frontiers | Research Topics

High-energy astrophysics research enabled by the probe-class mission concept HEX-P

Edited by
Gabriele Ponti, Murray Brightman, Esra Bulbul and Renee Ludlam

Coordinated by
Daniel Stern and Javier A. García

Published in
Frontiers in Astronomy and Space Sciences

FRONTIERS EBOOK COPYRIGHT STATEMENT

The copyright in the text of individual articles in this ebook is the property of their respective authors or their respective institutions or funders. The copyright in graphics and images within each article may be subject to copyright of other parties. In both cases this is subject to a license granted to Frontiers.

The compilation of articles constituting this ebook is the property of Frontiers.

Each article within this ebook, and the ebook itself, are published under the most recent version of the Creative Commons CC-BY licence. The version current at the date of publication of this ebook is CC-BY 4.0. If the CC-BY licence is updated, the licence granted by Frontiers is automatically updated to the new version.

When exercising any right under the CC-BY licence, Frontiers must be attributed as the original publisher of the article or ebook, as applicable.

Authors have the responsibility of ensuring that any graphics or other materials which are the property of others may be included in the CC-BY licence, but this should be checked before relying on the CC-BY licence to reproduce those materials. Any copyright notices relating to those materials must be complied with.

Copyright and source acknowledgement notices may not be removed and must be displayed in any copy, derivative work or partial copy which includes the elements in question.

All copyright, and all rights therein, are protected by national and international copyright laws. The above represents a summary only. For further information please read Frontiers' Conditions for Website Use and Copyright Statement, and the applicable CC-BY licence.

ISSN 1664-8714
ISBN 978-2-8325-6408-0
DOI 10.3389/978-2-8325-6408-0

About Frontiers

Frontiers is more than just an open access publisher of scholarly articles: it is a pioneering approach to the world of academia, radically improving the way scholarly research is managed. The grand vision of Frontiers is a world where all people have an equal opportunity to seek, share and generate knowledge. Frontiers provides immediate and permanent online open access to all its publications, but this alone is not enough to realize our grand goals.

Frontiers journal series

The Frontiers journal series is a multi-tier and interdisciplinary set of open-access, online journals, promising a paradigm shift from the current review, selection and dissemination processes in academic publishing. All Frontiers journals are driven by researchers for researchers; therefore, they constitute a service to the scholarly community. At the same time, the *Frontiers journal series* operates on a revolutionary invention, the tiered publishing system, initially addressing specific communities of scholars, and gradually climbing up to broader public understanding, thus serving the interests of the lay society, too.

Dedication to quality

Each Frontiers article is a landmark of the highest quality, thanks to genuinely collaborative interactions between authors and review editors, who include some of the world's best academicians. Research must be certified by peers before entering a stream of knowledge that may eventually reach the public - and shape society; therefore, Frontiers only applies the most rigorous and unbiased reviews. Frontiers revolutionizes research publishing by freely delivering the most outstanding research, evaluated with no bias from both the academic and social point of view. By applying the most advanced information technologies, Frontiers is catapulting scholarly publishing into a new generation.

What are Frontiers Research Topics?

Frontiers Research Topics are very popular trademarks of the *Frontiers journals series*: they are collections of at least ten articles, all centered on a particular subject. With their unique mix of varied contributions from Original Research to Review Articles, Frontiers Research Topics unify the most influential researchers, the latest key findings and historical advances in a hot research area.

Find out more on how to host your own Frontiers Research Topic or contribute to one as an author by contacting the Frontiers editorial office: frontiersin.org/about/contact

High-energy astrophysics research enabled by the probe-class mission concept HEX-P

Topic editors
Gabriele Ponti — Brera Astronomical Observatory, Italy
Murray Brightman — California Institute of Technology, United States
Esra Bulbul — Max Planck Institute for Extraterrestrial Physics, Germany
Renee Ludlam — Wayne State University, United States

Topic coordinators
Daniel Stern — NASA Jet Propulsion Laboratory (JPL), United States
Javier A. García — Goddard Space Flight Center, National Aeronautics and Space Administration, United States

Citation
Ponti, G., Brightman, M., Bulbul, E., Ludlam, R., Stern, D., García, J. A., eds. (2025). *High-energy astrophysics research enabled by the probe-class mission concept HEX-P*. Lausanne: Frontiers Media SA. doi: 10.3389/978-2-8325-6408-0

This Research Topic is organized by the researchers of the HEX-P mission. Authors and Guest Editors belong to the same consortium. Furthermore, Dr. Daniel Stern and Dr. Javier Garcia are the Principal Investigator and the Project Scientist of the mission respectively. All manuscripts will be peer-reviewed by researchers external to the collaboration.

Table of contents

07 Editorial: High-energy astrophysics research enabled by the probe-class mission concept HEX-P
Daniel Stern, Kristin Madsen and Javier A. García

10 The high energy X-ray probe: resolved X-ray populations in extragalactic environments
Bret D. Lehmer, Kristen Garofali, Breanna A. Binder, Francesca Fornasini, Neven Vulic, Andreas Zezas, Ann Hornschemeier, Margaret Lazzarini, Hannah Moon, Toni Venters, Daniel Wik, Mihoko Yukita, Matteo Bachetti, Javier A. García, Brian Grefenstette, Kristin Madsen, Kaya Mori and Daniel Stern

28 The high energy X-ray probe (*HEX-P*): studying extreme accretion with ultraluminous X-ray sources
Matteo Bachetti, Matthew J. Middleton, Ciro Pinto, Andrés Gúrpide, Dominic J. Walton, Murray Brightman, Bret Lehmer, Timothy P. Roberts, Georgios Vasilopoulos, Jason Alford, Roberta Amato, Elena Ambrosi, Lixin Dai, Hannah P. Earnshaw, Hamza El Byad, Javier A. García, Gian Luca Israel, Amruta Jaodand, Kristin Madsen, Chandreyee Maitra, Shifra Mandel, Kaya Mori, Fabio Pintore, Ken Ohsuga, Maura Pilia, Daniel Stern, George Younes and Anna Wolter

45 The high energy X-ray probe (HEX-P): a new window into neutron star accretion
R. M. Ludlam, C. Malacaria, E. Sokolova-Lapa, F. Fuerst, P. Pradhan, A. W. Shaw, K. Pottschmidt, S. Pike, G. Vasilopoulos, J. Wilms, J. A. García, K. Madsen, D. Stern, C. Maitra, M. Del Santo, D. J. Walton, M. C. Brumback and J. van den Eijnden

67 The high energy X-ray probe (HEX-P): Galactic PeVatrons, star clusters, superbubbles, microquasar jets, and gamma-ray binaries
Kaya Mori, Stephen Reynolds, Hongjun An, Aya Bamba, Roman Krivonos, Naomi Tsuji, Moaz Abdelmaguid, Jason Alford, Priyadarshini Bangale, Silvia Celli, Rebecca Diesing, Jordan Eagle, Chris L. Fryer, Stefano Gabici, Joseph Gelfand, Brian Grefenstette, Javier Garcia, Chanho Kim, Sajan Kumar, Ekaterina Kuznetsova, Brydyn Mac Intyre, Kristin Madsen, Silvia Manconi, Yugo Motogami, Hayato Ohsumi, Barbara Olmi, Jaegeun Park, Gabriele Ponti, Toshiki Sato, Ruo-Yu Shang, Daniel Stern, Yukikatsu Terada, Jooyun Woo, George Younes and Andreas Zoglauer

87 The High Energy X-ray Probe (HEX-P): supernova remnants, pulsar wind nebulae, and nuclear astrophysics
Stephen Reynolds, Hongjun An, Moaz Abdelmaguid, Jason Alford, Chris Fryer, Kaya Mori, Melania Nynka, Jaegeun Park, Yukikatsu Terada, Jooyun Woo, Aya Bamba, Priyadarshini Bangale, Rebecca Diesing, Jordan Eagle, Stefano Gabici, Joseph Gelfand, Brian Grefenstette, Javier Garcia, Chanho Kim, Sajan Kumar, Brydyn Mac Intyre, Kristin Madsen, Silvia Manconi, Yugo Motogami, Hayato Ohsumi, Barbara Olmi, Toshiki Sato, Ruo-Yu Shang, Daniel Stern, Naomi Tsuji, George Younes and Andreas Zoglauer

108 The high energy X-ray probe (HEX-P): probing the physics of the X-ray corona in active galactic nuclei
Elias Kammoun, Anne M. Lohfink, Megan Masterson, Dan R. Wilkins, Xiurui Zhao, Mislav Balokovic, Peter G. Boorman, Riley Connors, Paolo Coppi, Andrew Fabian, Javier A. García, Kristin K. Madsen, Nicole Rodriguez Cavero, Navin Sridhar, Daniel Stern, John Tomsick, Thomas Wevers, Dominic J. Walton, Stefano Bianchi, Johannes Buchner, Francesca M. Civano, Giorgio Lanzuisi, Labani Mallick, Giorgio Matt, Andrea Merloni, Emanuele Nardini, Joanna M. Piotrowska, Claudio Ricci, Ka-Wah Wong and Abderahmen Zoghbi

133 The High Energy X-ray Probe (HEX-P): probing accretion onto stellar mass black holes
Riley M. T. Connors, John A. Tomsick, Paul Draghis, Benjamin Coughenour, Aarran W. Shaw, Javier A. García, Dominic Walton, Kristin Madsen, Daniel Stern, Nicole Cavero Rodriguez, Thomas Dauser, Melania Del Santo, Jiachen Jiang, Henric Krawczynski, Honghui Liu, Joseph Neilsen, Michael Nowak, Sean Pike, Andrea Santangelo, Navin Sridhar, Andrew West and Jörn Wilms

150 The high energy X-ray probe (HEX-P): Resolving the nature of Sgr A* flares, compact object binaries and diffuse X-ray emission in the Galactic center and beyond
Kaya Mori, Gabriele Ponti, Matteo Bachetti, Arash Bodaghee, Jonathan Grindlay, Jaesub Hong, Roman Krivonos, Ekaterina Kuznetsova, Shifra Mandel, Antonio Rodriguez, Giovanni Stel, Shuo Zhang, Tong Bao, Franz Bauer, Maïca Clavel, Benjamin Coughenour, Javier A. García, Julian Gerber, Brian Grefenstette, Amruta Jaodand, Bret Lehmer, Kristin Madsen, Melania Nynka, Peter Predehl, Ciro Salcedo, Daniel Stern and John Tomsick

174 The high energy X-ray probe (HEX-P): magnetars and other isolated neutron stars
J. A. J. Alford, G. A. Younes, Z. Wadiasingh, M. Abdelmaguid, H. An, M. Bachetti, M. G. Baring, A. Beloborodov, A. Y. Chen, T. Enoto, J. A. García, J. D. Gelfand, E. V. Gotthelf, A. K. Harding, C-P. Hu, A. D. Jaodand, V. Kaspi, C. Kim, C. Kouveliotou, L. Kuiper, K. Mori, M. Nynka, J. Park, D. Stern, J. Valverde and D. J. Walton

188 The high energy X-ray probe (*HEX-P*): sensitive broadband X-ray observations of transient phenomena in the 2030s
Murray Brightman, Raffaella Margutti, Ava Polzin, Amruta Jaodand, Kenta Hotokezaka, Jason A. J. Alford, Gregg Hallinan, Elias Kammoun, Kunal Mooley, Megan Masterson, Lea Marcotulli, Arne Rau, Thomas Wevers, George A. Younes, Daniel Stern, Javier A. García and Kristin Madsen

200 The high energy X-ray probe (HEX-P): instrument and mission profile
Kristin K. Madsen, Javier A. García, Daniel Stern, Rashied Amini, Stefano Basso, Diogo Coutinho, Brian W. Grefenstette, Steven Kenyon, Alberto Moretti, Patrick Morrissey, Kirpal Nandra, Giovanni Pareschi, Peter Predehl, Arne Rau, Daniele Spiga, Jörn Wilms and William W. Zhang

210 The high energy X-ray probe (HEX-P): bringing the cosmic X-ray background into focus
F. Civano, X. Zhao, P. G. Boorman, S. Marchesi, T. Ananna, S. Creech, C.-T. Chen, R. C. Hickox, D. Stern, K. Madsen, J. A. García, R. Silver, J. Aird, D. M. Alexander, M. Baloković, W. N. Brandt, J. Buchner, P. Gandhi, E. Kammoun, S. LaMassa, G. Lanzuisi, A. Merloni, A. Moretti, K. Nandra, E. Nardini, A. Pizzetti, S. Puccetti, R. W. Pfeifle, C. Ricci, D. Spiga and N. Torres-Albà, on behalf of the HEX-P Collaboration

229 The high energy X-ray probe (HEX-P): constraining supermassive black hole growth with population spin measurements
J. M. Piotrowska, J. A. García, D. J. Walton, R. S. Beckmann, D. Stern, D. R. Ballantyne, D. R. Wilkins, S. Bianchi, P. G. Boorman, J. Buchner, C.-T. Chen, P. Coppi, T. Dauser, A. C. Fabian, E. Kammoun, K. Madsen, L. Mallick, G. Matt, G. Matzeu, E. Nardini, A. Pizzetti, S. Puccetti, C. Ricci, F. Tombesi, N. Torres-Albà and K.-W. Wong, on behalf of the HEX-P Collaboration

252 The High-Energy X-ray Probe (HEX-P): the circum-nuclear environment of growing supermassive black holes
P. G. Boorman, N. Torres-Albà, A. Annuar, S. Marchesi, R. W. Pfeifle, D. Stern, F. Civano, M. Baloković, J. Buchner, C. Ricci, D. M. Alexander, W. N. Brandt, M. Brightman, C. T. Chen, S. Creech, P. Gandhi, J. A. García, F. Harrison, R. Hickox, E. Kammoun, S. LaMassa, G. Lanzuisi, L. Marcotulli, K. Madsen, G. Matt, G. Matzeu, E. Nardini, J. M. Piotrowska, A. Pizzetti, S. Puccetti, D. Sicilian, R. Silver, D. J. Walton, D. R. Wilkins, X. Zhao and The HEX-P Collaboration

281 The high energy X-ray probe (HEX-P): the future of hard X-ray dual AGN science
Ryan W. Pfeifle, Peter G. Boorman, Kimberly A. Weaver, Johannes Buchner, Francesca Civano, Kristin Madsen, Daniel Stern, Núria Torres-Albà, Emanuele Nardini, Claudio Ricci, Stefano Marchesi, D. R. Ballantyne, Dominic Sicilian, Chien-Ting Chen, Elias Kammoun, Ryan C. Hickox, Javier A. García and Labani Mallick

297 The high energy X-ray probe (HEX-P): the most powerful jets through the lens of a superb X-ray eye
Lea Marcotulli, Marco Ajello, Markus Böttcher, Paolo Coppi, Luigi Costamante, Laura Di Gesu, Manel Errando, Javier A. García, Andrea Gokus, Ioannis Liodakis, Greg Madejski, Kristin Madsen, Alberto Moretti, Riccardo Middei, Felicia McBride, Maria Petropoulou, Bindu Rani, Tullia Sbarrato, Daniel Stern, Georgios Vasilopoulos, Michael Zacharias, Haocheng Zhang and the HEX-P Collaboration

328 The high energy X-ray probe (HEX-P): science overview
Javier A. García, Daniel Stern, Kristin Madsen, Miles Smith, Brian Grefenstette, Marco Ajello, Jason Alford, Adlyka Annuar, Matteo Bachetti, Mislav Baloković, Ricarda S. Beckmann, Stefano Bianchi, Daniela Biccari, Peter Boorman, Murray Brightman, Johannes Buchner, Esra Bulbul, Chien-Ting Chen, Francesca Civano, Joel Coley, Riley M. T. Connors, Melania Del Santo, Laura Di Gesu, Paul A. Draghis, P. Chris Fragile, Andrés Gúrpide, Manuele Gangi, Suvi Gezari, Fiona Harrison, Elias Kammoun, Giorgio Lanzuisi, Bret Lehmer, Anne Lohfink, Renee Ludlam, Stefano Marchesi, Lea Marcotulli, Raffaella Margutti, Megan Masterson, Andrea Merloni, Matthew Middleton, Kaya Mori, Alberto Moretti, Kirpal Nandra, Kerstin Perez, Ryan W. Pfeifle, Ciro Pinto, Joanna Piotrowska, Gabriele Ponti, Katja Pottschmidt, Peter Predehl, Simonetta Puccetti, Arne Rau, Stephen Reynolds, Andrea Santangelo, Daniele Spiga, John A. Tomsick, Núria Torres-Albà, Dominic J. Walton, Daniel Wilkins, Joern Wilms, Will Zhang and Xiurui Zhao, on behalf of the HEX-P Collaboration

frontiers | Frontiers in Astronomy and Space Sciences

TYPE Editorial
PUBLISHED 20 May 2025
DOI 10.3389/fspas.2025.1549342

Check for updates

OPEN ACCESS

EDITED AND REVIEWED BY
Julio Navarro,
University of Victoria, Canada

*CORRESPONDENCE
Daniel Stern,
daniel.k.stern@jpl.nasa.gov

RECEIVED 20 December 2024
ACCEPTED 30 April 2025
PUBLISHED 20 May 2025

CITATION
Stern D, Madsen K and García JA (2025) Editorial: High-energy astrophysics research enabled by the probe-class mission concept HEX-P.
Front. Astron. Space Sci. 12:1549342.
doi: 10.3389/fspas.2025.1549342

COPYRIGHT
© 2025 Stern, Madsen and García. This is an open-access article distributed under the terms of the Creative Commons Attribution License (CC BY). The use, distribution or reproduction in other forums is permitted, provided the original author(s) and the copyright owner(s) are credited and that the original publication in this journal is cited, in accordance with accepted academic practice. No use, distribution or reproduction is permitted which does not comply with these terms.

Editorial: High-energy astrophysics research enabled by the probe-class mission concept HEX-P

Daniel Stern[1]*, Kristin Madsen[2] and Javier A. García[2]

[1]Jet Propulsion Laboratory, California Institute of Technology, Pasadena, CA, United States, [2]X-ray Astrophysics Laboratory, NASA Goddard Space Flight Center, Greenbelt, MD, United States

KEYWORDS

X-ray, HEX-P, mission science, spectroscopy, black holes

Editorial on the Research Topic
High-energy astrophysics research enabled by the probe-class mission concept HEX-P

Introduction

The High Energy X-ray Probe (HEX-P) is a sensitive, broad-band (0.2–80 keV) X-ray mission concept submitted in response to NASA's Astrophysics Probe Explorer (APEX) Announcement of Opportunity in November 2023 (Figure 1). This was the first time NASA competed an Astrophysics mission of this scale, constrained to a cost cap of ≤$1.0 B, not including launch, managing the Guest Observer (GO) program, or contributions. Notably, this was also the first time NASA competed a GO facility. This Research Topic includes 17 papers that describe the HEX-P mission and its science. Madsen et al. provides an overview of the HEX-P instrument and mission profile and García et al. provides an overview of the HEX-P science. In brief, HEX-P entails two coaligned telescopes: the Low Energy Telescope (LET) which covers 0.2–20 keV with an angular resolution of $<5''$ (half-power diameter, or HPD), and the High Energy Telescope (HET) which covers 3–80 keV with an angular resolution of $<20''$ (at 20 keV, HPD).

APEX missions are intended primarily as community observatories. No data exclusive-use periods are allowed and at least 70% of the baseline 5-year mission must be allocated through competed GO opportunities. The remaining time is directed by the science team. For HEX-P, the latter science centers on three primary topics: supermassive black holes (SMBHs), resolved high-energy galactic populations, and time domain and multi-messenger (TDAMM) astrophysics. The PI-led science motivated the instrument and mission design, though providing a powerful, flexible GO capability to serve the broad astrophysics community was always at the core of the HEX-P design. Indeed, this was identified as a Major Strength by the NASA review which highlighted the ability of HEX-P to provide "*…a substantial program of GO observations that has a strong potential to produce significant scientific advances.*"

The independent peer review evaluated HEX-P as selectable, noting the mission's "*…significant science merit and science implementation strength, coupled with a modest level*

FIGURE 1
Cover of the submitted HEX-P proposal. [Image credit: JPL-Caltech/Shan Jiang (The Jacky Winter Group).].

of technical, management, and cost risk." However, HEX-P ultimately was not selected to proceed to a Phase A study. This is clearly not the end of broadband X-ray astrophysics, and the HEX-P team hopes that this Research Topic will serve as an inspiration for future projects that take on the mantel of addressing this science that is only accessible with an X-ray mission covering a wide bandpass.

Below, we briefly outline key science enabled by HEX-P, as described in greater detail in this Research Topic. These contributions were led co-investigators and collaborators on the HEX-P team, as well as the broader high-energy community.

Supermassive black hole growth and galaxy evolution

HEX-P will be a powerful facility for investigating how SMBHs grow and drive galaxy evolution, highlighted as a key question by Astro2020 Decadal Survey. Models and observations point to most black hole growth occurring in obscured sources, hidden at optical and low-energy X-rays by thick columns of absorbing material. High-energy (>10 keV) photons can penetrate this material, enabling HEX-P to study the full population of sources responsible for SMBH growth. Civano et al. simulates deep, pencil-beam surveys with HEX-P and shows how they will finally directly identify the sources responsible for the peak of the cosmic X-ray radiation, discovered more than 50 years ago. Boorman et al. discusses how HEX-P studies of nearby, heavily obscured accreting SMBHs will reveal the inner structure around the central engine, while Pfeifle et al. shows how HEX-P will be an unprecedented facility for the study of SMBH mergers, which preferentially occur in obscured systems and are therefore best studied by broadband X-ray facilities, sensitive above 10 keV.

Broadband X-ray spectroscopy also accesses spectral features that only appear above 10 keV. Kammoun et al. discusses how HEX-P will reveal the X-ray corona, the hot, shining plasma that exists just beyond the event horizon and produces most of the X-rays in the Universe. Measuring the temperature of the corona requires high-energy observations and is a key diagnostic of the poorly understood coronal physics. Observing samples of luminous and variable SMBHs, HEX-P will test theories of the corona and shed light on this foundational enigma of X-ray astrophysics. Broadband X-ray observations also constrain the spin of black holes by measuring relativistic broadening of the Fe K (~6.5 keV) and Compton hump (~30 keV) features. Piotrowska et al. show how a dedicated survey to measure SMBH spins of several dozen local, bright active galaxies over a range of black hole mass will reveal whether SMBHs grow primarily from accretion or mergers.

Resolved binary populations

With unrivaled angular resolution above 10 keV, HEX-P will investigate how binary systems live and die, highlighted as a key question by Astro2020. Mori et al. discusses the range of science enabled by HEX-P surveys of the Galactic Center and Galactic bulge, ranging from measuring the masses of white dwarfs to monitoring flares from Sgr A*, the four million solar mass SMBH at the center of the Milky Way. Lehmer et al. focuses on resolved binary populations in nearby galaxies. Crucially, while soft (<10 keV) X-ray observatories such as Chandra regularly identify off-nuclear sources in other galaxies, without access to higher energy X-rays, it remains unclear if these sources are stellar mass black holes or neutron stars. In addition, X-ray binaries are one of the best laboratories to study the accretion process and probe strong gravity. Connors et al. describes how HEX-P will study evolving accretion flows and coronae of binary compact object systems in the Milky Way and Local Group.

Time-domain and multi-messenger astrophysics

HEX-P will investigate what powers the diversity of extreme time domain and multi-messenger events, also identified as a Priority Area by Astro2020. Mori et al. describes how HEX-P will reveal the nature of the most extreme accelerators in our Galaxy by measuring high-energy (>40 keV) X-ray emission from Galactic gamma-ray sources. Brightman et al. surveys how HEX-P will explore the dynamic universe across the X-ray band, studying phenomena ranging from tidal disruption events to stellar explosions to electromagnetic radiation from gravitational wave merger events. Finally, Marcotulli et al. discusses how HEX-P will inform our understanding of the powerful, relativistic jets that are often associated with accreting SMBHs and are strong emitters from X-ray to gamma-ray energies. Notably, many of these phenomena, such as jets, mergers, and tidal disruptions, are also important multi-messenger events that produce cosmic rays, neutrinos, and/or gravitational waves.

HEX-P capabilities

The science described above requires sensitive broadband X-ray observations covering the full X-ray range and motivated the design

of the HEX-P mission. Madsen et al. details the HEX-P instrument and mission design. In brief, operating at L2 with a 20-m focal length and designed to achieve a low background, HEX-P reaches fainter fluxes in a fixed clock time than all current X-ray satellites. The LET reaches at least 2–10 times fainter fluxes below 10 keV in 1 M than the current flagship soft X-ray facilities, XMM-Newton and Chandra. The HET reaches ≥7 times fainter fluxes above 10 keV in 1 M than NuSTAR, the most sensitive hard X-ray telescope. The fields of view of the HEX-P instruments are $11.3' \times 11.3'$ for the LET and $13.7' \times 13.7'$ for the HET. HEX-P achieves an average response time of 12.3 h to target-of-opportunity observations, with a guaranteed response time of <24 hr.

Additional science

With the ability to obtain imaging, spectroscopic, and timing data for both bright and faint targets across the entire X-ray band, HEX-P will enable extensive science to excite a large, active GO community. Contributions to this Research Topic delve into just some of this potential, including HEX-P's contributions to studying neutron stars (Ludlam et al.), magnetars (Alford et al.), ultraluminous X-ray sources (Bachetti et al.), supernova remnants and pulsar wind nebulae (Reynolds et al.).

In summary, HEX-P is a powerful mission that will provide the most sensitive X-ray observations at both low and high energies. The program defined by the science team provides a legacy that directly addresses multiple key questions identified by the Astro2020 Decadal Survey, while the broad capabilities of the mission enable a diverse suite of science, from studying how stellar activity affects planet formation to finally understanding the physics and demographics of the accreting black holes that are responsible for most of the X-rays generated across cosmic time.

Author contributions

DS: Writing – original draft, Writing – review and editing. KM: Writing – original draft, Writing – review and editing. JG: Writing – original draft, Writing – review and editing.

Funding

The author(s) declare that no financial support was received for the research and/or publication of this article.

Conflict of interest

The authors declare that the research was conducted in the absence of any commercial or financial relationships that could be construed as a potential conflict of interest.

Generative AI statement

The authors declare that no Generative AI was used in the creation of this manuscript.

Publisher's note

All claims expressed in this article are solely those of the authors and do not necessarily represent those of their affiliated organizations, or those of the publisher, the editors and the reviewers. Any product that may be evaluated in this article, or claim that may be made by its manufacturer, is not guaranteed or endorsed by the publisher.

frontiers | Frontiers in Astronomy and Space Sciences

TYPE Original Research
PUBLISHED 23 November 2023
DOI 10.3389/fspas.2023.1293918

Check for updates

OPEN ACCESS

EDITED BY
Gabriele Ponti,
Brera Astronomical Observatory, Italy

REVIEWED BY
Anna Wolter,
INAF–Osservatorio Astronomico di Brera, Italy
Reinaldo Roberto Rosa,
National Institute of Space Research (INPE), Brazil

*CORRESPONDENCE
Bret D. Lehmer,
lehmer@uark.edu

RECEIVED 13 September 2023
ACCEPTED 30 October 2023
PUBLISHED 23 November 2023

CITATION
Lehmer BD, Garofali K, Binder BA, Fornasini F, Vulic N, Zezas A, Hornschemeier A, Lazzarini M, Moon H, Venters T, Wik D, Yukita M, Bachetti M, García JA, Grefenstette B, Madsen K, Mori K and Stern D (2023), The high energy X-ray probe: resolved X-ray populations in extragalactic environments.
Front. Astron. Space Sci. 10:1293918.
doi: 10.3389/fspas.2023.1293918

COPYRIGHT
© 2023 Lehmer, Garofali, Binder, Fornasini, Vulic, Zezas, Hornschemeier, Lazzarini, Moon, Venters, Wik, Yukita, Bachetti, García, Grefenstette, Madsen, Mori and Stern. This is an open-access article distributed under the terms of the Creative Commons Attribution License (CC BY). The use, distribution or reproduction in other forums is permitted, provided the original author(s) and the copyright owner(s) are credited and that the original publication in this journal is cited, in accordance with accepted academic practice. No use, distribution or reproduction is permitted which does not comply with these terms.

The high energy X-ray probe: resolved X-ray populations in extragalactic environments

Bret D. Lehmer[1,2]*, Kristen Garofali[3,4], Breanna A. Binder[5], Francesca Fornasini[6], Neven Vulic[7], Andreas Zezas[8,9,10], Ann Hornschemeier[3], Margaret Lazzarini[11], Hannah Moon[12], Toni Venters[3], Daniel Wik[12], Mihoko Yukita[4], Matteo Bachetti[13], Javier A. García[3,14], Brian Grefenstette[14], Kristin Madsen[3], Kaya Mori[15] and Daniel Stern[16]

[1]Department of Physics, University of Arkansas, Fayetteville, AR, United States, [2]Arkansas Center for Space and Planetary Sciences, University of Arkansas, Fayetteville, AR, United States, [3]X-ray Astrophysics Laboratory, NASA Goddard Space Flight Center, Greenbelt, MD, United States, [4]The Johns Hopkins University, Homewood Campus, Baltimore, MD, United States, [5]Department of Physics and Astronomy, California State Polytechnic University, Pomona, CA, United States, [6]Department of Physics and Astronomy, Stonehill College, Easton, MA, United States, [7]Eureka Scientific, Inc., Oakland, CA, United States, [8]Physics Department, Institute of Theoretical and Computational Physics, University of Crete, Heraklion, Crete, Greece, [9]Harvard-Smithsonian Center for Astrophysics, Cambridge, MA, United States, [10]Institute of Astrophysics, Foundation for Research and Technology-Hellas, Heraklion, Greece, [11]Department of Physics and Astronomy, California State University, Los Angeles, Los Angeles, CA, United States, [12]Department of Physics and Astronomy, The University of Utah, Salt Lake City, UT, United States, [13]INAF-Osservatorio Astronomico di Cagliari, Cagliari, Italy, [14]Cahill Center for Astronomy and Astrophysics, California Institute of Technology, Pasadena, CA, United States, [15]Columbia Astrophysics Laboratory, Columbia University, New York, NY, United States, [16]Jet Propulsion Laboratory, California Institute of Technology, Pasadena, CA, United States

We construct simulated galaxy data sets based on the *High Energy X-ray Probe* (HEX-P) mission concept to demonstrate the significant advances in galaxy science that will be yielded by the HEX-P observatory. The combination of high spatial resolution imaging (<20 arcsec FWHM), broad spectral coverage (0.2–80 keV), and sensitivity superior to current facilities (e.g., XMM-Newton and NuSTAR) will enable HEX-P to detect hard (4–25 keV) X-ray emission from resolved point-source populations within ~800 galaxies and integrated emission from ~6,000 galaxies out to 100 Mpc. These galaxies cover wide ranges of galaxy types (e.g., normal, starburst, and passive galaxies) and properties (e.g., metallicities and star-formation histories). In such galaxies, HEX-P will: 1) provide unique information about X-ray binary populations, including accretor demographics (black hole and neutron stars), distributions of accretion states and state transition cadences; 2) place order-of-magnitude more stringent constraints on inverse Compton emission associated with particle acceleration in starburst environments; and 3) put into clear context the contributions from X-ray emitting populations to both ionizing the surrounding interstellar medium in low-metallicity galaxies and heating the intergalactic medium in the $z > 8$ Universe.

KEYWORDS

early-type galaxies (429), star formation (1569), starburst galaxies (1570), X-ray binary stars (1811), X-ray astronomy (1810), compact objects (288)

1 Introduction

The quest to understand galaxy formation and evolution relies on a broad diversity of investigative tools that provide detailed insight into the variety of physical phenomena and source populations present within galaxies. For example, galaxy star-formation histories are effectively probed through color-magnitude diagram (CMD) isochrone analyses (e.g., Choi et al., 2016) and panchromatic spectral energy distribution fitting (e.g., Conroy, 2013; Carnall et al., 2019; Leja et al., 2019); galaxy interstellar medium (ISM) conditions of ionization and chemical abundances are constrained through UV-to-IR spectral line modeling (Kewley et al., 2019); and the cosmic history of star-formation and chemical enrichment among galaxy populations are probed by wide-and-deep multiwavelength extragalactic surveys (Blanton and Moustakas, 2009; Madau and Dickinson, 2014).

In the context of galaxy evolution, X-ray emission from normal galaxies, not dominated by active galactic nuclei (AGN), traces the most energetic of processes, providing critical information for a variety of phenomena. Supernovae and their remnants probe the detailed physics of exploding stars; diffuse emission from hot gas traces the impact of recent star formation on galactic and intergalactic scales and the depths of gravitational potential wells; and X-ray binaries (XRBs) provide unique constraints on compact object, binary, and massive-star population demographics, as well as the physics of accretion onto compact objects and its environmental impact.

For the last >20 years, Chandra and XMM-Newton, in conjunction with several multiwavelength facilities, have enabled many investigations of the roles of X-ray emitting phenomena in galaxy populations that span a broad range of properties (e.g., from starburst to passive ellipticals; see Gilfanov et al., 2022; Nardini et al., 2022, for recent reviews).

Due to its sensitivity above 10 keV, the advent of NuSTAR provided unique insight into the nature of luminous XRBs detected in galaxies out to ≈10 Mpc that had not been possible with previous X-ray observatories. In particular, relatively unobscured spectral signatures that distinguish accreting compact object types, black holes (BH) versus neutron stars (NS), in XRBs, and the state of accretion are most notable in the $E \approx 4$–30 keV spectral range (e.g., Remillard and McClintock, 2006; Done et al., 2007). Accretion disk state transitions in BHs, boundary layer emission from accreting NSs, and accretion columns in pulsars all have distinguishable spectral shapes in this energy range and can be efficiently classified via intensity-color and color-color diagrams.

Some of the highlights of NuSTAR-based studies of galaxies include: 1) direct measurement of the ratio of BH to NS XRBs in star-forming galaxies, indicating a rise in the BH fraction above a luminosity corresponding to the Eddington limit for 1.4 $M_{\odot}$ (Vulic et al., 2018); 2) identification of enhanced fractions of accreting pulsars and BH high-mass XRBs (HMXBs) in star-forming environments (e.g., the SMC, M33, NGC 253, and M83; Wik et al., 2014; Yukita et al., 2016; Lazzarini et al., 2019; 2023; Yang et al., 2022) versus weakly-magnetized Z-type/atoll NS low-mass XRBs (LMXBs) in passive environments (e.g., M31 and M81; Maccarone et al., 2016; Vulic et al., 2018); 3) first constraints on the level of inverse Compton emission in the starburst environment of NGC 253 (Wik et al., 2014); and 4) quantification of the growing dominance of ultraluminous X-ray sources (ULXs) in star-forming galaxy X-ray spectra with declining metallicity [e.g., measured by the characteristic $E > 7$ keV spectral turnover in ULXs (Lehmer et al., 2015; Garofali et al., 2020)]. These studies have provided critical insights into galaxy formation and evolution: XRB population classifications and spectral constraints inform population synthesis models and the role of X-ray radiation and mechanical feedback on the interstellar and intergalactic mediums (e.g., Simmonds et al., 2021; The HERA Collaboration et al., 2022; HERA Collaboration et al., 2023; Misra et al., 2023).

While the advances from NuSTAR, as described above, have demonstrated the power of using hard X-rays to uniquely constrain properties of XRBs, such studies are limited to only low signal-to-noise detections of the brightest X-ray sources (typically $\gtrsim$ few $\times 10^{38}$ erg s^{-1}) in galaxies in the nearby Universe. To make progress, we require the next-generation hard X-ray observatory to be capable of addressing:

1. What are the distributions of accretion states and compact object types (BHs, NSs, pulsars) across the full diversity of galactic environments in the Universe (i.e., spanning broad ranges of morphological types, star-formation histories, and metallicity)? How does the diversity of ULX spectral types vary across these properties? What does this tell us about the formation of the most massive stellar remnants in the Universe, the most extreme regimes of accretion, and the evolutionary pathways of LIGO/VIRGO gravitational wave sources?
2. What are the duty cycles of accretion state transitions in BH and NS XRB populations outside the Milky Way (MW)? How do these variability constraints inform the physics of accretion disks and corona across compact object and donor-star types?
3. What is the role of diffuse inverse Compton emission in starburst environments and do leptonic or hadronic particle accelerations drive these processes? What does this imply about mechanical feedback from supernovae?
4. How does star-formation history and metallicity impact the intrinsic and emergent broadband X-ray spectra of the source populations? How do X-ray emitting sources contribute to ionizing radiation in ISMs across galaxy types and the heating of the intergalactic medium in the $z \gtrsim 8$ Universe?

To uncover the scientific potential of the *High Energy X-ray Probe* (HEX-P; Madsen et al., 2018, Madsen et al., 2023) for addressing the above questions, we perform detailed simulations for a variety of galaxies. With our simulations, we demonstrate how HEX-P will revolutionize studies of X-ray emission from normal galaxies. Additional companion papers have been submitted providing additional details for how HEX-P will advance scientific insights from other X-ray emitting populations in galaxies, including, e.g., ULXs and AGN.

2 HEX-P mission design

The HEX-P probe-class mission concept offers sensitive broad-band coverage (0.2–80 keV) of the X-ray spectrum with exceptional spectral, timing and angular capabilities. It features two high-energy telescopes (HET) that focus hard X-rays, and soft X-ray coverage with a low-energy telescope (LET).

The LET consists of a segmented mirror assembly coated with Iron monocrystalline silicon that achieves a half power diameter (HPD) of 3.5″, and a low-energy DEPFET detector, of the same type as the Wide Field Imager (WFI Meidinger et al., 2020) onboard *Athena* (Nandra et al., 2013). It has 512× 512 pixels that cover a field of view (FOV) of $11.3' \times 11.3'$. It has an effective passband of 0.2–25 keV, and a full frame readout time of 2 ms, which can be operated in a 128 and 64 channel window mode for higher count-rates to mitigate pile-up and faster readout. Pile-up effects remain below an acceptable limit of ~1% for a flux up to ~100 mCrab (2–10 keV) in the smallest window configuration. Excising the core of the PSF, a common practice in X-ray astronomy, will allow for observations of brighter sources, with a typical loss of up to ~60% of the total photon counts.

The HET consists of two co-aligned telescopes and detector modules. The optics are made of Ni-electroformed full shell mirror substrates, leveraging the heritage of XMM-Newton (Jansen et al., 2001), and coated with Pt/C and W/Si multilayers for an effective passband of 2–80 keV. The high-energy detectors are of the same type as flown on NuSTAR (Harrison et al., 2013), and they consist of 16 CZT sensors per focal plane, tiled 4× 4, for a total of 128× 128 pixel spanning a FOV slightly larger than for the LET, of $13.4' \times 13.4'$. The HET utilizes the same optics technology as XMM-Newton and the PSF is energy dependent with an HPD of 10″ at 3 keV, ≈17″ at 20 keV, and increases at higher energies. For the purpose of simulations in this paper, an average HPD of 17″ was used across the entire bandpass.

For normal-galaxy studies, HEX-P will resolve XRB populations within galaxies out to $D \sim$ 30–50 Mpc and will constrain their broadband spectra to faint luminosity limits (typically $L < 10^{38}$ erg s^{-1}). For more distant galaxies, HEX-P will constrain the broadband X-ray spectra for thousands of galaxies out to ≈100–200 Mpc.

3 Galaxy sample and example science program

For the purpose of demonstrating how HEX-P will advance upon current constraints from existing X-ray observatories (e.g., NuSTAR) and could help address the key questions posed in Section 1, we perform HEX-P simulations of a sample of galaxies that span a diversity of properties (see Figure 1 and Table 1). Below, we describe the galaxy sample and the key scientific insights that can be afforded by studying these galaxies with HEX-P.

NGC 253: Due to its proximity ($D = 3.9$ Mpc; Karachentsev et al., 2004) and starburst nature (SFR/$M_\star \approx 10^{-10}$ yr^{-1}), NGC 253 represents an ideal target for investigating a variety of high-energy phenomena associated with star formation activity. For example, a few dozen XRBs have been observed across the span of the galactic disk, probing the formation of populations of compact objects and binaries (e.g., Pietsch et al., 2001). Diffuse thermal emission ($kT \approx 0.4$ keV) spans several arcminutes along the plane of the disk, with a hotter ~1 keV gas component observed in a collimated kpc-scale outflow emanating from the nuclear starburst (e.g., Strickland and Stevens, 2000; Strickland et al., 2002; Lopez et al., 2023). Finally, NGC 253 is one of only two starburst galaxies (the other being M82) that have been detected from hundreds of MeV to TeV energies, as a result of particle accelerations (e.g., Abramowski et al., 2012; H. E. S. S. Collaboration et al., 2018).

With ≈500 ks of cumulative NuSTAR exposure, only the most luminous X-ray binaries could be detected above 10 keV. These data indicated that ULX populations ($L > 10^{39}$ erg s^{-1}) commonly exhibit high-energy ($E \gtrsim 7$ keV) spectral turnovers associated with super-Eddington accretion (e.g., Pinto and Walton, 2023) and the majority of HMXBs with $L \gtrsim 3 \times 10^{38}$ erg s^{-1} (near the survey detection limit) have X-ray colors consistent with either hard-state/intermediate-state BH XRBs or *Z*-type NSs, albeit with large uncertainties (e.g., Wik et al., 2014). The data were further analyzed to place upper limits on the inverse Compton emission associated with starburst particle acceleration, in an attempt to distinguish between hadronic and leptonic particle dominance.

NuSTAR constraints on NGC 253 provided an enticing first demonstration of the scientific benefits afforded by focused hard X-ray imaging in a starburst environment not represented in the Local Group. However, performing meaningful tests of theoretical binary-population models and particle acceleration models requires hard X-ray detection and compact object/accretion-state characterization of all X-ray binaries in outburst, as well as the disentanglement of hard X-ray emission from point-sources and diffuse emission. HEX-P has been designed with these goals in mind, and the high spatial resolution and high-energy capabilities will provide the needed constraints.

The central bulge region of M31: M31 is the nearest large spiral galaxy outside of the Milky Way. At a distance of 776 kpc (e.g., Dalcanton et al., 2012), M31 is close enough to resolve and detect populations of individual X-ray sources at >10 keV with relatively short NuSTAR exposures (100 ks). The bulge region of M31 hosts a high concentration of stars and LMXBs associated with the older stellar population of the galaxy.

NuSTAR constraints indicate that the X-ray sources in the bulge region are dominated by hard-state BHs and atoll/Z-source NSs, with the brightest source above 10 keV being an accreting pulsar (Yukita et al., 2017). However, due to NuSTAR's relatively large PSF and the high density of sources, several bright sources in the nuclear region are undetected or have large photometric uncertainties due to source confusion. An observatory like HEX-P, which has both high spatial resolution and high-energy response, is needed to detect and classify the majority of the bright sources in the central bulge of M31 and monitor their accretion state transitions.

Maffei 1: Maffei 1 is one of the nearest ($D \approx$ 3–7 Mpc; e.g., Tikhonov and Galazutdinova, 2018) massive elliptical galaxies ($M_\star \sim 10^{11}\ M_\odot$), providing a unique target for studying a rich population of LMXBs in an old stellar environment in X-rays. LMXB populations in elliptical galaxies have been observed to have steeply declining numbers of sources between $L \approx 10^{37}$ erg s^{-1} and 10^{39} erg s^{-1}, with many of these bright sources crowded within small galactic footprints. This, combined with the fact that there are few very luminous LMXBs (i.e., most have $L < 10^{38}$ erg s^{-1}), has made it impossible to study such populations in hard X-rays with NuSTAR, which does not have the requisite angular resolution for resolving the populations.

A deep (177 ks) exposure with Chandra detected ≈150 X-ray sources (spanning $L \approx 10^{36}$–10^{38} erg s^{-1}) within a $10' \times 10'$ footprint centered on Maffei 1 (Ferrell et al. in-prep). NuSTAR imaging of the region reveals these sources as a few discrete concentrations of

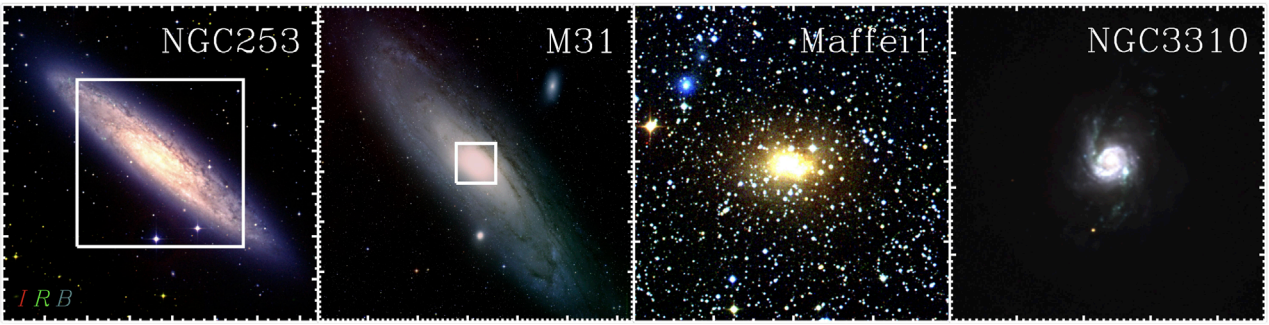

FIGURE 1
Optical images of the galaxy sample explored in this study. Digitized sky survey images in *BRI* (blue, green, red) are used for NGC 253, M31, and Maffei 1, with the exception of the *B*-band for NGC 253, which is from the Cerro Tololo Inter-american Observatory (CTIO). For NGC 3310, Sloan Digital Sky Survey (SDSS) *gri* bands are used. The white square regions shown for NGC 253 and M31, as well as the entire FOV shown for Maffei 1, represent the $13' \times 13'$ HEX-P HET FOV that we simulate. For NGC 3310, we show here the central $3.1' \times 3.1'$ region of the HET FOV, which we use throughout the remainder of this paper.

TABLE 1 Galaxy properties, Chandra observation log, and HEX-P simulation summary.

					Chandra Observations		HEX-P Simulation						
Galaxy	D^a	SFR^b	log$M_\star$ ^{b}	Z^b	t_{exp}	log(f_X^{min})	t_{exp}	HET			LET		log($L_{4\text{-}25keV}$)
Name	(Mpc)	($M_\odot$ yr^{-1})	($M_\odot$)	($Z_\odot$)	(ks)	(erg cm^{-2} s^{-1})	(ks)	N_B	N_M	N_H	N_S	N_M	(erg s^{-1})
(1)	(2)	(3)	(4)	(5)	(6)	(7)	(8)	(9)	(10)	(11)	(12)	(13)	(14)
NGC 253	3.94	5.6	10.8	1.0	156	−16.3	500	81	60	50	67	61	36.8
M31 bulge	0.776	<0.3	10.5	1.6	676	−16.3	50	81	64	49	73	67	36.0
Maffei 1	3.4	~0.0001	10.9	1.2	55	−15.6	200	64	45	25	51	43	37.0
NGC 3310	21.3	5.3	10.3	0.3	93	−15.9	250	11	11	7	11	11	39.0

Note—Col. (1): galaxy name. Col. (2)–(5): distance, SFR, logarithm of the stellar mass, and metallicity estimate for each galaxy/region simulated. Col. (6) and (7): archival Chandra observations cumulative exposure time and minimum 0.5–7 keV flux of the detected point sources. Col. (8): HEX-P simulation exposure time. Col. (9)–(11): numbers of sources detected in our HET simulations in the broad (B = 4–25 keV), medium (M = 6–12 keV), and hard (H = 12–25 keV) bands. Col. (12) and (13) numbers of sources detected in the LET soft (S = 4–6 keV) and medium bands. Col. (14): HEX-P HET simulation luminosity limit in the 4–25 keV band in units of erg s^{-1}.

[a]Values of distance were extracted from the NASA Extragalactic Database (NED; http://ned.ipac.caltech.edu/).

[b]Listed values of SFR, $M_\star$, and metallicity were obtained from the literature. For NGC 253 and NGC 3310 values of SFR and $M_\star$ were taken from the HECATE, source catalog (Kovlakas et al., 2021). For the M31 bulge, the SFR, was taken to be less than the total galaxy-wide SFR value of 0.3 $M_\odot$ yr−1 (Rahmani et al., 2016) and $M_\star$ was taken as ≈ 30% of the total galaxy-wide stellar mass following the estimate in Tamm et al. (2012). For Maffei 1, the SFR was derived using the absorption-corrected Hα luminosity from Buta and McCall (2003) and the L(Hα)–SFR relation from Kennicutt et al. (1994) and $M_\star$ was taken from McCall (2014). Metallicities are based on gas-phase emission line measurements for NGC 253 (Izotov et al., 2006), the M31 bulge (Sanders et al., 2012), and NGC 3310 (Engelbracht et al., 2008). For Maffei 1, the metallicity is approximated following the stellar mass versus metallicity relation from Kewley and Ellison (2008).

emission that trace the locations of the highest densities of sources. The NuSTAR data constrain the average spectral properties of the population out to ≈20 keV. However, to constrain the compact objects responsible for the accretion and the accretion states of this unique population requires hard X-ray data at high spatial resolution and sensitivity.

NGC 3310: NGC 3310 is a rare, yet nearby ($D \approx 20$ Mpc), low-metallicity galaxy (≈0.3 $Z_\odot$) that has a substantial SFR (≈8 $M_\odot$ yr^{-1}). Recent examinations of the metallicity-dependent formation rate of luminous HMXBs and ULXs in galaxies have shown an increase in the numbers of these sources with decreasing metallicity (Mapelli et al., 2010; Kovlakas et al., 2020; Lehmer et al., 2021). While population synthesis models predict such trends, the key drivers are not well understood and may have multiple causes, including, e.g., the presence of more massive compact object remnants and weaker binary-destroying supernova kicks for low-metallicity stars, as well as smaller orbital separations throughout the evolution of low-metallicity binary stars (Linden et al., 2010; Wiktorowicz et al., 2019). However, due to the rarity of low-metallicity galaxies in the local Universe, it has not been possible to search for key spectral and timing signatures that provide clues on the nature of HMXB populations in low metallicity galaxies in comparison to ULXs in higher metallicity galaxies.

Broadband (0.3–50 keV) measurements are capable of 1) characterizing contributions from accretion disks and coronae (e.g., Walton et al., 2018), 2) sensitively constraining cyclotron absorption lines (e.g., Brightman et al., 2022), and/or 3) detecting NS pulsations at hard X-rays (e.g., Bachetti et al., 2014) (a more detailed discussion

of ULX science with HEX-P is discussed in Bachetti et al., 2023, in-prep.). However, due to the rarity of low-metallicity galaxies in the local Universe, it has not been possible to search for key spectral and timing signatures that could provide concrete clues into the nature of luminous HMXBs and ULXs formed in low-metallicity environments.

As a result of its relatively high SFR, NGC 3310 contains a rich population of 14 Chandra-detected ULXs (Anastasopoulou et al., 2019), providing an excellent laboratory for studying the properties of luminous HMXBs and ULXs in a low-metallicity environment. However, at present, only Chandra and XMM-Newton are capable of observing and disentangling the X-ray properties of the individual ULXs, which are mainly present in a 20 arcsec diameter circumnuclear star-forming ring.

To investigate the hard X-ray spectrum of the aggregate population of ULXs in NGC 3310, a 140 ks NuSTAR observation was conducted (Lehmer et al., 2015). Chandra and NuSTAR data were combined to constrain the 0.5–30 keV spectrum for the galaxy. The galaxy-wide spectrum showed a steepening slope at $E \geq 7$ keV, characteristic of ULXs; however, it was not possible to investigate the ULX properties individually. HEX-P will alleviate this limitation by resolving the ULX population in NGC 3310 and other low-metallicity galaxies, providing first constraints on the nature of the sources themselves and the diversity of their spectral properties as of function of luminosity in a low-metallicity environment.

In Figure 1, we show optical color images of the above galaxies and highlight the specific HEX-P areal extents of the galaxies that we simulate.

4 Construction of simulated HEX-P data sets

4.1 SIXTE procedure

To simulate HEX-P data sets for the galaxy sample defined in Section 3, we made use of the SImulation of X-ray TElescopes software package (hereafter, SIXTE; Dauser et al., 2019).[1] SIXTE is a flexible Monte Carlo based simulator, designed to model realistic X-ray data sets for a variety of astrophysical sources. The simulation procedure in SIXTE begins with the definition of a simulation input (SIMPUT) file that contains the detailed astrophysical source population characteristics, including source sky locations, fluxes, spectra, intensity distributions, and time-dependent intensity variations.

Once a SIMPUT file is defined, SIXTE uses information about the observatory along with user-specified characteristics of the observation (exposure times, pointing direction, etc.) to generate a photon list (events list) for the observation. In this process, photons are generated using a Monte Carlo procedure that accounts for the astrophysical source spectral shape, the energy-dependent effective area (via an ancillary response file; ARF), the expected photon signal on the detector (via a redistribution matrix file; RMF), effects of vignetting, and the instrument PSF. Background photons can also be supplied for both instrumental and astrophysical sources, and SIXTE provides flexibility in how background is applied; such background sources are included in our work. As such, SIXTE simulations include all realistic sources of statistical noise for both sources and backgrounds that are expected in observations, and no two runs of the simulation are identical.

All the simulations presented below were produced using a set of response files that represent the observatory performance based on current best estimates as of Spring 2023 (see Madsen et al., 2023). The effective area is derived from ray tracing calculations for the mirror design including obscuration by all known structures. The detector responses are based on simulations performed by the respective hardware groups, with an optical blocking filter for the LET and a Be window and thermal insulation for the HET. The LET background was derived from a GEANT4 simulation (Eraerds et al., 2021) of the WFI instrument, and the HET background was derived from a GEANT4 simulation of the NuSTAR instrument. Both HEX-P background simulations assume an L1 orbit.

4.2 Sensitivity limit calculations and HEX-P exposure calculations

The depths of our simulated observations are mainly driven by the goal of detecting XRBs and classifying their compact objects and accretion states in a variety of extragalactic environments. To this end, our required exposures should be capable of both reaching interesting detection limits, while maintaining the ability to classify the X-ray sources.

To accomplish this, we have constructed the luminosity-color and color-color diagnostic diagrams shown in Figure 2A, which illustrate the HEX-P diagnostic capabilities similar to those used for Galactic XRBs [e.g., the "q" diagram of BH XRB accretion states (Belloni, 2010)]. These diagrams were constructed using samples of XRBs in the Milky Way observed at multiple epochs with RXTE, as well as extragalactic ULXs studied by NuSTAR (see, e.g., Wik et al., 2014; Vulic et al., 2018, for further information). The Milky Way samples include 2,568 total RXTE observations of 6 BH XRBs, 9 accreting pulsars, and 11 weakly magnetized NS XRBs (i.e., Atoll/Z-sources), while the ULX samples include only single-epoch NuSTAR observations of 7 unique objects. We note that our diagnostic diagrams are constructed from discrete observations of a finite number of bright sources that can be studied in detail, and that extragalactic populations are likely to span broader ranges of colors. However, the physical variations that make these spectral classes distinguishable across the 4–25 keV spectral range are physical in nature, e.g., accretion disk and corona variations in BHs/NSs, boundary layer emission in NSs, and accretion columns in pulsars. Thus, we expect that extragalactic XRBs will occupy similarly distinguishable regions of these color spaces.

The RXTE spectra at each epoch were fit using xspec, and best-fit models were convolved with HEX-P responses to determine count-rates in $S =$ 4–6 keV, $M =$ 6–12 keV, and $H =$ 12–25 keV bandpasses for both the LET and HET. These bandpasses were chosen to optimize the color variation between compact objects and accretion states, while simultaneously guarding against the impact of absorption on X-ray spectra below ~3 keV. We note that the effective areas of the LET and HET are less than a factor of 2 different from

1 See https://www.sternwarte.uni-erlangen.de/sixte/ for SIXTE code accessibility and documentation

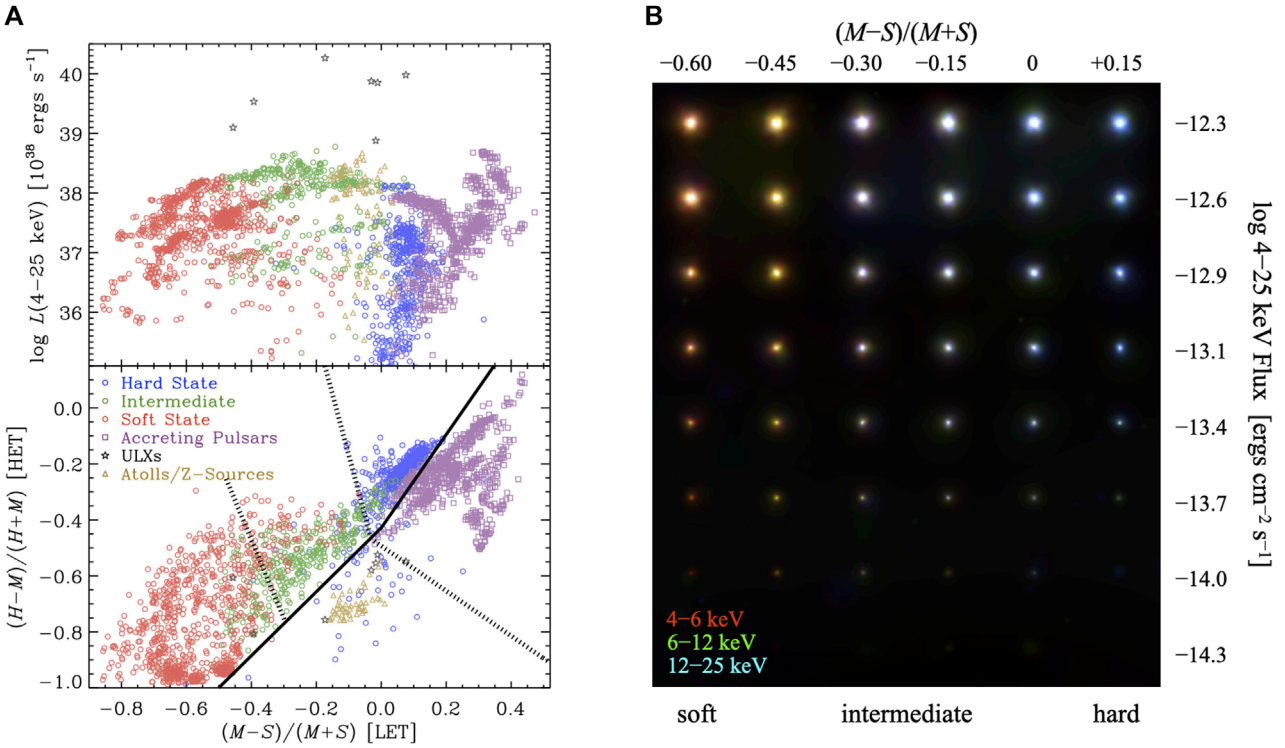

FIGURE 2
(A) 4–25 keV luminosity versus HEX-P LET medium-and-soft band color (*top*) and HEX-P HET hard-and-medium band versus LET medium-and-soft band color (*bottom*) for a variety of Galactic XRBs sampled at several times by RXTE. Bandpasses are defined as S = 4–6 keV and M = 6–12 keV, and H = 12–25 keV. Various BH (hard, intermediate, soft states), NS (accreting pulsars, atolls/Z-sources), and ULX source populations have been color coded (see annotations). **(B)** 500 ks SIXTE three-color HEX-P HET simulation (S = red, M = green, H = blue) of BH XRB spectra with different values of $(M-S)/(M+S)$ [LET] color (see top annotation of columns) and 4–25 keV flux (see right annotation of rows). The total number of 4–25 keV source counts is a weak function of color, however, this bandpass is most sensitive to detecting intermediate-state sources.

each other across the S and M bandpass, with the HET effective area being larger than the LET for both bandpasses. These differences result in our simulated sources having average factors of ≈1.2 and 1.6 more counts for the HET versus the LET for the S and M bands, respectively. However, due to the significantly sharper PSF of the LET compared to that of the HET, we find that the LET data were somewhat more sensitive than those of the HET. However, the much larger effective area of the HET than the LET above 10 keV provided significantly more sensitive measurements for the H band. Throughout the remainder of this paper, we therefore chose to adopt the LET color $(M-S)/(M+S)$ and HET color $(H-M)/(H+M)$ to illustrate the diagnostic power of HEX-P. More extensive analysis of HEX-P data, however, can simultaneously utilize redundant LET and HET color diagnostics, and direct spectral fitting for brighter source populations for source classification.

To determine the point-source detection limits as a function of accretion state (color) and flux, we first performed 500 ks SIXTE simulations of BH XRBs that span the full range of BH XRB LET $(M-S)/(M+S)$ colors at a variety of input fluxes. At the extremes of this range of colors are soft-state and hard-state BH XRBs, which show X-ray spectra that, respectively, drop and rise dramatically above 4 keV. Thus, soft-state and hard-state BH XRBs will be brightest in the S and H bands, respectively, but both populations will be detectable in a broader 4–25 keV bandpass.

In Figure 2B, we show a three-color (S = red, M = green, and H = blue) HEX-P HET image of our simulated sources at 500 ks depth, with each row representing a fixed 4–25 keV flux and each column representing a fixed spectral shape for BH XRBs (see annotations). We chose a flux range of 5×10^{-15} to 5×10^{-13} erg cm^{-2} s^{-1}, which corresponds to a luminosity range of 10^{37}–10^{39} erg s^{-1} at 4 Mpc (roughly the distance to NGC 253).

To search for sources, we ran the wavdetect wavelet algorithm, available through the CIAO v. 4.14 software package,[2] on our 4–25 keV image. Based on experimentation, we found that scales of 1.4, 2, 4, and 8 pixels and a false-positive probability threshold of 10^{-6} yielded reliable source lists and optimal numbers of real-source detections. At 500 ks HET depth, all sources with 4–25 keV fluxes above 10^{-14} erg cm^{-2} s^{-1} (≈2 ×10^{37} erg s^{-1} at 4 Mpc) were detected, regardless of accretion state, and two intermediate-color sources with 5×10^{-15} erg cm^{-2} s^{-1} (10^{37} erg s^{-1} at 4 Mpc) were also detected. In these particular simulations, we did not detect any false positive sources (e.g., background fluctuations). It is also clear from the three-color image in Figure 2 that the range of X-ray accretion states are clearly discriminated by their S, M, and H color down to the faintest source detections.

2 https://cxc.cfa.harvard.edu/ciao/

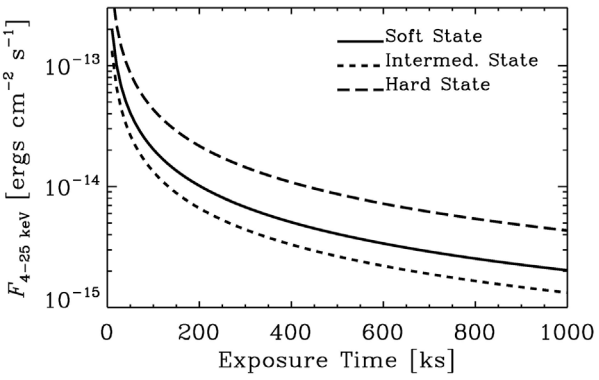

FIGURE 3
HET 4–25 keV flux detection limit as a function of exposure time for soft (*solid*), intermediate (*short-dashed*), and hard (*long-dashed*) state BH XRB spectral models.

To clarify how the sensitivity limit depends on XRB accretion state and exposure time, Figure 3 shows the approximate 3σ 4–25 keV detection limit as a function of exposure time. These curves are based on our HET sensitivity simulations (see Figure 2B), in which we estimated 3σ limits based on local count statistics (source and background) from 6 arcsec radii circular apertures for the sources given input 4–25 keV fluxes. We found good agreement between these curves and wavdetect source detections from our simulations.

As shown in Figure 3, the 4–25 keV HET sensitivity limit varies by a factor of ≈2 across accretion states and is most sensitive to sources in intermediate states, due to the combination of the spectral shape of this state and the shape of the effective area curve providing nearly optimal numbers of counts per unit flux. Although we restrict our analysis in this paper to sources with 4–25 keV band detections, significant additional sensitivity can be gained by searching for sources in subband images and using these source positions to extract local photometry in adjacent bands. For example, the 2–6 keV LET could be used to more sensitively detect soft-state sources, and harder band photometry/limits could be used to constrain the compact object types and/or accretion states for such sources.

In the simulations that we discuss below, we have adopted exposure times that demonstrate HEX-P's capability in addressing the key science goals outlined in Section 1. These exposures are listed in Table 1. Specifically, NGC 253 and Maffei 1 bookend the range of stellar environments, i.e., starburst and passive environments, for which we can study how compact object and accretion state distributions vary across star-formation histories. To characterize the properties of the bright XRBs in outburst requires that our observations reach 4–25 keV luminosity limits of $\approx 10^{37}$ erg s^{-1}. In the case of NGC 253, we can also demonstrate the expected constraints on diffuse thermal and inverse Compton emission in starburst. To achieve these goals, we adopt exposures of 500 and 200 ks for NGC 253 and Maffei 1, respectively.

To monitor accretion state transitions among XRBs in extragalactic environments requires short, repeated observations that reach deep luminosity limits. Given the proximity of a galaxy like M31 at ≈776 kpc, HEX-P can reach a 4–25 keV luminosity limit of $\approx 10^{36}$ erg s^{-1} in ≈50 ks. We therefore adopt this exposure in our simulations. We note that several other galaxies (e.g., M33 and the Magellanic Clouds) are also near enough for fast and deep observations and are thus ideal for monitoring.

While low-metallicity galaxies are present in the nearby Universe (i.e., within ≈10 Mpc) and can be studied with HEX-P, the majority of these objects are dwarf galaxies and contain few luminous XRBs and ULXs. This makes it difficult to explore the role of metallicity in the properties of the ULX population. NGC 3310 represents a more distant case ($D \approx 20$ Mpc) where multiple ULXs are observed in a single low-metallicity environment. We adopt a 250 ks HEX-P exposure to reach below the 4–25 keV detection limit of 10^{39} erg s^{-1}, corresponding to the typical definition of ULXs. Our simulation of NGC 3310 serves as a benchmark for studying the effects of metallicity on ULX populations in galaxies out to ≈50 Mpc.

4.3 Simulation assumptions for our galaxy sample

4.3.1 Point-source properties

As a starting point for each of our HEX-P galaxy simulations, we utilized archival Chandra data with FOVs that overlap with existing NuSTAR-observed fields to define input point-source catalogs (sky locations and 0.5–7 keV fluxes and luminosities) for each galaxy. We limited the regions of our analyses to $13' \times 13'$ fields, the approximate fields of view for the existing NuSTAR observations and simulated HEX-P footprints. The regions were centered on the central coordinates of the galaxies, which we list in Table 1. For all galaxies, except for M31, these regions cover the majority of the galactic footprints, as defined by ellipses that trace contours of constant $K_s \approx 20$ mag arcsec^{-2} galactic surface brightness (see Jarrett et al., 2003, for details). However, for M31, the FOV is limited to X-ray populations in the central bulge (see Figure 1 for context), which accounts for a small fraction of the full galactic extent.

We identified archival Chandra ACIS observations that had aim-points within 5 arcmin of the galactic centers, and in the case of M31, we limited our search to observations with exposures >20 ks, to avoid very long processing times for the many monitoring observations available. For all such ObsIds, we constructed merged data products and point-source catalogs following the procedures outlined in Section 3.2 of Lehmer et al. (2019). In Table 1, we provide the Chandra observation log for the observations that were used to create the point-source catalogs. The cumulative exposures of the Chandra observations are relatively long, ≈50–700 ks, which allows for very sensitive detections of point-source populations to faint limits.

In Figure 4, we show the 0.5–8 keV flux and luminosity distributions for the Chandra point-source catalogs for each of the galaxies in our sample. These point-source catalogs reach flux limits that are below the point-source detection limits of our simulated HEX-P exposures. As such, we consider our input catalogs to be sufficient for providing realistic simulated populations, including the fainter sources that contribute to the unresolved binaries and background AGN components, and we do not add additional contributions from X-ray point sources that are not contained in the Chandra catalogs.

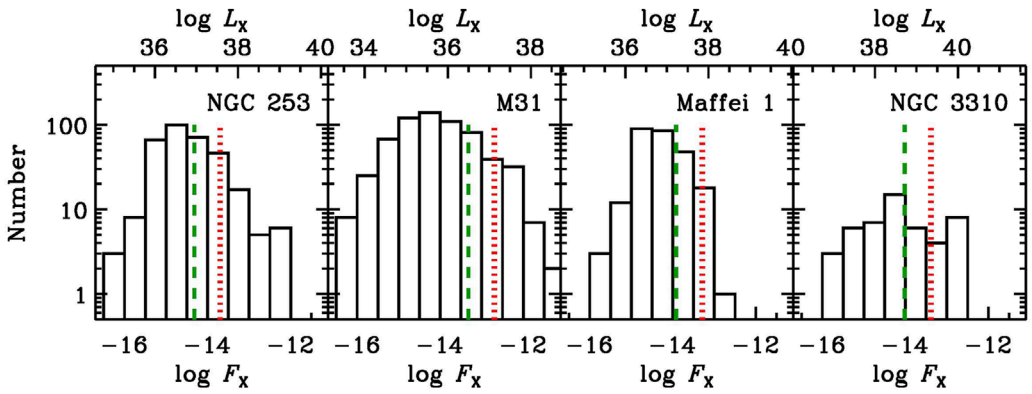

FIGURE 4
Distributions of input Chandra source catalog 0.5–8 keV fluxes (lower axis) and luminosities (upper axis) for each of the simulated galaxies in our sample. The vertical lines show the approximate point-source 3σ detection limits in our simulations for soft-state (*red dotted*) and hard-state (*green dashed*) BH XRB spectra and the simulation exposure times listed in Table 1. These limits indicate that even with the deepest simulated exposures, our input catalogs are likely to provide realistic accounting of X-ray source populations that include background contributions from sources below the individual source detection limits.

To build our simulations in SIXTE requires not only the source positions and flux estimates, which we obtain from Chandra, but also spectral models that cover the full HEX-P responses. Current Chandra constraints on the spectral shapes of the X-ray point sources are limited to the 0.5–8 keV band and have highly degenerate extrapolations to $E \gtrsim 8$ keV. This is a primary driver of unique HEX-P galaxy science. Creating realistic spectral models therefore involves making highly subjective choices regarding the nature of the X-ray sources. We adopt an approach in which we utilize the 0.5–8 keV luminosity of a given source to select 1) a compact object type, either a BH or NS, and 2) an appropriate accretion state, given the compact object type. The selection of luminosity, compact object type, and accretion state, along with some selection of galaxy-intrinsic absorption, uniquely defines a spectral model. Below, we describe this procedure in detail.

To assign a spectral model for a given point source within our galaxy catalogs, we first selected a compact object type using a hypothetical BH fraction, $f_{\rm BH}$ (i.e., the fraction of all X-ray sources that have BH compact object accretors), versus luminosity diagram; we show such a diagram in Figure 5. Recognizing that $f_{\rm BH}$ versus $L_{\rm X}$ is expected to vary with environment, we constructed two such curves, for star-forming and passive stellar host environments. For the star-forming environment, we utilized a function consistent with NuSTAR constraints from Vulic et al. (2018), while for the passive environment, we used a function consistent with the BH fraction inferred by population synthesis model X-ray luminosity functions (XLFs) produced for early-type galaxies NGC 3379 and NGC 4278 from Fragos et al. (2009). We utilized the star-forming BH fractions for NGC 253 and NGC 3310 simulations and the passive environment BH fractions for the bulge of M31 and Maffei 1. The compact object choice for a given source is selected by randomly drawing a number, a, from a uniform distribution in the domain of 0–1. If $a \leq f_{\rm BH}$ ($a > f_{\rm BH}$), then we adopt a BH (NS) compact object type for the source.

With a compact object choice adopted for a given source, we used the diagrams shown in Figure 2A to select an accretion state,

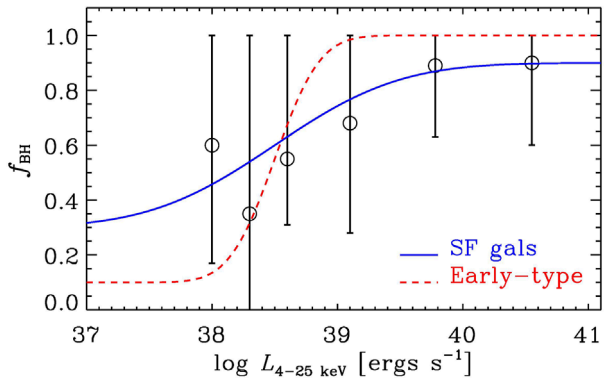

FIGURE 5
Current constraints on the BH fraction [$f_{\rm BH} = N_{\rm BH}/(N_{\rm BH} + N_{\rm NS})$] versus 4–25 keV luminosity for XRBs in star-forming galaxies studied by Vulic et al. (2018) (*open circles with 1σ error bars*). Our heuristic models, which we adopt for the purposes of constructing our SIXTE simulations, are displayed as a blue solid curve for star-forming galaxies (NGC 253 and NGC 3310) and a red dashed curve for passive environments (M31 bulge and Maffei 1).

which specifies a spectral model. We accomplished this by first constructing probability distribution functions (PDFs) of HEX-P LET $(M-S)/(M+S)$ color for various bins of 0.5–8 keV luminosity. Such PDFs were created for BHs and NSs separately using the data shown in Figure 2. For BHs in all environments, the PDFs were constructed from the full distribution of MW BHs (soft, intermediate, and hard states) and ULX source spectra. For NSs in star-forming environments, we constructed the PDFs using the MW pulsar color distribution, while for NSs in passive environments, we used the MW Atolls/Z-sources to construst the PDFs.

Given a value of LET $(M-S)/(M+S)$ as drawn from the most relevant PDF, we identified a unique spectral template that best matches the drawn color. These spectral templates contain

spectral shapes that are characterized in xspec as the sum of accretion disk (diskbb) and Comptonization (comptt) models that have varying parameters (i.e., they span ranges of disk temperature, Comptonization temperatures and optical depths, and relative normalizations) and a fixed intrinsic absorption column density ($N_{\rm H} = 10^{21}$ cm^{-2}). For a given simulated source, the best model is renormalized in SIXTE to the observed 0.5–8 keV flux, as constrained by Chandra.

We note that in this paper, we perform the above selection procedure once for our simulations, thus resulting in a discrete choice of compact object types and accretion states among the sources. Since this procedure is statistical, additional runs of the simulations will result in different draws of the numbers of sources in each category. In practice, the resulting uncertainties on numbers of sources from this procedure will follow Poisson distributions, the uncertainties of which can be propagated into calculations of demographics (e.g., X-ray luminosity functions of various source types).

4.3.2 Diffuse emission in NGC 253

For the case of NGC 253, we explicitly included diffuse emission in our simulations to explore the potential for HEX-P to differentiate diffuse emission and point-source populations and also constrain the inverse Compton emission within the central starburst. To model diffuse emission within SIXTE requires an input model "image" that contains the intensity distribution projected onto the sky. This input diffuse image can then be scaled to a user-chosen total flux with an X-ray spectrum specified. For NGC 253, we adopted separate diffuse emission images for the thermal emission that dominates at $E \lesssim 1$–2 keV and the inverse Compton emission that is expected to be primarily confined within the central starburst region.

To construct the thermal diffuse emission map, we made use of the Chandra point-source catalog and data products for NGC 253. We followed the Chandra X-ray center analysis thread for constructing a diffuse emission image after excluding known point sources.[3] The resulting point-source-free diffuse emission image was subsequently smoothed using CIAO task csmooth and sigma-clipped by setting map values that were $<1.5\sigma$ below the median map value to zero. The sigma clipping effectively removes pixels that are near the constant background value of the Chandra image and allows for the diffuse emission region to more effectively isolate true diffuse emission.

When modeling the thermal diffuse emission component spectral shape and galaxy-wide flux, we adopted the global constraints obtained by the Wik et al. (2014) Chandra-plus-NuSTAR investigation of NGC 253. Specifically, we assumed three apec models with temperatures of $kT = 0.2$, 0.6, and 2 keV; hereafter, cool, warm, and hot components, respectively. We assumed the warm and hot contributions were absorbed by column densities (tbabs) of $N_{\rm H} = 1$ and 7×10^{21} cm^{-2} and the intrinsic model normalization ratios were $A_{\rm cold}/A_{\rm hot} = 0.13$ and $A_{\rm warm}/A_{\rm hot} = 0.4$. When running our SIXTE simulations, the total thermal model was normalized to a galaxy-wide 0.5–7 keV flux of 5×10^{-12} erg cm^{-2} s^{-1}.

For the inverse Compton component, we constructed a diffuse emission map following assumptions that were adopted in Wik et al. (2014). Specifically, we defined a relatively small elliptical region centered on the galactic center with dimensions $a = 30''$ and $b = 8''$ that was rotated 55 deg east-of-north to align with the galactic disk. For the inverse Compton map, we chose to adopt a constant intensity across the elliptical region. In SIXTE we modeled the inverse Compton component using an absorbed power-law model with $N_{\rm H} = 3 \times 10^{21}$ cm^{-2} and $\Gamma = 1.52$, with a 2–7 keV flux of 3×10^{-13} erg cm^{-2} s^{-1}.

5 Results

5.1 Creation of data products and point-source catalogs

Using the SIMPUT catalogs and procedures discussed in Section 4, we ran HEX-P LET and HET SIXTE simulations for the galaxies in our sample using the exposure times discussed in Section 4.2 and listed in Table 1. We created events lists and images in various bandpasses. As our focus is on the characterization of point sources using intensity-color and color-color diagnostics, we chose to create images for both LET and HET in the broad B = 4–25 keV bandpass for source detection and S, M, and H bands for compact object and accretion-state diagnostic purposes. We also created LET 0.5–2 keV and 2–4 keV bandpasses and HET 25–50 keV and 50–80 keV bands.

In Figure 6A, we show three-color (S, M, and H bands) NuSTAR images of our galaxy sample. The FOVs of these images correspond to the regions indicated in the optical images shown in Figure 1. In Figure 6B, we show corresponding three-color HEX-P HET images in the S, M, and H bands, the same bandpasses as shown by NuSTAR. These simulated images alone provide a sense of the magnitude of science gained by HEX-P over NuSTAR. The sharper PSF and larger collecting area allow for substantially improved isolation of the point-source populations, enhanced sensitivity resulting in ~1 order of magnitude more sources detected, and ~1 order of magnitude more photons collected per source.

For each simulated galaxy, we searched the B, S, M, and H band images, for both the HET and LET, using the same procedure as employed in our calibration images: i.e., running wavdetect over scales of 1.4, 2, 4, and 8 pixels and a false-positive probability threshold of 10^{-6}. For simplicity, we created a catalog of sources based on the sources detected in the HET B-band images and cross-matched this source list to the S and M catalogs for the LET and the M, and H band catalogs of the HET for the purposes of obtaining photometry for diagnostic classification purposes (see Figure 2). When an HET B-band source was not detected in one of the subbands, 3σ upper limits were calculated on the local source counts and propagated when calculating hardness ratio limits.

For all bandpasses, we utilized source counts and background estimates from `wavdetect` photometry, and applied aperture corrections to the photometry based on the areas used by wavdetect and our knowledge of the PSFs. Typically, the photometry is extracted from regions that cover PSF fractions of ≈80%–90% for

3 https://cxc.cfa.harvard.edu/ciao/threads/diffuse_emission/

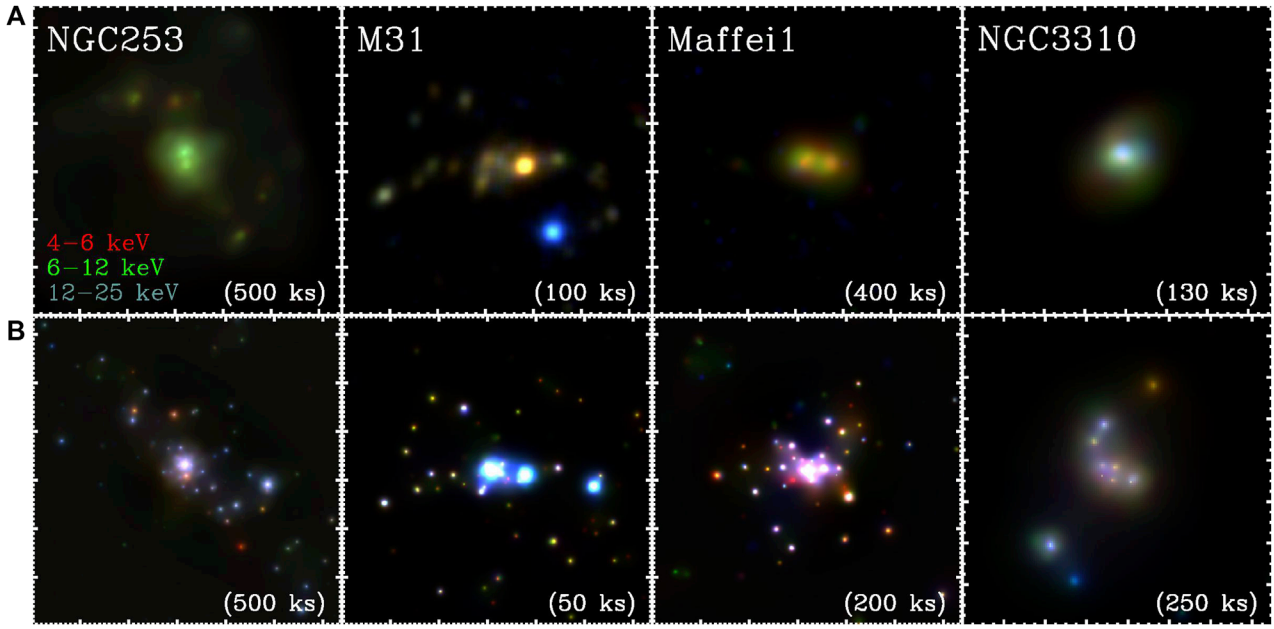

FIGURE 6
(A) NuSTAR three-color (red = 4–6 keV, green = 6–12 keV, blue = 12–25 keV) images of the galaxy sample outlined in Section 3. Each image has dimensions of $13' \times 13'$, except for NGC 3310, which has a $3.1' \times 3.1'$ FOV. These FOV correspond to the regions illustrated in the optical images of Figure 1. **(B)** Simulated three-color HEX-P HET images of the same regions and colors as those displayed in the top panels. Details of our simulations are described in Section 4. The improved PSF and throughput of HEX-P provide dramatic gains in sensitivity over NuSTAR, resulting in major improvements in point-source characterizations with much larger numbers of X-ray sources detectable. In addition to the HET data, the HEX-P LET will simultaneously provide imaging across the 0.2–20 keV bandpass with 4× higher angular resolution than the HET.

the LET and ≈40%–60% for the HET (approximately 1σ ranges). Uncertainties on the counts were based on Poisson estimates of the source and background count estimates, and these uncertainties are propagated to other calculations throughout the remainder of this paper.

In Table 1, we list the total numbers of sources detected in each of the bands of interest. The numbers of detected sources range from ≈10 for NGC 3310 to ≈80 for NGC 253 and the bulge of M31. As we describe below, one of our key goals is to characterize XRB compact object types and accretion states in a variety of environments. Accomplishing this requires accurate constraints on luminosities and colors that can enable such characterizations (see Figure 2). In Figure 7, we show how well we are able to recover 4–25 keV luminosity, $(M-S)/(M+S)$ color for the LET, and $(H-M)/(H+M)$ for the HET, given knowledge of the simulation input. We assessed the accuracy of recovering these parameters by performing a basic linear regression for each set of measured and input values, finding best-fitting relation slopes of 1.12 ± 0.02, 0.95 ± 0.05, and 1.01 ± 0.07 for 4–25 keV luminosity, $(M-S)/(M+S)$[LET], and $(H-M)/(H+M)$[HET], respectively. This indicates that the majority of the point-source properties are well-recovered in the galaxies and that HEX-P has the angular resolution to accurately disentangle the spectral properties of source populations in a variety of extragalactic environments, even with simple analysis prescriptions. We note, however, a subset of sources that lie in crowded regions (e.g., in NGC 3310 and the central regions of the other galaxies) have some offsets from the input parameters due to difficulty disentangling contributions from nearby sources, which we expect is driving the somewhat non-linear relation that we observe for the recovered 4–25 keV luminosity. For such cases, PSF fitting and source disentanglement procedures would need to be employed to obtain accurate photometry (see, e.g., Wik et al., 2014; Yukita et al., 2016; Vulic et al., 2018; Yang et al., 2022, for the implementation of such procedures with NuSTAR).

In the sections below, we utilize our simulated data products and catalogs to demonstrate HEX-P's power for addressing the scientific questions posed in Section 1.

5.2 A census of XRB compact object types and accretion states in diverse extragalactic environments

In Figure 8, we show the intensity-color (4–25 keV luminosity versus $(M-S)/(M+S)$ LET color) and color-color ($(H-M)/(H+M)$ [HET] versus $(M-S)/(M+S)$ [LET]) diagnostic plots for each galaxy, including MW XRB and ULX comparisons in the background (see Section 4 and Figure 2 for details). Without employing any quantitative assessments, we can see the signatures of our simulation assumptions coming through in these diagrams. For example, the star-forming galaxies, NGC 253 and NGC 3310, have source populations that occupy broad ranges of BH accretion states and contain substantial populations of pulsars. In contrast, the early-type environments, i.e., the bulge of M31 and Maffei 1, have larger fractions of non-pulsating NSs and BHs that are consistent with being in hard states.

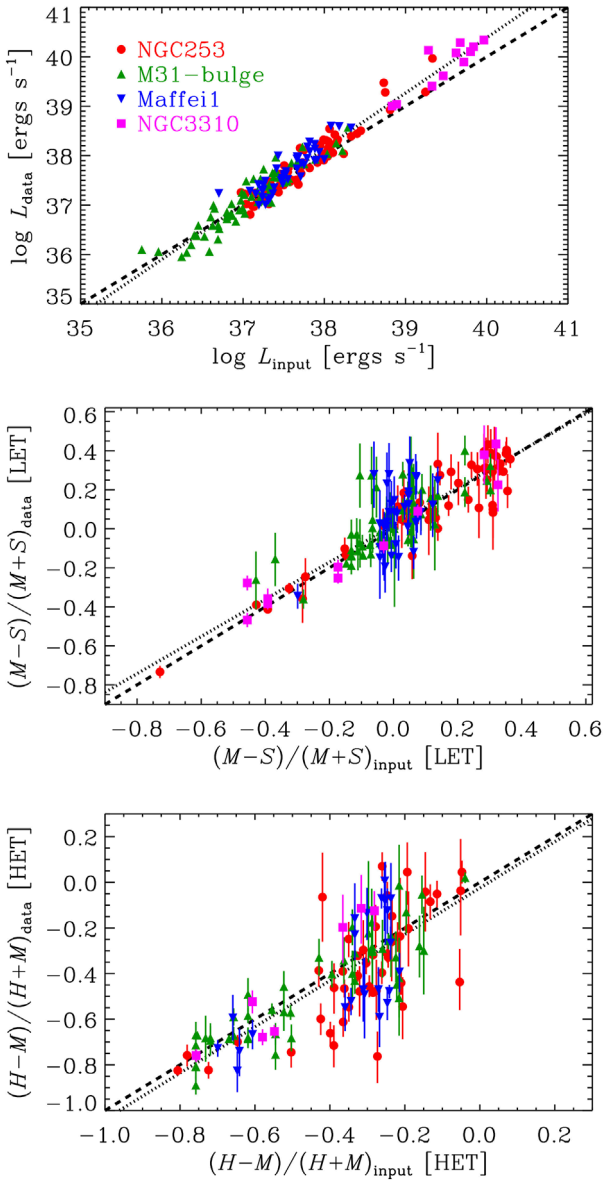

FIGURE 7
Assessments of the recovery of point-source properties from the four simulated galaxy data sets. We show the recovery of a given point-source parameter from our analysis of the simulated images (ordinate) versus the values of the input parameters (abscissa). In each panel, we show the one-to-one recovery line (*dashed black line*) and best-fit linear regression model (*dotted line*). From top-to-bottom, we show the 4–25 keV luminosity, $(M-S)/(M+S)$ for the LET, and $(H-M)/(H+M)$ for the HET. Most parameters are recovered well to within the uncertainties, with the exception of sources in crowded regions, where more detailed PSF fitting would be required.

While thorough probabilistic assessments would be required to properly classify sources as NSs and BHs, as well as characterize their accretion states, we can here provide first-order classifications of our sources based on their comparison with the MW and ULX comparison sample properties. Following the methodology in Vulic et al. (2018), we divided the intensity-color and color-color spaces into discrete zones of occupation for various MW and ULX comparison sources and classify the HEX-P simulated sources into compact object types and accretion states based on their zone location. We optimized the locations of these zones to maximize the correct classifications of these zones. For MW XRBs (non-ULXs), the following color division provides correct compact object type classifications for 98% of the sources:

$$\mathrm{HR}_2^{\rm CO} = \begin{cases} -0.428 + 1.142\mathrm{HR}_1 & (\mathrm{HR}_1 < 0) \\ -0.428 + 1.667\mathrm{HR}_1, & (\mathrm{HR}_1 \geq 0) \end{cases} \quad (1)$$

where $\mathrm{HR}_1 = (M-S)/(M+S)$ [LET] and $\mathrm{HR}_2 = (H-M)/(H+M)$ [HET]. Sources with HR_2 values above and below $\mathrm{HR}_2^{\rm CO}$, as defined by Eq. 1, are classified as BHs and NSs, respectively. In Figures 2, 8, we show this dividing boundary as a solid line.

We further divide sources into accretion states using a similar approach. We chose to divide sources into accretion states guided by the definitions illustrated in Figure 2. Specifically, we divided BH XRBs into soft, intermediate, and hard states, and NS XRBs into weakly magnetized atolls/*Z*-sources and accreting pulsars. Again, we defined color boundaries that optimized the number of correct classifications. For BHs, where $\mathrm{HR}_2 > \mathrm{HR}_2^{\rm CO}$, the accretion-state boundaries were defined as:

$$\mathrm{HR}_2^{\rm soft/int} = -1.593 - 2.804\mathrm{HR}_1, \quad (2)$$

$$\mathrm{HR}_2^{\rm int/hard} = -0.602 - 4.333\mathrm{HR}_1, \quad (3)$$

where soft-state BHs have $\mathrm{HR}_2 < \mathrm{HR}_2^{\rm soft/int}$, intermediate-state BHs have $\mathrm{HR}_2^{\rm soft/int} \leq \mathrm{HR}_2 < \mathrm{HR}_2^{\rm int/hard}$, and hard-state BHs have $\mathrm{HR}_2 > \mathrm{HR}_2^{\rm int/hard}$. For NSs, where $\mathrm{HR}_2 \leq \mathrm{HR}_2^{\rm CO}$, we used the equation,

$$\mathrm{HR}_2^{\rm mag} = -0.493 - 0.803\mathrm{HR}_1, \quad (4)$$

to divide between weakly-magnetized atoll/*Z*-sources ($\mathrm{HR}_2 < \mathrm{HR}_2^{\rm mag}$) and accreting pulsars ($\mathrm{HR}_2 \geq \mathrm{HR}_2^{\rm mag}$).

The above simple color selections reliably recover the correct accretion states for ≈90% of the MW XRB populations shown in Figure 2. These boundaries are overlaid onto Figures 2, 8 as dotted lines.

Using the above classification criteria and the measured constraints from our simulated data, as shown in Figure 8, we conducted basic classifications of the source populations based on either their measured colors or upper/lower limit constraints without detailed consideration of the uncertainties on these quantities. With this simple approach, we found that ≈78% of our sources had compact object classifications and ≈66% had accretion state classifications that matched our input assumptions. Sources with incorrect source classifications were primarily incorrectly classified due to photometric scatter, with some impact resulting from source crowding. As such, the fraction of correct classifications significantly increases with increasing source counts. The majority of the faint sources with incorrect classifications have uncertainties that overlap with the correct classification boundary. Thus, more thorough analyses that account for the ambiguity of source classifications for faint sources and account for photometric uncertainties would be required to rigorously interpret these results.

Despite the above limitations, we can use our basic classifications to demonstrate the promise of using HEX-P to infer information about XRBs in extragalactic environments. In Figure 9, we show

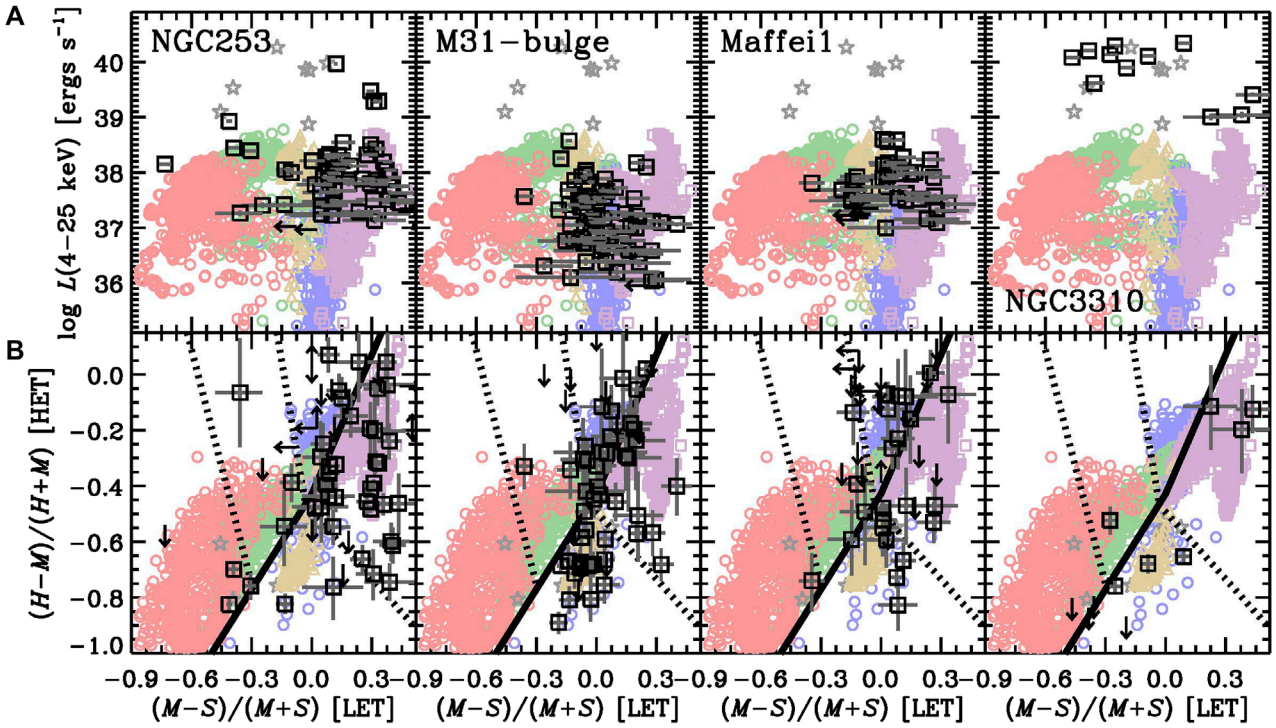

FIGURE 8
4–25 keV luminosity versus $(M-S)/(M+S)$ LET color **(A)** and $H-M/(H+M)$ HET color versus $(M-S)/(M+S)$ LET color **(B)** for each of our simulated galaxies. Color symbols represent Milky Way and nearby ULX diagnostic locations and have the same meaning as they did in Figure 2. HEX-P simulation constraints are shown as black open squares with 1σ uncertainties or black arrows representing 3σ upper limits. In **(B)**, lines represent divisions of classification that we adopt in this paper.

the 4–25 keV XLF for star-forming (NGC 253 and NGC 3310) and passive environments (bulge of M31 and Maffei 1) broken down into constituent compact object types and accretion states. While the detailed shapes of these observed XLFs are highly influenced by variable imaging depth, incompleteness, and variations in galaxy properties (star-formation history and metallicity) that were used to construct them, we are able to recover unique new insights into the nature of the sources that contribute to the XLFs in line with the assumptions of our simulations.

For instance, in star-forming galaxies, we can see the BH dominance among the bright-source populations and the pulsar dominance among the NS subpopulations. For passive galaxies, we recover the NS dominance among LMXBs and show that the weakly-magnetized NSs dominate the NS population. For both star-forming and passive galaxies, we see a steady rise in the fraction of hard-state BHs with decreasing luminosity, as the fraction of BHs in low-hard states outnumber soft/intermediate state sources. We stress again that more thorough analyses that incorporate the impact of photometric errors and source crowding on classifications would be needed to concretely quantify and test population synthesis models. Yet, our demonstration shows that these data will be extremely powerful for such tasks.

Of particular interest are the simulation results for the bulge region of M31. These results show that HEX-P will be capable of efficiently classifying XRBs in Local Group galaxies, even in crowded regions. Our relatively short 50 ks simulated exposure reaches HET 4–25 keV luminosities of $\approx 10^{36}$ erg s^{-1}. This demonstrates that HEX-P could provide powerful monitoring of XRB populations in Local Group galaxies ($D \lesssim 1$ Mpc), allowing for constraints on the duty cycles and the nature of accretion state transitions in XRB populations.

The Local Group includes galaxies representing diverse stellar populations, ranging from the actively star-forming Magellanic Clouds, dominated by stellar populations of <20 Myr and 30–70 Myr age for the SMC and the LMC, respectively (e.g., Harris and Zaritsky, 2004; 2009) to early type and late type spiral galaxies (M31, M33) and elliptical galaxies (M32). The availability of detailed star-formation history maps for these galaxies (e.g., Harris and Zaritsky, 2004; 2009; Lewis et al., 2015; Lazzarini et al., 2022) from HST data allow us to identify the X-ray counterparts of the X-ray sources, characterize their donor stars (e.g., supergiant, Be-XRB, giant, main-sequence donors), and associate them with individual star-formation events (e.g., Antoniou et al., 2010; Williams et al., 2013; Antoniou and Zezas, 2016; Lazzarini et al., 2018; 2021; 2023; Antoniou et al., 2019). Furthermore, these galaxies cover a wide range of metallicity, from 1/3 $Z_\odot$ for the SMC (e.g., Antoniou and Zezas, 2016) to solar metallicities for M31. HEX-P observations and monitoring of carefully selected fields, probing stellar populations of different ages (c.f. Antoniou et al., 2019), would allow us to study directly the dependence of the compact object types and accretion states on the stellar population age, a key test for XRB population synthesis models.

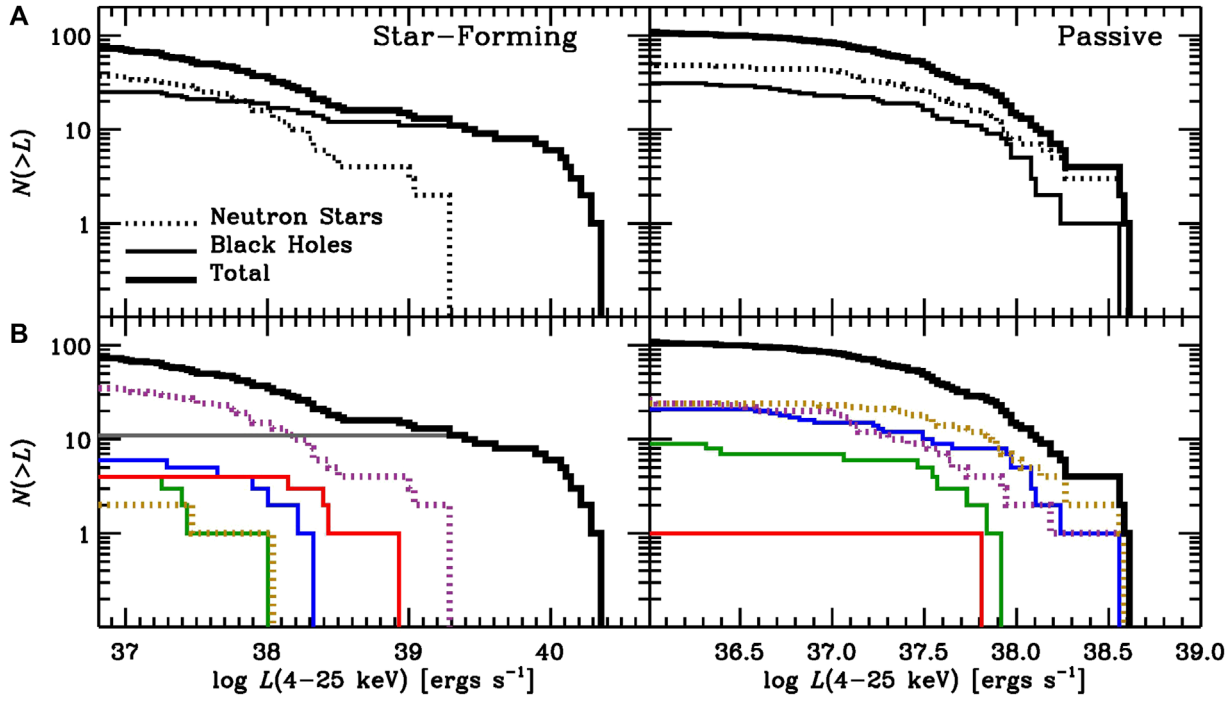

FIGURE 9
Observed 4–25 keV luminosity functions for star-forming (*left column*; NGC 253 and NGC 3310) and passive (*right column*; bulge of M31 and Maffei 1) environments from our simulations. The luminosity functions have been decomposed into compact object types **(A)** and accretion state **(B)**. The accretion states include various BH states (thin solid lines), ULXs (gray), soft (red), intermediate (green), and hard (blue), while the NSs (dotted lines) are divided into weakly magnetize atoll/*Z*-sources (gold) and accreting pulsars (purple). All classifications were based on the criteria defined in Section 5.2 based on the simulated data. The basic assumptions of our simulation inputs are recovered, including BH dominance for luminous sources in star-forming galaxies and NS dominance for XRBs in passive environments, and the dominance of pulsars and weakly magnetized NSs in star-forming and passive environments, respectively.

5.3 Spatial and spectral decomposition of X-ray emitting components in nearby galaxies

In addition to HEX-P's exquisite new capability for characterizing the nature of XRB populations using hard X-ray colors, the high spatial resolution and broadband coverage of HEX-P will work simultaneously to provide the best constraints to date on the broadband spectra of galaxies and the nature of the contributing components.

In our simulation of NGC 253, we included contributions from XRBs, thermal diffuse emission, and inverse Compton emission (see Section 4). For this galaxy, the high spatial resolution enables the detection and isolated study of the point sources, allowing for the direct quantification of the spectral contribution that these sources make to the galaxy, which can be spatially separated from the remaining diffuse emission components (thermal and inverse Compton). While this capability has been possible in the analysis of $\lesssim$10 keV galaxy data from Chandra, and to some extent XMM-Newton, HEX-P will uniquely provide improvements in these constraints across the vast 0.2–80 keV spectral range without requiring coordinated observations of multiple facilities (as is often required with NuSTAR observations). The LET will provide much improved spatial resolution over XMM-Newton, and much larger effective area than Chandra, allowing for better spectral constraints on the nature and absorption of point-sources (e.g., SNe and XRBs) and the thermal diffuse emission components in galaxies. The $\gtrsim$10 keV improved sensitivity from the HET over NuSTAR will enable better constraints on the compact object population types and accretion states, as well as the contribution of the inverse Compton component of the ISM, which is predicted to grow in intensity over other X-ray-emitting populations in this regime (see Section 3).

To demonstrate the analysis capabilities of HEX-P, we investigated the simulated spectrum of the central $1' \times 1'$ region, surrounding the galactic center where an ongoing starburst is present. In Figure 10A, we show the LET and HET spectral constraints as extracted from regions centered on the detected point-sources. We performed spectral fitting of the point-source data using an absorbed broken power-law to account for ULXs, which have spectral steepening above $\approx$10 keV, plus a single power-law to account for the more typical low-luminosity XRB populations. We show the best-fit "XRB model" in Figure 10 as a dashed blue curve.

In Figure 10B, we show the data extracted from the full $1' \times 1'$ region, including the point-sources and diffuse emission. We modeled the total spectrum using our XRB model, as constrained independently from the fit to the point-source data, plus a three-temperature thermal diffuse emission component and a single power-law with $\Gamma = 1.4$ to account for the inverse Compton emission. For simplicity the three temperatures of the thermal component were modeled assuming $kT = 0.2$, 0.6, and 2.0 keV, with

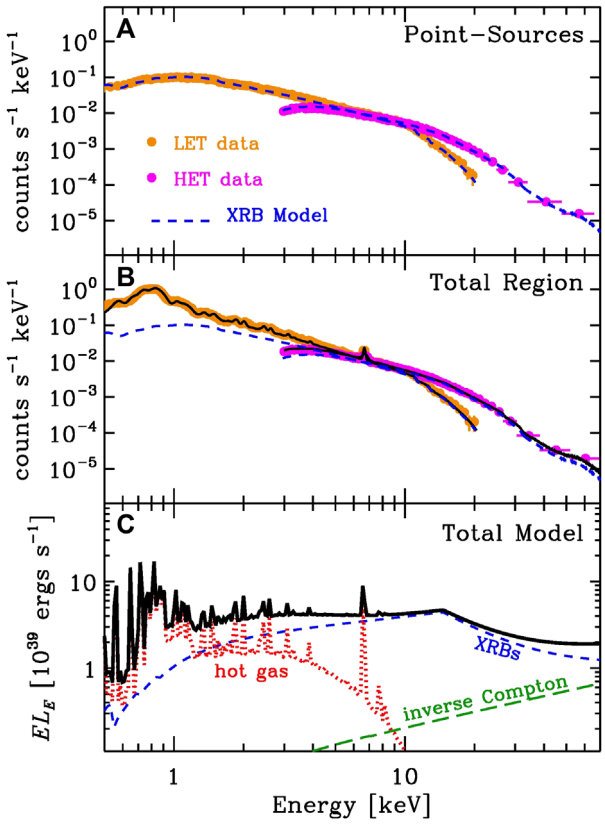

FIGURE 10
HEX-P LET and HET spectra and best-fit models for the central $1' \times 1'$ starburst region of NGC 253. Spectral fitting of the isolated point-source population data **(A)** can be used to constrain separately the XRB spectral contribution to the total spectrum **(B)**. LET and HET data are shown as orange and magenta points with spectral binning and 1σ uncertainties shown as error bars. In **(B,C)**, the model contributions from XRBs are shown as blue dashed curves, while the remainder of the total spectrum **(B)** is modeled due to diffuse thermal and inverse Compton emission. Our unfolded best-fit model to the total spectrum is shown in **(C)**, and includes contributions from thermal diffuse emission (red dotted), XRBs (blue short-dashed), and inverse Compton (green long-dashed).

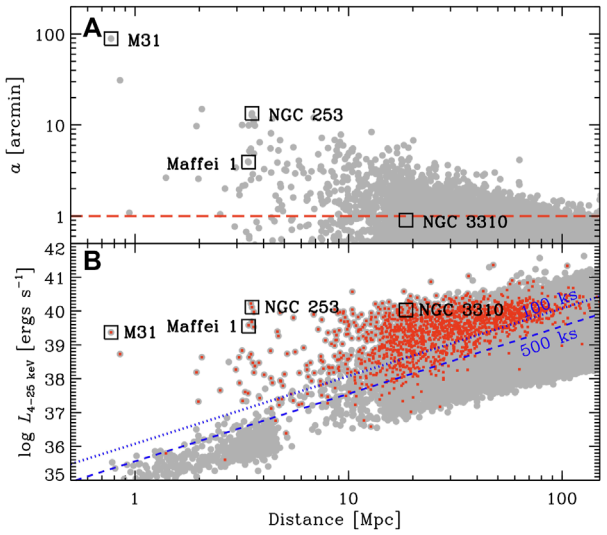

FIGURE 11
Estimated galactic semi-major axis **(A)** and scaling-relation estimated 4–25 keV luminosity **(B)** versus distance. The underlying galaxy sample is from the HECATE source catalog (Kovlakas et al., 2021), which is based on the HyperLEDA astronomical database (Makarov et al., 2014) For reference, we show the locations of our simulated galaxies in **(A,B)**. In **(A)**, we indicate with a horizontal dashed red line the approximate limit above which HEX-P can resolve galaxies into point-source populations. In **(B)**, we show the expected 4–25 keV detection limits for the HEX-P HET in 100 and 500 ks (blue lines) and indicate with small red squares galaxies with semi-major axes ≳1 arcmin, in which populations could be resolved by HEX-P. At 100 ks depth, HEX-P could study resolved populations in >1,000 extended galaxies (major axes ≳1 arcmin) and detect the X-ray emission from 10,000s of galaxies in the local Universe.

the normalizations on each of the components free to vary. In this fitting procedure, we found that all components of the model (thermal emission, XRBs, and inverse Compton) were required in order to obtain a good fit to the data. The solid curve in Figure 10B shows the best-fit overall model relative to the XRB contribution (blue dashed curve). Figure 10C shows the unfolded best-fit model in units of EL_E (νL_ν) with the model components overlaid.

While our constraints here are somewhat idealized by the assumptions of our modeling, the above procedure shows that HEX-P will provide powerful new constraints on the spectral contributions from star-forming galaxies like NGC 253.

5.4 Constraining the broad X-ray band spectra of galaxies for a variety of environments

Thus far, we have discussed the scientific advances from HEX-P observations of a few key nearby galaxies for addressing the scientific goals presented in Section 1; however, definitively addressing these goals would require additional observations of galaxies in the nearby Universe. To assess the reach of HEX-P for studying galaxies, we utilized the Heraklion Extragalactic CATaloguE [HECATE (Kovlakas et al., 2021)], which contains an extensive compilation of the properties (e.g., distances, sizes, SFR, and $M_\star$) of 204,733 galaxies (based on the HyperLEDA catalog) out to $D \approx 200$ Mpc. In the discussion that follows, we assume normal galaxy parameters for our estimates of X-ray emission, but note that AGN activity will impact the X-ray emission from a non-negligible fraction of galaxies. As discussed in other HEX-P papers focused on AGN, HEX-P will have excellent discriminating power for identifying AGN activity, even when heavily obscured or Compton thick.

Using the SFR and $M_\star$ values from the HECATE source catalog, we estimated the 4–25 keV luminosity of each galaxy using the scaling relation from Vulic et al. (2018):

$$L^{\rm scale}_{4-25\,{\rm keV}} \approx 3.56 \times 10^{29}\ M_\star + 1.90 \times 10^{39}\ {\rm SFR}, \quad (5)$$

where $L^{\rm scale}_{4-25\,{\rm keV}}$ has units of erg s^{-1}, $M_\star$ is in $M_\odot$ units, and SFR has units of $M_\odot$ yr^{-1}.

In Figure 11, we show the D_{25} semi-major axis (a) and $L^{\rm scale}_{4-25\,{\rm keV}}$ versus distance for galaxies in the HECATE sample, along with locations of our simulated sample galaxies annotated. From our simulation of NGC 3310, we showed that galaxies with extents smaller than ≈1 arcmin have XRB populations

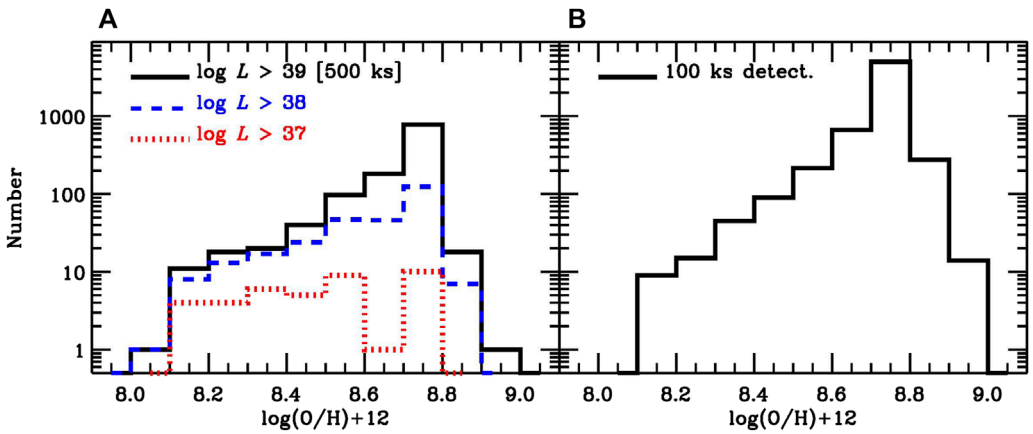

FIGURE 12
(A) Distributions of metallicities for galaxies that could be detected and resolved into X-ray point source populations with 500 ks HEX-P exposures down to limiting luminosities of 10^{37} (red dotted), 10^{38} (blue dashed), and 10^{39} erg s^{-1} (black solid). **(B)** Distribution of metallicities for galaxies that would be detected in 100 ks HEX-P exposures. These histograms illustrate that many galaxies will be within reach for studying both resolved X-ray populations and galaxy-integrated X-ray emission with HEX-P over a broad range of metallicity.

that are resolvable with HEX-P HET. From Figure 11A, we see that there are many such galaxies in the $D \lesssim 200$ Mpc Universe that could potentially be spatially resolved into their constituent point-source populations. However, actually detecting such sources depends on the sensitivity of the observations and the density of sources.

In Figure 11B, we show the point-source 4–25 keV detection limits achieved for the HET in 100 ks and 500 ks exposures. We find that for the extended galaxies ($a \gtrsim 1$ arcmin), ULXs (i.e., $L > 10^{39}$ erg s^{-1}) could be detected in ≳800 galaxies at 100 ks depth, and XRBs with $L \leq 10^{37}$ erg s^{-1} could be studied in ≈50 (10) galaxies with 500 ks (100 ks) depth exposures. In the quest to study the galaxy-integrated spectral properties of galaxy samples themselves, e.g., to explore how broadband X-ray spectra vary as a function of galaxy properties, we estimate that ≈6,000 galaxies could be detected at 100 ks depth, with ≳300 such galaxies predicted to have luminosities >10 times higher than the 100 ks detection limit.

To gain a sense of the diversity of metallicities that could be studied in these samples, we created Figure 12. In Figure 12A, we show the distributions of galaxy metallicities for galaxies that could be detected to various luminosity limits in 500 ks and resolved into point source populations (i.e., with semi-major axes $a > 1$ arcmin). In the right panel, we show the metallicity distribution of galaxies for which broadband constraints could be obtained in 100 ks depth exposures (Figure 12B). In this exercise, we utilized metallicity values in HECATE when available (≈47%) or estimates from the stellar mass versus metallicity relation from Table 2 of Kewley and Ellison (2008).

Figure 12 indicates that HEX-P will be capable of studying resolved XRB populations down to $L \approx 10^{37}$ erg s^{-1} and will obtain broadband SED constraints for galaxies spanning an order of magnitude in metallicity, spanning $Z \approx 0.2$–$2\ Z_{\odot}$ [i.e., 12+log(O/H) ≈ 8–9]. Such a range represents the approximate mean metallicity of galaxy populations spanning redshifts $z \approx$ 0–6, allowing for new interpretations for how the broadband X-ray spectra of galaxies, and their XRB constituents populations, evolved over the last ≳90% of cosmic history. Constraints on the metallicity dependence of these populations will help inform population synthesis models, provide new constraints on the ionization properties of XRB populations in low-metallicity galaxies, and provide insight into how galaxies in the very early Universe (e.g., $z \gtrsim 8$) contribute to the heating of the intergalactic medium (see discussion and references in Section 1).

The fiduciary simulations and analysis presented in the previous sections demonstrates the ability of HEX-P to revolutionize the fields of demographics of extragalactic XRBs by providing information on the compact object populations and accretion states for XRBs in a wide variety of galaxies. Starting from our Local Group observations of selected regions in its four main galaxies (SMC, LMC, M31, and M33), probing stellar populations of different ages will provide the first constraints on the compact object populations and accretion state duty cycle for XRBs in different environments.

In somewhat more distant galaxies (e.g., up to ≈10 Mpc), there are several spiral and dwarf galaxies covering broad ranges of star-formation history and metallicity, and many comprehensive panchromatic surveys of these galaxy samples have been conducted to provide subgalactic properties of the sources (e.g., Kennicutt et al., 2003; 2008; Dalcanton et al., 2009; Calzetti et al., 2015; Lee et al., 2022; Dale et al., 2023). Within the volume of $D < 10$ Mpc, there are 7 galaxies with SFR above 5 $M_{\odot}$ yr^{-1} and 15 galaxies with SFR between 1 and 5 $M_{\odot}$ yr^{-1}. Based on the scaling relation of Lehmer et al. (2019), we typically expect at least 10 to 20 sources with luminosity above 5×10^{38} erg s^{-1} per galaxy (the 100 ks 4–25 keV detection limit at 10 Mpc), for the galaxies with SFR >5 $M_{\odot}$ yr^{-1}. Therefore, HEX-P observations of even a few galaxies can

provide a statistically meaningful sample for which we will be able to study their compact object populations and accretion states. Deeper observations to $\approx 10^{37}$ erg s^{-1} for a few of these galaxies, as we have shown here for NGC 253 and Maffei 1, would allow us to extend these studies to lower luminosity sources and perform comparisons with the Local Group galaxies.

Larger volumes include more extreme galaxies with even lower metallicities or higher SFR/$M_\star$ and SFR. These are prime hosts of ULXs. In these galaxies, we can study in detail, with HEX-P, the accretion state and compact object populations of sources accreting close to or above the Eddington limit. In addition, we will obtain detailed demographics of the ULX population at energies $\gtrsim$10 keV, which together with focused spectroscopic and timing studies of nearby bright ULXs (e.g., Bacchetti et al., 2023; in prep.), will provide a more clear picture of their nature across the broader universe.

6 Conclusion

We have constructed simulations for the HEX-P Probe concept of a sample of four nearby galaxies that span ranges of star-formation history and metallicity to demonstrate the power of using high spatial resolution broadband X-ray data to constrain the nature of the underlying X-ray emitting populations. We have shown that the capabilities of HEX-P are well designed for obtaining powerful new insights into these populations. Specifically, we show that HEX-P has the capabilities required to provide the following important constraints:

1. *HEX-P* will place informative broadband X-ray constraints on large numbers of individual XRBs in galaxy populations that span broad ranges of morphology, star-formation history, and metallicity. In particular, the sensitivity across the 4–25 keV range allows for compact object types (BHs and NSs) and accretion states to be discriminable, avoiding degeneracies in classification due to absorption. With such data, it will be possible to investigate how the distributions of compact objects and accretion states vary as a function of formation age and metallicity, providing stringent new tests of stellar evolution including the impacts of binary evolution and close-binary interactions.
2. The improved sensitivity of HEX-P over NuSTAR will enable efficient detection and monitoring of the ~100s of bright XRBs in Local Group galaxies to understand how the accretion states of the source populations transition as a function of time. Such observations would allow for tests of accretion disk and corona modeling for a broadened range of binaries and mass-transfer scenarios.
3. The improved spatial resolution of the HEX-P LET over XMM-Newton, combined with the larger soft effective area over Chandra, will provide a new means for investigating thermal diffuse emission in galaxies without the contamination of bright XRBs. HEX-P HET constraints on the $\gtrsim$10 keV diffuse emission will provide powerful new constraints on the inverse Compton emission component that is predicted to be associated with particle accelerations in starburst galaxies. The constraints on inverse Compton will aid in discriminating between hadronic and leptonic scenarios for particle accelerators in starburst and will put into context the detected γ-ray emission from the nearby starburst galaxies NGC 253 and M82.
4. Taking a broader view, HEX-P will be capable of constraining XRB population compact objects and accretion states for 100s of nearby galaxies ($D \lesssim 50$ Mpc) and the broadband X-ray spectra of thousands of galaxies out to $D \approx$ 100–200 Mpc. As such, HEX-P can provide critical new constraints on populations of galaxies that span broad ranges of star-formation histories and metallicities, allowing for important new insights into how high-energy emitting sources emit throughout cosmic history.

Data availability statement

The raw data supporting the conclusion of this article will be made available by the authors, without undue reservation.

Author contributions

BL: Formal Analysis, Supervision, Validation, Visualization, Writing–original draft. KG: Conceptualization, Investigation, Writing–review and editing. BB: Writing–review and editing. FF: Writing–review and editing. NV: Conceptualization, Validation, Writing–review and editing. AZ: Conceptualization, Formal Analysis, Methodology, Writing–review and editing. AH: Conceptualization, Writing–review and editing. ML: Conceptualization, Validation, Writing–review and editing. HM: Investigation, Writing–review and editing. TV: Conceptualization, Writing–review and editing. DW: Conceptualization, Writing–review and editing. MY: Conceptualization, Writing–review and editing. MB: Methodology, Writing–review and editing. JG: Conceptualization, Supervision, Writing–review and editing. BG: Supervision, Writing–review and editing. KrM: Methodology, Resources, Writing–review and editing. KaM: Conceptualization, Writing–review and editing. DS: Conceptualization, Funding acquisition, Visualization, Writing–review and editing.

Funding

The authors declare financial support was received for the research, authorship, and/or publication of this article. BL gratefully acknowledges support from the National Aeronautics Space Administration (NASA) Astrophysics Data Analysis Program (80NSSC20K0444). NV acknowledges support for this work provided by the National Aeronautics and Space Administration through Chandra Award Number GO2-23065X issued by the Chandra X-ray Observatory Center, which is operated by the Smithsonian Astrophysical Observatory for and on behalf of NASA under contract NAS8-03060. KG was supported by an appointment to the NASA Postdoctoral Program at NASA Goddard Space Flight Center, administered by Oak Ridge Associated Universities under contract with NASA. The work of DS was carried out at the Jet

Propulsion Laboratory, California Institute of Technology, under a contract with NASA.

Acknowledgments

We are grateful to T. Dauser, M. Lorenz, and the SIXTE development team for their assistance with SIXTE simulations.

Conflict of interest

Author NV was employed by Eureka Scientific, Inc.

The remaining authors declare that the research was conducted in the absence of any commercial or financial relationships that could be construed as a potential conflict of interest.

Publisher's note

All claims expressed in this article are solely those of the authors and do not necessarily represent those of their affiliated organizations, or those of the publisher, the editors and the reviewers. Any product that may be evaluated in this article, or claim that may be made by its manufacturer, is not guaranteed or endorsed by the publisher.

References

Abramowski, A., Acero, F., Aharonian, F., Akhperjanian, A. G., Anton, G., Balzer, A., et al. (2012). Spectral analysis and interpretation of the γ-ray emission from the starburst galaxy NGC 253. *ApJ* 757, 158. doi:10.1088/0004-637X/757/2/158

Anastasopoulou, K., Zezas, A., Gkiokas, V., and Kovlakas, K. (2019). Do sub-galactic regions follow the galaxy-wide X-ray scaling relations? The example of NGC 3310 and NGC 2276. *MNRAS* 483, 711–733. doi:10.1093/mnras/sty3131

Antoniou, V., and Zezas, A. (2016). Star formation history and X-ray binary populations: the case of the Large Magellanic Cloud. *MNRAS* 459, 528–553. doi:10.1093/mnras/stw167

Antoniou, V., Zezas, A., Drake, J. J., Badenes, C., Haberl, F., Wright, N. J., et al. (2019). Deep Chandra survey of the small magellanic cloud. III. Formation efficiency of high-mass X-ray binaries. *ApJ* 887, 20. doi:10.3847/1538-4357/ab4a7a

Antoniou, V., Zezas, A., Hatzidimitriou, D., and Kalogera, V. (2010). Star Formation history and X-ray binary populations: the case of the small magellanic cloud. *ApJL* 716, L140–L145. doi:10.1088/2041-8205/716/2/L140

Bachetti, M., Harrison, F. A., Walton, D. J., Grefenstette, B. W., Chakrabarty, D., Fürst, F., et al. (2014). An ultraluminous X-ray source powered by an accreting neutron star. *Nature* 514, 202–204. doi:10.1038/nature13791

Bachetti, M., Middleton, M. J., Pinto, C., Gurpide, A., Walton, D. J., Brightman, M., et al. (2023). The high energy X-ray probe (HEX-P): studying extreme accretion with ultraluminous X-ray sources

Belloni, T. M. (2010). "States and transitions in black hole binaries," in *Lecture notes in physics*. Editor T. Belloni (Berlin Springer Verlag), 794, 53. doi:10.1007/978-3-540-76937-8/TNQDotTNQ/3

Blanton, M. R., and Moustakas, J. (2009). Physical properties and environments of nearby galaxies. *ARA&A* 47, 159–210. doi:10.1146/annurev-astro-082708-101734

Brightman, M., Kosec, P., Fürst, F., Earnshaw, H., Heida, M., Middleton, M. J., et al. (2022). An 8.56 keV absorption line in the hyperluminous X-ray source in NGC 4045: ultrafast outflow or cyclotron line? *ApJ* 929, 138. doi:10.3847/1538-4357/ac5e37

Buta, R., and McCall, M. L. (2003). Maffei 1 with the [ITAL]hubble space telescope[/ITAL]. *AJ* 125, 1150–1163. doi:10.1086/367789

Calzetti, D., Lee, J. C., Sabbi, E., Adamo, A., Smith, L. J., Andrews, J. E., et al. (2015). Legacy extragalactic UV survey (LEGUS) with the hubble space telescope. I. Survey description. *AJ* 149, 51. doi:10.1088/0004-6256/149/2/51

Carnall, A. C., Leja, J., Johnson, B. D., McLure, R. J., Dunlop, J. S., and Conroy, C. (2019). How to measure galaxy Star Formation histories. I. Parametric models. *ApJ* 873, 44. doi:10.3847/1538-4357/ab04a2

Choi, J., Dotter, A., Conroy, C., Cantiello, M., Paxton, B., and Johnson, B. D. (2016). Mesa isochrones and stellar tracks (MIST). I. Solar-Scaled models. *ApJ* 823, 102. doi:10.3847/0004-637X/823/2/102

Conroy, C. (2013). Modeling the panchromatic spectral energy distributions of galaxies. *ARA&A* 51, 393–455. doi:10.1146/annurev-astro-082812-141017

Dalcanton, J. J., Williams, B. F., Lang, D., Lauer, T. R., Kalirai, J. S., Seth, A. C., et al. (2012). The panchromatic hubble andromeda treasury. *ApJS* 200, 18. doi:10.1088/0067-0049/200/2/18

Dalcanton, J. J., Williams, B. F., Seth, A. C., Dolphin, A., Holtzman, J., Rosema, K., et al. (2009). The ACS nearby galaxy survey treasury. *ApJS* 183, 67–108. doi:10.1088/0067-0049/183/1/67

Dale, D. A., Boquien, M., Turner, J. A., Calzetti, D., Kennicutt, R. C., and Lee, J. C. (2023). Spectral energy distributions for 258 local volume galaxies. *AJ* 165, 260. doi:10.3847/1538-3881/accffe

Dauser, T., Falkner, S., Lorenz, M., Kirsch, C., Peille, P., Cucchetti, E., et al. (2019). SIXTE: a generic X-ray instrument simulation toolkit. *A&A* 630, A66. doi:10.1051/0004-6361/201935978

Done, C., Gierliński, M., and Kubota, A. (2007). Modelling the behaviour of accretion flows in X-ray binaries. Everything you always wanted to know about accretion but were afraid to ask. *A&ARv* 15, 1–66. doi:10.1007/s00159-007-0006-1

Engelbracht, C. W., Rieke, G. H., Gordon, K. D., Smith, J. D. T., Werner, M. W., Moustakas, J., et al. (2008). Metallicity effects on dust properties in starbursting galaxies. *ApJ* 678, 804–827. doi:10.1086/529513

Eraerds, T., Antonelli, V., Davis, C., Hall, D., Hetherington, O., Holland, A., et al. (2021). Enhanced simulations on the athena/wide field imager instrumental background. *J. Astronomical Telesc. Instrum. Syst.* 7, 034001. doi:10.1117/1.JATIS.7.3.034001

Fragos, T., Kalogera, V., Willems, B., Belczynski, K., Fabbiano, G., Brassington, N. J., et al. (2009). Transient low-mass X-ray binary populations in elliptical galaxies NGC 3379 and NGC 4278. *ApJL* 702, L143–L147. doi:10.1088/0004-637X/702/2/L143

Garofali, K., Lehmer, B. D., Basu-Zych, A., West, L. A., Wik, D., Yukita, M., et al. (2020). On the X-ray spectral energy distributions of star-forming galaxies: the 0.3-30 keV spectrum of the low-metallicity starburst galaxy VV 114. *ApJ* 903, 79. doi:10.3847/1538-4357/abba2d

Gilfanov, M., Fabbiano, G., Lehmer, B., and Zezas, A. (2022). *X-ray Binaries in external galaxies*. Singapore: Springer Nature Singapore, 1–38. doi:10.1007/978-981-16-4544-0_108-1

Harris, J., and Zaritsky, D. (2004). The Star Formation history of the small magellanic cloud. *AJ* 127, 1531–1544. doi:10.1086/381953

Harris, J., and Zaritsky, D. (2009). The Star Formation history of the large magellanic cloud. *AJ* 138, 1243–1260. doi:10.1088/0004-6256/138/5/1243

Harrison, F. A., Craig, W. W., Christensen, F. E., Hailey, C. J., Zhang, W. W., Boggs, S. E., et al. (2013). The nuclear spectroscopic telescope array (NuSTAR) high-energy X-ray mission. *ApJ* 770, 103. doi:10.1088/0004-637X/770/2/103

HERA Collaboration, Abdurashidova, Z., Adams, T., Aguirre, J. E., Alexander, P., Ali, Z. S., Baartman, R., et al. (2023). Improved constraints on the 21 cm EoR power spectrum and the X-ray heating of the IGM with HERA phase I observations. *ApJ* 945, 124. doi:10.3847/1538-4357/acaf50

H. E. S. S. Collaboration, Abdalla, H., Aharonian, F., Ait Benkhali, F., Angüner, E. O., Arakawa, M., Arcaro, C., et al. (2018). The starburst galaxy NGC 253 revisited by H.E.S.S. and Fermi-. *Lat. A&A* 617, A73. doi:10.1051/0004-6361/201833202

Izotov, Y. I., Stasińska, G., Meynet, G., Guseva, N. G., and Thuan, T. X. (2006). The chemical composition of metal-poor emission-line galaxies in the data release 3 of the sloan digital sky survey. *A&A* 448, 955–970. doi:10.1051/0004-6361:20053763

Jansen, F., Lumb, D., Altieri, B., Clavel, J., Ehle, M., Erd, C., et al. (2001). XMM-Newton observatory. I. The spacecraft and operations. *A&A* 365, L1–L6. doi:10.1051/0004-6361:20000036

Jarrett, T. H., Chester, T., Cutri, R., Schneider, S. E., and Huchra, J. P. (2003). The 2MASS large galaxy atlas. *AJ* 125, 525–554. doi:10.1086/345794

Karachentsev, I. D., Karachentseva, V. E., Huchtmeier, W. K., and Makarov, D. I. (2004). A catalog of neighboring galaxies. *A Catalog Neighboring Galaxies. AJ* 127, 2031–2068. doi:10.1086/382905

Kennicutt, J., Robert, C., Armus, L., Bendo, G., Calzetti, D., Dale, D. A., et al. (2003). SINGS: the SIRTF nearby galaxies survey. *PASP* 115, 928–952. doi:10.1086/376941

Kennicutt, J., Robert, C., Lee, J. C., Funes, J. G., Sakai, S., and Akiyama, S. (2008). An Hα imaging survey of galaxies in the local 11 Mpc volume. *ApJS* 178, 247–279. doi:10.1086/590058

Kennicutt, J., Robert, C., Tamblyn, P., and Congdon, C. E. (1994). Past and future Star Formation in disk galaxies. *ApJ* 435, 22. doi:10.1086/174790

Kewley, L. J., and Ellison, S. L. (2008). Metallicity calibrations and the mass-metallicity relation for star-forming galaxies. *ApJ* 681, 1183–1204. doi:10.1086/587500

Kewley, L. J., Nicholls, D. C., and Sutherland, R. S. (2019). Understanding galaxy evolution through emission lines. *ARA&A* 57, 511–570. doi:10.1146/annurev-astro-081817-051832

Kovlakas, K., Zezas, A., Andrews, J. J., Basu-Zych, A., Fragos, T., Hornschemeier, A., et al. (2020). A census of ultraluminous X-ray sources in the local Universe. *MNRAS* 498, 4790–4810. doi:10.1093/mnras/staa2481

Kovlakas, K., Zezas, A., Andrews, J. J., Basu-Zych, A., Fragos, T., Hornschemeier, A., et al. (2021). The Heraklion Extragalactic Catalogue (HECATE): a value-added galaxy catalogue for multimessenger astrophysics. *MNRAS* 506, 1896–1915. doi:10.1093/mnras/stab1799

Lazzarini, M., Hinton, K., Shariat, C., Williams, B. F., Garofali, K., Dalcanton, J. J., et al. (2023). *Multiwavelength characterization of the high mass X-ray binary population of M33*. arXiv e-prints , arXiv:2305.1639010.48550/arXiv.2305.16390.

Lazzarini, M., Hornschemeier, A. E., Williams, B. F., Wik, D., Vulic, N., Yukita, M., et al. (2018). Young accreting compact objects in M31: the combined power of NuSTAR, Chandra, and hubble. *ApJ* 862, 28. doi:10.3847/1538-4357/aacb2a

Lazzarini, M., Williams, B. F., Durbin, M., Dalcanton, J., Antoniou, V., Binder, B. A., et al. (2021). Multiwavelength characterization of the high-mass X-ray binary population of M31. *ApJ* 906, 120. doi:10.3847/1538-4357/abccca

Lazzarini, M., Williams, B. F., Durbin, M. J., Dalcanton, J. J., Smercina, A., Bell, E. F., et al. (2022). The panchromatic hubble andromeda treasury: triangulum extended region (PHATTER). II. The spatially resolved recent Star Formation history of M33. *ApJ* 934, 76. doi:10.3847/1538-4357/ac7568

Lazzarini, M., Williams, B. F., Hornschemeier, A. E., Antoniou, V., Vasilopoulos, G., Haberl, F., et al. (2019). Neutron stars and black holes in the small magellanic cloud: the SMC NuSTAR legacy survey. *ApJ* 884, 2. doi:10.3847/1538-4357/ab3f32

Lee, J. C., Whitmore, B. C., Thilker, D. A., Deger, S., Larson, K. L., Ubeda, L., et al. (2022). The PHANGS-HST survey: physics at high angular resolution in nearby galaxies with the hubble space telescope. *ApJS* 258, 10. doi:10.3847/1538-4365/ac1fe5

Lehmer, B. D., Eufrasio, R. T., Basu-Zych, A., Doore, K., Fragos, T., Garofali, K., et al. (2021). The metallicity dependence of the high-mass X-ray binary luminosity function. *ApJ* 907, 17. doi:10.3847/1538-4357/abcec1

Lehmer, B. D., Eufrasio, R. T., Tzanavaris, P., Basu-Zych, A., Fragos, T., Prestwich, A., et al. (2019). X-ray binary luminosity function scaling relations for local galaxies based on subgalactic modeling. *ApJS* 243, 3. doi:10.3847/1538-4365/ab22a8

Lehmer, B. D., Tyler, J. B., Hornschemeier, A. E., Wik, D. R., Yukita, M., Antoniou, V., et al. (2015). The 0.3-30 keV spectra of powerful starburst galaxies: NuSTAR and Chandra observations of NGC 3256 and NGC 3310. *ApJ* 806, 126. doi:10.1088/0004-637X/806/1/126

Leja, J., Carnall, A. C., Johnson, B. D., Conroy, C., and Speagle, J. S. (2019). How to measure galaxy Star Formation histories. II. Nonparametric models. *ApJ* 876, 3. doi:10.3847/1538-4357/ab133c

Lewis, A. R., Dolphin, A. E., Dalcanton, J. J., Weisz, D. R., Williams, B. F., Bell, E. F., et al. (2015). The panchromatic hubble andromeda treasury. XI. The spatially resolved recent Star Formation history of M31. *ApJ* 805, 183. doi:10.1088/0004-637X/805/2/183

Linden, T., Kalogera, V., Sepinsky, J. F., Prestwich, A., Zezas, A., and Gallagher, J. S. (2010). The effect of starburst metallicity on bright X-ray binary formation pathways. *ApJ* 725, 1984–1994. doi:10.1088/0004-637X/725/2/1984

Lopez, S., Lopez, L. A., Nguyen, D. D., Thompson, T. A., Mathur, S., Bolatto, A. D., et al. (2023). X-ray properties of NGC 253's starburst-driven outflow. *ApJ* 942, 108. doi:10.3847/1538-4357/aca65e

Maccarone, T. J., Yukita, M., Hornschemeier, A., Lehmer, B. D., Antoniou, V., Ptak, A., et al. (2016). Demonstrating the likely neutron star nature of five M31 globular cluster sources with Swift-NuSTAR spectroscopy. *MNRAS* 458, 3633–3643. doi:10.1093/mnras/stw530

Madau, P., and Dickinson, M. (2014). Cosmic star-formation history. *ARA&A* 52, 415–486. doi:10.1146/annurev-astro-081811-125615

Madsen, K. K, García, J. A., Stern, D., Armini, R., Basso, S., Coutinho, D., et al. (2023). The High Energy X-ray Probe (HEX-P): Instrument and Mission Profile. *arXiv*. doi:10.48550/arXiv.2312.04678

Madsen, K. K., Harrison, F., Broadway, D., Christensen, F. E., Descalle, M., Ferreira, D., et al. (2018). "Optical instrument design of the high-energy x-ray probe (HEX-P)," in *Space telescopes and instrumentation 2018: ultraviolet to gamma ray*. Editors J.-W. A. den Herder, S. Nikzad, and K. Nakazawa, 106996M. 10699 of Society of Photo-Optical Instrumentation Engineers (SPIE) Conference Series. doi:10.1117/12.2314117

Makarov, D., Prugniel, P., Terekhova, N., Courtois, H., and Vauglin, I. (2014). HyperLEDA. III. The catalogue of extragalactic distances. *A&A* 570, A13. doi:10.1051/0004-6361/201423496

Mapelli, M., Ripamonti, E., Zampieri, L., Colpi, M., and Bressan, A. (2010). Ultra-luminous X-ray sources and remnants of massive metal-poor stars. *MNRAS* 408, 234–253. doi:10.1111/j.1365-2966.2010.17048.x

McCall, M. L. (2014). A council of giants. *MNRAS* 440, 405–426. doi:10.1093/mnras/stu199

Meidinger, N., Albrecht, S., Beitler, C., Bonholzer, M., Emberger, V., Frank, J., et al. (2020). Development status of the wide field imager instrument for Athena. *Soc. Photo-Optical Instrum. Eng. (SPIE) Conf. Ser.*, 114440T. doi:10.1117/12.2560507

Misra, D., Kovlakas, K., Fragos, T., Lazzarini, M., Bavera, S. S., Lehmer, B. D., et al. (2023). X-ray luminosity function of high-mass X-ray binaries: studying the signatures of different physical processes using detailed binary evolution calculations. *A&A* 672, A99. doi:10.1051/0004-6361/202244929

Nandra, K., Barret, D., Barcons, X., Fabian, A., den Herder, J.-W., Piro, L., et al. (2013). *The hot and energetic universe: a white paper presenting the science theme motivating the Athena+ mission*. arXiv e-prints , arXiv:1306.230710.48550/arXiv.1306.2307.

Nardini, E., Kim, D.-W., and Pellegrini, S. (2022). *The hot interstellar medium*. arXiv e-prints , arXiv:2205.02855. doi:10.48550/arXiv.2205.02855

Pietsch, W., Roberts, T. P., Sako, M., Freyberg, M. J., Read, A. M., Borozdin, K. N., et al. (2001). XMM-Newton observations of NGC 253: resolving the emission components in the disk and nuclear area. *A&A* 365, L174–L180. doi:10.1051/0004-6361:20000068

Pinto, C., and Walton, D. J. (2023). *Ultra-luminous X-ray sources: extreme accretion and feedback*. arXiv e-prints , arXiv:2302.00006. doi:10.48550/arXiv.2302.00006

Rahmani, S., Lianou, S., and Barmby, P. (2016). Star formation laws in the Andromeda galaxy: gas, stars, metals and the surface density of star formation. *MNRAS* 456, 4128–4144. doi:10.1093/mnras/stv2951

Remillard, R. A., and McClintock, J. E. (2006). X-ray properties of black-hole binaries. *ARA&A* 44, 49–92. doi:10.1146/annurev.astro.44.051905.092532

Sanders, N. E., Caldwell, N., McDowell, J., and Harding, P. (2012). The metallicity profile of M31 from spectroscopy of hundreds of H II regions and PNe. *ApJ* 758, 133. doi:10.1088/0004-637X/758/2/133

Simmonds, C., Schaerer, D., and Verhamme, A. (2021). Can nebular He II emission be explained by ultra-luminous X-ray sources? *A&A* 656, A127. doi:10.1051/0004-6361/202141856

Strickland, D. K., Heckman, T. M., Weaver, K. A., Hoopes, C. G., and Dahlem, M. (2002). Chandra observations of NGC 253. II. On the origin of diffuse X-ray emission in the halos of starburst galaxies. *ApJ* 568, 689–716. doi:10.1086/338889

Strickland, D. K., and Stevens, I. R. (2000). Starburst-driven galactic winds - I. Energetics and intrinsic X-ray emission. *MNRAS* 314, 511–545. doi:10.1046/j.1365-8711.2000.03391.x

Tamm, A., Tempel, E., Tenjes, P., Tihhonova, O., and Tuvikene, T. (2012). Stellar mass map and dark matter distribution in M 31. *A&A* 546, A4. doi:10.1051/0004-6361/201220065

The HERA Collaboration, Abdurashidova, Z., Adams, T., Aguirre, J. E., Alexander, P., Ali, Z. S., et al. (2022). *Improved constraints on the 21 cm EoR power spectrum and the X-ray heating of the IGM with HERA phase I observations*. *arXiv e-prints*, arXiv:2210.04912. doi:10.48550/arXiv.2210.04912

Tikhonov, N. A., and Galazutdinova, O. A. (2018). Does the IC 342/maffei galaxy group really exist? *Astrophys. Bull.* 73, 279–292. doi:10.1134/S1990341318030021

Vulic, N., Hornschemeier, A. E., Wik, D. R., Yukita, M., Zezas, A., Ptak, A. F., et al. (2018). Black holes and neutron stars in nearby galaxies: insights from NuSTAR. *ApJ* 864, 150. doi:10.3847/1538-4357/aad500

Walton, D. J., Fürst, F., Heida, M., Harrison, F. A., Barret, D., Stern, D., et al. (2018). Evidence for pulsar-like emission components in the broadband ULX sample. *ApJ* 856, 128. doi:10.3847/1538-4357/aab610

Wik, D. R., Lehmer, B. D., Hornschemeier, A. E., Yukita, M., Ptak, A., Zezas, A., et al. (2014). Spatially resolving a starburst galaxy at hard X-ray energies: NuSTAR, Chandra, and VLBA observations of NGC 253. *ApJ* 797, 79. doi:10.1088/0004-637X/797/2/79

Wiktorowicz, G., Lasota, J.-P., Middleton, M., and Belczynski, K. (2019). The observed versus total population of ULXs. *ApJ* 875, 53. doi:10.3847/1538-4357/ab0f27

Williams, B. F., Binder, B. A., Dalcanton, J. J., Eracleous, M., and Dolphin, A. (2013). The ages of high-mass X-ray binaries in NGC 2403 and NGC 300. *ApJ* 772, 12. doi:10.1088/0004-637X/772/1/12

Yang, J., Wik, D. R., Lehmer, B. D., West, L. A., Williams, B. F., Maccarone, T. J., et al. (2022). Young black hole and neutron star systems in the nearby star-forming galaxy M33: the NuSTAR view. *ApJ* 930, 64. doi:10.3847/1538-4357/ac6351

Yukita, M., Hornschemeier, A. E., Lehmer, B. D., Ptak, A., Wik, D. R., Zezas, A., et al. (2016). A hard X-ray study of the normal star-forming galaxy M83 with NuSTAR. *ApJ* 824, 107. doi:10.3847/0004-637X/824/2/107

Yukita, M., Ptak, A., Hornschemeier, A. E., Wik, D., Maccarone, T. J., Pottschmidt, K., et al. (2017). Identification of the hard X-ray source dominating the$E>$ 25 keV emission of the nearby galaxy M31. *ApJ* 838, 47. doi:10.3847/1538-4357/aa62a3

frontiers | Frontiers in Astronomy and Space Sciences

TYPE Original Research
PUBLISHED 27 November 2023
DOI 10.3389/fspas.2023.1289432

Check for updates

OPEN ACCESS

EDITED BY
Renee Ludlam,
Wayne State University, United States

REVIEWED BY
Carlos Frajuca,
Federal University of Rio Grande, Brazil
Ryan Urquhart,
Michigan State University, United States
Federico García,
Argentine Institute of Radio Astronomy, Argentina

*CORRESPONDENCE
Matteo Bachetti,
matteo.bachetti@inaf.it

RECEIVED 05 September 2023
ACCEPTED 26 October 2023
PUBLISHED 27 November 2023

CITATION
Bachetti M, Middleton MJ, Pinto C, Gúrpide A, Walton DJ, Brightman M, Lehmer B, Roberts TP, Vasilopoulos G, Alford J, Amato R, Ambrosi E, Dai L, Earnshaw HP, El Byad H, García JA, Luca Israel G, Jaodand A, Madsen K, Maitra C, Mandel S, Mori K, Pintore F, Ohsuga K, Pilia M, Stern D, Younes G and Wolter A (2023), The high energy X-ray probe (*HEX-P*): studying extreme accretion with ultraluminous X-ray sources. *Front. Astron. Space Sci.* 10:1289432. doi: 10.3389/fspas.2023.1289432

COPYRIGHT
© 2023 Bachetti, Middleton, Pinto, Gúrpide, Walton, Brightman, Lehmer, Roberts, Vasilopoulos, Alford, Amato, Ambrosi, Dai, Earnshaw, El Byad, García, Luca Israel, Jaodand, Madsen, Maitra, Mandel, Mori, Pintore, Ohsuga, Pilia, Stern, Younes and Wolter. This is an open-access article distributed under the terms of the Creative Commons Attribution License (CC BY). The use, distribution or reproduction in other forums is permitted, provided the original author(s) and the copyright owner(s) are credited and that the original publication in this journal is cited, in accordance with accepted academic practice. No use, distribution or reproduction is permitted which does not comply with these terms.

The high energy X-ray probe (*HEX-P*): studying extreme accretion with ultraluminous X-ray sources

Matteo Bachetti[1]*, Matthew J. Middleton[2], Ciro Pinto[3], Andrés Gúrpide[2], Dominic J. Walton[4], Murray Brightman[5], Bret Lehmer[6], Timothy P. Roberts[7], Georgios Vasilopoulos[8], Jason Alford[9], Roberta Amato[10], Elena Ambrosi[3], Lixin Dai[11], Hannah P. Earnshaw[5], Hamza El Byad[1], Javier A. García[5,12], Gian Luca Israel[13], Amruta Jaodand[5], Kristin Madsen[12], Chandreyee Maitra[14], Shifra Mandel[9], Kaya Mori[9], Fabio Pintore[3], Ken Ohsuga[15], Maura Pilia[1], Daniel Stern[16], George Younes[12] and Anna Wolter[17]

[1]INAF-Osservatorio Astronomico di Cagliari, Cagliari, Selargius, Italy, [2]School of Physics and Astronomy, University of Southampton, Southampton, United Kingdom, [3]INAF—IASF Palermo, Palermo, Italy, [4]Centre for Astrophysics Research, University of Hertfordshire, Hatfield, United Kingdom, [5]Cahill Center for Astrophysics, California Institute of Technology, Pasadena, CA, United States, [6]Department of Physics, University of Arkansas, Fayetteville, NC, United States, [7]Centre for Extragalactic Astronomy, Department of Physics, Durham University, Durham, United Kingdom, [8]Department of Physics, National and Kapodistrian University of Athens, Athens, Greece, [9]Columbia Astrophysics Laboratory, Columbia University, New York, NY, United States, [10]Institut de Recherche en Astrophysique et Planétologie, Centre National d'Études Spatiales, Université de Toulouse, CNES, Toulouse, France, [11]Department of Physics, University of Hong Kong, Pokfulam, Hong Kong SAR, China, [12]X-ray Astrophysics Laboratory, NASA Goddard Space Flight Center, Greenbelt, MD, United States, [13]INAF—Osservatorio Astronomico di Roma, Rome, Italy, [14]Max-Planck-Institut für Extraterrestrische Physik, Garching, Germany, [15]Center for Computational Sciences, University of Tsukuba, Tsukuba, Japan, [16]Jet Propulsion Laboratory, California Institute of Technology, Pasadena, CA, United States, [17]INAF-Osservatorio Astronomico di Brera, Milano, Italy

Introduction: Ultraluminous X-ray sources (ULXs) represent an extreme class of accreting compact objects: from the identification of some of the accretors as neutron stars to the detection of powerful winds travelling at 0.1–0.2 c, the increasing evidence points towards ULXs harbouring stellar-mass compact objects undergoing highly super-Eddington accretion. Measuring their intrinsic properties, such as the accretion rate onto the compact object, the outflow rate, the masses of accretor/companion-hence their progenitors, lifetimes, and future evolution-is challenging due to ULXs being mostly extragalactic and in crowded fields. Yet ULXs represent our best opportunity to understand super-Eddington accretion physics and the paths through binary evolution to eventual double compact object binaries and gravitational-wave sources.

Methods: Through a combination of end-to-end and single-source simulations, we investigate the ability of HEX-P to study ULXs in the context of their host galaxies and compare it to XMM-Newton and NuSTAR, the current instruments with the most similar capabilities.

Results: HEX-P's higher sensitivity, which is driven by its narrow point-spread function and low background, allows it to detect pulsations and broad spectral features from ULXs better than XMM-Newton and NuSTAR.

Discussion: We describe the value of HEX-P in understanding ULXs and their associated key physics, through a combination of broadband sensitivity, timing resolution, and angular resolution, which make the mission ideal for pulsation detection and low-background, broadband spectral studies.

KEYWORDS

ultraluminous X-ray sources, *HEX-P*, pulsars, black holes, accretion, spectra

1 Introduction

Ultraluminous X-ray sources (ULXs, see Kaaret et al., 2017; Fabrika et al., 2021; King et al., 2023; Pinto and Walton, 2023 for recent reviews) are off-nuclear X-ray sources whose apparent luminosities exceed the Eddington limit for a stellar-mass black hole (e.g., $\sim 10^{39}$ erg s^{-1} for a $\sim 10 M_{\odot}$ black hole).

ULXs commonly have X-ray spectra consisting of two thermal components; the lower-energy component has a characteristic temperature of <1 keV, whereas the higher-energy component shows a cut off at >3 keV. The low-energy component was initially interpreted as evidence for standard, sub-Eddington accretion onto intermediate-mass black holes (Miller et al., 2003). However, the cutoff, hinted at in high-quality observations with *XMM-Newton* since the mid-2010s (Roberts et al., 2005; Stobbart et al., 2006; Middleton et al., 2015a), was interpreted as Comptonization of disk photons by an optically thick corona and super Eddington accretion (e.g., Gladstone et al., 2009). Hard X-ray coverage provided by *NuSTAR* (Harrison et al., 2013) gave the highest-significance detections of this higher-energy cutoff, confirming the likely super-Eddington nature of most ULXs (e.g., Bachetti et al., 2013; Walton et al., 2013; Rana et al., 2015). Following the first detection of pulsations in M82 X-2 with *NuSTAR* (Bachetti et al., 2014), a growing number of pulsating ULXs (PULXs, also referred to as ultraluminous pulsars, ULPs; e.g., Fürst et al., 2016; Israel et al., 2017; Carpano et al., 2018; Rodríguez Castillo et al., 2020) have been found, showing that neutron stars (NSs) are able to radiate at hundreds of times their Eddington limit. The pulsations tend to be associated with an additional hard spectral component above 10 keV, which is reminiscent of the hard, curved spectra found in accreting pulsars (e.g., Pintore et al., 2017; Walton et al., 2018b).

The detection of some Galactic super-Eddington NSs provide a possible link between high-luminosity X-ray binaries (XRBs) and ULXs (Wilson-Hodge et al., 2018, e.g., Swift J0243+6124); in general, studying the highest-luminosity end of Galactic XRBs in the Milky Way Galaxy and external galaxies might provide clues on the onset of the ULX regime [see Fabbiano (2006) for a review, and Connors et al. (2023), in this volume, for *HEX-P*'s contribution to studies of this Galactic population].

Except for the few cases where pulsations have been observed, implying a neutron star (NS) accretor, determining the nature of the compact object in ULXs remains a major challenge for current observatories and a key open question for the vast majority of sources. One way to address this issue is through population synthesis studies, which suggest that NS-ULXs may dominate the ULX population (King et al., 2017; Middleton and King, 2017; Wiktorowicz et al., 2019; Khan et al., 2021). PULXs can reach luminosities above 10^{41} erg s^{-1} (e.g., NGC 5907 X-1, Israel et al., 2017), and given the similarity of PULX spectra to much of the ULX population, NSs might indeed power the majority of ULXs (Pintore et al., 2017; Walton et al., 2018b). In addition, a very small number of ULXs have shown evidence for cyclotron resonance scattering features (CRSFs) in their spectra[1] (e.g., Walton et al., 2018a; Brightman et al., 2018), providing another route to identifying the presence of a NS, as well as a direct estimate of the magnetic field strength (likely indicating a weaker dipole but stronger multipolar field) close to the NS surface (Middleton et al., 2019a; Kong et al., 2022).

The mechanism for the very high luminosities of ULXs is still debated. It is likely that the emission is partially collimated by an optically thick, radiatively driven outflow (King et al., 2001) launched from the large scale-height disk expected at very high mass-transfer rates (Shakura and Sunyaev, 1973). Indeed, many ULXs show evidence of high-velocity winds and outflows likely inflating the ~100 pc interstellar bubbles found around many ULXs at various wavelengths (Stobbart et al., 2006; Middleton et al., 2014; 2015b; Pinto et al., 2016; Pakull and Mirioni, 2002; Gúrpide et al., 2022; Belfiore et al., 2020, see Section 2.1). However, these mass-loaded winds likely affect our ability to locate pulsing ULXs (e.g., Mushtukov et al., 2017), and collimation alone is difficult to reconcile with the high pulsed fraction concurrent with the high luminosities of PULXs (e.g., Israel et al., 2017). Another possibility is that a locally strong, possibly non-dipolar, magnetic field is capable of altering the local Thomson cross section (Basko and Sunyaev, 1976; Dall'Osso et al., 2015; Ekşi et al., 2015; Mushtukov et al., 2015; Israel et al., 2017; Brice et al., 2021). These processes might also operate together to a greater or lesser extent.

Most ULXs are known to have other bright X-ray sources within 1′, in particular those located outside the Local Group (see Section 3.1.2). A clear detection and isolation of sources is therefore not possible given the low resolution power of the high energy detectors in use, impeding a profound and detailed study of the whole population of ULXs. The understanding of ULXs could reach considerable advancement by the combination, in one instrument, of high angular resolution, high time resolution and sensitivity in the hard X-rays.

1 See Ludlam et al. (2023), this volume, for CRSF studies on bright Galactic sources with *HEX-P*.

The *High-Energy X-ray Probe* (*HEX-P*; Madsen et al., 2023) is a probe-class mission concept that offers sensitive broad-band X-ray coverage (0.2–80 keV) with an exceptional combination of spectral, timing and angular resolution capabilities. It features two high-energy telescopes (HETs) that focus hard X-rays, and one low-energy telescope (LET) that focuses lower energy X-rays.

The LET consists of a segmented mirror assembly, coated with iridium on monocrystalline silicon that achieves a half power diameter (HPD) of 3.5″, and a low-energy DEPFET detector, of the same type as the Wide Field Imager (WFI; Meidinger et al., 2020) onboard *Athena* (Nandra et al., 2013). It has 512 × 512 pixels that cover a field of view of 11.3′ × 11.3′, an effective passband of 0.2–25 keV, and a full frame readout time of 2 ms, which can be operated in a 128 and 64 channel window mode for higher count-rates, to mitigate pile-up and allow for faster readout. Pile-up effects remain below an acceptable limit of ~1% for fluxes up to ~100 mCrab–a lot higher than typical extragalactic ULX fluxes–in the smallest window configuration. The high angular resolution and low background result in a factor ~2 sensitivity improvement with respect to *XMM-Newton*.

The HET consists of two co-aligned telescopes and detector modules. The optics are made of Ni-electroformed full shell, mirror substrates, leveraging the heritage of *XMM-Newton* (Jansen et al., 2001), and coated with Pt/C and W/Si multilayers for an effective passband of 2–80 keV. The high-energy detectors are of the same type flown on *NuSTAR* (Harrison et al., 2013), consisting of 16 CZT sensors per focal plane, tiled 4 × 4, for a total of 128 × 128 pixels spanning a field of view of 13.4′ × 13.4′. This improvement in angular resolution allows for a much more sensitive instrument configuration compared to *NuSTAR*.

The broad *HEX-P* X-ray passband and superior sensitivity compared with existing facilities provides a powerful and important opportunity to study ULXs across a wide range of energies, luminosities, and timescales.

2 Challenges and open questions

A number of major questions in the field of ULXs and super-Eddington accretion remain unanswered, preventing us from achieving a comprehensive understanding of their phenomenology and detailed accretion physics. We briefly describe them here.

2.1 Where does the transferred mass go?

Understanding the fraction of matter being expelled in winds versus the fraction accreted is key to estimate the possible evolutionary paths of massive binary systems–for instance, the formation of double compact object binaries and systems that create large ionising flux at high redshifts (Fragos et al., 2013)—and for understanding potential supermassive black hole (SMBH) growth rates in the early universe. A possible means for measuring the current mass loss rate is via the absorption lines, which are indicators of quasi-relativistic winds [see Pinto et al. (2016)], requiring observations at <2 keV. Many ULXs are associated with optical or radio bubbles (Pakull and Mirioni, 2002; Soria et al., 2021), which are sometimes as large as 400 pc in diameter and mechanically inflated (Gúrpide et al., 2022), allowing an estimate for the integrated kinetic energy released by the winds. The mass inflow rate can be crudely estimated from soft X-ray spectra [see Poutanen et al. (2007)] or, should the mass transfer dominate the angular momentum distribution within the system, from the change in the orbital period [e.g., see Bachetti et al. (2022), who estimate the mass transfer rate from a decrease in the orbital period of M82 X-2 through pulsar timing].

Winds in XRBs are commonly identified via absorption lines in the Fe K band from hot plasmas (typically Fe XXV-XXVI), and in the soft band from a forest of H- and He-like ions of several elements from C to Fe [for a review see Neilsen and Degenaar (2023)]. Initial searches for Fe XXV-XXVI in ULXs did not result in detections [see, e.g., Walton et al. (2013)], most likely due to their soft spectra or high ionisation state of the gas [for a review on ULX winds see Pinto and Walton (2023)]. Evidence of atomic lines in low-resolution ULX X-ray spectra were found in the form of residuals around 1 keV with respect to the continuum model through high-count-rate *XMM-Newton* EPIC spectra (Stobbart et al., 2006; Middleton et al., 2014; 2015b). Later on, high-spatial-resolution instruments onboard *Chandra* showed that the residuals were associated with the ULX itself rather than the interstellar medium in the host galaxy (Sutton et al., 2015), which was supported by the anticorrelation between their strength and the ULX X-ray spectral hardness (Middleton et al., 2015b). The first unambiguous proof of winds was obtained through long observations (300–500 ks) with the high-spectral-resolution reflection grating spectrometer (RGS) onboard *XMM-Newton*. In particular, Pinto et al. (2016) discovered a forest of emission lines (at rest-frame laboratory wavelengths) and absorption lines (mainly O VII-VIII and Ne IX-X), blueshifted by ~0.2*c* in the two well-known ULXs NGC 1313 X-1 and NGC 5408 X-1, in excellent agreement with the predictions of winds driven by strong radiation pressure in super-Eddington accretion disks (Ohsuga and Mineshige, 2011; Jiang et al., 2014). Modelling of these lines permits an estimate of the kinetic power within the wind (affected by the uncertainties in the covering fraction), which matches well with the luminosities required to inflate the supersonically expanding ULX bubble nebulae [detected primarily in the optical and showing broad lines, see, e.g., recent work with the MUSE camera on the Very Large Telescope by Gúrpide et al. (2022)].

Features indicating a wind have been found in the majority of ULX RGS spectra with $\gtrsim 1{,}000$ net counts (Pinto et al., 2017; Kosec et al., 2018; Pinto et al., 2021), as well as in the *Chandra* gratings observation of the transient Galactic super-Eddington NS, Swift J0243.6+6124 (van den Eijnden et al., 2019). The luminosity of the plasma producing the emission lines varies slightly over time and is very large ($L_X \sim 10^{38}$ erg s^{-1}; Pinto et al., 2020a), orders of magnitude higher than in Eddington-limited Galactic XRBs (Psaradaki et al., 2018). Absorption lines at 8.6–8.8 keV from the hotter Fe K component of the wind were finally found (albeit at lower significance) in a few ULXs with hard spectra (Walton et al., 2016b; Brightman et al., 2022). The emission and absorption lines in the soft band (0.3–2 keV) have equivalent widths similar to those of Galactic XRBs [$EW \sim 5$–10 eV, see Kosec et al. (2021)]. The Fe K absorption features, albeit rarer, appear deeper ($EW \sim 50$–200 eV) and similar to the most extreme wind phases observed in Galactic XRBs (which have velocities of ~0.05*c*; e.g., King et al., 2012).

The very low detection rate of Fe K lines arises as a combination of low effective area in current instruments, high background, and low ionic fractions. The latter is a consequence of the soft radiation field of ULXs (e.g., Pinto and Walton, 2023). However, in ULXs likely seen at low inclinations [e.g., the hard ultraluminous, or HUL, systems of Sutton et al. (2013) with spectral slopes $\Gamma < 2$], the continuum is strong, likely overwhelming the lines in the soft band (e.g., Middleton et al., 2015b). The Fe K features might then be detected, as the irradiating continuum is hard, as long as the gas is not overionised in the wind cone and the instrumental background is sufficiently low at 7–9 keV.

Although absorption lines have proven elusive in HUL sources (such as Holmberg IX X-1 and most pulsating ULXs), should such features be detected, we could start to understand a) the 3D structure of the wind, and b) the actual mass outflow rate (and true kinetic power). The latter has important cosmological consequences for the net growth rate of SMBHs (e.g., Volonteri and Rees, 2005; Volonteri et al., 2015) and the overall role which ULXs play in their host galaxies, particularly at the peak of star formation (e.g., Prestwich et al., 2015). *HEX-P* will dramatically improve our ability to search for the Fe K wind component in ULXs thanks to its broader energy band (needed for modelling the continuum, which is crucial to search for shallow spectral features, see Figure 8), improved sensitivity compared to *XMM-Newton* and *NuSTAR* (for maximizing total source counts), and its narrower PSF (since ULXs tend to reside in crowded regions).

2.2 What is the content of the ULX population?

One of the open questions regarding the nature of ULXs is the prevalence of NS accretors and the strength of their magnetic fields. The detection of fast ($\gtrsim 1$ Hz) pulsations unequivocally identifies a ULX as a NS, and pulsar timing can be used to indirectly estimate the magnetic field (e.g., Ghosh and Lamb, 1979; Wang, 1996). The detection of cyclotron lines in X-ray spectra allows us to tackle these two problems simultaneously, as it enables us to identify the presence of a NS where pulsations may be undetectable or absent (Brightman et al., 2018), while simultaneously offering an indication of the magnetic field strength (Walton et al., 2018a; Middleton et al., 2019a). To date, only two potential CRSFs have been reported in extragalactic ULXs (Walton et al., 2018a; Brightman et al., 2018), and one Galactic super-Eddington source, Swift J0243+6124 (Kong et al., 2022). The broadband coverage of *HEX-P*–and its higher sensitivity above 10 keV (where these lines are typically detected in NS XRBs; Staubert et al., 2019)—will allow us to increase the population of identified NS-ULXs by detecting CRSFs (see Section 3.3.3).

At the moment, due to the limited amount of high quality data, the sample of well-studied ULXs is very small (a few tens, compared to the thousands known; Walton et al., 2022; Tranin et al., 2023), restricting our ability to perform deep searches for pulsations and CRSFs, and hence preventing us from assessing the fraction of NSs in the ULX population. Given the energy dependence of the pulsing component (e.g., Brightman et al., 2016) and the potential for the CRSF to be located at a wide range of energies (depending on the magnetic field strength), broad-band observations, especially at high energies, are crucial.

A similar energy dependence also characterizes other forms of variability in addition to pulsations, such as quasi-periodic oscillations (QPOs), which can in principle be used to classify accreting objects (Lewin et al., 1988; Belloni and Hasinger, 1990; van der Klis, 2005). ULXs are known to show QPOs (Atapin et al., 2019), some of which match the phenomenology observed in other accreting systems, e.g., QPOs that have been detected over a broad-band [like M82 X-1's 50–300 mHz QPO, see, e.g., El Byad (2021)] are more significant at higher energies ($\gtrsim 10$ keV). The broadband spectro-temporal study of a rich sample of ULXs will help single out possible candidate black hole ULXs (e.g., Wolter et al., 2018). In particular, it will be crucial for studying the brightest ULXs, also referred to as hyperluminous X-ray sources (HLXs; Farrell et al., 2009; MacKenzie et al., 2023, still considered among the best candidates to host intermediate-mass black holes (IMBHs) although are rare and mostly found in very distant galaxies.

2.3 What drives the changes in ULX brightness/spectral shape?

ULXs have been observed to change dramatically in brightness on timescales of days, weeks, and months (e.g., Walton et al., 2016a; Gúrpide et al., 2021a; b). Possible causes of this variability include precession of the disk and wind (e.g., Pasham and Strohmayer, 2013; Middleton et al., 2015b; Luangtip et al., 2016; Amato et al., 2023) driven by a variety of processes [see the discussion in Middleton et al. (2018), (2019b)], changes in accretion rate [for instance by the launching of a thermal wind at large radius (Middleton et al., 2022), or by modulating the mass transfer rate in a radiatively driven stellar wind], or the onset of a propeller state associated with a NS close to spin equilibrium. The latter has been extensively searched for (Earnshaw et al., 2018; Song et al., 2020), with the strongest evidence seen in the changing spin period of NGC 5907 ULX-1 (Fürst et al., 2023). With a well considered monitoring strategy, it should also be possible to identify propeller states accompanying smaller changes in luminosity by isolating changes in the spectrum at high energies [see Middleton et al. (2023)], provided that a broad energy bandpass is available. Determining the mechanism behind the long timescale changes in ULXs then requires several key ingredients: a) high energy coverage and sensitivity to locate and track pulsations, b) low energy coverage and sensitivity to explore how the wind responds to changes in the broad band spectrum (e.g., Middleton et al., 2015b; Pinto et al., 2020b), and c) broad simultaneous coverage at high and low energies in order to locate the hard component switching off (whilst the soft emission remains stable), which is an indicator of a likely propeller transition, and more generally to detect spectral transitions (Amato et al., 2023).

3 Simulations

To demonstrate the improved capabilities of *HEX-P* compared to the current primary instruments for ULX studies, *XMM-Newton*

and *NuSTAR*, we performed a detailed *HEX-P* simulation of NGC 253, a Galaxy with a large population of bright XRBs and ULXs, using the SImulation of X-ray TElescopes (SIXTE) software package (Dauser et al., 2019), with the procedure described in Section 3.1.1. This simulation provides precise estimates of the source and sky count rates, and the instrumental background, to set up reliable estimates for the detection and temporal and spectral characterization of sources in crowded fields. These estimates were refined through follow-up simulations, using the count rates and background from the SIXTE simulations as inputs.

All the simulations presented in this paper were produced with a set of response files that represent the observatory performance based on current best estimates as of Spring 2023 (see Madsen et al., 2023). The effective area is derived from a ray-trace of the mirror design including obscuration by all known structures. The detector responses are based on simulations performed by the respective hardware groups, with an optical blocking filter for the LET and a Be window and thermal insulation for the HET. The LET background was derived from a GEANT4 simulation (Eraerds et al., 2021) of the WFI instrument, and the HET background was derived from a GEANT4 simulation of the *NuSTAR* instrument; both simulations assume an L1 orbit for *HEX-P*. *XMM-Newton* and *NuSTAR* simulations were also performed for comparison, using the official set of response files distributed with SIXTE[2].

3.1 End-to-end simulations of an NGC 253-like galaxy

The *Chandra* Source Catalogue v.2.0 (Evans et al., 2010; 2020) contains 1583 ULXs [following the criteria from Walton et al. (2022)]. Among these ULXs, 14% have other X-ray sources within 5″, 45% within 20″, and 64% within 40″. The vast majority of the ULXs appear close to the nuclear region of their host galaxy, particularly for the ULXs residing in more distant galaxies. In these conditions, improvements in the angular resolution, whilst not degrading the effective area, timing capabilities, and hard X-ray response, are key for studying ULXs.

ULXs are mostly extragalactic objects; some galaxies, such as M51 (7.2 Mpc; Terashima and Wilson, 2004), NGC 253 (3.5 Mpc; Wik et al., 2014), and the Cartwheel Galaxy (150 Mpc; Wolter et al., 2018), are known to contain a relatively large number of bright accreting sources and ULXs, and so far, only *Chandra* is able to fully resolve their positions. It is possible that a population of elusive, highly absorbed ULXs (e.g., Luangtip et al., 2015; West et al., 2023), has still escaped detection (or identification as ULXs), awaiting high-energy response (and an ability to spatially separate them).

With its high sensitivity and angular resolution, *HEX-P* will be able to detect and characterize the spectra of many new ULXs. Simulations indicate that the effective area and background of *HEX-P* will allow us to not only identify ULXs from their characteristic spectra, but also detect important spectral features such as emission and absorption lines associated with strong winds, or cyclotron resonance features that allow for an estimate of NS magnetic fields (see Figure 8). Moreover, these capabilities are key for detecting pulsations from pulsars in crowded environments. We demonstrate this in the Sections below.

3.1.1 SIXTE setup

For complete, end-to-end simulations, we used the SIXTE software package (Dauser et al., 2019), a Monte Carlo simulation toolkit for X-ray astronomical instrumentation. This software is able to take into account very accurately the source properties, including simulating complicated fields-of-view with diffuse emission, and characteristics of the optics and detection system of the mission. The SIXTE team worked with the leads of the *HEX-P* mission to provide up-to-date instrument specification files for *HEX-P*. The SIXTE website also contains hardware specifications for a number of existing and future missions that allow an easy comparison between them.

To run a simulation with SIXTE, we first generate a source input (SIMPUT-format) file containing: 1) an image of the diffuse emission; 2) its spectral shape defined as a `Xspec`-format xcm file; and 3) a list of point sources, having different spectral shapes and timing properties, including pulsations and/or aperiodic variability. Through the script `run_sixt`, we then generate realistic simulations for *HEX-P*, *NuSTAR*, and *XMM-Newton*.

3.1.2 Galaxy and source parameters

We set up a SIMPUT file using a map of the diffuse emission of NGC 253, and 70 point sources[3].

The map of diffuse emission was obtained by removing all point sources from a deep *Chandra* map of the field. We assigned to it a thermal plasma spectrum [based on Wik et al. (2014); see the details in Lehmer et al. (2023), in this volume]. The total 0.5–7 keV flux of the diffuse emission was $9.6 \cdot 10^{-12}$ erg s^{-1} cm^{-2}. The 70 point sources selected were the 70 brightest sources from the *Chandra* catalogue. We only conserved the position and flux between 0.5 and 8 keV, but otherwise we changed the spectral and temporal properties of each source, as follows:

- each source had a ULX-like cutoff-powerlaw spectrum, with random parameters uniformly distributed in intervals deemed plausible by comparison with the spectral characteristics of known ULXs (e.g., Pintore et al., 2017): cutoff $E_{\rm cut}$ between 1 and 10 keV, and Γ between −2 and 0;
- pulsations with a pulsed fraction between 20% and 100% [NGC 300 ULX has ~80% pulsed fraction over the full band, see e.g., Carpano et al. (2018), Vasilopoulos et al. (2019)], a pulse period

2 They can be downloaded at https://www.sternwarte.uni-erlangen.de/sixte/instruments/

3 The galaxy does not have a bright AGN in the center. Such a source could, in some cases, dominate the emission close to the nucleus, and would be a source of confusion for the detection of ULXs for all instruments, plausibly more so for *XMM-Newton* and *NuSTAR*, that have a broader PSF.

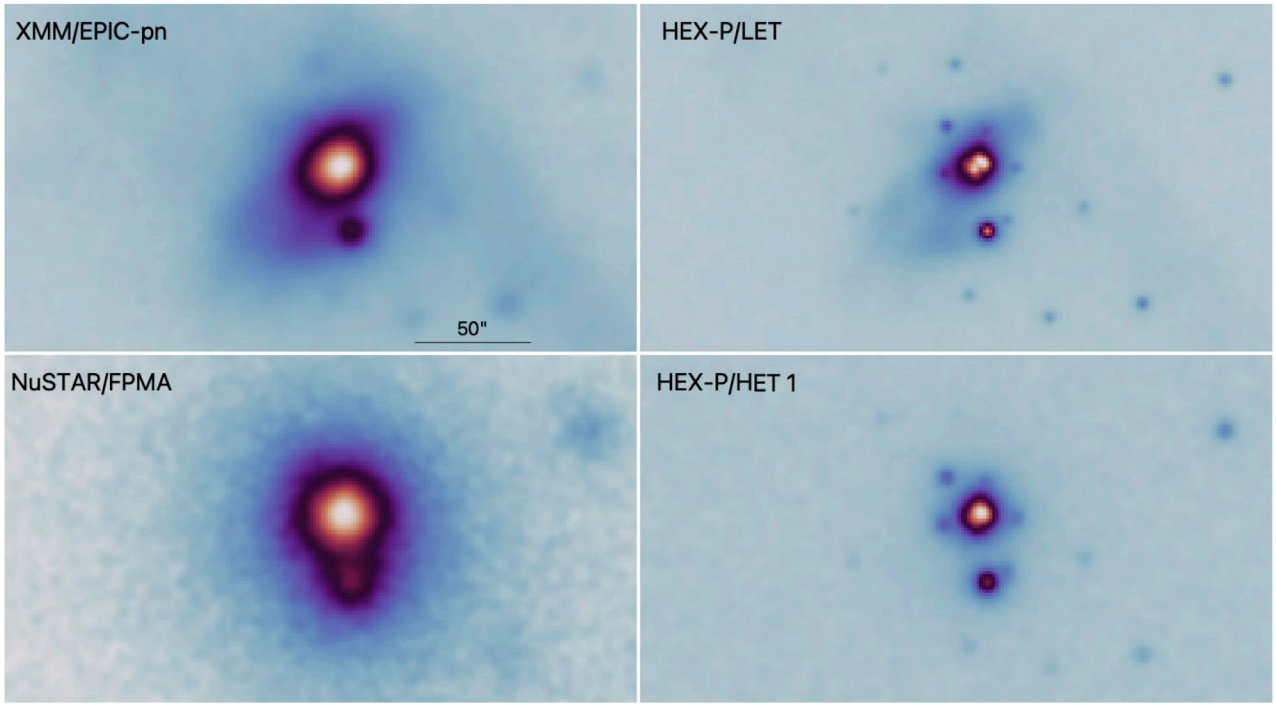

FIGURE 1
1-Ms Simulation of a NGC 253-like starburst galaxy showing the various components including diffuse hot gas and XRBs. Here we compare the performance of *XMM-Newton* and *NuSTAR* [compare to Pietsch et al. (2001), Wik et al. (2014)] with the instruments onboard *HEX-P*, using the procedure described in Section 3.1.2. *HEX-P* is able to resolve most of the bright X-ray sources in nearby galaxies, enabling a detailed study of both the source and diffuse emission. In particular, *HEX-P* is able to resolve and study in detail all ULXs, including the ones with known notable features (pulsations, lines, eclipses; see text), with better sensitivity and equivalent-or-better energy and timing resolution compared to *XMM-Newton* and *NuSTAR*.

between 1 ms and 100 s, and a pulse profile described by a Von Mises distribution with κ between 1 and 5.

We then ran full SIXTE simulations for *HEX-P*, *NuSTAR*, and *XMM-Newton* to produce images such as those shown in Figure 1. To analyze the simulations and estimate count rates from the sources and various components of the background, we used circular source regions centered at the source position with a radius corresponding to half of the half-power diameter of the point spread function used by SIXTE for the simulation.

For each source region, we used the internal description of data in SIXTE to estimate how many photons came from the source *n* (`SRC_ID = n`), how many from the instrumental background (`SRC_ID == -1`) and how many from the sky background `[(SRC_ID != -1)&(SRC_ID != n)]`.

3.2 Pulsar simulations

Assuming that one has averaged enough periodograms to yield normally-distributed powers, Lewin et al. (1988) estimates the significance of the detection of a broad feature against a Poisson background (e.g., a high frequency QPO) in a periodogram as

$$n_\sigma = \frac{1}{2} I r^2 \sqrt{\frac{T_{\rm obs}}{\Delta \nu}} \quad (1)$$

where I is the total count rate (sky, instrument, source), r the rms fractional variability of the QPO over the total flux, $T_{\rm obs}$ the observing time, and $\Delta\nu$ the width of the feature. This means that the observing time necessary to detect a QPO scales with the inverse *fourth power* of the rms.

Pulsar searches are usually performed with single periodograms, or proxies of them such as the Z^2_n statistic (Buccheri et al., 1983) or the Epoch Folding search (Leahy et al., 1983), for which one cannot assume normality of powers. However, it can be shown that a similar dependence on the rms is also valid in this case (Figure 2). Therefore, in order to perform a sensitive search for pulsations, the key ingredient is reducing all components of the background so that the rms amplitude is reduced to the intrinsic source rms. When pulsars are not dominating their fields-of-view, raw sensitivity of an instrument is less important than its ability to separate the target from the other sources. ULXs are borderline in this respect, as they are often relatively bright sources in their host galaxies, but being extragalactic, it is common to observe other ULXs or an active galactic nucleus (AGN) separated by less than a few arcminutes. The vast majority of known ULXs in nearby galaxies can be confidently separated by *HEX-P* (see Section 3.1). In addition, their hard X-ray tail, which is where the pulsed emission is strongest, is covered by the energy range where *HEX-P* is most sensitive. With the typical parameters of ULXs, *HEX-P* can detect pulsations in a fraction of the time it takes *NuSTAR* or *XMM-Newton*, and *HEX-P* can even outperform timing-dedicated, non-focusing instruments,

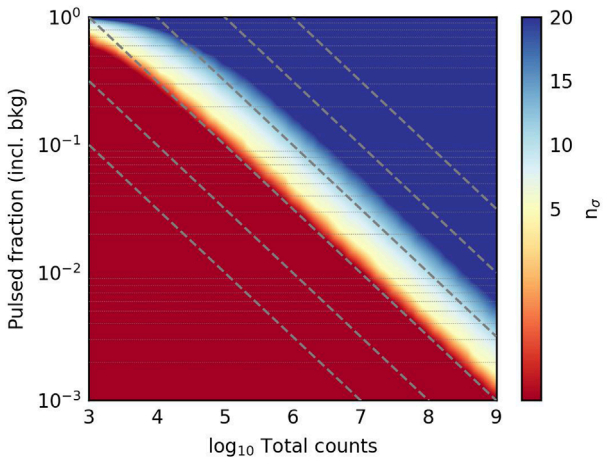

FIGURE 2
Comparison of the single-trial detection significance (in number of sigma) of a quasi-sinusoidal pulsed profile with a Z_n^2 search, given a total number of counts and the pulsed flux fraction (expressed as the counts in the pulse profile divided by the total counts). The sensitivity degrades rapidly when the pulsar is not dominating the emission, and a factor of ~5 lower in pulsed fraction can make a pulsar undetectable. Dashed lines show the expected dependence from a law that scales like Eq. 1.

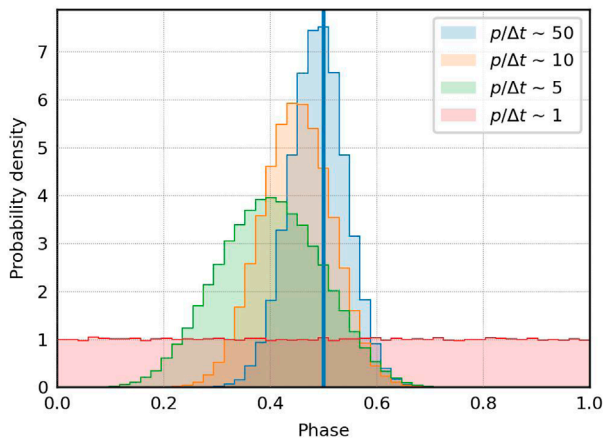

FIGURE 3
Distortion of a pulse profile when the pulse period p is comparable to the frame time Δt. This is relevant for CCD-based detectors like *XMM-Newton*'s cameras (5.7 ms frame time in small window mode) or *HEX-P*/LET (2 ms frame time).

which may have much larger effective areas but far poorer angular resolution.

3.2.1 Simulation setup

To simulate time-variable fluxes, we use inverse transform sampling. By appropriate normalization, a (positive definite) time series can be considered a probability density function. We first calculate its cumulative distribution function (CDF) by simple integration. Then, we generate random values of the CDF by extracting a series of values uniformly distributed between 0 and 1. We then invert this CDF by calculating (through any interpolation algorithm) the time values corresponding to that value of the CDF. This can be applied to a variable aperiodic light curve, for example, generated through the Timmer and Koenig (1995) method, or to the phases of a pulsar given its pulse profile. If we start from pulsar phases, further corrections to these phases can be made to accommodate spin derivatives, with the usual Taylor series expansion $\Delta\phi = \dot{\nu}t + 1/2\ddot{\nu}t^2 + \ldots$. We can further generate integer pulse *number* values, sum them to the pulse phases, and transform them into times by multiplying by the pulse period. These methods are already implemented in the `stingray` (Huppenkothen et al., 2019) and `HENDRICS` (Bachetti, 2018) packages that we use for standalone timing simulations, while the `SIXTE` package takes care of end-to-end simulations (Dauser et al., 2019, see below).

3.2.2 A note on frame time

The frame time of CCD-like detectors reduces the sensitivity to pulsations with periods below 10–50 frame times depending on the profile shape (because of the spread of each frame over multiple phases of the pulsations). Hence, we can expect that the 73 ms frame time in full window of the EPIC-pn camera onboard *XMM-Newton* will greatly reduce sensitivity to sinusoidal pulsations with periods $\lesssim$ 500 ms, and sharp pulsations (e.g., some rotation-powered pulsars) with even much longer periods. In Figure 3, we generated ~100,000 photons with phases following a Von Mises distribution of concentration ($\kappa = 10$), transformed the phases into arrival times by adding an integer pulse number and multiplying by the period, and applied a fixed frame time to the event times. Then, we folded the profiles using the standard procedure of adding a random number uniformly distributed around $\pm\Delta t/2$ to avoid artifacts[4]. The profiles are clearly distorted, losing sharpness and height as the pulse period approaches the sampling period, until the pulsation is not detectable anymore.

XMM-Newton has special data acquisition modes that reduce the frame time while sacrificing field-of-view. For example, the "small window" mode reaches a ~5.7 ms frame time by using only ~1/40th of the pixels. Moreover, the "timing" (0.03 ms) and "burst" (7 μs) modes also sacrifice angular resolution in order to further increase timing precision (Strüder et al., 2001). In contrast, the LET onboard *HEX-P* has a 2 ms frame time in its standard full frame operation mode, which allows the detection of significantly shorter pulse periods than *XMM-Newton*, even when conducting surveys or in crowded fields-of-view, making *HEX-P* a game-changer for extragalactic pulsar searches. The CdTe/CZT-based high-energy instruments such as *NuSTAR* and the HET onboard *HEX-P* have a ~10 μs timing resolution, which is more than enough to detect all known periodic and aperiodic phenomena expected in compact objects ($\lesssim$ 2,000 Hz). In the following, we assume that all pulsars have periods detectable by all the instruments that are being compared ($\gtrsim$ 1 s).

3.2.3 Pulsar searches

We carried out two different procedures to search for (and characterize) pulsations in the simulated data described in

4 See, e.g., the *XMM-Newton* science analysis software documentation, https://xmm-tools.cosmos.esa.int/external/xmm_user_support/documentation/sas_usg/USG/

Section 3.1, one blind search (to evaluate possible confusion of different unresolved candidates) and one directed at known pulsations (using the input periods, and evaluating the increase of detection significance with observing time).

For blind pulsation searches, we selected events from all the known source positions, using extraction regions equal to the HPD of each instrument. We then ran a standard Fourier search with a periodogram, to obtain a list of candidate frequencies (Lovelace and Sutton, 1969). Depending on the source position and the instrument used, there was significant contamination between the sources; this made frequency candidates from nearby sources appear in the search of others. This of course does not represent a problem. Around each pulsar candidate, we ran zoomed searches using the quasi-fast folding algorithm (Bachetti et al., 2020) as implemented in HENDRICS (Bachetti, 2018). This method allows a fast exploration of the frequency-frequency derivative plane around pulse candidates. As a metric for pulse detection we used the H test (de Jager et al., 1989) modified for binned profiles (Bachetti et al., 2021). We are mostly interested in the comparison between the instruments, and all parameters affecting the statistics are assumed the same for each[5] (principally the observing time, which increases the frequency resolution of the FFT and hence the number of trials). We selected a H test statistic of 50 in any instrument as criterion to declare a rough detection. This resulted in ~16 out of 70 sources being detected by one instrument or the other, and in particular some of the ones in the very center of the galaxy. For all these detections, we plot the value of the H test calculated from all instruments at the best frequency from the search in Figure 4. The results show that *HEX-P*'s instruments provide a comparable or higher sensitivity to pulsations compared to *XMM-Newton* and *NuSTAR*. Moreover, the two combined *HEX-P* instruments yield high sensitivity to pulsations in both soft and hard sources, something difficult to achieve with current instruments without complicated coordination. Finally, the LET's short frame time allows for sensitive searches of pulsations at frequencies well above *XMM-Newton*/EPIC-pn's limit.

To measure the expected detection significance of pulsars injected in the SIXTE simulation, we first evaluated the H-test at the injected frequency and the integrated pulse profile over the full simulation, and found the correct number of harmonics M to describe the pulsed profile. We then estimated the variation in the Z^2_M statistic for different exposures and source distances in the following way:

1. We created a grid of exposure times (E) and distances (D) for the source. For each value of E and D, we rescaled all sky counts (background and source) with a E/D^2 law, while the instrumental background was rescaled by exposure alone.
2. For each of the rescaled count estimates, we constructed a model pulse profile, as follows: 1) the theoretical pulse profile, including its intrinsic pulsed fraction, was normalized to an integrated value of 1 and multiplied by the number of source counts; 2) we added a background with the expected counts per bin from the sky and the instrument.

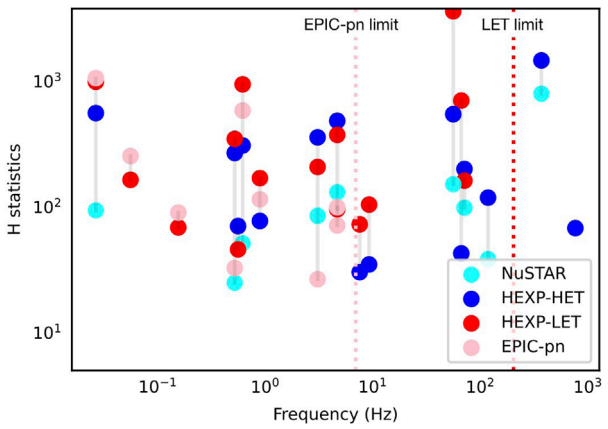

FIGURE 4
Results of a blind search of pulsations described in Section 3.2.3. Lines connect candidates for the same pulsar in different instruments. Some patterns appear: 1) *XMM-Newton*/EPIC-pn and *HEX-P*/LET have similar performance at low frequencies (the balance depends on pn's slightly larger effective area and LET's lower contamination), while HET is always better than *NuSTAR*; 2) EPIC-pn loses sensitivity above ~7 Hz due to its frame time, and LET above ~200 Hz.

3. Finally, we created 100 realizations of the pulse profile by simulating Poisson-distributed random numbers for each bin of the pulse profile, and we calculated the Z^2_M statistic for each realization. We then calculated the false-alarm probability for the average value of the Z^2_M statistic [using Buccheri et al. (1983), as adapted to folded pulsed profiles by Bachetti et al. (2021)] over all realizations, and expressed it in terms of Gaussian sigma values for ease of interpretation. This was then used to form the plots on the right hand side in Figure 5.

Figure 5 shows the detectability of two simulated bright pulsars (not even at a ULX level of brightness), near the nucleus of a galaxy modeled on NGC 253, with different instruments; these provide good examples of what happens when one looks for pulsations from sources in a crowded field and were selected to have a softer and harder spectrum respectively. The detectability of specific pulsars depends on the spectral shape, the fraction of pulsed flux, and the sky and instrumental background. Therefore, the same intrinsic pulsed flux ratio (PFR)[6] can result in very different total PFR (and hence, detectability) in different instruments, depending on sensitivity and angular resolution. In these two cases (and the same consideration is supported by the blind search as well, Figure 4), one can see why the instruments onboard *HEX-P* perform equivalently or better than current focussing instruments like *XMM-Newton* and *NuSTAR*, especially if the source is located in crowded fields or even in peripheral regions of the host galaxy. The angular resolution of *HEX-P* allows the emission from a large number of contaminating sources to be filtered out, improving

5 Here, we are neglecting data loss due to occultation or flaring during the orbit. Taking them into account would advantage *HEX-P* further, because the same exposure would be obtained in shorter observations.

6 Note that with PFR we are comparing the pulsed *flux*, the integral of the AC component of the pulse, to the total flux. The more commonly used pulsed fraction (PF), instead, compares the *amplitude* of the pulsation to the mean or the maximum of the pulse. Our definition is more independent of pulse shape.

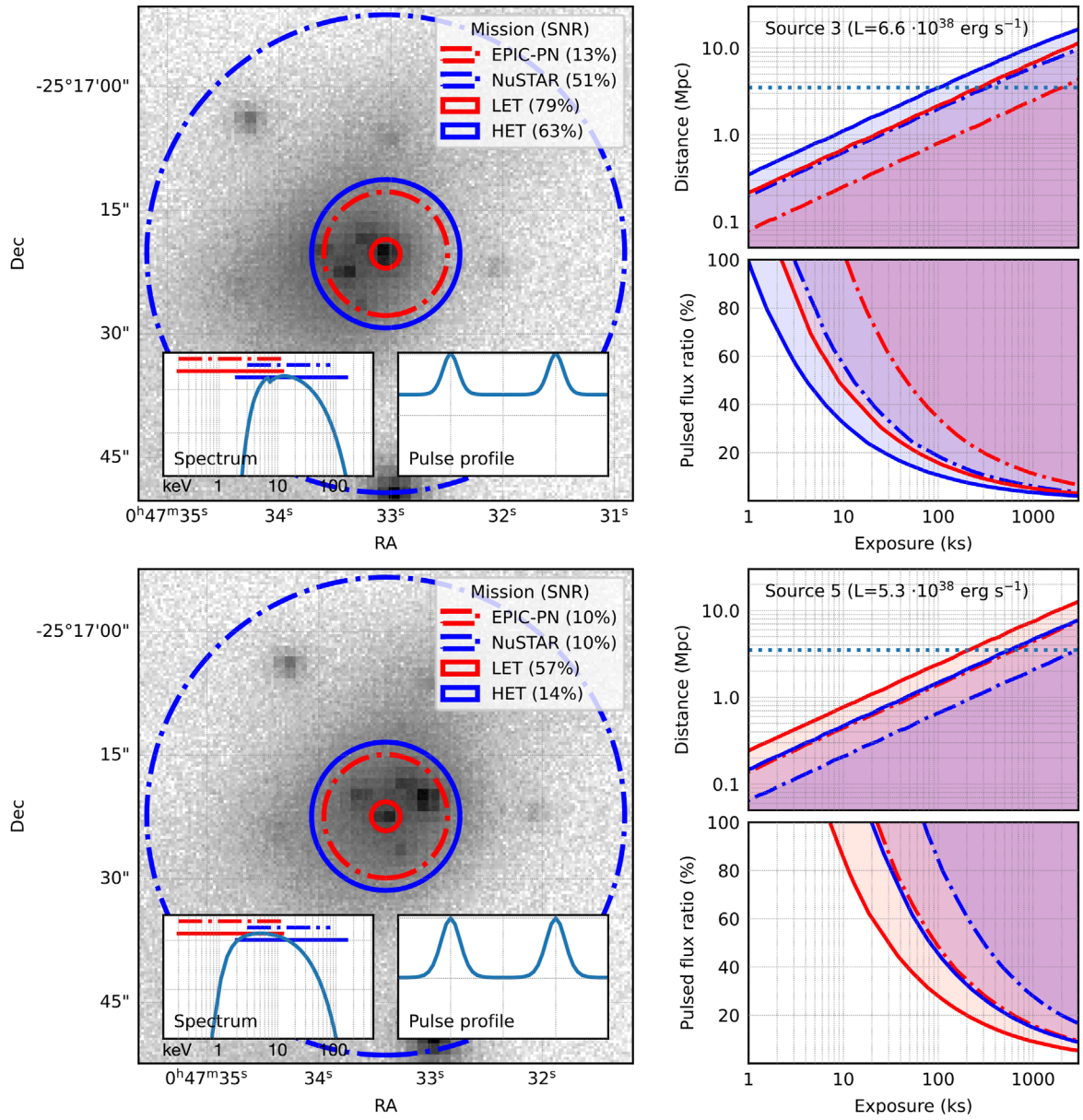

FIGURE 5
The maps on the left show a 1-Msec LET simulation of the central region of NGC 253 using the same setup as Figure 1. Each map is centered on one example source in this region, and the two insets show the spectrum and the pulse profile of the source. Circles indicate the HPD of each instrument. The two sources are only resolved by the LET. The shaded regions on the right of each map show (top) the limiting distance at which we can detect the pulsation (at 5 σ) at the given PFR with different exposures, and (bottom) the limiting intrinsic PFR detectable at the distance of NGC 253 (3.5 Mpc, marked in the top plot as a blue dashed line). Color coding for all line plots indicates different instruments (the band pass in the first inset). *NuSTAR* and *HEX-P*/HET include the flux from two modules. Percentages in the legend indicate the source to background (all components) flux ratio in the region.

the PFR and the pulsation sensitivity, even where the effective area is slightly lower (e.g., *XMM-Newton*/EPIC-pn compared to LET).

3.3 Spectral simulations

As discussed in Section 1, the X-ray spectral continuum of ULXs can be complex, characterized by up to three main components: a low-temperature (<1 keV) thermal component, a hotter 1–3 keV component, which appears broader than the cool one, and a hard component above 10 keV (e.g., Walton et al., 2018b). The latter can appear as a hard excess in the *NuSTAR* band, and may be related to Compton up-scattering of the disk emission, which is not included in the simple accretion disk models typically used [c.f. post-processing of general relativistic magnetohydrodynamical simulations of super-Eddington discs, (Mills et al., 2023)]. In some cases it is likely associated with the accretion column of a NS. The cool thermal component is often modelled with a simple disk-blackbody component (e.g., diskbb in `Xspec`) approximating the

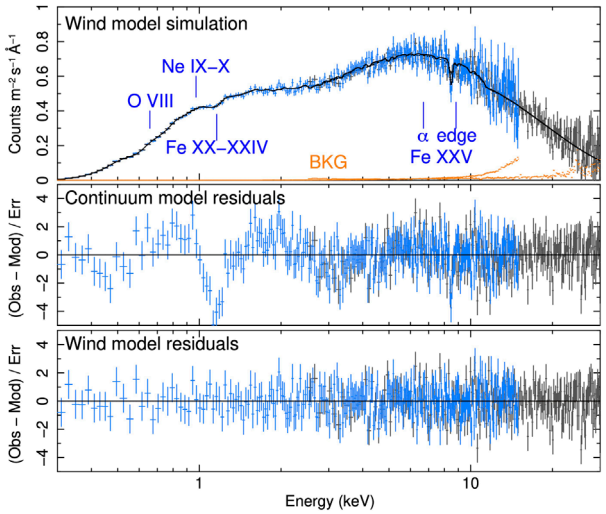

FIGURE 6
500ks *HEX-P* simulation of ULX NGC 1313 X-1 adopting the best-fit multiphase wind model of photoionised emitting and absorbing plasma (Pinto et al., 2020b). The middle panel shows the residuals assuming a continuum-only model (double blackbody plus cutoff powerlaw). The bottom panel shows the residuals to the full wind model. The rest-frame energies of the dominant transitions are labelled. Each component producing emission/absorption lines is detected at $\gtrsim 5\sigma$.

emission from the outer disk and/or wind. The hotter thermal component has a broader spectrum and can be equally described by a slim disk (e.g., diskpbb in `Xspec`) with a temperature-radius law $T \propto R^{-p}$ (with p taking values 0.5–0.75, e.g., Walton et al., 2020) or a thermal Comptonisation component (e.g., nthcomp in `Xspec`, Middleton et al., 2015a). Finally, when identified with a pulsation, the emission from the accretion column can be empirically modelled with a cutoff-powerlaw (CUTOFFPL) with slope $\Gamma = 0.59$ and high-energy cutoff $E_{\rm cut} = 7.9$ keV, which is based on the average parameters found for known ULX pulsars via phase-resolved spectroscopy (e.g., Walton et al., 2018a).

The study of the relationship between the luminosities and temperatures of the thermal components measured in different epochs may be useful in order to obtain valuable information on the evolution and structure of the inner accretion disk. The luminosity-temperature ($L-T$) trends often disagree with the theoretical predictions of sub-Eddington thin discs ($L \propto T^4$) and even show negative slopes consistent with the photosphere of a super-Eddington disk/wind (e.g., Robba et al., 2021). In this regard, *HEX-P* will provide an important improvement with respect to current missions thanks to its high effective area and broad energy coverage. In Walton et al. (2020) (in prep.), for instance, simulations of Holmberg IX X-1 have been performed showcasing how *HEX-P* will enable accurate estimates of the $L-T$ trends. In particular, it will be possible to distinguish the $L-T$ tracks observed at high and low source fluxes [also seen in NGC 1313 X-1 (Walton et al., 2020)], which can indicate dramatic changes in the inner accretion flow.

Once a satisfactory description of the continuum is achieved, spectral residuals can be located [almost ubiquitously: Middleton et al. (2015b)] and, eventually, searches for narrow lines can be performed. This is typically performed through scans that involve a moving Gaussian through a grid of centroid energies (e.g., Pinto et al., 2016). Monte Carlo simulations must be used in order to probe the statistical significance of any putative lines (e.g., Kosec et al., 2021). More recently, the exploration of a large parameter space has been employed through grids of plasma models, which account for multiple emission or absorption lines simultaneously. This boosted the detectability of weak lines such as those from ultrafast outflows (e.g., Kosec et al., 2018; Pinto et al., 2021). The emission lines are primarily produced by Ne K and Fe L ions around 1 keV and the absorption lines from blueshifted O VIII and Ne K/Fe L around 0.8 and 1.2 keV, respectively. Evidence of Fe K around 8–9 keV has also been found, showing the hottest, fastest and most powerful wind component (e.g., Walton et al., 2016b; Brightman et al., 2022). The emission and absorption lines can be well described with models of plasma in photoionization equilibrium, which is expected in the case of winds irradiated by the ULX continuum. Most work in this regard has made use of the `Spex` code (Kaastra et al., 1996), in particular through the `pion` component, although some work also made use of `Xstar` (Kallman and Bautista, 2001; Mendoza et al., 2021) coupled with `Xspec` (Arnaud, 1996). In the latter case, photoionization model grids are computed with `Xstar` and then loaded into `Xspec`, whilst in the former, `Spex` instantaneously fits the continuum, calculates the ionization balance and the model, and fits it to both lines and continuum. An example of *HEX-P*'s performance with regards to continuum modelling and line detection is shown in Section 3.3.2.

3.3.1 Simulation setup

A typical workflow for X-ray spectral simulations involves: 1) defining a theoretical model; 2) defining a count rate $\mathcal{C}$ and observation length $\mathcal{L}$; 3) specifying a set of instrument responses (RMF and ARF); 4) specifying an appropriate background file or a model providing an estimate of the instrumental and sky background contaminating the source region; 5) using a tool that generates a list of $\mathcal{CL}$[7] random X-ray energies following a statistical distribution obtained by the convolution of the spectral model with the instrumental responses.

In our case, the last step in the above list is executed with `Xspec`'s `fakeit` command, using the most recent response files available for each mission (see Sections 3.3.2, 3.3.3), following the procedure from the `Xspec` manual[8] or the equivalent procedure for PyXspec[9]. In order to simulate emission or absorption lines from plasmas in different types of equilibria (collisional or photoionisation) we also used the `Spex` code (Kaastra et al., 1996), which provides up-to-date atomic data, plasma models and a fitting package[10].

3.3.2 Wind features

In order to demonstrate the power of *HEX-P* in studying winds from ULXs by, e.g., achieving a highly significant ($\sim 5\,\sigma$) Fe K

7 Or better, a random number following a Poisson distribution around that value.

8 https://heasarc.gsfc.nasa.gov/xanadu/xspec/manual/node41.html

9 https://heasarc.gsfc.nasa.gov/xanadu/xspec/python/html/extended.html

10 https://spex-xray.github.io/spex-help/index.html

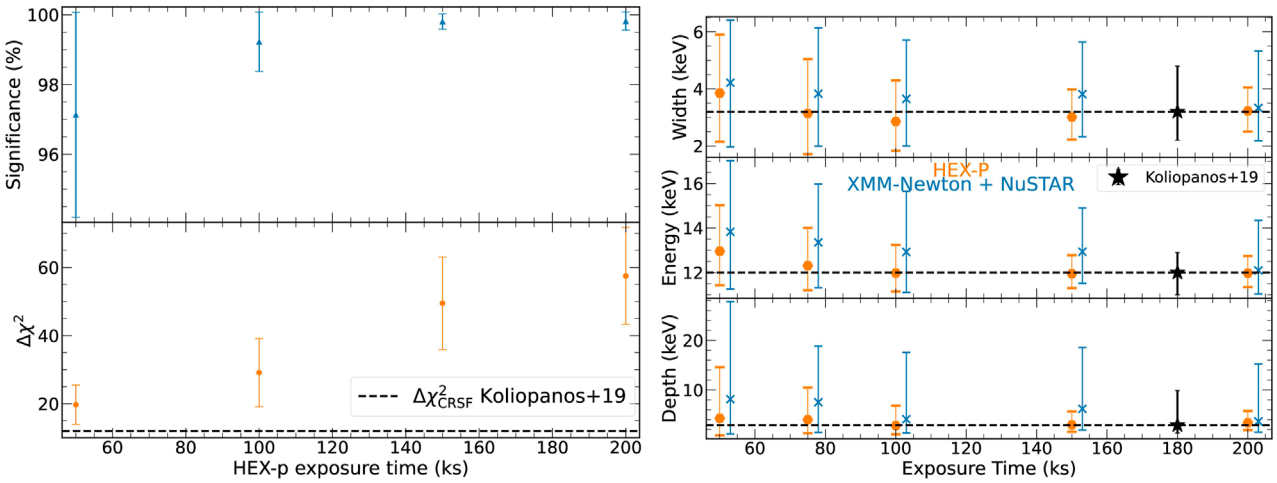

FIGURE 7
HEX-P detection levels and constraints on the putative NGC 300 ULX-1 CRSF. (Left) Line detection significance (top) and $\Delta\chi^2$ fit-improvement (bottom) as a function of exposure time. The error bars represent the spread over 10 realizations (see text for details). The $\Delta\chi^2$ fit-improvement obtained by Koliopanos et al. (2019) using a combined *XMM-Newton* and (~140 ks for EPIC-pn) *NuSTAR* (~180 ks) observation is shown as a dashed line for comparison. (Right) Constraints on the NGC 300 ULX-1 CRSF centroid energy (top) width (middle) and depth (bottom) as a function of exposure time for *HEX-P* (orange) and *XMM-Newton* + *NuSTAR* (blue, values have been shifted slightly horizontally for clarity). The mean best-fit value and mean (90% level) uncertainty are shown after averaging over 25 spectra per exposure time. The stars indicate the constraints obtained by Koliopanos et al. (2019) for comparison.

detection, we performed a simulation of the archetypal ULX NGC 1313 X-1, adopting the model described in Pinto et al. (2020b). The continuum consists of cool (0.2 keV) and hot (2 keV) thermal components and a cut-off powerlaw, the latter dominating above 10 keV with a slope of $\Gamma = 0.59$ and high-energy cutoff $E_{cut} = 7.9$ keV as mentioned above (Walton et al., 2020). Starting from previous work on NGC 1313 X-1, we simulated a deep *HEX-P* observation adopting the best-fit multiphase wind model of photoionised emission (at rest) and absorption (blueshifted by $0.2c$) plasmas [see Pinto et al. (2020b)]. This consists of one PION emission component and two XABS absorption components in Spex. The results are shown in Figure 6. The LET and HET simulated spectra in the top panel show a very strong absorption feature in the soft band above 1 keV from the cooler phase of the wind, and a narrow absorption line just above 8 keV from the hot phase of the wind [mainly Fe XXV; c.f., (Walton et al., 2016b)]. We also highlight the contribution of the wind by removing the emission and absorption lines from the model and refit the simulated spectra with a continuum-only model [double thermal component plus cutoff powerlaw; see Walton et al. (2020)]. Each of the three emission and absorption line components is detected[11] at $\gtrsim 5\sigma$ assuming an exposure of 500 ks, whilst for the weak Fe K lines confidence levels around 3σ are found with 300 ks observations, which are significantly shorter than the 700 ks total *XMM-Newton* and *NuSTAR* observations needed. Moreover, any observation that can detect the Fe K absorption will easily detect the lower energy (~1 keV) absorption as well since the latter typically requires exposures of a few tens of ks for bright ULXs. There are about 10 ULXs with fluence comparable to NGC 1313 X-1 in the Fe K band and a few dozen within a factor of a few (Walton et al., 2022). We therefore be confident that *HEX-P* will enable the first meaningful search for Fe K lines in a statistical sample of ULXs, which will place new constraints on the wind geometry, its outflow and kinetic energy, and improve our understanding of the overall accretion mechanism.

3.3.3 Cyclotron lines

Three (potential) CRSF features have been discussed for ULXs/related sources in the literature: an unusually low-energy ~4.5 keV feature in M51 ULX-8 that could be a proton CRSF [seen by *Chandra*; (Brightman et al., 2018)], an extremely high-energy feature at ~150 keV in the Galactic, Swift J0243+6124 [seen by HXMT; (Kong et al., 2022)], and a potential CRSF at ~13 keV in the ULX pulsar NGC300 ULX1 [seen in a coordinated *XMM-Newton* + *NuSTAR* observation; (Walton et al., 2018a)]. However, the detection of the latter is noted to be somewhat tentative, as the data can also be explained by a more complex continuum model with no CRSF, an issue also discussed by Koliopanos et al. (2019) who argued the more complex continuum model may actually be preferred by the data. Part of the uncertainty is the poorly understood continuum and the limited coverage above ~30 keV offered by *NuSTAR*, which makes it an excellent case-study for *HEX-P*.

In order to estimate the exposure time needed to unambiguously detect the putative line in NGC 300 ULX-1, we have simulated spectral models with and without the feature, using the models reported by Koliopanos et al. (2019) (see their Table 1 where they use a combination of two multi-color disk blackbodies and a powerlaw for the high energy emission, referred to as their MCAE model). We focus our simulations on the MCAE model with and without the line, as this gave the highest (Bayesian) evidence among

11 As determined through $\Delta\chi 2$, using the affected spectral bins as the number of free trials.

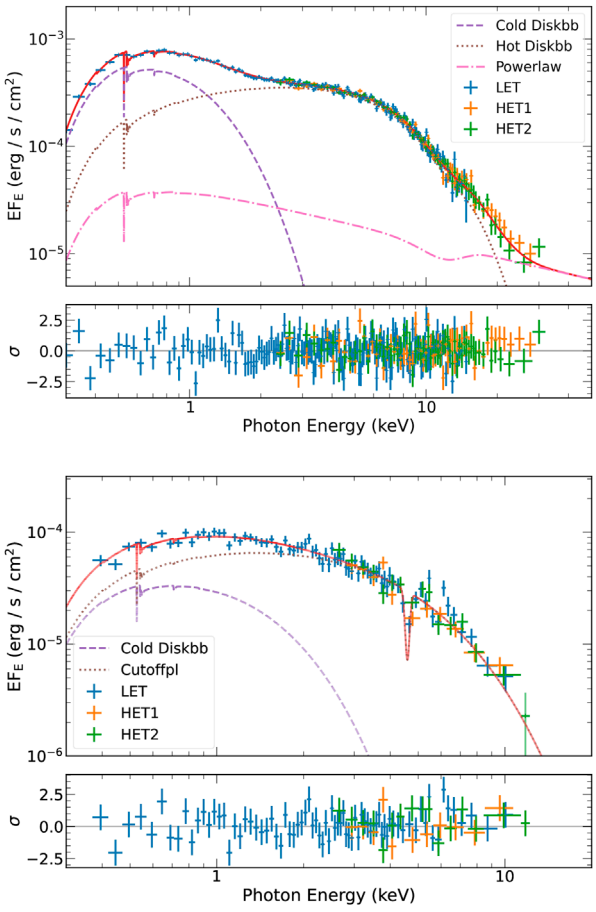

FIGURE 8
(Top) CRSF line in NGC 300 ULX-1 as observed by *HEX-P* in a 200 ks observation. (Bottom) CRSF line in M51 ULX-8 as observed by *HEX-P* in a 100 ks observation.

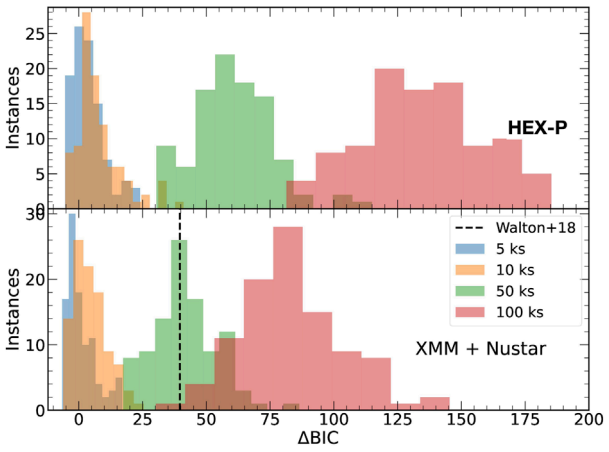

FIGURE 9
ΔBIC between the two competing models presented in Walton et al. (2018a) (a simpler continuum including the CRSF vs. a more complex featureless continuum) fitted to the pulsed component of NGC 3000 ULX1 for *HEX-P* (top) and combined *XMM-Newton* + *NuSTAR* observations (bottom) for different exposure times. 100 realizations are shown for each exposure time, as indicated by the colors. For comparison, we also show the value retrieved by Walton et al. (2018a) using 140 of EPIC-pn, 190 ks of combined EPIC-MOS, and 180 ks of combined *NuSTAR* observations (dashed line). We can see that *HEX-P* would be about a factor 1.5 more effective (notably above ~30 ks) in distinguishing these two different continuum models. Note that the exposure times are given for a quarter of the full pulse cycle and therefore total exposure times would be four times the values shown.

a set of competing models (see their Table 2), but below we also present an alternative case.

We estimated the CRSF detection significance α, using the method from Protassov et al. (2002). To this end, we simulated a single *HEX-P* spectrum (both LET and HET) using the MCAE model with a CRSF line [as reported in Koliopanos et al. (2019)] for exposure times of 50, 100, 150 and 200 ks. We fitted this spectrum with the null hypothesis model of the MCAE model *without* a line and then with the MCAE model *with* the CRSF, recording the single value of $\Delta\chi^2_{\rm CRSF}$ fit-improvement for each exposure time. We then simulated 1,000 spectra from the best-fit null hypothesis model and fitted these with both models, also recording the fit-improvement in each instance (obtaining the distribution of $\Delta\chi^2_{\rm null}$). We compared this fit-improvement distribution $\Delta\chi^2_{\rm null}$ with the $\Delta\chi^2_{\rm CRSF}$ value obtained from the *HEX-P* spectrum that included the CRSF, thereby obtaining the probability of observing a $\Delta\chi^2$ fit-improvement as high as that observed in the original *HEX-P* spectrum (i.e., the line detection significance α). We repeated the whole process 10 times per exposure to estimate the variations in $\Delta\chi^2_{\rm CRSF}$ and α due to Poisson fluctuations only.

The results of our simulations are shown in Figure 7. We see that for a 50 ks exposure, including the line represents a $\Delta\chi^2_{\rm CRSF} \sim 19 \pm 6$ the 1σ uncertainty comes from the spread of the 10 simulations improvement over the null continuum, which translates to a ~97% (2.2σ) detection significance, although the high-energy power-law will be marginally detected. Such a $\Delta\chi^2_{\rm CRSF}$ is already higher than, or comparable to, the value obtained by Koliopanos et al. (2019), who reported a $\Delta\chi^2_{\rm CRSF} = 12$ improvement based on the existing ~140 ks EPIC-pn and 180 ks *NuSTAR* exposure (see Figure 7 for details). For a 100 ks exposure time with *HEX-P*, the line is detected at the ~99% (~2.6σ) confidence level. Here the line provides a $\Delta\chi^2_{\rm CRSF} = 29 \pm 10$ fit-improvement. Finally for exposure times greater than 150 ks, we found the line will be detected comfortably above the 99.73% (3σ) level with $\Delta\chi^2_{\rm CRSF} \sim 50 \pm 14$ and 58 ± 14 for 150 and 200 ks respectively, with the high-energy power-law significantly detected. This final spectrum as seen by *HEX-P* is shown in Figure 8.

We also obtain simulated constraints on the line energy, width and depth, and compare these to those reported by Koliopanos et al. (2019) in Figure 7. We also simulated *XMM-Newton-NuSTAR* observations including all EPIC and both FMPA/B cameras, using responses from a similar epoch to the NGC 300 ULX-1 observations. We note that our latter simulations ignore calibration inaccuracies between *XMM-Newton* and *NuSTAR* detectors, which will only degrade the results presented here, particularly as compared to *HEX-P*. We can see from Figure 7 that *HEX-P* will allow us to obtain tighter constraints on the line properties compared to dedicated *XMM-Newton* + *NuSTAR* observations (about a factor two or even more). As stated above, one of the main uncertainties in the identification of the CRSF in NGC 300

ULX-1 was the nature of the underlying continuum. Walton et al. (2018a) proposed to tackle the problem by performing pulse-phase resolved spectroscopy. In particular, Walton et al. (2018a) isolated the pulsed spectrum by extracting data from the brightest and faintest quarter-phases of the pulse cycle of NGC 300 ULX-1 (and obtained the difference spectrum, i.e., "pulse-on"—"pulse-off"). By doing so, the uncertainty on the continuum is reduced as the 'constant' or non-pulsing component is eliminated. We thus performed additional simulations to examine the ability of *HEX-P* to distinguish between the two different continuum models presented by Walton et al. (2018a).

We simulated separate (LET and HET) spectra for the high (pulse on) and low (pulse off) phases of the pulse cycle of NGC 300 ULX-1 (each spanning 0.25 in phase) using the models of Walton et al. (2018a), i.e., a combination of two non-pulsing blackbodies and a high-energy GABS⊗CUTOFFPL ascribed to the accretion column. We subtracted the two and then fitted the pulsed component with the two competing models presented by Walton et al. (2018a) (a model containing the CRSF line, GABS ⊗ CUTOFFPL, and a more complex featureless continuum, CUTOFFPL ⊗ SIMPL) and retrieved the difference in Bayesian Information Criterion [ΔBIC; (Schwarz, 1978)] between the two models for 100 simulations per exposure time. From Figure 9 we can see that *HEX-P* would be about a factor 1.5 more effective (notably above ~50 ks per phase bin, corresponding to a total 200 ks) than *XMM-Newton* & *NuSTAR* in distinguishing different continuum models, therefore reducing uncertainties related to the presence of CRSF lines in the ULX spectra.

The same procedure as above was followed to explore the ability of *HEX-P* to detect the 4.5 keV CRSF originally detected in the *Chandra* spectrum of M51 ULX-8 by Brightman et al. (2018). We used the models reported by Middleton et al. (2019a), who carried out a more detailed analysis of the continuum (modelled with a soft DISKBB and a CUTOFFPL for the high energy emission). We found that a 50 ks *HEX-P* observation detects the line at the ~97% (2.2σ) level while a 100 ks exposure detects the line in excess of 99.73% (3σ) (to be compared with the 99.98% or 3.8σ detection by *Chandra* in 180 ks). Figure 8 shows the spectrum as observed by *HEX-P*.

Another unsolved problem *HEX-P* will tackle is determining the population of particles producing the CSRF lines. In the case of electrons, further associated lines at the harmonic frequencies are expected, whereas protons are expected to produce lines only at the fundamental frequency [see Staubert et al. (2019) and references therein]. Brightman et al. (2018) were unable to detect any harmonic feature at 9 keV, likely due to the low effective area of *Chandra* in this band. If we assume an additional line with the same properties (width and depth) as the fundamental but at twice the energy, the significance of the CRSF detection (now combined) would obviously increase (for 100 ks, an additional ~ $\Delta\chi^2 = 26$ compared to the case where only the fundamental is present in the spectrum). We found that an exposure of about 800 ks using *HEX-P* would allow us to detect the harmonic at the 99% (2.6σ) level *alone*. At this significance, combining both features will allow us to unambiguously identifying whether the CRSF is due to electrons or protons and thus accurately determine the magnetic field strength close to the NS.

4 Conclusion

As extragalactic sources, every ULX study–population, spectroscopy, temporal analysis–is affected by the sensitivity, angular resolution and instrumental background of X-ray telescopes. All major discoveries in the field of ULXs have been driven by instruments combining focusing capabilities and effective area over the ~0.3 – 30 keV band, such as the combination of *XMM-Newton* and *NuSTAR*. However, many galaxies containing ULXs are still unresolved by these two instruments, e.g., M51 and NGC 253. In addition, the effectiveness of multi-instrument analysis is lowered by the difficulties of retrieving simultaneous observations.

HEX-P's low- and high-energy telescopes ensure broadband simultaneous coverage of the X-ray spectrum and excellent angular resolution, significantly improved over both *XMM-Newton* (for the LET) and *NuSTAR* (for the HETs). Thanks to the lower background ensured by its small point-spread function, *HEX-P* facilitates the identification of ULXs through their distinct curved spectra even at large distances.

The design of the *HEX-P* mission would make it the ideal facility to shed light on a large number of questions regarding ULXs and super-Eddington accretion in general. In particular, broad-band and good energy resolution spectra would lead to a deep understanding of the balance between the mass inflow and outflow. *HEX-P* will also enrich ULX population studies, for example, by identifying the presence of NSs in ULXs through the detection of pulsations and CRSFs with significantly higher fidelity than existing missions. As shown in Section 3.2, *HEX-P* surpasses the sensitivity of *NuSTAR* and *XMM-Newton* in detecting pulsations from sources in crowded fields, especially ULXs. As a result, *HEX-P* extends the range for detecting pulsars to distances 2–5 times farther than currently achievable, thereby probing a much larger (8–125 times) volume. This will permit access to a statistically significant population of bright extragalactic X-ray pulsars for the very first time. Further demonstration of *HEX-P*'s capabilities in pulsar searches in crowded environments can be found in Mori et al. (Galactic Center) and Alford et al. (2023) (Magnetars, CCOs) in this volume.

In addition to the above, the L1 orbit of *HEX-P* enables a continuous observation of a large fraction of the sky, without Earth occultation (an issue for *NuSTAR*, which is located in a low Earth orbit) or increased particle background from the Van Allen belts (an issue for *XMM-Newton* and *Chandra*, with their highly elliptical orbits). This allows a significantly shorter "clock time" (actual time spent observing, as opposed to clean source exposure), while the broad bandpass of *HEX-P* eliminates the issues due to differing observation windows when coordinating satellites in different orbits (Middleton et al., 2017). This makes *HEX-P* more efficient, enabling observations of more sources in a given amount of time, with much longer exposure times for observations constrained by clock time (e.g., coordinated observations, orbital measurements).

In summary, the *HEX-P* mission concept holds tremendous promise for advancing our understanding of ULXs and the physics behind super-Eddington accretion. Its broad energy coverage, improved sensitivity, and exceptional spectral and timing capabilities establish it as a powerful tool for investigating ULXs and the fundamental physics at play.

Data availability statement

The raw data supporting the conclusion of this article will be made available by the authors, without undue reservation.

Author contributions

MaB: Conceptualization, Formal Analysis, Investigation, Software, Supervision, Visualization, Writing–original draft, Writing–review and editing. MM: Conceptualization, Supervision, Writing–original draft, Writing–review and editing. CP: Formal Analysis, Investigation, Methodology, Visualization, Writing–original draft. AG: Formal Analysis, Investigation, Methodology, Visualization, Writing–original draft. DW: Conceptualization, Supervision, Writing–review and editing. MuB: Writing–review and editing, Conceptualization. BL: Writing–review and editing, Methodology, Software. TR: Writing–review and editing, Conceptualization. GV: Writing–review and editing, Conceptualization, Investigation, Methodology. JA: Writing–review and editing. RA: Writing–review and editing. EA: Writing–review and editing. LD: Writing–review and editing. HEa: Writing–review and editing. HEl: Writing–review and editing. JG: Writing–review and editing, Funding acquisition, Supervision. GL: Writing–review and editing. AJ: Writing–review and editing. KMa: Writing–review and editing, Funding acquisition, Supervision. CM: Writing–review and editing. SM: Writing–review and editing. KMo: Writing–review and editing, Software. FP: Writing–review and editing. KO: Writing–review and editing. MP: Writing–review and editing. DS: Writing–review and editing, Funding acquisition, Supervision. GY: Writing–review and editing. AW: Writing–review and editing.

Funding

The author(s) declare financial support was received for the research, authorship, and/or publication of this article. MaB was funded in part by PRIN TEC INAF 2019 "SpecTemPolar!—Timing analysis in the era of high-throughput photon detectors." TR acknowledges funding from STFC as part of the consolidated grants ST/T000244/1 and ST/X001075/1. GV acknowledges support by Hellenic Foundation for Research and Innovation (H.F.R.I.) under the "3rd Call for H.F.R.I. Research Projects to support Postdoctoral Researchers" through the project ASTRAPE (Project ID 7802). The work of DS was carried out at the Jet Propulsion Laboratory, California Institute of Technology, under a contract with NASA.

Conflict of interest

The authors declare that the research was conducted in the absence of any commercial or financial relationships that could be construed as a potential conflict of interest.

Publisher's note

All claims expressed in this article are solely those of the authors and do not necessarily represent those of their affiliated organizations, or those of the publisher, the editors and the reviewers. Any product that may be evaluated in this article, or claim that may be made by its manufacturer, is not guaranteed or endorsed by the publisher.

References

Alford, J. A. J., Younes, G. A., Wadiasingh, Z., Abdelmaguid, M., An, H., Bachetti, M., et al. (2023). The high energy X-ray probe (HEX-P): magnetars and other isolated neutron stars. arXiv:2311.04739.

Amato, R., Gúrpide, A., Webb, N. A., Godet, O., and Middleton, M. J. (2023). The ultraluminous X-ray source M 81 X-6: a weakly magnetised neutron star with a precessing accretion disc? *Astronomy Astrophysics* 669, A130. doi:10.1051/0004-6361/202244576

Arnaud, K. A. (1996). "XSPEC: the first ten years," in *Astronomical data analysis software and systems V*. Editors G. H. Jacoby, and J. Barnes, 17.

Atapin, K., Fabrika, S., and Caballero-García, M. D. (2019). Ultraluminous X-ray sources with flat-topped noise and QPO. *Mon. Notices R. Astronomical Soc.* 486, 2766–2779. doi:10.1093/mnras/stz1027

Bachetti, M. (2018). *HENDRICS: high ENergy data reduction interface from the command shell*. Astrophysics Source Code Library. ascl:1805.019.

Bachetti, M., Harrison, F. A., Walton, D. J., Grefenstette, B. W., Chakrabarty, D., Fürst, F., et al. (2014). An ultraluminous X-ray source powered by an accreting neutron star. *Nat* 514, 202–204. doi:10.1038/nature13791

Bachetti, M., Heida, M., Maccarone, T., Huppenkothen, D., Israel, G. L., Barret, D., et al. (2022). Orbital decay in M82 X-2. *ApJ* 937, 125. doi:10.3847/1538-4357/ac8d67

Bachetti, M., Maccarone, T. J., Brightman, M., Brumback, M. C., Fürst, F., Harrison, F. A., et al. (2020). All at once: transient pulsations, spin-down, and a glitch from the pulsating ultraluminous X-ray source M82 X-2. *ApJ* 891, 44. doi:10.3847/1538-4357/ab6d00

Bachetti, M., Pilia, M., Huppenkothen, D., Ransom, S. M., Curatti, S., and Ridolfi, A. (2021). Extending the Z 2 n and H statistics to generic pulsed profiles. *ApJ* 909, 33. doi:10.3847/1538-4357/abda4a

Bachetti, M., Rana, V., Walton, D. J., Barret, D., Harrison, F. A., Boggs, S. E., et al. (2013). The ultraluminous X-ray sources NGC 1313 X-1 and X-2: a broadband study with NuSTAR and xmm-Newton. *ApJ* 778, 163. doi:10.1088/0004-637X/778/2/163

Basko, M. M., and Sunyaev, R. A. (1976). The limiting luminosity of accreting neutron stars with magnetic fields. *MNRAS* 175, 395–417. doi:10.1093/mnras/175.2.395

Belfiore, A., Esposito, P., Pintore, F., Novara, G., Salvaterra, R., De Luca, A., et al. (2020). Diffuse X-ray emission around an ultraluminous X-ray pulsar. *Nat. Astron.* 4, 147–152. doi:10.1038/s41550-019-0903-z

Belloni, T., and Hasinger, G. (1990). An atlas of aperiodic variability in HMXB. *A&A* 230, 103–119.

Brice, N., Zane, S., Turolla, R., and Wu, K. (2021). Super-eddington emission from accreting, highly magnetized neutron stars with a multipolar magnetic field. *Mon. Notices R. Astronomical Soc.* 504, 701–715. doi:10.1093/mnras/stab915

Brightman, M., Harrison, F., Walton, D. J., Fuerst, F., Hornschemeier, A., Zezas, A., et al. (2016). Spectral and temporal properties of the ultraluminous X-ray pulsar in M82 from 15 years of Chandra observations and analysis of the pulsed emission using NuSTAR. *ApJ* 816, 60. doi:10.3847/0004-637X/816/2/60

Brightman, M., Harrison, F. A., Fürst, F., Middleton, M. J., Walton, D. J., Stern, D., et al. (2018). Magnetic field strength of a neutron-star-powered ultraluminous X-ray source. *Nat. Astron.* 2, 312–316. doi:10.1038/s41550-018-0391-6

Brightman, M., Kosec, P., Fürst, F., Earnshaw, H., Heida, M., Middleton, M. J., et al. (2022). An 8.56 keV absorption line in the hyperluminous X-ray source in NGC 4045: ultrafast outflow or cyclotron line? *Astrophysical J.* 929, 138. doi:10.3847/1538-4357/ac5e37

Buccheri, R., Bennett, K., Bignami, G. F., Bloemen, J. B. G. M., Boriakoff, V., Caraveo, P. A., et al. (1983). Search for pulsed gamma-ray emission from radio pulsars in the COS-B data. *A&A* 128, 245–251.

Carpano, S., Haberl, F., Maitra, C., and Vasilopoulos, G. (2018). Discovery of pulsations from NGC 300 ULX1 and its fast period evolution. *MNRAS Let.* 476, L45–L49. doi:10.1093/mnrasl/sly030

Connors, R., Tomsick, J., Draghis, P., Coughenour, B., Shaw, A., Garcia, J., et al. (2023). The high energy X-ray probe (HEX-P): probing accretion onto stellar mass black holes. *arXiv e-prints*. arXiv:2311.04782.

Dall'Osso, S., Perna, R., and Stella, L. (2015). NuSTAR J095551+6940.8: a highly magnetized neutron star with super-Eddington mass accretion. *MNRAS* 449, 2144–2150. doi:10.1093/mnras/stv170

Dauser, T., Falkner, S., Lorenz, M., Kirsch, C., Peille, P., Cucchetti, E., et al. (2019). SIXTE: a generic X-ray instrument simulation toolkit. *Astronomy Astrophysics* 630, A66. doi:10.1051/0004-6361/201935978

de Jager, O. C., Raubenheimer, B. C., and Swanepoel, J. W. H. (1989). *A poweful test for weak periodic signals with unknown light curve shape in sparse data 221*, 180–190.

Earnshaw, H. P., Roberts, T. P., and Sathyaprakash, R. (2018). Searching for propeller-phase ULXs in the XMM-Newton serendipitous source catalogue. *MNRAS* 476, 4272–4277. doi:10.1093/mnras/sty501

Ekşi, K. Y., Andaç, I. C., Çıkıntoğlu, S., Gençali, A. A., Güngör, C., and Öztekin, F. (2015). The ultraluminous X-ray source NuSTAR J095551+6940.8: a magnetar in a high-mass X-ray binary. *MNRAS Let.* 448, L40–L42. doi:10.1093/mnrasl/slu199

El Byad, H. (2021). *Studying the aperiodic X-ray variability of the Ultraluminous X-ray sources in the M82 Galaxy*.

Eraerds, T., Antonelli, V., Davis, C., Hall, D., Hetherington, O., Holland, A., et al. (2021). Enhanced simulations on the athena/wide field imager instrumental background. *J. Astronomical Telesc. Instrum. Syst.* 7, 034001. doi:10.1117/1.JATIS.7.3.034001

Evans, I. N., Primini, F. A., Glotfelty, K. J., Anderson, C. S., Bonaventura, N. R., Chen, J. C., et al. (2010). THE CHANDRA SOURCE CATALOG. *ApJS* 189, 37–82. doi:10.1088/0067-0049/189/1/37

Evans, I. N., Primini, F. A., Miller, J. B., Evans, J. D., Allen, C. E., Anderson, C. S., et al. (2020). *Chandra Source Catalog — A Billion X-ray Photons* 235, 154–205.

Fabbiano, G. (2006). Populations of X-ray sources in galaxies. *Annu. Rev. Astronomy Astrophysics* 44, 323–366. doi:10.1146/annurev.astro.44.051905.092519

Fabrika, S. N., Atapin, K. E., Vinokurov, A. S., and Sholukhova, O. N. (2021). Ultraluminous X-ray sources. *Astrophys. Bull.* 76, 6–38. doi:10.1134/S1990341321010077

Farrell, S. A., Webb, N. A., Barret, D., Godet, O., and Rodrigues, J. M. (2009). An intermediate-mass black hole of over 500 solar masses in the galaxy ESO243-49. *Nat* 460, 73–75. doi:10.1038/nature08083

Fragos, T., Lehmer, B. D., Naoz, S., Zezas, A., and Basu-Zych, A. (2013). Energy feedback from X-ray binaries in the early universe. *ApJL* 776, L31. doi:10.1088/2041-8205/776/2/L31

Fürst, F., Walton, D. J., Harrison, F. A., Stern, D., Barret, D., Brightman, M., et al. (2016). Discovery of coherent pulsations from the ultraluminous X-ray source NGC 7793 P13. *ApJL* 831, L14. doi:10.3847/2041-8205/831/2/L14

Fürst, F., Walton, D. J., Israel, G. L., Bachetti, M., Barret, D., Brightman, M., et al. (2023). Probing the nature of the low state in the extreme ultraluminous X-ray pulsar NGC 5907 ULX1. *A&A* 672, A140. doi:10.1051/0004-6361/202245048

Ghosh, P., and Lamb, F. K. (1979). Accretion by rotating magnetic neutron stars. III - accretion torques and period changes in pulsating X-ray sources. *ApJ* 234, 296–316. doi:10.1086/157498

Gladstone, J. C., Roberts, T. P., and Done, C. (2009). The ultraluminous state. *MNRAS* 397, 1836–1851. doi:10.1111/j.1365-2966.2009.15123.x

Gúrpide, A., Godet, O., Koliopanos, F., Webb, N., and Olive, J. F. (2021a). Long-term X-ray spectral evolution of ultraluminous X-ray sources: implications on the accretion flow geometry and the nature of the accretor. *A&A* 649, A104. doi:10.1051/0004-6361/202039572

Gúrpide, A., Godet, O., Vasilopoulos, G., Webb, N. A., and Olive, J. F. (2021b). Discovery of a recurrent spectral evolutionary cycle in the ultra-luminous X-ray sources Holmberg II X-1 and NGC 5204 X-1. *A&A* 654, A10. doi:10.1051/0004-6361/202140781

Gúrpide, A., Parra, M., Godet, O., Contini, T., and Olive, J. F. (2022). MUSE spectroscopy of the ULX NGC 1313 X-1: a shock-ionised bubble, an X-ray photoionised nebula, and two supernova remnants. *A&A* 666, A100. doi:10.1051/0004-6361/202142229

Harrison, F. A., Craig, W. W., Christensen, F. E., Hailey, C. J., Zhang, W. W., Boggs, S. E., et al. (2013). The nuclear spectroscopic telescope array (NuSTAR) high-energy X-ray mission. *ApJ* 770, 103. doi:10.1088/0004-637X/770/2/103

Huppenkothen, D., Bachetti, M., Stevens, A. L., Migliari, S., Balm, P., Hammad, O., et al. (2019). Stingray: a modern Python library for spectral timing. *ApJ* 881, 39. doi:10.3847/1538-4357/ab258d

Israel, G. L., Belfiore, A., Stella, L., Esposito, P., Casella, P., De Luca, A., et al. (2017). An accreting pulsar with extreme properties drives an ultraluminous x-ray source in NGC 5907. *Science* 355, 817–819. doi:10.1126/science.aai8635

Jansen, F., Lumb, D., Altieri, B., Clavel, J., Ehle, M., Erd, C., et al. (2001). XMM-Newton observatory. I. The spacecraft and operations. *A&A* 365, L1–L6. doi:10.1051/0004-6361:20000036

Jiang, Y.-F., Stone, J. M., and Davis, S. W. (2014). A global three-dimensional radiation magneto-hydrodynamic simulation of super-eddington accretion disks. *ApJ* 796, 106. doi:10.1088/0004-637X/796/2/106

Kaaret, P., Feng, H., and Roberts, T. P. (2017). Ultraluminous X-ray sources. *Annu. Rev. Astronomy Astrophysics* 55, 303–341. doi:10.1146/annurev-astro-091916-055259

Kaastra, J. S., Mewe, R., and Nieuwenhuijzen, H. (1996). "SPEX: a new code for spectral analysis of X & UV spectra," in *UV and X-ray spectroscopy of astrophysical and laboratory plasmas*, 411–414.

Kallman, T., and Bautista, M. (2001). Photoionization and high-density gas. *Astrophysical J. Suppl. Ser.* 133, 221–253. doi:10.1086/319184

Khan, N., Middleton, M. J., Wiktorowicz, G., Dauser, T., Roberts, T. P., and Wilms, J. (2021). The impact of precession on the observed population of ULXs. *MNRAS*. doi:10.1093/mnras/stab3049

King, A., Lasota, J.-P., and Kluźniak, W. (2017). Pulsing ULXs: tip of the iceberg? *MNRAS Let.* 468, L59–L62. doi:10.1093/mnrasl/slx020

King, A., Lasota, J.-P., and Middleton, M. (2023). Ultraluminous X-ray sources. *New Astron. Rev.* 96, 101672. doi:10.1016/j.newar.2022.101672

King, A. L., Miller, J. M., Raymond, J., Fabian, A. C., Reynolds, C. S., Kallman, T. R., et al. (2012). An extreme X-ray disk wind in the black hole candidate IGR j17091-3624. *ApJL* 746, L20. doi:10.1088/2041-8205/746/2/L20

King, A. R., Davies, M. B., Ward, M. J., Fabbiano, G., and Elvis, M. (2001). Ultraluminous X-ray sources in external galaxies. *ApJ* 552, L109–L112. doi:10.1086/320343

Koliopanos, F., Vasilopoulos, G., Buchner, J., Maitra, C., and Haberl, F. (2019). Investigating ULX accretion flows and cyclotron resonance in NGC 300 ULX1. *A&A* 621, A118. doi:10.1051/0004-6361/201834144

Kong, L.-D., Zhang, S., Zhang, S.-N., Ji, L., Doroshenko, V., Santangelo, A., et al. (2022). Insight-HXMT discovery of the highest-energy CRSF from the first galactic ultraluminous X-ray pulsar Swift J0243.6+6124. *ApJL* 933, L3. doi:10.3847/2041-8213/ac7711

Kosec, P., Pinto, C., Reynolds, C. S., Guainazzi, M., Kara, E., Walton, D. J., et al. (2021). Ionized emission and absorption in a large sample of ultraluminous X-ray sources. *MNRAS* 508, 3569–3588. doi:10.1093/mnras/stab2856

Kosec, P., Pinto, C., Walton, D. J., Fabian, A. C., Bachetti, M., Brightman, M., et al. (2018). Evidence for a variable ultrafast outflow in the newly discovered ultraluminous pulsar NGC 300 ULX-1. *Mon. Notices R. Astronomical Soc.* 479, 3978–3986. doi:10.1093/mnras/sty1626

Leahy, D. A., Elsner, R. F., and Weisskopf, M. C. (1983). On searches for periodic pulsed emission - the Rayleigh test compared to epoch folding. *ApJ* 272, 256. doi:10.1086/161288

Lehmer, B. D., Garofali, K., Binder, B. A., Fornasini, F., Vulic, N., Zezas, A., et al. (2023). The high energy X-ray probe: resolved X-ray populations in extragalactic environments. *arXiv e-prints*. arXiv:2311.04735.

Lewin, W. H. G., van Paradijs, J., and van der Klis, M. (1988). A review of quasi-periodic oscillations in low-mass X-ray binaries. *SSRv* 46, 273–377. doi:10.1007/BF00212242

Lovelace, R. V. E., Sutton, J. M., and Salpeter, E. E. (1969). Digital search methods for pulsars. *Nat* 222, 231–233. doi:10.1038/222231a0

Luangtip, W., Roberts, T. P., and Done, C. (2016). The X-ray spectral evolution of the ultraluminous X-ray source Holmberg IX X-1. *MNRAS* 460, 4417–4432. doi:10.1093/mnras/stw1282

Luangtip, W., Roberts, T. P., Mineo, S., Lehmer, B. D., Alexander, D. M., Jackson, F. E., et al. (2015). A deficit of ultraluminous X-ray sources in luminous infrared galaxies. *Mon. Notices R. Astronomical Soc.* 446, 470–492. doi:10.1093/mnras/stu2086

Ludlam, R. M., Malacaria, C., Sokolova-Lapa, E., Fuerst, F., Pradhan, P., Shaw, A. W., et al. (2023). The high energy X-ray probe (HEX-P): a new window into neutron star accretion. *arXiv e-prints*. arXiv:2311.04687.

MacKenzie, A. D. A., Roberts, T. P., and Walton, D. J. (2023). The hyperluminous X-ray source population. *Astron. Nachrichten* 344, 20230028. easna. doi:10.1002/asna.20230028

Madsen, K. K, García, J. A., Stern, D., Armini, R., Basso, S., Coutinho, D., et al. (2023). The High Energy X-ray Probe (HEX-P): Instrument and Mission Profile. *arXiv*. doi:10.48550/arXiv.2312.04678

Meidinger, N., Albrecht, S., Beitler, C., Bonholzer, M., Emberger, V., Frank, J., et al. (2020). "Development status of the wide field imager instrument for Athena," in Society

of Photo-Optical Instrumentation Engineers (SPIE) Conference Series, 11444, 114440T. doi:10.1117/12.2560507

Mendoza, C., Bautista, M. A., Deprince, J., García, J. A., Gatuzz, E., Gorczyca, T. W., et al. (2021). The XSTAR atomic database. *Atoms* 9, 12. doi:10.3390/atoms9010012

Middleton, M., Gúrpide, A., and Walton, D. J. (2023). Propeller states in locally supercritical ULXs. *Mon. Notices R. Astronomical Soc.* 519, 2224–2234. doi:10.1093/mnras/stac3380

Middleton, M. J., Brightman, M., Pintore, F., Bachetti, M., Fabian, A. C., Fürst, F., et al. (2019a). On the magnetic field in M51 ULX-8. *MNRAS* 486, 2–9. doi:10.1093/mnras/stz436

Middleton, M. J., Casella, P., Gandhi, P., Bozzo, E., Anderson, G., Degenaar, N., et al. (2017). Paving the way to simultaneous multi-wavelength astronomy. *New Astron. Rev.* 79, 26–48. doi:10.1016/j.newar.2017.07.002

Middleton, M. J., Fragile, P. C., Bachetti, M., Brightman, M., Jiang, Y. F., Ho, W. C. G., et al. (2018). Lense-Thirring precession in ULXs as a possible means to constrain the neutron star equation of state. *MNRAS* 475, 154–166. doi:10.1093/mnras/stx2986

Middleton, M. J., Fragile, P. C., Ingram, A., and Roberts, T. P. (2019b). The Lense-Thirring timing-accretion plane for ULXs. *MNRAS* 489, 282–296. doi:10.1093/mnras/stz2005

Middleton, M. J., Heil, L., Pintore, F., Walton, D. J., and Roberts, T. P. (2015a). A spectral-timing model for ULXs in the supercritical regime. *MNRAS* 447, 3243–3263. doi:10.1093/mnras/stu2644

Middleton, M. J., Higginbottom, N., Knigge, C., Khan, N., and Wiktorowicz, G. (2022). Thermally driven winds in ultraluminous X-ray sources. *MNRAS* 509, 1119–1126. doi:10.1093/mnras/stab2991

Middleton, M. J., and King, A. (2017). Predicting ultraluminous X-ray source demographics from geometrical beaming. *MNRAS* 470, L69–L71. doi:10.1093/mnrasl/slx079

Middleton, M. J., Walton, D. J., Fabian, A., Roberts, T. P., Heil, L., Pinto, C., et al. (2015b). Diagnosing the accretion flow in ultraluminous X-ray sources using soft X-ray atomic features. *MNRAS* 454, 3134–3142. doi:10.1093/mnras/stv2214

Middleton, M. J., Walton, D. J., Roberts, T. P., and Heil, L. (2014). Broad absorption features in wind-dominated ultraluminous X-ray sources? *MNRAS* 438, L51–L55. doi:10.1093/mnrasl/slt157

Miller, J. M., Fabbiano, G., Miller, M. C., and Fabian, A. C. (2003). X-ray spectroscopic evidence for intermediate-mass black holes: cool accretion disks in two ultraluminous X-ray sources. *ApJ* 585, L37–L40. doi:10.1086/368373

Mills, B. S., Davis, S. W., Jiang, Y.-F., and Middleton, M. J. (2023). *Spectral calculations of 3D RMHD simulations of super-Eddington accretion onto a stellar-mass black hole. arXiv e-prints , arXiv:2304.*07977. doi:10.48550/arXiv.2304.07977

Mushtukov, A. A., Suleimanov, V. F., Tsygankov, S. S., and Ingram, A. (2017). Optically thick envelopes around ULXs powered by accreating neutron stars. *Mon. Notices R. Astronomical Soc.* 467, stx141–1208. doi:10.1093/mnras/stx141

Mushtukov, A. A., Suleimanov, V. F., Tsygankov, S. S., and Poutanen, J. (2015). On the maximum accretion luminosity of magnetized neutron stars: connecting X-ray pulsars and ultraluminous X-ray sources. *MNRAS* 454, 2539–2548. doi:10.1093/mnras/stv2087

Nandra, K., Barret, D., Barcons, X., Fabian, A., den Herder, J.-W., Piro, L., et al. (2013). *The hot and energetic universe: a white paper presenting the science theme motivating the Athena+ mission. arXiv e-prints , arXiv:1306.*2307. doi:10.48550/arXiv.1306.2307

Neilsen, J., and Degenaar, N. (2023). *High-resolution spectroscopy of X-ray binaries. arXiv e-prints , arXiv:2304.05412.* doi:10.48550/arXiv.2304.05412

Ohsuga, K., and Mineshige, S. (2011). Global structure of three distinct accretion flows and outflows around black holes from two-dimensional radiation-magnetohydrodynamic simulations. *ApJ* 736, 2. doi:10.1088/0004-637X/736/1/2

Pakull, M. W., and Mirioni, L. (2002). *Optical counterparts of ultraluminous X-ray sources.* arXiv e-prints , astro-ph/0202488. doi:10.48550/arXiv.astro-ph/0202488

Pasham, D. R., and Strohmayer, T. E. (2013). Can the 62 Day X-ray period of ULX M82 X-1 Be due to a precessing accretion disk? *ApJL* 774, L16. doi:10.1088/2041-8205/774/2/L16

Pietsch, W., Roberts, T. P., Sako, M., Freyberg, M. J., Read, A. M., Borozdin, K. N., et al. (2001). XMM-Newton observations of NGC 253: resolving the emission components in the disk and nuclear area. *Astronomy Astrophysics* 365, L174–L180. doi:10.1051/0004-6361:20000068

Pinto, C., Alston, W., Soria, R., Middleton, M. J., Walton, D. J., Sutton, A. D., et al. (2017). From ultraluminous X-ray sources to ultraluminous supersoft sources: NGC 55 ULX, the missing link. *MNRAS* 468, 2865–2883. doi:10.1093/mnras/stx641

Pinto, C., Mehdipour, M., Walton, D. J., Middleton, M. J., Roberts, T. P., Fabian, A. C., et al. (2020a). Thermal stability of winds driven by radiation pressure in super-Eddington accretion discs. *MNRAS* 491, 5702–5716. doi:10.1093/mnras/stz3392

Pinto, C., Middleton, M. J., and Fabian, A. C. (2016). Resolved atomic lines reveal outflows in two ultraluminous X-ray sources. *Nat* 533, 64–67. doi:10.1038/nature17417

Pinto, C., Soria, R., Walton, D. J., D'Aì, A., Pintore, F., Kosec, P., et al. (2021). XMM-Newton campaign on the ultraluminous X-ray source NGC 247 ULX-1: outflows. *MNRAS* 505, 5058–5074. doi:10.1093/mnras/stab1648

Pinto, C., and Walton, D. J. (2023). *Ultra-luminous X-ray sources: extreme accretion and feedback.* arXiv e-prints , arXiv:2302.00006. doi:10.48550/arXiv.2302.00006

Pinto, C., Walton, D. J., Kara, E., Parker, M. L., Soria, R., Kosec, P., et al. (2020b). XMM-Newton campaign on ultraluminous X-ray source NGC 1313 X-1: wind versus state variability. *MNRAS* 492, 4646–4665. doi:10.1093/mnras/staa118

Pintore, F., Zampieri, L., Stella, L., Wolter, A., Mereghetti, S., and Israel, G. L. (2017). Pulsator-like spectra from ultraluminous X-ray sources and the search for more ultraluminous pulsars. *Astrophysical J.* 836, 113. doi:10.3847/1538-4357/836/1/113

Poutanen, J., Lipunova, G., Fabrika, S., Butkevich, A. G., and Abolmasov, P. (2007). Supercritically accreting stellar mass black holes as ultraluminous X-ray sources. *MNRAS* 377, 1187–1194. doi:10.1111/j.1365-2966.2007.11668.x

Prestwich, A. H., Jackson, F., Kaaret, P., Brorby, M., Roberts, T. P., Saar, S. H., et al. (2015). Ultra-luminous X-ray sources in HARO II and the role of X-ray binaries in feedback in lyα emitting galaxies. *Astrophysical J.* 812, 166. doi:10.1088/0004-637X/812/2/166

Protassov, R., van Dyk, D. A., Connors, A., Kashyap, V. L., and Siemiginowska, A. (2002). Statistics, handle with care: detecting multiple model components with the likelihood ratio test. *ApJ* 571, 545–559. doi:10.1086/339856

Psaradaki, I., Costantini, E., Mehdipour, M., and Díaz Trigo, M. (2018). Modelling the disc atmosphere of the low mass X-ray binary EXO 0748-676. *A&A* 620, A129. doi:10.1051/0004-6361/201834000

Rana, V., Harrison, F. A., Bachetti, M., Walton, D. J., Fürst, F., Barret, D., et al. (2015). The broadband XMM-Newton and NuSTAR X-ray spectra of two ultraluminous X-ray sources in the galaxy IC 342. *ApJ* 799, 121. doi:10.1088/0004-637X/799/2/121

Robba, A., Pinto, C., Walton, D. J., Soria, R., Kosec, P., Pintore, F., et al. (2021). Broadband X-ray spectral variability of the pulsing ULX NGC 1313 X-2. *A&A* 652, A118. doi:10.1051/0004-6361/202140884

Roberts, T. P., Warwick, R. S., Ward, M. J., Goad, M. R., and Jenkins, L. P. (2005). XMM-Newton EPIC observations of the ultraluminous X-ray source NGC 5204 X-1. *MNRAS* 357, 1363–1369. doi:10.1111/j.1365-2966.2005.08758.x

Rodríguez Castillo, G. A., Israel, G. L., Belfiore, A., Bernardini, F., Esposito, P., Pintore, F., et al. (2020). Discovery of a 2.8 s pulsar in a 2 Day orbit high-mass X-ray binary powering the ultraluminous X-ray source ULX-7 in M51. *Astrophysical J.* 895, 60. doi:10.3847/1538-4357/ab8a44

Schwarz, G. (1978). Estimating the dimension of a model. *Ann. Stat.* 6, 461–464. Publisher: Institute of Mathematical Statistics. doi:10.1214/aos/1176344136

Shakura, N. I., and Sunyaev, R. A. (1973). Black holes in binary systems. Observational appearance. *A&A* 24, 337.

Song, X., Walton, D. J., Lansbury, G. B., Evans, P. A., Fabian, A. C., Earnshaw, H., et al. (2020). The hunt for pulsating ultraluminous X-ray sources. *MNRAS* 491, 1260–1277. doi:10.1093/mnras/stz3036

Soria, R., Pakull, M. W., Motch, C., Miller-Jones, J. C. A., Schwope, A. D., Urquhart, R. T., et al. (2021). The ultraluminous X-ray source bubble in NGC 5585. *MNRAS* 501, 1644–1662. doi:10.1093/mnras/staa3784

Staubert, R., Trümper, J., Kendziorra, E., Klochkov, D., Postnov, K., Kretschmar, P., et al. (2019). Cyclotron lines in highly magnetized neutron stars. *A&A* 622, A61. doi:10.1051/0004-6361/201834479

Stobbart, A. M., Roberts, T. P., and Wilms, J. (2006). XMM-Newton observations of the brightest ultraluminous X-ray sources. *MNRAS* 368, 397–413. doi:10.1111/j.1365-2966.2006.10112.x

Strüder, L., Briel, U., Dennerl, K., Hartmann, R., Kendziorra, E., Meidinger, N., et al. (2001). The European photon imaging camera on XMM-Newton: the pn-CCD camera. *Astronomy Astrophysics* 365, L18–L26. doi:10.1051/0004-6361:20000066

Sutton, A. D., Roberts, T. P., and Middleton, M. J. (2013). The ultraluminous state revisited: fractional variability and spectral shape as diagnostics of super-Eddington accretion. *MNRAS* 435, 1758–1775. doi:10.1093/mnras/stt1419

Sutton, A. D., Roberts, T. P., and Middleton, M. J. (2015). X-ray spectral residuals in NGC 5408 X-1: diffuse emission from star formation, or the signature of a super-eddington wind? *ApJ* 814, 73. doi:10.1088/0004-637X/814/1/73

Terashima, Y., and Wilson, A. S. (2004). The luminous X-ray source population in M51 observed with Chandra. *Astrophysical J.* 601, 735–758. doi:10.1086/380505

Timmer, J., and Koenig, M. (1995). On generating power law noise. *Astronomy Astrophysics* 300, 707.

Tranin, H., Webb, N., and Godet, O. (2023). *Statistical study of a large and cleaned sample of ultraluminous and hyperluminous X-ray sources*. doi:10.48550/arXiv.2304.11216

van den Eijnden, J., Degenaar, N., Schulz, N. S., Nowak, M. A., Wijnands, R., Russell, T. D., et al. (2019). Chandra reveals a possible ultrafast outflow in the super-Eddington Be/X-ray binary Swift J0243.6+6124. *MNRAS* 487, 4355–4371. doi:10.1093/mnras/stz1548

van der Klis, M. (2005). The QPO phenomenon. *Astron. Nachr.* 326, 798–803. doi:10.1002/asna.200510416

Vasilopoulos, G., Petropoulou, M., Koliopanos, F., Ray, P. S., Bailyn, C. B., Haberl, F., et al. (2019). NGC 300 ULX1: spin evolution, super-Eddington accretion, and outflows. *Mon. Notices R. Astronomical Soc.* 488, 5225–5231. doi:10.1093/mnras/stz2045

Volonteri, M., and Rees, M. J. (2005). Rapid growth of high-redshift black holes. *Astrophysical J.* 633, 624–629. doi:10.1086/466521

Volonteri, M., Silk, J., and Dubus, G. (2015). The case for supercritical accretion onto massive black holes at high redshift. *Astrophysical J.* 804, 148. doi:10.1088/0004-637X/804/2/148

Walton, D. J., Bachetti, M., Fürst, F., Barret, D., Brightman, M., Fabian, A. C., et al. (2018a). A potential cyclotron resonant scattering feature in the ultraluminous X-ray source pulsar NGC 300 ULX1 seen by NuSTAR and XMM-Newton. *Astrophysical J. Lett.* 857, L3. doi:10.3847/2041-8213/aabadc

Walton, D. J., Fuerst, F., Harrison, F., Stern, D., Bachetti, M., Barret, D., et al. (2013). An extremely luminous and variable ultraluminous X-ray source in the outskirts of circinus observed with NuSTAR. *ApJ* 779, 148. doi:10.1088/0004-637X/779/2/148

Walton, D. J., Fürst, F., Bachetti, M., Barret, D., Brightman, M., Fabian, A. C., et al. (2016a). A 78 Day X-ray period detected from NGC 5907 ULX1 by Swift. *ApJL* 827, L13. doi:10.3847/2041-8205/827/1/L13

Walton, D. J., Fürst, F., Heida, M., Harrison, F. A., Barret, D., Stern, D., et al. (2018b). Evidence for pulsar-like emission components in the broadband ULX sample. *Astrophysical J.* 856, 128. doi:10.3847/1538-4357/aab610

Walton, D. J., Mackenzie, A. D. A., Gully, H., Patel, N. R., Roberts, T. P., Earnshaw, H. P., et al. (2022). A multimission catalogue of ultraluminous X-ray source candidates. *Mon. Notices R. Astronomical Soc.* 509, 1587–1604. doi:10.1093/mnras/stab3001

Walton, D. J., Middleton, M. J., Pinto, C., Fabian, A. C., Bachetti, M., Barret, D., et al. (2016b). An iron K component to the ultrafast outflow in NGC 1313 X-1. *Astrophysical J.* 826, L26. doi:10.3847/2041-8205/826/2/L26

Walton, D. J., Pinto, C., Nowak, M., Bachetti, M., Sathyaprakash, R., Kara, E., et al. (2020). The unusual broad-band X-ray spectral variability of NGC 1313 X-1 seen with XMM-Newton, Chandra, and NuSTAR. *Mon. Notices R. Astronomical Soc.* 494, 6012–6029. doi:10.1093/mnras/staa1129

Wang, Y.-M. (1996). Location of the inner radius of a magnetically threaded accretion disk. *Astrophysical J.* 465, L111–L113. doi:10.1086/310150

West, L., Garofali, K., Lehmer, B. D., Prestwich, A., Eufrasio, R., Luangtip, W., et al. (2023). *The large deficit of HMXB emission from luminous infrared galaxies: the case of the circumnuclear starburst ring in NGC 7552*. doi:10.48550/arXiv.2305.19491

Wik, D. R., Lehmer, B. D., Hornschemeier, A. E., Yukita, M., Ptak, A., Zezas, A., et al. (2014). Spatially resolving a starburst galaxy at hard X-ray energies: NuSTAR, Chandra, and VLBA observations of NGC 253. *Astrophysical J.* 797, 79. doi:10.1088/0004-637X/797/2/79

Wiktorowicz, G., Lasota, J.-P., Middleton, M., and Belczynski, K. (2019). The observed versus total population of ULXs. *ApJ* 875, 53. doi:10.3847/1538-4357/ab0f27

Wilson-Hodge, C. A., Malacaria, C., Jenke, P. A., Jaisawal, G. K., Kerr, M., Wolff, M. T., et al. (2018). *NICER* and *fermi* GBM observations of the first galactic ultraluminous X-ray pulsar Swift J0243.6+6124. *ApJ* 863, 9. doi:10.3847/1538-4357/aace60

Wolter, A., Fruscione, A., and Mapelli, M. (2018). The X-ray luminosity function of ultraluminous X-ray sources in collisional ring galaxies. *Astrophysical J.* 863, 43. doi:10.3847/1538-4357/aacb34

frontiers | Frontiers in Astronomy and Space Sciences

TYPE Original Research
PUBLISHED 12 December 2023
DOI 10.3389/fspas.2023.1292500

Check for updates

OPEN ACCESS

EDITED BY
Gabriele Ponti,
Brera Astronomical Observatory, Italy

REVIEWED BY
Enrico Bozzo,
Swiss Institute of Comparative Law, Switzerland
Tolga Guver,
Istanbul University, Türkiye

*CORRESPONDENCE
R. M. Ludlam,
renee.ludlam@wayne.edu

RECEIVED 11 September 2023
ACCEPTED 20 November 2023
PUBLISHED 12 December 2023

CITATION
Ludlam RM, Malacaria C, Sokolova-Lapa E, Fuerst F, Pradhan P, Shaw AW, Pottschmidt K, Pike S, Vasilopoulos G, Wilms J, García JA, Madsen K, Stern D, Maitra C, Del Santo M, Walton DJ, Brumback MC and van den Eijnden J (2023), The high energy X-ray probe (HEX-P): a new window into neutron star accretion. *Front. Astron. Space Sci.* 10:1292500. doi: 10.3389/fspas.2023.1292500

COPYRIGHT
© 2023 Ludlam, Malacaria, Sokolova-Lapa, Fuerst, Pradhan, Shaw, Pottschmidt, Pike, Vasilopoulos, Wilms, García, Madsen, Stern, Maitra, Del Santo, Walton, Brumback and van den Eijnden. This is an open-access article distributed under the terms of the Creative Commons Attribution License (CC BY). The use, distribution or reproduction in other forums is permitted, provided the original author(s) and the copyright owner(s) are credited and that the original publication in this journal is cited, in accordance with accepted academic practice. No use, distribution or reproduction is permitted which does not comply with these terms.

The high energy X-ray probe (HEX-P): a new window into neutron star accretion

R. M. Ludlam[1]*, C. Malacaria[2], E. Sokolova-Lapa[3], F. Fuerst[4], P. Pradhan[5], A. W. Shaw[6], K. Pottschmidt[7,8], S. Pike[9], G. Vasilopoulos[10], J. Wilms[3], J. A. García[11,12], K. Madsen[11], D. Stern[13], C. Maitra[14], M. Del Santo[15], D. J. Walton[16], M. C. Brumback[17] and J. van den Eijnden[18]

[1]Department of Physics and Astronomy, Wayne State University, Detroit, MI, United States, [2]International Space Science Institute, Bern, Switzerland, [3]Dr. Karl Remeis-Observatory and Erlangen Centre for Astroparticle Physics, Friedrich-Alexander Universität Erlangen-Nürnberg, Bamberg, Germany, [4]Quasar Science Resources S.L for European Space Agency (ESA), European Space Astronomy Centre (ESAC), Madrid, Spain, [5]Physics and Astronomy Department, Embry Riddle Aeronautical University, Prescott, AZ, United States, [6]Department of Physics and Astronomy, Butler University, Indianapolis, IN, United States, [7]CRESST and CSST, University of Maryland, Baltimore County, Baltimore, MD, United States, [8]Astroparticle Physics Laboratory, NASA Goddard Space Flight Center, Greenbelt, MD, United States, [9]Department of Astronomy and Astrophysics, University of California, San Diego, San Diego, CA, United States, [10]Department of Physics, National and Kapodistrian University of Athens, University Campus Zografos, Athens, Greece, [11]X-ray Astrophysics Laboratory, NASA Goddard Space Flight Center, Greenbelt, MD, United States, [12]California Institute of Technology, Pasadena, CA, United States, [13]Jet Propulsion Laboratory, California Institute of Technology, Pasadena, CA, United States, [14]Max-Planck-Institut für Extraterrestrische Physik, Garching, Germany, [15]INAF, Istituto di Astrofisica Spaziale e Fisica Cosmica di Palermo, Palermo, Italy, [16]Centre for Astrophysics Research, University of Hertfordshire, Hatfield, United Kingdom, [17]Department of Physics, Middlebury College, Middlebury, VT, United States, [18]Department of Physics, University of Warwick, Coventry, United Kingdom

Accreting neutron stars (NSs) represent a unique laboratory for probing the physics of accretion in the presence of strong magnetic fields ($B \gtrsim 10^8$ G). Additionally, the matter inside the NS itself exists in an ultra-dense, cold state that cannot be reproduced in Earth-based laboratories. Hence, observational studies of these objects are a way to probe the most extreme physical regimes. Here we present an overview of the field and discuss the most important outstanding problems related to NS accretion. We show how these open questions regarding accreting NSs in both low-mass and high-mass X-ray binary systems can be addressed with the *High-Energy X-ray Probe* (*HEX-P*) via simulated data. In particular, with the broad X-ray passband and improved sensitivity afforded by a low X-ray background, *HEX-P* will be able to 1) distinguish between competing continuum emission models; 2) provide tighter upper limits on NS radii via reflection modeling techniques that are independent and complementary to other existing methods; 3) constrain magnetic field geometry, plasma parameters, and accretion column emission patterns by characterizing fundamental and harmonic cyclotron lines and exploring their behavior with pulse phase; 4) directly measure the surface magnetic field strength of highly magnetized NSs at the lowest accretion luminosities; as well as 5) detect cyclotron line features in extragalactic sources and probe their dependence on luminosity in the super-Eddington regime in order to distinguish between geometrical evolution and accretion-induced decay of the

magnetic field. In these ways *HEX-P* will provide an essential new tool for exploring the physics of NSs, their magnetic fields, and the physics of extreme accretion.

KEYWORDS

neutron stars, accretion, high-mass X-ray binary stars, low-mass X-ray binary stars, magnetic fields, high energy astrophysics, x-ray astronomy, X-ray telescopes

1 Introduction

1.1 Accreting neutron stars

Accretion is a ubiquitous process in the Universe, from the formation of stars and planets to supermassive black holes at the center of galaxies. X-ray binary systems are composed of a compact object (CO), either a black hole (BH) or neutron star (NS), that accretes from a stellar companion. These systems can be further categorized based on the mass of the stellar companion: low-mass and high-mass (see Longair, 2011 for a more detailed review). Figure 1 shows a simple schematic for accretion onto NSs in several types of binary systems. Low-mass X-ray binaries (LMXBs) have a $\lesssim 1\ M_{\odot}$ companion that transfers matter via Roche-lobe overflow to form an accretion disk around the compact object. High-mass X-ray binaries (HMXBs) have a more massive ($\gtrsim 5\ M_{\odot}$), early-type stellar companion and accretion onto the CO can occur in various ways, including periodic Roche lobe overflow (such as when the CO passes through the decretion disk of a Be type star), or capture of material ejected through dense stellar winds. We note that there is a rare class of LMXBs that accrete from the slow winds of a late-type stellar companion and exhibit properties akin to HMXBs (see Bozzo et al. 2022 and references therein)[1].

NSs are the densest known objects with a surface in the Universe. The matter inside a NS exists in an ultra-dense, cold state that cannot be replicated in terrestrial laboratories. The only way to discern how matter behaves under these conditions is by determining the equation of state (EoS). The EoS sets the mass and radius of the NS through the Tolman-Oppenheimer-Volkoff equations (Tolman, 1934; 1939; Oppenheimer and Volkoff, 1939) and astronomical measurements of NS masses and radii are therefore crucial for determining which theoretical EoS models are viable (see, e.g., Lattimer, 2011). In particular, accretion onto NSs probes the properties and behavior of matter in the presence of a strong magnetic field ($B \sim 10^{8-9}$ G for LMXBs and $B \sim 10^{12}$ G for HMXBs; see Caballero and Wilms, 2012).

In order to fully encapsulate the accretion emission from these systems, a broad X-ray passband is necessary (see Section 2 for LMXBs and Section 3 for HMXBs). Currently, *NuSTAR* (Harrison et al., 2013) is the only focusing hard X-ray telescope with a passband from 3 to 80 keV. Energies below 3 keV have to be supplemented with other X-ray telescopes, such as *NICER* (Gendreau et al., 2012), *Swift* (Gehrels et al., 2004), or *XMM-Newton* (Jansen et al., 2001), to construct a broad energy passband. While observations can be scheduled to occur during the same observing period, often the data are not strictly simultaneous due to the different orbits of the missions resulting in various degrees of overlap. Since NS binary systems are highly variable, sometimes on time-scales comparable to or shorter than the typical exposure itself, simultaneous observations over a broad X-ray passband are invaluable for studying these systems.

1.2 The high energy X-ray probe: HEX-P

The *High Energy X-ray Probe* (*HEX-P*; Madsen et al., 2023) is a probe-class mission concept that offers sensitive broad-band X-ray coverage (0.2–80 keV) with exceptional spectral, timing and angular capabilities. It features two high-energy telescopes (HETs) that focus hard X-rays and one low-energy telescope (LET) that focuses lower-energy X-rays.

The LET consists of a segmented mirror assembly coated with Ir on monocrystalline silicon that achieves an angular resolution of 3.5″, and a low-energy DEPFET detector, of the same type as the Wide Field Imager (WFI; Meidinger et al., 2020) onboard *Athena* (Nandra et al., 2013). It has 512×512 pixels that cover a field of view of $11.3' \times 11.3'$. The LET has an effective passband of 0.2–25 keV, and a full frame readout time of 2 m, which can be operated in a 128 and 64 channel window mode for higher count-rates to mitigate pile-up and faster readout. Pile-up effects remain below an acceptable limit of ~ 1% for fluxes up to ~ 100 mCrab in the smallest window configuration. Excising the core of the PSF, a common practice in X-ray astronomy, will allow for observations of brighter sources, with a typical loss of up to ~ 60% of the total photon counts.

The HET consists of two co-aligned telescopes and detector modules. The optics are made of Ni-electroformed full shell mirror substrates, leveraging the heritage of *XMM-Newton*, and coated with Pt/C and W/Si multilayers for an effective passband of 2–80 keV. The high-energy detectors are of the same type as flown on *NuSTAR*, and they consist of 16 CZT sensors per focal plane, tiled 4×4, for a total of 128×128 pixel spanning a field of view of $13.4' \times 13.4'$.

This paper highlights interesting existing open questions about NSs and accretion in strong magnetic fields, and demonstrates *HEX-P*'s unique ability to address these with the current best estimate (CBE) mission capabilities. All simulations presented here were produced with a set of response files that represents the observatory performance based on CBEs as of Spring 2023 (see Madsen et al., 2023; *in prep.*). The effective area is derived from raytracing calculations for the mirror design including obscuration by all known structures. The detector responses are based on simulations performed by the respective hardware groups, with an optical blocking filter for the LET and a Be window and thermal insulation for the HET. The LET background was derived from a

1 Although we do not discuss this special class of objects further, some of the science cases we explore (e.g., cyclotron line studies) are applicable to these sources as well.

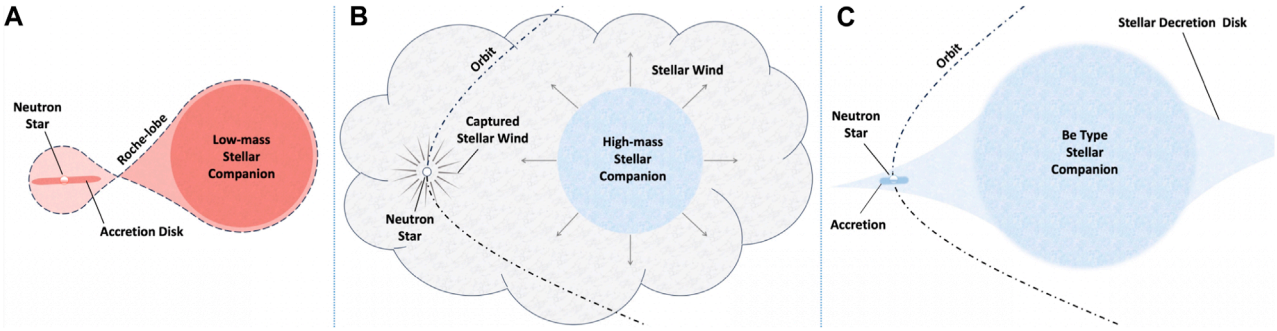

FIGURE 1
Simple schematic diagrams of several types of X-ray binary systems: **(A)** a LMXB system where the NS accretes from a stellar companion via Roche-lobe overflow, **(B)** a NS in a HMXB that accretes from material captured from stellar winds that are launched from the companion, and **(C)** a NS accreting from the decretion disk of a Be type stellar companion.

GEANT4 simulation (Eraerds et al., 2021) of the WFI instrument, and the HET background was derived from a GEANT4 simulation of the *NuSTAR* instrument. Both assume *HEX-P* is in an L1 orbit. The broad X-ray passband and superior sensitivity will provide a unique opportunity to study accretion onto NSs across a wide range of energies, luminosity, and dynamical regimes.

2 Low-mass X-ray binaries

2.1 Background

Persistently accreting NS LMXBs are divided into two types based upon characteristic shapes that are traced out in hardness-intensity diagrams and color-color diagrams (Hasinger and van der Klis, 1989): "Z" sources and "atoll" sources. Z sources trace out a Z-shaped pattern with three distinct branches: the horizontal, normal, and flaring branch (HB, NB, and FB, respectively), with the FB being the softest spectral state. They can be further divided into two subgroups, Sco-like and Cyg-like, based upon how much time they spend in the different branches. Sco-like sources spend little to no time in the HB and extended periods of time in the FB (>12 hours), whereas Cyg-like sources have a strong HB and spend little time in the FB (Kuulkers et al., 1997). Atoll sources are either observed in the soft "banana" state or hard "island" state. A difference in mass accretion rate is thought to be the primary driver between the behavioral differences between atoll and Z sources. Atoll sources probe a lower range in Eddington luminosity (~ 0.01–$0.5 L_{\rm Edd}$) in comparison to the near-Eddington Z sources (~ 0.5–$1.0 L_{\rm Edd}$: van der Klis, 2005). Further evidence that the average mass accretion rate is responsible for the observed difference between the two classes comes from observing transient NS LMXBs that have transitioned between the two classes during outburst (e.g., XTE J1701−462: Homan et al., 2010).

NS LMXBs occupy a number of spectral states which vary considerably in terms of the models and spectral parameters needed to describe the continuum emission (Barret, 2001). In the very hard state, the spectrum is dominated by Comptonization that can be modeled with an absorbed power-law component with a photon index $\Gamma \sim 1$ (Ludlam et al., 2016; Parikh et al., 2017) or two thermal Comptonization components assuming two distinct populations of seed photons from different plasma temperatures (Fiocchi et al., 2019). In the hard state, the spectrum is dominated by a hard Comptonization component with $\Gamma = 1.5$–2.0 and a soft thermal component arising from a single temperature blackbody component or multi-color disk blackbody with a temperature $\lesssim 1$ keV (Barret et al., 2000; Church and Balucińska-Church, 2001). In the soft state, the spectrum becomes thermally dominated with weakly Comptonized emission. Model choices for the thermal and Comptonization components in the soft state vary in the literature leading to two classical descriptions. The "Eastern" model, after Mitsuda et al. (1989), uses a multi-color disk blackbody in combination with a Comptonized blackbody component, while the "Western" model, after White et al. (1988), uses a single-temperature blackbody and a Comptonized disk component. Lin et al. (2007) devised a hybrid model for hard and soft state spectra based upon *RXTE* observations of two transient atoll systems that resulted in a coherent picture of the spectral evolution (e.g., the thermal components follow the expected $L_x \propto T^4$ relation). In this model, the soft state assumes two thermal components (i.e., a single-temperature blackbody and a disk blackbody) and weak Comptonization accounts for the power-law component. This hybrid double thermal model has been used in many NS LMXBs studies (e.g., Cackett et al., 2008; 2009; Lin et al., 2010), though not exclusively. For instance, a recent study using thermal Comptonization from a blackbody and a multi-color accretion disk blackbody (akin to the "Eastern" model) to model the X-ray spectra of the atoll 4U 1820-30 found good agreement with the observed jet variability in this system (Marino et al., 2023). In the absence of multi-wavelength data to support a choice of continuum model, it is difficult to ascertain which prescription of the spectra is appropriate. Due to the soft spectral shape in these states, the source spectrum typically becomes background dominated above 30 keV even when observed with *NuSTAR*. A broad X-ray passband with large effective collecting area and low X-ray background that can observe a large number of sources at various luminosity levels

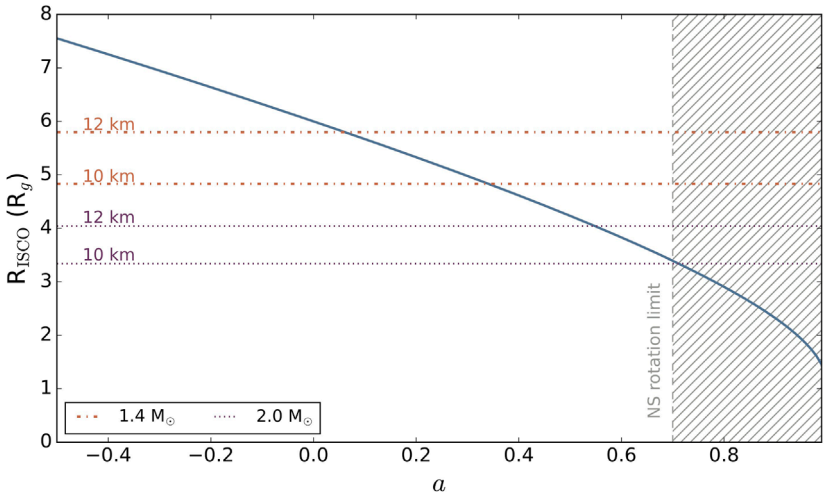

FIGURE 2
Position of the innermost stable circular orbit (ISCO) in units of gravitational radii *versus* the dimensionless spin parameter *a* of the CO. The hatched region indicates where the NS surpasses the rotational limit and would break apart. The horizontal dot-dashed lines indicate the corresponding values of 10 km and 12 km radius for a canonical NS mass of 1.4 $M_{\odot}$. The horizontal dotted lines indicate the same radius values for a more massive NS of 2.0 $M_{\odot}$.

and spectral states is needed to further our understanding of these sources.

The accretion disks in these systems can be externally illuminated by hot electrons in the corona (Sunyaev et al., 1991) or from the thermal emission of the NS or boundary layer region (Popham and Sunyaev, 2001). We note that the exact geometry of the corona is unclear (see Degenaar et al. 2018 for some possible geometries), but X-ray polarization measurements with *IXPE* are beginning to shed light on coronal orientation and presence of boundary layer regions in some systems (e.g., Cocchi et al. 2023; Farinelli et al. 2023; Jayasurya et al. 2023; Ursini et al. 2023); building up our understanding of the accretion geometry when coupled with X-ray energy spectral studies. Regardless of the hard X-ray source, the disk reprocesses the hard X-ray emission and re-emits discrete emission lines superimposed upon a reprocessed continuum known as the 'reflection' spectrum (Ross and Fabian, 2005; García and Kallman, 2010). The spectrum is then relativistically blurred due to the extreme environment close to the NS, where accreting material reaches relativistic velocities as it falls into the NS's deep gravitational well (Fabian et al., 1989; Dauser et al., 2013). Studying reflection in NS LMXBs allows for properties of NSs and the disk itself to be measured, such as the NS magnetic field strength (Cackett et al., 2009; Ibragimov and Poutanen, 2009; Ludlam et al., 2017b), extent of the boundary layer (Popham and Sunyaev, 2001; King et al., 2016; Ludlam et al., 2021), and NS radius (Cackett et al., 2008; Ludlam et al., 2017a; 2022). Of particular interest is both the inner disk radius, $R_{\rm in}$, and dimensionless spin parameter, $a = cJ/GM^2$ (which is the mass normalized total angular momentum J of the CO); the latter is typically fixed in current studies due to limitations in data quality. The spin parameter has important consequences for both accreting NSs and BHs (see Connors et al., 2023, *in prep.*, and Piotrowska et al., 2023, *in prep.*, for *HEX-P* science with BH X-ray binaries and supermassive BHs, respectively). The spin sets the location of the innermost stable circular orbit (ISCO) where a higher spin corresponds to a smaller ISCO (Bardeen et al., 1972). Consequently, the position of the inner disk radius for higher spin values cannot be replicated by lower spin if the data is of sufficient quality to recover $R_{\rm in}$ accurately. The majority of NSs in LMXBs have spin $a \lesssim 0.3$ (Galloway et al., 2008; Miller et al., 2011) and the difference in the location of the ISCO decreases from 6 gravitational radii ($R_g = GM/c^2$) at $a = 0$ to 4.98 R_g at $a = 0.3$ (see Figure 2). Therefore, targeting an accreting NS with a higher spin, as indicated through a high measured spin frequency, can decrease the upper limit on NS radii obtained from reflection modeling by roughly 2–3 km.

In order to capture the entire reflection spectrum (i.e., the low-energy O VIII and iron (Fe) L emission lines near 1 keV (Madej et al., 2014; Ludlam et al., 2018; Ludlam et al., 2021), the Fe K emission lines at 6.4–6.97 keV, and the Compton backscattering hump above 15 keV), determine the appropriate continuum model, and measure the absorption column along the line of sight, a broad X-ray passband is necessary. Hence, the broad X-ray sensitivity provided by the LET and HETs on *HEX-P* is crucial for studying accreting NS LMXBs.

2.2 Simulated science cases for LMXBs

All simulations in this section were conducted in XSPEC (Arnaud, 1996) via the "fakeit" command, which draws photons from a randomized seed distribution, with V07 of the *HEX-P* response files selecting an 80% PSF correction, assuming the data would be extracted from a 15 arcsec region for the HET and 8 arcsec region for the LET, as well as the anticipated background for the telescope at L1. The simulated spectra were

TABLE 1 Input model parameters for simulating reflection model data with *HEX-P*. Values are taken from Table 3: RNS1 of Ludlam et al. (2022) for Cygnus X-2 in the NB and updated using the public version of RELXILLNS (v2.2). Additionally, we show one case of the recovered model parameters from a simulated *HEX-P* spectrum after performing a Markov Chain Monte Carlo (MCMC) analysis with a burn-in of 10^6 and chain length of 5×10^5 to emulate a standard analysis of the data. Errors are reported at the 1σ confidence level, though the errors for R_{in} and a are drawn from the bivariate distribution between the two due to their correlated nature.

Model component	Parameter	Input	Recovered for $a = 0.3$
Tbfeo	N_H (10^{22} cm^{-2})	0.39	0.39[a]
	O	1.16	1.16[a]
	Fe	1.00	1.00[a]
Diskbb	T_{in} (keV)	1.74	1.74 ± 0.01
	norm	117	117 ± 1
Powerlaw	Γ	3.49	3.49 ± 0.01
	norm	6.0	5.9 ± 0.1
Rexillns	q	2.21	2.21 ± 0.04
	a	0, 0.17, 0.30	0.3 ± 0.2
	i (°)	65	65[a]
	R_{in} (R_{ISCO})	1.00	$1.02^{+0.10}_{-0.02}$
	R_{out} (R_g)	1000	1000[a]
	kT_{bb} (keV)	2.49	2.49 ± 0.01
	log(ξ/[erg cm s^{-1}])	2.00	$2.04^{+0.03}_{-0.10}$
	A_{Fe}	5.9	$4.9^{+0.7}_{-0.8}$
	log(N[cm^{-3}])	18	17.9 ± 0.1
	f_{refl}	1.0	1.0 ± 0.1
	norm (10^{-3})	3.23	3.2 ± 0.1

[a]= fixed, $\chi 2/d.o.f$ 3132.3/3102 for the recovered fit in the final column.

grouped via GRPPHA to have a minimum of 25 counts per bin to allow for the use of χ^2 statistics. The flux for each of the following simulations can be found in Supplementary Table S1.

2.2.1 Distinguishing between continuum models

To demonstrate *HEX-P*'s ability to distinguish between different continuum models, we base our simulations on the models used to fit simultaneous *NICER* and *NuSTAR* observations of the accreting atoll 4U 1735–44 published in Ludlam et al. (2020). Model 1 is based on the hybrid double thermal continuum model of Lin et al. (2007) while Model 2 is based on the "Eastern" model of Mitsuda et al. (1989). Both models provide an adequate description of the data in the 0.3–30 keV energy band (the *NuSTAR* observations were background dominated above 30 keV) when neglecting the reflection spectrum, but data at higher energies would distinguish between these two continuum models. We take the continuum model and parameter values for Model 1 and Model 2 from Table 1 of Ludlam et al. (2020) as input for the *HEX-P* simulation; the exact values can be found in Supplementary Table S2. The overall models[2] are as follows: (a) Model 1: TBABS*(DISKBB + BBODY + POW) and (b) Model 2: TBABS*(DISKBB + NTHCOMP). Note that we fix the absorption column index to a value between the ones used in Model 1 and Model 2, $N_H = 4 \times 10^{21}$ cm^{-2}, to focus on the difference in the spectral shape due to the model component choices rather than a difference in absorption column between the models. We chose an exposure time of 20 ks, roughly equivalent to the exposure time of the *NuSTAR* observation in the aforementioned study.

The simulated *HEX-P* spectra remain above the background in the HET bands up to 80 keV, though they dive into the LET background below 1 keV. This could be remedied by increasing

2 The definition of each model component and their parameters can be found in the XSPEC manual: https://heasarc.gsfc.nasa.gov/xanadu/xspec/manual/node128.html.

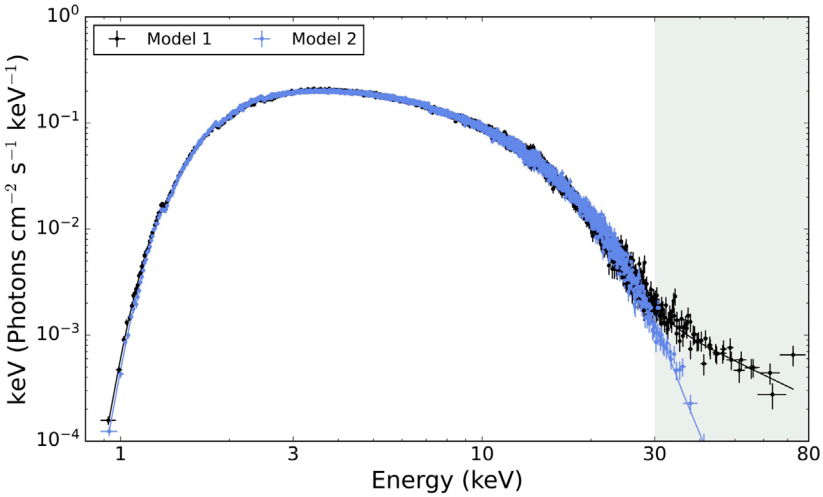

FIGURE 3
Comparison of simulated 20 ks *HEX-P* (LET+2 HETs) observation for two different continuum models typically used to describe NS LMXB soft state spectra: a double thermal continuum model with weak Comptonization (Model 1: black) and an accretion disk with blackbody Comptonization (Model 2: blue). The models diverge above 30 keV where currently available missions quickly become background dominated for the same exposure time. To emphasize this point, the same S/N near 30 keV could be achieved with *NuSTAR* in an exposure time of 96.6 ks. The broad X-ray passband and improved sensitivity of *HEX-P* will differentiate the models.

the exposure time, though, notably, the spectrum above 30 keV is where the models diverge. The reduced χ^2 is ≤1.03 when fitting each simulation with its own input model. Attempting to fit each simulated spectrum with the opposing model description provides an inadequate fit with $\Delta\chi^2 > 1{,}000$ for the same number of degrees of freedom (*d.o.f.*). Figure 3 shows the *HEX-P* spectrum for the Model 2 input of a thermal disk with a Comptonized blackbody from a boundary layer region. For direct comparison, we show a simulated spectrum using Model 1 (the double thermal continuum model with weak Comptonization) with parameter values from fitting the simulated spectrum of Model 2 below 30 keV, since these models perform equally well within this energy regime. This highlights that though these models are nearly identical below 30 keV, they diverge at higher energies inaccessible by current operating missions. The weakly Comptonized emission above 30 keV cannot be replicated by Model 2, and demonstrates the potential for a broadband X-ray mission like *HEX-P* to discern between competing continuum models that would otherwise equally describe the data below 30 keV.

2.2.2 Neutron star radius constraints from relativistic reflection modeling

To demonstrate that *HEX-P* would improve the radius constraints obtained by reflection modeling of NSs, we base our simulations on the results of a recent investigation of Cygnus X-2 that utilized simultaneous data from *NICER* and *NuSTAR* (Ludlam et al., 2022). This source is of particular interest since it has a dynamical NS mass measurement of $M_{\rm NS} = 1.71 \pm 0.21\ M_{\odot}$ (Casares et al., 2010). The source was analyzed in the NB, HB, and the vertex between those branches. Fixing the spin at $a = 0$, Ludlam et al. (2022) found that the inner disk radius remained close to $R_{\rm ISCO}$. In the current literature it is customary to find studies in which the spin of the NS has been fixed while fitting models to the data given the highly degenerate nature of $R_{\rm in}$ and a. We set up our simulations using the Cygnus X-2 data in the NB modeled with the latest public release of the self-consistent reflection model tailored for thermal emission illuminating the accretion disk, RELXILLNS (v2.2: García et al., 2022). The input parameters for the simulation[3] are provided in Table 1. We leave $R_{\rm in}$ at 1 $R_{\rm ISCO}$ for all simulations while varying the input spin since the disk remained consistent with this value while the source was in the various branches. We chose three spin values as test cases: non-rotating ($a = 0$), the highest value expected for a NS LMXB ($a = 0.3$), and $a = 0.17$ which is an approximation based on the spin frequency of the source (Mondal et al., 2018). We use an exposure time of 100 ks and investigate how well $R_{\rm in}$ and spin can be recovered independently.

Given the degenerate nature of the parameters of interest and that each spectrum simulated is created via a randomized photon generation, the results obtained can vary with each iteration. We therefore simulate 10^4 spectra per spin value to determine the likelihood of constraining $R_{\rm in}$ and a. The LET data were modeled in the 0.3–15 keV energy band while the HET data were modeled in the 2–80 keV band. We impose an upper limit on the spin ($a \leq 0.7$) when fitting the simulated spectra so as to not surpass the rotational break-up limit of a NS (Lattimer and Prakash, 2004). We fit each spectrum and then perform error scans to ensure that each iteration reached a minimum goodness of fit of χ^2/d.o.f. ≤ 1.1 prior to obtaining values

3 Note that there was an update to the publicly available RELXILL model's definition of the reflection fraction parameter for non-lamppost type models. As a result the values we use do not exactly match those of Ludlam et al. (2022), which used a proprietary developmental version of RELXILLNS. We have verified that the main results are consistent within errors when fitting the *NuSTAR* spectrum in the NB.

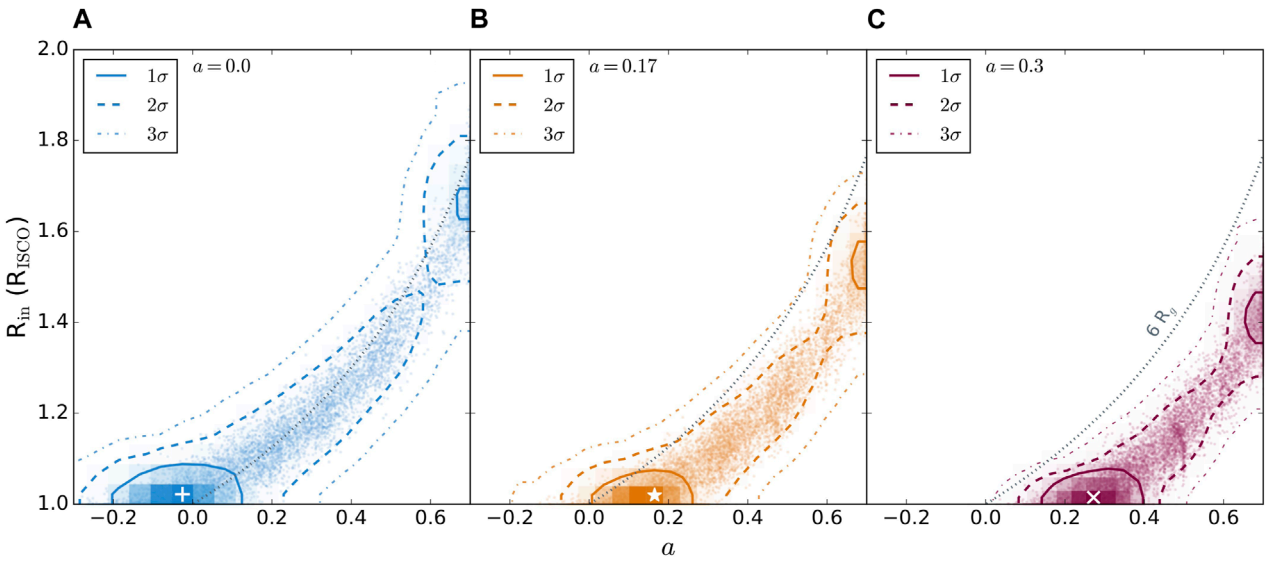

FIGURE 4
Posterior distribution of a and R_{in} for 10^4 iterations of simulating *HEX-P* spectra for three spin values: **(A)** a = 0.0, **(B)** a = 0.17, and **(C)** a = 0.3. The 1σ, 2σ, and 3σ contours are shown. The white points indicate the highest probability value. The dotted grey line indicates a constant line of 6 R_g which corresponds to the ISCO for a = 0. The distribution tightens at high values of spin as relativistic effects become stronger. However, the distributions show that the data are able to trace out unique values of inner disk radii by trending towards lower values of R_g at higher a.

for inner disk radius and spin from each simulated spectrum, thus building up the posterior distribution shown in Figure 4.

Errors are drawn from the bivariate posterior distribution due to their correlated nature and reported at the 1σ confidence level. We find that for an input of $a = 0$, we recover $a = -0.03^{+0.15}_{-0.17}$ and $R_{in} = 1.02^{+0.07}_{-0.02}$ R_{ISCO}. For an input of $a = 0.17$, we recover $a = 0.17^{+0.09}_{-0.16}$ and $R_{in} = 1.02^{+0.05}_{-0.02}$ R_{ISCO}. Lastly, for an input of $a = 0.30$, we recover $a = 0.27 \pm 0.13$ and $R_{in} = 1.02^{+0.05}_{-0.02}$ R_{ISCO}. The ability to recover the input parameters improves at higher spin as the relativistic effects become stronger. Recall that the position of the inner disk radius for higher spin values cannot be replicated by lower spin, thus if the data is of sufficient quality to recover R_{in} accurately this will become apparent. For example, an input of $R_{in} = 1R_{ISCO}$ for a spin of $a = 0$ corresponds to $6R_g$. This value can be mimicked by a higher spin and R_{in} beyond 1 R_{ISCO} (e.g., $6R_g$ is equal to $1.2R_{ISCO}$ for $a = 0.3$). However, an input of $R_{in} = 1R_{ISCO}$ for $a = 0.3$ corresponds to $4.98R_g$ and cannot be replicated by a lower spin so long as the upper limit recovered when fitting the data returns a value of $R_{in} < 1.2R_{ISCO}$. We note that Cygnus X-2 is a bright LMXB (~ 0.7 Crab) and would thus need to be observed in a configuration that would reduce pile-up effects in the LET. However, we obtain consistent results at the 1σ level when performing the same exercise with just the HETs, which do not suffer from pile-up, though the 3σ level can no longer rule out a non-rotating NS as is the case when the LET is included. Hence the combined observing power of the HETs and LET provide an improvement over the current capabilities of existing missions.

Figure 5 shows the improvement provided by *HEX-P* for reflection modeling of spinning NS LMXBs in comparison to simultaneous *NICER* and *NuSTAR* results with fixed spin. Additionally, the current best constraints from gravitational wave events of binary NS mergers and pulsar light curve modeling demonstrate how the various methods can work in concert to narrow down the allowable region for the EoS. Each method has its own underlying systematic uncertainties, so the firmest EoS constraints will require multiple measurement approaches. Utilizing the dynamical NS mass estimate of Cygnus X-2 ($M_{NS} = 1.71 \pm 0.21$ $M_\odot$: Casares et al., 2010), Ludlam et al. (2022) reported an upper limit on the radius of $R_{NS} = 19.5$ km for $M_{NS} = 1.92$ $M_\odot$ and $R_{NS} = 15.3$ km for $M_{NS} = 1.5$ $M_\odot$. The lower limit on spin and upper limit on R_{in} return a conservative upper limit on the NS radius. From the *HEX-P* simulations we calculate an upper limit of $R_{NS} = 16.7$ km for $M_{NS} = 1.92$ $M_\odot$ and $R_{NS} = 13.2$ km for $M_{NS} = 1.5$ $M_\odot$ for an input of $a = 0.3$. This demonstrates the power of *HEX-P* to study rotating NSs with reflection studies. For comparison, we conducted the same simulation with *NuSTAR* response files. For the highest spin value of $a = 0.3$, *NuSTAR* recovers $a = 0.67^{+0.03}_{-0.54}$ and $R_{in} = 1.02^{+0.16}_{-0.02}$ R_{ISCO}. The conservative upper limit on the NS radius from the location of the inner disk radius is larger than 6 R_g and therefore does not provide an improvement over current reflection studies that assume the spin is fixed at $a = 0$. Performing this test with the combination of *NICER* and *NuSTAR* marginally improves the recovered spin value to $a = 0.68^{+0.02}_{-0.50}$, but with a larger upper limit on $R_{in} = 1.02^{+0.18}_{-0.02}$ R_{ISCO}, which is still >1 km larger than the constraints obtained from *HEX-P* (i.e., $R_{NS} = 18.5$ km for $M_{NS} = 1.92$ $M_\odot$ and $R_{NS} = 14.4$ km for $M_{NS} = 1.5$ $M_\odot$).

We demonstrate that these results do not depend on drawing from a posterior distribution of simulated spectra by conducting Markov Chain Monte Carlo (MCMC) analysis on one of the simulated *HEX-P* spectra with an input spin of $a = 0.3$. The results of this test are shown in Table 1 with the inclination fixed at the median value from optical and X-ray studies (Orosz and Kuulkers, 1999; Ludlam et al., 2022). The lower limit on spin of $a = 0.1$ and upper

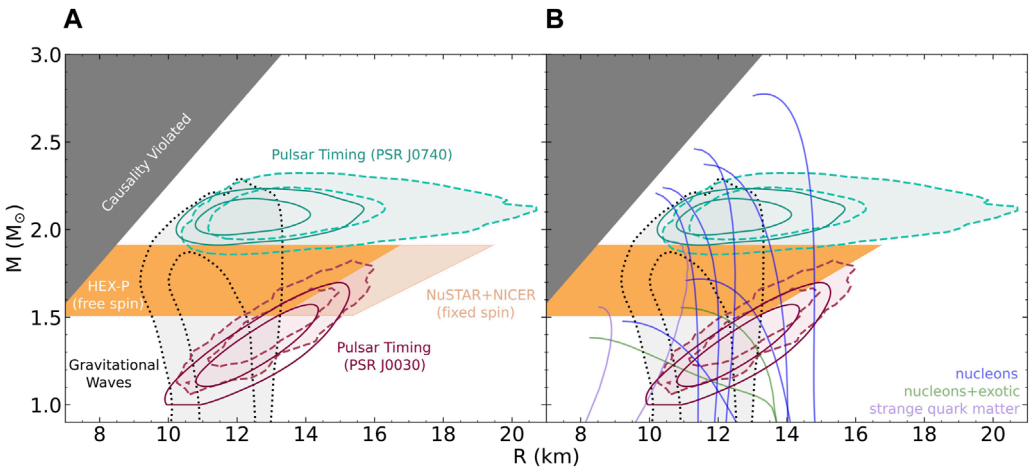

FIGURE 5
Mass and radius constraints from reflection modeling compared to NS gravitational wave events and *NICER* pulsar light curve modeling. The darker solid orange region indicates the improved radius constraints for reflection modeling of *HEX-P* data based on Cygnus X-2 for the case of high *a*. Note that both R_{in} and *a* are free parameters when fitting the *HEX-P* data, while the *NuSTAR* plus *NICER* analysis fixes $a = 0$ (lighter solid orange region in panel **(A)**; Ludlam et al., 2022). The solid gray region indicates where causality is violated (i.e., the sound speed within the NS exceeds the speed of light). Pulsar light curve modeling of *NICER* data for PSR J0740 + 6620 is indicated in teal (dashed lines: Miller et al., 2021; solid lines; Riley et al., 2021). Maroon indicates the results for light curve modeling of PSR J0030 + 0452 (dashed lines: Miller et al., 2019; solid lines; Riley et al., 2019). The black dotted line denotes the mass-radius constraints from the combined GW170817 (Abbott et al., 2019) and GW190425 (The LIGO Scientific Collaboration et al., 2020) signatures using a piece-wise polytropic model as reported in Raaijmakers et al. (2021). Confidence contours correspond to the 68% and 95% credible regions. Panel **(B)** shows select EoS models from Lattimer and Prakash (2001) to demonstrate the behavior of different internal compositions on the mass-radius plane.

limit on $R_{in} = 1.12\, R_{ISCO}$ still provides an improvement over current *NICER* and *NuSTAR* analyses, which fix $a = 0$. The MCMC analysis finds an upper limit of $R_{NS} = 18$ km for $M_{NS} = 1.92\, M_{\odot}$ and $R_{NS} = 14.1$ km for $M_{NS} = 1.5\, M_{\odot}$.

For completeness we note that the Kerr metric is used to describe the space-time close to the NS in the relativistic reflection model. As the angular momentum (i.e., spin) increases, the NS can become oblate, thus causing deviations in space-time from the Kerr metric due to an induced quadrupole moment. The exact induced deviation depends upon the EoS of the NS, but this has an effect <10% (Sibgatullin and Sunyaev, 1998) in the anticipated range of spin parameters for NS LMXBs ($a \lesssim 0.3$). Given that our 1σ errors for R_{in} are larger than this deviation from the Kerr metric, the *HEX-P* spectra would not be sensitive enough to measure this effect. However, our conservative upper limits on NS radius are still at larger radii than the deviation in the R_{ISCO} and hence are not in conflict even if we are insensitive to an induced quadrupole moment. Therefore, reflection studies of accreting NS LMXBs with *HEX-P* would provide improved upper limits on NS radii in comparison to current studies.

3 High-mass X-ray binaries

3.1 Background

NSs in HMXBs are typically highly magnetized, with a dipolar magnetic field strength of $\sim 10^{12}$G. The pressure of the TeraGauss magnetic field disrupts the inflow of the accreting matter, channelling it onto the magnetic poles (Davies and Pringle, 1981). There, the kinetic energy of the matter is released as radiation in a highly anisotropic manner. Since the NS rotates, the sources are visible as X-ray pulsars. Studying this emission is crucial to understanding the physics of plasma accretion and the interaction of radiation with high magnetic fields that are orders of magnitude stronger than those achievable in laboratories on Earth. Due to their extreme surface magnetic field strength, quantum effects take place at the site of emission. In particular, the electron motion in the direction perpendicular to the magnetic field lines becomes quantized. This affects the electron scattering cross section, leading to a resonance at an energy that is proportional to the magnetic field strength (Meszaros, 1992). As a result, the spectra of X-ray pulsars (XRPs) can contain absorption line-like features called cyclotron resonant scattering features (CRSFs), or cyclotron lines, at an energy of

$$E_{cyc} \approx \frac{n}{(1+z_g)} 11.6\, B_{12}\ \text{keV}, \tag{1}$$

where z_g is the gravitational redshift (typically 0.3 for standard NS mass and radius) and B_{12} is the NS (polar) magnetic field strength in units of 10^{12}G, while *n* is the number of Landau levels involved[4]. Cyclotron lines represent the most direct way to probe the NS magnetic field on or close to the NS surface. Up to now, cyclotron lines have been confirmed in the spectra of about 40 sources (Staubert et al., 2019). Figure 6 shows a schematic description of the formation of cyclotron harmonics.

4 In the following, the cyclotron line energy correspondent to $n = 1$ is labeled as *fundamental*, while for $n > 1$ lines are labeled as the n_i *harmonic*, with $i = n$.

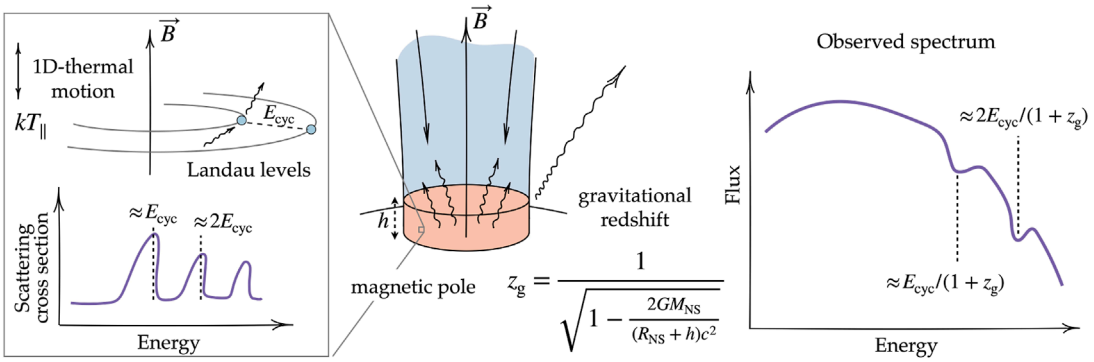

FIGURE 6
Simplified depiction of the formation of cyclotron lines in the spectra of accreting highly magnetized neutron stars due to photon scattering off electrons, whose motion perpendicular to the field lines is restricted by Landau quantization. The latter leads to strong cyclotron resonances in the Compton scattering cross section, broadened by the electron thermal motion parallel to the magnetic field. The centroid energies of the cyclotron lines in observed spectra approximately correspond to the redshited energies of the resonances (with some correction for the scattering redistribution effects during the lines' formation). The gravitational redshift is dependent on the height of the line-forming region, h, above the surface of the neutron star.

When observed at typical outburst luminosity of $\gtrsim 10^{36}$ erg s^{-1}, the spectra of XRPs have been described with phenomenological models (a power-law with high-energy cutoff) modified by interstellar absorption, an Fe Kα emission line around 6.4 keV, low-temperature blackbody components and, at times, a component called the 10 keV feature (Mushtukov and Tsygankov, 2022, and references therein). However, at lower luminosity accretion regimes, the spectrum often exhibits a transition to a double-hump shape (Tsygankov et al., 2019a) which has recently been explained in terms of a low-energy thermal component peaking at ~ 5 keV and a high-energy Comptonized component peaking at ~ 35 keV representing the broadened red wing of the cyclotron line (Mushtukov et al., 2021; Sokolova-Lapa et al., 2021). A dip between the two components was sometimes interpreted as a cyclotron line (see, e.g., Doroshenko et al. (2012), for the case of X Per), but is likely a continuum feature, as was shown for sources with a known fundamental cyclotron line at higher energies after the transition to a low-luminosity state (see, e.g., Tsygankov et al. (2019a)).

These low luminosity states of accretion characterized by two-hump spectra are generally associated with braking of the accretion flow in the NS atmosphere [Mushtukov et al., 2021; Sokolova-Lapa et al., 2021, although a model assuming an extended collisionless shock instead was recently proposed by Becker and Wolff, (2022)]. Rapid deceleration of the plasma in the atmosphere proceeds mainly by Coulomb collisions and leads to the formation of an overheated outermost layer with electron temperatures of ~ 30 keV. Such high temperatures significantly enhance Comptonization and together with resonant redistribution lead to the formation of the high-energy excess in the spectra around the cyclotron line. When the mass-accretion rate onto the poles is increased, the pressure of the emitted radiation starts affecting the dynamics of the accretion flow. The radiation becomes capable of decelerating the flow above the surface, reducing direct heating of the atmosphere and giving rise to a radiation-dominated shock (Basko and Sunyaev, 1976). The onset of this regime is typically associated with a critical luminosity ($L_{crit} \sim 10^{37}$ erg s^{-1}: Basko and Sunyaev, 1976; Becker et al., 2012; Mushtukov et al., 2015) and growth of the accretion column as an emitting structure. Modeling emission from accretion columns is a very challenging problem due to its dynamic nature, multi-dimensional geometry, and the necessity of including general relativistic effects. On the other hand, studying the low-luminosity regime with emission from the heated atmosphere of the polar cap allows easier access to fundamental parameters of accreting NSs (see Section 3.2.3 for more details).

Cyclotron lines exhibit variations with accretion luminosity, pulse phase, and over secular time scales. Variation of the cyclotron line centroid energy E_{cyc} with X-ray luminosity L_X can be exploited to gain insight into the accretion regime. For example, low-luminosity XRPs often show a positive correlation between E_{cyc} and L_X, while high-luminosity XRPs show a negative correlation [see, e.g., Klochkov et al. (2011)]. The two trends are assumed to be separated by the critical luminosity and thus are related to the transition between the different accretion regimes described above. On the other hand, studying the pulse-phase dependence of the E_{cyc} (as well as the line depth and width) can shed light upon the geometrical configuration of the NS (Nishimura, 2011). Moreover, some sources show evidence of a pulse phase-transient cyclotron line; i.e., a CRSF that only appears at certain pulse phases (Klochkov et al., 2008; Kong et al., 2022). Finally, secular variation of the cyclotron line has been attributed to a geometric reconfiguration of the polar field or to a magnetic field burial due to continued accretion (Bala et al., 2020; Staubert et al., 2020).

One of the biggest challenges for the detection and characterization of cyclotron lines is determining a robust broadband continuum model. The centroid energy of the line as well as its other parameters can show significantly different best-fit values when modelled with different continua. Due to this model-dependence, the very presence of a cyclotron line has been questioned at times (Di Salvo et al., 1998; Doroshenko et al., 2012; Doroshenko et al., 2020) as has its luminosity dependence

(Müller et al., 2013). A similar argument also holds for the continuum best-fit values. The "true" continuum model can only be inferred if data cover a sufficiently wide energy passband to constrain absorption affecting the softer X-ray energies and the various spectral components at harder X-ray energies (Sokolova-Lapa et al., 2021; Malacaria et al., 2023a). Moreover, properly constraining the broadband continuum is necessary when multiple cyclotron line harmonics are present, as in the cases of 4U 0115 + 63 (Heindl et al., 2004) and V 0332 + 53 (Pottschmidt et al., 2005). In addition, observing the broadband continuum from accreting XRPs can help constraining physical parameters of the NSs thanks to the recent development of physically motivated spectral models (e.g., Farinelli et al. 2016; Becker and Wolff 2022, and references therein). This is especially important at low-luminosity, where the accretion flow free-falls on the NS surface and our understanding of the physical mechanisms is more uncertain concerning, e.g., how the flow transitions from radiation-dominated to gas-dominated, or the detailed production of seed photons from cyclotron, bremsstrahlung, and blackbody mechanisms at the site of impact. *HEX-P* will bring crucial contributions also in this field, as it will be able to probe broadband spectral emission from intrinsically dim sources whose required observing exposure with current facilities would be prohibitive.

Last but not least measuring phase-dependent spectral components with the highest sensitivity is required in order to develop consistent physical models for the emission process that include X-ray polarization properties. Recent *IXPE* observations of accreting pulsars like Cen X-3, Vela X-1, EXO 2030 + 375 and others provided new constraints as they showed low, energy-dependent polarization degrees of <10% (Tsygankov et al., 2022; Malacaria et al., 2023b; Forsblom et al., 2023). Radiative transfer models of highly magnetized plasmas predict considerably higher polarization degrees of 50%–80% (Meszaros et al., 1988; Caiazzo and Heyl, 2021; Sokolova-Lapa et al., 2023). Initial candidates for explaining the difference highlight the potential importance of the temperature structure of the plasma in the accretion column, of angle-dependent beaming, and of the propagation of X-rays in the magnetosphere for lowering the polarization degree. Furthermore it has been demonstrated that the X-ray continuum and cyclotron line profile can be expected to directly show subtle, complex imprints of polarization effects (Sokolova-Lapa et al., 2023). This is an intriguing possible reason for the occasionally observed and notoriously difficult to constrain "10 keV feature" mentioned above, as well as for the fact that some accreting pulsars do not show cyclotron lines.

Advancing our understanding of HMXBs in general and cyclotron line sources in particular therefore requires broadband spectra with high sensitivity throughout the relevant energy passband, with a limited background as provided by focusing X-ray facilities, and medium spectral energy resolution (Wolff et al., 2019). Thanks to its leap in observational capabilities, *HEX-P* will be capable of overcoming all above-mentioned challenges and push our understanding of accretion onto XRPs forward. In the next section, we simulate a few exemplary cases highlighting the gains enabled by *HEX-P* with respect to currently available X-ray facilities for which the investigated cyclotron lines centroid energy, accretion regime, or the necessary exposure time prevent a comprehensive study of the physical mechanisms at work.

3.2 Simulated science cases for HMXBs

The following simulations show *HEX-P*'s potential to tackle different cyclotron line science cases using several example sources. Each source has been chosen to represent a specific science case, either because it allows us to observe a certain accretion regime and luminosity range or due to its specific cyclotron line properties, such as the existence of $n > 1$ harmonics. We begin with the prototypical persistent cyclotron line sources Cen X-3 and Vela X-1, which show moderate to high fluxes and luminosities, and allow for exquisitely detailed and sensitive parameter constraints with *HEX-P*. Then we focus on transient accreting pulsars for which *HEX-P* will provide unprecedented access to low fluxes, allowing study of extreme luminosity regimes, e.g., for GX 304-1 in quiescence or for super-Eddington outbursts of extragalactic sources like SMC X-2. Similar to Section 2.2, all simulations were performed via the "fakeit" command in XSPEC (Arnaud, 1996) or ISIS (Houck and Denicola, 2000), employing version v07 of the *HEX-P* response files, selecting an 80% PSF correction, assuming a 15″ extraction region for the HETs and 8″ for the LET, as well as taking the expected background at L1 into account. The flux for each of the following simulations can be found in Supplementary Table S1.

3.2.1 Constraining magnetic field geometry from cyclotron line harmonics

As discussed earlier, cyclotron lines result from transitions between quantized Landau energy levels of electrons in the presence of a magnetic field (Meszaros, 1992). Measuring the energy, width, and strength of cyclotron lines in HMXBs is crucial for understanding the underlying physics of these systems. The energy of cyclotron lines provides insights into the line-forming region in the accretion column. The width of cyclotron lines provides valuable information about the geometry, temperature distribution, and plasma conditions within the accretion column [see e.g., Becker et al. (2012); Staubert et al. (2014) and references therein]. Broadening of cyclotron lines can be influenced by factors such as electron thermal motion, turbulence, and relativistic effects. In the last few decades, comprehensive analyses of HMXBs have directly unveiled many important properties of these systems [see, e.g., Staubert et al. (2019); Pradhan et al. (2021) and references therein]. In addition to the fundamental, higher harmonics of the cyclotron line are also sometimes present in the X-ray spectrum. They arise due to higher-order interactions between X-rays and the Landau levels. By detecting and analyzing fundamental cyclotron lines and their higher harmonics, one can determine the magnetic field strength in different regions of the accretion column. Furthermore, the strength or intensity of fundamental cyclotron lines and their higher harmonics relative to the fundamental line provide insight into the scattering efficiency and the fraction of scattered photons, improving our understanding of the emission processes and properties of the compact object [e.g., see Alexander and Meszaros, 1991; Schwarm et al., 2017 and references therein].

Given the limited passband and/or higher background of instruments like *RXTE* and *Suzaku*, there have been few studies to date of cyclotron lines higher harmonics in HMXBs (see Table 3 of Pradhan et al., 2021). More recent instruments like *NuSTAR* and *Insight*/HXMT provide a significant improvement, but as we look into the future, these studies will be revolutionized by a mission with

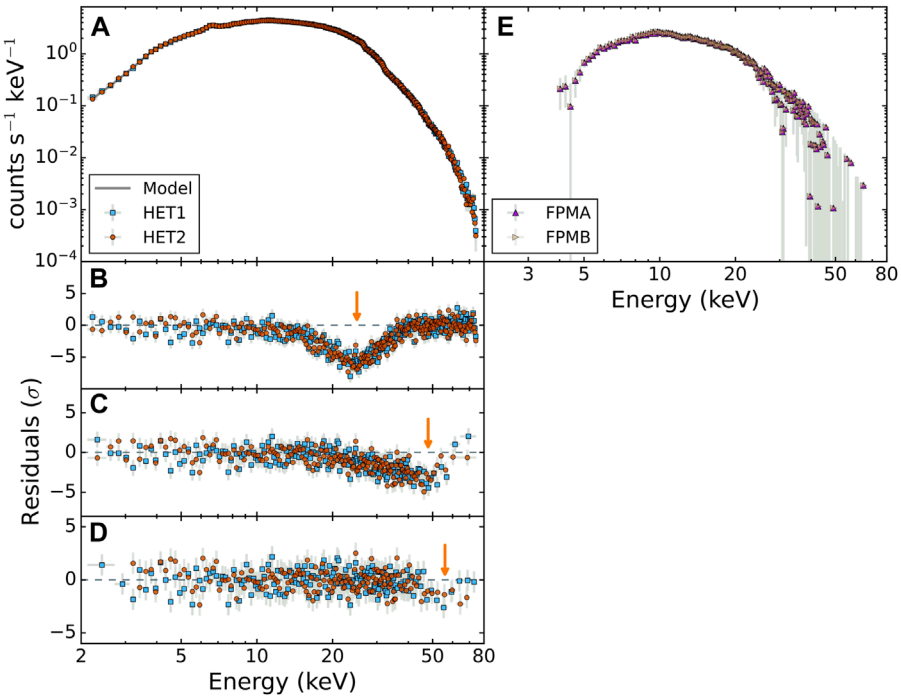

FIGURE 7
Simulated 20 ks HET spectra for Cen X-3, as well as the best-fit model are shown in panel **(A)**. Panels **(B–D)** show the residuals obtained when we set the strength of fundamental, n_2 harmonic, and n_3 harmonic to zero, respectively. We re-binned the data visually and provide arrows for the cyclotron line components to aid with clarity. For comparison, we provide a simulated *NuSTAR* spectrum for using the same model and exposure time which is shown in panel **(E)**. The *NuSTAR* data are strongly background dominated at these flux levels, which makes constraining the higher energy harmonics difficult even at much longer exposure times (see text for more details).

a broad passband coupled with very low background like *HEX-P*. In order to test this, we simulated a 20 ks *HEX-P* spectrum of Cen X-3 in XSPEC. Due to its bright nature and that Cen X-3 is a strong hard X-ray emitter (see Supplementary Table S1), we concentrate on the HETs only which are devoid of pile-up although we have verified that the results below are consistent when including the LET. Cen X-3, an eclipsing HMXB, consists of an O star and a pulsar with a rotational period of ~4.8 s (Chodil et al., 1967; Giacconi et al., 1971; Schreier et al., 1972). The X-ray spectrum of this source exhibits multiple emission lines (Fe, Si, Mg, Ne: Iaria et al., 2005; Tugay and Vasylenko, 2009; Naik and Paul, 2012; Aftab et al., 2019; Sanjurjo-Ferrín et al., 2021), and the X-ray emission has been detected beyond 70 keV. The fundamental cyclotron line occurs near 29 keV (Tomar et al., 2021) with a possible n_2 harmonic at ~47 keV (Yang et al., 2023) as seen from recent HXMT results. With the passband of *HEX-P* extending up to 80 keV and significantly less background, we investigated the possibility of detecting an n_3 harmonic in the source.

The baseline model for our simulation is NPEX (Eq. 2; Mihara, 1995; Makishima et al., 1999) and the values of model parameters are taken from Table 1 (ObsID P010131101602) of Yang et al. (2023). The functional form of NPEX is given by

$$\mathrm{NPEX}(E) = \left(AE^{-\Gamma_1} + BE^{+\Gamma_2}\right) e^{-E/E_{\mathrm{fold}}} \quad (2)$$

where Γ_1 and Γ_2 are the negative and positive power-law indices, respectively. Γ_2, which approximates a Wien hump, was fixed at 2.0, $\Gamma_1 = 0.8$, the folding energy $E_{\mathrm{fold}} = 6.9$ keV, and the absorption column $N_{\mathrm{H}} = 2.06\times 10^{22}$ cm^{-2}.

The CRSFs are modeled with a multiplicative model of a line with a Gaussian optical depth profile with energy E_i, strength d_i, and width σ_i. The fundamental line, $i = 1$, is at ~29 keV with $d_1 \sim 1.4$ and $\sigma_1 = 7.6$ keV. The n_2 harmonic line, $i = 2$, is at ~47 keV, with $d_2 \sim 2.3$ and $\sigma_2 = 9.7$ keV. The 2–75 keV flux is $\sim 1\times 10^{-8}$ erg cm^{-2} s^{-1}. In order to showcase the unparalleled accuracy of *HEX-P* in measuring magnetic fields correspondent to cyclotron line energies above 50 keV, we incorporated a representative example into our model: we include an n_3 harmonic line at 70 keV ($i = 3$), with the width (σ_3) and strength (d_3) set to match those of the n_2 harmonic line. By doing so, we investigate the ability of *HEX-P* to effectively detect these parameters in the n_3 harmonic line, from which we can constrain the magnetic field strength and details about the magnetic field structure.

A 20 ks observation *HEX-P* is able to constrain the energy of the n_3 harmonic well, to within 7% (see Figure 7). We also applied an F-test to calculate the probability of chance improvement, with and without the n_3 harmonic line, and found that the probability of chance improvement when adding the n_3 harmonic line is below 0.06%, confirming the robustness of the detection. We reiterate here that the clear improvement of *HEX-P* over its predecessors in terms of broadband coverage and sensitivity makes it possible to investigate higher harmonic features–which have clearly eluded *NuSTAR* [see e.g., Tomar et al. (2021)].

Since cyclotron lines result from the resonant scattering of photons by electrons whose energies are quantized into Landau levels by the strong magnetic field, and the quantized energy levels of the electrons are harmonically spaced, one would naively expect the energy of the $n > 1$ harmonics to be the integer multiples of the fundamental line. It has however been observed in various X-ray pulsars that this is generally not the case (see Yang et al., 2023; Orlandini et al., 2012 and discussions within). The discrepancy can be understood by assuming a difference in line formation *mechanisms* or in line-forming *regions* for the fundamental and higher harmonics. In the former case, the fundamental would primarily arise from resonant scattering, while the higher harmonics involve additional effects like multiple scattering and photon spawning [see e.g., Nishimura, (2003); Schönherr et al. (2007)]. This, however, can not be the only reason because some systems show an an-harmonic spacing larger than predicted by this effect. One way to explain this difference is to take into account that the optical depths of the fundamental and the higher harmonics can be different if they are formed at different heights above the NS. The higher harmonics could be closer to the NS surface and the fundamental line situated at a height with weaker magnetic field strength [see, e.g., Fürst et al. (2018)]. Another possibility is to consider a displacement of the magnetic dipole, which would also explain the energy difference of the two lines if the lines originate from the different poles of the NS (Rodes-Roca et al., 2009). Therefore, a significant phase dependence of the strength of the fundamental and higher harmonics is expected, which is not possible to probe with the current data sets. Here, too, *HEX-P* can provide revolutionary new capabilities though (see Section 3.2.2).

Finally, note that while the n_2 harmonic of Cen X-3 at 47 keV technically falls within the energy range covered by *NuSTAR*, meaningful constraints could not be derived with *NuSTAR* (see panel (e) of Figure 7) due to the dominant background in that energy range even when the exposure was set to 500 ks. However, with *HEX-P*, the parameters associated with the cyclotron line can be much better constrained, while also alleviating the degeneracies with the continuum. To emphasize the latter point, we present a contour plot in Figure 8 depicting the relationship between the fundamental cyclotron line energy and the cutoff energy for both *HEX-P* and *NuSTAR* data for the same model and exposure of 20 ks for Cen X-3. The plot clearly demonstrates that *HEX-P* provides significantly more stringent constraints compared to *NuSTAR*. Such accurate measurements in short exposure times will enable detailed pulse phase-resolved spectra to explore the accretion physics in the accretion column in unprecedented detail, as discussed in the following section.

Note that Cen X-3 is highly variable, the X-ray flux varies by up-to two orders of magnitude even outside eclipses. Therefore, we also fit the actual *NuSTAR* data in bright flux state (ObsID 30101055002; exposure 21 ks), which has a flux an order of magnitude more than our simulations, and find the harmonics were not detected in the *NuSTAR* spectrum [see, Tomar et al. (2021)]. In order to make a comparison of *HEX-P* vs. *NuSTAR* for this bright state of Cen X-3, we simulated an HET spectrum using the *NuSTAR* model in bright state, while keeping the parameters of harmonics as above. We find that, even for this bright state of Cen X-3, *NuSTAR* will be able to obtain the same signal-to-noise as *HEX-P* only if the exposure is increased by 20 times (i.e., 420 ks).

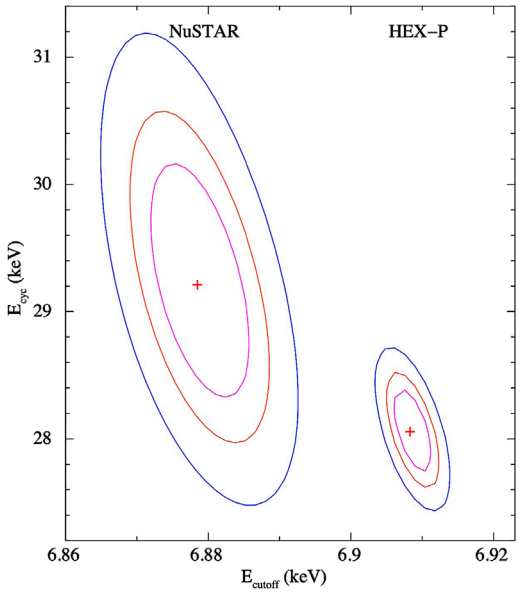

FIGURE 8
Contour plots (68%, 90%, and 99% confidence levels) for cutoff energy *versus* the fundamental cyclotron line energy for Cen X-3 using the same model and exposure for *NuSTAR* and *HEX-P*. As evident from the plot, *HEX-P* will provide better constraints on the continuum and cyclotron line parameters; thereby mitigating degeneracies between the two. Note that the cutoff energies are slightly shifted to aid visualization.

3.2.2 Constraining accretion column emission geometry through pulse phase-resolved spectroscopy

Vela X-1 is an archetypical HMXB. It has been well studied with all current and past X-ray missions (see Kretschmar et al., 2021, for a recent review). While not being exceptionally luminous ($\sim 10^{36}$ erg s^{-1}), its close distance ($d = 1.9$ kpc) and X-ray eclipses make it an ideal system to study NS magnetic fields and their interaction with the stellar wind of the companion (i.e., the mass donor). The X-ray spectrum of Vela X-1 shows two CRSFs, the fundamental at around 25 keV and the n_2 harmonic around 55 keV (see Fürst et al., 2014, and references therein). These line energies are ideally covered by the *HEX-P* energy band. However, in Vela X-1, the fundamental line around 25 keV is much weaker and shallower than the n_2 harmonic line at 55 keV. In fact, the 25 keV line is so weak that there has been a long-standing discussion in the literature about its existence, which could only be settled once *NuSTAR* data were available (Kreykenbohm et al., 2002; Maitra and Paul, 2013; Fürst et al., 2014). The cyclotron lines in Vela X-1 therefore represent a good test case to explore *HEX-P*'s sensitivity to broad and shallow spectral features.

We performed simulations to study how well *HEX-P* can measure the energy, width, and depth of both CRSFs, in particular as a function of rotational phase of the NS. Variations of CRSF parameters as a function of phase constrain the magnetic field geometry and emission geometry of the accretion column [see, e.g., Iwakiri et al. (2019); Liu et al. (2020)].

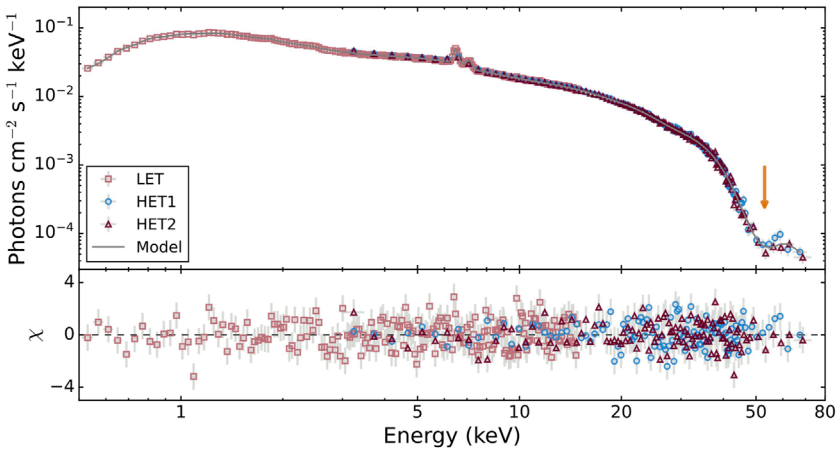

FIGURE 9
Simulated Vela X-1 spectrum for the bin covering phases 0–0.1 (see Figure 10 for the spectral values in that bin). The n_2 harmonic cyclotron line is clearly visible as a strong dip at the highest energies as indicated by the arrow.

We base our simulations on the spectral fits of *NuSTAR* data presented by Diez et al. (2022). In particular, the continuum is modeled by a powerlaw with an exponential cutoff at high energies (using the model "FDcut" in XSPEC, Eq. 3; Tanaka, 1986), modified by neutral absorption column at low energies:

$$\mathrm{FDCUT}\,(E) = A\ E^{-\Gamma}\ \frac{1}{1+\mathrm{e}^{(E-E_{\mathrm{cut}})/E_{\mathrm{fold}}}} \tag{3}$$

where Γ is the power-law index, E_{cut} is the cutoff energy, and E_{fold} is the folding energy. In addition to the continuum model used by Diez et al. (2022) we also include soft X-ray emission lines at 6.4 keV (Fe Kα), 2.4 keV (S Kα), 1.8 keV (Si Kα), 1.4 keV (Mg Lα), and 0.9 keV (Ne IX), representing various atomic features in the spectrum (Diez et al., 2023). A simulated spectrum is shown in Figure 9.

As mentioned in Section 3.2.1, CRSFs are modeled using a multiplicative line model with a Gaussian optical depth profile described by its energy E_i, its strength d_i, and its width σ_i. Here the subscript i denotes either the fundamental line around 25 keV ($i = 1$) or the n_2 harmonic line around 55 keV ($i = 2$). The width σ_1 is set to $0.5 \times \sigma_2$ (Diez et al., 2022). Instead of relying on the [rather uncertain; see, e.g., Maitra et al. (2018)] current knowledge of the phase-resolved behavior of the CRSF parameters, we simulate that the four most relevant parameters (E_1, E_2, d_1, d_2) vary sinusoidally with random phase shifts to each other. This approach demonstrates the power of *HEX-P* to resolve small changes in any of the parameters, even for relatively weak lines. In particular, we assume that the fundamental line E_1 varies by about ±3.5 keV as a function of phase, while the n_2 harmonic line energy E_2 varies by ±5 keV. The strength d_1 and d_2 vary by ±0.3 keV and ±5.0 keV, respectively.

In addition, we also allow the absorption column of the partial absorber to vary, with $\pm 5 \times 10^{22}$ cm^{-2} around the average value of 32.1×10^{22} cm^{-2}. While we do not necessarily expect that the absorption column will vary significantly as function of pulse phase, this variability highlights the capabilities of the *HEX-P*/LET to measure small changes in absorbing columns on time-scales as short as 5 ks. These variations have been observed in time-resolved spectroscopy and allow us to study the physical properties, like density and clump sizes of the accreted medium (Diez et al., 2023). At the same time, the changes in N_{H} do not influence the high energy spectrum where the CRSFs are present.

For our simulations, we assume that LET will be operated in a fast readout mode to avoid pile-up and with negligible deadtime. We simulate spectra with 50 ks exposure time each, and split the data into 10 phase-bins so that each one has an exposure time of 5 ks We simulate 100 individual spectra for each phase-bin and calculate the standard deviation (SD) of that sample as uncertainties for each parameter. We additionally calculate the 90% and 10% percentile of the 90% uncertainties of each realization as a realistic estimate of the expected uncertainties in a real 50 ks observation. Using multiple realizations for each phase bin allows us to avoid issues with any one particular realization and shows that our uncertainties are properly sampled over the Poisson noise inherent to counting statistics. The results are shown in Figure 10.

All parameters can be very well reconstructed, with the fundamental energy having uncertainties <0.5 keV for phases where its strength is >0.4 keV (i.e., phases 0.5–1.0). Even for weaker lines (despite having larger uncertainties of about ±1 keV), the line can be still significantly detected. This is a significant improvement over *NuSTAR*, for which Fürst et al. (2018) found that the energy was basically unconstrained for line strengths <0.5 keV.

The n_2 harmonic line energy can be very well constrained (with uncertainties <2 keV) for central energies of the line <57 keV. Due to the exposure time of only 5 ks per phase-bin and the low cutoff energy of ~25 keV, the line appears at the very edge of the useful range of the spectrum. Therefore, higher energies become more difficult to constrain, as most of the line is outside the useful passband; however, we still find typical constraints of ±3–4 keV, even for a simulated line energy of 61 keV.

These results represent a significant improvement over previous phase-resolved studies of Vela X-1. For example, using *RXTE*, Kreykenbohm et al. (1999) found variations of the CRSF energies for both the fundamental and the n_2 harmonic line, but could only use 10 phase bins and still had average uncertainties of 2–3 keV for

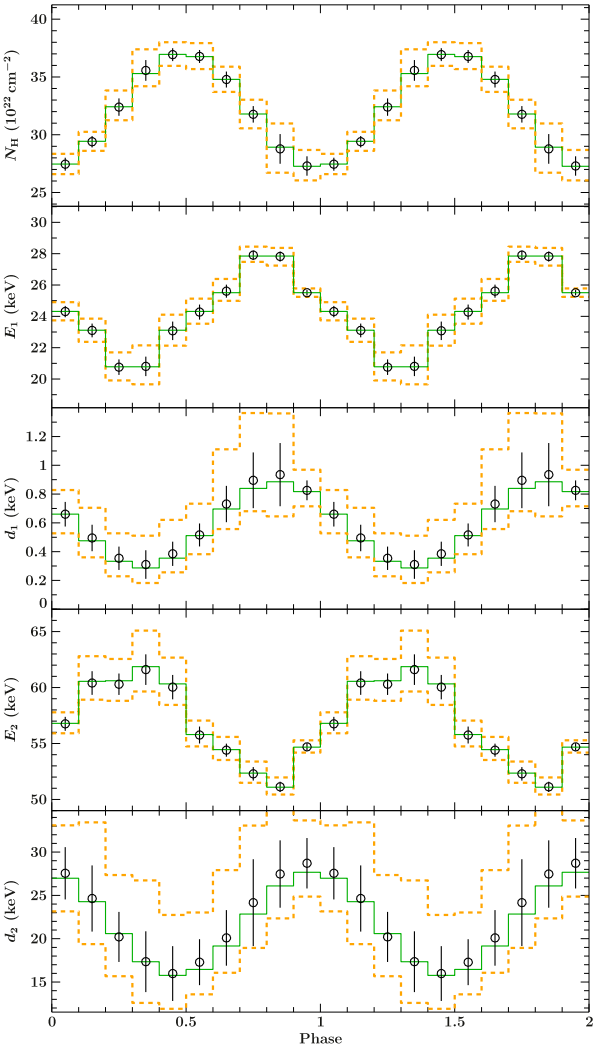

FIGURE 10
Absorption column and cyclotron line variability in Vela X-1, calculated from simulated phase-resolved *HEX-P* spectra using the results of Diez et al. (2022) with an average flux of 6.7×10^{-9} erg s^{-1} cm^{-2} in the 3–80 keV band. The parameters from top to bottom are: absorption column N_H, fundamental line energy (E_1), fundamental line strength (d_1), n_2 harmonic line energy (E_2), and n_2 harmonic line strength (d_2). Note that the fundamental line width is set to half of the n_2 harmonic width. The black uncertainties show the standard deviation for a sample of 100 simulations per phase bin. The orange dashed histogram indicates the expected 90% uncertainties on each individual realization. The green line indicates the input values for each phase bin. For details about the simulation set-up see Section 3.2.2; Supplementary Table S3.

the fundamental line, and 5–10 keV for the n_2 harmonic. Recently, Liu et al. (2022) published results obtained on Vela X-1 with *Insight*/HXMT. Using 16 phase-bins for a ~100 ks exposure, they found average uncertainties comparable to our *HEX-P* simulations for the n_2 harmonic line, but with significantly larger uncertainties (a few keV) for the fundamental line. We also note that Liu et al. (2022) found the n_2 harmonic line at energies between 40 and 50 keV, i.e., at much lower energies than simulated here and therefore in a part of the spectrum with a much higher signal-to-noise ratio.

HEX-P observations would therefore be a big step forward in being able to obtain phase-resolved spectroscopy of bright HMXBs, where we can constrain the CRSF parameters, in particular the energy, much better than with existing instruments in shorter exposure times. This reduction in exposure time means that we can either observe more sources in less time or slice the phase-resolved spectra finer to obtain a more detailed look at the emission and magnetic field geometry of the accretion column (Nishimura, 2003; Schönherr et al., 2007; Schwarm et al., 2017).

3.2.3 Constraining the surface magnetic field strength from quiescent observations of Be X-ray binaries

Details regarding the formation of cyclotron lines in the spectra of accreting NSs in HMXBs are highly debated in the literature. The observed positive and negative correlations of the cyclotron energy with luminosity are often interpreted as a change of the dynamics of the accretion process in different accretion regimes, distinguished by a critical luminosity where a radiation-dominated shock forms in the column above the NS surface. For high-luminosity regimes, when it is assumed that $L_X > L_{crit}$, several mechanisms for the formation of cyclotron lines have been suggested that explain the observed negative line energy *versus* luminosity correlation. These scenarios involve different locations for the line production: above the NS surface in an accretion column that is growing with increasing luminosity [see, e.g., Becker et al. (2012)] or in the illuminated atmosphere of the NS at lower magnetic latitudes, where the column radiation is reprocessed [as suggested by Poutanen et al. (2013); see, however; Kylafis et al. (2021)]. For lower luminosities, $L_X \lesssim L_{crit}$, the formation of cyclotron lines is usually attributed to comparatively lower heights in the accretion column. In this case, a positive line energy *versus* luminosity correlation can be explained by the formation of a collisionless shock [see, e.g., Rothschild et al. (2017); Vybornov et al. (2017)] that is moving closer to the NS surface for higher luminosities or by the redshift due to bulk motion of the accretion flow (Nishimura, 2014; Mushtukov et al., 2015). However, to apply these models in a consistent way and to distinguish between their predictions, it is required to know the surface field at the magnetic pole of the NS. This can then serve as a reference to estimate, for example, the characteristic height of the line-forming region in the column or the velocity of the accretion flow near the surface.

Recent evidence of accretion in Be X-ray binaries in quiescence, i.e., with $L_X \ll L_{crit}$, and the simple emission region geometry expected in this case (i.e., a hot spot on the NS surface) together represent a unique opportunity to observe cyclotron lines at the energy corresponding to the surface value of the magnetic field. From current observational examples it seems that for this accretion state to occur, the magnetic field of the source might have to be sufficiently high, $B \gtrsim 5 \times 10^{12}$ G, and the spin period might have to be comparatively long, $\gtrsim 100$ s (as, e.g., for GX 304–1 and GRO J1008–57: Tsygankov et al., 2019b; Lutovinov et al., 2021). The low flux level, however, makes the detection of cyclotron lines at high energies very challenging. GX 304–1 is one of the first sources which unambiguously exhibited stable quiescent accretion (Rouco Escorial et al., 2018) with a cyclotron line known from outburst observations (Mihara et al., 2010; Malacaria et al., 2015). The corresponding flux level in the 2–10 keV energy band,

~ 0.4 mCrab, is below the sensitivity of *Insight*/HXMT. With *NuSTAR* we can access the high-energy emission, but are typically unable to constrain the turnover of the second hump of the characteristic double-hump spectrum (see Section 3.1) and the cyclotron line (Tsygankov et al., 2019b, Zainab et al., in prep.).

The best way to probe the above mentioned science cases is to observe the source during the quiescent accretion regime, i.e., at a low-luminosity state that is typically below the detection threshold for X-ray all sky monitors and accessible only with pointed observations subsequent to an X-ray outburst. Such a regime is also of importance since the simplified physics of plasma stopping at the nearly-static NS atmosphere allows for more detailed modeling of emission processes. The tenuous flow of matter stops at the NS atmosphere by Coulomb collisions, resulting in a high temperature gradient from ~ 30 keV at the top down to ~ 2 keV in the lower layers, separated by only ~ 10 m [see, e.g., Sokolova-Lapa et al. (2021)]. The intrinsic emission is mainly produced by magnetic bremsstrahlung (for sufficiently low magnetic fields, cyclotron photons are produced as well from collisional excitations of electrons moving in bulk; Mushtukov et al., 2021), which is then modified by Compton scattering. This regime of accretion allows, for the first time, to combine modeling of the temperature and density structure of the emission region with a *joint* simulation of the continuum and cyclotron line formation (Mushtukov et al., 2021; Sokolova-Lapa et al., 2021).

In this way, existing physically-motivated models principally provide access to information about the field strength at the poles of accreting highly magnetized NSs. However, the limitations of current high-energy missions do not permit us to constrain the corresponding cyclotron lines in the spectra. *HEX-P* will open a new avenue for the accreting NSs community by allowing us to detect such features with sufficiently long exposures.

In order to demonstrate *HEX-P*'s capabilities to measure the surface magnetic field strength of a NS in quiescence, we simulate observations of the quiescent state of the Be X-ray binary GX 304–1, the first system for which a transition to the two-component spectrum was observed by *NuSTAR* (Tsygankov et al., 2019b). We use the physical model POLCAP presented by Sokolova-Lapa et al. (2021), which describes emission for the low-luminosity accretion regime. Here, we adopt an updated parametrization of the model (using the same underlying pre-calculated spectra; E. Sokolova-Lapa, priv. comm.). The parameters are the mass flux, $\dot{M}/\pi r_0^2$, where $\dot{M}$ is the mass-accretion rate and r_0 is the polar cap radius; the cyclotron energy, $E_{\rm cyc}$, corresponding to the polar magnetic field strength, B; and the normalization given in terms of r_0^2/D^2, where D is the distance to the source. We set the normalization and the mass flux based on the flux level and the shape of the spectrum as observed previously by *NuSTAR*. The magnetic field strength is set to $B = \times 5.3510^{12}$ G, derived from the centroid energy of the cyclotron line observed during the previous outburst [~ 50 keV, Jaisawal et al. (2016)] and corrected by the gravitational redshift near the surface of the NS ($z_g \approx 0.24$, assuming standard NS parameters). The corresponding spectrum calculated with the POLCAP model and the exact values of the parameters used for the simulations are shown in Figure 11. Due to internal averaging over the emission angles to obtain the total flux in the NS rest-frame [see details in Sokolova-Lapa et al. (2021)], the cyclotron line in the corresponding spectrum is located at ≈ 60 keV. Taking into account the gravitational redshift, the cyclotron line in the observed spectrum is therefore expected at ≈ 48 keV. We simulate a 60 ks observation for all three *HEX-P* instruments, combining the POLCAP model with TBABS (Wilms et al., 2000) to account for interstellar absorption (i.e., TBABS*POLCAP), fixing $N_{\rm H}$ to the Galactic value of 1.1×10^{22} cm^{-2} in the direction of the source. The resulting luminosity in the 1–80 keV range is $\sim 8 \times 10^{33}$ erg s^{-1}.

We compare the *HEX-P* spectra against a *NuSTAR* observation of the same exposure. We first fit both, the simulated *HEX-P* and existing *NuSTAR* observations, using a model that includes two independent Comptonized components (COMPTT; Titarchuk, 1994), TBABS*(COMPTT$_1$ + COMPTT$_2$). This model, with or without a multiplicative Gaussian-like cyclotron line (GABS), is commonly used to describe the two-component spectra of low-luminosity states [see, e.g., Tsygankov et al. (2019a); Lutovinov et al. (2021); Doroshenko et al. (2021)]. Similarly to earlier analyses (Tsygankov et al., 2019b), we obtain a good description of the *NuSTAR* data with this model, with $\chi^2_{\rm red} = 136.93/107 = 1.28$ for the best fit.

For the simulated *HEX-P* data, the same model consistent of two absorbed Comptonized components provides a formally satisfactory fit ($\chi^2_{\rm red} = 322.64/275 = 1.17$), however, the residuals are flat only at low and intermediate energies, but indicate a dip at around 40–60 keV, where the cyclotron line is expected from the underlying physical model (see Figure 11). The best fit for a model which includes an additional Gaussian absorption line at high energies to describe the cyclotron line, provides the line's centroid energy of $46.5^{+4.1}_{-2.7}$ keV, width $8.2^{+3.1}_{-2.1}$ keV, and strength 54^{+41}_{-21} keV, with the $\chi^2_{\rm red} = 261.23/276 = 0.95$. The centroid energy corresponds (within its uncertainties) to the redshifted cyclotron line from the physical model, which is expected to be at $\approx 60/(1+z_g)$ keV ≈ 48 keV, assuming the standard NS parameters to estimate the redshift, $z_g = 0.24$. Figure 12 shows the resulting spectra and the corresponding best-fit models for the real *NuSTAR* and the simulated *HEX-P* observations.

This example shows that even at this exposure, which is relatively low for the quiescent state of Be X-ray binaries, we can constrain the cyclotron line energy and thus the surface magnetic field to within ~ 20%. This capability is crucial for systems which have never been observed at high-luminosity states, that is, for which cyclotron lines have never been observed in the spectra. This class of Be X-ray binaries accreting in quiescence is actively growing, e.g., through *NuSTAR* follow-up of Be X-ray binary candidates found during the first eROSITA All Sky Survey [see, e.g., Doroshenko et al. (2022)]. More similar discoveries are expected as deeper X-ray survey data from eROSITA become available. The spectral shape of the latter sources, in particular, the location of the high-energy excess associated with the energies below the cyclotron resonance, suggests a similar magnetic field strength as in GX 304–1. The search for high-energy cyclotron lines, which makes it possible to unambiguously constrain the surface magnetic field of an accreting neutron star, requires superior sensitivity at hard X-rays, as will be provided by *HEX-P*.

For a discussion of NS science that can be done with *HEX-P* for B-fields in excess of ~ 10^{14}G (i.e., magnetars), we refer the reader to Alford et al. (2023), (*in prep.*).

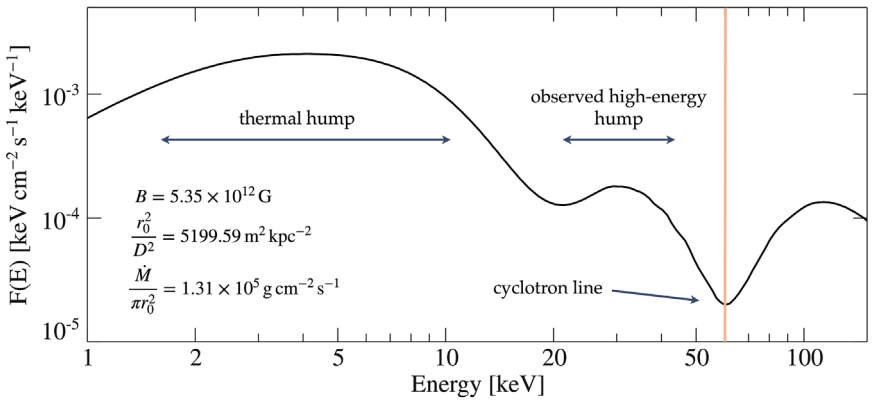

FIGURE 11
Model used to simulate the observation of the Be X-ray binary GX 304–1 in quiescence. The vertical orange line indicates the center of the cyclotron line. The cyclotron line and the continuum are calculated together using polarized radiative transfer simulations (Sokolova-Lapa et al., 2021). The low-energy "thermal" hump and the high-energy hump below the cyclotron line (the red wing of the cyclotron line) are typically observed as a "two-hump" spectrum from Be X-ray binaries in quiescence.

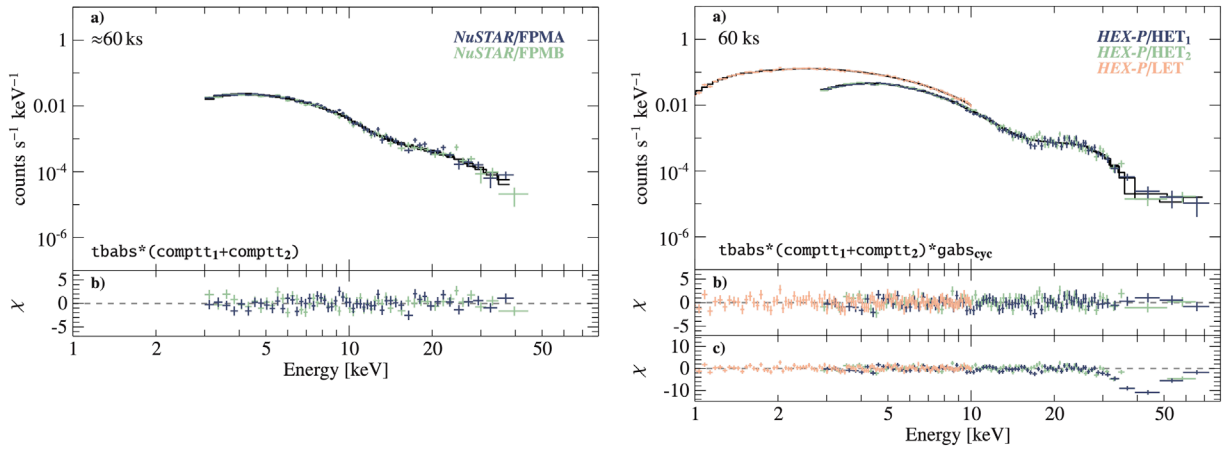

FIGURE 12
NuSTAR observation [left, (a)] and simulated *HEX-P* [right, (a)] spectra of a 60 ks observation of the Be X-ray GX 304–1 in quiescence and corresponding best-fit models. Both panels (b) show residuals for the best-fit models. For the simulated *HEX-P* spectra, we also show the residuals for the case when the cyclotron line strength is set to zero [left, (c)]. The high-energy cyclotron line can be constrained from the *HEX-P* data, with the centroid energy $46.5^{+4.1}_{-2.7}$ keV.

3.2.4 Constraining super-critical accretion and the critical luminosity via cyclotron line evolution in extragalactic sources

A correlation between cyclotron line energy and X-ray luminosity has been reported for a handful of X-ray pulsars [see Staubert et al., 2019, and above]. The dependence of the line energy on luminosity can be attributed to changes in the height of the accretion column and can be positive or negative for low and high X-ray luminosity, respectively (Becker et al., 2012). However, in a couple of sources a secondary effect has been reported: for equal levels of luminosity, the energy of the cyclotron line can be different (up to 10% change) between the rise and the decay of an outburst or between different outbursts (e.g., V 0332 + 53, Cusumano et al. (2016) and SMC X-2; Jaisawal et al., 2023). Doroshenko et al. (2017) proposed that this effect is likely caused by a change of the emission region geometry (e.g., different combinations of height and width of the accretion column), while an alternative explanation is that it is due to accretion-induced decay of the NS's magnetic field (Cusumano et al., 2016; Jaisawal et al., 2023).

Given this complex observational behavior, it is critical to detect CRSFs in more transient systems and to study their evolution over luminous outbursts. Although a significant population of HMXBs is found in the Milky Way, interpreting results from observing its members is often hampered by their uncertain distance and large foreground absorption. In that sense nearby galaxies like the star-forming Large and Small Magellanic Clouds (LMC and SMC) offer a unique laboratory to complement our studies of luminous Galactic HMXBs. Sources in these galaxies have well determined distances of ~50 kpc (LMC) or ~60 kpc (SMC) and low Galactic foreground absorption (~ 10^{20} cm^{-2}) making them ideal targets for spectral and temporal studies during major outbursts. Based on past observations and recent statistics, an

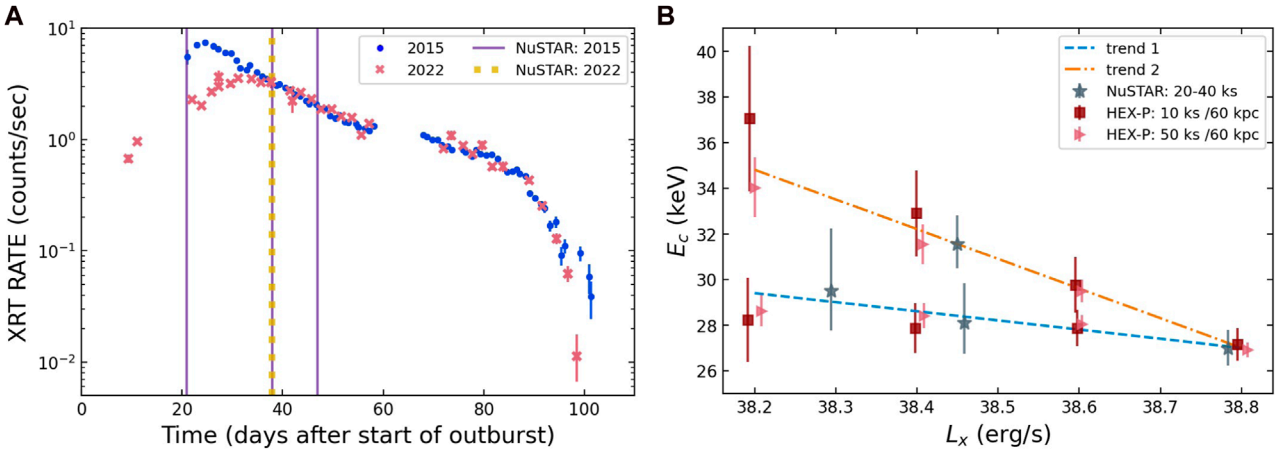

FIGURE 13
(A): The 2015 and 2022 super-critical outbursts of SMC X-2 observed by *Swift*/XRT. The vertical lines mark the epochs of four *NuSTAR* observations of the system. **(B)**: The cyclotron line dependence on luminosity. The star symbols mark the measured CRSF values for SMC X-2 for the *NuSTAR* observations (Jaisawal et al., 2023). Note that the *NuSTAR* points on the trend 1 line are from the 2015 outburst, while the point on the trend 2 line was measured during the 2022 outburst; hence different cyclotron line energies can be measured even when the source is at nearly the same luminosity during outburst indicating an inherent difference between outbursts. We demonstrate *HEX-P*'s capabilities to discern between different possible trends in cyclotron line energy as a function of luminosity in these types of systems in as little at 10 ks, though greatly improved for 50 ks exposures.

outburst that peaks above 2×10^{38} erg s^{-1} occurs in the Magellanic Clouds every few years [e.g., Vasilopoulos et al. (2014); Koliopanos and Vasilopoulos, (2018); Maitra et al. (2018); Vasilopoulos et al. (2020)]. Such outbursts are brighter than the Eddington luminosity for a typical NS, more precisely, they are brighter than the critical luminosity[5], $L_{\rm crit} \sim 10^{37}$ erg s^{-1}, for a typical accretion column (see Section 3.1). They are therefore called super-Eddington or super-critical outbursts.

SMC X-2 is a good example to demonstrate *HEX-P*'s capabilities to detect and follow the evolution of a CRSF during a bright outburst. This BeXRB pulsar has exhibited two outbursts which reached luminosities above the Eddington limit over the last decade, one in 2015 and another in 2022. Both outbursts were followed up with *Swift*/XRT, as well as with *NuSTAR* ToOs (three observations in 2015 and one in 2022), covering a broad range in luminosity of $(2–6) \times 10^{38}$ erg s^{-1} (see Figures 13A). When comparing the CRSF energy for the two outbursts at the same luminosity level, the line energy was about 2 keV higher during the 2022 outburst than observed previously in 2015 (see Figures 13B). This corresponds to a difference in magnetic field strength of $B \sim 2 \times 10^{11}$ G, akin to the difference reported by Cusumano et al. (2016) for V 0332 + 53.

In order to test *HEX-P*'s capabilities to detect CRSF features for extragalactic sources and determine if the data would be sufficient to distinguish trends with luminosity, we performed several simulations based on the spectral properties of SMC X-2 as measured by *NuSTAR* (Jaisawal et al., 2023). For all simulations we used both HET and LET detectors. For the continuum we used an absorbed (TBABS with $N_{\rm H} = 10^{20}$ cm^{-2}; Wilms et al., 2000) cut-off power-law model (i.e., CUTOFFPL) and a cyclotron absorption feature with the GABS model. We limited our simulations to the super-critical regime and a bolometric luminosity of 1.5–6 $\times 10^{38}$ ergs s^{-1} which yields an absorbed flux range of 2–8 $\times 10^{-10}$ ergs cm^{-2} s^{-1} (1–50 keV). We simulated spectra where the CRSF energy varied with luminosity assuming two arbitrary inverse linear energy dependencies (trend 1 and trend 2 in Figure 13). We then fit the spectra and derived the best-fit parameters for the line with corresponding uncertainties. The results are shown in Figures 13B. *HEX-P* can constrain the CRSF parameters (here the central line energy) at least two times better than *NuSTAR* and with an exposure time (10 ks) that is only between half and a fourth that of *NuSTAR*, as well as discern between different trend inputs. For a longer exposure time of 50 ks the line parameters can be measured with unparalleled accuracy at the distance of the SMC. Thus, *HEX-P* will be able to detect and follow cyclotron line evolution for super-critical outbursts in the Magellanic Clouds and thereby test competing physical models (i.e., similar to V 0332 + 53 Cusumano et al., 2016; Vybornov et al., 2018). Note that the flux regime for which these trends are simulated (see Supplementary Table S1) and the science cases of the previous subsections suggest that trends in CRSF energy can also be probed at sub-critical through super-critical luminosities in galactic sources. For science that can be executed with *HEX-P* regarding pulsations and cyclotron lines in extragalactic ultraluminous X-ray (ULX) sources which reach even higher luminosities of >100× their Eddington limit, we refer the reader to Bachetti et al. (*in prep.*).

In addition, it is expected that accreting XRPs crossing the critical luminosity should show a reversal of the cyclotron line energy *versus* luminosity correlation. To date only marginal evidence has been observed for such a trend reversal and in only a couple of sources (Doroshenko et al., 2017; Malacaria et al., 2022). As mentioned above, the Magellanic Clouds host comparatively many transient accreting pulsars displaying high-luminosity outbursts. *HEX-P*'s ability to constrain the cyclotron line energy with unprecedented accuracy across orders of magnitude in luminosity (and thus over distinct accretion regimes) will provide us with the

5 The critical luminosity is sometimes called the "local Eddington limit" which is descriptive but formally not well defined.

opportunity to trace more and well defined trend reversals. This will allow us to constrain the critical luminosity for a given source which, in turn, places constraints on physical parameters of the observed system, such as the NS magnetic field strength or source distance (Becker et al., 2012).

4 Conclusion

We have presented open questions about NSs and accretion onto strongly magnetized sources, and demonstrated *HEX-P*'s unique ability to address these questions. The broad X-ray passband, improved sensitivity, and low X-ray background make *HEX-P* ideally suited to understand accretion in X-ray soft sources, down into low accretion rate regimes. In particular for LMXBs, we have shown that *HEX-P* observations will discriminate between competing continuum emission models that diverge above 30 keV; an energy band inaccessible to current focusing X-ray telescopes for these soft spectrum sources. Additionally, leveraging the improved sensitivity and broad X-ray passband, *HEX-P* will achieve tighter constraints on NS radius measurements through reflection modeling. These measurements are complementary and independent to other methodologies, and will narrow the allowed region on the NS mass-radius plane for viable EoS models for ultra-dense, cold matter, providing fundamental physics information in a regime inaccessible to terrestrial laboratories.

For the case of NSs in HMXBs, *HEX-P* will vastly improve our ability to: 1) detect multiple cyclotron line features in a single observation, aiding in our understanding of the magnetic field strength in different regions of the accretion column and the poorly known physical mechanisms behind the formation of higher harmonic features; 2) obtain detailed phase-resolved spectra to track the dependence of CRSFs on pulse phase in order to explore the geometric configuration of the accretion column emission in unprecedented details; 3) constrain the surface magnetic field strength of accreting NSs at the lowest accretion regime and characterize the continuum spectral formation to provide updated physically-motivated spectral models for future observations; and 4) identify CRSFs in extragalactic sources and follow the evolution of their line energy as a function of luminosity in order to distinguish between competing theories regarding changing emission region geometry or accretion-induced decay of the NS *B*-field.

HEX-P will provide a new avenue for testing magnetic field configuration, emission pattern, and accretion column physics close to the surface of NSs, as well as enhance our understanding of extreme accretion physics in both LMXBs and HMXBs.

Data availability statement

The raw data supporting the conclusions of this article will be made available by the authors, without undue reservation.

Author contributions

RL: Conceptualization, Data curation, Formal Analysis, Investigation, Methodology, Supervision, Validation, Visualization, Writing–original draft, Writing–review and editing. CM: Conceptualization, Investigation, Methodology, Writing–original draft, Writing–review and editing. ES-L: Conceptualization, Formal Analysis, Investigation, Methodology, Writing–original draft, Writing–review and editing. FF: Conceptualization, Formal Analysis, Investigation, Methodology, Writing–original draft, Writing–review and editing. PP: Conceptualization, Formal Analysis, Investigation, Methodology, Writing–original draft, Writing–review and editing. AS: Conceptualization, Formal Analysis, Investigation, Methodology, Validation, Writing–original draft, Writing–review and editing. KP: Conceptualization, Supervision, Validation, Writing–original draft, Writing–review and editing. SP: Conceptualization, Writing–review and editing. GV: Conceptualization, Formal Analysis, Investigation, Methodology, Writing–original draft, Writing–review and editing. JW: Conceptualization, Validation, Writing–review and editing. JG: Writing–review and editing. KM: Writing–review and editing. DS: Writing–review and editing. CM: Writing–review and editing. MD: Writing–review and editing. DW: Writing–review and editing. MB: Writing–review and editing. JE: Writing–review and editing.

Funding

The author(s) declare financial support was received for the research, authorship, and/or publication of this article. The material is based upon work supported by NASA under award number 80GSFC21M0002. GV acknowledges support by the Hellenic Foundation for Research and Innovation, (H.F.R.I.) through the project ASTRAPE (Project ID 7802). The work of DS was carried out at the Jet Propulsion Laboratory, California Institute of Technology, under a contract with NASA. ES-L and JW acknowledge partial funding under Deutsche Forschungsgemeinschaft grant WI 1860/11-2 and Deutsches Zentrum für Luft-und Raumfahrt grant 50 QR 2202.

Acknowledgments

RL and AS would like to thank Dr. Kazuhiko Shinki for providing consultation on statistical methods of Section 2.2.2. The authors thank the reviewers for their detailed comments that enhanced the science cases presented within the manuscript.

Conflict of interest

The authors declare that the research was conducted in the absence of any commercial or financial relationships that could be construed as a potential conflict of interest.

Publisher's note

All claims expressed in this article are solely those of the authors and do not necessarily represent those of

their affiliated organizations, or those of the publisher, the editors and the reviewers. Any product that may be evaluated in this article, or claim that may be made by its manufacturer, is not guaranteed or endorsed by the publisher.

Supplementary material

The Supplementary Material for this article can be found online at: https://www.frontiersin.org/articles/10.3389/fspas.2023.1292500/full#supplementary-material

References

Abbott, B. P., Abbott, R., Abbott, T. D., Acernese, F., Ackley, K., Adams, C., et al. (2019). Properties of the binary neutron star merger GW170817. *Phys. Rev. X* 9, 011001. doi:10.1103/PhysRevX.9.011001

Aftab, N., Paul, B., and Kretschmar, P. (2019). X-ray reprocessing: through the eclipse spectra of high-mass X-ray binaries with XMM-Newton. *ApJ Suppl.* 243, 29. doi:10.3847/1538-4365/ab2a77

Alexander, S. G., and Meszaros, P. (1991). Cyclotron harmonics in accreting pulsars and gamma-ray bursters: effect of two-photon processes. *ApJ* 372, 565. doi:10.1086/170001

Arnaud, K. A. (1996). "XSPEC: the first ten years," in *Astronomical data analysis software and systems V. San francisco: astron. Soc. Pacific)*. Editors G. H. Jacoby, and J. Barnes, 17. 101 of Astron. Soc. Pacific Conf. Ser.

Bala, S., Bhattacharya, D., Staubert, R., and Maitra, C. (2020). Time evolution of cyclotron line of Her X-1: a detailed statistical analysis including new AstroSat data. *MNRAS* 497, 1029–1042. doi:10.1093/mnras/staa1988

Bardeen, J. M., Press, W. H., and Teukolsky, S. A. (1972). Rotating black holes: locally nonrotating frames, energy extraction, and scalar synchrotron radiation. *ApJ* 178, 347–370. doi:10.1086/151796

Barret, D. (2001). The broad band x-ray/hard x-ray spectra of accreting neutron stars. *Adv. Space Res.* 28, 307–321. doi:10.1016/S0273-1177(01)00414-8

Barret, D., Olive, J. F., Boirin, L., Done, C., Skinner, G. K., and Grindlay, J. E. (2000). Hard X-ray emission from low-mass X-ray binaries. *ApJ* 533, 329–351. doi:10.1086/308651

Basko, M. M., and Sunyaev, R. A. (1976). The limiting luminosity of accreting neutron stars with magnetic fields. *MNRAS* 175, 395–417. doi:10.1093/mnras/175.2.395

Becker, P. A., Klochkov, D., Schönherr, G., Nishimura, O., Ferrigno, C., Caballero, I., et al. (2012). Spectral formation in accreting X-ray pulsars: bimodal variation of the cyclotron energy with luminosity. *A&A* 544, A123. doi:10.1051/0004-6361/201219065

Becker, P. A., and Wolff, M. T. (2022). A generalized analytical model for thermal and bulk comptonization in accretion-powered X-ray pulsars. *ApJ* 939, 67. doi:10.3847/1538-4357/ac8d95

Bozzo, E., Romano, P., Ferrigno, C., and Oskinova, L. (2022). The symbiotic X-ray binaries Sct X-1, 4U 1700+24, and IGR J17329-2731. *MNRAS* 513, 42–54. doi:10.1093/mnras/stac907

Caballero, I., and Wilms, J. (2012). X-ray pulsars: a review. *MemSAI* 83, 230. doi:10.48550/arXiv.1206.3124

Cackett, E. M., Altamirano, D., Patruno, A., Miller, J. M., Reynolds, M., Linares, M., et al. (2009). Broad relativistic iron emission line observed in SAX J1808.4−3658. *ApJ* 694, L21–L25. doi:10.1088/0004-637X/694/1/L21

Cackett, E. M., Miller, J. M., Bhattacharyya, S., Grindlay, J. E., Homan, J., van der Klis, M., et al. (2008). Relativistic iron emission lines in neutron star low-mass X-ray binaries as probes of neutron star radii. *ApJ* 674, 415–420. doi:10.1086/524936

Caiazzo, I., and Heyl, J. (2021). Polarization of accreting X-ray pulsars - II. Hercules X-1. *MNRAS* 501, 129–136. doi:10.1093/mnras/staa3429

Casares, J., González Hernández, J. I., Israelian, G., and Rebolo, R. (2010). On the mass of the neutron star in Cyg X-2. *MNRAS* 401, 2517–2520. doi:10.1111/j.1365-2966.2009.15828.x

Chodil, G., Mark, H., Rodrigues, R., Seward, F. D., and Swift, C. D. (1967). X-ray intensities and spectra from several cosmic sources. *ApJ* 150, 57. doi:10.1086/149312

Church, M. J., and Balucińska-Church, M. (2001). Results of a LMXB survey: variation in the height of the neutron star blackbody emission region. *A&A* 369, 915–924. doi:10.1051/0004-6361:20010150

Cocchi, M., Gnarini, A., Fabiani, S., Ursini, F., Poutanen, J., Capitanio, F., et al. (2023). Discovery of strongly variable X-ray polarization in the neutron star low-mass X-ray binary transient XTE J1701−462. *A&A* 674, L10. doi:10.1051/0004-6361/202346275

Cusumano, G., La Parola, V., D'Aì, A., Segreto, A., Tagliaferri, G., Barthelmy, S. D., et al. (2016). An unexpected drop in the magnetic field of the X-ray pulsar V0332+53 after the bright outburst occurred in 2015. *MNRAS* 460, L99–L103. doi:10.1093/mnrasl/slw084

Dauser, T., García, J., Wilms, J., Böck, M., Brenneman, L. W., Falanga, M., et al. (2013). Irradiation of an accretion disc by a jet: general properties and implications for spin measurements of black holes. *MNRAS* 430, 1694–1708. doi:10.1093/mnras/sts710

Davies, R. E., and Pringle, J. E. (1981). Spindown of neutron stars in close binary systems - II. *MNRAS* 196, 209–224. doi:10.1093/mnras/196.2.209

Degenaar, N., Ballantyne, D. R., Belloni, T., Chakraborty, M., Chen, Y.-P., Ji, L., et al. (2018). Accretion disks and coronae in the X-ray flashlight. *Space Sci. Rev.* 214, 15. doi:10.1007/s11214-017-0448-3

Diez, C. M., Grinberg, V., Fürst, F., El Mellah, I., Zhou, M., Santangelo, A., et al. (2023). Observing the onset of the accretion wake in Vela X-1. *A&A* 674, A147. doi:10.1051/0004-6361/202245708

Diez, C. M., Grinberg, V., Fürst, F., Sokolova-Lapa, E., Santangelo, A., Wilms, J., et al. (2022). Continuum, cyclotron line, and absorption variability in the high-mass X-ray binary Vela X-1. *A&A* 660, A19. doi:10.1051/0004-6361/202141751

Di Salvo, T., Burderi, L., Robba, N. R., and Guainazzi, M. (1998). The two-component X-ray broadband spectrum of X persei observed by BeppoSAX. *ApJ* 509, 897–903. doi:10.1086/306525

Doroshenko, R., Piraino, S., Doroshenko, V., and Santangelo, A. (2020). Revisiting BeppoSAX and NuSTAR observations of KS 1947+300 and the missing cyclotron line. *MNRAS* 493, 3442–3448. doi:10.1093/mnras/staa490

Doroshenko, V., Santangelo, A., Kreykenbohm, I., and Doroshenko, R. (2012). The hard X-ray emission of X Persei. *A&A* 540, L1. doi:10.1051/0004-6361/201218878

Doroshenko, V., Santangelo, A., Tsygankov, S. S., and Ji, L. (2021). SGR 0755−2933: a new high-mass X-ray binary with the wrong name. *A&A* 647, A165. doi:10.1051/0004-6361/202039785

Doroshenko, V., Staubert, R., Maitra, C., Rau, A., Haberl, F., Santangelo, A., et al. (2022). SRGA J124404.1-632232/SRGA J124404.1−632232/SRGU J124403.8−632231: new X-ray pulsar discovered in the all-sky survey by the SRG. *A&A* 661, A21. doi:10.1051/0004-6361/202141147

Doroshenko, V., Tsygankov, S. S., Mushtukov, A. A., Lutovinov, A. A., Santangelo, A., Suleimanov, V. F., et al. (2017). Luminosity dependence of the cyclotron line and evidence for the accretion regime transition in V 0332+53. *MNRAS* 466, 2143–2150. doi:10.1093/mnras/stw3236

Eraerds, T., Antonelli, V., Davis, C., Hall, D., Hetherington, O., Holland, A., et al. (2021). Enhanced simulations on the athena/wide field imager instrumental background. *J. Astronomical Telesc. Instrum. Syst.* 7, 034001. doi:10.1117/1.JATIS.7.3.034001

Fabian, A. C., Rees, M. J., Stella, L., and White, N. E. (1989). X-ray fluorescence from the inner disc in Cygnus X-1. *MNRAS* 238, 729–736. doi:10.1093/mnras/238.3.729

Farinelli, R., Fabiani, S., Poutanen, J., Ursini, F., Ferrigno, C., Bianchi, S., et al. (2023). Accretion geometry of the neutron star low mass X-ray binary Cyg X-2 from X-ray polarization measurements. *MNRAS* 519, 3681–3690. doi:10.1093/mnras/stac3726

Farinelli, R., Ferrigno, C., Bozzo, E., and Becker, P. A. (2016). A new model for the X-ray continuum of the magnetized accreting pulsars. *A&A* 591, A29. doi:10.1051/0004-6361/201527257

Fiocchi, M., Bazzano, A., Bruni, G., Ludlam, R., Natalucci, L., Onori, F., et al. (2019). Quasi-simultaneous INTEGRAL, SWIFT, and NuSTAR observations of the new X-ray clocked burster 1RXS j180408.9-342058. *ApJ* 887, 30. doi:10.3847/1538-4357/ab4d59

Forsblom, S. V., Poutanen, J., Tsygankov, S. S., Bachetti, M., Di Marco, A., Doroshenko, V., et al. (2023). IXPE observations of the quintessential wind-accreting X-ray pulsar Vela X-1. *ApJ* 947, L20. doi:10.3847/2041-8213/acc391

Fürst, F., Falkner, S., Marcu-Cheatham, D., Grefenstette, B., Tomsick, J., Pottschmidt, K., et al. (2018). Multiple cyclotron line-forming regions in GX 301−2. *A&A* 620, A153. doi:10.1051/0004-6361/201732132

Fürst, F., Pottschmidt, K., Wilms, J., Tomsick, J. A., Bachetti, M., Boggs, S. E., et al. (2014). NuSTAR discovery of a luminosity dependent cyclotron line energy in Vela X-1. *ApJ* 780, 133. doi:10.1088/0004-637X/780/2/133

Galloway, D. K., Muno, M. P., Hartman, J. M., Psaltis, D., and Chakrabarty, D. (2008). Thermonuclear (type I) X-ray bursts observed by the rossi X-ray timing explorer. *ApJ Suppl.* 179, 360–422. doi:10.1086/592044

García, J., and Kallman, T. R. (2010). X-Ray reflected spectra from accretion disk models. I. Constant density atmospheres. *ApJ* 718, 695–706. doi:10.1088/0004-637X/718/2/695

García, J. A., Dauser, T., Ludlam, R., Parker, M., Fabian, A., Harrison, F. A., et al. (2022). Relativistic X-ray reflection models for accreting neutron stars. *ApJ* 926, 13. doi:10.3847/1538-4357/ac3cb7

Gehrels, N., Chincarini, G., Giommi, P., Mason, K. O., Nousek, J. A., Wells, A. A., et al. (2004). The*Swift*Gamma-ray burst mission. *ApJ* 611, 1005–1020. doi:10.1086/422091

Gendreau, K. C., Arzoumanian, Z., and Okajima, T. (2012). "The Neutron star Interior Composition ExploreR (NICER): an Explorer mission of opportunity for soft x-ray timing spectroscopy," in *Space telescopes and instrumentation 2012: ultraviolet to gamma ray*. *SPIE*). Editors T. Takahashi, S. S. Murray, J.-W. A. den Herder, and W. A. Bellingham, 8443. of Society of Photo-Optical Instrumentation Engineers (SPIE) Conference Series. doi:10.1117/12.926396844313

Giacconi, R., Gursky, H., Kellogg, E., Schreier, E., and Tananbaum, H. (1971). Discovery of periodic X-ray pulsations in centaurus X-3 from UHURU. *ApJ* 167, L67. doi:10.1086/180762

Harrison, F. A., Craig, W. W., Christensen, F. E., Hailey, C. J., Zhang, W. W., Boggs, S. E., et al. (2013). The nuclear spectroscopic telescope array (NuSTAR) high-energy X-ray mission. *ApJ* 770, 103. doi:10.1088/0004-637X/770/2/103

Hasinger, G., and van der Klis, M. (1989). Two patterns of correlated X-ray timing and spectral behaviour in low-mass X-ray binaries. *A&A* 225, 79–96.

Heindl, W. A., Rothschild, R. E., Coburn, W., Staubert, R., Wilms, J., Kreykenbohm, I., et al. (2004). "Timing and spectroscopy of accreting X-ray pulsars: the state of cyclotron line studies," in *X-Ray timing 2003: rossi and beyond*. Editors P. Kaaret, F. K. Lamb, and J. H. Swank, 714, 323–330. of American Institute of Physics Conference Series. doi:10.1063/1.1781049

Homan, J., van der Klis, M., Fridriksson, J. K., Remillard, R. A., Wijnands, R., Méndez, M., et al. (2010). XTE J1701–462 and its implications for the nature of subclasses in low-magnetic-field neutron star low-mass X-ray binaries. *ApJ* 719, 201–212. doi:10.1088/0004-637X/719/1/201

Houck, J. C., and Denicola, L. A. (2000). "ISIS: an interactive spectral interpretation system for high resolution X-ray spectroscopy," in *Astronomical data analysis software and systems IX. San francisco: astron. Soc. Pacific*. Editors N. Manset, C. Veillet, and D. Crabtree, 216, 591. of Astron. Soc. Pacific Conf. Ser.

Iaria, R., Di Salvo, T., Robba, N. R., Burderi, L., Lavagetto, G., and Riggio, A. (2005). Resolving the Fe xxv triplet with chandra in centaurus X-3. *ApJ* 634, L161–L164. doi:10.1086/499040

Ibragimov, A., and Poutanen, J. (2009). Accreting millisecond pulsar SAX J1808.4–3658 during its 2002 outburst: evidence for a receding disc. *MNRAS* 400, 492–508. doi:10.1111/j.1365-2966.2009.15477.x

Iwakiri, W. B., Pottschmidt, K., Falkner, S., Hemphill, P. B., Fürst, F., Nishimura, O., et al. (2019). Spectral and timing analysis of the accretion-powered pulsar 4U 1626–67 observed with Suzaku and NuSTAR. *ApJ* 878, 121. doi:10.3847/1538-4357/ab1f87

Jaisawal, G. K., Naik, S., and Epili, P. (2016). Suzaku view of the Be/X-ray binary pulsar GX 304–1 during Type I X-ray outbursts. *MNRAS* 457, 2749–2760. doi:10.1093/mnras/stw085

Jaisawal, G. K., Vasilopoulos, G., Naik, S., Maitra, C., Malacaria, C., Chhotaray, B., et al. (2023). On the cyclotron absorption line and evidence of the spectral transition in SMC X-2 during 2022 giant outburst. *MNRAS* 521, 3951–3961. doi:10.1093/mnras/stad781

Jansen, F., Lumb, D., Altieri, B., Clavel, J., Ehle, M., Erd, C., et al. (2001). XMM-Newton observatory. I. The spacecraft and operations. *A&A* 365, L1–L6. doi:10.1051/0004-6361:20000036

Jayasurya, K. M., Agrawal, V. K., and Chatterjee, R. (2023). Detection of significant X-ray polarization from transient NS-LMXB XTE J1701-462 with IXPE and its implication on the coronal geometry. *MNRAS* 525, 4657–4662. doi:10.1093/mnras/stad2601

King, A. L., Tomsick, J. A., Miller, J. M., Chenevez, J., Barret, D., Boggs, S. E., et al. (2016). Measuring a truncated disk in aquila X-1. *ApJ* 819, L29. doi:10.3847/2041-8205/819/2/L29

Klochkov, D., Santangelo, A., Staubert, R., and Ferrigno, C. (2008). Giant outburst of EXO 2030+375: pulse-phase resolved analysis of INTEGRAL data. *A&A* 491, 833–840. doi:10.1051/0004-6361:200810673

Klochkov, D., Staubert, R., Santangelo, A., Rothschild, R. E., and Ferrigno, C. (2011). Pulse-amplitude-resolved spectroscopy of bright accreting pulsars: indication of two accretion regimes. *A&A* 532, A126. doi:10.1051/0004-6361/201116800

Koliopanos, F., and Vasilopoulos, G. (2018). Accreting, highly magnetized neutron stars at the Eddington limit: a study of the 2016 outburst of SMC X-3. *A&A* 614, A23. doi:10.1051/0004-6361/201731623

Kong, L.-D., Zhang, S., Zhang, S.-N., Ji, L., Doroshenko, V., Santangelo, A., et al. (2022). Insight-HXMT discovery of the highest-energy CRSF from the first galactic ultraluminous X-ray pulsar Swift J0243.6+6124. *ApJ* 933, L3. doi:10.3847/2041-8213/ac7711

Kretschmar, P., El Mellah, I., Martínez-Núñez, S., Fürst, F., Grinberg, V., Sander, A. A. C., et al. (2021). Revisiting the archetypical wind accretor Vela X-1 in depth. Case study of a well-known X-ray binary and the limits of our knowledge. *A&A* 652, A95. doi:10.1051/0004-6361/202040272

Kreykenbohm, I., Coburn, W., Wilms, J., Kretschmar, P., Staubert, R., Heindl, W. A., et al. (2002). Confirmation of two cyclotron lines in Vela X-1. *A&A* 395, 129–140. doi:10.1051/0004-6361:20021181

Kreykenbohm, I., Kretschmar, P., Wilms, J., Staubert, R., Kendziorra, E., Gruber, D. E., et al. (1999). VELA X-1 as seen by RXTE. *A&A* 341, 141–150. doi:10.48550/arXiv.astro-ph/9810282

Kuulkers, E., van der Klis, M., Oosterbroek, T., van Paradijs, J., and Lewin, W. H. G. (1997). GX17+2: X-ray spectral and timing behaviour of a bursting Z source. *MNRAS* 287, 495–514. doi:10.1093/mnras/287.3.495

Kylafis, N. D., Trümper, J. E., and Loudas, N. A. (2021). Cyclotron line formation by reflection on the surface of a magnetic neutron star. *A&A* 655, A39. doi:10.1051/0004-6361/202039361

Lattimer, J. M. (2011). Neutron stars and the dense matter equation of state. *Astrophys. Space Sci.* 336, 67–74. doi:10.1007/s10509-010-0529-1

Lattimer, J. M., and Prakash, M. (2001). Neutron star structure and the equation of state. *ApJ* 550, 426–442. doi:10.1086/319702

Lattimer, J. M., and Prakash, M. (2004). The physics of neutron stars. *Science* 304, 536–542. doi:10.1126/science.1090720

Lin, D., Remillard, R. A., and Homan, J. (2007). Evaluating spectral models and the X-ray states of neutron star X-ray transients. *ApJ* 667, 1073–1086. doi:10.1086/521181

Lin, D., Remillard, R. A., and Homan, J. (2010). Suzaku and BeppoSAX X-ray spectra of the persistently accreting neutron-star binary 4U 1705–44. *ApJ* 719, 1350–1361. doi:10.1088/0004-637X/719/2/1350

Liu, B.-S., Tao, L., Zhang, S.-N., Li, X.-D., Ge, M.-Y., Qu, J.-L., et al. (2020). A peculiar cyclotron line near 16 keV detected in the 2015 outburst of 4U 0115+63? *ApJ* 900, 41. doi:10.3847/1538-4357/aba4a5

Liu, Q., Wang, W., Chen, X., Ding, Y. Z., Lu, F. J., Song, L. M., et al. (2022). Variations of cyclotron resonant scattering features in Vela X-1 revealed with Insight-HXMT. *MNRAS* 514, 2805–2814. doi:10.1093/mnras/stac1520

Longair, M. S. (2011). *High energy astrophysics*. Cambridge: Cambridge Univ. Press.

Ludlam, R. M., Cackett, E. M., García, J. A., Miller, J. M., Bult, P. M., Strohmayer, T. E., et al. (2020). NICER-NuSTAR observations of the neutron star low-mass X-ray binary 4U 1735–44. *ApJ* 895, 45. doi:10.3847/1538-4357/ab89a6

Ludlam, R. M., Cackett, E. M., García, J. A., Miller, J. M., Stevens, A. L., Fabian, A. C., et al. (2022). Radius constraints from reflection modeling of Cygnus X-2 with NuSTAR and NICER. *ApJ* 927, 112. doi:10.3847/1538-4357/ac5028

Ludlam, R. M., Jaodand, A. D., García, J. A., Degenaar, N., Tomsick, J. A., Cackett, E. M., et al. (2021). Simultaneous NICER and NuSTAR observations of the ultracompact X-ray binary 4U 1543-624. *ApJ* 911, 123. doi:10.3847/1538-4357/abedb0

Ludlam, R. M., Miller, J. M., Arzoumanian, Z., Bult, P. M., Cackett, E. M., Chakrabarty, D., et al. (2018). Detection of reflection features in the neutron star low-mass X-ray binary serpens X-1 with NICER. *ApJ* 858, L5. doi:10.3847/2041-8213/aabee6

Ludlam, R. M., Miller, J. M., Bachetti, M., Barret, D., Bostrom, A. C., Cackett, E. M., et al. (2017a). A hard look at the neutron stars and accretion disks in 4U 1636–53, GX 17+2, and 4U 1705–44 with NuStar. *ApJ* 836, 140. doi:10.3847/1538-4357/836/1/140

Ludlam, R. M., Miller, J. M., Cackett, E. M., Fabian, A. C., Bachetti, M., Parker, M. L., et al. (2016). NuSTAR and XMM-Newton observations of the neutron star X-ray binary 1RXS j180408.9-34205. *ApJ* 824, 37. doi:10.3847/0004-637X/824/1/37

Ludlam, R. M., Miller, J. M., Degenaar, N., Sanna, A., Cackett, E. M., Altamirano, D., et al. (2017b). Truncation of the accretion disk at one-third of the Eddington limit in the neutron star low-mass X-ray binary aquila X-1. *ApJ* 847, 135. doi:10.3847/1538-4357/aa8b1b

Lutovinov, A., Tsygankov, S., Molkov, S., Doroshenko, V., Mushtukov, A., Arefiev, V., et al. (2021). SRG/ART-XC and NuSTAR observations of the X-ray pulsar GRO J1008−57 in the lowest luminosity state. *ApJ* 912, 17. doi:10.3847/1538-4357/abec43

Madej, O. K., García, J., Jonker, P. G., Parker, M. L., Ross, R., Fabian, A. C., et al. (2014). X-ray reflection in oxygen-rich accretion discs of ultracompact X-ray binaries. *MNRAS* 442, 1157–1165. doi:10.1093/mnras/stu884

Madsen, K. K., García, J. A., Stern, D., Armini, R., Basso, S., Coutinho, D., et al. (2023). The High Energy X-ray Probe (HEX-P): Instrument and Mission Profile. *arXiv*. doi:10.48550/arXiv.2312.04678

Maitra, C., and Paul, B. (2013). Pulse-phase-resolved spectroscopy of Vela X-1 with Suzaku. *ApJ* 763, 79. doi:10.1088/0004-637X/763/2/79

Maitra, C., Paul, B., Haberl, F., and Vasilopoulos, G. (2018). Detection of a cyclotron line in SXP 15.3 during its 2017 outburst. *MNRAS* 480, L136–L140. doi:10.1093/mnrasl/sly141

Makishima, K., Mihara, T., Nagase, F., and Tanaka, Y. (1999). Cyclotron resonance effects in two binary X-ray pulsars and the evolution of neutron star magnetic fields. *ApJ* 525, 978–994. doi:10.1086/307912

Malacaria, C., Bhargava, Y., Coley, J. B., Ducci, L., Pradhan, P., Ballhausen, R., et al. (2022). Accreting on the edge: a luminosity-dependent cyclotron line in the Be/X-Ray binary 2S 1553-542 accompanied by accretion regimes transition. *ApJ* 927, 194. doi:10.3847/1538-4357/ac524f

Malacaria, C., Ducci, L., Falanga, M., Altamirano, D., Bozzo, E., Guillot, S., et al. (2023a). The unaltered pulsar: GRO J1750−27, a supercritical X-ray neutron star that does not blink an eye. *A&A* 669, A38. doi:10.1051/0004-6361/202245123

Malacaria, C., Heyl, J., Doroshenko, V., Tsygankov, S. S., Poutanen, J., Forsblom, S. V., et al. (2023b). A polarimetrically oriented X-ray stare at the accreting pulsar EXO 2030+375. *A&A* 675, A29. doi:10.1051/0004-6361/202346581

Malacaria, C., Klochkov, D., Santangelo, A., and Staubert, R. (2015). Luminosity-dependent spectral and timing properties of the accreting pulsar GX 304−1 measured with INTEGRAL. *A&A* 581, A121. doi:10.1051/0004-6361/201526417

Marino, A., Russell, T. D., Del Santo, M., Beri, A., Sanna, A., Coti Zelati, F., et al. (2023). *The accretion/ejection link in the neutron star X-ray binary 4U 1820-30 I: a boundary layer-jet coupling? arXiv e-prints*. arXiv:2307.16566. doi:10.48550/arXiv.2307.16566

Meidinger, N., Albrecht, S., Beitler, C., Bonholzer, M., Emberger, V., Frank, J., et al. (2020). "Development status of the wide field imager instrument for Athena," in *Space telescopes and instrumentation 2020: ultraviolet to gamma ray*. Editors J.-W. A. den Herder, S. Nikzad, and K. Nakazawa (of Society of Photo-Optical Instrumentation Engineers (SPIE) Conference Series), 11444, 114440T. doi:10.1117/12.2560507

Meszaros, P. (1992). *High-energy radiation from magnetized neutron stars*. Chicago: Univ. Chicago Press.

Meszaros, P., Novick, R., Szentgyorgyi, A., Chanan, G. A., and Weisskopf, M. C. (1988). Astrophysical implications and observational prospects of X-ray polarimetry. *ApJ* 324, 1056. doi:10.1086/165962

Mihara, T. (1995). *Observational study of X-ray spectra of binary pulsars with Ginga*. Ph.D. thesis. Dept. of Physics, Univ. of Tokyo (M95).

Mihara, T., Yamamoto, T., Sugizaki, M., and Yamaoka, K. (2010). Discovery of the cyclotron line at 51 keV from GX 304−1. *ATEL*, 2796.

Miller, J. M., Maitra, D., Cackett, E. M., Bhattacharyya, S., and Strohmayer, T. E. (2011). A fast X-ray disk wind in the transient pulsar IGR J17480−2446 in terzan 5. *ApJ* 731, L7. doi:10.1088/2041-8205/731/1/L7

Miller, M. C., Lamb, F. K., Dittmann, A. J., Bogdanov, S., Arzoumanian, Z., Gendreau, K. C., et al. (2019). PSR J0030+0451 mass and radius from NICER data and implications for the properties of neutron star matter. *ApJ* 887, L24. doi:10.3847/2041-8213/ab50c5

Miller, M. C., Lamb, F. K., Dittmann, A. J., Bogdanov, S., Arzoumanian, Z., Gendreau, K. C., et al. (2021). The radius of PSR J0740+6620 from NICER and XMM-Newton data. *ApJ* 918, L28. doi:10.3847/2041-8213/ac089b

Mitsuda, K., Inoue, H., Nakamura, N., and Tanaka, Y. (1989). Luminosity-related changes of the energy spectrum of X 1608−522. *PASJ* 41, 97−111.

Mondal, A. S., Dewangan, G. C., Pahari, M., and Raychaudhuri, B. (2018). NuSTAR view of the Z-type neutron star low-mass X-ray binary Cygnus X-2. *MNRAS* 474, 2064−2072. doi:10.1093/mnras/stx2931

Müller, S., Ferrigno, C., Kühnel, M., Schönherr, G., Becker, P. A., Wolff, M. T., et al. (2013). No anticorrelation between cyclotron line energy and X-ray flux in 4U 0115+634. *A&A* 551, A6. doi:10.1051/0004-6361/201220359

Mushtukov, A., and Tsygankov, S. (2022). *Accreting strongly magnetised neutron stars: X-ray Pulsars. arXiv e-prints*. arXiv:2204.14185. doi:10.48550/arXiv.2204.14185

Mushtukov, A. A., Suleimanov, V. F., Tsygankov, S. S., and Portegies Zwart, S. (2021). Spectrum formation in X-ray pulsars at very low mass accretion rate: Monte Carlo approach. *MNRAS* 503, 5193−5203. doi:10.1093/mnras/stab811

Mushtukov, A. A., Suleimanov, V. F., Tsygankov, S. S., and Poutanen, J. (2015). The critical accretion luminosity for magnetized neutron stars. *MNRAS* 447, 1847−1856. doi:10.1093/mnras/stu2484

Naik, S., and Paul, B. (2012). Investigation of variability of iron emission lines in Centaurus X-3. *Bull. Astronomical Soc. India* 40, 503.

Nandra, K., Barret, D., Barcons, X., Fabian, A., den Herder, J.-W., Piro, L., et al. (2013). *The Hot and Energetic Universe: a White Paper presenting the science theme motivating the Athena+ mission. arXiv e-prints*. arXiv:1306.2307. doi:10.48550/arXiv.1306.2307

Nishimura, O. (2003). *The influence of a dipole magnetic field on the structures of cyclotron lines*, 55. Publications of the Astronomical Society of Japan, 849−857. doi:10.1093/pasj/55.4.849

Nishimura, O. (2011). Superposition of cyclotron lines in accreting X-ray pulsars. I. Long spin period. *ApJ* 730, 106. doi:10.1088/0004-637X/730/2/106

Nishimura, O. (2014). Variations of cyclotron line energy with luminosity in accreting X-ray pulsars. *ApJ* 781, 30. doi:10.1088/0004-637X/781/1/30

Oppenheimer, J. R., and Volkoff, G. M. (1939). On massive neutron cores. *Phys. Rev.* 55, 374−381. doi:10.1103/PhysRev.55.374

Orlandini, M., Frontera, F., Masetti, N., Sguera, V., and Sidoli, L. (2012). BeppoSAX observations of the X-ray pulsar MAXI J1409−619 in low state: discovery of cyclotron resonance features. *ApJ* 748, 86. doi:10.1088/0004-637X/748/2/86

Orosz, J. A., and Kuulkers, E. (1999). The optical light curves of Cygnus X-2 (V1341 Cyg) and the mass of its neutron star. *MNRAS* 305, 132−142. doi:10.1046/j.1365-8711.1999.t01-1-02420.x

Parikh, A. S., Wijnands, R., Degenaar, N., Altamirano, D., Patruno, A., Gusinskaia, N. V., et al. (2017). Very hard states in neutron star low-mass X-ray binaries. *MNRAS* 468, 3979−3984. doi:10.1093/mnras/stx747

Popham, R., and Sunyaev, R. (2001). Accretion disk boundary layers around neutron stars: X-ray production in low-mass X-ray binaries. *ApJ* 547, 355−383. doi:10.1086/318336

Pottschmidt, K., Kreykenbohm, I., Wilms, J., Coburn, W., Rothschild, R. E., Kretschmar, P., et al. (2005). RXTE discovery of multiple cyclotron lines during the 2004 december outburst of V0332+53. *ApJ* 634, L97−L100. doi:10.1086/498689

Poutanen, J., Mushtukov, A. A., Suleimanov, V. F., Tsygankov, S. S., Nagirner, D. I., Doroshenko, V., et al. (2013). A reflection model for the cyclotron lines in the spectra of X-ray pulsars. *ApJ* 777, 115. doi:10.1088/0004-637X/777/2/115

Pradhan, P., Paul, B., Bozzo, E., Maitra, C., and Paul, B. C. (2021). Comprehensive broad-band study of accreting neutron stars with Suzaku: is there a bi-modality in the X-ray spectrum? *Mon. Notices R. Astronomical Soc.* 502, 1163−1190. doi:10.1093/mnras/stab024

Raaijmakers, G., Greif, S. K., Hebeler, K., Hinderer, T., Nissanke, S., Schwenk, A., et al. (2021). Constraints on the dense matter equation of state and neutron star properties from NICER's mass-radius estimate of PSR J0740+6620 and multimessenger observations. *ApJ* 918, L29. doi:10.3847/2041-8213/ac089a

Riley, T. E., Watts, A. L., Bogdanov, S., Ray, P. S., Ludlam, R. M., Guillot, S., et al. (2019). A NICER view of PSR J0030+0451: millisecond pulsar parameter estimation. *ApJ* 887, L21. doi:10.3847/2041-8213/ab481c

Riley, T. E., Watts, A. L., Ray, P. S., Bogdanov, S., Guillot, S., Morsink, S. M., et al. (2021). A NICER view of the massive pulsar PSR J0740+6620 informed by radio timing and XMM-Newton spectroscopy. *ApJ* 918, L27. doi:10.3847/2041-8213/ac0a81

Rodes-Roca, J. J., Torrejón, J. M., Kreykenbohm, I., Martínez Núñez, S., Camero-Arranz, A., and Bernabéu, G. (2009). The first cyclotron harmonic of 4U 1538−52. *A&A* 508, 395−400. doi:10.1051/0004-6361/200912815

Ross, R. R., and Fabian, A. C. (2005). A comprehensive range of X-ray ionized-reflection models. *MNRAS* 358, 211−216. doi:10.1111/j.1365-2966.2005.08797.x

Rothschild, R. E., Kühnel, M., Pottschmidt, K., Hemphill, P., Postnov, K., Gornostaev, M., et al. (2017). Discovery and modelling of a flattening of the positive cyclotron line/luminosity relation in GX 304−1 with RXTE. *MNRAS* 466, 2752−2779. doi:10.1093/mnras/stw3222

Rouco Escorial, A., van den Eijnden, J., and Wijnands, R. (2018). Discovery of accretion-driven pulsations in the prolonged low X-ray luminosity state of the Be/X-ray transient GX 304−1. *A&A* 620, L13. doi:10.1051/0004-6361/201834572

Sanjurjo-Ferrín, G., Torrejón, J. M., Postnov, K., Oskinova, L., Rodes-Roca, J. J., and Bernabeu, G. (2021). X-ray variability of the HMXB Cen X-3: evidence for inhomogeneous accretion flows. *MNRAS* 501, 5892−5909. doi:10.1093/mnras/staa3953

Schönherr, G., Wilms, J., Kretschmar, P., Kreykenbohm, I., Santangelo, A., Rothschild, R. E., et al. (2007). A model for cyclotron resonance scattering features. *A&A* 472, 353−365. doi:10.1051/0004-6361:20077218

Schreier, E., Levinson, R., Gursky, H., Kellogg, E., Tananbaum, H., and Giacconi, R. (1972). Evidence for the binary nature of centaurus X-3 from UHURU X-ray observations. *ApJ* 172, L79. doi:10.1086/180896

Schwarm, F. W., Ballhausen, R., Falkner, S., Schönherr, G., Pottschmidt, K., Wolff, M. T., et al. (2017). Cyclotron resonant scattering feature simulations. II. Description of the CRSF simulation process. *A&A* 601, A99. doi:10.1051/0004-6361/201630250

Sibgatullin, N. R., and Sunyaev, R. A. (1998). Disk accretion in the gravitational field of a rapidly rotating neutron star with a rotationally induced quadrupole mass distribution. *Astron. Lett.* 24, 774−787. doi:10.48550/arXiv.astro-ph/9811028

Sokolova-Lapa, E., Gornostaev, M., Wilms, J., Ballhausen, R., Falkner, S., Postnov, K., et al. (2021). X-ray emission from magnetized neutron star atmospheres at low mass-accretion rates. I. Phase-averaged spectrum. *A&A* 651, A12. doi:10.1051/0004-6361/202040228

Sokolova-Lapa, E., Stierhof, J., Dauser, T., and Wilms, J. (2023). Vacuum polarization alters the spectra of accreting X-ray pulsars. *A&A* 674, L2. doi:10.1051/0004-6361/202346265

Staubert, R., Ducci, L., Ji, L., Fürst, F., Wilms, J., Rothschild, R. E., et al. (2020). Cyclotron line energy in Hercules X-1: stable after the decay. *A&A* 642, A196. doi:10.1051/0004-6361/202038855

Staubert, R., Klochkov, D., Wilms, J., Postnov, K., Shakura, N. I., Rothschild, R. E., et al. (2014). Long-term change in the cyclotron line energy in Hercules X-1. *A&A* 572, A119. doi:10.1051/0004-6361/201424203

Staubert, R., Trümper, J., Kendziorra, E., Klochkov, D., Postnov, K., Kretschmar, P., et al. (2019). Cyclotron lines in highly magnetized neutron stars. *A&A* 622, A61. doi:10.1051/0004-6361/201834479

Sunyaev, R. A., Arefev, V. A., Borozdin, K. N., Gilfanov, M. R., Efremov, V. V., Kaniovskii, A. S., et al. (1991). Broadband X-ray spectra of black-hole candidates X-ray pulsars and low-mass binary X-ray systems - KVANT module results. *Sov. Astron. Lett.* 17, 409.

Tanaka, Y. (1986). "Observations of compact X-ray sources,". *IAU colloq. 89: radiation hydrodynamics in stars and compact objects*. Editors D. Mihalas, and K.-H. A. Winkler (Berlin, Heidelberg: Springer), 255, 198. doi:10.1007/3-540-16764-1_12

The LIGO Scientific Collaboration, The Virgo Collaboration, B. P., Abbott, R., Abbott, T. D., Abraham, S., Acernese, F., et al. (2020). GW190425: observation of a compact binary coalescence with total mass ~ 3.4 $M_{\odot}$. *ApJ* 892, L3. doi:10.3847/2041-8213/ab75f5

Titarchuk, L. (1994). Generalized comptonization models and application to the recent high-energy observations. *ApJ* 434, 570. doi:10.1086/174760

Tolman, R. C. (1934). *Relativity, thermodynamics, and cosmology*. Oxford: Clarendon Press.

Tolman, R. C. (1939). Static solutions of einstein's field equations for spheres of fluid. *Phys. Rev.* 55, 364–373. doi:10.1103/PhysRev.55.364

Tomar, G., Pradhan, P., and Paul, B. (2021). New measurements of the cyclotron line energy in Cen X-3. *MNRAS* 500, 3454–3461. doi:10.1093/mnras/staa3477

Tsygankov, S. S., Doroshenko, V., Mushtukov, A. A., Suleimanov, V. F., Lutovinov, A. A., and Poutanen, J. (2019a). Cyclotron emission, absorption, and the two faces of X-ray pulsar A 0535+262. *MNRAS* 487, L30–L34. doi:10.1093/mnrasl/slz079

Tsygankov, S. S., Doroshenko, V., Poutanen, J., Heyl, J., Mushtukov, A. A., Caiazzo, I., et al. (2022). The X-ray polarimetry view of the accreting pulsar cen X-3. *ApJ* 941, L14. doi:10.3847/2041-8213/aca486

Tsygankov, S. S., Rouco Escorial, A., Suleimanov, V. F., Mushtukov, A. A., Doroshenko, V., Lutovinov, A. A., et al. (2019b). Dramatic spectral transition of X-ray pulsar GX 304−1 in low luminous state. *MNRAS* 483, L144–L148. doi:10.1093/mnrasl/sly236

Tugay, A. V., and Vasylenko, A. A. (2009). "XMM-Newton observations of X-ray pulsar cen X-3,". *Young scientists 16th proceedings*. Editors V. Y. Choliy, and G. Ivashchenko, 58–61.

Ursini, F., Farinelli, R., Gnarini, A., Poutanen, J., Bianchi, S., Capitanio, F., et al. (2023). X-ray polarimetry and spectroscopy of the neutron star low-mass X-ray binary GX 9+9: an in-depth study with IXPE and NuSTAR. *A&A* 676, A20. doi:10.1051/0004-6361/202346541

van der Klis, M. (2005). Timing neutron stars. *Electromagn. Spectr. Neutron Stars* 210, 283. of NATO Advanced Study Institute (ASI) Series B.

Vasilopoulos, G., Haberl, F., Sturm, R., Maggi, P., and Udalski, A. (2014). Spectral and temporal properties of RX J0520.5-6932 (LXP 8.04) during a type-I outburst. *A&A* 567, A129. doi:10.1051/0004-6361/201423934

Vasilopoulos, G., Ray, P. S., Gendreau, K. C., Jenke, P. A., Jaisawal, G. K., Wilson-Hodge, C. A., et al. (2020). The 2019 super-Eddington outburst of RX J0209.6-7427: detection of pulsations and constraints on the magnetic field strength. *MNRAS* 494, 5350–5359. doi:10.1093/mnras/staa991

Vybornov, V., Doroshenko, V., Staubert, R., and Santangelo, A. (2018). Changes in the cyclotron line energy on short and long timescales in V 0332+53. *A&A* 610, A88. doi:10.1051/0004-6361/201731750

Vybornov, V., Klochkov, D., Gornostaev, M., Postnov, K., Sokolova-Lapa, E., Staubert, R., et al. (2017). Luminosity-dependent changes of the cyclotron line energy and spectral hardness in Cepheus X-4. *A&A* 601, A126. doi:10.1051/0004-6361/201630275

White, N. E., Stella, L., and Parmar, A. N. (1988). The X-ray spectral properties of accretion discs in X-ray binaries. *ApJ* 324, 363. doi:10.1086/165901

Wilms, J., Allen, A., and McCray, R. (2000). On the absorption of X-rays in the interstellar medium. *ApJ* 542, 914–924. doi:10.1086/317016

Wolff, M., Becker, P. A., Coley, J., Fürst, F., Guillot, S., Harding, A. K., et al. (2019). The physics of accretion onto highly magnetized neutron stars. *Bull. AAS* 51, 386. doi:10.48550/arXiv.1904.00108

Yang, W., Wang, W., Liu, Q., Chen, X., Wu, H. J., Tian, P. F., et al. (2023). Discovery of two cyclotron resonance scattering features in X-ray pulsar Cen X-3 by Insight-HXMT. *MNRAS* 519, 5402–5409. doi:10.1093/mnras/stad048

frontiers | Frontiers in Astronomy and Space Sciences

TYPE Original Research
PUBLISHED 22 December 2023
DOI 10.3389/fspas.2023.1303197

Check for updates

OPEN ACCESS

EDITED BY
Esra Bulbul,
Max Planck Institute for Extraterrestrial Physics, Germany

REVIEWED BY
Ruizhi Yang,
University of Science and Technology of China, China
Ruoyu Liu,
Nanjing University, China

*CORRESPONDENCE
Kaya Mori,
kaya@astro.columbia.edu

RECEIVED 27 September 2023
ACCEPTED 04 December 2023
PUBLISHED 22 December 2023

CITATION
Mori K, Reynolds S, An H, Bamba A, Krivonos R, Tsuji N, Abdelmaguid M, Alford J, Bangale P, Celli S, Diesing R, Eagle J, Fryer CL, Gabici S, Gelfand J, Grefenstette B, Garcia J, Kim C, Kumar S, Kuznetsova E, Mac Intyre B, Madsen K, Manconi S, Motogami Y, Ohsumi H, Olmi B, Park J, Ponti G, Sato T, Shang R-Y, Stern D, Terada Y, Woo J, Younes G and Zoglauer A (2023), The high energy X-ray probe (HEX-P): Galactic PeVatrons, star clusters, superbubbles, microquasar jets, and gamma-ray binaries.
Front. Astron. Space Sci. 10:1303197.
doi: 10.3389/fspas.2023.1303197

COPYRIGHT
© 2023 Mori, Reynolds, An, Bamba, Krivonos, Tsuji, Abdelmaguid, Alford, Bangale, Celli, Diesing, Eagle, Fryer, Gabici, Gelfand, Grefenstette, Garcia, Kim, Kumar, Kuznetsova, Mac Intyre, Madsen, Manconi, Motogami, Ohsumi, Olmi, Park, Ponti, Sato, Shang, Stern, Terada, Woo, Younes and Zoglauer. This is an open-access article distributed under the terms of the Creative Commons Attribution License (CC BY). The use, distribution or reproduction in other forums is permitted, provided the original author(s) and the copyright owner(s) are credited and that the original publication in this journal is cited, in accordance with accepted academic practice. No use, distribution or reproduction is permitted which does not comply with these terms.

The high energy X-ray probe (HEX-P): Galactic PeVatrons, star clusters, superbubbles, microquasar jets, and gamma-ray binaries

Kaya Mori[1]*, Stephen Reynolds[2], Hongjun An[3], Aya Bamba[4,5,6], Roman Krivonos[7], Naomi Tsuji[8], Moaz Abdelmaguid[9], Jason Alford[9], Priyadarshini Bangale[10], Silvia Celli[11], Rebecca Diesing[12,13,14], Jordan Eagle[15], Chris L. Fryer[16], Stefano Gabici[17], Joseph Gelfand[9], Brian Grefenstette[18], Javier Garcia[15], Chanho Kim[3], Sajan Kumar[19], Ekaterina Kuznetsova[7], Brydyn Mac Intyre[20], Kristin Madsen[15], Silvia Manconi[21], Yugo Motogami[22], Hayato Ohsumi[22], Barbara Olmi[23,24], Jaegeun Park[3], Gabriele Ponti[25,26], Toshiki Sato[27], Ruo-Yu Shang[28], Daniel Stern[29], Yukikatsu Terada[22,30], Jooyun Woo[1], George Younes[15,31] and Andreas Zoglauer[32]

[1]Columbia Astrophysics Laboratory, Columbia University, New York, NY, United States, [2]Department of Physics, North Carolina State University, Raleigh, NC, United States, [3]Department of Astronomy and Space Science, Chungbuk National University, Cheongju, Republic of Korea, [4]Department of Physics, The University of Tokyo, Tokyo, Japan, [5]Research Center for the Early Universe, School of Science, The University of Tokyo, Tokyo, Japan, [6]Trans-Scale Quantum Science Institute, The University of Tokyo, Tokyo, Japan, [7]Space Research Institute (IKI), Russian Academy of Sciences, Moscow, Russia, [8]Faculty of Science, Kanagawa University, Yokohama, Kanagawa, Japan, [9]Department of Physics, New York University, Abu Dhabi, United Arab Emirates, [10]Department of Physics and Astronomy, The Bartol Research Institute, University of Delaware, Newark, DE, United States, [11]Department of Physics, Sapienza University of Rome and INFN Sezione di Roma, Rome, Italy, [12]Department of Astronomy and Astrophysics, The University of Chicago, Chicago, IL, United States, [13]The School of Natural Sciences, The Institute for Advanced Study, Princeton, NJ, United States, [14]Columbia Astrophysics Laboratory, Columbia University, New York, NY, United States, [15]NASA Goddard Space Flight Center, Greenbelt, MD, United States, [16]Center for Non Linear Studies, Los Alamos National Laboratory, Los Alamos, NM, United States, [17]Universite Paris Cite, Centre national de la recherche scientifique, Astroparticule et Cosmologie, Paris, France, [18]Space Radiation Laboratory, California Institute of Technology, Pasadena, CA, United States, [19]Department of Physics, University of Maryland, College Park, MD, United States, [20]Department of Physics and Astronomy, University of Manitoba, Winnipeg, MB, Canada, [21]Laboratoire d'Annecy-le-Vieux de Physique Theorique, CNRS, Université Savoie Mont Blanc, Annecy, France, [22]Graduate School of Science and Engineering, Saitama University, Sakura, Saitama, Japan, [23]INAF–Osservatorio Astrofisico di Arcetri, Firenze, Italy, [24]INAF–Osservatorio Astronomico di Palermo, Palermo, Italy, [25]INAF–Osservatorio Astronomico di Brera, Merate, Italy, [26]Max-Planck-Institut für extraterrestrische Physik, Garching, Germany, [27]Department of Physics, School of Science and Technology, Meiji University, Kawasaki, Kanagawa, Japan, [28]Department of Physics and Astronomy, Barnard College, New York, NY, United States, [29]Jet Propulsion Laboratory, California Institute of Technology, Pasadena, CA, United States, [30]Japan Aerospace Exploration Agency (JAXA), Institute of Space and Astronautical Science, Sagamihara, Japan, [31]Department of Physics, The George Washington University, Washington, DC, United States, [32]Space Sciences Laboratory, UC Berkeley, Berkeley, CA, United States

HEX-P is a probe-class mission concept that will combine high spatial resolution X-ray imaging (<10″ FWHM) and broad spectral coverage (0.2–80 keV) with an effective area far superior to current facilities (including XMM-Newton and NuSTAR) to enable revolutionary new insights into a variety of important astrophysical problems. With the recent discoveries of over 40 ultra-high-energy gamma-ray sources (detected above 100 TeV) and neutrino emission in the Galactic Plane, we have entered a new era of multi-messenger astrophysics facing the exciting reality of Galactic PeVatrons. In the next decade, as more Galactic PeVatrons and TeV gamma-ray sources are expected to be discovered, the identification of their acceleration and emission mechanisms will be the most pressing issue in both particle and high-energy astrophysics. In this paper, along with its companion papers, we will present that HEX-P is uniquely suited to address important problems in various cosmic-ray accelerators, including Galactic PeVatrons, through investigating synchrotron X-ray emission of TeV–PeV electrons produced by both leptonic and hadronic processes. For Galactic PeVatron candidates and other TeV gamma-ray sources, HEX-P can fill in a large gap in the spectral-energy distributions (SEDs) of many objects observed in radio, soft X-rays, and gamma rays, constraining the maximum energies to which electrons can be accelerated, with implications for the nature of the Galactic PeVatrons and their contributions to the spectrum of Galactic cosmic rays beyond the knee at ~3 PeV. In particular, X-ray observation with HEX-P and TeV observation with CTAO will provide the most powerful multi-messenger diagnostics to identify Galactic PeVatrons and explore a variety of astrophysical shock mechanisms. We present simulations of each class of Galactic TeV–PeV sources, demonstrating the power of both the imaging and spectral capabilities of HEX-P to advance our knowledge of Galactic cosmic-ray accelerators. In addition, we discuss HEX-P's unique and complementary roles to upcoming gamma-ray and neutrino observatories in the 2030s.

KEYWORDS

particle accelerators, Galactic PeVatrons, star clusters, superbubbles, microquasars, gamma-ray binaries, X-ray telescopes, multimessenger astronomy

1 Introduction

Over the last few decades, it has become clear that energetic particles (cosmic rays, CRs) make up a significant component of the Universe. In galaxies, cosmic rays can power galactic winds, support galactic coronae, and control star formation through ionization of molecular clouds. They can influence the structure of large-scale galactic magnetic fields and their propagation can drive turbulence in the interstellar medium. [See, e.g., Heintz and Zweibel (2022) and references therein]. The most energetic cosmic rays, with energies from 10^{15} eV (1 PeV) up to and above 10^{19} eV, appear to fill the Universe, traveling enormous distances to arrive at Earth–the only form of extragalactic matter we will be able to directly examine.

X-ray astronomy has brought powerful insights into the mechanisms by which Nature accelerates particles to energies many orders of magnitude above thermal energies. While radio astronomy even from its infancy gave evidence of electrons with GeV energies (through the diffuse Galactic synchrotron background discovered by chance by Karl Jansky in 1932, though its origin was not clear for decades), it was known long before the advent of space astronomy that far higher energies were exhibited by some particles, to the extent that high-energy physics experiments were conducted on mountaintops to tap the flux of incoming cosmic rays, long before the advent of terrestrial particle accelerators. But clues to the origin of the highest-energy particles required the ability to image sources in photons above the optical window. Quasar continua supplied evidence for optical synchrotron radiation, but the details of the process could not be deduced from unresolved observations. X-ray astronomy first allowed the inference of the presence of TeV particles at their sources, with the detection of the featureless X-ray spectrum of SN 1006 and its interpretation as synchrotron emission from electrons with such energies.

The advent of diffusive shock acceleration (DSA) as a mechanism for the production of suprathermal particles in shocks constituted a major advance in understanding, along with the observational data supplied by several generations of X-ray satellites, most importantly *Chandra* and *XMM*. It has been well-established that TeV electrons are present in most young shell supernova remnants (SNRs), with about ten objects dominated by non-thermal synchrotron emission, and clear non-thermal spectral components in others alongside thermal emission. The initial hope that young SNRs could furnish the origin of all cosmic rays was dashed by the realization based on very general considerations that standard SNR evolution could produce energies only up to several PeV, where a steepening of the integrated cosmic ray spectrum suggests a decreasing efficiency of cosmic-ray production by Galactic sources.

More detailed study strongly suggests that reaching even that energy may be difficult [e.g., Lagage and Cesarsky (1983)]. See Blasi (2013) for a review.

More recently, gamma-ray astronomy has revealed many Galactic sources with energies in the GeV range (observed by *Fermi*-LAT) to above 1 PeV (observed by ground-based imaging atmospheric Cerenkov telescopes (IACTs), such as VERITAS, MAGIC, and H.E.S.S., or extensive air-shower arrays (EASAs), such as HAWC and LHAASO). Recently, a new exciting discovery has been made by IceCube as they have identified neutrino emission in the Galactic Plane (IceCube Collaboration et al., 2023). Angular resolutions of these instruments often do not allow unambiguous identification with sources at lower photon energies, let alone provide morphological clues to the origins of the fast particles in those sources. The imaging capabilities of X-ray telescopes, current and planned, can address the gaps in our understanding resulting from the mismatch between high-resolution radio observations of GeV electrons, and the observations of particles (electrons or hadrons) of up to and above 1 PeV.

Various classes of objects are now known to produce energetic particles: SNRs, pulsar-wind nebulae (PWNe) at the termination shock of the pulsar's relativistic wind forming the inner boundary of the PWN, superbubbles driven by multiple supernovae, and termination shocks of jets from "microquasars" such as SS433. Arguments have been made for each of these as the primary source of the most energetic Galactic cosmic rays, but in no case do we have conclusive determinations.

A full understanding of the physics of particle acceleration in shocks, and elsewhere, and in particular, of the nature of the most energetic sources ("PeVatrons"), will require a new generation of instruments. In the context of DSA, we still do not understand the details of how electrons become initially accelerated; how the accelerated-particle population, both electrons and ions, develops and affects the local environment (magnetic field, thermal fluid); what determines the fractions of shock energy going into particles and magnetic field; and what determines the maximum energy to which particles are accelerated, with possibly different limitations applying to electrons and hadrons. For the wind termination shocks of PWNe, the additional complications of special-relativistic effects are present.

In particular, an attack on the problem of the nature of "PeVatrons" can be divided into two fronts: a better understanding of the basic physics of particle acceleration, conducted in those objects which can be most fully characterized, and direct observational studies of candidate PeVatrons themselves. The latter project is hampered by the large point-spread functions (PSFs) of Cherenkov detectors (of order a significant fraction of a degree), often containing multiple possible counterparts in the crowded Galactic plane. In the former approach, one works to improve our knowledge of the basic physics of shock acceleration by studying better-understood objects, but ones fairly certain not to be the PeVatrons themselves. The proposed HEX-P mission can contribute on both fronts.

In this paper, we present a wealth of HEX-P programs for investigating a diverse class of cosmic-ray accelerators and exotic radioactive sources in our Galaxy. In Section 2, we review the key radiative processes as a primer for understanding multi-wavelength electromagnetic emission from cosmic-ray accelerators. Sections 3, 4 describe the current telescope design and HEX-P's primary observation program for Galactic cosmic-ray accelerators, respectively. The HEX-P's primary observation program has been optimally determined based on extensive simulations with the Simulations of X-ray Telescopes (SIXTE) suite and with NASA's HEASARC XSPEC software, as well as consulting with the current and future gamma-ray and neutrino telescope groups, including CTAO, HAWC, VERITAS, IceCube, and COSI. Note that two primary classes of Galactic particle accelerators, SNRs and PWNe, are discussed in a companion paper (Reynolds et al., 2023). Section 5 discusses the unique and complementary role of HEX-P in the future multi-messenger observations of Galactic PeVatrons, which is arguably the most exciting field in astroparticle physics currently and in the 2030s Section 6 presents HEX-P observations of star clusters and superbubbles which represent a primary class of hadronic particle accelerators. Section 7 focuses on the HEX-P survey of W50 lobes, a unique particle accelerator powered by the microquasar SS433. Section 8 presents how HEX-P observations can deepen our understanding of intrabinary shock physics and interactions between pulsars and circumstellar disks in rare TeV gamma-ray binaries. Section 9 concludes the paper with various HEX-P survey ideas in synergy with future telescopes in other wavelengths.

2 Radiative processes

Accelerated particles make their presence known through a variety of radiative processes: synchrotron radiation, bremsstrahlung, and inverse-Compton scattering for the electrons or positrons (leptonic processes), and, for protons and nuclei, decay into gamma rays of π^0 mesons produced in inelastic scattering from target atoms (hadronic process).

Relativistic electrons (or positrons) of energy E radiating in a magnetic field **B** produce synchrotron radiation with a spectrum peaking at photon energy $E_\gamma = 15\langle B_{\mu G}\rangle\, E^2_{\rm PeV}$ keV, after averaging over the angle between **B** and the line of sight. These particles can also upscatter any ambient photon fields through inverse-Compton scattering (ICS). Both cosmic microwave background (CMB) photons and optical-IR (OIR) photons can serve as relevant seed photon populations. The scattering cross-section is constant at its Thomson value $\sigma_T \equiv 6.65\times10^{-25}$ cm^2 for small values of the Klein-Nishina (KN) parameter $x_{\rm KN} \equiv 4E\,E_{yi}/(m_ec^2)^2$, where E_{yi} is the seed photon energy. But as $x_{\rm KN}$ approaches and exceeds 1, the cross-section decreases (Klein-Nishina suppression). The maximum outgoing photon energy E_γ is given, for $x_{\rm KN} \ll 1$, by $E_\gamma = 4(E/m_ec^2)^2E_{yi} = x_{\rm KN}E$, but as $x_{\rm KN}$ approaches 1, E_γ asymptotes to E, independent of the seed photon energy. For CMB seeds ($E_{yi} \sim 0.2$ meV), requiring $x_{\rm KN} \le 0.1$ to remain safely in the Thomson limit, the peak scattered photon energy is about 3 TeV, produced by electrons with $E \sim 30$ TeV. Higher-energy photons can be produced, but with decreasing efficiency. For OIR seeds ($E_{yi} \sim 1$ eV), again requiring $x_{\rm KN} < 0.1$ limits scattered photon energies to about 400 MeV, produced by electrons with $E \sim 7$ GeV. Thus ICS from the CMB can produce very high-energy (VHE, 100 GeV–100 TeV) gamma-rays detectable with IACTs, while ICS from starlight seeds is most important below 1 GeV photon energies, observable with satellites. Finally, relativistic electrons can also produce relativistic bremsstrahlung with photon energies up to

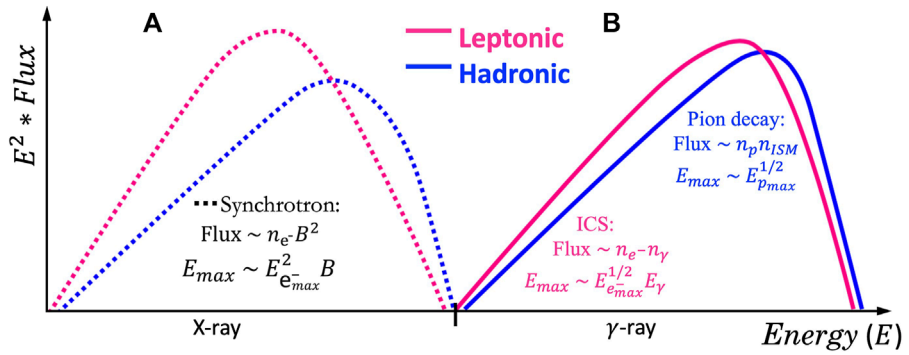

FIGURE 1
(A): Cartoon multiwavelength (MW) SED models for leptonic and hadronic accelerators. **(B)**: Example leptonic (black) and hadronic (red) SED models for a hypothetical gamma-ray emitting particle accelerator. The two SED models with nearly identical gamma-ray spectra were produced using NAIMA (Zabalza, 2015). Note that the synchrotron X-ray spectra appear differently in both fluxes and slopes in the HEX-P bandpass (0.2–80 keV). The secondary electrons in the hadronic case are modeled following the recipe of Kelner et al. (2006).

$E_\gamma \sim E/3$, but for the regions of parameter space relevant to the particle acceleration sources in this paper, bremsstrahlung is rarely dominant.

Cosmic-ray protons and nuclei can produce gamma-ray emission through inelastic collisions with ambient gas, resulting in the production of pions (hadronic process). The charged pions decay to secondary electrons and positrons, while the π^0 particles decay to gamma rays. These collisions result in a fixed ratio of gamma rays to secondary leptons, an unavoidable consequence of the process. For kinematic reasons, pions cannot be produced until proton energies reach 280 MeV, at which point it becomes possible to produce π^0's.

The synchrotron process does not contribute to gamma-ray emission, but it plays a crucial role in providing evidence for the highest-energy electrons. Electrons with energies above a few tens of TeV scatter CMB photons much less efficiently, so their gamma-ray emission may be faint or lost below hadronic gamma-ray processes. However, their maximum energy can be constrained through their synchrotron radiation, in the energy range targeted by HEX-P.

Thus a population of relativistic leptons and hadrons produces broadband emission from radio to above PeV energies, through all four processes in general. Characterizing those populations requires observations at all wavelengths, to create a spectral-energy distribution (SED). Radio emission, produced only by ~ GeV-range electrons, can anchor the lepton distribution. The gamma-ray part of the spectrum above 70 MeV could be produced by two leptonic and one hadronic process, and sorting out which is responsible is an essential task for the investigation of particle acceleration. Of particular interest are instruments capable of observing very high-energy and ultra high-energy (UHE, >100 TeV) gamma rays. While most of these instruments have angular resolutions of a significant fraction of a degree, the Cherenkov Telescope Array (CTA), currently under construction and scheduled to begin full operation in the mid-2020s, is of particular interest for the HEX-P mission. Two CTAO sites in the northern and southern hemispheres will be able to survey the entire sky in the 0.1–100 TeV band with ~1 arcmin angular resolution.

In general, synchrotron X-ray emission ($F_X \propto n_e \cdot B^2$), ICS gamma-ray emission ($F_\gamma \propto n_e \cdot n_\gamma$), and hadronic gamma-ray emission ($F_\gamma \propto n_p \cdot n_{\rm ISM}$), where n_e, n_γ, n_p and $n_{\rm ISM}$ are electron, seed photon, proton, and ISM densities, represent different components from the same underlying particle energy distribution (Figure 1). Hence, in numerous Galactic TeV sources, multiwavelength morphology and SED studies with X-ray and IACT TeV data helped to distinguish between the leptonic and hadronic scenarios and to constrain model parameters (Kargaltsev et al., 2013; Mori et al., 2021). For instance, Figure 1 illustrates the distinct X-ray spectra expected in leptonic and hadronic models, despite predicting nearly identical gamma-ray spectra. Additional constraints come from the fact that the same population of relativistic electrons can produce both synchrotron and inverse-Compton emission. The ratio of total power radiated by an electron in the two processes is given by the ratio of magnetic-field energy density to seed photon energy density, i.e., $P_{\rm synch}/P_{\rm IC} = [(B^2/8\pi)/u_{\rm rad}]$. The radiated spectra have the same slope up to peak energies related to the maximum electron energy. The synchrotron peak depends on the magnetic field, while the IC peak depends on which seed photons are scattered. Therefore, the ratio of the peak photon energies can give an estimate of the magnetic-field strength, while the ratio of the peak fluxes there can give the magnetic-field filling factor (i.e., if the volume of radiating electrons is not uniformly filled with B). See Aharonian and Atoyan (1999) and Lazendic et al. (2004) for detailed expressions.

While gamma-ray detections provide evidence of particle acceleration, studying synchrotron X-ray emission from primary and secondary electrons provides unique and complementary information to gamma-ray observations. However, X-ray telescopes operating only below 10 keV are hampered by the contamination by unrelated thermal X-ray components, which can hinder the detection of non-thermal X-ray emission.

3 HEX-P mission design and simulation

The High-Energy X-ray Probe (HEX-P; Madsen et al., 2023; in preparation) is a probe-class mission concept that offers sensitive broad-band coverage (0.2–80 keV) of the X-ray spectrum with exceptional spectral, timing, and angular capabilities. It features two

high-energy telescopes (HET) that focus hard X-rays, and a low-energy telescope (LET) providing soft X-ray coverage. Overall, LET and HET will achieve a factor of ~3 and ~10 or better improvements in sensitivity over *XMM*-EPIC and *NuSTAR* telescopes in the 0.2–20 and 3–70 keV bands, respectively.

The LET consists of a segmented mirror assembly coated with Ir on monocrystalline silicon that achieves a half power diameter of 3.5″, and a low-energy DEPFET detector, of the same type as the Wide Field Imager [WFI; Meidinger et al. (2020)] onboard Athena (Nandra et al., 2013). It has 512 × 512 pixels that cover a field of view of $11.3' \times 11.3'$. It has an effective bandpass of 0.2–25 keV and a full-frame readout time of 2 m, and can be operated in a 128 and 64 channel window mode for higher count-rates to mitigate pile-up and faster readout. Pile-up effects remain below an acceptable limit of ~1% for sources up to ~100 mCrab in the smallest window configuration (64w). Excising the core of the PSF, a common practice in X-ray astronomy, will allow for observations of brighter sources, with a maximum loss of ~60% of the total photon counts.

The HET consists of two co-aligned telescopes and detector modules. The optics are made of Ni-electroformed full shell mirror substrates, leveraging the heritage of *XMM* (Jansen et al., 2001), and coated with Pt/C and W/Si multilayers for an effective bandpass of 2–80 keV. The high-energy detectors are of the same type as those flown on *NuSTAR* (Harrison et al., 2013), and they consist of 16 CZT sensors per focal plane, tiled 4×4, for a total of 128×128 pixel spanning a field of view slightly larger than for the LET, of $13.4' \times 13.4'$.

All the simulations presented here were produced with a set of response files that represent the observatory performance based on current best estimates (see Madsen et al., 2023, in preparation). The effective area is derived from a ray-trace of the mirror design including obscuration by all known structures. The detector responses are based on simulations performed by the respective hardware groups, with an optical blocking filter for the LET and a Be window and thermal insulation for the HET. The LET background was derived from a GEANT4 simulation (Eraerds et al., 2021) of the WFI instrument, and the one for the HET from a GEANT4 simulation of the *NuSTAR* instrument, both positioned at L1. Throughout the paper, we present our simulation results for *HEX-P* using the SIXTE (Dauser et al., 2019) and XSPEC toolkits (Arnaud, 1996). To ensure the most realistic simulation results, we incorporated recent high-resolution X-ray images (mostly from *Chandra* or other wavelength observations), the best-known spectral information, and theoretical model predictions. Various exposure times have been considered for the feasibility studies presented in the following sections.

4 HEX-P observation program overview

One of the main objectives for the HEX-P mission is to comprehensively explore all types of cosmic-ray accelerators in our Galaxy, including the recently discovered PeVatron candidates. HEX-P's primary mission will include observations of a diverse class of Galactic particle accelerators as outlined in Table 1. Broadly speaking, understanding particle acceleration, propagation, and cooling entails tackling four-dimensional problems that involve spatial distribution (X, Y), particle energy (E), and time (t). Modeling and observing particle acceleration/injection sites serve as the initial step for this exploration. While pulsars act as single-point central engines for producing PWNe, SNRs exhibit multiple acceleration sites, such as forward and reverse shock waves. Once particles are accelerated and injected into the ambient medium, they propagate and lose kinetic energy through various mechanisms, including radiative loss, adiabatic cooling, and collisions with the ISM and molecular clouds. Different regions away from the central engines contain particles injected at different times, requiring multi-zone investigations to track particle transport and cooling. Resolving the multi-wavelength radiation from multiple regions is vital to grasp the entire picture of how particle acceleration, propagation, and cooling interplay with each other. Furthermore, to assess the contribution of specific types of particle accelerators to the local and global CR populations in our Galaxy, it is crucial to examine objects at different stages of evolution.

Typically, energetic and powerful particle accelerators have been discovered through gamma-ray observations. Since the directional and intrinsic energy information of CRs is lost by the interstellar magnetic fields, the CR acceleration and propagation can only be probed indirectly through associated TeV gamma-ray sources. While gamma-ray detections indicate the presence of particle acceleration, the limited angular resolution of TeV gamma-ray telescopes often prevented source identifications. Multi-wavelength observations are required to determine source types and acceleration mechanisms, utilizing telescopes at lower energies and with sub-arcminute angular resolutions.

While CTAO is expected to revolutionize our views of Galactic particle accelerators in the TeV band, its high-quality gamma-ray data alone cannot fully identify the source types and acceleration mechanisms since broader spectral data are required to separate out different potential emission components (ICS, pion-decay, and synchrotron radiation). It has long been realized that multi-wavelength observations are crucial for identifying the sources and elucidating their emission/acceleration mechanisms. At lower energies, X-ray and radio observations play a unique and complementary role to the gamma-ray data by detecting synchrotron radiation from GeV–PeV electrons. Furthermore, broad-band X-ray spectral data provide unique diagnostics for determining the highest energy cutoff region of hadronic PeVatrons (Celli et al., 2020). To do this, the detailed shape of the X-ray spectrum, in particular the existence of curvature or spectral breaks must be well characterized.

Above all, the necessary condition for studying any particle accelerator in the X-ray band is the clean detection of non-thermal X-ray emission apart from soft, thermal X-rays. While previous and current X-ray telescopes such as *NuSTAR* achieved some success in this respect, HEX-P surpasses them as the ultimate non-thermal X-ray detector, given its unprecedented sensitivity above 10 keV. HEX-P excels in spatially resolving thermal and non-thermal (synchrotron) X-ray emission, providing valuable broadband X-ray morphology and spectroscopy data. Moreover, determining the distribution of magnetic fields around the acceleration sites is important for understanding particle transport and cooling processes. For example, low ambient B-fields may offer insights into why some PeVatron candidates seem to sustain extended TeV

TABLE 1 HEX-P primary observation program of Galactic cosmic-ray accelerators.

Source name	Source type	Exposure time (ks)	Section
LHAASO sources	Unidentified PeVatrons	5 × 200 ks	Section 5
Cas A	Young SNR	200 ks	SNR/PWN paper (Section 3.3)
Tycho	Young SNR	200 ks	SNR/PWN paper (Section 3.4)
G1.9 + 0.3	Young SNR	200 ks	SNR/PWN paper (Section 3.5)
SN 1987A	Young SNR + PWN	300 ks	SNR/PWN paper (Section 3.6)
Crab	Young PWN	Calibration source	SNR/PWN paper (Section 4.3)
G21.5–0.9	Young PWN	Calibration source	SNR/PWN paper (Section 4.3)
Lighthouse nebula	Middle-aged PWN	100 ks	SNR/PWN paper (Section 4.3)
G0.9 + 0.1	Young PWN	100 ks	SNR/PWN paper (Section 4.3)
Arches cluster	Star cluster	100 ks	Section 6.1
30 Dor C	Superbubble	300 ks	Section 6.2
SS433/W50 lobes	Microquasar jets	300 ks	Section 7
Sgr A*	Supermassive BH	500 ks	GC paper (Section 4)

Note: 3.3 Ms total exposure. Some of the sources are described in our companion SNR/PWN (Reynolds et al., 2023) and GC papers (Mori et al., 2021).

emission without undergoing fast synchrotron cooling. Variability studies with HEX-P, as well as modeling small-scale features, can constrain magnetic field strengths. HEX-P alone or in synergy with future TeV telescopes, provides the most powerful diagnostic tools to investigate the creation and propagation of the most energetic particles as well as their environments (e.g., magnetic field), ultimately shaping the CR populations both below and above the knee at ~3 PeV. A golden combination of HEX-P and CTAO can usher in a new and exciting era of multi-zone and multi-wavelength approaches to studying Galactic particle accelerators.

Below we summarize the primary HEX-P programs for studying a diverse class of Galactic particle accelerators as well as for investigating nucleosynthesis in young SNRs and potential neutron-star mergers. More detailed descriptions and simulation results on each program can be found in the subsequent sections.

4.1 Investigation of a variety of astrophysical shocks in the primary CR accelerators

Through synchrotron X-ray emission of TeV–PeV electrons: (1) DSA in SNRs, (2) PWN termination shock, (3) interactions between the SNR reverse shock and PWN, (4) intra-binary shock in gamma-ray binaries, (5) microquasar jet-driven shock, (6) colliding wind shock in star clusters, and (7) supermassive blackhole at Sgr A*. As outlined in Table 1, the primary science program will observe all these types of particle accelerators and prompt follow-up HEX-P observations.

4.2 Broad-band X-ray census of Galactic PeVatron candidates

In the most exciting and unexplored regime of astroparticle physics, HEX-P will play a pivotal role in multi-wavelength astrophysics by identifying Galactic PeVatrons and their acceleration/emission mechanisms in synergy with the upcoming CTAO observatory. Currently, 43 PeVatron candidates have been detected by LHAASO (Cao et al., 2023a), but most of them have not yet been identified with known sources, and even the leptonic or hadronic nature of the emission is not known. By the 2030s, more PeVatron candidates (at least ~100) are expected to be discovered. In addition, measuring the maximum particle energy exceeding ~1 PeV is necessary to establish that the LHAASO sources are indeed PeVatrons. HEX-P and CTAO will determine both the accelerator types and maximum particle energies through multi-wavelength SED studies.

4.3 Providing a dynamic view of X-ray filaments and knots in young SNRs

HEX-P will be able to detect year-scale variability from X-ray knots in young SNRs due to ongoing particle acceleration, magnetic field amplification, and fast synchrotron cooling (e.g., $\tau < 6$ years for electrons emitting synchrotron X-rays at $E_\gamma > 40$ keV and $B = 0.1$ mG). HEX-P will identify the most energetic acceleration sites and determine if young SNRs contain localized PeVatrons associated with hard X-ray knots. This investigation is uniquely conducted with HEX-P by measuring local B-fields and maximum

electron energies. See more details in the HEX-P SNR/PWN paper (Reynolds et al., 2023).

4.4 Dissecting particle acceleration, propagation, and cooling mechanisms in PWNe

HEX-P can provide spatially-resolved X-ray spectroscopy and broad-band X-ray morphology data of young and evolved PWNe. The pulsar X-ray emission can be separated and studied by timing analysis thanks to HEX-P's <2 ms temporal resolution. HEX-P alone enables comprehensive multi-zone investigations to understand how particle acceleration, propagation, and cooling operate across various stages of PWN evolution. See more details in the HEX-P SNR/PWN paper (Reynolds et al., 2023).

4.5 Searching for non-thermal X-ray emission from star clusters and superbubbles

HEX-P will search for non-thermal X-ray emission arising from colliding winds in the prominent star clusters and superbubbles such as Arches, Westerlund 1 and 2, Cygnus OB region and 30 Dor C. These star clusters are recognized as primary sites for hadronic acceleration and are largely responsible for producing extended gamma-ray cocoons.

4.6 Surveying particle accelerators and CR distributions in the Galactic Center (GC)

In the GC, HEX-P will conduct surveys of the primary accelerators, including the supermassive BH at Sgr A*, the youngest SNR in our Galaxy (G1.9 + 0.3) and bright TeV sources such as PWN G0.9 + 0.1. HEX-P will also map the spatial and energy distributions of CRs in the central molecular zone and through X-ray filaments in the GC. See more details on Sgr A* flares, X-ray filaments and Arches cluster in the HEX-P GC paper (Mori et al., 2021).

5 Galactic PeVatrons

With the advent of extensive air-shower arrays (EASAs) such as HAWC and LHAASO operating in the ultra-high energy (UHE) band ($E_\gamma \gtrsim 100$ TeV), we are reaching the unprecedented regime of astroparticle physics by discovering PeVatrons that can accelerate CRs to PeV energies, far beyond the maximum energies reachable by the terrestrial particle accelerators (~TeV). The presence of Galactic PeVatrons is a new, exciting reality since LHAASO detected 43 UHE sources in the Galactic disk (Figure 2; Cao et al., 2021b; a; Aharonian et al., 2021; Cao et al., 2023a). Similarly, HAWC and Tibet AS γ detected Galactic TeV sources above ~50 TeV, overlapping with most of the LHAASO sources (Abeysekara et al., 2020; Amenomori et al., 2021). Remarkably, some of the LHAASO sources were detected above 1 PeV, representing the most extreme known particle accelerators in our Galaxy. More Galactic PeVatrons are expected to be discovered as LHAASO and HAWC observatories accumulate more data over the next decade. PeVatrons in the southern sky remain unexplored where H.E.S.S reported several PeVatron candidates, such as HESS J1702−420A, whose gamma-ray spectra extend up to ~100 TeV (Abdalla et al., 2021). The South Wide-field Gamma-ray Observatory (SWGO) is expected to discover PeVatrons in the southern sky, complementing the northern sky coverage of LHAASO and HAWC (Hinton and SWGO Collaboration, 2022). The recent discoveries of the UHE sources by the EASAs marked a paradigm shift in high energy astrophysics from "Do PeVatrons exist in our Galaxy?" to "What are the Galactic PeVatrons detected by EASAs?" and "What is the contribution of Galactic PeVatrons to the UHE cosmic-ray population from the knee (~10^{15} eV) to the ankle (~10^{18} eV)?".

TeV gamma-ray sources, including the Galactic PeVatrons, are usually classified as primarily leptonic or hadronic accelerators. A substantial fraction of energetic $e^{+/-}$ at GeV–PeV energies could be generated by PWNe and pulsar halos (Cholis and Krommydas, 2022; López-Coto et al., 2022). A PWN is generally assumed to be a pure leptonic accelerator, with synchrotron and ICS emission from the expanding bubble of shocked, highly relativistic $e^{+/-}$ pulsar wind continuously injected by the pulsar. However, the possible presence of hadrons in the pulsar wind (see, e.g., Atoyan and Aharonian, 1996; Amato et al., 2003; Guépin et al., 2020) has not been ruled out by present observations (Amato and Olmi, 2021). In the hadronic accelerators, energetic CR ions diffuse out from the accelerator site, collide with any ambient dense material, and produce copious pionic showers which decay into neutrinos, γ-rays and (secondary) $e^{+/-}$. SNRs near clouds, massive star clusters, and superbubbles are considered the primary hadronic accelerators (Aharonian et al., 2019; Cristofari, 2021). Black holes in different mass scales have been recognized as another class of Galactic particle accelerators or possibly PeVatron candidates, associated with X-ray binaries (Kantzas et al., 2022), microquasars (Safi-Harb et al., 2022b), and the supermassive black hole at Sgr A* (HESS Collaboration et al., 2016).

5.1 Multi-wavelength observations of Galactic PeVatrons with HEX-P and CTA

While the EASAs such as LHAASO serve as PeVatron search engines, their UHE sources (above 0.1 PeV) are poorly localized or spatially extended due to their limited angular resolutions. The position and extent of the LHAASO sources usually have an uncertainty of ~0.1° and ~0.3°, respectively (Cao et al., 2021b; Cao et al., 2023a). Therefore, observations at lower energy γ-ray band ($E_\gamma \lesssim 50$ TeV) by IACTs such as VERITAS, H.E.S.S, and MAGIC are crucial for resolving the UHE sources with $\lesssim 0.1°$ angular resolutions. However, the current IACTs have resolved only two UHE sources (LHAASO J2108 + 3651 and J1825-1326) into multiple distinct TeV sources so far, possibly because the UHE sources are largely extended, obscured by diffuse TeV emission in the Galactic Plane or fainter than the current IACT's sensitivity limits (Aliu et al., 2014; S. S. Collaboration et al., 2020). Similarly, in the GeV band, *Fermi*-LAT sources were detected near some UHE sources, but the unique identification of GeV counterparts is often difficult due to the low angular resolution of *Fermi*-LAT.

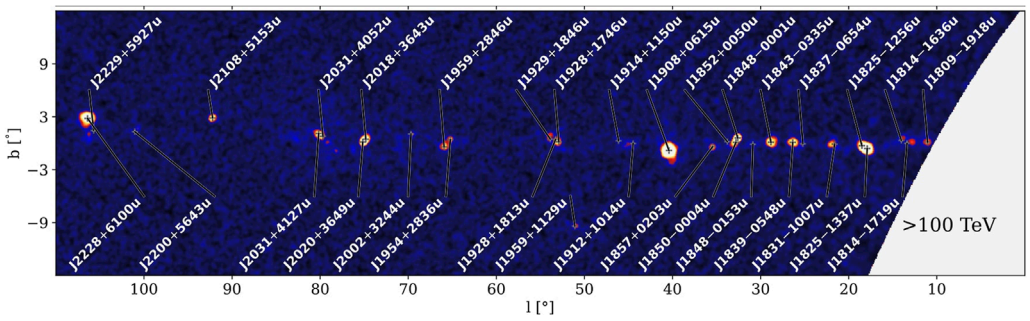

FIGURE 2
LHAASO $E > 100$ TeV significance map of the Galactic Plane ($10° < l < 115°$) excerpted from Cao et al. (2023a).

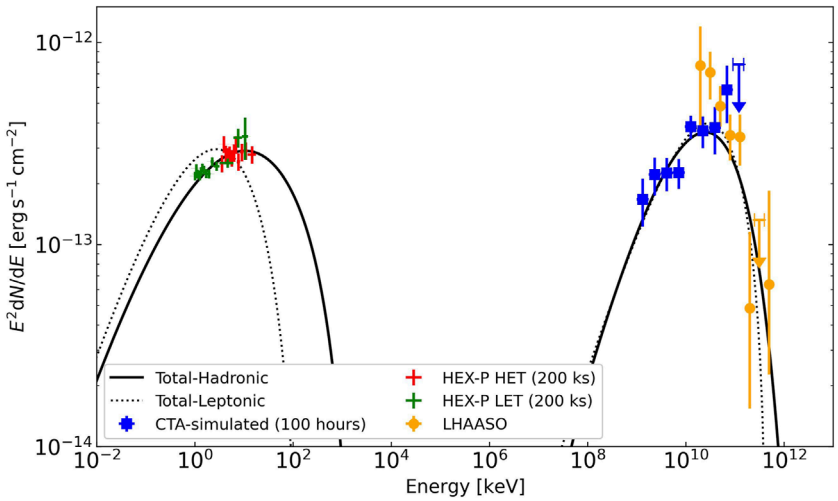

FIGURE 3
Multi-wavelength SED models for LHAASO J2108 + 5157 including both hadronic (black solid line) and leptonic (black dotted line) models. The flux points from LHAASO-KM2A Cao et al. (2023a) are overlaid as yellow circles. The CTAO flux points (blue square) are from a 100-h simulation using the Small-Sized Telescopes (SST) and Medium-Sized Telescopes (MST). The HEX-P LET and HET flux points, the green and red crosses, respectively, are from 200-ks simulations.

Resolving the UHE sources will need to wait until CTAO, the next-generation IACT, becomes fully operational in the mid-2020s. Observing Galactic PeVatrons is a key science project (KSP) for the CTAO mission, and it is recognized as one of the important science goals in the gamma-ray and astroparticle physics communities (Cherenkov Telescope Array Consortium et al., 2019). CTAO is expected to resolve and localize the most energetic particle acceleration sites in the Galactic PeVatrons.

In the X-ray band, given its broadband coverage and high sensitivity up to 80 keV, HEX-P will be uniquely suited for exploring the nature and acceleration mechanisms of Galactic PeVatrons in synergy with CTA. HEX-P will be optimal for detecting diffuse non-thermal X-ray emission and characterizing the known counterparts (e.g., PWNe, SNRs, star clusters) of the UHE targets. Both HEX-P and CTAO, reaching the regime of the highest energy particles in the PeVatrons, are alike for their broad-band energy coverages and versatile functionality equipped with excellent angular, energy, and timing resolutions. CTAO will be able to resolve the LHAASO/HAWC sources with ~1′ angular resolution and guide HEX-P in pinpointing their central engines and primary high-energy emission sites. Hard X-ray emission should originate from more compact regions (which will likely be covered by a single or few pointings with HEX-P) as observed from many of the known Galactic TeV sources (e.g., Coerver et al., 2019). In both leptonic or hadronic particle accelerators, synchrotron X-ray radiation is expected from Galactic TeV sources through primary electrons and secondary electrons from pionic showers. Accurate measurements of the B-field are crucial since synchrotron radiation is typically the dominant particle cooling process for TeV-PeV electrons. Unfortunately, *NuSTAR* observations of many extended X-ray sources have been limited by high background contamination, often resulting in detections up to only 20 keV. Expanding on the previous X-ray + TeV observations (e.g., *NuSTAR* + HAWC + VERITAS, H.E.S.S + *Suzaku* surveys), multi-wavelength SED data obtained by HEX-P and CTAO will enable identifying the nature of Galactic PeVatrons in the 2030s. An example, shown in

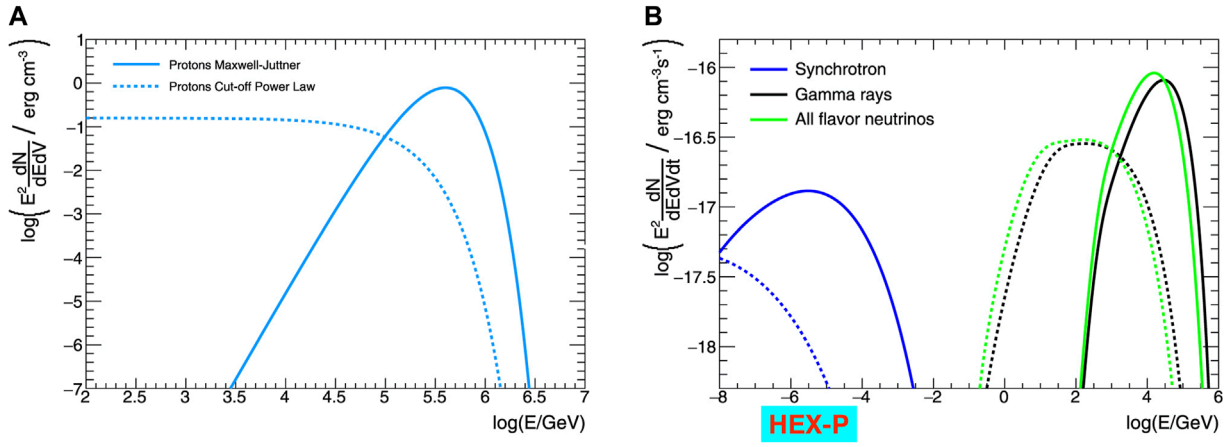

FIGURE 4
Primary proton energy distributions **(A)** and multi-wavelength SED models **(B)** for hadronic PeVatrons, excerpted from Celli et al. (2020). Two types of primary proton spectral models are considered: Maxwellian-like (solid lines) and power-law with an exponential cutoff (dashed lines). The synchrotron X-ray spectra are quite distinct between the two scenarios (assuming $B = 1$ mG). HEX-P will thus play a complementary role in constraining the primary CR spectra to the gamma-ray and neutrino telescopes.

Figure 3, depicts the fit of LHAASO and simulated CTAO SED data of one of the dark PeVatron accelerators (LHAASO J2108 + 5157) using both leptonic and hadronic models. The SED plot highlights a stark contrast in the X-ray fluxes and slopes within the HEX-P band. Moreover, Figure 4 displays multi-wavelength SEDs of a hadronic PeVatron with two different primary proton spectra. The synchrotron X-ray emission from secondary electrons provides the most sensitive diagnostics for determining the proton energy distribution, particularly in the cutoff PeV energy band, unlike gamma-ray and neutrino SEDs (Celli et al., 2020).

In summary, HEX-P will play a crucial role in the multi-messenger investigations of PeVatron astrophysics. As part of the primary science program, HEX-P aims to observe five Galactic PeVatron candidates, while CTAO is expected to survey most of the PeVatron candidates through their KSP program. Very recently and excitingly, IceCube detected TeV–PeV neutrinos in the Galactic Plane as the first evidence of Galactic hadronic PeVatrons (IceCube Collaboration et al., 2023). HEX-P will survey various types of PeVatron candidates, including leptonic, hadronic, and dark accelerators (with no apparent low-energy counterparts or association with known astrophysical sources), paving the way for more extensive PeVatron observations through the PI-led GTO or GO programs.

6 Star clusters and superbubbles

Star clusters, observed in broad ranges of masses, ages, and stellar densities (Pfalzner, 2009; Krumholz et al., 2019) might be found in different types of galaxies with high star-forming rates (Whitmore, 2000; Adamo et al., 2020). The evolution of the galactic environment is closely related to star formation, which is a key phenomenon that binds together important constituents from molecular gas to magnetic fields and cosmic rays in a close relationship. Star-forming regions both in the Milky Way and in starburst galaxies are known sources of broadband non-thermal radiation from radio to gamma rays, indicating the presence of relativistic particles. A significant part of massive stars is believed to evolve as clusters, which are gravitationally bound groups of stars of a common origin. Of particular interest are massive star clusters (MSCs) found in many regions of star formation. MSCs are sources of both thermal and non-thermal X-ray radiation, and they are considered effective cosmic ray accelerators (e.g., Bykov, 2014; Aharonian et al., 2019). The Milky Way contains a number of well-studied MSCs, such as NGC 3603 (Drissen et al., 1995), Westerlund 1/2 (Clark et al., 2005; Zeidler et al., 2015), Arches (Figer et al., 2002), and Quintuplet (Figer et al., 1999), which contain dozens and even hundreds of bright OB, Wolf-Rayet (WR), cool super- and hypergiant stars in the cluster cores of a parsec scale size.

In recent years, MSCs and superbubbles have been recognized as one of the primary classes of hadronic accelerators, possibly accounting for some of the PeVatrons in our Galaxy (Aharonian et al., 2019). In hadronic accelerators, energetic CRs diffuse out from the accelerator site (star cluster), collide with ambient medium and molecular clouds, and produce copious pionic showers which decay into neutrinos, gamma-rays, and electrons/positrons. MSCs contain a number of massive stars ($M > 20M_{\odot}$) and sometimes form large-scale H II regions, the so-called superbubbles, by ionizing and heating the surrounding gas. Colliding winds in massive binaries (composed of OB and WR stars) can also accelerate particles efficiently and emit non-thermal high-energy radiation (Pittard et al., 2020; Morlino et al., 2021). An important clue to support the MSC origin of PeVatrons has arisen from a recent discovery of diffuse gamma-ray sources around a handful of the MSCs and superbubbles. Remarkably, H.E.S.S. and *Fermi*-LAT discovered the so-called γ-ray cocoons extending over ~ 50–300 pc around two MSCs (Westerlund 1 and 2) and two superbubbles (Cygnus and 30 Dor C in the LMC). A leptonic origin for the γ-ray cocoons is ruled out since TeV–PeV electrons will cool down before traveling over the cocoon size distance. There

are two key features observed from the γ-ray cocoons that suggest they are likely hadronic PeVatrons. First, H.E.S.S. and *Fermi*-LAT detected hard γ-ray spectra with $\Gamma \approx 2$ up to $E \gtrsim 10$ TeV with no spectral cutoff–this is a potential signature of PeVatrons (Yang et al., 2019). Secondly, the CR proton densities decrease as $1/r$ where r is the distance from the star cluster (Yang et al., 2019). The $1/r$ profile indicates that the CRs must be injected from the source continuously over ~10^6 years. SNRs alone are unlikely to produce γ-ray cocoons since an unreasonably high SNR birth rate of more than one per 100 years is required in the region (Yang et al., 2019). Similarly, the MSCs such as Arches and Quintuplet clusters have been proposed as alternative particle accelerators which cause diffuse TeV emission in the central molecular zone (CMZ) of the Galactic Center, in addition to the (currently dormant) supermassive black hole at Sgr A* (Aharonian et al., 2019) Hence, the most plausible hypothesis is that MSCs continuously injected TeV–PeV CRs into the ambient molecular clouds, along with episodic supernova explosions, over the past ~10^6 years and formed the γ-ray cocoons and superbubbles extending over ~50–300 pc (Vieu et al., 2022; Gabici, 2023). This hypothesis needs to be tested by multi-wavelength observations.

6.1 Star clusters

In order to explore the formation of gamma-ray cocoons, firstly, it is essential to study how their central engines (i.e., MSCs) accelerate particles using X-ray and TeV data. Given that the gamma-ray cocoon profiles suggested continuous particle injections, their star clusters should be presently accelerating particles. The TeV emission mechanism from MSCs is still unsettled partially due to the lack of associated non-thermal X-ray detection. TeV gamma-rays could be produced by hadronic interactions in the colliding winds or ambient molecular clouds or ICS emission due to the high radiation densities within the clusters. It remains uncertain whether the prominent MSCs such as Westerlund 1 exhibit non-thermal X-ray emission caused by colliding wind shocks, apart from the thermal X-rays from numerous massive stars. Note that *NuSTAR* data of Westerlund 1 and Cygnus OB associations are severely contaminated by background photons from nearby magnetar and X-ray binaries (Borghese et al., 2019; Mossoux et al., 2020). From Westerlund 2, a hard X-ray component has been detected up to ~20 keV by SRG/ART-XC but its origin remains undetermined between non-thermal ($\Gamma \sim 2$) and thermal plasma ($kT \sim 5$ keV) emission (Bykov et al., 2023). For the Arches cluster, variable non-thermal X-ray emission was detected by *NuSTAR* from its nearby molecular clouds, but not from the star cluster itself (Krivonos et al., 2014). So far, *NuSTAR* has identified non-thermal X-ray emission only from Eta Carina (Hamaguchi et al., 2018). Eta Carina has been considered an exception as it is the supermassive and most luminous binary star system in our Galaxy.

Without detecting non-thermal X-ray emission, it remains elusive whether numerous massive stars and binaries can emit strong winds and accelerate particles collectively in the MSCs. Given its higher angular resolution and sensitivity than *NuSTAR*, HEX-P is best suited for resolving non-thermal X-rays from predominant thermal X-ray emission spatially and spectrally. HET is particularly important since the MSCs are usually crowded with other non-thermal X-ray sources such as magnetars and PWNe. A good example is Westerlund 1 where *NuSTAR* data are severely contaminated by X-ray photons from the magnetar CXOU J164710.2−455216 in the region. Overall, broad-band LET + HET spectra will be able to characterize both thermal and non-thermal X-ray components from star clusters with significantly reduced background levels than *NuSTAR*. For example, Figures 5A displays simulated HEX-P spectra for Westerlund 2, whose non-thermal X-ray component is detected up to ~30 keV. In addition to Westerlund 1and2 and the Cygnus regions, HEX-P's GC survey program will cover Arches and Quintuplet star clusters which have been considered as one of the primary particle accelerators in the GC region (Aharonian et al., 2019). HEX-P observations of Orion and Carina nebulae will allow us to explore X-ray source populations and potential particle acceleration sites in younger star clusters (Mori et al., 2021).

The star clusters Arches and Quintuplet, located in the GC, are known X-ray emitters: thermal and possibly non-thermal X-ray emission was detected by *Chandra* (Law and Yusef-Zadeh, 2004; Wang et al., 2006). The nature of the non-thermal X-ray emission of the Arches cluster is not completely known. Tatischeff et al. (2012) mapped the molecular cloud in 6.4 pkeV Fe fluorescent line and made an assumption about collisional ionization by low energy CR (LECR) particles. Furthermore, Krivonos et al. (2014) studied the extended X-ray emission of the Arches complex, containing star cluster and nearby molecular cloud, at energies above 10 keV with *NuSTAR* data (see also Kuznetsova et al., 2019). They showed that non-thermal emission is consistent with the X-ray reflection scenario, but also in broad agreement with the bombardment of the neutral matter by LECR protons. Clavel et al. (2014) showed that the X-ray flux from the Arches molecular cloud in the 6.4 keV line and continuum has been decreasing since 2012, which indicates cloud ionization from a possible Sgr A* flare. Since then, studies of non-thermal emission from the Arches complex have not been carried out, and after a few years, a significant decrease in the flux can be expected. This opens a possibility to observe the Arches star cluster isolated, i.e., without strong contribution from non-thermal emission of the molecular cloud, and to detect possible non-thermal emission of the star cluster itself.

To investigate the prospects of *HEX-P* to discover the intrinsic non-thermal emission from the Arches star cluster, we consider the observed total X-ray emission in 2015–2016 with *NuSTAR* and *XMM-Newton* (Krivonos et al., 2014; Kuznetsova et al., 2019). The properties of the cluster's thermal emission are well known; for example, Kuznetsova et al. (2019) uses collisionally ionized plasma with a temperature of 1.95 keV and an unabsorbed 2–10 keV flux $F_{apec} = 1.16 \times 10^{-12}$ ergs cm^{-2} s^{-1}. Due to the unknown spectral form of the expected Arches cluster non-thermal emission, we consider a power-law model with a photon index $\Gamma = 1$ and $\Gamma = 2$. To constrain the normalization of the power-law model, we imposed the 10–40 keV flux not to exceed the observed total emission of $F_{10-40\ \mathrm{keV}} = 4 \times 10^{-13}$ ergs cm^{-2} s^{-1} within 50″ from the cluster's center (Kuznetsova et al., 2019). For an exposure of 150 ks, we estimate the non-thermal flux to be detected at the significance of 8σ for both spectral indexes, with the uncertainty of spectral index at the level of 30% and 10% for $\Gamma = 1$ and $\Gamma = 2$, respectively (see Figures 5B for $\Gamma = 1$). The simulated thermal flux of the Arches cluster 1.3×10^{-14} ergs cm^{-2} s^{-1} in 10–40 keV band can be

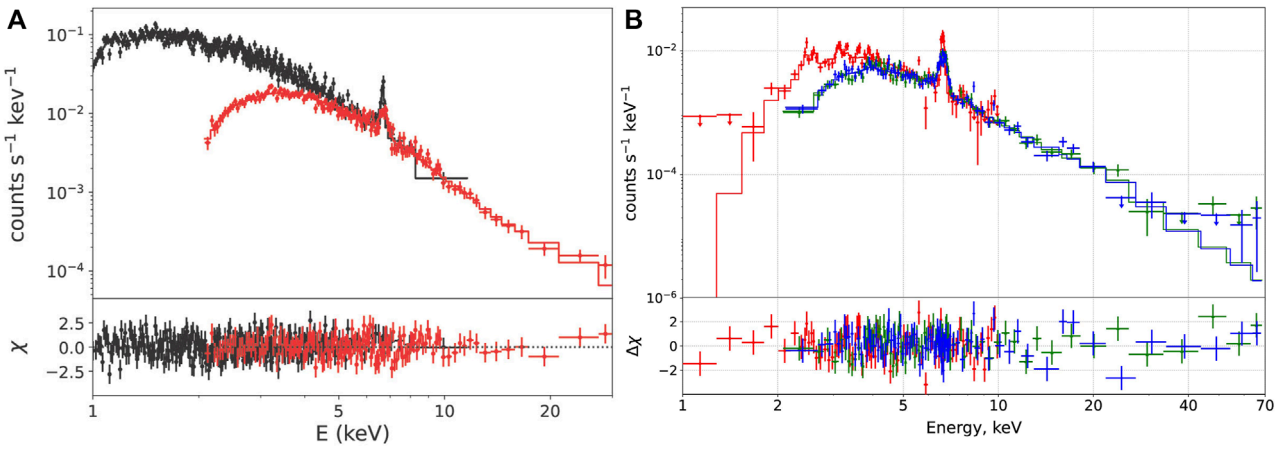

FIGURE 5
(A): Simulated *HEX-P* LET + HET spectra of Westerlund 2 ($r < 90''$ around the core of the cluster). We input an absorbed APEC + power-law model, which was also fit to the simulated spectra. The spectral parameters used in the model ($kT = 2.6$ keV and $\Gamma = 2$) were determined by *NuSTAR* analysis of the same region. Note that the photon index is not well constrained by *NuSTAR* data due to the poor signal-to-noise ratio above 10 keV, also making the detection of a non-thermal emission component ambiguous. For comparison, we fit an absorbed double-APEC model to the simulated HEX-P spectra and found that the second thermal plasma component yielded an unreasonable and unconstrained plasma temperature of $kT > 27$ keV. **(B)**: Simulated spectrum of the Arches cluster emission expected from the circular region with $R = 50''$ Krivonos et al. (2017), Kuznetsova et al. (2019). The spectrum is presented for *HEX-P* (red for LET and blue and green for HET) in the 1–70 keV energy band with the 150 ks exposure time. The non-thermal emission was simulated for a case of $\Gamma = 1$ and the non-thermal flux of 7% of the total flux in the 2–10 keV energy band.

considered as a threshold, above which the non-thermal component can be revealed.

The angular resolution of the *LET* module will allow resolving bright point sources in the dense cluster's core. To model the spatial morphology of the cluster seen by *LET*, we utilize the spatial and spectral information of the bright sources A1N, A1S, and A2 in the Arches cluster detected with *Chandra* by Wang et al. (2006). Figure 6 demonstrates the 150-ks LET simulation which allows resolving A2 from A1N and A1S. We conclude that LET will provide an opportunity to investigate the spatial morphology of the Arches cluster thermal emission in detail. In addition, Figure 6 clearly demonstrates different source morphologies seen by HET for different cases of non-thermal emission likely to be emitted by point sources of the Arches cluster.

6.2 Superbubbles

While star clusters are the primary sites of accelerating and injecting particles, superbubbles extending over hundreds of parsecs emerge as a result of energetic particles propagating into the surrounding medium over millions of years. 30 Dor C is the only superbubble detected with non-thermal X-rays (Bamba et al., 2004) up to 20 keV (Lopez et al., 2020) and TeV gamma-rays (S. S. Collaboration et al., 2015). The non-thermal X-ray luminosity is 10 times brighter than that of SN 1006, and similar to that of RX J1713.7−3946 (Nakamura et al., 2012), implying that 30 Dor C hosts a powerful particle accelerator. Bykov (2001, Bykov, 2006) proposed that episodic supernova explosions in star clusters can generate multiple shock waves and their interactions within the superbubbles result in energetic particle acceleration. This idea is supported by the *XMM* detection of a young SNR inside 30 Dor C (Kavanagh et al., 2015). However, we still lack a global picture of which physical parameters control the particle acceleration mechanism since no other superbubbles have non-thermal X-ray emission detected yet (Yamaguchi et al., 2010). The acceleration mechanism of superbubbles seems to operate differently from that of SNRs since the superbubble is filled with less dense, optically-thin hot plasma. Due to the smaller Mach numbers of the SN shocks in the superbubbles, the shock waves expand without deceleration until they abruptly slow down upon colliding with the surrounding dense gas. Given the complex interactions between SN shock waves and ambient gas, it is challenging to model the maximum energy of accelerated particles and their energy evolution. To determine the contribution of superbubbles to the Galactic cosmic-ray populations, it is crucial to measure the maximum electron energies through broadband non-thermal X-ray spectra from superbubbles. HEX-P observations of superbubbles, leading to measuring their X-ray spectral indices and roll-off energies, will allow us to elucidate how their particle acceleration processes are different from those of SNRs (e.g., Cas A and Tycho). For example, a simulated HEX-P HET image of 30 Dor C is presented in the Figures 7B. Note that 30 Dor C will be covered by the 300 ks HEX-P observation of SN 1987A in the same FOV. The simulation clearly shows hard X-ray emission up to 20 keV with only 300 ks (compared to the *NuSTAR* observations with ~3 Ms yielding similar results (Lopez et al., 2020)), highlighting HEX-P's capability of detecting extended sources in the hard X-ray band.

7 SS433/W50 lobes

The Manatee Nebula W50 is one of the most prominent radio sources in the sky, associated with the microquasar SS 433 located

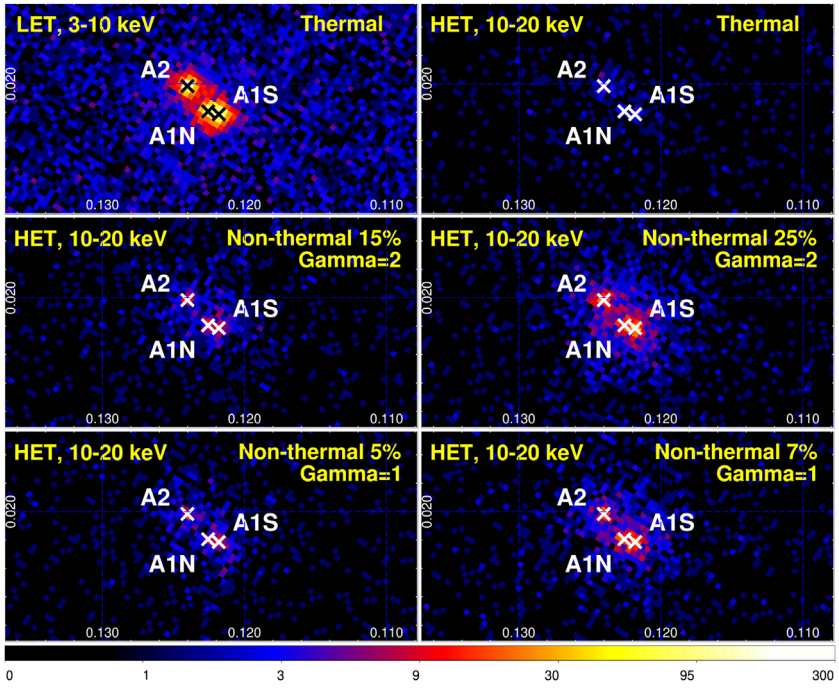

FIGURE 6
150-ks simulations of various scenarios of thermal and non-thermal emission from the Arches cluster for LET and HET. The crosses correspond to the positions of the brightest point sources within the Arches cluster detected by *Chandra* (Wang et al., 2006). The assumed fraction of the non-thermal flux to the total flux in the 2–10 keV energy band and the photon index of the power-law component are labeled at the upper right corner of each figure.

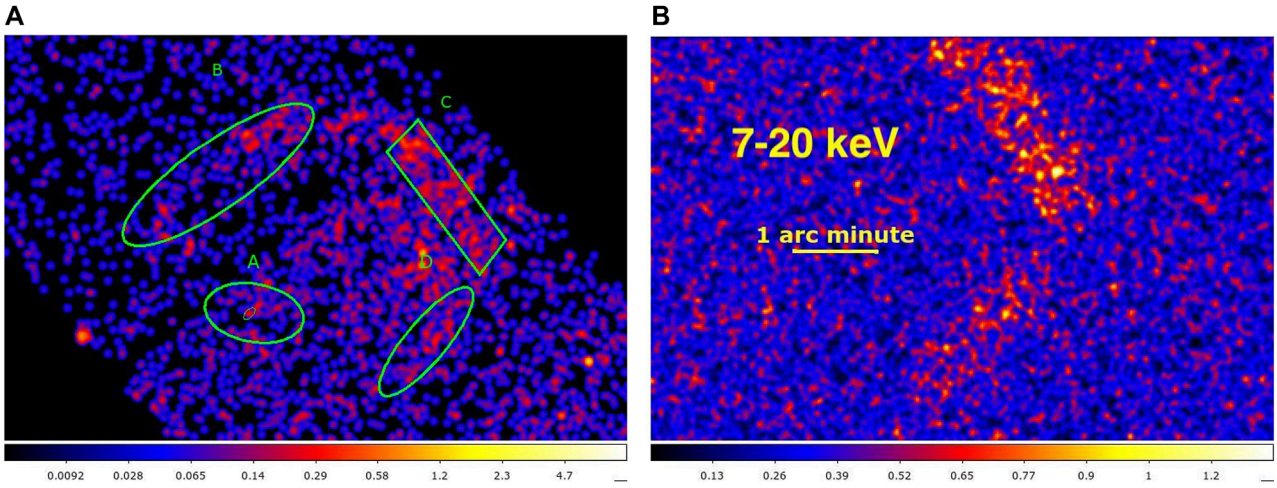

FIGURE 7
(A): *Chandra* image around 30 Dor C in the 2–7 keV band used as an input for SIXTE simulations. We input the best-fit spectral parameters from four shell-like regions, which correspond to the regions A–D shown in Figure 1 in Bamba et al. (2004). **(B)**: Simulated HEX-P HET image of 30 Dor C in the 7–20 keV band in a linear scale. One can see clear emission from its shells up to 20 keV with only 300 ks exposure.

at a distance of 5.5 kpc (Figure 8 and, e.g.,; Dubner et al. (1998)). The bipolar jets launched from SS 433 interact with the ISM and W50 nebula, producing distinct features in multiwavelength bands. Of particular interest are knot-like structures at both the eastern and western lobes, referred to as e1–2 and w1–2, recently shown to be sites of TeV gamma-ray emission (HAWC Collaboration et al., 2020; Cao et al., 2023a). The initial ASCA/ROSAT/RXTE/XMM surveys identified distinct X-ray knots in the eastern (e1–e3) and western (w1–w2) lobes (Safi-Harb and Ögelman, 1997; Safi-Harb and Petre, 1999; Brinkmann et al., 2007) with non-thermal

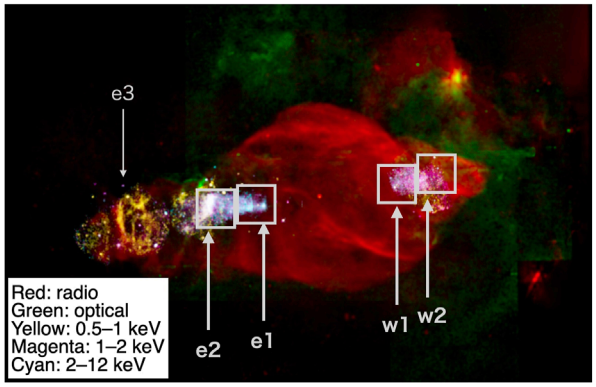

FIGURE 8
Entire image of the SS 433/W50 system, taken from Safi-Harb et al. (2022a). White boxes show the FoV of HEX-P and our proposed pointings.

X-ray emission dominating the inner regions, likely synchrotron radiation from accelerated electrons. Only e3 has an apparent counterpart in the radio band known as the eastern ear. The HAWC discovery of TeV gamma-ray emission from the eastern and western lobes, recently also detected by LHAASO (Cao et al., 2023a), indicated that the SS 433/W50 system could represent another class of extreme particle accelerators powered by microquasar jets (HAWC Collaboration et al., 2020).

The detection of TeV emission by HAWC has motivated extensive studies of the W50 system, including multi-wavelength surveys below the TeV band, theoretical modeling, and numerical simulations. Among various follow-up observations, *XMM* unveiled that there exists a relatively compact structure at the e1 knot, dubbed the head region (Figure 8). Broadband X-ray spectra with *XMM* and *NuSTAR* were characterized by a power-law model with $\Gamma \sim 1.5$ up to ~30 keV in the head region (Safi-Harb et al., 2022a). In the western lobe, using the archival *Chandra* data (Moldowan et al., 2005; Kayama et al., 2022) recently extracted a detailed profile of spectral parameters along the western lobe (w1–w2), revealing that non-thermal X-ray emission begins at w1 (where the particle acceleration is initiated and most energetic) and becomes gradually softer toward w2 due to synchrotron cooling. In the radio band, an extensive VLA survey in the 1.4 GHz band was conducted over the entire W50 system, mapping synchrotron radiation emitted by lower-energy (GeV) electrons (Sakemi et al., 2021). As shown in Figure 8), the W50 "mini-AGN" system manifests all elements of astrophysical jets: acceleration sites (the inner lobes); particle propagation/cooling along the jet; and thermalization at the termination region. Motivated by the HAWC discovery in 2018, a handful of particle acceleration models have been developed, including leptonic and hadronic SED models (Kimura et al., 2020a; Sudoh et al., 2020) as well as MHD simulations (Ohmura et al., 2021).

Despite the extensive X-ray surveys with *XMM*, *Chandra*, and *NuSTAR*, we are still not at the stage of fully testing these theoretical model predictions, let alone deciding the origin of TeV emission between the leptonic and hadronic acceleration mechanisms. The *NuSTAR* data of the head regions (e1 and w1) are severely contaminated by ghost-ray background photons from SS 433 (Safi-Harb et al., 2022b) above ~30 keV. The TeV emission needs to be resolved with $\lesssim 20''$ angular resolution so that it can be compared well with the X-ray and radio data. Apparently, we need multi-zone, multi-wavelength observations and modeling tied together, in order to completely determine how particles get accelerated and propagate, while cooling, throughout the bipolar jets. As mentioned repeatedly for other types of particle accelerators, HEX-P and CTAO will make the highest impact on understanding this complex system, including local MHD phenomena such as magnetic-field amplification and knot formation.

7.1 Scientific objectives with HEX-P

A HEX-P X-ray survey of the SS 433/W50 system will be able to resolve the spectral and spatial profiles and will offer a unique opportunity to investigate particle acceleration by microquasar jets and their interactions with the surrounding environment. During the primary science program, HEX-P plans to survey the SS 433/W50 region with four observations pointing at the e1, e2, w1, and w2 knots, as shown in Figure 8. To assess the feasibility of HEX-P observations, we conducted simulations with the SIXTE and XSPEC packages. For instance, Figure 9 illustrates simulated HET images of the western lobe in different energy bands with an exposure of 75 ks? The simulations use as input the *Chandra* flux image in 0.5–7 keV and spatial distributions of spectral parameters, N_H, flux, and Γ, which were adopted from Figure 6 in Kayama et al. (2022). Note that the w1 knot, which exhibits a harder X-ray spectrum, remains clearly visible up to ~80 keV, while the softer w2 knot can be detected up to ~25 keV. Hence, HEX-P will have the capability of fully characterizing the X-ray spectral and spatial distributions, tracking the evolution of relativistic particles along the jets.

7.1.1 Determining the particle acceleration mechanism

The origin of the TeV emission from the inner lobes remains uncertain since the current multi-wavelength SED data do not provide conclusive evidence for distinguishing between the leptonic and hadronic models (Kimura et al., 2020b). Similar to other TeV sources, gamma-ray information alone is insufficient to discriminate between the leptonic and hadronic scenarios or to constrain model parameters. Instead, broad-band X-ray spectroscopy and morphology studies with HEX-P, along with CTAO, will be critical in elucidating the origin of the TeV emission and constraining key model parameters such as magnetic field (B) and electron/proton spectral indices. The morphology data obtained by HEX-P, capturing non-thermal X-rays, will enable us to spatially correlate synchrotron X-ray emission with molecular clouds (Yamamoto et al., 2022) and radio features (Sakemi et al., 2021). Note that the molecular cloud and radio maps track the target material distribution for hadronic interactions and the magnetic field distribution, respectively. The identification of hot spots in hard X-rays, coinciding spatially with molecular clouds and high-density optical filaments, would lend support to the hadronic case where synchrotron X-ray radiation originates from secondary electrons (produced by proton-proton collisions and subsequent pion decays) (Kimura et al., 2020b). Conversely, in the leptonic

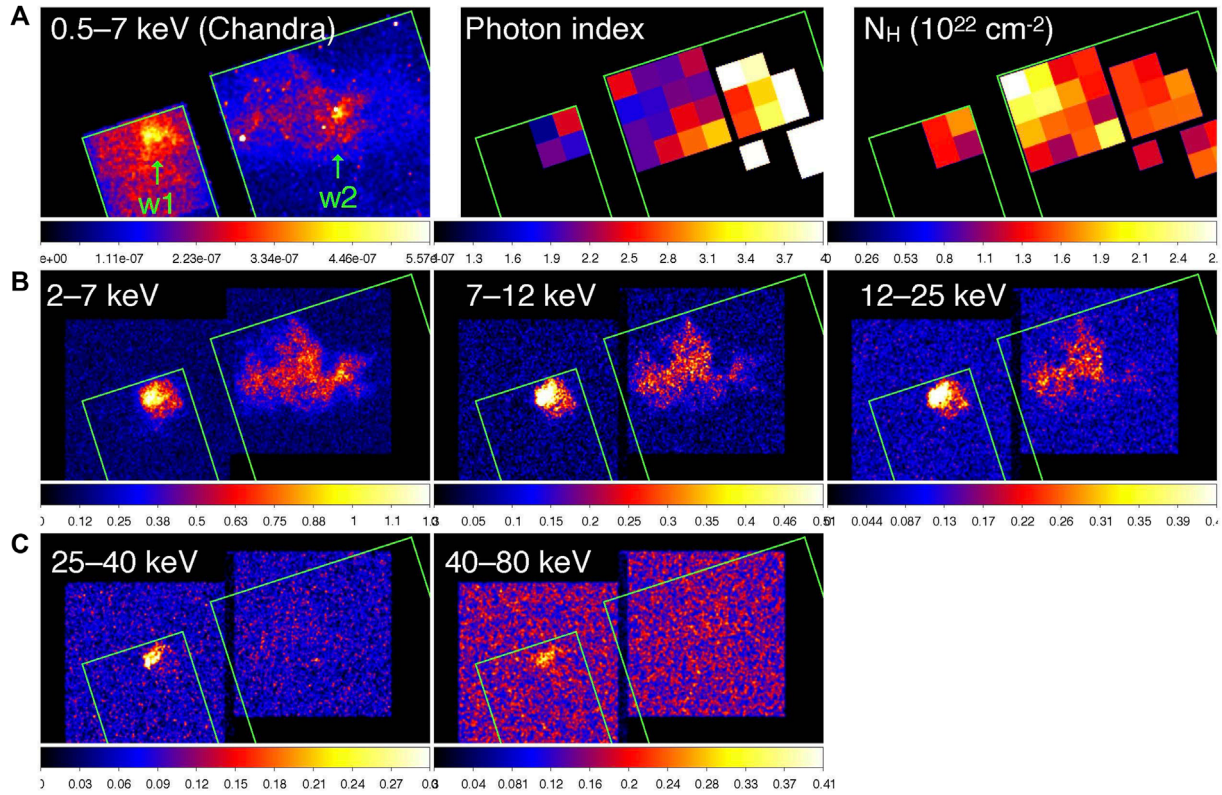

FIGURE 9
(A): Input *Chandra* flux, photon index, and column density maps of SS433/W50 western lobe in 0.5–7 keV. **(B,C)**: Simulated HET images in five different energy bands of w1–2 with exposure of 75 ks Green lines show the FoV of *Chandra* ObsID 3843.

case, a more gradual X-ray spectral softening is expected from the acceleration site (w1/e1) to the termination region (w2/e2 or e3) as propagating electrons cool down via synchrotron radiation (Sudoh et al., 2020). A combination of multi-wavelength SED analysis and the localization of energetic electrons, for which the hard X-ray band coverage of HEX-P plays a crucial role, can distinguish between the leptonic and hadronic scenarios robustly (Kimura et al., 2020a).

7.1.2 Constraining acceleration efficiency along the jets

Measuring the cutoff energy (E_c) in the synchrotron X-ray spectrum offers direct insights into the particle acceleration mechanism by constraining an "acceleration efficiency factor" $\eta_{\rm acc} \equiv c\,\tau_{acc}/r_L$, where τ_{acc} is the acceleration time to energy E and r_L the Larmor radius (Sudoh et al., 2020). That is, $\eta_{\rm acc}$ is the dimensionless acceleration time, measured in units of the inverse of the Larmor frequency. Particularly, in the case of DSA and cooling-limited electrons, the combination of E_c and shock velocity provides a robust means to derive $\eta_{\rm acc}$ independent of the B-field. In the standard diffusion scenario, $\eta_{\rm acc}$ is characterized by the gyrofactor η_g, the ratio of the mean free path of a particle to its gyroradius ($\eta_g = 1$ is the "Bohm limit"). Ultimately, $\eta_{\rm acc}$ and E_c can be used to determine the maximum energies of accelerated particles, assuming an age-limited case. Of particular importance is the determination of whether $\eta_{\rm acc}$ is smaller than 10^2, as it implies the acceleration of particles to PeV energies in the formalism of (Sudoh et al., 2020). Previous observations with *NuSTAR* detected non-thermal X-ray emission in the head regions, where the particle acceleration is considered to be most active, up to ~20–30 keV, but a cutoff was difficult to determine because of the high background level. In contrast, HEX-P holds a great premise of extending its sensitivity up to 80 keV, enabling the more accurate determination of cutoff energies and further constraining the acceleration efficiency factors.

In order to demonstrate the unique capabilities of HEX-P determining parameters related to particle acceleration, we conducted simulations based on the leptonic model developed by Sudoh et al. (2020), covering a wide range of $\eta_{\rm acc}$ values. For the case of DSA, the $\eta_{\rm acc}$ parameter and the gyrofactor $\eta_{\rm g}$ are related: $\eta_{\rm acc} \simeq 10^2(\eta_g/2)(v_{\rm sh}/0.26c)^{-2}$ (see Sudoh et al. (2020) for details). Figure 10 displays the simulated HET spectra of the e1 knot with an exposure time of 75 ks? We found that a spectral cutoff energy can be measured with <10% accuracy, which is sufficient to distinguish between $\eta_{\rm acc} = 10$, 10^2, 10^3, and 10^4. In the w1 knot where its X-ray flux is fainter, a 75-ks HEX-P observation can unambiguously determine whether the acceleration is in the Bohm ($\eta_g \sim 1$) or non-Bohm ($\eta_g \gg 1$) regime. A longer exposure time will constrain $\eta_{\rm acc}$ values in the w1 knot similarly to the e1 knot. The determination of acceleration efficiency within the microquasar jets will provide valuable insights among accelerators with different scales, such as $\eta_g \sim 1$ (the most efficient acceleration

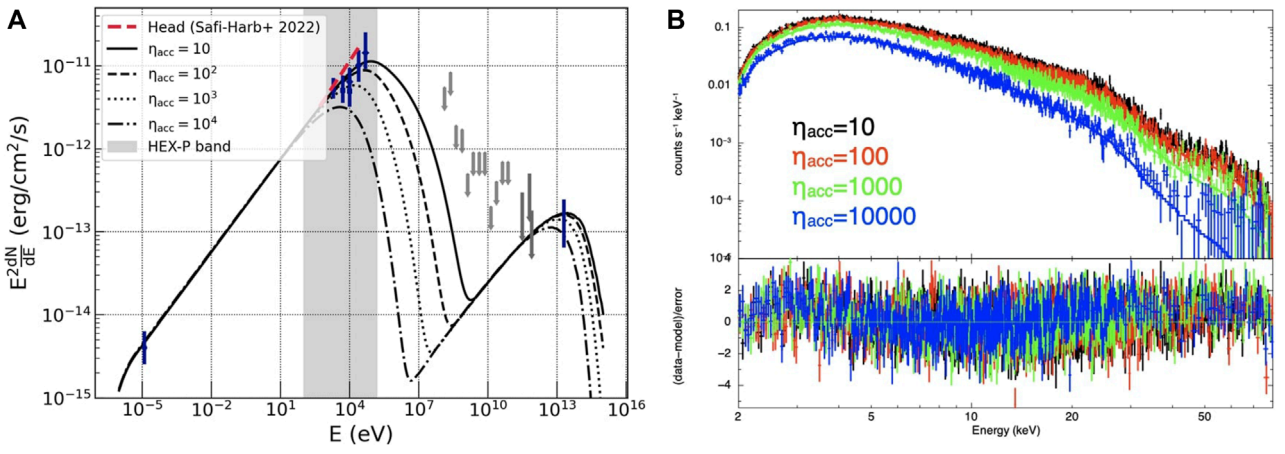

FIGURE 10
(A): multiwavelength SED of e1 and theoretical models with different acceleration efficiency (η_{acc}) by Sudoh et al. (2020). **(B)**: simulated HET spectra of e1 with exposure of 75 ks.

case) at SNR shells (e.g., Tsuji et al., 2021) and $\eta_g \sim 10^6$ at AGN jets (e.g., Araudo et al., 2015; Inoue and Tanaka, 2016). By combining HEX-P and CTAO observations with the existing radio data, it will be possible to perform the most refined multiwavelength SED analyses at various X-ray knot locations, as shown in Figures 10A, at sub-arcminute scales. This panchromatic approach will yield mapping of the distribution of acceleration efficiency and boost our understanding of particle acceleration and evolution along the microquasar jets/lobes.

7.1.3 Knot formation in the microquasar jets/lobes

The formation and evolution of X-ray knots along the jets, not only in the case of W50 but also in AGN jets, remain uncertain and represent a long-standing question in astrophysics. Theoretical studies have proposed that the interaction of the jets with the ambient medium produces knot-like structures, as demonstrated by MHD simulations (Ohmura et al., 2021). The proximity of W50 provides a unique opportunity for correlating the X-ray knots and known ambient features such as molecular clouds and filaments. Furthermore, it is not fully understood whether the knot sizes are determined by radiation loss, adiabatic cooling, magnetic field amplification, and re-acceleration (Sudoh et al., 2020). A recent X-ray study suggested synchrotron cooling, in combination with amplified B-fields, dominates in several locations of the western lobe (e.g., w2), in order to reproduce the X-ray spectral profile obtained by *Chandra* observations (Kayama et al., 2022). If synchrotron cooling is indeed predominant in most or all of the X-ray knots, HEX-P will contribute to the determination of local B-fields by measuring the presumably energy-dependent sizes of the X-ray knots. The broad-band X-ray morphology traces the production site and cooling timescales of TeV-PeV electrons by detecting synchrotron burn-off effects. By directly measuring local B-fields, HEX-P can uniquely investigate the origin of X-ray knot formation and test the leading theoretical hypothesis of B-field amplification (Sudoh et al., 2020). Consequently, a HEX-P survey of W50 will provide valuable insights into the processes involved in knot formation and contribute to our fundamental understanding of astrophysical jets.

8 TeV gamma-ray binaries

TeV gamma-ray binaries (TGBs) are unique binary systems composed of a compact object and a massive companion, typically an O- or B-type star. To date, fewer than 10 TGBs have been discovered within our Galaxy, with one additional TGB in the LMC (Corbet et al., 2016). In three of these TGBs, the compact object was identified as a pulsar. While TGBs belong to a subclass of high-mass X-ray binaries (HMXBs), they possess distinct properties, notably their predominantly non-thermal SEDs peaking above MeV energies. Except for the intense optical blackbody (BB) emission from their companions, multi-wavelength SEDs of the known TGBs exhibit a double-humped feature (e.g., Figure 11). The low-energy hump, observed from radio to X-ray band, arises from synchrotron radiation emitted by energetic electrons present in either the jets of a BH [microquasar model, e.g., Marcote et al. (2015)] or the intra-binary shock (IBS) formed by interactions between the pulsar and companion star winds [pulsar-wind model, e.g., Dubus (2013)]. The high-energy bump, observed in the ≥100 GeV band, is due to ICS between relativistic electrons and BB photons from the companion. The X-ray emission above ~10 keV and the >TeV emission imply the presence of highly energetic (TeV) particles within TGBs. Furthermore, the broadband emission from TGBs exhibits strong orbital modulation, which can be attributed to the Doppler beaming of shocked particle flow and orbital variations of the ICS geometry.

For the TGB systems in which the compact object is known to be a pulsar (PSR B1259−63, PSR J2032 + 4127, and LS I +61° 303; Johnston et al., 1992; Abdo et al., 2009; Weng et al., 2022), an IBS in the pulsar-wind scenario are responsible for the broadband non-thermal emission. These systems all contain a Be-type companion with an equatorial disk. Broadband emission properties of these TGBs have been best studied for the archetypal

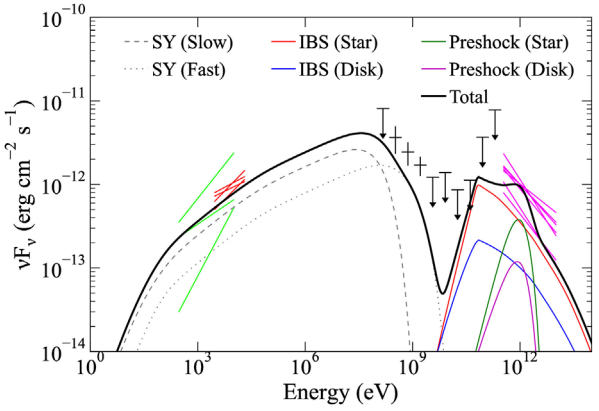

FIGURE 11
Broadband SED of the TGB HESS J0632 + 057 and an IBS model [figure taken from Kim et al. (2022). SEDs measured with *Swift* (lime), *NuSTAR* (red), and H.E.S.S. (magenta) are displayed with line segments with each line representing a measurement at an orbital phase. The data points at ~GeV are LAT-measured fluxes, which may include the putative pulsar's magnetospheric emission. The dashed or colored curves show various model components and the thick curve is the sum of them.

object PSR B1259−63. The pulsar crosses the disk at orbital phases near the periastron, and the pulsar-disk interaction produces dramatic X-ray and TeV flares at the crossings, accompanied by delayed orphan GeV flares. The physical mechanisms responsible for these flares are not well understood yet but are speculated to be related to the pulsar–disk interaction which could enhance seed photon density and/or (partial) disruption of the IBS by the disk. *NuSTAR* observations of PSR B1259−63 during such orbital intervals (including the GeV flare periods) revealed that the spectra were well fit by a hard $\Gamma_X = 1.5$ power-law model, whereas the source spectra were softer ($\Gamma_X \approx$ 1.8–2.0) at the periastron and disk-crossing phases (Chernyakova et al., 2015). These observed spectral variations are likely caused by a change in the particle injection spectrum and/or enhanced cooling at the disk-crossing phase. In the former case, we expect a power-law X-ray spectrum extending to ~ MeV energies, where the synchrotron cooling break is expected in TGBs (e.g., An and Romani, 2017). In the latter case, however, the amplified B-field of the IBS, caused by compression from the circumstellar disk (Tokayer et al., 2021), may increase the synchrotron cooling rate, leading to a spectral break in the X-ray band. Thus, accurate measurements of the X-ray and gamma-ray spectral shapes are important to elucidate the particle acceleration and flow processes within relativistic shocks.

8.1 Scientific objectives with HEX-P

Previous *NuSTAR* observations in the soft state of PSR B1259−63 were consistent with a simple power-law model to 79 keV. However, the sensitivity of *NuSTAR* data was limited in detecting a break or cutoff at >30 keV due to the high background level. Given the large effective area, higher angular resolution, and reduced background, HEX-P will significantly improve the current measurements of the X-ray spectra during the disk crossing phases. Figure 12 displays simulation results for a 50-ks HEX-P observation during a disk-crossing phase. For the simulations, we used an exponential-cutoff power law ($K(E/1\ \mathrm{keV})^{-\Gamma_X}\exp(-[E/E_c]^{\alpha})$), where K and Γ_X were obtained from the *NuSTAR* results of PSR B1259−63 at the crossing phase (power law with $\Gamma_X = 1.84$ and $F_{1-10\ \mathrm{keV}} = 2.84 \times 10^{-11}$ erg s^{-1} cm^{-2}; Chernyakova et al., 2015). We held the exponential index α fixed at 5 and varied E_c. We then fit the simulated spectra with a power-law and an exponential-cutoff power-law model, and we employed the *F*-test to discern between the two models. Our results, shown in the Figures 12C, suggest that HEX-P will be capable of detecting an exponential cut-off at $E_c \leq 70$ keV with 50-ks exposure, and even a milder cut-off (e.g., a smaller exponential index) can be detectable with HEX-P. Moreover, the more accurate spectral measurements and identification of spectral features at different orbital phases can contribute to distinguishing between various emission components in TGBs, such as the IBS vs. preshock emission (e.g., Kim et al., 2022).

Furthermore, HEX-P offers opportunities for other interesting studies. Since TGBs belong to a rare and intriguing class of Galactic TeV sources, dedicated multi-wavelength investigations for all known systems (~10 TGBs) have been performed with a number of X-ray, GeV, and TeV observations (e.g., Takahashi et al., 2009; Ackermann et al., 2012; Adams et al., 2021). These studies uncovered diverse physical phenomena, including strong orbit-to-orbit variability (e.g., Tokayer et al., 2021), correlations between Γ_X and F_X (e.g., Bosch-Ramon et al., 2005; An et al., 2013), variable N_{H} (e.g., Malyshev et al., 2019; Tokayer et al., 2021), and X-ray flares in certain sources (e.g., Chernyakova et al., 2015). These findings highlight the complicated interactions between the particle flow, the companion's wind, disk (e.g., Kefala and Bosch-Ramon, 2023), and particle evolution in the IBS. The hard X-ray data from *NuSTAR* have added important insights into TGBs, e.g., possible magnetar-like X-ray pulsations in LS 5039 (Yoneda et al., 2020) (although claimed to be spurious later; see Volkov et al., 2021) and the extension of simple power-law emission to 20–30 keV (e.g., An et al., 2015; Tokayer et al., 2021) suggesting that particle cooling is not severe. Although these previous X-ray and gamma-ray studies revealed the complex emission mechanisms of the TGBs (e.g., Dubus et al., 2015), our understanding of the diverse phenomena specific to TGBs remains incomplete. More precise characterization of X-ray spectral variability (Γ_X, F_X, and N_{H}), achievable by HEX-P, thanks to its contemporaneous observations in the broad 0.2–80 keV band enabled by LET + HET, will help in discerning variabilities caused by the injection and cooling of relativistic particles and their interactions with the environment.

The future prospects for TGB science are promising with the advent of CTAO and HEX-P. CTAO is expected to discover more TGBs (Dubus et al., 2017) and measure the TeV spectral variations of known TGBs on timescales as short as ~30 min (Chernyakova et al., 2019). A larger sample size of TGBs will expand the parameter space and facilitate a deeper understanding of their diverse nature. Dedicated observation programs with HEX-P and CTAO will by far surpass the current studies involving *NuSTAR*, VERITAS, and H.E.S.S. Overall, HEX-P is poised to make significant contributions to TGB astrophysics, enhancing our knowledge of these enigmatic binary systems and elucidating their complex

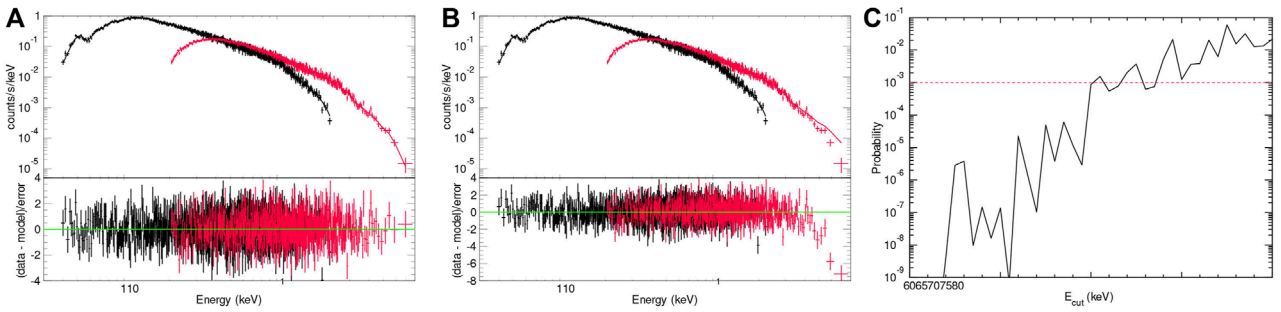

FIGURE 12
Results of simulations for 50-ks HEX-P observations of PSR B1259–63 at a disk-crossing phase. Simulated HEX-P spectra with a cutoff at 60 keV, along with the best-fit cut-off power-law and simple power-law models, are displayed in the **(A,B)**. The residuals in the bottom show that the spectral cutoff at 60 keV is clearly detectable by HEX-P. *F*-test probabilities for detecting an exponential cutoff for a range of E_{cut} values are presented in the **(C)** where the red horizontal line marks $p = 10^{-3}$.

TABLE 2 Potential HEX-P survey programs.

Program description	Sources	Comments
Galactic PeVatrons	TBD (e.g., Dark PeVtrons)	CTAO, LHAASO, HAWC, SWGO
Hadronic PeVatrons	IceCube neutrino sources	IceCube
Leptonic PeVatrons	PWNe detected above 100 TeV	CTAO, LHAASO, HAWC, SWGO
Young SNRs (X-ray variability)	Cas A, Tycho, G1.9 + 0.3	Multi-epoch observations
Young SNRs (^{44}Ti science)	Cas A, Tycho, G1.9 + 0.3, G350.1–0.1	Combine multi-epoch observations*
Sgr A* monitoring	Supermassive BH	EHT, GRAVITY, CTAO
Galactic NSM candidates	TBD	COSI

Note: These are potential HEX-P survey ideas other than the primary science program listed in Table 1.
*^{44}Ti science program will benefit from combining HEX-P data obtained from multi-epoch observations, which are intended for detecting X-ray variabilities from young SNRs.

emission mechanisms associated with relativistic shocks and jets in TGBs.

9 Conclusion

As our simulations demonstrate, HEX-P is poised to revolutionize X-ray views of Galactic particle accelerators, unraveling the origin of CRs up to the knee and beyond. Along with CTAO, HEX-P will play a crucial role in identifying numerous PeVatron candidates and their acceleration mechanisms. An extensive HEX-P survey of various types and stages of the particle accelerators associated with known SNRs, PWNe, star clusters, binaries, and BHs, will provide a broad picture of how particle acceleration, propagation, and cooling operate in different sources and environments. Finally, HEX-P will foster multi-messenger observation programs with other future missions such as CTAO, IceCube gen2, and COSI (see Table 2 for potential HEX-P survey programs). HEX-P clearly stands out as the foremost X-ray observatory for particle acceleration astrophysics in the 2030s.

Data availability statement

The raw data supporting the conclusions of this article will be made available by the authors, without undue reservation.

Author contributions

KM: Writing–original draft, Writing–review and editing. SR: Writing–original draft, Writing–review and editing. HA: Writing–original draft, Writing–review and editing. AB: Writing–original draft, Writing–review and editing. RK: Writing–original draft, Writing–review and editing. NT: Writing–original draft, Writing–review and editing. MA: Writing–review and editing. JA: Writing–review and editing. PB: Writing–review and editing. SC: Writing–review and editing. RD: Writing–review and editing. JE: Writing–review and editing. CF: Writing–review and editing. SG: Writing–review and editing. JoG: Writing–review and editing. BG: Writing–review and editing. JaG: Writing–review and editing. CK: Writing–review and editing. SK: Writing–review and editing. EK: Writing–review and editing.

BM: Writing–review and editing. KM: Writing–review and editing. SM: Writing–review and editing. YM: Writing–review and editing. HO: Writing–review and editing. BO: Writing–review and editing. JP: Writing–review and editing. GP: Writing–review and editing. TS: Writing–review and editing. R-YS: Writing–review and editing. DS: Writing–review and editing. YT: Writing–review and editing. JW: Writing–review and editing. GY: Writing–review and editing. AZ: Writing–review and editing.

Funding

The author(s) declare financial support was received for the research, authorship, and/or publication of this article. This work was financially supported by Japan Society for the Promotion of Science Grants-in-Aid for Scientific Research (KAKENHI) Grant Numbers, JP23H01211 (AB), 22K14064 (NT), 20K04009 (YT).

Acknowledgments

We are grateful to J. Wilms, T. Dauser, C. Kirsch, M. Lorenz, L. Dauner, and the SIXTE development team for their assistance with SIXTE simulations. HA acknowledges support from the National Research Foundation of Korea (NRF) grant funded by the Korean Government (MSIT) (NRF-2023R1A2C1002718). In Section 7 (SS 433/W50 lobes), we thank Takahiro Sudoh and Kazuho Kayama for providing their results and Samar Safi-Harb for the image. We thank Ke Fang, Lu Lu, and Kelly Malone for their helpful discussion.

Conflict of interest

The authors declare that the research was conducted in the absence of any commercial or financial relationships that could be construed as a potential conflict of interest.

Publisher's note

All claims expressed in this article are solely those of the authors and do not necessarily represent those of their affiliated organizations, or those of the publisher, the editors and the reviewers. Any product that may be evaluated in this article, or claim that may be made by its manufacturer, is not guaranteed or endorsed by the publisher.

References

Abdalla, H., Aharonian, F., Ait Benkhali, F., Angüner, E. O., Arcaro, C., Armand, C., et al. (2021). Evidence of 100 TeV γ-ray emission from HESS J1702-420: a new PeVatron candidate. *A&A* 653, A152. doi:10.1051/0004-6361/202140962

Abdo, A. A., Ackermann, M., Ajello, M., Anderson, B., Atwood, W. B., Axelsson, M., et al. (2009). Detection of 16 gamma-ray pulsars through blind frequency searches using the Fermi LAT. *Science* 325, 840. doi:10.1126/science.1175558

Abeysekara, A. U., Albert, A., Alfaro, R., Angeles Camacho, J. R., Arteaga-Velázquez, J. C., Arunbabu, K. P., et al. (2020). Multiple galactic sources with emission above 56 TeV detected by HAWC. *PRL* 124, 021102. doi:10.1103/PhysRevLett.124.021102

Ackermann, M., Ajello, M., Ballet, J., Barbiellini, G., Bastieri, D., Belfiore, A., et al. (2012). Periodic emission from the gamma-ray binary 1FGL j1018.6-5856. *Science* 335, 189. doi:10.1126/science.1213974

Adamo, A., Zeidler, P., Kruijssen, J. M. D., Chevance, M., Gieles, M., Calzetti, D., et al. (2020). Star clusters near and far; tracing star formation across cosmic time. *SSRv* 216, 69. doi:10.1007/s11214-020-00690-x

Adams, C. B., Benbow, W., Brill, A., Buckley, J. H., Capasso, M., Chromey, A. J., et al. (2021). Observation of the gamma-ray binary HESS J0632+057 with the H.E.S.S., MAGIC, and VERITAS telescopes. *ApJ* 923, 241. doi:10.3847/1538-4357/ac29b7

Aharonian, F., An, Q., Axikegu, L. X., BaiBai, Y. X., Bao, Y. W., Bastieri, D., et al. (2021). Extended very-high-energy gamma-ray emission surrounding PSR J 0622 +3749 observed by LHAASO-km2a. *PhRvL* 126, 241103. doi:10.1103/PhysRevLett.126.241103

Aharonian, F., Yang, R., and de Oña Wilhelmi, E. (2019). Massive stars as major factories of Galactic cosmic rays. *Nat. Astron.* 3, 561–567. doi:10.1038/s41550-019-0724-0

Aharonian, F. A., and Atoyan, A. M. (1999). On the origin of TeV radiation of SN 1006. *A&A* 351, 330–340. doi:10.48550/arXiv.astro-ph/9911158

Aliu, E., Archambault, S., Aune, T., Behera, B., Beilicke, M., Benbow, W., et al. (2014). Long-term TeV and X-ray observations of the gamma-ray binary HESS J0632+057. *ApJ* 780, 168. doi:10.1088/0004-637X/780/2/168

Amato, E., Guetta, D., and Blasi, P. (2003). Signatures of high energy protons in pulsar winds. *A&A* 402, 827–836. doi:10.1051/0004-6361:20030279

Amato, E., and Olmi, B. (2021). The crab pulsar and nebula as seen in gamma-rays. *Universe* 7, 448. doi:10.3390/universe7110448

Amenomori, M., Bao, Y. W., Bi, X. J., Chen, D., Chen, T. L., and Chen, H. (2021). Gamma-ray observation of the Cygnus region in the 100-TeV energy region. *PhRvL* 127, 031102. doi:10.1103/PhysRevLett.127.031102

An, H., Bellm, E., Bhalerao, V., Boggs, S. E., Christensen, F. E., Craig, W. W., et al. (2015). Broadband X-ray properties of the gamma-ray binary 1FGL j1018.6-5856. *ApJ* 806, 166. doi:10.1088/0004-637X/806/2/166

An, H., Dufour, F., Kaspi, V. M., and Harrison, F. A. (2013). Swift observations of 1FGL j1018.6-5856. *ApJ* 775, 135. doi:10.1088/0004-637X/775/2/135

An, H., and Romani, R. W. (2017). Light curve and SED modeling of the gamma-ray binary 1FGL j1018.6-5856: constraints on the orbital geometry and relativistic flow. *ApJ* 838, 145. doi:10.3847/1538-4357/aa6623

Araudo, A. T., Bell, A. R., and Blundell, K. M. (2015). Particle acceleration and magnetic field amplification in the jets of 4C74.26. *Astrophysical J.* 806, 243. doi:10.1088/0004-637X/806/2/243

Arnaud, K. A. (1996). "XSPEC: the first ten years," in *Astronomical data analysis software and systems V of astronomical society of the pacific conference series*. Editors G. H. Jacoby, and J. Barnes (USA: IEEE), 17.

Atoyan, A. M., and Aharonian, F. A. (1996). On the mechanisms of gamma radiation in the Crab Nebula. *MNRAS* 278, 525–541. doi:10.1093/mnras/278.2.525

Bamba, A., Ueno, M., Nakajima, H., and Koyama, K. (2004). Thermal and nonthermal X-rays from the large magellanic cloud superbubble 30 doradus C. *ApJ* 602, 257–263. doi:10.1086/380957

Blasi, P. (2013). The origin of galactic cosmic rays. *AAPR* 21, 70. doi:10.1007/s00159-013-0070-7

Borghese, A., Rea, N., Turolla, R., Pons, J. A., Esposito, P., Coti Zelati, F., et al. (2019). The multi-outburst activity of the magnetar in Westerlund I. *MNRAS* 484, 2931–2943. doi:10.1093/mnras/stz084

Bosch-Ramon, V., Paredes, J. M., Ribó, M., Miller, J. M., Reig, P., and Martí, J. (2005). Orbital X-ray variability of the microquasar LS 5039. *ApJ* 628, 388–394. doi:10.1086/429901

Brinkmann, W., Pratt, G. W., Rohr, S., Kawai, N., and Burwitz, V. (2007). XMM-Newton observations of the eastern jet of SS 433. *Astronomy Astrophysics* 463, 611–619. doi:10.1051/0004-6361:20065570

Bykov, A. M. (2001). Particle acceleration and nonthermal phenomena in superbubbles. *SSRv* 99, 317–326. doi:10.1023/A:1013817721725

Bykov, A. M. (2006). "High-energy radiation generated by winds and shocks: SNRs and superbubbles," in *Populations of high energy sources in galaxies*. Editors E. J. A. Meurs, and G. Fabbiano (USA: IEEE), 230, 111–119. doi:10.1017/S1743921306008039

Bykov, A. M. (2014). Nonthermal particles and photons in starburst regions and superbubbles. *AAPR* 22, 77. doi:10.1007/s00159-014-0077-8

Bykov, A. M., Uvarov, Y. A., Kalyashova, M. E., Badmaev, D. V., Lapshov, I. Y., Lutovinov, A. A., et al. (2023). X-ray emission from Westerlund 2 detected by SRG/ART-XC and Chandra: search for radiation of TeV leptons. *MNRAS* 525, 1553–1561. doi:10.1093/mnras/stad2356

Cao, Z., Aharonian, F., An, Q., AxikeguBai, L. X., Bai, Y. X., et al. (2021a). Discovery of a new gamma-ray source, LHAASO J0341+5258, with emission up to 200 TeV. *ApJL* 917, L4. doi:10.3847/2041-8213/ac0fd5

Cao, Z., Aharonian, F., An, Q., AxikeguBai, Y. X., Bao, Y. W., et al. (2023a). *The first LHAASO catalog of gamma-ray sources*.

Cao, Z., Aharonian, F. A., An, Q., Axikegu, L. X., BaiBai, Y. X., Bao, Y. W., et al. (2021b). Ultrahigh-energy photons up to 1.4 petaelectronvolts from 12 γ-ray Galactic sources. *Nature* 594, 33–36. doi:10.1038/s41586-021-03498-z

Celli, S., Aharonian, F., and Gabici, S. (2020). Spectral signatures of PeVatrons. *ApJ* 903, 61. doi:10.3847/1538-4357/abb805

Cherenkov Telescope Array Consortium, Acharya, B. S., Agudo, I., Al Samarai, I., Alfaro, R., Alfaro, J., et al. (2019). *Science with the Cherenkov telescope array*. doi:10.1142/10986

Chernyakova, M., Malyshev, D., Paizis, A., La Palombara, N., Balbo, M., Walter, R., et al. (2019). Overview of non-transient γ-ray binaries and prospects for the Cherenkov telescope array. *A&A* 631, A177. doi:10.1051/0004-6361/201936501

Chernyakova, M., Neronov, A., van Soelen, B., Callanan, P., O'Shaughnessy, L., Babyk, I., et al. (2015). Multi-wavelength observations of the binary system PSR B1259-63/LS 2883 around the 2014 periastron passage. *MNRAS* 454, 1358–1370. doi:10.1093/mnras/stv1988

Cholis, I., and Krommydas, I. (2022). Utilizing cosmic-ray positron and electron observations to probe the averaged properties of Milky Way pulsars. *PhRvD* 105, 023015. doi:10.1103/PhysRevD.105.023015

Clark, J. S., Negueruela, I., Crowther, P. A., and Goodwin, S. P. (2005). On the massive stellar population of the super star cluster <ASTROBJ>Westerlund 1</ASTROBJ&gt. *A&A* 434, 949–969. doi:10.1051/0004-6361:20042413

Clavel, M., Soldi, S., Terrier, R., Tatischeff, V., Maurin, G., Ponti, G., et al. (2014). Variation of the X-ray non-thermal emission in the Arches cloud. *MNRAS* 443, L129–L133. doi:10.1093/mnrasl/slu100

Coerver, A., Wilcox, P., Zhang, H., Dingus, B. L., Gotthelf, E. V., Hailey, C. J., et al. (2019). Multiwavelength investigation of pulsar wind nebula DA 495 with HAWC, VERITAS, and NuSTAR. *ApJ* 878, 126. doi:10.3847/1538-4357/ab21d0

Corbet, R. H. D., Chomiuk, L., Coe, M. J., Coley, J. B., Dubus, G., Edwards, P. G., et al. (2016). A luminous gamma-ray binary in the large magellanic cloud. *ApJ* 829, 105. doi:10.3847/0004-637X/829/2/105

Cristofari, P. (2021). The hunt for pevatrons: the case of supernova remnants. *Universe* 7, 324. doi:10.3390/universe7090324

Dauser, T., Falkner, S., Lorenz, M., Kirsch, C., Peille, P., Cucchetti, E., et al. (2019). SIXTE: a generic X-ray instrument simulation toolkit. *A&A* 630, A66. doi:10.1051/0004-6361/201935978

Drissen, L., Moffat, A. F. J., Walborn, N. R., and Shara, M. M. (1995). The dense galactic starburst NGC 3603. I. HST/FOS spectroscopy of individual stars in the core and the source of ionization and kinetic energy. *AJ* 110, 2235. doi:10.1086/117684

Dubner, G. M., Holdaway, M., Goss, W. M., and Mirabel, I. F. (1998). A high-resolution radio study of the W50-SS 433 system and the surrounding medium. *AJ* 116, 1842–1855. doi:10.1086/300537

Dubus, G. (2013). Gamma-ray binaries and related systems. *AAPR* 21, 64. doi:10.1007/s00159-013-0064-5

Dubus, G., Guillard, N., Petrucci, P.-O., and Martin, P. (2017). Sizing up the population of gamma-ray binaries. *A&A* 608, A59. doi:10.1051/0004-6361/201731084

Dubus, G., Lamberts, A., and Fromang, S. (2015). Modelling the high-energy emission from gamma-ray binaries using numerical relativistic hydrodynamics. *A&A* 581, A27. doi:10.1051/0004-6361/201425394

Eraerds, T., Antonelli, V., Davis, C., Hall, D., Hetherington, O., Holland, A., et al. (2021). Enhanced simulations on the athena/wide field imager instrumental background. *J. Astronomical Telesc. Instrum. Syst.* 7, 034001. doi:10.1117/1.JATIS.7.3.034001

Figer, D. F., McLean, I. S., and Morris, M. (1999). Massive stars in the quintuplet cluster. *ApJ* 514, 202–220. doi:10.1086/306931

Figer, D. F., Najarro, F., Gilmore, D., Morris, M., Kim, S. S., Serabyn, E., et al. (2002). Massive stars in the Arches cluster. *ApJ* 581, 258–275. doi:10.1086/344154

Gabici, S. (2023). *Star clusters as cosmic ray accelerators*.

Guépin, C., Cerutti, B., and Kotera, K. (2020). Proton acceleration in pulsar magnetospheres. *A&A* 635, A138. doi:10.1051/0004-6361/201936816

Hamaguchi, K., Corcoran, M. F., Pittard, J. M., Sharma, N., Takahashi, H., Russell, C. M. P., et al. (2018). Non-thermal X-rays from colliding wind shock acceleration in the massive binary Eta Carinae. *Nat. Astron.* 2, 731–736. doi:10.1038/s41550-018-0505-1

Harrison, F. A., Craig, W. W., Christensen, F. E., Hailey, C. J., Zhang, W. W., Boggs, S. E., et al. (2013). The nuclear spectroscopic telescope array (NuSTAR) high-energy X-ray mission. *ApJ* 770, 103. doi:10.1088/0004-637X/770/2/103

HAWC Collaboration, Abeysekara, A. U., Albert, A., and Alfaro, R. (2020). Multiple galactic sources with emission above 56 TeV detected by HAWC. *PhRvL* 124, 021102. doi:10.1103/PhysRevLett.124.021102

Heintz, E., and Zweibel, E. G. (2022). Galaxies at a cosmic ray eddington limit. *ApJ* 941, 78. doi:10.3847/1538-4357/ac9e9e

HESS Collaboration, Abramowski, A., Aharonian, F., and Benkhali, F. A. (2016). Acceleration of petaelectronvolt protons in the galactic centre. *Nature* 531, 476–479. doi:10.1038/nature17147

Hinton, J., and SWGO Collaboration (2022). The southern wide-field gamma-ray observatory: status and prospects. *37th Int. Cosm. Ray Conf.* 23. doi:10.22323/1.395.0023

IceCube Collaboration, Abbasi, R., Ackermann, M., Adams, J., Aguilar, J. A., Ahlers, M., et al. (2023). Observation of high-energy neutrinos from the galactic plane. *Science* 380, 1338–1343. doi:10.1126/science.adc9818

Inoue, Y., and Tanaka, Y. T. (2016). Baryon loading erriciency and particle acceleration erriciency of relativistic jets: cases for low luminosity bl lacs. *Astrophysical J.* 828, 13. doi:10.3847/0004-637X/828/1/13

Jansen, F., Lumb, D., Altieri, B., Clavel, J., Ehle, M., Erd, C., et al. (2001). XMM-Newton observatory. I. The spacecraft and operations. *A&A* 365, L1–L6. doi:10.1051/0004-6361:20000036

Johnston, S., Manchester, R. N., Lyne, A. G., Bailes, M., Kaspi, V. M., Qiao, G., et al. (1992). PSR 1259-63: a binary radio pulsar with a Be star companion. *ApJL* 387, L37. doi:10.1086/186300

Kantzas, D., Markoff, S., Lucchini, M., Ceccobello, C., Grinberg, V., Connors, R. M. T., et al. (2022). The prototype X-ray binary GX 339-4: using TeV γ-rays to assess LMXBs as Galactic cosmic ray accelerators. *MNRAS* 510, 5187–5198. doi:10.1093/mnras/stac004

Kargaltsev, O., Rangelov, B., and Pavlov, G. G. (2013). *Gamma-ray and X-ray properties of pulsar wind nebulae and unidentified galactic TeV sources*.

Kavanagh, P. J., Sasaki, M., Bozzetto, L. M., Filipović, M. D., Points, S. D., Maggi, P., et al. (2015). XMM-Newton study of 30 doradus C and a newly identified MCSNR j0536-6913 in the large magellanic cloud. *A&A* 573, A73. doi:10.1051/0004-6361/201424354

Kayama, K., Tanaka, T., Uchida, H., Tsuru, T. G., Sudoh, T., Inoue, Y., et al. (2022). Spatially resolved study of the SS 433/W 50 west region with Chandra: X-ray structure and spectral variation of non-thermal emission. *Publ. Astronomical Soc. Jpn.* 74, 1143–1156. doi:10.1093/pasj/psac060

Kefala, E., and Bosch-Ramon, V. (2023). Modeling the effects of clumpy winds in the high-energy light curves of γ-ray binaries. *A&A* 669, A21. doi:10.1051/0004-6361/202244531

Kelner, S. R., Aharonian, F. A., and Bugayov, V. V. (2006). Energy spectra of gamma rays, electrons, and neutrinos produced at proton-proton interactions in the very high energy regime. *PhRvD* 74, 034018. doi:10.1103/PhysRevD.74.034018

Kim, J., An, H., and Mori, K. (2022). Investigation of the broadband emission of the gamma-ray binary HESS J0632+057 using an intrabinary shock model. *ApJ* 936, 32. doi:10.3847/1538-4357/ac8663

Kimura, S. S., Murase, K., and Mészáros, P. (2020a). Deciphering the origin of the GeV–TeV gamma-ray emission from SS 433. *ApJ* 904, 188. doi:10.3847/1538-4357/abbe00

Kimura, S. S., Murase, K., and Mészáros, P. (2020b). Deciphering the origin of the GeV–TeV gamma-ray emission from SS 433. *Astrophysical J.* 904, 188. doi:10.3847/1538-4357/abbe00

Krivonos, R. A., Tomsick, J. A., Bauer, F. E., Baganoff, F. K., Barriere, N. M., Bodaghee, A., et al. (2014). First hard X-ray detection of the non-thermal emission around the Arches cluster: morphology and spectral studies with NuSTAR. *ApJ* 781, 107. doi:10.1088/0004-637X/781/2/107

Krivonos, R. A., Tsygankov, S. S., Mereminskiy, I. A., Lutovinov, A. A., Sazonov, S. Y., and Sunyaev, R. A. (2017). New hard X-ray sources discovered in the ongoing INTEGRAL Galactic plane survey after 14 yr of observations. *MNRAS* 470, 512–516. doi:10.1093/mnras/stx1276

Krumholz, M. R., McKee, C. F., and Bland-Hawthorn, J. (2019). Star clusters across cosmic time. *ARA&A* 57, 227–303. doi:10.1146/annurev-astro-091918-104430

Kuznetsova, E., Krivonos, R., Clavel, M., Lutovinov, A., Chernyshov, D., Hong, J., et al. (2019). Investigating the origin of the faint non-thermal emission of the Arches cluster using the 2015-2016 NuSTAR and XMM-Newton X-ray observations. *MNRAS* 484, 1627–1636. doi:10.1093/mnras/stz119

Lagage, P. O., and Cesarsky, C. J. (1983). The maximum energy of cosmic rays accelerated by supernova shocks. *A&A* 125, 249–257.

Law, C., and Yusef-Zadeh, F. (2004). X-ray observations of stellar clusters near the galactic center. *ApJ* 611, 858–870. doi:10.1086/422307

Lazendic, J. S., Slane, P. O., Gaensler, B. M., Reynolds, S. P., Plucinsky, P. P., and Hughes, J. P. (2004). A high-resolution study of nonthermal radio and X-ray emission from supernova remnant g347.3-0.5. *ApJ* 602, 271–285. doi:10.1086/380956

Lopez, L. A., Grefenstette, B. W., Auchettl, K., Madsen, K. K., and Castro, D. (2020). Evidence of particle acceleration in the superbubble 30 doradus C with NuSTAR. *ApJ* 893, 144. doi:10.3847/1538-4357/ab8232

López-Coto, R., de Oña Wilhelmi, E., Aharonian, F., Amato, E., and Hinton, J. (2022). *Gamma-ray halos around pulsars as the key to understanding cosmic ray transport in the Galaxy*.

Madsen, Kristin K., García, Javier A., Stern, D., Armini, R., Basso, S., Coutinho, D., et al. (2023). The high energy x-ray probe (HEX-P): instrument and mission profile. doi:10.48550/arXiv.2312.04678

Malyshev, D., Chernyakova, M., Santangelo, A., and Pühlhofer, G. (2019). Decade-long X-ray observations of HESS J0632+057. *Astron. Nachrichten* 340, 465–474. doi:10.1002/asna.201913605

Marcote, B., Ribó, M., Paredes, J. M., and Ishwara-Chandra, C. H. (2015). Physical properties of the gamma-ray binary LS 5039 through low- and high-frequency radio observations. *MNRAS* 451, 59–73. doi:10.1093/mnras/stv940

Meidinger, N., Albrecht, S., Beitler, C., Bonholzer, M., Emberger, V., Frank, J., et al. (2020). "Development status of the wide field imager instrument for athena," in *Space telescopes and instrumentation 2020: ultraviolet to gamma ray*. Editors J.-W. A. den Herder, K. Nakazawa, and S. Nikzad (USA: IEEE). doi:10.1117/12.2560507

Moldowan, A., Safi-Harb, S., Fuchs, Y., and Dubner, G. (2005). A multi-wavelength study of the western lobe of W50 powered by the galactic microquasar SS 433. *Adv. Space Res.* 35, 1062–1065. doi:10.1016/j.asr.2005.01.086

Mori, K., An, H., Burgess, D., Capasso, M., Dingus, B., Gelfand, J., et al. (2021). *NuSTAR broad-band X-ray observational campaign of energetic pulsar wind nebulae in synergy with VERITAS, HAWC and Fermi gamma-ray telescopes*.

Morlino, G., Blasi, P., Peretti, E., and Cristofari, P. (2021). Particle acceleration in winds of star clusters. *MNRAS* 504, 6096–6105. doi:10.1093/mnras/stab690

Mossoux, E., Pittard, J. M., Rauw, G., and Nazé, Y. (2020). Search for non-thermal X-ray emission in the colliding wind binary Cygnus OB2 #8A. *A&A* 636, A109. doi:10.1051/0004-6361/201936735

Nakamura, R., Bamba, A., Dotani, T., Ishida, M., Yamazaki, R., and Kohri, K. (2012). Evolution of synchrotron X-rays in supernova remnants. *ApJ* 746, 134. doi:10.1088/0004-637X/746/2/134

Nandra, K., Barret, D., Barcons, X., Fabian, A., den Herder, J.-W., Piro, L., et al. (2013). *The hot and energetic Universe: a white paper presenting the science theme motivating the Athena+ mission*.

Ohmura, T., Ono, K., Sakemi, H., Tashima, Y., Omae, R., and Machida, M. (2021). Continuous jets and backflow models for the Formation of W50/SS 433 in magnetohydrodynamics simulations. *Astrophysical J.* 910, 149. doi:10.3847/1538-4357/abe5a1

Pfalzner, S. (2009). Universality of young cluster sequences. *A&A* 498, L37–L40. doi:10.1051/0004-6361/200912056

Pittard, J. M., Vila, G. S., and Romero, G. E. (2020). Colliding-wind binary systems: diffusive shock acceleration and non-thermal emission. *MNRAS* 495, 2205–2221. doi:10.1093/mnras/staa1099

Reynolds, S., An, H., Abdelmaguid, M., Alford, J., Fryer, C., Mori, K., et al. (2023). High-energy astrophysics research enabled by the probe-class mission concept HEX-P. *Front. Astron. Space Sci.* 10. doi:10.3389/fspas.2023.1321278

Safi-Harb, S., Mac Intyre, B., Zhang, S., Pope, I., Zhang, S., Saffold, N., et al. (2022a). *Hard X-ray emission from the eastern jet of SS 433 powering the W50 "Manatee" nebula: evidence for particle re-acceleration*

Safi-Harb, S., Mac Intyre, B., Zhang, S., Pope, I., Zhang, S., Saffold, N., et al. (2022b). Hard X-ray emission from the eastern jet of SS 433 powering the W50 "manatee" nebula: evidence for particle reacceleration. *ApJ* 935, 163. doi:10.3847/1538-4357/ac7c05

Safi-Harb, S., and Ögelman, H. (1997). ROSAT and ASCA observations of W50 associated with the peculiar source SS 433. *Astrophysical J.* 483, 868. doi:10.1086/304274

Safi-Harb, S., and Petre, R. (1999). Rossi X-ray timing explorer observations of the eastern lobe of W50 associated with SS 433. *Astrophysical J.* 512, 784. doi:10.1086/306803

Sakemi, H., Omae, R., Ohmura, T., and Machida, M. (2021). Energy estimation of high-energy particles associated with the SS 433/W 50 system through radio observation at 1.4 GHz. *Publ. Astronomical Soc. Jpn.* 73, 530–544. doi:10.1093/pasj/psab018

S. S. Collaboration, Abramowski, A., Aharonian, F., Ait Benkhali, F., Akhperjanian, A. G., Angüner, E. O., et al. (2015). The exceptionally powerful TeV γ-ray emitters in the Large Magellanic Cloud. *Science* 347, 406–412. doi:10.1126/science.1261313

S. S. Collaboration, Abdalla, H., Adam, R., Aharonian, F., Ait Benkhali, F., Angüner, E. O., et al. (2020). An extreme particle accelerator in the Galactic plane: HESS J1826-130. *A&A* 644, A112. doi:10.1051/0004-6361/202038851

Sudoh, T., Inoue, Y., and Khangulyan, D. (2020). Multiwavelength emission from galactic jets: the case of the microquasar SS433. *ApJ* 889, 146. doi:10.3847/1538-4357/ab6442

Takahashi, T., Kishishita, T., Uchiyama, Y., Tanaka, T., Yamaoka, K., Khangulyan, D., et al. (2009). Study of the spectral and temporal characteristics of X-ray emission of the gamma-ray binary LS 5039 with Suzaku. *ApJ* 697, 592–600. doi:10.1088/0004-637X/697/1/592

Tatischeff, V., Decourchelle, A., and Maurin, G. (2012). Nonthermal X-rays from low-energy cosmic rays: application to the 6.4 keV line emission from the Arches cluster region. *A&A* 546, A88. doi:10.1051/0004-6361/201219016

Tokayer, Y. M., An, H., Halpern, J. P., Kim, J., Mori, K., and Hailey, C. J. e. a. (2021). Multiwavelength observation campaign of the TeV gamma-ray binary HESS J0632 + 057 with NuSTAR, VERITAS, MDM, and Swift. *ApJ* 923, 17. doi:10.3847/1538-4357/ac2c6a

Tsuji, N., Uchiyama, Y., Khangulyan, D., and Aharonian, F. (2021). Systematic study of acceleration efficiency in young supernova remnants with nonthermal X-ray observations. *Astrophysical J.* 907, 117. doi:10.3847/1538-4357/abce65

Vieu, T., Gabici, S., Tatischeff, V., and Ravikularaman, S. (2022). Cosmic ray production in superbubbles. *MNRAS* 512, 1275–1293. doi:10.1093/mnras/stac543

Volkov, I., Kargaltsev, O., Younes, G., Hare, J., and Pavlov, G. (2021). NuSTAR observation of LS 5039. *ApJ* 915, 61. doi:10.3847/1538-4357/abfe0e

Wang, Q. D., Lu, F. J., and Gotthelf, E. V. (2006). G359.95-0.04: an energetic pulsar candidate near Sgr A. *Mon. Notices R. Astronomical Soc.* 367, 937–944. doi:10.1111/j.1365-2966.2006.09998.x

Weng, S.-S., Qian, L., Wang, B.-J., Torres, D. F., Papitto, A., Jiang, P., et al. (2022). Radio pulsations from a neutron star within the gamma-ray binary LS I +61° 303. *Nat. Astron.* doi:10.1038/s41550-022-01630-1

Whitmore, B. C. (2000). *The Formation of star clusters*.

Yamaguchi, H., Sawada, M., and Bamba, A. (2010). Searching for diffuse nonthermal X-rays from the superbubbles N11 and N51D in the large magellanic cloud. *ApJ* 715, 412–420. doi:10.1088/0004-637X/715/1/412

Yamamoto, H., Okamoto, R., Murata, Y., Nakanishi, H., Imai, H., and Kurahara, K. (2022). Physical properties of the molecular cloud, N4, in SS433; Evidence for an interaction of molecular cloud with the jet from SS433

Yang, R.-z., Aharonian, F., and de Oña Wilhelmi, E. (2019). Massive star clusters as the an alternative source population of galactic cosmic rays. *Rendiconti Lincei. Sci. Fis. Nat.* 30, 159–164. doi:10.1007/s12210-019-00819-3

Yoneda, H., Makishima, K., Enoto, T., Khangulyan, D., Matsumoto, T., and Takahashi, T. (2020). Sign of hard-X-ray pulsation from the γ -ray binary system LS 5039. *PhRvL* 125, 111103. doi:10.1103/PhysRevLett.125.111103

Zabalza, V. (2015). naima: a python package for inference of relativistic particle energy distributions from observed nonthermal spectra. *Proc. Int. Cosmic Ray Conf.* 2015, 922. doi:10.22323/1.236.0922

Zeidler, P., Sabbi, E., Nota, A., Grebel, E. K., Tosi, M., Bonanos, A. Z., et al. (2015). A high-resolution multiband survey of Westerlund 2 with the hubble space telescope. I. Is the massive star cluster double? *AJ* 150, 78. doi:10.1088/0004-6256/150/3/78

frontiers | Frontiers in Astronomy and Space Sciences

TYPE Original Research
PUBLISHED 22 December 2023
DOI 10.3389/fspas.2023.1321278

Check for updates

OPEN ACCESS

EDITED BY
Gabriele Ponti,
Brera Astronomical Observatory, Italy

REVIEWED BY
Filiberto Hueyotl-Zahuantitla,
Cátedra CONACYT-UNACH, Mexico
Carlos Frajuca,
Federal University of Rio Grande, Brazil

*CORRESPONDENCE
Kaya Mori,
kaya@astro.columbia.edu

RECEIVED 13 October 2023
ACCEPTED 20 November 2023
PUBLISHED 22 December 2023

CITATION
Reynolds S, An H, Abdelmaguid M, Alford J, Fryer C, Mori K, Nynka M, Park J, Terada Y, Woo J, Bamba A, Bangale P, Diesing R, Eagle J, Gabici S, Gelfand J, Grefenstette B, Garcia J, Kim C, Kumar S, Intyre BM, Madsen K, Manconi S, Motogami Y, Ohsumi H, Olmi B, Sato T, Shang R-Y, Stern D, Tsuji N, Younes G and Zoglauer A (2023), The High Energy X-ray Probe (HEX-P): supernova remnants, pulsar wind nebulae, and nuclear astrophysics.
Front. Astron. Space Sci. 10:1321278.
doi: 10.3389/fspas.2023.1321278

COPYRIGHT
© 2023 Reynolds, An, Abdelmaguid, Alford, Fryer, Mori, Nynka, Park, Terada, Woo, Bamba, Bangale, Diesing, Eagle, Gabici, Gelfand, Grefenstette, Garcia, Kim, Kumar, Intyre, Madsen, Manconi, Motogami, Ohsumi, Olmi, Sato, Shang, Stern, Tsuji, Younes and Zoglauer. This is an open-access article distributed under the terms of the Creative Commons Attribution License (CC BY). The use, distribution or reproduction in other forums is permitted, provided the original author(s) and the copyright owner(s) are credited and that the original publication in this journal is cited, in accordance with accepted academic practice. No use, distribution or reproduction is permitted which does not comply with these terms.

The High Energy X-ray Probe (HEX-P): supernova remnants, pulsar wind nebulae, and nuclear astrophysics

Stephen Reynolds[1], Hongjun An[2], Moaz Abdelmaguid[3], Jason Alford[3], Chris Fryer[4], Kaya Mori[5]*, Melania Nynka[6], Jaegeun Park[2], Yukikatsu Terada[7,8], Jooyun Woo[5], Aya Bamba[9,10,11], Priyadarshini Bangale[12], Rebecca Diesing[13], Jordan Eagle[14], Stefano Gabici[15], Joseph Gelfand[3], Brian Grefenstette[16], Javier Garcia[14], Chanho Kim[2], Sajan Kumar[17], Brydyn Mac Intyre[18], Kristin Madsen[14], Silvia Manconi[19], Yugo Motogami[7], Hayato Ohsumi[7], Barbara Olmi[20,21], Toshiki Sato[22], Ruo-Yu Shang[23], Daniel Stern[24], Naomi Tsuji[25], George Younes[14] and Andreas Zoglauer[26]

[1]Department of Physics, North Carolina State University, Raleigh, NC, United States, [2]Department of Astronomy and Space Science, Chungbuk National University, Cheongju, Republic of Korea, [3]Department of Physics, New York University, Abu Dhabi, United Arab Emirates, [4]Center for Non Linear Studies, Los Alamos National Laboratory, Los Alamos, NM, United States, [5]Columbia Astrophysics Laboratory, Columbia University, New York, NY, United States, [6]Kavli Institute for Astrophysics and Space Research, Massachusetts Institute of Technology, Cambridge, MA, United States, [7]Graduate School of Science and Engineering, Saitama University, Sakura, Saitama, Japan, [8]Japan Aerospace Exploration Agency (JAXA), Institute of Space and Astronautical Science, Sagamihara, Japan, [9]Department of Physics, The University of Tokyo, Tokyo, Japan, [10]Research Center for the Early Universe, School of Science, The University of Tokyo, Tokyo, Japan, [11]Trans-Scale Quantum Science Institute, The University of Tokyo, Tokyo, Japan, [12]Department of Physics and Astronomy, Bartol Research Institute, University of Delaware, Newark, DE, United States, [13]Department of Astronomy and Astrophysics, The University of Chicago, Chicago, IL, United States, [14]NASA Goddard Space Flight Center, Greenbelt, MD, United States, [15]Universite Paris Cite, Centre National de la Recherche Scientifique, Astroparticule et Cosmologie, Paris, France, [16]Space Radiation Laboratory, California Institute of Technology, Pasadena, CA, United States, [17]Department of Physics, University of Maryland, College Park, MD, United States, [18]Department of Physics and Astronomy, University of Manitoba, Winnipeg, MB, Canada, [19]Laboratoire d'Annecy-le-Vieux de Physique Theorique, Centre National de la Recherche Scientifique, Université Savoie Mont Blanc, Annecy, France, [20]INAF—Osservatorio Astrofisico di Arcetri, Firenze, Italy, [21]INAF—Osservatorio Astronomico di Palermo, Palermo, Italy, [22]Department of Physics, School of Science and Technology, Meiji University, Kanagawa, Japan, [23]Department of Physics and Astronomy, Barnard College, New York, NY, United States, [24]Jet Propulsion Laboratory, California Institute of Technology, Pasadena, CA, United States, [25]Faculty of Science, Kanagawa University, Kanagawa, Japan, [26]Space Sciences Laboratory, University of California, Berkeley, Brkeley, CA, United States

HEX-P is a probe-class mission concept that will combine high spatial resolution X-ray imaging (<10″ full width at half maximum) and broad spectral coverage (0.2–80 keV) with an effective area far superior to current facilities (including *XMM*-Newton and *NuSTAR*) to enable revolutionary new insights into a variety of important astrophysical problems. HEX-P is ideally suited to address important problems in the physics and astrophysics of supernova remnants (SNRs) and pulsar wind nebulae (PWNe). For shell SNRs, HEX-P can greatly improve our understanding via more accurate spectral characterization and localization of non-thermal X-ray emission from both

non-thermal-dominated SNRs and those containing both thermal and non-thermal components, and can discover previously unknown non-thermal components in SNRs. Multi-epoch HEX-P observations of several young SNRs (e.g., Cas A and Tycho) are expected to detect year-scale variabilities of X-ray filaments and knots, thus enabling us to determine fundamental parameters related to diffusive shock acceleration, such as local magnetic field strengths and maximum electron energies. For PWNe, HEX-P will provide spatially-resolved, broadband X-ray spectral data separately from their pulsar emission, allowing us to study how particle acceleration, cooling, and propagation operate in different evolution stages of PWNe. HEX-P is also poised to make unique and significant contributions to nuclear astrophysics of Galactic radioactive sources by improving detections of, or limits on, ^{44}Ti in the youngest SNRs and by potentially discovering rare nuclear lines as evidence of double neutron star mergers. Throughout the paper, we present simulations of each class of objects, demonstrating the power of both the imaging and spectral capabilities of HEX-P to advance our knowledge of SNRs, PWNe, and nuclear astrophysics.

KEYWORDS

supernova remnants, pulsar wind nebulae, nuclear astrophysics, X-ray astrophysics, future missions frontiers

1 Introduction

In the Galactic ecosystem, fast particles play a crucial role in ionization of molecular material (influencing star and planet formation), in regulating the interstellar magnetic field, and perhaps in driving a Galactic wind. We observe a highly filtered subset of those particles as cosmic rays at Earth, but their origins lie in a range of high-energy-density Galactic environments. Strong shock waves from supernova remnants (SNRs) remain the prime candidate for accelerating the bulk of Galactic cosmic-ray electrons and ions up to energies of the order of PeV, through the diffusive shock acceleration (DSA) mechanism. An additional leptonic component (electrons and positrons) is thought to originate in pulsar wind nebulae (PWNe), probably at the termination shock of the initially relativistic cold outflow. These classes of object exhibit the physics of particle acceleration in particularly accessible ways, through spatially resolved nonthermal emission in radio, X-ray, and gamma-ray bands. That emission is due to some combination of four important processes, three involving leptons and one due to hadrons. The leptonic processes, described in more detail in Mori et al. (2021), are synchrotron radiation producing radio through hard X-ray emission, inverse-Compton upscattering of ambient photon fields producing GeV to TeV gamma rays, and nonthermal bremsstrahlung producing hard X-rays through gamma rays. Of these, the latter is rarely dominant. The hadronic process begins with inelastic collisions of energetic ions with ambient thermal gas, producing charged and neutral pions (once the kinematic threshold of about 140 MeV is surpassed). The charged pions decay, ultimately, to secondary electrons and positrons which can produce synchrotron radiation, in an inescapable consequence of the hadronic process. The neutral pions decay to gamma rays, which can range in energy up to ten percent or so of that of the initiating hadron. One of the fundamental questions in interpreting potential Galactic cosmic-ray sources involves deciding which process is responsible for their gamma-ray emission.

This paper demonstrates the potential contributions to understanding these issues that can be provided by a high resolution, high sensitivity hard X-ray imaging capability. In addition to access to the continuum processes described above, the hard X-ray spectral region offers a window into some of the most energetic stellar-scale processes in Nature: along with supernovae and SNRs, the kilonovae resulting from merging binary neutron stars. In both these arenas, nucleosynthesis is important and can be diagnosed through the production of unstable species with a range of half-lives which decay with the production of different hard X-ray lines. Of particular relevance for SNe and young SNRs are the 68 and 78 keV lines produced in the decay of ^{44}Ti, but merging neutron stars are also expected to produce potentially observable lines for a sufficiently nearby event. Information from such decays gives insight into nucleosynthesis unavailable in any other channel.

The HEX-P instrument can bring to the study of these issues unmatched sensitivity and angular resolution above 10 keV. Below, we lay out the contributions HEX-P can make to characterizing the nature and evolution of SNRs and PWNe. §2 describes the current telescope design and HEX-P simulation tools. §3 demonstrates HEX-P's spectro-imaging capabilities for characterizing thermal and non-thermal X-ray emission from young SNRs by showing simulation results for Cas A, Tycho, G1.9 + 0.3, and SN 1987A. §4 presents HEX-P's observation program of investigating different evolutionary stages of PWNe and exploring this primary class of leptonic particle accelerators in our Galaxy. HEX-P's broad-band X-ray data, in conjunction with the upcoming Cherenkov Telescope Array (CTA) mission, will allow us to dissect the particle acceleration, propagation, and cooling processes in PWNe. §5 discusses HEX-P's unique role in nuclear astrophysics, such as detecting ^{44}Ti lines from the youngest SNRs and nuclear lines from double neutron star mergers in our Galaxy. In our

companion paper (Mori et al., submitted to FrASS), we will discuss other types of Galactic particle accelerators such as unidentified PeVatron candidates, star clusters, superbubbles, microquasar jets, TeV gamma-ray binaries and the supermassive black hole in Sgr A*. The science we describe here has considerable overlap with that discussed in parallel HEX-P papers. Our planned studies of PWNe will of course also produce important new information on the pulsars they contain (see Jaodand et al., submitted to FrASS), with possible bearing on magnetars (Alford et al., submitted to FrASS) and general properties of neutron stars (Ludlum et al., submitted to FrASS) as well. Various classes of binary X-ray source are also described in Connors et al. (submitted to FrASS). Several of our target sources may be observed as part of the Galactic Center effort (Mori et al., submitted to FrAss), while others lie in nearby galaxies (Lehmer et al., submitted to FrASS). SN 1987A is on our list of primary targets, and we describe here some of the nuclear astrophysics possible with SNe or neutron-star mergers, more likely to be found among nearby galaxies than in our own.

2 HEX-P mission design and simulation

The High-Energy X-ray Probe (Madsen et al., 2023) is a probe-class mission concept that offers sensitive broad-band coverage (0.2–80 keV) of the X-ray spectrum with exceptional spectral, timing, and angular capabilities. It features two high-energy telescopes (HET) that focus hard X-rays, and a low-energy telescope (LET) providing soft X-ray coverage.

The LET consists of a segmented mirror assembly coated with Ir on monocrystalline silicon that achieves a half power diameter of 3.5″, and a low-energy DEPFET detector, of the same type as the Wide Field Imager (WFI; Meidinger et al., 2020) onboard Athena (Nandra et al., 2013). It has 512 × 512 pixels that cover a field of view of $11.3' \times 11.3'$. It has an effective bandpass of 0.2–25 keV and a full-frame readout time of 2 ms, and can be operated in 128 and 64 channel window modes for higher count-rates to mitigate pile-up and allow faster readout. Pile-up effects remain below an acceptable limit of ~1% for sources up to ~100 mCrab in the smallest window configuration (64w). Excising the core of the point-spread function (PSF), a common practice in X-ray astronomy, will allow for observations of brighter sources, with a maximum loss of ~60% of the total photon counts.

The HET consists of two co-aligned telescopes and detector modules. The optics are made of Ni-electroformed full shell mirror substrates, leveraging the heritage of *XMM* (Jansen et al., 2001), and coated with Pt/C and W/Si multilayers for an effective bandpass of 2–80 keV. The high-energy detectors are of the same type as those flown on *NuSTAR* (Harrison et al., 2013), and they consist of 16 CZT sensors per focal plane, tiled 4×4, for a total of 128×128 pixels spanning a field of view slightly larger than for the LET, of $13.4' \times 13.4'$.

All the simulations presented here were produced with a set of response files that represent the observatory performance based on current best estimates (Madsen et al., 2023). The effective area is derived from a ray-trace of the mirror design including obscuration by all known structures. The detector responses are based on simulations performed by the respective hardware groups, with an optical blocking filter for the LET and a Be window and thermal insulation for the HET. The LET background was derived from a GEANT4 simulation (Eraerds et al., 2021) of the WFI instrument, and the one for the HET from a GEANT4 simulation of the *NuSTAR* instrument, both positioned at L1. Throughout the paper, we present our simulation results for *HEX-P* using the SIXTE (Dauser et al., 2019) and XSPEC toolkits (Arnaud, 1996). To ensure the most realistic simulation results, we incorporated recent high-resolution X-ray images (mostly from *Chandra* or other wavelength observations), the best-known spectral information, and theoretical model predictions. Various exposure times have been considered for the feasibility studies presented in the following sections.

3 Supernova remnants

The best understood of all sources of high-energy particles are probably the shell SNRs, where independent measures of the ambient densities, shock speeds, and magnetic-field strengths are all possible. However, the evidence for those high-energy particles is primarily synchrotron X-ray emission, unambiguously separable from thermal emission only at energies above 10 keV or so. *NuSTAR* showed the promise of studying particle acceleration in SNRs with a few observations of young bright SNRs with strong nonthermal emission relative to thermal, but those observations raised more questions than they answered. HEX-P will be able to identify and characterize hard nonthermal X-ray emission in many more remnants, and will be able to address many of the questions raised by earlier observations. Older SNRs with somewhat slower shock velocities, predicted by theory to accelerate electrons to X-ray-emitting energies but too faint for prior study, can be examined by HEX-P, along with potential new sources turned up by upcoming surveys such as that performed by eROSITA, and newly occurring transients that may appear. Below we illustrate the capabilities of HEX-P with simulations of Cas A, Tycho, G1.9 + 0.3 (youngest Galactic SNR), and SN 1987A.

3.1 Thermal emission

Supernova remnants in X-rays are chiefly thermal sources, with temperatures from a few tenths to a few keV, and rich line spectra providing essential information on plasma composition, and given sufficient energy resolution, on radial velocities and ionization state. See Vink (2012) for a review. Most young remnants (estimated ages less than a few thousand years) also show spatial and spectral evidence for nonthermal X-rays, often in the form of thin rims at the remnant periphery, and in hard continuum components sometimes apparent in relatively line-free regions of the spectrum between 4 and 6 keV. Some of the continuum emission in this spectral region is certainly thermal bremsstrahlung, and interpreting the Fe Kα line complex at 6.4–6.7 keV requires knowing the thermal fraction. The nonthermal component can be followed to higher energies. Non-imaging instruments before *Chandra* and *XMM* found hard continua in the integrated spectra of a few remnants, the most spectacular being Cas A, with emission extending to at least 100 keV (Vink et al., 2000). But few remnants are bright enough to be studied in this way. *NuSTAR* was able to detect non-thermal continua in a

few young remnants, to 20 keV or (in a few cases) 30 keV. But in others, where small features in Chandra images are found to be line-free, the integrated emission at energies above 10 keV is not strong enough to be examined with *NuSTAR*.

The ability to identify thermal and nonthermal emission components in SNRs below about 10 keV would provide a powerful tool for diagnosing the detailed relation between particle acceleration and the properties of the thermal plasma. HEX-P's two instruments will provide such a tool. One simple but critical distinction would be to differentiate shocked ejecta from shocked surrounding material (undisturbed interstellar medium [ISM], for remnants of SNe Ia, or modified stellar wind or circumstellar material for remnants of core-collapse SNe), requiring good spatial and spectral resolution in the line-rich region from 0.5 to 4 keV, as well as at the crucial Fe Kα line. While it is possible to piece together some of this information by combining *Chandra* or *XMM* observations with, say, *NuSTAR* data, the task is complex in practice. Having two instruments aboard the same spacecraft will significantly improve our ability to cross-calibrate and will result in unbroken spectra from as low energies as interstellar absorption typically permits ($\gtrsim 0.2$ keV) up to 80 keV if such photons are present. SNR plasmas are generally multitemperature, and while they can sometimes be fairly well represented by two components, a higher-temperature component is easy to confuse with nonthermal emission, with important effects on interpreting, say, the equivalent width of the Fe Kα line complex. In fact, the LET instrument alone, coupled with HEX-P's large effective area, will improve the purely thermal diagnosis of many SNRs. Particle backgrounds constitute significant impediments above 8 or 9 keV for both *Chandra* and *XMM*, but can be expected to be significantly lower at the L1 position of HEX-P.

3.2 Nonthermal continuum

The presence in most young SNRs of strong thermal X-ray emission is both a bug and a feature: below 10 keV, the fraction of nonthermal emission is often quite uncertain, but as described above, thermal emission provides essential information on densities and shock speeds, and composition. Observing those objects at X-ray energies above 10 keV where the thermal contribution is small or negligible then allows the separate characterization of the nonthermal-electron energy spectrum. Basic questions afflict our understanding of electron acceleration to high energies in young SNRs. Where, exactly, does the acceleration take place? What are the physical conditions there, as indicated by observations at other wavelengths? What are the spectral shapes? To how high photon energies does emission extend, and are there spatial variations in spectral shape? The current fleet of X-ray observatories has produced important information on some of these questions, but the acceleration to the highest energies remains mysterious. Only *NuSTAR* has been able to image SNRs well above thermal energies, and spatial resolution, effective area, and background limitations have confined those studies to a few objects. But what has been learned is alarming: especially in Cas A, both spectral and spatial expectations for the highest-energy synchrotron emission were impressively upended. Neither the forward nor the reverse shock seems to be the site of the strongest emission between 15 and 50 keV. The spectra, while steeper than radio, show no indication of further curvature, indicating that the highest-energy electrons have not yet been observed. Observations of the handful of other young SNRs bright enough above 10 keV for *NuSTAR* hint at similar deficiencies.

But this problem is an opportunity. The study of particle acceleration in shocks has seemed to be an essentially solved problem, with the only remaining tasks to measure the parameters of the standard models. But those standard models are clearly incomplete, in the face of the *NuSTAR* data. More detailed observations above 10 keV of not only the historical remnants but other young objects less well-known, stand to produce qualitatively new information most relevant to basic questions of efficiency and maximum energies attainable (e.g., Diesing and Caprioli (2021)) that may apply to acceleration sites elsewhere in the Universe.

3.3 Cassiopeia A

Cassiopeia A (Cas A) is the youngest remnant of a core-collapse supernova event in our Galaxy. Light-echo observations of the scattered optical emission from the supernova event (Krause et al., 2008a) have established the supernova subtype as IIb—the explosion of a massive star that lost most of its hydrogen envelope, and has expanded into the pre-SN stellar wind. Its radio emission is dramatically stronger than that from any other Galactic SNR, perhaps partly due to the blast wave having encountered dense stellar wind at earlier times. The strongest radio emission from electrons with GeV energies is found not at the outer blast wave but at a bright inner ring between the forward and reverse shocks, where strong magnetic turbulence is likely to be present, boosting synchrotron emissivity because of a stronger magnetic field but also perhaps further accelerating nonthermal particles. These properties distinguish Cas A from young remnants of Type Ia supernovae such as Tycho and Kepler, which expand into inhomogeneous, but probably not radially varying, interstellar medium, and whose radio emission tends to be concentrated at the forward shock.

While the bright radio ring in Cas A indicates a large population of GeV-energy electrons, it was expected that the highest-energy X-ray-emitting particles would be found at the primary acceleration sites in the remnant, probably the forward blast wave. Evidence for particle acceleration at reverse shocks in young SNRs is ambiguous at best. The *NuSTAR* observations (Grefenstette et al., 2015), however, told a different story, showing diffuse hard X-ray (> 15 keV) emission from the remnant interior, with the brightest emission from two compact knots inside the blast wave to the west. Hard emission is present and associated with the outer blast wave, but it is considerably fainter. There are approximate correspondences between the bright knots and features in radio or soft X-rays (Bleeker et al., 2001; Helder and Vink, 2008; Maeda et al., 2009), where they are much less prominent. The angular resolution and sensitivity of *NuSTAR* were insufficient to allow a detailed search for corresponding small-scale features at optical wavelengths, where proper motions and/or radial velocities might give clues as to the nature of these hotspots of electron acceleration.

HEX-P, with improved angular resolution and sensitivity, will allow for resolving faint features such as shown in Figure 1. Non-thermal spectra will be mapped at the forward shock, reverse shock, and interior of the remnant. This spatially resolved

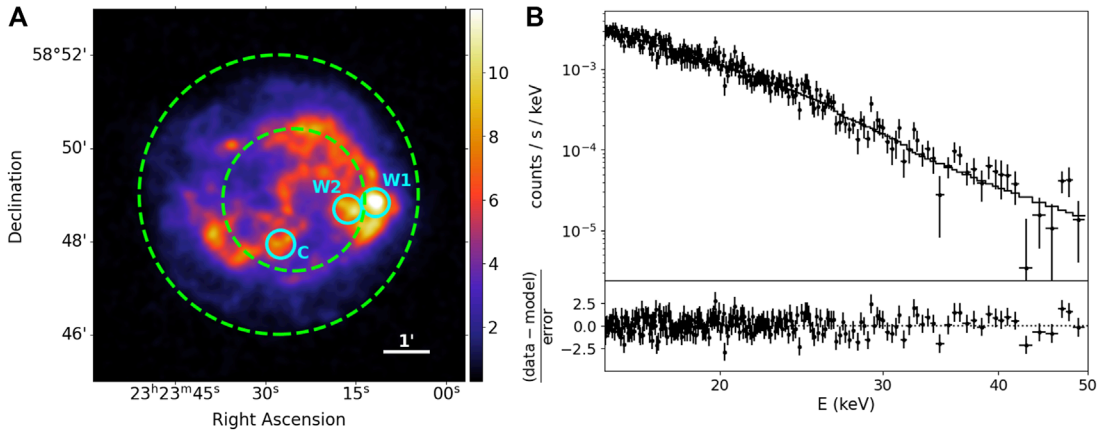

FIGURE 1
(A) Simulated HEX-P image of Cas A (15–50 keV) for a 200 ks exposure. The green dotted lines mark the forward (outer ring) and reverse (inner ring) shock, respectively. The cyan circles (C, W1, W2) are the brightest hard X-ray knots detected by *NuSTAR* (Grefenstette et al., 2015). **(B)** Simulated HEX-P spectrum of Cas A (W1 region in the left figure, $r = 18''$) for 200 ks exposure. We input a power-law model with the best-fit parameters determined by archival *NuSTAR* data ($\Gamma = 3.32$). Fits to the simulated spectrum recovered the input value of the photon index with 2% precision ($\Gamma = 3.38 \pm 0.06$).

spectroscopy will provide the best opportunity to study the variability on timescales of a few years of non-thermal emission at the hard X-ray knots suggested by Sato et al. (2018) and Uchiyama and Aharonian (2008). Such flux variability requires enhanced magnetic fields (0.1–1 mG) perhaps at "inward shocks" induced by a density gradient due to molecular clouds (Fraschetti et al., 2018) or asymmetric circumstellar material (Orlando et al. (2022) and references therein). While Sato et al. (2018) left open the possibility of variable thermal emission ($kT \sim 1$–3 keV) from *Chandra* observations, the high-energy sensitivity of HEX-P HET will minimize the complication with thermal emission and probe clean non-thermal continuum with photon index $\Gamma = 3$–3.5 above 15 keV as seen by *NuSTAR*. Independent estimates of the magnetic field (such as those based on "thin rim" morphology; Parizot et al., 2006) are also of order 0.2 mG, giving synchrotron cooling timescales of 1–10 years. Our simulation shows that a 200-ks observation with HEX-P can measure the flux of the hard X-ray knots ($r = 18''$ circles) at 2% precision. At this level of angular resolution and precision of flux measurement, the magnetic field can be accurately measured not only at the inward shock but also at other smaller hard X-ray knots throughout the entire remnant. Such a study will reveal the magnetic field structure of the remnant at the location of the highest-energy electrons, in synergy with the polarization measurement by IXPE (Vink et al., 2022). The connection between such observations and the highly detailed radio polarimetric studies, which reflect the much larger regions populated by GeV-energy electrons, can help in following the evolution of nonthermal particles beyond their acceleration sites and in filling out our general picture of the production and evolution of relativistic particles in a supernova remnant.

3.4 Tycho

SNR G120.1 + 1.4, famously known as Tycho, belongs to a class referred to as "Historical Supernovae" due to its association with the supernova explosion SN 1572. Its classification as the remnant of a normal Type Ia supernova was confirmed with light echos (Krause et al., 2008b). Tycho was one of the first Galactic radio sources identified ("Cassiopeia B"), shown to be separate from the much brighter nearby Cassiopeia A by Hanbury Brown and Hazard (1952), and was only the second radio source, after the Crab, to be identified with a known supernova. That radio synchrotron emission demonstrates the presence of electrons accelerated to GeV energies. Non-thermal X-ray emission was detected up to 25 keV with HEAO-1 (Pravdo and Smith, 1979), indicating for the first time the presence of electrons with TeV energies in Tycho. Following this detection, *Chandra* observations located most non-thermal emission in narrow filaments around Tycho's rim (Hwang et al., 2002; Bamba et al., 2005; Warren et al., 2005). Following that, several non-thermal "stripes" inside Tycho were revealed by follow-up deeper *Chandra* observations (Eriksen et al., 2011). The spacing of these stripes was argued to be of the order of the gyroradius of the highest-energy protons present, giving (for a magnetic field of order 30 μG) proton energies above 10^{15} eV, near the "knee" of the cosmic-ray spectrum around 3 PeV. Subsequent variability studies (Okuno et al., 2020) gave an even higher estimate of ~100 μG, but the relation to the maximum proton energy relies on several untested assumptions.

Lopez et al. (2015) used *NuSTAR* to perform a spatially resolved spectroscopic analysis of the synchrotron emission and radioactive ^{44}Ti in Tycho's SNR using a deep (~750 ks) *NuSTAR* observation. The hard (>10 keV) X-rays were found to be concentrated in the southwest of the remnant, where the earlier *Chandra* observation had found the high emissivity "stripes". No evidence was found for ^{44}Ti, and only upper limits were put on its presence. Spatially resolved spectra were fit with a simple model of synchrotron emission from a power-law electron energy distribution with an exponential cutoff, which produces a slower-than-exponential rolloff of emission characterized by the frequency $\nu_{\rm roll}$ at which the spectrum has dropped by a factor of 10 below its extrapolation from lower frequencies. Values of rolloff energy $h\nu_{\rm roll}$ were found to vary over a factor of 5 at different regions around the rim

(Lopez et al., 2015), and were shown to rise as a steep function of the shock velocity obtained from radio expansion measurements (Reynoso et al., 1997).

In addition to Tycho's well-characterized X-ray emission, gamma rays were detected by *Fermi*-LAT at GeV energies (Giordano et al., 2012) and by VERITAS at TeV energies (Acciari et al., 2011). The detection in the TeV range proves that efficient particle acceleration to very high energies is taking place, presumably at the SNR's shock. Whether the gamma rays are due to leptonic or hadronic processes is not clear. The gamma-ray spectrum of Tycho was modeled and found to be consistent with diffusive shock acceleration (DSA) of electrons, in a two-zone leptonic model, (Atoyan and Dermer, 2012), but a hadronic model invoking shock-accelerated cosmic-ray protons was also possible (Berezhko et al., 2013). HEX-P will allow better constraints on high-energy spectral structure which will aid in this discrimination.

3.4.1 Imaging and spectral simulations

Figure 2 shows the broadband (0.7–9 keV) *Chandra* image of Tycho. Regions previously identified with strong nonthermal emission include the thin rims seen around most of the periphery, as well as structures in the west. *Chandra* spectra from the annulus ("rim") and irregular hard-spectrum west region ("W hard") were extracted and fit with power-law models, which were used to simulate images in the LET and HET instruments. Models for the rim were power-laws with photon index $\Gamma = 2.67$ and 3.48 (compared in Figure 3). The same model for the W hard region was used in each. A purely thermal spectrum of the remainder of the remnant was assumed. The models can clearly be distinguished; the rim is clearly resolvable separately from the W interior region, allowing model discrimination not possible with the *NuSTAR* sensitivity and angular resolution.

Figure 4 shows simulated spectra using XSPEC and the V7 response files for the HET and LET. In all cases, an input power-law index of $\Gamma = 3.0$ was assumed, with normalization based on the *Chandra* image. All spectra are consistent with the data in the *Chandra* band, but with different assumptions about behavior at higher energies. In a 200-ks exposure, parameters of XSPEC simulated straight power-laws can be recovered to within ~5% accuracy, while models with broken power-laws (with $\Delta\Gamma = 3$) do a distinctly poorer job, as quantified by the increase in C statistics. A second set of input models, broken power-law simulated data also steepening by $\Delta\Gamma = 3$ at various assumed energies $E_{\rm break}$, produce the simulations shown in Figure 4. Fits with the same models recover the two photon indices and $E_{\rm break}$ to within ≈2.5%, ≈ 5%, and ≈10% for break energies of 20, 30 and 40 keV, respectively. These accuracy levels will enable the detection of hard X-ray variabilities from several prominent X-ray features where particle acceleration is considered to be more energetic and active. These simulations demonstrate the ability of the HET, especially, to characterize the spectral shape in hard X-rays from Tycho, with important implications for the nature of electron acceleration. The detection of steepening, either as smooth curvature or more abrupt spectral breaks, is essential for determining the maximum energies of electrons.

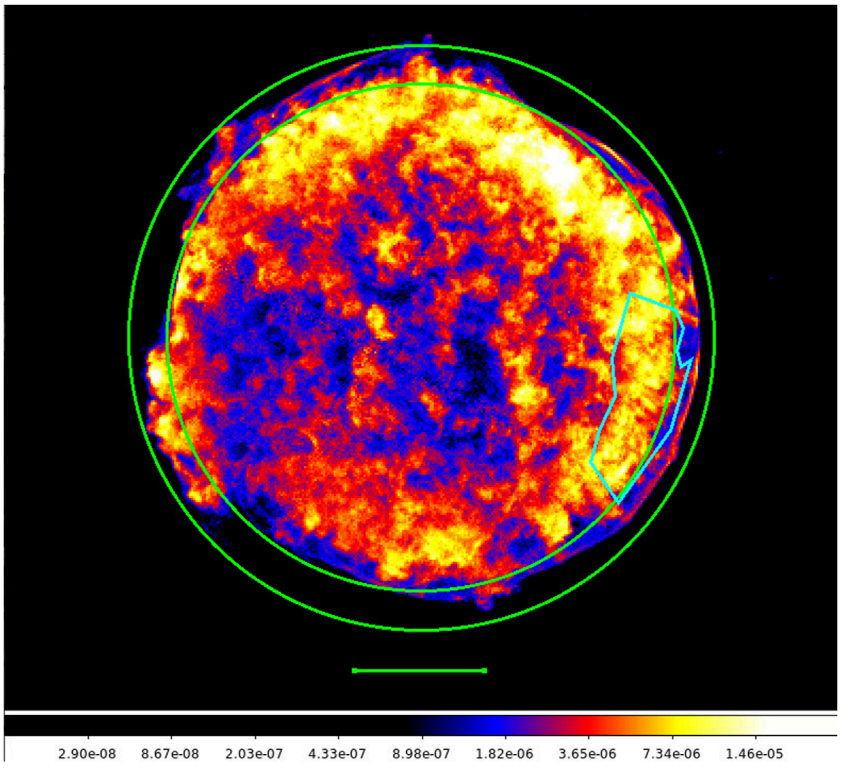

FIGURE 2
Chandra image of Tycho (0.7–9 keV), binned by a factor of 4. Brightness scale is logarithmic; units are erg cm^{-2} s^{-1}. The scale bar has length 2′. The annulus defines the "rim" region, which contains a high percentage of nonthermal emission. The irregular cyan region in the west has a harder spectrum than most of the remnant. Simulated HEX-P spectra from each, based on *Chandra* data, are shown below.

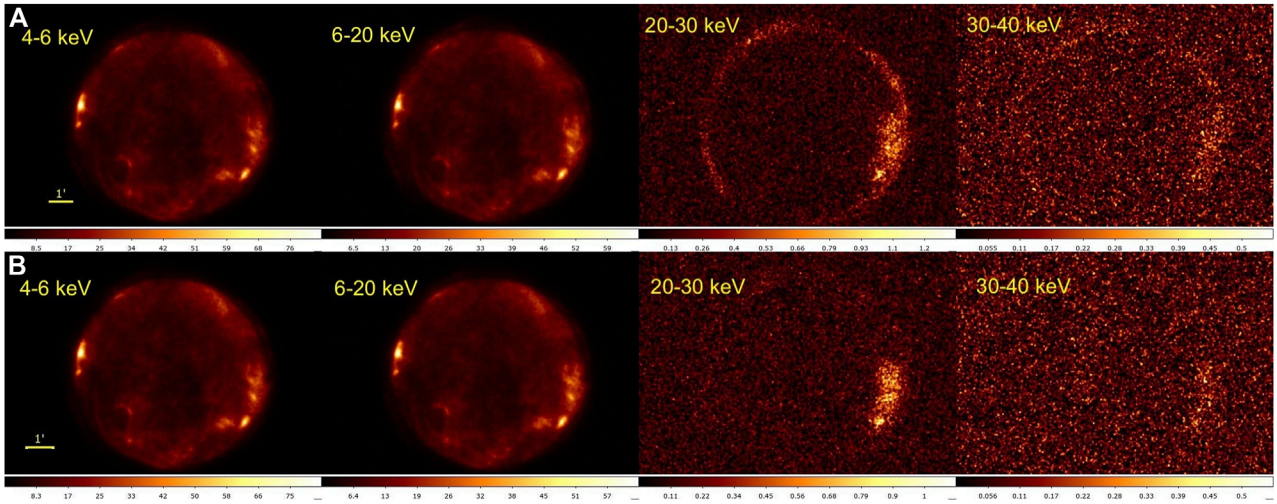

FIGURE 3
Simulated 100 ks HEX-P images of Tycho's SNR. Input spectral models include a power-law for the W hard interior region, one of two power-law models for the rim region ($\Gamma = 2.67$ or 3.48) and a thermal shock model for the remaining interior (parameters not specified as this component contributes negligibly above 8 keV). Units are integrated counts in the indicated energy ranges. **(A)** Rim power-law, $\Gamma = 2.67$. **(B)** Rim power-law model, $\Gamma = 3.48$. The different rim models can clearly be distinguished.

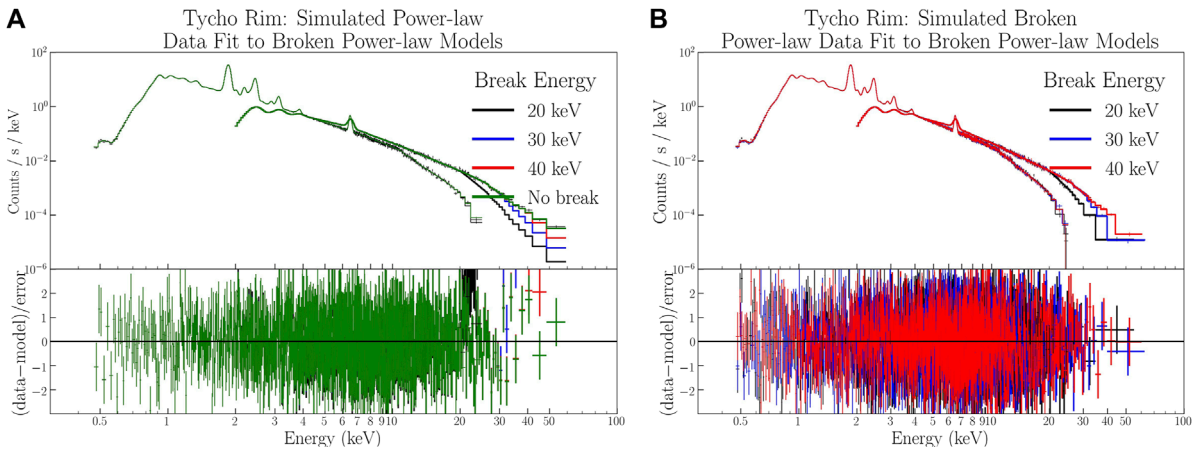

FIGURE 4
Simulated spectra for a 200-ks observation of Tycho. **(A)** Simulated spectra from parameters given by pure power-law fits to *Chandra* rim data, fit with one pure and three broken power-law models for a 200-ks observation of Tycho. C-statistic values are 398.0 for the power-law fit, and rapidly deteriorate for fits using broken power-law models: 433.7, 662.4, and 2,273.8 for increasingly severe break energies (40, 30, and 20 keV respectively), clearly ruling out the broken power-law models. **(B)** Simulated spectra from parameters given by broken power-law fits to the *Chandra* data, fit with broken power-law models. Input values are recovered to ≈2.5%, ≈ 5%, and ≈10% accuracy for break energies of 20, 30, and 40 keV, respectively (Cstat values of 418.9, 414.2, and 414.0.

3.5 G1.9 + 0.3

G1.9 + 0.3 is the remnant of the most recent supernova in the Milky Way (Reynolds et al., 2008), with an expansion age of order 140 years (an upper limit to the true age) and (based on hydrodynamic models of the deceleration) a likely explosion date of around 1900 (Carlton et al., 2011). It has an X-ray spectrum dominated by synchrotron emission, with one of the highest rolloff energies of any SNR (over 2 keV; Reynolds et al., 2009). However, thermal emission is detected in small regions, with line widths of up to 14,000 km s^{-1} (Borkowski et al., 2010), the fastest seen in any Galactic SNR, and consistent with the measured expansion at an assumed distance of 8.5 kpc. The remnant is sufficiently young that particle acceleration (at least in conventional theories) is limited by the remnant age—that is, the maximum electron energy is not set by synchrotron losses, and is the same as the maximum ion energy. This would make G1.9 + 0.3 a unique case where the maximum ion energy can be inferred directly from X-ray observations. The remnant is also the only Galactic SNR still increasing in brightness, at both radio and X-ray wavelengths (Carlton et al., 2011), and it is

expected that the maximum particle energy is also continuing to increase. *NuSTAR* observations (Zoglauer et al., 2015) showed the presence of X-rays out to about 25 keV before the signal was lost in the background. Those observations were unable to discriminate between straight power-laws and power-laws with relatively low (~ 15 keV) cutoff energies, a crucial difference in characterizing the highest-energy electron spectrum. As the simulations of Figure 5 show, HEX-P can resolve this problem. As time goes on, G1.9 + 0.3 provides us with a view of the evolving process of particle acceleration.

3.6 SN 1987A

SN 1987A is the closest supernova known since its explosion 36 years ago in the Large Magellanic Cloud (LMC) located 51 kpc away. While it has been best known for the detection of neutrinos from the supernova event, SN 1987A has exhibited spatial and spectral evolution across a wide range of wavelength bands from radio to X-ray. Shortly after the explosion, X-rays were detected from SN 1987A (e.g., Frank et al., 2016). The X-ray emission, composed of soft and hard components which vary separately, is primarily thermal, considered to arise from the interaction between the expanding shock wave and the surrounding circumstellar material.

One of the key questions associated with SN 1987A is whether the supernova left a neutron star or black hole. Some hints on the presence of a NS at the core were suggested by recent ALMA radio and *NuSTAR* hard X-ray observations. ALMA detected a bright spot, suggesting that local dust is being heated by the NS's thermal emission (Cigan et al., 2019). *NuSTAR* observed non-thermal X-ray emission above 10 keV, suggesting the presence of a PWN (Greco et al., 2021). However, despite the *NuSTAR* observations with 3.3 Ms total exposure, the detection of a PWN component is still under debate (Alp et al., 2021; Greco et al., 2022), and more sensitive hard X-ray observations are required for making a firm detection of the putative PWN. A contribution to the hard X-rays from synchrotron emission from electrons accelerated in the SN blast wave cannot be ruled out, as the blast wave radius is smaller than an arcsecond. Note that only the hard X-ray band above 10 keV can be observed from the core region due to severe photo-absorption by heavy-element ejecta (Alp et al., 2018). HEX-P's energy coverage from 0.2 to 80 keV will be essential for fully characterizing both thermal and non-thermal X-ray components. Figure 6 shows simulated HEX-P spectra of SN 1987A. While SN 1987A is a point source to HEX-P as it is for *NuSTAR*, HEX-P's better angular resolution means smaller background in a resolution element, enhancing the sensitivity to unconfirmed non-thermal emission above 10 keV compared to *NuSTAR*.

Since the multi-wavelength emission components from SN 1987A are expected to vary on year timescales, as seen over the last 35 years, HEX-P will be able to provide a broadband and high-resolution X-ray view of how both thermal and non-thermal X-ray emission appears and evolves in the 2030s. Since CTA selected the LMC survey as one of CTA's key science projects (Cherenkov Telescope Array Consortium, 2023), HEX-P and CTA will jointly reveal hard X-ray and TeV emission from synchrotron and inverse-Compton radiation associated with the SNR and possibly emerging PWN, respectively.

4 Pulsar wind nebula

A pulsar wind nebula (PWN) is a bubble of non-thermal radiation from a magnetized, primarily electron/positron plasma which is supplied by an energetic pulsar. The confinement of the initially relativistic pulsar wind by its environment results in a termination shock. Particles are thought to be accelerated to high

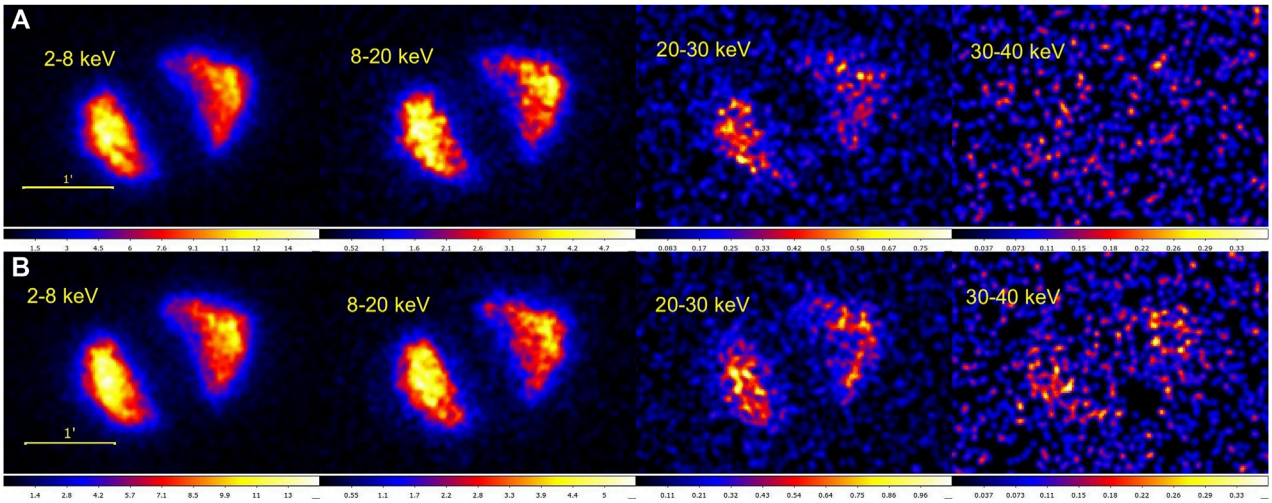

FIGURE 5
Simulated 100 ks HEX-P images of G1.9 + 0.3, based on two spectral fits indistinguishable to *NuSTAR* (Zoglauer et al., 2015). **(A)** Power-laws with an exponential cutoff in photon energy (E limb: $\Gamma = 2.09$, $E_{break} = 14.9$ keV; W limb, $\Gamma = 2.07$, $E_{break} = 13.9$ keV. **(B)** Straight power-laws (E limb: $\Gamma = 2.59$; W limb, $\Gamma = 2.66$). Units are counts.

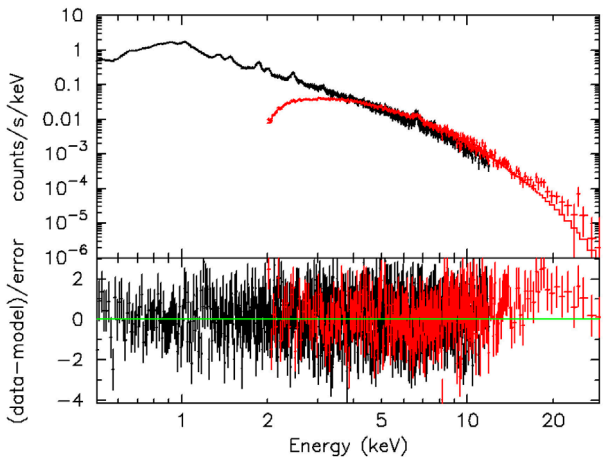

FIGURE 6
Simulated HEX-P LET (black) and HET (red) spectra of SN 1987A assuming a 300 ks exposure. The input spectral parameters for the three thermal components ($kT_1 = 0.48, kT_2 = 0.96, kT_3 = 3.2$ keV) and a power-law component ($\Gamma = 2.6$) were adopted from the *Chandra*, *XMM* and *NuSTAR* observations obtained in 2020 (Greco et al., 2022). The simulated *HEX-P* spectra are fit with the thermal components only to illustrate the presence of the non-thermal emission above 10 keV. The non-thermal component is detected with 7σ significance and its photon index is well constrained to $\Gamma = 2.4^{+0.2}_{-0.1}$, much improved from the 2020 *NuSTAR* observation with 350 ks exposure ($\Gamma = 2.6^{+0.7}_{-1.8}$) (Greco et al., 2022).

energies in the shock and flow and diffuse outward to produce a PWN. PWNe are expected to evolve through three phases: an initial phase in which the young PWN expands into the cooled expanding ejecta of its natal SNR; a second phase in which the SNR's reverse shock wave has returned toward the center and recompressed the PWN, distorting it and perhaps moving it off-center in the SNR; and a third phase, after the pulsar has either left the SNR or outlived it, and its wind is interacting with undisturbed ISM. Since pulsars are typically born with substantial kick velocities, in this third phase they are normally moving supersonically in the ISM and their PWN is in the form of a bow-shock nebula. Most modeling has been done for the earlier stages. Kennel and Coroniti (1984a; Kennel and Coroniti, 1984b) modeled the Crab Nebula with a spherically symmetric magnetohydrodynamic model assuming pure advection of particles behind the termination shock, successfully explaining its basic features. Later detailed MHD simulations have reproduced many features of the X-ray morphology of the Crab Nebula, including small-scale structures such as jets and tori (e.g., Del Zanna et al., 2004; Komissarov and Lyubarsky, 2004), features found in many other PWNe (Ng and Romani, 2004, and references therein). While these MHD models capture the main properties of the Crab Nebula, they do less well in describing properties common in other PWNe that the Crab does not share, such as uniformly steepening spectra with distance from the pulsar. In general, there is a great deal more to be learned about the diversity of PWN phenomenology that the MHD models cannot answer. TeV and even PeV photons are observed in PWNe (Cao et al., 2021), meaning that they accelerate electrons to even higher energies. These particles can escape from the PWNe and could contribute significantly to the flux of energetic electrons and positrons detected on Earth (e.g., Abeysekara et al., 2017a).

Particle acceleration in PWNe is thought to occur at the relativistic termination shock via DSA or magnetic reconnection as demonstrated by particle-in-cell (PIC) simulations (e.g., Sironi and Spitkovsky, 2009; Sironi and Spitkovsky, 2014). However, it is still unclear to what energy the particles are accelerated, how they evolve as they flow and diffuse, and how they escape from the PWNe. These can be addressed by high-quality X-ray and gamma-ray data. In particular, synchrotron X-rays probe the highest-energy electrons, as their inverse-Compton gamma-ray emission is suppressed by the Klein-Nishina effect. Sensitive X-ray and gamma-ray observatories have helped to address these questions during the previous 2 decades, but many important questions remain unanswered. We list questions (1)–(3) as shown below.

4.1 Important questions to address on PWN physics

4.1.1 Particle acceleration in relativistic shocks

Numerous PWNe emit TeV (even PeV) photons, implying that there must be very energetic particles accelerated at their termination shocks or elsewhere. Indeed, half of the unidentified TeV sources discovered in H.E.S.S. Galactic plane surveys are now categorized as middle-aged or old PWNe (H.E.S.S. Collaboration, 2018), and half of the sources listed in the first LHASSO source catalog are linked with pulsars and/or PWNe (Cao et al., 2023). Most of them are theoretically compatible with being powered by a pulsar (de Oña Wilhelmi et al., 2022). Because the energy distribution of the particles is imprinted in their radiation spectrum, accurate measurements of PWN spectra will give us clues to particle acceleration processes in relativistic shocks. Although PeV-energy particles are already detected in the Crab Nebula, an important question is whether or not other PWNe can generally accelerate particles to such energies (i.e., constitute leptonic PeVatrons). As in other sources, Klein-Nishina suppression of inverse-Compton scattering from the highest-energy electrons means that their energy distribution, up to those highest energies, is best probed not by gamma rays but by sensitive high-energy X-ray observations of synchrotron emission. Modeling of X-ray and gamma-ray data of various PWNe has given maximum particle energies of ~PeV not only in young sources ($\lesssim 10^4$ years; e.g., Torres et al., 2014; Abdelmaguid et al., 2023) but also in middle-aged ones ($\sim 10^4$–10^5 years; e.g., Burgess et al., 2022; Park et al., 2023a; Woo et al., 2023). While these estimates depend strongly on B within the PWN (an electron of energy E emits its peak synchrotron power at a photon energy $h\nu_m \propto E^2\, B$), broadband spectral-energy-distribution (SED) models can constrain B, especially if spectral features such as spectral breaks or cut-offs, spatial variation of the spectrum, and/or energy-dependent morphology are measured. An independent B estimation is possible if the seed-photon radiation energy density $u^\star$ in the PWN region is known, since $P_{\rm synch}/P_{\rm IC} = u_B/u^\star$ (in the Thomson regime), where $u_B \equiv B^2/8\pi$ is the energy density in magnetic field. The state-of-the-art code GALPROP (Porter et al., 2022, and references therein) provides models for Galactic distributions of cosmic rays as well as of the

interstellar radiation field.[1] The latter provides models for $u^\star$ within the Galaxy, thereby allowing an independent estimation of B in PWNe. High-quality X-ray data will facilitate measurements of the aforementioned spectral and spatial features with high precision, and these, combined with improved $u^\star$ estimations, will improve our understanding of particle acceleration processes in PWNe.

4.1.2 Particle injection into the interstellar medium

The origin of the cosmic-ray positron flux detected on Earth at energies higher than a few GeV is a longstanding puzzle (e.g., Aguilar et al., 2019), and it was suggested that nearby pulsars and their PWNe are an important source of these particles (e.g., Cholis and Hooper, 2013; Della Torre et al., 2015; Xi et al., 2019; Manconi et al., 2020). Radiative energy losses restrict possible sources of the highest-energy terrestrial cosmic-ray leptons with $E \gtrsim 1$ TeV to within about 1 kpc, but studying numerous PWNe in a larger volume can aid in understanding energetic leptons within the Galaxy. After being accelerated at the relativistic termination shock of the pulsar wind, leptons evolve in the PWN under radiative and advective cooling (e.g., Reynolds, 2009; Van Etten and Romani, 2011; Park et al., 2023b). Young systems are expected to efficiently confine the nebular plasma, and in general they might not be an efficient source of energetic cosmic-ray electrons in the Galaxy, since their electrons rapidly lose energy to radiation via synchrotron emission in the strong magnetic fields typical of such objects. However, we do have direct evidence of an efficient escape of particles in the outer medium from middle-aged and more evolved systems (see e.g., Olmi and Bucciantini, 2023, for a recent review of systems in different phases and their observational signatures).

A first clear indication is TeV halos seen around old PWNe (e.g., Yüksel et al., 2009; Bamba et al., 2010; Sudoh et al., 2019; Abeysekara et al., 2017a; H.E.S.S. Collaboration, 2023). These TeV halos are likely due to the sum of all particles which have escaped over time during the lives of the PWNe. A second piece of evidence is the presence of extended (from 1 to several pc), asymmetric and collimated X-ray features protruding from some high-speed bow shock PWNe (e.g., Kargaltsev et al., 2017), showing a strong misalignment with respect to the pulsar direction of motion. These intriguing features can be explained as formed by energetic particles leaving the PWN, advected away along the ambient magnetic field lines (Olmi and Bucciantini, 2019). Some degree of amplification of the ambient field is necessary to explain the observed emission as due to synchrotron radiation (Bandiera, 2008), possibly produced by the particles themselves. An excellent example is the Lighthouse PWN (IGR J11014−6103) powered by the old 120 kyr pulsar PSR J1101−6101 (Halpern et al., 2014). It shows a ∼6′ long and bright collimated outflow to the west (Pavan et al., 2016), with evidence for spectral evolution along the feature in the combined observations from *Chandra* and *NuSTAR* (Klingler et al., 2022). The possibility of investigating the spectrum of such features in the very extended energy band of HEX-P, and with its angular resolution, is a key ingredient to understand not only the properties of escaped particles (and thus of the PWN) but also how they interact with the ambient medium, with important consequences for our understanding of the physics of transport and diffusion in the vicinity of sources. All these points are then intimately connected both with point (1)—how and to what energy particles are accelerated at the pulsar wind termination shock—and the following point (3)—how particle acceleration and escape change as the PWN evolves.

4.1.3 Co-evolution of the PWN and its SNR

The evolution of a PWN is tightly linked to that of its host SNR. The entire evolutionary history affects the particle energy distribution within the PWN today, which is imprinted in the emission SED. The size and expansion speed of PWNe provide additional information on the co-evolution since the PWN expansion is influenced by, first, the surrounding SNR ejecta, and later by the reverse shock (e.g., Hattori et al., 2020). Effects of PWN/SNR co-evolution (e.g., Bandiera et al., 2020; 2023) are particularly important in understanding cosmic-ray electrons since we need to consider the entire history of particle injection by PWNe to compare with cosmic rays detected today. The co-evolution is very complex, and hydrodynamic (HD) simulations have been carried out to study the dynamic evolution of PWN-SNR systems (e.g., Bucciantini et al., 2003; Kolb et al., 2017). In these works, the broadband spectral properties of the PWNe have not been considered. Gelfand et al. (2009) developed a dynamic and radiative evolution model by treating the PWN-SNR co-evolution in a semi-analytic way (Reynolds and Chevalier, 1984), in a one-zone model with spherical symmetry. This evolutionary PWN model has successfully fit the SED, size, and expansion speed of some PWNe (e.g., Abdelmaguid et al., 2023), and the model-inferred properties of the SN and SNR seem to agree reasonably well with other SNR evolution models (e.g., HD simulations). While PWN evolution models are very useful for understanding PWN physics and can provide a supplementary tool for understanding SNR physics, the models have many covarying parameters, and one-zone models fail to capture the obvious inhomogeneities and morphological complexities of almost all PWNe. Moreover, recent higher-resolution HD studies (e.g., Bandiera et al., 2020; 2023) found deviations from the prescriptions used for the dynamic evolution in the radiative evolution model of Gelfand et al. (2009). These deviations may be manifest in the spatially-varying emission properties and can have a significant impact on the highest-energy particles. Measurements of the spatially-integrated SED, size, and expansion speed are certainly insufficient for studying the co-evolution in detail and precise measurements of the PWN properties (e.g., spatially-resolved spectra) are necessary to enrich our understanding of PWNe and SNRs.

4.2 HEX-P contribution to PWN physics

Accurate characterizations of the PWN emission properties are crucial to address the aforementioned questions. Question 1 requires sensitive measurements of high-energy X-ray spectra of PWNe. For Questions 2 and 3, accurate measurements of spatially-resolved emission properties are necessary, along with an emission model that takes into account the temporal and spatial evolution of particles within the PWN. While existing X-ray observatories have helped address these questions, their sensitivity to faint emission

1 https://galprop.stanford.edu/code.php?option=theory

and to spectral detail is not yet sufficient to provide firm answers. *Chandra* and *XMM* have measured PWN images and spectra in great detail, but their lack of sensitivity above 10 keV precludes detailed investigation of the most energetic electrons. While this could be supplemented by *NuSTAR*'s hard X-ray data (see Reynolds, 2016; Mori et al., 2021), cross-calibration uncertainties between the observatories cause some problem (e.g., Madsen et al., 2015a; 2017a; Hattori et al., 2020; Abdelmaguid et al., 2023). In addition, the low angular resolution (60″ HPD), limited effective area, and strong and inhomogeneous backgrounds of *NuSTAR* (e.g., Wik et al., 2014; Madsen et al., 2017b) have been a concern for measurements of spatially-integrated and resolved spectra of PWNe above 20 keV.

The HEX-P observatory can revolutionize our studies of PWNe. The broadband coverage of the combined LET and HET instruments provides a large lever arm for spectral measurements, and thus the properties of emission by highest-energy electrons, which may be manifested as a spectral cutoff, can be well measured. Figure 7 shows detectability of a strong spectral break at $E_{\rm brk}$ (broken from $\Gamma_l = 2$ to $\Gamma_h = 5$ as was suggested for 3C 58; An, 2019), simulated for a generic $R = 3'$ PWN assuming a 100 ks observation with HEX-P. Note that other gradual cut-off shapes, e.g., exponential cutoffs at $E_{\rm cut}$, are more easily detected because the spectral shape starts to change at low energies as compared to the broken power-law case. We also mark fluxes of some bright PWNe in the figure for reference. The simulations show that we can detect a spectral break up to 50 keV if the source is bright (e.g., $F \geq 10^{-10}$ erg s^{-1} cm^{-2} in the 2–10 keV band) and if its spectrum indeed exhibits a spectral cutoff. This experiment will be particularly useful for some PWNe in which a spectral curvature or cutoff was measured (e.g., Crab, G21.5–0.9, PSR J1400−6325, and PSR J1813−1749; Madsen et al., 2015a; Nynka et al., 2014; Hitomi Collaboration et al., 2018; Renaud et al., 2010; Bamba et al., 2022; Hattori et al., 2020) or suggested (e.g., 3C 58 and N157B; An, 2019; Bamba et al., 2022). This will help address Question 1. Note that *NuSTAR* data have some systematic uncertainty due to the inhomogeneous background which is very difficult to assess for diffuse PWNe. HEX-P, in addition to having twice the effective area and lower backgrounds, would not suffer from such inhomogeneous background. Hence the improvement can be substantial.

In studying PWN emission using an evolutionary model, it is crucial to measure the emission SED as precisely as possible. This can provide additional information to break parameter covariance of the evolutionary model since the SED shape changes depending sensitively on the cooling history of the particles (e.g., Gelfand et al., 2009). In this regard, the broadband coverage of LET + HET of HEX-P is particularly helpful. The right panel of Figure 7 shows HEX-P's sensitivity to a small degree of curvature in the emission spectrum investigated using the `logpar` model in *XSPEC* ($dN/dE = K(E/E_p)^{-a-b\log(E/E_p)}$ with $E_p = 5$ keV) for $R = 3'$ PWN emission. This value of the pivot energy E_p was chosen as it is near the center of HEX-P's full LET + HET bandpass, thus posing the most stringent test for sensitivity to departures from a power-law. Simulations of a 100-ks exposure show that HEX-P will be able to measure a shallow curvature with $b < 0.1$ (corresponding to ~20% SED change over the 0.3–80 keV band) if the source flux in the 2–10 keV band is $\geq 10^{-11}$ erg s^{-1} cm^{-2}. This is sufficient for measuring spectral breaks detected in some young PWNe, which will provide important clues to the particle acceleration mechanisms and PWN-SNR co-evolution. In particular, Klingler et al. (2022) found in outflow regions of the Lighthouse PWN that the soft X-ray (*Chandra*) spectra are discrepant with the hard X-ray (*NuSTAR*) ones, implying that the effects of particle evolution (e.g., cooling) are best seen at >8 keV. However, this could not be confidently stated because of cross-calibration issues and non-uniform background in the *NuSTAR* data. HEX-P observations will help to clarify this since the suggested spectral curvature is large enough for detection, and can shed light on the properties of the particles escaping the PWN and their effect on the ambient medium (Question 2).

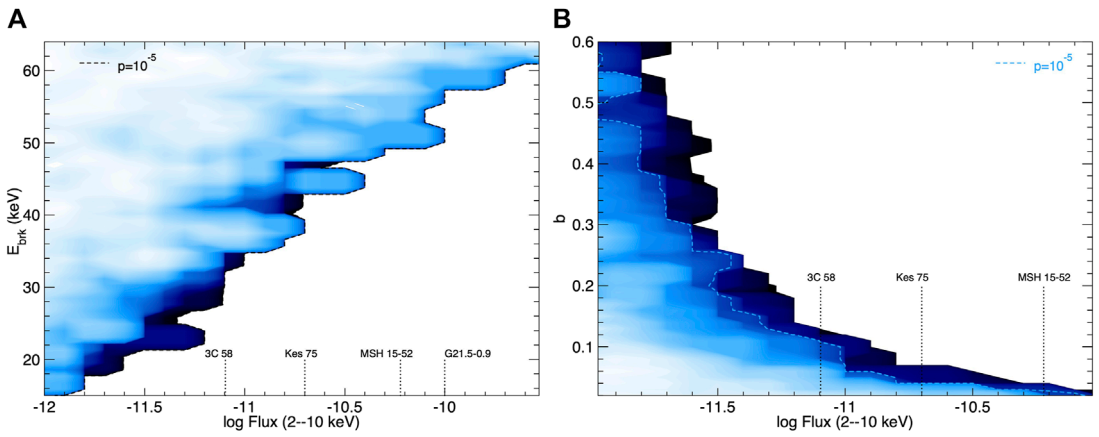

FIGURE 7
Results of HEX-P simulations of a generic $R = 3'$ extended PWN. **(A)** *F*-test probability contours between a power law (PL) and a broken power-law (BPL) model. Simulated HEX-P data (100-ks) for a BPL spectrum having $\Gamma_l = 2$ and $\Gamma_h = 5$ at break energy $E_{\rm brk}$ are fit by a BPL and a PL, and the addition of the break was tested using the *F* statistic. **(B)** Same as the left, but the simulations were carried out for a `logpar` model with varying *b* (see text). The vertical dashed lines mark fluxes of some young and bright PWNe: 3C 58 (An, 2019), Kes 75 (Gotthelf et al., 2021), MSH 15–52 (An et al., 2014), and G21.5–0.9 (Nynka et al., 2014).

HEX-P will also allow measurements above 10 keV of faint emission in the outer regions of extended (and evolved) PWNe. This will help to characterize synchrotron burn-off effects as well as particle flow near the outer boundary of the PWNe, and to provide new insights into the evolution of PWNe after their young phase (Question 3). We can then estimate the amount and spectrum of electrons that escape from the X-ray PWN and propagate to larger TeV emission regions. With the advent of high-resolution TeV observatories (e.g., CTA), the HEX-P data will tell us about how the electron spectrum evolves as electrons propagate from the X-ray PWN to the TeV emission region, and eventually to the interstellar medium. This will help address Question 2. In our 100-ks simulations of a HEX-P observation of a $R = 4'$ PWN, we found that we could measure the photon index of an annular region with the inner and outer radii of $3'$ and $4'$ to within 0.1 if the 2–10 keV flux is higher than 3×10^{-13} erg s^{-1} cm^{-2}. In other PWNe, the injection regions may be too faint for accurate measurement of the spectrum. These faint regions can still be identified by images, and our simulations of HEX-P observations for a hypothetical PWN suggest that faint source emission within an annular region with the inner and outer radii of $4'$ and $4.25'$ (i.e., width of $15''$) can be detected with 3σ confidence if the flux is higher than 3×10^{-14} erg s^{-1} cm^{-2}.

4.3 HEX-P simulations for the Crab Nebula, G21.5–0.9, Lighthouse PWN and G0.9 + 0.1

HEX-P plans to observe the Crab, G21.5–0.9, Lighthouse PWN and G0.9 + 0.1 in the primary science program. The improved PSF of HEX-P HET will resolve substructures in the sources much better than *NuSTAR* could. In addition, HEX-P's large effective area will allow more accurate spectral characterization of the sources. Figure 8 shows simulated images of the sources made with the SIXTE suite. Compared to *NuSTAR*'s images of the sources (Nynka et al., 2014; Madsen et al., 2015a; Klingler et al., 2022), the morphologies of the PWNe are much better resolved. The torus and jets of the Crab Nebula and the northern spur and eastern limb of G21.5–0.9 were seen by *NuSTAR* only after deconvolving the PSF from the images, and thus their spectra could not be measured. The HET of HEX-P can resolve those structures as in the simulated images (Figure 8), allowing spectral measurements. Nonthermal emission from the northern spur and the eastern limb of G21.5–0.9 that were suggested based on deconvolved images (Nynka et al., 2014) can be better characterized by HEX-P observations. This also applies to other sources in which NuSTAR's resolution was insufficient to resolve various structures in them, requiring deconvolution (e.g., G11.2–0.3; Madsen et al., 2020).

The Lighthouse PWN is particularly intriguing thanks to its long (~$6'$) and misaligned tail, which connects to a diffuse emission region (Pavan et al., 2016). The morphological change from a collimated jet to a diffuse region in this PWN can tell us much about electron injection from the old PWN into the ISM. The *NuSTAR* measurement of the spectrum of the diffuse region ($\Gamma = 2.21 \pm 0.08$) was discrepant with the *Chandra* result ($\Gamma = 1.74 \pm 0.05$) (Klingler et al., 2022), suggesting that the electrons had experienced strong cooling. However, this was uncertain because of unknown systematic effects in the data, e.g., cross-calibration between the observatories and inhomogeneous background in the *NuSTAR* data (the latter was a particular concern; see Klingler et al., 2022). Our HEX-P simulations for a 100-ks observation of the Lighthouse PWN, based on the previous *NuSTAR* results, found that HEX-P would be able to detect the diffuse emission at $\geq 6'$ up to ~20 keV (Figure 8) and to measure its spectrum accurately, e.g., constraining Γ_X to within 0.04. This will provide sufficient sensitivity for discriminating between the hard vs. soft injection spectra as measured by *Chandra* and *NuSTAR*. More importantly, HEX-P data (LET + HET) will not suffer from systematic effects due to cross-calibration across the 0.2–80 keV band or to inhomogeneous background. Hence, HEX-P observations of the Lighthouse PWN will considerably improve the *Chandra* and *NuSTAR* measurements, and thereby provide

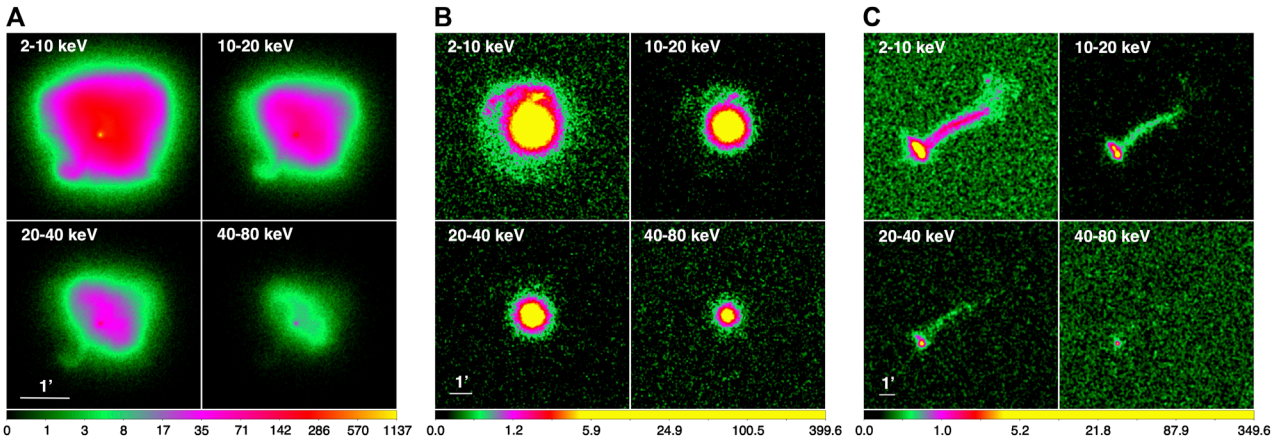

FIGURE 8
Simulated HEX-P HET images of the Crab Nebula [1 ks; **(A)**], G21.5–0.9 [50 ks; **(B)**] and the Lighthouse PWN [**(C)**; 100 ks] made with the SIXTE suite. Units are total counts; scales are logarithmic. Chandra images were used as the inputs, and spectral variations within the PWNe as measured by Chandra (Mori et al., 2004; Pavan et al., 2016; Guest et al., 2019) were included.

crucial clues to how the PWN electrons are injected into the ISM.

G0.9 + 0.1 is a composite-type supernova remnant (SNR) and pulsar wind nebula (PWN) located only one degree from the Galactic Center, long studied in the X-ray regime. As the system is quite young with a spin-down age of $\tau_c = 5.3$ kyr (Camilo et al., 2009), the SNR shell has not interacted with the $d \sim 2'$ PWN core (Helfand and Becker, 1987) leaving the nebula an ideal candidate for probing the physical mechanisms responsible for accelerating high-energy particles. X-ray observations below 10 keV by *Chandra* (Gaensler et al., 2001) and *XMM* (Porquet et al., 2003; Holler et al., 2012) reveal prototypical non-thermal emission with a radially dependent power-law index, a signature of PWN synchrotron cooling. Despite its young age and energetic pulsar, the nebula has coincident γ-ray emission (Aharonian et al., 2005; Adams et al., 2021) that is relatively underluminous for its pulsar luminosity, making this an interesting target to probe high-energy particle acceleration. *NuSTAR* observations were able... were able to detect the non-thermal PWN emission up to 30 keV. However, stray light caused by the proximity to the Galactic Center reduces the quality of the data and the spectral parameters are only moderately constrained. HEX-P simulations of G0.9 + 0.1 show a significant improvement in the >10 keV range (Figure 9A). Broadband studies with multi-wavelength SEDs have attempted to probe the underlying acceleration processes. Several one-zone time-dependent leptonic models (e.g., Fiori et al., 2020) have been adopted with various constraints applied to input parameters, while other models explored lepto-hadronic scenarios (Holler et al., 2012), multiple zones, or incorporated significant adiabatic cooling (Tanaka and Takahara, 2011). While these complex models fit the available data, they often leave crucial parameters, such as the injected electron spectral index, unconstrained. HEX-P provides critical coverage at the energy band where the majority of models predict a turnover in the SED curve (Figure 9B). HEX-P data added to broadband SED analysis will provide a deeper understanding of the extreme particle acceleration processes within PWNe.

4.4 Summary

The broadband coverage, superior angular resolution, and low background of HEX-P HET will provide significant improvement in our understanding of PWNe. In addition to the spectral improvement, the HET of HEX-P will measure the morphologies of PWNe in greater detail compared to *NuSTAR* as presented in Figure 8. Hard X-ray emission from substructures (e.g., torus, jets, and knots) in PWNe will be better probed. HEX-P will observe the Crab Nebula and G21.5−0.9 as calibration targets, and these observations will provide unprecedented data for these two young and bright PWNe, allowing precise SED studies. In addition, a 100 ks HEX-P observation of the Lighthouse PWN will measure the spectra of the outflow regions out to $\geq 5'$ without systematic effects due to inhomogeneous background. This will probe how the electrons in the outflows evolve and merge into the ISM.

5 Nucleosynthesis in the galaxy

While HEX-P can revolutionize the study of hard X-ray nonthermal continua from particle accelerators, the spectral region above 10 keV holds little information on thermal line emission. However, HEX-P can make a major improvement in line spectroscopy of another sort: radioactive decay of freshly synthesized unstable isotopes from supernovae or from double neutron-star mergers. In supernovae, the well-known hard X-ray nuclear decay lines at 68 and 78 keV emitted in the decay chain of ^{44}Ti contain invaluable information on the synthesis of iron-group elements. One of the most important results from *NuSTAR* was the detection of these spectral lines from SN 1987A, and more significantly, their imaging as well, from Cas A. Unlike lines from collisionally ionized iron which must be shocked to high temperatures, these lines are emitted independent of temperature, so show the presence of titanium both before and after interaction with the reverse shock in a supernova interior. The imaging of ^{44}Ti in Cas A violated the widely held expectation that its

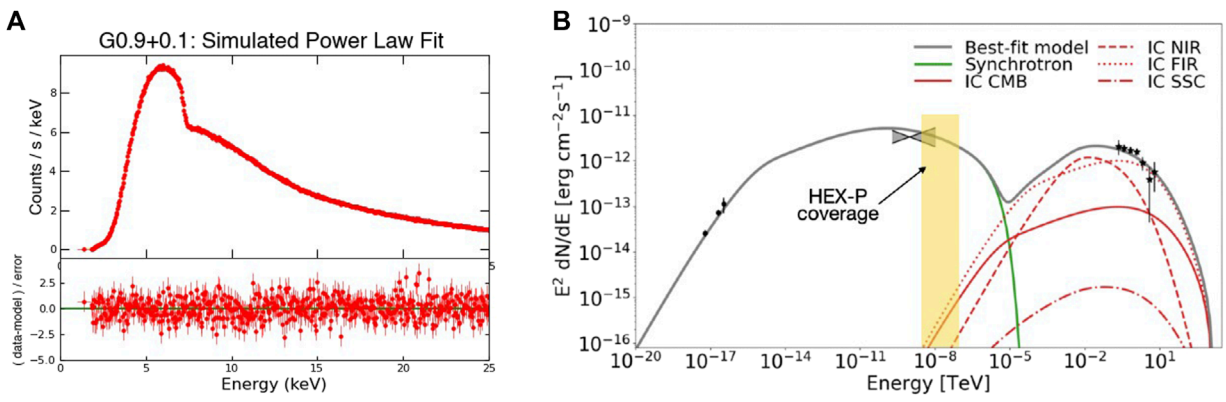

FIGURE 9
(A) Simulated 50 ks HEX-P HET spectra of the absorbed non-thermal emission from the PWN G0.9 + 0.1. The spectrum is well detected up to 40 keV and all the parameters are recovered with 1% or better. **(B)** A one-zone time-independent SED model for G0.9 + 0.1 incorporating broadband data from existing radio, X-ray, and γ-ray data (Fiori et al., 2020). The HEX-P energy band is shown in yellow, covering a critical portion of the SED.

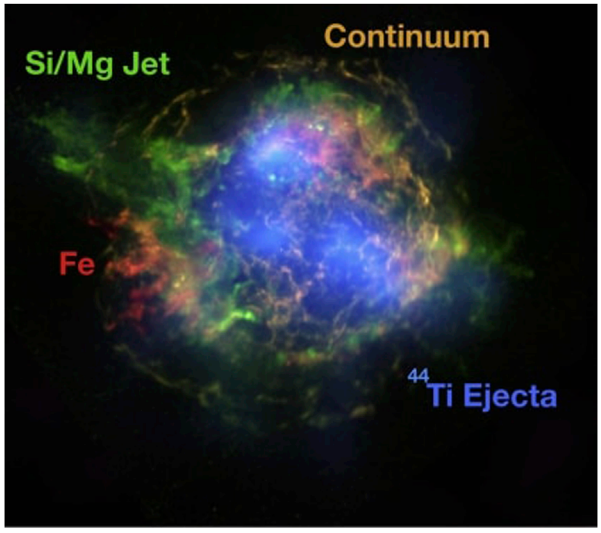

FIGURE 10
Comparison of the spatial distribution of ^{44}Ti with that of other components of Cas A (Grefenstette et al., 2017). Particularly relevant is the poor correspondence with (shocked) iron.

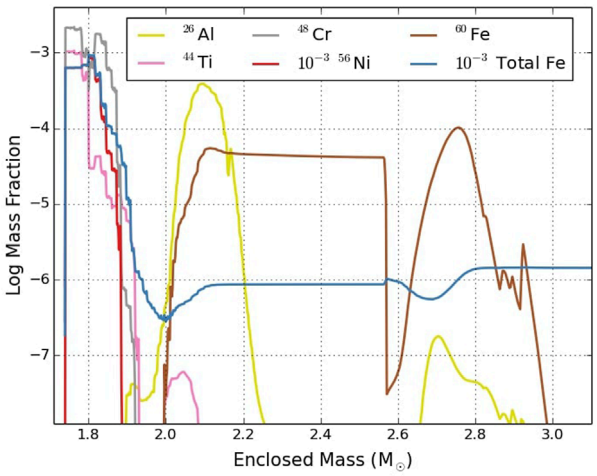

FIGURE 11
Distribution of ^{26}Al, ^{44}Ti, ^{48}Cr, ^{56}Ni, ^{60}Fe, and total Fe as a function of mass. Like ^{56}Ni and ^{48}Cr, ^{44}Ti traces the innermost ejecta. Of the isotopes probing the innermost ejecta, ^{44}Ti is uniquely observable in young supernova remnants.

distribution would mirror that of ^{56}Ni and its stable decay product ^{56}Fe. The famous *NuSTAR* image (Figure 10) shows fairly poor correspondence. However, even *NuSTAR*'s 2.4 Ms integration time was not sufficient to fully characterize the distribution at lower flux levels, and the spatial resolution, far poorer than that of the Fe Kα image produced by Chandra, did not permit more detailed examinations of Ti/Fe ratios. Both these limitations will be much less severe with HEX-P, which can improve on the *NuSTAR* detections, but also search for ^{44}Ti from other young supernova remnants (both core-collapse and Type Ia, though significant titanium production in SNe Ia probably requires high degrees of explosion asymmetry). Most excitingly, HEX-P could examine a sufficiently nearby binary neutron star merger event, with the prospect of obtaining information inaccessible to optical or soft X-ray instruments.

5.1 ^{44}Ti line emission from young SNRs

In a supernova explosion, ^{44}Ti is produced in the innermost ejecta (either in the convective region or just above it; Magkotsios et al. (2010); Fryer et al. (2023)) and is one of the most direct tracers of the supernova engine (Figure 11). ^{44}Ti production is extremely sensitive to the strength of the shock and can probe explosion asymmetries (Magkotsios et al., 2010; Vance et al., 2020). But the Cas A observations (Figure 10) highlighted issues with our understanding of the explosion mechanism.

^{44}Ti provides an ideal probe of the supernova engine. Because ^{44}Ti is produced near the engine, it traces the explosion asymmetries caused by this engine. *NuSTAR* observations of the ^{44}Ti distribution provided the most direct evidence to date supporting the convective-engine paradigm behind core-collapse supernovae (Grefenstette et al., 2014; 2017; Wongwathanarat et al., 2017; Vance et al., 2020). More precise maps of the ^{44}Ti distribution will further constrain the asymmetries in the models. In addition, the amount of ^{44}Ti produced and the ratio of ^{44}Ti to iron or other iron-peak elements provide further probes of the engine and, ultimately, the nuclear physics producing these yields.

5.1.1 Cas A

Cas A provides the only example of spatially resolved ^{44}Ti emission from a young SNR (Grefenstette et al., 2014; Grefenstette et al., 2017; Figure 10). The distribution of the ^{44}Ti already provides constraints on the asymmetries of the explosion. When these observations were obtained, constraints on the iron and other iron-peak elements were limited to iron located through X-ray emission from highly ionized states, meaning that only material having passed through the reverse shock could be observed. The long *NuSTAR* observation (2.4 Ms) was limited by spatial resolution and by background; it is possible that fainter ^{44}Ti emission could be detected and would provide quantitative measures or limits on the local Ti/Fe ratio, especially for redshifted features where both the 68 and 78 keV spectral lines could be observed. Combining more detailed HEX-P maps with recent JWST observations of this remnant (measuring unshocked iron) will allow scientists to study details of both the shock properties and the nuclear physics. Figure 12 shows the simulated HEX-P image in 67–69 keV using Chandra's Fe Kα map as a guide for the ^{44}Ti map. We emphasize that, as Figure 10 graphically demonstrates (Grefenstette et al., 2014; 2017), the ^{44}Ti distribution in Cas A does not trace the distribution of Fe Kα. Currently, the only available ^{44}Ti map is from the *NuSTAR* observations at a resolution of ~1′, so to exhibit the effect of HEX-P's superior angular resolution, we use the *Chandra* Fe Kα image as input, knowing that the resultant simulated image is a demonstration only (compare the resolution of Figure 12 to the *NuSTAR* image Figure 10). However,

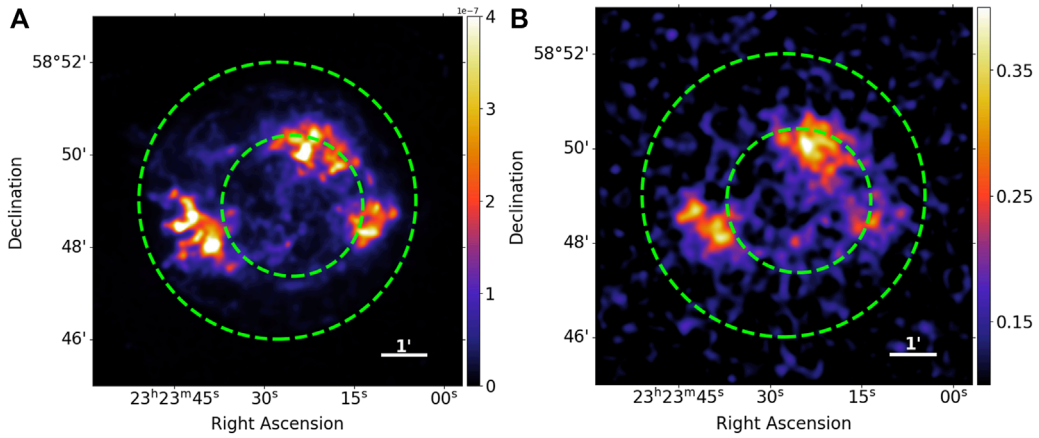

FIGURE 12
(A) Chandra Fe Kα map (6.54–6.92 keV). **(B)** Simulated HEX-P image of ^{44}Ti emission from Cas A (67–69 keV) for 1.5 Ms exposure using the Chandra Fe Kα map as the input image. The green dotted lines mark the forward (outer ring) and reverse (inner ring) shock, respectively. This image is merely to demonstrate HEX-P's high spatial resolution, as we have no access to the "true" distribution of ^{44}Ti.

the integrated flux in the simulated image is that measured by *NuSTAR*.

5.1.2 Other possible sources

The 85-year mean life of ^{44}Ti means that only SNRs less than a few hundred years old will be detectable sources. Our primary target list includes (in addition to Cas A) two such objects, SN 1987A, and Tycho's SNR. SN 1987A was detected by *NuSTAR* in a 2.6 Ms exposure, with a flux in the 68 keV line of $(3.5 \pm 0.7) \times 10^{-6}$ photons cm^{-2} s^{-1}, at a mean epoch of 27 years after the SN. In our proposed 300 ks HEX-P exposure, and assuming an observation year of 2029, we estimate about 10% of the signal, which should allow a detection, though not an improvement over *NuSTAR*. Type Ia supernovae such as the one that produced Tycho are not expected to synthesize large masses of ^{44}Ti, but asymmetric explosion models have predicted values of $(1–3) \times 10^{-5}$ $M_\odot$ (Maeda et al., 2010), or about 10% of the mass of 1.4×10^{-4} $M_\odot$ inferred for Cas A (Grefenstette et al., 2017). A similar scaling of the flux from Cas A to the distance (2.3 kpc; Chevalier et al., 1980) and age (451 years) of Tycho, and assuming 0.1 times the ^{44}Ti mass of Cas A, gives a line flux of about 6% of that of Cas A.

In addition to Cas A, two other remnants of core-collapse supernovae have ages of order a few hundred years, as inferred from expansion measurements. Kes 75 (G29.7-0.3), a combination shell SNR/PWN/pulsar system, has an age of 480 ± 50 years (Reynolds et al., 2018). At a distance of 5.8 kpc, it could produce a detectable signal. Again scaling the observed line flux from Cas A to the distance and age of Kes 75, we estimate a flux of about 7% of that of Cas A. Similarly, the remarkable iron-rich rapidly expanding SNR G350.1-0.3 (Borkowski et al., 2020) is at most 600 years old (the expansion age of the fastest-moving ejecta and an upper limit to the true age, since deceleration has certainly occurred). For an age of 600 years and a distance of 4.5 kpc, again scaling to Cas A predicts a flux of 0.027 of that of Cas A for the 68 keV line. Figure 13 shows a simulation assuming (as is not the case in Cas A!) that the titanium distribution follows that of shocked iron. The strong Fe Kα emission from G350.1-0.3 is redshifted by up to 2,600 km s^{-1}, which if true of titanium as well, would allow both the 68 and 78 keV lines to be observed, which was not the case for Cas A, potentially doubling the relative sensitivity. The required exposure times for HEX-P detections of these targets at such flux levels are too long for the proposed primary observation program, but are certainly within reach for the extended mission. We mention them here as a reminder that HEX-P can bring this unique capability to the study of supernovae.

5.2 r-process nucleosynthesis in binary NS-NS mergers

The creation of cosmic isotopes heavier than the iron group is primarily attributed to the so-called r-process, which involves rapid neutron captures compared to β-decay lifetimes (Burbidge et al., 1957; Cameron, 1957). However, it remains unclear where this nucleosynthesis occurs, as it requires neutron-rich environments with low electron fraction Y_e. Recent observations of thermal kilonova emission from ejecta produced in binary neutron-star mergers (NSMs) in gravitational wave events like GW170817 (Abbott et al., 2017) or in short gamma-ray bursts (e.g., GRB 130603B; Tanvir et al., 2013) strongly suggest a significant r-process component. In fact, these observations have established NSMs as a promising r-process site, possibly even more important than the standard case involving core-collapse supernovae (SNe) (Lattimer and Schramm, 1974). While MeV gamma-rays from r-process nuclei should provide direct evidence for NSMs, their fluxes immediately following binary NSM events are estimated to be very low (~10^{-8} photons s^{-1} cm^{-2} keV^{-1}) even at a close distance of 3 Mpc (Hotokezaka et al., 2016). This is below the sensitivity of current and near-future MeV gamma-ray missions. An alternative and more promising approach to explore the r-process site is to search for gamma-rays from long-lived r-process nuclei in Galactic NSMs (Wu et al., 2019; Korobkin et al.,

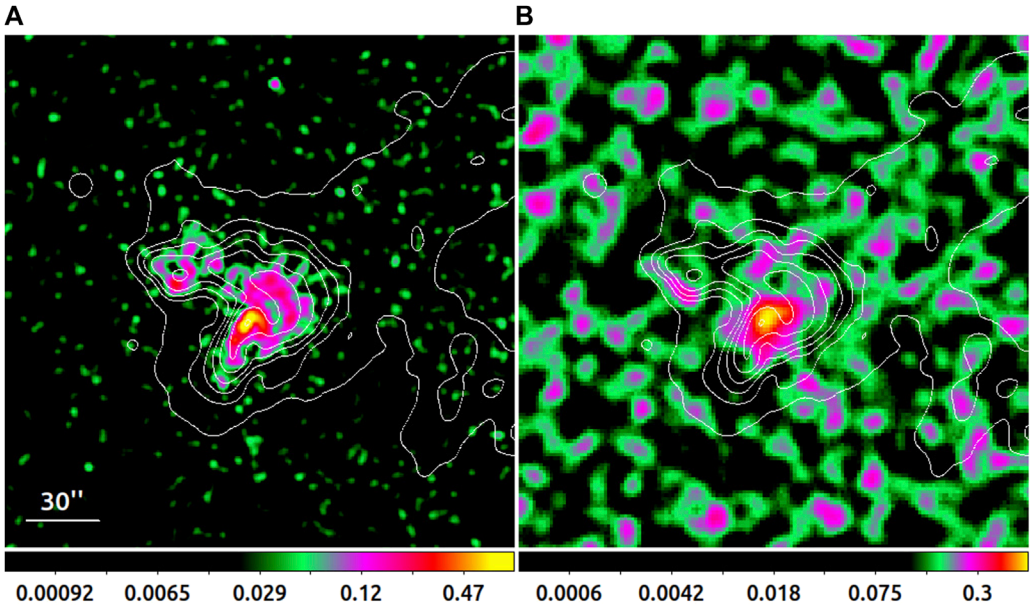

FIGURE 13
(A) Chandra Fe Kα image of G350.1–0.1 measured in the 6.3–6.8 keV band (270 ks exposure). Color bar units are counts. The white contours show the Chandra continuum image. **(B)** Simulated HEX-P image of ^{44}Ti emission from G350.1–0.1 (67–69 keV) for 2 Ms exposure. For this simulation, the Chandra Fe Kα map **(A)** was used as the input image.

2020; Wang et al., 2020; Terada et al., 2022). The radiation from r-process nuclei appears mainly in the sub-MeV band, but in older remnants, it can extend down to the hard X-ray band. The hard X-ray signals from the decay of r-process isotopes can be detected by HEX-P, making it a unique probe to study the r-process from Galactic NSMs and establishing synergy with gravitational wave observations in the multi-messenger era.

In order to assess the feasibility of detecting gamma-rays from Galactic NSMs with HEX-P, we compared the gamma-ray spectra from Galactic NSMs, at ages of τ of 100, 10^4, and 10^6 years old and located at 10 kpc, with the sensitivities of hard X-ray to gamma-ray telescopes including HEX-P (Figure 14). Since most Galactic NSMs are expected to be ~8 kpc away (Wu et al., 2019), HEX-P can detect younger NSM remnants with τ less than a few hundred years. Additionally, HEX-P may be able to detect nuclear gamma-ray lines from middle-aged NSM remnants (τ less than about a few $\times 10^3$ years), since the Doppler broadening caused by the fast motion of ejecta is much less significant than in younger remnants. Figure 14 shows that the nuclear lines from ^{229}Th (11.3 keV), ^{126}Sn (23.4 keV), ^{241}Am (26.8 keV, 59.6 keV), ^{225}Ra (40.3 keV), and ^{243}Am (43.9 keV) from Galactic NSMs with 10^4 years old are above the sensitivity of HEX-P.

Since HEX-P is not a survey-type mission, it is important to select optimal NSM candidates in advance. This can be done through a pilot survey utilizing the current hard X-ray and gamma-ray missions, such as *INTEGRAL*, *Swift*, *MAXI*, etc., or by discovering NSMs serendipitously, for instance in the HEX-P's Galactic Center

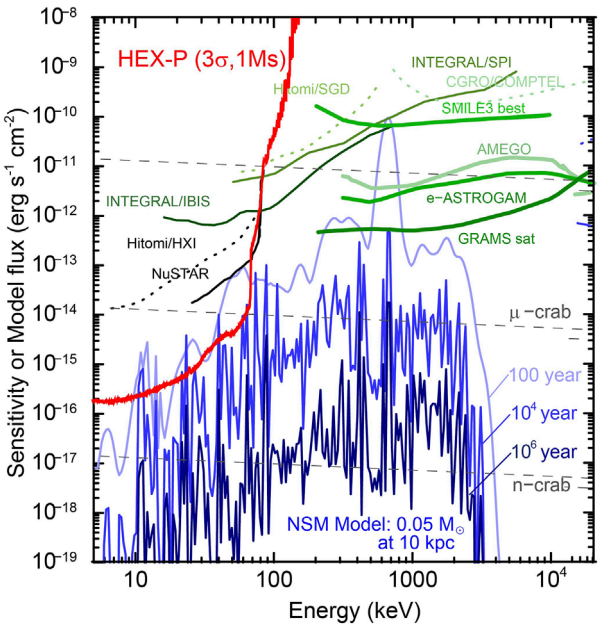

FIGURE 14
Gamma-ray spectra from NSM remnants estimated by Terada et al. (2022) at a distance of 10 kpc and with ages of 100, 10^4, and 10^6 years since the merging are shown in cyan, blue, and dark blue lines, respectively. The 3-σ sensitivities of the hard X-ray to gamma-ray missions are shown as the labeled lines. The 3-σ sensitivity of HEX-P with 1 Ms exposure is shown in red. For others, please see Figure 14 in Terada et al. (2022).

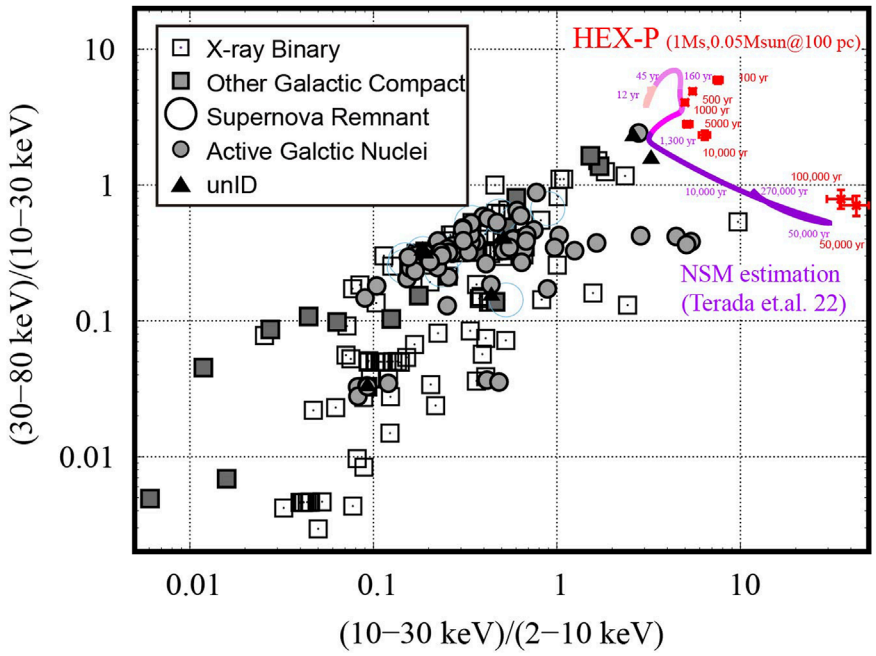

FIGURE 15
A color–color diagram of the flux ratio between the 30–80 and 10–30 keV bands versus that between the 10–30 and 2–10 keV bands. Our estimation, following the same procedure as Figure 8 in Terada et al. (2022), is shown in the purple line, and those of the X-ray objects listed in the *INTEGRAL* catalog (version 0043) are plotted in gray. The red crosses represent the expectation with 3σ errors for the NSMs at 100 pc using HEX-P with 1 Ms exposure.

survey (Mori et al., submitted to FrASS). One of the effective ways based on a pilot survey with the current gamma-ray instruments is to diagnose the spectral shape of NSMs using the color-color diagram shown in Figure 8 in Terada et al. (2022). Figure 15 displays the same diagram, but recalculated for HEX-P's energy band from 2 to 80 keV, using the simulation code adopted from Terada et al. (2022). Our simulations demonstrate that very young NSMs ($\tau < 10^3$ y) and old NSMs ($\tau > 10^4$ y) can be distinguished from other types of hard X-ray sources such as SNRs, AGNs, and XRBs. The figure also demonstrates the numerical results for the case of a nearby NSM (within 100 pc) observed by HEX-P with long exposure times (shown in red crosses in Figure 15).

Once an NSM remnant is identified by the color-color diagram analysis, a handful of nuclear lines from r-process nuclei may be detected with deeper observations of HEX-P, as already shown in Figure 14. Nuclear lines in the hard X-ray band originate mostly from nuclei in the relatively low Y_e environment, compared with those in the MeV band. Note that the hard X-ray nuclear lines are unique signatures of NSMs, while MeV gamma-ray lines could be emitted from SNe. Therefore, the hard X-ray lines potentially detectable with HEX-P, namely, ^{229}Th, ^{126}Sn, ^{241}Am, ^{225}Ra, and ^{243}Am, will provide strong evidence of r-process nucleosynthesis in NSM remnants. Among them, it is anticipated that the nuclear lines from ^{241}Am, ^{243}Am, and ^{126}Sn have constant luminosities for $\tau \sim 10^2$–10^5 years (Figure 9 in Terada et al. (2022)), yielding a few hundred photon counts with 1 Msec exposure, and therefore, making them suitable as a standard candle for estimating the source distance. Overall, searching for r-process nucleosynthesis sites in our Galaxy is a unique scientific objective of HEX-P in the 2030s that, while somewhat risky, has the potential for significant scientific gains.

6 Conclusion

The physical processes involved in the acceleration of particles at strong shocks are particularly well exhibited in shell SNRs, for nonrelativistic shocks, and in PWNe, for relativistic shocks. These processes ought to operate across the Universe, in many environments where sources are too compact to be spatially resolved. Galactic SNRs and PWNe, closely examined by HEX-P, can serve as laboratories in which to investigate details of these processes. Major breakthroughs in understanding occurred with hard X-ray observations of the famous shell SNR SN 1006, and of the even more famous Crab Nebula. A great deal more can be learned about objects in each class with the new capabilities promised by HEX-P. The simulations described above demonstrate the kinds of advances possible in the study of particular SNRs and PWNe, and of Galactic particle acceleration in general (see Mori et al., 2021 for other types of particle accelerators). The additional, unique capability of HEX-P to study nuclear-decay line emission will improve our knowledge of the ^{44}Ti distribution in Cas A, and may detect lines from other young SNRs or in the unlikely but exciting possibility of a sufficiently nearby neutron-star binary merger event. HEX-P clearly stands out as the foremost X-ray observatory for cosmic accelerators and nuclear astrophysics in the 2030s.

Data availability statement

The original contributions presented in the study are included in the article. Further inquiries may be directed to the corresponding author.

Author contributions

SR: Writing–original draft. HA: Writing–original draft. MA: Writing–original draft. JA: Writing–original draft. CF: Writing–original draft. KM: Writing–original draft. MN: Writing–original draft. JP: Writing–original draft. YT: Writing–original draft. JW: Writing–original draft. AB: Writing–review and editing. PB: Writing–review and editing. RD: Writing–review and editing. JE: Writing–review and editing. SG: Writing–review and editing. JoG: Writing–review and editing. BG: Writing–review and editing. JaG: Project administration, Writing–review and editing. CK: Writing–review and editing. SK: Writing–review and editing. BI: Writing–review and editing. KM: Project administration, Writing–review and editing. SM: Writing–review and editing. YM: Writing–review and editing. HO: Writing–review and editing. BO: Writing–review and editing. TS: Writing–review and editing. R-YS: Writing–review and editing. DS: Project administration, Writing–review and editing. NT: Writing–review and editing. GY: Writing–review and editing. AZ: Writing–review and editing.

Funding

The author(s) declare that financial support was received for the research, authorship, and/or publication of this article. The work of DS was carried out at the Jet Propulsion Laboratory, California Institute of Technology, under a contract with NASA. This work was financially supported by Japan Society for the Promotion of Science Grants-in-Aid for Scientific Research (KAKENHI) Grant Numbers, JP23H01211 (AB), 22K14064 (NT), 20K04009 (YT). HA acknowledges support from the National Research Foundation of Korea (NRF) grant funded by the Korean Government (MSIT) (NRF-2023R1A2C1002718).

Acknowledgments

We are grateful to J. Wilms, T. Dauser, C. Kirsch, M. Lorenz, L. Dauner, and the SIXTE development team for their assistance with SIXTE simulations. We thank K. Fang, L. Lu, and K. Malone for assistance.

Conflict of interest

The authors declare that the research was conducted in the absence of any commercial or financial relationships that could be construed as a potential conflict of interest.

Publisher's note

All claims expressed in this article are solely those of the authors and do not necessarily represent those of their affiliated organizations, or those of the publisher, the editors and the reviewers. Any product that may be evaluated in this article, or claim that may be made by its manufacturer, is not guaranteed or endorsed by the publisher.

References

Abbott, B. P., Abbott, R., Abbott, T. D., Acernese, F., Ackley, K., Adams, C., et al. (2017). GW170817: observation of gravitational waves from a binary neutron star inspiral. *PhRvL* 119, 161101. doi:10.1103/PhysRevLett.119.161101

Abdelmaguid, M., Gelfand, J. D., Gotthelf, E., and Straal, S. (2023). Broadband X-ray spectroscopy of the pulsar wind nebula in HESS j1640-465. *ApJ* 946, 40. doi:10.3847/1538-4357/acbd30

Abeysekara, A. U., Albert, A., Alfaro, R., Alvarez, C., Álvarez, J. D., Arceo, R., et al. (2017a). Extended gamma-ray sources around pulsars constrain the origin of the positron flux at Earth. *Science* 358, 911–914. doi:10.1126/science.aan4880

Acciari, V. A., Aliu, E., Arlen, T., Aune, T., Beilicke, M., Benbow, W., et al. (2011). Discovery of TeV gamma-ray emission from Tycho's supernova remnant. *ApJL* 730, L20. doi:10.1088/2041-8205/730/2/L20

Adams, C. B., Benbow, W., Brill, A., Brose, R., Buchovecky, M., Capasso, M., et al. (2021). VERITAS observations of the galactic center region at multi-TeV gamma-ray energies. *ApJ* 913, 115. doi:10.3847/1538-4357/abf926

Aguilar, M., Ali Cavasonza, L., Alpat, B., Ambrosi, G., Arruda, L., Attig, N., et al. (2019). Towards understanding the origin of cosmic-ray electrons. *PhRvL* 122, 101101. doi:10.1103/PhysRevLett.122.101101

Aharonian, F., Akhperjanian, A. G., Aye, K.-M., Bazer-Bachi, A. R., Beilicke, M., Benbow, W., et al. (2005). Very high energy gamma rays from the composite SNR G 0.9+0.1. *A&A* 432, L25–L29. doi:10.1051/0004-6361:200500022

Alp, D., Larsson, J., and Fransson, C. (2021). Thermal emission and radioactive lines, but No pulsar, in the broadband X-ray spectrum of supernova 1987A. *ApJ* 916, 76. doi:10.3847/1538-4357/ac052d

Alp, D., Larsson, J., Fransson, C., Indebetouw, R., Jerkstrand, A., Ahola, A., et al. (2018). The 30 Year search for the compact object in SN 1987A. *ApJ* 864, 174. doi:10.3847/1538-4357/aad739

An, H. (2019). NuSTAR hard X-ray studies of the pulsar wind nebula 3C 58. *ApJ* 876, 150. doi:10.3847/1538-4357/ab18a6

An, H., Madsen, K. K., Reynolds, S. P., Kaspi, V. M., Harrison, F. A., Boggs, S. E., et al. (2014). High-energy X-ray imaging of the pulsar wind nebula MSH 15-52: constraints on particle acceleration and transport. *ApJ* 793, 90. doi:10.1088/0004-637X/793/2/90

Arnaud, K. A. (1996). "XSPEC: the first ten years," in *Astronomical data analysis software and systems V*. Editors G. H. Jacoby, and J. Barnes (USA: IEEE), 17.

Atoyan, A., and Dermer, C. D. (2012). Gamma rays from the Tycho supernova remnant: multi-zone versus single-zone modeling. *ApJL* 749, L26. doi:10.1088/2041-8205/749/2/L26

Bamba, A., Anada, T., Dotani, T., Mori, K., Yamazaki, R., Ebisawa, K., et al. (2010). X-Ray evolution of pulsar wind nebulae. *ApJL* 719, L116–L120. doi:10.1088/2041-8205/719/2/L116

Bamba, A., Shibata, S., Tanaka, S. J., Mori, K., Uchida, H., Terada, Y., et al. (2022). Spectral break of energetic pulsar wind nebulae detected with wideband X-ray observations. *PASJ* 74, 1186–1197. doi:10.1093/pasj/psac062

Bamba, A., Yamazaki, R., Yoshida, T., Terasawa, T., and Koyama, K. (2005). A spatial and spectral study of nonthermal filaments in historical supernova remnants: observational results with Chandra. *ApJ* 621, 793–802. doi:10.1086/427620

Bandiera, R. (2008). On the X-ray feature associated with the Guitar nebula. *A&A* 490, L3–L6. doi:10.1051/0004-6361:200810666

Bandiera, R., Bucciantini, N., Martín, J., Olmi, B., and Torres, D. F. (2020). Reverberation of pulsar wind nebulae (I): impact of the medium properties and other parameters upon the extent of the compression. *MNRAS* 499, 2051–2062. doi:10.1093/mnras/staa2956

Bandiera, R., Bucciantini, N., Martín, J., Olmi, B., and Torres, D. F. (2023). Reverberation of pulsar wind nebulae - II. Anatomy of the 'thin-shell' evolution. *MNRAS* 520, 2451–2472. doi:10.1093/mnras/stad134

Berezhko, E. G., Ksenofontov, L. T., and Völk, H. J. (2013). The nature of gamma-ray emission of Tycho's supernova remnant. *ApJ* 763, 14. doi:10.1088/0004-637X/763/1/14

Bleeker, J. A. M., Willingale, R., van der Heyden, K., Dennerl, K., Kaastra, J. S., Aschenbach, B., et al. (2001). Cassiopeia A: on the origin of the hard X-ray continuum and the implication of the observed O VIII Ly-α/Ly-β distribution. *A&A* 365, L225–L230. doi:10.1051/0004-6361:20000048

Borkowski, K. J., Miltich, W., and Reynolds, S. P. (2020). Expansion and age of the supernova remnant g350.1-0.3: high-velocity iron ejecta from a core-collapse event. *ApJL* 905, L19. doi:10.3847/2041-8213/abcda7

Borkowski, K. J., Reynolds, S. P., Green, D. A., Hwang, U., Petre, R., Krishnamurthy, K., et al. (2010). Radioactive scandium in the youngest galactic supernova remnant G1.9+0.3. *ApJL* 724, L161–L165. –L165. doi:10.1088/2041-8205/724/2/L161

Bucciantini, N., Blondin, J. M., Del Zanna, L., and Amato, E. (2003). Spherically symmetric relativistic MHD simulations of pulsar wind nebulae in supernova remnants. *A&A* 405, 617–626. doi:10.1051/0004-6361:20030624

Burbidge, E. M., Burbidge, G. R., Fowler, W. A., and Hoyle, F. (1957). Synthesis of the elements in stars. *Rev. Mod. Phys.* 29, 547–650. doi:10.1103/RevModPhys.29.547

Burgess, D. A., Mori, K., Gelfand, J. D., Hailey, C. J., Tokayer, Y. M., Woo, J., et al. (2022). The eel pulsar wind nebula: a PeVatron-candidate origin for hawc j1826-128 and hess j1826-130. *ApJ* 930, 148. doi:10.3847/1538-4357/ac650a

Cameron, A. G. W. (1957). Nuclear reactions in stars and nucleogenesis. *PASP* 69, 201. doi:10.1086/127051

Camilo, F., Ransom, S. M., Gaensler, B. M., and Lorimer, D. R. (2009). Discovery of the energetic pulsar j1747-2809 in the supernova remnant G0.9+0.1. *ApJL* 700, L34–L38. –L38. doi:10.1088/0004-637X/700/1/L34

Cao, Z., Aharonian, F., An, Q., Axikegu, Bai, Y. X., Bao, Y. W., et al. (2023). *The first LHAASO catalog of gamma-ray sources*, arXiv:2305.1703010.48550/arXiv

Cao, Z., Aharonian, F. A., An, Q., Axikegu, Bai, L. X., Bai, Y. X., et al. (2021). Ultrahigh-energy photons up to 1.4 petaelectronvolts from 12 γ-ray Galactic sources. *Nature* 594, 33–36. doi:10.1038/s41586-021-03498-z

Carlton, A. K., Borkowski, K. J., Reynolds, S. P., Hwang, U., Petre, R., Green, D. A., et al. (2011). Expansion of the youngest galactic supernova remnant G1.9+0.3. *ApJL* 737, L22. doi:10.1088/2041-8205/737/1/L22

Cherenkov Telescope Array Consortium, T. (2023). *Sensitivity of the Cherenkov telescope Array to TeV photon emission from the large magellanic cloud*. arXiv:2305.1670710.48550/arXiv.

Chevalier, R. A., Kirshner, R. P., and Raymond, J. C. (1980). The optical emission from a fast shock wave with application to supernova remnants. *ApJ* 235, 186–195. doi:10.1086/157623

Cholis, I., and Hooper, D. (2013). Dark matter and pulsar origins of the rising cosmic ray positron fraction in light of new data from the AMS. *PhRvD* 88, 023013. doi:10.1103/PhysRevD.88.023013

Cigan, P., Matsuura, M., Gomez, H. L., Indebetouw, R., Abellán, F., Gabler, M., et al. (2019). High angular resolution ALMA images of dust and molecules in the SN 1987A ejecta. *ApJ* 886, 51. doi:10.3847/1538-4357/ab4b46

Dauser, T., Falkner, S., Lorenz, M., Kirsch, C., Peille, P., Cucchetti, E., et al. (2019). SIXTE: a generic X-ray instrument simulation toolkit. *A&A* 630, A66. doi:10.1051/0004-6361/201935978

Della Torre, S., Gervasi, M., Rancoita, P. G., Rozza, D., and Treves, A. (2015). Pulsar Wind Nebulae as a source of the observed electron and positron excess at high energy: the case of Vela-X. *J. High Energy Astrophysics* 8, 27–34. doi:10.1016/j.jheap.2015.08.001

Del Zanna, L., Amato, E., and Bucciantini, N. (2004). Axially symmetric relativistic MHD simulations of Pulsar Wind Nebulae in Supernova Remnants. On the origin of torus and jet-like features. *A&A* 421, 1063–1073. doi:10.1051/0004-6361:20035936

de Oña Wilhelmi, E., López-Coto, R., Amato, E., and Aharonian, F. (2022). On the potential of bright, young pulsars to power ultrahigh gamma-ray sources. *ApJL* 930, L2. doi:10.3847/2041-8213/ac66cf

Diesing, R., and Caprioli, D. (2021). Steep cosmic-ray spectra with revised diffusive shock acceleration. *ApJ* 922, 1. doi:10.3847/1538-4357/ac22fe

Eraerds, T., Antonelli, V., Davis, C., Hall, D., Hetherington, O., Holland, A., et al. (2021). Enhanced simulations on the athena/wide field imager instrumental background. *J. Astronomical Telesc. Instrum. Syst.* 7, 034001. doi:10.1117/1.JATIS.7.3.034001

Eriksen, K. A., Hughes, J. P., Badenes, C., Fesen, R., Ghavamian, P., Moffett, D., et al. (2011). Evidence for particle acceleration to the knee of the cosmic ray spectrum in Tycho's supernova remnant. *ApJL* 728, L28. doi:10.1088/2041-8205/728/2/L28

Fiori, M., Zampieri, L., Burtovoi, A., Caraveo, P., and Tibaldo, L. (2020). Constraining models of the pulsar wind nebula in SNR G0.9+0.1 via simulation of its detection properties using the Cherenkov Telescope Array. *MNRAS* 499, 3494–3509. doi:10.1093/mnras/staa3039

Frank, K. A., Zhekov, S. A., Park, S., McCray, R., Dwek, E., and Burrows, D. N. (2016). Chandra observes the end of an era in SN 1987A. *ApJ* 829, 40. doi:10.3847/0004-637X/829/1/40

Fraschetti, F., Katsuda, S., Sato, T., Jokipii, J. R., and Giacalone, J. (2018). Vortical amplification of the magnetic field at an inward shock of supernova remnant cassiopeia a. *Phys. Rev. Lett.* 120, 251101. doi:10.1103/PhysRevLett.120.251101

Fryer, C. L., Burns, E., Hungerford, A., Safi-Harb, S., Wollaeger, R. T., Miller, R. S., et al. (2023). Multi-messenger diagnostics of the engine behind core-collapse supernovae. *arXiv e-prints* , arXiv:2305.0613410.48550/arXiv.2305.06134

Gaensler, B. M., Pivovaroff, M. J., and Garmire, G. P. (2001). [ITAL]Chandra[/ITAL] observations of the pulsar wind nebula in supernova remnant G0.9+0.1. *ApJL* 556, L107–L111. –L111. doi:10.1086/322982

Gelfand, J. D., Slane, P. O., and Zhang, W. (2009). A dynamical model for the evolution of a pulsar wind nebula inside a nonradiative supernova remnant. *ApJ* 703, 2051–2067. –2067. doi:10.1088/0004-637X/703/2/2051

Giordano, F., Naumann-Godo, M., Ballet, J., Bechtol, K., Funk, S., Lande, J., et al. (2012). Fermi large area telescope detection of the young supernova remnant Tycho. *ApJL* 744, L2. doi:10.1088/2041-8205/744/1/L2

Gotthelf, E. V., Safi-Harb, S., Straal, S. M., and Gelfand, J. D. (2021). X-ray spectroscopy of the highly magnetized pulsar PSR j1846-0258, its wind nebula, and hosting supernova remnant kes 75. *ApJ* 908, 212. doi:10.3847/1538-4357/abd32b

Greco, E., Miceli, M., Orlando, S., Olmi, B., Bocchino, F., Nagataki, S., et al. (2021). Indication of a pulsar wind nebula in the hard X-ray emission from SN 1987A. *ApJL* 908, L45. doi:10.3847/2041-8213/abdf5a

Greco, E., Miceli, M., Orlando, S., Olmi, B., Bocchino, F., Nagataki, S., et al. (2022). Additional evidence for a pulsar wind nebula in the heart of SN 1987A from multiepoch X-ray data and MHD modeling. *ApJ* 931, 132. doi:10.3847/1538-4357/ac679d

Grefenstette, B. W., Fryer, C. L., Harrison, F. A., Boggs, S. E., DeLaney, T., Laming, J. M., et al. (2017). The distribution of radioactive ^{44}Ti in cassiopeia A. *ApJ* 834, 19. doi:10.3847/1538-4357/834/1/19

Grefenstette, B. W., Harrison, F. A., Boggs, S. E., Reynolds, S. P., Fryer, C. L., Madsen, K. K., et al. (2014). Asymmetries in core-collapse supernovae from maps of radioactive ^{44}Ti in CassiopeiaA. *Nature* 506, 339–342. doi:10.1038/nature12997

Grefenstette, B. W., Reynolds, S. P., Harrison, F. A., Humensky, T. B., Boggs, S. E., Fryer, C. L., et al. (2015). Locating the most energetic electrons in cassiopeia A. *ApJ* 802, 15. doi:10.1088/0004-637X/802/1/15

Guest, B. T., Safi-Harb, S., and Tang, X. (2019). The deepest Chandra X-ray study of the plerionic supernova remnant G21.5-0.9. *MNRAS* 482, 1031–1042. doi:10.1093/mnras/sty2635

Halpern, J. P., Tomsick, J. A., Gotthelf, E. V., Camilo, F., Ng, C. Y., Bodaghee, A., et al. (2014). Discovery of X-ray pulsations from the INTEGRAL source IGR j11014-6103. *ApJL* 795, L27. doi:10.1088/2041-8205/795/2/L27

Hanbury Brown, R., and Hazard, C. (1952). Radio-frequency radiation from Tycho brahe's supernova (A.D. 1572). *Nature* 170, 364–365. doi:10.1038/170364a0

Harrison, F. A., Craig, W. W., Christensen, F. E., Hailey, C. J., Zhang, W. W., Boggs, S. E., et al. (2013). The nuclear spectroscopic telescope Array (NuSTAR) high-energy X-ray mission. *ApJ* 770, 103. doi:10.1088/0004-637X/770/2/103

Hattori, S., Straal, S. M., Zhang, E., Temim, T., Gelfand, J. D., and Slane, P. O. (2020). The nonstandard properties of a "standard" PWN: unveiling the mysteries of PWN g21.5-0.9 using its IR and X-ray emission. *ApJ* 904, 32. doi:10.3847/1538-4357/abba32

Helder, E. A., and Vink, J. (2008). Characterizing the nonthermal emission of cassiopeia A. *ApJ* 686, 1094–1102. doi:10.1086/591242

H.E.S.S. Collaboration, Abdalla, H., Abramowski, A., Aharonian, F., Ait Benkhali, F., Akhperjanian, A. G., Andersson, T., et al. (2018). The population of TeV pulsar wind nebulae in the H.E.S.S. Galactic Plane Survey. *A&A* 612, A2. doi:10.1051/0004-6361/201629377

H.E.S.S. Collaboration, Aharonian, F., Ait Benkhali, F., Aschersleben, J., Ashkar, H., Backes, M., Barbosa Martins, V., et al. (2023). Detection of extended γ-ray emission around the Geminga pulsar with H.E.S.S *A&A* 673, A148. doi:10.1051/0004-6361/202245776

Helfand, D. J., and Becker, R. H. (1987). G0.9+0.1 and the emerging class of composite supernova remnants. *ApJ* 314, 203. doi:10.1086/165050

Hitomi Collaboration, Aharonian, F., Akamatsu, H., Akimoto, F., Allen, S. W., Angelini, L., Audard, M., et al. (2018). Hitomi X-ray observation of the pulsar wind nebula G21.5-0.9. *PASJ* 70, 38. doi:10.1093/pasj/psy027

Holler, M., Schöck, F. M., Eger, P., Kießling, D., Valerius, K., and Stegmann, C. (2012). Spatially resolved X-ray spectroscopy and modeling of the nonthermal emission of the pulsar wind nebula in G0.9+0.1. *A&A* 539, A24. doi:10.1051/0004-6361/201118121

Hotokezaka, K., Wanajo, S., Tanaka, M., Bamba, A., Terada, Y., and Piran, T. (2016). Radioactive decay products in neutron star merger ejecta: heating efficiency and γ-ray emission. *MNRAS* 459, 35–43. doi:10.1093/mnras/stw404

Hwang, U., Decourchelle, A., Holt, S. S., and Petre, R. (2002). Thermal and nonthermal X-ray emission from the forward shock in Tycho's supernova remnant. *ApJ* 581, 1101–1115. doi:10.1086/344366

Jansen, F., Lumb, D., Altieri, B., Clavel, J., Ehle, M., Erd, C., et al. (2001). XMM-Newton observatory. I. The spacecraft and operations. *A&A* 365, L1–L6. doi:10.1051/0004-6361:20000036

Kargaltsev, O., Pavlov, G. G., Klingler, N., and Rangelov, B. (2017). Pulsar wind nebulae created by fast-moving pulsars. *J. Plasma Phys.* 83, 635830501. doi:10.1017/S0022377817000630

Kennel, C. F., and Coroniti, F. V. (1984a). Confinement of the Crab pulsar's wind by its supernova remnant. *ApJ* 283, 694–709. doi:10.1086/162356

Kennel, C. F., and Coroniti, F. V. (1984b). Magnetohydrodynamic model of Crab nebula radiation. *ApJ* 283, 710–730. doi:10.1086/162357

Klingler, N., Hare, J., Kargaltsev, O., Pavlov, G. G., and Tomsick, J. (2022). *A NuSTAR and Chandra investigation of the misaligned outflow of PSR j1101-6101 and the Lighthouse pulsar wind nebula*. arXiv:2212.0395210.48550/arXiv.2212.03952.

Kolb, C., Blondin, J., Slane, P., and Temim, T. (2017). Evolution of a pulsar wind nebula within a composite supernova remnant. *ApJ* 844, 1. doi:10.3847/1538-4357/aa75ce

Komissarov, S. S., and Lyubarsky, Y. E. (2004). Synchrotron nebulae created by anisotropic magnetized pulsar winds. *MNRAS* 349, 779–792. doi:10.1111/j.1365-2966.2004.07597.x

Korobkin, O., Hungerford, A. M., Fryer, C. L., Mumpower, M. R., Misch, G. W., Sprouse, T. M., et al. (2020). Gamma rays from kilonova: a potential probe of r-process nucleosynthesis. *ApJ* 889, 168. doi:10.3847/1538-4357/ab64d8

Krause, O., Birkmann, S. M., Usuda, T., Hattori, T., Goto, M., Rieke, G. H., et al. (2008a). The cassiopeia A supernova was of type IIb. *Science* 320, 1195–1197. doi:10.1126/science.1155788

Krause, O., Tanaka, M., Usuda, T., Hattori, T., Goto, M., Birkmann, S., et al. (2008b). Tycho Brahe's 1572 supernova as a standard typeIa as revealed by its light-echo spectrum. *Nature* 456, 617–619. doi:10.1038/nature07608

Lattimer, J. M., and Schramm, D. N. (1974). Black-hole-neutron-star collisions. *ApJL* 192, L145. doi:10.1086/181612

Lopez, L. A., Grefenstette, B. W., Reynolds, S. P., An, H., Boggs, S. E., Christensen, F. E., et al. (2015). A spatially resolved study of the synchrotron emission and titanium in Tycho's supernova remnant using NuSTAR. *ApJ* 814, 132. doi:10.1088/0004-637X/814/2/132

Madsen, K. K., García, J. A., Stern, D., Armini, R., Basso, S., Coutinho, D., et al. (2023). The High Energy X-ray Probe (HEX-P): instrument and mission profile. arXiv.2312.04678.

Madsen, K. K., Beardmore, A. P., Forster, K., Guainazzi, M., Marshall, H. L., Miller, E. D., et al. (2017a). IACHEC cross-calibration of Chandra, NuSTAR, Swift, suzaku, XMM-Newton with 3C 273 and PKS 2155-304. *AJ* 153, 2. doi:10.3847/1538-3881/153/1/2

Madsen, K. K., Christensen, F. E., Craig, W. W., Forster, K. W., Grefenstette, B. W., Harrison, F. A., et al. (2017b). *Observational artifacts of NuSTAR: ghost rays and stray light*. arXiv:1711.0271910.48550/arXiv. 1711.02719.

Madsen, K. K., Fryer, C. L., Grefenstette, B. W., Lopez, L. A., Reynolds, S., and Zoglauer, A. (2020). NuSTAR observations of g11.2-0.3. *ApJ* 889, 23. doi:10.3847/1538-4357/ab54ca

Madsen, K. K., Reynolds, S., Harrison, F., An, H., Boggs, S., Christensen, F. E., et al. (2015a). Broadband X-ray imaging and spectroscopy of the Crab nebula and pulsar with NuSTAR. *ApJ* 801, 66. doi:10.1088/0004-637X/801/1/66

Maeda, K., Röpke, F. K., Fink, M., Hillebrandt, W., Travaglio, C., and Thielemann, F. K. (2010). Nucleosynthesis in two-dimensional delayed detonation models of type Ia supernova explosions. *ApJ* 712, 624–638. doi:10.1088/0004-637X/712/1/624

Maeda, Y., Uchiyama, Y., Bamba, A., Kosugi, H., Tsunemi, H., Helder, E. A., et al. (2009). Suzaku X-ray imaging and spectroscopy of cassiopeia A. *PASJ* 61, 1217–1228. doi:10.1093/pasj/61.6.1217

Magkotsios, G., Timmes, F. X., Hungerford, A. L., Fryer, C. L., Young, P. A., and Wiescher, M. (2010). Trends in ^{44}Ti and ^{56}Ni from core-collapse supernovae. *ApJS* 191, 66–95. doi:10.1088/0067-0049/191/1/66

Manconi, S., Di Mauro, M., and Donato, F. (2020). Contribution of pulsars to cosmic-ray positrons in light of recent observation of inverse-Compton halos. *PhRvD* 102, 023015. doi:10.1103/PhysRevD.102.023015

Mori, K., An, H., Burgess, D., Capasso, M., Dingus, B., Gelfand, J., et al. (2021). *NuSTAR broad-band X-ray observational campaign of energetic pulsar wind nebulae in synergy with VERITAS, HAWC and Fermi gamma-ray telescopes*. arXiv:2108.00557.

Mori, K., Burrows, D. N., Hester, J. J., Pavlov, G. G., Shibata, S., and Tsunemi, H. (2004). Spatial variation of the X-ray spectrum of the Crab nebula. *ApJ* 609, 186–193. doi:10.1086/421011

Ng, C. Y., and Romani, R. W. (2004). Fitting pulsar wind tori. *ApJ* 601, 479–484. doi:10.1086/380486

Nynka, M., Hailey, C. J., Reynolds, S. P., An, H., Baganoff, F. K., Boggs, S. E., et al. (2014). NuSTAR study of hard X-ray morphology and spectroscopy of PWN g21.5-0.9. *ApJ* 789, 72. doi:10.1088/0004-637X/789/1/72

Okuno, T., Tanaka, T., Uchida, H., Aharonian, F. A., Uchiyama, Y., Tsuru, T. G., et al. (2020). Time variability of nonthermal X-ray stripes in Tycho's supernova remnant with Chandra. *ApJ* 894, 50. doi:10.3847/1538-4357/ab837e

Olmi, B., and Bucciantini, N. (2019). On the origin of jet-like features in bow shock pulsar wind nebulae. *MNRAS* 490, 3608–3615. doi:10.1093/mnras/stz2819

Olmi, B., and Bucciantini, N. (2023). The dawes review 11: from young to old: the evolutionary path of pulsar wind nebulae. *PASA* 40, e007. doi:10.1017/pasa.2023.5

Orlando, S., Wongwathanarat, A., Janka, H. T., Miceli, M., Nagataki, S., Ono, M., et al. (2022). Evidence for past interaction with an asymmetric circumstellar shell in the young SNR Cassiopeia A. *A&A* 666, A2. A2. doi:10.1051/0004-6361/202243258

Parizot, E., Marcowith, A., Ballet, J., and Gallant, Y. A. (2006). Observational constraints on energetic particle diffusion in young supernovae remnants: amplified magnetic field and maximum energy. *A&A* 453, 387–395. doi:10.1051/0004-6361:20064985

Park, J., Kim, C., Woo, J., An, H., Mori, K., Reynolds, S. P., et al. (2023a). A broadband X-ray study of the rabbit pulsar wind nebula powered by PSR j1418-6058. *ApJ* 945, 66. doi:10.3847/1538-4357/acba0e

Park, J., Kim, C., Woo, J., An, H., Mori, K., Reynolds, S. P., et al. (2023b). X-ray studies of the pulsar PSR j1420-6048 and its TeV pulsar wind nebula in the kookaburra region. *ApJ* 945, 33. doi:10.3847/1538-4357/acb1b0

Pavan, L., Pühlhofer, G., Bordas, P., Audard, M., Balbo, M., Bozzo, E., et al. (2016). Closer view of the IGR J11014-6103 outflows. *A&A* 591, A91. doi:10.1051/0004-6361/201527703

Porquet, D., Decourchelle, A., and Warwick, R. S. (2003). XMM-Newton spectral analysis of the Pulsar Wind Nebula within the composite SNR G0.9+0.1. *A&A* 401, 197–203. doi:10.1051/0004-6361:20021670

Porter, T. A., Jóhannesson, G., and Moskalenko, I. V. (2022). The GALPROP cosmic-ray propagation and nonthermal emissions framework: release v57. *ApJS* 262, 30. doi:10.3847/1538-4365/ac80f6

Pravdo, S. H., and Smith, B. W. (1979). X-ray evidence for electron-ion equilibrium and ionization nonequilibrium in Young supernova remnants. *ApJL* 234, L195. doi:10.1086/183138

Renaud, M., Marandon, V., Gotthelf, E. V., Rodriguez, J., Terrier, R., Mattana, F., et al. (2010). Discover of a highly eneregtic pulsar associated with igr j14003–6326 in the young uncataloged galaactic supernova remnant G310.6–1.6. *ApJ* 716, 663–670. doi:10.1088/0004-637X/716/1/663

Reynolds, S. P. (2009). Synchrotron-loss spectral breaks in pulsar-wind nebulae and extragalactic jets. *ApJ* 703, 662–670. doi:10.1088/0004-637X/703/1/662

Reynolds, S. P. (2016). Hard X-ray emission from pulsar-wind nebulae. *J. Plasma Phys.* 82, 635820501. doi:10.1017/S0022377816000751

Reynolds, S. P., Borkowski, K. J., Green, D. A., Hwang, U., Harrus, I., and Petre, R. (2008). The youngest galactic supernova remnant: G1.9+0.3. *ApJL* 680, L41–L44. doi:10.1086/589570

Reynolds, S. P., Borkowski, K. J., Green, D. A., Hwang, U., Harrus, I., and Petre, R. (2009). X-ray spectral variations in the youngest galactic supernova remnant G1.9+0.3. *ApJL* 695, L149–L153. doi:10.1088/0004-637X/695/2/L149

Reynolds, S. P., Borkowski, K. J., and Gwynne, P. H. (2018). Expansion and brightness changes in the pulsar-wind nebula in the composite supernova remnant Kes 75. *ApJ* 856, 133. doi:10.3847/1538-4357/aab3d3

Reynolds, S., An, H., Abdelmaguid, M., Alford, J., Fryer, C., Mori, K., et al. (2023). High-energy astrophysics research enabled by the probe-class mission concept HEX-P. Front. Astron. Space Sci. 10. doi:10.3389/fspas.2023.1321278

Reynolds, S. P., and Chevalier, R. A. (1984). Evolution of pulsar-driven supernova remnants. *ApJ* 278, 630–648. doi:10.1086/161831

Reynoso, E. M., Moffett, D. A., Goss, W. M., Dubner, G. M., Dickel, J. R., Reynolds, S. P., et al. (1997). A VLA study of the expansion of Tycho's supernova remnant. *ApJ* 491, 816–828. doi:10.1086/304997

Sato, T., Katsuda, S., Morii, M., Bamba, A., Hughes, J. P., Maeda, Y., et al. (2018). X-ray measurements of the particle acceleration properties at inward shocks in Cassiopeia A. *ApJ* 853, 46. doi:10.3847/1538-4357/aaa021

Sironi, L., and Spitkovsky, A. (2009). Particle acceleration in relativistic magnetized collisionless pair shocks: dependence of shock acceleration on magnetic obliquity. *ApJ* 698, 1523–1549. doi:10.1088/0004-637X/698/2/1523

Sironi, L., and Spitkovsky, A. (2014). Relativistic reconnection: an efficient source of non-thermal particles. *ApJL* 783, L21. doi:10.1088/2041-8205/783/1/L21

Sudoh, T., Linden, T., and Beacom, J. F. (2019). TeV halos are everywhere: prospects for new discoveries. *PhRvD* 100, 043016. doi:10.1103/PhysRevD.100.043016

Tanaka, S. J., and Takahara, F. (2011). Study of four young TeV pulsar wind nebulae with a spectral evolution model. *ApJ* 741, 40. doi:10.1088/0004-637X/741/1/40

Tanvir, N. R., Levan, A. J., Fruchter, A. S., Hjorth, J., Hounsell, R. A., Wiersema, K., et al. (2013). A 'kilonova' associated with the short-duration γ-ray burst GRB 130603B. *Nature* 500, 547–549. doi:10.1038/nature12505

Terada, Y., Miwa, Y., Ohsumi, H., Fujimoto, S.-i., Katsuda, S., Bamba, A., et al. (2022). Gamma-ray diagnostics of r-process nucleosynthesis in the remnants of galactic binary neutron-star mergers. *ApJ* 933, 111. doi:10.3847/1538-4357/ac721f

Torres, D. F., Cillis, A., Martín, J., and de Oña Wilhelmi, E. (2014). Time-dependent modeling of TeV-detected, young pulsar wind nebulae. *J. High Energy Astrophysics* 1, 31–62. doi:10.1016/j.jheap.2014.02.001

Uchiyama, Y., and Aharonian, F. A. (2008). Fast variability of nonthermal X-ray emission in cassiopeia A: probing electron acceleration in reverse-shocked ejecta. *ApJL* 677, L105–L108. doi:10.1086/588190

Vance, G. S., Young, P. A., Fryer, C. L., and Ellinger, C. I. (2020). Titanium and iron in the cassiopeia A supernova remnant. *ApJ* 895, 82. doi:10.3847/1538-4357/ab8ade

Van Etten, A., and Romani, R. W. (2011). Multi-zone modeling of the pulsar wind nebula hess j 1825–137. *Astrophysical J.* 742, 62. doi:10.1088/0004-637x/742/2/62

Vink, J. (2012). Supernova remnants: the X-ray perspective. *AAPR* 20, 49. doi:10.1007/s00159-011-0049-1

Vink, J., Kaastra, J. S., Bleeker, J. A. M., and Bloemen, H. (2000). The hard X-ray emission and 44ti emission of Cas A. *Adv. Space Res.* 25, 689–694. doi:10.1016/S0273-1177(99)00823-6

Vink, J., Prokhorov, D., Ferrazzoli, R., Slane, P., Zhou, P., Asakura, K., et al. (2022). X-ray polarization detection of cassiopeia A with IXPE. *ApJ* 938, 40. doi:10.3847/1538-4357/ac8b7b

Wang, X., N3AS Collaboration, Vassh, N., FIRE collaboration, Sprouse, T., Mumpower, M., Vogt, R., Randrup, J., et al. (2020). MeV gamma rays from fission: a distinct signature of actinide production in neutron star mergers. *ApJL* 903, L3. doi:10.3847/2041-8213/abbe18

Warren, J. S., Hughes, J. P., Badenes, C., Ghavamian, P., McKee, C. F., Moffett, D., et al. (2005). Cosmic-ray acceleration at the forward shock in Tycho's supernova remnant: evidence from Chandra X-ray observations. *ApJ* 634, 376–389. doi:10.1086/496941

Wik, D. R., Hornstrup, A., Molendi, S., Madejski, G., Harrison, F. A., Zoglauer, A., et al. (2014). NuSTAR observations of the bullet cluster: constraints on inverse compton emission. *ApJ* 792, 48. doi:10.1088/0004-637X/792/1/48

Wongwathanarat, A., Janka, H.-T., Müller, E., Pllumbi, E., and Wanajo, S. (2017). Production and distribution of ^{44}Ti and ^{56}Ni in a three-dimensional supernova model resembling cassiopeia A. *ApJ* 842, 13. doi:10.3847/1538-4357/aa72de

Woo, J., An, H., Gelfand, J. D., Hailey, C. J., Mori, K., Mukherjee, R., et al. (2023). *Hard X-ray observation and multiwavelength study of the PeVatron candidate pulsar wind nebula "Dragonfly"*. arXiv:2306.0734710. 48550/arXiv.2306.07347.

Wu, M.-R., Banerjee, P., Metzger, B. D., Martínez-Pinedo, G., Aramaki, T., Burns, E., et al. (2019). Finding the remnants of the Milky way's last neutron star mergers. *ApJ* 880, 23. doi:10.3847/1538-4357/ab2593

Xi, S.-Q., Liu, R.-Y., Huang, Z.-Q., Fang, K., and Wang, X.-Y. (2019). GeV observations of the extended pulsar wind nebulae constrain the pulsar interpretations of the cosmic-ray positron excess. *ApJ* 878, 104. doi:10.3847/1538-4357/ab20c9

Yüksel, H., Kistler, M. D., and Stanev, T. (2009). TeV gamma rays from geminga and the origin of the GeV positron excess. *PhRvL* 103, 051101. doi:10.1103/PhysRevLett.103.051101

Zoglauer, A., Reynolds, S. P., An, H., Boggs, S. E., Christensen, F. E., Craig, W. W., et al. (2015). The hard X-ray view of the young supernova remnant G1.9+0.3. *ApJ* 798, 98. doi:10.1088/0004-637X/798/2/98

frontiers | Frontiers in Astronomy and Space Sciences

TYPE Original Research
PUBLISHED 05 January 2024
DOI 10.3389/fspas.2023.1308056

Check for updates

OPEN ACCESS

EDITED BY
Paola Marziani,
Osservatorio Astronomico di Padova (INAF), Italy

REVIEWED BY
Pierre-olivier Petrucci,
UMR5274 Institut de Planétologie et d'Astrophysique de Grenoble (IPAG), France
Thanassis Akylas,
National Observatory of Athens, Greece

*CORRESPONDENCE
Elias Kammoun,
ekammoun.astro@gmail.com

RECEIVED 05 October 2023
ACCEPTED 11 December 2023
PUBLISHED 05 January 2024

CITATION
Kammoun E, Lohfink AM, Masterson M, Wilkins DR, Zhao X, Balokovic M, Boorman PG, Connors R, Coppi P, Fabian A, García JA, Madsen KK, Rodriguez Cavero N, Sridhar N, Stern D, Tomsick J, Wevers T, Walton DJ, Bianchi S, Buchner J, Civano FM, Lanzuisi G, Mallick L, Matt G, Merloni A, Nardini E, Piotrowska JM, Ricci C, Wong K-W and Zoghbi A (2024), The high energy X-ray probe (HEX-P): probing the physics of the X-ray corona in active galactic nuclei.
Front. Astron. Space Sci. 10:1308056.
doi: 10.3389/fspas.2023.1308056

COPYRIGHT
© 2024 Kammoun, Lohfink, Masterson, Wilkins, Zhao, Balokovic, Boorman, Connors, Coppi, Fabian, García, Madsen, Rodriguez Cavero, Sridhar, Stern, Tomsick, Wevers, Walton, Bianchi, Buchner, Civano, Lanzuisi, Mallick, Matt, Merloni, Nardini, Piotrowska, Ricci, Wong and Zoghbi. This is an open-access article distributed under the terms of the Creative Commons Attribution License (CC BY). The use, distribution or reproduction in other forums is permitted, provided the original author(s) and the copyright owner(s) are credited and that the original publication in this journal is cited, in accordance with accepted academic practice. No use, distribution or reproduction is permitted which does not comply with these terms.

The high energy X-ray probe (HEX-P): probing the physics of the X-ray corona in active galactic nuclei

Elias Kammoun[1,2,3]*, Anne M. Lohfink[4], Megan Masterson[5], Dan R. Wilkins[6], Xiurui Zhao[7], Mislav Balokovic[8,9], Peter G. Boorman[10], Riley Connors[11], Paolo Coppi[12], Andrew Fabian[13], Javier A. García[10,14], Kristin K. Madsen[14], Nicole Rodriguez Cavero[15], Navin Sridhar[10,16], Daniel Stern[17], John Tomsick[18], Thomas Wevers[1,9], Dominic J. Walton[20], Stefano Bianchi[1], Johannes Buchner[21], Francesca M. Civano[14], Giorgio Lanzuisi[22], Labani Mallick[10,23,24], Giorgio Matt[1], Andrea Merloni[21], Emanuele Nardini[3], Joanna M. Piotrowska[10], Claudio Ricci[25,26], Ka-Wah Wong[27] and Abderahmen Zoghbi[28,29,30]

[1]Roma Tre University, Rome, Italy, [2]UMR5277 Institut de Recherche en Astrophysique et Planétologie (IRAP), Toulouse, France, [3]Osservatorio Astrofisico di Arcetri (INAF), Florence, Tuscany, Italy, [4]Department of Physics, College of Letters and Science, Montana State University, Bozeman, MT, United States, [5]MIT Kavli Institute for Astrophysics and Space Research, School of Science, Massachusetts Institute of Technology, Cambridge, MA, United States, [6]Kavli Institute for Particle Astrophysics and Cosmology, Stanford University, Stanford, CA, United States, [7]Center for Astrophysics, Harvard University, Cambridge, MA, United States, [8]Center for Astronomy and Astrophysics, Yale University, New Haven, CT, United States, [9]Department of Physics, Faculty of Arts and Sciences, Yale University, New Haven, CT, United States, [10]California Institute of Technology, Pasadena, CA, United States, [11]Department of Astrophysics and Planetary Science, Villanova University, Villanova, PA, United States, [12]Department of Astronomy, Faculty of Arts and Sciences, Yale University, New Haven, CT, United States, [13]Institute of Astronomy, Faculty of Physics and Chemistry, School of Physical Sciences, University of Cambridge, Cambridge, England, United Kingdom, [14]X-ray Astrophysics Laboratory, Goddard Space Flight Center, National Aeronautics and Space Administration, Greenbelt, MD, United States, [15]Department of Physics, Faculty of Arts and Sciences, Washington University in St. Louis, St. Louis, MO, United States, [16]Department of Astronomy, Columbia University, New York, NY, United States, [17]NASA Jet Propulsion Laboratory (JPL), La Cañada Flintridge, CA, United States, [18]Space Sciences Laboratory, University of California, Berkeley, Berkeley, CA, United States, [19]Space Telescope Science Institute (NASA), Baltimore, MD, United States, [20]Centre for Astrophysics Research, School of Physics Astronomy and Mathematics, University of Hertfordshire, Hatfield, United Kingdom, [21]Max Planck Institute for Extraterrestrial Physics, Garching, Germany, [22]Osservatorio di Astrofisica e Scienza dello Spazio di Bologna (INAF), Bologna, Emilia-Romagna, Italy, [23]University of Manitoba, Winnipeg, MB, Canada, [24]Department of Physics, Faculty of Arts and Science, Canadian Institute for Theoretical Astrophysics, University of Toronto, Toronto, ON, Canada, [25]Diego Portales University, Santiago, Chile, [26]The Kavli Institute for Astronomy and Astrophysics, School of Physics, Faculty of Science, Peking University, Beijing, China, [27]SUNY Brockport, Brockport, NY, United States, [28]Department of Astronomy, College of Computer, Mathematical and Natural Sciences, University of Maryland, College Park, College Park, MD, United States, [29]Goddard Space Flight Center, National Aeronautics and Space Administration, Greenbelt, MD, United States, [30]Center for Research and Exploration in Space Science and Technology, University of Maryland, College Park, Greenbelt, MD, United States

The hard X-ray emission in active galactic nuclei (AGN) and black hole X-ray binaries is thought to be produced by a hot cloud of electrons referred to as the corona. This emission, commonly described by a power law with a high-energy cutoff, is suggestive of Comptonization by thermal electrons. While several hypotheses have been proposed to explain the origin, geometry,

and composition of the corona, we still lack a clear understanding of this fundamental component. *NuSTAR* has been playing a key role improving our knowledge of X-ray coronæ thanks to its unprecedented sensitivity above 10 keV. However, these constraints are limited to bright, nearby sources. The *High Energy X-ray Probe* (*HEX-P*) is a probe-class mission concept combining high spatial resolution X-ray imaging and broad spectral coverage (0.2–80 keV) with a sensitivity superior to current facilities. In this paper, we highlight the major role that *HEX-P* will play in further advancing our insights of X-ray coronæ notably in AGN. We demonstrate how *HEX-P* will measure key properties and track the temporal evolution of coronæ in unobscured AGN. This will allow us to determine their electron distribution and test the dominant emission mechanisms. Furthermore, we show how *HEX-P* will accurately estimate the coronal properties of obscured AGN in the local Universe, helping address fundamental questions about AGN unification. In addition, *HEX-P* will characterize coronæ in a large sample of luminous quasars at cosmological redshifts for the first time and track the evolution of coronæ in transient systems in real time. We also demonstrate how *HEX-P* will enable estimating the coronal geometry using spectral-timing techniques. *HEX-P* will thus be essential to understand the evolution and growth of black holes over a broad range of mass, distance, and luminosity, and will help uncover the black holes' role in shaping the Universe.

KEYWORDS

accretion, x-ray astronomy, black holes, active galactic nuclei, quasars, tidal disruption events

1 Introduction

Active galactic nuclei (AGN) are known to be prolific X-ray emitters. The hard X-rays from AGN are thought to be generated through Compton scattering of thermal UV-soft X-ray seed photons from the accretion disk by a hot electron plasma located in the vicinity of the black hole, known as the corona (e.g., Vaiana and Rosner, 1978; Rybicki and Lightman, 1979; Haardt and Maraschi, 1991; 1993). The resulting X-ray continuum spectrum is usually approximated by a power law of photon index Γ, with a high-energy cutoff ($E_{\rm cut}$) at tens to hundreds of keV (e.g., Fabian et al., 2017; Tortosa et al., 2018; 2023). Within the Comptonization framework, Γ and $E_{\rm cut}$ can be mapped into the electron temperature[1] ($kT_{\rm e}$) and the coronal optical depth (τ) plane (see, e.g., Titarchuk and Lyubarskij, 1995; Zdziarski et al., 1996; Beloborodov, 1999; Petrucci et al., 2001a; b; Middei et al., 2019). The X-ray corona thus holds key information about the physical processes occurring near the supermassive black hole (SMBH), offering insights into the energetic phenomena associated with AGN. Understanding the physics of the X-ray corona in AGN is crucial for unraveling the accretion process, comprehending the origin of the emission from AGN, studying black hole feedback and its impact on galaxy evolution, probing strong gravity regimes, and investigating magnetic fields and particle acceleration.

1.1 The geometry of the X-ray corona

Constraining the geometry (e.g., size and location) of the X-ray corona offers an opportunity to test models for the formation of the corona as each mechanism predicts a distinct geometry. For example, the "two-phase" corona model proposed by Haardt and Maraschi (1991) predicts an extended corona. In contrast, within the framework of the failed jet model proposed by Ghisellini et al. (2004), the corona is expected to be compact. To date, the most promising constraints come from microlensing variability. The microlensing of quasars by stellar components in the lensing galaxy results in a complex magnification pattern (e.g., Wambsganss, 2006). The relative motion of the lensed quasar, the galaxy and its stellar components, and the observer leads to uncorrelated variability. The variability amplitude depends significantly on the size of the emitting region, with a larger amplitude from a smaller emitting region. Thus, the size of the source region can be estimated by modelling the light curve of a lensed quasar (e.g., Chartas et al., 2002; Kochanek et al., 2007; Chartas et al., 2009; Mosquera et al., 2013; Chartas et al., 2016). Reis and Miller (2013) compiled measurements of the X-ray-emitting region in lensed quasars and found the sizes range from ~ one to tens of gravitational radii ($r_{\rm g} = GM_{\rm BH}/c^2$, where G is the gravitational constant, $M_{\rm BH}$ is the mass of the black hole, and c the speed of light). We highlight that current results are based on only a few strongly lensed quasars.

X-ray spectral and spectral-timing properties of nearby bright Seyfert galaxies, notably the detection of X-ray reverberation lags, led to the similar conclusion that the X-ray source is compact and lies within a few gravitational radii of the black hole (Fabian et al., 2009;

1 The cutoff energy is commonly estimated to be ~2 – 3 times the electron temperature (Petrucci et al., 2001a).

De Marco et al., 2013; Cackett et al., 2014; Emmanoulopoulos et al., 2014; Uttley et al., 2014; Kara et al., 2016). Modelling the continuum optical-to-X-ray spectral energy distribution (SED) of a few bright Seyfert galaxies also yields similar estimates of the corona size (e.g., Done et al., 2013; Petrucci et al., 2013; Porquet et al., 2019). This has been recently applied also to a bright quasar at intermediate redshift (Kammoun et al., 2023). Further evidence of a small physical size of the corona emerges from varying obscuration of the corona by clouds in the broad line region (e.g., Risaliti et al., 2011; Sanfrutos et al., 2013; Gallo et al., 2021). These results motivated the adoption of the lamp-post geometry to describe the disk–corona system, where the X-ray corona is assumed to be a point-like source located on the symmetry axis of the disk (e.g., Matt et al., 1991; Martocchia and Matt, 1996; Miniutti and Fabian, 2004). Such a geometry could be physically realized by collisions and shocks within an ejection flow or a failed jet (e.g., Henri and Pelletier, 1991; Henri and Petrucci, 1997; Ghisellini et al., 2004), and has been assumed in detailed models for the calculation of reflection spectra (e.g., Dauser et al., 2013; García et al., 2014; Niedźwiecki et al., 2016; Ingram et al., 2019; Mastroserio et al., 2021; Dovčiak et al., 2022). We note that recently several works are considering a variety of more realistic 3D coronal geometries (e.g., Wilkins et al., 2016; Gonzalez et al., 2017; Zhang W. et al., 2019).

Several works have adopted an approach similar to the one of Soltan (1982) to constrain the radiative efficiency (η) of accreting SMBHs (e.g., Fabian and Iwasawa, 1999; Yu and Tremaine, 2002; Marconi et al., 2004; Shankar et al., 2004; 2009; 2020; Raimundo and Fabian, 2009; Raimundo et al., 2012; Aversa et al., 2015; Zhang and Lu, 2017). This cosmology-independent approach enables constraining the radiative efficiency by comparing the energy density of quasar/AGN radiation with the local mean SMBH mass density. All these works resulted in constraining η to be larger than 0.1. More recently, Shankar et al. (2020) favor $\eta \sim 0.12$–0.2 which is in line with spinning SMBH, suggesting an average spin value larger than ~0.5. For these spin values half of the accretion disk emission is produced within the inner $20r_g$ (see, e.g., Agol and Krolik, 2000; Dovčiak et al., 2022). The inner edge of the accretion disk is thus required to extend close to the black hole. Consequently, the bulk of the emission should be emitted from a compact region, which is in agreement with the results obtained from X-ray observations.

1.2 The heating and cooling mechanisms of the X-ray corona

While the heating mechanism of the corona is still uncertain, magnetic reconnection has been suggested to play an important role (e.g., Galeev et al., 1979; Di Matteo et al., 1997; Merloni and Fabian, 2001a; b; Sironi and Beloborodov, 2020; Sridhar et al., 2021; 2023; Gupta et al., 2023). Within this scenario, the magnetized coronæ could generate cyclo/synchrotron radiation that can be observed in the radio/mm band (e.g., Laor and Behar, 2008; Inoue and Doi, 2014; Panessa et al., 2019). In fact, low levels of radio emission has been almost ubiquitously detected in radio-quiet AGN. In many cases, the emitting region is unresolved and associated with a compact, sub-kpc nuclear region (see, e.g., Smith et al., 2016; Panessa et al., 2019, and references therein). Given the expected physical size of the X-ray emitting region, the coronal mm-wave synchrotron emission is expected to be self-absorbed, and it would therefore be more easily detectable in the mm than in the radio. The size (R) of the self-absorbed synchrotron source decreases with frequency following $R \propto \nu^{-7/4}$. Thus, the synchrotron emission from an X-ray corona sized source would peak at ~100 GHz (e.g., Raginski and Laor, 2016; Inoue and Doi, 2018). Several observational studies hint towards a coronal origin of the mm-wave nuclear emission in non-jetted AGN (e.g., Behar et al., 2015; 2018; Doi and Inoue, 2016; Inoue and Doi, 2018; Kawamuro et al., 2022; 2023; Petrucci et al., 2023). In particular, correlations between mm continuum emission and X-ray emission have been found in various samples of AGN, with an average ratio between the ~100 – 200 GHz and X-ray continuum of $\sim 10^{-5} - 10^{-4}$ (Behar et al., 2015; 2018; Kawamuro et al., 2022; Ricci et al., 2023). Interestingly, this relation is consistent with what has been observed in coronally active stars (Guedel and Benz, 1993), which are magnetically heated, similar to what is expected for AGN coronæ, further supporting the proposed coronal origin for the 100–200 GHz continuum emission, and in turn the idea that the corona is magnetically heated.

A physically compact X-ray corona is expected to be radiatively compact, meaning that the luminosity to radius ratio (L/R_c) is large. The compactness is usually described by the dimensionless parameter $\ell = \frac{L}{R_c}\frac{\sigma_T}{m_e c^3}$, where σ_T is the Thompson scattering cross section and m_e is the electron mass (Guilbert et al., 1983). For large values of ℓ, the number density of the high-energy photons can lead to electron-positron pair production due to photon-photon collisions. In this case, feeding the corona with more energy will lead to the production of more particles to share the energy, which will limit the increase of the temperature of the corona and prevent pair production from becoming a runaway process and exceed annihilation. This can be assimilated to an ℓ-dependent thermostat (Svensson, 1984; Zdziarski and Lightman, 1985; Stern et al., 1995). Observational constraints on the coronal parameters so far obtained are in agreement with the hypothesis that pair production and annihilation may act as an effective thermostat controlling the coronal temperature (Fabian et al., 2015; 2017). It is common to assume that the coronal plasma is thermal. However, several AGN show electron temperatures that are much lower than expected for a purely thermal pair plasma (see, e.g., Baloković et al., 2015; Ursini et al., 2016; Kara et al., 2017; Tortosa et al., 2018; Reeves et al., 2021; Bertola et al., 2022). These low temperatures could be indicative of a hybrid plasma composed of a mixture of thermal and non-thermal particles (Ghisellini et al., 1993; Zdziarski et al., 1993; Fabian et al., 2017). Only a small fraction of non-thermal electrons with energy above 1 MeV would be needed to result in runaway pair production. In this case, the cooled pairs share the energy which reduces the temperature of the corona.

It is common to model the Comptonization spectrum using a phenomenological power law with a high energy cutoff. Various physical models are also used and all of them describe the current data equally well. These models differ in their assumptions for the spectrum of the seed photons and the geometry of the Comptonizing region. Various analytic Comptonization models such as `CompTT` (Titarchuk, 1994) and `CompPS` (Poutanen and Svensson, 1996) are used, allowing different simple geometries. Recently, more physically

self-consistent calculations such as EQPAIR (Coppi, 1999), BELM (Belmont et al., 2008), MoCa (Tamborra et al., 2018), and MONK (Zhang W. et al., 2019) include a variety of geometries, hybrid coronæ, and polarization.

1.3 Observational constraints

The unprecedented sensitivity of *NuSTAR* (Harrison et al., 2013) above 10 keV has been instrumental to study the hard X-ray spectra of AGN. *NuSTAR* enabled high-energy cut-off measurements from single epoch observations for a relatively large sample of local (Ballantyne et al., 2014; Matt et al., 2014; Baloković et al., 2015; 2020; Ricci et al., 2017; Tortosa et al., 2018; Akylas and Georgantopoulos, 2021; Kamraj et al., 2022; Tortosa et al., 2023) and intermediate-redshift AGN for the first time (see, e.g., Kammoun et al., 2017; 2023; Lanzuisi et al., 2019; Bertola et al., 2022; Marinucci et al., 2022b, and references therein). It should be mentioned that previous studies (with *BeppoSAX, RXTE, INTEGRAL*, etc.) allowed these measurements for a much smaller sample of the brightest nearby AGN (e.g., Nicastro et al., 2000; Petrucci et al., 2004; Malizia et al., 2014; Lubiński et al., 2016). *NuSTAR* observations allowed us not only to constrain the coronal temperature by accurately measuring values of $E_{\rm cut}$, but also to probe its variability (e.g., Ballantyne et al., 2014; Zoghbi et al., 2017) the origin of which remains unclear.

The *Swift*/BAT AGN sample comprises all AGN detected by the all-sky 14–195 keV BAT survey (Baumgartner et al., 2013; Oh et al., 2018). Ricci et al. (2017) have estimated a median high-energy cutoff of local unobscured AGN (i.e., $\log(N_{\rm H}/{\rm cm}^{-2}) < 22$) of $E_{\rm cut} = 210 \pm 36$ keV. Ricci et al. (2018) subsequently found evidence for an inverse correlation between $E_{\rm cut}$ and Eddington ratio ($\lambda_{\rm Edd}$) where the median $E_{\rm cut}$ increases from $E_{\rm cut} = 160 \pm 41$ keV to $E_{\rm cut} = 370 \pm 51$ keV considering AGN with $\lambda_{\rm Edd}$ larger and smaller than 0.1, respectively. This could be suggestive that the properties of the X-ray corona evolve with the accretion rate. More recently, Kamraj et al. (2022) included *NuSTAR* observations of this sample and estimated the mean electron temperature to be $kT_{\rm e} = 84 \pm 9$ keV, which is consistent with the values reported previously in the literature. However, the authors were not able to recover the correlation between the electron temperature and any of the accretion parameters. It is worth mentioning that differences in coronal spectra may be expected between obscured and unobscured AGN, within the framework of the orientation-based unified model of AGN (Antonucci, 1993; Urry and Padovani, 1995), especially if the corona has a net velocity perpendicular to the accretion disk (most likely related to jet formation; see, e.g., Malzac et al., 2001; Markoff et al., 2005). However, Baloković et al. (2020) estimated a median $E_{\rm cut} = 290 \pm 20$ keV for a sample of 130 local obscured AGN, consistent within the current large uncertainties with the values found by Ricci et al. (2017) for unobscured AGN.

More recently, the launch of the *Imaging X-ray Polarimetry Explorer* (*IXPE*; Weisskopf et al., 2022) has enabled studies of X-ray polarization in AGN for the first time (in the 2–8 keV range). X-ray polarization is a powerful technique to explore the geometry of the X-ray emitting region (see, e.g., Schnittman and Krolik, 2010; Beheshtipour et al., 2017; Tamborra et al., 2018; Zhang W. et al., 2019). So far, a total of four non-blazar AGN have been observed (NGC 4151, MCG–05-23-16, the Circinus galaxy, and IC 4329A). Only upper limits could be determined for MCG–05-23-16 (Marinucci et al., 2022b; Tagliacozzo et al., 2023) and IC 4329A (Ingram et al., 2023), which are not conclusive on the geometry of the X-ray source. The Circinus galaxy shows a polarization of 28 ± 7 per cent (at 68 per cent confidence level), with a polarization angle of $18° \pm 5°$, roughly perpendicular to the radio jet (Ursini et al., 2023). Given the large obscuration in this source, this polarization is most likely due to reflection off cold material in the torus (e.g., Ghisellini et al., 1994; Goosmann and Matt, 2011; Marin et al., 2018; Ratheesh et al., 2021) and cannot be interpreted as the intrinsic polarization of the X-ray source. As for NGC 4151, a polarization of 4.9 ± 1.1 per cent with a polarization angle of $86° \pm 7°$ (at the 68 per cent confidence level) are reported by Gianolli et al. (2023). This is consistent with a radially extended source of polarization that is perpendicular to the radio jet, i.e., parallel to the accretion disk. Similar results have also been observed in the black hole X-ray binary Cygnus X-1 (Krawczynski et al., 2022).

The *High-Energy X-ray Probe* (*HEX-P*; Madsen et al., 2023; in preparation) will address many of the open questions related to the physics of the X-ray corona in AGN. In this paper, we showcase how *HEX-P* will play a major role in advancing our understanding of the physics of the X-ray coronæ in AGN. In Section 2 we briefly present the properties of the mission. Characterisations of the X-ray coronæ in unobscured and obscured AGN with *HEX-P* are discussed in Section 3 and Section 4, respectively. Section 5 shows how studying the X-ray coronæ in high-redshift quasars will be possible with *HEX-P*. Section 6 addresses the capabilities of *HEX-P* in studying the X-ray coronæ of transient sources. Section 7 demonstrates how *HEX-P* will allow us to better constrain the coronal geometry. Finally, we present a summary and a brief discussion in Section 9.

2 Mission design

HEX-P is a probe-class mission concept that offers sensitive broad-band coverage (0.2–80 keV) of the X-ray spectrum with exceptional spectral, timing, and angular capabilities. It features two high-energy telescopes (HETs) that focus hard X-rays, and one low-energy telescope (LET) that focuses lower energy X-rays.

The LET consists of a segmented mirror assembly coated with Ir on monocrystalline silicon that achieves a half power diameter of 3.5″, and a low-energy DEPFET detector, of the same type as the Wide Field Imager (WFI; Meidinger et al., 2020) onboard *Athena* (Nandra et al., 2013). It has 512×512 pixels that cover a field of view of $11.3' \times 11.3'$. It has an effective passband of 0.2–20 keV, and a full frame readout time of 2 ms, which can be operated in a 128 and 64 channel window mode for higher count-rates to mitigate pile-up and faster readout. Pile-up effects remain below an acceptable limit of ~1% for fluxes up to ~100 mCrab in the smallest window configuration. Excising the core of the PSF, a common practice in X-ray astronomy, will allow for observations of brighter sources, with a typical loss of up to ~60% of the total photon counts.

The HET consists of two co-aligned telescopes and detector modules. The optics are made of Ni-electroformed full shell mirror

substrates, leveraging the heritage of *XMM-Newton* (Jansen et al., 2001), and coated with Pt/C and W/Si multilayers for an effective passband of 2–80 keV. The high-energy detectors are of the same type as flown on *NuSTAR* (Harrison et al., 2013), and they consist of 16 CZT sensors per focal plane, tiled 4×4, for a total of 128×128 pixels spanning a slightly larger field of view than the LET, $13.4' \times 13.4'$.

The broad X-ray band pass and superior sensitivity will provide a unique opportunity to study the X-ray corona physics across a wide range of energies, luminosity, and dynamical regimes.

2.1 Simulations

All the simulations presented here were produced with a set of response files that represent the observatory performance based on current best estimates (see Madsen et al., 2023; in preparation). The effective area is derived from a ray-trace of the mirror design including obscuration by all known structures. The detector responses are based on simulations performed by the respective hardware groups, with an optical blocking filter for the LET and a Be window and thermal insulation for the HET. The LET background was derived from a GEANT4 simulation (Eraerds et al., 2021) of the WFI instrument, and the HET background was derived from a GEANT4 simulation of the *NuSTAR* instrument; both simulations assume *HEX-P* is orbiting at the first Earth-Sun Lagrangian point (L1).

3 Physics of the corona in unobscured AGN

Unobscured AGN ($\log(N_{\rm H}/{\rm cm}^{-2}) < 22$) with their clean view of the central engine have provided most of the knowledge we have today regarding AGN coronæ, as outlined in Section 1. The view of the whole Comptonization spectrum, and of the X-ray reflection arising from the interaction with the disk, is what makes X-ray observations of unobscured AGN so valuable. The constraints provided on these sources are key as we move towards refining our picture of AGN coronæ with *HEX-P*.

NuSTAR observations of unobscured AGN have provided many coronal temperature measurements, which are consistent with the runaway pair production scenario discussed above. Interestingly, in some AGN the coronal temperatures have been found to be much lower than what would be expected for pair-regulated thermal coronæ. One likely explanation for this is that the energy distribution of the electrons in the corona is not entirely thermal but has a non-thermal contribution. Such a hybrid corona would have a lower observed coronal temperature as the non-thermal high energy electrons create pairs even when the bulk of the electrons have lower temperatures.

The hybrid nature of the electron distribution can be detected directly from the X-ray spectrum. Comptonization from thermal electrons results in a power-law like X-ray continuum with a fairly abrupt cut-off at high energies. Consequently, an addition of non-thermal electrons, following a power-law like distribution beyond the thermal peak, leads to an increase in hard X-rays, as there are now electrons with even higher energies. This additional hard X-ray emission beyond the thermal cut-off is usually referred to as a "hard tail".

Using these differences in the resulting Comptonization spectrum, i.e., the X-ray continuum, some evidence has been found in black hole X-ray binaries that the X-ray continuum is caused by hybrid Comptonization (e.g., Cadolle Bel et al., 2006; Cangemi et al., 2021; Zdziarski et al., 2021). The presence of hybrid Comptonization in AGN has been widely hypothesized but a direct detection of the hard tail itself is beyond the capabilities of current and proposed future instruments. *HEX-P*, however, will allow indirect confirmation of the presence of hybrid Comptonization in AGN and determine the strength of its contribution.

There are two primary methods to indirectly detect hybrid Comptonization: one relies on the reflection spectrum of the high energy continuum (García et al., 2015, see also Section 9), and the other tests temperature regulation by electron-positron pair production. The latter case can be made by studying the evolution of a source with unusually low coronal temperature over a period of time. If the source is variable, we can study the evolution of its compactness and coronal temperature with time. If the coronal temperature is set by pair production and the accretion geometry remains unchanged[2] then as the source flux increases, the coronal temperature will decrease. If, on the other hand, the coronal temperature is not regulated by pairs then the temperature may not change or change in a different fashion. If we see the expected trend of lower coronal temperature with increased flux, and if the observed coronal temperatures are much lower than expected for thermal Comptonization, that would be strongly indicative of hybrid Comptonization. The findings can then also be compared to theoretical predictions. In rare cases, this is already possible with today's instrumentation for some of the brightest X-ray binaries (see Buisson et al., 2019, for an example), but has remained out of reach for AGN. For the observations to yield meaningful constraints our measurements need to be more accurate at low fluxes than is possible with current instruments. However, *HEX-P* is able to obtain much tighter constraints on the coronal temperatures due to its low background at high energies (Figure 1, left), enabling a high-quality study of coronal temperature variations in AGN for the first time.

To demonstrate this, we explored the feasibility of a study with *HEX-P* that targets the evolution of the coronal temperature in the bright, local narrow-line Seyfert 1 galaxy Ark 564. Ark 564 is ideally suited for such a study as it exhibits a low measured coronal temperature (Kara et al., 2017; Lewin et al., 2022) as well as observed coronal temperature and flux variations (Barua et al., 2020). Our *HEX-P* simulations of Ark 564 are based on the absorbed 2–10 keV fluxes observed with *RXTE* over a 4-year period ranging from 1999 to 2003 and our simulations are further assuming a scenario where the coronal size remains unchanged with luminosity[3]. During this period the observed 2–10 keV flux varies between $1.0–5.0 \times 10^{-11}$ $erg\ s^{-1}\ cm^{-2}$ (Rivers et al., 2013). We simulate spectra at five evenly spaced levels within the observed flux range assuming a model that consists of a thermal

2 This can be assessed by studying the X-ray reflection spectrum.

3 Our final conclusions do not depend on this assumption, as the coronal size can also be estimated from the spectral modeling.

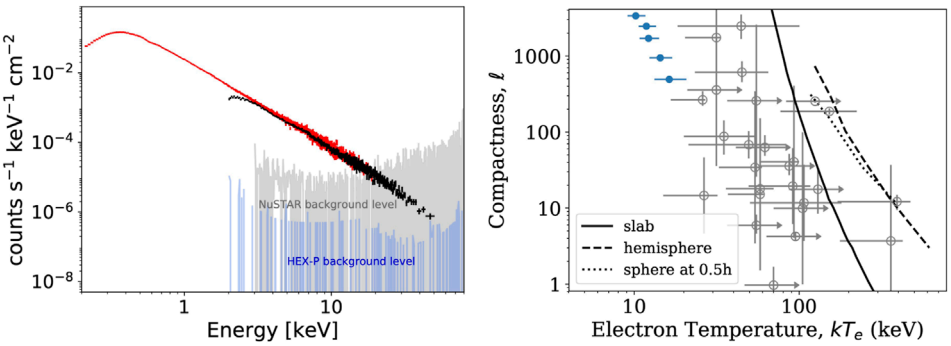

FIGURE 1
Left: Simulated LET (red) and HET (black) spectra of Ark 564, assuming Γ =2.48, kT_e = 13 keV and an exposure time of 90 ks. The figure also shows the background levels of *NuSTAR* (grey) and *HEX-P*-HET (blue): the background of *HEX-P* is significantly lower than that of *NuSTAR*. Right: Corona compactness as function of electron temperature. The blue circles correspond to simulated observations of Ark 564 with *HEX-P* at five different flux levels and five different coronal temperatures from 15 to 10 keV (see text). For clarity, uncertainities in the compactness of Ark 564 are not plotted. The grey empty circles represent typical estimates of kT_e from other AGN performed with *NuSTAR*.

Comptonization continuum and its associated reflection spectrum, both of which are treated with the relativistic reflection model `relxilllpcP` (Dauser et al., 2020). The second lowest flux level of 2.0×10^{-11} erg s^{-1} cm^{-2} corresponds very well to the 2018 joint *XMM-Newton* + *NuSTAR* observations of the source, which were studied in detail in Lewin et al. (2022). We therefore adopt the spectral parameters from their detailed modeling for this flux level (Table 3 in their paper), in particular they have determined that $\Gamma = 2.48$ and $kT_e = 14.7$ keV at this particular flux level. Then as we vary the flux level, we not only adjust the normalization of our spectral model but also evolve the photon index from 2.40 to 2.56 to mimic a softer-when-brighter effect and the coronal temperature from 15.1 to 10.0 keV to have the coronal evolve mildly with flux, the reflection parameters are kept unchanged. To determine how much exposure time was needed at each flux level, we simulated spectra with increasingly longer exposure times until we were able to recover the coronal temperature with an accuracy of ±2.5 keV or better at 90% confidence. From the simulations, we found that a study of Ark 564 with *HEX-P* with a total exposure time of 445 ks targeting the source at different flux levels will constrain the coronal temperature to ≤2.5 keV and could yield important data points in the compactness-temperature plane (blue points, Figure 1, right). At higher flux levels it is easy for us to exceed the accuracy requirement of 2.5 keV and the error bars are therefore smaller. We note here that accuracy of the coronal temperature constraint for a certain simulated exposure time is model-dependent, where more complex models lead to less accurate constraints.

To place the findings from the Ark 564 study into the context of the wider population of radio-quiet, unobscured AGN, ideally a few similar studies of other sources would also be conducted. Suitable study targets display large variability on timescales of weeks to months and possess a low coronal temperature, several of such sources have already been identified. Together, with the findings from one-time observation of unobscured AGN and high redshift targets, this will highlight whether Ark 564 is special in any way or whether its coronal variations can be considered representative for the population as a whole.

The much lower background of *HEX-P* at higher energies and the therefore much improved constraints on the spectral shape in this energy range with shorter exposure times will likely not only lead to a better understanding of hybrid Comptonization, but also to a more accurate spectral decomposition of unobscured AGN. This aspect is studied in more detail in Piotrowska et al. (2023).

4 Physics of the corona in obscured AGN

Within the framework of the orientation-based unified model for AGN (Antonucci, 1993), differences in coronal spectra between obscured ($\log(N_H/\mathrm{cm}^{-2}) \geq 22$) and unobscured AGN could be expected if the corona has significant velocity perpendicular to the accretion disk, possibly related to jet formation (Beloborodov, 1999; Markoff et al., 2005; Liu et al., 2014). Hard X-rays (≥15 keV) are essential to study the intrinsic properties of obscured AGN, as the obscuring material is optically thin to these photons. Constraints on coronæ in obscured AGN remain extremely scarce in the literature despite the prevalence of obscured AGN both in the local universe and, particularly, at high redshift (50%–75% of the population; Hickox and Alexander, 2018). A few constraints based on data from non-focusing hard X-ray instruments are available from, e.g., *BeppoSAX* (Dadina, 2007), *Suzaku* (Tazaki et al., 2011), *INTEGRAL* (de Rosa et al., 2012), *Swift*/BAT (Ricci et al., 2018), or a combination thereof (Molina et al., 2013). However, the cutoff of the power-law continuum at high energies, E_{cut}, has been well constrained using *NuSTAR* data for only about a dozen bright, obscured AGN (e.g., Baloković et al., 2015; Fabian et al., 2017; Buisson et al., 2018; Tortosa et al., 2018; Ursini et al., 2019), while larger samples representative of the obscured AGN population provide ensemble-level constraints mostly based on short *NuSTAR* observations with limited photon statistics (Baloković et al., 2020). In addition to E_{cut}, we note that constraining the photon index in obscured AGN is crucial to study the intrinsic AGN spectrum and understand the accretion process.

Thanks to its low background, and broad-band energy coverage, *HEX-P* will provide better constraints on the properties of the X-ray corona in obscured AGN. We performed simulations of various configurations of absorbed AGN to test the capabilities of *HEX-P* in constraining coronal parameters, assuming uniform exposure times of 100 ks (typical exposure for the planned *HEX-P* surveys; see Civano et al., 2023). We used the `borus02` model (Baloković et al., 2018), which self-consistently computes the reprocessed emission from a sphere with conical cutouts at both poles, approximating a torus with variable covering factor. We considered a torus with a half-opening angle of 45° and an inclination of 60°. We also considered a photon index of the incident power law of $\Gamma = [1.6, 1.9, 2.2]$, and a high-energy cutoff $E_{\rm cut} = [50, 150, 300]$ keV. The incident luminosity was estimated to match the average values observed by Ricci et al. (2017) for $z = 0.02$ and $z = 0.5$, resulting in unabsorbed 2–10 keV luminosities in the range $10^{42.9-45.5}$ erg s^{-1}. We considered three values for the column densities $\log(N_{\rm H}/{\rm cm}^{-2}) = [22, 23, 24]$. For simplicity, we assume a homogeneous torus with the line-of-sight column density equal to the equatorial value. In addition, the soft X-ray spectrum in obscured AGN is typically characterized by the emission from photoionized gas in the narrow line region. For simplicity, we include a soft `APEC` component, which is commonly used in the literature to model this emission in absorbed AGN. For this component we assume a temperature of 0.9 keV and a normalization that is equal to 10% that of the power law, as

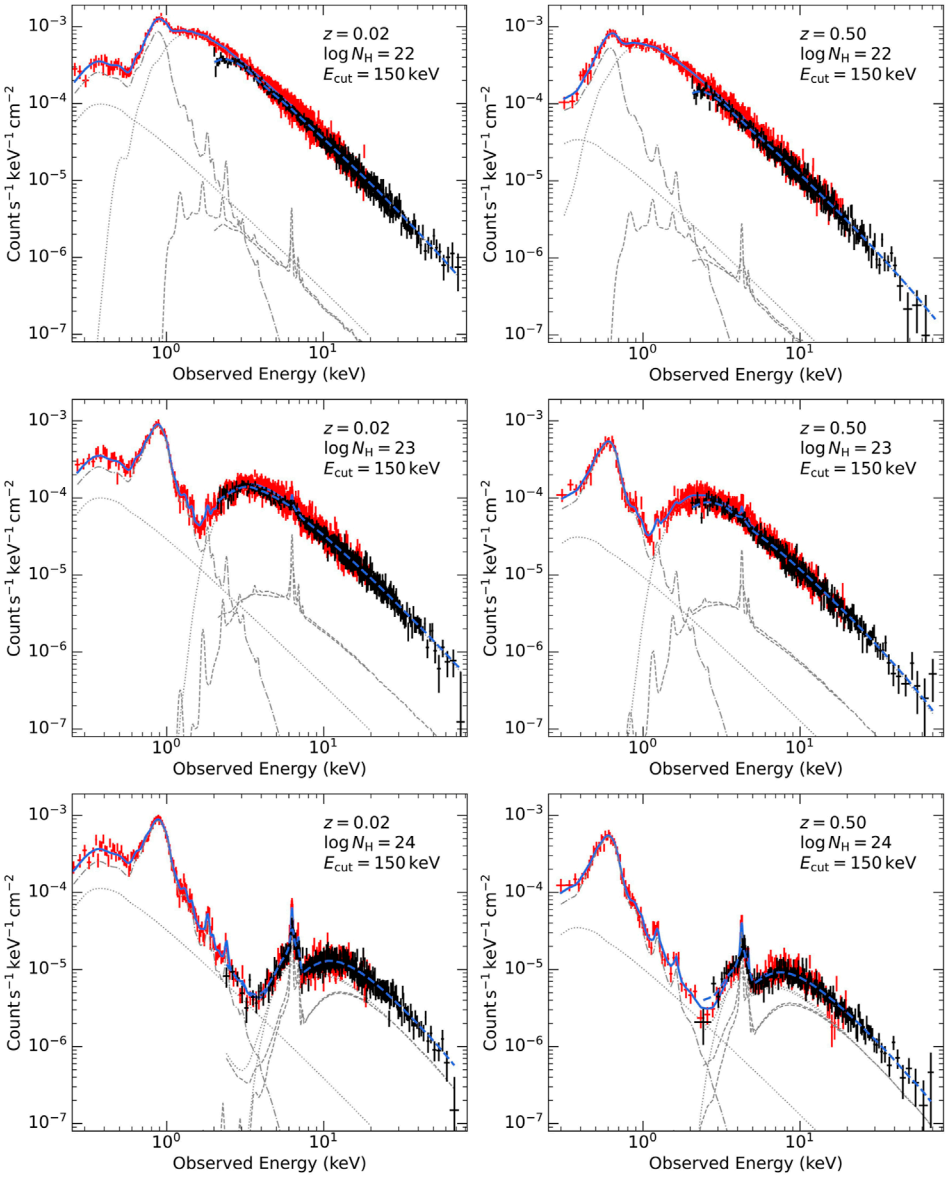

FIGURE 2
Simulated LET (red) and HET (black) spectra of an absorbed AGN at $z = 0.02$ (left) and $z = 0.5$ (right), assuming $\log(N_{\rm H}/{\rm cm}^{-2}) = 22, 23, 24$ (top to bottom), $\Gamma = 1.9$, $E_{\rm cut} = 150$ keV, and an exposure time of 100 ks. The grey dotted lines represent the power law components, the grey dashed lines represent the neutral reflection component, and the grey dash-dotted lines represent the thermal component.

typically seen in local AGN (see, e.g., Kammoun et al., 2020). The total model results observed 2–10 keV fluxes in the range $2.5–8.5 \times 10^{-12}$ erg s^{-1} cm^{-2} Figure 2 shows example *HEX-P* spectra for an intermediate configuration for all the simulated N_H values, assuming $\Gamma = 1.9$, and $E_{cut} = 150$ keV, for $z = 0.02$ and $z = 0.5$ (left and right panels, respectively). Figure 3 shows the E_{cut}-vs-Γ contours at the 3σ confidence level for all the configurations considered. *HEX-P* accurately measures the photon index over a broad range of parameters. The uncertainty on Γ is larger for higher column densities, since increasing amounts of absorption limits the access to the power law portion of the continuum to increasingly hard X-rays. This yields larger uncertainties on E_{cut} as well. The uncertainty on E_{cut} also increases with increasing E_{cut}; only lower limits could be estimated for $E_{cut} = 300$ keV. We note that the observed flux decreases by a factor of ~3 between $z = 0.02$ and $z = 0.5$, which lead to an increase in the uncertainty on the parameters higher redshift. For comparison with current facilities, we simulate a joint 30-ks *XMM-Newton* plus 100-ks *NuSTAR* (accounting for both modules, FPMA and FPMB) observation, which are typical exposures with these facilities. For all cases, we adopt $z = 0.02$ as it results in tighter constraints than the $z = 0.5$ case. The $\Gamma - E_{cut}$ constraints are shown as black dotted contours in Figure 3, demonstrating the improvements enabled by *HEX-P*. We note that, for the flux levels of these sources and the exposure time, many of these sources will be easily detected in the *HEX-P* surveys (see Civano et al., 2023).

We would like to note that our `borus02` model is setup in coupled mode in which the line-of-sight and global column densities scale together. The reflection component will be higher at higher line-of-sight column densities, possibly contributing to the increased uncertainties in the higher N_H regime that we show in Figure 3. To definitively test this would require knowledge of the dependence between global column density and a wide range of different physical AGN parameters as well as a wide range of different model prescriptions for the obscurer, which is outside the scope of the current work. It is also worth mentioning that

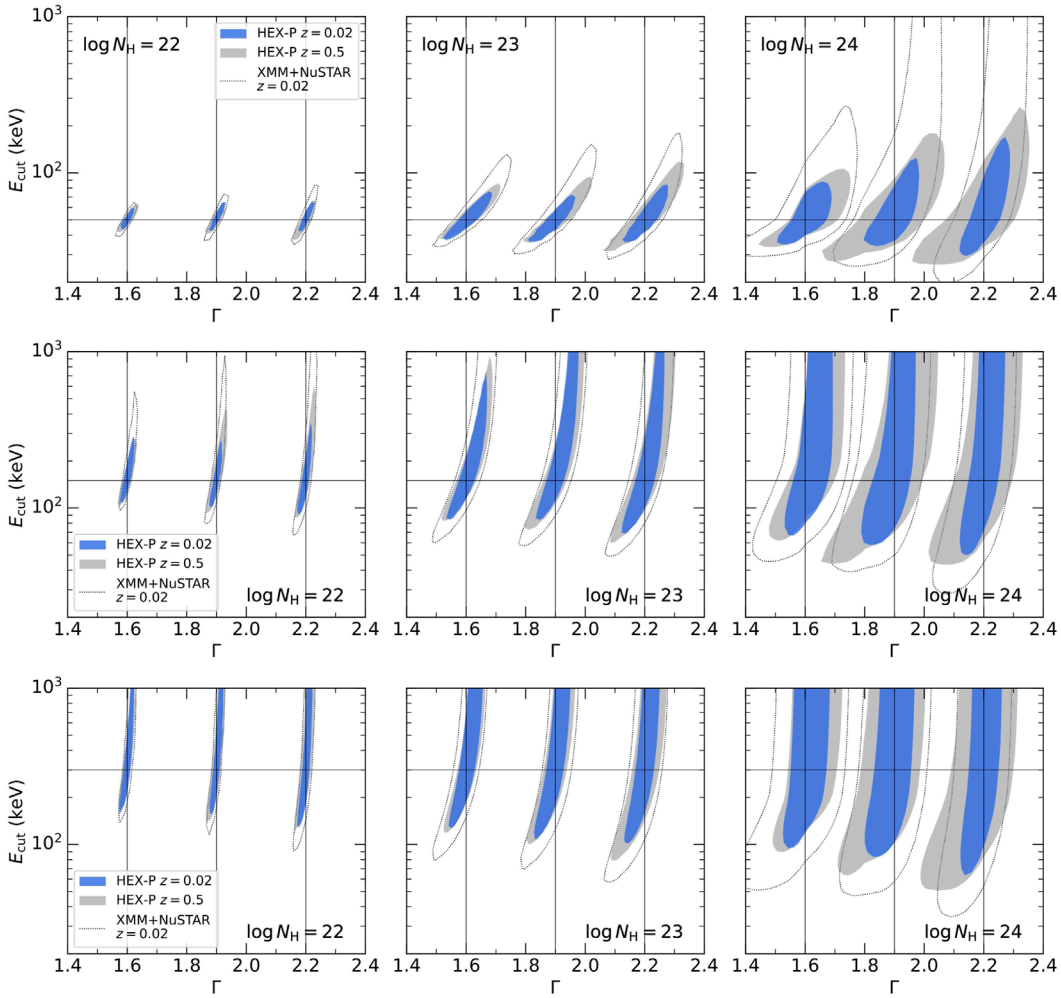

FIGURE 3
$\Gamma - E_{cut}$ contour plots (3σ confidence level) for $z = 0.02$ and 0.5 (blue and grey contours, respectively) assuming $\log(N_H/cm^{-2}) = [22,23,24]$ (left to right), $E_{cut} = 50,150$, and 300 *keV* (top to bottom), and simulating a 100-ks *HEX-P* observation. The black dotted contours correspond to the 3σ confidence level constraints for a source at $z = 0.02$ with 30-ks exposure by *XMM-Newton* combined with a 100-ks exposure by *NuSTAR* (including both modules, FPMA and FPMB). Horizontal and vertical lines indicate the input values of Γ and E_{cut}, respectively.

near and above the Compton-thick regime, the measurement of the energy cut-off is degenerate with the assumed obscurer model. Different obscurer geometries have different Compton-scattering behaviour, altering the reprocessed spectrum up to 400 keV (e.g., Buchner et al., 2019; 2021). Thus the obscurer geometry and the energy cut-off are degenerate. Merely assuming an obscurer geometry may bias the energy cut-off measurement. Here, for simplicity, a fixed obscurer model (borus02) was used for generating and modeling the data. The complex task of inferring the true obscurer geometry and the true energy cut-off thus would have to be achieved simultaneously, but this is beyond the scope of this paper. Boorman et al. (in prep.) discusses *HEX – P*′s ability to infer torus geometries in heavily obscured AGN in more detail.

5 Physics of the corona in intermediate-/high-redshift quasars

The high-energy cutoff in the X-ray spectrum (at tens to hundreds keV) can be directly linked to the properties of the corona. Thanks to *NuSTAR*, whose hard X-ray sensitivity is orders of magnitude better than previous missions, a large sample of AGN were observed with unprecedented data quality at hard X-rays. The majority of the observed sources are AGN with low luminosity ($L_{2-10\,\mathrm{keV}} = 10^{42}$–$10^{44}$ erg s^{-1}; see, e.g., Kamraj et al., 2018; Ricci et al., 2018; Baloković et al., 2020), so they are in a region of the $kT_e - \ell$ plane where a broad range of E_{cut} is allowed within the framework of the runaway pair production hypothesis. This can be seen in the left panel of Figure 4 (we assume here $E_{cut} = 2\,kT_e$, $R_c \sim 10\,r_g$, and coronal luminosity $L_c = L_{0.1-200\,\mathrm{keV}} \sim 4 \times L_{2-10\,\mathrm{keV}}$). Furthermore, most of these sources are in the nearby Universe ($z < 0.1$, Figure 4, right). Therefore, only lower limits to their cutoff energy were measured at 90% confidence level due to the limited bandpass in the rest frame of local sources (<80 keV), covered by *NuSTAR*.

On the contrary, high-redshift ($z \geq 1$) radio-quiet quasars (mostly with luminosity $L_{2-10\,\mathrm{keV}} > 10^{45}$ erg s^{-1}) are ideal sources to constrain high-energy cutoffs thanks to the limited allowed E_{cut} range on the $kT_e - \ell$ plane (assuming kT_e is indeed limited by runaway pair production; see Figure 4, left) and the cosmological redshifting of E_{cut} to the *NuSTAR* observable band. Therefore, they constitute a promising sample to constrain the AGN coronal properties at high luminosity and test the runaway pair production theory. So far, only three $z > 1$ quasars were observed with *NuSTAR* and had their high-energy cutoffs constrained (Lanzuisi et al., 2019; Bertola et al., 2022; Figure 4, right). All three quasars (with $L_{2-10\,\mathrm{keV}} > 3 \times 10^{45}$ erg s^{-1}) were found below the critical line on the $kT_e - \ell$ plane as per pair-production models expectations, though note the large uncertainties for two of the sources which leave ambiguous results (Figure 4, left). The well constrained cutoff energies of the three high-z quasars ($\lambda_{Edd} > 0.1$) were 1.5–2.5 times lower than the 160 keV measured by Ricci et al. (2018) for sources with high Eddington ratio. Therefore, observing high-redshift quasars, where the coronal properties could be well constrained, is crucial to study the possible evolution of the corona with the accretion parameters such as the accretion rate and the SMBH mass.

Despite the recent progress in constraining the coronal properties of high-redshift, high-luminosity quasars, the observations are extremely time-consuming. A total of ~375 ks *NuSTAR* and 150 ks XMM observations were spent on the above three sources. The long exposures required in these observations lead to a strong limitation in constraining AGN coronal properties statistically.

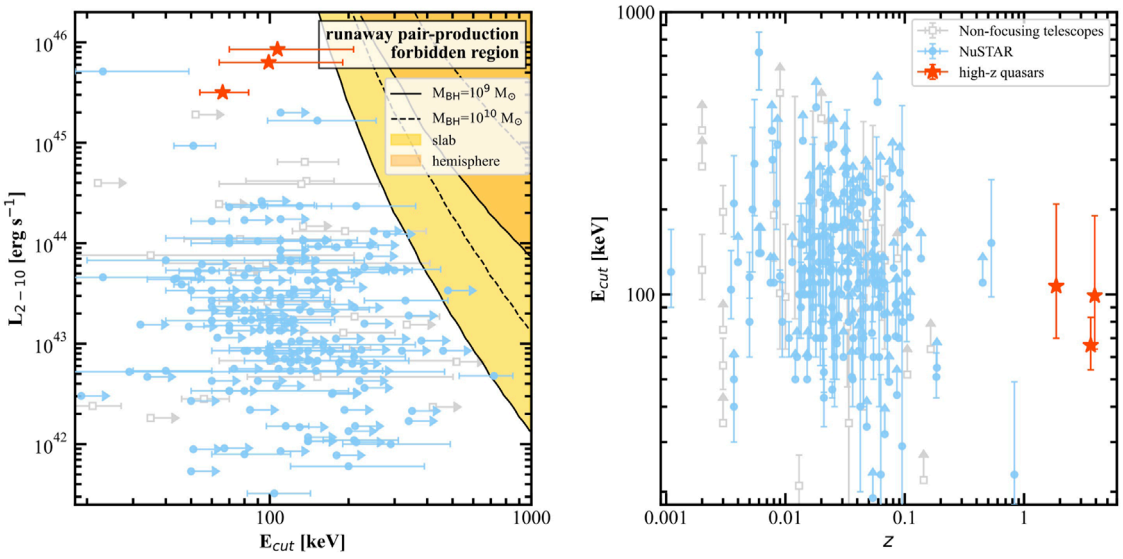

FIGURE 4
High-energy cutoff of AGN as a function of 2–10 keV luminosity (left) and redshift (right) by *NuSTAR* (light blue circles) and non-focusing telescopes (gray squares), based on Bertola et al. (2022). The pair-production forbidden regions assuming different coronal geometries are plotted in orange (hemisphere) and yellow (slab). So far, E_{cut} was only measured in three quasars at $z > 1$ (red stars). E_{cut} is not constrained for most of the low-redshift and low-luminosity AGN.

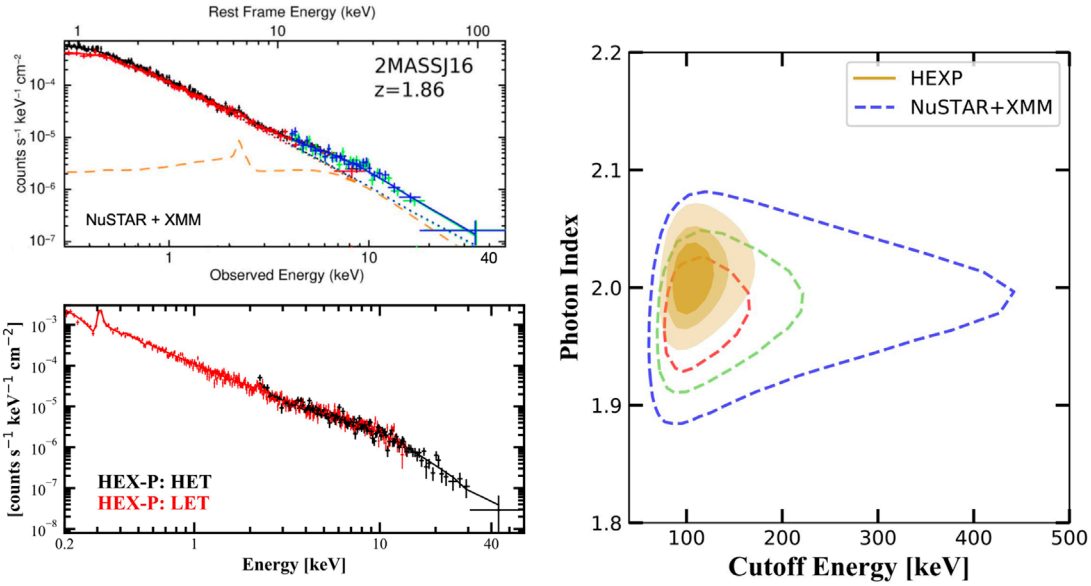

FIGURE 5
Left, upper panel: 140 ks *NuSTAR* (blue) and 69 ks *XMM-Newton* (red) spectra of 2MASS J1614346 + 470,420 at z 1.86 (adapted from Lanzuisi et al., 2019). *Left, lower panel:* 140 ks *HEX-P* simulation of the same quasar (HET in black, LET in red). *Right:* contours of E_{cut} and photon index of the *NuSTAR* + *XMM-Newton* observations (red, green, and blue correspond to 68%, 90%, and 99% confidence level, respectively) and *HEX-P* simulations (dark yellow, yellow, and light yellow correspond to 68%, 90%, and 99% confidence level, respectively).

HEX-P, with larger effective area, lower background, and broad band coverage, is well suited to efficiently study the coronal properties of high-redshift, high-luminosity quasars. We compare the 140 ks *NuSTAR*+ 69 ks *XMM-Newton* observation of 2MASS J1614346 + 470,420 ($z = 1.86$) from Lanzuisi et al. (2019) to a simulated 140 ks *HEX-P* observation in Figure 5. Note that L1 orbit of *HEX-P* implies that the *HEX-P* observation would take half the total observatory time compared to the *NuSTAR* observation, since *NuSTAR* is in low-Earth orbit and does not re-point during Earth occultations. The 90% confidence level constraints on E_{cut} are 106^{+100}_{-40} keV from *NuSTAR* + *XMM-Newton* and 103^{+30}_{-20} keV from the simulated *HEX-P* spectra, implying significantly improved constraints on E_{cut} by *HEX-P* in the same exposure time and half the clock time. The high-energy cutoff and the photon index contours (at 68%, 90%, and 99% confidence levels) derived from *NuSTAR* + *XMM-Newton* and simulated *HEX-P* spectra are plotted in the right panel of Figure 5. The contours show that *HEX-P* can constrain E_{cut} at high confidence.

HEX-P will not only provide better constraints on AGN coronal properties but it will also efficiently probe AGN coronæ in a large sample of high-redshift, high-luminosity quasars. We demonstrate the constraining power of *HEX-P* for coronal cutoff energy measurements of intermediate-/high-redshift, high-luminosity quasars. We simulated nine *HEX-P* observations of quasars with 50 ks exposures assuming an input 2–10 keV flux of $F_{2-10\,keV} = 10^{-12}$ erg s^{-1} cm^{-2}. We note that cosmic X-ray background population synthesis models predict ~ 200 quasars at $z > 1$ with such flux level (see, e.g., Gilli et al., 2007). The input redshifts range goes from $z = 0.65$ to $z = 4.5$, so that their 2–10 keV intrinsic luminosity range over $\log(L_{2-10\,keV}/\mathrm{erg\ s^{-1}}) = 45.25–47.25$. We simulated source spectra assuming a cutoff power law with a Galactic absorption of 10^{20} cm^{-2} and photon index of $\Gamma = 1.90$. We simulated three different high-energy cutoffs, $E_{cut} = 50$, 100, and 200 keV, to explore the parameter space. Assuming the same supermassive black hole mass, $\log(M_{BH}/M_{\odot}) = 9.2$ and a 2–10 keV luminosity to bolometric luminosity conversion factor of 20 (e.g., Vasudevan and Fabian, 2007; Lusso et al., 2012), the Eddington ratios of the sample range over $\lambda_{Edd} = 0.2–20$.

Figure 6 shows the $E_{cut} - \Gamma$ contours measured from the simulated spectra of the quasars with different redshifts and different high-energy cutoffs. The best-fit high-energy cutoffs of each simulated spectrum with its 90% confidence level uncertainties are indicated on the upper right corner of each panel. As expected, E_{cut} is better constrained at higher redshift thanks to the cosmological redshifting, given the fact that we conserve the flux ($F_{2-10\,keV} = 10^{-12}$ erg s^{-1} cm^{-2}) of each simulated source at different redshifts. Likewise, sources with $E_{cut} = 50$ keV are better constrained than higher E_{cut} sources at all redshifts due to the band coverage of *HEX-P*. We found that it is difficult to constrain the high-energy cutoff of intermediate redshifts ($z < 1.1$) sources with $E_{cut} = 200$ keV in a 50 ks exposure.

We tested the E_{cut} constrained by *HEX-P* assuming different photon indices ($\Gamma = 1.60$, 1.90, and 2.20) under a few redshifts ($z = 0.85$, 1.40, 2.20, and 3.50) assuming the same flux as above. The results are reported in Table 1. We found that harder photon index provides better constraints on E_{cut} than softer photon index at all redshifts because more high energy photons are obtained for harder photon indices and a given 2–10 keV flux. The differences of the constraints on E_{cut} between softer and harder photon indices are much larger at lower redshifts than at higher redshifts. Nevertheless,

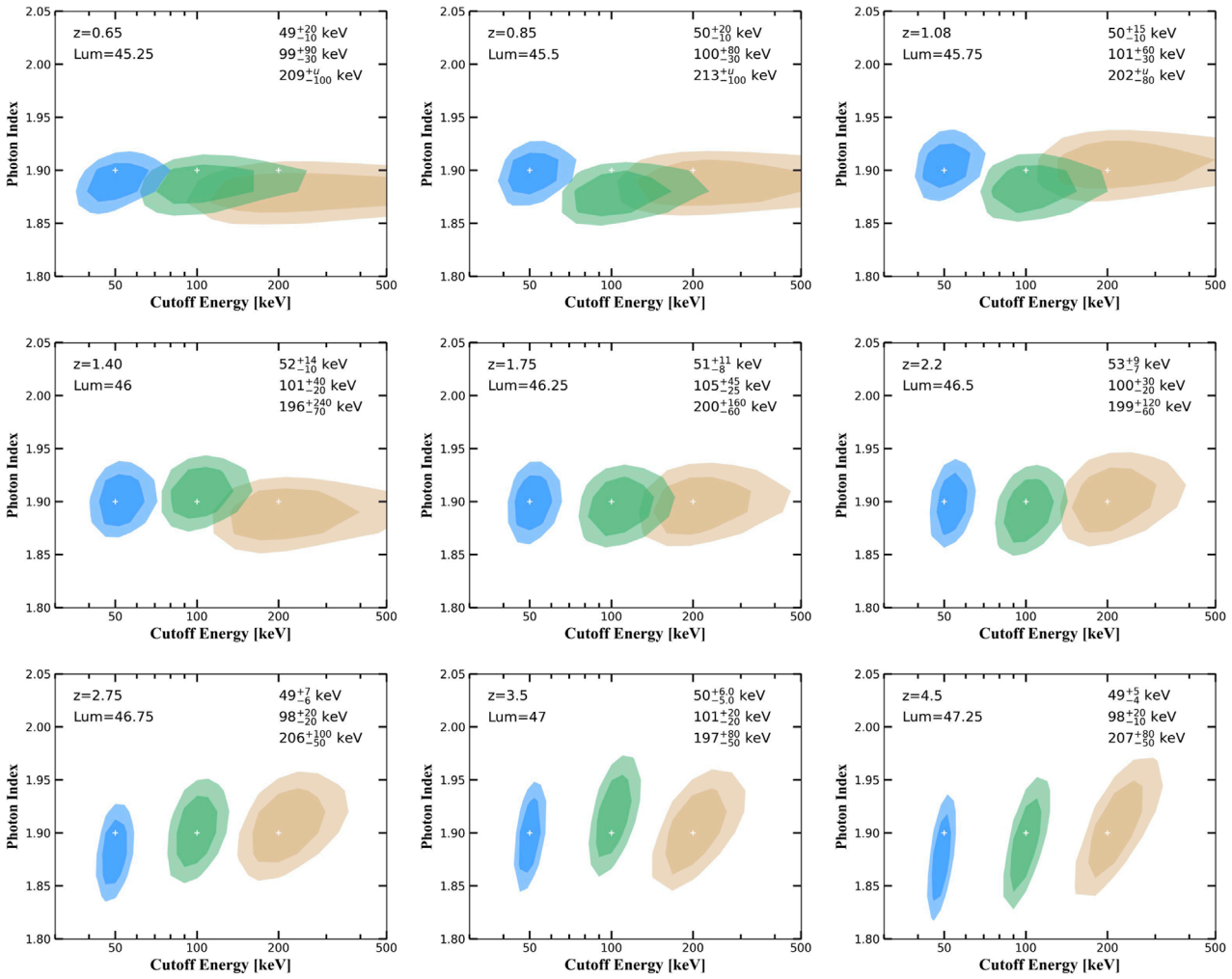

FIGURE 6
$E_{cut} - \Gamma$ contour plots (68% and 90% confidence levels) measured from the simulated spectra of the quasars with different redshifts ($0.65 < z < 4.5$), assuming an input 2–10 keV flux of 1×10^{-12} erg s^{-1} cm^{-2} and a *HEX-P* exposure of 50 ks We simulated three set of high-energy cutoff for each source, E_{cut} = 50, 100, and 200 keV (blue, green, and yellow). The white crosses indicate the input values. The best-fit value of each spectrum with its 90% confidence level uncertainty is indicated on the upper right corner of each panel.

TABLE 1 Constraints on the high-energy cutoff with different photon indices under different redshifts.

z	$\Gamma = 1.6$	$\Gamma = 1.9$	$\Gamma = 2.2$	$\Gamma = 1.6$	$\Gamma = 1.9$	$\Gamma = 2.2$	$\Gamma = 1.6$	$\Gamma = 1.9$	$\Gamma = 2.2$
	50 keV			100 keV			200 keV		
0.85	51^{+12}_{-9}	50^{+17}_{-10}	51^{+42}_{-15}	100^{+42}_{-24}	100^{+78}_{-31}	95^{+104}_{-34}	205^{+237}_{-74}	213^{+u}_{-96}	213^{+u}_{-117}
1.40	51^{+9}_{-7}	52^{+14}_{-9}	51^{+23}_{-12}	102^{+30}_{-20}	101^{+40}_{-20}	96^{+70}_{-30}	205^{+140}_{-60}	196^{+240}_{-70}	205^{+u}_{-90}
2.20	50^{+6}_{-6}	53^{+9}_{-7}	50^{+11}_{-8}	99^{+23}_{-16}	100^{+30}_{-19}	101^{+39}_{-23}	197^{+80}_{-50}	199^{+120}_{-60}	190^{+175}_{-55}
3.50	50^{+6}_{-5}	50^{+6}_{-5}	51^{+7}_{-6}	99^{+20}_{-15}	101^{+20}_{-15}	101^{+23}_{-17}	197^{+80}_{-45}	197^{+80}_{-45}	197^{+80}_{-45}

HEX-P could constrain the E_{cut} in most circumstances even for the sources with quite soft photon index, $\Gamma = 2.20$.

eROSITA (Predehl et al., 2021) observations will provide an all-sky survey of X-ray sources, which will be the deepest survey in the soft X-rays ever performed. With the ongoing SDSS and DESI surveys, and future *Euclid*, 4MOST, Subaru Prime Focus Spectrograph, and *SPHEREx* spectroscopic surveys, a large number of high-redshift, high-luminosity, radio-quiet AGN are expected

to be discovered prior to the launch of *HEX-P*. The combination of these large surveys should therefore provide a large sample of high-redshift quasars for *HEX-P* coronal physics studies in the next decade.

6 Physics of the corona in transient sources: changing-look/changing-state AGN and tidal disruption events

The growing number of time-domain surveys across the electromagnetic spectrum are revealing extreme variability in the accretion process onto supermassive black holes. These objects break from the standard stochastic variability seen in steadily accreting AGN, and thus provide a unique window into the formation, stability, and heating of the corona.

Changing-look AGN (CLAGN; also often referred to as changing-state AGN) show rapid changes between optical spectral types through either the appearance or disappearance of broad emission lines on timescales of months to years (for a recent review, see Ricci and Trakhtenbrot, 2022). These sources challenge the classic unified model for AGN, whereby the appearance of broad emission lines is solely a function of viewing angle. Instead, the change between optical spectral types is often coupled with an associated increase or decrease in the observed optical and X-ray flux, suggesting that the accretion rate is another key factor in AGN unification (e.g., Elitzur et al., 2014). The driving mechanism behind these changing-look events is still under debate, with theories including state transitions reminiscent of the behavior in black hole binaries (Noda and Done, 2018; Ruan et al., 2019), radiation pressure disk instabilities (Sniegowska et al., 2020), propagating cooling fronts linked to changes in the magnetic torques in the innermost regions of the accretion flow (Ross et al., 2018; Stern et al., 2018), and transient events like tidal disruption events (TDEs; e.g., Merloni et al., 2015; Ricci et al., 2020).

Although CLAGN are still a relatively rare phenomenon with only about 100 such systems known to date, they provide unique insights into the dynamic behavior of the inner accretion flow and unveil physics that is impossible to probe in standard steady-state AGN. One extreme example is evidenced by the recent discovery of the disappearance and recreation of the X-ray corona in 1 ES 1927 + 654. In late 2017, the source underwent one of the fastest changing-look events to date, whereby broad emission lines were caught forming on timescales of months (Trakhtenbrot et al., 2019). Shortly after the start of the changing-look event, X-ray observations of 1 ES 1927 + 654 revealed negligible hard X-ray emission, indicating that the X-ray corona had vanished in this source (Ricci et al., 2020; 2021). The corona began to reappear as the source brightened in the X-ray, although it remained extremely soft compared to standard AGN ($\Gamma \approx 3$–3.5; Ricci et al., 2021; Masterson et al., 2022). Two competing theories have been suggested to explain the behavior in this kind of system: a TDE occurring in an AGN (Ricci et al., 2020), or an inversion in the magnetic flux polarity (Scepi et al., 2021; Laha et al., 2022). Both theories can effectively cut off the energy supply to the corona, leading to its destruction.

TABLE 2 Spectral models and parameters used in simulations of 1ES 1927 + 654 with *HEX-P*.

Phase	XSPEC model	Γ	E_{cut} (keV)	kT_{bb} (eV)
1	tbabs × ztbabs × (zbbody + zpower + gsmooth (xillverTDE))	3.4	–[†]	88
2	tbabs × ztbabs × (zbbody + zcutoffpl + gsmooth (xillverTDE))	3.6	8.1	205
3	tbabs × ztbabs × (zcutoffpl + relxillCp)	2.3	23.4	–

[†]In this epoch, the source was too soft for proper determination of the cutoff energy, and hence, we used a simple power law to model the spectrum. Note that in the first joint *XMM-Newton*/*NuSTAR*, observation of 1 ES, 1927 + 654, the source was undetected above 3 keV with *XMM-Newton* and was not detected with *NuSTAR*.

As a unique opportunity to witness, for the first time, the formation of the corona in an AGN, there have been extensive X-ray resources used to study this enigmatic outburst of 1ES 1927 + 654. To date, *NICER* has observed the target for more than 1 Ms, and there have been 8 simultaneous *XMM-Newton*/*NuSTAR* monitoring periods, totalling more than 400 ks with each telescope. *NuSTAR* observations have been crucial for disentangling the soft photon index and low cutoff energy as the corona formed, which is not possible with either *XMM-Newton* or *NICER* alone due to their limited bandpasses. However, both *XMM-Newton* and *NICER* have been critical to unlocking information about the inner accretion flow with their soft X-ray spectra, including providing crucial information about rapid variability of the soft X-ray flux and the broad 1 keV line, that was recently linked to reflection from the inner disk (Masterson et al., 2022). To fully understand this system therefore requires a broad bandpass, which is provided by a single observatory in *HEX-P*.

To assess the contributions *HEX-P* can make to our understanding of the corona in CLAGN, we simulated the three different phases in the outburst of 1ES 1927 + 654 as would be seen with the LET and HET on *HEX-P*. For each phase, we simulated *HEX-P* spectra using the best-fitting *XMM-Newton*/*NuSTAR* models from Masterson et al. (2022) with six exposure times ranging from 10 to 150 ks The model used for each phase, along with the key coronal parameters used in the simulations, are given in Table 2. Figure 7 shows the resulting constraints on key coronal parameters Γ and E_{cut} for each evolutionary phase, as well as constraints on kT_{bb} of the dominant thermal component in the early super-soft phase (in which constraints on E_{cut} were not possible given the super-soft nature of the source). We compare these constraints to the ones achieved by 50-ks joint *XMM-Newton*/*NuSTAR* observations, which vary with the changing spectral shape and flux of the source. We find that *HEX-P* can reach similar constraints as from joint *XMM-Newton*/*NuSTAR* observations in a fraction of the exposure time. These simulations show that *HEX-P* could probe the evolution of the cutoff energy and photon index on roughly 10–25 ks timescales, meaning that either the source could be visited relatively frequently to track the evolution over weeks-months timescales, or that a single long stare could be broken into many 10–25 ks segments

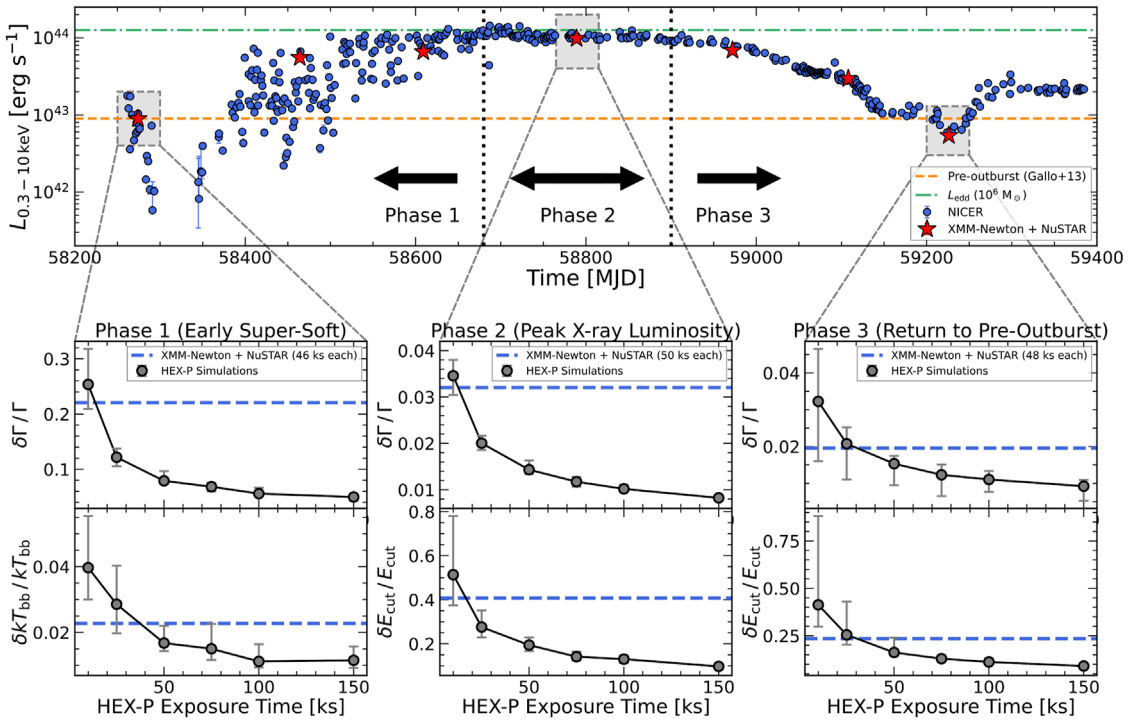

FIGURE 7
Top: X-ray light curve of 1 ES 1927 + 654 from Masterson et al. (2022), including 7 simultaneous *XMM-Newton*/*NuSTAR* observations and ~ 500 NICER observations. The pre-outburst X-ray luminosity is shown as an orange dashed line, and the Eddington luminosity for a 10^6 $M_\odot$ black hole is shown as a green dot-dashed line. The three evolutionary phases are indicated with vertical black dotted lines. The three *XMM-Newton*/*NuSTAR* epochs simulated with *HEX-P* are shown with grey boxes. *Bottom:* Fractional uncertainty on Γ, E_{cut}, and kT_{bb} for *HEX-P* simulations of the changing-look AGN 1 ES 1927 + 654 in three different evolutionary stages during its 2018–2021 outburst. The left-most panel shows simulations during the early super-soft phase (June 2018/Epoch 1), the middle panel shows simulations during the peak X-ray luminosity phase (Nov. 2019/Epoch 4), and the right panel shows simulations during the return to the post-outburst phase (Jan. 2021/Epoch 7). For each evolutionary phase, we simulated 25 spectra for 6 different *HEX-P* exposure times based on the best-fit *XMM-Newton*/*NuSTAR* model from Masterson et al. (2022). The blue dashed lines show the joint *XMM-Newton*/*NuSTAR* constraints on Γ and E_{cut} (or kT_{bb} for the early super-soft state, in which the cutoff energy cannot be constrained), which can be reached with *HEX-P* with much shorter exposure times (10–25 ks). The spectral models and key coronal parameters used to simulate the *HEX-P* spectra are given in Table 2.

in which the evolution of Γ and E_{cut} could be studied. The X-ray flux of 1ES 1927 + 654 varied by an order of magnitude in timescales as short as 8 h while the corona was in the process of forming (Ricci et al., 2020), which would allow *HEX-P* to provide unprecedented constraints on the evolution of the temperature and compactness of a newly forming corona for the first time. Since the discovery of 1ES 1927 + 654, other sources with similarly dramatic X-ray variability have been discovered (e.g., a repeating TDE discovered by eROSITA, which shows a repetitive creation and collapse of the X-ray corona; Liu et al., 2023).

Moreover, non-jetted TDEs present another opportunity to witness the formation of the corona around SMBHs, and *HEX-P* will play a major role in improving our understanding of various aspects of TDEs. Although detailed simulations go beyond the scope of the current manuscript, we highlight some of these science cases below. The majority of X-ray emitting, non-jetted TDEs show dominant thermal emission, presumably from the accretion disk, but a handful of sources have shown evidence for the formation of a corona in late-time (~ few years after ignition) X-ray observations (e.g., Wevers et al., 2021; Yao et al., 2022). As TDEs are believed to transition from super-to sub-Eddington when the mass fallback rate drops as stellar debris is accreted, they are another powerful probe of how the corona evolves with changes to the accretion state. A correlation between the Eddington ratio and X-ray spectral state has been already observed in a (small) sample study (Wevers, 2020), with a slope that is remarkably similar to that seen in AGN samples (see, e.g., Lusso and Risaliti, 2016). *HEX-P* studies will enable constraints on the formation and evolution of the corona while *simultaneously* constraining the high-energy cutoff energy over a wide range of accretion rates in individual SMBHs. This direct probe the disk-corona connection during different accretion states will allow for a comparison to state transitions in black hole binaries (Remillard and McClintock, 2006) and serve as a test of the scale-invariant nature of accretion.

X-ray observations of TDEs can also provide independent estimates of SMBH masses and spins, which are otherwise difficult to probe in dormant SMBHs. Detailed X-ray spectral modelling of the thermal continuum in TDEs can provide constraints on the mass and the spin of the central black hole (e.g., Wen et al., 2020). With its wide energy coverage, *HEX-P* will be able to advance this technique by mitigating the inherent uncertainties and bias introduced by the presence of an X-ray corona. Furthermore, X-ray variability is also a powerful probe of SMBH properties. In particular, the SMBH spin can be estimated through the detection

of X-ray quasi-periodic oscillations and/or disk precession (e.g., Pasham et al., 2019), and the SMBH mass can be measured with the break frequency of the power spectral distribution (PSD) (McHardy et al., 2006). In TDEs, the PSD behaviour has been shown to change with Eddington ratio (Saxton et al., 2012; Wevers et al., 2021), and hence can provide an independent estimate of the SMBH mass in TDEs. Additionally, if TDEs form a corona at late times when the accretion rate has dropped and the disk is geometrically thin, then the Fe Kα line can be used to constrain the corona geometry and SMBH spin (e.g., Yao et al., 2022). Thanks to its broad energy coverage, high throughput, low background, and L1 orbit permitting long observations, *HEX-P* will be able to improve our understanding of TDEs using all of these techniques. This will provide several independent mass and spin measurements of quiescent black holes, which would add invaluable information to constrain the demographics of quiescent low mass SMBHs ($<10^7 M_\odot$) that is not readily available through other means.

7 Coronal geometry

One of the key advances in recent years has been the ability to measure the location, geometry and structure of the corona using X-ray reflection and reverberation from the inner regions of the accretion disk. Determining the structure of the corona in this way places important constraints on the mechanism by which the corona is formed and energized by the accretion flow, for example, distinguishing between a corona that is formed in a jet or failed jet, from a corona that is formed over the surface of the inner accretion disk.

In addition to understanding the physics of the corona itself, measurements of the location and geometry of the corona are important to validate assumptions that underpin the use of X-ray reflection spectroscopy to measure fundamental properties of the black hole, such as its spin (Fabian et al., 1989; Dauser et al., 2013; Risaliti et al., 2013; Mallick et al., 2022). One of the predominant techniques employed to measure black hole spin is based upon identifying the innermost radius of the accretion disk (assumed to coincide with the innermost stable circular orbit, ISCO) from the extremal redshift detected in emission lines (namely, the iron K line) within the reflection spectrum (see Brenneman and Reynolds, 2006; Reynolds, 2021; Piotrowska et al., 2023). The intensity of the reflection and the line emission profile, however, depends upon the geometry of the corona, which provides the primary source of illumination. Typically, either a point source (or "lamppost") is assumed, or a phenomenological power law is used to model the emissivity profile of the disk (i.e., the intensity of the reflected flux as a function of radius). If the model corona or power law over-predicts reflection from the inner disk, the corona is at a greater height or is more extended than assumed in the model, and it is possible that the spin of the black hole is underestimated (Fabian et al., 2014). First-hand measurements of the location and geometry of the corona reduce this systematic uncertainty and the degeneracy that arises between extended coronæ and low spins.

HEX-P will enable measurements of the location, geometry and structure of the corona via both broadband X-ray spectroscopy and timing. The former is based upon direct measurement of the emissivity profile of the disk from the reflection observed in time-averaged X-ray spectra. The latter technique utilizes the light travel time between the corona and disk as variations in the luminosity of the primary X-ray emission reverberate off of the accretion disk. In addition, further constrains on the geometry of the X-ray corona are available from X-ray polarisation measurements, which can distinguish between X-ray emission from a compact corona, a corona associated with a jet, or an extended slab-like corona extending over the inner accretion disk (see, e.g., Marinucci et al., 2022a; Gianolli et al., 2023; Tagliacozzo et al., 2023; Ursini et al., 2023).

7.1 Measurements of the corona via X-ray spectroscopy

The emissivity profile of the disk is encoded in the profile of the relativistically broadened emission lines. The emission line we observe is the line emission integrated over the entire disk, and is comprised of photons experiencing different Doppler shifts and gravitational redshifts, which vary as a function of position on the disk. This means that it is possible to fit the observed line profile as the sum of contributions from different radii on the disk, and the relative contribution of the line model from each radius provides a measurement of the emissivity profile (Wilkins and Fabian, 2011). The measured profile can then be compared to theoretical predictions for the illumination of the disk by coronæ with different geometries and at different locations (Wilkins and Fabian, 2012; Dauser et al., 2013). Alternatively, a geometry can be assumed for the corona (usually a point source, or lamppost), and a model can be fit directly to full reflection spectrum to make a measurement of the coronal parameters; namely, the height of the corona for the lamppost (Dauser et al., 2016). The emissivity profile of the disk is sensitive to the coronal height in the case of a lamppost geometry, or to the radial extent of the corona if it were extended over the surface of the disk (Wilkins and Fabian, 2012).

A further measurement of the corona comes from the ratio of the reflected flux to the flux of the continuum that is observed directly from the corona, referred to as the reflection fraction (Wilkins and Gallo, 2015; Dauser et al., 2016). In the case of an isotropically emitting point source above an infinite accretion disk in a flat spacetime, we expect a reflection fraction $R_f = 1$, since exactly half of the emission from the corona is emitted downwards to illuminate the disk, and half is emitted upwards to escape to be observed as the continuum. Light bending around the black hole causes a greater fraction of the rays to be focused towards the inner accretion disk, enhancing the reflection fraction relative to the continuum when the corona is confined to a more compact region of space, closer to the black hole, providing another probe of the compactness of the corona (Fabian et al., 2012; Parker et al., 2014; Walton et al., 2021). On the other hand, the reflection fraction can be reduced below unity if it is outflowing at a mildly relativistic velocity (for example, if the corona is part of a jet or failed jet). In this case, the coronal emission is relativistically beamed away from the accretion disk, enhancing the fraction of rays that are able to escape to be observed as part of the continuum (Beloborodov, 1999; Gonzalez et al., 2017). The broad bandpass of *HEX-P* is vital to obtain an accurate measurement of the total reflection fraction.

In addition, by combining measurements of the reflection fraction with measurements of the relativistically broadened iron K line and the associated reverberation time lags, *HEX-P* will be able to obtain measurements of the location, the geometry, and the motion of the X-ray emitting coronæ around black holes.

7.2 X-ray reverberation from the inner accretion disk

The measurement of X-ray reverberation time lags adds a further dimension to the picture of the corona. The reflection and line emission from the accretion disk responds to short-timescale changes in luminosity of the primary X-ray emission from the corona. There is, however, a time delay between variations in the continuum and the correlated variations in the reflection due to the additional light travel time between the corona and disk (Fabian et al., 2009; Uttley et al., 2014). In the sample of AGN in which reverberation has been detected, the measured time delays are short and correspond to the light crossing time across distances of between approximately one and ten gravitational radii (this is approximately equal to the radial co-ordinate of the event horizon of a maximally spinning black hole). Such short time delays indicate that the corona must be compact and confined to a small region of space close to the black hole and innermost accretion flow (e.g., De Marco et al., 2013; Kara et al., 2016; Mallick et al., 2021). The reverberation time scale is primarily sensitive to the scale height of the corona above the disk (Wilkins and Fabian, 2013; Cackett et al., 2014). In recent years, there have also been advances in simultaneously modelling the X-ray spectrum and time lag measurements under the assumption of a point-like corona, using models such as RELTRANS (Ingram et al., 2019). With simultaneous fitting, it is possible to obtain simultaneous constraints on both the height of the corona and the mass of the black hole (e.g., Mastroserio et al., 2020).

HEX-P measurements of X-ray reflection and reverberation were simulated for nearby AGN, typical of those in which reverberation from the inner disk has been detected (e.g., Kara et al., 2015; 2016; Mallick et al., 2021). These are predominantly narrow line Seyfert 1 (NLS1) AGN (Gallo, 2006), which show strong, relativistically broadened iron K lines from the inner accretion disk and a high degree of short-timescale variability in their X-ray light curves (see, e.g., Gallo, 2018, for a review). The observations were simulated from a full spectral-timing reverberation model, which begins with general relativistic ray tracing calculations between a point-like corona, the accretion disk, and the observer, using the CUDAKERR code of Wilkins and Fabian (2012) and Wilkins et al. (2016). These ray tracing calculations self-consistently predict the illumination of the disk by the corona, and the energy shifts and time delays of the observed reflection and reverberation in the form of the impulse response function (Reynolds and Begelman, 1997; Cackett et al., 2014; Uttley et al., 2014). The response function is then convolved with the XILLVER model for the reflection spectrum produced in the rest frame of the material in the disk (García et al., 2013) to predict the full spectral-timing response. The simulations generate the observed X-ray spectrum (including the instrumental background), and the light curves that would be observed in different energy bands, folded through the response functions of the *HEX-P* telescopes and detectors, allowing measurements of the spectrum and time lags to be conducted as they would be for real observations.

The left panel of Figure 8 shows the simulated broadband X-ray spectrum and time lag spectrum for a typical Seyfert-like AGN displaying X-ray reverberation for a deep 500 ks observation with *HEX-P*. Reverberation is simulated around a maximally spinning ($a = 0.998$) black hole with a mass of $10^7\ M_\odot$ at a redshift of $z = 0.025$. The observed flux is equivalent to accretion at 0.3 times the Eddington limit, and 5 per cent of the total bolometric luminosity is produced by the corona. Parameters of the corona and accretion disk are selected to be representative of the typical reflection spectra observed in nearby AGN (e.g., Jiang et al., 2018; Mallick et al., 2018). The X-ray spectrum shows the characteristic features of X-ray reflection from the inner disk: a) the iron K line around 6.4 keV, with an extended redshifted wing comprised of the line photons emitted from the innermost radii of the accretion disk; b) the Compton hump around 20 keV; and c) a soft excess formed as soft X-ray lines are blended together by relativistic broadening. The ability to simultaneously measure the soft X-ray band, the broad iron K line, and the Compton hump will allow *HEX-P* observations to unambiguously separate reflection from the accretion disk from other spectral components (e.g., Walton et al., 2014).

The characteristic form of the reflection spectrum is also evident in the time lag spectrum. The energy bands dominated by reprocessed emission from the disk, namely, the soft excess, the iron K line, and the Compton hump, are seen to respond to variations at later times than the energy bands dominated by continuum emission observed directly from the corona (1.5–3 keV and 8–10 keV). The broad bandpass covered by the combination of the LET and HET on *HEX-P*, combined with the available effective area, mean that *HEX-P* is sensitive to reverberation time lags across the full range of the reflection spectrum. It will be possible to measure the differential time lag between the redshifted wing of the iron K line, which arises from the inner disk, closer to the black hole and corona, and the 6.4 keV core of the iron K line from larger radii. The difference in time lag between the inner and outer disk is a sensitive probe of the structure of the corona (Wilkins et al., 2016). *HEX-P* will be able to routinely measure the reverberation time delays associated with the Compton hump, only hints of which have so far appeared in *NuSTAR* observations (Kara et al., 2015; Zoghbi et al., 2017).

7.3 Simulation of *HEX-P* reverberation measurements

To demonstrate the sensitivity of *HEX-P* to X-ray reverberation and its effectiveness in measuring the structure of the corona across the supermassive black hole mass spectrum, iron K reverberation measurements were simulated for a sample representative of the 25 brightest nearby AGN in the BASS catalog, each observed for 300 ks with *HEX-P*. For each of these simulated AGN, the mass, bolometric luminosity, redshift and absorption were drawn from the BASS catalog (Koss et al., 2022). The remaining parameters of the black hole, accretion disk and corona were drawn randomly from distributions representing the reverberation sample (since

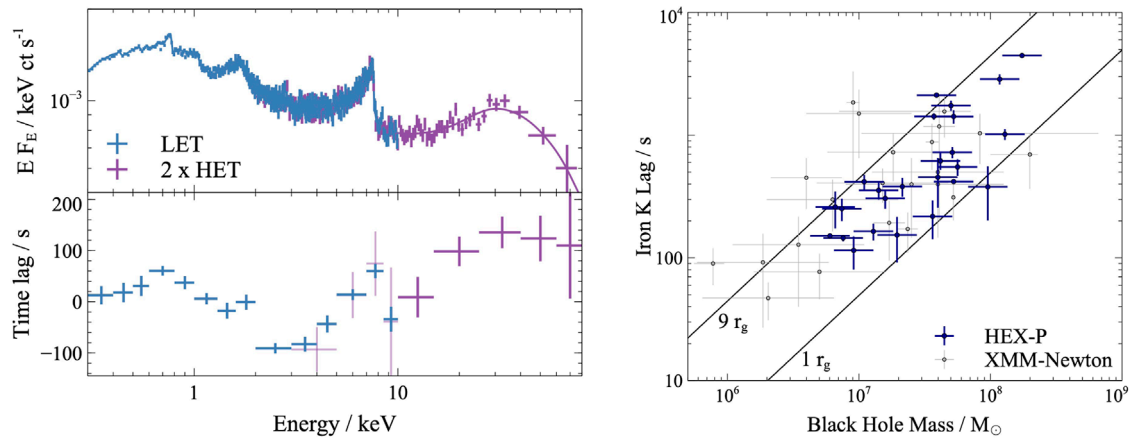

FIGURE 8
Left: Simulated 500 ks *HEX-P* observation of a typical nearby AGN, showing X-ray reflection and reverberation from the inner accretion disk. The top panel shows the simulated X-ray spectra obtained with the LET and HET. The relativistically broadened iron K line (around 6.4 keV) and Compton hump (around 25 kev) that are characteristic of reflection from the inner disk are clearly visible. The bottom panel shows the measured time lag vs. energy spectrum, which shows the relative time at which different energy bands respond as variations in the continuum emission reverberate off the disk. The energy bands dominated by reflection from the disk (the soft X-ray excess, below 1 keV, the broad iron line, and the Compton hump) lag behind the bands dominated by the primary continuum observed directly from the corona. This time delay arises from the additional light travel time between the corona and accretion disk, and is a sensitive probe of the location and geometry of the corona. *Right:* Simulated iron K reverberation lag measurements as a function of black hole mass for a simulated sample of AGN based upon the BASS sample. For each simulated AGN, the mass, luminosity, and redshift are representative of the real sample, and the remaining parameters of the black hole, disk, and corona are drawn from random distributions. Each of the simulated AGN is observed for 300 ks with *HEX-P*. Error bars on the black hole mass values assume mass measurements can be made via optical reverberation, and correspond to a representative uncertainty of 0.15 dex.

detailed spectral analyses are not available for all of the BASS AGN[4]). The reverberation measurement was simulated as described above, predicting the time lag vs. Fourier frequency that would be measured by *HEX-P* between the continuum-dominated 1.2–4 keV band and the 4–7 keV iron K band. We select the frequency bin with the highest signal-to-noise (i.e., the ratio between the lag and the lag uncertainty) as the representative iron K lag value.

The right panel of Figure 8 shows the simulated iron K reverberation lag measurements as a function of black hole mass for the BASS AGN sample, compared to the equivalent measurements made in a sample of nearby Seyfert galaxies using *XMM-Newton* (Kara et al., 2016). *HEX-P* will significantly detect reverberation in the iron K line and trace the relationship between the reverberation time lag and the mass of the black hole. From these simulations, we expect that *HEX-P* will be able to measure iron K lags in a sample of AGN between redshifts of $z = 0.005$ and $z = 0.14$, with bolometric luminosities between 3×10^{43} and 10^{46} erg s^{-1} (assuming 5 per cent of this is emitted across the broad 0.1–100 keV X-ray band). The simulations show that iron K lags will be measured to high precision, with a median uncertainty of 13 per cent across the sample from 300 ks observations. Longer observations of around 500 ks will enable an additional reverberation measurement to be made in the Compton hump to constrain the broadband time lag spectrum, to which more detailed reverberation models can be fit (as demonstrated in the left panel).[5]

Notably, *HEX-P* will also be able to detect reverberation around the most massive black holes in the sample ($\gtrsim 10^8\ M_\odot$), where the reverberation timescale is expected to be longer (if it scales simply with the gravitational radius around the black hole). The ability to measure long-timescale lags using common Fourier techniques (Uttley et al., 2014) is limited by the duration of continuous light curves that can be obtained. The highly elliptical orbit of *XMM-Newton* limits individual observations, and hence individual light curve segments, to ~125 ks. At its L1 orbit, *HEX-P* will be able to perform much longer continuous exposures (in principle up to 12 days), greatly lengthening the timescales that can be probed. Combined with the fact that the highest mass AGN are some of the brightest in the BASS sample, iron K reverberation is expected to be detected at high significance.

8 Black hole X-ray binary coronæ

This work has focused on coronæ in the vicinity of extragalactic SMBHs, primarily observed through hard X-ray emission from AGN. However, Galactic black hole X-ray binaries (BHXRBs) can

4 The probability distributions from which the parameter values are drawn were chosen to be consistent with the range of parameter values from the sub-set of the BASS AGN sample for which spectroscopic measurements are available, detailed at www.bass-survey.com and in Ricci et al. (2017).

5 In Figure 8, the error bars on mass measurements assume that the mass can be measured by optical reverberation. We assume a representative uncertainty of 0.15 dex on the black hole mass, the median of those obtained by reverberation measurements in the Black Hole Mass Database (Bentz and Katz, 2015).

be viewed broadly as scaled-down versions of AGN, particularly from the point of view of the compact regions close to the BH (Falcke et al., 2004; Körding et al., 2006; McHardy et al., 2006; Walton et al., 2012). Many BHXRBs–those with low-mass companion stars–are transient sources, undergoing outbursts lasting weeks to years, during which they display a full repertoire of accretion states and regularly exceed X-ray fluxes of 1 Crab (see, e.g., Remillard and McClintock, 2006; Tetarenko et al., 2016). Given the broad dynamical range one can probe via studies of BHXRBs, much can be learned about the long-term behaviour and evolution of AGN through observations possible on human timescales. In addition, the high fluxes of outbursting BHXRBs allow for characterization of the broadband X-ray continuum with exquisite detail, making them a primary target for *HEX-P*.

As briefly discussed in Section 3, today's X-ray observatories already allow us to probe the coronal temperatures of BHXRBs as they decrease with increasing source flux (Buisson et al., 2019; Cangemi et al., 2021; Zdziarski et al., 2021), and these measurements have contributed greatly to our understanding of BH coronæ. However, degeneracies remain in the broadband X-ray continuum emission and geometry of BHXRB coronæ, as well as the AGN ones, and this has been a hindrance to reflection studies aimed at characterizing the inner accretion flow and measuring BH spin. With its broadband coverage, large collecting area, and high energy sensitivity, *HEX-P* will: (i) break degeneracies in the geometry of the irradiating corona intrinsic to reflection models; and (ii) measure deviations from purely thermal Comptonization models, allowing explicit constraints on the non-thermal fraction of BHXRB coronæ. The broadband spectral coverage of *HEX-P* in the 0.2–80 keV range, combined with its high-energy sensitivity (owing to low X-ray background) will be especially powerful in constraining the weaker power law emission in BHXRB soft states, advancing coronal constraints spanning orders of magnitude in luminosity and across the spectral states. We refer the reader to Connors et al. (2023) for a full description of *HEX-P* simulations of BHXRB coronæ.

9 Discussion and conclusion

In this paper, we show the advances that *HEX-P* will make in understanding the physics of the X-ray corona in different types of AGN, ranging from local Seyferts to quasars at cosmological redshifts. The broad passband, large effective area, low background, and the ability to have continuous long exposures will enable addressing many open questions regarding the physics of the X-ray corona in AGN. *HEX-P* will allow an accurate estimate of the continuum emission spectrum of the corona by measuring the photon index and the high-energy cutoff. Assuming a certain geometry, these parameters can then be mapped into optical depth and electron temperature within the framework of Comptonization (see, e.g., Middei et al., 2019). We demonstrate how *HEX-P* will improve our understanding of the electron distribution in AGN coronæ, measure coronal properties of obscured sources, and extend these analyses to $z \geq 1$. Furthermore, we show that *HEX-P* will track variations of bright transient events such as CLAGN and TDEs on timescales of a few hours. *HEX-P* will allow us to study the properties of the X-ray corona and probe the innermost regions of the accretion disk via reverberation mapping. This will be crucial for understanding how the corona interacts with the accretion disk, studying disk reflection and consequently measure the BH spin in AGN over a broad range of mass and luminosity, and probing AGN feedback (see Piotrowska et al., 2023). Furthermore, *HEX-P* will allow a detailed study of obscuration in AGN and identify the fraction of Compton-thick AGN in deep surveys (see Boorman et al., 2023; Civano et al., 2023). All this will help achieving a more complete picture of how SMBHs grow and evolve across cosmic time, and the role they play in galaxy evolution.

Simultaneous observations with LET and HET, covering the 0.2–80 keV range, will allow an accurate measurement of $E_{\rm cut}$ up to ~1 MeV in bright sources where ionized disk reflection is important. This has been discussed in detail by García et al. (2015) who showed that the soft part of the reflection spectrum, rich in fluorescent lines and atomic features, depends strongly on the properties of the corona, illuminating the accretion disk. García et al. (2015) demonstrated this in the case of joint *NuSTAR* and *Suzaku* spectra. Here, we revisit the analysis presented by those authors for *HEX-P*. We consider a simple spectrum comprised of neutral Galactic absorption (`TBabs`; Wilms et al., 2000) and a power law plus ionized reflection (`relxill`; Dauser et al., 2013; García et al., 2014). In `XSPEC` parlance, the model is written as: `Model = TBabs × relxill`. We assume a Galactic absorption $N_{\rm H} = 5 \times 10^{20}$ cm^{-2}. As for the reflection component, we assume a photon index $\Gamma = 2$, a black hole spin $a^* = 0.998$, a disk ionization parameter $\log(\xi/\mathrm{erg\ cm\ s^{-1}}) = 1.5$, an inclination $i = 45°$, a disk emissivity index $q = 3$, and an iron abundance equal to the solar value. García et al. (2015) used similar parameters except for the reflection fraction which they assumed to be $R_{\rm f} = 3$. This enhances the reflection features in the spectrum. We choose a more conservative value of $R_{\rm f} = 1$. We then simulate 100-ks observations of *HEX-P* for $E_{\rm cut}$ ranging between 50 keV and 1 MeV for 2–10 keV flux levels of 1 mCrab, 10 mCrab, 100 mCrab, and 500 mCrab. These simulations are intended to represent a wide range of Galactic and extragalactic accreting black holes. We fit the simulated spectra using only the HET and by using both LET and HET simultaneously. Similarly to García et al. (2015), we find that *HEX-P* will allow us to accurately estimate $E_{\rm cut}$ up to ~1 MeV for bright sources (Figure 9). In addition, we also find that the inclusion of LET significantly reduces the uncertainty on $E_{\rm cut}$. We note that these results assume that the soft X-ray excess is in totality caused by the ionized relativistic reflection from the inner parts of the disk. In fact, the nature of this excess is still a matter of debate as it has been suggested that it could also be caused by the presence of a warm optically thick corona (e.g., Petrucci et al., 2018; 2020). Studying the effect of such model on the properties of the hot corona is beyond the scope of this paper.

9.1 Synergies with other facilities

We have demonstrated the power of *HEX-P* as a stand-alone instrument to advance our understanding of the physics of X-ray coronæ in accreting black holes. However, simultaneous broadband X-ray and multi-wavelength coverage will provide a more comprehensive physical picture of accretion onto these objects.

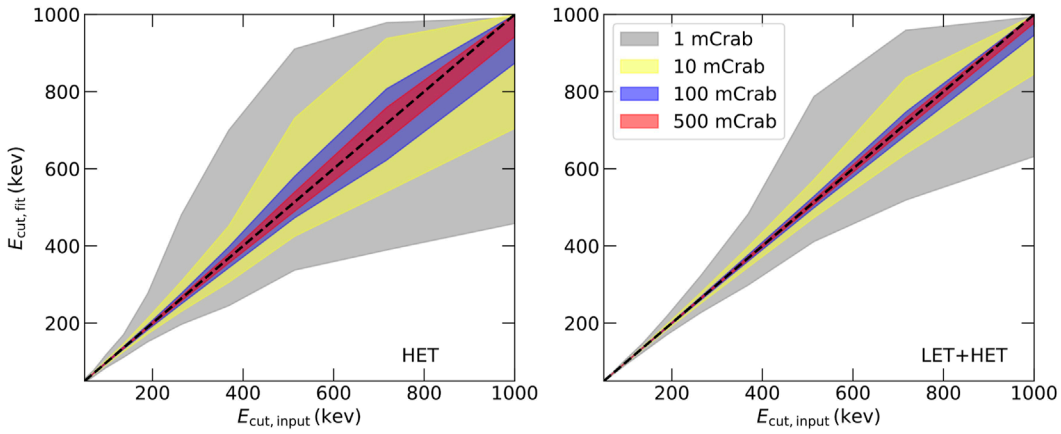

FIGURE 9
Results of fitting *HEX-P* simulations assuming relativistic reflection, by employing only HET (left) and by adding the soft X-rays LET + HET (right). The grey, yellow, blue, and red areas correspond to the 90% confidence level on estimating E_{cut} for observed flux levels of 1 mCrab, 10 mCrab, 100 mCrab, and 500 mCrab, respectively.

HEX-P will play an instrumental role in such studies thanks to its broad passband and high energy sensitivity as demonstrated throughout this paper. The ability to probe the emission from the X-ray corona for a variety of sources with a wide range of mass, luminosity, distance, and variability timescales will make *HEX-P* an essential tool to provide a comprehensive understanding of the behavior and physics of AGN coronæ, which is the dominant source of X-rays in the universe.

For example, the recent advancements made by *IXPE*, observing X-ray polarization in AGN for the first time, required a full characterization of the broadband X-ray spectrum. This has been ensured via simultaneous observations with *XMM-Newton*, *NuSTAR*, and *Chandra*. *HEX-P* will provide equivalent energy coverage to the combination of *XMM-Newton*/*Chandra* and *NuSTAR*, with significant improvements to the high energy sensitivity. *HEX-P* will be an essential complementary observatory to future X-ray polarization missions such as the *X-ray Polarization Probe* (*XPP*; Krawczynski et al., 2019; Jahoda et al., 2019) and the *enhanced X-ray Timing and Polarimetry* mission (*eXTP*; Zhang S. et al., 2019).

As mentioned earlier, a correlation between the hard X-ray emission and mm-band continuum has been observed in various samples of AGN (see, e.g., Behar et al., 2018; Kawamuro et al., 2022; Ricci et al., 2023). *HEX-P* will accurately measure the optical depth and temperature of the X-ray corona, as well as determine the fraction of non-thermal electrons producing the X-ray emission for a large sample of AGN. In coordination with ALMA and similar facilities, these parameters can then be used to model the continuum emission in the mm-band and probe the magnetic field powering the corona. *HEX-P* will also complement observations with the Square Kilometer Array and the next-generation of cosmic microwave background experiments (e.g., CMB-S4; Carlstrom et al., 2019; Abazajian et al., 2022).

Moreover, *HEX-P* will play a crucial part in connecting soft X-ray and soft gamma-ray (i.e., up to a few MeV) observations of BHXRBs. In particular, a primary science goal of the *Compton Spectrometer and Imager* (*COSI*; Tomsick et al., 2019), scheduled for launch in 2027 as a NASA Small Explorer (SMEX) mission, is to characterize the Galactic 511 keV positron annihilation line and the gamma-ray polarization of compact objects. *COSI* will be able to detect a broadened and redshifted pair line from pair-dominated coronæ. The broadband X-ray coverage of *HEX-P* will help constrain the continuum coronal emission, which will be important for modeling the higher energy emission and polarization measurements provided by *COSI*. *HEX-P* will also play a major role in constraining the X-ray emission from gamma-ray emitting AGN detected by *COSI* (see Marcotulli et al., 2023), which will probe the connection between the accretion disk and jets (Ajello et al., 2019), shedding yet more light on the nature of the X-ray corona.

Recent systematic studies of the optical night sky, such as All Sky Automated Survey for Super Novæ (ASASSN; Shappee et al., 2014), the Asteroid Terrestrial-impact Last Alert System (ATLAS; Tonry et al., 2018), and the Zwicky Transient Facility (ZTF; Bellm, 2014; Graham et al., 2019), are providing large numbers of Galactic and extragalactic transients, which are often associated with accretion onto compact objects. The discovery rate of nuclear transients with dramatic X-ray variability, similar to 1ES 1927 + 654, is expected to increase significantly in the next decade with the continued advance of large-scale, time-domain surveys in the optical (e.g., photometry from the Vera Rubin Observatory, spectroscopy from SDSS-V) and UV (e.g., *ULTRASAT*; Sagiv et al., 2014). Therefore, *HEX-P* will be well-positioned to make significant discoveries and contributions to the X-ray evolution and nature of the corona in transient accretion systems (as discussed in Section 6).

Finally, *HEX-P* will play a major role in the era of the high-resolution X-ray spectroscopy, with the development of microcalorimeters achieving a resolving power ($E/\Delta E$) larger than 1,000 at energies up to 7 keV. The Resolve instrument on *XRISM* (Tashiro et al., 2018; XRISM Science Team, 2022) launched in August 2023, and the X-ray Integral Field Unit (X-IFU) on *Athena*

(Nandra et al., 2013; Barret et al., 2023), expected to be launched in the late 2030s, will revolutionize our view of accretion onto compact objects. These instruments will probe the fine structure in absorption and emission from gas around accreting black holes. However, these gaseous structures are dictated by the hard ionizing X-rays, and the accurate measurements of such features will require a proper estimate of the underlying X-ray continuum out to tens of keV. This energy coverage can be provided by *NuSTAR* in the 2020s and *HEX-P* will extend and improve this coverage in the decades to come. In particular, *HEX-P* will be able to constrain the coronal emission and reflection spectrum at hard X-rays. This will be crucial for determining the illumination profile of the accretion disk by the X-ray corona, and accurately measuring BH spin for a broad range of mass and luminosity (see Piotrowska et al., 2023). Combining the resolving power of the future generation of microcalorimeters to the broad energy coverage of *HEX-P* will allow us to address important questions about black hole growth and evolution, and to understand the role of these objects in shaping the Universe.

9.2 Conclusion

We have demonstrated that *HEX-P* will provide an unprecedented look at the X-ray coronæ of accreting black holes with a main focus on AGN, thanks to its high sensitivity and broad energy coverage. The main results of the paper can be summarised as follows:

- *HEX-P* will accurately estimate the coronal properties of unobscured AGN. In particular, it will study evolution of coronal temperature in bright, variable AGN. This will allow us to measure the non-thermal fraction of electrons in AGN coronæ and test the runaway pair production hypothesis.
- *HEX-P* will also accurately estimate the coronal properties of obscured AGN up to $z \sim 0.5$. This will be a crucial test of the orientation-based unified model of AGN.
- *HEX-P* will efficiently constrain the coronal properties of high-redshift quasars ($z > 1.40$) even with high energy cutoff up to 200 keV. *HEX-P* will also extend the estimates of the coronal properties of powerful quasars beyond cosmic noon up to $z \simeq 4.5$. This will allow us to study the evolution of the X-ray properties of AGN across cosmic times.
- *HEX-P* will play a major role in studying transient events such as CLAGN and TDEs. It will allow us to witness the destruction, formation, and evolution of the X-ray corona in these extreme events.
- Finally, the high sensitivity of *HEX-P* that extends to hard X-rays and the possibility of long continuous observations of bright AGN will enable accurate reverberation mapping of the innermost regions of the accretion disk. This will allow us to estimate the location of the corona and its illuminating profile over a broad mass range.

Data availability statement

The raw data supporting the conclusion of this article will be made available by the authors, without undue reservation.

Author contributions

EK: Methodology, Visualization, Writing–original draft, Writing–review and editing. AL: Visualization, Writing–original draft, Writing–review and editing. MM: Writing–original draft, Writing–review and editing. DWi: Writing–original draft, Writing–review and editing. XZ: Writing–original draft, Writing–review and editing. MB: Writing–original draft, Writing–review and editing. PB: Writing–original draft, Writing–review and editing. RC: Writing–original draft, Writing–review and editing. PC: Conceptualization, Writing–review and editing. AF: Writing–review and editing. JG: Writing–original draft, Writing–review and editing. KM: Writing–original draft. NR: Investigation, Writing–review and editing. NS: Writing–original draft, Writing–review and editing. DS: Writing–review and editing. JT: Writing–review and editing. TW: Writing–review and editing. DWa: Writing–review and editing. SB: Writing–review and editing. JB: Writing–review and editing, Writing–original draft. FC: Writing–review and editing. GL: Writing–review and editing. LM: Writing–review and editing. GM: Writing–review and editing. AM: Writing–review and editing. EN: Writing–review and editing. JP: Writing–review and editing. CR: Writing–review and editing. K-WW: Writing–review and editing. AZ: Writing–review and editing.

Funding

The author(s) declare financial support was received for the research, authorship, and/or publication of this article. LM is supported by the CITA National Fellowship. The work of DS was carried out at the Jet Propulsion Laboratory, California Institute of Technology, under a contract with NASA.

Acknowledgments

EK acknowledges financial support from the Centre National d'Etudes Spatiales (CNES). MB acknowledges support from the YCAA Prize Postdoctoral Fellowship. CR acknowledges support from Fondecyt Regular grant 1230345 and ANID BASAL project FB210003. XZ acknowledges NASA support under contract number 80NSSC22K0012.

Conflict of interest

The authors declare that the research was conducted in the absence of any commercial or financial relationships that could be construed as a potential conflict of interest.

The author(s) declared that they were an editorial board member of Frontiers, at the time of submission. This had no impact on the peer review process and the final decision.

The reviewer P-OP declared a past co-authorship with the authors SB, GM, and EK to the handling Editor.

Publisher's note

All claims expressed in this article are solely those of the authors and do not necessarily represent those of their affiliated organizations, or those of the publisher, the editors and the reviewers. Any product that may be evaluated in this article, or claim that may be made by its manufacturer, is not guaranteed or endorsed by the publisher.

References

Abazajian, K., Abdulghafour, A., Addison, G. E., Adshead, P., Ahmed, Z., Ajello, M., et al. (2022). *Snowmass 2021 CMB-S4 white paper*. arXiv e-prints, Available at: https://doi.org/10.48550/arXiv.2203.08024.

Agol, E., and Krolik, J. H. (2000). Magnetic stress at the marginally stable orbit: altered disk structure, radiation, and black hole spin evolution. *ApJ* 528, 161–170. doi:10.1086/308177

Ajello, M., Paliya, V., Marcotulli, L., Perkins, J. S., Prandini, E., D'Ammando, F., et al. (2019). Supermassive black holes at high redshifts. *BAAS* 51, 289.

Akylas, A., and Georgantopoulos, I. (2021). Distribution of the coronal temperature in Seyfert 1 galaxies. *A&A* 655, A60. doi:10.1051/0004-6361/202141186

Antonucci, R. (1993). Unified models for active galactic nuclei and quasars. *ARA&A* 31, 473–521. doi:10.1146/annurev.aa.31.090193.002353

Aversa, R., Lapi, A., de Zotti, G., Shankar, F., and Danese, L. (2015). Black hole and galaxy coevolution from continuity equation and abundance matching. *ApJ* 810, 74. doi:10.1088/0004-637X/810/1/74

Ballantyne, D. R., Bollenbacher, J. M., Brenneman, L. W., Madsen, K. K., Baloković, M., Boggs, S. E., et al. (2014). NuSTAR reveals the comptonizing corona of the broad-line radio galaxy 3C 382. *ApJ* 794, 62. doi:10.1088/0004-637X/794/1/62

Baloković, M., Brightman, M., Harrison, F. A., Comastri, A., Ricci, C., Buchner, J., et al. (2018). New spectral model for constraining torus covering factors from broadband X-ray spectra of active galactic nuclei. *ApJ* 854, 42. doi:10.3847/1538-4357/aaa7eb

Baloković, M., Harrison, F. A., Madejski, G., Comastri, A., Ricci, C., Annuar, A., et al. (2020). NuSTAR survey of obscured swift/BAT-selected active galactic nuclei. II. Median high-energy cutoff in Seyfert II hard X-ray spectra. *ApJ* 905, 41. doi:10.3847/1538-4357/abc342

Baloković, M., Matt, G., Harrison, F. A., Zoghbi, A., Ballantyne, D. R., Boggs, S. E., et al. (2015). Coronal properties of the Seyfert 1.9 galaxy MCG-05-23-016 determined from hard X-ray spectroscopy with NuSTAR. *ApJ* 800, 62. doi:10.1088/0004-637X/800/1/62

Barret, D., Albouys, V., Herder, J.-W. d., Piro, L., Cappi, M., Huovelin, J., et al. (2023). The Athena X-ray Integral Field Unit: a consolidated design for the system requirement review of the preliminary definition phase. *Exp. Astron.* 55, 373–426. doi:10.1007/s10686-022-09880-7

Barua, S., Jithesh, V., Misra, R., Dewangan, G. C., Sarma, R., and Pathak, A. (2020). NuSTAR observation of Ark 564 reveals the variation of coronal temperature with flux. *MNRAS* 492, 3041–3046. doi:10.1093/mnras/staa067

Baumgartner, W. H., Tueller, J., Markwardt, C. B., Skinner, G. K., Barthelmy, S., Mushotzky, R. F., et al. (2013). The 70 Month swift-BAT all-sky hard X-ray survey. *ApJS* 207, 19. doi:10.1088/0067-0049/207/2/19

Behar, E., Baldi, R. D., Laor, A., Horesh, A., Stevens, J., and Tzioumis, T. (2015). Discovery of millimetre-wave excess emission in radio-quiet active galactic nuclei. *MNRAS* 451, 517–526. doi:10.1093/mnras/stv988

Behar, E., Vogel, S., Baldi, R. D., Smith, K. L., and Mushotzky, R. F. (2018). The mm-wave compact component of an AGN. *MNRAS* 478, 399–406. doi:10.1093/mnras/sty850

Beheshtipour, B., Krawczynski, H., and Malzac, J. (2017). The X-ray polarization of the accretion disk coronae of active galactic nuclei. *ApJ* 850, 14. doi:10.3847/1538-4357/aa906a

Bellm, E. (2014). "The Zwicky transient facility," in *The third hot-wiring the transient universe workshop*. Editors P. R. Wozniak, M. J. Graham, A. A. Mahabal, and R. Seaman (Santa Fe: NASA/ADS), 27–33. doi:10.48550/arXiv.1410.8185

Belmont, R., Malzac, J., and Marcowith, A. (2008). Simulating radiation and kinetic processes in relativistic plasmas. *A&A* 491, 617–631. doi:10.1051/0004-6361:200809982

Beloborodov, A. M. (1999). Plasma ejection from magnetic flares and the X-ray spectrum of Cygnus X-1. *ApJ* 510, L123–L126. doi:10.1086/311810

Bentz, M. C., and Katz, S. (2015). The AGN black hole mass Database. *PASP* 127, 67–73. doi:10.1086/679601

Bertola, E., Vignali, C., Lanzuisi, G., Dadina, M., Cappi, M., Gilli, R., et al. (2022). The properties of the X-ray corona in the distant (z = 3.91) quasar APM 08279+5255. *A&A* 662, A98. doi:10.1051/0004-6361/202142642

Boorman, P. G., Torres-Albà, N., Annuar, A., Marchesi, S., Pfeifle, R., Stern, D., et al. (2023). The high energy X-ray probe (HEX-P): the circum-nuclear environment of growing supermassive black holes. *arXiv e-prints*, arXiv:2311.04949. doi:10.48550/arXiv.2311.04949

Brenneman, L. W., and Reynolds, C. S. (2006). Constraining black hole spin via X-ray spectroscopy. *ApJ* 652, 1028–1043. doi:10.1086/508146

Buchner, J., Brightman, M., Baloković, M., Wada, K., Bauer, F. E., and Nandra, K. (2021). Physically motivated X-ray obscurer models. *A&A* 651, A58. doi:10.1051/0004-6361/201834963

Buchner, J., Brightman, M., Nandra, K., Nikutta, R., and Bauer, F. E. (2019). X-ray spectral and eclipsing model of the clumpy obscurer in active galactic nuclei. *A&A* 629, A16. doi:10.1051/0004-6361/201834771

Buisson, D. J. K., Fabian, A. C., Barret, D., Fürst, F., Gandhi, P., García, J. A., et al. (2019). MAXI J1820+070 with NuSTAR I. An increase in variability frequency but a stable reflection spectrum: coronal properties and implications for the inner disc in black hole binaries. *MNRAS* 490, 1350–1362. doi:10.1093/mnras/stz2681

Buisson, D. J. K., Fabian, A. C., and Lohfink, A. M. (2018). Coronal temperatures of the AGN ESO 103-035 and IGR 2124.7+5058 from NuSTAR observations. *MNRAS* 481, 4419–4426. doi:10.1093/mnras/sty2609

Cackett, E. M., Zoghbi, A., Reynolds, C., Fabian, A. C., Kara, E., Uttley, P., et al. (2014). Modelling the broad Fe Kα reverberation in the AGN NGC 4151. *MNRAS* 438, 2980–2994. doi:10.1093/mnras/stt2424

Cadolle Bel, M., Sizun, P., Goldwurm, A., Rodriguez, J., Laurent, P., Zdziarski, A. A., et al. (2006). The broad-band spectrum of Cygnus X-1 measured by INTEGRAL. *A&A* 446, 591–602. doi:10.1051/0004-6361:20053068

Cangemi, F., Beuchert, T., Siegert, T., Rodriguez, J., Grinberg, V., Belmont, R., et al. (2021). Potential origin of the state-dependent high-energy tail in the black hole microquasar Cygnus X-1 as seen with INTEGRAL. *A&A* 650, A93. doi:10.1051/0004-6361/202038604

Carlstrom, J., Abazajian, K., Addison, G., Adshead, P., Ahmed, Z., Allen, S. W., et al. (2019). CMB-S4. *Bull. Am. Astronomical Soc.* 51, 209. doi:10.48550/arXiv.1908.01062

Chartas, G., Brandt, W. N., Gallagher, S. C., and Garmire, G. P. (2002). CHANDRA detects relativistic broad absorption lines from APM 08279+5255. *ApJ* 579, 169–175. doi:10.1086/342744

Chartas, G., Kochanek, C. S., Dai, X., Poindexter, S., and Garmire, G. (2009). X-ray microlensing in rxj1131-1231 and HE1104-1805. *ApJ* 693, 174–185. doi:10.1088/0004-637X/693/1/174

Chartas, G., Rhea, C., Kochanek, C., Dai, X., Morgan, C., Blackburne, J., et al. (2016). Gravitational lensing size scales for quasars. *Astron. Nachrichten* 337, 356–361. doi:10.1002/asna.201612313

Civano, F., Zhao, X., Boorman, P., Marchesi, S., Ananna, T., Creech, S., et al. (2023). The high energy X-ray probe (HEX-P): bringing the cosmic X-ray background into focus. arXiv e-prints. Available at: https://doi.org/10.48550/arXiv.2311.04832.

Connors, R., Tomsick, J., Draghis, P., Coughenour, B., Shaw, A., Garcia, J., et al. (2023). The high energy X-ray probe (HEX-P): probing accretion onto stellar mass black holes. arXiv e-prints, Available at: https://doi.org/10.48550/arXiv.2311.04782.

Coppi, P. S. (1999). "The physics of hybrid thermal/non-thermal plasmas," in *High energy processes in accreting black holes. Vol. 161 of astronomical society of the pacific conference series, 375*. Editors J. Poutanen, and R. Svensson (California, United States: Astronomical Society of the Pacific). doi:10.48550/arXiv.astro-ph/9903158

Dadina, M. (2007). BeppoSAX observations in the 2–100 keV band of the nearby Seyfert galaxies: an atlas of spectra. *A&A* 461, 1209–1252. doi:10.1051/0004-6361:20065734

Dauser, T., García, J., Parker, M. L., Fabian, A. C., Wilms, J., Lohfink, A., et al. (2020). *relxill: reflection models of black hole accretion disks*. record ascl:2010.015. Astrophysics Source Code Library.

Dauser, T., García, J., Walton, D. J., Eikmann, W., Kallman, T., McClintock, J., et al. (2016). Normalizing a relativistic model of X-ray reflection. Definition of the reflection fraction and its implementation in relxill. *A&A* 590, A76. doi:10.1051/0004-6361/201628135

Dauser, T., Garcia, J., Wilms, J., Böck, M., Brenneman, L. W., Falanga, M., et al. (2013). Irradiation of an accretion disc by a jet: general properties and implications for spin measurements of black holes. *MNRAS* 430, 1694–1708. doi:10.1093/mnras/sts710

De Marco, B., Ponti, G., Cappi, M., Dadina, M., Uttley, P., Cackett, E. M., et al. (2013). Discovery of a relation between black hole mass and soft X-ray time lags in active galactic nuclei. *MNRAS* 431, 2441–2452. doi:10.1093/mnras/stt339

de Rosa, A., Panessa, F., Bassani, L., Bazzano, A., Bird, A., Landi, R., et al. (2012). Broad-band study of hard X-ray-selected absorbed active galactic nuclei. *MNRAS* 420, 2087–2101. doi:10.1111/j.1365-2966.2011.20167.x

Di Matteo, T., Celotti, A., and Fabian, A. C. (1997). Cyclo-synchrotron emission from magnetically dominated active regions above accretion discs. *MNRAS* 291, 805–810. doi:10.1093/mnras/291.4.805

Doi, A., and Inoue, Y. (2016). High-frequency excess in the radio continuum spectrum of the type-1 Seyfert galaxy NGC 985. *PASJ* 68, 56. doi:10.1093/pasj/psw052

Done, C., Jin, C., Middleton, M., and Ward, M. (2013). A new way to measure supermassive black hole spin in accretion disc-dominated active galaxies. *MNRAS* 434, 1955–1963. doi:10.1093/mnras/stt1138

Dovčiak, M., Papadakis, I. E., Kammoun, E. S., and Zhang, W. (2022). Physical model for the broadband energy spectrum of X-ray illuminated accretion discs: fitting the spectral energy distribution of NGC 5548. *A&A* 661, A135. doi:10.1051/0004-6361/202142358

Elitzur, M., Ho, L. C., and Trump, J. R. (2014). Evolution of broad-line emission from active galactic nuclei. *MNRAS* 438, 3340–3351. doi:10.1093/mnras/stt2445

Emmanoulopoulos, D., Papadakis, I. E., Dovčiak, M., and McHardy, I. M. (2014). General relativistic modelling of the negative reverberation X-ray time delays in AGN. *MNRAS* 439, 3931–3950. doi:10.1093/mnras/stu249

Eraerds, T., Antonelli, V., Davis, C., Hall, D., Hetherington, O., Holland, A., et al. (2021). Enhanced simulations on the athena/wide field imager instrumental background. *J. Astronomical Telesc. Instrum. Syst.* 7, 034001. doi:10.1117/1.JATIS.7.3.034001

Fabian, A. C., and Iwasawa, K. (1999). The mass density in black holes inferred from the X-ray background. *MNRAS* 303, L34–L36. doi:10.1046/j.1365-8711.1999.02404.x

Fabian, A. C., Lohfink, A., Belmont, R., Malzac, J., and Coppi, P. (2017). Properties of AGN coronae in the NuSTAR era - II. Hybrid plasma. *MNRAS* 467, 2566–2570. doi:10.1093/mnras/stx221

Fabian, A. C., Lohfink, A., Kara, E., Parker, M. L., Vasudevan, R., and Reynolds, C. S. (2015). Properties of AGN coronae in the NuSTAR era. *MNRAS* 451, 4375–4383. doi:10.1093/mnras/stv1218

Fabian, A. C., Parker, M. L., Wilkins, D. R., Miller, J. M., Kara, E., Reynolds, C. S., et al. (2014). On the determination of the spin and disc truncation of accreting black holes using X-ray reflection. *MNRAS* 439, 2307–2313. doi:10.1093/mnras/stu045

Fabian, A. C., Rees, M. J., Stella, L., and White, N. E. (1989). X-ray fluorescence from the inner disc in Cygnus X-1. *MNRAS* 238, 729–736. doi:10.1093/mnras/238.3.729

Fabian, A. C., Zoghbi, A., Ross, R. R., Uttley, P., Gallo, L. C., Brandt, W. N., et al. (2009). Broad line emission from iron K- and L-shell transitions in the active galaxy 1H0707-495. *Nature* 459, 540–542. doi:10.1038/nature08007

Fabian, A. C., Zoghbi, A., Wilkins, D., Dwelly, T., Uttley, P., Schartel, N., et al. (2012). 1H 0707-495 in 2011: an X-ray source within a gravitational radius of the event horizon. *MNRAS* 419, 116–123. doi:10.1111/j.1365-2966.2011.19676.x

Falcke, H., Körding, E., and Markoff, S. (2004). A scheme to unify low-power accreting black holes. Jet-dominated accretion flows and the radio/X-ray correlation. *A&A* 414, 895–903. doi:10.1051/0004-6361:20031683

Galeev, A. A., Rosner, R., and Vaiana, G. S. (1979). Structured coronae of accretion disks. *ApJ* 229, 318–326. doi:10.1086/156957

Gallo, L. (2018). X-ray perspective of Narrow-line Seyfert 1 galaxies. *Revisiting Narrow-Line Seyfert 1 Galaxies their Place Universe* 328, 35. doi:10.22323/1.328.0034

Gallo, L. C. (2006). Investigating the nature of narrow-line Seyfert 1 galaxies with high-energy spectral complexity. *MNRAS* 368, 479–486. doi:10.1111/j.1365-2966.2006.10137.x

Gallo, L. C., Gonzalez, A. G., and Miller, J. M. (2021). Eclipsing the X-ray emitting region in the active galaxy NGC 6814. *ApJ* 908, L33. doi:10.3847/2041-8213/abdcb5

García, J., Dauser, T., Lohfink, A., Kallman, T. R., Steiner, J. F., McClintock, J. E., et al. (2014). Improved reflection models of black hole accretion disks: treating the angular distribution of X-rays. *ApJ* 782, 76. doi:10.1088/0004-637X/782/2/76

García, J., Dauser, T., Reynolds, C. S., Kallman, T. R., McClintock, J. E., Wilms, J., et al. (2013). X-ray reflected spectra from accretion disk models. III. A complete grid of ionized reflection calculations. *ApJ* 768, 146. doi:10.1088/0004-637X/768/2/146

García, J. A., Dauser, T., Steiner, J. F., McClintock, J. E., Keck, M. L., and Wilms, J. (2015). On estimating the high-energy cutoff in the x-ray spectra of black holes via reflection spectroscopy. *Astrophysical J. Lett.* 808, L37. doi:10.1088/2041-8205/808/2/L37

Ghisellini, G., Haardt, F., and Fabian, A. C. (1993). On re-acceleration, pairs and the high-energy spectrum of AGN and galactic black hole candidates. *MNRAS* 263, L9–L12. doi:10.1093/mnras/263.1.L9

Ghisellini, G., Haardt, F., and Matt, G. (1994). The contribution of the obscuring torus to the X-ray spectrum of Seyfert galaxies: a test for the unification model. *MNRAS* 267, 743–754. doi:10.1093/mnras/267.3.743

Ghisellini, G., Haardt, F., and Matt, G. (2004). Aborted jets and the X-ray emission of radio-quiet AGNs. *A&A* 413, 535–545. doi:10.1051/0004-6361:20031562

Gianolli, V. E., Kim, D. E., Bianchi, S., Agís-González, B., Madejski, G., Marin, F., et al. (2023). Uncovering the geometry of the hot X-ray corona in the Seyfert galaxy NGC 4151 with IXPE. *MNRAS* 523, 4468–4476. doi:10.1093/mnras/stad1697

Gilli, R., Comastri, A., and Hasinger, G. (2007). The synthesis of the cosmic X-ray background in the Chandra and XMM-Newton era. *A&A* 463, 79–96. doi:10.1051/0004-6361:20066334

Gonzalez, A. G., Wilkins, D. R., and Gallo, L. C. (2017). Probing the geometry and motion of AGN coronae through accretion disc emissivity profiles. *MNRAS* 472, 1932–1945. doi:10.1093/mnras/stx2080

Goosmann, R. W., and Matt, G. (2011). Spotting the misaligned outflows in NGC 1068 using X-ray polarimetry. *MNRAS* 415, 3119–3128. doi:10.1111/j.1365-2966.2011.18923.x

Graham, M. J., Kulkarni, S. R., Bellm, E. C., Adams, S. M., Barbarino, C., Blagorodnova, N., et al. (2019). The Zwicky transient facility: science objectives. *PASP* 131, 078001. doi:10.1088/1538-3873/ab006c

Guedel, M., and Benz, A. O. (1993). X-Ray/Microwave relation of different types of active stars. *ApJ* 405, L63. doi:10.1086/186766

Guilbert, P. W., Fabian, A. C., and Rees, M. J. (1983). Spectral and variability constraints on compact sources. *MNRAS* 205, 593–603. doi:10.1093/mnras/205.3.593

Gupta, S., Sridhar, N., and Sironi, L. (2023). Comptonization by reconnection plasmoids in black hole coronae III: dependence on the guide field in pair plasma. arXiv e-prints, Available at: https://doi.org/10.48550/arXiv.2310.04233.

Haardt, F., and Maraschi, L. (1991). A two-phase model for the X-ray emission from Seyfert galaxies. *ApJ* 380, L51. doi:10.1086/186171

Haardt, F., and Maraschi, L. (1993). X-ray spectra from two-phase accretion disks. *ApJ* 413, 507. doi:10.1086/173020

Harrison, F. A., Craig, W. W., Christensen, F. E., Hailey, C. J., Zhang, W. W., Boggs, S. E., et al. (2013). The nuclear spectroscopic telescope Array (NuSTAR) high-energy X-ray mission. *ApJ* 770, 103. doi:10.1088/0004-637X/770/2/103

Henri, G., and Pelletier, G. (1991). Relativistic electron-positron beam formation in the framework of the two-flow model for active galactic nuclei. *ApJ* 383, L7. doi:10.1086/186228

Henri, G., and Petrucci, P. O. (1997). Anisotropic illumination of AGN's accretion disk by a non thermal source. I. General theory and application to the Newtonian geometry. *A&A* 326, 87–98. doi:10.48550/arXiv.astro-ph/9705233

Hickox, R. C., and Alexander, D. M. (2018). Obscured active galactic nuclei. *ARA&A* 56, 625–671. doi:10.1146/annurev-astro-081817-051803

Ingram, A., Ewing, M., Marinucci, A., Tagliacozzo, D., Rosario, D. J., Veledina, A., et al. (2023). The X-ray polarisation of the Seyfert 1 galaxy IC 4329A. arXiv e-prints, Available at: https://doi.org/10.48550/arXiv.2305.13028.

Ingram, A., Mastroserio, G., Dauser, T., Hovenkamp, P., van der Klis, M., and García, J. A. (2019). A public relativistic transfer function model for X-ray reverberation mapping of accreting black holes. *MNRAS* 488, 324–347. doi:10.1093/mnras/stz1720

Inoue, Y., and Doi, A. (2014). Unveiling the nature of coronae in active galactic nuclei through submillimeter observations. *PASJ* 66, L8. doi:10.1093/pasj/psu079

Inoue, Y., and Doi, A. (2018). Detection of coronal magnetic activity in nearby active supermassive black holes. *ApJ* 869, 114. doi:10.3847/1538-4357/aaeb95

Jahoda, K., Krawczynski, H., Kislat, F., Marshall, H., Okajima, T., Agudo, I., et al. (2019). The X-ray Polarization Probe mission concept. arXiv e-prints , Available at: https://doi.org/10.48550/arXiv.1907.10190.

Jansen, F., Lumb, D., Altieri, B., Clavel, J., Ehle, M., Erd, C., et al. (2001). XMM-Newton observatory. I. The spacecraft and operations. *A&A* 365, L1–L6. doi:10.1051/0004-6361:20000036

Jiang, J., Parker, M. L., Fabian, A. C., Alston, W. N., Buisson, D. J. K., Cackett, E. M., et al. (2018). The 1.5 Ms observing campaign on IRAS 13224-3809 - I. X-ray spectral analysis. *MNRAS* 477, 3711–3726. doi:10.1093/mnras/sty836

Kammoun, E. S., Igo, Z., Miller, J. M., Fabian, A. C., Reynolds, M. T., Merloni, A., et al. (2023). The first X-ray look at SMSS J114447.77-430859.3: the most luminous quasar in the last 9 Gyr. *MNRAS* 522, 5217–5237. doi:10.1093/mnras/stad952

Kammoun, E. S., Miller, J. M., Koss, M., Oh, K., Zoghbi, A., Mushotzky, R. F., et al. (2020). A hard look at local, optically selected, obscured Seyfert galaxies. *ApJ* 901, 161. doi:10.3847/1538-4357/abb29f

Kammoun, E. S., Risaliti, G., Stern, D., Jun, H. D., Graham, M., Celotti, A., et al. (2017). Coronal properties of the luminous radio-quiet quasar QSO B2202-209. *MNRAS* 465, 1665–1671. doi:10.1093/mnras/stw2897

Kamraj, N., Brightman, M., Harrison, F. A., Stern, D., García, J. A., Baloković, M., et al. (2022). X-ray coronal properties of swift/BAT-selected Seyfert 1 active galactic nuclei. *ApJ* 927, 42. doi:10.3847/1538-4357/ac45f6

Kamraj, N., Harrison, F. A., Baloković, M., Lohfink, A., and Brightman, M. (2018). Coronal properties of swift/BAT-selected Seyfert 1 AGNs observed with NuSTAR. *ApJ* 866, 124. doi:10.3847/1538-4357/aadd0d

Kara, E., Alston, W. N., Fabian, A. C., Cackett, E. M., Uttley, P., Reynolds, C. S., et al. (2016). A global look at X-ray time lags in Seyfert galaxies. *MNRAS* 462, 511–531. doi:10.1093/mnras/stw1695

Kara, E., García, J. A., Lohfink, A., Fabian, A. C., Reynolds, C. S., Tombesi, F., et al. (2017). The high-Eddington NLS1 Ark 564 has the coolest corona. *MNRAS* 468, 3489–3498. doi:10.1093/mnras/stx792

Kara, E., Zoghbi, A., Marinucci, A., Walton, D. J., Fabian, A. C., Risaliti, G., et al. (2015). Iron K and Compton hump reverberation in SWIFT J2127.4+5654 and NGC 1365 revealed by NuSTAR and XMM-Newton. *MNRAS* 446, 737–749. doi:10.1093/mnras/stu2136

Kawamuro, T., Ricci, C., Imanishi, M., Mushotzky, R. F., Izumi, T., Ricci, F., et al. (2022). BASS XXXII: studying the nuclear millimeter-wave continuum emission of AGNs with ALMA at scales ≲100-200 pc. *ApJ* 938, 87. doi:10.3847/1538-4357/ac8794

Kawamuro, T., Ricci, C., Mushotzky, R. F., Imanishi, M., Bauer, F. E., Ricci, F., et al. (2023). BASS XXXIV: a catalog of the nuclear mm-wave continuum emission properties of AGNs constrained on scales ≲ 100–200 pc. arXiv e-prints, Available at: https://doi.org/10.48550/arXiv.2309.02776.

Kochanek, C. S., Dai, X., Morgan, C., Morgan, N., Poindexter, G., and Chartas, S. (2007). "Turning AGN microlensing from a curiosity into a tool," in *Statistical challenges in modern astronomy IV*. Editors G. J Babu, and E. D Feigelson. vol. 371 of Astronomical Society of the Pacific Conference Series, 43. doi:10.48550/arXiv.astro-ph/0609112

Körding, E. G., Jester, S., and Fender, R. (2006). Accretion states and radio loudness in active galactic nuclei: analogies with X-ray binaries. *MNRAS* 372, 1366–1378. doi:10.1111/j.1365-2966.2006.10954.x

Koss, M. J., Ricci, C., Trakhtenbrot, B., Oh, K., den Brok, J. S., Mejía-Restrepo, J. E., et al. (2022). BASS. XXII. The BASS DR2 AGN catalog and data. *ApJS* 261, 2. doi:10.3847/1538-4365/ac6c05

Krawczynski, H., Matt, G., Ingram, A. R., Taverna, R., Turolla, R., Kislat, F., et al. (2019). Astro2020 science white paper: using X-ray polarimetry to probe the physics of black holes and neutron stars. arXiv e-prints, Available at: https://doi.org/10.48550/arXiv.1904.09313.

Krawczynski, H., Muleri, F., Dovčiak, M., Veledina, A., Rodriguez Cavero, N., Svoboda, J., et al. (2022). Polarized x-rays constrain the disk-jet geometry in the black hole x-ray binary Cygnus X-1. *Science* 378, 650–654. doi:10.1126/science.add5399

Laha, S., Meyer, E., Roychowdhury, A., Becerra Gonzalez, J., Acosta-Pulido, J. A., Thapa, A., et al. (2022). A radio, optical, UV, and X-ray view of the enigmatic changing-look active galactic nucleus 1ES 1927+654 from its pre-to postflare states. *ApJ* 931, 5. doi:10.3847/1538-4357/ac63aa

Lanzuisi, G., Gilli, R., Cappi, M., Dadina, M., Bianchi, S., Brusa, M., et al. (2019). NuSTAR measurement of coronal temperature in two luminous, high-redshift quasars. *ApJ* 875, L20. doi:10.3847/2041-8213/ab15dc

Laor, A., and Behar, E. (2008). On the origin of radio emission in radio-quiet quasars. *MNRAS* 390, 847–862. doi:10.1111/j.1365-2966.2008.13806.x

Lewin, C., Kara, E., Wilkins, D., Mastroserio, G., García, J. A., Zhang, R. C., et al. (2022). X-ray reverberation mapping of Ark 564 using Gaussian process regression. *ApJ* 939, 109. doi:10.3847/1538-4357/ac978f

Liu, T., Wang, J.-X., Yang, H., Zhu, F.-F., and Zhou, Y.-Y. (2014). Are X-ray emitting coronae around supermassive black holes outflowing? *ApJ* 783, 106. doi:10.1088/0004-637X/783/2/106

Liu, Z., Malyali, A., Krumpe, M., Homan, D., Goodwin, A. J., Grotova, I., et al. (2023). Deciphering the extreme X-ray variability of the nuclear transient eRASSt J045650.3−203750. A likely repeating partial tidal disruption event. *A&A* 669, A75. doi:10.1051/0004-6361/202244805

Lubiński, P., Beckmann, V., Gibaud, L., Paltani, S., Papadakis, I. E., Ricci, C., et al. (2016). A comprehensive analysis of the hard X-ray spectra of bright Seyfert galaxies. *MNRAS* 458, 2454–2475. doi:10.1093/mnras/stw454

Lusso, E., Comastri, A., Simmons, B. D., Mignoli, M., Zamorani, G., Vignali, C., et al. (2012). Bolometric luminosities and Eddington ratios of X-ray selected active galactic nuclei in the XMM-COSMOS survey. *MNRAS* 425, 623–640. doi:10.1111/j.1365-2966.2012.21513.x

Lusso, E., and Risaliti, G. (2016). The tight relation between X-ray and ultraviolet luminosity of quasars. *ApJ* 819, 154. doi:10.3847/0004-637X/819/2/154

Madsen, K. K., García, J. A., Stern, D., Armini, R., Basso, S., Coutinho, D., et al. (2023). The high energy X-ray probe (HEX-P): instrument and mission profile. *arXiv e-prints*, arXiv:2312.04678. doi:10.48550/arXiv.2312.04678

Malizia, A., Molina, M., Bassani, L., Stephen, J. B., Bazzano, A., Ubertini, P., et al. (2014). The INTEGRAL high-energy cut-off distribution of type 1 active galactic nuclei. *ApJ* 782, L25. doi:10.1088/2041-8205/782/2/L25

Mallick, L., Alston, W. N., Parker, M. L., Fabian, A. C., Pinto, C., Dewangan, G. C., et al. (2018). A high-density relativistic reflection origin for the soft and hard X-ray excess emission from Mrk 1044. *MNRAS* 479, 615–634. doi:10.1093/mnras/sty1487

Mallick, L., Fabian, A. C., García, J. A., Tomsick, J. A., Parker, M. L., Dauser, T., et al. (2022). High-density disc reflection spectroscopy of low-mass active galactic nuclei. *MNRAS* 513, 4361–4379. doi:10.1093/mnras/stac990

Mallick, L., Wilkins, D. R., Alston, W. N., Markowitz, A., De Marco, B., Parker, M. L., et al. (2021). Discovery of soft and hard X-ray time lags in low-mass AGNs. *MNRAS* 503, 3775–3783. doi:10.1093/mnras/stab627

Malzac, J., Beloborodov, A. M., and Poutanen, J. (2001). X-ray spectra of accretion discs with dynamic coronae. *MNRAS* 326, 417–427. doi:10.1046/j.1365-8711.2001.04450.x

Marconi, A., Risaliti, G., Gilli, R., Hunt, L. K., Maiolino, R., and Salvati, M. (2004). Local supermassive black holes, relics of active galactic nuclei and the X-ray background. *MNRAS* 351, 169–185. doi:10.1111/j.1365-2966.2004.07765.x

Marcotulli, L., Ajello, M., Böttcher, M., Coppi, P., Costamante, L., Di Gesu, L., et al. (2023). The High Energy X-ray Probe (HEX-P): the most powerful jets through the lens of a superb X-ray eye. arXiv e-prints, Available at: https://doi.org/10.48550/arXiv.2311.04801.

Marin, F., Dovčiak, M., Muleri, F., Kislat, F. F., and Krawczynski, H. S. (2018). Predicting the X-ray polarization of type 2 Seyfert galaxies. *MNRAS* 473, 1286–1316. doi:10.1093/mnras/stx2382

Marinucci, A., Muleri, F., Dovciak, M., Bianchi, S., Marin, F., Matt, G., et al. (2022a). Polarization constraints on the X-ray corona in Seyfert galaxies: MCG-05-23-16. *MNRAS* 516, 5907–5913. doi:10.1093/mnras/stac2634

Marinucci, A., Vietri, G., Piconcelli, E., Bianchi, S., Guainazzi, M., Lanzuisi, G., et al. (2022b). Breaking the rules at $z \simeq 0.45$: the rebel case of RBS 1055. *A&A* 666, A169. doi:10.1051/0004-6361/202244272

Markoff, S., Nowak, M. A., and Wilms, J. (2005). Going with the flow: can the base of jets subsume the role of compact accretion disk coronae? *ApJ* 635, 1203–1216. doi:10.1086/497628

Martocchia, A., and Matt, G. (1996). Iron Kα line intensity from accretion discs around rotating black holes. *MNRAS* 282, L53–L57. doi:10.1093/mnras/282.4.L53

Masterson, M., Kara, E., Ricci, C., García, J. A., Fabian, A. C., Pinto, C., et al. (2022). Evolution of a relativistic outflow and X-ray corona in the extreme changing-look AGN 1ES 1927+654. *ApJ* 934, 35. doi:10.3847/1538-4357/ac76c0

Mastroserio, G., Ingram, A., and van der Klis, M. (2020). Multi-timescale reverberation mapping of Mrk 335. *MNRAS* 498, 4971–4982. doi:10.1093/mnras/staa2735

Mastroserio, G., Ingram, A., Wang, J., García, J. A., van der Klis, M., Cavecchi, Y., et al. (2021). Modelling correlated variability in accreting black holes: the effect of high density and variable ionization on reverberation lags. *MNRAS* 507, 55–73. doi:10.1093/mnras/stab2056

Matt, G., Marinucci, A., Guainazzi, M., Brenneman, L. W., Elvis, M., Lohfink, A., et al. (2014). The soft-X-ray emission of Ark 120. XMM-Newton, NuSTAR, and the importance of taking the broad view. *MNRAS* 439, 3016–3021. doi:10.1093/mnras/stu159

Matt, G., Perola, G. C., and Piro, L. (1991). The iron line and high energy bump as X-ray signatures of cold matter in Seyfert 1 galaxies. *A&A* 247, 25.

McHardy, I. M., Koerding, E., Knigge, C., Uttley, P., and Fender, R. P. (2006). Active galactic nuclei as scaled-up Galactic black holes. *Nature* 444, 730–732. doi:10.1038/nature05389

Meidinger, N., Albrecht, S., Beitler, C., Bonholzer, M., Emberger, V., Frank, J., et al. (2020). "Development status of the wide field imager instrument for Athena," in *Society of photo-optical instrumentation engineers (SPIE) conference series*. vol. 11444 of Society of Photo-Optical Instrumentation Engineers (SPIE) Conference Series. doi:10.1117/12.2560507

Merloni, A., Dwelly, T., Salvato, M., Georgakakis, A., Greiner, J., Krumpe, M., et al. (2015). A tidal disruption flare in a massive galaxy? Implications for the fuelling mechanisms of nuclear black holes. *MNRAS* 452, 69–87. doi:10.1093/mnras/stv1095

Merloni, A., and Fabian, A. C. (2001a). Accretion disc coronae as magnetic reservoirs. *MNRAS* 321, 549–552. doi:10.1046/j.1365-8711.2001.04060.x

Merloni, A., and Fabian, A. C. (2001b). Thunderclouds and accretion discs: a model for the spectral and temporal variability of Seyfert 1 galaxies. *MNRAS* 328, 958–968. doi:10.1046/j.1365-8711.2001.04925.x

Middei, R., Bianchi, S., Marinucci, A., Matt, G., Petrucci, P. O., Tamborra, F., et al. (2019). Relations between phenomenological and physical parameters in the hot coronae of AGNs computed with the MoCA code. *A&A* 630, A131. doi:10.1051/0004-6361/201935881

Miniutti, G., and Fabian, A. C. (2004). A light bending model for the X-ray temporal and spectral properties of accreting black holes. *MNRAS* 349, 1435–1448. doi:10.1111/j.1365-2966.2004.07611.x

Molina, M., Bassani, L., Malizia, A., Stephen, J. B., Bird, A. J., Bazzano, A., et al. (2013). Hard-X-ray spectra of active galactic nuclei in the INTEGRAL complete sample. *MNRAS* 433, 1687–1700. doi:10.1093/mnras/stt844

Mosquera, A. M., Kochanek, C. S., Chen, B., Dai, X., Blackburne, J. A., and Chartas, G. (2013). The structure of the X-ray and optical emitting regions of the lensed quasar Q 2237+0305. *ApJ* 769, 53. doi:10.1088/0004-637X/769/1/53

Nandra, K., Barret, D., Barcons, X., Fabian, A., den Herder, J.-W., Piro, L., et al. (2013). The hot and energetic universe: a white paper presenting the science theme motivating the Athena+ mission. arXiv e-prints, Available at: https://doi.org/10.48550/arXiv.1306.2307.

Nicastro, F., Piro, L., De Rosa, A., Feroci, M., Grandi, P., Fiore, F., et al. (2000). A long observation of NGC 5548 by BeppoSAX: the high-energy cutoff, intrinsic spectral variability, and a truly warm absorber. *ApJ* 536, 718–728. doi:10.1086/308950

Niedźwiecki, A., Zdziarski, A. A., and Szanecki, M. (2016). On the lamppost model of accreting black holes. *ApJ* 821, L1. doi:10.3847/2041-8205/821/1/L1

Noda, H., and Done, C. (2018). Explaining changing-look AGN with state transition triggered by rapid mass accretion rate drop. *MNRAS* 480, 3898–3906. doi:10.1093/mnras/sty2032

Oh, K., Koss, M., Markwardt, C. B., Schawinski, K., Baumgartner, W. H., Barthelmy, S. D., et al. (2018). The 105-month swift-BAT all-sky hard X-ray survey. *ApJS* 235, 4. doi:10.3847/1538-4365/aaa7fd

Panessa, F., Baldi, R. D., Laor, A., Padovani, P., Behar, E., and McHardy, I. (2019). The origin of radio emission from radio-quiet active galactic nuclei. *Nat. Astron.* 3, 387–396. doi:10.1038/s41550-019-0765-4

Parker, M. L., Wilkins, D. R., Fabian, A. C., Grupe, D., Dauser, T., Matt, G., et al. (2014). The NuSTAR spectrum of Mrk 335: extreme relativistic effects within two gravitational radii of the event horizon? *MNRAS* 443, 1723–1732. doi:10.1093/mnras/stu1246

Pasham, D. R., Remillard, R. A., Fragile, P. C., Franchini, A., Stone, N. C., Lodato, G., et al. (2019). A loud quasi-periodic oscillation after a star is disrupted by a massive black hole. *Science* 363, 531–534. doi:10.1126/science.aar7480

Petrucci, P. O., Gronkiewicz, D., Rozanska, A., Belmont, R., Bianchi, S., Czerny, B., et al. (2020). Radiation spectra of warm and optically thick coronae in AGNs. *A&A* 634, A85. doi:10.1051/0004-6361/201937011

Petrucci, P. O., Haardt, F., Maraschi, L., Grandi, P., Malzac, J., Matt, G., et al. (2001a). Testing comptonization models using BeppoSAX observations of Seyfert 1 galaxies. *ApJ* 556, 716–726. doi:10.1086/321629

Petrucci, P. O., Maraschi, L., Haardt, F., and Nandra, K. (2004). Physical interpretation of the NGC 7469 UV/X-ray variability. *A&A* 413, 477–487. doi:10.1051/0004-6361:20031499

Petrucci, P. O., Merloni, A., Fabian, A., Haardt, F., and Gallo, E. (2001b). The effects of a Comptonizing corona on the appearance of the reflection components in accreting black hole spectra. *MNRAS* 328, 501–510. doi:10.1046/j.1365-8711.2001.04897.x

Petrucci, P. O., Paltani, S., Malzac, J., Kaastra, J. S., Cappi, M., Ponti, G., et al. (2013). Multiwavelength campaign on Mrk 509. XII. Broad band spectral analysis. *A&A* 549, A73. doi:10.1051/0004-6361/201219956

Petrucci, P. O., Piétu, V., Behar, E., Clavel, M., Bianchi, S., Henri, G., et al. (2023). Simultaneous millimetric and X-ray intraday variability in the radio-quiet AGN MCG+08-11-11. *A&A* 678, L4. doi:10.1051/0004-6361/202347495

Petrucci, P. O., Ursini, F., De Rosa, A., Bianchi, S., Cappi, M., Matt, G., et al. (2018). Testing warm Comptonization models for the origin of the soft X-ray excess in AGNs. *A&A* 611, A59. doi:10.1051/0004-6361/201731580

Piotrowska, J. M., García, J. A., Walton, D. J., Beckmann, R. S., Stern, D., Ballantyne, D. R., et al. (2023). The high energy X-ray probe (HEX-P): constraining supermassive black hole growth with population spin measurements. arXiv e-prints, Available at: https://doi.org/10.48550/arXiv.2311.04752.

Porquet, D., Done, C., Reeves, J. N., Grosso, N., Marinucci, A., Matt, G., et al. (2019). A deep X-ray view of the bare AGN Ark 120. V. Spin determination from disc-Comptonisation efficiency method. *A&A* 623, A11. doi:10.1051/0004-6361/201834448

Poutanen, J., and Svensson, R. (1996). The two-phase pair corona model for active galactic nuclei and X-ray binaries: how to obtain exact solutions. *ApJ* 470, 249. doi:10.1086/177865

Predehl, P., Andritschke, R., Arefiev, V., Babyshkin, V., Batanov, O., Becker, W., et al. (2021). The eROSITA X-ray telescope on SRG. *A&A* 647, A1. doi:10.1051/0004-6361/202039313

Raginski, I., and Laor, A. (2016). AGN coronal emission models - I. The predicted radio emission. *MNRAS* 459, 2082–2096. doi:10.1093/mnras/stw772

Raimundo, S. I., and Fabian, A. C. (2009). Eddington ratio and accretion efficiency in active galactic nuclei evolution. *MNRAS* 396, 1217–1221. doi:10.1111/j.1365-2966.2009.14796.x

Raimundo, S. I., Fabian, A. C., Vasudevan, R. V., Gandhi, P., and Wu, J. (2012). Can we measure the accretion efficiency of active galactic nuclei? *MNRAS* 419, 2529–2544. doi:10.1111/j.1365-2966.2011.19904.x

Ratheesh, A., Matt, G., Tombesi, F., Soffitta, P., Pesce-Rollins, M., and Di Marco, A. (2021). Exploring the accretion-ejection geometry of GRS 1915+105 in the obscured state with future X-ray spectro-polarimetry. *A&A* 655, A96. doi:10.1051/0004-6361/202140701

Reeves, J. N., Braito, V., Porquet, D., Lobban, A. P., Matzeu, G. A., and Nardini, E. (2021). The flaring X-ray corona in the quasar PDS 456. *MNRAS* 500, 1974–1991. –1991. doi:10.1093/mnras/staa3377

Reis, R. C., and Miller, J. M. (2013). On the size and location of the X-ray emitting coronae around black holes. *ApJ* 769, L7. doi:10.1088/2041-8205/769/1/L7

Remillard, R. A., and McClintock, J. E. (2006). X-ray properties of black-hole binaries. *ARA&A* 44, 49–92. doi:10.1146/annurev.astro.44.051905.092532

Reynolds, C. S. (2021). Observational constraints on black hole spin. *ARA&A* 59, 117–154. doi:10.1146/annurev-astro-112420-035022

Reynolds, C. S., and Begelman, M. C. (1997). Iron fluorescence from within the innermost stable orbit of black hole accretion disks. *ApJ* 488, 109–118. doi:10.1086/304703

Ricci, C., Chang, C.-S., Kawamuro, T., Privon, G., Mushotzky, R., Trakhtenbrot, B., et al. (2023). A tight correlation between millimeter and X-ray emission in accreting massive black holes from < 100 milliarcsecond-resolution ALMA observations. arXiv e-prints , Available at: https://doi.org/10.48550/arXiv.2306.04679.

Ricci, C., Ho, L. C., Fabian, A. C., Trakhtenbrot, B., Koss, M. J., Ueda, Y., et al. (2018). BAT AGN Spectroscopic Survey - XII. The relation between coronal properties of active galactic nuclei and the Eddington ratio. *MNRAS* 480, 1819–1830. doi:10.1093/mnras/sty1879

Ricci, C., Kara, E., Loewenstein, M., Trakhtenbrot, B., Arcavi, I., Remillard, R., et al. (2020). The destruction and recreation of the X-ray corona in a changing-look active galactic nucleus. *ApJ* 898, L1. doi:10.3847/2041-8213/ab91a1

Ricci, C., Loewenstein, M., Kara, E., Remillard, R., Trakhtenbrot, B., Arcavi, I., et al. (2021). The 450 Day X-ray monitoring of the changing-look AGN 1ES 1927+654. *ApJS* 255, 7. doi:10.3847/1538-4365/abe94b

Ricci, C., and Trakhtenbrot, B. (2022). Changing-look active galactic nuclei. arXiv e-prints, Available at: https://doi.org/10.48550/arXiv.2211.05132.

Ricci, C., Trakhtenbrot, B., Koss, M. J., Ueda, Y., Del Vecchio, I., Treister, E., et al. (2017). BAT AGN spectroscopic survey. V. X-ray properties of the Swift/BAT 70-month AGN catalog. *ApJS* 233, 17. doi:10.3847/1538-4365/aa96ad

Risaliti, G., Harrison, F. A., Madsen, K. K., Walton, D. J., Boggs, S. E., Christensen, F. E., et al. (2013). A rapidly spinning supermassive black hole at the centre of NGC 1365. *Nature* 494, 449–451. doi:10.1038/nature11938

Risaliti, G., Nardini, E., Salvati, M., Elvis, M., Fabbiano, G., Maiolino, R., et al. (2011). X-ray absorption by broad-line region clouds in Mrk 766. *MNRAS* 410, 1027–1035. doi:10.1111/j.1365-2966.2010.17503.x

Rivers, E., Markowitz, A., and Rothschild, R. (2013). Full spectral survey of active galactic nuclei in the rossi X-ray timing explorer archive. *ApJ* 772, 114. doi:10.1088/0004-637X/772/2/114

Ross, N. P., Ford, K. E. S., Graham, M., McKernan, B., Stern, D., Meisner, A. M., et al. (2018). A new physical interpretation of optical and infrared variability in quasars. *MNRAS* 480, 4468–4479. doi:10.1093/mnras/sty2002

Ruan, J. J., Anderson, S. F., Eracleous, M., Green, P. J., Haggard, D., MacLeod, C. L., et al. (2019). The analogous structure of accretion flows in supermassive and stellar mass black holes: new insights from faded changing-look quasars. *ApJ* 883, 76. doi:10.3847/1538-4357/ab3c1a

Rybicki, G. B., and Lightman, A. P. (1979). *Radiative processes in astrophysics*. New Jersey: John Wiley and Sons, Ltd.

Sagiv, I., Gal-Yam, A., Ofek, E. O., Waxman, E., Aharonson, O., Kulkarni, S. R., et al. (2014). Science with a wide-field UV transient explorer. *AJ* 147, 79. doi:10.1088/0004-6256/147/4/79

Sanfrutos, M., Miniutti, G., Agís-González, B., Fabian, A. C., Miller, J. M., Panessa, F., et al. (2013). The size of the X-ray emitting region in SWIFT J2127.4+5654 via a broad line region cloud X-ray eclipse. *MNRAS* 436, 1588–1594. doi:10.1093/mnras/stt1675

Saxton, R. D., Read, A. M., Esquej, P., Komossa, S., Dougherty, S., Rodriguez-Pascual, P., et al. (2012). A tidal disruption-like X-ray flare from the quiescent galaxy SDSS J120136.02+300305.5⋆. *Astronomy Astrophysics* 541, A106. doi:10.1051/0004-6361/201118367

Scepi, N., Begelman, M. C., and Dexter, J. (2021). Magnetic flux inversion in a peculiar changing look AGN. *MNRAS* 502, L50–L54. doi:10.1093/mnrasl/slab002

Schnittman, J. D., and Krolik, J. H. (2010). X-Ray polarization from accreting black holes: coronal emission. *ApJ* 712, 908–924. doi:10.1088/0004-637X/712/2/908

Shankar, F., Salucci, P., Granato, G. L., De Zotti, G., and Danese, L. (2004). Supermassive black hole demography: the match between the local and accreted mass functions. *MNRAS* 354, 1020–1030. doi:10.1111/j.1365-2966.2004.08261.x

Shankar, F., Weinberg, D. H., Marsden, C., Grylls, P. J., Bernardi, M., Yang, G., et al. (2020). Probing black hole accretion tracks, scaling relations, and radiative efficiencies from stacked X-ray active galactic nuclei. *MNRAS* 493, 1500–1511. doi:10.1093/mnras/stz3522

Shankar, F., Weinberg, D. H., and Miralda-Escudé, J. (2009). Self-consistent models of the AGN and black hole populations: duty cycles, accretion rates, and the mean radiative efficiency. *ApJ* 690, 20–41. doi:10.1088/0004-637X/690/1/20

Shappee, B. J., Prieto, J. L., Grupe, D., Kochanek, C. S., Stanek, K. Z., De Rosa, G., et al. (2014). The man behind the curtain: X-rays drive the UV through NIR variability in the 2013 active galactic nucleus outburst in NGC 2617. *ApJ* 788, 48. doi:10.1088/0004-637X/788/1/48

Sironi, L., and Beloborodov, A. M. (2020). Kinetic simulations of radiative magnetic reconnection in the coronae of accreting black holes. *ApJ* 899, 52. doi:10.3847/1538-4357/aba622

Smith, K. L., Mushotzky, R. F., Vogel, S., Shimizu, T. T., and Miller, N. (2016). Radio properties of the BAT AGNs: the FIR-radio relation, the fundamental plane, and the main sequence of star formation. *ApJ* 832, 163. doi:10.3847/0004-637X/832/2/163

Sniegowska, M., Czerny, B., Bon, E., and Bon, N. (2020). Possible mechanism for multiple changing-look phenomena in active galactic nuclei. *A&A* 641, A167. doi:10.1051/0004-6361/202038575

Soltan, A. (1982). Masses of quasars. *MNRAS* 200, 115–122. doi:10.1093/mnras/200.1.115

Sridhar, N., Sironi, L., and Beloborodov, A. M. (2021). Comptonization by reconnection plasmoids in black hole coronae I: magnetically dominated pair plasma. *MNRAS* 507, 5625–5640. doi:10.1093/mnras/stab2534

Sridhar, N., Sironi, L., and Beloborodov, A. M. (2023). Comptonization by reconnection plasmoids in black hole coronae II: electron-ion plasma. *MNRAS* 518, 1301–1315. doi:10.1093/mnras/stac2730

Stern, B. E., Poutanen, J., Svensson, R., Sikora, M., and Begelman, M. C. (1995). On the geometry of the X-ray–emitting region in Seyfert galaxies. *ApJ* 449, L13. doi:10.1086/309617

Stern, D., McKernan, B., Graham, M. J., Ford, K. E. S., Ross, N. P., Meisner, A. M., et al. (2018). A mid-IR selected changing-look quasar and physical scenarios for abrupt AGN fading. *ApJ* 864, 27. doi:10.3847/1538-4357/aac726

Svensson, R. (1984). Steady mildly relativistic thermal plasmas - processes and properties. *MNRAS* 209, 175–208. doi:10.1093/mnras/209.2.175

Tagliacozzo, D., Marinucci, A., Ursini, F., Matt, G., Bianchi, S., Baldini, L., et al. (2023). The geometry of the hot corona in MCG-05-23-16 constrained by X-ray polarimetry. arXiv e-prints, Available at: https://doi.org/10.48550/arXiv.2305.10213.

Tamborra, F., Matt, G., Bianchi, S., and Dovčiak, M. (2018). MoCA: a Monte Carlo code for Comptonisation in Astrophysics. I. Description of the code and first results. *A&A* 619, A105. doi:10.1051/0004-6361/201732023

Tashiro, M., Maejima, H., Toda, K., Kelley, R., Reichenthal, L., Lobell, J., et al. (2018). "Concept of the X-ray astronomy recovery mission," in *Space telescopes and instrumentation 2018: ultraviolet to gamma ray*. Editors J.-W. A den Herder, S Nikzad, and K Nakazawa. vol. 10699 of Society of Photo-Optical Instrumentation Engineers (SPIE) Conference Series. doi:10.1117/12.2309455

Tazaki, F., Ueda, Y., Terashima, Y., and Mushotzky, R. F. (2011). Suzaku view of the Swift/BAT active galactic nuclei. IV. Nature of two narrow-line radio galaxies (3C 403 and IC 5063). *ApJ* 738, 70. doi:10.1088/0004-637X/738/1/70

Tetarenko, B. E., Sivakoff, G. R., Heinke, C. O., and Gladstone, J. C. (2016). WATCHDOG: a comprehensive all-sky Database of galactic black hole X-ray binaries. *ApJS* 222, 15. doi:10.3847/0067-0049/222/2/15

Titarchuk, L. (1994). Generalized comptonization models and application to the recent high-energy observations. *ApJ* 434, 570. doi:10.1086/174760

Titarchuk, L., and Lyubarskij, Y. (1995). Power-law spectra as a result of comptonization of the soft radiation in a plasma cloud. *ApJ* 450, 876. doi:10.1086/176191

Tomsick, J., Zoglauer, A., Sleator, C., Lazar, H., Beechert, J., Boggs, S., et al. (2019). The Compton spectrometer and imager. *Bull. Am. Astronomical Soc.* 51, 98. doi:10.48550/arXiv.1908.04334

Tonry, J. L., Denneau, L., Heinze, A. N., Stalder, B., Smith, K. W., Smartt, S. J., et al. (2018). ATLAS: a high-cadence all-sky survey system. *PASP* 130, 064505. doi:10.1088/1538-3873/aabadf

Tortosa, A., Bianchi, S., Marinucci, A., Matt, G., and Petrucci, P. O. (2018). A NuSTAR census of coronal parameters in Seyfert galaxies. *A&A* 614, A37. doi:10.1051/0004-6361/201732382

Tortosa, A., Ricci, C., Ho, L. C., Tombesi, F., Du, P., Inayoshi, K., et al. (2023). Systematic broad-band X-ray study of super-Eddington accretion on to supermassive black holes - I. X-ray continuum. *MNRAS* 519, 6267–6283. doi:10.1093/mnras/stac3590

Trakhtenbrot, B., Arcavi, I., MacLeod, C. L., Ricci, C., Kara, E., Graham, M. L., et al. (2019). 1ES 1927+654: an AGN caught changing look on a timescale of months. *ApJ* 883, 94. doi:10.3847/1538-4357/ab39e4

Urry, C. M., and Padovani, P. (1995). Unified schemes for radio-loud active galactic nuclei. *PASP* 107, 803. doi:10.1086/133630

Ursini, F., Bassani, L., Malizia, A., Bazzano, A., Bird, A. J., Stephen, J. B., et al. (2019). The coronal temperature of NGC 4388 and NGC 2110 measured with INTEGRAL. *A&A* 629, A54. doi:10.1051/0004-6361/201936273

Ursini, F., Marinucci, A., Matt, G., Bianchi, S., Marin, F., Marshall, H. L., et al. (2023). Mapping the circumnuclear regions of the Circinus galaxy with the imaging X-ray polarimetry explorer. *MNRAS* 519, 50–58. doi:10.1093/mnras/stac3189

Ursini, F., Petrucci, P. O., Matt, G., Bianchi, S., Cappi, M., De Marco, B., et al. (2016). High-energy monitoring of NGC 4593 with XMM-Newton and NuSTAR. X-ray spectral analysis. *MNRAS* 463, 382–392. doi:10.1093/mnras/stw2022

Uttley, P., Cackett, E. M., Fabian, A. C., Kara, E., and Wilkins, D. R. (2014). X-ray reverberation around accreting black holes. *A&ARv* 22, 72. doi:10.1007/s00159-014-0072-0

Vaiana, G. S., and Rosner, R. (1978). Recent advances in coronal physics. *ARA&A* 16, 393–428. doi:10.1146/annurev.aa.16.090178.002141

Vasudevan, R. V., and Fabian, A. C. (2007). Piecing together the X-ray background: bolometric corrections for active galactic nuclei. *MNRAS* 381, 1235–1251. doi:10.1111/j.1365-2966.2007.12328.x

Walton, D. J., Baloković, M., Fabian, A. C., Gallo, L. C., Koss, M., Nardini, E., et al. (2021). Extreme relativistic reflection in the active galaxy ESO 033-G002. *MNRAS* 506, 1557–1572. doi:10.1093/mnras/stab1290

Walton, D. J., Reis, R. C., Cackett, E. M., Fabian, A. C., and Miller, J. M. (2012). The similarity of broad iron lines in X-ray binaries and active galactic nuclei. *MNRAS* 422, 2510–2531. doi:10.1111/j.1365-2966.2012.20809.x

Walton, D. J., Risaliti, G., Harrison, F. A., Fabian, A. C., Miller, J. M., Arevalo, P., et al. (2014). NuSTAR and XMM-Newton observations of NGC 1365: extreme absorption variability and a constant inner accretion disk. *ApJ* 788, 76. doi:10.1088/0004-637X/788/1/76

Wambsganss, J. (2006). "Part 4: gravitational microlensing," in *Saas-fee advanced course 33: gravitational lensing: strong, weak and micro*. Editors G Meylan, P Jetzer, P North, P Schneider, C. S Kochanek, and J Wambsganss, 453–540.

Weisskopf, M. C., Soffitta, P., Baldini, L., Ramsey, B. D., O'Dell, S. L., Romani, R. W., et al. (2022). Imaging X-ray polarimetry explorer: prelaunch. *J. Astronomical Telesc. Instrum. Syst.* 8, 026002. doi:10.1117/1.JATIS.8.2.026002

Wen, S., Jonker, P. G., Stone, N. C., Zabludoff, A. I., and Psaltis, D. (2020). Continuum-fitting the X-ray spectra of tidal disruption events. *ApJ* 897, 80. doi:10.3847/1538-4357/ab9817

Wevers, T. (2020). Fainter harder brighter softer: a correlation between α_{ox}, X-ray spectral state, and Eddington ratio in tidal disruption events. *MNRAS* 497, L1–L6. doi:10.1093/mnrasl/slaa097

Wevers, T., Pasham, D. R., van Velzen, S., Miller-Jones, J. C. A., Uttley, P., Gendreau, K. C., et al. (2021). Rapid accretion state transitions following the tidal disruption event AT2018fyk. *ApJ* 912, 151. doi:10.3847/1538-4357/abf5e2

Wilkins, D. R., Cackett, E. M., Fabian, A. C., and Reynolds, C. S. (2016). Towards modelling X-ray reverberation in AGN: piecing together the extended corona. *MNRAS* 458, 200–225. doi:10.1093/mnras/stw276

Wilkins, D. R., and Fabian, A. C. (2011). Determination of the X-ray reflection emissivity profile of 1H 0707-495. *MNRAS* 414, 1269–1277. doi:10.1111/j.1365-2966.2011.18458.x

Wilkins, D. R., and Fabian, A. C. (2012). Understanding X-ray reflection emissivity profiles in AGN: locating the X-ray source. *MNRAS* 424, 1284–1296. doi:10.1111/j.1365-2966.2012.21308.x

Wilkins, D. R., and Fabian, A. C. (2013). The origin of the lag spectra observed in AGN: reverberation and the propagation of X-ray source fluctuations. *MNRAS* 430, 247–258. doi:10.1093/mnras/sts591

Wilkins, D. R., and Gallo, L. C. (2015). Driving extreme variability: the evolving corona and evidence for jet launching in Markarian 335. *MNRAS* 449, 129–146. doi:10.1093/mnras/stv162

Wilms, J., Allen, A., and McCray, R. (2000). On the absorption of X-rays in the interstellar medium. *ApJ* 542, 914–924. doi:10.1086/317016

XRISM Science Team (2022). *XRISM quick reference*. arXiv e-prints, Available at: https://doi.org/10.48550/arXiv.2202.05399.

Yao, Y., Lu, W., Guolo, M., Pasham, D. R., Gezari, S., Gilfanov, M., et al. (2022). The tidal disruption event AT2021ehb: evidence of relativistic disk reflection, and rapid evolution of the disk-corona system. *ApJ* 937, 8. doi:10.3847/1538-4357/ac898a

Yu, Q., and Tremaine, S. (2002). Observational constraints on growth of massive black holes. *MNRAS* 335, 965–976. doi:10.1046/j.1365-8711.2002.05532.x

Zdziarski, A. A., Johnson, W. N., and Magdziarz, P. (1996). Broad-band γ-ray and X-ray spectra of NGC 4151 and their implications for physical processes and geometry. *MNRAS* 283, 193–206. doi:10.1093/mnras/283.1.193

Zdziarski, A. A., Jourdain, E., Lubiński, P., Szanecki, M., Niedźwiecki, A., Veledina, A., et al. (2021). Hybrid comptonization and electron-positron pair production in the black-hole X-ray binary MAXI J1820+070. *ApJ* 914, L5. doi:10.3847/2041-8213/ac0147

Zdziarski, A. A., and Lightman, A. P. (1985). Nonthermal electron-positron pair production and the 'universal' X-ray spectrum of active galactic nuclei. *ApJ* 294, L79–L83. doi:10.1086/184513

Zdziarski, A. A., Lightman, A. P., and Maciolek-Niedzwiecki, A. (1993). Acceleration efficiency in nonthermal sources and the soft gamma rays from NGC 4151 observed by OSSE and SIGMA. *ApJ* 414, L93. doi:10.1086/187004

Zhang, S., Santangelo, A., Feroci, M., Xu, Y., Lu, F., Chen, Y., et al. (2019a). The enhanced X-ray Timing and Polarimetry mission—eXTP. *Sci. China Phys. Mech. Astronomy* 62, 29502. doi:10.1007/s11433-018-9309-2

Zhang, W., Dovčiak, M., and Bursa, M. (2019b). Constraining the size of the corona with fully relativistic calculations of spectra of extended coronae. I. The Monte Carlo radiative transfer code. *ApJ* 875, 148. doi:10.3847/1538-4357/ab1261

Zhang, X., and Lu, Y. (2017). On the mean radiative efficiency of accreting massive black holes in AGNs and QSOs. *Sci. China Phys. Mech. Astronomy* 60, 109511. doi:10.1007/s11433-017-9062-1

Zoghbi, A., Matt, G., Miller, J. M., Lohfink, A. M., Walton, D. J., Ballantyne, D. R., et al. (2017). A long look at MCG-5-23-16 with NuSTAR. I. Relativistic reflection and coronal properties. *ApJ* 836, 2. doi:10.3847/1538-4357/aa582c

frontiers | Frontiers in Astronomy and Space Sciences

TYPE Original Research
PUBLISHED 08 January 2024
DOI 10.3389/fspas.2023.1292682

Check for updates

OPEN ACCESS

EDITED BY
Renee Ludlam,
Wayne State University, United States

REVIEWED BY
Anna Lia Longinotti,
Universidad Nacional Autonoma de Mexico, Mexico
Keigo Fukumura,
James Madison University, United States

*CORRESPONDENCE
Riley M. T. Connors,
riley.connors@villanova.edu

RECEIVED 11 September 2023
ACCEPTED 09 November 2023
PUBLISHED 08 January 2024

CITATION
Connors RMT, Tomsick JA, Draghis P, Coughenour B, Shaw AW, García JA, Walton D, Madsen K, Stern D, Rodriguez NC, Dauser T, Del Santo M, Jiang J, Krawczynski H, Liu H, Neilsen J, Nowak M, Pike S, Santangelo A, Sridhar N, West A and Wilms J (2024), The High Energy X-ray Probe (HEX-P): probing accretion onto stellar mass black holes.
Front. Astron. Space Sci. 10:1292682.
doi: 10.3389/fspas.2023.1292682

COPYRIGHT
© 2024 Connors, Tomsick, Draghis, Coughenour, Shaw, García, Walton, Madsen, Stern, Rodriguez, Dauser, Del Santo, Jiang, Krawczynski, Liu, Neilsen, Nowak, Pike, Santangelo, Sridhar, West and Wilms. This is an open-access article distributed under the terms of the Creative Commons Attribution License (CC BY). The use, distribution or reproduction in other forums is permitted, provided the original author(s) and the copyright owner(s) are credited and that the original publication in this journal is cited, in accordance with accepted academic practice. No use, distribution or reproduction is permitted which does not comply with these terms.

The High Energy X-ray Probe (HEX-P): probing accretion onto stellar mass black holes

Riley M. T. Connors[1]*, John A. Tomsick[2], Paul Draghis[3], Benjamin Coughenour[2], Aarran W. Shaw[4], Javier A. García[5,6], Dominic Walton[7], Kristin Madsen[5], Daniel Stern[8], Nicole Cavero Rodriguez[9], Thomas Dauser[10], Melania Del Santo[11], Jiachen Jiang[12], Henric Krawczynski[9], Honghui Liu[13], Joseph Neilsen[1], Michael Nowak[14], Sean Pike[15], Andrea Santangelo[16], Navin Sridhar[6,17,18], Andrew West[9] and Jörn Wilms[10]

[1]Department of Physics, Villanova University, Villanova, PA, United States, [2]Space Sciences Laboratory, University of California, Berkeley, Berkeley, CA, United States, [3]Department of Astronomy, University of Michigan, Ann Arbor, MI, United States, [4]Department of Physics and Astronomy, Butler University, Indianapolis, IN, United States, [5]X-ray Astrophysics Laboratory, NASA Goddard Space Flight Center, Greenbelt, MD, United States, [6]Cahill Center for Astronomy and Astrophysics, California Institute of Technology, Pasadena, CA, United States, [7]Centre for Astrophysics Research, University of Hertfordshire, College Lane, Hatfield, United Kingdom, [8]Jet Propulsion Laboratory, California Institute of Technology, Pasadena, CA, United States, [9]Physics Department, McDonnell Center for the Space Sciences, and Center for Quantum Leaps, Washington University, St. Louis, MO, United States, [10]Karl Remeis-Observatory and Erlangen Centre for Astroparticle Physics, Freidrich-Alexander-Universität Erlangen-Nürnberg, Bamberg, Germany, [11]Instituto Nazionale Di Astrofisica, Istituto di Astrofisica Spaziale e Fisica Cosmica di Palermo, Palermo, Italy, [12]Institute of Astronomy, University of Cambridge, Cambridge, United Kingdom, [13]Center for Field Theory and Particle Physics and Department of Physics, Fudan University, Shanghai, China, [14]Physics Department, Washington University, St Louis, MO, United States, [15]Department of Astronomy and Astrophysics, University of California, San Diego, San Diego, CA, United States, [16]Institute of Astronomy and Astrophysics, University of Tüebingen, Tüebingen, Germany, [17]Department of Astronomy, Columbia University, New York, NY, United States, [18]Theoretical High Energy Astrophysics (THEA) Group, Columbia University, New York, NY, United States

Accretion is a universal astrophysical process that plays a key role in cosmic history, from the epoch of reionization to galaxy and stellar formation and evolution. Accreting stellar-mass black holes in X-ray binaries are one of the best laboratories to study the accretion process and probe strong gravity—and most importantly, to measure the angular momentum, or spin, of black holes, and its role as a powering mechanism for relativistic astrophysical phenomena. Comprehensive characterization of the disk-corona system of accreting black holes, and their co-evolution, is fundamental to measurements of black hole spin. Here, we use simulated data to demonstrate how key unanswered questions in the study of accreting stellar-mass black holes will be addressed by the *High Energy X-ray Probe* (*HEX-P*). *HEX-P* is a probe-class mission concept that will combine high spatial resolution X-ray imaging and broad spectral coverage (0.2–80 keV) with a sensitivity superior to current facilities (including *XMM-Newton* and *NuSTAR*) to enable revolutionary new insights into a variety of important astrophysical problems. We illustrate the capability of *HEX-P* to: 1) measure the evolving structures of black hole binary accretion flows down to low ($\lesssim$ 0.1%) Eddington-scaled luminosities via detailed X-ray reflection spectroscopy; 2) provide unprecedented spectral observations of the coronal plasma, probing its elusive geometry and energetics; 3) perform

detailed broadband studies of stellar mass black holes in nearby galaxies, thus expanding the repertoire of sources we can use to study accretion physics and determine the fundamental nature of black holes; and 4) act as a complementary observatory to a range of future ground and space-based astronomical observatories, thus providing key spectral measurements of the multi-component emission from the inner accretion flows of black hole X-ray binaries.

KEYWORDS

accretion, x-ray astronomy, black holes, binaries, high energy astrophysics

1 Introduction

Accretion is one of the most fundamental astrophysical processes in the Universe. It is seen across an extremely wide range of mass-scales, from young stellar objects (YSOs) still in the earliest stages of stellar evolution (Scaringi et al., 2015), to the supermassive black holes powering active galactic nuclei (AGN; Urry and Padovani, 1995; McHardy et al., 2006). Channeled through this diverse repertoire of compact engines, the accretion process has driven a significant portion of the most fundamental evolutionary stages of the cosmos, such as the epoch of reionization (Loeb and Barkana, 2001; Power et al., 2009), galaxy evolution (Kormendy and Ho, 2013), and stellar birth and evolution (Boyle and Terlevich, 1998; Davies et al., 2007; Merloni and Heinz, 2013). One of the best ways to study accretion is through observations of X-ray binaries, which consist of a compact object (a black hole: BH, or neutron star: NS) accreting matter from a stellar companion via an accretion disk. X-ray binaries are typically split into two main classes, governed by the mass of the companion star. Low-mass X-ray binaries (LMXBs) contain low-mass ($\lesssim M_{BH}$) donors that overflow their Roche lobes. LMXBs often spend long periods in a quiescent state, followed by bright outbursts during which the source luminosity increases by several orders of magnitude (see, e.g., Tanaka and Lewin, 1995; Remillard and McClintock, 2006; Kalemci et al., 2022). High-mass X-ray binaries (HMXBs), on the other hand, contain massive ($\gtrsim 10M_{\odot}$), typically early-type, companions, the stellar winds of which are often powerful enough to drive the accretion process in the absence of Roche lobe overflow (Liu et al., 2006). HMXBs are also persistently active, though much rarer than LMXBs, and X-ray studies of the inner accretion flows of HMXBs are often hampered by contamination from interactions with the companion's stellar wind. Therefore, the focus of this study will be the more commonly occurring LMXB outbursts, objects we can probe across a wide range of luminosities. We note also that many LMXBs, almost exclusively NS-LMXBs, are also persistently active; here we focus only on BH-LMXBs that are transient in nature, objects that are attract the primary attention of the black hole astrophysics community, and thus *HEX-P* science.

Stellar-mass BHs in X-ray binaries are often viewed as scaled-down versions of AGN (e.g., Falcke et al., 2004; Körding et al., 2006; McHardy et al., 2006) and, as such, studying them can provide important clues on the complex physical processes of accretion, on timescales much more accessible than those offered by AGN. BH-LMXBs, in particular, often transition through a series of different "accretion states" throughout the course of an outburst that can last weeks to years (see Tetarenko et al., 2016 for a comprehensive overview of known Galactic BH X-ray binaries). In the soft state, BH-LMXBs exhibit an X-ray spectrum dominated by thermal radiation from the accretion disk and show little to no variability (see, e.g., Done et al., 2007; Muñoz-Darias et al., 2011). Conversely, in the hard state, they exhibit an X-ray spectrum that can be well-described by a power law of index $\Gamma \sim 1.5$–2, traditionally attributed to the presence of an optically thin 'corona' of hot thermal electrons ($kT_e \sim$ 10s–100s of keV) that Compton up-scatter photons from the disk (Bisnovatyi-Kogan and Blinnikov, 1977; Haardt and Maraschi, 1991; Haardt and Maraschi, 1993; Dove et al., 1997). The presence of radio emission in the hard state has led many to theorize that the X-ray corona could be associated with the base of a compact jet (e.g., Markoff et al., 2005) but its true origin remains poorly understood. Additional alternative models exist to explain coronal formation and the Compton scattering process, including magnetic reconnection of local magnetic fields threaded through the accretion disk (Liu et al., 2003), and Comptonization due to the bulk motion of the coronal plasma can also play a role (e.g., Beloborodov, 2017; Sironi and Beloborodov, 2020; Sridhar et al., 2021; Gupta et al., 2023; Sridhar et al., 2023).

Despite more than 50 years of studies of BH X-ray binaries (BH-XRBs), many unanswered questions remain. For example, study of the rotation (spin; $a_* \equiv Jc/GM^2$, where J is the BH angular momentum, c is the speed of light, G is the gravitational constant, and M is the BH mass) of BHs has led to the discovery that the observed distribution of spins of BHs in X-ray binaries is significantly different from the observed spin distribution of merging binary BHs in gravitational wave (GW) events (Reynolds, 2021; Fishbach and Kalogera, 2022; Draghis et al., 2023) detected by the Laser Interferometer Gravitational-Wave Observatory (LIGO; Abbott et al., 2016)—see Figure 1. Such studies can provide critical clues about the formation and evolution of different populations of BHs. However, in-depth studies of BH spin in X-ray binaries have mostly been restricted to the brightest sources. Spin estimation in BH-XRBs is often performed by measuring the spectrum of photons from the corona that illuminate the disk and are ultimately reprocessed via a process called relativistic reflection (George and Fabian, 1991; Dauser et al., 2014; García et al., 2014). However, the geometry of the aforementioned corona is not well known, and assumptions regarding coronal geometry can introduce systematic uncertainties to spin measurements (Dauser et al., 2013). In addition, a fundamental assumption behind BH spin measurements via reflection spectroscopy is that the accretion disk extends to the innermost stable circular orbit (ISCO) during the soft state and at least the more luminous

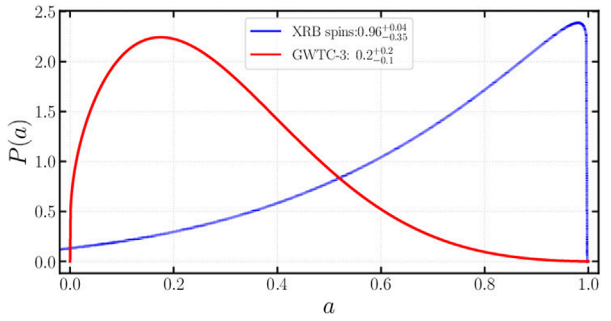

FIGURE 1
Probability density functions of different BH spin distributions. The red curve shows the distribution inferred based on the pre-merger BH spins calculated and reported in the third edition of the Gravitational Wave Transient Catalog (GWTC-3; The LIGO Scientific Collaboration et al., 2021). The blue curve shows the distribution inferred based on all the values measured using X-ray spectroscopy of BH X-ray binary systems. The numbers reported in the figure legend represent the modes of the distributions, along with the 1σ credible intervals of the values. The observed spin distributions are in clear disagreement, suggesting different formation and evolution mechanisms of BHs in binary BH systems observed to merge through GW observations and the BHs observed in XRB systems.

hard spectral states (Reynolds and Begelman, 1997; Young et al., 1998; Reynolds and Fabian, 2008; Fabian et al., 2014). Herein lies just one key issue contributing to an impasse in BH-XRB studies as a whole, and most importantly for recovering BH spin constraints. Despite the wealth of X-ray spectral data garnered to date, with modern instruments such as the *Nuclear Spectroscopic Telescope Array* (*NuSTAR*; Harrison et al., 2013), *XMM-Newton* (Jansen et al., 2001), the *Neutron Star Interior Composition Explorer* (*NICER*; Gendreau et al., 2016), the X-ray Telescope onboard the *Neil Gehrels Swift Observatory* (*Swift*-XRT Gehrels et al., 2004; Burrows et al., 2005), and the *INTErnational Gamma-Ray Astrophysics Laboratory* (*INTEGRAL* Jensen et al., 2003), orders-of-magnitude disagreements persist regarding the degree of disk truncation in hard spectral states of BH-XRBs, with some finding the disk is close to the ISCO (e.g., Reis et al., 2008; Tomsick et al., 2008; Reis et al., 2010; García et al., 2015b; Fürst et al., 2015; Parker et al., 2015; García et al., 2018b; García et al., 2019; Sridhar et al., 2019; Sridhar et al., 2020; Connors et al., 2022), and others deriving truncation on the order of 10 s–100 s of gravitational radii (e.g., Tomsick et al., 2009; Plant et al., 2015; Marino et al., 2021; Zdziarski et al., 2021; Zdziarski et al., 2022). This disk truncation debate is just one among many sources of degeneracy in modeling of relativistic reflection, others include: the geometry of the corona; the microphysics of the accretion disk, i.e., ionization and atomic abundances; contamination from other spectral components, such as reprocessing in a disk wind. Resolving these disagreements is key to obtaining accurate measurements of BH spin with the reflection method.

Furthermore, it is not only the macrophysics of the corona/disk system in BH-XRBs that contains uncertainties, but the microphysics/energetics too, i.e., the composition of the coronal plasma (e.g., electron-positron pairs vs. baryon enrichment; Sridhar et al., 2023), the particle energy distribution (Sironi and Beloborodov, 2020; Sridhar et al., 2021), and thus the emergent high-energy non-thermal X-ray continuum, and the orientation of the magnetic field in the corona (Gupta et al., 2023). Both the geometry of the disk/corona and the energetics of the coronal plasma are key components to accurate BH spin measurements via reflection spectroscopy.

It is also worth noting that our current knowledge of accretion in BH-XRBs has mostly come from observations of sources in our own Galaxy. Comprehensive studies of extragalactic systems are scarce (see Liu et al., 2008; Barnard et al., 2014; Binder et al., 2021 for some examples), mostly due to the limitations of current instrumentation and, as such, we are unable to make detailed comparisons of these populations with the Milky Way population of BHs. Whilst it is clear that this limitation is a function of the sensitivity of our instruments due to the reduction in source flux with distance, it can also be overcome by improving X-ray spatial resolution to isolate point sources in nearby galaxies.

It is clear that, in order to advance our understanding of the complex accretion processes in BH-XRBs—and thus make strides in the characterization of accretion physics and the fundamental properties of black holes—we need to be able to study sources across a large range of fluxes, with a broad passband. In this paper, we discuss a number of open questions surrounding accreting BHs, and how we will be able to answer them with the *High-Energy X-ray Probe* (*HEX-P*; Madsen et al., 2023) probe-class mission concept. In the subsections that follow (§ 1.1 and § 1.2) we introduce the *HEX-P* mission design and outline the specifications used to produce simulations in this work. In Section 2 we present a series of simulations demonstrating the scientific advances *HEX-P* will make in studies of Galactic BH-XRBs, with a focus on low-to-high flux constraints on the accretion flow structure of transient sources (§ 2.1) and characterization of the geometry and physics of the hard X-ray BH corona (§ 2.2). In Section 3 we present simulations of detailed broadband studies of BH-XRBs in nearby galaxies with *HEX-P*. Finally, in Section 4 we present an overview of our simulation results and discuss the implications of future advances *HEX-P* will make in the study of black holes and their accretion flows.

1.1 Mission design

HEX-P (Madsen et al., 2023) is a probe-class mission concept that offers sensitive broad-band coverage (0.2–80 keV) of the X-ray spectrum with exceptional spectral, timing and angular capabilities. It features two high-energy telescopes (HET) that focuses hard X-rays, and soft X-ray coverage with a low-energy telescope (LET).

The LET consists of a segmented mirror assembly coated with Ir on monocrystalline silicon that achieves a half power diameter of 3.5", and a low-energy DEPFET detector, of the same type as the Wide Field Imager (WFI; Meidinger et al., 2020) planned for *NewAthena* (Nandra et al., 2013; Barret et al., 2020). It has 512 × 512 pixels that cover a field of view of $11.3' \times 11.3'$. It has an effective passband of 0.2–25 keV, and a full frame readout time of 2 ms, which can be operated in a 128 and 64 channel window mode for higher count-rates to mitigate pile-up and faster readout. Pile-up effects remain below an acceptable limit of ~1% for sources up to ~100 mCrab in the smallest window configuration (64w). Excising the core of the PSF, a common practice in X-ray astronomy, will allow for observations of brighter sources, with a maximum loss of

~60% of the total photon counts. We describe results of simulations and illustrate the use of this method specifically for the LET in the Supplementary Appendix.

The HET consists of two co-aligned telescopes and detector modules. The optics are made of Ni-electroformed full shell mirror substrates, leveraging the heritage of *XMM-Newton* (Jansen et al., 2001), and coated with Pt/C and W/Si multilayers for an effective passband of 2–80 keV. The high-energy detectors are of the same type as those onboard *NuSTAR* (Harrison et al., 2013), and they consist of 16 CZT sensors per focal plane, tiled 4 × 4, for a total of 128 × 128 pixel spanning a field of view slightly larger than for the LET, of 13.4′x13.4′.

The broad X-ray passband and superior sensitivity will provide a unique opportunity to study accretion onto stellar mass BHs across a wide range of energies, luminosity, and dynamical regimes.

1.2 Simulations

All the simulations presented here were produced with a set of response files that represent the observatory performance based on current best estimates (Madsen et al., 2023). The effective area is derived from a ray-trace of the mirror design including obscuration by all known structures. The detector responses are based on simulations performed by the respective hardware groups, with an optical blocking filter for the LET and a be window and thermal insulation for the HET. The LET background was derived from a GEANT4 simulation (Eraerds et al., 2021) of the WFI instrument, and the one for the HET from a GEANT4 simulation of the *NuSTAR* instrument, both positioned at L1.

2 Galactic black hole X-ray binaries

We have introduced two key areas in the study of accretion onto stellar mass BHs in which progress must be made to advance our understanding of accretion physics, strong gravity, and the spins of BHs: 1) the inner accretion flow structure, and 2) the geometry and physics of the corona. We argue that it is imperative that we break modeling degeneracies in order to resolve these outstanding problems. Achieving this requires advancements in broadband X-ray spectral observations capable of probing a wide range of source fluxes, with a particular focus on sensitivity to higher energy emission (originating from the X-ray corona). Here, we present simulations that demonstrate the advancements *HEX-P* will make in characterizing the complex disk-corona connection in BH-XRBs. In the subsection that follows (2.1) we show *HEX-P* simulations of the full outburst evolution of a typical BH-XRB, and in Section 2.2 we demonstrate how *HEX-P* will allow constraints on the coronal geometry and microphysics (and thus the BH-XRB continuum emission).

2.1 Tracking the evolution of black hole X-ray binary outbursts

As outlined in Section 1, most BH-XRBs undergo serendipitous outbursts during which the X-ray luminosity of the sources increases by a few orders of magnitude on rapid timescales, followed by a decay occurring on time scales of weeks to months. Throughout the outbursts, the sources often undergo state transitions, evolving from hard states in which the coronal and reflected emission dominate the spectra, to soft states in which the thermal emission from the accretion disk dominates the observed spectra, but strong reflection features are still present (Gierliński et al., 1999; Zdziarski et al., 1999; Del Santo et al., 2008; Del Santo et al., 2016; Steiner et al., 2016). Often times, sources are observed at multiple epochs throughout the duration of their outbursts in order to characterize their time evolution. Figure 2 shows ratio of data to model produced when fitting 6 *NuSTAR* observations of the galactic BH-XRB EXO 1846-031 with models that ignore relativistic reflection effects, and only account for the thermal emission from the accretion disk and the coronal contribution. The blue points represent the spectra from the *NuSTAR* FPMA detector. We simulated *HEX-P* spectra with the same exposure as the existing *NuSTAR* observations, using the best-performing models that *do* account for relativistic reflection (`relxill`; García et al., 2014; Dauser et al., 2014). We fit these simulated *HEX-P* observations with models that *do not* account for relativistic reflection, and the residuals produced are shown in Figure 2, with *HEX-P* HET shown in red and LET shown in orange. Not only do the disk and coronal contributions evolve throughout the duration of the outburst, but the features of relativistic reflection also change in time. Owing to the increased energy coverage of *HEX-P* and the increased sensitivity at high energies, the continuum emission is characterized differently when fitting either *HEX-P* or *NuSTAR* data alone. By constraining the underlying continuum over a larger energy band with *HEX-P*, the degeneracy with the reflection features is further reduced, enabling placing better constraints on the parameters of the reflected spectrum, including black hole spin, inner disk radius and viewing inclination, accretion disk density, ionization, and Fe abundance, and coronal properties. In cases where the underlying continuum emission is similarly characterized (i.e., for Obs 1), the residuals produced by the reflection features appear similar. However, in all the other cases, fitting NuSTAR data alone produces different, incomplete characterizations of the continuum emission, leading to a distinct visual difference in the reflection residuals. Due to the wider energy coverage of HEX-P, ensured by pairing the LET and HET instruments, the continuum emission will be reliably characterized even when reflection features are not accounted for, more clearly highlighting present residuals.

Draghis et al. (2020) measured the spin of the BH in EXO 1846-031 to be $a_\star = 0.997^{+0.001}_{-0.002}$ based only on the first *NuSTAR* observation. However, the precision of this measurement is overestimated by not fully exploring all possible sources of systematic uncertainty. One such possible source of uncertainty comes from variability of the observed sources on timescales ranging from seconds to the entire duration of typical observations, which can lead to changes in the spectral features that become blurred when treating the observations in a time-averaged way. In order to successfully perform time-resolved spectroscopy, it is necessary to obtain a large number of counts throughout observations, and the most pragmatic way to reach that is to increase the sensitivity of our instruments.

Owing to its high sensitivity across a broad passband, *HEX-P* will provide spectra with unprecedented signal to noise, and will allow complete, simultaneous characterization of the thermal

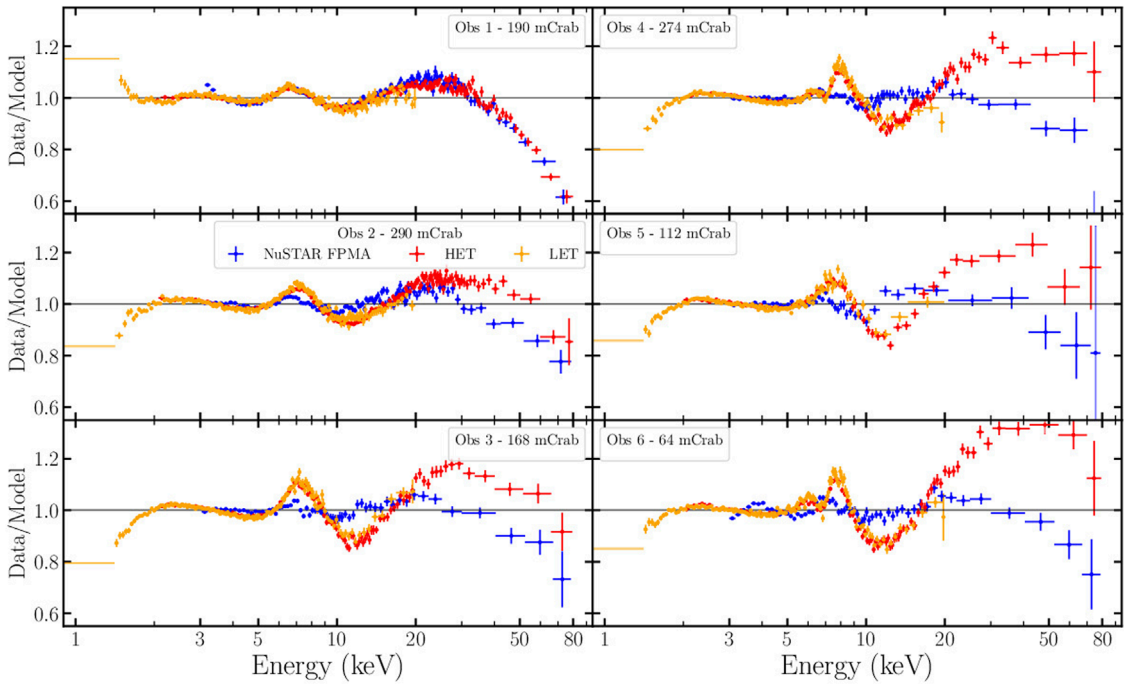

FIGURE 2
Ratio of data to model produced when using models that do not account for relativistic reflection to fit the FPMA spectra from the 6 existing *NuSTAR* observations of EXO 1846-031 (blue) and similar simulated *HEX-P* LET (orange) and HET (red) spectra. The *NuSTAR* observations were taken during the 2019 outburst of EXO 1846-031. The *HEX-P* spectra were simulated to have an exposure equal to the existing *NuSTAR* observations, using the best-fit parameters determined when fitting the *NuSTAR* spectra with models that do account for relativistic reflection. The increased energy coverage of *HEX-P* paired with its increased sensitivity at high energies enables stronger constraints on the underlying continuum emission, reducing the degeneracy with the reflected radiation, enabling placing stronger constraints on the physical properties of the system.

continuum emission from the accretion disk and the galactic absorption at low energies, the direct coronal emission up to high energies, and the features of relativistic reflection, namely, the Fe K complex and the Compton hump. When compared to current generation instruments such as *NuSTAR*, *HEX-P* spectra will enable placing reliable constraints on the parameters of the structure of the accretion disk in significantly fainter sources, or from relatively short observations of bright sources. The broadband coverage of both low and high energy instruments on board (LET and HET) will provide a key advantage as well, avoiding the necessity for complex cross-telescope scheduling (i.e., between *NuSTAR* and *NICER* or *XMM-Newton*); though we should stress that *HEX-P* will nonetheless be capable of slewing to transient sources on short timescales, and will thus be a key instrument for simultaneous observations, which remain a key strategy for calibration checks and validation. As an example, here we focus on the ability of *HEX-P* spectra to measure the radius of the inner accretion disk. Characterizing the accretion flow in very faint sources will solve the currently elusive problem of inner disk truncation at mid-to-low Eddington fractions, 0.1% $L_{\rm Edd} \leq L_{\rm X} \leq 1\%\ L_{\rm Edd}$, while placing rapid constraints on the geometry of the accretion disk from very short observations of bright sources will lead to a complete characterization of the physical mechanisms behind highly variable sources. Expanding our understanding of the physics of accretion in BH-XRBs will help constrain the uncertainties introduced to BH spin measurements. At the same time, *HEX-P* observations will permit time-resolved spectroscopy of bright sources and will enable us to perform detailed broadband spectral modeling of sources down to fluxes inaccessible with current instruments (due to lack of sensitivity and higher X-ray backgrounds), thus expanding our sample sizes. This will lead to a better understanding of systematic uncertainties.

In order to illustrate the capabilities of *HEX-P* we simulated an array of observations of a source with spectral properties similar to those of the well-known BH-LMXB GX 339-4, in both hard and soft spectral states, with varying luminosity. The model used to generate the simulated spectra includes galactic absorption through the `TBabs` component (Wilms et al., 2000), and describes the thermal emission from the accretion disk using the `diskbb` component (Mitsuda et al., 1984; Makishima et al., 1986), the hard emission from the compact corona using the `nthcomp` component (Zdziarski et al., 1996; Życki et al., 1999), and the relativistic reflection features through the `relxillCp` component (Dauser et al., 2014; García et al., 2014). We assumed a Galactic column density of $N_{\rm H} = 10^{22}$ cm^{-2}, Fe abundance $A_{\rm Fe} = 6.6$ times the solar value (see Table 3 in García et al., 2019), in agreement with the distribution of Fe abundance measured using current generation data and relativistic reflection models in AGN and XRBs (see Figure 3 in García et al., 2018a), limited the ionization parameter to an intermediate value of $\log(\xi) = 3.1$ (where $\xi = 4\pi F_x/n_{\rm e}$, $F_{\rm x}$ is the irradiating flux, and $n_{\rm e}$ is the disk density, and the units are erg cm s^{-1}), the spin of the BH $a_\star = 0.95$, and kept the inclination of the inner accretion disk to $\theta = 45°$. For simplicity, we restricted the inner and outer emissivity parameters of the compact corona to $q_1 = q_2 = 3$, the reflection fraction in the `relxillCp` component

to $R = -1$ in order to only generate the reflected component, and the coronal temperature to $kT_e = 400$ keV. This choice of coronal temperature was made following the results of the analysis of García et al. (2015b) on GX 339-4, which measure a high energy cutoff ≥900 keV in the hard state at a low luminosity. For simplicity, and in order to reduce the complications of measuring the high energy cutoff with a limited passband, as the ability to constrain the inner accretion disk radius is likely unaffected by the choice of coronal temperature, we adopted this value for both a soft and hard spectral state, regardless of source flux; we note however that we would expect the coronal temperature to vary with luminosity in reality. The remaining source properties such as the disk temperature and power-law index were adjusted to match the ones measured by Liu et al. (2023a) by using *Insight*–HXMT observations of the source in the two different spectral states. For the soft state, we adopted a disk temperature of $kT_{\rm in} = 0.75$ keV and a power-law index $\Gamma = 2.5$, while during the hard state we used $kT_{\rm in} = 0.5$ keV and $\Gamma = 1.7$. We adjusted the normalizations of the components in order to match the ratio of the fluxes between the different components described by Liu et al. (2023a) during the two spectral states. In our experiment, we simulated 100 s, 1 ks, and 10 ks exposures of sources with fluxes varying from 1 m Crab to 500 m Crab, for an array of inner disk radii varying from $R_{\rm in} = R_{\rm ISCO}$ to $R_{\rm in} = 400R_{\rm ISCO}$; we note that during the soft state it is already well established that the disk sits close to, or at, the ISCO, but we simulate truncated spectra nonetheless as an exercise in consistency between the spectral states. We then fit these simulated spectra with the same models, allowing the parameters to vary freely. Figure 3 shows constraints on inner disk radius for different simulated model values as a function of source flux, for the three different effective exposure times, while in hard (left) and soft (right) spectral states, respectively.

For bright sources, *HEX-P* observations will place tight constraints on the inner disk radius even from short, 100s snapshots, enabling tests of the rapid evolution of the physics of the inner accretion flow. At the same time, owing to its increased sensitivity and low background, *HEX-P* will probe reflection in sources fainter than ever before, with fluxes ≤1 mCrab, through relatively modest duration observations of a few ks, expanding our understanding of the physics of accretion at Eddington fractions ≤0.1% $L_{\rm Edd}$. To better highlight the improvement over current generation instruments, Figure 4 illustrates the ability to measure the inner disk radius based on *HEX-P* (left) and *NuSTAR* (right) observations of bright (500 mCrab) and faint (25 mCrab) sources using 1ks and 10ks observations. Figure 4 clearly highlights the ability of *HEX-P* to surpass the extraordinary legacy of *NuSTAR* by probing the properties of accreting BH-XRBs on much shorter time scales, in significantly fainter sources.

2.2 Geometry and physics of the corona

2.2.1 Coronal geometry

To demonstrate *HEX − P*'s ability to distinguish between different coronal geometries, we consider a recent study of a BH-XRB in which two distinct geometries describe the data equally well. The geometry of the BH corona, which provides the hard X-ray flux that illuminates the inner accretion disk to produce reflection, is a topic of active current research. Combining X-ray timing analysis with reflection spectroscopy suggests a variable, compact corona ($r \sim 10R_{\rm g}$) in both AGN (Wilkins et al., 2017; Alston et al., 2020) and BH-XRBs (Kara et al., 2019). Another avenue towards classifying the nature and geometry of BH coronae is with spectral and polarization measurements, which is an ongoing effort with the recent launch of IXPE (Weisskopf et al., 2016; Krawczynski et al., 2022; Weisskopf et al., 2022). With spectral analysis alone, different reflection models are often degenerate, such that the different assumptions about the coronal geometry can reproduce the same data (e.g., Miller et al., 2015; García et al., 2018b; Draghis et al., 2020; Draghis et al., 2021; Connors et al., 2022). While some models rely on a 'lamppost' geometry with a compact corona directly above the spin axis of the BH, others are more flexible in allowing for different configurations of the BH corona.

Reflection modeling of the recently discovered BH transient MAXI J1803−298 by Coughenour et al. (2023) could not distinguish between two distinct coronal geometries. Using the lamppost geometry, a distant corona with a height of $h \gtrsim 25R_g$ was preferred, while models which parameterize the emissivity of the inner accretion disk suggest a closer (and potentially extended) corona. Statistically, both models provided an excellent fit to the *NuSTAR* data and were consistent with one another with respect to the BH spin, disk inclination, ionization, temperature, and other key parameters. Therefore, despite relying on the longest *NuSTAR* observation of MAXI J1803−298 which was taken at the peak of its outburst, spectral analysis alone was unable to identify the nature of the corona.

To investigate whether *HEX − P*'s improved sensitivity and broadband energy coverage will distinguish between these two distinct coronal geometries, we simulated a *HEX-P* observation comparable to the 32 ks *NuSTAR* observation analyzed in Coughenour et al. (2023). Following that work, we compared a lamppost corona (using `relxilllpD`) and a model which utilizes a broken power law disk emissivity (`relxillD`). Both models are high-density flavors of the *relxill* suite of reflection models (Dauser et al., 2014; García et al., 2014). We simulated *HEX-P* spectra using both models, applying a correction factor to the LET spectra in order to account for the mitigation of pileup given a source flux of ~500 mCrab (see Supplementary Appendix; note also that the HET is much less impacted by pileup due to its triggered readout capability, and so we only consider these effects in the LET). Slight differences between the two models, resulting from the different coronal geometries, can be seen as deviations from unity in the ratio plot shown in Figure 5. The simulated *HEX-P* spectrum, produced under the assumption that our second model (which suggests a closer and potentially extended corona) is the true description of the data, deviates significantly from the lamppost model, particularly at the extreme ends of the spectrum (below ~2 keV and above ~50 keV) as well as near the Fe line (6–7 keV).

To quantify how well *HEX-P* would distinguish the two coronal geometries, we also fit each simulated dataset with both models. While Figure 5 highlights the differences between the two scenarios, re-fitting the *HEX-P* spectra with each model tests the possibility that these differences might be resolved. However, when the alternate model is applied, we find $\Delta\chi^2 \geq 28$ (for 3069 degrees of freedom), as well as a disagreement between notable parameters like the disk inclination. Therefore, *HEX-P* would in this instance be able to distinguish between these two coronal geometries relying on the

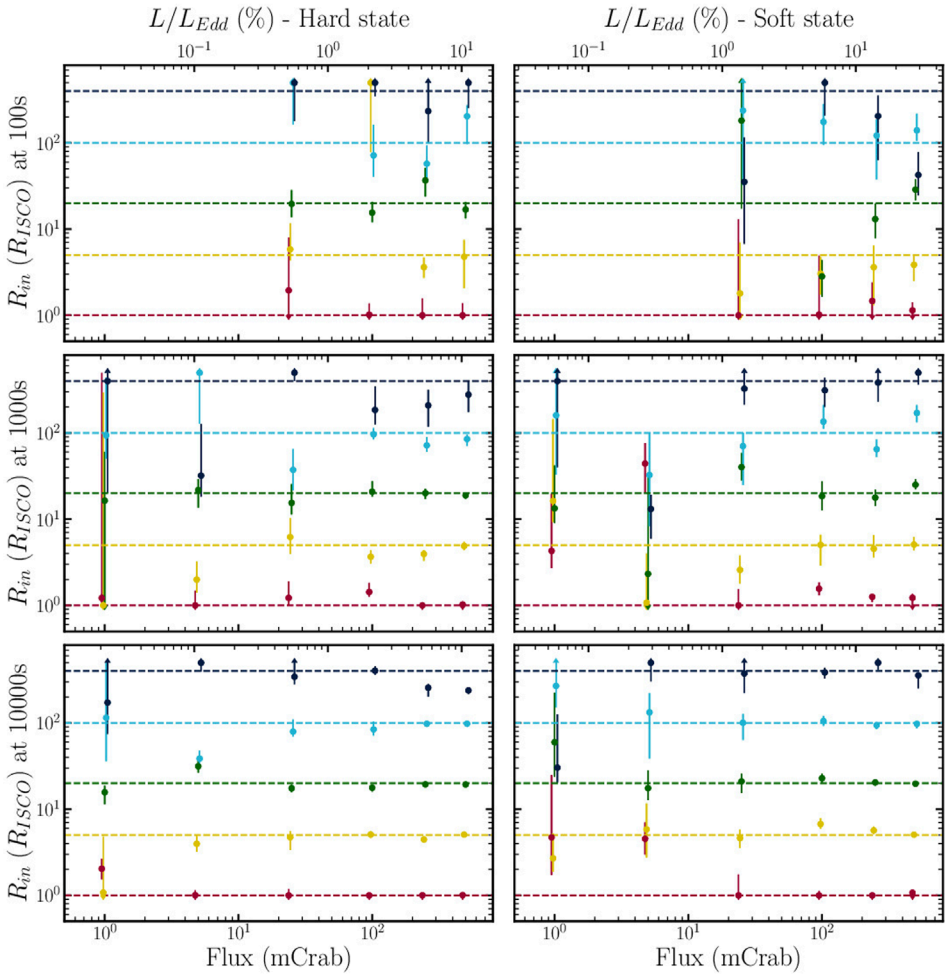

FIGURE 3
Ability to recover the inner disk radius assumed when simulating *HEX-P* spectra of a source similar to GX 339-4 in a hard (left) and soft (right) state, with fluxes varying between 1 mCrab and 500 mCrab, in 100 s, 1 ks, and 10 ks observations. The horizontal lines show the value of R_{in} used when simulating the spectra, in units of the size of the BH ISCO. The colored points represent the measurement of the inner disk radius based on the spectra simulated with the different values of R_{in}. The error bars represent 1σ uncertainties on the measurements. Spectra simulated to reproduce 100 s exposures of 1 and 5 mCrab sources do not produce enough signal to ensure meaningful spectral fits, so those points were excluded from the figure.

quality of spectra alone, and will be able to do so in more cases and with shorter exposures than current missions.

2.2.2 Coronal physics: Hybrid Comptonization

As already discussed at the beginning of this Section and Section 1, one of the primary causes of disagreements in X-ray spectral reflection measurements of the spins of accreting stellar mass BHs is the disagreement, or uncertainty, regarding the proximity of the accretion disk to the ISCO. However, a key driver of this uncertainty is the degeneracy between the irradiating X-ray continuum and the reflected component (Zdziarski et al., 2021), combined with degeneracies in spectral fitting of those continuum models. This is an issue that, whilst highlighted with great care over a decade ago (Nowak et al., 2011), still persists today. For example, several recent works have shown that measurements of the inner radius of the reflecting accretion disk will yield wildly different constraints depending on the continuum model assumed, even with broad X-ray coverage provided by previous and current instruments (e.g., Zdziarski et al., 2021; Connors et al., 2022; Zdziarski et al., 2022). One fundamental component of these degeneracies concerns the coronal Comptonization continuum. Often, with the X-ray coverage out to ~80 keV provided by, e.g., *NuSTAR*, the coronal continuum can be well described by a purely thermal Comptonization model, with some notable exceptions in which *NuSTAR* captures a high energy tail beyond 50 keV (e.g., Liu et al., 2023b). However, measurements out to higher energies typically show the corona in BH-XRBs is not a purely thermal plasma, but instead is comprised of a hybrid mixture of thermal and non-thermal electrons, identified by a high energy tail beyond ~100 keV (e.g., Grove et al., 1998; Gierliński et al., 1999; Del Santo et al., 2008; Bouchet et al., 2009; Roques et al., 2015; Del Santo et al., 2016; Roques and Jourdain, 2019; Cangemi et al., 2021). These findings were not surprising on physical grounds, since one expects luminous compact sources to have radiative cooling rates far greater than thermalization rates (Ghisellini et al., 1993; Zdziarski et al., 1993; Fabian et al., 2015; Fabian et al., 2017). An

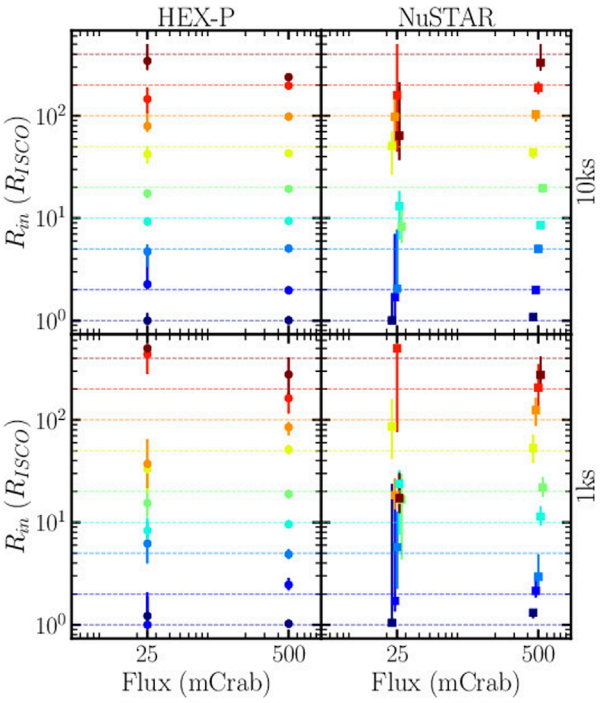

FIGURE 4
Ability to recover the inner disk radius assumed when simulating *HEX-P* (left) and *NuSTAR* (right) spectra of a source similar to GX 339-4, with fluxes of 25mCrab and 500mCrab, in 1ks (bottom), and 10ks (top) observations. The horizontal lines show the value of R_{in} used when simulating the spectra, in units of the size of the BH ISCO. The colored points represent the measurement of the inner disk radius based on the spectra simulated with the different values of R_{in}. The error bars represent 1σ uncertainties on the measurements.

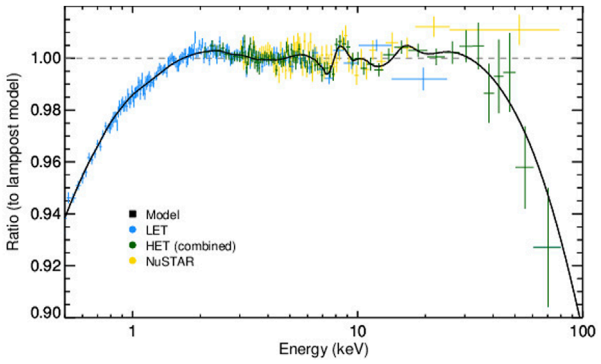

FIGURE 5
Ratio of a broken power law disk emissivity to a lamppost geometry for MAXI J1803−298, along with a 32 ks simulated *HEX-P* spectrum based on the disk emissivity model. *HEX − P*'s sensitivity and broad energy coverage allow it to distinguish between two distinct coronal geometries represented by the different models. Despite their differences, each model provides an acceptable fit to the *NuSTAR* data alone.

improved characterization of the BH corona is not only key to our understanding of BH accretion as a whole (and, e.g., supermassive BH growth), but critical for accurate measurements of BH spin via reflection spectroscopy (García et al., 2015a).

We have performed a series of simulations to investigate *HEX − P*'s capabilities to measure the subtle differences between purely thermal and hybrid thermal/non-thermal coronal Comptonization spectra with the combined broadband coverage of the LET (0.2–25 keV) and HET (2–80 keV). We set up canonical hard and soft state models using the Xspec model `eqpair` (Coppi, 1999). The `eqpair` model computes, self-consistently, the microphysical processes in a coronal plasma of mixed thermal/non-thermal leptons, including Coulomb collisions, bremsstrahlung, Compton scattering, and photon-photon pair production/annihilation. We refer the reader to Coppi (1999) for a complete description of this model, and simply note the key parameters of interest here, which are: i) l_s, the soft photon compactness; ii) l_h/l_s, the hard-to-soft compactness (i.e., l_h tells us the power supplied to the coronal electron plasma that upscatters the soft photons from the disk); iii) l_{nth}/l_h, the fraction of coronal power in non-thermal particles, from here on referred to as the non-thermal fraction; iv) kT_{bb}, seed photon temperature (assumed to be the inner disk temperature of a pseudo-Newtonion disk model, `diskpn`; see Gierliński et al., 1999); v) τ_p, the Thomson scattering optical depth; vi) Γ_{inj}, power law slope of the accelerated non-thermal electrons.

To represent a propotypical hard and soft spectral state with the `eqpair` model, we use the broadband X-ray spectral modeling of canonical bright sources such as Cyg X-1 and MAXI J1820+070 as a guide (Nowak et al., 2011; Del Santo et al., 2013; Parker et al., 2015; Cangemi et al., 2021; Zdziarski et al., 2021). The shape of the X-ray continuum is governed primarily by the compactness ratios l_h/l_s and l_{nth}/l_h, the scattering optical depth τ_p, the seed photon temperature kT_{bb}, and the slope of the injected accelerated electrons Γ_{inj}. The overall compactness is set by the soft compactness l_s, which will not alter the spectral shape significantly as long as $l_s < 100$. In accordance with previous works we fix its value to $l_s = 10$ for soft states, and $l_s = 1$ for hard states. For hard states, we assume $l_h/l_s = 10$, $kT_{bb} = 0.1$ keV, $\tau_p = 1.5$, and $\Gamma_{inj} = 3$ for our simulations, and a range of non-thermal fractions $l_{nth}/l_h = 0.1, 0.3, 0.5, 0.7, 0.9$. We assume all available soft photons pass through the corona in the hard state, i.e., a covering factor of 1, such that we only include the scattered component in our total model.

To model the soft state, we must take into account the dominance of the unscattered thermal disk blackbody spectrum, with a higher peak inner disk temperature, $kT_{bb} = 1$ keV. We increase the soft photon compactness in accordance to $l_s = 10$, and assume $l_h/l_s = 0.1$, $\tau_p = 2$, and $\Gamma_{inj} = 3$, and again simulate spectra with a range of non-thermal fractions $l_{nth}/l_h = 0.1, 0.3, 0.5, 0.7, 0.9$. We then separate the total spectrum into the scattered `eqpair` component, and an unscattered disk blackbody spectrum given by `diskpn`, where we assume a conservative covering factor for the corona (to soft photons) of just 10%. We note that we have performed the simulations that follow with the reflected component omitted. Since the reflection spectrum is intrinsically dependent on the continuum emission at higher energies (above 80 keV), including it naturally introduces additional constraints, whereas in these simulations we want to investigate how well *HEX-P* captures the underlying continuum. Thus we focus instead on the broadband shape of the irradiating continuum, and simply note that the presence

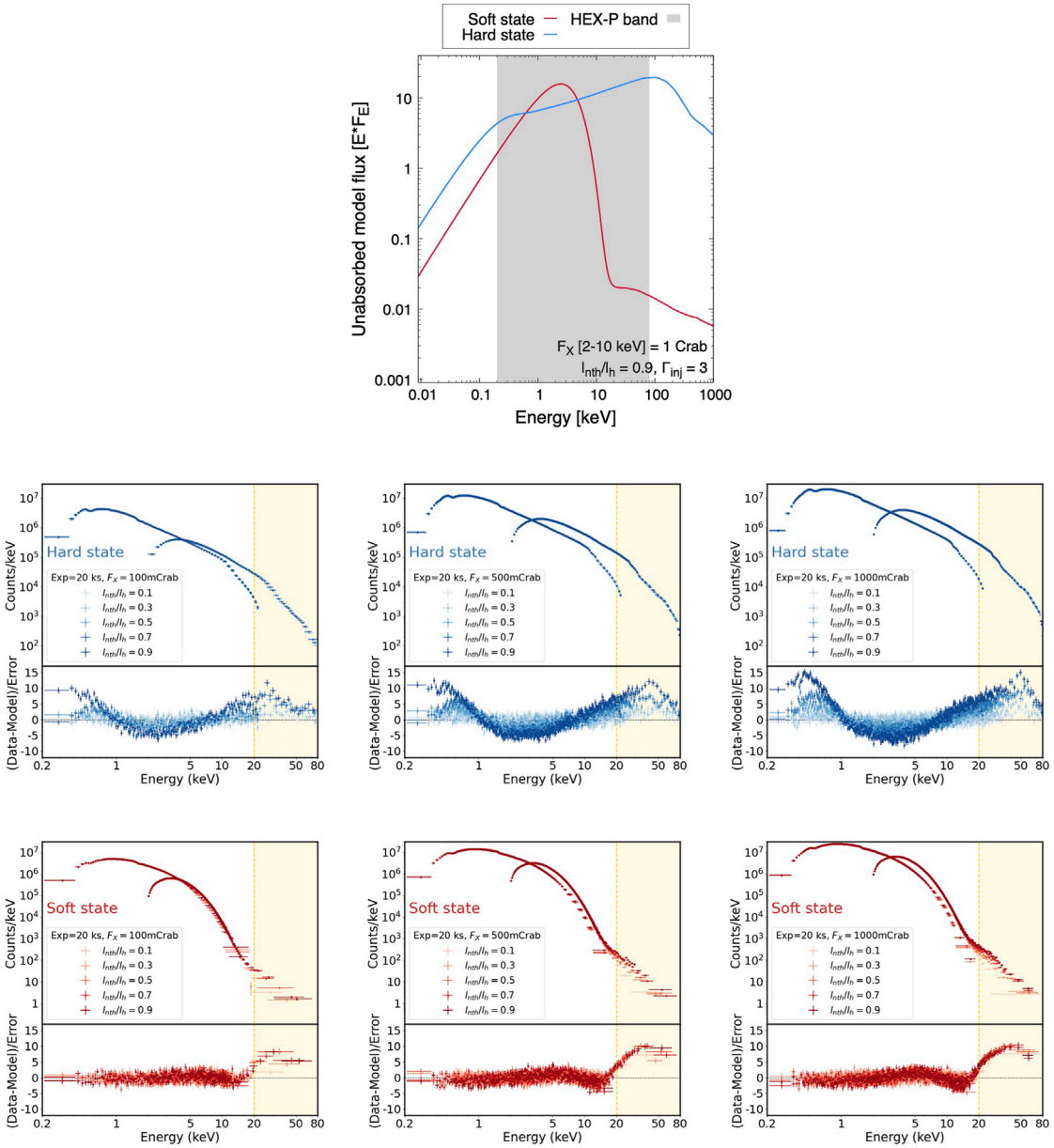

FIGURE 6
Top: Examples of the hybrid corona models used in *HEX-P* simulations of hard and soft BH-XRB spectral states. Middle/bottom: simulated *HEX-P* spectra of a prototypical Galactic BH-XRB hard (middle) and soft (bottom) state assuming different non-thermal electron fractions in a corona comprised of a hybrid of thermal/non-thermal electrons (using the `eqpair` model; Coppi, 1999). The model 2–10 keV X-ray source fluxes are 100 mCrab, 500 mCrab, and 1 Crab respectively from left to right. All data are simulated assuming a source exposure of 20 ks. The legend shows the non-thermal fraction ($l_{\rm nth}/l_{\rm h}$) and the shaded region highlights the 20–80 keV high energy band; simulations of the hard spectral state contain 10^5–10^6 counts in this band, soft state simulations typically contain 100–1000 counts.

of reflection features in observed X-ray spectra does not limit the capability of *HEX-P* to probe the underlying continuum. A comparison of the hard and soft state models is shown in the top panel of Figure 6.

The total spectral model is `TBabs*(diskpn+eqpair)`, and we fix the hydrogen column density to $N_{\rm H} = 10^{21}$ cm^{-2}. We simulate a series of hard and soft state spectra assuming a 2–10 keV source flux of 100 mCrab, 500 mCrab, and 1 Crab. As before, we apply a correction factor to the LET spectra to account for pileup mitigation according to the 64 channel window mode (64w) shown in Supplementary Appendix Table S3, depending on spectral state. We then fit each simulated spectrum (for both hard and soft states) with a purely thermal plasma model, i.e., $l_{\rm nth}/l_{\rm h} = 0$, and inspect the deviations of the model from the simulated data, shown in the middle/bottom panels of Figure 6. During hard states, the HET of *HEX-P* detects upwards of 10^5 counts in the 20–80 keV band for a conservative source flux of 100 mCrab, allowing us to measure statistically significant deviations from a purely thermal scattering spectral model for non-thermal fractions of $l_{\rm nth}/l_{\rm h} > 0.5$. More realistic non-thermal fractions in bright hard states are likely within

the 0.1–0.3 range (Buisson et al., 2019), which *HEX-P* can detect for sources approaching 1 Crab (wherein the HET would detect $>10^6$ counts in the 20–80 keV band). The high-energy sensitivity of *HEX-P* is best demonstrated, however, by its capability to detect the weak power law tail in BH-XRB soft states. Even given the stringent limits we placed on the flux contained within the scattered component (10%), the HET will capture the power law tail beyond 20 keV with high statistical significance (detecting upwards of ~100 counts) for the full range of non-thermal fractions and source fluxes. We note that the constraint provided by the LET of the soft disk component of the spectrum is also a key factor here, demonstrating the advantages of *HEX − P*'s broadband energy coverage via the combination of both the LET and HET.

These simulations show that *HEX-P* will be an important tool for studies of the microphysics of the corona, i.e., its particle content. However, in addition to there being further degeneracies in the coronal geometry itself (demonstrated in § 2.2.1), the modeling landscape is more complex than presented here: the non-thermal vs. thermal particle content of the corona is just one key model parameter among many. For example, the microphysics of the accretion disk atmosphere, typically parameterized in reflection models via disk ionization, $\log\xi$, iron abundance, $A_{\rm Fe}$, and disk density, $n_{\rm e}$, is necessarily degenerate with the irradiating continuum. Furthermore, there remain theoretical developments that must be made in order to improve models—not only spectroscopic ones—to better understand the high quality data *HEX-P* will provide. One such example is the physical size and shape of the corona in BH-XRBs. Estimates of the coronal extent have been made, typically by utilizing measurements of rapid X-ray variability (e.g., Kara et al., 2019), but they are often difficult to perform reliably due to the small spatial extent of the inner accretion flows of BH-XRBs. Recent polarimatric measurements have allowed us to begin probing the spatial extent and shape of the corona (e.g., Krawczynski et al., 2022), but again, such measurements are novel. From a theoretical standpoint, we must continue to improve our models to reflect the apparent complexity of the X-ray corona, and this applies to its size and shape, as well as microphysics. Such advances will be crucial if we are to take full advantage of *HEX-P*.

3 Black hole X-ray binaries in nearby galaxies

With *HEX − P*'s improvements in angular resolution (≥4× better than *NuSTAR*) and sensitivity, detailed broadband studies of BH-XRBs in other galaxies are finally within reach (see Lehmer et al., 2023, for detailed simulations of resolved X-ray source populations in nearby galaxies). To date, X-ray spectra have been obtained for only a small number of BH-XRBs with similar properties to those in our Galaxy (e.g., hard or soft spectral states, sub-Eddington luminosities, etc.). M33 X-7 is an example of a BH-XRB that was studied with *Chandra* in the soft state, and with its well-known distance (840 ± 20 kpc) and the fact that it is an eclipsing source, it was possible to determine the black hole mass and spin (Liu et al., 2008). IC10 X-1 and NGC300 X-1 are two other examples that have been observed by *XMM-Newton* and *Chandra* (Barnard et al., 2014; Binder et al., 2021). They have interesting but complex properties due to absorption by the winds from their Wolf-Rayet companions. The sample is far too small to make a meaningful comparison to the BH-XRBs in our Galaxy. Extending detailed spectral and timing studies to nearby galaxies opens a new window on our understanding of accreting BHs. *HEX-P* will vastly improve the BH-XRB population statistics due to its ability to resolve more point sources in nearby galaxies than, for example, *NuSTAR*. Lehmer et al. (2023) show, via simulations of *HEX-P* observations of extragalactic binaries, that *HEX-P* will be capable of detecting ~100 BH-XRBs above 4–25 keV luminosities of 10^{37} erg s^{-1} and ~10 above 4–25 keV luminosities of 10^{38} erg s^{-1}, per nearby galaxy (from a sample of hundreds of galaxies). We therefore expect a sizeable population of extragalactic BH-XRBs to perform statistical studies, including X-ray spectral modeling.

We illustrate *HEX − P*'s capabilities by considering spectra measured for a Galactic BH transient, MAXI J1820+070. This transient was well-studied during its outburst in 2018, and showed excellent examples of hard and soft states (Kalemci et al., 2022). The distance to the source and the BH mass have been well-determined (3 kpc and 8 solar masses, respectively), showing that it reached a luminosity of 1.5×10^{38} erg s^{-1}, which is 15% of the Eddington limit. Thus, this source is clearly in the category of BH-XRBs rather than being an ultraluminous X-ray source. Figure 7 shows simulated spectra for the case of a BH transient like MAXI J1820+070 in M31 (at 765 kpc) observed by *HEX-P* for 1 Ms (such an observation may be plausible with *HEX-P* as part of planned deep surveys of XRB populations in nearby galaxies, see Lehmer et al., 2023). The flux is near 2×10^{-12} erg cm^{-2} s^{-1}, and *HEX-P* will be capable of obtaining high-quality spectra. In the case of the hard state, the source is well-detected from 0.2 to 80 keV. The input model for the hard state spectrum includes a reflection component, and fitting the spectrum without a reflection component provides a poor fit with $\chi^2/\nu = 556/421$, indicating a detection of reflection. The residuals show that *HEX − P*'s high-energy sensitivity is the reason for the detection. Also, the simulated soft state spectrum shows that an excellent measurement of the thermal component will be obtained. It is worth mentioning that even with the vast improvements *HEX-P* will allow us to make in spectral studies of sources in nearby galaxies, in most cases the measurements of the reflection component will not allow tight constraints on spin.

4 Discussion

We have presented a range of detailed simulations demonstrating advances *HEX-P* will make in the science of BH-XRBs. *HEX-P* will make considerable strides in our understanding of the inner accretion flows of BH-XRBs, and the geometry and properties of the coronal plasma. Furthermore, *HEX-P* will make detailed spectral studies of BH-XRBs in other galaxies possible, opening a novel avenue on our understanding of BH accretion. Here we discuss our results and their broader implications.

4.1 Inner accretion flow structure and black hole spin

Measurements of disk truncation in BH-XRBs are fundamental to BH spin constraints, since spin estimates rely on the assumption

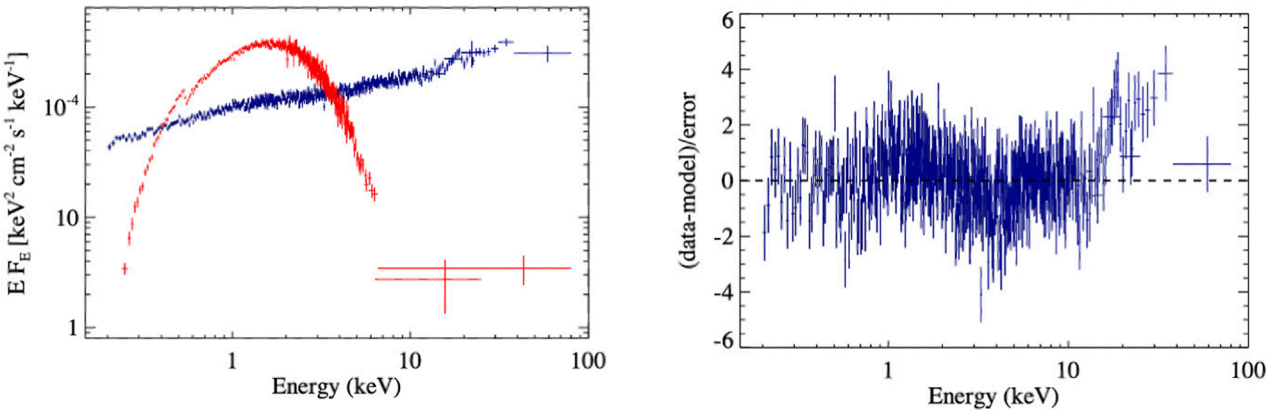

FIGURE 7
Simulated *HEX-P* spectra for studies of a BH transient like MAXI J1820+070 in M31. The spectra (left panel) include LET and HET with 1 Ms of exposure time. The blue spectrum is for the hard state, and the red spectrum is for the soft state. The residuals (right panel) are for a fit to the hard state spectrum without the reflection component.

that the inner edge of the accretion disk is located at the ISCO, and thus the gravitational signatures are dependent on the BH angular momentum (Reynolds and Fabian, 2008). In principle, BH spin constraints should be regarded as lower limits, since minor truncation beyond the ISCO is equivalent to the ISCO for a less rapidly spinning BH. Spin constraints nonetheless rely on accurate modeling of the underlying continuum, or else one can misinterpret curvature in the continuum as broadened line features. Up to now, whilst there is strong evidence for BH-XRB hard states in which the accretion disk extends to the ISCO (and thus estimates of spin from X-ray reflection spectroscopy are reliable; García et al., 2015b; Buisson et al., 2019; Sridhar et al., 2019; Connors et al., 2022; Liu et al., 2023b), disagreements persist (Basak and Zdziarski, 2016; Basak et al., 2017; Zdziarski et al., 2021; Zdziarski et al., 2022), and these are driven primarily by uncertainties in the shape and geometry of the irradiating coronal Comptonization continuum. This disk truncation dilemma is particularly pertinent now, given the recent extension of BH studies to the realm of merging BBHs via gravitational wave events (Abbott et al., 2016; Reynolds, 2021). A debate has ensued as to whether the populations of BH-XRBs and BBHs are distinct or not, and this debate hinges primarily on the spins of the BHs constituting these two classes of binary (Belczynski et al., 2021; Fishbach and Kalogera, 2022). Addressing this question is crucial to our understanding of BH formation and binary evolutionary channels (e.g., Ma and Fuller, 2019; Qin et al., 2019). BH-XRB observational data provided by current X-ray instruments have thus far struggled to unambiguously separate the coronal plasma emission from the reflected emission in many cases; as such, this debate over BH-XRB disk truncation (and thus spin) remains unsettled. *HEX-P* will finally address the issue of disk truncation due to its capability to probe the evolution of the inner disk over several orders of magnitude in luminosity, and on short timescales (§ 2.1). Similarly, *HEX-P* will be capable of probing the continuum emission of accreting neutron stars (NSs), and measure their radii via reflection modeling (see Ludlam et al., 2023, for a full description of NS accretion studies with *HEX-P*).

Finally, it is worth briefly mentioning the importance of ionized disk winds to comprehensive studies of BH-XRBs, especially in the context of contamination of key discrete reflection spectral signatures, i.e., the iron line complex. Ionized disk winds are typically detected via a series of blueshifted absorption signatures in the broadband X-ray spectrum, primarily in the soft band (see, e.g., Ponti et al., 2012). In addition, reprocessing can occur in gases surrounding the accretion flow that leads to emission lines (see, e.g., King et al., 2015; Shaw et al., 2022). The presence of such absorption and emission signatures in the X-ray spectra of BH-XRBs is typically circumvented by making use of instruments with high spectral energy resolution. *HEX-P* will have a spectral resolution that is improved beyond current high-energy X-ray missions such as *NuSTAR*, but it will not be capable of identifying all discreet signatures and separating those from disk reflection in all cases. We simply state this as a key caveat to our reflection spectroscopy simulations, since further study of the interplay between winds and reflection is beyond the scope of our work.

4.2 Black hole coronae

Determining the nature of the corona is fundamental to a broader understanding of the physics of accretion, and obtaining BH spin constraints. There exists a strong relationship, however, between the properties of the corona, the inflowing optically thick gases (i.e., the disk), and the strong gravity of the BH, and thus its spin. We have demonstrated this degeneracy, and shown how *HEX-P* will contribute to breaking it in BH-XRBs, due to the combination of its broadband coverage, competitive spectral resolution, and high energy sensitivity. Our simulations of *HEX-P* observations of the X-ray continuum shape of hybrid (containing both non-thermal and thermal electrons) coronal emission (§ 2.2.2) demonstrate a broader proof of concept of probes of weak coronal emission, i.e., during BH-XRB soft states. Basic constraints on the Comptonization spectrum, whether it is comprised of hybrid or purely thermal electrons, are challenging in soft states, due to the intrinsically low coronal

power (typically the bright, soft disk emission dwarfs the hard continuum flux by orders of magnitude; Remillard and McClintock, 2006; Done et al., 2007). *HEX-P* will make significant improvements over *NuSTAR*, the best available instrument we currently have to study weak coronal emission, due mostly to *HEX − P*'s low hard X-ray background. This will allow for full characterization of the corona across BH-XRB spectral states, which is not only crucial to breaking degeneracies with the reflected component of emission, but also fundamental to understanding coronal physics more broadly (Fabian et al., 2015; Fabian et al., 2017; Buisson et al., 2019).

As discussed above, the composition, energetics, and geometry of the corona are key to the studies of accretion in BH-XRBs, and this is also true more broadly across the entire BH mass scale (see, e.g., Kammoun et al., 2023). Recently, kinetic plasma simulations of radiative magnetic reconnection in electron-positron and electron-ion coronae have started shedding light on the long-standing problem of coronal energization (Sridhar et al., 2021; Sridhar et al., 2023). Particle-in-cell simulations have shown that the electrons in the coronal plasma will be cooled down to non-relativistic temperatures in the presence of strong inverse-Compton cooling (due to disk photons), and that the chain of trans-relativistically moving cold plasmoids could engage in Comptonization. The properties of the Comptonized spectra in this paradigm are primarily set by plasma magnetization (defined as the ratio of magnetic field to particle energy densities). Note that the plasma's magnetization is strongly dependent on its composition and location in the system (e.g., a corona composed of pair plasma near the jet would have a higher magnetization than a baryon-loaded corona right above the disk). *HEX-P*, with its reduced background at higher energies, will have the sensitivity to measure hard coronal emission down to low fluxes (as we showed in Section 2.2.2). As such, *HEX-P* is an ideal instrument to discern the subtle differences in the spectra around and beyond the high-energy spectral cutoff (for similar effective electron temperatures and spectral indices) arising due to different plasma magnetizations, and thus potentially constrain the coronal composition and location.

4.3 Synergies with other observatories

We have demonstrated the power of *HEX-P* as a stand-alone instrument to advance our understanding of accretion onto stellar-mass BHs. However, comprehensive studies of BH-XRBs benefit hugely from synergies between different observatories, with simultaneous broadband X-ray (and multiwavelength) coverage continuously proving key to building a complete physical picture of accretion (e.g., Miller-Jones et al., 2012; Dinçer et al., 2014; Kalemci et al., 2016; Buisson et al., 2019; Saikia et al., 2022, and references therein). *HEX-P* will be especially advantageous in this regard due to its broadband energy coverage (0.2–80 keV) and high energy sensitivity. As demonstrated throughout this paper, this combination gives us a clean view of both the soft thermal disk and hard X-ray coronal components of BH-XRBs from hard-to-soft spectral states. This ability to probe multiple BH-XRB emission components with a single observation will make *HEX-P* the connecting tissue between any given targeted observation of specific components and a broader understanding of the behaviour of the source.

For example, recent developments have been made in X-ray polarization studies of BH-XRBs. The *Imaging X-ray Polarimetry Explorer* (*IXPE*; Weisskopf et al., 2016; Weisskopf et al., 2022), which detects polarization in the 2–8 keV band, recently measured the X-ray polarization degree and angle of the coronal emission in Cyg X-1, concluding, among other things, that the corona must be spatially extended (Krawczynski et al., 2022). This conclusion required full characterization of the broadband X-ray spectrum, obtained via simultaneous observations with *NICER*, *NuSTAR*, *Swift*, and *INTEGRAL*. *HEX-P* will provide equivalent energy coverage to the combination of *NICER* and *NuSTAR*, with significant improvements to the high energy sensitivity, and will be crucial to future polarimetric observations of BH-XRBs. *HEX-P* will be a critical complementary observatory to future polarimetry missions such as the *X-ray Polarization Probe* (*XPP*; Krawczynski et al., 2019; Jahoda et al., 2019) and the *Enhanced X-ray Timing and Polarimetry* mission (*eXTP*; Zhang et al., 2016).

HEX-P will also play a key role in bridging the gap between X-ray and gamma-ray observations of BH-XRBs with, for example, the *Compton Spectrometer and Imager* (*COSI*; Tomsick et al., 2019), selected for launch in 2027 as a NASA Small Explorer (SMEX) mission. A key science goal of *COSI*, which will observe in the 0.2–5 MeV range, is to characterize the Galactic 511 keV positron annihilation line and the gamma-ray polarization of compact objects. The broadband X-ray coverage of *HEX-P* will provide constraints on the coronal continuum emission of BH-XRBs and thus serve as a benchmark for models to explain the higher energy emission and polarization measurements provided by *COSI*.

Furthermore, recent advances in systematic studies of the optical night sky with surveys provided by facilities such as the Zwicky Transient Facility (ZTF; Bellm et al., 2019) and ATLAS (Tonry et al., 2018) are paving the way for large scale rapid transient detections. Such surveys can result in serendipitous discoveries of Galactic transients of interest to the community studying accretion onto compact objects. For example, ATLAS recently discovered an optical transient named AT2019wey (Tonry et al., 2019), first thought to be a Supernova (Mereminskiy et al., 2020). However, full X-ray follow-up with *NICER*, *NuSTAR*, *Chandra*, *Swift*, and *MAXI* resulted in a revision of the source identification, and AT2019wey was shown to be an XRB (Yao et al., 2021b), and subsequently a candidate BH-XRB (Yao et al., 2021a). This shows that follow-up broadband X-ray observations of sources detected with wide-field optical (and indeed multiwavelength) transient surveys will be critical to identifiying and capitalizing on the discovery of new BH transients. *HEX-P* will be a key player in this regard, since it will be capable of providing constraints on multiple spectral components of accreting sources over several orders of magnitude in flux, with a single, short source exposure of just a few ks (see Section 2.1).

Shifting focus to high-resolution spectroscopy, we are fast approaching the era of high resolving power ($E/\Delta E$) X-ray astronomy at energies beyond a few keV with the development of microcalorimeters capable of achieving spectral energy resolutions of $E/\Delta E \geq 1000$. For example, *XRISM* (Tashiro et al., 2018) launched in September 2023, and *NewAthena* (Nandra et al., 2013; Barret et al., 2020) is due to follow in the 2030s. These

instruments will be revolutionary in the study of accretion onto compact objects (such as in BH-XRBs). At such high revolving powers, we will be able to probe the subtle narrow features due to absorption and emission from the ionized gases in and around BH accretion disks. However, it has always been the case that accurate measurements of spectral features require proper characterization of the underlying X-ray continuum emission out to energies beyond 10 keV, just as the resolving power allows us to then separate these components. The spectral coverage needed for this is currently provided by instruments such as *NuSTAR*, but we will *need* this coverage in the decades to come. As we have demonstrated in Sections 2 and 3, *HEX-P* will make significant improvements on high energy observatories like *NuSTAR* in terms of broadband energy coverage and high energy sensitivity. As such, *HEX-P* will be the workhorse that complements the key science goals of upcoming microcalorimetry missions.

Finally, *HEX-P* will be a key instrument in future detections of the electromagnetic (EM) counterparts of GW events. Beyond the recent and ongoing GW detections provided by the LIGO-Virgo collaboration (Abbott et al., 2016), future instruments such as Einstein (Punturo et al., 2010; Maggiore et al., 2020), the Cosmic Explorer (Reitze et al., 2019), and the space-based Laser Interferometer Space Antenna (LISA; Amaro-Seoane et al., 2017) will push the science of compact object mergers into the 2030s and beyond. Broadband X-ray coverage will be fundamental to EM follow-ups of such detections—for which source localization and precise temporal predictions of the merger will be possible—in the decade to come, and *HEX-P* will be central to those efforts. We refer the reader to Brightman et al. (2023) for a detailed study of *HEX-P* contributions to GW science.

4.4 Conclusions

We summarize the main conclusions of our simulations of BH-XRB *HEX-P* observations—and the discussion of our results—as follows.

- *HEX-P* will allow us to study the broadband spectral evolution of BH-XRBs over a wide range of X-ray luminosities, providing full characterization of the disk and coronal spectral components. In particular, *HEX-P* will make strides forward in resolving the debate regarding the structure of inner accretion flows as BH-XRBs evolve, by constraining, for example, the inner disk edge $R_{\rm in}$ with high precision across a large dynamical and luminosity range (down to below 0.1% of the Eddington luminosity), with source exposures of just a few ks.
- *HEX-P*, due to its broadband coverage (0.2–80 keV) and high energy sensitivity (a feature of its reduced background), will break some key parameter degeneracies in both the geometry and Comptonization spectral shape of BH-XRB coronae. This leap forward in our understanding of the BH corona is key to BH spin measurements and our broader understanding of the corona as a power source for astrophysical phenomena on both Galactic and cosmological scales.
- *HEX-P* will expand the detailed spectral analysis of BH-XRBs into the extragalactic realm. We will be able to probe the high energy emission of these bright accretors out to larger distances (nearby galaxies at ~500–1000 kpc). Although detailed X-ray reflection spoctrscopy of extragalactic sources will still be limited to only the very brightest, super-Eddington sources, *HEX-P* will conduct science typically reserved for Galactic compact stellar sources.
- *HEX-P* will serve as a multi-faceted accompanying observatory to many other future advanced facilites, such as X-ray polarization missions, optical transient survey telescopes, and GW observatories. The broadband coverage of *HEX-P*–and thus its ability to probe multiple spectral components simultaneously—will make it the leading mission in X-ray spectral measurements of BH-XRBs, providing connections to modern multi-messenger astronomical observations and maximizing their scientific output.

Data availability statement

The raw data supporting the conclusion of this article will be made available by the authors, without undue reservation.

Author contributions

RC: Conceptualization, Data curation, Formal Analysis, Investigation, Methodology, Supervision, Writing–original draft, Writing–review and editing. JT: Conceptualization, Data curation, Formal Analysis, Investigation, Methodology, Project administration, Supervision, Writing–original draft, Writing–review and editing. PD: Conceptualization, Data curation, Formal Analysis, Investigation, Methodology, Writing–original draft, Writing–review and editing. BC: Conceptualization, Data curation, Formal Analysis, Investigation, Methodology, Writing–original draft, Writing–review and editing. AS: Investigation, Methodology, Writing–review and editing. JG: Conceptualization, Methodology, Supervision, Writing–review and editing. DW: Conceptualization, Methodology, Supervision, Writing–review and editing. KM: Writing–review and editing, Data curation, Resources, Software. DS: Writing–review and editing, Funding acquisition, Project administration, Resources, Supervision, Validation. NCR: Writing–review and editing. TD: Writing–review and editing, Resources, Software. MS: Writing–review and editing. JJ: Writing–review and editing, Conceptualization. HK: Conceptualization, Methodology, Writing–review and editing. HL: Conceptualization, Writing–review and editing. JN: Conceptualization, Investigation, Writing–review and editing. MN: Investigation, Methodology, Writing–review and editing. SP: Investigation, Writing–review and editing. AS: Writing–review and editing. NS: Investigation, Writing–review and editing. AW: Conceptualization, Data curation, Investigation, Writing–review and editing. JW: Conceptualization, Investigation, Writing–review and editing.

Funding

The author(s) declare financial support was received for the research, authorship, and/or publication of this article. The work of DS was carried out at the Jet Propulsion Laboratory, California Institute of Technology, under a contract with NASA.

Conflict of interest

The authors declare that the research was conducted in the absence of any commercial or financial relationships that could be construed as a potential conflict of interest.

Publisher's note

All claims expressed in this article are solely those of the authors and do not necessarily represent those of their affiliated organizations, or those of the publisher, the editors and the reviewers. Any product that may be evaluated in this article, or claim that may be made by its manufacturer, is not guaranteed or endorsed by the publisher.

Supplementary material

The Supplementary Material for this article can be found online at: https://www.frontiersin.org/articles/10.3389/fspas.2023.1292682/full#supplementary-material

References

Abbott, B. P., Abbott, R., Abbott, T. D., Abernathy, M. R., Acernese, F., Ackley, K., et al. (2016). Binary black hole mergers in the first advanced LIGO observing run. *Phys. Rev. X* 6, 041015. doi:10.1103/PhysRevX

Alston, W. N., Fabian, A. C., Kara, E., Parker, M. L., Dovciak, M., Pinto, C., et al. (2020). A dynamic black hole corona in an active galaxy through X-ray reverberation mapping. *Nat. Astron.* 4, 597–602. doi:10.1038/s41550-019-1002-x

Amaro-Seoane, P., Audley, H., Babak, S., Baker, J., Barausse, E., Bender, P., et al. (2017). *Laser interferometer space Antenna. arXiv e-prints,* aarXiv:1702.

Barnard, R., Steiner, J. F., Prestwich, A. F., Stevens, I. R., Clark, J. S., and Kolb, U. C. (2014). Energy-dependent evolution in IC10 X-1: hard evidence for an extended corona and implications. *ApJ* 792, 131. doi:10.1088/0004-637X/792/2/131

Barret, D., Decourchelle, A., Fabian, A., Guainazzi, M., Nandra, K., Smith, R., et al. (2020). The Athena space X-ray observatory and the astrophysics of hot plasma. *Astron. Nachrichten* 341, 224–235. doi:10.1002/asna.202023782

Basak, R., and Zdziarski, A. A. (2016). Spectral analysis of the XMM-Newton data of GX 339-4 in the low/hard state: disc truncation and reflection. *MNRAS* 458, 2199–2214. doi:10.1093/mnras/stw420

Basak, R., Zdziarski, A. A., Parker, M., and Islam, N. (2017). Analysis of NuSTAR and Suzaku observations of Cyg X-1 in the hard state: evidence for a truncated disc geometry. *MNRAS* 472, 4220–4232. doi:10.1093/mnras/stx2283

Belczynski, K., Done, C., and Lasota, J. P. (2021). *All Apples: comparing black holes in X-ray binaries and gravitational-wave sources. arXiv e*-prints, arXiv:2111.

Bellm, E. C., Kulkarni, S. R., Graham, M. J., Dekany, R., Smith, R. M., Riddle, R., et al. (2019). The Zwicky transient facility: system overview, performance, and first results. *PASP* 131, 018002. doi:10.1088/1538-3873/aaecbe

Beloborodov, A. M. (2017). Radiative magnetic reconnection near accreting black holes. *ApJ* 850, 141. doi:10.3847/1538-4357/aa8f4f

Binder, B. A., Sy, J. M., Eracleous, M., Christodoulou, D. M., Bhattacharya, S., Cappallo, R., et al. (2021). The wolf-rayet + black hole binary NGC 300 X-1: what is the mass of the black hole? *ApJ* 910, 74. doi:10.3847/1538-4357/abe6a9

Bisnovatyi-Kogan, G. S., and Blinnikov, S. I. (1977). Disk accretion onto a black hole at subcritical luminosity. *AAP* 59, 111–125.

Bouchet, L., del Santo, M., Jourdain, E., Roques, J. P., Bazzano, A., and DeCesare, G. (2009). Unveiling the high energy tail of 1E 1740.7-2942 with INTEGRAL. *ApJ* 693, 1871–1876. doi:10.1088/0004-637X/693/2/1871

Boyle, B. J., and Terlevich, R. J. (1998). The cosmological evolution of the QSO luminosity density and of the star formation rate. *MNRAS* 293, L49–L51. doi:10.1046/j.1365-8711.1998.01264.x

Buisson, D. J. K., Fabian, A. C., Barret, D., Fürst, F., Gandhi, P., García, J. A., et al. (2019). MAXI J1820+070 with NuSTAR I. An increase in variability frequency but a stable reflection spectrum: coronal properties and implications for the inner disc in black hole binaries. *MNRAS* 490, 1350–1362. doi:10.1093/mnras/stz2681

Burrows, D. N., Hill, J. E., Nousek, J. A., Kennea, J. A., Wells, A., Osborne, J. P., et al. (2005). The Swift X-ray telescope. *SSR* 120, 165–195. doi:10.1007/s11214-005-5097-2

Cangemi, F., Beuchert, T., Siegert, T., Rodriguez, J., Grinberg, V., Belmont, R., et al. (2021). Potential origin of the state-dependent high-energy tail in the black hole microquasar Cygnus X-1 as seen with INTEGRAL. *AAP* 650, A93. doi:10.1051/0004-6361/202038604

Connors, R. M. T., García, J. A., Tomsick, J., Mastroserio, G., Grinberg, V., Steiner, J. F., et al. (2022). The long-stable hard state of XTE J1752-223 and the disk truncation dilemma. *ApJ* 935, 118. doi:10.3847/1538-4357/ac7ff2

Coppi, P. S. (1999) "The physics of hybrid thermal/non-thermal plasmas," in *High energy processes in accreting black holes*J. Poutanen, and R. Svensson (Astronomical Society of the Pacific (ASP)). doi:10.48550/arXiv.astro-ph/9903158

Coughenour, B. M., Tomsick, J. A., Mastroserio, G., Steiner, J. F., Connors, R. M. T., Jiang, J., et al. (2023). Reflection and timing study of the transient black hole X-ray binary MAXI J1803-298 with NuSTAR. *ApJ* 949, 70. doi:10.3847/1538-4357/acc65c

Dauser, T., Falkner, S., Lorenz, M., Kirsch, C., Peille, P., Cucchetti, E., et al. (2019). SIXTE: a generic X-ray instrument simulation toolkit. *AAP* 630, A66. doi:10.1051/0004-6361/201935978

Dauser, T., Garcia, J., Parker, M. L., Fabian, A. C., and Wilms, J. (2014). The role of the reflection fraction in constraining black hole spin. *MNRAS* 444, L100–L104. doi:10.1093/mnrasl/slu125

Dauser, T., Garcia, J., Wilms, J., Böck, M., Brenneman, L. W., Falanga, M., et al. (2013). Irradiation of an accretion disc by a jet: general properties and implications for spin measurements of black holes. *MNRAS* 430, 1694–1708. doi:10.1093/mnras/sts710

Davies, R. I., Müller Sánchez, F., Genzel, R., Tacconi, L. J., Hicks, E. K. S., Friedrich, S., et al. (2007). A close look at star formation around active galactic nuclei. *ApJ* 671, 1388–1412. doi:10.1086/523032

Del Santo, M., Belloni, T. M., Tomsick, J. A., Sbarufatti, B., Cadolle Bel, M., Casella, P., et al. (2016). Spectral and timing evolution of the bright failed outburst of the transient black hole Swift J174510.8-262411. *MNRAS* 456, 3585–3595. doi:10.1093/mnras/stv2901

Del Santo, M., Malzac, J., Belmont, R., Bouchet, L., and De Cesare, G. (2013). The magnetic field in the X-ray corona of Cygnus X-1. *MNRAS* 430, 209–220. doi:10.1093/mnras/sts574

Del Santo, M., Malzac, J., Jourdain, E., Belloni, T., and Ubertini, P. (2008). Spectral variability of GX339-4 in a hard-to-soft state transition. *MNRAS* 390, 227–234. doi:10.1111/j.1365-2966.2008.13672.x

Dinçer, T., Kalemci, E., Tomsick, J. A., Buxton, M. M., and Bailyn, C. D. (2014). Complete multiwavelength evolution of galactic black hole transients during outburst decay. II. Compact jets and X-ray variability properties. *ApJ* 795, 74. doi:10.1088/0004-637X/795/1/74

Done, C., Gierliński, M., and Kubota, A. (2007). Modelling the behaviour of accretion flows in X-ray binaries. Everything you always wanted to know about accretion but were afraid to ask. *AAPR* 15, 1–66. doi:10.1007/s00159-007-0006-1

Dove, J. B., Wilms, J., Maisack, M., and Begelman, M. C. (1997). Self-consistent thermal accretion disk corona models for compact objects. II. Application to Cygnus X-1. *ApJ* 487, 759–768. doi:10.1086/304647

Draghis, P. A., Miller, J. M., Cackett, E. M., Kammoun, E. S., Reynolds, M. T., Tomsick, J. A., et al. (2020). A new spin on an old black hole: NuSTAR spectroscopy of EXO 1846-031. *ApJ* 900, 78. doi:10.3847/1538-4357/aba2ec

Draghis, P. A., Miller, J. M., Zoghbi, A., Kammoun, E. S., Reynolds, M. T., and Tomsick, J. A. (2021). The spin and orientation of the black hole in XTE J1908+094. *ApJ* 920, 88. doi:10.3847/1538-4357/ac1270

Draghis, P. A., Miller, J. M., Zoghbi, A., Reynolds, M., Costantini, E., Gallo, L. C., et al. (2023). A systematic view of ten new black hole spins. *ApJ* 946, 19. doi:10.3847/1538-4357/acafe7

Eraerds, T., Antonelli, V., Davis, C., Hall, D., Hetherington, O., Holland, A., et al. (2021). Enhanced simulations on the athena/wide field imager instrumental background. *J. Astronomical Telesc. Instrum. Syst.* 7, 034001. doi:10.1117/1.JATIS.7.3.034001

Fabian, A. C., Lohfink, A., Belmont, R., Malzac, J., and Coppi, P. (2017). Properties of AGN coronae in the NuSTAR era - II. Hybrid plasma. *MNRAS* 467, 2566–2570. doi:10.1093/mnras/stx221

Fabian, A. C., Lohfink, A., Kara, E., Parker, M. L., Vasudevan, R., and Reynolds, C. S. (2015). Properties of AGN coronae in the NuSTAR era. *MNRAS* 451, 4375–4383. doi:10.1093/mnras/stv1218

Fabian, A. C., Parker, M. L., Wilkins, D. R., Miller, J. M., Kara, E., Reynolds, C. S., et al. (2014). On the determination of the spin and disc truncation of accreting black holes using X-ray reflection. *MNRAS* 439, 2307–2313. doi:10.1093/mnras/stu045

Falcke, H., Körding, E., and Markoff, S. (2004). A scheme to unify low-power accreting black holes. Jet-dominated accretion flows and the radio/X-ray correlation. *AAP* 414, 895–903. doi:10.1051/0004-6361:20031683

Fishbach, M., and Kalogera, V. (2022). Apples and oranges: comparing black holes in X-ray binaries and gravitational-wave sources. *ApJL* 929, L26. doi:10.3847/2041-8213/ac64a5

Fürst, F., Nowak, M. A., Tomsick, J. A., Miller, J. M., Corbel, S., Bachetti, M., et al. (2015). The complex accretion geometry of GX 339-4 as seen by NuSTAR and Swift. *ApJ* 808, 122. doi:10.1088/0004-637X/808/2/122

García, J., Dauser, T., Lohfink, A., Kallman, T. R., Steiner, J. F., McClintock, J. E., et al. (2014). Improved reflection models of black hole accretion disks: treating the angular distribution of X-rays. *ApJ* 782, 76. doi:10.1088/0004-637X/782/2/76

García, J. A., Dauser, T., Steiner, J. F., McClintock, J. E., Keck, M. L., and Wilms, J. (2015a). On estimating the high-energy cutoff in the X-ray spectra of black holes via reflection spectroscopy. *ApJL* 808, L37. doi:10.1088/2041-8205/808/2/L37

García, J. A., Kallman, T. R., Bautista, M., Mendoza, C., Deprince, J., Palmeri, P., et al. (2018a). The problem of the high iron abundance in accretion disks around black holes. *Workshop Astrophysical Opacities* 515. doi:10.48550/arXiv.1805.00581

García, J. A., Steiner, J. F., Grinberg, V., Dauser, T., Connors, R. M. T., McClintock, J. E., et al. (2018b). Reflection spectroscopy of the black hole binary XTE J1752-223 in its long-stable hard state. *ApJ* 864, 25. doi:10.3847/1538-4357/aad231

García, J. A., Steiner, J. F., McClintock, J. E., Remillard, R. A., Grinberg, V., and Dauser, T. (2015b). X-ray reflection spectroscopy of the black hole GX 339–4: exploring the hard state with unprecedented sensitivity. *ApJ* 813, 84. doi:10.1088/0004-637X/813/2/84

García, J. A., Tomsick, J. A., Sridhar, N., Grinberg, V., Connors, R. M. T., Wang, J., et al. (2019). The 2017 failed outburst of GX 339-4: relativistic X-ray reflection near the black hole revealed by NuSTAR and Swift spectroscopy. *ApJ* 885, 48. doi:10.3847/1538-4357/ab384f

Gehrels, N., Chincarini, G., Giommi, P., Mason, K. O., Nousek, J. A., Wells, A. A., et al. (2004). The*Swift* Gamma-ray burst mission. *ApJ* 611, 1005–1020. doi:10.1086/422091

Gendreau, K. C., Arzoumanian, Z., Adkins, P. W., Albert, C. L., Anders, J. F., Aylward, A. T., et al. (2016). "The neutron star interior composition explorer (NICER): design and development," in *Space telescopes and instrumentation 2016: ultraviolet to gamma ray* Editors J.-W. A. den Herder, T. Takahashi, and M. Bautz (Proceedings of The International Society for Optics and Photonics (SPIE)). doi:10.1117/12.2231304

George, I. M., and Fabian, A. C. (1991). X-ray reflection from cold matter in active galactic nuclei and X-ray binaries. *MNRAS* 249, 352–367. doi:10.1093/mnras/249.2.352

Ghisellini, G., Haardt, F., and Fabian, A. C. (1993). On re-acceleration, pairs and the high-energy spectrum of AGN and galactic black hole candidates. *MNRAS* 263, L9–L12. doi:10.1093/mnras/263.1.l9

Gierliński, M., Zdziarski, A. A., Poutanen, J., Coppi, P. S., Ebisawa, K., and Johnson, W. N. (1999). Radiation mechanisms and geometry of Cygnus X-1 in the soft state. *MNRAS* 309, 496–512. doi:10.1046/j.1365-8711.1999.02875.x

Grove, J. E., Johnson, W. N., Kroeger, R. A., McNaron-Brown, K., Skibo, J. G., and Phlips, B. F. (1998). Gamma-ray spectral states of galactic black hole candidates. *ApJ* 500, 899–908. doi:10.1086/305746

Gupta, S., Sridhar, N., and Sironi, L. (2023). *Comptonization by reconnection plasmoids in black hole coronae III: dependence on the guide field in pair plasma*. *arXiv e-prints*, arXiv:2310.04233.

Haardt, F., and Maraschi, L. (1991). A two-phase model for the X-ray emission from seyfert galaxies. *ApJL* 380, L51. doi:10.1086/186171

Haardt, F., and Maraschi, L. (1993). X-ray spectra from two-phase accretion disks. *ApJ* 413, 507. doi:10.1086/173020

Harrison, F. A., Craig, W. W., Christensen, F. E., Hailey, C. J., Zhang, W. W., Boggs, S. E., et al. (2013). The nuclear spectroscopic telescope array (NuSTAR) high-energy X-ray mission. *ApJ* 770, 103. doi:10.1088/0004-637X/770/2/103

Jahoda, K., Krawczynski, H., Kislat, F., Marshall, H., Okajima, T., Agudo, I., et al. (2019). *The X-ray Polarization Probe mission concept*. *arXiv e-prints*, arXiv:1907.

Jansen, F., Lumb, D., Altieri, B., Clavel, J., Ehle, M., Erd, C., et al. (2001). XMM-Newton observatory. I. The spacecraft and operations. *AAP* 365, L1–L6. doi:10.1051/0004-6361:20000036

Jensen, P. L., Clausen, K., Cassi, C., Ravera, F., Janin, G., Winkler, C., et al. (2003). The INTEGRAL spacecraft - in-orbit performance. *AAP* 411, L7–L17. doi:10.1051/0004-6361:20031173

Kalemci, E., Begelman, M. C., Maccarone, T. J., Dinçer, T., Russell, T. D., Bailyn, C., et al. (2016). Wind, jet, hybrid corona and hard X-ray flares: multiwavelength evolution of GRO J1655-40 during the 2005 outburst rise. *MNRAS* 463, 615–627. doi:10.1093/mnras/stw2002

Kalemci, E., Kara, E., and Tomsick, J. A. (2022). Black holes: timing and spectral properties and evolution. *Handb. X-ray Gamma-ray Astrophysics* 9, 1–43. doi:10.1007/978-981-16-4544-0_100-1

Kara, E., Steiner, J. F., Fabian, A. C., Cackett, E. M., Uttley, P., Remillard, R. A., et al. (2019). The corona contracts in a black-hole transient. *Nature* 565, 198–201. doi:10.1038/s41586-018-0803-x

Kammoun, E., Lohfink, A. M., Masterson, M., Wilkins, D. R., Zhao, X., Balokovic, M., et al. (2023). The high energy X-ray probe (HEX-P): probing the physics of the X-ray corona in active galactic nuclei. *Front. Astron. Space Sci.* arXiv:2311.04679.

King, A. L., Miller, J. M., Raymond, J., Reynolds, M. T., and Morningstar, W. (2015). High-resolution Chandra HETG spectroscopy of V404 cygni in outburst. *ApJL* 813, L37. doi:10.1088/2041-8205/813/2/L37

Körding, E. G., Jester, S., and Fender, R. (2006). Accretion states and radio loudness in active galactic nuclei: analogies with X-ray binaries. *MNRAS* 372, 1366–1378. doi:10.1111/j.1365-2966.2006.10954.x

Kormendy, J., and Ho, L. C. (2013). Coevolution (or not) of supermassive black holes and host galaxies. *ARAA* 51, 511–653. doi:10.1146/annurev-astro-082708-101811

Krawczynski, H., Matt, G., Ingram, A. R., Taverna, R., Turolla, R., Kislat, F., et al. (2019). *Astro2020 science white paper: using X-ray polarimetry to probe the physics of black holes and neutron stars*. *arXiv e-prints*, arXiv:1904.09313. doi:10.48550/arXiv.1904.09313

Krawczynski, H., Muleri, F., Dovčiak, M., Veledina, A., Rodriguez Cavero, N., Svoboda, J., et al. (2022). Polarized x-rays constrain the disk-jet geometry in the black hole x-ray binary Cygnus X-1. *Science* 378, 650–654. doi:10.1126/science.add5399

Lehmer, B., Garofali, K., Binder, B. A., Fornasini, F., Vulic, N., Zezas, A., et al. (2023). The high energy X-ray probe: resolved X-ray populations in extragalactic environments. *Front. Astron. Space Sci.* ArXiv:2311.04735.

Liu, B. F., Mineshige, S., and Ohsuga, K. (2003). Spectra from a magnetic reconnection-heated corona in active galactic nuclei. *ApJ* 587, 571–579. doi:10.1086/368282

Liu, H., Bambi, C., Jiang, J., García, J. A., Ji, L., Kong, L., et al. (2023a). The hard-to-soft transition of GX 339-4 as seen by insight-HXMT. *ApJ* 950, 5. doi:10.3847/1538-4357/acca17

Liu, H., Jiang, J., Zhang, Z., Bambi, C., Fabian, A. C., García, J. A., et al. (2023b). High-density reflection spectroscopy of black hole X-ray binaries in the hard state. *ApJ* 951, 145. doi:10.3847/1538-4357/acd8b9

Liu, J., McClintock, J. E., Narayan, R., Davis, S. W., and Orosz, J. A. (2008). Precise measurement of the spin parameter of the stellar-mass black hole M33 X-7. *ApJL* 679, L37–L40. doi:10.1086/588840

Liu, Q. Z., van Paradijs, J., and van den Heuvel, E. P. J. (2006). Catalogue of high-mass X-ray binaries in the Galaxy (4th edition). *AAP* 455, 1165–1168. doi:10.1051/0004-6361:20064987

Loeb, A., and Barkana, R. (2001). The reionization of the universe by the first stars and quasars. *ARAA* 39, 19–66. doi:10.1146/annurev.astro.39.1.19

Ludlam, R., Malacaria, C., Sokolova-Lapa, E., Fuerst, F., Pradhan, P., Shaw, A. W., et al. (2023). The high energy X-ray probe (HEX-P): a new window into neutron star accretion. *Front. Astron. Space Sci.* ArXiv:2311.04687.

Ma, L., and Fuller, J. (2019). Angular momentum transport in massive stars and natal neutron star rotation rates. *MNRAS* 488, 4338–4355. doi:10.1093/mnras/stz2009

Madsen, K. K., García, J. A., Stern, D., Armini, R., Basso, S., Coutinho, D., et al. (2023). The High Energy X-ray Probe (HEX-P): instrument and mission profile. *Instrumentation and Methods for Astrophysics* 10. doi:10.48550/arXiv.2312.04678

Maggiore, M., Van Den Broeck, C., Bartolo, N., Belgacem, E., Bertacca, D., Bizouard, M. A., et al. (2020). Science case for the Einstein telescope. *JCAP* 2020, 050. doi:10.1088/1475-7516/2020/03/050

Makishima, K., Maejima, Y., Mitsuda, K., Bradt, H. V., Remillard, R. A., Tuohy, I. R., et al. (1986). Simultaneous X-ray and optical observations of GX 339-4 in an X-ray high state. *ApJ* 308, 635. doi:10.1086/164534

Marino, A., Barnier, S., Petrucci, P. O., Del Santo, M., Malzac, J., Ferreira, J., et al. (2021). Tracking the evolution of the accretion flow in MAXI J1820+070 during its hard state with the JED-SAD model. *AAP* 656, A63. doi:10.1051/0004-6361/202141146

Markoff, S., Nowak, M. A., and Wilms, J. (2005). Going with the flow: can the base of jets subsume the role of compact accretion disk coronae? *ApJ* 635, 1203–1216. doi:10.1086/497628

McHardy, I. M., Koerding, E., Knigge, C., Uttley, P., and Fender, R. P. (2006). Active galactic nuclei as scaled-up Galactic black holes. *Nature* 444, 730–732. doi:10.1038/nature05389

Meidinger, N., Albrecht, S., Beitler, C., Bonholzer, M., Emberger, V., Frank, J., et al. (2020). Development status of the wide field imager instrument for Athena. *Soc. Photo-Optical Instrum. Eng. (SPIE) Conf. Ser.* 11444, 114440T. doi:10.1117/12.2560507

Mereminskiy, I., Medvedev, P., Semena, A., Pavlinsky, M., Molkov, S., Lutovinov, A., et al. (2020). SRG discovery of SRGA J043520.9+552226 = SRGE J043523.3+552234, an X-ray counterpart of optical transient ATLAS19bcxp. *Astronomer's Telegr.* 13571, 1–11. doi:10.1017/S1368980020003389

Merloni, A., and Heinz, S. (2013). "Evolution of active galactic nuclei," in *Planets, stars and stellar systems. Volume 6: extragalactic astronomy and cosmology* Editors T. D. Oswalt, and W. C. Keel (springer). doi:10.1007/978-94-007-5609-0_11

Miller, J. M., Tomsick, J. A., Bachetti, M., Wilkins, D., Boggs, S. E., Christensen, F. E., et al. (2015). New constraints on the black hole low/hard state inner accretion flow with NuSTAR. *ApJL* 799, L6. doi:10.1088/2041-8205/799/1/L6

Miller-Jones, J. C. A., Sivakoff, G. R., Altamirano, D., Coriat, M., Corbel, S., Dhawan, V., et al. (2012). Disc-jet coupling in the 2009 outburst of the black hole candidate H1743-322. *MNRAS* 421, 468–485. doi:10.1111/j.1365-2966.2011.20326.x

Mitsuda, K., Inoue, H., Koyama, K., Makishima, K., Matsuoka, M., Ogawara, Y., et al. (1984). Energy spectra of low-mass binary X-ray sources observed from TENMA. *PASJ* 36, 741–759.

Muñoz-Darias, T., Motta, S., and Belloni, T. M. (2011). Fast variability as a tracer of accretion regimes in black hole transients. *MNRAS* 410, 679–684. doi:10.1111/j.1365-2966.2010.17476.x

Nandra, K., Barret, D., Barcons, X., Fabian, A., den Herder, J.-W., Piro, L., et al. (2013). *The hot and energetic universe: a white paper presenting the science theme motivating the Athena+ mission*. *arXiv e*-prints , arXiv:1306.2307.

Nowak, M. A., Hanke, M., Trowbridge, S. N., Markoff, S. B., Wilms, J., Pottschmidt, K., et al. (2011). Corona, jet, and relativistic line models for suzaku/RXTE/Chandra-HETG observations of the Cygnus X-1 hard state. *ApJ* 728, 13. doi:10.1088/0004-637X/728/1/13

Parker, M. L., Tomsick, J. A., Miller, J. M., Yamaoka, K., Lohfink, A., Nowak, M., et al. (2015). NuSTAR and suzaku observations of the hard state in Cygnus X-1: locating the inner accretion disk. *ApJ* 808, 9. doi:10.1088/0004-637X/808/1/9

Plant, D. S., Fender, R. P., Ponti, G., Muñoz-Darias, T., and Coriat, M. (2015). The truncated and evolving inner accretion disc of the black hole GX 339-4. *AAP* 573, A120. doi:10.1051/0004-6361/201423925

Ponti, G., Fender, R. P., Begelman, M. C., Dunn, R. J. H., Neilsen, J., and Coriat, M. (2012). Ubiquitous equatorial accretion disc winds in black hole soft states. *MNRAS* 422, L11–L15. doi:10.1111/j.1745-3933.2012.01224.x

Power, C., Wynn, G. A., Combet, C., and Wilkinson, M. I. (2009). Primordial globular clusters, X-ray binaries and cosmological reionization. *MNRAS* 395, 1146–1152. doi:10.1111/j.1365-2966.2009.14628.x

Punturo, M., Abernathy, M., Acernese, F., Allen, B., Andersson, N., Arun, K., et al. (2010). The Einstein Telescope: a third-generation gravitational wave observatory. *Class. Quantum Gravity* 27, 194002. doi:10.1088/0264-9381/27/19/194002

Qin, Y., Marchant, P., Fragos, T., Meynet, G., and Kalogera, V. (2019). On the origin of black hole spin in high-mass X-ray binaries. *ApJL* 870, L18. doi:10.3847/2041-8213/aaf97b

Reis, R. C., Fabian, A. C., and Miller, J. M. (2010). Black hole accretion discs in the canonical low-hard state. *MNRAS* 402, 836–854. doi:10.1111/j.1365-2966.2009.15976.x

Reis, R. C., Fabian, A. C., Ross, R. R., Miniutti, G., Miller, J. M., and Reynolds, C. (2008). A systematic look at the very high and low/hard state of GX339-4: constraining the black hole spin with a new reflection model. *MNRAS* 387, 1489–1498. doi:10.1111/j.1365-2966.2008.13358.x

Reitze, D., Adhikari, R. X., Ballmer, S., Barish, B., Barsotti, L., Billingsley, G., et al. (2019). Cosmic explorer: the U.S. Contribution to gravitational-wave astronomy beyond LIGO. *Bull. Am. Astronomical Soc.* 51, 35. doi:10.48550/arXiv.1907.04833

Remillard, R. A., and McClintock, J. E. (2006). X-ray properties of black-hole binaries. *ARAA* 44, 49–92. doi:10.1146/annurev.astro.44.051905.092532

Reynolds, C. S. (2021). Observational constraints on black hole spin. *ARAA* 59, 117–154. doi:10.1146/annurev-astro-112420-035022

Reynolds, C. S., and Begelman, M. C. (1997). Iron fluorescence from within the innermost stable orbit of black hole accretion disks. *ApJ* 488, 109–118. doi:10.1086/304703

Reynolds, C. S., and Fabian, A. C. (2008). Broad iron-Kα emission lines as a diagnostic of black hole spin. *ApJ* 675, 1048–1056. doi:10.1086/527344

Roques, J.-P., and Jourdain, E. (2019). On the high-energy emissions of compact objects observed with INTEGRAL SPI: event selection impact on source spectra and scientific results for the bright sources Crab nebula, GS 2023+338 and MAXI J1820+070. *ApJ* 870, 92. doi:10.3847/1538-4357/aaf1c9

Roques, J.-P., Jourdain, E., Bazzano, A., Fiocchi, M., Natalucci, L., and Ubertini, P. (2015). First INTEGRAL observations of V404 cygni during the 2015 outburst: spectral behavior in the 20-650 keV energy range. *ApJL* 813, L22. doi:10.1088/2041-8205/813/1/L22

Saikia, P., Russell, D. M., Baglio, M. C., Bramich, D. M., Casella, P., Diaz Trigo, M., et al. (2022). A multiwavelength study of GRS 1716-249 in outburst: constraints on its system parameters. *ApJ* 932, 38. doi:10.3847/1538-4357/ac6ce1

Scaringi, S., Maccarone, T. J., Kording, E., Knigge, C., Vaughan, S., Marsh, T. R., et al. (2015). Accretion-induced variability links young stellar objects, white dwarfs, and black holes. *Sci. Adv.* 1, e1500686. doi:10.1126/sciadv.1500686

Shaw, A. W., Miller, J. M., Grinberg, V., Buisson, D. J. K., Heinke, C. O., Plotkin, R. M., et al. (2022). High resolution X-ray spectroscopy of V4641 Sgr during its 2020 outburst. *MNRAS* 516, 124–137. doi:10.1093/mnras/stac2213

Sironi, L., and Beloborodov, A. M. (2020). Kinetic simulations of radiative magnetic reconnection in the coronae of accreting black holes. *ApJ* 899, 52. doi:10.3847/1538-4357/aba622

Sridhar, N., Bhattacharyya, S., Chandra, S., and Antia, H. M. (2019). Broad-band reflection spectroscopy of MAXI J1535-571 using AstroSat: estimation of black hole mass and spin. *MNRAS* 487, 4221–4229. doi:10.1093/mnras/stz1476

Sridhar, N., García, J. A., Steiner, J. F., Connors, R. M. T., Grinberg, V., and Harrison, F. A. (2020). Evolution of the accretion disk-corona during the bright hard-to-soft state transition: a reflection spectroscopic study with GX 339-4. *ApJ* 890, 53. doi:10.3847/1538-4357/ab64f5

Sridhar, N., Sironi, L., and Beloborodov, A. M. (2021). Comptonization by reconnection plasmoids in black hole coronae I: magnetically dominated pair plasma. *MNRAS* 507, 5625–5640. doi:10.1093/mnras/stab2534

Sridhar, N., Sironi, L., and Beloborodov, A. M. (2023). Comptonization by reconnection plasmoids in black hole coronae II: electron-ion plasma. *MNRAS* 518, 1301–1315. doi:10.1093/mnras/stac2730

Steiner, J. F., Remillard, R. A., García, J. A., and McClintock, J. E. (2016). Stronger reflection from black hole accretion disks in soft X-ray states. *ApJL* 829, L22. doi:10.3847/2041-8205/829/2/L22

Tanaka, Y., and Lewin, W. H. G. (1995). Black hole binaries. *X-ray Bin.* 1995, 126–174.

Tashiro, M., Maejima, H., Toda, K., Kelley, R., Reichenthal, L., Lobell, J., et al. (2018). "Concept of the X-ray astronomy recovery mission," in *Space telescopes and instrumentation 2018: ultraviolet to gamma ray* Editors J.-W. A. den Herder, S. Nikzad, and K. Nakazawa (Proceedings of the SPIE), 1069922. doi:10.1117/12.2309455

Tetarenko, B. E., Sivakoff, G. R., Heinke, C. O., and Gladstone, J. C. (2016). WATCHDOG: a comprehensive all-sky database of galactic black hole X-ray binaries. *ApJS* 222, 15. doi:10.3847/0067-0049/222/2/15

The LIGO Scientific Collaboration, the Virgo Collaboration, the KAGRA Collaboration, Abbott, R., Abbott, T. D., Acernese, F., et al. (2021). *GWTC-3: compact binary coalescences observed by LIGO and virgo during the second part of the third observing run*. *arXiv e*-prints, arXiv:2111.03606

Tomsick, J., Zoglauer, A., Sleator, C., Lazar, H., Beechert, J., Boggs, S., et al. (2019). The Compton spectrometer and imager. *Bull. Am. Astronomical Soc.* 51, 98. doi:10.48550/arXiv.1908.04334

Tomsick, J. A., Kalemci, E., Kaaret, P., Markoff, S., Corbel, S., Migliari, S., et al. (2008). Broadband X-ray spectra of GX 339-4 and the geometry of accreting black holes in the hard state. *ApJ* 680, 593–601. doi:10.1086/587797

Tomsick, J. A., Yamaoka, K., Corbel, S., Kaaret, P., Kalemci, E., and Migliari, S. (2009). Truncation of the inner accretion disk around a black hole at low. *Luminosity* 707, L87–L91. –L91. doi:10.1088/0004-637X/707/1/L87

Tonry, J., Denneau, L., Heinze, A., Weiland, H., Flewelling, H., Stalder, B., et al. (2019). *ATLAS transient discovery report for 2019-12-08*, 1. Transient Name Server Discovery Report 2019-2553.

Tonry, J. L., Denneau, L., Heinze, A. N., Stalder, B., Smith, K. W., Smartt, S. J., et al. (2018). ATLAS: a high-cadence all-sky survey system. *PASP* 130, 064505. doi:10.1088/1538-3873/aabadf

Urry, C. M., and Padovani, P. (1995). Unified schemes for radio-loud active galactic nuclei. *PASP* 107, 803. doi:10.1086/133630

Weisskopf, M. C., Ramsey, B., O'Dell, S., Tennant, A., Elsner, R., Soffitta, P., et al. (2016). "The imaging X-ray polarimetry explorer (IXPE)," in *Space telescopes and instrumentation 2016: ultraviolet to gamma ray* Editors J.-W. A. den Herder, T. Takahashi, and M. Bautz. (Proceedings of the SPIE). doi:10.1117/12.2235240.990517

Weisskopf, M. C., Soffitta, P., Baldini, L., Ramsey, B. D., O'Dell, S. L., Romani, R. W., et al. (2022). Imaging X-ray polarimetry explorer: prelaunch. *J. Astronomical Telesc. Instrum. Syst.* 8, 026002. doi:10.1117/1.JATIS.8.2.026002

Wilkins, D. R., Gallo, L. C., Silva, C. V., Costantini, E., Brandt, W. N., and Kriss, G. A. (2017). Revealing structure and evolution within the corona of the Seyfert galaxy I Zw 1. *MNRAS* 471, 4436–4451. doi:10.1093/mnras/stx1814

Wilms, J., Allen, A., and McCray, R. (2000). On the absorption of X-rays in the interstellar medium. *ApJ* 542, 914–924. doi:10.1086/317016

Yao, Y., Kulkarni, S. R., Burdge, K. B., Caiazzo, I., De, K., Dong, D., et al. (2021a). Multi-wavelength observations of AT2019wey: a new candidate black hole low-mass X-ray binary. *ApJ* 920, 120. doi:10.3847/1538-4357/ac15f9

Yao, Y., Kulkarni, S. R., Gendreau, K. C., Jaisawal, G. K., Enoto, T., Grefenstette, B. W., et al. (2021b). A comprehensive X-ray report on AT2019wey. *ApJ* 920, 121. doi:10.3847/1538-4357/ac15f8

Young, A. J., Ross, R. R., and Fabian, A. C. (1998). Iron line profiles including emission from within the innermost stable orbit of a black hole accretion disc. *MNRAS* 300, L11–L15. –L15. doi:10.1046/j.1365-8711.1998.02058.x

Zdziarski, A. A., Johnson, W. N., and Magdziarz, P. (1996). Broad-band γ-ray and X-ray spectra of NGC 4151 and their implications for physical processes and geometry. *MNRAS* 283, 193–206. doi:10.1093/mnras/283.1.193

Zdziarski, A. A., Jourdain, E., Lubiński, P., Szanecki, M., Niedźwiecki, A., Veledina, A., et al. (2021). Hybrid comptonization and electron-positron pair production in the black-hole X-ray binary MAXI J1820+070. *ApJL* 914, L5. doi:10.3847/2041-8213/ac0147

Zdziarski, A. A., Lightman, A. P., and Maciolek-Niedzwiecki, A. (1993). Acceleration efficiency in nonthermal sources and the soft gamma rays from NGC 4151 observed by OSSE and SIGMA. *ApJL* 414, L93. doi:10.1086/187004

Zdziarski, A. A., Lubiński, P., and Smith, D. A. (1999). Correlation between Compton reflection and X-ray slope in Seyferts and X-ray binaries. *MNRAS* 303, L11–L15. –L15. doi:10.1046/j.1365-8711.1999.02343.x

Zdziarski, A. A., You, B., Szanecki, M., Li, X.-B., and Ge, M. (2022). Insight-HXMT, NuSTAR, and INTEGRAL data show disk truncation in the hard state of the black hole X-ray binary MAXI J1820+070. *ApJ* 928, 11. doi:10.3847/1538-4357/ac54a7

Zhang, S. N., Feroci, M., Santangelo, A., Dong, Y. W., Feng, H., Lu, F. J., et al. (2016). "eXTP: enhanced X-ray timing and polarization mission," in *Space telescopes and instrumentation 2016: ultraviolet to gamma ray* Editors J.-W. A. den Herder, T. Takahashi, and M. Bautz (Edinburgh, UK: Proceedings of the SPIE) 99051Q. doi:10.1117/12.2232034

Życki, P. T., Done, C., and Smith, D. A. (1999). The 1989 May outburst of the soft X-ray transient GS 2023+338 (V404 Cyg). *MNRAS* 309, 561–575. doi:10.1046/j.1365-8711.1999.02885.x

frontiers | Frontiers in Astronomy and Space Sciences

TYPE Original Research
PUBLISHED 08 January 2024
DOI 10.3389/fspas.2023.1292130

Check for updates

OPEN ACCESS

EDITED BY
Murray Brightman,
California Institute of Technology,
United States

REVIEWED BY
Jakob Van Den Eijnden,
University of Warwick, United Kingdom
Ruth Daly,
Penn State Berks, United States

*CORRESPONDENCE
Kaya Mori,
kaya@astro.columbia.edu

RECEIVED 11 September 2023
ACCEPTED 05 December 2023
PUBLISHED 08 January 2024

CITATION
Mori K, Ponti G, Bachetti M, Bodaghee A, Grindlay J, Hong J, Krivonos R, Kuznetsova E, Mandel S, Rodriguez A, Stel G, Zhang S, Bao T, Bauer F, Clavel M, Coughenour B, García JA, Gerber J, Grefenstette B, Jaodand A, Lehmer B, Madsen K, Nynka M, Predehl P, Salcedo C, Stern D and Tomsick J (2024), The high energy X-ray probe (HEX-P): Resolving the nature of Sgr A* flares, compact object binaries and diffuse X-ray emission in the Galactic center and beyond.
Front. Astron. Space Sci. 10:1292130.
doi: 10.3389/fspas.2023.1292130

COPYRIGHT
© 2024 Mori, Ponti, Bachetti, Bodaghee, Grindlay, Hong, Krivonos, Kuznetsova, Mandel, Rodriguez, Stel, Zhang, Bao, Bauer, Clavel, Coughenour, García, Gerber, Grefenstette, Jaodand, Lehmer, Madsen, Nynka, Predehl, Salcedo, Stern and Tomsick. This is an open-access article distributed under the terms of the Creative Commons Attribution License (CC BY). The use, distribution or reproduction in other forums is permitted, provided the original author(s) and the copyright owner(s) are credited and that the original publication in this journal is cited, in accordance with accepted academic practice. No use, distribution or reproduction is permitted which does not comply with these terms.

The high energy X-ray probe (HEX-P): Resolving the nature of Sgr A* flares, compact object binaries and diffuse X-ray emission in the Galactic center and beyond

Kaya Mori[1]*, Gabriele Ponti[2,3], Matteo Bachetti[4], Arash Bodaghee[5], Jonathan Grindlay[6], Jaesub Hong[6], Roman Krivonos[7], Ekaterina Kuznetsova[7], Shifra Mandel[1], Antonio Rodriguez[8], Giovanni Stel[2], Shuo Zhang[9], Tong Bao[10], Franz Bauer[11], Maïca Clavel[12], Benjamin Coughenour[13], Javier A. García[14], Julian Gerber[1], Brian Grefenstette[8], Amruta Jaodand[8], Bret Lehmer[15], Kristin Madsen[14], Melania Nynka[16], Peter Predehl[3], Ciro Salcedo[1], Daniel Stern[17] and John Tomsick[13]

[1]Columbia Astrophysics Laboratory, Columbia University, New York, NY, United States, [2]INAF—Osservatorio Astronomico di Brera, Merate, Italy, [3]Max-Planck-Institut für extraterrestrische Physik, Garching, Germany, [4]INAF-Osservatorio Astronomico di Cagliari, Selargius, Italy, [5]Department of Chemistry, Physics and Astronomy, Georgia College & State University, Milledgeville, GA, United States, [6]Harvard-Smithsonian Center for Astrophysics, Harvard University, Cambridge, MA, United States, [7]Space Research Institute (IKI), Russian Academy of Sciences, Moscow, Russia, [8]Cahill Center for Astronomy and Astrophysics, California Institute of Technology, Pasadena, CA, United States, [9]Department of Physics and Astronomy, Michigan State University, East Lansing, MI, United States, [10]School of Astronomy and Space Science, Nanjing University, Nanjing, China, [11]Instituto de Astrofísica, Millennium Institute of Astrophysics, Pontificia Universidad Católica de Chile, Santiago, Chile, [12]University Grenoble Alpes, CNRS, IPAG, Grenoble, France, [13]Space Sciences Laboratory, UC Berkeley, Berkeley, CA, United States, [14]X-ray Astrophysics Laboratory, NASA Goddard Space Flight Center, Greenbelt, MD, United States, [15]Department of Physics, University of Arkansas, Fayetteville, AR, United States, [16]Kavli Institute for Astrophysics and Space Research, Massachusetts Institute of Technology, Cambridge, MA, United States, [17]Jet Propulsion Laboratory, California Institute of Technology, Pasadena, CA, United States

HEX-P is a probe-class mission concept that will combine high spatial resolution X-ray imaging (<10″ FWHM) and broad spectral coverage (0.2–80 keV) with an effective area far superior to current facilities' (including *XMM-Newton* and *NuSTAR*). These capabilities will enable revolutionary new insights into a variety of important astrophysical problems. We present scientific objectives and simulations of *HEX-P* observations of the Galactic Center (GC) and Bulge. We demonstrate the unique and powerful capabilities of the *HEX-P* observatory for studying both X-ray point sources and diffuse X-ray emission. *HEX-P* will be uniquely equipped to explore a variety of major topics in Galactic astrophysics, allowing us to 1) investigate broad-band properties of X-ray flares emitted from the supermassive black hole (BH) at Sgr A* and probe the associated particle acceleration and emission mechanisms; 2) identify hard X-ray sources detected by *NuSTAR* and determine X-ray point source populations in different regions

and luminosity ranges; 3) determine the distribution of compact object binaries in the nuclear star cluster and the composition of the Galactic Ridge X-ray emission; 4) identify X-ray transients and measure fundamental parameters such as black hole spin; 5) find hidden pulsars in the Galactic Center; 6) search for BH–OB binaries and hard X-ray flares from young stellar objects in young massive clusters; 7) measure white dwarf (WD) masses of magnetic CVs to deepen our understanding of CV evolution and the origin of white dwarf magnetic fields; 8) explore primary particle accelerators in the GC in synergy with future TeV and neutrino observatories; 9) map out cosmic-ray distributions by observing non-thermal X-ray filaments; 10) explore past X-ray outbursts from Sgr A* through X-ray reflection components from giant molecular clouds.

KEYWORDS

galaxy: centre, black hole physics, X-rays: binaries, stars: cataclysmic variables, accretion, acceleration of particles, pulsars: general

1 Introduction

The Galactic Center (GC) harbors an extremely dense and diverse population of stars, compact objects, X-ray binaries (XRBs), molecular clouds, magnetic filaments, and energetic cosmic-ray accelerators within its central few degrees. Sgr A*, the radiative counterpart of the supermassive black hole (SMBH), plays a crucial role in the gas dynamics and binary formation processes in the central few parsecs, where stars and XRBs cluster (Muno et al., 2003; Mori et al., 2021). Despite its faint quiescent X-ray emission, Sgr A* intermittently accelerates particles and emits daily X-ray flares. In the past, Sgr A* is believed to have been far more active, possibly fueling the Fermi GeV bubbles (Cheng et al., 2011), X-ray chimneys (Ponti et al., 2021), and, as recently as a few hundred years ago, X-ray emission from the GC molecular clouds (Ponti et al., 2010; Clavel et al., 2013). The population of relativistic cosmic rays, including leptons and hadrons, is evident in radio/X-ray filaments and TeV emission from molecular clouds (Zhang et al., 2014; Zhang et al., 2020).

X-ray observations provide valuable insights into compact objects, their binary systems, and particle accelerators in the GC region, since those sources are frequently observed to emit X-rays. However, conducting X-ray studies in this densely populated region, which is located at a large distance of 8 kpc, poses challenges. Furthermore, the GC is filled with numerous point and diffuse X-ray sources, requiring high-angular-resolution X-ray telescopes to resolve them. Over the past two decades, extensive surveys of the GC and bulge regions in the soft X-ray band (<10 keV) have been carried out by *Chandra*, *XMM-Newton* and *Suzaku*. In a $2° \times 0.8°$ region, *Chandra* detected ~10,000 X-ray point sources below 8 keV (Wang et al., 2002; Muno et al., 2009; Zhu et al., 2018). Studies of diffuse X-ray emission in the GC and Bulge regions have been conducted by *Suzaku* and *XMM-Newton*, revealing extensive hot plasma emission (Koyama et al., 2009; Ponti et al., 2015b; Anastasopoulou et al., 2023). Frequent X-ray monitoring of the GC with *Swift*-XRT resulted in the detection of ~20 X-ray transients in the GC (Degenaar et al., 2015). Follow-up X-ray observations with *Chandra*, *XMM-Newton* and *NuSTAR* enabled the identification of some of those transients (Mori et al., 2013; Mori et al., 2019).

In the GC and bulge regions, soft X-ray data is limited to $E > 2$ keV due to significant X-ray absorption and scattering. Consequently, the narrow-band (2–10 keV) X-ray data obtained by *Chandra* and *XMM-Newton* are often insufficient for identifying source types and accurately measuring spectral parameters (e.g., plasma temperatures and photon indices) due to the parameter degeneracy with neutral hydrogen column density ($N_{\rm H}$). In the GC, $N_{\rm H}$ is typically high ($N_{\rm H} \sim (5–20) \times 10^{22}$ cm^{-2}) and variable across different regions (Johnson et al., 2009), complicating our ability to constrain other spectral parameters in the soft X-ray band. In the higher energy band above 10 keV, *INTEGRAL*/IBIS and *Suzaku*-HXD unveiled diffuse hard X-ray emission and a handful of bright XRBs (Revnivtsev et al., 2004; Yuasa et al., 2008). Subsequently, *NuSTAR* surveyed ~2/3 of the central $2° \times 0.8°$ region, resolving the hard X-ray emission better with its sub-arcminute angular resolution. However, the *NuSTAR* GC observations are significantly affected by contamination from stray-light and ghost-ray background photons. As a result, several GC and bulge regions, including the Limiting Window (one of the low extinction windows where *Chandra* detected hundreds of soft X-ray point sources), Sgr C (one of the GC molecular clouds), and the southern part of the central $2° \times 0.8°$ region, remain unobserved by *NuSTAR* due to the elevated background levels. While *Chandra*, *XMM-Newton* and *Suzaku* have provided a comprehensive *soft* X-ray view of the GC region, our *broad-band* knowledge of the X-ray point and diffuse sources in the GC remains relatively limited.

In this paper, we highlight the unique capabilities of *HEX-P* to significantly advance our understanding of X-ray-emitting objects within the GC, Bulge and other regions in our Galaxy. Specifically, *HEX-P*'s exceptional angular resolution and broad-band X-ray coverage extending up to 80 keV are crucial for resolving X-ray sources, characterizing their X-ray emission, and identifying their nature. Given its energy band—extending to 25 keV with 3.5″ angular resolution, LET will be highly advantageous for investigating X-ray sources in crowded fields like the GC. On the other hand, HET will allow us to investigate hard X-ray sources and non-thermal X-ray emission with far better sensitivity than *NuSTAR*. X-ray spectral and timing properties of transients will be fully characterized by *HEX-P* thanks to its fast readout time. Both LET and HET will provide excellent Fe line diagnostics at $E = 6–7$ keV; detecting and

resolving highly-ionized Fe lines at 6.7 and 6.9 keV will enable us to discern between thermal and non-thermal X-ray sources. Moreover, a neutral Fe fluorescence line at 6.4 keV can be utilized to constrain X-ray reflection models for molecular clouds and magnetic CVs (mCVs). Additionally, both LET and HET possess high-resolution timing capabilities, making them valuable tools for identifying pulsars and millisecond pulsars (Alford et al., 2023; Jaodand et al., 2023). During the 2030s, *HEX-P* is poised to make unique contributions to multi-messenger astrophysics of the GC, Bulge and Plane, in synergy with existing and upcoming telescopes across various wavelengths. These include the CTAO for TeV gamma-ray observations, the IceCube gen2 neutrino experiment, radio telescopes such as EHT (Event Horizon telescope), SKA (Square Kilometer Array) and next-generation VLA, as well as infrared telescopes like JWST and GRAVITY.

The paper is organized as follows. §2 describes the current design of the *HEX-P* telescope and simulation tools. §3 briefly introduces key science cases in the primary GC observation program. More detailed descriptions can be found about Sgr A* flares (§4), X-ray source populations in the GC and Bulge (§5 and diffuse X-ray sources in the GC (§6). §7.1 and §7.2 demonstrate some examples for potential *HEX-P* GO program observations of star-forming regions and CVs. §8 concludes the paper. Additional figures and tables, including a table defining all acronyms used in this paper, can be found in the Supplementary Material.

2 *HEX-P* mission design and simulation

The *High Energy X-ray Probe* (*HEX-P*; Madsen et al., 2023) is a probe-class mission concept that offers sensitive broad-band X-ray coverage (0.2–80 keV) with exceptional spectral, timing and angular capabilities. It features two high-energy telescopes (HETs) that focus hard X-rays and one low-energy telescope (LET) that focuses lower-energy X-rays.

The LET consists of a segmented mirror assembly coated with Ir on monocrystalline silicon that achieves an angular resolution of 3.5″, and a low-energy DEPFET detector, of the same type as the Wide Field Imager (WFI; Meidinger et al., 2020) onboard *Athena* (Nandra et al., 2013). It has 512 × 512 pixels that cover a field of view of 11.3′ × 11.3′. The LET has an effective passband of 0.2–25 keV, and a full frame readout time of 2 ms, which can be operated in a 128 and 64 channel window mode for higher count rates to mitigate pile-up with faster readout. Pile-up effects remain below an acceptable limit of ~ 1% for fluxes up to ~ 100 mCrab in the smallest window configuration. Excising the core of the PSF, a common practice in X-ray astronomy, will allow for observations of brighter sources, with a typical loss of up to ~ 60% of the total photon counts.

The HET consists of two co-aligned telescopes and detector modules. The optics are made of Ni-electroformed full shell mirror substrates, leveraging the heritage of *XMM-Newton*, and coated with Pt/C and W/Si multilayers for an effective passband of 2–80 keV. The high-energy detectors are of the same type as those flown on *NuSTAR*, and they consist of 16 CZT sensors per focal plane, tiled 4 × 4, for a total of 128 × 128 pixel spanning a field of view of 13.4′ × 13.4′. The HET utilizes the same optics technology as *XMM-Newton* and the PSF is energy-dependent with an HPD of 10″ at 3 keV, ~17″ at 20 keV, and increases at higher energies. For the purpose of simulations in this paper, an average HPD of 17″ was used across the entire bandpass.

All simulations presented here were produced with a set of response files that represent the observatory performance based on current best estimates (see Madsen et al., 2023). The effective area is derived from a ray-trace of the mirror design including obscuration by all known structures. The detector responses are based on simulations performed by the respective hardware groups, with an optical blocking filter for the LET and a Be window and thermal insulation for the HET. The LET background was derived from a GEANT4 simulation (Eraerds et al., 2021) of the WFI instrument, and the one for the HET from a GEANT4 simulation of the *NuSTAR* instrument, both positioned at L1. Throughout the paper, we present our simulation results for *HEX-P* using the SIXTE (Dauser et al., 2019) and XSPEC toolkits (version 12.13.0 (Arnaud, 1996)). To ensure the most realistic simulation results, we incorporated recent high-resolution X-ray images (mostly from *Chandra* or other wavelength observations), the best-known spectral information, and theoretical model predictions. Various exposure times have been considered for the feasibility studies presented in the following sections.

3 *HEX-P*'s Galactic center observation program

Throughout the paper, we present how *HEX-P* will have a high impact on exploring and understanding a variety of high-energy sources in the GC. With its versatile and well-balanced capabilities, including 1) large effective area in 0.2–80 keV, 2) high energy resolution for resolving atomic lines, 3) low background levels, 4) <3.5″ (LET) and <20″ (HET) angular resolutions, and 5) <2 ms timing resolution, *HEX-P* is an ideal X-ray probe mission for investigating a diverse class of X-ray point and diffuse sources. We have outlined the targets for *HEX-P*'s primary science program in Table 1 and briefly described them below. Figure 1 displays the survey regions covered by the primary science program, along with *Chandra* X-ray and MeerKAT radio images of the GC region.

1) Broad-band X-ray investigation of Sgr A* X-ray flares (§4): *HEX-P* observations of Sgr A* X-ray flares will play a unique and impactful role in the multi-messenger astrophysics of studying how the supermassive BH accelerates particles and emit flares in various ways. *HEX-P* will fully characterize the spectral and timing properties of bright flares thanks to the broadband and continuous coverage without earth occultation. In the 2030s, *HEX-P* in synergy with other telescopes in the radio (EHT), IR (GRAVITY) and TeV (CTA) bands will provide a wealth of multi-wavelength SED and lightcurve data on Sgr A* flares. These legacy data sets will make a significant impact on understanding the particle acceleration and emission mechanisms of Sgr A* flares.

2) Revealing X-ray point source populations in the GC (§5.1, 5.2, 5.3): The broadband X-ray spectral and timing capabilities of *HEX-P* will provide a variety of useful diagnostic tools for identifying X-ray point sources and transients in the GC, Bulge, and beyond. These diagnostic tools encompass Fe line analysis, broad-band X-ray spectroscopy, pulsation detection, and X-ray variability study. In the primary science program, *HEX-P* is expected to detect ~1,000

TABLE 1 *HEX-P*'s primary observation program of the Galactic Center region.

Target name	Exposure time (ks)	Science objectives
Sgr A* and the central 10 pc	500	Sgr A* flares, NSC and filaments
Sgr A complex	300 (with 4 tiles)	Molecular clouds, filaments, star clusters, point sources
Sgr B2	100	Molecular clouds and point sources
Sgr C	100	Molecular clouds and point sources
Limiting Window	300	Point sources
1° × 0.7° survey	850 (17 tiles × 50 ks)	Point sources
SNR G1.9 + 0.3	100	Youngest SNR in our Galaxy
PWN G0.9 + 0.1	50	One of the brightest TeV sources

Note: 2.3 Ms total exposure is currently allocated to the *HEX-P*'s primary science observations of the GC regions as listed above.

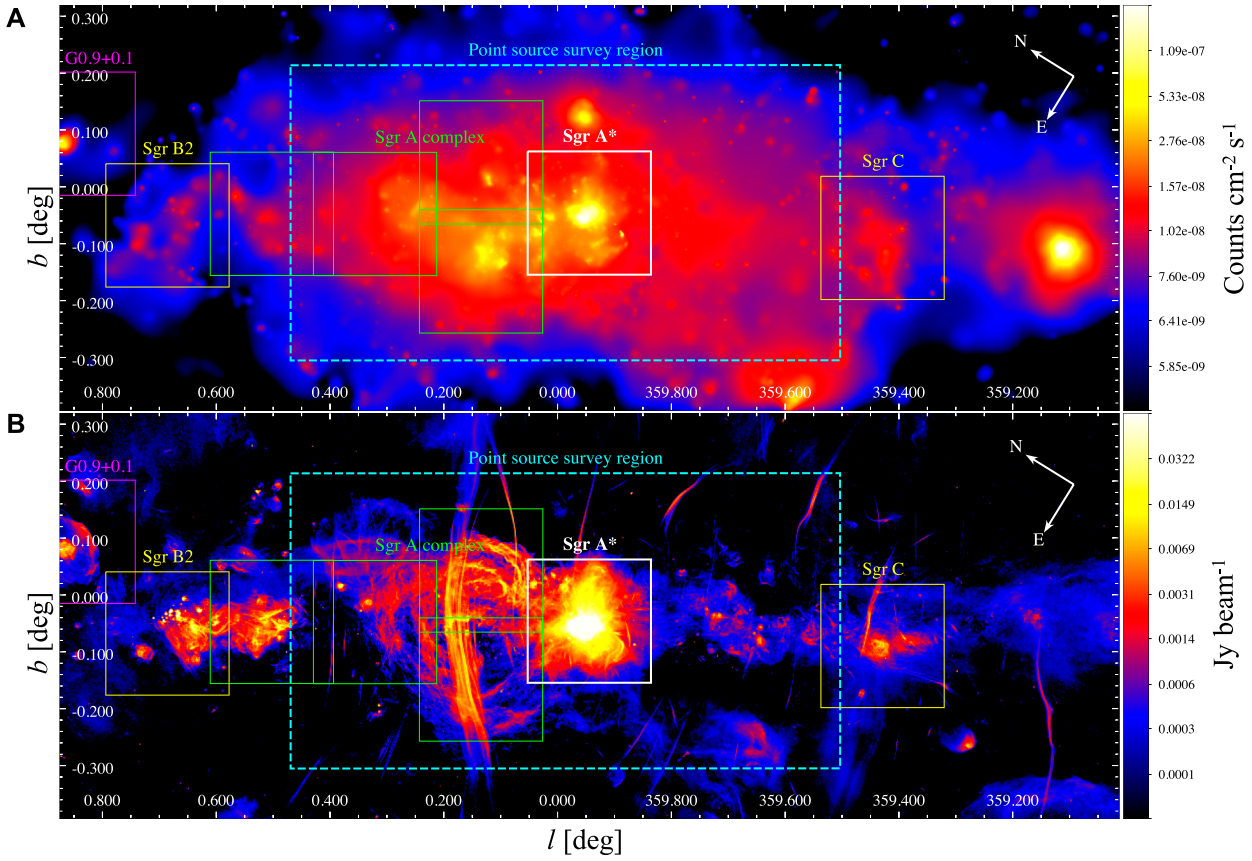

FIGURE 1
The GC regions surveyed by the *HEX-P* primary observation program, overlaid with *Chandra* X-ray **(A)** and MeerKAT radio images **(B)**. SNR G1.9 + 0.3 and the LW are located outside the images above. *Chandra* image credit: Wang et al. (2002); Muno et al. (2009). MeerKAT image credit: Heywood et al. (2022).

X-ray sources above 8 keV and identify/classify them with existing or future IR and X-ray observation data. In particular, *HEX-P* will probe the X-ray luminosity range of $L_X \sim 10^{32}$–10^{33} erg s^{-1}, poorly explored by *NuSTAR* due to the limited sensitivity. This is the regime where a large number of the *Chandra* sources, mostly composed of compact object binaries, remain unclassified. As demonstrated by *NuSTAR*, *HEX-P* will obtain broadband X-ray spectral and timing data of X-ray transients, will be instrumental in detecting pulsations

(in the case of transient magnetars) and BH spins (in the case of BH transients) as well as characterizing X-ray properties of very faint X-ray transients (VFXTs).

3) Resolving the central 10 parsec region above 10 keV (§5.4): The nuclear star cluster (NSC), spanning over $r \lesssim 10$ pc around Sgr A*, contains an extremely high concentration of stars and X-ray sources where the central hard X-ray emission (CHXE) was discovered by *NuSTAR*. *HEX-P* will be able to resolve the CHXE in the 20–40 keV band with better spatial resolution than *NuSTAR*, and determine whether the core of the CHXE is cuspy or not. This refined hard X-ray view of the NSC/CHXE will enable testing theoretical models on the formation of X-ray binaries through interactions with Sgr A* BH and other stars. Moreover, *HEX-P* will obtain the most pristine images of non-thermal X-ray sources in the vicinity of Sgr A* over 40 keV, including the central PWN, X-ray filaments, and unidentified hard X-ray sources.

4) Probing the composition of the Galactic Ridge X-ray emission (§5.5): The Limiting Window, known as one of the low extinction regions where *Chandra* resolved Fe line emission to a few hundred X-ray point sources, holds the key to unravel the composition of the Galactic Ridge X-ray emission (GRXE). Due to the narrow-band *Chandra* observations below 8 keV, their true plasma temperatures, possibly varying between different X-ray luminosities (which may reflect different types of CVs in the LW), remain unknown. *HEX-P* is expected to classify a majority of the *Chandra* sources by performing X-ray spectral analysis on bright sources individually and analyzing stacked spectral data. Consequently, we will be able to accurately measure the plasma temperatures of the X-ray sources across different X-ray luminosity ranges. Such measurements will lead to identifying which types of X-ray sources predominantly constitute the GRXE.

5) Surveying the central molecular zone (§6.1): Within the central molecular zone (CMZ), a handful of molecular clouds have exhibited X-ray emission. This emission consists of variable X-ray reflections of Sgr A* outbursts in the past and/or steady X-ray emission originating from cosmic-ray interactions with the clouds. In the primary observation program, *HEX-P* will conduct a survey of the Sgr A complex, Sgr B1, B2 and C, aiming to map their neutral Fe fluorescent line emission and X-ray continuum emission. The initial survey data will play a pivotal role in guiding subsequent *HEX-P* observations, dissecting the X-ray emission mechanisms, and gaining valuable insights into the past activities of Sgr A* and cosmic-ray distributions around the clouds.

6) Investigating energetic particle accelerators and mapping cosmic-ray distributions (§6.2 and Renolds et al. 2023): As an integral part of the major observation program aimed at exploring Galactic particle accelerators, *HEX-P* will observe prominent cosmic-ray acceleration sites, including the youngest SNR in our Galaxy (G1.9 + 0.3), the most luminous TeV sources (e.g., PWN G0.9 + 0.1), and star clusters (e.g., Arches) in synergy with future CTAO TeV observatory (Reynolds et al., 2023; Mori et al., 2021). Furthermore, *HEX-P* will characterize the synchrotron radiation emitted by X-ray filaments in conjunction with high-resolution radio data. Through broadband X-ray spectral data of these filaments, we will create a detailed map of the distribution of TeV–PeV electrons in the GC. Ultimately, *HEX-P* will explore how and where the relativistic cosmic rays are accelerated and then propagate through the GC region.

4 Sgr A* flares

Sgr A* is the radiative counterpart of the supermassive BH at the center of the Milky Way. Sgr A* has been proposed as one of the energetic particle accelerators powered by accretion flow among other PeVatrons candidates in the GC, such as PWNe and star clusters (HESS Collaboration et al., 2016). However, the quiescent emission from Sgr A* remains so faint with $L_{Bol} \sim 10^{36}$ erg s^{-1} and $L_X \sim 2 \times 10^{33}$ erg s^{-1}, that it casts doubts about its role as a persistent particle accelerator (Genzel et al., 2010). On the other hand, Sgr A* emits flares frequently, during which its X-ray luminosity can increase by up to two orders of magnitude (Baganoff et al., 2001; Neilsen et al., 2013; Barrière et al., 2014; Ponti et al., 2015a; Haggard et al., 2019). Similarly, IR flares have been observed daily (Genzel et al., 2003; Ghez et al., 2004). Interestingly, whenever an X-ray flare is observed, an IR counterpart is present, whereas the opposite is not always true. These flares are considered to originate from synchrotron or synchrotron self-Compton scattering radiation emitted from accelerated electrons to high Lorentz factors ($\gamma_e \sim 10^{5-6}$ in the synchrotron case). Typically, X-ray flares last for a few thousand seconds before they decay via radiative cooling or particle escaping. While simultaneous, multi-wavelength observations of Sgr A* flares in the IR and X-ray band are important, *HEX-P* will uniquely explore the particle acceleration and emission mechanisms of the highest energy electrons produced by the supermassive BH at Sgr A*.

Previous *Chandra* observations of Sgr A* flares suggest an average rate of 1-2 flares per day (Nowak et al., 2012; Neilsen et al., 2013). With fainter X-ray flares occurring more frequently, the expected number of detectable flares depends on the telescope's sensitivity. For instance, Ponti et al. (2015a) detected 11 flares with *XMM-Newton* in 1.6 Ms until 2014, yielding a lower rate of 0.6 flares per day. Note that *HEX-P* will be more sensitive to detecting fainter X-ray flares than *XMM-Newton*. It was reported that, since 2014, bright X-ray flares with 2–10 keV fluence above $\sim 1.7 \times 10^{-8}$ erg cm^{-2} have seemed to occur more frequently, at a rate of 0.8 flares per day (Mossoux et al., 2020). Assuming these flare detection rates, 3.5–5 flares will be detected by *HEX-P* during the 500 ks exposure allocated to *HEX-P* observations of Sgr A* in the primary science program. We anticipate more *HEX-P* observations of Sgr A* will be carried out through subsequent GO or PI-led GTO programs, jointly with other telescopes. Presently, *NuSTAR*, *XMM-Newton* and *Chandra* observe Sgr A* each year, in conjunction with EHT and GRAVITY, with a total exposure of $\gtrsim 500$ ks. Assuming that similar multi-wavelength observation campaigns will be undertaken in the 2030s, it is projected that *HEX-P* will detect 18–25 X-ray flares during the first 5 years of operation. The orbit of *HEX-P* at L1 enables uninterrupted coverage of Sgr A*. This is a tremendous advantage for characterizing the flare lightcurve profiles, whereas previous *NuSTAR* observations were hampered as parts of the flares were missed due to earth occultation.

The primary objective of investigating synchrotron X-ray emission during Sgr A* flares is to determine their photon indices and potential spectral cutoffs. X-ray photon indices are directly linked to the intrinsic energy distributions of electrons, while X-ray spectral cutoffs reflect the maximum energy at which electrons are accelerated or a synchrotron cooling break. These X-ray spectral

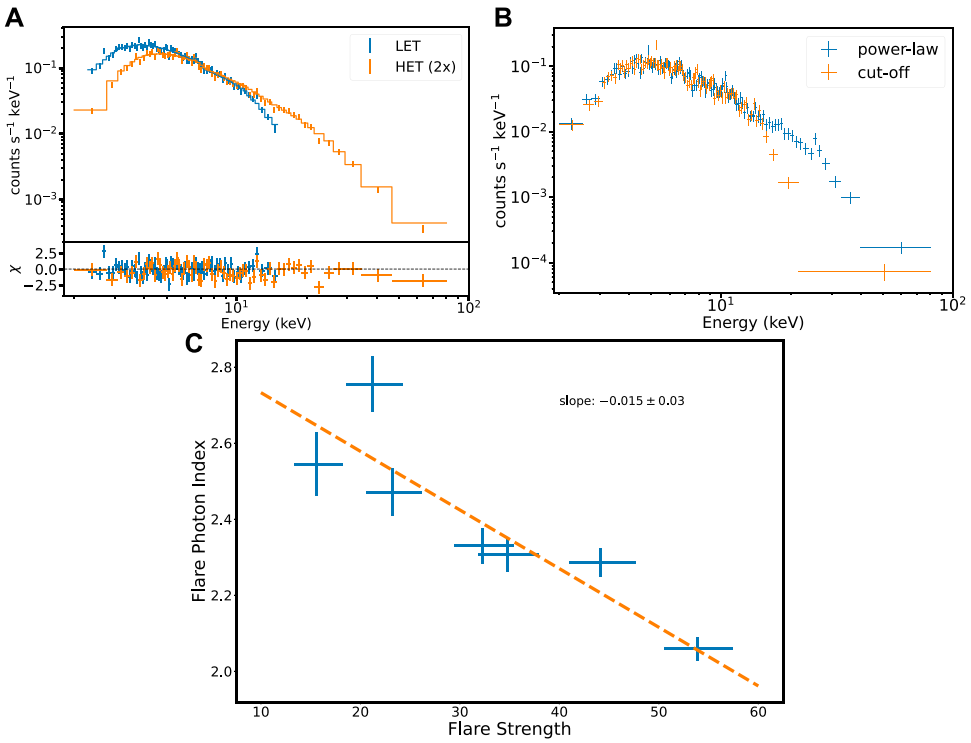

FIGURE 2
(A) Simulated *HEX-P* spectra of a bright flare. The flare has a mean luminosity of 54 times the quiescent level in 2–10 keV and lasts for 5,900 s. **(B)** Simulated HET spectra of a bright Sgr A* flare, with a cutoff at 15 keV (orange) and without it (blue). In both cases above, we adopted the astrophysical background spectra from *XMM-Newton* observations of Sgr A* in the 2–10 keV band, and extrapolated them up to 80 keV. **(C)** A scattered plot of the X-ray photon indices and flare strengths measured by *HEX-P*, assuming a similar ensemble of X-ray flares as that studied in Zhang et al. (2017). The flare strength is defined as the mean luminosity of a flare divided by the quiescent luminosity in the 2–10 keV band.

characteristics are likely to vary between different flares, such as faint vs. bright or short vs. long flares, and *HEX-P* is the most suitable for these measurements due to its broader energy coverage (compared to *Chandra* and *XMM-Newton*) and higher sensitivity (compared to *NuSTAR*). For example, Figure 2 shows simulated *HEX-P* spectra of a bright X-ray flare from Sgr A* assuming different spectral shapes. These simulation results represent a significant advance as *HEX-P* will be able to detect spectral cutoffs from Sgr A* flares, which was not achievable by *NuSTAR* due to the limited sensitivity. Overall, *HEX-P* will provide much greater insight into the particle acceleration mechanism near the event horizon.

Furthermore, *HEX-P* will eventually collect a large sample of X-ray flares from Sgr A* revealing their statistical properties. Based on seven bright flares observed with *NuSTAR* in ≃ 1 Ms, Zhang et al. (2017) reported a potential but unconfirmed correlation between the photon index and flux data. Figure 2C presents a scattered plot of the photon indices and the flare strengths measured by *HEX-P*, assuming the same flux distribution observed with *NuSTAR* and that the potential correlation reported in Zhang et al. (2017) exists. With about five-seven bright flares, *HEX-P* will be able to establish the correlation at $\gtrsim 3\sigma$, and more significantly from a larger number of flares detectable by *HEX-P* in the first few years.

4.1 Synergy with radio, IR, and TeV gamma-ray telescopes

Simultaneous X-ray and IR observations have proven to provide a more in-depth investigation of the particle acceleration and cooling mechanisms of Sgr A*, as recently realized by a few such successful observations. For instance, EHT directly images the SMBH and its environment in the sub-millimeter band, potentially capturing hot spots swirling around the event horizon following X-ray flares (Wielgus et al., 2022). In the IR band, GRAVITY has pinpointed Sgr A* and detected flares with its exceptional sensitivity of the adaptive optics. Since the X-ray and IR emission represent different components of the entire synchrotron radiation emitted from Sgr A* flares, multi-wavelength SED data will enable not only distinguishing between various emission models but also determining the magnetic field strengths through cooling breaks between the IR and X-ray bands (Dodds-Eden et al., 2009; Ponti et al., 2017).

Previous IR and sub-millimeter observations have revealed that flares originate from an area that extends over one gravitational radius, and they orbit around ~5 Schwarzschild radii from the SMBH at a non-Keplerian speed (GRAVITY Collaboration et al., 2018; GRAVITY Collaboration et al., 2020). However, these observations are less sensitive in determining the acceleration

mechanism since the electron cooling times in these bands are orders of magnitude longer than those for X-ray-emitting electrons. Therefore, only X-ray observations can be used to identify the central engine of accelerating particles to the highest energies and whether it is powered by magnetic reconnection, shock acceleration, etc. As mentioned earlier, by studying bright flares through *HEX-P* with simultaneous IR observations, we can directly measure the energy distribution and maximum energy of the accelerated electrons ($\gamma \sim 10^4$–10^6 for synchrotron, combined with the magnetic field strength determined by IR and X-ray SED data). Tracking the evolution of the electron spectra during a very bright flare may be feasible as *HEX-P* will yield ample photon statistics of X-ray flares with continuous coverage. Sensitive X-ray observations with *HEX-P* can also reveal the formation and evolution of the acceleration source on a timescale comparable with the light crossing time, which is of the order of the Schwarzschild radius. These are unique opportunities that can be pursued by *HEX-P* but are not feasible with the limited bandpass of *Chandra* and *XMM-Newton*.

Recent *NuSTAR* observations suggested somehow softer photon indices of Sgr A* flares compared with those measured by *XMM-Newton* and *Chandra*. This could indicate the presence of a high energy cut-off above 10 keV (GRAVITY Collaboration et al., 2021) or an artifact caused by the high background level in *NuSTAR* data. In contrast, *HEX-P* observations of Sgr A* flares over a broader X-ray band and with significantly reduced background contamination provide more direct insights into how particles are accelerated at a few Schwarzschild radii from the SMBH and will help to constrain the acceleration models and their physical parameters. If Sgr A* is indeed accelerating electrons to high Lorentz factors above $\gamma_e \sim 10^6$, which will be evident from detecting hard X-rays with *HEX-P*, these electrons will also emit TeV gamma-rays through the inverse Compton scattering process. Thus, hard X-ray detections by *HEX-P* will motivate simultaneous TeV observations with the upcoming CTAO mission and ultimately determine whether the supermassive BH at Sgr A* is a PeVatron accelerator at the present time.

5 X-ray source population in the GC and bulge

Extensive *Chandra* surveys have detected over 10,000 X-ray sources in the $2° \times 0.8°$ GC field (Wang et al., 2002; Muno et al., 2009; Zhu et al., 2018). Even excluding foreground sources, which constitute about 25% of the total, these *Chandra* sources represent the densest X-ray source population in our Galaxy. This is illustrated in Figure 3, which shows the *Chandra* X-ray flux distributions in different regions of the GC and Bulge. In the GC and bulge regions, where optical, UV, and soft X-ray ($E \lesssim 2$ keV) observations are hindered due to significant extinction and dust scattering, the hard X-ray band provides a singular opportunity to explore the populations of compact objects and their binaries. Thus far, multi-decade X-ray observations of the GC, Bulge, and Ridge have revealed that 1) the X-ray point sources are predominantly mCVs, with a modest fraction of XRBs (Xu et al., 2019a); 2) a small population of non-thermal X-ray sources exist, and they are likely LMXBs or runaway pulsars (Hailey et al., 2018); 3) ~20 X-ray transients have been detected, a majority of them in the central few pc (Mori et al., 2021); 4) diffuse hard X-ray emission is largely composed of unresolved CVs (Hailey et al., 2016). As described briefly below, these results indicate distinct spatial distributions and compositions of X-ray sources in the GC and Bulge. Identifying these X-ray sources and the underlying X-ray populations is important for testing the fundamental theories and recent N-body simulation results of XRB/CV formation in the vicinity of Sgr A*, the NSC and beyond (Generozov et al., 2018; Szölgyén and Kocsis, 2018; Panamarev et al., 2019), with implications ranging from the rates of gravitational wave events to the nature of dark matter.

1) Magnetic CV population in the GC and Bulge: Stacked X-ray spectra of the *Chandra* sources were well fit with an optically thin thermal plasma model with $kT \gtrsim 8$ keV, indicating that they are predominantly mCVs (Hong et al., 2016). MCVs possess WD magnetic fields strong enough to truncate or quench accretion disks, and they are generally classified into two classes: intermediate polars (IPs) and polars. An IP is a type of mCV that has non-synchronized orbits and WD magnetic fields ($B \sim 0.1$–10 MG) strong enough to truncate the inner accretion disk; they are copious emitters of hard X-rays ($kT \sim 20$–40 keV). On the other hand, polars are magnetically synchronized mCVs with higher B-field strength (typically $B \sim 10$–240 MG) and thus possess softer X-ray spectra ($kT \sim 10$–20 keV) than IPs due to faster cyclotron cooling. By contrast, non-magnetic CVs (nmCVs) have lower B-fields ($B \lesssim 0.1$ MG), and their accretion disks extend to the WD surface. NmCVs exhibit softer and fainter X-ray emission ($kT \lesssim 10$ keV) than those of mCVs (Byckling et al., 2010). Since only a few % of the *Chandra* sources in the GC have been detected by *NuSTAR* above 10 keV (Hong et al., 2016), their source types remain elusive. To distinguish between nmCVs, IPs, and polars, it is important to characterize both broad-band X-ray continuum and Fe emission lines at 6–7 keV (Mukai, 2017; Xu et al., 2019b).

2) X-ray binaries and pulsars: A fraction of the *Chandra* sources are characterized by non-thermal X-ray spectra with no or weak Fe lines. These non-thermal X-ray sources are likely quiescent LMXBs (containing NSs or BHs) or pulsars (Mori et al., 2021). Subsequently, multi-decade X-ray observations of the Sgr A* region with *Chandra*, *XMM-Newton*, *Swift* and *NuSTAR* revealed a cusp of LMXBs in the central pc (Hailey et al., 2018; Mori et al., 2021). Finding a concentration of pulsars in the Galactic Bulge will have significant implications for the origin of the GeV gamma-ray excess emission detected by *Fermi*-LAT (Dexter and O'Leary, 2014).

3) X-ray transients: Daily *Swift*/XRT monitoring since 2006, combined with other frequent X-ray observations of the GC, resulted in the detection of 20 X-ray transients in the central ~50 pc (Muno et al., 2005; Degenaar et al., 2015). Six of the GC transients were identified as NS-LMXBs through the detection of type I X-ray bursts or pulsations (Degenaar et al., 2012), while *NuSTAR* observations identified two recent *Swift* transients as outbursting BH-LMXBs (Mori et al., 2019). Otherwise, ~10 VFXTs have been detected with peak luminosities of $L_X \sim 10^{34}$–10^{36} erg s^{-1} (Degenaar et al., 2015) but their identity remains elusive despite extensive investigations by *Swift*-XRT (Degenaar et al., 2015).

4) Diffuse hard X-ray emission: In the Bulge, Ridge and central 10 pc regions, diffuse hard X-ray emission with different plasma temperatures ranging from $kT \sim 8$ to 35 keV have been detected by *Suzaku*, *INTEGRAL*/IBIS and *NuSTAR* (Türler et al., 2010; Yuasa et al., 2012; Perez et al., 2019; 2015). This diffuse X-ray

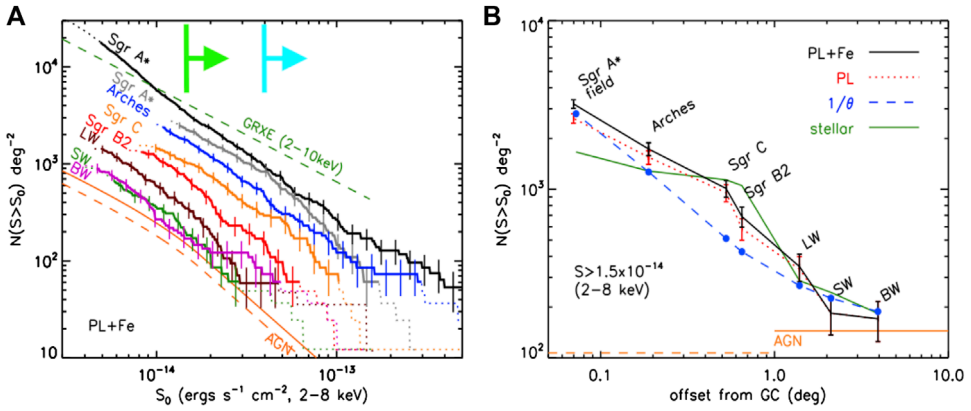

FIGURE 3
LogN-logS **(A)** and radial **(B)** distributions of *Chandra* X-ray sources in the GC. The plots are excerpted and modified from Hong et al. (2016). The 2–10 keV flux limits are indicated by the vertical cyan and green lines with arrows for source identification by individual X-ray spectral analysis (1) and classification by hardness ratio analysis described (2), respectively. Note that we assumed 100 ks exposure per source, and these conditions for source identification and classification do not apply to crowded fields such as the Arches cluster and the central 10 pc region where the source density is much higher **(A)**. These X-ray flux limits correspond to $L_X = 3 \times 10^{32}$ and 1×10^{32} erg s^{-1} at the GC distance (8 kpc), respectively.

emission is believed to originate from unresolved populations of X-ray point sources. Only a few low-extinction regions in the bulge and ridge, such as the Limiting Window (LW), have been observed by *Chandra* and resolved into hundreds of X-ray point sources, most of which remain unidentified due to the lack of hard X-ray observations.

As we present below, *HEX-P* will greatly enhance our understanding of X-ray source populations in the GC and Bulge, covering a wide range of X-ray luminosity (L_X). *HEX-P* will conduct deep observations of prominent regions such as the Sgr A complex, the Arches cluster, Sgr B2, Sgr C, and the LW. These investigations will fully utilize the broadband spectral and timing capabilities of *HEX-P* to reveal the X-ray source populations within those regions. Our primary focus will be on classifying X-ray source populations in the range of $L_X \sim 10^{32}$–10^{33} erg s^{-1} at the GC distance (8 kpc), and examining how they vary with L_X and distance from the GC. This unexplored parameter space of X-ray sources holds considerable interest, as we expect to unveil a number of mCVs, XRBs, and pulsars that have not yet been discovered in the GC. In contrast, a significant portion of fainter X-ray sources is likely background AGNs and coronally active dwarfs (Ebisawa et al., 2005; DeWitt et al., 2010; Morihana et al., 2022), which are unrelated to the compact object populations in the GC and Bulge.

5.1 X-ray source population

The *NuSTAR* GC survey covered ~2/3 of the central 2° × 0.8° region, resulting in detecting a total of 77 hard X-ray sources above 10 keV (Hong et al., 2016). These sources exhibit either thermal X-ray spectra with $kT > 20$ keV or non-thermal X-ray spectra with $\Gamma = 1.5$–2, indicating that they are mCVs or XRBs, respectively (Hong et al., 2016). The *NuSTAR* data analysis of the GC sources has been largely limited below ~20 keV due to high stray-light background levels (Mori et al., 2015). Consequently, despite extensive studies combining *NuSTAR* observations with archived *Chandra* and *XMM-Newton* data, the majority of *individual NuSTAR* sources remain unidentified because their existing X-ray spectra do not allow us to distinguish between thermal (mCVs) or non-thermal sources (XRBs), and lack accurate measurements of plasma temperatures or photon indices. Furthermore, ~1/3 of the 2° × 0.8° GC region, as well as the LW, were not surveyed by *NuSTAR* due to substantial background contamination. In addition to identifying the known hard X-ray sources detected by *NuSTAR*, *HEX-P* will survey the unexplored regions, allowing us to detect new hard X-ray sources and determine their source types.

The goals and capabilities of *HEX-P* in classifying and identifying X-ray sources in the GC are specified in Supplementary Table S2 in the Supplementary Material section and in the numbered paragraphs below. The primary GC survey program involves surveying the central 1° × 0.7° region with multiple tiled observations with a typical exposure time of ~100 ks per field. Each tile will have a 50 ks exposure, likely divided into multiple, shorter exposures for obtaining X-ray variability data. These tiles will overlap with each other to achieve ~100 ks exposure at a given location in the survey area. Additionally, *HEX-P* plans to conduct deeper observations of Sgr A*, Sgr A, and the LW (Table 1).

We conducted extensive simulations based on existing data to demonstrate the remarkable capabilities of our proposed surveys. In order to determine the detectability of X-ray sources with *HEX-P*, we adopted the X-ray flux data of 6,760 *Chandra* sources from Muno et al. (2009), excluding foreground sources. We assumed that these sources have $kT = 15$–30 keV, which are typical plasma temperatures for mCVs. Assuming a 100 ks exposure per field and $kT = 15$ keV, HET will be able to detect >600 sources at >4σ significance; with a temperature of $kT = 30$ keV, that number rises to ~1000 sources within the 2° × 0.8° GC field (Figure 4). HET will be able to extract X-ray photometry data cleanly from these sources since they are separated from each other by at least 8.5″ (half the HET HPD), allowing us to obtain broadband logN-logS distribution, hardness ratio, and variability data in the 2–40 keV band. This is a significant improvement compared to the 77 hard

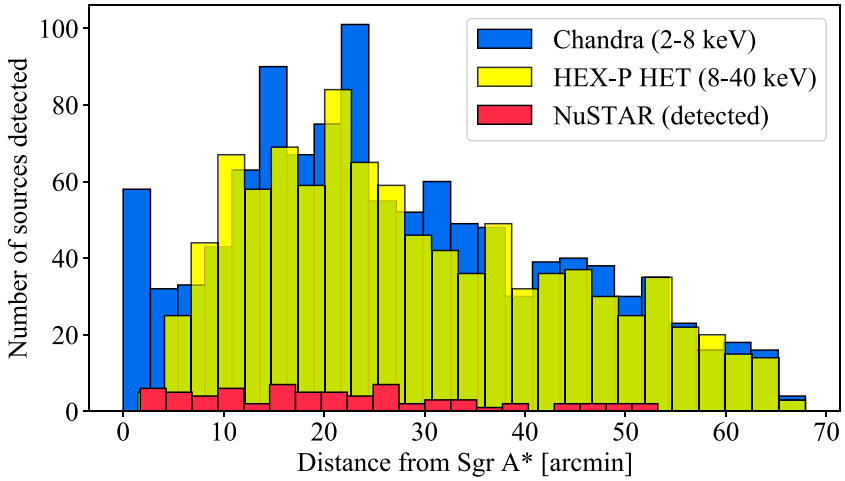

FIGURE 4
The radial distributions of point sources that will be detectable by *HEX-P* HET in the 8–40 keV band above the 4σ level (yellow). The distribution only includes non-foreground sources for which the "nearest neighbor" is at least 8.5″ away, corresponding to half of HET's HPD (Pfeifle et al., 2023). For comparison, the blue histogram shows the point sources detected by *Chandra* with >4σ significance. By contrast, *NuSTAR* was only able to detect 70 sources (red) within the same region.

TABLE 2 X-ray source classification.

Source type	L_X[a] [erg s^{-1}]	Fe lines[b]	X-ray continuum	Variability	IR detection[c]
LMXB	10^{31}–10^{33}	Weak	Thermal + Power-law[e]	Yes	Yes (MS donor)
HMXB	$\gtrsim 10^{33}$	Strong	Thermal + Power-law	Yes	Yes (O/B donor)
UCXB	$\lesssim 10^{33}$	Weak	Thermal ($kT_{BB} \sim 0.1$–2 keV)	Yes	No (H-poor donor)
Pulsar	10^{32}–10^{34}	No	Power-law ($\Gamma \sim 1.3$–1.5)	No	No
IP	10^{32}–10^{34}	Strong	Thermal ($kT \sim 15$–40 keV)	Low	Yes (MS donor)
Polar	10^{31}–10^{33}	Strong	Thermal ($kT \sim 5$–15 keV)	High	Yes (MS donor)
Non-magnetic CV	$\lesssim 10^{31}$	Strong	Thermal ($kT \lesssim 8$ keV)	Low	Yes (MS donor)
AM CVn	$\lesssim 10^{33}$	Weak	Thermal ($kT \lesssim 1$ keV)	Yes	No (H-poor donor)
BH/NS transient	10^{36}–10^{38}	Strong	Thermal + Power-law	Yes	Yes (MS donor)
VFXT[d]	10^{34}–10^{36}	Weak	Thermal + Power-law	Yes	Yes (if MS donor)

[a]Unless otherwise noted, these values refer to typical quiescent luminosities.
[b]Strong and weak Fe lines refer to the combined equivalent width of neutral, He-like and H-like lines at 6.4, 6.7 and 7.0 keV above ~300 eV and below ~100 eV, respectively.
[c]This refers to the detection of IR counterparts at Galactic center distances.
[d]VFXTs (very faint X-ray transients) could be outbursting UCXBs.
[e]Some LMXBs, particularly low-accretion neutron stars, exhibit primarily thermal emission; others, especially quiescent BH-LMXBs, are predominantly non-thermal.

X-ray sources detected by *NuSTAR*. As described below, *HEX-P* will be able to identify and classify ~1,000 X-ray sources in the GC using broadband X-ray spectral and timing data, combined with the archived *Chandra* and IR data. Table 2 (in Section 10) lists various types of X-ray sources that can be identified by extensive *HEX-P* observations in the GC and other regions in our Galaxy.

1) Identification of Chandra and IR counterparts: 18 out of the 77 *NuSTAR* sources do not have clear associations with *Chandra* sources because the limited angular resolution of *NuSTAR* (18″ FWHM) hinders their correlation with *Chandra* positions, as well as their IR counterparts. *HEX-P*'s angular resolution, superior to *NuSTAR*'s, will allow us to identify *Chandra* counterparts to hard X-ray sources with high confidence. Consequently, *Chandra*'s sub-arcsecond angular resolution will enable us to find the NIR counterparts to those X-ray sources and determine their nature using the combined X-ray and NIR spectral and temporal properties of those systems (Table 2). Accreting binaries are expected to

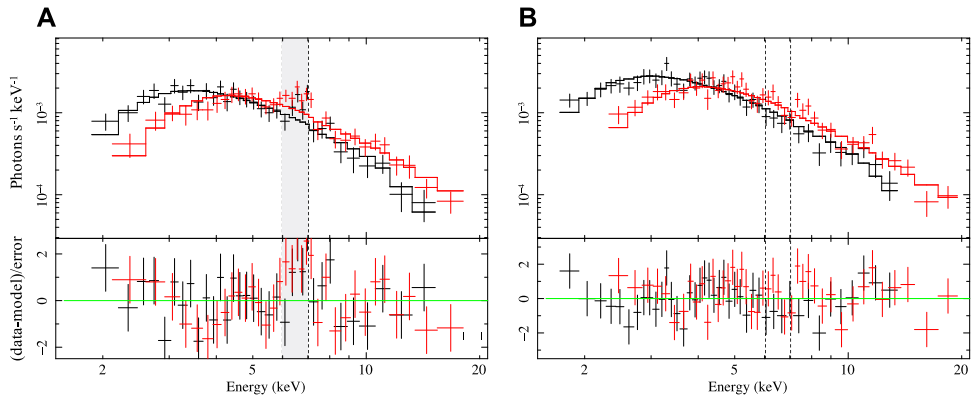

FIGURE 5
Simulated *HEX-P* LET (black) and HET (red) spectra of thermal **(A)** and non-thermal **(B)** X-ray sources in the GC, assuming 100 ks exposure. We fit an absorbed power-law model to both sources. The thermal source exhibits Fe line residuals at 6–7 keV (shaded area), which are detected with 5 – σ significance.

display ellipsoidal modulations in their NIR light curves, which result from the distortion of Roche-lobe-filling donor stars due to the tidal forces exerted by the compact object. Currently ongoing—and upcoming—JWST surveys will be able to detect such periodic variability even from low-mass companions, thanks to their unprecedented depth (Schoedel et al., 2023). Combining deep NIR and X-ray data will open a new window into the nature and evolution of accreting compact objects. Furthermore, unambiguous *Chandra* counterpart identification will enable joint X-ray spectral and variability analysis with archived *Chandra* and *XMM-Newton* data, allowing us to understand the temporal properties of those sources over a timescale of decades.

2) X-ray spectral analysis: Hard X-ray detections above 10 keV suggest the *NuSTAR* sources could be either mCVs or XRBs (Hong et al., 2016). To accurately identify these sources, Fe line diagnostics are crucial. Typically, mCVs exhibit thermal X-ray spectra with strong Fe emission lines at 6–7 keV (Xu et al., 2016), while quiescent XRBs show non-thermal X-ray spectra with weak or no Fe lines. However, the majority of the *NuSTAR* sources lack clear Fe line determinations because their *NuSTAR* spectra are largely contaminated by diffuse X-ray emission, which also exhibits strong Fe lines. With both the LET and HET covering the 6–7 keV band, *HEX-P* will greatly improve Fe line diagnostics thanks to its superior angular resolution and significantly reduced background levels compared to *NuSTAR*. Figure 5 (top) illustrates how *HEX-P* can discern between thermal and non-thermal X-ray models by resolving the Fe line complex region at 6–7 keV. For faint X-ray sources that lack sufficient source counts for individual spectral analysis, *HEX-P* will be highly effective in classifying source types via hardness ratios and stacked X-ray spectra. Given its broad energy band, *HEX-P* is less susceptible to X-ray absorption below a few keV, which can cause parameter degeneracy with intrinsic spectral parameters like kT and Γ. Unlike the limited bandpass of *Chandra* and *XMM-Newton* data, *HEX-P* can investigate the broad-band hardness or quantile ratios, which are more intrinsic to source types and properties. For instance, one can define hardness ratios between 3–10 and 10–40 keV bands, which are nearly unaffected by X-ray absorption and dust scattering effects.

3) Detection of X-ray variability and periodic signals: Multi-epoch *HEX-P* observations of the GC regions can provide long-term X-ray variability data over the course of days and weeks. Year-scale X-ray variabilities can be investigated by combining *HEX-P* with archived X-ray data obtained by *NuSTAR*, *Chandra* and *XMM-Newton*over the past decades. These long-term X-ray variability data can be useful in identifying mCV types. For example: compared to IPs, polars often display significant flux variations (by more than an order of magnitude) in the optical and X-ray band due to higher variability in mass accretion rates. In the GC and bulge regions, optical observations are hindered by significant extinction and dust scattering, whereas IR emission of mCVs is usually dominated by companion stars. *Chandra* observations have shown promise in detecting orbital periods from a handful of mCVs in the LW (Hong et al., 2012; Bao and Li, 2020), which *HEX-P* could also achieve by using several sophisticated timing methods with only hundreds of source counts. Based on the simulation-based detection rate from Bao and Li (2020), in the case of a sinusoidal light curve, the detection completeness with significance over 99% by GL algorithm (Gregory and Loredo, 1992) was generally $\gtrsim$ 20% and 50% for source counts $\gtrsim$ 100 and 300, respectively. Moreover, at high amplitude variation ($F_{max}/F_{min} \gtrsim 4$), which is typical for polars, the detection completeness will be ~90%.

5.2 X-ray transients

The GC region hosts a dense population of XRBs and X-ray transients, as revealed by deep X-ray surveys and long-term monitoring over the last two decades (Muno et al., 2005; Degenaar and Wijnands, 2010; Hailey et al., 2018; Mori et al., 2021). In the crowded GC region, *HEX-P* is uniquely suited to make these requisite hard X-ray (>10 keV) observations due to its superior angular resolution. *HEX-P* will be sensitive in obtaining broad-band X-ray spectral and timing data of VFXTs,

which belong to a unique class of X-ray transients with peak luminosities of $L_X \sim 10^{34}$–10^{36} erg s^{-1}(Degenaar et al., 2015). Given its combination of broad energy band and fast readout time, *HEX-P* is ideal for characterizing bright X-ray transients through spectral and timing analysis without significant deadtime effects. Some distinct features often observed in BH and NS transients, such as thermal disk emission, Comptonization, and relativistic Fe lines, will be fully characterized in *HEX-P* broad-band X-ray spectral data. Fitting the broad-band *HEX-P* spectra with relativistic X-ray reflection models will yield the spin measurements of a BH transient within 100 pc of the GC as demonstrated by *NuSTAR* observations of two BH transients in 2016 (Mori et al., 2019). Given the high concentration of XRBs in the GC, a combination of frequent X-ray monitoring (e.g., *Star-X* or *Swift*-XRT) and *HEX-P* ToO observations will provide an efficient way to measure BH spins from new stellar-mass BH transients (Connors et al. submitted to FrASS). In addition, *HEX-P* has superb capabilities of detecting pulsations and QPO signals in a wide frequency range from mHz to kHz, thanks to the drastic reduction of background noise which results in an increase of fractional r.m.s. Variability (e.g., Bachetti et al., this volume; Alford et al., this volume).

5.3 Pulsars

In 2009, *Fermi*-LAT detected an excess of GeV gamma-ray emission extending over the central ~10° of the Milky Way Galaxy (Goodenough and Hooper, 2009). The nature of the GeV excess still remains one of the great puzzles in astrophysics, with often-conflicting studies that suggest either a dark matter origin or a large population of unresolved pulsars (Hooper and Linden, 2011; Brandt and Kocsis, 2015; Gautam et al., 2022). In addition, recent N-body simulations predict run-away NSs from the NSC due to their natal kicks or interactions with the supermassive BH and surrounding stars (Bortolas et al., 2017). However, despite extensive searches, no such population of pulsars or milli-second pulsars has ever been observed, resulting in the "missing pulsar problem". As demonstrated by the discovery of a transient magnetar in the vicinity of Sgr A* (Mori et al., 2013), finding even a few pulsars in the GC and bulge regions will have profound implications for the underlying NS population and test the hypothesis of NS ejection from the NSC (Dexter and O'Leary, 2014; Bortolas et al., 2017). However, it is extremely challenging to detect radio pulsars in the GC due to large dispersion measures until SKA becomes fully operational (Keane et al., 2015). With the sub-millisecond timing resolution, *HEX-P* is uniquely suited for finding pulsars in the X-ray band and complementary to future radio pulsar searches in the GC and Bulge.

There are a handful of pulsar candidates such as non-thermal, hard X-ray sources detected by *Chandra* and *NuSTAR*. For instance, a runaway NS called the "Cannonball", detected in the radio and X-ray bands (Zhao et al., 2013), exhibited non-thermal X-ray emission extending up to 30 keV (Nynka et al., 2013). Furthermore, two PWNe (G359.95-0.04 and G0.13-0.11) are associated with TeV sources (Mori et al., 2015; Zhang et al., 2020). While *Chandra* has resolved PWNe X-ray point sources within both PWNe, no pulsations have been detected yet. Since the search for radio pulsations is severely hampered by significant dispersion measures, X-ray telescopes equipped with high angular and timing resolution, such as *HEX-P*, would be an ideal pulsar finder in the GC and Bulge. Figure 6 illustrates the sensitivity of *HEX-P* in detecting a ~10 Hz pulsation from G359.95-0.04, located ~10″ away from Sgr A*. Higher or lower pulse frequencies would change this plot only slightly, due to a weak dependence of significance on the number of trials used in a blind search[1,2] Compared to *XMM-Newton* EPIC-PN and *NuSTAR*, *HEX-P* will be far more sensitive in detecting pulsars due to its <1 msec temporal resolution, high angular resolution, and hard X-ray coverage (> 10 keV), where pulsar emission is more dominant over the PWN and thermal diffuse X-ray emission. During the planned Sgr A* observations (500 ks total), both LET and HET will be able to detect a pulsation signal at >5σ level if the pulsed fraction is higher than ~10%. For other pulsar candidates, such as the Cannonball and G0.13-0.11, we anticipate that pulsations will be more easily detectable due to lower background rates from the surrounding regions. We also note that HEX-P, being in a Lagrangian point, will also guarantee much longer stretches of uninterrupted observations with little or no periods of occultation or flaring, which will improve stability for the study of slow variability and the detection of the slowest pulsars (e.g. RCW 103 with a 6.7-h pulsation (De Luca et al., 2006)).

5.4 Probing the distribution of compact object binaries in the nuclear star cluster

The central 10 pc region of our Galaxy contains a dense concentration of stars and compact objects around the SMBH at Sgr A*. Within the NSC, which boasts the densest stellar environment in our Galaxy, *Chandra* detected a few hundred X-ray point sources (Zhu et al., 2018). Above 20 keV, *NuSTAR* discovered diffuse hard X-ray emission spanning an area of approximately 8 pc × 4 pc, which coincides with the NSC (Perez et al., 2015). This emission, known as the central hard X-ray emission (CHXE), is predominantly attributed to an unresolved population of mCVs with a mean WD mass of $M_{\rm WD} \sim 0.9 M_\odot$ (Hailey et al., 2016). However, the core of the CHXE/NSC within the central few pc region could not be resolved by *NuSTAR* due to the limited angular resolution and presence of hard X-ray filaments.

The central ~3 pc region corresponds to the influence radius of Sgr A*, where the immense gravity of the SMBH affects the motion of stars and compact objects. Since NSCs in other galactic nuclei cannot be spatially resolved in the X-ray band due to Mpc distances, the NSC in the GC offers a unique opportunity to study its X-ray source compositions with *HEX-P*. The gravitational interactions between Sgr A* and surrounding stars significantly boost the rates of binary formation; evaporation is also significantly enhanced within $r \lesssim 3$ pc. As a result, this region should be largely inhabited by binaries with more massive compact objects, such as stellar-mass BHs, and with tighter orbits, as suggested by recent *Chandra* studies of the non-thermal X-ray sources detected in $r \lesssim 1$

1 The number of spectral bins, and so the number of trials, is proportional to the frequency and, for the FFT, to the observation length (because $\Delta\nu = 1/T$).

2 For example, a $Z_2^2 = 100$ is a 8.22σ detection with 10,000 trials, and a 7.65σ detection with 1,000,000 trials.

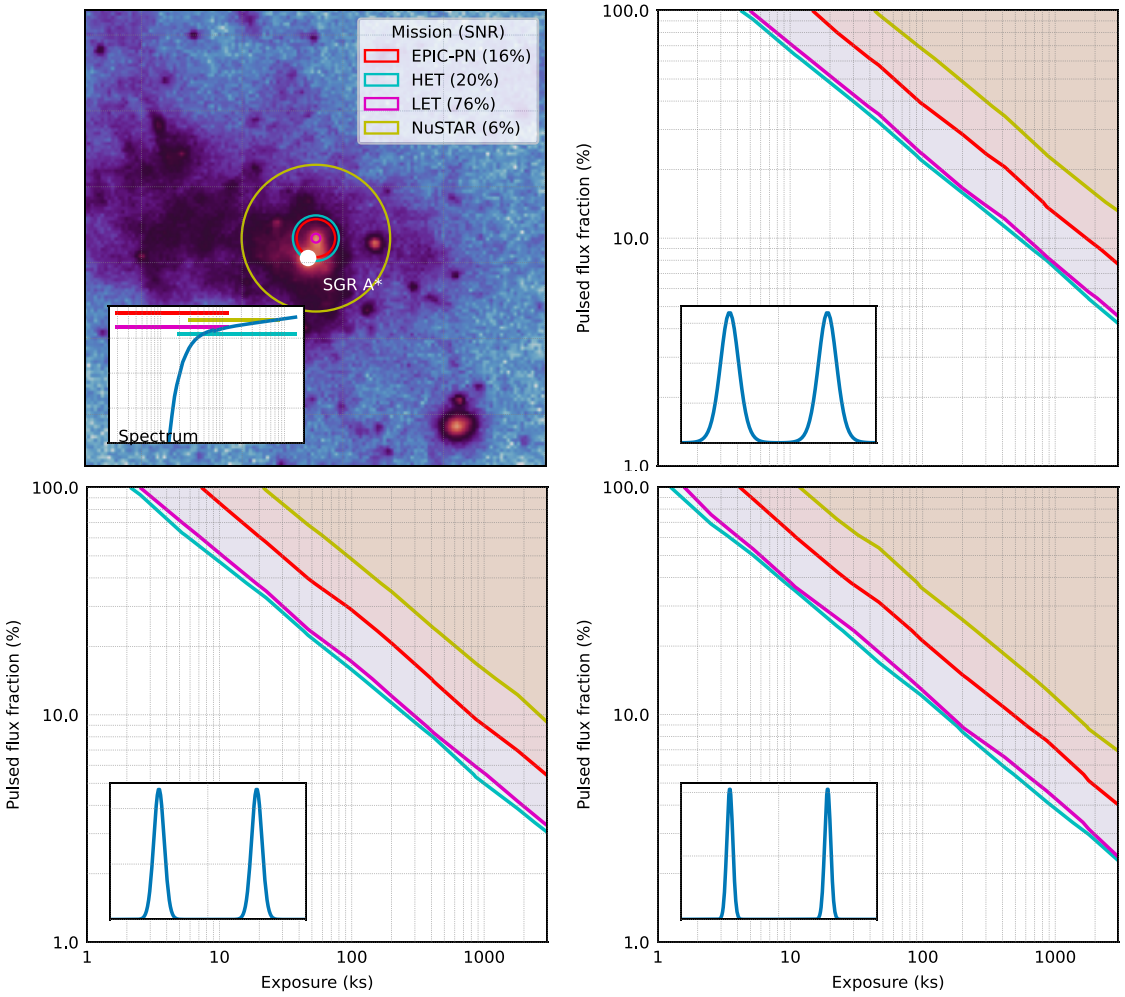

FIGURE 6
The map on the top left shows a simulated LET image of the pulsar wind nebula G359.95-0.04 and its surrounding region, using SIXTE. Equivalent maps were produced for the three additional instruments listed in the plot, and were used to estimate the source flux and the sky and instrumental background in the circular sources shown (calibrated on the mean HPD of the telescope). Simulated *NuSTAR* and *HEX-P* HET data take into account the flux from two modules. The color coding is consistent in the plots (e.g., cyan for *HEX-P*-HET). Percentages in the legend indicate the source to background (all components) flux ratio in the region. The shaded regions in the other plots show the pulsed flux fraction (ratio between the pulsed flux and the total flux) detectable at >5 σ with different instruments, for different exposures.

pc (Hailey et al., 2018; Mori et al., 2021). If the CHXE/NSC is indeed composed of hundreds of mCVs, an extremely intriguing question is whether its core shows a lower or higher concentration of X-ray point sources (predominantly mCVs), compared to the cuspy stellar distribution revealed by IR observations (Schödel et al., 2018). MCVs with heavier WD masses and shorter binary separations are more likely to survive in the NSC core. While heavier WD masses make X-ray spectra harder due to higher shock temperatures in their accretion columns, smaller binary orbits should correspond to reduced mass accretion rates (Hillman et al., 2020), and thus lower X-ray luminosities. A hard X-ray view of the NSC and its core within $r < 3$ pc (<75″) with higher angular resolution than *NuSTAR* may reveal energy-dependent spatial profiles above 10 keV, where diffuse soft X-ray emission from the SNR Sgr A East becomes negligible. Depending on the (unknown) WD mass and binary separation distributions within $r < 3$ pc, *HEX-P* may unveil a sharply lower or higher hard X-ray flux compared to the CHXE, which extends out to $r \sim 8$ pc. In the NSC region, a unique population of mCVs, whose thermal X-ray emission is typically characterized by plasma temperatures $kT \sim 10$–40 keV, can be probed most sensitively in the 20–40 keV band. Figure 7 shows simulated radial profiles of 20–40 keV hard X-ray emission resolved by *HEX-P* for two possible scenarios representing a lower ("deficit") and higher ("cusp") concentration of mCVs within $r < 3$ pc. The two radial profiles are clearly distinct from each other, thanks to the higher angular resolution of *HEX-P*, which can resolve the CHXE *and* its core from other non-thermal X-ray sources.

5.5 Resolving the composition of the GRXE through the Limiting Window

While a majority of the thousands of sources detected by *Chandra* in the GC are believed to be mCVs (Muno et al.,

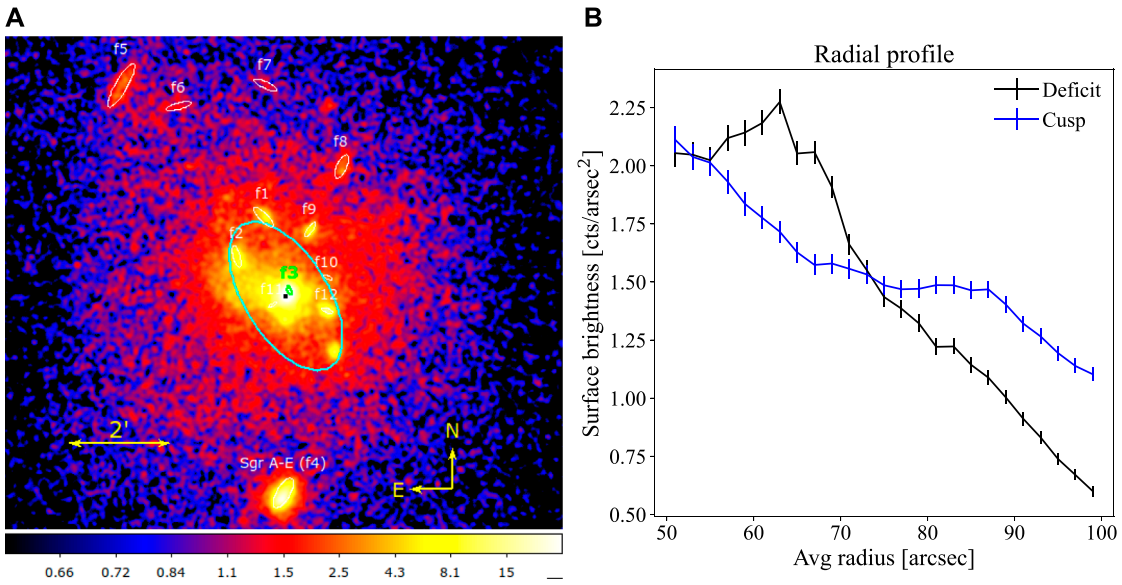

FIGURE 7
(A) Simulated *HEX-P*/HET image of the central 10 pc region in the 20–40 keV band. Sgr A* and the CHXE are indicated by a black dot and a cyan ellipse, respectively. X-ray filaments are denoted by f1, f2, f3, etc. A complete list of the corresponding filament names and their spectral parameters can be found in Supplementary Table S3 in the Supplementary Material. **(B)** Simulated radial profiles of hard X-ray emission (20–40 keV) in the central 4 pc, assuming a cusp (blue) or deficit (black) of hard IPs at $r < 3$ pc around Sgr A*.

2009), their specific source types, average WD masses, and their dependence on the X-ray luminosity (L_X) and radial distance from Sgr A* are still largely unknown. It is the study of diffuse X-ray emission that has revealed the presence of distinct populations of CVs between the GC and ridge. In contrast to the CHXE, which has $kT \sim 35$ keV, the Galactic ridge exhibits softer diffuse X-ray emission with $kT \sim 8$–15 keV (Türler et al., 2010; Yuasa et al., 2012; Perez et al., 2019). Several studies of this diffuse X-ray emission suggest that the softer ridge X-ray emission is due to an unresolved population of polars and/or nmCVs (Hailey et al., 2016; Xu et al., 2016). However, it is challenging to separate the diffuse X-ray emission into distinct CV populations (with varying L_X and kT distributions) solely through analysis of diffuse hard X-ray continuum or Fe line emission.

The Limiting Window (LW), located 1.4° south of Sgr A*, is a region with low extinction that allows for the study of X-ray sources in the GC and Bulge regions without significant obscuration. A deep exposure of the LW with *Chandra* has resolved a large portion of the Fe line emission (≳80%) into ~300 point sources (Revnivtsev et al., 2009). This discovery has been considered a crucial indication of the point source nature of the GRXE, as opposed to being truly diffuse in origin. However, it is still unclear what types of point sources constitute the GRXE. Revnivtsev et al. (2009) suggest that relatively faint coronal sources, such as active binaries (ABs), may constitute a major portion of the GRXE. On the other hand, it was suggested that relatively bright accretion sources, particularly mCVs, dominate the GRXE (Hong et al., 2012; Schmitt et al., 2022). These conflicting findings highlight the need for further investigation to determine the contribution of different source types in the LW and shed light on the understanding of the X-ray emission in the Bulge and Ridge regions. Indeed, the identification of the bright X-ray sources in the LW is crucial, and their individual spectral and timing properties can provide valuable insights. For instance, it is difficult to identify soft coronal sources like ABs in other typical GC and Bulge regions due to heavy obscuration, while the bright point source population in other low extinction windows in the Bulge such as Baade's window is dominated by AGNs (Figure 3). *HEX-P*'s hard X-ray coverage above 10 keV can decisively determine the coronal vs. accretion nature of X-ray emission from these sources.

For our simulations, we considered different X-ray source compositions in the LW. For example, we assigned $kT = 8, 15$ or 35 keV to the X-ray sources in the LW. Figure 8 shows simulated LET (0.2–25 keV) and HET (3–40 keV) images of a section of the LW. Known mCVs from Hong et al. (2012) were given their best-fit model parameters specific to each source, while all other *Chandra* sources within this region were assumed to have spectra characterized by an absorbed APEC model with $kT = 15$ keV. *HEX-P* is expected to detect 53 and 29 sources above 4σ significance among 235 and 261 *Chandra* sources used as an input to SIXTE simulation for LET and HET, respectively. For different plasma temperatures ($kT = 8$ and 35 keV), we found that *HEX-P* can detect a similar number of *Chandra* sources in broad energy bands beyond 8 keV. Eventually, broad-band X-ray spectral data obtained by *HEX-P* will allow us to determine the X-ray source composition in the LW. More specifically, we aim to measure 1) plasma temperatures of the known mCVs, 2) the mean plasma temperature of other bright X-ray sources ($L_X \gtrsim 10^{32}$ erg s^{-1}), and 3) the mean plasma temperature of faint X-ray sources ($L_X \lesssim 10^{32}$ erg s^{-1}). For group 1), we will analyze *HEX-P* and archived *Chandra* spectra of the known mCVs individually. For groups 2) and 3), stacking their LET and HET spectra, along with archived *Chandra* data, will allow us to measure their mean plasma temperatures. In all cases, the

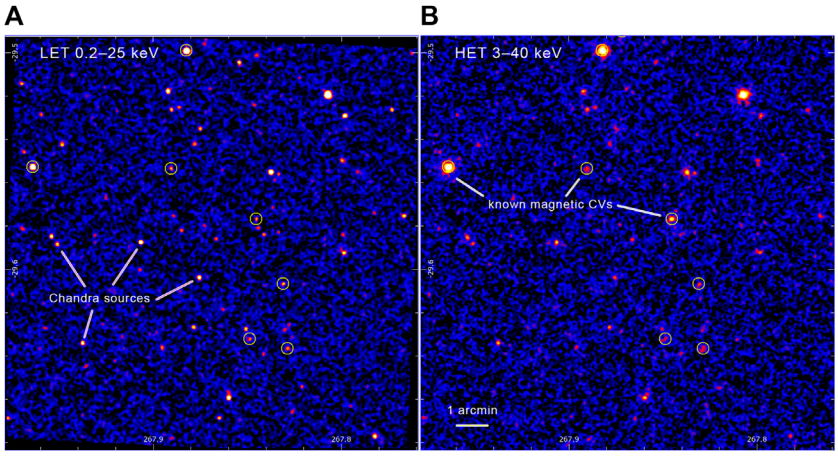

FIGURE 8
Simulated *HEX-P* LET **(A)** and HET **(B)** images of a section of the LW based on Chandra source positions and fluxes (Hong et al., 2009) assuming an absorbed APEC model ($kT = 15$ keV). Magnetic CVs identified in Hong et al. (2012) are encircled in yellow.

hard X-ray coverage by *HEX-P* is crucial to determine their plasma temperatures accurately (with ~20% error), which can be compared with those measured in the Bulge (8 keV), Ridge (15 keV) and CHXE (35 keV). It is possible that the three groups of X-ray sources may reveal different plasma temperatures. For instance, group 1) and 2) could have higher temperatures $kT \sim 35$ (predominantly IPs) and 15 keV (predominantly polars), respectively, while group 3) may have lower temperatures of $kT \lesssim 8$ keV (predominantly nmCVs and ABs) for 3). This is how *HEX-P* is capable of dissecting the composition of X-ray source populations in different luminosity ranges. Moreover, *HEX-P* may be able to detect orbital periods from more X-ray sources in the LW as an alternate way of classifying them as polars or IPs (Hong et al., 2012; Bao and Li, 2020).

6 Diffuse X-ray sources in the Galactic center

The GC hosts a zoo of various, unique types of diffuse X-ray sources, containing both powerful particle accelerators (e.g., Sgr A* BH, SNRs, PWNe, star clusters) and targets bombarded by relativistic cosmic rays and X-rays (e.g., molecular clouds and filaments). *HEX-P* will survey all primary particle accelerators, molecular clouds (MCs), and X-ray filaments to obtain a whole picture of the CR spatial and energy distributions in the GC. Broad-band X-ray spectroscopy and excellent spatial resolution of *HEX-P* are crucial for distinguishing thermal and non-thermal diffuse X-ray emission. Combined with the CTAO GC survey, *HEX-P* will obtain the most accurate multi-wavelength SED data over the X-ray and TeV bands.

6.1 Molecular clouds

While the SMBH at Sgr A* is currently dormant, only occasionally emitting X-ray flares (see §4), a series of X-ray observations of the CMZ that Sgr A* used to be more active in the recent past. Following the first detection of hard X-ray emission from Sgr B2, it was suggested that the molecular cloud (MC) reflected bright X-ray flares, presumably emitted from Sgr A* (Sunyaev et al., 1993). The X-ray reflection exhibits Compton scattering, fluorescent Fe emission lines at 6.4 and 7.06 keV, and photo-absorption. In addition, both the X-ray continuum and Fe fluorescent lines have been observed to decrease over the last two decades as the X-ray flare propagated through the Sgr B2 cloud (Koyama et al., 1996; Sunyaev and Churazov, 1998; Terrier et al., 2010; 2018; Nobukawa et al., 2011; Zhang et al., 2015). Propagation of X-ray echoes is also detected from other MCs in the CMZ (e.g. Muno et al., 2007; Ponti et al., 2010; Clavel et al., 2013; Ryu et al., 2013; Chuard et al., 2018; Terrier et al., 2018). High energy observations with *INTEGRAL* (Sgr B2) and *NuSTAR* (Sgr A and B2) have shown that the reflection signal extends above 10 keV and has been detected up to 100 keV (Revnivtsev et al., 2004; Terrier et al., 2010; Mori et al., 2015; Zhang et al., 2015; Kuznetsova et al., 2022). *NuSTAR* played a crucial role in resolving hard X-ray continuum emission from Sgr B2 and Sgr A complex clouds, while Sgr C has not been observed with *NuSTAR* due to the high background contamination (Mori et al., 2015; Zhang et al., 2015; Rogers et al., 2022).

While the variable X-ray emission is primarily caused by single Compton scatterings, another non-variable X-ray component may emerge after the X-ray light front passes the clouds. This "constant" X-ray emission component may be caused by 1) multiply-scattered X-ray photons confined within dense cloud cores (Sunyaev and Churazov, 1998; Molaro et al., 2016; Khabibullin et al., 2020; Sazonov et al., 2020) and/or 2) non-thermal X-ray emission and collisional ionization by cosmic-rays (Tatischeff et al., 2012). Recent X-ray observations indicated that clouds in Sgr B2 (Kuznetsova et al., 2022; Rogers et al., 2022) and the Arches cluster (Kuznetsova et al., 2019) may have entered the constant X-ray emission phase. Diffuse TeV gamma-ray emission was observed to coincide with the MCs in the GC

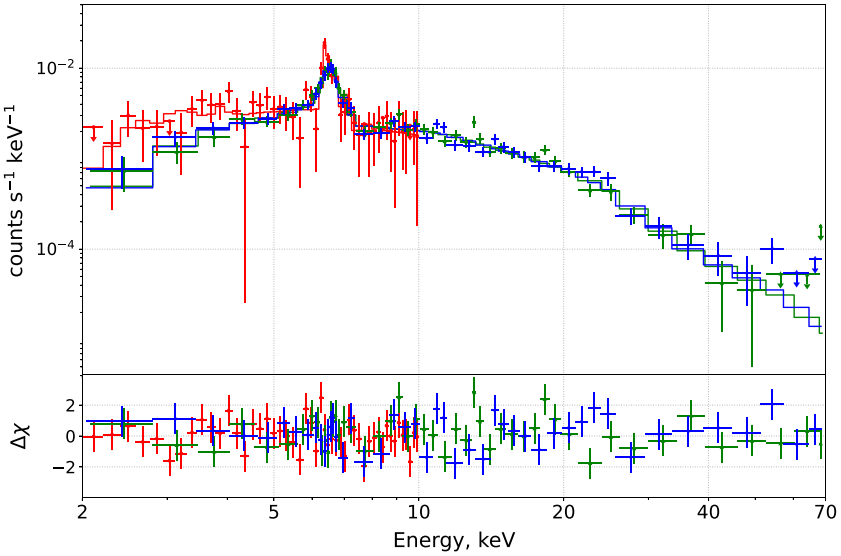

FIGURE 9
Simulated *HEX-P* spectra of the Sgr B2 core ($r < 90''$) based on our phenomenological model (see text and Zhang et al., 2015) obtained with 100 ks exposure time. The model was corrected for foreground absorption and consisted of a thermal background emission with a temperature of $kT = 1.9$ keV, an intrinsically absorbed power-law with a photon index of $\Gamma = 1.9$ and two Gaussian emission lines Fe Kα (6.4 keV) and Kβ (7.06 keV), with an unabsorbed non-thermal flux in the 10–40 keV energy band of $F_{10-40keV} = 1.9 \times 10^{-12}$ erg cm^{-2} s^{-1} (other parameters are listed in Table 2 in Zhang et al., 2015). Red points correspond to the simulated LET data (2–10 keV), blue and green to the HET data (2–70 keV). Arrows show 2σ upper limits. The total model is represented by stepped solid lines of the colors corresponding to the data.

region, indicating that the clouds are bombarded by energetic CRs (Aharonian et al., 2006; van Eldik and H. E. S. S. Collaboration, 2008; Beilicke and VERITAS Collaboration, 2012; Sinha et al., 2022). Overall, extensive X-ray observations over the last two decades revealed that the MCs exhibit different time evolution and X-ray properties, likely due to multiple X-ray outbursts from Sgr A* and different cosmic-ray bombardment mechanisms.

HEX-P will survey all prominent MCs, including Sgr A, B1, B2 and C, in the primary GC observation program (Table 1). The *HEX-P* survey will capture the X-ray landscape of the MCs through both the Fe fluorescent line at 6.4 keV and non-thermal X-ray continuum emission in the early 2030s. *HEX-P* will likely conduct follow-up observations of these clouds later to monitor X-ray variabilities. All MC complexes with X-ray variability will be covered with at least 100 ks exposure. Detection of changes in the morphology and spectral parameters of the MC emission will determine whether X-ray echoes are still propagating through the clouds or the cosmic-ray bombardment component is dominating. The significantly lower stray-light background will allow us to investigate the hard X-ray morphology of the CMZ with *HEX-P* far more precisely than *NuSTAR*. To demonstrate the capability of *HEX-P* on the MC science, we present simulation results for Sgr B2, whose emission has been decreasing since the 1990s and has now likely reached a faint constant level. We adopted the latest *NuSTAR* (Zhang et al., 2015; Rogers et al., 2022) and *INTEGRAL* (Kuznetsova et al., 2022) observation results for XSPEC simulations (Zhang et al., 2015). Figure 9 shows the simulated *HEX-P* spectra of the Sgr B2 core. Our simulation demonstrates that the non-thermal X-ray component will be detected at ~17σ significance, and the photon index and the equivalent width of the 6.4 keV emission line will be measured with ≤10% error.

Furthermore, we investigated whether *HEX-P* can discriminate between different emission models based on broad-band X-ray spectral data. We considered two main scenarios: 1) reflection of past X-ray flares and 2) non-thermal bremsstrahlung emission and collisional excitation by low-energy cosmic-ray protons (LECRp). In the reflection scenario, the spectrum can be dominated by single or multiple scatterings, depending on the location of the X-ray light front. To clarify whether these scenarios can be discerned by *HEX-P*, we simulated Sgr B2 spectra for three models using 2013 *NuSTAR* flux measurements; the same low-energy component (absorption and astrophysical background) and either LECRp parameters (model described in Tatischeff et al., 2012) from *NuSTAR* (Zhang et al., 2015) or reflection parameters (CREFL16 model from Churazov et al., 2017) from *INTEGRAL* observations to account for the emission of Sgr B2 at high energies (Revnivtsev et al., 2004; Kuznetsova et al., 2022). Figure 10 illustrates the three different models and corresponding spectra simulated for the 90″-region of Sgr B2.

The Compton shoulder is clearly present below the Fe fluorescent lines (both for Kα and Kβ) for the reflection models (Khabibullin et al., 2020), while the LECR spectra exhibit only the narrow emission lines (Tatischeff et al., 2012). The multiple-scattering case in the middle panel can be identified well by the large line ratio (~1) between the Compton shoulder and 6.4 keV line, which should be ≈1 as a result of multiple Compton scatterings (Khabibullin et al., 2020).

Overall, *HEX-P*'s Fe line spectroscopy and broad-band X-ray data can distinguish between the X-ray reflection and cosmic-ray

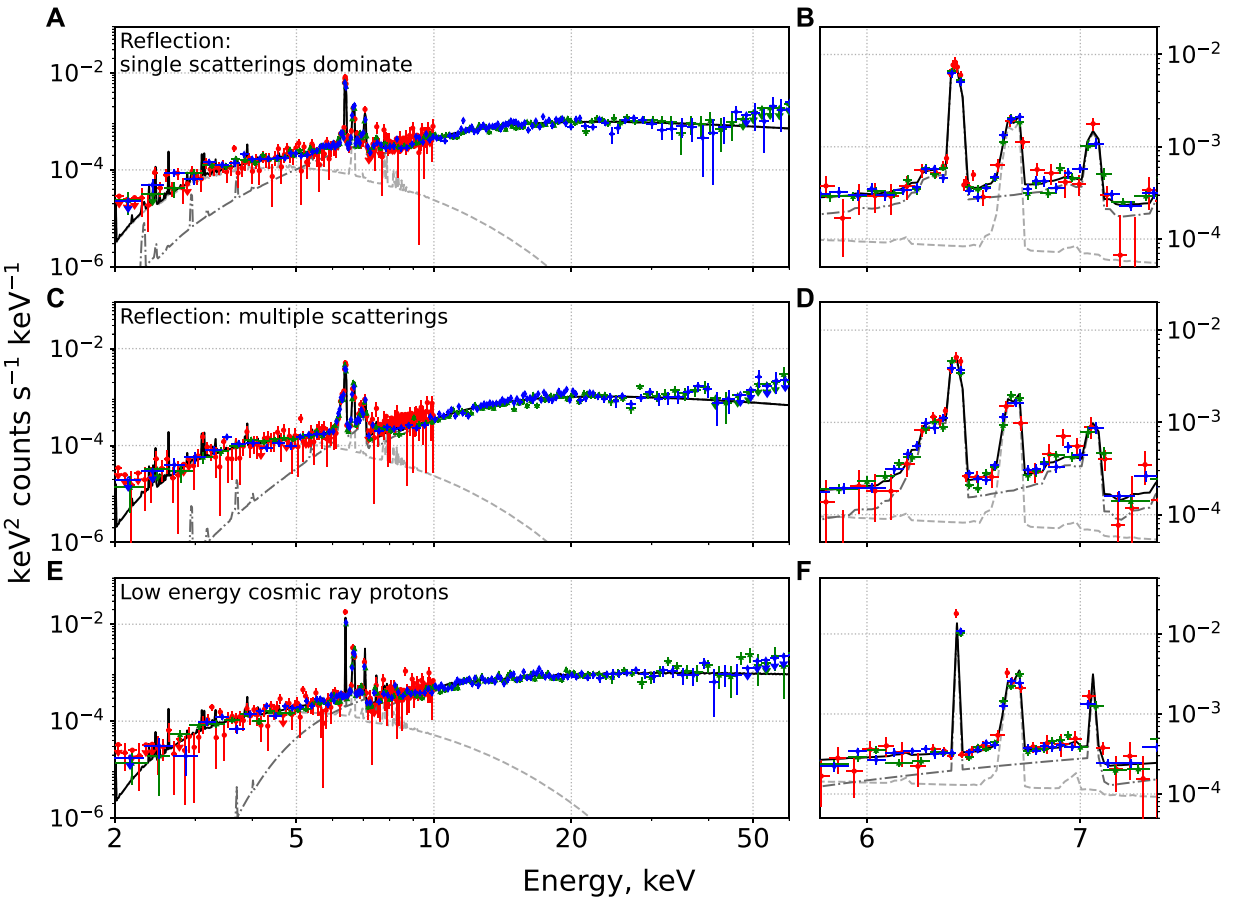

FIGURE 10
Sgr B2 spectra simulated based on the CREFL16 **(A,B)**, CREFL16 multiple scatterings only **(C,D)**, LECRp **(E,F)** models in the 2–70 keV energy band with 300 ks exposure. Arrows show 2σ upper limits. The right panels represent the strongest emission lines of the Sgr B2 spectrum. Red points correspond to the simulated LET data in the 2–10 keV energy band, blue and green to the HET data in 2–70 keV. The right panels show the Fe Kα and Kβ emission lines, at 6.40 and 7.06 keV energies, respectively, caused by non-thermal processes. Between them, there is the Fe 6.7 keV emission line related to the thermal emission component. For illustration purposes, the spectra plotted were further grouped to reach either 7σ or 7 bins of the fitted spectra per bin.

models unambiguously. *HEX-P*'s spatial and spectral resolutions will allow us to trace the X-ray morphology evolution and characterize the Fe line profiles in detail, respectively. *HEX-P*'s broadband X-ray spectral data will lead to measuring the spectral index of past X-ray flares from Sgr A* and bombarding CRs. In the former case, this is a unique opportunity to investigate the mechanism of Sgr A* X-ray flares that occurred a few hundred years ago. For the latter, we can map out the population of CRs in the GC region in conjunction with future TeV observations by CTAO.

6.2 X-ray filaments

A unique phenomenon in the GC region is the existence of numerous radio and X-ray filaments (Yusef-Zadeh et al., 1984; Morris and Serabyn, 1996). The origin and formation of these filaments have been a long-standing question for decades. Within the central ~2° region, MeerKAT radio surveys have revealed over 150 filaments, which seem to be associated with bi-polar radio bubbles (Heywood et al., 2019; Yusef-Zadeh et al., 2023). The emission mechanism of non-thermal radio filaments has been pinned down to synchrotron emission thanks to the detection of linear polarization. Within the filaments, the magnetic field strengths are found to be 1–2 orders of magnitude higher than the surroundings at $B \sim 1$ mG and aligned with the major axis of a filament (e.g. (Morris and Serabyn, 1996)). High-resolution JVLA observations further revealed complex sub-filaments entangled with each other within many of the radio filaments (Morris et al., 2014). It suggests that radio filaments are magnetic structures, where strong and highly-organized magnetic fields trap GeV electrons and produces synchrotron emission (Zhang et al., 2014).

At higher energies, filaments at smaller spatial scales have also been detected in the X-ray band. About 30 parsec-long X-ray filaments have been detected so far, some of which have radio counterparts (Lu et al., 2008; Muno et al., 2008; Johnson et al., 2009; Zhang et al., 2014; Ponti et al., 2015a; Zhang et al., 2020). Out of ~30 known X-ray filaments, *NuSTAR* was able to detect only the four brightest ones (Zhang et al., 2014; Mori et al., 2015; Zhang et al., 2020). The brightest X-ray filament Sgr A-E exhibits a featureless power-law spectrum extending up to 50 keV, which

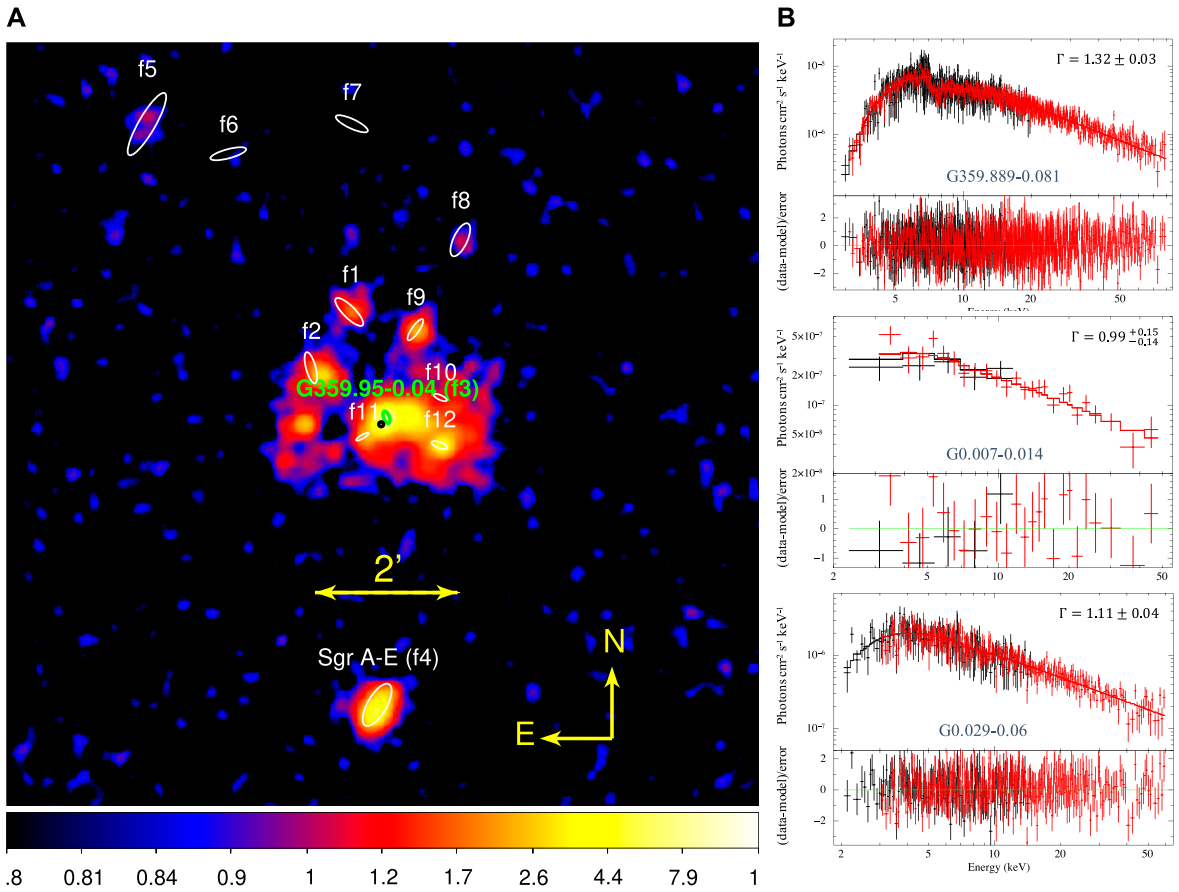

FIGURE 11
(A) Simulated *HEX-P* 40–80 keV image of the GC region. Eight of the 12 simulated non-thermal X-ray filaments are resolved. A list of the filaments and their spectral parameters is given in Supplementary Table S3 in the Supplementary Material. **(B)** Simulated *HEX-P* spectra of three of those filaments. LET and HET spectra are shown in black and red, respectively. *HEX-P* will be able to constrain their spectral indices far better than current instruments.

requires electron energies of multi-hundred TeV electrons that are most likely produced by hadronic interactions between primary PeV protons and nearby MCs (Zhang et al., 2020). Therefore, mapping out even a subset of the X-ray filaments could serve as a powerful way of indirectly probing PeVatron particle distribution in the GC.

HEX-P data above 40 keV will provide an unprecedentedly pristine view of non-thermal X-ray emission in the central 10 pc region. While the central PWN G359.95-0.04 and several X-ray filaments have been detected by *NuSTAR* above 40 keV (Mori et al., 2015; Nynka et al., 2015), other (potentially hidden) non-thermal X-ray sources remain largely unresolved. These non-thermal X-ray sources in the GC represent energetic particle accelerators (e.g., PWNe) or tracers of TeV–PeV electrons emitting synchrotron X-rays. It is still unclear just how high the maximum energy of X-rays emitted from the filaments around Sgr A* can reach (Li et al., 2013). This information is crucial for measuring the maximum energies of relativistic electrons in the region. *HEX-P* is poised to resolve high-energy X-ray emission from a much larger number of X-ray filaments than *NuSTAR* and potentially discover new filaments. For example, a 500 ks *HEX-P* simulation of the central $13' \times 13'$field results in detecting 8 out of the 12 known X-ray filaments above 40 keV (Figure 11). A full list of all filaments included in this simulation—along with their spectral parameters—is provided in Supplementary Table S3 in the Supplementary Material. Figure 11B shows simulated *HEX-P* spectra for three filaments with 100 ks exposure: Sgr A-E (G359.889–0.081), G0.007–0.014 and G0.029–0.06, respectively. The simulated spectra can be fitted well with an absorbed power-law model extending beyond 50 keV. For brighter filaments like Sgr A-E and G0.029-0.06, spectral indices can be constrained to less than 5%. A spectral break or cutoff below 50 keV can be ruled out. Determination of the maximum X-ray photon energy is essential to infer the energy of parent electrons. Unlike the current and proposed soft X-ray telescopes operating below 8–10 keV, broadband X-ray spectroscopy with *HEX-P* can measure the X-ray spectral shapes robustly with minimal parameter degeneracy issues with $N_{\rm H}$. Multi-wavelength SED and morphology studies of these filaments with MeerKAT/SKA and HEX-P will allow us to determine ambient B-field and broadband particle energy distribution. In summary, *HEX-P* observation of X-ray and radio filaments will help to reveal the origin of relativistic particles in the GC, whether they are driven by common PeVatron accelerators in the GC (e.g., Sgr A* BH) or associated with local particle accelerators such as PWNe, SNRs, stellar winds or magnetic reconnections within the filaments.

7 *HEX-P* science in other regions of the Milky Way

Besides the primary observation program of the GC and Bulge regions described above, below we list several unique *HEX-P* science cases that can be explored through GO observations. These observation ideas have not been feasible with *NuSTAR* or stem from expanding the previous *NuSTAR* observations.

7.1 Investigation of X-ray sources in star-forming regions

Outside the GC and Bulge, a *HEX-P* survey of several young massive clusters (YMCs) and star-formation regions in our Galaxy can be conducted to search for hidden BH–OB binaries, detect hard X-ray flares from young stellar objects (affecting the dynamics of protostellar disks) and identify hard X-ray sources previously detected by *NuSTAR*. YMCs, ranging in age from approximately 1 to 10 million years, are characterized by the presence of massive star-forming regions. These clusters offer valuable insights into ongoing star formation and often host compact objects such as NSs and stellar-mass BHs. This is due to the relatively short lifetimes of massive stars, which eventually undergo core-collapse supernovae. The Orion Nebula is particularly well-suited for studying a wide range of X-ray activities, including hard X-ray emission from BH binaries and flares from massive young stars. The Norma spiral arm, where *NuSTAR* detected ~30 hard X-ray sources, could be surveyed with *HEX-P* searching for HMXBs (Fornasini et al., 2017).

7.1.1 Search for black hole binaries with OB stars

It is estimated that the Milky Way harbors a substantial number of stellar mass BHs, ranging from 10^8 to 10^9. However, only around 20 BHs have been dynamically confirmed, and approximately 50 candidates have been identified mainly based on their X-ray characteristics. This discrepancy highlights the scarcity of confirmed BHs compared to the estimated population. In addition, these confirmed BH systems are predominantly LMXBs, in contrast to the dearth of BH-HMXBs. Currently, there are only six known HMXBs that contain a BH companion. Among them, Cygnus X-1 is the only system with an undisputed BH companion. Thus, the discovery of X-ray emission from just a few new BH–OB systems would significantly impact our understanding of these systems and their evolution.

The majority of massive stars are formed as binary or high multiple systems, as supported by studies such as Moe and Di Stefano (2017). Langer et al. (2020) estimated that ~3% of massive OB stars have companions in the form of BHs, resulting in ~1,200 BH–OB systems existing within our Galaxy. The discovery of these systems would provide valuable insights into various aspects of astrophysics, including star formation processes, stellar and binary evolution, galaxy evolution, supernova rates, and gravitational wave events. Through precise proper motion measurements conducted by the *Gaia* mission, two BH binary systems named Gaia BH1 and BH2 have been recently discovered using their astrometric orbital solutions (El-Badry et al., 2023a; b; Chakrabarti et al., 2023). These groundbreaking findings have opened new avenues of research in the field. It is anticipated that *Gaia* Data Release 3 will unveil ~190 BH–OB binaries (Janssens et al., 2022), which may revolutionize our understanding of these systems. It is worth noting that *Gaia* would be sensitive to detecting the BH binary systems with long orbital periods ($\gtrsim$ 10 days). These binaries are non-interacting in nature, similar to the initial two detections (Gaia BH1 with an orbital period of 185.6 days and Gaia BH2 with 1,277 days; see Figure 12 in El-Badry et al., 2023b).

While *Gaia*'s sensitivity does extend to systems with shorter orbital periods, the detection of BH–OB systems with periods $\lesssim$ 10 days can be facilitated by observing X-ray emission resulting from wind accretion onto the BH (Gomez and Grindlay, 2021). This is because BH–OB systems in close binaries with short orbital periods are more likely to have accretion onto the BH from the powerful stellar wind of the OB star, leading to the generation of X-ray emission. In particular, the presence of hard X-ray emission above 10 keV serves as a definitive signature of the BH's existence, especially when combined with knowledge of the orbital mass (which allows for differentiation between BH–OB and NS–OB systems). This is due to the fact that single OB stars or (massive) active binaries rarely emit hard X-rays. Eta Carinae stands as the sole known massive binary system exhibiting hard X-rays above 10 keV. Thus, observing such hard X-ray emission can provide crucial evidence for the presence of a BH in an BH–OB system.

In Gomez and Grindlay (2021), a novel method for identifying BH–OB systems is presented. The approach involves initially compiling a list of single-line spectroscopic binaries that exhibit no observable stellar spectrum of the secondary (with absorption lines) companion (hence, the binary is a SB1). Such systems are strong candidates to have secondary companions that are evolved stellar remnants: either a NS or a stellar-mass BH. These selected systems are then subjected to follow-up observations using *NuSTAR* to investigate the presence of hard X-ray emission originating from the binary. The critical signature of a NS or BH secondary is that the X-ray spectrum is detectable above 10 keV since isolated O stars have soft thermal spectra with $kT \sim$ 1–3 keV and $L_X \sim 10^{-7} L_{bol} \sim 10^{31}$ erg s^{-1}. According to El-Badry et al. (2023a,b), BH binary systems with $P_{\rm orb} \lesssim 10$ days are expected to exhibit X-ray fluxes greater than $\sim 10^{-13}$ erg s^{-1} cm^{-2}. These estimations suggest that both soft and hard X-ray emission from close BH–OB systems in nearby massive clusters are detectable with *HEX-P*, for example, by surveying the central $23' \times 23'$ field of the Orion nebula, containing 1,600 *Chandra* X-ray sources (Getman et al., 2005), with 2×2 pointings (60 ks exposure each) and an additional 60 ksec observation at the center. *HEX-P*'s hard X-ray search for BH–OB binary candidates in several YMCs (alternatively, hard X-ray sources identified by *HEX-P* in these fields can be further investigated using follow-up optical/infrared spectroscopic studies to measure orbital mass) will complement the BH systems discovered through astrometric orbital solutions with *Gaia*, which are primarily sensitive to non-interacting, long-period systems.

7.1.2 Hard X-ray flares from young stellar objects

Flares from stars are the most energetic events in their star systems, but our understanding of them, including flare distributions and their long-term influence on orbiting planets, is limited, primarily to our own sun. The situation becomes even more uncertain for flares from young stellar objects (YSOs), such as pre-main sequence stars (PMS). Deep X-ray surveys, like COUP, offer

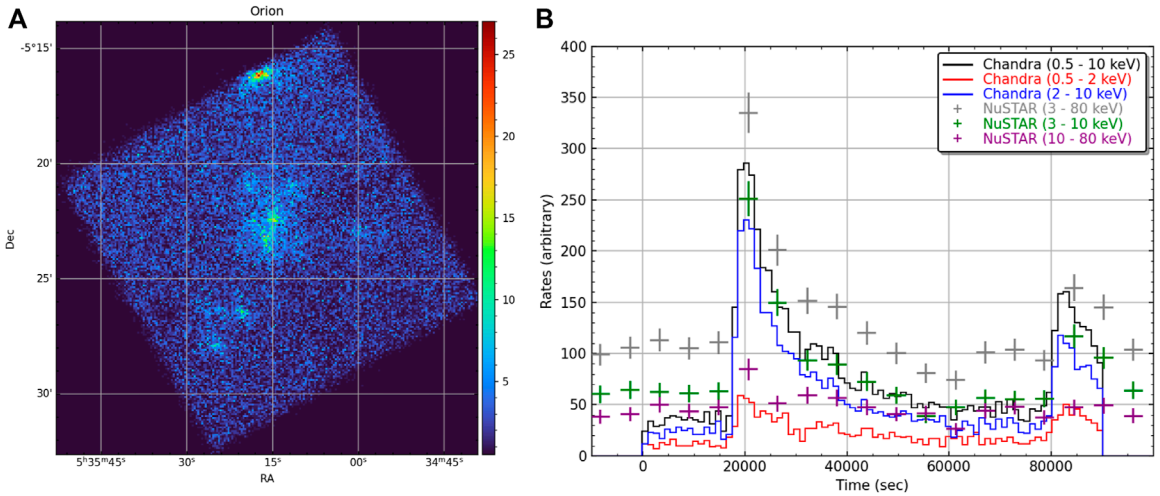

FIGURE 12
NuSTAR images of the Orion Nebula Cluster **(A)** and light curve of one of the variables **(B)**. The hard (>10 keV) X-ray component (purple crosses) is heavily contaminated by neighboring sources, which makes hard X-ray flares difficult to distinguish with *NuSTAR*. *HEX-P*'s superior angular resolution and sensitivity will enable us to identify many more flares from YSOs.

valuable opportunities to gain knowledge about flares originating from YSOs. According to the standard picture, a flare occurs due to magnetic reconnection, which accelerates non-thermal electrons along magnetic field lines, resulting in the heating of the chromosphere and corona. Based on the largest flares observed in COUP, Favata et al. (2005) suggested the existence of additional flare channels in YSOs, where reconnection events in magnetic field lines connect the star and the protoplanetary disk. Getman et al. (2008a,b) also found that the brightest flare distribution, in terms of peak luminosity or temperatures, significantly deviates from expectations based on extrapolations from main sequence stars.

The evolution of a protoplanetary disk relies on the strength of the interaction between the magnetic field and ionized matter within the disk. High-temperature flares emit energetic photons that play a significant role in ionizing the disk, creating what is known as an active zone since they penetrate deep into the disk. The active zone, in turn, facilitates the transport of matter throughout the disk (Glassgold et al., 2004) through mechanisms such as the magnetorotational instability (Glassgold et al., 1997). The influence of hard X-rays is particularly important as they penetrate deeper into the disk, making the hard X-ray luminosity a key factor in determining the accretion rate of a protostar.

The simultaneous observation of the Orion Nebula using *NuSTAR* and *Chandra* aimed to study the properties of flares from YSOs in the hard X-ray range (>10 keV) (Guenther 2023 in preparation). The *NuSTAR* data revealed a wide range of hard X-ray activity in the region, as depicted in Figure 12. However, the angular resolution of *NuSTAR* is relatively poor, leading to contamination from nearby sources in this densely populated area, which limits the hard X-ray investigation. Although ~8 flares and ~6 variables were detected, and some exhibited a similar pattern in their lightcurves between soft and hard X-rays, the *NuSTAR* lightcurves exhibited significant fluctuations due to low statistics and contamination from neighboring sources (Figure 12). In contrast, due to its significantly improved sensitivities compared to *NuSTAR*, *HEX-P* will enable a comprehensive study of five times more flares in both the soft and hard X-ray bands. Such a study will provide valuable insights into the evolution of protoplanetary disks and the formation of planets.

7.2 Magnetic cataclysmic variables

The knowledge of WD masses, metallicities, and source types (e.g., magnetic vs. nmCVs) offers valuable insights into the formation and evolution of CVs in various environments within our Galaxy (Mukai, 2017). The high sensitivity and wide spectral coverage of *HEX-P* present a unique opportunity to investigate the spatial evolution of the seemingly distinct CV populations in the GC, Bulge, Ridge and solar neighborhood. Also, as described in the next section, accurately measuring the WD masses of mCVs—a task that *HEX-P* is uniquely suited for—allows us to probe the fundamental properties of these systems, such as 1) the long-term mass evolution of mCVs toward the Chandrasekhar mass limit with IPs, and 2) the origin of WD magnetic fields with polars. In the near future, *eROSITA*, ZTF, and Rubin all-sky surveys are expected to discover a large number of mCVs in the Galactic Disk, including rare classes of CVs such as AM CVn stars, novae, and fast-spinning CVs (Rodriguez et al., 2023). *HEX-P* will provide broad-band X-ray spectral and timing data of these exotic CVs, allowing us to study and understand those new populations with physically meaningful interpretations.

7.2.1 White dwarf mass measurements from magnetic CVs

Whether mCVs gain or lose mass is of great significance for probing the two competing channels for type Ia supernovae (SNIa) (Pala and Gänsicke, 2017). In the double-degenerate case, two WDs in a binary system merge to form a WD with $M > M_{Ch}$

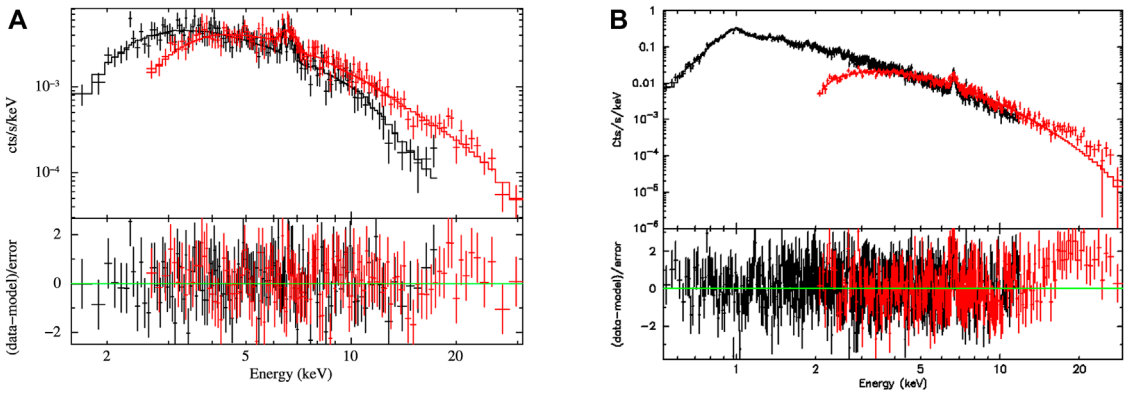

FIGURE 13
(A) Simulated *HEX-P* LET (black) and HET (red) spectra of an IP with $M_{WD} = 0.8M_{\odot}$. **(B)** Simulated 100-ks *HEX-P* LET (black) and HET (red) spectra of AE Aqr. The input model is composed of two thermal (APEC) and power-law components adopted from (Kitaguchi et al., 2014). The simulated *HEX-P* spectra are fit only with the two thermal components to illustrate the hard non-thermal X-ray excess above 10 keV.

(the Chandrasekhar mass limit, $M_{WD} \sim 1.4M_{\odot}$); in the alternative single-degenerate model, a CO WD increases its mass at it accretes matter from its companion, eventually exceeding the Chandrasekhar limit. It is, however, still unknown whether CVs increase in mass over time due to accretion or lose mass through episodic nova eruptions. Interestingly, some of the newly identified IPs originally detected by *INTEGRAL* were found to have WD masses close to the Chandrasekhar limit (Tomsick et al., 2016; Tomsick et al., 2023). However, the *INTEGRAL* sources are intrinsically biased toward a population of more massive IPs, which generally possess harder X-ray spectra. In order to robustly test the CV mass evolution models such as the eCAML model (Schreiber et al., 2016), it is necessary to collate WD masses and characterize their distribution from a larger, unbiased sample of IPs. Polars, on the other hand, are more suited for studying the WD mass and B-field correlation, in order to test the common envelope (CE) model. The CE model is a leading but unconfirmed candidate for WD B-field formation where differential rotation between the decaying binary orbit and the CE leads to a magnetic dynamo, enhancing the B-field in the WD. One of the most robust predictions of CE models is an anti-correlation between B and M_{WD} (Briggs, 2019). Measuring the WD masses of polars will allow us to explore the B vs. M correlation because their B-fields ($B = 7$–240 MG) are well determined in the optical band. Since polars are typically fainter and more variable than IPs, *HEX-P*'s high sensitivity in the broad X-ray band will be crucial for determining their WD masses accurately.

X-ray spectral modeling of the accretion flow over a broad energy range (extending beyond ~10 keV) is a particularly effective method for measuring WD masses (Shaw et al., 2020; Vermette et al., 2023). In mCVs, infalling material is funneled onto the WD poles along B-field lines and heated to temperatures ($kT_{shock} \sim 10$–80 keV) that scale with the WD mass. Below a standoff shock where the plasma temperature is highest, a column of infalling material cools via thermal bremsstrahlung and cyclotron radiation as it approaches the WD surface with varying temperatures and densities. Since hard X-rays are emitted from the post-shock region, hard X-ray data above $E \sim 10$ keV provide the most accurate measurements of WD masses (Hailey et al., 2016). With the advent of more sophisticated X-ray spectral models for mCVs (e.g., Suleimanov et al., 2019; Hayashi et al., 2021), *NuSTAR*'s broadband X-ray spectral data led to measuring WD masses of ~30 IPs (Shaw et al., 2020), including new IPs discovered in the Bulge accurately ($\lesssim 20\%$) (Mondal et al., 2022; Mondal et al., 2023). *HEX-P* will expand this program to measure WD masses from over 100 mCVs in the solar neighborhood ($d \lesssim$ few $\times$ 100 pc), allowing us to parse WD mass data into different types, regions, and accretion rates. Figure 13A shows simulated *HEX-P* spectra of an IP yielding WD mass measurements with 10% error.

7.2.2 Exotic classes of magnetic CVs

Among the thousands of CVs discovered by extensive optical and X-ray surveys, several rare classes of CVs have been identified, such as AM CVn stars (compact CVs with short orbital periods), recurrent novae, and fast-spinning CVs. While rare, the populations and high-energy emission mechanisms of these exotic CVs are considered extremely important in contemporary astrophysics. For example, given their tight orbits, AM CVn stars are among the most likely gravitational wave sources detectable by the future *LISA* observatory. In another example, recurrent novae such as RS Oph, which undergo episodic thermonuclear explosions on the WD surface that produce shocks from the ejecta slamming into the surrounding circumstellar winds, are of great interest for their strong X-ray and gamma-ray emission (Cheung et al., 2022). Of particular and increasing interest is a rare class of fast-spinning CVs (FSCVs) with $P_{spin} \lesssim$ a few minutes. These FSCVs discovered so far are unique and distinct from regular accretion-powered CVs, including the WD "pulsar" systems (AR Sco and J191213.72-441045.1) and propeller CV (AE Aqr) (Pelisoli et al., 2023). In the near future, a larger population of undetected FSCVs may be revealed by the *Rubin* and *eROSITA* all-sky surveys (Pretorius and Mukai, 2014). *HEX-P*'s higher sensitivity and broad-band X-ray coverage will allow us to study a large number of FSCVs better than *NuSTAR*. For example, *HEX-P* will be able to detect the putative non-thermal X-ray component from AE Aqr above 10 keV (Figure 13B). As demonstrated for AR Sco (Takata et al., 2018), multi-wavelength observations of new WD pulsars will be

invaluable for understanding their particle acceleration and non-thermal emission mechanisms.

8 Conclusion

In conclusion, *HEX-P*, as a probe-class mission, will offer an unprecedented opportunity to revolutionize our understanding of various astrophysical phenomena in the GC and broadly in Galactic astrophysics. With its high spatial resolution X-ray imaging, broad spectral coverage, and superior effective area, *HEX-P* is poised to provide groundbreaking insights into a variety of important questions in the GC. These include the past and current X-ray flares from the SMBH at Sgr A*, the populations of compact object binaries from the NSC to the GRXE, the primary particle accelerators, and cosmic-ray distributions in the GC. Outside the GC, *HEX-P* is expected to accurately measure WD masses of hundreds of mCVs, explore broadband X-ray spectral and timing properties of X-ray transients (including determining BH spins from Galactic BH transients), detect pulsars, and search for BH–OB binaries in young star clusters. These scientific objectives can be uniquely achieved by *HEX-P* or in synergy with other currently operating or future telescopes such as EHT, GRAVITY, MeerKAT, Roman, CTAO, and IceCube gen2. This paper, along with other Galactic science papers, highlights *HEX-P*'s enormous potential to uncover significant new insights into the most important astrophysical problems in the field of Galactic astrophysics in the 2030s.

Data availability statement

The raw data supporting the conclusion of this article will be made available by the authors, without undue reservation.

Author contributions

KM: Data curation, Methodology, Supervision, Writing–original draft, Writing–review and editing, Conceptualization. GP: Supervision, Writing–review and editing, Writing–original draft. MB: Writing–review and editing, Data curation, Formal Analysis, Investigation, Visualization. AB: Investigation, Writing–review and editing, Visualization. JG: Writing–review and editing, Supervision. JH: Writing–original draft, Data curation, Visualization. RK: Supervision, Writing–review and editing. EK: Investigation, Visualization, Writing–original draft. SM: Investigation, Methodology, Visualization, Writing–original draft, Writing–review and editing. AR: Writing–review and editing, Writing–original draft. GS: Investigation, Visualization, Writing–original draft. SZ: Supervision, Writing–original draft. TB: Writing–review and editing, Investigation. FB: Writing–review and editing. MC: Writing–review and editing. BC: Writing–review and editing. JaG: Writing–review and editing. JuG: Investigation, Writing–review and editing. BG: Writing–review and editing. AJ: Writing–review and editing. BL: Writing–review and editing. KM: Writing–review and editing. MN: Writing–review and editing. PP: Writing–review and editing. CS: Investigation, Visualization, Writing–review and editing. DS: Writing–review and editing. JT: Writing–review and editing.

Funding

The author(s) declare that no financial support was received for the research, authorship, and/or publication of this article.

Acknowledgments

We are grateful to J. Wilms, T. Dauser, C. Kirsch, M. Lorenz, L. Dauner, and the SIXTE development team for their assistance with SIXTE simulations. We would like to thank the reviewers for their thoughtful feedback, which helped improve an earlier draft of this paper.

Conflict of interest

The authors declare that the research was conducted in the absence of any commercial or financial relationships that could be construed as a potential conflict of interest.

Publisher's note

All claims expressed in this article are solely those of the authors and do not necessarily represent those of their affiliated organizations, or those of the publisher, the editors and the reviewers. Any product that may be evaluated in this article, or claim that may be made by its manufacturer, is not guaranteed or endorsed by the publisher.

Supplementary material

The Supplementary Material for this article can be found online at: https://www.frontiersin.org/articles/10.3389/fspas.2023.1292130/full#supplementary-material

References

Aharonian, F., Akhperjanian, A. G., Bazer-Bachi, A. R., Beilicke, M., Benbow, W., Berge, D., et al. (2006). Discovery of very-high-energy γ-rays from the galactic centre ridge. *Nature* 439, 695–698. doi:10.1038/nature04467

Anastasopoulou, K., Ponti, G., Sormani, M. C., Locatelli, N., Haberl, F., Morris, M. R., et al. (2023). Study of the excess Fe XXV line emission in the central degrees of the Galactic centre using XMM-Newton data. *Astronomy Astrophysics* 671, A55. doi:10.1051/0004-6361/202245001

Arnaud, K. A. (1996). "XSPEC: the first ten years," in *Astronomical data analysis software and systems V, A.S.P. Conference series, vol. 101*. Editors G. H. Jacoby, and J. Barnes, 17.

Baganoff, F. K., Bautz, M. W., Brandt, W. N., Chartas, G., Feigelson, E. D., Garmire, G. P., et al. (2001). Rapid X-ray flaring from the direction of the supermassive black hole at the Galactic Centre. *Nature* 413, 45–48. doi:10.1038/35092510

Bao, T., and Li, Z. (2020). Periodic X-ray sources in the Galactic bulge: application of the Gregory-Loredo algorithm. *MNRAS* 498, 3513–3534. doi:10.1093/mnras/staa2603

Barrière, N. M., Tomsick, J. A., Baganoff, F. K., Boggs, S. E., Christensen, F. E., Craig, W. W., et al. (2014). NuSTAR detection of high-energy X-ray emission and rapid variability from Sagittarius A* flares. *Astrophysical J.* 786, 46. doi:10.1088/0004-637X/786/1/46

Beilicke, M., and VERITAS Collaboration (2012). The Galactic Center region imaged by VERITAS. *Nucl. Instrum. Methods Phys. Res. A* 692, 208–211. doi:10.1016/j.nima.2012.01.045

Bortolas, E., Mapelli, M., and Spera, M. (2017). Supernova kicks and dynamics of compact remnants in the Galactic Centre. *MNRAS* 469, 1510–1520. doi:10.1093/mnras/stx930

Brandt, T. D., and Kocsis, B. (2015). Disrupted globular clusters can explain the galactic center gamma-ray excess. *ApJ* 812, 15. doi:10.1088/0004-637X/812/1/15

Briggs, G. P. (2019). *The genesis of magnetic fields in white dwarfs. arXiv e-prints*, arXiv:1907.04513.

Byckling, K., Mukai, K., Thorstensen, J. R., and Osborne, J. P. (2010). Deriving an X-ray luminosity function of dwarf novae based on parallax measurements. *MNRAS* 408, 2298–2311. doi:10.1111/j.1365-2966.2010.17276.x

Chakrabarti, S., Simon, J. D., Craig, P. A., Reggiani, H., Brandt, T. D., Guhathakurta, P., et al. (2023). A noninteracting galactic black hole candidate in a binary system with a main-sequence star. *Astrophysical J.* 166, 6. doi:10.3847/1538-3881/accf21

Cheng, K. S., Chernyshov, D. O., Dogiel, V. A., Ko, C. M., and Ip, W. H. (2011). Origin of the Fermi bubble. *Astrophysical J. Lett.* 731, L17. doi:10.1088/2041-8205/731/1/L17

Cheung, C. C., Johnson, T. J., Jean, P., Kerr, M., Page, K. L., Osborne, J. P., et al. (2022). Fermi LAT gamma-ray detection of the recurrent nova RS ophiuchi during its 2021 outburst. *Astrophysical J.* 935, 44. doi:10.3847/1538-4357/ac7eb7

Chuard, D., Terrier, R., Goldwurm, A., Clavel, M., Soldi, S., Morris, M. R., et al. (2018). Glimpses of the past activity of Sgr A* inferred from X-ray echoes in Sgr C. *A&A* 610, A34. doi:10.1051/0004-6361/201731864

Churazov, E., Khabibullin, I., Ponti, G., and Sunyaev, R. (2017). Polarization and long-term variability of Sgr A* X-ray echo. *MNRAS* 468, 165–179. doi:10.1093/mnras/stx443

Clavel, M., Terrier, R., Goldwurm, A., Morris, M. R., Ponti, G., Soldi, S., et al. (2013). Echoes of multiple outbursts of Sagittarius A*revealed by*Chandra*. *A&A* 558, A32. doi:10.1051/0004-6361/201321667

Dauser, T., Falkner, S., Lorenz, M., Kirsch, C., Peille, P., Cucchetti, E., et al. (2019). SIXTE: a generic X-ray instrument simulation toolkit. *A&A* 630, A66. doi:10.1051/0004-6361/201935978

Degenaar, N., and Wijnands, R. (2010). A four-year baseline Swift study of enigmatic X-ray transients located near the Galactic center. *A&A* 524, A69. doi:10.1051/0004-6361/201015322

Degenaar, N., Wijnands, R., Cackett, E. M., Homan, J., in't Zand, J. J. M., Kuulkers, E., et al. (2012). A four-year XMM-Newton/Chandra monitoring campaign of the Galactic centre: analysing the X-ray transients. *A&A* 545, A49. doi:10.1051/0004-6361/201219470

Degenaar, N., Wijnands, R., Miller, J. M., Reynolds, M. T., Kennea, J., and Gehrels, N. (2015). The Swift X-ray monitoring campaign of the center of the Milky Way. *J. High Energy Astrophysics* 7, 137–147. doi:10.1016/j.jheap.2015.03.005

De Luca, A., Caraveo, P. A., Mereghetti, S., Tiengo, A., and Bignami, G. F. (2006). A long-period, violently variable X-ray source in a young supernova remnant. *Science* 313, 814–817. doi:10.1126/science.1129185

DeWitt, C., Bandyopadhyay, R. M., Eikenberry, S. S., Blum, R., Olsen, K., Sellgren, K., et al. (2010). Near-infrared counterparts of Chandra X-ray sources toward the galactic center. *Astrophysical J.* 721, 1663–1679. doi:10.1088/0004-637X/721/2/1663

Dexter, J., and O'Leary, R. M. (2014). The peculiar pulsar population of the central parsec. *Astrophysical J. Lett.* 783, L7. doi:10.1088/2041-8205/783/1/L7

Dodds-Eden, K., Porquet, D., Trap, G., Quataert, E., Haubois, X., Gillessen, S., et al. (2009). Evidence for X-ray synchrotron emission from simultaneous mid-infrared to X-ray observations of a strong Sgr A* flare. *Astrophysical J.* 698, 676–692. doi:10.1088/0004-637X/698/1/676

Ebisawa, K., Tsujimoto, M., Paizis, A., Hamaguchi, K., Bamba, A., Cutri, R., et al. (2005). Chandra deep X-ray observation of a typical galactic plane region and near-infrared identification. *Astrophysical J.* 635, 214–242. doi:10.1086/497284

El-Badry, K., Rix, H.-W., Cendes, Y., Rodriguez, A. C., Conroy, C., Quataert, E., et al. (2023a). A red giant orbiting a black hole. *MNRAS* 521, 4323–4348. doi:10.1093/mnras/stad799

El-Badry, K., Rix, H.-W., Quataert, E., Howard, A. W., Isaacson, H., Fuller, J., et al. (2023b). A Sun-like star orbiting a black hole. *MNRAS* 518, 1057–1085. doi:10.1093/mnras/stac3140

Eraerds, T., Antonelli, V., Davis, C., Hall, D., Hetherington, O., Holland, A., et al. (2021). Enhanced simulations on the athena/wide field imager instrumental background. *J. Astronomical Telesc. Instrum. Syst.* 7, 034001. doi:10.1117/1.JATIS.7.3.034001

Favata, F., Flaccomio, E., Reale, F., Micela, G., Sciortino, S., Shang, H., et al. (2005). Bright X-ray flares in orion young stars from COUP: evidence for star-disk magnetic fields? *Astrophysical J. Suppl. Ser.* 160, 469–502. doi:10.1086/432542

Fornasini, F. M., Tomsick, J. A., Hong, J., Gotthelf, E. V., Bauer, F., Rahoui, F., et al. (2017). The NuSTAR hard X-ray survey of the norma arm region. *Astrophysical J. Suppl. Ser.* 229, 33. doi:10.3847/1538-4365/aa61fc

Gautam, A., Crocker, R. M., Ferrario, L., Ruiter, A. J., Ploeg, H., Gordon, C., et al. (2022). Millisecond pulsars from accretion-induced collapse as the origin of the Galactic Centre gamma-ray excess signal. *Nat. Astron.* 6, 703–707. doi:10.1038/s41550-022-01658-3

Generozov, A., Stone, N. C., Metzger, B. D., and Ostriker, J. P. (2018). An overabundance of black hole X-ray binaries in the Galactic Centre from tidal captures. *MNRAS* 478, 4030–4051. doi:10.1093/mnras/sty1262

Genzel, R., Eisenhauer, F., and Gillessen, S. (2010). The Galactic Center massive black hole and nuclear star cluster. *Rev. Mod. Phys.* 82, 3121–3195. doi:10.1103/RevModPhys.82.3121

Genzel, R., Schödel, R., Ott, T., Eckart, A., Alexander, T., Lacombe, F., et al. (2003). Near-infrared flares from accreting gas around the supermassive black hole at the Galactic Centre. *Nature* 425, 934–937. doi:10.1038/nature02065

Getman, K. V., Feigelson, E. D., Broos, P. S., Micela, G., and Garmire, G. P. (2008a). X-ray flares in orion young stars. I. Flare characteristics. *Astrophysical J.* 688, 418–436. doi:10.1086/592033

Getman, K. V., Feigelson, E. D., Micela, G., Jardine, M. M., Gregory, S. G., and Garmire, G. P. (2008b). X-ray flares in orion young stars. II. Flares, magnetospheres, and protoplanetary disks. *ApJ* 688, 437–455. doi:10.1086/592034

Getman, K. V., Flaccomio, E., Broos, P. S., Grosso, N., Tsujimoto, M., Townsley, L., et al. (2005). Chandra orion ultradeep project: observations and source lists. *Astrophysical J. Suppl. Ser.* 160, 319–352. doi:10.1086/432092

Ghez, A. M., Wright, S. A., Matthews, K., Thompson, D., Le Mignant, D., Tanner, A., et al. (2004). Variable infrared emission from the supermassive black hole at the center of the Milky way. *ApJL* 601, L159–L162. doi:10.1086/382024

Glassgold, A. E., Najita, J., and Igea, J. (1997). X-ray ionization of protoplanetary disks. *ApJ* 480, 344–350. doi:10.1086/303952

Glassgold, A. E., Najita, J., and Igea, J. (2004). Heating protoplanetary disk atmospheres. *ApJ* 615, 972–990. doi:10.1086/424509

Gomez, S., and Grindlay, J. E. (2021). Optical analysis and modeling of HD96670, a new black hole X-ray binary candidate. *ApJ* 913, 48. doi:10.3847/1538-4357/abf24c

Goodenough, L., and Hooper, D. (2009). *Possible evidence for dark matter annihilation in the inner Milky way from the Fermi gamma ray space telescope. arXiv e-prints*, arXiv:0910.2998. doi:10.48550/arXiv.0910.2998

GRAVITY Collaboration, Abuter, R., Amorim, A., Bauböck, M., Berger, J. P., Bonnet, H., et al. (2018). Detection of orbital motions near the last stable circular orbit of the massive black hole SgrA. *A&A* 618, L10. doi:10.1051/0004-6361/201834294

GRAVITY Collaboration, Bauböck, M., Dexter, J., Abuter, R., Amorim, A., Berger, J. P., et al. (2020). Modeling the orbital motion of Sgr A*'s near-infrared flares. *A&A* 635, A143. doi:10.1051/0004-6361/201937233

GRAVITY Collaboration, Abuter, R., Amorim, A., Bauböck, M., Baganoff, F., Berger, J. P., et al. (2021). Constraining particle acceleration in Sgr A* with simultaneous GRAVITY, spitzer, NuSTAR, and Chandra observations. *A&A* 654, A22. doi:10.1051/0004-6361/202140981

Gregory, P. C., and Loredo, T. J. (1992). A new method for the detection of a periodic signal of unknown shape and period. *ApJ* 398, 146. doi:10.1086/171844

Haggard, D., Nynka, M., Mon, B., de la Cruz Hernandez, N., Nowak, M., Heinke, C., et al. (2019). Chandra spectral and timing analysis of Sgr A*'s brightest X-ray flares. *ApJ* 886, 96. doi:10.3847/1538-4357/ab4a7f

Hailey, C. J., Mori, K., Bauer, F. E., Berkowitz, M. E., Hong, J., and Hord, B. J. (2018). A density cusp of quiescent X-ray binaries in the central parsec of the Galaxy. *Nature* 556, 70–73. doi:10.1038/nature25029

Hailey, C. J., Mori, K., Perez, K., Canipe, A. M., Hong, J., Tomsick, J. A., et al. (2016). Evidence for intermediate polars as the origin of the galactic center hard X-ray emission. *ApJ* 826, 160. doi:10.3847/0004-637X/826/2/160

Hayashi, T., Kitaguchi, T., and Ishida, M. (2021). Application of a new X-ray reflection model to V1223 Sagittarii. *MNRAS* 504, 3651–3661. doi:10.1093/mnras/stab809

HESS Collaboration, Abramowski, A., Aharonian, F., Benkhali, F. A., Akhperjanian, A. G., Angüner, E. O., et al. (2016). Acceleration of petaelectronvolt protons in the galactic centre. *Nature* 531, 476–479. doi:10.1038/nature17147

Heywood, I., Camilo, F., Cotton, W. D., Yusef-Zadeh, F., Abbott, T. D., Adam, R. M., et al. (2019). Inflation of 430-parsec bipolar radio bubbles in the Galactic Centre by an energetic event. *Nature* 573, 235–237. doi:10.1038/s41586-019-1532-5

Heywood, I., Rammala, I., Camilo, F., Cotton, W. D., Yusef-Zadeh, F., Abbott, T. D., et al. (2022). The 1.28 GHz MeerKAT galactic center mosaic. *ApJ* 925, 165. doi:10.3847/1538-4357/ac449a

Hillman, Y., Shara, M. M., Prialnik, D., and Kovetz, A. (2020). A unified theory of cataclysmic variable evolution from feedback-dominated numerical simulations. *Nat. Astron.* 4, 886–892. doi:10.1038/s41550-020-1062-y

Hong, J., Mori, K., Hailey, C. J., Nynka, M., Zhang, S., Gotthelf, E., et al. (2016). NuSTAR hard X-ray survey of the galactic center region. II. X-ray point sources. *ApJ* 825, 132. doi:10.3847/0004-637X/825/2/132

Hong, J., van den Berg, M., Grindlay, J. E., Servillat, M., and Zhao, P. (2012). Discovery of a significant magnetic cataclysmic variable population in the limiting window. *ApJ* 746, 165. doi:10.1088/0004-637X/746/2/165

Hong, J. S., van den Berg, M., Grindlay, J. E., and Laycock, S. (2009). Radial distribution of X-ray point sources near the galactic center. *ApJ* 706, 223–237. doi:10.1088/0004-637X/706/1/223

Hooper, D., and Linden, T. (2011). On the origin of the gamma rays from the galactic center. *Phys. Rev. D.* 84, 1230005. doi:10.1103/PhysRevD.84.123005

Janssens, S., Shenar, T., Sana, H., Faigler, S., Langer, N., Marchant, P., et al. (2022). Uncovering astrometric black hole binaries with massive main-sequence companions with Gaia. *A&A* 658, A129. doi:10.1051/0004-6361/202141866

Johnson, S. P., Dong, H., and Wang, Q. D. (2009). A large-scale survey of X-ray filaments in the Galactic Centre. *Mon. Notices R. Astronomical Soc.* 399, 1429–1440. doi:10.1111/j.1365-2966.2009.15362.x

Keane, E., Bhattacharyya, B., Kramer, M., Stappers, B., Keane, E. F., Bhattacharyya, B., et al. (2015). "A cosmic census of radio pulsars with the SKA," in Advancing Astrophysics with the Square Kilometre Array (AASKA14), Giardini Naxos, Italy, 8 – 13 June, 2014, 40. doi:10.22323/1.215.0040

Khabibullin, I., Churazov, E., Sunyaev, R., Federrath, C., Seifried, D., and Walch, S. (2020). X-raying molecular clouds with a short flare: probing statistics of gas density and velocity fields. *MNRAS* 495, 1414–1432. doi:10.1093/mnras/staa1262

Kitaguchi, T., An, H., Beloborodov, A. M., Gotthelf, E. V., Hayashi, T., Kaspi, V. M., et al. (2014). NuSTAR and Swift observations of the fast rotating magnetized white dwarf AE aquarii. *ApJ* 782, 3. doi:10.1088/0004-637X/782/1/3

Koyama, K., Maeda, Y., Sonobe, T., Takeshima, T., Tanaka, Y., and Yamauchi, S. (1996). ASCA view of our galactic center: remains of past activities in X-rays? *PASJ* 48, 249–255. doi:10.1093/pasj/48.2.249

Koyama, K., Takikawa, Y., Hyodo, Y., Inui, T., Nobukawa, M., Matsumoto, H., et al. (2009). Spatial distribution of the galactic center diffuse X-rays and the spectra of the brightest 6.4keV clumps. *PASJ* 61, S255–S262. doi:10.1093/pasj/61.sp1.S255

Kuznetsova, E., Krivonos, R., Clavel, M., Lutovinov, A., Chernyshov, D., Hong, J., et al. (2019). Investigating the origin of the faint non-thermal emission of the Arches cluster using the 2015-2016 NuSTAR and XMM-Newton X-ray observations. *MNRAS* 484, 1627–1636. doi:10.1093/mnras/stz119

Kuznetsova, E., Krivonos, R., Lutovinov, A., and Clavel, M. (2022). Sgr B2 hard X-ray emission with INTEGRAL after 2009: still detectable? *MNRAS* 509, 1605–1613. doi:10.1093/mnras/stab3004

Langer, N., Schürmann, C., Stoll, K., Marchant, P., Lennon, D. J., Mahy, L., et al. (2020). Properties of OB star-black hole systems derived from detailed binary evolution models. *A&A* 638, A39. doi:10.1051/0004-6361/201937375

Li, Z., Morris, M. R., and Baganoff, F. K. (2013). Evidence for a parsec-scale jet from the galactic center black hole: interaction with local gas. *ApJ* 779, 154. doi:10.1088/0004-637X/779/2/154

Lu, F. J., Yuan, T. T., and Lou, Y.-Q. (2008). An imaging and spectral study of 10 X-ray filaments around the galactic center. *ApJ* 673, 915–927. doi:10.1086/524369

Madsen, K. K., García, J. A., Stern, D., Armini, R., Basso, S., Coutinho, D., et al. (2023). The high energy X-ray probe (HEX-P): instrument and mission profile. *arXiv e-prints* arXiv:2312.04678

Meidinger, N., Albrecht, S., Beitler, C., Bonholzer, M., Emberger, V., Frank, J., et al. (2020). "Development status of the wide field imager instrument for Athena," in *Space telescopes and instrumentation 2020: ultraviolet to gamma ray* (SPIE). doi:10.1117/12.2560507

Moe, M., and Di Stefano, R. (2017). Mind your ps and qs: the interrelation between period (P) and mass-ratio (Q) distributions of binary stars. *ApJS* 230, 15. doi:10.3847/1538-4365/aa6fb6

Molaro, M., Khatri, R., and Sunyaev, R. A. (2016). Probing the clumping structure of giant molecular clouds through the spectrum, polarisation and morphology of X-ray reflection nebulae. *A&A* 589, A88. doi:10.1051/0004-6361/201527760

Mondal, S., Ponti, G., Haberl, F., Anastasopoulou, K., Campana, S., Mori, K., et al. (2022). An intermediate polar candidate toward the Galactic plane. *A&A* 666, A150. doi:10.1051/0004-6361/202244264

Mondal, S., Ponti, G., Haberl, F., Mori, K., Rea, N., Morris, M. R., et al. (2023). Discovery of periodicities in two highly variable intermediate polars towards the Galactic centre. *A&A* 671, A120. doi:10.1051/0004-6361/202245553

Mori, K., Gotthelf, E. V., Zhang, S., An, H., Baganoff, F. K., Barrière, N. M., et al. (2013). NuSTAR discovery of a 3.76 s transient magnetar near Sagittarius A. *ApJL* 770, L23. doi:10.1088/2041-8205/770/2/L23

Mori, K., Hailey, C. J., Krivonos, R., Hong, J., Ponti, G., Bauer, F., et al. (2015). NuSTAR hard X-ray survey of the galactic center region I: hard X-ray morphology and spectroscopy of the diffuse emission. *ApJ* 814, 94. doi:10.1088/0004-637X/814/2/94

Mori, K., Hailey, C. J., Mandel, S., Schutt, Y. E., Bachetti, M., Coerver, A., et al. (2019). NuSTAR and Chandra observations of new X-ray transients in the central parsec of the Galaxy. *ApJ* 885, 142. doi:10.3847/1538-4357/ab4b47

Mori, K., Hailey, C. J., Schutt, T. Y. E., Mandel, S., Heuer, K., Grindlay, J. E., et al. (2021). The X-ray binary population in the galactic center revealed through multi-decade observations. *ApJ* 921, 148. doi:10.3847/1538-4357/ac1da5

Morihana, K., Tsujimoto, M., Ebisawa, K., and Gandhi, P. (2022). Deep near-infrared imaging observation of the faint X-ray point sources constituting the Galactic bulge X-ray emission. *PASJ* 74, 283–297. doi:10.1093/pasj/psab124

Morris, M., and Serabyn, E. (1996). The galactic center environment. *Annu. Rev. Astronomy Astrophysics* 34, 645–701. doi:10.1146/annurev.astro.34.1.645

Morris, M. R., Zhao, J. H., and Goss, W. M. (2014). "Nonthermal filamentary radio features within 20 pc of the Galactic center," in *The galactic center: feeding and feedback in a normal galactic nucleus*. Editors L. O. Sjouwerman, C. C. Lang, and J. Ott, 369–373.

Mossoux, E., Finociety, B., Beckers, J. M., and Vincent, F. H. (2020). Continuation of the X-ray monitoring of Sgr A*: the increase in bright flaring rate confirmed. *A&A* 636, A25. doi:10.1051/0004-6361/201937136

Mukai, K. (2017). X-ray emissions from accreting white dwarfs: a review. *Publ. Astronomical Soc. Pac.* 129, 062001. doi:10.1088/1538-3873/aa6736

Muno, M. P., Baganoff, F. K., Bautz, M. W., Brandt, W. N., Broos, P. S., Feigelson, E. D., et al. (2003). A deep Chandra catalog of X-ray point sources toward the galactic center. *ApJ* 589, 225–241. doi:10.1086/374639

Muno, M. P., Baganoff, F. K., Brandt, W. N., Morris, M. R., and Starck, J.-L. (2008). A catalog of diffuse X-ray-emitting features within 20 pc of Sagittarius A*: twenty pulsar wind nebulae? *ApJ* 673, 251–263. doi:10.1086/521641

Muno, M. P., Baganoff, F. K., Brandt, W. N., Park, S., and Morris, M. R. (2007). Discovery of variable iron fluorescence from reflection nebulae in the galactic center. *ApJL* 656, L69–L72. doi:10.1086/512236

Muno, M. P., Bauer, F. E., Baganoff, F. K., Bandyopadhyay, R. M., Bower, G. C., Brandt, W. N., et al. (2009). A catalog of X-ray point sources from two megaseconds of Chandra observations of the galactic center. *ApJS* 181, 110–128. doi:10.1088/0067-0049/181/1/110

Muno, M. P., Pfahl, E., Baganoff, F. K., Brandt, W. N., Ghez, A., Lu, J., et al. (2005). An overabundance of transient X-ray binaries within 1 parsec of the galactic center. *ApJL* 622, L113–L116. doi:10.1086/429721

Nandra, K., Barret, D., Barcons, X., Fabian, A., den Herder, J.-W., Piro, L., et al. (2013). *The hot and energetic universe: a white paper presenting the science theme motivating the Athena+ mission. arXiv e-prints*, arXiv:1306.2307. doi:10.48550/arXiv.1306.2307

Neilsen, J., Nowak, M. A., Gammie, C., Dexter, J., Markoff, S., Haggard, D., et al. (2013). A Chandra/HETGS census of X-ray variability from Sgr A* during 2012. *ApJ* 774, 42. doi:10.1088/0004-637X/774/1/42

Nobukawa, M., Ryu, S. G., Tsuru, T. G., and Koyama, K. (2011). New evidence for high activity of the supermassive black hole in our galaxy. *ApJL* 739, L52. doi:10.1088/2041-8205/739/2/L52

Nowak, M. A., Neilsen, J., Markoff, S. B., Baganoff, F. K., Porquet, D., Grosso, N., et al. (2012). Chandra/HETGS observations of the brightest flare seen from Sgr A. *ApJ* 759, 95. doi:10.1088/0004-637X/759/2/95

Nynka, M., Hailey, C. J., Mori, K., Baganoff, F. K., Bauer, F. E., Boggs, S. E., et al. (2013). High-energy X-rays from j174545.5-285829, the Cannonball: a candidate pulsar wind nebula associated with Sgr A East. *ApJL* 778, L31. doi:10.1088/2041-8205/778/2/L31

Nynka, M., Hailey, C. J., Reynolds, S. P., An, H., Baganoff, F. K., Boggs, S. E., et al. (2015). G359.97-0.038: a hard X-ray filament associated with a supernova shell-molecular cloud interaction. *ApJ* 800, 119. doi:10.1088/0004-637X/800/2/119

Pala, A. F., and Gänsicke, B. T. (2017). "Dynamical masses of accreting white dwarfs," in *20th European white dwarf workshop*. Editors P. E. Tremblay, B. Gaensicke, and T. Marsh (San Francisco: Astronomical Society of the Pacific), 91.

Panamarev, T., Just, A., Spurzem, R., Berczik, P., Wang, L., and Arca Sedda, M. (2019). Direct N-body simulation of the Galactic centre. *MNRAS* 484, 3279–3290. doi:10.1093/mnras/stz208

Pelisoli, I., Marsh, T. R., Buckley, D. A. H., Heywood, I., Potter, S. B., Schwope, A., et al. (2023). A 5.3-min-period pulsing white dwarf in a binary detected from radio to X-rays. *Nat. Astron.* 7, 931–942. doi:10.1038/s41550-023-01995-x

Perez, K., Hailey, C. J., Bauer, F. E., Krivonos, R. A., Mori, K., Baganoff, F. K., et al. (2015). Extended hard-X-ray emission in the inner few parsecs of the Galaxy. *Nature* 520, 646–649. doi:10.1038/nature14353

Perez, K., Krivonos, R., and Wik, D. R. (2019). The galactic bulge diffuse emission in broadband X-rays with NuSTAR. *ApJ* 884, 153. doi:10.3847/1538-4357/ab4590

Pfeifle, R. W., Boorman, R. G., Weaver, K. A., Buchner, J., Civano, F., Madsen, K., et al. (2023). The high energy X-ray Probe (HEX-P): the future of hard X-ray dual AGN science. *arXiv e-prints*. doi:10.48550/arXiv.2311.05154

Ponti, G., De Marco, B., Morris, M. R., Merloni, A., Muñoz-Darias, T., Clavel, M., et al. (2015a). Fifteen years of XMM-Newton and Chandra monitoring of Sgr A*: evidence for a recent increase in the bright flaring rate. *MNRAS* 454, 1525–1544. doi:10.1093/mnras/stv1537

Ponti, G., George, E., Scaringi, S., Zhang, S., Jin, C., Dexter, J., et al. (2017). A powerful flare from Sgr A* confirms the synchrotron nature of the X-ray emission. *MNRAS* 468, 2447–2468. doi:10.1093/mnras/stx596

Ponti, G., Morris, M. R., Churazov, E., Heywood, I., and Fender, R. P. (2021). The Galactic center chimneys: the base of the multiphase outflow of the Milky Way. *A&A* 646, A66. doi:10.1051/0004-6361/202039636

Ponti, G., Morris, M. R., Terrier, R., Haberl, F., Sturm, R., Clavel, M., et al. (2015b). The XMM-Newton view of the central degrees of the Milky Way. *MNRAS* 453, 172–213. doi:10.1093/mnras/stv1331

Ponti, G., Terrier, R., Goldwurm, A., Belanger, G., and Trap, G. (2010). Discovery of a superluminal Fe K echo at the galactic center: the glorious past of Sgr A* preserved by molecular clouds. *ApJ* 714, 732–747. doi:10.1088/0004-637X/714/1/732

Pretorius, M. L., and Mukai, K. (2014). Constraints on the space density of intermediate polars from the Swift-BAT survey. *MNRAS* 442, 2580–2585. doi:10.1093/mnras/stu990

Revnivtsev, M., Sazonov, S., Churazov, E., Forman, W., Vikhlinin, A., and Sunyaev, R. (2009). Discrete sources as the origin of the galactic x-ray ridge emission. *Nature* 458, 1142–1144. doi:10.1038/nature07946

Revnivtsev, M. G., Churazov, E. M., Sazonov, S. Y., Sunyaev, R. A., Lutovinov, A. A., Gilfanov, M. R., et al. (2004). Hard X-ray view of the past activity of Sgr A* in a natural Compton mirror. *A&A* 425, L49–L52. doi:10.1051/0004-6361:200400064

Rodriguez, A. C., Galiullin, I., Gilfanov, M., Kulkarni, S. R., Khamitov, I., Bikmaev, I., et al. (2023). *SRGeJ045359.9+622444: a 55-min period eclipsing AM CVn discovered from a joint SRG/eROSITA + ZTF search*. arXiv e-prints, arXiv:2306.13133. doi:10.48550/arXiv.2306.13133

Rogers, F., Zhang, S., Perez, K., Clavel, M., and Taylor, A. (2022). New constraints on cosmic particle populations at the galactic center using X-ray observations of the molecular cloud Sagittarius B2. *ApJ* 934, 19. doi:10.3847/1538-4357/ac7717

Ryu, S. G., Nobukawa, M., Nakashima, S., Tsuru, T. G., Koyama, K., and Uchiyama, H. (2013). X-ray echo from the Sagittarius C complex and 500-year activity history of Sagittarius A. *PASJ* 65, 33. doi:10.1093/pasj/65.2.33

Sazonov, S., Paizis, A., Bazzano, A., Chelovekov, I., Khabibullin, I., Postnov, K., et al. (2020). The galactic LMXB population and the galactic centre region. *New Astron. Rev.* 88, 101536. doi:10.1016/j.newar.2020.101536

Schmitt, J. H. M. M., Czesla, S., Schneider, P. C., Freund, S., and Robrade, J. (2022). The nature of the X-ray sources constituting the 6.7 keV Galactic ridge emission. *A&A* 661, A88. doi:10.1051/0004-6361/202142876

Schödel, R., Gallego-Cano, E., Dong, H., Nogueras-Lara, F., Gallego-Calvente, A. T., Amaro-Seoane, P., et al. (2018). The distribution of stars around the Milky Way's central black hole. II. Diffuse light from sub-giants and dwarfs. *A&A* 609, A27. doi:10.1051/0004-6361/201730452

Schoedel, R., Longmore, S., Henshaw, J., Ginsburg, A., Bally, J., Feldmeier, A., et al. (2023). *The JWST galactic center survey – a white paper*. arXiv e-prints, arXiv:2310.11912. doi:10.48550/arXiv.2310.11912

Schreiber, M. R., Zorotovic, M., and Wijnen, T. P. G. (2016). Three in one go: consequential angular momentum loss can solve major problems of CV evolution. *MNRAS* 455, L16–L20. doi:10.1093/mnrasl/slv144

Shaw, A. W., Heinke, C. O., Mukai, K., Tomsick, J. A., Doroshenko, V., Suleimanov, V. F., et al. (2020). Measuring the masses of magnetic white dwarfs: a NuSTAR legacy survey. *MNRAS* 498, 3457–3469. doi:10.1093/mnras/staa2592

Sinha, A., Baghmanyan, V., Peron, G., Gallant, Y., Casanova, S., Holler, M., et al. (2022). "Search for enhanced TeV gamma ray emission from Giant Molecular Clouds using H.E.S.S," in 37th International Cosmic Ray Conference, Berlin, Germany, 12-23 July 2021. doi:10.22323/1.395.0790

Suleimanov, V. F., Doroshenko, V., and Werner, K. (2019). Hard X-ray view on intermediate polars in the Gaia era. *MNRAS* 482, 3622–3635. doi:10.1093/mnras/sty2952

Sunyaev, R., and Churazov, E. (1998). Equivalent width, shape and proper motion of the iron fluorescent line emission from molecular clouds as an indicator of the illuminating source X-ray flux history. *MNRAS* 297, 1279–1291. doi:10.1046/j.1365-8711.1998.01684.x

Sunyaev, R. A., Markevitch, M., and Pavlinsky, M. (1993). The center of the Galaxy in the recent past - a view from GRANAT. *ApJ* 407, 606–610. doi:10.1086/172542

Szölgyén, Á., and Kocsis, B. (2018). Black hole disks in galactic nuclei. *Phys. Rev. Lett.* 121, 101101. doi:10.1103/PhysRevLett.121.101101

Takata, J., Hu, C. P., Lin, L. C. C., Tam, P. H. T., Pal, P. S., Hui, C. Y., et al. (2018). A non-thermal pulsed X-ray emission of AR scorpii. *ApJ* 853, 106. doi:10.3847/1538-4357/aaa23d

Tatischeff, V., Decourchelle, A., and Maurin, G. (2012). Nonthermal X-rays from low-energy cosmic rays: application to the 6.4 keV line emission from the Arches cluster region. *A&A* 546, A88. doi:10.1051/0004-6361/201219016

Terrier, R., Clavel, M., Soldi, S., Goldwurm, A., Ponti, G., Morris, M. R., et al. (2018). An X-ray survey of the central molecular zone: variability of the Fe Kα emission line. *A&A* 612, A102. doi:10.1051/0004-6361/201730837

Terrier, R., Ponti, G., Bélanger, G., Decourchelle, A., Tatischeff, V., Goldwurm, A., et al. (2010). Fading hard X-ray emission from the galactic center molecular cloud Sgr B2. *ApJ* 719, 143–150. doi:10.1088/0004-637X/719/1/143

Tomsick, J. A., Kumar, S. G., Coughenour, B. M., Shaw, A. W., Mukai, K., Hare, J., et al. (2023). *Classifying IGR J15038-6021 as a magnetic CV with a massive white dwarf. arXiv e-prints*, arXiv:2306.04691. doi:10.48550/arXiv.2306.04691

Tomsick, J. A., Rahoui, F., Krivonos, R., Clavel, M., Strader, J., and Chomiuk, L. (2016). Identifying IGR J14091-6108 as a magnetic CV with a massive white dwarf using X-ray and optical observations. *MNRAS* 460, 513–523. doi:10.1093/mnras/stw871

Türler, M., Chernyakova, M., Courvoisier, T. J.-L., Lubiński, P., Neronov, A., Produit, N., et al. (2010). INTEGRAL hard X-ray spectra of the cosmic X-ray background and Galactic ridge emission. *A&A* 512, A49. doi:10.1051/0004-6361/200913072

van Eldik, C., and H. E. S. S. Collaboration (2008). The H.E.S.S. view of the Galactic Centre region. *Nucl. Instrum. Methods Phys. Res. A* 588, 72–75. doi:10.1016/j.nima.2008.01.025

Vermette, B., Salcedo, C., Mori, K., Gerber, J., Yoon, K. D., Bridges, G., et al. (2023). *Constraining white dwarf mass and magnetic field strength of a new intermediate polar through X-ray observations. arXiv e-prints*, arXiv:2307.11910. doi:10.48550/arXiv.2307.11910

Wang, Q. D., Gotthelf, E. V., and Lang, C. C. (2002). A faint discrete source origin for the highly ionized iron emission from the Galactic Centre region. *Nature* 415, 148–150. doi:10.1038/415148a

Wielgus, M., Moscibrodzka, M., Vos, J., Gelles, Z., Martí-Vidal, I., Farah, J., et al. (2022). Orbital motion near Sagittarius A*. Constraints from polarimetric ALMA observations. *A&A* 665, L6. doi:10.1051/0004-6361/202244493

Xu, X.-j., Li, Z., Zhu, Z., Cheng, Z., Li, X.-d., and Yu, Z.-l. (2019a). Massive white dwarfs in the galactic center: a Chandra X-ray spectroscopy of cataclysmic variables. *ApJ* 882, 164. doi:10.3847/1538-4357/ab32df

Xu, X.-j., Wang, Q. D., and Li, X.-D. (2016). Fe line diagnostics of cataclysmic variables and Galactic Ridge X-Ray emission. *ApJ* 818, 136. doi:10.3847/0004-637X/818/2/136

Xu, X.-j., Yu, Z.-l., and Li, X.-d. (2019b). The Fe line flux ratio as a diagnostic of the maximum temperature and the white dwarf mass of cataclysmic variables. *ApJ* 878, 53. doi:10.3847/1538-4357/ab1fe1

Yuasa, T., Makishima, K., and Nakazawa, K. (2012). Broadband spectral analysis of the Galactic Ridge X-Ray emission. *ApJ* 753, 129. doi:10.1088/0004-637X/753/2/129

Yuasa, T., Tamura, K.-I., Nakazawa, K., Kokubun, M., Makishima, K., Bamba, A., et al. (2008). Suzaku detection of extended/diffuse hard X-ray emission from the galactic center. *PASJ* 60, S207–S221. doi:10.1093/pasj/60.sp1.S207

Yusef-Zadeh, F., Arendt, R. G., Wardle, M., and Heywood, I. (2023). The population of the galactic center filaments: position angle distribution reveals a degree-scale collimated outflow from Sgr A* along the galactic plane. *ApJL* 949, L31. doi:10.3847/2041-8213/acd54b

Yusef-Zadeh, F., Morris, M., and Chance, D. (1984). Large, highly organized radio structures near the galactic centre. *Nature* 310, 557–561. doi:10.1038/310557a0

Zhang, S., Baganoff, F. K., Ponti, G., Neilsen, J., Tomsick, J. A., Dexter, J., et al. (2017). Sagittarius A* high-energy X-ray flare properties during*NuStar*Monitoring of the galactic center from 2012 to 2015. *ApJ* 843, 96. doi:10.3847/1538-4357/aa74e8

Zhang, S., Hailey, C. J., Baganoff, F. K., Bauer, F. E., Boggs, S. E., Craig, W. W., et al. (2014). High-energy X-ray detection of g359.89-0.08 (Sgr A-E): magnetic flux tube emission powered by cosmic rays? *ApJ* 784, 6. doi:10.1088/0004-637X/784/1/6

Zhang, S., Hailey, C. J., Baganoff, F. K., Bauer, F. E., Boggs, S. E., Craig, W. W., et al. (2015). Hard X-ray morphological and spectral studies of the galactic center molecular cloud Sgr B2: constraining past Sgr A* flaring activity. *Astrophysical J.* 815, 132. doi:10.1088/0004-637X/815/2/132

Zhang, S., Zhu, Z., Li, H., Pasham, D., Li, Z., Clavel, M., et al. (2020). NuSTAR and Chandra observations of the galactic center nonthermal X-ray filament g0.13-0.11: a pulsar-wind-nebula-driven magnetic filament. *ApJ* 893, 3. doi:10.3847/1538-4357/ab7dc1

Zhao, J.-H., Morris, M. R., and Goss, W. M. (2013). Radio detection of a candidate neutron star associated with galactic center supernova remnant Sagittarius A East. *ApJ* 777, 146. doi:10.1088/0004-637X/777/2/146

Zhu, Z., Li, Z., and Morris, M. R. (2018). An ultradeep Chandra catalog of X-ray point sources in the galactic center star cluster. *ApJS* 235, 26. doi:10.3847/1538-4365/aab14f

frontiers | Frontiers in Astronomy and Space Sciences

TYPE Original Research
PUBLISHED 09 January 2024
DOI 10.3389/fspas.2023.1294449

Check for updates

OPEN ACCESS

EDITED BY
Renee Ludlam,
Wayne State University, United States

REVIEWED BY
Alice Borghese,
Instituto de Astrofisica de Canarias, Spain
Silvia Zane,
University College London,
United Kingdom

*CORRESPONDENCE
J. A. J. Alford,
alford@nyu.edu

RECEIVED 14 September 2023
ACCEPTED 06 December 2023
PUBLISHED 09 January 2024

CITATION
Alford JAJ, Younes GA, Wadiasingh Z, Abdelmaguid M, An H, Bachetti M, Baring MG, Beloborodov A, Chen AY, Enoto T, García JA, Gelfand JD, Gotthelf EV, Harding AK, Hu C-P, Jaodand AD, Kaspi V, Kim C, Kouveliotou C, Kuiper L, Mori K, Nynka M, Park J, Stern D, Valverde J and Walton DJ (2024), The high energy X-ray probe (HEX-P): magnetars and other isolated neutron stars.
Front. Astron. Space Sci. 10:1294449.
doi: 10.3389/fspas.2023.1294449

COPYRIGHT
© 2024 Alford, Younes, Wadiasingh, Abdelmaguid, An, Bachetti, Baring, Beloborodov, Chen, Enoto, García, Gelfand, Gotthelf, Harding, Hu, Jaodand, Kaspi, Kim, Kouveliotou, Kuiper, Mori, Nynka, Park, Stern, Valverde and Walton. This is an open-access article distributed under the terms of the Creative Commons Attribution License (CC BY). The use, distribution or reproduction in other forums is permitted, provided the original author(s) and the copyright owner(s) are credited and that the original publication in this journal is cited, in accordance with accepted academic practice. No use, distribution or reproduction is permitted which does not comply with these terms.

The high energy X-ray probe (HEX-P): magnetars and other isolated neutron stars

J. A. J. Alford[1]*, G. A. Younes[2], Z. Wadiasingh[3,4,5], M. Abdelmaguid[1], H. An[6], M. Bachetti[7], M. G. Baring[8], A. Beloborodov[9], A. Y. Chen[10], T. Enoto[11], J. A. García[12], J. D. Gelfand[1], E. V. Gotthelf[9], A. K. Harding[13], C-P. Hu[14], A. D. Jaodand[15], V. Kaspi[16], C. Kim[6], C. Kouveliotou[2], L. Kuiper[17], K. Mori[9], M. Nynka[18], J. Park[6], D. Stern[19], J. Valverde[20] and D. J. Walton[21]

[1]NYU Abu Dhabi, Abu Dhabi, United Arab Emirates, [2]Department of Physics, The George Washington University, Washington, DC, United States, [3]Astrophysics Science Division, NASA/GSFC, Greenbelt, MD, United States, [4]Department of Astronomy, University of Maryland, College Park, MD, United States, [5]Center for Research and Exploration in Space Science and Technology, NASA/GSFC, Greenbelt, MD, United States, [6]Department of Astronomy and Space Science, Chungbuk National University, Cheongju, Republic of Korea, [7]INAF-Osservatorio Astronomico di Cagliari, Selargius, Italy, [8]Department of Physics and Astronomy—MS 108, Rice University, Houston, TX, United States, [9]Columbia Astrophysics Laboratory, Columbia University, New York, NY, United States, [10]Physics Department and McDonnell Center for the Space Sciences, Washington University in St. Louis, St. Louis, MO, United States, [11]Extreme Natural Phenomena RIKEN Hakubi Research Team, Cluster for Pioneering Research, RIKEN, Wako, Saitama, Japan, [12]X-ray Astrophysics Laboratory, NASA Goddard Space Flight Center, Greenbelt, MD, United States, [13]Theoretical Division, Los Alamos National Laboratory, Los Alamos, NM, United States, [14]Department of Physics, National Changhua University of Education, Changhua, Taiwan, [15]Division of Physics, California Institute of Technology, Pasadena, CA, United States, [16]Department of Physics, McGill University, 3600 rue University, Montreal, QC, Canada, [17]SRON-Netherlands Institute for Space Research, Leiden, Netherlands, [18]Kavli Institute For Astrophysics and Space Research, Massachusetts Institute of Technology, Cambridge, MA, United States, [19]Jet Propulsion Laboratory, California Institute of Technology, Pasadena, CA, United States, [20]Department of Physics and Center for Space Sciences and Technology, University of Maryland Baltimore County, Baltimore, MD, United States, [21]Centre for Astrophysics Research, University of Hertfordshire, College Lane, Hatfield, United Kingdom

The hard X-ray emission from magnetars and other isolated neutron stars remains under-explored. An instrument with higher sensitivity to hard X-rays is critical to understanding the physics of neutron star magnetospheres and also the relationship between magnetars and Fast Radio Bursts (FRBs). High sensitivity to hard X-rays is required to determine the number of magnetars with hard X-ray tails, and to track transient non-thermal emission from these sources for years post-outburst. This sensitivity would also enable previously impossible studies of the faint non-thermal emission from middle-aged rotation-powered pulsars (RPPs), and detailed phase-resolved spectroscopic studies of younger, bright RPPs. The High Energy X-ray Probe (HEX-P) is a probe-class mission concept that will combine high spatial resolution X-ray imaging (<5 arcsec half-power diameter (HPD) at 0.2–25 keV) and broad spectral coverage (0.2–80 keV) with a sensitivity superior to current facilities (including XMM-Newton and NuSTAR). HEX-P has the required timing resolution to perform follow-up observations of sources identified by other facilities and positively identify candidate pulsating neutron stars. Here we discuss how HEX-P is ideally

suited to address important questions about the physics of magnetars and other isolated neutron stars.

KEYWORDS

X-ray sources, HEX-P, pulsars, magnetars, neutron stars, spectra Frontiers

1 Introduction

Massive stars ($\gtrsim 8\ M_\odot$) end their lives in spectacular supernovae, leaving behind either a neutron star (NS) or a black hole (BH) (Heger et al., 2003). NSs are very compact (having masses of ≈1.4 $M_\odot$ and radii of ≈10 km), and isolated NSs typically have strong magnetic fields ($B \gtrsim 10^{12}$ G, though see the discussion of central compact objects (CCOs) below). The telltale sign for the existence of an NS is the detection of their spin ephemerides, most notably their spin periods P and, if multi-epoch observations exist, their period derivatives $\dot{P}$. These two observational properties can be used to estimate three key fundamental physical scales under the assumption of a rotating dipole magnet in vacuum (Figure 1): 1) rotational energy loss $|\dot{E}| \propto \dot{P}/P^3$, 2) characteristic spin-down age $\tau_{\rm char} = P/2\dot{P}$, and 3) surface dipolar magnetic field strength $B_{\rm dip} \propto \sqrt{P\dot{P}}$.

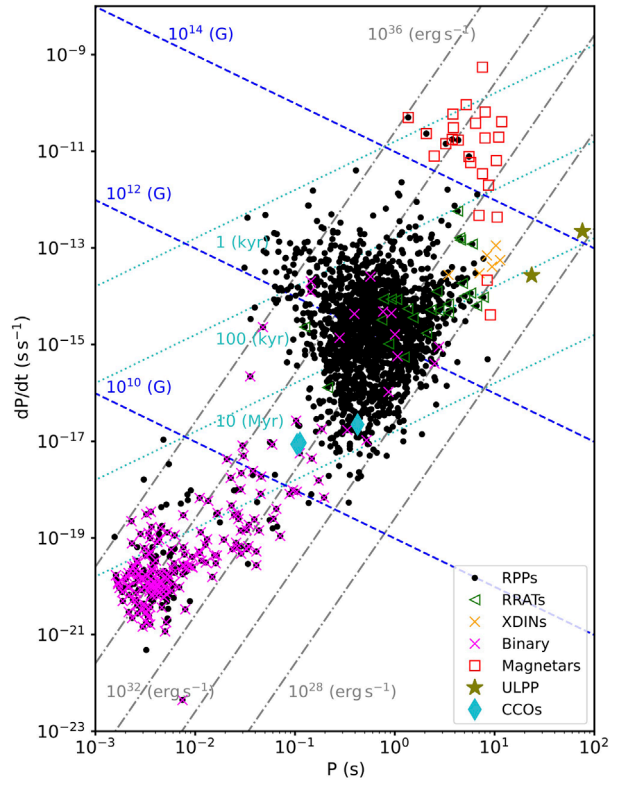

FIGURE 1
Pulsar period period-derivative diagram highlighting the range of neutron star classes. Note lines of constant rotational energy loss $|\dot{E}| \propto \dot{P}/P^3$, characteristic spin-down age $\tau_{\rm char} = P/2\dot{P}$, and surface dipolar magnetic field strength $B_{\rm dip} \propto \sqrt{P\dot{P}}$. Data are from the ATNF pulsar catalog version 1.65 (Manchester et al., 2005).

Since their discovery, a number of unique classes of isolated NSs (INSs) have been identified through differences in their broadband emission characteristics, location/environment, and timing behavior. The most common of the INS population are the rotation-powered pulsars (RPPs), aptly named given that their large spin-down power $\dot{E}$ far exceeds their total radiative luminosity. Then, there are the magnetars, which possess periods typically in the range of about 1–15 s and large spin-down rates ($\dot{P} \sim 10^{-11}$ s s^{-1}), thus occupying a unique space in the P-$\dot{P}$ diagram (Figure 1, red squares). Assuming magnetic dipole braking, the magnetar timing properties translate to dipole field strengths of the order of 10^{14} G (two orders of magnitude larger than RPPs, Kouveliotou et al., 1998; Kouveliotou et al., 1999; Kaspi et al., 2003), average spin-down ages of 10^4 years (confirmed through the association of a few with young, X-ray bright supernova remnants (SNRs), see, e.g., Vasisht and Gotthelf 1997), and low spin-down power $|\dot{E}| \sim 10^{32}$ erg s^{-1} (Olausen and Kaspi, 2014). Despite the latter, magnetars are observed as hot thermal emitters with surface thermal temperatures $kT \approx 0.5$ keV (factors of ~2 larger than young RPPs; see, e.g., Figure 1 of Olausen and Kaspi, 2014), and X-ray luminosities $\gtrsim 10^{33}$ erg s^{-1}. Hence, magnetar radiative power is attributed to the decay of their extreme external and internal B-fields (Thompson and Duncan, 1995; Kaspi and Beloborodov, 2017).

Then there are the dozen known CCOs, which are perhaps the least understood class of INSs (De Luca, 2017). The three CCOs with measured spin ephemerides are indicated with blue diamonds in Figure 1. These point-like X-ray sources are found in young X-ray bright SNRs, and lack both emission at other wavelengths and any associated pulsar wind nebula. While there are relatively few identified CCOs, their locations in young SNRs suggests that they may represent a significant fraction of NS births. CCOs are also known as "anti-magnetars," since some of them have the smallest spin-down-measured dipole magnetic field strengths among all known young NSs (Gotthelf et al., 2013), at odds with their relatively bright thermal X-ray emission.

X-ray dim isolated NSs (XDINSs, yellow crosses in Figure 1) constitute a population with observational characteristics that do not quite fit the above classes. They are nearby (within a few hundred parsecs, Kaplan, 2008), radio-quiet (but see Rigoselli et al., 2019), yet thermally-emitting with surface temperatures in the range of 45–110 eV and luminosities $L_{\rm X} < 10^{32}$ erg s^{-1}. This emission is pulsed at a spin-period of a few seconds, while slowing down with a rate of $\dot{P} \approx 10^{-14}$ s s^{-1}, implying $B_{\rm dip} \sim 10^{13}$ G, $\tau \gtrsim 1$ Myr, and an average $\dot{E} \sim 5 \times 10^{30}$ erg s^{-1}. Given their small $|\dot{E}|$ compared to their surface thermal emission, XDINS are thought to be powered by their relatively large B-fields, akin to magnetars, which are thought to be their younger counterparts according to magneto-thermal evolutionary models.

Recently, a new class of long-period radio-emitting NSs have been discovered with spin periods of tens of seconds and relatively large spin-down rates (Tan et al., 2018; Caleb et al., 2022; green stars

in Figure 1). Their dipole-inferred fields are comparable to those of magnetars and XDINs. They are also relatively nearby with distances of the order of 1 kpc, yet deep X-ray observations have not detected their high energy counterpart with upper-limits comparable to those of XDINs (Rea et al., 2022; Beniamini et al., 2023). These limits are consistent with the old magnetar interpretation, though how they maintain dipolar-fields of 10^{14} G is less clear (Caleb et al., 2022; Beniamini et al., 2023).

Our understanding of the young INS population has been predominantly shaped by radio and X-ray observations. Radio surveys of large areas of the Galaxy provide understanding of the birth rate and properties of NSs (e.g., Arzoumanian et al., 2002; Faucher-Giguère and Kaspi, 2006), while X-ray observations established several of the above sub-classes, and highlighted the connections among them; e.g., RPPs and CCOs showing magnetar-like bursting and outburst abilities (Gavriil et al., 2008; Archibald et al., 2016b; Rea et al., 2016), the existence of low *B*-field magnetars (Rea et al., 2010), and bona-fide magnetars with RPP characteristics such as radio emission and pulsar wind nebulae (Camilo et al., 2006; Camilo et al., 2007; Younes et al., 2016). All of these X-ray discoveries have led to several attempts at unifying these sub-classes (Kaspi and Boydstun, 2010), mainly through magneto-thermal evolution models (Viganò et al., 2013; Gourgouliatos et al., 2016). Lastly, in a breakthrough discovery, the long-held view that Fast Radio Bursts (FRBs) might be powered by magnetar activity was confirmed after the detection of an FRB (CHIME/FRB Collaboration et al., 2020; Bochenek et al., 2020) simultaneous with a hard X-ray burst (e.g., Mereghetti et al., 2020; Li et al., 2021) from a Galactic magnetar in outburst (see Zhang (2023) for a review of FRBs).

In this paper, we present the case for the probe-class mission HEX-P as the next-generation X-ray satellite to build upon the legacy of all past and current X-ray satellites, and open up avenues for new discoveries in the timely field of high energy studies of young INSs. A companion paper, Ludlam et al. (in prep.), discusses the power of HEX-P to study neutron stars in low- and high-mass binary systems.

2 Mission design

The High-Energy X-ray Probe (HEX-P; Madsen et al., 2015) is a probe-class mission concept that offers sensitive broad-band coverage (0.2–80 keV) of the X-ray spectrum with exceptional spectral, timing and angular capabilities. It features two high-energy telescopes (HETs) that focus hard X-rays and one low-energy telescope (LET) that focuses lower-energy X-rays. The HET and LET will observe simultaneously, and both telescopes are well suited for timing studies (e.g., periodicity searches), with timing resolution ~1 μs and 1 m. The HEX-P LET and HET will achieve a factor of ~3 and ~10 or better improvements in sensitivity over XMM-EPIC and NuSTAR telescopes in the 0.2–20 and 3–70 keV bands, respectively. These sensitivity improvements are partially due to the high earth orbit (HEO), in contrast to NuSTAR's low earth orbit (LEO).

The LET consists of a segmented mirror assembly coated with Ir on monocrystalline silicon that achieves a half power diameter of 3.5″, and a low-energy DEPFET detector, of the same type as the Wide Field Imager (WFI; Meidinger et al., 2020) onboard Athena (Nandra et al., 2013). It has 512 × 512 pixels that cover a field of view of 11.3′ × 11.3′ (1.32″/pixel). It has an effective passband of 0.2–25 keV, and a full frame readout time of 2 m, which can be operated in a 128 and 64 channel window mode for higher count-rates to mitigate pile-up and faster readout. Pile-up effects remain below an acceptable limit of ~1% for fluxes up to ~100 mCrab in the smallest window configuration. Excising the core of the point spread function (PSF), a common practice in X-ray astronomy, will allow for observations of brighter sources, with a typical loss of up to ~60% of the total photon counts.

The HET consists of two co-aligned telescopes and detector modules. The optics are made of Ni-electroformed full shell mirror substrates, leveraging the heritage of XMM-Newton (Jansen et al., 2001), and coated with Pt/C and W/Si multilayers for an effective passband of 2–80 keV. The high-energy detectors are of the same type as flown on NuSTAR (Harrison et al., 2013), and they consist of 16 CZT sensors per focal plane, tiled 4 × 4, for a total of 128 × 128 pixel spanning a field of view of 13.4′ × 13.4′.

The broad X-ray passband and superior sensitivity will provide a unique opportunity to study INSs across a wide range of energies, luminosity, and dynamical regimes.

3 Simulations

All the simulations presented here were produced with a set of response files that represent the observatory performance based on current best estimates as of Spring 2023 (see Madsen et al., 2023). The effective area is derived from a ray-trace of the mirror design including obscuration by all known structures. The detector responses are based on simulations performed by the respective hardware groups, with an optical blocking filter for the LET and a Be window and thermal insulation for the HET. The LET background was derived from a GEANT4 simulation (Eraerds et al., 2021) of the WFI instrument, and the HET background was derived from a GEANT4 simulation of the NuSTAR instrument, with both simulations adopting a Lagrange point L1 orbit for HEX-P.

We utilize Xspec version 12.13.0c to simulate point source spectra, implementing HEX-P LET and HET response matrices, ancillary, and background files version v07 (Arnaud, 1996). All simulated spectra are binned to have 5 counts per energy channel. For spectral fitting, we utilize the Cash-statistic (C-stat in Xspec, Cash, 1979), to derive the best fit model parameters and corresponding uncertainties. To assess the goodness of fit, we utilize the goodness command which simulates 1000 spectral realizations from a given model and compares their fit statistic to that of the data; if the data is drawn from the model, or, in other words, the model is a good fit to the data, the fit statistic should lie around the 50% mark.

4 Magnetars

4.1 Persistent broadband X-ray emission

Magnetar persistent emission consists of two components, a thermal emission likely emanating from surface hot-spots with temperatures of ~ 0.4–0.5 keV, and a non-thermal component

with photon index $\Gamma = 0.0$–1.5, i.e., rising in νF_ν, known as the hard X-ray tail. The latter likely originates from inverse Compton scattering of soft photons by relativistic electrons in non-potential magnetospheric loops energized by twists and currents, tied to footpoints whose evolution is driven internally by the crust of the magnetar. Due to the large magnetic fields, the scattering in the magnetosphere is resonant at the electron cyclotron frequency, which is efficient at boosting the photon energies by orders of magnitude relative to the non-resonant case, a process known as Resonant Inverse Compton Scattering (RICS).

Hard X-ray tails were first discovered in 2004 with INTEGRAL and RXTE (Kuiper et al., 2004). Prior to the NuSTAR launch, only a handful of magnetars were detected at energies >10 keV (Kuiper et al., 2006; den Hartog et al., 2008b; den Hartog et al., 2008a; Enoto et al., 2010). NuSTAR, with its superior sensitivity at hard X-rays, has doubled the pool of detected sources, which is currently standing at 10 (e.g., Enoto et al., 2017). The faintest known magnetar hard X-ray tail has a 10–100 keV flux of $\sim 10^{-12}$ erg s^{-1} cm^{-2}; an order of magnitude fainter than detections by NuSTAR predecessors. HEX-P, owing to its superior sensitivity, simultaneous broad-band coverage, and more efficient orbit, will detect magnetar hard X-ray tails an order of magnitude fainter again, and characterize their spectral curvature (i.e., a possible energy dependence of the photon index Γ). This is demonstrated through a 100 ks HEX-P simulation of a typical magnetar spectrum, i.e., $kT = 0.45$ keV, $\Gamma = 1.0$, and $N_{\rm H} = 10^{22}$ cm^{-2}, with absorption-corrected fluxes in the 1–10 keV and 10–100 keV band of 5.0×10^{-14} erg s^{-1} cm^{-2} and 10^{-13} erg s^{-1} cm^{-2}, respectively (Figure 2). The former flux level represents the faint end of the soft X-ray flux level from the currently known magnetar population while the latter is an order of magnitude fainter than the faintest magnetar hard X-ray tail known (SGR 0526–66; Park et al., 2020). The hard tail is detected up to 35 keV with a count rate of $(2.3 \pm 0.2) \times 10^{-3}$ counts s^{-1} (i.e., a 10σ detection significance), and the spectral curvature of the hard tail is constrained to 30% ($\Gamma = 1.0 \pm 0.3$). For comparison, we also perform a 100 ks simulated observation of the broad-band X-ray spectrum of the magnetar SGR 0526–66 in the Large Magellanic Cloud based on results from Chandra and NuSTAR (Park et al., 2020). HEX-P observations will produce a 10–80 keV count rate of $(44.3 \pm 0.2) \times 10^{-3}$ counts s^{-1} and a 0.5–10 keV rate of $(11.6 \pm 0.1) \times 10^{-2}$ counts s^{-1}, providing excellent quality data for a detailed spectral and temporal analysis. We note that, under the above spectral considerations, a simple 3.5σ detection of a fiducial magnetar at energies >10 keV with HET is achieved for fluxes as low as 4×10^{-14} erg s^{-1} cm^{-2}.

According to the current magnetar $\log N$-$\log S$ distribution (Figure 2, left panel), where S is the 10–100 keV flux, the HEX-P sensitivity limit will enable hard X-ray tail detection and characterization in about 30 magnetars, tripling the current number. Consequently, this will permit a far more comprehensive population-wide correlation analysis between the soft and hard X-ray properties (Marsden and White, 2001; Enoto et al., 2010; Kaspi and Boydstun, 2010; Enoto et al., 2017; Seo et al., 2023), in turn informing on the evolution of internal and external B-field and globally or locally twisted magnetospheres (Beloborodov, 2009; Parfrey et al., 2013; Viganò et al., 2013; Chen and Beloborodov, 2017).

Older magnetars, with spin-down ages $\gtrsim 10$ kyr, are less efficient at sustaining bright hard X-ray emission; their 1–100 keV luminosity is dominated by the soft thermal component from their surfaces (Enoto et al., 2010; Enoto et al., 2017). Hence, the LET is more suitable for the detection of older, fainter magnetars. We derive its detectability limit by considering a magnetar with a spectral model consisting of an absorbed ($N_{\rm H} = 10^{22}$ cm^{-2}) blackbody model with temperature $kT = 0.3$ keV (note that the magnetar surface temperature decreases with age, Viganò et al. 2013). We find that a 3.5σ detection can be achieved for observed fluxes of the order of 10^{-15} erg cm^{-2} s^{-1} (1–5 keV count rate of about $(5.5 \pm 1.5) \times 10^{-4}$ counts s^{-1}), rivaling the detection limit from XMM-Newton as well as Chandra. Hence, the LET provides an excellent opportunity to extend the legacy of the latter two observatories for the detection of the faint persistent counterparts to transient magnetars (Section 4.2).

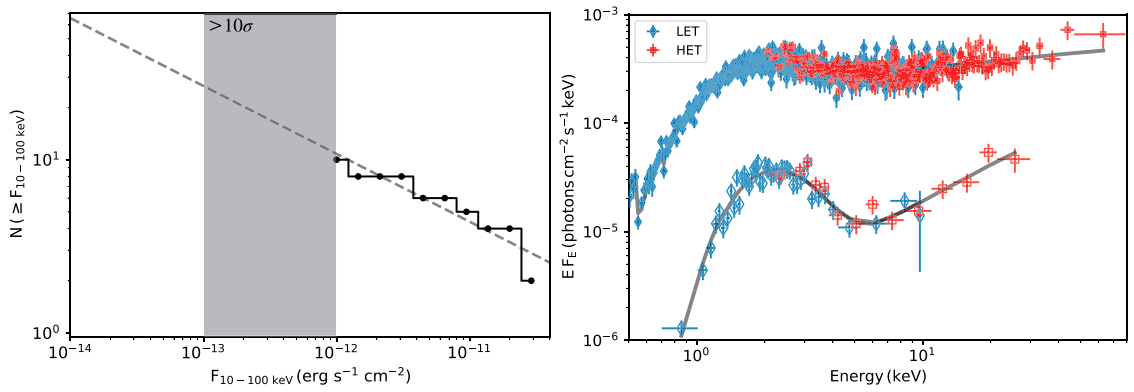

FIGURE 2
Left panel. Magnetar $\log N - \log S$ distribution in the hard (10–100 kev) X-ray band. NuSTAR doubled the number of magnetar detected at >10 keV, which currently stands at 10. The faintest hard X-ray tail known has a flux of the order 10^{-12} erg s^{-1} cm^{-2} (SGR 0526–66, Park et al., 2020. HEX-P, with its superior sensitivity, will triple the current number of hard X-ray tails detected from magnetars (gray shaded area). *Right panel.* 100 ks HEX-P simulation of the SGR 0526–66 broad-band spectrum (filled symbols) and of a generic magnetar with a hard X-ray flux in the 10–100 keV band an order of magnitude weaker than SGR 0526–66, i.e., $F_{10-100\ \rm keV} \sim 10^{-13}$ erg s^{-1} cm^{-2} (empty symbols).

For the brightest magnetars, HEX-P will also provide the most detailed look at the 0.3–80 keV spectro-temporal properties that are crucial to guide the theoretical development of radiation transport in the high B-field ($>10^{14}$ G) regime, inaccessible to terrestrial laboratories, such as photon splitting. Early predictions for the phase-resolved spectra and energy dependent profiles in the 10–80 keV band are presented in Wadiasingh et al. (2018), also see: Baring and Harding 2007; Fernández and Thompson 2007; Beloborodov 2013; Caiazzo et al., 2022; Taverna et al., 2020), and more sophisticated models are in development (e.g., Wadiasingh et al., 2019; Wadiasingh et al., 2022) Yet, the current data quality above 10 keV for even the brightest magnetars (i.e., 4U 0142 + 61 and 1RXS J170849.0−400,910), is inadequate for the detailed phase-resolved spectroscopy required to confront these models. HEX-P, providing far superior broad-band data for the brightest magnetars, will allow us to answer fundamental questions which currently remain open: 1) Where are the locales of particle acceleration within magnetar magnetospheres? 2) What are the Lorentz factors of the energetic particles? 3) How do the physical properties governing the hard X-ray tails evolve with age and field strength? 4) Is the hard X-ray emission for persistently emitting magnetars dominated by the dipolar field, or do higher order, crustal fields dominate?

RICS emission is highly anisotropic and sensitive to where cyclotron resonance in the magnetosphere is sampled by an observer. Moreover, beginning around 30 keV, photon splitting can begin to impact spectra depending in the viewing angle or, equivalently, pulse phase (Hu et al., 2019; Hu et al., 2022; Wadiasingh et al., 2022). As such, RICS radiation models may obtain a variety of phase-dependent spectral energy distributions (or equivalently, energy dependent pulse profiles) depending on viewing geometry and zones of activation of relativistic particle populations (Figure 3). Detailed fitting of phase-resolved spectra to models of RICS emission is sensitive to the activated zones and observer viewing geometry, providing answers to the open questions laid out above. Furthermore, a comparison of viewing and field geometries will test related constraints obtained for soft thermal emission hot spot modeling from IXPE observations of bright magnetars (Taverna et al., 2022; Zane et al., 2023).

RICS constraints on the relativistic electron population, along with 0.2–80 keV broadband spectroscopy provided by HEX-P will also test if return currents and particle bombardment play a significant role in heating surface layers of magnetars. Moreover, HEX-P will provide a detailed population-level phase-resolved spectral survey of magnetars. This will inform evolutionary traits in the RICS parameters with age, and determine if beaming is compatible with the lack of observed hard X-ray emission in some moderately bright X-ray magnetars. We note that fitting phase-resolved spectra with RICS models has not yet been attempted due to the paucity of pulsed counts at high energies (>10 keV). For instance, the brightest magnetar at hard X-rays, 1E 1841–045, has a *NuSTAR* count rate in the 10–79 keV band of 0.16 counts s^{-1}, which, for the 350 ks existing observation (An et al., 2015), results in 56,000 phase-averaged counts, and 11,200 pulsed counts. For a modest phase-resolved spectroscopic analysis with 10 phase bins, the 1100 counts in each bin were able to constrain the hard X-ray photon index to about ≈20% (An et al., 2015). In contrast, the HEX-P count rate for 1E 1841–045 in the same energy range is predicted to be 0.62 counts s^{-1}, which, for the same considerations above, would result in ~ 4350 counts per phase bin, allowing us to search for phase variability in the hard X-ray tail down to the $\lesssim 5$ percent level, notably aided by the LET instrument which will constrain the soft thermal part of the spectrum. Furthermore, observing from L1 rather than from low-Earth orbit like NuSTAR, HEX-P has nearly twice the observing efficiency of NuSTAR.

Lastly, we note that magnetars have attracted interest from the dark matter community as testbeds for certain axion-like particle (ALP) models. ALPs produced in the magnetar core are predicted to convert into photons in the magnetosphere. ALP models generally predict an opposite hard X-ray phase dependence to RICS, thereby enabling HEX-P to provide important constraints to the dark matter community (e.g., Maruyama et al., 2018; Fortin et al., 2021).

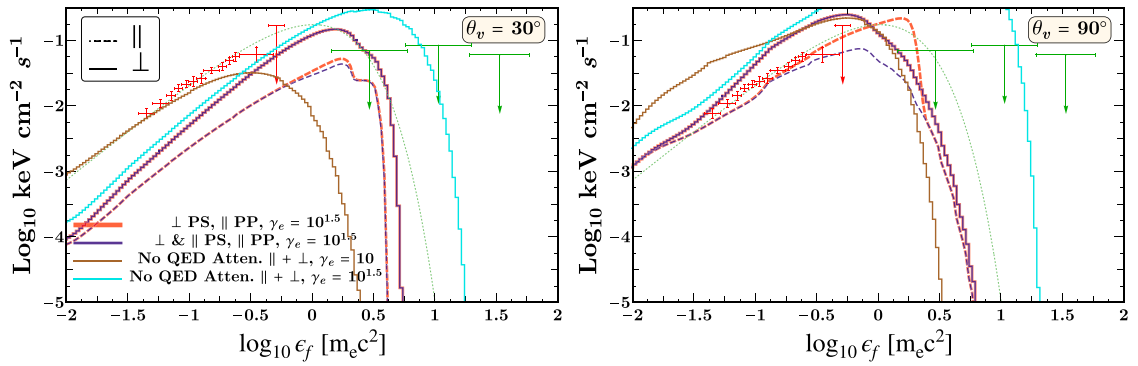

FIGURE 3
Phase-resolved RICS spectra overlaid on INTEGRAL data for 4U 0142 + 61 (orange data points, Kuiper et al., 2006), along with a power-law with exponential cutoff at 350 keV (dotted green). The model emission is computed for surface photons of temperature 5×10^6 K scattered by $\gamma_e = 10$-$10^{1.5}$ electrons uniformly populating field bundle from magnetic footpoint colatitudes 12°–45°. The assumed dipole field strength is 4×10^{14} G. Brown and dark blue lines show total intensities, while red and light blue curves show the case with QED attenuation. *Left panel.* Observer angle to magnetic axis $\theta_v = 30°$. *Right panel.* $\theta_v = 90°$. The RICS emission is predicted to be highly phase dependent, as shown here. Adapted from Wadiasingh et al. (2019).

4.2 Transient behavior–crustal and magnetospheric dynamics

In addition to the persistent magnetars, with X-ray luminosities $\sim 10^{35}$ erg s^{-1}, there are also 'transient' magnetars, which only reach $\sim 10^{35}$ erg s^{-1} during outbursts, when their X-ray fluxes can increase by up to over two orders of magnitude (Coti Zelati et al., 2018). We emsphasize that persistent magnetars also experience outbursts, with the distinction between 'persistent' and 'transient' magnetar dependent on the initial quiescent luminosity of each source Pons and Rea (2012). Transient magnetar outbursts decay on exponential timescales ranging from months to years (Rea et al., 2009; Kaspi et al., 2014; Coti Zelati et al., 2018). The outburst spectra feature both thermal emission and transient non-thermal emission. The non-thermal emission is observed only during outbursts, and is believed to have a magnetospheric origin. The thermal emission is observed both during quiescence and outburst, is brighter and harder during outbursts, and is thought to originate from the NS surface.

During the decay phase, thermal hot spots are observed to cool and shrink in size. This behaviour is consistent with currents circulating through a twisted magnetosphere, depositing heat at the surface footpoints of magnetic current loops Beloborodov (2009). Alternatively, this behavior might be due to internal heating of the crust through magnetic stresses associated with evolving toroidal fields (Lander et al., 2015; Lander and Gourgouliatos, 2019; Lander, 2023). While the decay of the thermal emission has been well observationally constrained, the hard, non-thermal X-ray emission fades beyond current detection limits fairly quickly (over the course of weeks). It is therefore unknown whether the non-thermal emission decays in tandem with the soft X-ray emission, as expected in the case of surface bombardment by accelerated particles in the magnetosphere, or whether the two evolve independently. This might be the case if the surface heating is indeed induced internally (e.g., Kouveliotou et al., 2004; Pons and Rea, 2012; Deibel et al., 2017), independent of the external magnetospheric emission. This is a major open question in transient magnetars given its potential to investigate crustal micro- and macro-physical properties, which are poorly known, and are highly relevant to the NS equation of state. HEX-P's sensitivity and broadband X-ray coverage are uniquely capable of addressing this fundamental open question.

The left panel of Figure 4 shows simulated HEX-P and NuSTAR spectra, both with 100 ks exposure time, based on the X-ray spectrum of the transient magnetar XTE J1810-197 during its late 2018 outburst (Gotthelf et al., 2019). These simulations highlight the essential role that the LET plays in constraining the soft <2 keV spectrum, especially in the case of less absorbed sources such as for XTE J1810-197, and the ~5x increase in counts for the HET vs. NuSTAR.

The right panel of Figure 4 shows HEX-P and NuSTAR simulations, both with 100 ks exposure time, of the hard X-ray spectrum of SGR J1745−2900 following its 2013 outburst. The spectral parameters are set based on NuSTAR and Chandra observations of the beginning of the 2013 outburst (Kaspi et al., 2014). The hard non-thermal emission could only be tracked for ~4 months post-outburst, due to the crowded nature of the galactic center (GC) region. On the other hand, we know that the soft thermal emission temperature and luminosity followed a multi-year evolution observed by Chandra (Figure 5, left panel) (Rea et al., 2020). Since Chandra's excellent angular resolution enabled multi-year tracking of the soft emission, it is natural so to ask how long HEX-P can track the evolution of the hard X-ray emission. We emphasize that such observation are only possible due to HEX-P's *combined* excellent angular resolution (important in the GC region) and larger effective area than NuSTAR. We perform our simulations by setting the luminosity of the non-thermal emission equal to what was observed by NuSTAR at the beginning of the outburst, and set the non-thermal emission to decay proportionally to the thermal luminosity. All observations are simulated with a 100 ks exposure time. While NuSTAR tracked the SGR J1745−2900 non-thermal emission for only 4 months post-outburst, we calculate that HEX-P will be capable of tracking a similar magnetar outburst for 2 years (Figure 5, right panel). While the biggest advantage of HEX-P in this scenario (vs. previous observatories, e.g., Chandra)

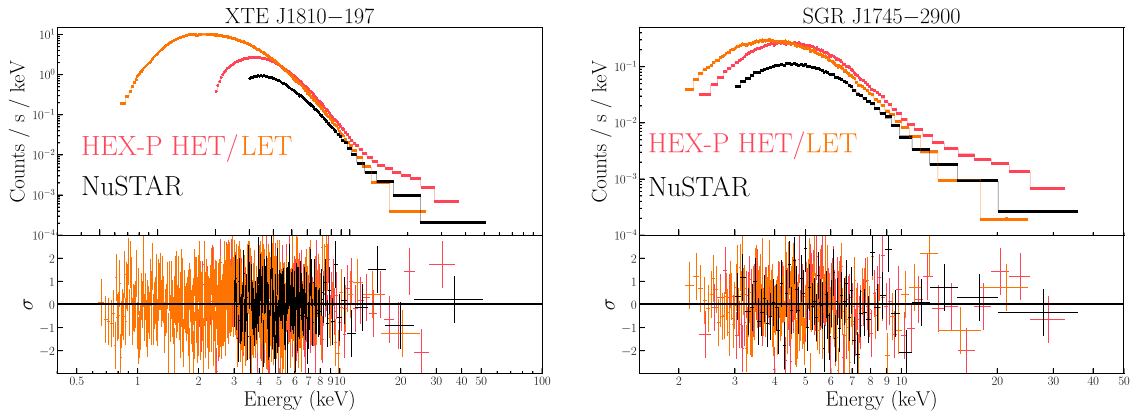

FIGURE 4
Simulated HEX-P broadband X-ray spectra of two transient magnetars near the peak of their outbursts: XTE J1810–197 (left) and SGR J1745–2900 (right) based on data from their 2018 and 2013 outbursts, respectively. LET and HET data are shown in orange and red, respectively. Note that SGR J1745–2900 is highly absorbed due to its location in the Galactic center region.

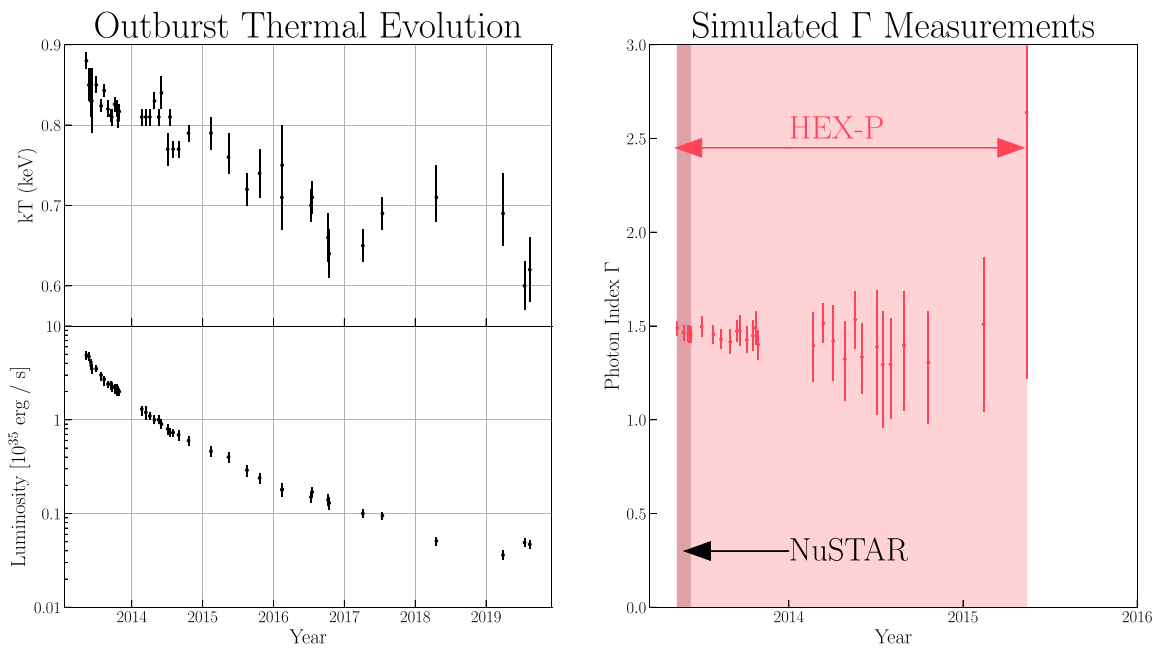

FIGURE 5
Simulated HEX-P measurements of the photon index Γ following the 2013 outburst of SGR 1745–2900 based on NuSTAR and Chandra observations. The upper panel of the left figure shows the evolution of the blackbody temperature, where the evolution of the 0.3–10.0 keV X-ray luminosity is shown in the lower panel of the left figure. The right figure shows the evolution of Γ obtained with NuSTAR and HEX-P. HEX-P's improved sensitivity will enable monitoring of these outbursts significantly longer than NuSTAR.

is its ability to track the hard X-ray decay, we also mention that its broadband coverage will also allow for more precise measurements of the soft thermal emission temperature and flux. This will provide data critical to our understanding of NS crustal and magnetospheric dynamics, unique observational characteristics of magnetars following an outburst.

4.3 Fast radio bursts

Fast Radio Bursts (FRBs) are millisecond, bright radio bursts (fluence ~ few Jy ms) observed over a broad range of frequencies, from ~120 MHz to a few GHz. They were first reported in 2007 (Lorimer et al., 2007), and since then several hundred have been detected by a suite of radio dishes across the Earth, e.g., Parkes, Arecibo, ASKAP, FAST, and CHIME (Petroff et al., 2022). FRBs are distributed nearly isotropically across the sky and show very large dispersion measures, indicating an extragalactic origin. Hence, their large fluences translate into very bright luminosities, ~9 orders of magnitude brighter than the Crab's giant pulses. While most FRBs appear as single events, a few have associated with a single position on the sky, i.e., repeating FRBs (Fonseca et al., 2020). The origin of FRBs is currently a matter of intense debate, and while many theoretical possibilities exist (Platts et al., 2019), one of the leading models is a NS or magnetar central engine.

In a breakthrough discovery, observational evidence for the magnetar model as a source of FRBs occurred on 2020 April 28, when an FRB-like radio burst was detected from the Galactic magnetar SGR 1935 + 2154 (CHIME/FRB Collaboration et al., 2020; Bochenek et al., 2020), in the winding hours of a major burst storm (Younes et al., 2020); it had a fluence rivaling those of the faint end of extragalactic FRBs. Moreover, the FRB occurred simultaneously with a bright, short X-ray burst, connecting it to magnetar activity and providing crucial evidence for its triggering mechanism (e.g., Mereghetti et al., 2020; Li et al., 2021; Ridnaia et al., 2021). In the following years, SGR 1935 + 2154 has shown several more radio bursts (Kirsten et al., 2020), most notably at times of bursting activity. Though most radio bursts occur simultaneous to X-ray bursts, the majority of X-ray bursts occur without a simultaneous radio signal (Lin et al., 2020b; Bailes et al., 2021) suggesting special circumstances for the emission of FRB-like bursts from magnetars. Indeed, a comparison of the X-ray burst associated with the FRB and NICER + Fermi bursts belonging to the same burst storm of April 2020 reveal the former to have a distinctive spectrum. This is a clue to either its emission mechanism or triggering locale (Younes et al., 2021), and has been seen in data from INTEGRAL (Mereghetti et al., 2020), Fermi/GBM (Lin et al., 2020a), Konus-Wind (Ridnaia et al., 2021), and Insight-HXMT (Li et al., 2021), among others.

The discovery of FRB-like bursts from magnetars opened up new avenues for the study of extragalactic FRBs (e.g., Wadiasingh and Timokhin, 2019), radio emission from young INSs (Philippov and Kramer, 2022), and, more generally, plasma and pair production in magnetar magnetospheres (e.g., Beloborodov, 2020; Yuan et al., 2020; Mahlmann et al., 2022). Yet, as is the case with every new fundamental discovery, more questions arise in its aftermath, e.g., 1) What is unique about the FRB-associated X-ray bursts, and why do the majority of X-ray bursts lack a radio counterpart? (2) What

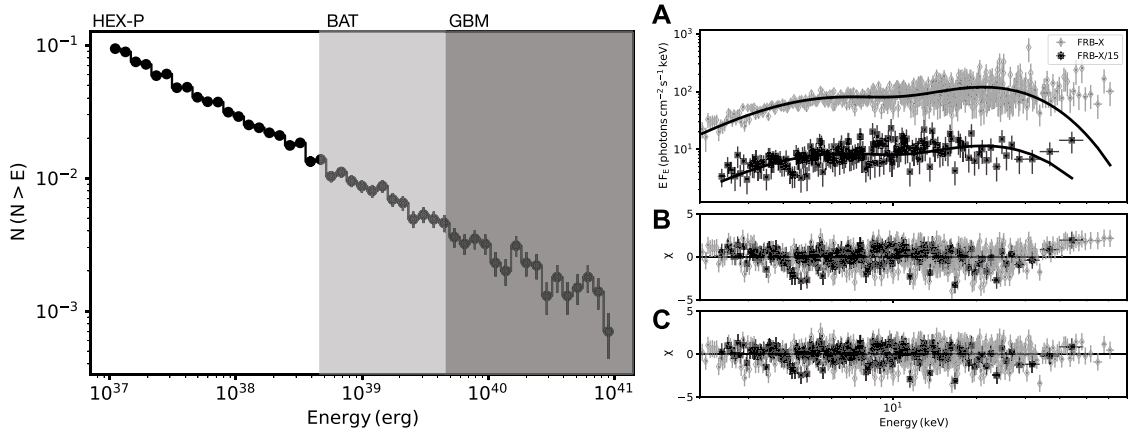

FIGURE 6
Left panel. $\log N - \log E$ distribution of magnetar short bursts, where E is the burst total energy. The light and dark shaded areas are the sensitivity limits (>5σ detection) of Swift/BAT and Fermi/GBM, respectively, assuming a source distance of 20 kpc. HEX-P is sensitive to the full burst energy distribution for every magnetar in the Galaxy. *Right panel.* Panel **(A)** shows a HEX-P Xspec simulation of the FRB200428-associated X-ray burst spectrum (gray diamonds) assuming a non-thermal cutoff power-law as measured with Insight-HXMT (Li et al., 2021). The solid line is the best-fit thermal double blackbody (2BB) model. Black squares are a simulated spectrum with the same assumptions, but with a fluence that is a factor 15 smaller. Panel **(B)** shows the residuals from the thermal fit in units of 1σ, with the same grey and black symbols. Panel **(C)** shows the residuals from the non-thermal fit in units of 1σ, again with the same grey and black symbols. HEX-P will distinguish the thermal vs. non-thermal nature of short X-ray bursts for fluences that are over an order of magnitude weaker than FRB-X (see text).

is the distribution of the spectral properties for FRB-associated X-ray bursts? Are their distinctive spectral properties universal across radio fluence? 3) Is the radio to X-ray flux ratio (L_R/L_X) constant for all FRB-like radio bursts? 4) What is the radio-X-ray time-lag across burst fluence?

The answers to these open questions are critical for improving our understanding of the FRB phenomenon, both Galactic and extragalactic. Answering these questions will require 1) a broad X-ray coverage given that the spectral energy distributions of magnetar bursts peak in the 20–30 keV range, 2) high timing resolution ($\lesssim$ 1 ms) for accurately measuring the radio-X-ray lag in burst arrival time (Mereghetti et al., 2020), 3) sensitivity to faint X-ray bursts, i.e., fluence $<10^{-7}$ erg cm^{-2}, to sample a large fraction of the X-ray and radio burst fluence distribution given their steep shapes ($N \propto S^{-0.6}$, Figure 6; Younes et al., 2020). HEX-P is the only facility to satisfy all the above criteria. Its only limitation is the small field-of-view, yet, most radio FRB bursts detected from the Galactic magnetar SGR 1935 + 2154 occurred at the time of major burst storms, which last up to a few days. This is sufficient time for HEX-P to slew to the target. We also note that NuSTAR was observing SGR 1935 + 2154 at the time of its 2022 October FRB-like burst, though the source was Earth-occulted (Dong and Chime/Frb Collaboration, 2022; Enoto et al., 2022). Due to the L1 orbit of HEX-P, such misfortune is naturally avoided.

The left panel of Figure 6 shows a simulated $\log N - \log S$ magnetar burst energy distribution, which follows a power-law of the form $dN/dE \propto E^{-1.6}$ (GöğüŞ et al., 1999; Göğüş et al., 2000; Gavriil et al., 2004; van der Horst et al., 2012; Younes et al., 2020). The Fermi/GBM >5σ sensitivity to typical short bursts from a magnetar at a distance of 20 kpc is shown in dark gray (Meegan et al., 2009) while that for Swift/BAT is shown in light gray (Lien et al., 2016). At that distance, HEX-P will detect bursts with energies comparable to the persistent emission, i.e., ~10^{37} erg (in a 1-s interval), covering significantly more of the short burst energy distribution. This will ensure the detection of X-ray bursts associated with faint radio bursts and provide answers to questions (3) and (4).

To address questions (1) and (2), we performed HEX-P HET simulations of an X-ray burst with spectral properties similar to that of the FRB-associated X-ray burst (which we call FRB-X) as determined by Insight-HXMT (Li et al., 2021); i.e., a cutoff power-law with $\Gamma = 1.6$ and $E_{cut} = 80$ keV, and a fluence of 5.0×10^{-7} erg cm^{-2} (Figure 6, gray diamonds in panel (a)), and a burst-duration of 1 s. We then fit this spectrum with a thermal 2 blackbody (2BB) model (shown as a solid black line). The thermal model fails to provide a statistically acceptable fit to the data (panel (b)), unlike the non-thermal model (panel (c)). This is confirmed through Xspec simulations which show that $\gg$ 99% of simulated spectra drawn from the thermal model have better fit statistics. This indicates that Het alone will discern the non-thermal nature of any bursts similar to FRB-X. We then performed a set of simulations assuming the same spectral model as FRB-X, while decreasing the fluence by increments of factor 2. We then fit each spectrum to a thermal 2BB model, and assess the fit quality through simulations. We find that we can discern (at the ≈3σ level) between the thermal and non-thermal model down to a fluence of ~3×10^{-8} erg cm^{-2}, i.e., a factor 15 fainter than FRB-X (Figure 6, black squares).

5 Central compact objects

The CCO class of NSs are defined by the following observational characteristics: steady, soft thermal X-ray emission, lack of a surrounding pulsar wind nebula, and non-detection at all other wavelengths. X-ray pulses have been detected from only three of the dozen known CCOs (Gotthelf et al., 2013). Two of these three, the CCOs in the Puppis A and Kes 79 SNRs, have the lowest spin

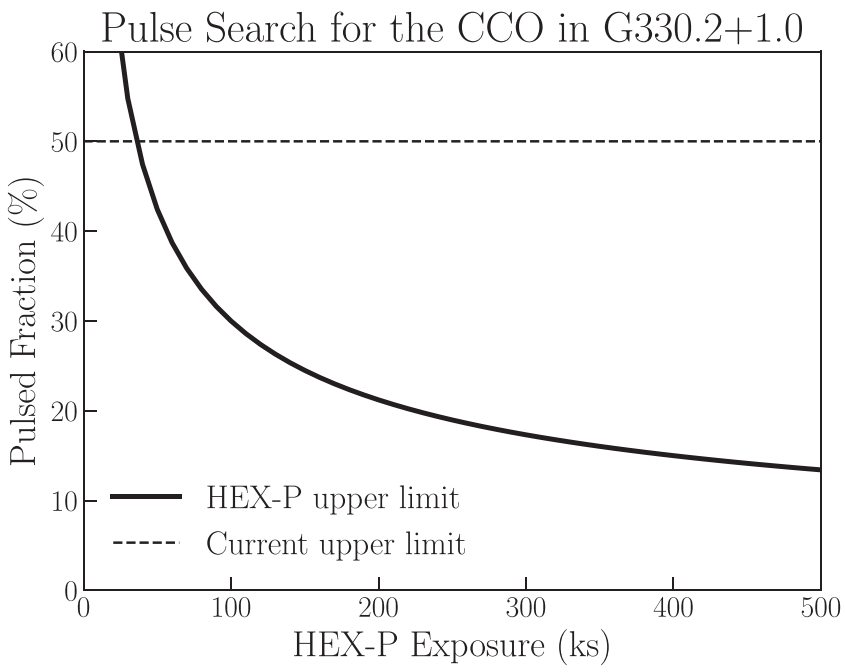

FIGURE 7
HEX-P pulsed fraction upper limits as a function of exposure for the CCO in G330.2 + 1.0.

down measured magnetic fields among young neutron stars, with $B_s \sim 3 \times 10^{10}$ G.

While only a dozen CCOs are currently known, their locations in young SNRs indicates they may represent a significant fraction of all NS births. Hence, understanding how young NSs are born with such small dipole magnetic fields is important to address how CCOs fit within the broad INS family. Increasing the number of CCO spin period and period derivative measurements is critical. Because CCOs are only detected at X-ray wavelengths, these spin period searches can only be done in the X-ray band. This is an area where HEX-P can shine as a follow-up observatory, capable of both searching for X-ray pulsations and, after identifying a spin period, making the required phase resolved spectroscopic measurements.

As an example, the CCO in G330.2 + 1.0 is a promising target for HEX-P thermal pulse searches. Previous searches with XMM-Newton were limited by the high background from the surrounding SNR thermal emission (Alford and Halpern, 2023). This is highlighted in Eq. 1 which relates the calculated pulsed fraction upper limit $f_p^{\max}$ to the number of total counts N, source counts N_s, background counts N_b, and intrinsic signal power P_s:

$$f_p^{\max} = 2\left(1 + N_b/N_s\right)\sqrt{P_s/N}, \quad (1)$$

Since CCOs are found in young supernova remnants, in many cases the thermal background emission from the remnant can be significant, hindering the ability to detect the underlying NS pulsations. To overcome these obstacles, both high X-ray timing and angular resolution are required. HEX-P's 3.5 arcsec PSF (for the LET detector) will allow for a significantly reduced background. Detailed comparisons of the performance of HEX-P in pulsar searches compared to XMM-Newton and NuSTAR can be found in Bachetti et al., in prep. (ULXs and extragalactic pulsars) and Mori et al., in prep. (the Galactic Center). Figure 7 presents the pulsed fraction upper limits as a function of exposure time for the CCO in G330.2 + 1.0. HEX-P will significantly reduce the current pulsed fraction upper limit, likely leading to a secure determination of the spin period.

Once an X-ray pulse period is found, a measurement of the period derivative can easily follow, as well as the characterization of the timing properties of these sources, e.g., B-field strength and spin down luminosity $\dot{E}$. Moreover, such observations will allow us to study the thermal pulse profiles of new CCOs. Energy-dependent pulse profile modeling is a powerful tool to map the surface thermal emission (Bogdanov, 2014; Alford et al., 2022). The HEX-P LET has the required effective area, timing resolution, low background, and angular resolution to produce more detailed maps, while increasing the pool of studied sources.

6 Rotation-powered pulsars

In contrast to the magnetically-powered magnetars and passively cooling CCOs, many pulsars are powered by the loss of their rotational kinetic energy. The 33 ms Crab pulsar is perhaps the best known pulsar in this class, with significant rotationally powered emission extending into the hard X-ray band (Madsen et al., 2015). HEX-P observations of the Crab pulsar will be a significant improvement over NuSTAR. For instance, HEX-P will enable low background phase-resolved studies of the Crab pulsar, by resolving the Crab pulsar from the bright pulsar wind nebula (PWN) background emission.

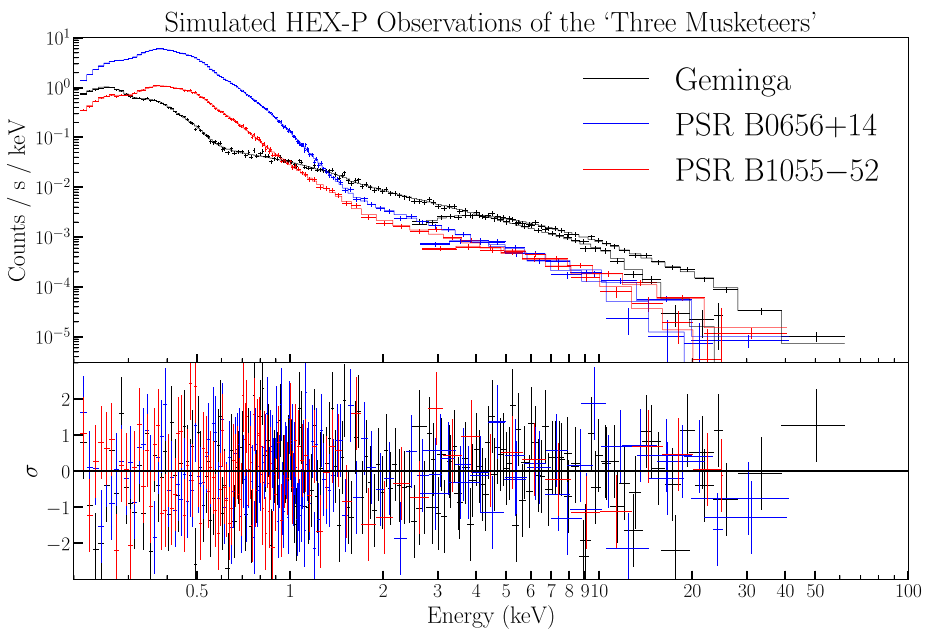

FIGURE 8
Simulated HEX-P observations of the Geminga pulsar, PSR B0656 + 14, and PSR B1055-52. HEX-P will be capable of extending the current hard X-ray detection limit for Geminga from 20 keV to 50 keV.

HEX-P will allow us to observe in detail the faint, middle-aged (~10^5 yr) pulsars which offer an opportunity to study how pulsars evolve and eventually "die," ceasing as X-ray and radio emitting sources. As RPPs age, their X-ray luminosity will decrease with their spin down power, making observations more challenging compared to younger RPPs.

There are three well-known nearby middle-aged pulsars that have been dubbed the "three musketeers": PSR B0656 + 14, PSR B1055−52 and Geminga. These three pulsars all exhibit thermal surface emission and non-thermal magnetospheric emission. They have similar ~10^{12} G spin down magnetic fields and 10^{34} erg s^{-1} spin down luminosities (De Luca et al., 2005). Despite their relative proximity, open questions remain regarding the physics of their surface thermal emission, and the extent of their non-thermal emission.

Open questions about Geminga are particularly interesting given its potentially large contribution to the local leptonic cosmic ray flux, and its status as the second brightest gamma-ray source in the sky. Mori et al. (2014) reported on a 150 ks NuSTAR observation of Geminga and found several spectral models were consistent with the data. Figure 8 shows a simulated 200 ks HEX-P observation of Geminga based on the two blackbody plus powerlaw model, with $\Gamma = 1.7$, $kT_1 = 44$ eV, and $kT_2 = 195$ eV. The cooler thermal component corresponds to emission from the whole NS surface, and the hot component, if its existence is confirmed, may correspond to emission from a hot polar cap. We find that, if the powerlaw extends to higher energies, HEX-P will extend the detection of non-thermal emission from ~20 keV to ~50 keV. The X-ray emission of Geminga above 20 keV is unexplored territory, and the detection of changes in the spectrum could be important clues to the physics of its magnetosphere.

Figure 8 also shows simulated HEX-P observations of PSR B0656 + 14 and PSR B1055−52, performed using the spectral parameters from De Luca et al. (2005). We find that 150 ks HEX-P observations will measure the photon indices Γ of all three of these faint pulsars to better than 10%.

HEX-P will also potentially address a fundamental mystery regarding PSR B0656 + 14, PSR B1055−52 and Geminga. B0656 + 14, and PSR B1055−52 clearly have small surface thermal hot spots, presumably corresponding to the heated pulsar polar caps. If Geminga has a similar hot spot, then its luminosity is at least two orders of magnitude dimmer (Jackson and Halpern, 2005). HEX-P's high throughput and broad coverage of Geminga's X-ray spectrum will allow us to answer this question.

7 Potential discovery space

Present and future large field-of-view facilities at all wavelengths from radio to PeV energies will result in a large number of unidentified sources, especially within the Galactic plane. This is already evident at GeV energies and beyond, i.e., Fermi/LAT, H.E.S.S, and LHASSO, where the number of unknown sources outweigh the number of identified ones, a problem that will only be exacerbated with the Cherenkov Telescope Array Observatory (CTAO). These high energy sources represent the most efficient particle accelerators in the universe, and for the Galactic ones, their most likely counterpart involves a pulsar (Mori et al., 2014 (in prep.)). At X-ray energies, eROSITA (Predehl et al., 2021, and potentially STAR-X Zhang et al., 2022) will provide some of the deepest wide-field X-ray surveys of our Galaxy, with a >10× increase in the number of X-ray sources compared to ROSAT. A large

fraction of these X-ray sources will be of unknown origin, and a non-negligible fraction should be INSs (Pires et al., 2017). Deeper, targeted exposures, as possible with HEX-P, will be required to identify them. Finally, in the radio, the Square Kilometer Array and Deep Synoptic Array 2000 are expected to increase the number of currently known pulsars by a factor of 10 (i.e., to ~20,000 pulsars), as well as detect a large number of new SNR shells and candidate wind nebulae.

Simply detecting X-ray point sources in the error region of unidentified gamma-ray and radio sources will not yield a secure identification. Furthermore, providing a high quality soft X-ray spectrum of eROSITA/STAR-X sources will not be enough to firmly distinguish their origin. High timing resolution is required to discern the pulsar nature from other types of X-ray emitters, such as low-mass X-ray binaries, cataclysmic variables, background active galaxies, etc. Moreover, being limited to a soft X-ray detector will hamper our ability to probe deep into the Galaxy due to absorption, stressing the need for hard X-ray coverage. Last but not least, high spatial resolution is required for crowded regions such as Sgr A* (Mori et al., 2014 (in prep.)), and to isolate the pulsar emission from any surrounding SNR and/or nebula (as noted in §5 with regards to candidate CCOs). These issues have already been demonstrated with NuSTAR. For instance, although a candidate soft X-ray counterpart to the TeV γ-ray source HESS J1640-465 had been proposed, only NuSTAR was able to detect pulsed emission confirming its pulsar nature (Gotthelf et al., 2019). This was mainly due to the combination of heavy absorption (10^{23} cm^{-2}) in the source direction and non-negligible contamination by the PWN (Gotthelf et al., 2019). Continued NuSTAR follow-up of this pulsar found the braking index $n > 3$, possibly pointing to a magnetic quadrupole in the source (Archibald et al., 2016a).

HEX-P presents the ideal satellite to follow-up Galactic gamma-ray sources, INS candidates from wide-area X-ray surveys, and pulsar/pulsar candidates from deep radio surveys. Increasing the number of isolated X-ray pulsars, such as XDINs, CCOs, RPPs, and magnetars, will enable a deeper understanding of their physics, X-ray properties, environment (e.g., wind nebulae, SNRs and nearby cosmic ray acceleration sites), and progenitors, in turn teaching us about NS formation and evolutionary tracks through, e.g., population synthesis modeling (e.g., Gullón et al., 2015; Dirson et al., 2022) and magneto-thermal evolution models (e.g., Viganò et al., 2013; Gourgouliatos et al., 2016).

Data availability statement

The original contributions presented in the study are included in the article/Supplementary Material, further inquiries can be directed to the corresponding author.

Author contributions

JA: Conceptualization, Investigation, Software, Writing–original draft, Writing–review and editing. GY: Writing–original draft, Writing–review and editing. ZW: Writing–review and editing, Writing–original draft. MA: Writing–review and editing. HA: Writing–review and editing. MBc: Writing–review and editing. MBr: Writing–review and editing. AB: Writing–review and editing. AC: Writing–review and editing. TE: Writing–review and editing. JAG: Writing–review and editing. JDG: Writing–review and editing. EG: Writing–review and editing. AH: Writing–review and editing. C-PH: Writing–review and editing. AJ: Writing–review and editing. VK: Writing–review and editing. CKi: Writing–review and editing. CKo: Writing–review and editing. LK: Writing–review and editing. KM: Writing–review and editing. MN: Writing–review and editing. JP: Writing–review and editing. DS: Writing–review and editing. JV: Writing–review and editing. DW: Writing–review and editing.

Funding

The author(s) declare financial support was received for the research, authorship, and/or publication of this article. The work of DS was carried out at the Jet Propulsion Laboratory, California Institute of Technology, under a contract with NASA. ZW acknowledges support by NASA under award number 80GSFC21M0002. This work has made use of the NASA Astrophysics Data System.

Conflict of interest

The authors declare that the research was conducted in the absence of any commercial or financial relationships that could be construed as a potential conflict of interest.

The reviewer AB declared a past co-authorship with the author GY to the handling editor.

Publisher's note

All claims expressed in this article are solely those of the authors and do not necessarily represent those of their affiliated organizations, or those of the publisher, the editors and the reviewers. Any product that may be evaluated in this article, or claim that may be made by its manufacturer, is not guaranteed or endorsed by the publisher.

References

Alford, J. A. J., Gotthelf, E. V., Perna, R., and Halpern, J. P. (2022). Measuring the nonaxially symmetric surface temperature distribution of the central compact object in Puppis A. *ApJ* 927, 233. doi:10.3847/1538-4357/ac4d9a

Alford, J. A. J., and Halpern, J. P. (2023). Do central compact objects have carbon atmospheres? *ApJ* 944, 36. doi:10.3847/1538-4357/acaf55

An, H., Archibald, R. F., Hascoët, R., Kaspi, V. M., Beloborodov, A. M., Archibald, A. M., et al. (2015). Deep NuSTAR and Swift monitoring observations of the magnetar 1E 1841-045. *ApJ* 807, 93. doi:10.1088/0004-637X/807/1/93

Archibald, R. F., Gotthelf, E. V., Ferdman, R. D., Kaspi, V. M., Guillot, S., Harrison, F. A., et al. (2016a). A high braking index for a pulsar. *ApJL* 819, L16. doi:10.3847/2041-8205/819/1/L16

Archibald, R. F., Kaspi, V. M., Tendulkar, S. P., and Scholz, P. (2016b). A magnetar-like outburst from a high-B radio pulsar. *ApJL* 829, L21. doi:10.3847/2041-8205/829/1/L21

Arnaud, K. A. (1996). "XSPEC: the first ten years," in *Astronomical data analysis software and systems V of astronomical society of the pacific conference series*. Editors G. H. Jacoby, and J. Barnes 101, 17.

Arzoumanian, Z., Chernoff, D. F., and Cordes, J. M. (2002). The velocity distribution of isolated radio pulsars. *ApJ* 568, 289–301. doi:10.1086/338805

Bailes, M., Bassa, C. G., Bernardi, G., Buchner, S., Burgay, M., Caleb, M., et al. (2021). Multifrequency observations of SGR J1935+2154. *MNRAS* 503, 5367–5384. doi:10.1093/mnras/stab749

Baring, M. G., and Harding, A. K. (2007). Resonant Compton upscattering in anomalous X-ray pulsars. *APSS* 308, 109–118. doi:10.1007/s10509-007-9326-x

Beloborodov, A. M. (2009). Untwisting magnetospheres of neutron stars. *ApJ* 703, 1044–1060. doi:10.1088/0004-637X/703/1/1044

Beloborodov, A. M. (2013). On the mechanism of hard X-ray emission from magnetars. *ApJ* 762, 13. doi:10.1088/0004-637X/762/1/13

Beloborodov, A. M. (2020). Blast waves from magnetar flares and fast radio bursts. *ApJ* 896, 142. doi:10.3847/1538-4357/ab83eb

Beniamini, P., Wadiasingh, Z., Hare, J., Rajwade, K. M., Younes, G., and van der Horst, A. J. (2023). Evidence for an abundant old population of Galactic ultra-long period magnetars and implications for fast radio bursts. *MNRAS* 520, 1872–1894. doi:10.1093/mnras/stad208

Bochenek, C. D., Ravi, V., Belov, K. V., Hallinan, G., Kocz, J., Kulkarni, S. R., et al. (2020). A fast radio burst associated with a Galactic magnetar. *Nature* 587, 59–62. doi:10.1038/s41586-020-2872-x

Bogdanov, S. (2014). Modeling the X-rays from the central compact object PSR J1852+0040 in kesteven 79: evidence for a strongly magnetized neutron star. *ApJ* 790, 94. doi:10.1088/0004-637X/790/2/94

Caiazzo, I., González-Caniulef, D., Heyl, J., and Fernández, R. (2022). Probing magnetar emission mechanisms with X-ray spectropolarimetry. *MNRAS* 514, 5024–5034. doi:10.1093/mnras/stac1571

Caleb, M., Heywood, I., Rajwade, K., Malenta, M., Stappers, B. W., Barr, E., et al. (2022). Discovery of a radio-emitting neutron star with an ultra-long spin period of 76 s. *Nat. Astron.* 6, 828–836. doi:10.1038/s41550-022-01688-x

Camilo, F., Ransom, S. M., Halpern, J. P., and Reynolds, J. (2007). 1E 1547.0-5408: a radio-emitting magnetar with a rotation period of 2 seconds. *ApJL* 666, L93–L96. doi:10.1086/521826

Camilo, F., Ransom, S. M., Halpern, J. P., Reynolds, J., Helfand, D. J., Zimmerman, N., et al. (2006). Transient pulsed radio emission from a magnetar. *Nature* 442, 892–895. doi:10.1038/nature04986

Cash, W. (1979). Parameter estimation in astronomy through application of the likelihood ratio. *ApJ* 228, 939–947. doi:10.1086/156922

Chen, A. Y., and Beloborodov, A. M. (2017). Particle-in-Cell simulations of the twisted magnetospheres of magnetars. I. *ApJ* 844, 133. doi:10.3847/1538-4357/aa7a57

CHIME/FRB Collaboration, Andersen, B. C., Bandura, K. M., Bhardwaj, M., Bij, A., Boyce, M. M., et al. (2020). A bright millisecond-duration radio burst from a Galactic magnetar. *Nature* 587, 54–58. doi:10.1038/s41586-020-2863-y

Coti Zelati, F., Rea, N., Pons, J. A., Campana, S., and Esposito, P. (2018). Systematic study of magnetar outbursts. *MNRAS* 474, 961–1017. doi:10.1093/mnras/stx2679

Deibel, A., Cumming, A., Brown, E. F., and Reddy, S. (2017). Late-time cooling of neutron star transients and the physics of the inner crust. *ApJ* 839, 95. doi:10.3847/1538-4357/aa6a19

De Luca, A. (2017). Central compact objects in supernova remnants. *J. Phys. Conf. Ser. J. Phys. Conf. Ser.* 932, 012006. doi:10.1088/1742-6596/932/1/012006

De Luca, A., Caraveo, P. A., Mereghetti, S., Negroni, M., and Bignami, G. F. (2005). On the polar caps of the three musketeers. *ApJ* 623, 1051–1069. doi:10.1086/428567

den Hartog, P. R., Kuiper, L., and Hermsen, W. (2008a). Detailed high-energy characteristics of AXP 1RXS J170849-400910. Probing the magnetosphere using INTEGRAL, RXTE, and XMM-Newton. *A&A* 489, 263–279. doi:10.1051/0004-6361:200809772

den Hartog, P. R., Kuiper, L., Hermsen, W., Kaspi, V. M., Dib, R., Knödlseder, J., et al. (2008b). Detailed high-energy characteristics of AXP 4U 0142+61. Multi-year observations with INTEGRAL, RXTE, XMM-Newton, and ASCA. *A&A* 489, 245–261. doi:10.1051/0004-6361:200809390

Dirson, L., Pétri, J., and Mitra, D. (2022). The Galactic population of canonical pulsars. *A&A* 667, A82. doi:10.1051/0004-6361/202243305

Dong, F. A., and Chime/Frb Collaboration (2022). *CHIME/FRB detection of a bright radio burst from SGR 1935+2154*. The Astronomer's Telegram, 15681.

Enoto, T., Hu, C.-P., Guver, T., Younes, G., Gendreau, K. C., Arzoumanian, Z., et al. (2022). *NICER and NuSTAR observations of SGR 1935+2154 bracketing the time of the bright radio burst*. The Astronomer's Telegram, 15690.

Enoto, T., Nakazawa, K., Makishima, K., Rea, N., Hurley, K., and Shibata, S. (2010). Broadband study with suzaku of the magnetar class. *ApJL* 722, L162–L167. doi:10.1088/2041-8205/722/2/L162

Enoto, T., Shibata, S., Kitaguchi, T., Suwa, Y., Uchide, T., Nishioka, H., et al. (2017). Magnetar broadband X-ray spectra correlated with magnetic fields: suzaku archive of SGRs and AXPs combined with NuSTAR, Swift, and RXTE. *ApJS* 231, 8. doi:10.3847/1538-4365/aa6f0a

Eraerds, T., Antonelli, V., Davis, C., Hall, D., Hetherington, O., Holland, A., et al. (2021). Enhanced simulations on the athena/wide field imager instrumental background. *J. Astronomical Telesc. Instrum. Syst.* 7, 034001. doi:10.1117/1.JATIS.7.3.034001

Faucher-Giguère, C.-A., and Kaspi, V. M. (2006). Birth and evolution of isolated radio pulsars. *ApJ* 643, 332–355. doi:10.1086/501516

Fernández, R., and Thompson, C. (2007). Resonant cyclotron scattering in three dimensions and the quiescent nonthermal X-ray emission of magnetars. *ApJ* 660, 615–640. doi:10.1086/511810

Fonseca, E., Andersen, B. C., Bhardwaj, M., Chawla, P., Good, D. C., Josephy, A., et al. (2020). Nine new repeating fast radio burst sources from CHIME/FRB. *ApJL* 891, L6. doi:10.3847/2041-8213/ab7208

Fortin, J.-F., Guo, H.-K., Harris, S. P., Sheridan, E., and Sinha, K. (2021). Magnetars and axion-like particles: probes with the hard X-ray spectrum. *JCAP* 2021, 036. doi:10.1088/1475-7516/2021/06/036

Gavriil, F. P., Gonzalez, M. E., Gotthelf, E. V., Kaspi, V. M., Livingstone, M. A., and Woods, P. M. (2008). Magnetar-like emission from the young pulsar in kes 75. *Science* 319, 1802–1805. doi:10.1126/science.1153465

Gavriil, F. P., Kaspi, V. M., and Woods, P. M. (2004). A comprehensive study of the X-ray bursts from the magnetar candidate 1E 2259+586. *ApJ* 607, 959–969. doi:10.1086/383564

Göğüş, E., Woods, P. M., Kouveliotou, C., van Paradijs, J., Briggs, M. S., Duncan, R. C., et al. (2000). Statistical properties of SGR 1806-20 bursts. *ApJL* 532, L121–L124. doi:10.1086/312583

GöğüŞ, E., Woods, P. M., Kouveliotou, C., van Paradijs, J., Briggs, M. S., Duncan, R. C., et al. (1999). Statistical properties of SGR 1900+14 bursts. *ApJL* 526, L93–L96. doi:10.1086/312380

Gotthelf, E. V., Halpern, J. P., and Alford, J. (2013). The spin-down of PSR j0821-4300 and PSR j1210-5226: confirmation of central compact objects as anti-magnetars. *ApJ* 765, 58. doi:10.1088/0004-637X/765/1/58

Gotthelf, E. V., Halpern, J. P., Alford, J. A. J., Mihara, T., Negoro, H., Kawai, N., et al. (2019). The 2018 X-ray and radio outburst of magnetar XTE j1810-197. *ApJL* 874, L25. doi:10.3847/2041-8213/ab101a

Gourgouliatos, K. N., Wood, T. S., and Hollerbach, R. (2016). Magnetic field evolution in magnetar crusts through three-dimensional simulations. *Proc. Natl. Acad. Sci.* 113, 3944–3949. doi:10.1073/pnas.1522363113

Gullón, M., Pons, J. A., Miralles, J. A., Viganò, D., Rea, N., and Perna, R. (2015). Population synthesis of isolated neutron stars with magneto-rotational evolution - II. From radio-pulsars to magnetars. *MNRAS* 454, 615–625. doi:10.1093/mnras/stv1644

Harrison, F. A., Craig, W. W., Christensen, F. E., Hailey, C. J., Zhang, W. W., Boggs, S. E., et al. (2013). The nuclear spectroscopic telescope Array (NuSTAR) high-energy X-ray mission. *ApJ* 770, 103. doi:10.1088/0004-637X/770/2/103

Heger, A., Fryer, C. L., Woosley, S. E., Langer, N., and Hartmann, D. H. (2003). How massive single stars end their life. *ApJ* 591, 288–300. doi:10.1086/375341

Hu, K., Baring, M. G., Harding, A. K., and Wadiasingh, Z. (2022). High-energy photon opacity in the twisted magnetospheres of magnetars. *ApJ* 940, 91. doi:10.3847/1538-4357/ac9611

Hu, K., Baring, M. G., Wadiasingh, Z., and Harding, A. K. (2019). Opacities for photon splitting and pair creation in neutron star magnetospheres. *MNRAS* 486, 3327–3349. doi:10.1093/mnras/stz995

Jackson, M. S., and Halpern, J. P. (2005). A refined ephemeris and phase-resolved X-ray spectroscopy of the Geminga pulsar. *ApJ* 633, 1114–1125. doi:10.1086/491615

Jansen, F., Lumb, D., Altieri, B., Clavel, J., Ehle, M., Erd, C., et al. (2001). XMM-Newton observatory. I. The spacecraft and operations. *A&A* 365, L1–L6. doi:10.1051/0004-6361:20000036

Kaplan, D. L. (2008). "Nearby, thermally emitting neutron stars," in *Astrophysics of compact objects of American Institute of physics conference series*. Editors Y.-F. Yuan, X.-D. Li, and D. Lai, 968, 129–136. doi:10.1063/1.2840384

Kaspi, V. M., Archibald, R. F., Bhalerao, V., Dufour, F., Gotthelf, E. V., An, H., et al. (2014). Timing and flux evolution of the galactic center magnetar SGR j1745-2900. *ApJ* 786, 84. doi:10.1088/0004-637X/786/2/84

Kaspi, V. M., and Beloborodov, A. M. (2017). Magnetars. *ARAA* 55, 261–301. doi:10.1146/annurev-astro-081915-023329

Kaspi, V. M., and Boydstun, K. (2010). On the X-ray spectra of anomalous X-ray pulsars and soft gamma repeaters. *ApJL* 710, L115–L120. doi:10.1088/2041-8205/710/2/L115

Kaspi, V. M., Gavriil, F. P., Woods, P. M., Jensen, J. B., Roberts, M. S. E., and Chakrabarty, D. (2003). A major soft gamma repeater-like outburst and rotation glitch in the No-longer-so-anomalous X-ray pulsar 1E 2259+586. *ApJL* 588, L93–L96. doi:10.1086/375683

Kirsten, F., Snelders, M. P., Jenkins, M., Nimmo, K., van den Eijnden, J., Hessels, J. W. T., et al. (2020). Detection of two bright radio bursts from magnetar SGR 1935 + 2154. *Nat. Astron.* 5, 414–422. doi:10.1038/s41550-020-01246-3

Kouveliotou, C., Dieters, S., Strohmayer, T., van Paradijs, J., Fishman, G. J., Meegan, C. A., et al. (1998). An X-ray pulsar with a superstrong magnetic field in the soft γ-ray repeater SGR1806 - 20. *Nature* 393, 235–237. doi:10.1038/30410

Kouveliotou, C., Strohmayer, T., Hurley, K., van Paradijs, J., Finger, M. H., Dieters, S., et al. (1999). Discovery of a magnetar associated with the soft gamma repeater SGR 1900+14. *ApJL* 510, L115–L118. doi:10.1086/311813

Kouveliotou, C., Woosley, S. E., Patel, S. K., Levan, A., Blandford, R., Ramirez-Ruiz, E., et al. (2004). Chandra observations of the X-ray environs of SN 1998bw/GRB 980425. *ApJ* 608, 872–882. doi:10.1086/420878

Kuiper, L., Hermsen, W., den Hartog, P. R., and Collmar, W. (2006). Discovery of luminous pulsed hard X-ray emission from anomalous X-ray pulsars 1RXS j1708-4009, 4U 0142+61, and 1E 2259+586 by INTEGRAL and RXTE. *ApJ* 645, 556–575. doi:10.1086/504317

Kuiper, L., Hermsen, W., and Mendez, M. (2004). Discovery of hard nonthermal pulsed X-ray emission from the anomalous X-ray pulsar 1E 1841-045. *ApJ* 613, 1173–1178. doi:10.1086/423129

Lander, S. K. (2023). The game of life on a magnetar crust: from gamma-ray flares to FRBs. *ApJL* 947, L16. doi:10.3847/2041-8213/acca1f

Lander, S. K., Andersson, N., Antonopoulou, D., and Watts, A. L. (2015). Magnetically driven crustquakes in neutron stars. *MNRAS* 449, 2047–2058. doi:10.1093/mnras/stv432

Lander, S. K., and Gourgouliatos, K. N. (2019). Magnetic-field evolution in a plastically failing neutron-star crust. *MNRAS* 486, 4130–4143. doi:10.1093/mnras/stz1042

Li, C. K., Lin, L., Xiong, S. L., Ge, M. Y., Li, X. B., Li, T. P., et al. (2021). HXMT identification of a non-thermal X-ray burst from SGR J1935+2154 and with FRB 200428. *Nat. Astron.* 5, 378–384. doi:10.1038/s41550-021-01302-6

Lien, A., Sakamoto, T., Barthelmy, S. D., Baumgartner, W. H., Cannizzo, J. K., Chen, K., et al. (2016). The third Swift burst alert telescope gamma-ray burst catalog. *ApJ* 829, 7. doi:10.3847/0004-637X/829/1/7

Lin, L., Göğüş, E., Roberts, O. J., Baring, M. G., Kouveliotou, C., Kaneko, Y., et al. (2020a). Fermi/GBM view of the 2019 and 2020 burst active episodes of SGR J1935+2154. *ApJL* 902, L43. doi:10.3847/2041-8213/abbefe

Lin, L., Zhang, C. F., Wang, P., Gao, H., Guan, X., Han, J. L., et al. (2020b). No pulsed radio emission during a bursting phase of a Galactic magnetar. *Nature* 587, 63–65. doi:10.1038/s41586-020-2839-y

Lorimer, D. R., Bailes, M., McLaughlin, M. A., Narkevic, D. J., and Crawford, F. (2007). A bright millisecond radio burst of extragalactic origin. *Science* 318, 777–780. doi:10.1126/science.1147532

Madsen, K. K., Reynolds, S., Harrison, F., An, H., Boggs, S., Christensen, F. E., et al. (2015). Broadband X-ray imaging and spectroscopy of the Crab nebula and pulsar with NuSTAR. *ApJ* 801, 66. doi:10.1088/0004-637X/801/1/66

Madsen, K. K., García, J. A., Stern, D., Armini, R., Basso, S., Coutinho, D., et al. (2023). The high energy x-ray probe (HEX-P): instrument and mission profile. *arXiv*. doi:10.48550/arXiv.2312.04678

Mahlmann, J. F., Philippov, A. A., Levinson, A., Spitkovsky, A., and Hakobyan, H. (2022). Electromagnetic fireworks: fast radio bursts from rapid reconnection in the compressed magnetar wind. *ApJL* 932, L20. doi:10.3847/2041-8213/ac7156

Manchester, R. N., Hobbs, G. B., Teoh, A., and Hobbs, M. (2005). The Australia telescope national facility pulsar catalogue. *AJ* 129, 1993–2006. doi:10.1086/428488

Marsden, D., and White, N. E. (2001). Correlations between spectral properties and spin-down rate in soft gamma-ray repeaters and anomalous X-ray pulsars. *ApJL* 551, L155–L158. doi:10.1086/320025

Maruyama, T., Balantekin, A. B., Cheoun, M.-K., Kajino, T., and Mathews, G. J. (2018). Axion production from Landau quantization in the strong magnetic field of magnetars. *Phys. Lett. B* 779, 160–165. doi:10.1016/j.physletb.2018.01.084

Meegan, C., Lichti, G., Bhat, P. N., Bissaldi, E., Briggs, M. S., Connaughton, V., et al. (2009). The *fermi*gamma-ray burst monitor. *ApJ* 702, 791–804. doi:10.1088/0004-637X/702/1/791

Meidinger, N., Albrecht, S., Beitler, C., Bonholzer, M., Emberger, V., Frank, J., et al. (2020). "Development status of the wide field imager instrument for Athena," in *Society of photo-optical instrumentation engineers (SPIE) conference series*, 11444, 114440T. doi:10.1117/12.2560507

Mereghetti, S., Savchenko, V., Ferrigno, C., Götz, D., Rigoselli, M., Tiengo, A., et al. (2020). INTEGRAL discovery of a burst with associated radio emission from the magnetar SGR 1935+2154. *ApJL* 898, L29. doi:10.3847/2041-8213/aba2cf

Mori, K., Gotthelf, E. V., Dufour, F., Kaspi, V. M., Halpern, J. P., Beloborodov, A. M., et al. (2014). A broadband X-ray study of the Geminga pulsar with NuSTAR and XMM-Newton. *ApJ* 793, 88. doi:10.1088/0004-637X/793/2/88

Nandra, K., Barret, D., Barcons, X., Fabian, A., den Herder, J.-W., Piro, L., et al. (2013). The hot and energetic universe: a white paper presenting the science theme motivating the Athena+ mission. arXiv e-prints, arXiv:1306.2307 Available at: https://arxiv.org/abs/1306.2307.

Olausen, S. A., and Kaspi, V. M. (2014). The McGill magnetar catalog. *ApJS* 212, 6. doi:10.1088/0067-0049/212/1/6

Parfrey, K., Beloborodov, A. M., and Hui, L. (2013). Dynamics of strongly twisted relativistic magnetospheres. *ApJ* 774, 92. doi:10.1088/0004-637X/774/2/92

Park, S., Bhalerao, J., Kargaltsev, O., and Slane, P. O. (2020). NuSTAR detection of quiescent hard X-ray emission from SGR 0526-66 in the large magellanic Cloud. *ApJ* 894, 17. doi:10.3847/1538-4357/ab83f8

Petroff, E., Hessels, J. W. T., and Lorimer, D. R. (2022). Fast radio bursts at the dawn of the 2020s. *AAPR* 30, 2. doi:10.1007/s00159-022-00139-w

Philippov, A., and Kramer, M. (2022). Pulsar magnetospheres and their radiation. *ARAA* 60, 495–558. doi:10.1146/annurev-astro-052920-112338

Pires, A. M., Schwope, A. D., and Motch, C. (2017). Follow-up of isolated neutron star candidates from the eROSITA survey. *Astron. Nachrichten* 338, 213–219. doi:10.1002/asna.201713333

Platts, E., Weltman, A., Walters, A., Tendulkar, S. P., Gordin, J. E. B., and Kandhai, S. (2019). A living theory catalogue for fast radio bursts. *Phys. Rep.* 821, 1–27. doi:10.1016/j.physrep.2019.06.003

Pons, J. A., and Rea, N. (2012). Modeling magnetar outbursts: flux enhancements and the connection with short bursts and glitches. *ApJL* 750, L6. doi:10.1088/2041-8205/750/1/L6

Predehl, P., Andritschke, R., Arefiev, V., Babyshkin, V., Batanov, O., Becker, W., et al. (2021). The eROSITA X-ray telescope on SRG. *A&A* 647, A1. doi:10.1051/0004-6361/202039313

Rea, N., Borghese, A., Esposito, P., Coti Zelati, F., Bachetti, M., Israel, G. L., et al. (2016). Magnetar-like activity from the central compact object in the SNR RCW103. *ApJL* 828, L13. doi:10.3847/2041-8205/828/1/L13

Rea, N., Coti Zelati, F., Dehman, C., Hurley-Walker, N., de Martino, D., Bahramian, A., et al. (2022). Constraining the nature of the 18 min periodic radio transient GLEAM-X j162759.5-523504.3 via multiwavelength observations and magneto-thermal simulations. *ApJ* 940, 72. doi:10.3847/1538-4357/ac97ea

Rea, N., Coti Zelati, F., Viganò, D., Papitto, A., Baganoff, F., Borghese, A., et al. (2020). The X-ray outburst of the galactic center magnetar over six years of Chandra observations. *ApJ* 894, 159. doi:10.3847/1538-4357/ab8387

Rea, N., Esposito, P., Turolla, R., Israel, G. L., Zane, S., Stella, L., et al. (2010). A low-magnetic-field soft gamma repeater. *Science* 330, 944–946. doi:10.1126/science.1196088

Rea, N., Israel, G. L., Turolla, R., Esposito, P., Mereghetti, S., Götz, D., et al. (2009). The first outburst of the new magnetar candidate SGR0501+4516. *MNRAS* 396, 2419–2432. doi:10.1111/j.1365-2966.2009.14920.x

Ridnaia, A., Svinkin, D., Frederiks, D., Bykov, A., Popov, S., Aptekar, R., et al. (2021). A peculiar hard X-ray counterpart of a Galactic fast radio burst. *Nat. Astron.* 5, 372–377. doi:10.1038/s41550-020-01265-0

Rigoselli, M., Mereghetti, S., Suleimanov, V., Potekhin, A. Y., Turolla, R., Taverna, R., et al. (2019). XMM-Newton observations of PSR J0726-2612, a radio-loud XDINS. *A&A* 627, A69. doi:10.1051/0004-6361/201935485

Seo, J., Lee, J., and An, H. (2023). Correlation study of temporal and emission properties of quiescent magnetars. *J. Korean Astronomical Soc.* 56, 41–57. doi:10.5303/JKAS.2023.56.1.41

Tan, C. M., Bassa, C. G., Cooper, S., Dijkema, T. J., Esposito, P., Hessels, J. W. T., et al. (2018). LOFAR discovery of a 23.5 s radio pulsar. *ApJ* 866, 54. doi:10.3847/1538-4357/aade88

Taverna, R., Turolla, R., Muleri, F., Heyl, J., Zane, S., Baldini, L., et al. (2022). Polarized x-rays from a magnetar. *Science* 378, 646–650. doi:10.1126/science.add0080

Taverna, R., Turolla, R., Suleimanov, V., Potekhin, A. Y., and Zane, S. (2020). X-ray spectra and polarization from magnetar candidates. *MNRAS* 492, 5057–5074. doi:10.1093/mnras/staa204

Thompson, C., and Duncan, R. C. (1995). The soft gamma repeaters as very strongly magnetized neutron stars - I. Radiative mechanism for outbursts. *MNRAS* 275, 255–300. doi:10.1093/mnras/275.2.255

van der Horst, A. J., Kouveliotou, C., Gorgone, N. M., Kaneko, Y., Baring, M. G., Guiriec, S., et al. (2012). SGR J1550–5418 bursts detected with the *fermi* gamma-ray burst monitor during its most prolific activity. *ApJ* 749, 122. doi:10.1088/0004-637X/749/2/122

Vasisht, G., and Gotthelf, E. V. (1997). The discovery of an anomalous X-ray pulsar in the supernova remnant K[CLC]es 73[/CLC]. *ApJL* 486, L129–L132. doi:10.1086/310843

Viganò, D., Rea, N., Pons, J. A., Perna, R., Aguilera, D. N., and Miralles, J. A. (2013). Unifying the observational diversity of isolated neutron stars via

magneto-thermal evolution models. *Mon. Notices R. Astronomical Soc.* 434, 123–141. doi:10.1093/mnras/stt1008

Wadiasingh, Z., Baring, M., Hu, K., Harding, A., Younes, G., and Gonthier, P. (2022). Phase-resolved spectropolarimetric models of magnetar hard X-ray emission with QED photon splitting attenuation. *AAS/High Energy Astrophys. Div.* 54, 47.

Wadiasingh, Z., Baring, M. G., Gonthier, P. L., and Harding, A. K. (2018). Resonant inverse Compton scattering spectra from highly magnetized neutron stars. *ApJ* 854, 98. doi:10.3847/1538-4357/aaa460

Wadiasingh, Z., and Timokhin, A. (2019). Repeating fast radio bursts from magnetars with low magnetospheric twist. *ApJ* 879, 4. doi:10.3847/1538-4357/ab2240

Wadiasingh, Z., Younes, G., Baring, M. G., Harding, A. K., Gonthier, P. L., Hu, K., et al. (2019). Magnetars as astrophysical laboratories of extreme quantum electrodynamics: the case for a Compton telescope. *BAAS* 51, 292. doi:10.48550/arXiv.1903.05648

Younes, G., Baring, M. G., Kouveliotou, C., Arzoumanian, Z., Enoto, T., Doty, J., et al. (2021). Broadband X-ray burst spectroscopy of the fast-radio-burst-emitting Galactic magnetar. *Nat. Astron.* 5, 408–413. doi:10.1038/s41550-020-01292-x

Younes, G., Güver, T., Kouveliotou, C., Baring, M. G., Hu, C.-P., Wadiasingh, Z., et al. (2020). NICER view of the 2020 burst storm and persistent emission of SGR 1935+2154. *ApJL* 904, L21. doi:10.3847/2041-8213/abc94c

Younes, G., Kouveliotou, C., Kargaltsev, O., Gill, R., Granot, J., Watts, A. L., et al. (2016). The wind nebula around magnetar Swift j1834.9-0846. *ApJ* 824, 138. doi:10.3847/0004-637X/824/2/138

Yuan, Y., Beloborodov, A. M., Chen, A. Y., and Levin, Y. (2020). Plasmoid ejection by alfvén waves and the fast radio bursts from SGR 1935+2154. *ApJL* 900, L21. doi:10.3847/2041-8213/abafa8

Zane, S., Taverna, R., González-Caniulef, D., Muleri, F., Turolla, R., Heyl, J., et al. (2023). A strong X-ray polarization signal from the magnetar 1RXS j170849.0-400910. *ApJL* 944, L27. doi:10.3847/2041-8213/acb703

Zhang, B. (2023). The physics of fast radio bursts. *Rev. Mod. Phys.* 95, 035005. doi:10.1103/RevModPhys.95.035005

Zhang, W., Basu-Zych, A., Bautz, M., Brandt, W., Cenko, S., Chan, K.-W., et al. (2022). The survey and time-domain astrophysical research explorer (STAR-X). *AAS/High Energy Astrophys. Div.* 54, 45.

frontiers | Frontiers in Astronomy and Space Sciences

TYPE Original Research
PUBLISHED 10 January 2024
DOI 10.3389/fspas.2023.1292656

Check for updates

OPEN ACCESS

EDITED BY
Esra Bulbul,
Max Planck Institute for Extraterrestrial Physics, Germany

REVIEWED BY
Sergio Campana,
National Institute of Astrophysics (INAF), Italy
Kohta Murase,
The Pennsylvania State University (PSU), United States

*CORRESPONDENCE
Murray Brightman,
murray@srl.caltech.edu

†NHFP Einstein Fellow

RECEIVED 11 September 2023
ACCEPTED 15 December 2023
PUBLISHED 10 January 2024

CITATION
Brightman M, Margutti R, Polzin A, Jaodand A, Hotokezaka K, Alford JAJ, Hallinan G, Kammoun E, Mooley K, Masterson M, Marcotulli L, Rau A, Wevers T, Younes GA, Stern D, García JA and Madsen K (2024), The high energy X-ray probe (*HEX-P*): sensitive broadband X-ray observations of transient phenomena in the 2030s. *Front. Astron. Space Sci.* 10:1292656. doi: 10.3389/fspas.2023.1292656

COPYRIGHT
© 2024 Brightman, Margutti, Polzin, Jaodand, Hotokezaka, Alford, Hallinan, Kammoun, Mooley, Masterson, Marcotulli, Rau, Wevers, Younes, Stern, García and Madsen. This is an open-access article distributed under the terms of the Creative Commons Attribution License (CC BY). The use, distribution or reproduction in other forums is permitted, provided the original author(s) and the copyright owner(s) are credited and that the original publication in this journal is cited, in accordance with accepted academic practice. No use, distribution or reproduction is permitted which does not comply with these terms.

The high energy X-ray probe (*HEX-P*): sensitive broadband X-ray observations of transient phenomena in the 2030s

Murray Brightman[1]*, Raffaella Margutti[2,3], Ava Polzin[4], Amruta Jaodand[1], Kenta Hotokezaka[5], Jason A. J. Alford[6], Gregg Hallinan[1], Elias Kammoun[7,8], Kunal Mooley[1], Megan Masterson[9], Lea Marcotulli[10,11†], Arne Rau[12], Thomas Wevers[13,14], George A. Younes[6], Daniel Stern[15], Javier A. García[16,1] and Kristin Madsen[16]

[1]Cahill Center for Astrophysics, California Institute of Technology, Pasadena, CA, United States, [2]Department of Astronomy, University of California, Berkeley, Berkeley, CA, United States, [3]Department of Physics, University of California, Berkeley, Berkeley, CA, United States, [4]Department of Astronomy and Astrophysics, The University of Chicago, Chicago, IL, United States, [5]Research Center for the Early Universe, Graduate School of Science, University of Tokyo, Tokyo, Japan, [6]Department of Physics, The George Washington University, Washington, DC, United States, [7]Institut de Recherche en Astrophysique et Planétologie, Université de Toulouse, French National Center for Scientific Research, Paul Sabatier University – Toulouse III, Centre national d'études spatiales, Toulouse, France, [8]INAF—Osservatorio Astrofisico di Arcetri, Firenze, Italy, [9]MIT Kavli Institute for Astrophysics and Space Research, Massachusetts Institute of Technology, Cambridge, MA, United States, [10]Yale Center for Astronomy and Astrophysics, New Haven, CT, United States, [11]Department of Physics, Yale University, New Haven, CT, United States, [12]Max-Planck-Institut für Extraterrestrische Physik, Garching, Germany, [13]Space Telescope Science Institute, Baltimore, MD, United States, [14]European Southern Observatory, Santiago, Chile, [15]Jet Propulsion Laboratory, California Institute of Technology, Pasadena, CA, United States, [16]X-Ray Astrophysics Laboratory, NASA Goddard Space Flight Center, Greenbelt, MD, United States

HEX-P is a probe-class mission concept that will combine high spatial resolution X-ray imaging (<10″ FWHM) and broad spectral coverage (0.2–80 keV) with an effective area superior to *NuSTAR* above 10 keV to enable revolutionary new insights into a variety of astrophysical problems, especially those related to compact objects, accretion and outflows. *HEX-P* will launch at a time when the sky is being routinely scanned for transient gravitational wave, electromagnetic and neutrino phenomena that will require the capabilities of a sensitive, broadband X-ray telescope for follow up studies. These include the merger of compact objects such as neutron stars and black holes, stellar explosions, and the birth of new compact objects. A response time to target of opportunity observation requests of <24 hours and a field of regard of 3π steradians will allow *HEX-P* to probe the accretion and ejecta from these transient phenomena through the study of relativistic outflows and reprocessed emission, provide unique capabilities for understanding jet physics, and potentially revealing the nature of the central engine.

KEYWORDS

transients: neutron star mergers, transients: black hole-neutron star mergers, transients: black hole mergers, transients: supernovae, transients: fast blue optical transients

1 Introduction

X-ray transients comprise some of the most interesting and energetic events in the Universe, and are usually powered by the birth of, accretion onto, and mergers of compact objects such as black holes and neutron stars. Surveys for astrophysical transients are now possible through electromagnetic, gravitational wave, and neutrino searches. As these transient surveys become more prevalent and more sensitive, it will be essential to have the capability to study the X-ray emission from the transients they uncover over a wide a range in energy and fluxes in order to understand the physics at their core.

Starting in the 2030s, the next-generation of gravitational-wave observatories are expected to come online, namely, the Einstein Telescope (Punturo et al., 2010; Maggiore et al., 2020), the Cosmic Explorer (Reitze et al., 2019), and the space-based *Laser Interferometer Space Antenna* (*LISA*; Amaro-Seoane et al., 2017). These observatories will detect the mergers of neutron stars and black holes out to large cosmological distances with improved sky localizations that will significantly increase the chances to identify their electromagnetic counterparts. The future of optical transients will be dominated by the Vera Rubin Observatory and its large synoptic survey where 1–2 million alerts are expected per night, as well as one million new supernovae from Rubin's Legacy Survey of Space and Time (LSST; Ivezić et al., 2019). A rich sample of transients at longer wavelengths will also be found by the next-generation radio observatories, particularly by the Square-Kilometer Array (SKA; Dewdney et al., 2009) and its pathfinders which are already in operation, such as the Australian SKA Pathfinder (ASKAP, Johnston et al., 2008) and the South African MeerKAT (Jonas et al., 2016). In the UV, *ULTRASAT* is approved for launch and will deliver a large number of UV transients (Shvartzvald et al., 2023). NASA is also currently concluding the down-select for the next Medium Explorer, both of which emphasize time-domain capabilities: either the *Ultraviolet Explorer* (*UVEX*) observing at UV energies providing large field of view UV photometry and rapid spectroscopy, or the *Survey and Time-domain Astrophysical Research eXplorer* (*STAR-X*) observing at soft X-ray and UV energies, is expected to launch at the end of this decade. Finally, the next-generation of neutrino detectors, namely, the KM3NeT in the Mediterranean Sea (Katz, 2006), the Gigaton Volume Detector in Lake Baikal (Baikal-GVD; Belolaptikov et al., 1997), and IceCube-Gen2 at the South Pole (Aartsen et al., 2014) also promise to yield a rich new view of the high-energy Universe, including stellar explosions.

Polzin et al. (2022) presents a compilation of all known classes of X-ray transients to date, covering a wide range in type, flux, and timescale (Figure 1). These range from low-luminosity events typically seen in our Galaxy, such as X-ray binary outbursts, to high-luminosity events seen in other galaxies, such as tidal disruption events (TDEs–e.g., Rees, 1988; Evans and Kochanek, 1989; Auchettl et al., 2017; Gezari, 2021). Both of these examples are produced by the accretion of stellar material onto a compact object such as a neutron star or a black hole. Polzin et al. (2022) also includes X-ray transients produced by the possible formation of a compact object, such as supernovae (SNe–e.g., Chevalier and Fransson, 2017) and more recently discovered fast blue optical transients (FBOTs–e.g., Drout et al., 2014; Arcavi et al., 2016; Ho et al., 2021), which might also be manifestations of (super-Eddington) accreting compact-objects.

The Probe-class *HEX-P* mission (Madsen et al., 2023) will provide sensitive broadband X-ray observations including roughly an order of magnitude improvement in the 10–30 keV band over *NuSTAR*, with significantly sharper angular resolution than either *XMM-Newton* (below 10 keV) or *NuSTAR* (above 10 keV). This sensitivity over a broad X-ray band will revolutionize the field of high-energy transient science, as shown in Figure 2 (adapted from Polzin et al., 2022), which shows that the faintest well-sampled lightcurves of each transient type to date will all be easily detected by *HEX-P* in the 10–30 keV band at early times.

Below we describe the *HEX-P* mission and the transient science for which we expect *HEX-P* to provide invaluable insights. We begin with the electromagnetic counterparts to gravitational wave events, followed by FBOTs, and SNe. We will also describe how *HEX-P* will yield insights into changing-look AGN (CLAGN), TDEs, blazars and fast radio bursts (FRBs) which are covered in more detail in separate papers (Kammoun et al., 2023; Marcotulli et al., 2023; Alford et al., 2023).

2 Mission design

The *High-Energy X-ray Probe* (*HEX-P*, Madsen et al., 2023) is a probe-class mission concept that offers sensitive broad-band X-ray coverage (0.2–80 keV) with exceptional spectral, timing and angular capabilities. It features two high-energy telescopes (HETs) that focus hard X-rays and one low-energy telescope (LET) that focuses lower-energy X-rays.

The LET consists of a segmented mirror assembly coated with Ir on monocrystalline silicon that achieves an angular resolution of 3.5″, and a low-energy DEPFET detector, of the same type as the Wide Field Imager (WFI; Meidinger et al., 2020) onboard *Athena* (Nandra et al., 2013). It has 512×512 pixels that cover a field of view of $11.3' \times 11.3'$. The LET has an effective passband of 0.2–25 keV, and a full frame readout time of 2 ms, which can be operated in a 128 and 64 channel window mode for higher count-rates to mitigate pile-up and faster readout. Pile-up effects remain below an acceptable limit of ~ 1% for fluxes up to ~ 100 mCrab in the smallest window configuration. Excising the core of the PSF, a common practice in X-ray astronomy, will allow for observations of brighter sources, with a typical loss of up to ~ 60% of the total photon counts.

The HET consists of two co-aligned telescopes and detector modules. The optics are made of Ni-electroformed full shell mirror substrates, leveraging the heritage of *XMM-Newton* (Jansen et al., 2001), and coated with Pt/C and W/Si multilayers for an effective passband of 2–80 keV. The high-energy detectors are of the same type and flown on *NuSTAR* (Harrison et al., 2013), and they consist of 16 CZT sensors per focal plane, tiled 4×4, for a total of 128×128 pixel spanning a field of view slightly larger than for the LET, of $13.4' \times 13.4'$.

The response time to target of opportunity (ToO) observation requests will be <24 hours enabling fast observations of transient events. As shown in Figure 2 this will be more than enough to observe and detect and characterize all known X-ray transients in the 10–30 keV band while they are still bright. Furthermore,

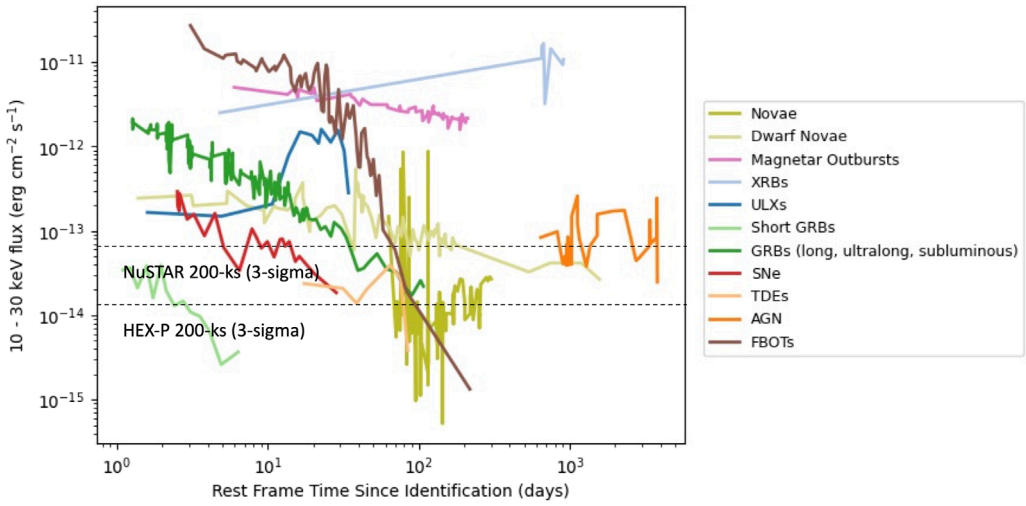

FIGURE 1
10–30 keV X-ray lightcurves of known X-ray transients, adapted from Polzin et al. (2022), with the sensitivities of *HEX-P* and *NuSTAR* shown with dashed lines. *HEX-P* will probe deeper in sensitivity than *NuSTAR* while matching *XMM-Newton* and *Chandra* at lower energies. This will enable sensitive broadband studies of all known X-ray transient types from ≤ 1 day post identification.

FIGURE 2
Artist impression of *HEX-P* showing the two high-energy telescopes (HETs) that focus hard X-rays and one low-energy telescope (LET) that focuses lower-energy X-rays. To achieve the high energies, HEX-P features a 20-m extendable boom, wrapped in a thermal sock to reduce motions.

HEX-P's location at L1 will allow a large fraction of the sky to be observed at any one time - the field of regard will be 3π steradians. This will also enable the fast observation of transient events.

The broad X-ray passband, superior sensitivity, fast response time and large field of regard will provide a unique opportunity to enable revolutionary new insights into the wealth of transient astrophysical phenomena that the facilities discussed above are expected to discover.

3 Simulations

All simulations presented in the following sections, specifically Section 4.3 and 4.4, were produced with a set of response files that represents the observatory performance based on current best estimates as of Spring 2023 (see Madsen et al., 2023). The effective area, ~340 cm^2 at both 1 keV and 30 keV when combining the LET and HET, is derived from raytracing calculations for the mirror design including obscuration by all known structures. The detector responses are based on simulations performed by the respective hardware groups, with an optical blocking filter for the LET and a Be window and thermal insulation for the HET. The LET background was derived from a GEANT4 simulation (Eraerds et al., 2021) of the WFI instrument, and the HET background was derived from a GEANT4 simulation of the *NuSTAR* instrument. Both assume *HEX-P* is in an L1 orbit.

4 New insights into transient phenomena by HEX-P

4.1 Probing the ejecta and remnant emission from the mergers of neutron stars and black holes detected in gravitational waves

With the detection of the first binary black hole merger in 2015 (Abbott et al., 2016), LIGO-Virgo opened a new gravitational wave window onto the Universe. This new era of multi-messenger astronomy with gravitational waves expanded with the LIGO-Virgo detection of GWs and photons from the binary neutron star merger GW170817 (Abbott et al., 2017), which yielded a wide range of scientific results, informing us about gravitational physics, nucleosynthesis, extreme states of nuclear matter, relativistic explosions and jets, and cosmology (e.g., Cowperthwaite et al.,

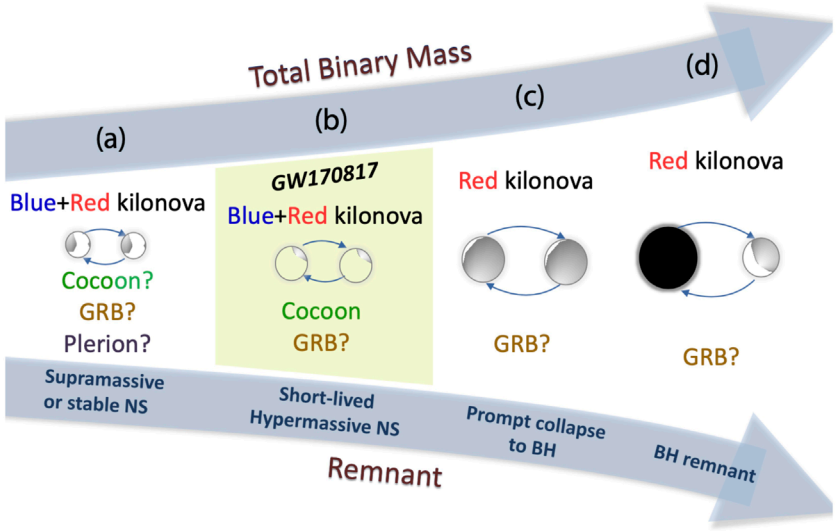

FIGURE 3
The range of binary neutron star and neutron star-black hole merger events expected to produce an X-ray afterglow being **(A)** a supramassive or stable NS, **(B)** a short-lived Hypermassive NS, **(C)** a prompt collapse to BH or **(D)** a BH remnant. *HEX-P* will provide a powerful tool for studying and understanding these extreme events.

2017; Margutti et al., 2017a; Troja et al., 2017; Margutti et al., 2018; Mooley et al., 2018b; a; Margutti and Chornock, 2021; Mooley et al., 2022).

The X-ray emission from GW170817 was produced by the collision between the fastest moving collimated ejecta and the circumburst medium (Margutti et al., 2017a; Troja et al., 2017; Margutti et al., 2018; D'Avanzo et al., 2018; Hajela et al., 2022). GW170817 represents only an initial exploration of a rich scientific landscape populated by stellar evolution, explosions, and eventual mergers of massive binary systems, and there are still many unknowns regarding the outcome of binary neutron star and neutron star-black hole mergers. The total binary mass and binary mass ratio, as well as the nature of the final remnant, governs the mass, velocity, and direction of ejecta outflows and should lead to a diverse range of electromagnetic counterparts. For example, the properties of the associated explosion, known as a kilonova, is expected to depend on how long lived a hypermassive neutron star (HMNS) may last before collapsing to form a black hole (Figure 3). If black hole formation is prompt, a red kilonova that peaks in the near-infrared is expected, otherwise, a longer-lived HMNS could produce a bluer kilonova (e.g., Metzger and Fernández, 2014). The neutron star equation of state is also expected to affect the kilonova properties (Zhao et al., 2023).

For binaries with significantly lower total mass than GW170817, does a long-lived supermassive or stable neutron star remnant form? *HEX-P* has the potential to observe emission from the merger remnant, be it a black hole or neutron star. Murase et al. (2018b) calculates the expected X-ray emission from the merger remnant, which, depending on the nature of the remnant, they predict would come from the disk of a newly formed black hole or the pulsar wind nebula (plerion) of a newly formed neutron star. In both cases, the emission would be highly absorbed at early times due to the remnant being buried in the merger ejecta (Figure 4). Hard X-rays would thus be the first to emerge, followed by softer X-rays as the ejecta become optically thin. Indeed, in the recent example of SN 2023ixf in the nearby Pinwheel Galaxy (M101; d = 6.9 Mpc), Grefenstette et al. (2023) report on *NuSTAR* observations a highly absorbed X-ray spectrum 4 days after the explosion and likely would have detected it sooner if the observation had taken place earlier. Soft X-ray observations by *Swift* did not detect the supernova until 4.25 days post-explosion (Panjkov et al., 2023). Naturally, an X-ray observatory with hard X-ray sensitivity such as *HEX-P* will be well suited to detect this kind of early and evolving remnant emission.

Assuming a distance of 40 Mpc, Murase et al. (2018b) predicts that the 30 keV emission from a black hole merger remnant would peak at $\sim 10^{-14}$ erg cm^{-2} s^{-1} approximately $\sim 10^{6} - 10^{7}$ s post-merger (i.e., weeks to month timescales). *HEX-P* could reach these sensitivities at 30 keV (3σ) in a 500 ks observation. The emission from a neutron star is expected to be significantly brighter and therefore detectable to larger distances and/or shorter exposures.

X-ray lightcurves for events as bright as GW170817 provide a powerful means of probing ejecta properties such as energy and angular structure. From these bright events we can determine which binary neutron star mergers are capable of launching ultra-relativistic jets (e.g., Nathanail et al., 2021; Sun et al., 2022). Potentially, all binary neutron star mergers generate ultrarelativistic jets. If only some do, what determines the behavior? *HEX-P* will be able to detect the afterglow emission from a neutron star-neutron star merger at distances up to 200 Mpc under a range of jet scenarios, and characterize its lightcurve across multiple energy bands, thereby answering these questions. We illustrate this in Figure 5 which shows lightcurves calculated from hydrodynamic simulations of a binary neutron star merger based on the semi-analytic code used in Lazzati et al. (2018). The model has five free parameters: the viewing angle θ_v, the microphysical parameters ϵ_e (the fraction of shock energy given to electrons) and ϵ_B (the fraction of shock energy given to tangled magnetic field), the electrons population distribution index p, and the external medium density

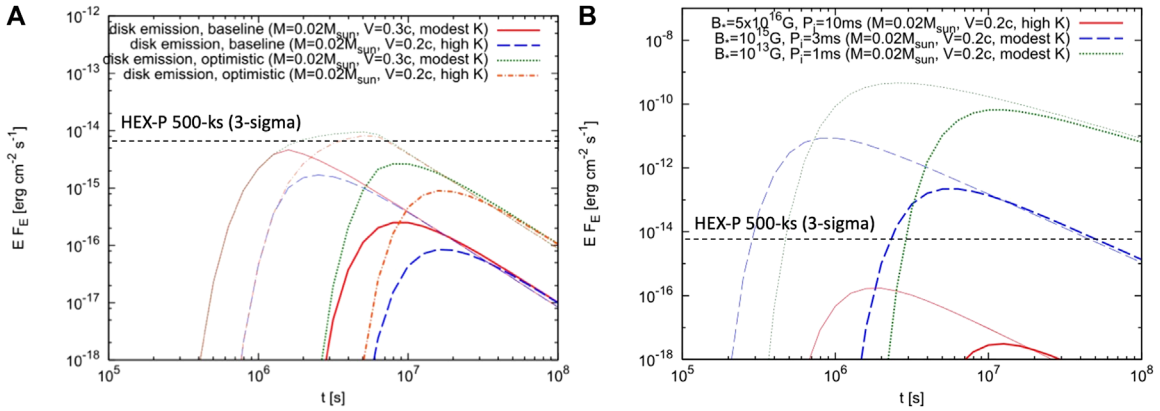

FIGURE 4
Predicted X-ray lightcurves of emission from an accretion disk of a black hole remnant **(A)** and emission from a pulsar wind nebula of a neutron star remnant **(B)** taken from Murase et al. (2018b) with *HEX-P* sensitivities at 30 keV shown. In both cases, emission at 30 keV (thin lines) emerges prior to and is stronger than emission at 3 keV (thick lines) due to the remnant being buried in the merger ejecta which is initially optically thick.

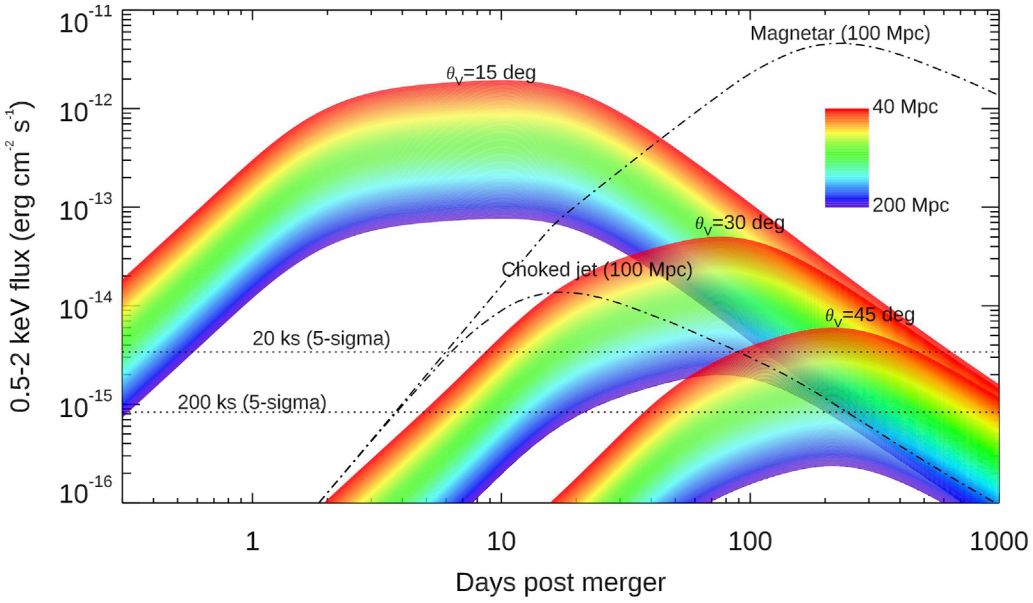

FIGURE 5
X-ray lightcurves calculated from hydrodynamic simulations of a binary neutron star merger at distances of 40–200 Mpc and circumburst density of 0.1 cm^{-3}. Our simulation includes outflow from the jet interacting with the interstellar medium, with viewing angles of $\theta_V = 15$, 30 and 45°. We also plot a prediction for a choked jet and the magnetar model. *HEX-P* sensitivities are shown with dotted lines.

$n_{\rm ISM}$, which was assumed to be 0.1 cm^{-3} and constant. The total kinetic energy of the fireball and its initial Lorentz factor, both dependent on the viewing angle, were taken from a hydrodynamic numerical simulation previously described in Lazzati et al. (2017). Specifically, the energy of the blast wave, set by the numerical simulation, is 6×10^{49} erg. Our simulation includes outflow from the jet interacting with the interstellar medium, with viewing angles of $\theta_V = 15$, 30 and 45°.

For a binary merger with significantly more mass than GW170817, we might expect a prompt collapse to a black hole. Although the formation of jets and cocoons is uncertain, the detection of the X-ray and radio afterglows may be able to disambiguate binary neutron star mergers from neutron star-black hole mergers of similar total mass. For neutron star-black hole mergers where the neutron star is disrupted beyond the innermost stable circular orbit, the tidal ejecta is expected to have much higher mass ($\sim 0.1 M_\odot$) than in a binary neutron star merger, and could yield a bright red kilonova. An absence of polar ejecta in this case would imply that jets, if launched, would escape to produce a short gamma-ray burst. However, there are large uncertainties and many unknowns in these predictions. *HEX-P*, with spectral and timing capabilities over a wide bandpass, as well as <24 hr response time

and good sky visibility, will be well positioned to observe the range of X-ray emission from the ejecta of neutron star-neutron star and neutron star-black hole mergers.

4.2 Black hole-black hole mergers in AGN accretion disks

Binary black hole mergers come from two broad classes: a binary star evolutionary channel and a dynamical, or hierarchical, channel (for a recent review, see Mapelli, 2021). Among dynamical mergers, sub-channels include mergers in globular clusters, mergers in quiescent galactic nuclei, and mergers in the accretion disks of active galactic nuclei (AGN). Since the most massive stars end their lived in pair instability supernovae which leave no compact remnant, the explosive deaths of massive stars are not thought capable of producing black holes in the "upper mass gap" range above ~$50M_{\odot}$. Massive binary black hole merger progenitors above ~$100M_{\odot}$ therefore strongly imply a hierarchical merger origin, i.e., from consecutive merger events. This, in turn, implies a dynamical origin, not a field binary origin.

Since black holes can receive a strong kick at merger, mergers remnants are more easily retained in deep gravitational potentials, such as in the nuclei of galaxies. A promising location for hierarchical mergers are therefore AGN (McKernan et al., 2019). Merger kicks, even of large magnitude, are insufficient to escape an AGN environment, making AGN ideal for retaining and growing black holes via hierarchical mergers. AGN are expected to dominate the rate of mergers in the deep potential wells of galactic nuclei. Besides massive binary black hole mergers, other pointers to a significant contribution to binary black hole mergers from the AGN channel include highly asymmetric mass ratio black hole mergers and the observed anti-correlation between binary black hole mass ratio and effective spin (Callister et al., 2021), which at present can only be explained in the context of the AGN channel (McKernan et al., 2022).

Unlike all other merger channels, detectable counterparts are expected from compact object mergers in AGN due to the baryon-rich, high density environment. Simple scaling arguments imply that the luminosity of the counterpart should scale roughly linearly with the binary total mass (McKernan et al., 2019), implying more massive gravitational wave events create more luminous flares. Indeed, the first event with a candidate optical counterpart, reported by (Graham et al., 2020), was later identified as the most massive LIGO/Virgo merger observed to date, with a total mass of $150M_{\odot}$ (Abbott et al., 2020). Kimura et al. (2021) present a model of how compact object mergers in AGN accretion disks should appear, with outflows creating a bubble in the AGN accretion disk, and the merger remnant black hole subsequently recoiling into the dense AGN disk and producing strong X-ray outflow-breakout emission that can outshine the AGN.

Though we are currently at very early stages, both theoretically and observationally, for understanding binary black hole mergers in AGN accretion disks, there are strong arguments to expect that this is an important gravitational wave merger channel, and that broadband X-ray emission will be a key tool for studying such events. We also note that counterparts to black hole mergers in accretion disks provide a test of the dynamics of the merger and a probe of fundamental AGN disk properties (Vajpeyi et al., 2022). In addition, associated counterparts (i.e., spectroscopic redshifts) to gravitational wave mergers enable their use as a standard siren, providing a new, independent measurement of the Hubble constant (Chen et al., 2022). *HEX-P* is well posed to become an important tool for studying both binary black hole mergers in AGN accretion disks, as well as the larger population of gravitational wave merger events over a range of environments.

4.3 Observing a potentially newly-formed compact object in fast blue optical transients

With the wealth of large area optical surveys such as the Zwicky Transient Facility (ZTF) and the upcoming Vera Rubin Observatory, a vast array of optical transients have been uncovered, with orders of magnitude more sources expected in the 2030s. Fast evolving luminous transients, or fast blue optical transients (FBOTs) are one such new class (Drout et al., 2014; Arcavi et al., 2016; Ho et al., 2021). Their fast evolution with rise times of <10 days and high luminosity in excess of 10^{43} erg s^{-1} imply a power source incompatible with the standard radioactive decay model for supernovae and can be explained by prolonged energy injection from a central compact object. Only a handful of such events have been discovered so far and are thought to comprise <0.1% of the local supernova population (Ho et al., 2023).

The best studied FBOT to date is AT 2018cow which, at a distance 60 Mpc, reached a peak X-ray luminosity of ~4×10^{44} erg s^{-1} (Margutti et al., 2019). One of the defining properties of this event was its luminous and variable X-ray emission unprecedented among optical transients. A *NuSTAR* observation ~7.7 days after discovery revealed an excess of hard X-ray emission above the soft X-ray power-law which is well modeled by reflection from Compton-thick material, i.e., the reprocessing of X-rays in an optically-thick medium such as an accretion disk. Reflection spectra are characterized by the presence of Fe K fluorescence emission lines near 6.4–6.9 keV, an absorption Fe K-edge at ~ 7–9 keV, and a broad featureless hump peaking at 20–30 keV produced by electron scattering. Modeling the high-energy spectrum of AT 2018cow required aspherical ejecta. The reflection features faded rapidly and could not be constrained by *NuSTAR* in observations a few days later, precluding a detailed study of its nature. One possible explanation for the origin of the reflected component was a funnel formed by a super-Eddington accretion flow, is often used to explain the spectra of ultraluminous X-ray sources (Margutti et al., 2019). Similar funnel-like geometries for super-Eddington accretion have been invoked in TDEs too (Kara et al., 2016; Dai et al., 2018, e.g.).

Due to its proximity and X-ray brightness, AT 2018cow is the only transient to show such a Compton reflection feature so far. With the greater sensitivity and improved target-of-opportunity capabilities afforded by *HEX-P*, studies of FBOTs will become more detailed and possible to larger distances and volume, allowing the determination of the central engine. We show a simulated *HEX-P* spectrum of AT 2018cow in Figure 6, compared to the *NuSTAR* actual data. We produced this by assuming the reflection + corona model (`relxill` + cutoffpl in XSPEC) described in (Margutti et al.,

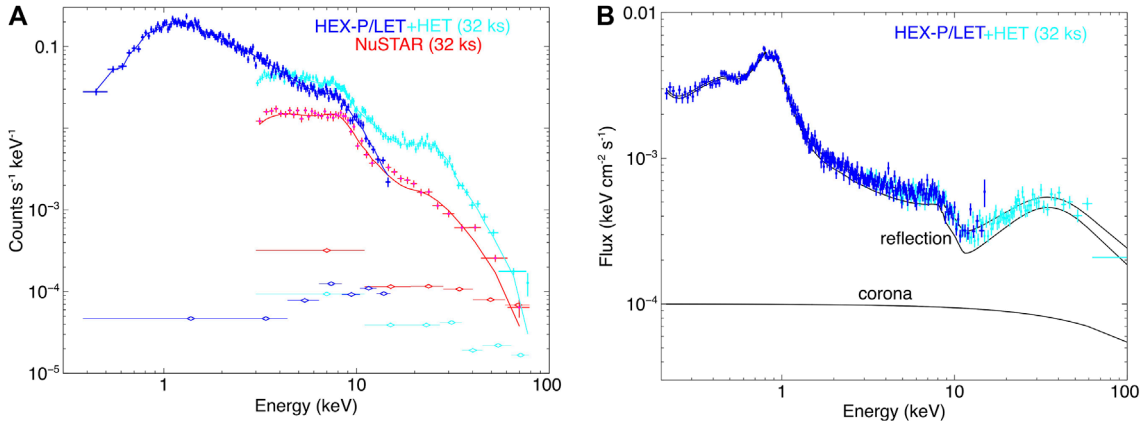

FIGURE 6
(A) A simulated spectrum of AT 2018cow with *HEX-P* compared to what *NuSTAR* observed (crosses). *HEX-P* would have detected the transient over the 0.2–80 keV range, which combined with greater effective area and lower background (diamonds) than *NuSTAR* would have allowed a detailed study of its spectral components. **(B)**. Unfolded *HEX-P* spectrum of AT 2018cow showing the reflection and corona components.

2019) with dimensionless spin parameter a = 0.7, X-ray spectral index $\Gamma = 1.0$, ionization parameter $\log\xi = 3.3$, iron abundance $A_{\rm Fe} = 4.9$, high-energy cut off $E_{\rm cut} = 170$ keV and reflection fraction $R_{\rm refl} = -12$ as shown in the right panel of Figure 6 and with the same 32-ks exposure time as the *NuSTAR* observation. Not only will *HEX-P* provide the simultaneous soft X-ray data, it will provide a larger effective area and lower background than *NuSTAR* above 10 keV that will enable a more sensitive broadband X-ray spectral investigation of these sources, including detection of reflection components.

HEX-P will also be able to detect AT 2018cow-like events with a 10–30 keV signal-to-noise of 5 in a 20-ks observation up to 10 times further (600 Mpc), and in 1,000 times the volume, which will undoubtedly lead to a leap in understanding of these events.

4.4 Mapping the most extreme mass loss history of massive stars in interacting supernovae

Along with possible engine-powered optical transients like AT 2018cow, a plethora of supernovae types will be detected by upcoming optical surveys. These include interacting supernovae where the ejecta from the stellar explosion interact with the ISM, producing high-temperature shocked emission that can reveal the mass loss history of the massive star (Chevalier and Fransson, 2017). The high temperature of the shock can only be constrained with sensitive hard X-ray observations which have only been done with *NuSTAR* so far (Ofek et al., 2014; Chandra et al., 2015; Margutti et al., 2017b; Grefenstette et al., 2023, e.g., SNe 2010jli, 2014C and 2023ixf). For the case of SN 2014C at a distance of 14.7 Mpc, the shock produced bright hard X-ray emission that was observed with *Chandra* and *NuSTAR* (Margutti et al., 2017b). The hard X-ray coverage allowed for the measurement of the absorption and shock temperature (10–20 keV) as a function of time, which has only been achieved for SN 2014C so far. These data constrain the density profile of the environment of the supernova.

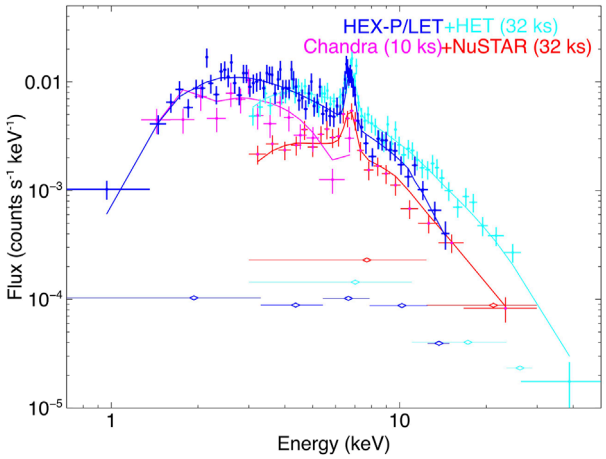

FIGURE 7
A simulated spectrum of SN 2014C with *HEX-P* compared to what *Chandra* and *NuSTAR* observed (crosses). *HEX-P* would have provided simultaneous data over the 0.2–50 keV range, which combined with greater effective area and lower background than *NuSTAR* (diamonds) would have provided a more detailed constraint on the shock properties.

Recently, *NuSTAR* observations of SN 2023ixf from 4 days post-explosion have provided the earliest constraints on the absorption and shock temperature to date (Grefenstette et al., 2023) and follow up observation promise to reveal more about the mass-loss history of its progenitor (Margutti et al. in prep.).

We show a simulated *HEX-P* spectrum of SN 2014C in Figure 7. We produce these spectra by assuming the absorbed thermal bremsstrahlung with Gaussian line component spectral model described in Margutti et al. (2017b) (tbabs*bremss + gaussian in XSPEC) with parameters $N_{\rm H} = 3 \times 10^{22}$ cm^{-2} and $kT = 18$ keV with a 0.3–10 keV flux of 10^{-12} erg cm^{-2} s^{-1} and the same 32-ks exposure time as *NuSTAR*. Compared to *Chandra* and *NuSTAR*, *HEX-P*

would have yielded a spectrum with signal-to-noise twice that of *NuSTAR* in the 3–30 keV band, providing better constraints on the shock temperature and absorption, where the uncertainties would be reduced by more than 50%. The spectral resolution of *HEX-P* at 6 keV is expected to be 0.14 keV, better than *NuSTAR* and similar to *Chandra*/ACIS. More importantly, *HEX-P* will also be able to detect SN 2014C-like events with a 10–30 keV signal-to-noise of 5 in a 20-ks observation up to 3 times further (45 Mpc), and in 27 times the volume.

As with binary neutron star mergers embedded in their ejecta, and AT 2018cow and SN 2014C like events, *HEX-P*'s hard X-ray sensitivity will be invaluable for studying explosive transients of all types that occur in dense environments. These may include high-redshift GRBs which are expected to occur in dense environments where optical and soft X-rays are likely to be obscured, but mid-infrared and hard X-rays can penetrate. For this reason there exists potential synergies between *HEX-P* and *JWST*.

4.5 Nuclear transients: Changing-look AGN, tidal disruption events and quasi-periodic eruptions

4.5.1 Changing look AGN

The advance of time-domain surveys is also revealing extreme variability in the accretion process onto supermassive black holes. Transient accretion events provide unique windows into the formation and evolution of accretion disks, the heating of the X-ray corona, and the connection between accretion and ejection via winds and jets. The X-ray band, in particular, is crucial to probing the innermost portions of the accretion flow, where strong outflows are launched and much of the gravitational energy is released.

Recently there has been a class of AGN discovered that undergo rapid transitions on timescales of months to years, in which broad lines either appear or disappear in the optical spectrum. These sources are known as changing-look AGN (CLAGN; for a recent review, see Ricci and Trakhtenbrot, 2022), and they challenge the classic unified model for AGN, whereby the presence of broad emission lines is solely a function of viewing angle. A particularly extreme source and the first CLAGN that was caught in the act of changing states, 1ES 1927 + 654 showed dramatic and unprecedented X-ray variability as optical broad lines formed (Trakhtenbrot et al., 2019; Ricci et al., 2020). Shortly after the optical outburst, the canonical X-ray corona was destroyed (Ricci et al., 2020). Extensive X-ray monitoring revealed its reappearance, allowing for one of the first studies of how an AGN corona is formed (Ricci et al., 2021; Masterson et al., 2022). This dramatic behavior has been explained by either a TDE occurring in an AGN (Ricci et al., 2020) or an inversion in the magnetic flux polarity (Scepi et al., 2021; Laha et al., 2022). *NuSTAR* observations were crucial for disentangling the soft photon index and low cutoff energy as the corona formed, while softer instruments like *XMM-Newton* and *NICER* probed the evolution of the inner accretion flow in 1 ES 1927 + 654, including rapid variability of the soft X-ray flux and a relativistic outflow launched from the inner disk (Masterson et al., 2022). Thus, broad energy coverage in the X-ray band is crucial to fully understanding this and other CLAGN. With its 0.2–80 keV bandpass, *HEX-P* will be uniquely situated to probe the X-ray evolution, variability, and coupling between the inner disk and the corona in CLAGN.

4.5.2 Tidal disruption events

TDEs also hold key insights into how the X-ray corona is powered and formed, as numerous TDEs have shown spectral hardening and the formation of a corona at late-times (~ a few years after the initial disruption; e.g., Wevers et al., 2021; Yao et al., 2022; Guolo et al., 2023). They can also serve as probes of extreme accretion, as dramatic X-ray spectral variability, similar to that of 1ES 1927 + 654, has also been seen in TDE candidates (e.g., a repeating TDE discovered by eROSITA, which shows a repetitive creation and collapse of the X-ray corona; Liu et al., 2023).

Likewise, as TDEs can also transition from super-to sub-Eddington as the mass fallback rate drops, *HEX-P* can also be used to study the disk-corona connection during these transitions, thereby allowing for comparisons to state transitions in black hole binaries (Remillard and McClintock, 2006) and tests of the scale-invariant nature of accretion. Moreover, X-ray observations of TDEs can help illuminate the underlying accretion disk evolution, which is especially hard to probe with optical emission alone.

X-rays from TDEs also serve as an independent way of measuring black hole mass and spin, but this is currently quite difficult to do with existing facilities. Detailed X-ray spectral modeling of the thermal continuum emission in TDEs can provide constraints on the mass and spin of the black hole (e.g., Wen et al., 2020). However, there are inherent uncertainties related to the presence of an X-ray corona, which can introduce biases. Likewise, the detection of X-ray quasi-periodic oscillations (QPOs) can be used to constrain the black hole spin (e.g., Pasham et al., 2019), but are difficult to detect with low count rates and short observations. Finally, through time-lags between the continuum and reflected components, Fe Kα reverberation mapping provides constraints on the disk and coronal geometrics, as well as black hole spin in systems with geometrically thin disks truncated at the ISCO. To date, only one source, the relativistically jetted TDE Swift J1644, has shown an Fe Kα reverberation signal, potentially due to the fact that the corona often appears at late times in TDEs when the emission becomes faint (Kara et al., 2016). With its high throughput, good spectral energy resolution, low background, and ability to do long pointed observations, *HEX-P* studies of TDEs will advance all three of these techniques for measuring BH mass and spin. These studies will add invaluable constraints on the demographics of quiescent, low-mass SMBHs, which are not readily available through other means.

Theoretical studies of TDEs have proposed that the apparent X-ray/optical dichotomy among TDEs is a result of viewing angle dependence (Dai et al., 2018), which has been recently supported by *Swift* and *XMM-Newton* observations of numerous optically-selected TDEs (e.g., Guolo et al., 2023). *HEX-P* will be able to provide frequent and systematic X-ray follow-up of optically-selected TDEs, which are expected to become far more numerous in the next decade (e.g., Bricman and Gomboc, 2020). This is vital for understanding sample biases, as well as probing other interesting accretion phenomena, such as the fraction of TDEs that can launch powerful outflows and their evolution over time, as well as the physical conditions that are required to launch them.

Finally, TDEs are also powerful probes of relativistic and multi-messenger astrophysics, with powerful on-axis jets detected in a few

sources (Burrows et al., 2011; Cenko et al., 2012; Andreoni et al., 2022; Pasham et al., 2023) and recent discoveries of high-energy neutrinos coincident with three optical TDE candidates (contributing a sizeable fraction of the astrophysical high-energy neutrino flux, despite being found in non-jetted systems; e.g., Stein et al., 2021; van Velzen et al., 2021; Reusch et al., 2022). Probing future jetted and neutrino-emitting TDEs in the X-ray band with *HEX-P* will help to disentangle particle acceleration mechanisms and models for both jet and neutrino production.

4.5.3 Quasi-periodic eruptions

A recently discovered phenomenon whose origins remain elusive are quasi-periodic eruptions (QPEs) of nearby low mass galaxies (e.g., Miniutti et al., 2019; Giustini et al., 2020; Arcodia et al., 2021; Chakraborty et al., 2021; Guolo et al., 2023). With recurrence times between 2 h and ~22 days, potential explanations range from rapid limit-cycle oscillations in the inner accretion disk of an AGN, to various flavors of stellar mass companions on a bound orbit about a massive black hole. While the discovery of new systems requires a large area survey, detailed follow-up studies with *HEX-P* can help to further constrain their trigger mechanism by accurately measuring their X-ray properties and evolution over time. In particular, the presence and role of the X-ray corona remains unclear in the known sources and our current knowledge is limited by the effective area of existing telescopes (taking into account the sharp decrease in signal of QPEs at >1 keV energies). The high throughput and low background of *HEX-P* would enable more detailed constraints on the behaviour of the >1 keV energy emission in QPEs, while its high throughput down to 0.2 keV will allow for efficient photon collection compared to existing missions, as this is where the QPE emission peaks.

HEX-P will make significant contributions to our understanding of extreme accretion physics in these nuclear transients, including improving key constraints on the evolution of coronal parameters like Γ and $E_{\rm cut}$ by a factor of ~2 with respect to *XMM-Newton* and *NuSTAR* (Kammoun et al., 2023). More details on the coronal physics that we can glean from these transients with *HEX-P*, as well as SMBH coronal physics in general, are described in Kammoun et al. (2023). Separately, Connors et al. (2023) describe the coronal physics of accreting stellar-mass BHs.

4.6 Blazars

Many AGN are known to launch relativistic jets which can extend up to kiloparsecs in length. These jets emit across the electromagnetic spectrum (radio to γ-ray) and are also multi-messenger (neutrino) emitters. When the viewing angle is close to on axis (viewing angles, $\theta_{\rm V} < 5°–10°$) we observe a blazar, while at larger viewing angles we classify them as misaligned AGNs or radio galaxies (e.g., Urry and Padovani, 1995; Hovatta et al., 2009).

Blazars are believed to be able to accelerate protons to very high energies. This was potentially confirmed by the claimed association of the γ-ray flaring blazar TXS 0506 + 056 with the IceCube neutrino event IceCube-170922A (Aartsen et al., 2018). In order to probe the transition between the synchrotron and high-energy emission part of the spectrum, where signatures of electromagnetic cascades associated with the neutrino-producing photo-hadronic interactions should emerge (Murase et al., 2018a) simultaneous broadband coverage from X-ray to MeV γ-rays is required, and has so far been lacking. This was shown in previous studies of a previous neutrino flare potentially linked to TXS 0506 + 056 where the lack of sensitive simultaneous broad-band X-ray spectral and temporal coverage did not allow for any conclusion on the emission mechanism (e.g., Reimer et al., 2019; Zhang et al., 2020). Simultaneous broadband coverage of neutrino alerts in the direction of blazar sources could be the tipping point for jet models as well as confirming AGN as one of the sources of high-energy cosmic rays.

For the first time *HEX-P* will allow us to detect the spectral signatures that will conclusively yield the preferred high-energy emission mechanisms in jets, and, by extension, their composition. Furthermore, combined with current and upcoming observatories such as COSI, IXPE, CTA, IceCube Gen 2, *HEX-P* will reveal the preferred particle acceleration and emission mechanism of the brightest objects in the Universe, fulfilling the promises of multi-wavelength and multi-messenger science. The contribution to blazar science by *HEX-P* is described in more detail in Marcotulli et al. (2023).

4.7 Fast radio bursts

Fast Radio Bursts (FRBs) are millisecond duration transients discovered through their luminous sweeps in multi-band radio detectors (Petroff et al., 2019). Initially, FRBs were thought of as non-recurrent phenomena. However in the last decade advent of radio facilities such as MeerKAT, MeerTRAP and CHIME which could regularly monitor the known population of FRBs have led to a deluge of fast radio burst transients spanning a wide range of the parameter space. While most of the ~10^3 FRBs detected so far do not seem to repeat yet, 24 of them have occasionally shown high burst rates clustered over a short duration. The emission models for both non-repeating and repeating FRBs are not yet well-constrained.

In a breakthrough discovery, observational evidence for the magnetar model as a source of FRBs occurred on 2020 April 28, when an FRB-like radio burst was detected from the Galactic magnetar SGR 1935 + 2,154 (Andersen et al., 2020; Bochenek et al., 2020), in the winding hours of a major burst storm (Younes et al., 2020); it had a fluence rivaling those of the faint end of extragalactic FRBs. Moreover, the FRB occurred simultaneously with a bright, short X-ray burst, hence, relating it to magnetar activity and providing crucial evidence for its triggering mechanism (e.g., Mereghetti et al., 2020; Li et al., 2021; Ridnaia et al., 2021).

The discovery of FRB-like bursts from magnetars opened up new avenues for the study of extragalactic FRBs (e.g., Wadiasingh and Timokhin, 2019). This discovery opened up new questions such as 1) What is unique about the FRB-associated X-ray bursts, and why do the majority of X-ray bursts lack a radio counterpart? 2) What is the distribution of the spectral properties for FRB-associated X-ray bursts? Are their distinctive spectral properties universal across radio fluence? 3) Is the radio to X-ray flux ratio ($L_{\rm R}/L_{\rm X}$) constant for all FRB-like radio bursts? 4) What is the radio-X-ray time-lag across burst fluence? Answering these questions will require 1) a broad X-ray coverage given that the spectral energy distribution of magnetar burst peaks in the 20–30 keV range, 2) high timing resolution ($\lesssim$ 1 ms) for accurately measuring the radio-X-ray lag in

burst arrival time (Mereghetti et al., 2020), 3) sensitivity to faint X-ray bursts, i.e., fluence $<10^{-7}$ erg cm^{-2}, to sample a large fraction of the X-ray and radio burst fluence distribution given their steep shapes ($N \propto S^{-0.6}$, Younes et al., 2020). *HEX-P* is the only facility to satisfy all the above criteria. The contribution to FRB science by *HEX-P* is described in detail in Alford et al. (2023).

5 Conclusion

The 2030s will be an exciting era for time domain and multi-messenger astronomy, with a veritable orchestra of new facilities providing new views of new events in the Universe. We are virtually guaranteed to discover events that are barely dreamed of currently. Given this evolving landscape, it is essential that a sensitive, versatile, and flexible X-ray observatory will be available in the 2030s, able to do broadband X-ray studies, including imaging, spectroscopy, and timing, to understand the nature and the physics of these events. From the early days of X-ray astronomy, it was revealed that the high-energy sky is highly variable–and that X-rays provide a powerful and essential tool for understanding the range of phenomena. This paper describes how *HEX-P* will provide that needed capability for the 2030s.

Data availability statement

Publicly available datasets were analyzed in this study. This data can be found here: https://heasarc.gsfc.nasa.gov/db-perl/W3Browse/w3browse.pl.

Author contributions

MB: Writing–original draft, Writing–review and editing. RM: Writing–review and editing. AP: Writing–review and editing. AJ: Writing–review and editing. KH: Writing–review and editing. JA: Writing–review and editing. GH: Writing–review and editing. EK: Writing–review and editing. KuM: Writing–review and editing. MM: Writing–review and editing. LM: Writing–review and editing. AR: Writing–review and editing. GY: Writing–review and editing. DS: Writing–review and editing. JG: Writing–review and editing. KrM: Writing–review and editing.

Funding

The author(s) declare financial support was received for the research, authorship, and/or publication of this article. The work of DS was carried out at the Jet Propulsion Laboratory, California Institute of Technology, under a contract with NASA. EK acknowledges financial support from the Centre National d?Etudes Spatiales (CNES). GH and KM acknowledge support from the National Science Foundation Grant AST-1911199.

Conflict of interest

The authors declare that the research was conducted in the absence of any commercial or financial relationships that could be construed as a potential conflict of interest.

Publisher's note

All claims expressed in this article are solely those of the authors and do not necessarily represent those of their affiliated organizations, or those of the publisher, the editors and the reviewers. Any product that may be evaluated in this article, or claim that may be made by its manufacturer, is not guaranteed or endorsed by the publisher.

References

Aartsen, M. G., Ackermann, M., Adams, J., Aguilar, J. A., Ahlers, M., Ahrens, M., et al. (2018). Multimessenger observations of a flaring blazar coincident with high-energy neutrino IceCube-170922A. *Science* 361, eaat1378. doi:10.1126/science.aat1378

Aartsen, M. G., Ackermann, M., Adams, J., Aguilar, J. A., Ahlers, M., Ahrens, M., et al. (2014). *IceCube-Gen2: a vision for the future of neutrino astronomy in Antarctica*. Available at: https://arxiv.org/abs/1412.5106.

Abbott, B. P., Abbott, R., Abbott, T. D., Abernathy, M. R., Acernese, F., Ackley, K., et al. (2016). Observation of gravitational waves from a binary black hole merger. *Phys. Rev. Lett.* 116, 061102. doi:10.1103/PhysRevLett.116.061102

Abbott, B. P., Abbott, R., Abbott, T. D., Acernese, F., Ackley, K., Adams, C., et al. (2017). GW170817: observation of gravitational waves from a binary neutron star inspiral. *Phys. Rev. Lett.* 119, 161101. doi:10.1103/PhysRevLett.119.161101

Abbott, R., Abbott, T. D., Abraham, S., Acernese, F., Ackley, K., Adams, C., et al. (2020). GW190521: a binary black hole merger with a total mass of 150 $M_{\odot}$. *PRL* 125, 101102. doi:10.1103/PhysRevLett.125.101102

Amaro-Seoane, P., Audley, H., Babak, S., Baker, J., Barausse, E., Bender, P., et al. (2017). *Laser interferometer space Antenna*. Available at: https://arxiv.org/abs/1702.00786.

Andersen, B. C., Bandura, K. M., Bhardwaj, M., Bij, A., Boyce, M. M., Boyle, P. J., et al. (2020). A bright millisecond-duration radio burst from a Galactic magnetar. *Nature* 587, 54–58. doi:10.1038/s41586-020-2863-y

Andreoni, I., Coughlin, M. W., Perley, D. A., Yao, Y., Lu, W., Cenko, S. B., et al. (2022). A very luminous jet from the disruption of a star by a massive black hole. *Nature* 612, 430–434. doi:10.1038/s41586-022-05465-8

Arcavi, I., Wolf, W. M., Howell, D. A., Bildsten, L., Leloudas, G., Hardin, D., et al. (2016). Rapidly rising transients in the supernova—superluminous supernova gap. *ApJ* 819, 35. doi:10.3847/0004-637X/819/1/35

Arcodia, R., Merloni, A., Nandra, K., Buchner, J., Salvato, M., Pasham, D., et al. (2021). X-ray quasi-periodic eruptions from two previously quiescent galaxies. *Nature* 592, 704–707. doi:10.1038/s41586-021-03394-6

Auchettl, K., Guillochon, J., and Ramirez-Ruiz, E. (2017). New physical insights about tidal disruption events from a comprehensive observational inventory at X-ray wavelengths. *ApJ* 838, 149. doi:10.3847/1538-4357/aa633b

Belolaptikov, I. A., Bezrukov, L. B., Borisovets, B. A., Budnev, N. M., Bugaev, E. V., Chensky, A. G., et al. (1997). The Baikal underwater neutrino telescope: design, performance, and first results. *Astropart. Phys.* 7, 263–282. doi:10.1016/S0927-6505(97)00022-4

Bochenek, C. D., Ravi, V., Belov, K. V., Hallinan, G., Kocz, J., Kulkarni, S. R., et al. (2020). A fast radio burst associated with a Galactic magnetar. *Nature* 587, 59–62. doi:10.1038/s41586-020-2872-x

Bricman, K., and Gomboc, A. (2020). The prospects of observing tidal disruption events with the large synoptic survey telescope. *ApJ* 890, 73. doi:10.3847/1538-4357/ab6989

Burrows, D. N., Kennea, J. A., Ghisellini, G., Mangano, V., Zhang, B., Page, K. L., et al. (2011). Relativistic jet activity from the tidal disruption of a star by a massive black hole. *Nature* 476, 421–424. doi:10.1038/nature10374

Callister, T. A., Haster, C.-J., Ng, K. K. Y., Vitale, S., and Farr, W. M. (2021). Who ordered that? Unequal-Mass binary black hole mergers have larger effective spins. *ApJL* 922, L5. doi:10.3847/2041-8213/ac2ccc

Cenko, S. B., Krimm, H. A., Horesh, A., Rau, A., Frail, D. A., Kennea, J. A., et al. (2012). Swift J2058.4+0516: discovery of a possible second relativistic tidal disruption flare? *ApJ* 753, 77. doi:10.1088/0004-637X/753/1/77

Chakraborty, J., Kara, E., Masterson, M., Giustini, M., Miniutti, G., and Saxton, R. (2021). Possible X-ray quasi-periodic eruptions in a tidal disruption event candidate. *ApJL* 921, L40. doi:10.3847/2041-8213/ac313b

Chandra, P., Chevalier, R. A., Chugai, N., Fransson, C., and Soderberg, A. M. (2015). X-ray and radio emission from type IIn supernova SN 2010jl. *ApJ* 810, 32. doi:10.1088/0004-637X/810/1/32

Chen, H.-Y., Haster, C.-J., Vitale, S., Farr, W. M., and Isi, M. (2022). A standard siren cosmological measurement from the potential GW190521 electromagnetic counterpart ZTF19abanrhr. *MNRAS* 513, 2152–2157. doi:10.1093/mnras/stac989

Chevalier, R. A., and Fransson, C. (2017). "Thermal and non-thermal emission from circumstellar interaction," in *Handbook of supernovae*. Editors A. W. Alsabti, and P. Murdin, 875. doi:10.1007/978-3-319-21846-5_34

Cowperthwaite, P. S., Berger, E., Villar, V. A., Metzger, B. D., Nicholl, M., Chornock, R., et al. (2017). The electromagnetic counterpart of the binary neutron star merger LIGO/virgo GW170817. II. UV, optical, and near-infrared light curves and comparison to kilonova models. *ApJL* 848, L17. doi:10.3847/2041-8213/aa8fc7

Dai, L., McKinney, J. C., Roth, N., Ramirez-Ruiz, E., and Miller, M. C. (2018). A unified model for tidal disruption events. *ApJL* 859, L20. doi:10.3847/2041-8213/aab429

D'Avanzo, P., Campana, S., Salafia, O. S., Ghirlanda, G., Ghisellini, G., Melandri, A., et al. (2018). The evolution of the X-ray afterglow emission of GW 170817/GRB 170817A in XMM-Newton observations. *AAP* 613, L1. doi:10.1051/0004-6361/201832664

Dewdney, P. E., Hall, P. J., Schilizzi, R. T., and Lazio, T. J. L. W. (2009). The square kilometre array. *IEEE Proc.* 97, 1482–1496. doi:10.1109/JPROC.2009.2021005

Drout, M. R., Chornock, R., Soderberg, A. M., Sanders, N. E., McKinnon, R., Rest, A., et al. (2014). Rapidly evolving and luminous transients from pan-STARRS1. *ApJ* 794, 23. doi:10.1088/0004-637X/794/1/23

Eraerds, T., Antonelli, V., Davis, C., Hall, D., Hetherington, O., Holland, A., et al. (2021). Enhanced simulations on the athena/wide field imager instrumental background. *J. Astronomical Telesc. Instrum. Syst.* 7, 034001. doi:10.1117/1.JATIS.7.3.034001

Evans, C. R., and Kochanek, C. S. (1989). The tidal disruption of a star by a massive black hole. *ApJL* 346, L13. doi:10.1086/185567

Gezari, S. (2021). Tidal disruption events. *ARAA* 59, 21–58. doi:10.1146/annurev-astro-111720-030029

Giustini, M., Miniutti, G., and Saxton, R. D. (2020). X-ray quasi-periodic eruptions from the galactic nucleus of RX J1301.9+2747. *AAP* 636, L2. doi:10.1051/0004-6361/202037610

Graham, M. J., Ford, K. E. S., McKernan, B., Ross, N. P., Stern, D., Burdge, K., et al. (2020). Candidate electromagnetic counterpart to the binary black hole merger gravitational-wave event S190521g*. *PRL* 124, 251102. doi:10.1103/PhysRevLett.124.251102

Grefenstette, B. W., Brightman, M., Earnshaw, H. P., Harrison, F. A., and Margutti, R. (2023). Early hard X-rays from the nearby core-collapse supernova SN 2023ixf. *ApJL* 952, L3. doi:10.3847/2041-8213/acdf4e

Guolo, M., Gezari, S., Yao, Y., van Velzen, S., Hammerstein, E., Cenko, S. B., et al. (2023). *A systematic analysis of the X-ray emission in optically selected tidal disruption events: observational evidence for the unification of the optically and X-ray selected populations*. Available at: https://arxiv.org/abs/2308.13019.

Hajela, A., Margutti, R., Bright, J. S., Alexander, K. D., Metzger, B. D., Nedora, V., et al. (2022). Evidence for X-ray emission in excess to the jet-afterglow decay 3.5 yr after the binary neutron star merger GW 170817: a new emission component. *ApJL* 927, L17. doi:10.3847/2041-8213/ac504a

Harrison, F. A., Craig, W. W., Christensen, F. E., Hailey, C. J., Zhang, W. W., Boggs, S. E., et al. (2013). The nuclear spectroscopic telescope array (NuSTAR) high-energy X-ray mission. *ApJ* 770, 103. doi:10.1088/0004-637X/770/2/103

Ho, A. Y. Q., Perley, D. A., Gal-Yam, A., Lunnan, R., Sollerman, J., Schulze, S., et al. (2021). *A search for extragalactic fast blue optical transients in ZTF and the rate of AT2018cow-like transients*. Available at: https://arxiv.org/abs/2105.08811.

Ho, A. Y. Q., Perley, D. A., Gal-Yam, A., Lunnan, R., Sollerman, J., Schulze, S., et al. (2023). A search for extragalactic fast blue optical transients in ZTF and the rate of AT2018cow-like transients. *ApJ* 949, 120. doi:10.3847/1538-4357/acc533

Hovatta, T., Valtaoja, E., Tornikoski, M., and Lähteenmäki, A. (2009). Doppler factors, Lorentz factors and viewing angles for quasars, BL Lacertae objects and radio galaxies. *AAP* 494, 527–537. doi:10.1051/0004-6361:200811150

Ivezić, Ž., Kahn, S. M., Tyson, J. A., Abel, B., Acosta, E., Allsman, R., et al. (2019). LSST: from science drivers to reference design and anticipated data products. *ApJ* 873, 111. doi:10.3847/1538-4357/ab042c

Jansen, F., Lumb, D., Altieri, B., Clavel, J., Ehle, M., Erd, C., et al. (2001). XMM-Newton observatory. I. The spacecraft and operations. *AAP* 365, L1–L6. doi:10.1051/0004-6361:20000036

Johnston, S., Taylor, R., Bailes, M., Bartel, N., Baugh, C., Bietenholz, M., et al. (2008). Science with ASKAP. The Australian square-kilometre-array pathfinder. *Exp. Astron.* 22, 151–273. doi:10.1007/s10686-008-9124-7

Kara, E., Miller, J. M., Reynolds, C., and Dai, L. (2016). Relativistic reverberation in the accretion flow of a tidal disruption event. *Nature* 535, 388–390. doi:10.1038/nature18007

Katz, U. F. (2006). KM3NeT: towards a km^3 Mediterranean neutrino telescope. *Nucl. Instrum. Methods Phys. Res. A* 567, 457–461. doi:10.1016/j.nima.2006.05.235

Kimura, S. S., Murase, K., and Bartos, I. (2021). Outflow bubbles from compact binary mergers embedded in active galactic nuclei: cavity formation and the impact on electromagnetic counterparts. *ApJ* 916, 111. doi:10.3847/1538-4357/ac0535

Laha, S., Meyer, E., Roychowdhury, A., Becerra Gonzalez, J., Acosta-Pulido, J. A., Thapa, A., et al. (2022). A radio, optical, UV, and X-ray view of the enigmatic changing-look active galactic nucleus 1ES 1927+654 from its pre-to postflare states. *ApJ* 931, 5. doi:10.3847/1538-4357/ac63aa

Lazzati, D., López-Cámara, D., Cantiello, M., Morsony, B. J., Perna, R., and Workman, J. C. (2017). Off-axis prompt X-ray transients from the cocoon of short gamma-ray bursts. *ApJL* 848, L6. doi:10.3847/2041-8213/aa8f3d

Lazzati, D., Perna, R., Morsony, B. J., Lopez-Camara, D., Cantiello, M., Ciolfi, R., et al. (2018). Late time afterglow observations reveal a collimated relativistic jet in the ejecta of the binary neutron star merger GW170817. *PRL* 120, 241103. doi:10.1103/PhysRevLett.120.241103

Li, C. K., Lin, L., Xiong, S. L., Ge, M. Y., Li, X. B., Li, T. P., et al. (2021). HXMT identification of a non-thermal X-ray burst from SGR J1935+2154 and with FRB 200428. *Nat. Astron.* 5, 378–384. doi:10.1038/s41550-021-01302-6

Liu, Z., Malyali, A., Krumpe, M., Homan, D., Goodwin, A. J., Grotova, I., et al. (2023). Deciphering the extreme X-ray variability of the nuclear transient eRASSt J045650.3−203750. A likely repeating partial tidal disruption event. *AAP* 669, A75. doi:10.1051/0004-6361/202244805

Madsen, K. K., García, J. A., Stern, D., Armini, R., Basso, S., Coutinho, D., et al. (2023). *The high energy X-ray probe (HEX-P): instrument and mission profile*. Available at: https://arxiv.org/abs/2312.04678.

Maggiore, M., Van Den Broeck, C., Bartolo, N., Belgacem, E., Bertacca, D., Bizouard, M. A., et al. (2020). Science case for the Einstein telescope. *JCAP* 2020, 050. doi:10.1088/1475-7516/2020/03/050

Mapelli, M. (2021). "Formation channels of single and binary stellar-mass black holes," in *Handbook of gravitational wave astronomy*. 16. doi:10.1007/978-981-15-4702-7/TNQDotTNQ/16-1

Margutti, R., Alexander, K. D., Xie, X., Sironi, L., Metzger, B. D., Kathirgamaraju, A., et al. (2018). The binary neutron star event LIGO/virgo GW170817 160 Days after merger: synchrotron emission across the electromagnetic spectrum. *ApJL* 856, L18. doi:10.3847/2041-8213/aab2ad

Margutti, R., Berger, E., Fong, W., Guidorzi, C., Alexander, K. D., Metzger, B. D., et al. (2017a). The electromagnetic counterpart of the binary neutron star merger LIGO/virgo GW170817. V. Rising X-ray emission from an off-axis jet. *ApJL* 848, L20. doi:10.3847/2041-8213/aa9057

Margutti, R., and Chornock, R. (2021). First multimessenger observations of a neutron star merger. *ARAA* 59, 155–202. doi:10.1146/annurev-astro-112420-030742

Margutti, R., Kamble, A., Milisavljevic, D., Zapartas, E., de Mink, S. E., Drout, M., et al. (2017b). Ejection of the massive hydrogen-rich envelope timed with the collapse of the stripped SN 2014C. *ApJ* 835, 140. doi:10.3847/1538-4357/835/2/140

Margutti, R., Metzger, B. D., Chornock, R., Vurm, I., Roth, N., Grefenstette, B. W., et al. (2019). An embedded X-ray source shines through the aspherical at 2018cow: revealing the inner workings of the most luminous fast-evolving optical transients. *ApJ* 872, 18. doi:10.3847/1538-4357/aafa01

Masterson, M., Kara, E., Ricci, C., García, J. A., Fabian, A. C., Pinto, C., et al. (2022). Evolution of a relativistic outflow and X-ray corona in the extreme changing-look AGN 1ES 1927+654. *ApJ* 934, 35. doi:10.3847/1538-4357/ac76c0

McKernan, B., Ford, K. E. S., Bartos, I., Graham, M. J., Lyra, W., Marka, S., et al. (2019). Ram-pressure stripping of a kicked hill sphere: prompt electromagnetic emission from the merger of stellar mass black holes in an AGN accretion disk. *ApJL* 884, L50. doi:10.3847/2041-8213/ab4886

McKernan, B., Ford, K. E. S., Callister, T., Farr, W. M., O'Shaughnessy, R., Smith, R., et al. (2022). LIGO-Virgo correlations between mass ratio and effective inspiral spin: testing the active galactic nuclei channel. *MNRAS* 514, 3886–3893. doi:10.1093/mnras/stac1570

Meidinger, N., Albrecht, S., Beitler, C., Bonholzer, M., Emberger, V., Frank, J., et al. (2020). "Development status of the wide field imager instrument for Athena," in *Society of photo-optical instrumentation engineers (SPIE) conference series. Vol. 11444*

of society of photo-optical instrumentation engineers (SPIE) conference series, 114440T. doi:10.1117/12.2560507

Mereghetti, S., Savchenko, V., Ferrigno, C., Götz, D., Rigoselli, M., Tiengo, A., et al. (2020). INTEGRAL discovery of a burst with associated radio emission from the magnetar SGR 1935+2154. *ApJL* 898, L29. doi:10.3847/2041-8213/aba2cf

Metzger, B. D., and Fernández, R. (2014). Red or blue? A potential kilonova imprint of the delay until black hole formation following a neutron star merger. *MNRAS* 441, 3444–3453. doi:10.1093/mnras/stu802

Miniutti, G., Saxton, R. D., Giustini, M., Alexander, K. D., Fender, R. P., Heywood, I., et al. (2019). Nine-hour X-ray quasi-periodic eruptions from a low-mass black hole galactic nucleus. *Nature* 573, 381–384. doi:10.1038/s41586-019-1556-x

Mooley, K. P., Anderson, J., and Lu, W. (2022). Optical superluminal motion measurement in the neutron-star merger GW170817. *Nature* 610, 273–276. doi:10.1038/s41586-022-05145-7

Mooley, K. P., Deller, A. T., Gottlieb, O., Nakar, E., Hallinan, G., Bourke, S., et al. (2018a). Superluminal motion of a relativistic jet in the neutron-star merger GW170817. *Nature* 561, 355–359. doi:10.1038/s41586-018-0486-3

Mooley, K. P., Nakar, E., Hotokezaka, K., Hallinan, G., Corsi, A., Frail, D. A., et al. (2018b). A mildly relativistic wide-angle outflow in the neutron-star merger event GW170817. *Nature* 554, 207–210. doi:10.1038/nature25452

Murase, K., Oikonomou, F., and Petropoulou, M. (2018a). Blazar flares as an origin of high-energy cosmic neutrinos? *ApJ* 865, 124. doi:10.3847/1538-4357/aada00

Murase, K., Toomey, M. W., Fang, K., Oikonomou, F., Kimura, S. S., Hotokezaka, K., et al. (2018b). Double neutron star mergers and short gamma-ray bursts: long-lasting high-energy signatures and remnant dichotomy. *ApJ* 854, 60. doi:10.3847/1538-4357/aaa48a

Nandra, K., Barret, D., Barcons, X., Fabian, A., den Herder, J.-W., Piro, L., et al. (2013). *The hot and energetic Universe: a white paper presenting the science theme motivating the Athena+ mission*. Available at: https://arxiv.org/abs/1306.2307.

Nathanail, A., Gill, R., Porth, O., Fromm, C. M., and Rezzolla, L. (2021). 3D magnetized jet break-out from neutron-star binary merger ejecta: afterglow emission from the jet and the ejecta. *MNRAS* 502, 1843–1855. doi:10.1093/mnras/stab115

Ofek, E. O., Zoglauer, A., Boggs, S. E., Barriére, N. M., Reynolds, S. P., Fryer, C. L., et al. (2014). SN 2010jl: optical to hard X-ray observations reveal an explosion embedded in a ten solar mass cocoon. *ApJ* 781, 42. doi:10.1088/0004-637X/781/1/42

Panjkov, S., Auchettl, K., Shappee, B. J., Do, A., Lopez, L. A., and Beacom, J. F. (2023). *Probing the soft X-ray properties and multi-wavelength variability of SN2023ixf and its progenitor*. Available at: https://arxiv.org/abs/2308.13101.

Pasham, D. R., Lucchini, M., Laskar, T., Gompertz, B. P., Srivastav, S., Nicholl, M., et al. (2023). The birth of a relativistic jet following the disruption of a star by a cosmological black hole. *Nat. Astron.* 7, 88–104. doi:10.1038/s41550-022-01820-x

Pasham, D. R., Remillard, R. A., Fragile, P. C., Franchini, A., Stone, N. C., Lodato, G., et al. (2019). A loud quasi-periodic oscillation after a star is disrupted by a massive black hole. *Science* 363, 531–534. doi:10.1126/science.aar7480

Petroff, E., Hessels, J. W. T., and Lorimer, D. R. (2019). Fast radio bursts. *AAPR* 27, 4. doi:10.1007/s00159-019-0116-6

Polzin, A., Margutti, R., Coppejans, D., Auchettl, K., Page, K. L., Vasilopoulos, G., et al. (2022). *The luminosity phase space of galactic and extragalactic X-ray transients out to intermediate redshifts*. Available at: https://arxiv.org/abs/2211.01232.

Punturo, M., Abernathy, M., Acernese, F., Allen, B., Andersson, N., Arun, K., et al. (2010). The Einstein Telescope: a third-generation gravitational wave observatory. *Class. Quantum Gravity* 27, 194002. doi:10.1088/0264-9381/27/19/194002

Rees, M. J. (1988). Tidal disruption of stars by black holes of 106–108 solar masses in nearby galaxies. *Nature* 333, 523–528. doi:10.1038/333523a0

Reimer, A., Böttcher, M., and Buson, S. (2019). Cascading constraints from neutrino-emitting blazars: the case of TXS 0506+056. *ApJ* 881, 46. doi:10.3847/1538-4357/ab2bff

Reitze, D., Adhikari, R. X., Ballmer, S., Barish, B., Barsotti, L., Billingsley, G., et al. (2019). "Cosmic explorer: the U.S. Contribution to gravitational-wave astronomy beyond LIGO," in *Bulletin of the American astronomical society*. vol. 51, 35. Available at: https://arxiv.org/abs/1907.04833.

Remillard, R. A., and McClintock, J. E. (2006). X-ray properties of black-hole binaries. *ARAA* 44, 49–92. doi:10.1146/annurev.astro.44.051905.092532

Reusch, S., Stein, R., Kowalski, M., van Velzen, S., Franckowiak, A., Lunardini, C., et al. (2022). Candidate tidal disruption event AT2019fdr coincident with a high-energy neutrino. *PRL* 128, 221101. doi:10.1103/PhysRevLett.128.221101

Ricci, C., Kara, E., Loewenstein, M., Trakhtenbrot, B., Arcavi, I., Remillard, R., et al. (2020). The destruction and recreation of the X-ray corona in a changing-look active galactic nucleus. *ApJL* 898, L1. doi:10.3847/2041-8213/ab91a1

Ricci, C., Loewenstein, M., Kara, E., Remillard, R., Trakhtenbrot, B., Arcavi, I., et al. (2021). The 450 Day X-ray monitoring of the changing-look AGN 1ES 1927+654. *ApJS* 255, 7. doi:10.3847/1538-4365/abe94b

Ricci, C., and Trakhtenbrot, B. (2022). *Changing-look active galactic nuclei*. Available at: https://arxiv.org/abs/2211.05132.

Ridnaia, A., Svinkin, D., Frederiks, D., Bykov, A., Popov, S., Aptekar, R., et al. (2021). A peculiar hard X-ray counterpart of a Galactic fast radio burst. *Nat. Astron.* 5, 372–377. doi:10.1038/s41550-020-01265-0

Scepi, N., Begelman, M. C., and Dexter, J. (2021). Magnetic flux inversion in a peculiar changing look AGN. *MNRAS* 502, L50–L54. doi:10.1093/mnrasl/slab002

Shvartzvald, Y., Waxman, E., Gal-Yam, A., Ofek, E. O., Ben-Ami, S., Berge, D., et al. (2023). *ULTRASAT: a wide-field time-domain UV space telescope*. Available at: https://arxiv.org/abs/2304.14482.

Stein, R., van Velzen, S., Kowalski, M., Franckowiak, A., Gezari, S., Miller-Jones, J. C. A., et al. (2021). A tidal disruption event coincident with a high-energy neutrino. *Nat. Astron.* 5, 510–518. doi:10.1038/s41550-020-01295-8

Sun, L., Ruiz, M., Shapiro, S. L., and Tsokaros, A. (2022). Jet launching from binary neutron star mergers: incorporating neutrino transport and magnetic fields. *PRD* 105, 104028. doi:10.1103/PhysRevD.105.104028

Trakhtenbrot, B., Arcavi, I., MacLeod, C. L., Ricci, C., Kara, E., Graham, M. L., et al. (2019). 1ES 1927+654: an AGN caught changing look on a timescale of months. *ApJ* 883, 94. doi:10.3847/1538-4357/ab39e4

Troja, E., Piro, L., van Eerten, H., Wollaeger, R. T., Im, M., Fox, O. D., et al. (2017). The X-ray counterpart to the gravitational-wave event GW170817. *Nature* 551, 71–74. doi:10.1038/nature24290

Urry, C. M., and Padovani, P. (1995). Unified schemes for radio-loud active galactic nuclei. *PASP* 107, 803. –+. doi:10.1086/133630

Vajpeyi, A., Thrane, E., Smith, R., McKernan, B., and Saavik Ford, K. E. (2022). Measuring the properties of active galactic nuclei disks with gravitational waves. *ApJ* 931, 82. doi:10.3847/1538-4357/ac6180

van Velzen, S., Stein, R., Gilfanov, M., Kowalski, M., Hayasaki, K., Reusch, S., et al. (2021). *Establishing accretion flares from massive black holes as a major source of high-energy neutrinos*. Available at: https://arxiv.org/abs/2111.09391.

Wadiasingh, Z., and Timokhin, A. (2019). Repeating fast radio bursts from magnetars with low magnetospheric twist. *ApJ* 879, 4. doi:10.3847/1538-4357/ab2240

Wen, S., Jonker, P. G., Stone, N. C., Zabludoff, A. I., and Psaltis, D. (2020). Continuum-fitting the X-ray spectra of tidal disruption events. *ApJ* 897, 80. doi:10.3847/1538-4357/ab9817

Wevers, T., Pasham, D. R., van Velzen, S., Miller-Jones, J. C. A., Uttley, P., Gendreau, K. C., et al. (2021). Rapid accretion state transitions following the tidal disruption event AT2018fyk. *ApJ* 912, 151. doi:10.3847/1538-4357/abf5e2

Yao, Y., Lu, W., Guolo, M., Pasham, D. R., Gezari, S., Gilfanov, M., et al. (2022). The tidal disruption event AT2021ehb: evidence of relativistic disk reflection, and rapid evolution of the disk-corona system. *ApJ* 937, 8. doi:10.3847/1538-4357/ac898a

Younes, G., Güver, T., Kouveliotou, C., Baring, M. G., Hu, C.-P., Wadiasingh, Z., et al. (2020). NICER view of the 2020 burst storm and persistent emission of SGR 1935+2154. *ApJL* 904, L21. doi:10.3847/2041-8213/abc94c

Zhang, B. T., Petropoulou, M., Murase, K., and Oikonomou, F. (2020). A neutral beam model for high-energy neutrino emission from the blazar TXS 0506+056. *ApJ* 889, 118. doi:10.3847/1538-4357/ab659a

Zhao, C., Lu, Y., Chu, Q., and Zhao, W. (2023). The luminosity functions of kilonovae from binary neutron star mergers under different equation of states. *MNRAS* 522, 912–936. doi:10.1093/mnras/stad1028

frontiers | Frontiers in Astronomy and Space Sciences

TYPE Review
PUBLISHED 01 March 2024
DOI 10.3389/fspas.2024.1357834

Check for updates

OPEN ACCESS

EDITED BY
Renee Ludlam,
Wayne State University, United States

REVIEWED BY
Herman Marshall,
Massachusetts Institute of Technology, United States
Richard Rothschild,
University of California, San Diego, United States

*CORRESPONDENCE
Kristin K. Madsen,
kristin.c.madsen@nasa.gov

RECEIVED 18 December 2023
ACCEPTED 30 January 2024
PUBLISHED 01 March 2024

CITATION
Madsen KK, García JA, Stern D, Amini R, Basso S, Coutinho D, Grefenstette BW, Kenyon S, Moretti A, Morrissey P, Nandra K, Pareschi G, Predehl P, Rau A, Spiga D, Wilms J and Zhang WW (2024), The high energy X-ray probe (HEX-P): instrument and mission profile. *Front. Astron. Space Sci.* 11:1357834. doi: 10.3389/fspas.2024.1357834

COPYRIGHT
© 2024 Madsen, García, Stern, Amini, Basso, Coutinho, Grefenstette, Kenyon, Moretti, Morrissey, Nandra, Pareschi, Predehl, Rau, Spiga, Wilms and Zhang. This is an open-access article distributed under the terms of the Creative Commons Attribution License (CC BY). The use, distribution or reproduction in other forums is permitted, provided the original author(s) and the copyright owner(s) are credited and that the original publication in this journal is cited, in accordance with accepted academic practice. No use, distribution or reproduction is permitted which does not comply with these terms.

The high energy X-ray probe (HEX-P): instrument and mission profile

Kristin K. Madsen[1]*, Javier A. García[1,2], Daniel Stern[3], Rashied Amini[3], Stefano Basso[4], Diogo Coutinho[5], Brian W. Grefenstette[2], Steven Kenyon[1], Alberto Moretti[4], Patrick Morrissey[3], Kirpal Nandra[5], Giovanni Pareschi[4], Peter Predehl[5], Arne Rau[5], Daniele Spiga[4], Jörn Wilms[6] and William W. Zhang[1]

[1]X-ray Astrophysics Laboratory, NASA Goddard Space Flight Center, Greenbelt, MD, United States, [2]Cahill Center for Astrophysics, California Institute of Technology, Pasadena, CA, United States, [3]Jet Propulsion Laboratory, California Institute of Technology, Pasadena, CA, United States, [4]INAF-Osservatorio Astronomico di Brera, Brera, Italy, [5]Max Planck Institute for Extraterrestrial Physics, Garching, Germany, [6]Department of Physics Dr. Karl Remeis-Observatory Bamberg, Friedrich-Alexander-Universität, Erlangen-Nürnberg, Erlangen, Bayern, Germany

The High Energy X-ray Probe (HEX-P) is a proposed NASA probe-class mission that combines the power of high angular resolution with a broad X-ray bandpass to provide the necessary leap in capabilities to address the important astrophysical questions of the next decade. HEX-P achieves breakthrough performance by combining technologies developed by experienced international partners. To meet the science goals, the payload consists of a suite of co-aligned X-ray telescopes designed to cover the 0.2–80 keV bandpass. The High Energy Telescope (HET) has an effective bandpass of 2–80 keV, and the Low Energy Telescope (LET) has an effective bandpass of 0.2–20 keV. HEX-P will be launched into L1 to enable high observing efficiency, and the combination of bandpass and high observing efficiency delivers a powerful platform for broad science to serve a wide community. The baseline mission is 5 years, with 30% of the observing time dedicated to the PI-led program and 70% to a General Observer (GO) program. The General Observer program will be executed along with the PI-led program.

KEYWORDS

X-ray, HEX-P, mission, future concept, instrumentation

1 Introduction

The current landscape for large X-ray missions is dominated by oversubscribed observatories far into their extended operation phase. The next planned flagship-class X-ray observatory is the ESA Athena mission, currently scheduled to launch no earlier than 2037. With the current outlook, the science community faces a non-negligible risk of being without a sensitive X-ray GO observatory in the 2030s, which is particularly alarming given the extensive number of time domain and multi-messenger astrophysics (TDAMM) facilities coming online over the next decade and the critical role high-energy observations play in understanding the physics of explosive and energetic phenomena (e.g., Brightman et al., 2023). HEX-P is designed to bridge this gap and complement Athena once

it launches, with instrumentation that will deliver capabilities to advance our understanding of the X-ray Universe across a breadth of topics.

The *Nuclear Spectroscopic Telescope Array* (*NuSTAR*) (Harrison et al., 2013), a NASA Small Explorer mission, opened the high-energy (> 10 keV) X-ray band by establishing the power of focused broad-band X-ray spectroscopy (3–80 keV). HEX-P builds on this legacy with a mission concept submitted to the 2023 NASA Astrophysics Probe Explorer (APEX) call, which was directed by the 2020 Decadal Survey on Astronomy and Astrophysics[1]. HEX-P combines the power of high angular resolution with broad bandpass coverage to provide the necessary leap in capabilities to address important astrophysical questions of the next decade. These questions were formulated in the 2020 Decadal Survey and motivated new observational capabilities across the electromagnetic and multi-messenger regimes to resolve the rich workings of planets, stars, and galaxies on all scales. HEX-P fills the important gap between soft X-rays and γ-rays where compact objects, from stellar remnants (neutron stars and black holes) up to supermassive black holes, emit vast amounts of energy through the process of accretion.

HEX-P will be launched into L1, which provides ≥90% observing efficiency, a large instantaneous field of regard, and the capability to do long uninterrupted observations. HEX-P's combination of bandpass and high observing efficiency delivers a powerful General Observer (GO) platform for a broad range of science that services a wide community base. The advantage of combining the soft and hard X-ray bandpasses in a single observatory allows for the exploration of science that is currently challenging due to the necessity of coordinating multiple observatories across several agencies. *NuSTAR*, the only available focusing hard X-ray satellite currently in orbit, spends > 50% of its observing time coordinating with other observatories. This is limited by the time each agency is willing to share for coordination and is becoming increasingly challenging as the desire for coordinated hard and soft X-ray observations has risen, e.g., with the recent launches of NASA's *Imaging X-ray Polarimetry Explorer* (*IXPE*) and JAXA's *X-ray Imaging and Spectroscopy Mission* (*XRISM*). The demand for simultaneous observations is oversubscribed by a factor of five and increases each cycle. As an example, HEX-P's plan to measure the spin distribution of 100 AGN (Piotrowska et al., 2023) would take approximately 30 years with the current level of coordination between observatories in their GO programs (Figure 1).

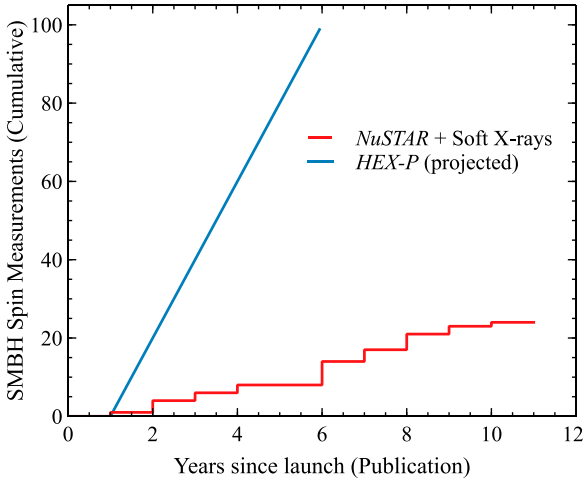

FIGURE 1
Time to obtain 100 supermassive black hole (SMBH) spin measurements with HEX-P compared to *NuSTAR* observations coordinated with soft X-ray observatories (primarily *XMM-Newton*). The number of spin measurements obtained with *NuSTAR* are collected from published papers and demonstrates that at the current rate, which is limited by the coordinated observing time, it would take about 30 years to obtain 100 spin measurements through GO programs.

2 Observatory and mission overview

The HEX-P payload consists of a suite of three co-aligned X-ray telescopes designed to cover the 0.2–80 keV bandpass. The High Energy Telescope (HET) has an effective bandpass of 2–80 keV and is composed of two High Energy Mirror Assemblies (HEMAs), which utilize thin electroformed Ni shells coated with Pt/C and W/Si multilayer coatings for high energy response. These focus on two High Energy Detector Assemblies (HEDAs), which are photon counting CdZnTe (CZT) hybrid detectors based on the *NuSTAR* design. The Low Energy Telescope (LET) has an effective bandpass of 0.2–20 keV and is composed of a Low Energy Mirror Assembly (LEMA) optimized for improved spatial resolution that capitalizes on Si segmented mirror technology developed at the NASA Goddard Space Flight Center (GSFC). The LEMA focuses on the Low Energy Detector Assembly (LEDA), which utilizes a Depleted P-Channel Field Effect Transistor (DEPFET).

The HEX-P instrumentation is shown in Figure 2. The three Wolter type I (Wolter-I) telescope mirror assemblies are mounted to a Northrop Grumman three-axis stabilized spacecraft bus that serves as the base for a three-sided, coilable boom, extended after launch to place the detector bench at a focal length of 20 m. The coilable boom is enclosed in a thermal Kapton sock to suppress stray light and bremsstrahlung activation of the boom components by solar X-ray flux. The boom deploys with an array of three aperture stops to mitigate stray light from sources outside the field of view (FoV) and the cosmic X-ray background (CXB).

A metrology system (MET), comprised of three parallel diode lasers mounted to the optics bench and co-aligned with the telescopes, forms a reference for three position-sensitive detectors (PSDs) mounted at the focal plane bench. The MET tracks the motions of the boom during observations, while three bus-mounted star trackers provide an absolute pointing reference that is combined with the laser metrology to reconstruct data on the ground.

The baseline mission is 5 years, with 30% of the observing time dedicated to the PI-led program and 70% to a GO program. The GO program will run alongside the PI-led program, and all data will be made available without proprietary time.

1 https://www.nationalacademies.org/our-work/decadal-survey-on-astronomy-and-astrophysics-2020-astro2020

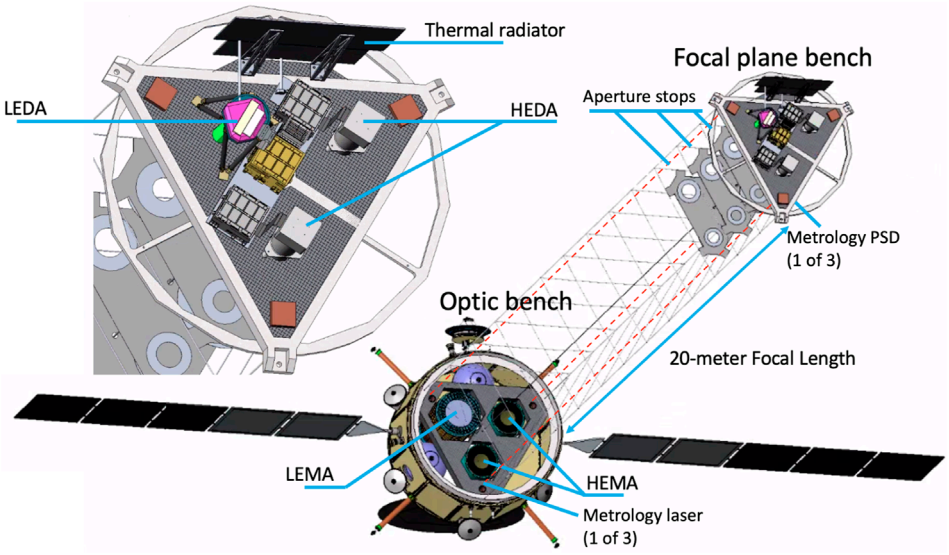

FIGURE 2
Three Wolter-I mirror assemblies are mounted rigidly onto the spacecraft structure and connected to a composite focal plane bench by a 20-m long, three-sided, coilable boom. A metrology system comprised of three laser-detector pairs provides real-time tracking of displacements between the benches that are used to reconstruct images from time-resolved data during post-processing. The aperture stops interior to the boom provide background mitigation from stray-light and the diffuse cosmic X-ray background.

3 Payload instruments

3.1 The high energy telescope: HET

The HET consists of the two HEMA optics, which are co-aligned and observe the same field. These two mirror assemblies are identical and coated with Pt/C and W/Si multilayers to achieve the broad bandpass response. The HET optics design and implementation rely on previous developments carried out in Italy for the Simbol-X and NHXM mission studies (Pareschi et al., 2009; Basso et al., 2011; Spiga et al., 2011). The two HEMAs are matched to the HEDAs, which are photon-counting CZT hybrid detectors based on the *NuSTAR* design built by Caltech. The HET has a FoV of $13.7' \times 13.7'$, driven by the detector size, and the mirrors are expected to provide a half-power diameter (HPD) angular resolution of $10''$ at 6 keV and $23''$ at 60 keV.

The performance presented in this paper corresponds to the instrument specifications that are summarized in Table 1, analogous to the version 7 (v07) instrument design, which was distributed in April 2023 (and are available at https://hexp.org/response-files-2/). For the submission of the proposal in November 2023, the number of HEMA shells was reduced from 60 to 57, resulting in a 12% loss of the HET effective area at energies below 20 keV.

3.1.1 The high energy mirror assembly: HEMA

The two HEMAs are made from pseudo-cylindrical monolithic shells, replicated from high-accuracy mandrels by means of Ni electroforming (see, e.g., Vernani et al., 2011). This technology has been successfully used for the Ni gold-coated X-ray mirrors of *BeppoSAX* (launched in 1996), *XMM-Newton* (1999), *Neil Gehrels Swift Observatory* (2004), *SRG*/eROSITA (2019), and the forthcoming *Einstein Probe* (Vernani et al., 2022).

Each HEMA has 60 (v07) nested Wolter-I paraboloid-hyperboloid mirror shells. The primary design constraint requires that the grazing incidence angle be less than 3.2 mrad. For a focal length of 20 m, this corresponds to an outermost diameter at the parabola-hyperbola intersection plane of approximately 500 mm. Figure 3 shows the reflectivity of a Pt/C multilayer coating optimized for the bandpass, demonstrating that at these angles, the coatings have >50% efficiency for energies up to 50 keV. Long mirrors provide a higher effective area per shell, and for this reason, the HEMA shells are 660 mm tall, constrained by the maximum shell length that can be produced using the current Media Lario facilities.

The multilayers for the HEMA are optimized for bandpass and performance in a well-established process (Madsen et al., 2004; Cotroneo et al., 2009; Madsen et al., 2022). The number of bilayers is <100 and the maximum bilayer thickness <30 nm, making them both simpler and thinner than was done for *NuSTAR* (Madsen et al., 2009). The W K-edge is at 69.5 keV, and the Pt K-edge is at 78.4 keV; beyond these energies, the respective coating efficiencies drop precipitously. Because the W/Si coating is smoother and easier to deposit, the HEMAs will have shells coated with W/Si at the outermost radii where the coatings only reflect <70 keV. The innermost shells, which can achieve 70–80 keV, will be coated with Pt/C.

On the basis of the previous experience gained with Ni electroformed shells, in particular eROSITA, an angular resolution of HPD $\leq 10''$ at energies <10 keV is anticipated. This estimate is obtained from a simulation of the achievable power spectral density (PSD) of the shells surface for the HEMA geometry and a finite element analysis (FEM) of the structural alignment, both of which

TABLE 1 HEX-P instrument performance (v07).

	LET	HET
# optic; detectors	1	2
Focal Length	20 m	20 m
Bandpass	0.2–20 keV	2–80 keV
Detectors	LEDA	HEDA
Field of view	$11.3' \times 11.3'$	$13.7' \times 13.7'$
Detector sensor	DEPFET Si	CnZnTe (CZT) pixel hybrid
Sensor format	512 × 512 pixels	32 × 32 pixels
# Sensors	1	16 (4 × 4)
Sensor thickness	450 μm	3 mm
Pixel pitch	130 μm	604.8 μm
Time resolution	full-frame: 2 ms (w64: 250 μs)	1 μs
Mirrors	LEMA	HEMA
Mirror technology	Monocrystalline Si	Ni electroformed
# Shells	24 [30]	60 [57]
Half-power diameter	$3.5''$ [$2.9''$]	$10''$, $17''$, $23''$ @ 10, 30, 60 keV
Maximum radius	350 mm	250 mm
Shell length	800 mm	660 mm
Shell thickness	0.8 mm	0.32–0.55 mm
Mirror coating	Ir with C overcoat	Pt/C and W/Si graded multilayers

[] Value in brackets are baseline changes not included in the instrument performance presented here.

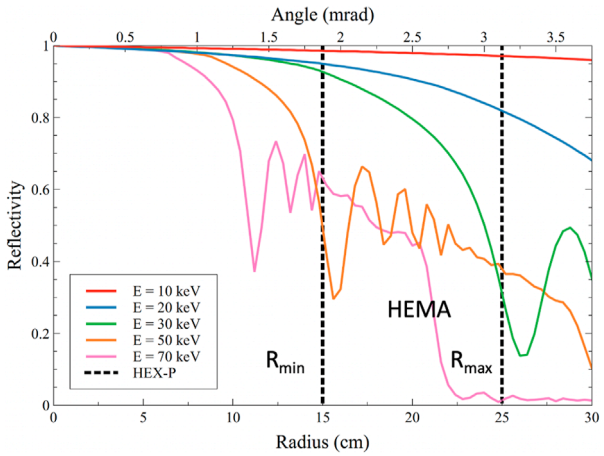

FIGURE 3
Reflectivity curve of a Pt/C multilayer coating as a function of energy.

are improved by the 20-m focal length. The HPD trend at higher energies is dominated by the surface roughness, which is responsible for the X-ray scattering. The HEMA HPD is estimated from the PSD of the eROSITA mirror modules. Extrapolating eROSITA in-flight performance to the energy range and angles of HEX-P, the HPD angular resolution is anticipated to be $<25''$ for energies ≤80 keV. A sample of HPDs calculated for selected energies is shown in Table 1, and a more detailed description of the HEX-P mirror design can be found in Madsen et al. (2023a).

3.1.2 The high energy detector assembly: HEDA

The design of the HEDA is adapted from flight-proven hard X-ray detectors flown on *NuSTAR* with over a decade of successful operation in space (Harrison et al., 2013). These hybrid detectors are composed of a monolithic crystal of CZT flip-chip bonded to an Application Specific Integrated Circuit (ASIC) (Chen et al., 2004). To improve the high-energy quantum efficiency (QE), the HEDA uses 3-mm thick CZT rather than the 2-mm thick CZT used on *NuSTAR*. The dimensions of the individual hybrid detectors remain the same, and due to the longer focal length, each HEDA will use an array of 4 × 4 detectors compared to the *NuSTAR* 2 × 2 layout. This conserves the FoV to be $13.7' \times 13.7'$, as it is for *NuSTAR*.

The energy resolution is comparable to *NuSTAR*, with a 500 eV full-width at half-maximum (FWHM) energy resolution below 10 keV, increasing to 850 eV at 60 keV. Improvements to the digital processing and analog-to-digital conversion rates increase the overall throughput of the system by up to 1,000 cps from 400 cps in *NuSTAR*. The detectors can handle an incidence count rate of 10,000 cps before pile-up becomes an issue. Like *NuSTAR*, the HEDA is surrounded by an anti-coincidence shield to reduce the background due to charged particles.

3.1.3 HET background

The similarities between the *NuSTAR* focal plane module (FPM) and the HEDA allow the use of a scaled mass model for a *NuSTAR* FPM to estimate the non-X-ray background (NXB) contribution from the charged particle flux at L1 using GEANT4 modeling (Madsen et al., 2023b). To eliminate the Cs and I lines between 23 and 28 keV, which arise from the anticoincidence shield that was used on *NuSTAR*, the HEX-P baseline is BiGeO (BGO), which will produce Ge Kα lines at 9–11 keV and Bi Kα lines at 74–77 keV. For comparison with *NuSTAR*, simulations were performed for CsI, and the results were used to scale the *NuSTAR* background. The background was fit with an empirical model, and the Cs and I lines were removed before producing the background instrument file for the simulations.

The HET background contribution from the CXB is determined by the solid angle of the sky that subtends the detectors. Because of *NuSTAR*'s open structure, it is the dominant background component to the *NuSTAR* detectors below 20 keV. This is mitigated on HEX-P with a set of aperture stops held inside the boom, which combine with a graded-Z plate to prevent transmission through the bench on the optic bench and narrow the solid angle of the HEDA down to 0.0023 sr. As shown in Figure 4A,

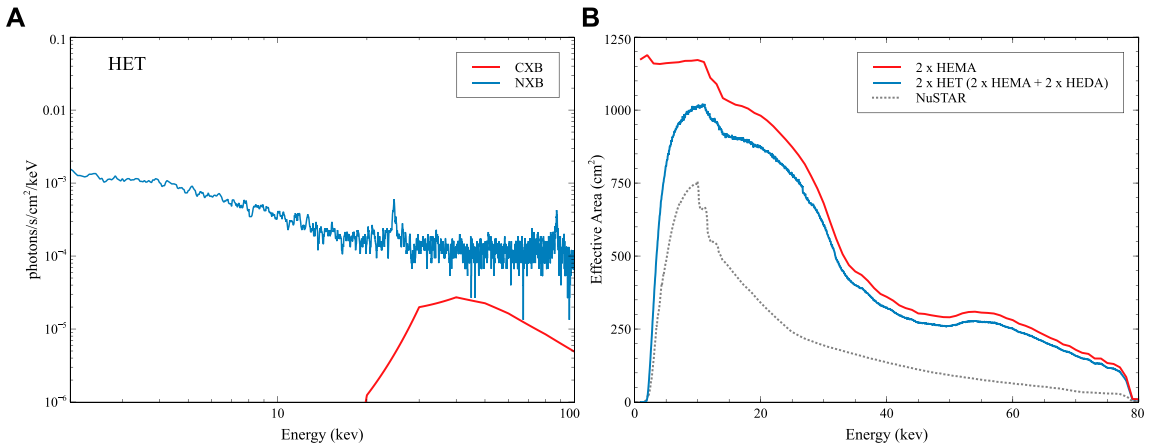

FIGURE 4
(A) The HET instrument background is separated into the CXB and NXB. **(B)** The effective area of the HET, with and without the detector efficiency and other absorbing elements in the X-ray path.

this eliminates the CXB background contribution below 20 keV (Madsen et al., 2023b).

The Sun is a prompt source of soft X-rays and particles, producing a series of flares on timescales of days with rapid decays. Since the periods of high background can be excluded, they are not included in the persistent NXB background estimate.

3.1.4 HET effective area

The effective area of the HEMA was derived from a full ray trace, including all known effects of obscuration, surface micro-roughness, and mirror reflection from multilayers. The QE and redistribution matrix of the HEDA were simulated using the charge transport and detector effects modeling code developed for *NuSTAR* and validated against flight data. Figure 4B shows the current best estimate of the effective area of the HEMA folded through the HEDA detector redistribution function. The sag in the area around 40 keV can be mitigated with different multilayer prescriptions at a cost in the area around 20 keV.

3.2 The Low Energy Telescope: LET

The LET is composed of one LEMA mirror, which is optimized for improved spatial resolution up to 20 keV and capitalizes on the Si segmented mirror technology developed at the NASA GSFC. At the focus of the LEMA is the LEDA, which utilizes the DEPFET technology developed by the Max Planck Institute for Extraterrestrial Physics (MPE; Garching, Germany) for the Wide Field Imager (WFI) (Meidinger et al., 2020) on the ESA L-class Athena mission (Ayre et al., 2018; Bavdaz et al., 2021). The FoV of the LET is $11.3' \times 11.3'$, and the anticipated angular resolution of the LET is projected to be HPD $\leq 3''$.

The performance presented in this paper corresponds to the instrument specifications that are summarized in Table 1, and analogous to the 'v07's estimated performance that were distributed in and are available at https://hexp.org/response-files-2/. For the submitted proposal, the number of shells of the LEMA was increased from 24 to 30, resulting in a 35% increase in effective area. In addition, the current best estimate of the LET HPD improved from $3.5''$ to $2.9''$.

3.2.1 The Low Energy Mirror Assembly: LEMA

The LEMA uses the single crystal Si mirror technology that has been under development at GSFC by the Next-Generation X-ray Optics team since 2010. It consists of semiconductor-grade monocrystalline segments, approximately 100×100 mm^2 and 0.8 mm in thickness, that are cut out of a block of Si and polished to an arcsecond figure using lapping and polishing techniques, including ion-beam figuring (Riveros et al., 2022).

The optical design and curvature of the primary and secondary mirror follow a variant of the Wolter-I design that employs a hyperbolic-hyperbolic prescription (Harvey et al., 2001; Saha and Zhang, 2022). In this design, the Wolter-I parabolic primary is replaced with a hyperbolic curvature, which provides superior off-axis angular performance over a conventional Wolter-I design. The LEMA is a segmented mirror with sub-components collected into 18 mirror modules that are arranged in a ring. Due to the long focal length, the mirror modules are required to be 800 mm in length, and each mirror module contains 8 (axial) and 24 (radial) mirror segments (for the v07 design).

The LEMA is baselined with a 10 nm layer of Ir with an 8 nm C overcoat. This coating prescription is identical to what is proposed for Athena (Svendsen et al., 2022). The benefit of the C overcoat is demonstrated in Figure 5: C mitigates absorption occurring from the Ir M-complex, providing a significant improvement in low-energy performance. Further details on the mirror design and coating performance are presented in Madsen et al. (2023a).

3.2.2 The Low Energy Detector Assembly: LEDA

The LEDA utilizes one built-to-print detector quadrant of the WFI and packages it into a new housing. At the heart

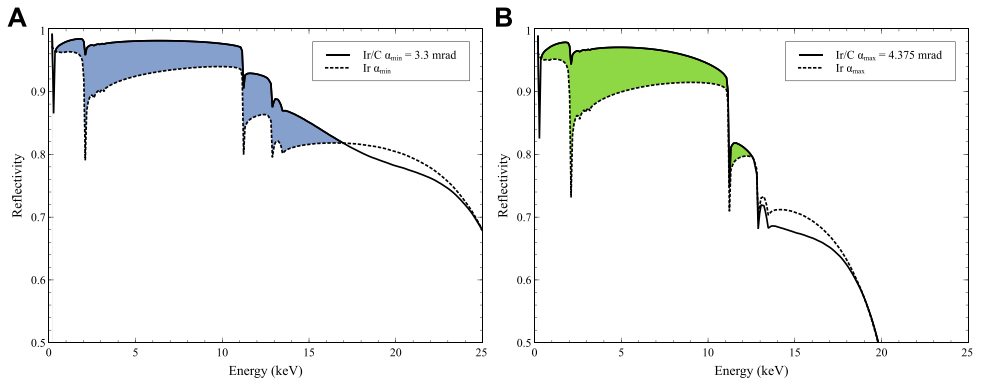

FIGURE 5
The C overcoat provides a significant improvement in reflectivity below 10 keV for a small trade between 15 and 20 keV. **(A)** Difference in reflectivity between a single Ir coated layer and Ir with a C overcoat for the minimum grazing incidence angle α_{min} = 3.3 mrad. **(B)** Difference in reflectivity between a single Ir coated layer and Ir with a C overcoat for the minimum grazing incidence angle α_{max} = 4.375 mrad.

of the detector is the Si DEPFET sensor, which is a sensor-amplifier structure combined with a MOSFET integrated onto a fully depleted Si bulk. The DEPFET sensor is read out using two types of ASICs: the Switcher and the Veritas (Herrmann et al., 2018). These comprise the front-end electronics of the DEPFET detector. The Switcher controls the row-steering of the DEPFET sensor in a rolling shutter mode by applying a sequence of voltages, where rows are read out sequentially, and all pixels of one row are read simultaneously. The Veritas is a low-noise, multichannel amplifier, and shaper circuit with an analog output that serializes the analog signals of the DEPFET pixels, clocking out at a rate of 25.6 MHz. Each pair of Veritas/Switcher handles 64 rows of the DEPFET, and each detector contains 8 ASICs of each type.

The DEPFET detector facilitates state-of-the-art spectral resolution over the required broad energy band from 0.2 to 20 keV, with a FWHM of 80 eV at 1 keV and 150 eV at 7 keV (Figure 6). High QE is achieved by back-illumination of the 450 μm thick sensor. A 5-μm thick benzocyclobutene (C_8H_8) layer on the off-mirror side is used for passivation, and a 90-nm thick Al coating on the mirror side of the detector serves as an on-chip filter to reduce contamination of the X-ray signal by optical light. A filter wheel provides a 40 nm Al filter for additional optical blocking and contamination control.

The LEDA is operated at 2 ms frame time (the WFI operates at 5 ms) in full frame mode (i.e., all pixels) at a small cost in energy resolution, as shown in Figure 6A. For bright sources that cause pile-up, the detector can be operated in a window mode that enables a faster readout for fewer rows (in multiples of 64). For the smallest window (w64: 64 × 512 pixels), the detector readout is 250 μs. A Monte Carlo simulation using the SImulation of X-ray TElescopes (SIXTE) (Dauser et al., 2019) software was used to estimate the LEDA pileup percentage as a function of incident count rate using a spectrum of the Crab with a slope of Γ = 2.1. SIXTE contains the DEPFET simulator and can faithfully replicate the readout speed. Combined with the LET mirror effective area, SIXTE can predict the pileup fraction as a function of source flux. This was simulated for the full frame detector and for window modes using 128 or 64 rows. Figure 6B shows that 1% pileup fraction is reached at 20 mCrab for the full detector and 150 mCrab for the 64-row mode. A higher flux limit could be allowed for a flatter spectrum.

Due to the potential for radiation damage from soft protons from the Sun, the LEDA has a magnetic diverter that deflects protons with energies $E < 75$ keV (Madsen et al., 2023b).

3.2.3 LET Background

The LEDA builds strongly on efforts made for Athena/WFI, and the radiation requirements on the shielding are directly inherited from the WFI (Eraerds et al., 2021). The charged particle background, NXB, is the dominant term and, based on the work done for the WFI (Madsen et al., 2023b), has a mean rate of 6.7×10^{-3} photons s^{-1} cm^{-2} keV^{-1} between 0.2–20 keV. This is considered an upper limit since the GEANT4 modeling was performed on the WFI instrument, which has approximately four times the mass of the LEDA.

As for the HET, a set of apertures and a graded-Z shielding plate on the optics bench combine to limit the solid angle of sky subtended by the detectors. Due to the larger aperture of the LEMA, the aperture stop openings also have to be larger than for the HET, and the solid angle of the sky is 0.0048 sr, about twice as large as for the HET. This results in a CXB component of a mean rate of 1.0×10^{-5} photons s^{-1} cm^{-2} keV^{-1}, two orders of magnitude below the NXB as shown in Figure 7A.

The Sun is a prompt source of soft X-rays and particles, producing a series of flares on timescales of days with rapid decays. Since the periods of high background can be excluded, they are not included in the persistent NXB background estimate.

3.2.4 LET Effective Area

The effective area of the LEMA was derived from a full ray trace, including all known effects of obscuration, surface micro-roughness, and multilayer reflection. The QE and redistribution matrix of the LEDA were simulated

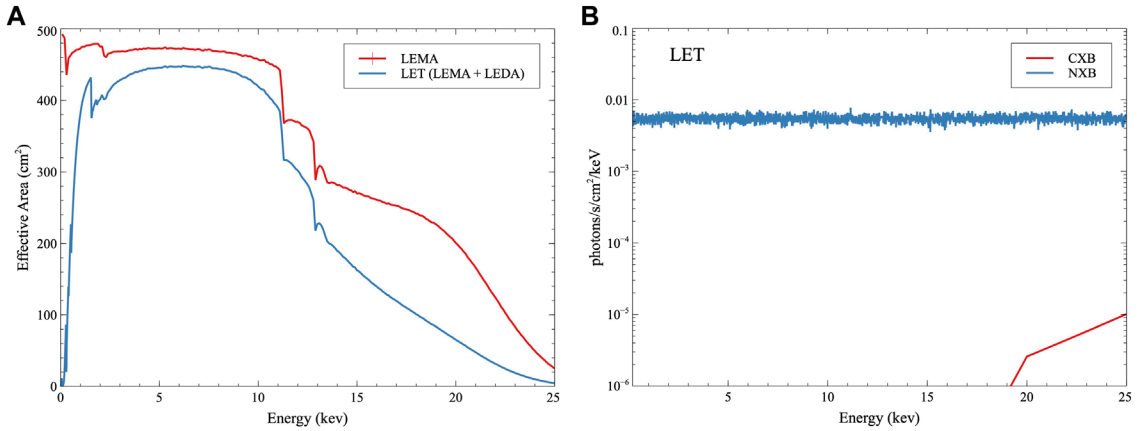

FIGURE 6
(A) Spectral performance of the DEPFET. The listed times are the exposure times and, therefore, the time resolution of the sensor. For the readout, the full exposure time is used, which allows for a better performance at a lower time resolution. The increasing difference between the theoretical Fano limit and the measured performance for lower photon energies is caused by charge losses at the entrance window. Low-energy photons have a lower penetration depth and increased probability of charge losses. **(B)** Simulated pile-up fraction for HEX-P in full frame or window modes with either 64 (w64) or 128 (w128) rows.

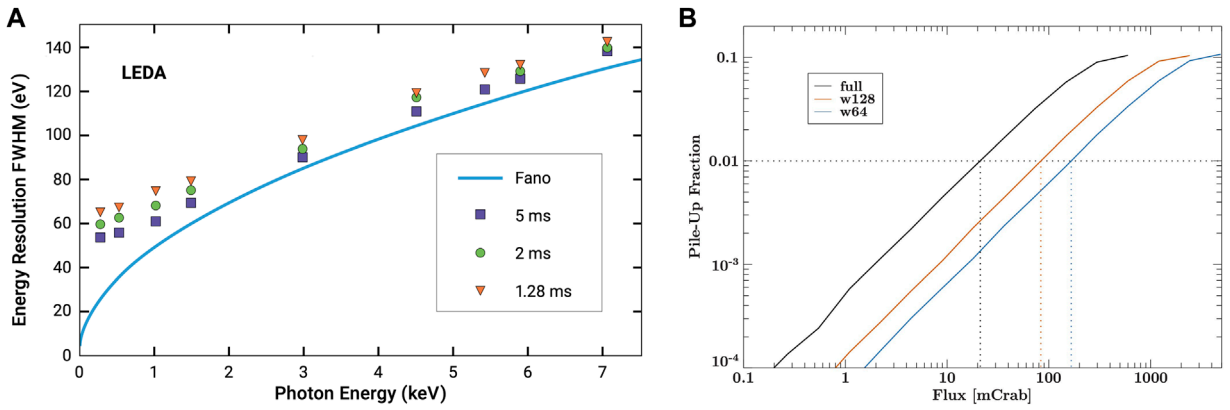

FIGURE 7
(A) The LET instrument background is separated into the CXB and NXB. **(B)** The effective area of the LET, with and without the detector efficiency and optical blocking filters.

using the SIXTE detector simulator and verified against laboratory data. Figure 7B shows the best current estimate of the effective area of LEMA (v07) folded through the redistribution function of the LEDA detector and the optical blocking filters.

4 Instrument sensitivity

Due to the broadband nature of the science objectives and the diversity of spectral features targeted in the source spectra, the HEX-P performance metric is expressed as the minimum detectable flux of a signal-to-noise ratio, $\sigma = S/\sqrt{S+B}$, where S and B are the source and background counts in the bandpass of interest in the exposure time, t, in the Poisson regime. This quadratic equation can be solved for S to find the minimum counts of the source for a given σ and background B. Using the energy-dependent instrument response functions, the counts can be turned into a minimum detectable flux over a bin, ΔE, by

$$F_{min} = \int \frac{\sigma^2 + \sqrt{\sigma^4 + 4\sigma^2\left(btA_{\mathrm{PSF}}\right)}}{2\left(A_{\mathrm{Eff}}(E)\,t\right)} dE \tag{1}$$

where b is the background flux, t is the exposure time, A_{PSF} is the energy-dependent area on the detector covered by the PSF, and A_{Eff} is the energy-dependent effective area. The PSF detector area, A_{PSF}, is optimized to maximize the signal in the background and has a diameter of ~2×HPD. This flux can be expressed as: 1) the instrumental minimum detectable flux density, F_E, and 2) the minimum detectable flux in a specific bandpass, F_{E1-E2}, which gives the integrated flux of a specified spectrum between E1 and E2.

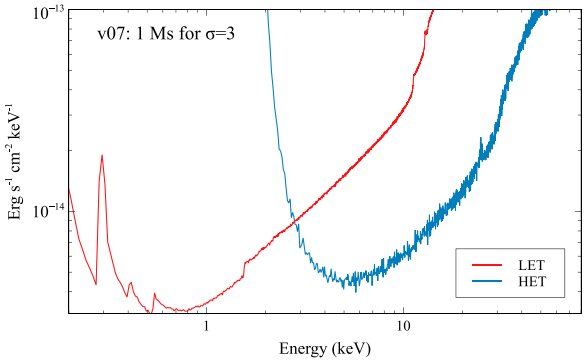

FIGURE 8
The differential flux, *dF*/*dE*, of the LET and HET based on the responses for the v07 instrument summarized in Table 1.

TABLE 2 Sensitivity of the LET and HET.

HET		LET	
Band	Sensitivity (erg s^{-1} cm^{-2})	Band	Sensitivity (erg s^{-1} cm^{-2})
2–10 keV	1.1×10^{-15}	0.2–5 keV	3.6×10^{-16}
10–20 keV	1.4×10^{-15}	5.0–10 keV	1.4×10^{-15}
20–40 keV	5.2×10^{-15}	0.5–10 keV	6.0×10^{-16}
40–80 keV	3.9×10^{-14}	10–20 keV	7.5×10^{-15}

Minimum detectable flux for Γ = 1.9, σ = 3, time = 1 Ms

The differential flux of the instrument is shown in Figure 8 and Table 2 summarizes the sensitivity of the instrument for different bands, calculated for 1 Ms assuming an optimized signal-to-noise extraction region of 6″ (LET) and 12″ (HET) for a minimum detectable flux at $\sigma = 3$ of a source with a power law photon index $\Gamma = 1.9$.

5 Mission profile

The proposed HEX-P mission baseline is 5 years, with 30% of the observing time dedicated to the PI-led program and 70% to the GO program. The spacecraft carries consumables for 20 years, and in the extended mission phase, 100% of the observing time will be dedicated to the GO program. During the baseline mission, the GO program is executed alongside the PI-led program.

The two instruments, HET and LET, are co-aligned and simultaneously observe the same field to provide the required broadband coverage. At L1, the mission achieves an observing efficiency ≥90%, with the remaining 10% used for overhead, calibration observations, and engineering for slews, desaturation, and station-keeping maneuvers. Solar shields maintain a 60° solar keep-out zone for an instantaneous $\geq 3\pi$ field-of-regard for Target of Opportunity (ToO) observations. The observatory has a 24-h on-target response time to ToOs, which is limited by the availability of uplink opportunities. The HEX-P Science Center (HSC) is located at Caltech, and ToOs will be evaluated by the science team and approved by the mission PI. The HSC will conduct an automated transient search on all data, sending out transient alerts through established systems.

The HSC manages the Science Data Center, where all data undergo a quality assurance check before being sent to the High-Energy Astrophysics Science Archive Research Center (HEASARC) at GSFC to be archived and distributed to the community. Within 2 weeks of being taken, all science data are made publicly available without a proprietary period, in compliance with SPD-41a.

The HSC will produce a serendipitous HEX-P Source Catalog, updated annually, to support the use of archival data. This catalog, based on the *XMM-Newton* Serendipitous Survey (Webb et al., 2020) and the *Chandra* Source Catalog (Evans et al., 2010), will provide easy access to HEX-P observations with standardized data products.

6 Summary

In summary, the HEX-P payload instrument has been designed to address the astrophysical questions highlighted by the 2020 Decadal Survey on Astronomy and Astrophysics. Instrument responses have been derived using advanced and detailed modeling of the instruments and the background, and they reflect the current best estimate of performance as of Spring 2023. The instrument responses have been made publicly available and in a format for use with XSPEC and SIXTE.

HEX-P will be launched into L1 with an observing efficiency ≥90%, and the 5-year mission profile has been designed to maximize the GO program with a 24-h ToO response time. The PI-led and GO programs are executed in parallel, and data are made available without a proprietary period.

Author contributions

KM: Conceptualization, Data curation, Formal Analysis, Investigation, Methodology, Project administration, Software, Supervision, Validation, Writing–original draft, Writing–review and editing. JG: Conceptualization, Writing–original draft, Writing–review and editing. DS: Conceptualization, Writing–original draft, Writing–review and editing. RA: Formal Analysis, Investigation, Software, Writing–original draft, Writing–review and editing. SB: Formal Analysis, Investigation, Software, Writing–original draft, Writing–review and editing. DC: Formal Analysis, Investigation, Writing–original draft, Writing–review and editing. BG: Formal Analysis, Investigation, Writing–original draft, Writing–review and editing. SK: Formal Analysis, Investigation, Writing–original draft, Writing–review and editing. AM: Investigation, Writing–original draft, Writing–review and editing. PM: Investigation, Writing–original draft, Writing–review and editing. KN: Writing–original draft, Writing–review and editing. GP: Investigation, Writing–original draft, Writing–review and editing. PP: Writing–original draft, Writing–review and editing. AR: Formal Analysis, Investigation, Writing–original draft, Writing–review and editing. DS: Formal Analysis, Investigation, Software, Writing–original

draft, Writing–review and editing. Joern JW: Software, Writing–original draft, Writing–review and editing. WZ: Investigation, Writing–original draft, Writing–review and editing.

Funding

The author(s) declare that no financial support was received for the research, authorship, and/or publication of this article.

Acknowledgments

The work of DS was carried out at the Jet Propulsion Laboratory, California Institute of Technology, under a contract with NASA.

Conflict of interest

The authors declare that the research was conducted in the absence of any commercial or financial relationships that could be construed as a potential conflict of interest.

Publisher's note

All claims expressed in this article are solely those of the authors and do not necessarily represent those of their affiliated organizations, or those of the publisher, the editors and the reviewers. Any product that may be evaluated in this article, or claim that may be made by its manufacturer, is not guaranteed or endorsed by the publisher.

References

Ayre, M., Bavdaz, M., Ferreira, I., Wille, E., Fransen, S., Stefanescu, A., et al. (2018). "ATHENA: system studies and optics accommodation,". *Space telescopes and instrumentation 2018: ultraviolet to gamma ray*. Editors J.-W. A. den Herder, S. Nikzad, and K. Nakazawa (International Society for Optics and Photonics), 10699. doi:10.1117/12.2313305

Basso, S., Pareschi, G., Citterio, O., Spiga, D., Tagliaferri, G., Raimondi, L., et al. (2011). "The optics system of the New Hard X-ray Mission: status report,". *Optics for EUV, X-ray, and gamma-ray Astronomy V*. Editors S. L. O'Dell, and G. Pareschi (International Society for Optics and Photonics), 8147. doi:10.1117/12.895324

Bavdaz, M., Wille, E., Ayre, M., Ferreira, I., Shortt, B., Fransen, S., et al. (2021). *The athena x-ray optics development and accommodation*, 72. doi:10.1117/12.2599341

Brightman, M., Margutti, R., Polzin, A., Jaodand, A., Hotokezaka, K., Alford, J. A. J., et al. (2023). *The High Energy X-ray Probe (HEX-P): sensitive broadband X-ray observations of transient phenomena in the 2030s*. arXiv:2311.04856. doi:10.48550/arXiv.2311.04856

Chen, C., Cook, W., Harrison, F., Lin, J., Mao, P., and Schindler, S. (2004). Characterization of the heft cdznte pixel detectors. *Proc. SPIE* 5198. doi:10.1117/12.506075

Cotroneo, V., Pareschi, G., Spiga, D., and Tagliaferri, G. (2009). "Optimization of the reflecting coatings for the new hard x-ray mission,". *Optics for EUV, X-ray, and gamma-ray Astronomy IV*. Editors S. L. O'Dell, and G. Pareschi (International Society for Optics and Photonics), 7437. doi:10.1117/12.827347

Dauser, T., Falkner, S., Lorenz, M., Kirsch, C., Peille, P., Cucchetti, E., et al. (2019). Sixte: a generic x-ray instrument simulation toolkit. *A&A* 630, A66. doi:10.1051/0004-6361/201935978

Eraerds, T., Antonelli, V., Davis, C., Hall, D. J., Hetherington, O., Holland, A. D., et al. (2021). Enhanced simulations on the athena/wide field imager instrumental background. *J. Astronomical Telesc. Instrum. Syst.* 7, 034001. doi:10.1117/1.JATIS.7.3.034001

Evans, I. N., Primini, F. A., Glotfelty, K. J., Anderson, C. S., Bonaventura, N. R., Chen, J. C., et al. (2010). The chandra source catalog. *Astrophysical J. Suppl. Ser.* 189, 37–82. doi:10.1088/0067-0049/189/1/37

Harrison, F. A., Craig, W. W., Christensen, F. E., Hailey, C. J., Zhang, el, al., et al. (2013). The nuclear spectroscopic telescope array (NuSTAR) high-energy X-ray mission. *ApJ* 770, 103. doi:10.1088/0004-637X/770/2/103

Harvey, J. E., Krywonos, A., Thompson, P. L., and Saha, T. T. (2001). Grazing-incidence hyperboloid–hyperboloid designs for wide-field x-ray imaging applications. *Appl. Opt.* 40, 136–144. doi:10.1364/AO.40.000136

Herrmann, S., Koch, A., Obergassel, S., Treberspurg, W., Bonholzer, M., and Meidinger, N. (2018). "VERITAS 2.2: a low noise source follower and drain current readout integrated circuit for the wide field imager on the Athena x-ray satellite,". *High energy, optical, and infrared detectors for Astronomy VIII*. Editors A. D. Holland, and J. Beletic (International Society for Optics and Photonics), 10709. doi:10.1117/12.2314335

Madsen, K. K., Broadway, D., and Ferreira, D. D. M. (2022). "Single-layer and multilayer coatings for astronomical X-ray mirrors," in *Handbook of X-ray and gamma-ray astrophysics*. Editors C. Bambi, and A. Santangelo, 71. doi:10.1007/978-981-16-4544-0_4-1

Madsen, K. K., Christensen, F. E., Jensen, C. P., Ziegler, E., Craig, W. W., Gunderson, K. S., et al. (2004). "X-ray study of W/Si multilayers for the HEFT hard x-ray telescope,". *Optics for EUV, X-ray, and gamma-ray Astronomy*. Editors O. Citterio, and S. L. O'Dell (of Proc. SPIE), 5168, 41–52. doi:10.1117/12.505665

Madsen, K. K., Corsetti, J., Kenyon, S., Okajima, T., Rohrback, S., Tamura, K., et al. (2023a). "Mirror design for the high-energy x-ray probe (HEX-P),". *Optics for EUV, X-ray, and gamma-ray Astronomy XI*. Editors S. L. O'Dell, J. A. Gaskin, G. Pareschi, and D. Spiga (International Society for Optics and Photonics), 12679, 126791E. doi:10.1117/12.2677554

Madsen, K. K., Fleischhack, H., Violette, D. P., Grefenstette, B. W., Zoglauer, A., Arenberg, J., et al. (2023b). "Background simulations for the high energy x-ray probe (HEX-P),". *UV, X-ray, and gamma-ray space instrumentation for Astronomy XXIII*. Editors O. H. Siegmund, and K. Hoadley (International Society for Optics and Photonics), 12678, 126781B. doi:10.1117/12.2676891

Madsen, K. K., Harrison, F. A., Mao, P. H., Christensen, F. E., Jensen, C. P., Brejnholt, N., et al. (2009). "Optimizations of Pt/SiC and W/Si multilayers for the nuclear spectroscopic telescope array," in *Optics for EUV, X-ray, and gamma-ray Astronomy IV* (of Proc. SPIE), 7437. doi:10.1117/12.826669

Meidinger, N., Albrecht, S., Beitler, C., Bonholzer, M., Emberger, V., Frank, J., et al. (2020). "Development status of the wide field imager instrument for Athena,". *Space telescopes and instrumentation 2020: ultraviolet to gamma ray*. Editors J.-W. A. den Herder, S. Nikzad, and K. Nakazawa (International Society for Optics and Photonics), 11444, 114440T. doi:10.1117/12.2560507

Pareschi, G., Tagliaferri, G., Attinà, P., Basso, S., Borghi, G., Citterio, O., et al. (2009). "Design and development of the optics system for the NHXM hard X-ray and polarimetric mission,". *Optics for EUV, X-ray, and gamma-ray Astronomy IV*. Editors S. L. O'Dell, and G. Pareschi (International Society for Optics and Photonics), 7437. doi:10.1117/12.828142

Piotrowska, J. M., García, J. A., Walton, D. J., Beckmann, R. S., Stern, D., Ballantyne, D. R., et al. (2023). "The high energy X-ray probe (HEX-P)," in *Constraining supermassive black hole growth with population spin measurements*. arXiv:2311.04752. doi:10.48550/arXiv.2311.04752

Riveros, R. E., Allgood, K. D., Biskach, M. P., DeVita, T. A., Hlinka, M., Kearney, J. D., et al. (2022). "Fabrication of lightweight silicon x-ray mirrors,". *Space telescopes and instrumentation 2022: ultraviolet to gamma ray*. Editors J.-W. A. den Herder, S. Nikzad, and K. Nakazawa (International Society for Optics and Photonics), 12181. doi:10.1117/12.26290171218111

Saha, T. T., and Zhang, W. W. (2022). Optical design of type-1 x-ray telescopes and their application to star-x. *Appl. Opt.* 61, 505–516. doi:10.1364/AO.446958

Spiga, D., Raimondi, L., Furuzawa, A., Basso, S., Binda, R., Borghi, G., et al. (2011). "Angular resolution measurements at SPring-8 of a hard x-ray optic for the New Hard X-ray Mission,". *Optics for EUV, X-ray, and gamma-ray Astronomy V*. Editors S. L.

O'Dell, and G. Pareschi (International Society for Optics and Photonics), 8147. 81470A. doi:10.1117/12.894488

Svendsen, S., Massahi, S., Ferreira, D. D., Gellert, N. C., Jegers, A. S., Christensen, F. E., et al. (2022). "Characterisation of iridium and low-density bilayer coatings for the Athena optics,". *Space telescopes and instrumentation 2022: ultraviolet to gamma ray*. Editors J.-W. A. den Herder, S. Nikzad, and K. Nakazawa (International Society for Optics and Photonics), 12181, 121810Z. doi:10.1117/12.2629976

Vernani, D., Bianucci, G., Grisoni, G., Marioni, F., Valsecchi, G., Keereman, A., et al. (2022). "Follow-up x-ray telescope (FXT) mirror module for the Einstein probe mission,". *Space telescopes and instrumentation 2022: ultraviolet to gamma ray*. Editors J.-W. A. den Herder, S. Nikzad, and K. Nakazawa, 12181. doi:10.1117/12.2630147

Vernani, D., Borghi, G., Calegari, G., Castelnuovo, M., Citterio, O., Ferrario, I., et al. (2011). "Performance of a mirror shell replicated from a new flight quality mandrel for eROSITA mission,". *Optics for EUV, X-ray, and gamma-ray Astronomy V*. Editors S. L. O'Dell, and G. Pareschi (International Society for Optics and Photonics), 8147. doi:10.1117/12.895329

Webb, N. A., Coriat, M., Traulsen, I., Ballet, J., Motch, C., Carrera, F. J., et al. (2020). Thexmm-newtonserendipitous survey: ix. the fourthxmm-newtonserendipitous source catalogue. *Astronomy Astrophysics* 641, A136. doi:10.1051/0004-6361/201937353

frontiers | Frontiers in Astronomy and Space Sciences

TYPE Original Research
PUBLISHED 18 March 2024
DOI 10.3389/fspas.2024.1340719

Check for updates

OPEN ACCESS

EDITED BY
Daniel Stern,
NASA Jet Propulsion Laboratory (JPL),
United States

REVIEWED BY
Zhiyuan Ma,
University of Massachusetts Amherst,
United States
Martin Hardcastle,
University of Hertfordshire, United Kingdom

*CORRESPONDENCE
F. Civano,
francesca.m.civano@nasa.gov

RECEIVED 18 November 2023
ACCEPTED 26 February 2024
PUBLISHED 18 March 2024

CITATION
Civano F, Zhao X, Boorman PG, Marchesi S, Ananna T, Creech S, Chen C-T, Hickox RC, Stern D, Madsen K, García JA, Silver R, Aird J, Alexander DM, Baloković M, Brandt WN, Buchner J, Gandhi P, Kammoun E, LaMassa S, Lanzuisi G, Merloni A, Moretti A, Nandra K, Nardini E, Pizzetti A, Puccetti S, Pfeifle RW, Ricci C, Spiga D and Torres-Albà N (2024), The high energy X-ray probe (HEX-P): bringing the cosmic X-ray background into focus. *Front. Astron. Space Sci.* 11:1340719. doi: 10.3389/fspas.2024.1340719

COPYRIGHT
© 2024 Civano, Zhao, Boorman, Marchesi, Ananna, Creech, Chen, Hickox, Stern, Madsen, García, Silver, Aird, Alexander, Baloković, Brandt, Buchner, Gandhi, Kammoun, LaMassa, Lanzuisi, Merloni, Moretti, Nandra, Nardini, Pizzetti, Puccetti, Pfeifle, Ricci, Spiga and Torres-Albà. This is an open-access article distributed under the terms of the Creative Commons Attribution License (CC BY). The use, distribution or reproduction in other forums is permitted, provided the original author(s) and the copyright owner(s) are credited and that the original publication in this journal is cited, in accordance with accepted academic practice. No use, distribution or reproduction is permitted which does not comply with these terms.

The high energy X-ray probe (HEX-P): bringing the cosmic X-ray background into focus

F. Civano[1]*, X. Zhao[2], P. G. Boorman[3], S. Marchesi[4,5], T. Ananna[6], S. Creech[7,8], C.-T. Chen[9,10], R. C. Hickox[11], D. Stern[12], K. Madsen[1], J. A. García[1], R. Silver[1,13], J. Aird[14], D. M. Alexander[15], M. Baloković[16,17], W. N. Brandt[18,19,20], J. Buchner[21], P. Gandhi[22], E. Kammoun[23,24], S. LaMassa[25], G. Lanzuisi[4], A. Merloni[21], A. Moretti[26], K. Nandra[21], E. Nardini[23], A. Pizzetti[5], S. Puccetti[27], R. W. Pfeifle[1,13], C. Ricci[28,29], D. Spiga[30] and N. Torres-Albà[5], on behalf of the HEX-P Collaboration

[1]NASA Goddard Space Flight Center, Greenbelt, MD, United States, [2]Harvard-Smithsonian Center for Astrophysics, Cambridge, MA, United States, [3]Cahill Center for Astrophysics, California Institute of Technology, Pasadena, CA, United States, [4]INAF—Osservatorio di Astrofisica e Scienza dello Spazio di Bologna, Bologna, Italy, [5]Department of Physics and Astronomy, Kinard Lab of Physics, Clemson University, Clemson, SC, United States, [6]Department of Physics and Astronomy, Wayne State University, Detroit, MI, United States, [7]Department of Physics and Astronomy, University of Utah, Salt Lake City, UT, United States, [8]Astrophysics Science Division, SURA/GSFC/CRESST II, Greenbelt, MD, United States, [9]Science and Technology Institute, Universities Space Research Association, Huntsville, AL, United States, [10]Astrophysics Office, NASA Marshall Space Flight Center, Huntsville, AL, United States, [11]Department of Physics and Astronomy, Dartmouth College, Hanover, NH, United States, [12]Jet Propulsion Laboratory, California Institute of Technology, Pasadena, CA, United States, [13]NASA NPP Program, Oak Ridge Associated Universities, Oak Ridge, TN, United States, [14]Institute for Astronomy, Royal Observatory, University of Edinburgh, Edinburgh, United Kingdom, [15]Department of Physics, Centre for Extragalactic Astronomy, Durham University, Durham, United Kingdom, [16]Yale Center for Astronomy and Astrophysics, New Haven, CT, United States, [17]Department of Physics, Yale University, New Haven, CT, United States, [18]Department of Astronomy & Astrophysics, The Pennsylvania State University, University Park, PA, United States, [19]Institute for Gravitation and the Cosmos, The Pennsylvania State University, University Park, PA, United States, [20]Department of Physics, The Pennsylvania State University, University Park, PA, United States, [21]Max-Planck-Institut für Extraterrestrische Physik, Garching, Germany, [22]Department of Physics and Astronomy, Faculty of Physical Sciences and Engineering, University of Southampton, Southampton, United Kingdom, [23]INAF–Osservatorio Astrofisico di Arcetri, Florence, Italy, [24]Dipartimento di Matematica e Fisica, Università Roma Tre, Rome, Italy, [25]Space Telescope Science Institute, Baltimore, MD, United States, [26]INAF, Osservatorio Astronomico di Brera, Milano, Italy, [27]ASI—Agenzia Spaziale Italiana, Rome, Italy, [28]Núcleo de Astronom ía de la Facultad de Ingeniería, Universidad Diego Portales, Santiago, Chile, [29]Kavli Institute for Astronomy and Astrophysics, Peking University, Beijing, China, [30]INAF, Osservatorio Astronomico di Brera, Merate, Italy

Since the discovery of the cosmic X-ray background (CXB), astronomers have strived to understand the accreting supermassive black holes (SMBHs) contributing to its peak in the 10–40 keV band. Existing soft X-ray telescopes could study this population up to only 10 keV, and, while *NuSTAR* (focusing on 3–24 keV) made great progress, it also left significant uncertainties in characterizing the hard X-ray population, crucial for calibrating current population synthesis models. This paper presents an in-depth analysis of simulations of two extragalactic surveys (deep and wide) with the *High-Energy X-ray Probe* (*HEX-P*), each observed for 2 Ms. Applying established source detection techniques, we show that *HEX-P* surveys will reach a flux of ~10^{-15} erg s^{-1} cm^{-2} in the 10–40 keV band, an order of magnitude fainter than current *NuSTAR* surveys. With the large sample of new hard X-ray detected sources

(~2000), we showcase *HEX-P*'s ability to resolve more than 80% of the CXB up to 40 keV into individual sources. The expected precision of *HEX-P*'s resolved background measurement will allow us to distinguish between population synthesis models of SMBH growth. *HEX-P* will leverage accurate broadband (0.5–40 keV) spectral analysis and the combination of soft and hard X-ray colors to provide obscuration constraints even for the fainter sources, with the overall objective of measuring the Compton-thick fraction. With unprecedented sensitivity in the 10–40 keV band, *HEX-P* will explore the hard X-ray emission from AGN to flux limits never reached before, thus expanding the parameter space for serendipitous discoveries. Consequently, it is plausible that new models will be needed to capture the population *HEX-P* will unveil.

KEYWORDS

X-ray, surveys, AGN, obscuration, models, cosmic X-ray background, Compton-thick

1 Introduction

The cosmic X-ray background (CXB), i.e., the diffuse emission from 0.1 to 100 keV discovered in the early 1960s by Giacconi et al. (1962), has been a focal point at the center of X-ray astronomy research since then. As most of the emission between 10 and 100 keV is expected to come from accretion of matter onto supermassive black holes (SMBHs; see Ueda et al., 1999; Gandhi and Fabian, 2003; Gilli et al., 2007; Comastri et al., 2015; Ananna et al., 2019), the CXB provides a crucial verification for current models of SMBH growth across cosmic time. The growth of these SMBHs, which are known as active galactic nuclei (AGN) during phases of accretion, is intricately linked to the evolution of galaxies and their episodes of star formation (see Harrison, 2017). Consequently, studying the population contributing to the CXB offers invaluable insights into the co-evolution of SMBHs and galaxies.

We now understand that the CXB represents the total integrated emission of faint X-ray sources across the sky. Thanks to the extragalactic surveys (e.g., Civano et al., 2016; Luo et al., 2017; Chen et al., 2018) performed over the past ~25 years, particularly with the use of focusing soft X-ray telescopes like *Chandra* and XMM-*Newton*, we have been able to resolve and study the accreting SMBHs that contribute to approximately ~80%–85% of the CXB at energies below 10 keV (e.g., Moretti et al., 2003, Moretti et al., 2012; Worsley et al., 2005; Hickox and Markevitch, 2006; Xue et al., 2012; Cappelluti et al., 2017). The large samples of AGN in these soft band surveys have allowed us to constrain various properties including, e.g., the evolution of the X-ray luminosity functions of AGN out to $z \sim 5$ (Vito et al., 2014; Aird et al., 2015b; Buchner et al., 2015) and the evolution of the unobscured ($N_{\rm H} < 10^{22}$ cm^{-2}) and obscured ($N_{\rm H} > 10^{22}$ cm^{-2}) fraction to comparable redshifts (e.g., Marchesi et al., 2016b; Vito et al., 2018; Peca et al., 2023).

Compton-thick AGN (CT; $N_{\rm H} > 10^{24}$ cm^{-2}) are a crucial piece of the CXB that still remains unresolved. Soft X-ray surveys have faced challenges to detect CT AGN as the low–energy photons (<10 keV) are easily absorbed by heavily obscuring column densities. In particular, at low redshifts, most of the emission from CT AGN can only be observed at energies greater than 10 keV, making softer energy X-ray surveys less suitable to detect these populations. In contrast, hard X-ray photons (>10 keV) can penetrate higher column densities. High-redshift ($z > 1$–2) CT sources can be detected in soft surveys due to their main signature, the Compton-hump (20–30 keV), moving to <10 keV. However, collecting large samples requires deep exposures at very faint fluxes, limiting observations to only a few fields and introducing significant uncertainties on the fraction of CT AGN (e.g., Brightman et al., 2014; Buchner et al., 2014; Lanzuisi et al., 2018; Yan et al., 2023).

The launch of *NuSTAR* (Harrison et al., 2013) and the extragalactic surveys that were performed in the hard X-rays (3–24 keV) have provided a breakthrough, enabling us to observe the high-energy X-ray universe where obscuration is less of an issue, and CT sources can be more easily detected. *NuSTAR* adopted the classic "wedding cake" survey strategy by observing the most notable extragalactic fields (COSMOS, ECDFS, EGS, CDFN and UDS; Civano et al., 2015; Mullaney et al., 2015; Masini et al., 2018a), and a survey of all the serendipitous sources in *NuSTAR* observations (Alexander et al., 2013; Lansbury et al., 2017a). Moreover, *NuSTAR* is currently observing the deepest survey ever performed in the 3–24 keV range in the North Ecliptic Pole, a *JWST* Time Domain Field, reaching fluxes of 3.7×10^{-14} erg s^{-1} cm^{-2} (over 50% of the area) in the 8–24 keV band (Zhao et al., 2021, Zhao et al., 2024). These *NuSTAR* surveys have probed the demographics of hard X-ray emitting AGN up to $z \sim 3$, providing the most precise measurements of the hard X-ray flux distribution ($\log N - \log S$) and luminosity function (Aird et al., 2015a; Harrison et al., 2016; Zhao et al., 2024) and directly resolving 35% of the CXB in the 8–24 keV range with detected sources (Harrison et al., 2016; Hickox, 2024). Interestingly, *NuSTAR* surveys have uncovered a local CT AGN that was previously misidentified by the soft X-ray surveys alone in the same field (Civano et al., 2015), and that luminous obscured AGN selected at other wavelengths (e.g., *WISE*) remain extremely weak or undetected in deep *NuSTAR* exposures, implying $N_{\rm H} > 10^{25}$ cm^{-2} (Stern et al., 2014; Yan et al., 2019; Carroll et al., 2023). Spectral analysis of the 63 brightest hard X-ray sources in *NuSTAR* surveys (Zappacosta et al., 2018) has shown that broadband data covering the 0.5–24 keV band (*Chandra* or XMM-*Newton* combined with *NuSTAR*) are essential for constraining the spectral parameters such as photon index, column density, reflection and luminosity. Similarly, Marchesi et al. (2017, 2018, 2019) have shown that the combination of non-simultaneous soft X-ray data with *Swift*-BAT

can lead to an overestimation of the line-of-sight column density which results in an overestimate of the CT-AGN fraction. While *NuSTAR* has made substantial progress in measuring the spectral properties of CT AGN in the local Universe, there are still significant inconsistencies between the observed and predicted CT fraction (see Boorman et al., 2023, and references therein). At higher redshift, the CT fraction remains unconstrained, with an upper limit of 66% at 90% confidence level (Zappacosta et al., 2018). Similarly, results solely from hardness ratio analysis have led to very large uncertainties on the CT fraction at $z > 0.1$ (Civano et al., 2015; Masini et al., 2018a; Zhao et al., 2021, Zhao et al., 2024).

Population synthesis models (e.g., Comastri et al., 1995; Ballantyne et al., 2006; Gilli et al., 2007; Treister et al., 2009; Ueda et al., 2014; Ananna et al., 2019) combine AGN spectral shapes and AGN space densities in luminosity, obscuration, and redshift bins to reproduce the intensity and shape of the CXB. The space densities are constrained using the results from existing X-ray surveys described above. The completeness and robustness of such results are limited by the energy band probed (most of the sources are only detected by *Chandra* and XMM-*Newton* below 10 keV) and by the survey's flux limits. AGN samples from higher energy surveys such as *NuSTAR* are quite scarce, and most of the hard X-ray constraints are from *Swift*-BAT, therefore limited to bright, low redshift sources (Ricci et al., 2017; Oh et al., 2018). The typical AGN spectrum is another piece of the puzzle when calibrating population synthesis models: without high-energy X-ray data, constraining spectral parameters such as the reflection scaling factor (relevant at 20–40 keV) and the high-energy cutoff (relevant at $E >$ 60 keV) remains challenging (Ricci et al., 2017; Ananna et al., 2020; Kammoun et al., 2023). As the dominant AGN contribution to the CXB is expected to be in the 10–100 keV energy band, poorly constrained spectral parameters can hinder the accuracy of population synthesis models. To justify the low resolved fraction of the CXB at high energy, the latest models have either changed assumptions on AGN spectral shapes (e.g., Akylas et al., 2012) or predicted that a large fraction of the sources contributing to the CXB must be extremely obscured or CT, and that the fraction should reach ~50% at faint fluxes ($<10^{-15}$ erg s^{-1} cm^{-2} at 20–30 keV; Ananna et al., 2019). Similar results are obtained in cosmological hydrodynamical simulations (Ni et al., 2022). Recent observational evidence of an extremely obscured and possibly CT AGN at $z = 10.1$ detected behind the Abell 2644 cluster (Bogdan et al., 2023; Goulding et al., 2023) supports these models, implying a large CT fraction at high redshift. Moreover, results from *JWST* indicating a steepening at the faint end of the AGN luminosity function (Harikane et al., 2023; Maiolino et al., 2023a; Maiolino et al., 2023b) could suggest that, as we are finding more faint unobscured AGN than expected, the intensity of the CXB could be a factor of 10 higher than what was constrained before (Padmanabhan and Loeb, 2023).

Resolving the population contributing to the CXB in the 10–40 keV band, determining their spectral properties and constraining the CT fraction at faint fluxes with the goal of providing strong constraints on population synthesis models are the major goals of the *High-Energy X-ray Probe* (*HEX-P*; Madsen et al., 2023). In this paper, we present the results obtained from accurate simulations (carried out using the observatory performance based on current best estimates as of Spring 2023) of a deep narrow (~0.16 deg^2) and a shallow wide (~1.1 deg^2) extragalactic survey, employing 2 Ms of exposure time each. We assume such surveys will be performed in well-known extragalactic fields, providing rich datasets (e.g., including data from Rubin, *JWST*, *Roman*) for a multiwavelength characterization of *HEX-P* detections.

The paper is structured as follows: Section 2 describes the telescope's characteristics; Section 3 explains the details of the survey simulations; Section 4 presents the source properties; Section 5 discusses the findings regarding the CXB resolved fraction; Section 6 presents the results related to obscured sources detected in the surveys, spectral analysis, and the CT fraction; and Section 7 includes a concise summary.

2 The high energy X-ray probe

HEX-P is a probe-class mission concept that offers sensitive broad-band coverage (0.2–80 keV) of the X-ray spectrum with exceptional spectral, timing and angular capabilities. It features two high-energy telescopes (hereafter HET; 2–80 keV) that focus hard X-rays, and a low-energy telescope (hereafter LET; 0.2–25 keV) that has soft X-ray coverage.

The LET consists of a segmented mirror assembly coated with Ir on monocrystalline silicon that achieves a half-power diameter of 3.5″, and a low-energy DEPFET detector of the same type as the Wide Field Imager (WFI; Meidinger et al., 2020) onboard Athena (Nandra et al., 2013). It has 512 × 512 pixels that cover a field of view of 11.3′ × 11.3′. It has an effective passband of 0.2–25 keV, and a full frame readout time of 2 ms, which can be operated in a 128 and 64-channel window mode for higher count-rates to mitigate pile-up and faster readout. Pile-up effects remain below an acceptable limit of ~1% for a flux up to ~100 mCrab (2–10 keV) in the smallest window configuration. Excising the core of the point spread function (PSF), a common practice in X-ray astronomy, will allow for observations of brighter sources, with a typical loss of up to ~60% of the total photon counts.

The HET consists of two co-aligned telescopes and detector modules. The optics are made of Ni-electroformed full shell mirror substrates, leveraging the heritage of XMM-*Newton* (Jansen et al., 2001), and coated with Pt/C and W/Si multilayers for an effective passband of 2–80 keV. The high-energy detectors are of the same type as flown on *NuSTAR* (Harrison et al., 2013), and they consist of 16 CZT sensors per focal plane, tiled 4 × 4, for a total of 128 × 128 pixels spanning a field of view of 13.4′×13.4′, slightly larger than that of the LET.

The broad X-ray passband of *HEX-P* and superior sensitivity to *NuSTAR* will provide a unique opportunity to probe the evolution of AGN in extragalactic surveys over a wide range of obscuration regimes that is not possible with soft X-ray instruments alone. The spectral constraints provided by simultaneous coverage of the soft and hard X-ray bands will remove any issues associated with variability and provide spectral constraints for new sources detected above 10 keV. By resolving a high fraction of the CXB in hard X-rays, *HEX-P* will ultimately enable far more sensitive population synthesis of SMBH growth in the context of the evolution of their host galaxies as probed by a plethora of multiwavelength observations.

3 *HEX-P* survey simulations

The approach we used to perform end-to-end simulations of surveys with *HEX-P* is essentially identical to the one adopted in Marchesi et al. (2020), to which we refer the reader for a detailed explanation while providing an overview here. The analysis of our simulated data was developed based on *NuSTAR* extragalactic surveys (Civano et al., 2015; Mullaney et al., 2015; Masini et al., 2018a; Zhao et al., 2021). Here, we briefly present the tool we used to perform the simulations, as well as the input mock catalogs of AGN and non-active galaxies and the analysis of such simulated data.

3.1 The SIXTE simulation tool

The *HEX-P* surveys presented in this paper have been simulated using the Monte Carlo code Simulation of X-ray Telescopes (hereafter SIXTE, Dauser et al., 2019). This software enables the simulation of observations using an X-ray telescope in the following manner. Initially, the tool creates a photon list, which includes the arrival time, energy and position of each photon. To generate this initial information, SIXTE reads the instrument configuration from an *xml* file. This first step uses the instrument's effective area, the field of view and pointing. The photon list created in the first step is then convolved with the instrument PSF and vignetting. In doing so, SIXTE generates an impact list that contains the energy and arrival time of each photon, as well as its position on the detector. The final event file is obtained from this intermediate list and reprocessed to take into account the simulated detector read-out properties and redistribution matrix file.

The *HEX-P* simulations presented in this work were produced with a set of response files that represent the observatory performance based on current best estimates as of Spring 2023 (v07; see Madsen et al., 2023). The effective area is derived from ray-tracing the mirror design, including obscuration by all known structures. The detector responses are based on simulations performed by the hardware groups, with an optical blocking filter for the LET and a Be window and thermal insulation for the HET. The LET background was derived from a GEANT4 simulation (Eraerds et al., 2021) of the WFI instrument. The HET background was derived from a GEANT4 simulation of the *NuSTAR* instrument. Both simulations adopt the planned L1 orbit for *HEX-P*. The SIXTE team has included the above *HEX-P* configuration files (i.e., telescope setup, response matrices, vignetting, point spread function) for both the HET and LET in their system, ready to be used.

3.2 Active galactic nuclei mock catalog

In order to perform the steps above and to produce a realistic representation of the X-ray sky, SIXTE needs an input source list generated in the SIMPUT data format. In this paper, we use the mock catalogs of AGN and non-active galaxies presented in Marchesi et al. (2020). The catalogs we used are available online in FITS format and ready to be used within SIXTE.

The mocks have been calibrated to reproduce known trends between AGN number densities and luminosity, redshift and column density. In detail, each AGN in the catalog has intrinsic 0.5–2 keV luminosities, redshift and column density, computed by resampling the X-ray luminosity function of unabsorbed AGN given by Hasinger et al. (2005), scaled up by a luminosity–dependent factor to account for the whole AGN population (see Gilli et al., 2007). No assumption is made on AGN or host clustering. AGN have been simulated down to a 0.5–2 keV luminosity $L_{0.5-2} = 10^{40}$ erg s^{-1} and up to $z = 10$. The mock AGN number counts match the observed ones over the whole range of fluxes sampled by current X-ray surveys. The mock AGN sample average CT fraction is $f_{CT} = 39\%$. As a reference, this is a similar figure to that found in the current AGN population synthesis models: Ueda et al. (2014, $f_{CT} = 33\%$), Buchner et al. (2015, $f_{CT} = 38\%$), and Ananna et al. (2019, $f_{CT} = 50\%$). These are all average values; however, all models adopt a luminosity-dependent CT fraction, consistent with what is observed in X-ray surveys of AGN (see, e.g., Ricci et al., 2015; Marchesi et al., 2016a).

Finally, while the Gilli et al. (2007) model is generally in close agreement with the observational results from X-ray surveys, in the high-redshift regime (i.e., at $z > 3$, where the AGN space density starts declining) the discrepancy becomes more prominent, with the model underestimating the expected number of sources with respect to the observational evidence. For this reason, Marchesi et al. (2020) developed a separate $z > 3$ catalog using as a reference the Vito et al. (2014) $z > 3$ AGN luminosity function, which describes the observational evidence from the deepest X-ray surveys currently available (e.g., Vito et al., 2018).

In the simulations of *HEX-P* surveys presented in this work, we also include the non-active galaxies mock catalogs presented in Marchesi et al. (2020) and derived from the peakM and peakG model $\log N - \log S$ by Ranalli et al. (2005). The galaxies in the mock have X-ray flux information but lack redshifts and luminosity, so we do not include them in our source detection analysis. The presence of the galaxies in the simulation, however, ensures that the overall simulated emission closely matches the CXB intensity.

3.3 *HEX-P* surveys layout and tiling strategy

We simulated two *HEX-P* fields, a Deep and a Wide survey. Each survey has been simulated both with the LET camera and with the two HET cameras. The two HET cameras are then co-added for the analysis. The total exposure for each survey is 2 Ms. Since the LET field of view ($\sim 11.3' \times 11.3'$) is slightly smaller than the HET field of view ($\sim 13.4' \times 13.4'$), we used two slightly different tiling strategies for the Wide and Deep surveys to ensure uniform coverage at low energies.

The *HEX-P* Deep Field is obtained by combining four 500 ks observations. The survey tiling is a 2×2 grid where the pointing centers are offset by $11.3'$ (i.e., a whole LET field of view) in right ascension or declination. Because the LET is smaller in size than the HET, the HET pointings are slightly overlapping by about $2'$. The overall HET survey area is $A_{deep} = 0.1668$ deg^2, while the overall LET survey area is 0.1469 deg^2 (see blue dashed curves in Figures 1, 3). The *HEX-P* Wide Field survey consists of 81 overlapping pointings, each having nominal exposures of 25 ks, in a 9×9 grid. The survey tiling is done using the half-a-field shift strategy, which was successfully used in the *NuSTAR* COSMOS

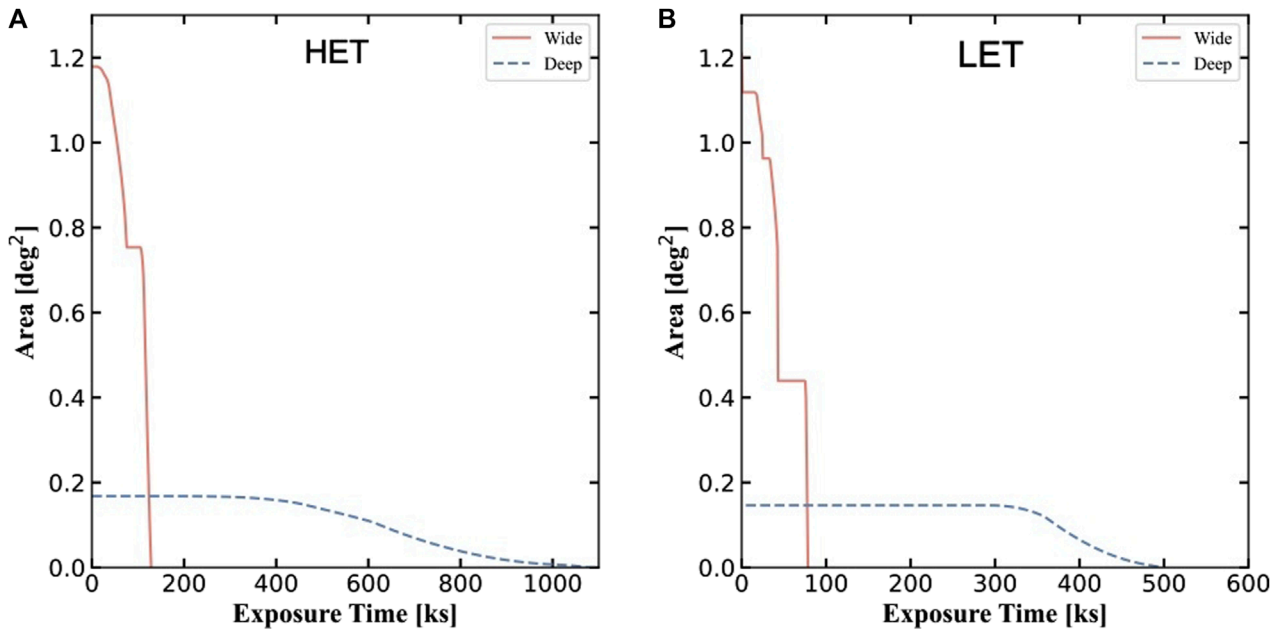

FIGURE 1
Survey area as a function of the effective, i.e., vignetting-corrected, exposure time for the HET **(A)** in the 3–24 keV band and LET **(B)** in the 0.5–2 keV band. The deep and wide surveys are in blue and salmon, respectively.

survey (Civano et al., 2015): the center of each pointing is offset by 6.7′ (i.e., half a HET field of view) in right ascension or declination with respect to the previous one. The overall survey exposure per detector is therefore 25 ks × 81 pointings = 2.025 Ms. The overall HET survey area is $A_{\rm wide}$ = 1.083 deg × 1.083 deg = 1.174 deg^2, while the overall LET area is 1.12 deg^2 (see salmon curves in Figures 1, 3).

The area versus exposure for the deep (blue) and wide (salmon) surveys are shown in Figure 1 for the HET (left) and the LET (right). A zoomed in section of the wide survey mosaics for the LET (0.5–2 keV), HET (2 telescopes summed, 3–24 keV) and *NuSTAR* (2 telescopes summed, 3–24 keV) is shown in Figure 2. The areas at lower exposure due to the overlapping of the tiles in the LET is visible but does not really affect the source detection (see Section 3.4). While hundreds of sources are visible by eye in the HET and LET images, only one source is clearly visible in a *NuSTAR* simulation of the same field that was done using the same exposure and tiling strategy (25 ks × 81 pointings = 2.025 Ms).

3.4 Source detection

We performed source detection on the simulated data in five energy bands for the HET (3–8, 8–24, 3–24, 10–40 and 35–55 keV) and two bands for the LET (0.5–2 and 2–10 keV) following the procedure used in previous *NuSTAR* surveys (Civano et al., 2015; Mullaney et al., 2015; Masini et al., 2018a; Zhao et al., 2021). All the parameters used at each step (smoothing and matching radius, probability and significance thresholds, etc) were chosen to maximize the detection rate, the completeness and the reliability in the simulated *HEX-P* surveys. We summarize the process in the following.

First, we used *Source-Extractor* (Bertin and Arnouts, 1996) on the false-probability maps of the two surveys, which measures the probability ($P_{\rm false}$) that a signal is due to a background fluctuation rather than a real source. The false-probability maps were generated from the smoothed simulated maps (with a 7.5″ and 3″ smoothing radius for the HET and LET, respectively) and the background mosaics at each pixel using the incomplete Gamma function. The detection limit in *Source-Extractor* is set to be $P_{\rm false} \leq 10^{-p}$ (where p is determined to maximize the detection rate). The coordinates of the detected sources were then used to extract the Poisson probability ($P_{\rm random}$) of each source, which is used to characterize the probability that a detection is due to a random fluctuation of the background. The Poisson probability is calculated using the total and background counts extracted from the simulated maps and the background maps at the coordinate of the detection using a circular aperture of 10″ and 5″ radius for the HET and LET, respectively. We then define the maximum likelihood (DET ML) of each detection as the inverse logarithm of the Poisson probability, i.e., DET ML = $-\ln P_{\rm random}$. Therefore, a lower $P_{\rm random}$ (i.e., a higher DET ML) suggests a lower chance that the signal arises from a background fluctuation. Multiple detections of the same X-ray source (~2%) were removed using a radius of 20″. The detections were then matched with the input mock catalog using 10″ and 7″ searching radii for the HET and LET catalogs, respectively.

3.5 Reliability, completeness and survey sensitivity

To evaluate and maximize the accuracy and efficiency of the source detection in real observations, we compute the survey's

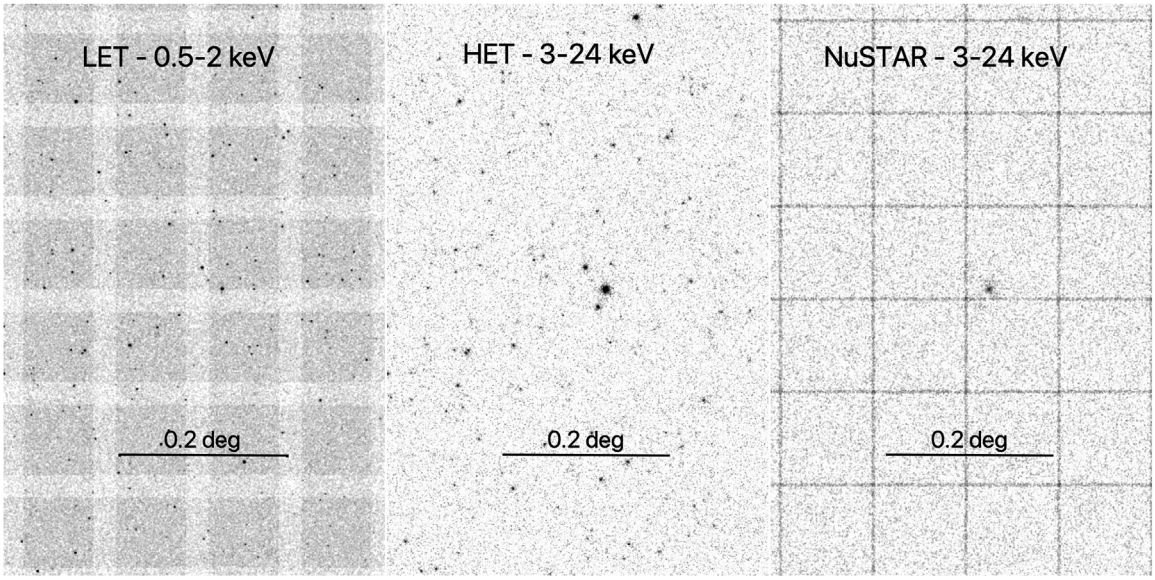

FIGURE 2
A zoomed in section of the wide survey mosaics for the LET (0.5–2 keV), HET (2 telescopes summed, 3–24 keV) and *NuSTAR* (2 telescopes summed, 3–24 keV; this simulation was performed with SIXTE). Hundreds of sources are visible in the HET and LET mosaics.

reliability and completeness. Reliability is the ratio of the number of detected sources matched to input sources to the total number of detected sources at or above a particular DET ML. Completeness is defined as the ratio of the number of detected sources matched to the input catalog and above a chosen reliability threshold to the number of sources in the input catalog at a particular flux level. The definition of reliability and completeness can be found in Zhao et al. (2021), and references therein.

For the *HEX-P* surveys presented in this paper, we choose to set a reliability of 99%, which implies a 1% spurious detection rate. Reliability and completeness depend on exposure, and if the observation tiling is planned in a way to have the field exposure uniform, it is possible to adopt a single DET ML threshold. The DET ML values are listed in Table 1 along with the number of sources detected and matched to the input catalogs above the threshold in each energy band.

The sky coverage (or the sensitivity) of the survey at a given flux can be derived from the completeness curve: if, at the chosen detection threshold, the completeness is sufficiently high (with reliability also high), the number of detected sources should correspond to the number of input sources with DET ML greater than the threshold value. In this case, the sky coverage is the normalized version of the completeness curve to the total area of the survey. The sensitivity curves for the LET and HET wide and deep surveys are shown in Figure 3 compared with current *NuSTAR* surveys for the HET and *Chandra* and XMM-*Newton* surveys for the LET. Thanks to the large effective area, the lower background and the smaller PSF, *HEX-P* surveys reach significantly fainter fluxes than any previous *NuSTAR* survey. The *HEX-P* wide area survey is comparable in area and total exposure time (1.2 deg^2 and 2 Ms) to the COSMOS *NuSTAR* survey (1.7 deg^2 and 3 Ms) and reaches a ~20 times fainter flux limit in the 8–24 keV band, as shown in Figure 3. The deep *HEX-P* survey is comparable in area and exposure to the *NuSTAR* North Ecliptic Pole (*NuSTAR*-NEP; 0.16 deg^2 and 1.6 Ms) survey (Zhao et al., 2021), the deepest survey that *NuSTAR* has ever performed, but it is a factor of 25 times deeper in flux in the 8–24 keV band. In the lower energy regime, the wide LET survey is comparable in area covered with literature *Chandra* and XMM-*Newton* COSMOS surveys (Cappelluti et al., 2009; Civano et al., 2016;), but reach flux limits 4–5 times deeper employing roughly the same exposure time (e.g., *Chandra* COSMOS Legacy Survey used 4.6 Ms to cover 2.2 deg^2, XMM-COSMOS is slightly shallower and used 1.5 Ms to cover 2.2 deg^2, while the *HEX-P* wide survey employs 2 Ms of time to cover 1.1 deg^2).

Because one of *HEX-P*'s major goals is to detect the sources that contribute to the peak of the CXB, we have also performed the detection in higher energy bands, 10–40 and 35–55 keV, which have never been effectively exploited and explored before. The sensitivities in the two bands are presented in Figure 4. While a previous attempt to detect sources in the 35–55 keV band was performed by Masini et al. (2018b) combining the COSMOS, ECDFS and UDS *NuSTAR* surveys, no sources were detected above the reliability threshold due to the very shallow flux limit in that band (brighter than 10^{-13} erg s^{-1} cm^{-2}; see Figure 4B). Their derived upper limit on the expected number counts is consistent with population synthesis model predictions (e.g., Gilli et al., 2007; Ananna et al., 2019), *HEX-P* instead will provide detected number counts for the first time up to at least 55 keV to stringently test the model predictions.

4 Source statistics and properties

In Table 1, the number of detected sources with DET ML above the thresholds are reported for the wide and deep surveys in five energy bands for the HET and two energy bands for the LET. The total number of sources detected in the HET is >20 times the number of sources detected in previous *NuSTAR* surveys (with

TABLE 1 Summary of simulation results on detection and sensitivity in 7 different bands.

	3–8 keV	8–24 keV	3–24 keV	10–40 keV	35–55 keV	Total	0.5–2 keV	2–10 keV	Total
Wide									
DET ML(99%) threshold	4.04	3.12	2.64	3.12	2.62		2.65	2.53	
$N_{detection}$	892	771	1,632	806	36		2,261	2,816	
Sensitivity (20%-area) 10^{-15} cgs	2.00	3.90	2.74	4.66	14.5	1,702	0.22	0.58	3,611
Sensitivity (50%-area) 10^{-15} cgs	3.2	6.25	4.63	7.62	27.8		0.51	1.28	
Deep									
DET ML(99%) threshold	3.75	1.0	4.11	3.77	3.16		3.03	3.46	
$N_{detection}$	476	434	521	387	36		859	940	
Sensitivity (20%-area) 10^{-16} cgs	3.6	6.6	9.3	12.0	33.9	608	0.47	1.43	1,188
Sensitivity (50%-area) 10^{-16} cgs	7.1	11.5	17.1	21.7	65.4		0.92	2.74	

similar exposure and area covered). Such a large sample will allow, for the first time, not only to resolve the sources contributing to the peak of the CXB but also to perform a statistically significant analysis of their X-ray properties and eventually study the correlations with the properties of their host galaxies. The advantage of having a high–and a low–energy telescope is that the majority of the sources detected in the HET will have a lower-energy counterpart, as shown from the numbers in Table 1. This allows for broad-band analysis as well as using the sharper lower energy PSF for multiwavelength associations and characterization. The simulations show that we can recover the position of the input sources with a median uncertainty of 2″ (2.3″) and 3″ (3.6″) for the LET and HET detections in the deep (wide) survey, respectively.

As mentioned above, the detection in the hardest X-ray band (35–55 keV) did not find any sources in previous *NuSTAR* surveys. In the *HEX-P* simulations, we detect more than ~1,000 sources in the 10–40 keV band and ~70 sources in the 35–55 keV band, combining deep and wide surveys. These results show that *HEX-P* will be able to provide the first detections in a band encompassing the entire peak of the CXB and above it.

Thanks to the information in the original mock catalog used for populating the sources of the *HEX-P* simulations, we associate a redshift and a column density to each detected source. By the time *HEX-P* is launched, extensive spectroscopic campaigns and photometric survey data will be available in the majority of the well-known fields (e.g., COSMOS, CDFS, UDS) and also new and larger surveys, using data from *JWST*, *Euclid* (Euclid Collaboration et al., 2022), *Roman* (Troxel et al., 2023; Yung et al., 2023) as well as ground-based telescopes like Rubin (Brandt et al., 2018; Scolnic et al., 2018), 4MOST and SDSS Kollmeier et al. (2017). This will allow the complete characterization of the multiwavelength properties of *HEX-P*–detected AGN. In Figure 5, the luminosity distributions for the HET and LET sources from the deep and wide surveys are plotted. The reported luminosities were not corrected for intrinsic absorption. The *HEX-P* detections are compared with samples in the literature including the *Swift*-BAT 105 months all-sky survey sample (black open circles; Oh et al., 2018), the catalog of *NuSTAR* extragalactic survey sources, including COSMOS (Civano et al., 2015), ECDFS (Mullaney et al., 2015), UDS (Masini et al., 2018a), and the 40-month serendipitous (Lansbury et al., 2017b) surveys. While the *NuSTAR* surveys already reach luminosities two orders of magnitude fainter than the *Swift*-BAT sample and extend to significantly higher redshift, with *HEX-P* sources, it will be possible to explore a new area of the high-energy luminosity-redshift space by reaching Seyfert-like luminosities up to redshift $z \sim 3$. *HEX-P* will also detect in the hard X-rays a statistically significant sample of sources at $z > 2$, thanks to the combination of flux and area covered. Even in the low energy band, the LET surveys will achieve luminosity and redshift limits comparable or deeper than archival *Chandra* and XMM-*Newton* surveys.

5 CXB resolved fraction

Before *NuSTAR*, the spectrum of the CXB in the hard X-ray band (>10 keV) was used as an integral constraint due to the non-focusing nature of hard X-ray telescopes. As mentioned in Section 1, thanks

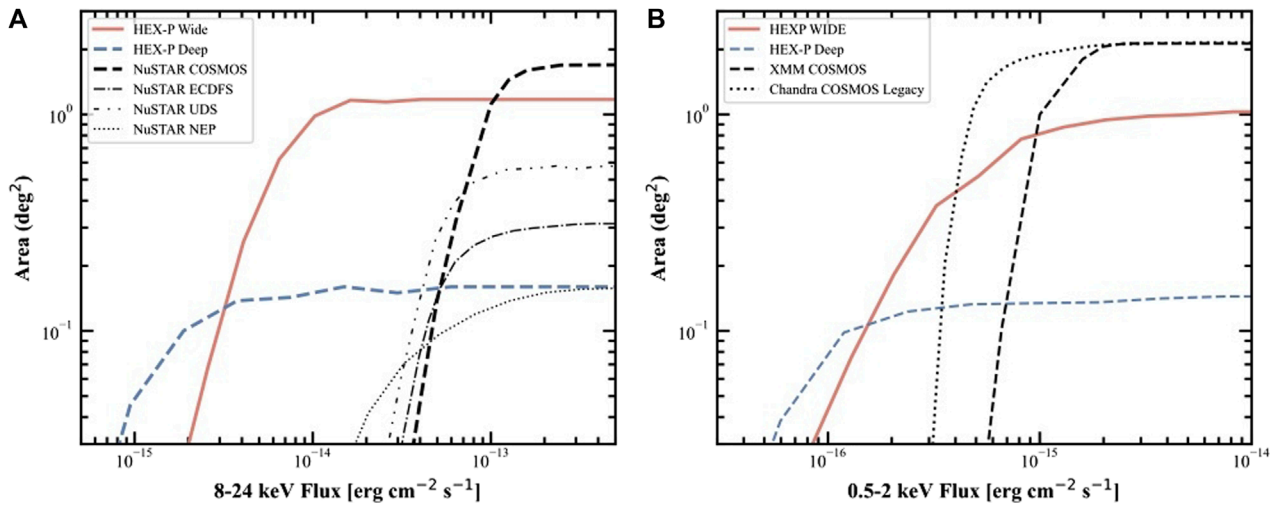

FIGURE 3
Survey sensitivity for the HET **(A)** in the 8–24 keV band and LET **(B)** in the 0.5–2 keV band. The deep and wide surveys are in blue and salmon, respectively. In each panel, the predicted sensitivities are compared with surveys published in the literature using *NuSTAR* in the left panel and *Chandra* and XMM-*Newton* in the right panel.

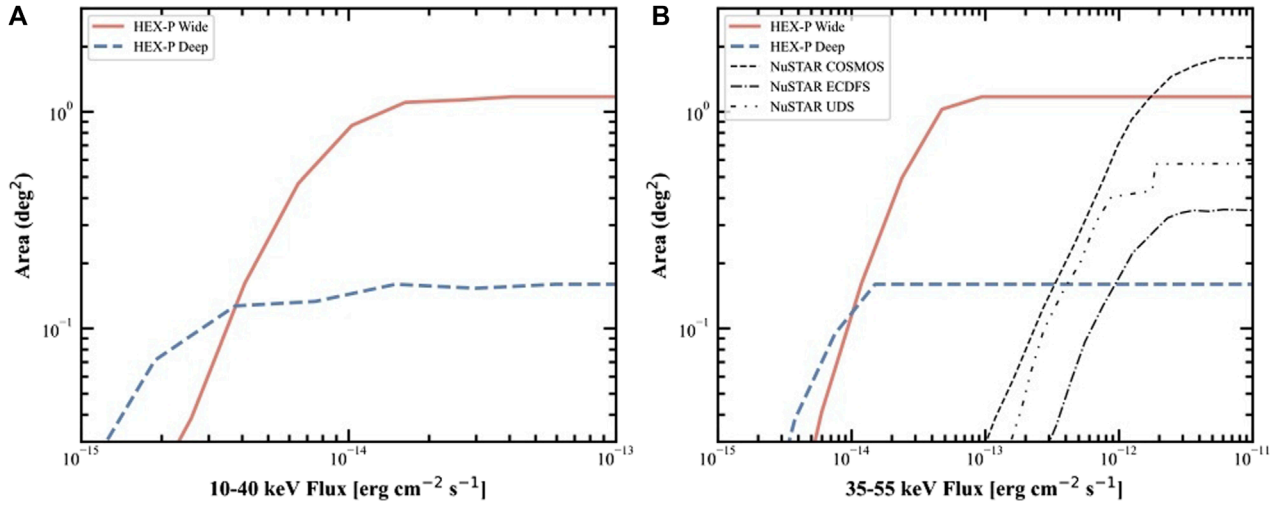

FIGURE 4
Survey sensitivity for the HET **(A)** in the 10–40 keV **(B)** and 35–55 keV (right) bands. The deep and wide surveys are in blue and salmon, respectively. The dashed, dot-dashed and dot-dot-dashed lines in the right panel shows the sensitivity in the same band computed for the COSMOS, ECDFS and UDS *NuSTAR* surveys (Masini et al., 2018b).

to *NuSTAR* we are able to resolve, for the first time, ~30%–35% of the CXB above 8 keV.

With *HEX-P*, it will be possible to measure the resolved fraction up to energies of ~40 keV. Because we used the well-calibrated mock catalog from Marchesi et al. (2020), computing the resolved fraction in the simulated *HEX-P* surveys is straightforward.

To this end, we have summed the input fluxes of the HET–detected sources in the deep and wide surveys separately in four different bands (3–8 keV, 8–16 keV, 8–24 keV, and 10–40 keV) that were chosen *a posteriori* to minimize the uncertainty on the resolved fraction. We then summed the fluxes of all the sources in the total input mock catalog in each energy band, which indeed returns the total intensity of the CXB (within a few percent) as reported and shown in Figure 5 of Marchesi et al. (2020). The CXB resolved fraction in the wide and deep surveys was then calculated by dividing the sum of the input fluxes of the detected sources by the total fluxes from the input catalog in each of the four aforementioned energy bands.

The uncertainty on the resolved fraction was derived from the uncertainty on the measured net counts of the detected sources. The net counts of each detected source are the background subtracted counts, extracted from a circular region centered at the source detected position with a 8.5″ radius (corresponding to an energy encircled fraction of 50%). The uncertainty on the net counts ($\sigma_{\rm net}$)

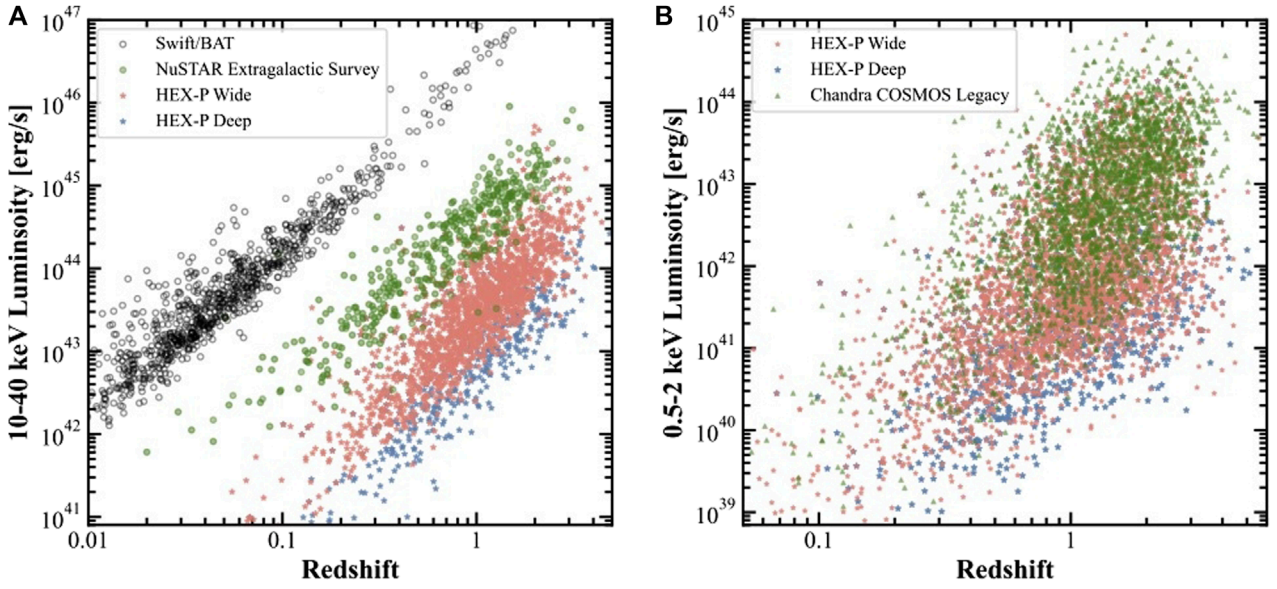

FIGURE 5
(A) 10–40 keV rest frame luminosity versus redshift of the HET detected sources in the deep (blue) and wide (salmon) surveys. **(B)** 0.5–2 keV rest frame luminosity versus redshift of the LET detected sources in the deep (blue) and wide (salmon) surveys. In both panels, the *HEX-P* surveys are compared with surveys in the literature using *NuSTAR* and *Swift*-BAT in the left panel and *Chandra* in the right panel.

of each source is the combination of the uncertainties on the total (σ_{tot}) and background counts (σ_{bkg}) in quadrature ($\sigma^2_{net} = \sigma^2_{tot} + \sigma^2_{bkg}$). The uncertainties on the total and background counts are calculated using equation (9) in Gehrels (1986), which is optimized for sources with small numbers of observed photon counts. Here, we use the 90% confidence level uncertainties. The net count uncertainty of the entire sample of detected sources ($\sigma^2_{net,sample}$) is calculated by adding up the net count uncertainty of each detected source in the sample in quadrature ($\sigma^2_{net,sample} = \sum \sigma^2_{net}$). The uncertainty on the CXB resolved fraction divided by the CXB resolved fraction is thus the net count (or flux) uncertainty of the entire sample divided by the net count (or flux) of the entire sample.

As a result, the measured CXB resolved fractions (and errors) in the simulated wide survey are 73% ± 2%, 73% ± 2%, 73% ± 6%, and 74% ± 3% in the 3–8, 8–16, 16–24, and 10–40 keV energy bands, respectively and the measured CXB resolved fractions (and errors) in the simulated deep survey are 86% ± 2%, 85% ± 2%, 86% ± 6%, and 86% ± 3% in the four energy bands, respectively. The measured CXB resolved fraction is shown in Figure 6 together with the *Chandra* and *NuSTAR* measurements. The width of the x-axis error bar on each of the *HEX-P* point corresponds to the width of the energy band used for that measurement. We note that the measured resolved fraction is almost constant across a wide energy range and this is due to the combination of the deep flux limit reached in these simulations that enables the detection of all the bright unobscured and also obscured sources contributing to the CXB and also to the use of the source input flux in the computation of the resolved fraction and not the measured flux (see below).

Just using the detected sources in the HET, we predict that *HEX-P* will reach a resolved fraction comparable with the results obtained from *Chandra* deep surveys below 8 keV (e.g., Xue et al., 2012) but reaching above the peak of the CXB up to 40 keV (see Figure 6). While ~70 sources are detected in the 35–55 keV band as shown in Table 1, this sample is too small to obtain strong constraints on the resolved fraction and provides only an upper limit (not reported in Figure 6). While the actual intensity of the CXB remains still uncertain, as recently shown by Rossland et al. (2023), the resolved fraction measured here is self-consistent as the input source fluxes are drawn from the mock catalog of Marchesi et al. (2020) and the total flux used is the sum of all the sources from the same mock catalog. Therefore, the uncertainties affecting the intensity of the CXB do not play a role in ou r measurement.

A fraction of the detected sources might be affected by Eddington bias, and their measured fluxes might be over-estimated compared to the input fluxes. This excess (over-estimation) of the measured fluxes mostly affects the sources at the flux limit of a survey (see, e.g., Figure 11 in Zhao et al., 2021). In this paper, the input fluxes from the mock catalog were used to compute the resolved fraction, and consequently, the Eddington bias does not affect our measurement. However, we did assess how Eddington bias will affect the measured resolved CXB fraction in real *HEX-P* surveys compared to the resolved CXB fraction computed above. For this analysis, we used the 50%-area sensitivity reported in Table 1 as the indicator of the turnover in a flux-flux distribution, following the method in Zhao et al. (2021), and derived that fluxes below the 50% area sensitivity in the wide survey might be overestimated by 2%, 6%, 10%, and 3% for the 3–8, 8–16, 16–24, and 10–40 keV bands. On the other hand, the fluxes of the sources in the deep survey are predicted to be overestimated by less than 1%–2%. Therefore, we anticipate that the resolved CXB fraction computed from future *HEX-P* surveys might be higher than the resolved CXB fraction presented in this paper by 2%–10% in the wide survey (depending on the energy band) and <2% in the deep survey.

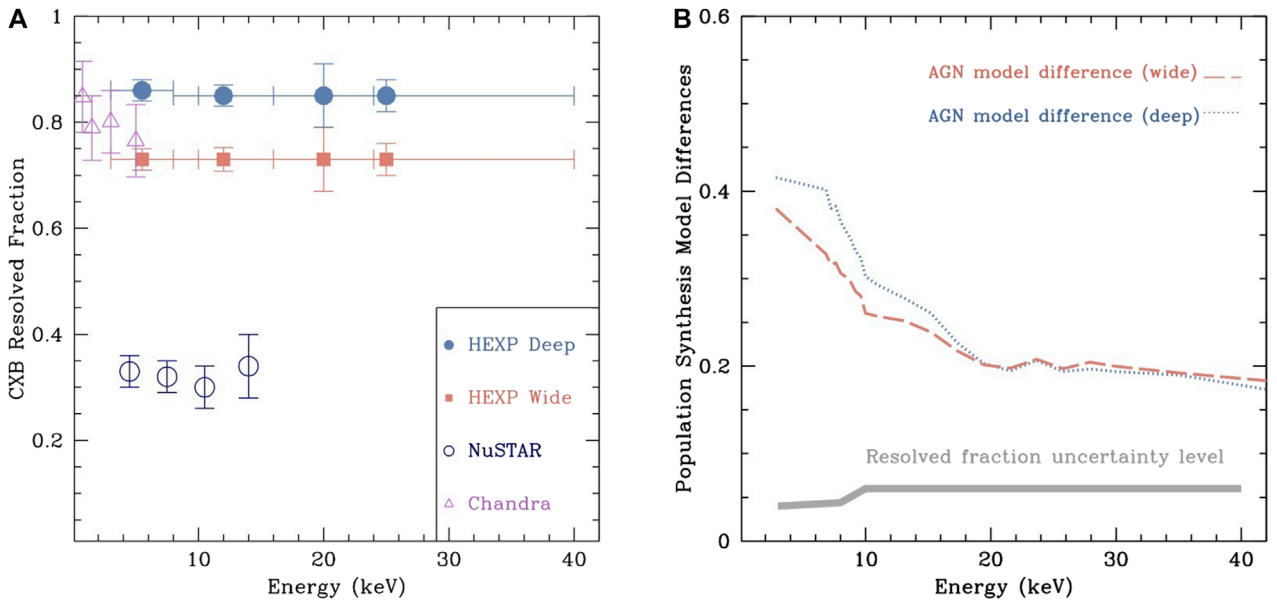

FIGURE 6
(A) Resolved fraction of the CXB as a function of energy as measured by *Chandra* (open violet triangles), *NuSTAR* deep surveys (open blue circles) and predicted for *HEX-P* deep (solid teal circles) and wide (solid salmon squares). **(B)** Difference between population synthesis models compared to the level of uncertainties (grey) measured for the CXB resolved fraction. The population synthesis models from Gilli et al. (2007) and Ananna et al. (2019) are folded with the deep (teal) and wide (salmon) survey sensitivity curves.

5.1 Comparison with population synthesis models

As shown in Figure 5, the luminosity-redshift space sampled by *HEX-P* will fill an important gap in our understanding of the AGN population. Currently, there are significant disagreements between population synthesis models, in particular at the faintest fluxes where the lack of detected sources makes it impossible to constrain the models. The faintest fluxes are populated by low-luminosity and/or heavily obscured AGN (see Figures 12 and 15 from Ananna et al., 2019). Sampling these parts of the population is one of the goals of the *HEX-P* surveys and will be of extreme importance for calibrating the next-generation of synthesis models.

The wide survey will also provide high-energy information on the poorly sampled population of luminous AGN which are rare and require larger volumes to be found (see the right panel of Figure 5). Although different population synthesis models predict different fractions of AGN at each obscuration level, usually these contributions sum to the same value of CXB (e.g., the CXB broken into bins of obscuration is given in Figure 11 of Ananna et al., 2019). One way to break the degeneracy is by applying different flux limits in different energy bands, as that leads to varying predictions between models of the CXB resolved fraction.

Comparing the measured resolved fraction with population synthesis models in this work would not return valuable information as the mock catalog used in these simulations is drawn from the Gilli et al. (2007) model and therefore the obtained results are in agreement with it. However, we can use the measurement uncertainties to showcase *HEX-P*'s capability to distinguish between model differences. In Figure 6B, the uncertainty level measured on the CXB resolved fraction (gray band) is compared with the typical difference between resolved fractions predicted by population synthesis models at the *HEX-P* flux limits in the wide and deep surveys. We used the models from Gilli et al. (2007) and Ananna et al. (2019) for this comparison, all of which were folded with the deep and wide survey sensitivities. Several other models were considered, but the above models captured the typical discrepancy between model predictions. We find that the difference between models is significantly larger than the simulated *HEX-P* measurement uncertainties, which will help us converge toward the most accurate population synthesis model.

HEX-P will focus X-rays in an energy range where it has never been achieved by any instruments before, allowing us to study the hard X-ray emission of AGN to flux limits never reached before. This will open the parameter space for new serendipitous discoveries. It is possible, even likely, that no existing model will perfectly predict the population that *HEX-P* will observe, as has happened in the past when new facilities reached unprecedented capabilities (Ananna et al., 2019; Kirkpatrick et al., 2023).

6 Obscured sources in surveys

Besides the detection of the sources contributing to the peak of the CXB, one of the main goals of *HEX-P* extragalactic surveys will be to characterize AGN spectral properties such as spectral indices, cut-off temperatures, reflection scaling factors and circum-nuclear obscuration covering factors (Boorman et al., 2023; Kammoun et al., 2023; Piotrowska et al., 2023). Extragalactic field surveys will contribute to this analysis by providing deep exposures for faint sources. While the CXB is an aggregate population statistic, data from *HEX-P* can be directly incorporated into models and

can contribute greatly towards constraining one of the biggest uncertainties in AGN populations: the fraction of heavily obscured (i.e., CT) objects.

Zappacosta et al. (2018) carried out a systematic broad-band (0.5–24 keV) spectral analysis of 63 sources detected in *NuSTAR* extragalactic surveys with a flux brighter than 7×10^{-14} erg s^{-1} cm^{-2} (8–24 keV) to characterize their spectral properties, obtain a column density distribution and measure the absorbed/CT fractions to compare with predictions from population-synthesis models. However, their sample lacks large statistics, its soft band data (needed to perform the spectral fitting) was taken at a different epoch and the spectral analysis can be affected by variability. As a consequence, the results on the derived properties, like the obscured and CT fractions, have large uncertainties or are basically unconstrained (CT = 0.02–0.56 or <0.66 at 90% c.l.). Clearly, increasing the number of sources with good quality spectra in the hard X-ray band paired with simultaneous good quality low-energy data would be crucial (as shown in Marchesi et al., 2018, Marchesi et al., 2019) to constrain the CT fraction at a flux limit never reached before. *HEX-P* surveys will provide such a sample.

In Figure 7, the net counts distribution in 10″ and 5″ radius apertures (~30% of the PSF) for the HET and LET detections in the simulated surveys are reported. As shown by Zappacosta et al. (2018), above 40 counts in the 3–24 keV band, it is possible to obtain good (>3σ) constraints on spectral parameters with spectral fitting. The sample in *HEX-P* surveys will include several hundreds of sources with broadband coverage and enough counts in the 0.5–40 keV energy band to perform good quality spectral analysis (see Section 6.1). Besides the obscuration distribution, for the bright sources in the sample, it will also be possible to measure other spectral properties like the high-energy cut-off as shown by Kammoun et al. (2023) for both unobscured and obscured AGN (see their Section 5; Figures 5, 6) extending their results to fainter luminosities/fluxes.

The good quality X-ray spectra will also allow us to investigate further potential observational biases caused by rapidly spinning black holes with strong reflection components that mimic obscured spectra (Gandhi et al., 2007; Vasudevan et al., 2016). Deconvolving spin-related reflection signatures from obscuration will reval SMBH growth with cosmic time.

While spectral analysis is the best tool to measure intrinsic source properties (spectral index, column density, luminosity), the hardness ratio (HR = H-S/H+S where H and S are typically the number of counts in a given hard and soft band respectively) has been used before in XMM-*Newton*, *Chandra* and *NuSTAR* surveys (Civano et al., 2015; Marchesi et al., 2016a; Zhao et al., 2021) to obtain a rough measurement of obscuration. As shown in Zhao et al. (2021), the hardness ratio computed using *NuSTAR* bands (3–8 and 8–24 keV) is more sensitive to obscuration above $N_{\rm H} > 10^{24}$ cm^{-2} than just using softer bands (0.5–2 and 2–10 keV), which can better distinguish column densities below $N_{\rm H} < 10^{23}$ cm^{-2}. However, usually, soft and hard X-ray data are not simultaneous in extragalactic surveys, and therefore the estimate of obscuration using non-simultaneous hardness ratios can give erroneous results. With *HEX-P*, HET detections will have soft energy data readily available to build a color-color diagram spanning the 0.5–40 keV band. Figure 8A shows such a color-color diagram using the hard X-ray HR$_{HET}$ (with H = 10–40 keV and S = 3–8 keV counts) compared to the soft X-ray HR$_{LET}$ (with H = 2–10 keV and S = 0.5–2 keV counts); the sources are color-coded according to their column density from the input mock catalog. Only detections in the 10–40 keV and 3–8 keV bands are used. As most of these sources will be in the low-counts regime, the best estimate of the HR will be obtained using a Bayesian tool such as BEHR (Park et al., 2006). The spread of the points on the x-axis for each given column density is due to the degeneracy of hardness ratio with redshift. Still, we foresee that most, if not all, of the sources in the *HEX-P* extragalactic surveys will have a spectroscopic or photometric redshift measure. The contours represent number densities associated with 1, 2 and 3 σ from a two-dimensional Gaussian distribution, according to different input obscuration values. Thanks to the coverage at energies above 10 keV, it will be possible to distinguish the CT AGN from the less obscured ones as the CT AGN are separated by the rest of the sources mainly on the HR$_{HET}$ axis/color. Adding multi-wavelength information (e.g., redshifts, infrared fluxes, etc) will constrain the column density to even higher precision and accuracy (e.g., Carroll et al., 2021, Carroll et al., 2023; Silver et al., 2023) and therefore deliver a robust sample of CT AGN.

Another method to select candidate obscured and CT sources is to use a simple band ratio (H/S) as done in *NuSTAR* by Mullaney et al. (2015). Previously, an anti-correlation was observed between band ratio (H/S) and count rates in the chosen soft band (S), attributed to the decrease of soft band counts with increasing obscuration (Della Ceca et al., 1999; Ueda et al., 1999; Mushotzky et al., 2000; Tozzi et al., 2001; Alexander et al., 2003). We have used the 10–40 keV to 3–8 keV input flux ratio and compared it with the detected counts ratio in the same band to test the reliability of the band ratio to find CT sources (Figure 8B). The two quantities correlate when considering the 10–40 keV detected sample with fluxes above the 50%-area flux limit and with detections in both the 10–40 and 3–8 keV bands. When including upper limits on the 3–8 keV flux, the correlation between the two band ratios is not equally strong due to few unobscured sources, which are just detected in the 10–40 keV band, possibly due to Eddington bias.

6.1 Spectral analysis of obscured sources

To quantify the spectral constraints attainable from *HEX-P* surveys and compare with the quality of the best sources in *NuSTAR*'s surveys, we simulated known CT and obscured Compton-thin ($log(N_{\rm H}) < 24$) AGN detected in the *NuSTAR* COSMOS (Civano et al., 2015) and serendipitous (Lansbury et al., 2017a) surveys which were both presented in Zappacosta et al. (2018). The observed/measured spectral properties (from Zappacosta et al., 2018) are summarized in Table 2. We used the spectra from Zappacosta et al. (2018) and performed broadband spectral fitting using the Bayesian X-ray Analysis (BXA) code from Buchner (2016) with the UXCLUMPY model (Buchner et al., 2019). The original *Chandra*, XMM-*Newton* and *NuSTAR* spectra and their best-fit models are shown in Figure 9. As presented by Zappacosta et al. (2018), two of the three sources (nuid117 and cnuid330) are classified as CT, and one (cnuid272) is obscured but Compton-thin.

Using the best-fit UXCLUMPY models found by BXA, we simulated *HEX-P* spectra for both the LET and HET. For the bright CT source (cnuid330), we simulated exposure times consistent

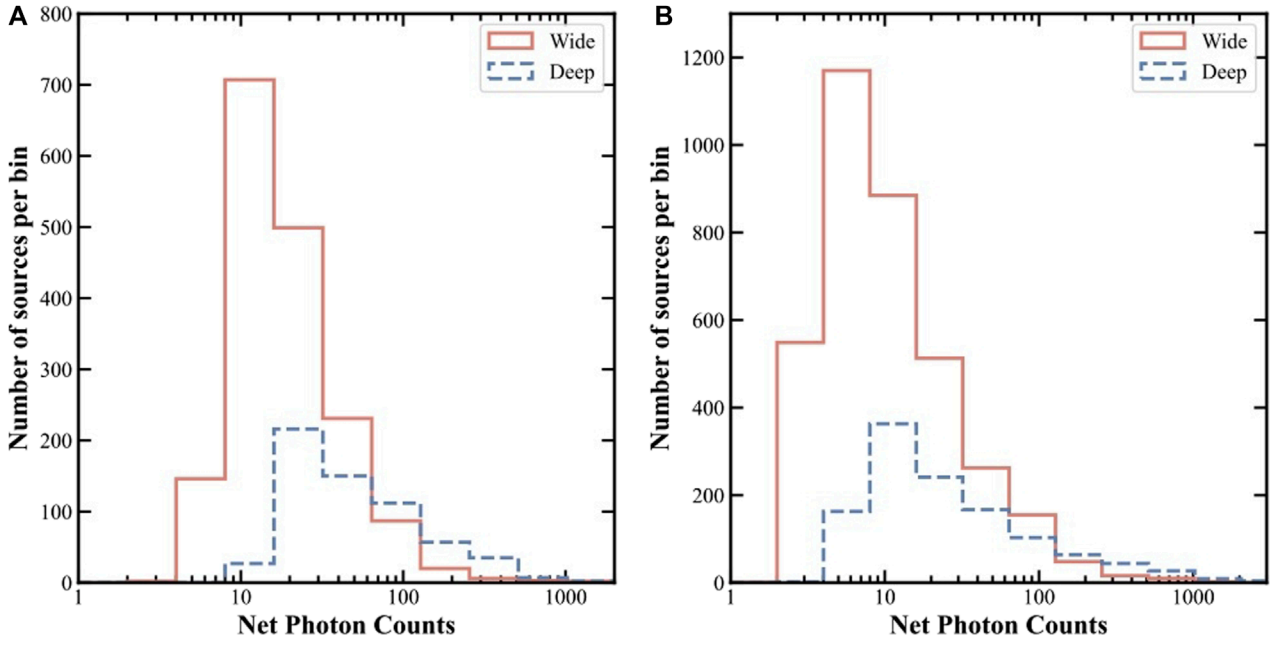

FIGURE 7
Source count distributions showcasing how many counts we will have in HET **(A)** and LET **(B)** over the bandpass to perform spectral analysis. The counts were extracted in the 0.5–15 keV band for the LET and the 3–40 keV band for the HET (summing two telescopes). The sources from the deep survey are in blue, those from the wide survey are in salmon.

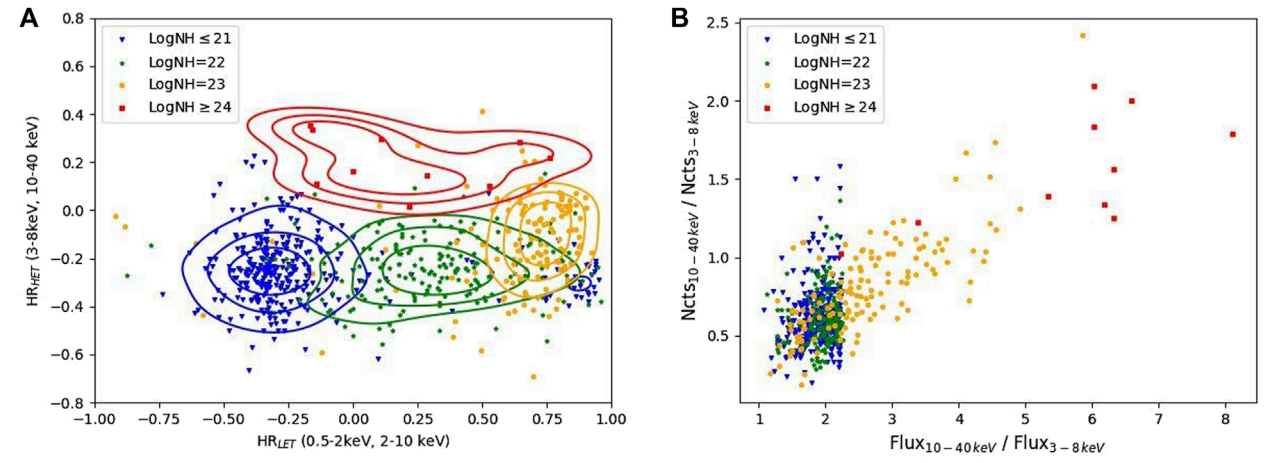

FIGURE 8
(A) HR_{HET} versus HR_{LET} for sources detected in the 10–40 keV band. The sources are color-coded by obscuration from the input catalog. The density contours represent 1, 2 and 3 σ from a two-dimensional Gaussian distribution. **(B)** 10–40 and 3–8 keV observed counts ratio plotted against the input flux ratio in the same bands. The sources are color-coded by obscuration from the input catalog.

TABLE 2 Properties of targets chosen for spectral analysis simulations.

Object ID	z	*NuSTAR* exp (ks)	$log(N_H)$ (cm^{-2})	2–10 keV flux (10^{-13} erg s^{-1} cm^{-2})	8–24 keV flux (10^{-13} erg s^{-1} cm^{-2})
cnuid330	0.04	52	24.13	4.75	3.54
cnuid272	0.67	106	22.62	0.65	1.03
nuid117	0.78	22	24.61	0.25	0.88

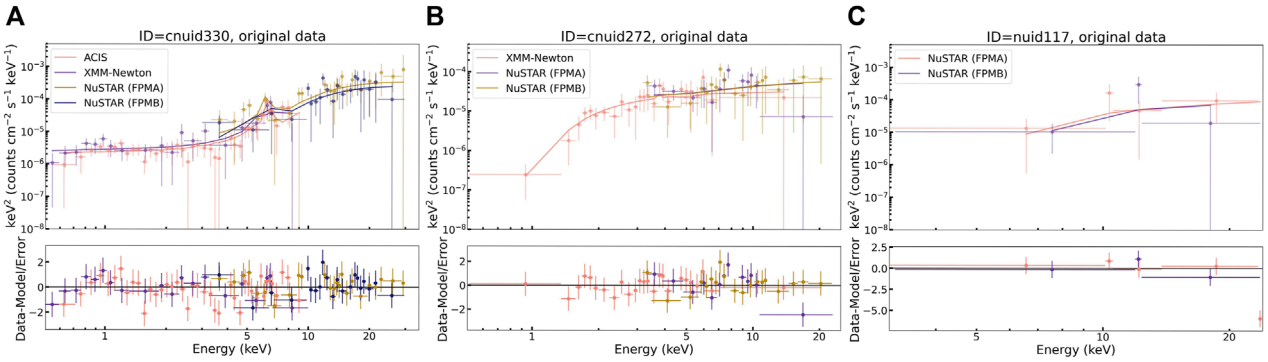

FIGURE 9
The original spectra for cnuid330 **(A)**, cnuid272 **(B)** and nuid117 **(C)**, unfolded with the best-fit UXCLUMPY model (denoted with solid lines) found using BXA.

with the proposed wide field survey (50, 60, and 100 ks; see Figure 1, salmon curves) which is likely to detect similarly bright CT sources. For the two fainter sources (nuid117 and cnuid272), we used exposure times consistent with the *HEX-P* deep survey (250, 500, and 700 ks; see Figure 1, blue curves), which probes the faint population.

The goal of these simulations is to test the ability of *HEX-P* to differentiate the subtle effects that the geometry of obscuring material has on the AGN spectral shape. As described by Buchner et al. (2019), the UXCLUMPY model includes an optional CT inner ring of obscuring material that can help to explain the features of some, but not all, CT AGN at hard energies ($\gtrsim 10$ keV). For example, Buchner et al. (2019) shows that this additional component is needed to efficiently model the broadband X-ray spectrum of the prototypical CT-AGN in the Circinus Galaxy. The inner ring is parameterized by the covering fraction of the material (CTK-COVER, which ranges from 0.0 to 0.6). For the faint and higher redshift AGN (nuid117 and cnuid272), CTK-COVER is not constrained with previous data. *HEX-P*'s effective area beyond 20 keV will allow us to discern the subtle effects (e.g., a general sharpening of the Compton hump at >10 keV) that CTK-COVER has on the hard-band spectra of these AGN. To show this, we have simulated obscured *HEX-P* spectra with CTK-COVER = 0.0, 0.3, and 0.6. The other parameters were set to the best-fit values found by BXA on the original *NuSTAR* spectra as in Table 2. The simulated spectra and models of these objects are shown in Figure 10. The effects of different values of CTK-COVER for these X-ray faint obscured AGN (nuid117 and cnuid330) are clearly observable in *HEX-P* spectra. The corresponding constraints on CTK-COVER are plotted against $N_{\rm H}$ in Figure 11 for simulations of nuid117 and cnuid330 using the 500 ks and 100 ks exposures. Constraints on CTK-COVER and 99.73% percentile values derived from the posterior distribution for cnuid272 in the deep survey (500 ks) are $0.31^{+0.19}_{-0.30}$ (true CTK-COVER = 0.0), $0.37^{+0.19}_{-0.36}$ (true CTK-COVER = 0.3), and >0.11 (true CTK-COVER = 0.6). For cnuid330 in the wide survey (100 ks), the constraints are $0.06^{+0.496}_{-0.064}$ (true CTK-COVER = 0.0), $0.37^{+0.23}_{-0.36}$ (true CTK-COVER = 0.3), and $0.59^{+0.01}_{-0.57}$ (true CTK-COVER = 0.6). As a side note, it's worth remembering that the spectral analysis discussed here was not conducted in Zappacosta et al. (2018) as the quality of the spectra did not allow it, while *HEX-P* will provide excellent constraints even on the geometrical properties of the circum-nuclear obscurer itself. spectral covering fraction.

For obscured, Compton-thin AGN, the effects of CTK-COVER are negligible within *HEX-P*'s energy range. But it is still of interest to constrain $N_{\rm H}$ of these AGN. In the case of cnuid272, this constraint is shown for 500 ks simulation of the object at its nominal flux, as well as an identical object that is ten times fainter as well as to the $N_{\rm H}$ constraints of the existing *NuSTAR* observation in Figure 12. Similar constraints as *NuSTAR* will be achieved for a source that is 10 times fainter with *HEX-P*. It may be noted that the maximum *a posteriori* value of $N_{\rm H}$ derived by BXA (which is taken as the "truth" value for the simulations) does not align with the peak of the distribution. This shift can occur when analyzing a multi-dimensional parameter space where one or more parameters become limits. In these cases, it is difficult to define a best-fit model, and therefore, it is more useful to compare the posterior distribution of the parameters, which is done here.

6.2 Predictions on the compton-thick fraction

Constraining the space densities of CT objects has remained elusive due to a lack of high-energy X-ray telescopes capable of detecting faint sources. *HEX-P* can help fill this gap in several ways. Combining spectral analysis of the brightest sources with hardness and band ratio analyses, it will be possible to place constraints on the CT fraction at fluxes ten times, or more, fainter than has been reported before (Burlon et al., 2011; Civano et al., 2015; Ricci et al., 2015; Masini et al., 2018a; Torres-Albà et al., 2021). To visualise the importance of flux limits in assessing the CT fraction, we show the contribution to the CXB from CT objects using the Ananna et al. (2019) model with two different assumed CT fractions (30% and 50%) as solid lines in Figure 13. For a series of increasing flux depths, we then considered the detected CT sources above that flux level and re-sampled a random number of not-CT AGN detected above that flux level to give a fraction as close as possible to the value given by

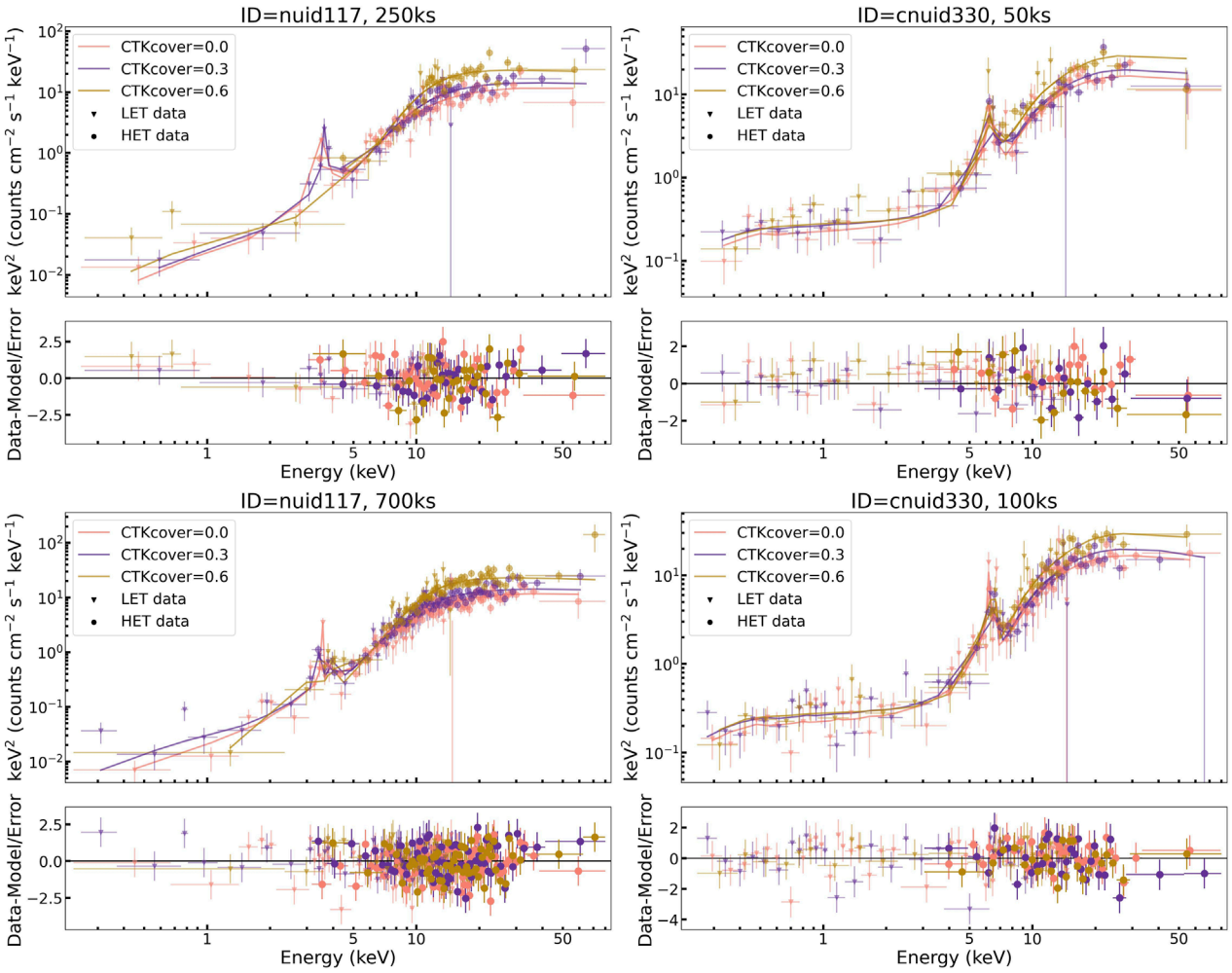

FIGURE 10
Unfolded *HEX-P* spectra for two CT sources (nuid117, left and cnuid330, right) simulated for the minimum (top) and maximum (bottom) exposure times of the deep (nuid117, left) and wide (cnuid330, right) surveys. LET and HET data are plotted as triangles and circles, respectively. The theoretical spectra on which the simulations were based are shown by solid lines. The three colors denote simulations with different values of UXCLUMPY's CTK-cover parameter. The spectra of nuid117 have been normalized at 6 keV and of cnuid330 have been normalized at 5 keV.

each model. We note that since the simulations performed in this work follow a mock catalog based on Gilli et al. (2007), we are not directly comparing the measured CT fraction in simulations with the Ananna et al. (2019) models. Still, we derive uncertainties on the curves in Figure 13 based on the binomial uncertainties associated with the number of CT sources detected in the surveys above a given flux. For the comparison in Figure 13, the sources detected in the 10–40 keV band in the combined deep and wide surveys were considered.

At the flux level sampled by *NuSTAR* surveys ($>2\times10^{-14}$ erg s^{-1} cm^{-2} in the 10–40 keV band), the models are indistinguishable. At deeper flux levels, the number of CT sources that *HEX-P* surveys will detect are sufficient to constrain the CT fraction to a flux limit of $\sim10^{-15}$ erg s^{-1} cm^{-2} in the 10–40 keV and inform population synthesis models.

There are several other ways in which *HEX-P* will help us constrain CT space densities. One important approach would be to consider the entire population detected by *HEX-P* and infer the CT fraction with multi-wavelength diagnostics and machine learning algorithms, in particular using infrared colors (Stern et al., 2005; Stern et al., 2012; Mateos et al., 2013; Assef et al., 2015; Carroll et al., 2021, Carroll et al., 2023; Silver et al., 2023). Moreover, given the improved PSF of *HEX-P* compared to *NuSTAR*, it will be possible to perform stacking analysis (see the results in Hickox, 2024) at the position of non-X-ray detected candidate CT AGN selected from multiwavelength analysis. We can then apply the *HEX-P* wide and deep survey flux limits in the 10–40 keV energy window to population synthesis models and compare the results with the *HEX-P* observed sample to find the most accurate models. This will be a useful check not only for CT sources but also for relatively unobscured sources, as there are significant disagreements between population synthesis models at Compton-thin obscuration levels as well (as these models have to add up to reproduce the CXB, overestimation in one obscuration level needs to be compensated for by reducing the contribution in others, and *vice versa*). Overall, *HEX-P*'s data promises a deeper, more nuanced insight into AGN space densities, shedding light on the evolution of AGN across cosmic time.

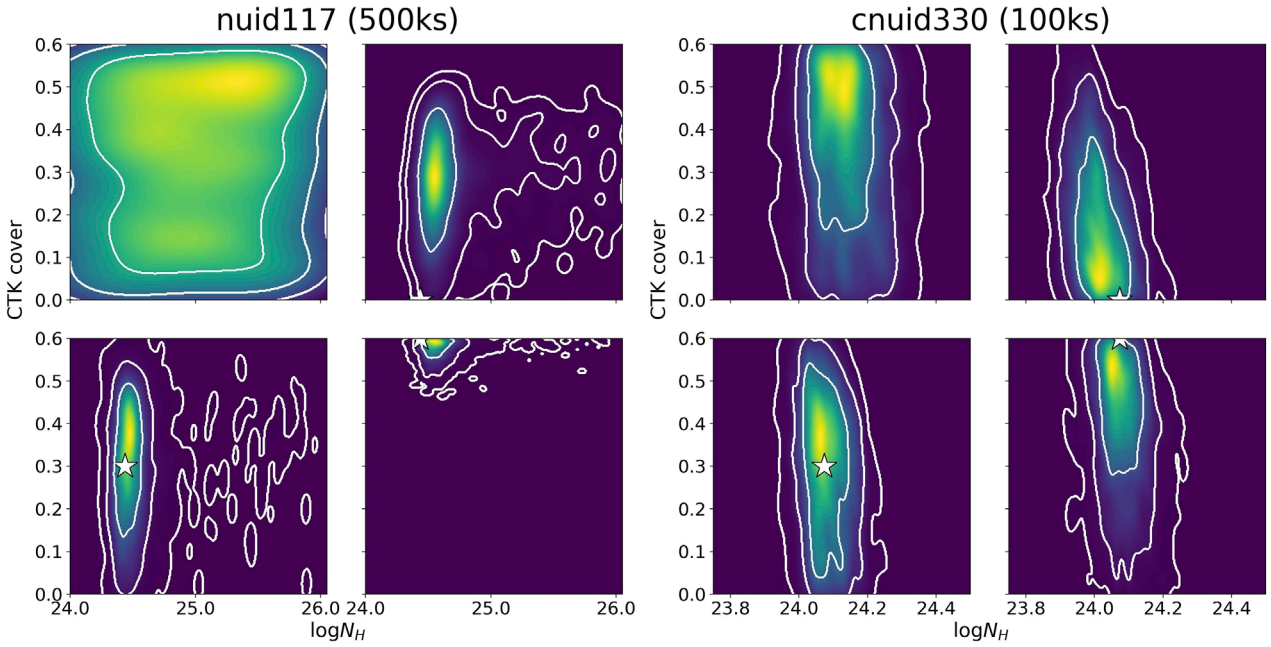

FIGURE 11
Constraints on N_H and CTK-COVER for nuid117/cnuid330 (left/right). Constraints are shown for the original data (top-left) and 500 ks/100 ks *HEX-P* simulations with CTK-COVER = 0.0 (top-right), 0.3 (bottom-left), and 0.6 (bottom-right). The white contour lines demonstrate 1σ, 2σ, and 3σ constraints and a white star denotes the nominal parameter values for the simulations.

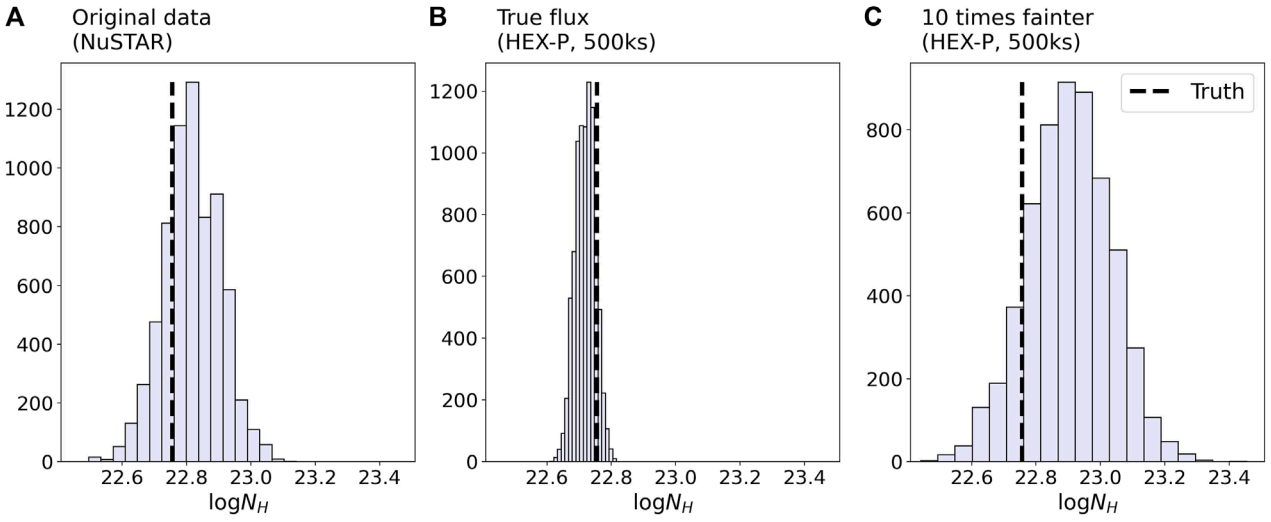

FIGURE 12
The N_H constraints for cnuid272 (a Compton-thin source) found using the original data **(A)** and 500 ks *HEX-P* simulation **(B)** and a simulated object ten times fainter than (but otherwise identical to) cnuid272 **(C)**. The dashed black line in all three panels marks the best-fit N_H for the original data, which is set to the "truth" value for the simulated spectra.

7 Summary

In this paper, we have presented a small selection of the results that will be obtained by performing wide and deep extragalactic surveys with the *High Energy X-ray Probe*. These findings are based on extensive simulations using AGN mock catalogs derived from Marchesi et al. (2020). We followed the standard survey detection process to analyze these simulations, leading to the detection of several thousand sources above 3 keV, in contrast to the few hundred sources detected in all of *NuSTAR*'s surveys performed to date. Notably, we predict the detection of the first sample of AGN in the 35–55 keV energy band.

The analysis of these simulations demonstrates that *HEX-P* will, for the first time, have the capability to significantly constrain

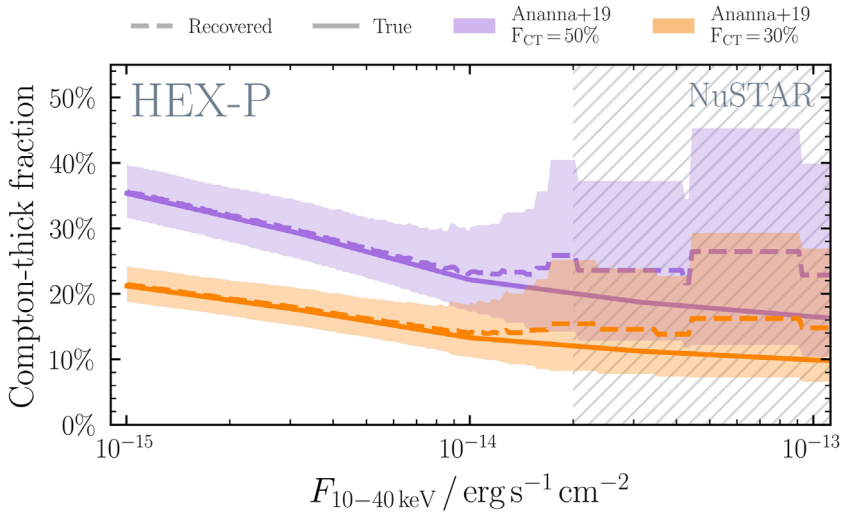

FIGURE 13
The ability to distinguish between population synthesis model predictions of the CT fraction as a function of flux limit in the 10–40 keV band with the simulated wide and deep *HEX-P* surveys combined. The true predicted CT fractions from the population synthesis models of Ananna et al. (2019) are shown with solid lines for 30% and 50% in orange and purple, respectively. The CT fraction recovered purely from CT sources detected above each flux limit on the x-axis is shown with dashed lines and associated binomial uncertainty shading. Clearly the two models can be differentiated by reaching fainter flux levels than *NuSTAR* is currently able to (hatched shading).

the contribution of AGN to the CXB around its peak (3–40 keV). We anticipate reaching a resolved fraction of approximately ~86% in the 3–40 keV energy range, comparable to what *Chandra* has resolved in the 0.5–8 keV range. This result was achieved using HET detections alone, and even higher resolved fractions can be obtained by performing a stacking analysis of the HET data at the position of LET sources. Furthermore, the resolved fraction could be computed in the 0.5–15 keV energy band exclusively from LET detections.

With the large samples of sources *HEX-P* will detect, it will be possible to compute the resolved fraction by separating sources in different classes based on X-ray (obscured, unobscured, CT or C-Thin) or optical classifications, allowing to study their relative contribution (and spectrum) at different energies to the total CXB with the ultimate goal of informing population synthesis models and understanding the full cosmic history of black hole growth.

Understanding the spectrum of the AGN population is a crucial aspect when calibrating population synthesis models. *HEX-P*'s simultaneous broadband coverage will enable spectral analysis for ~1,000 sources (combining the LET and HET detections) with sufficient counts to measure and strongly constrain spectral parameters beside obscuration and spectral slope, including, e.g., the covering factor and high-energy cut-off. For sources with low-count spectra, we have shown that the combination of soft and hard X-ray colors can estimate their obscuration level by comparing these colors with the simulations presented in this paper and future simulations. For the first time, we will measure the CT fraction in the 10–40 keV band at a flux limit that is one order of magnitude fainter than *NuSTAR* with a sample of CT AGN large enough to finally calibrate the next-generation of population synthesis models.

When comparing the uncertainty on the measured CXB resolved fraction with the typical difference between AGN population synthesis models, it becomes evident that these new *HEX-P* measurements will be able to disentangle models. It is also plausible that no currently existing model will offer a perfect fit to the population that *HEX-P* will uncover. Together with dedicated observations of local CT AGN (Boorman et al., 2023), the survey data will open the door to a recalibration of existing population synthesis models, facilitating the integration of more precise constraints on both space densities and AGN spectra.

The potential residing in *HEX-P* surveys extends far beyond what is covered in this paper. For example, we have not discussed the great potential of serendipitous detections of AGN pairs in surveys (see discussion in Pfeifle et al., 2023) nor the measurements of SMBH spins for the brighter AGN (Piotrowska et al., 2023) and also the possible detection of blazars in the wide area survey (Marcotulli et al., 2023). By the time *HEX-P* is launched, comprehensive spectroscopic campaigns and photometric data will be available for the majority of the extragalactic fields that *HEX-P* will target from major ground and space-based observatories. These data will allow the complete characterization of the multiwavelength properties of *HEX-P* detected AGN as well as the properties of their host galaxies. Understanding the connection between SMBH growth and host galaxy evolution is one of the main goals of the Astro2020 Decadal Survey (National Academies of Sciences, Engineering, and Medicine, 2021) and the *HEX-P* survey samples, combined with these exquisite and rich multiwavelength datasets, will allow us to finally address this goal in the early 2030s.

Data availability statement

The raw data supporting the conclusion of this article will be made available by the authors, without undue reservation.

Author contributions

FC: Writing–original draft, Writing–review and editing. XZ: Formal Analysis, Writing–review and editing. PB: Writing–review and editing. SM: Writing–review and editing. TA: Writing–review and editing. SC: Writing–review and editing. C-TC: Writing–review and editing. RH: Writing–review and editing. DS: Writing–review and editing. KM: Writing–review and editing. JG: Writing–review and editing. RS: Writing–review and editing. JA: Writing–review and editing. DA: Writing–review and editing. MB: Writing–review and editing. WB: Writing–review and editing. JB: Writing–review and editing. PG: Writing–review and editing. EK: Writing–review and editing. SL: Writing–review and editing. GL: Writing–review and editing. AMe: Writing–review and editing. AMo: Writing–review and editing. KN: Writing–review and editing. EN: Writing–review and editing. AP: Writing–review and editing. SP: Writing–review and editing. RP: Writing–review and editing. CR: Writing–review and editing. DS: Writing–review and editing. NT-A: Writing–review and editing.

Funding

The author(s) declare financial support was received for the research, authorship, and/or publication of this article. RS acknowledges support from the *NuSTAR* grant number 19-NuSTAR-0036. CR acknowledges support from the Fondecyt Regular grant 1230345 and ANID BASAL project FB210003. The work of DS was carried out at the Jet Propulsion Laboratory, California Institute of Technology, under a contract with NASA. SC work is supported by NASA under award number 80GSFC21M0002.

Conflict of interest

Author SP was employed by ASI—Agenzia Spaziale Italiana.

The remaining authors declare that the research was conducted in the absence of any commercial or financial relationships that could be construed as a potential conflict of interest.

Publisher's note

All claims expressed in this article are solely those of the authors and do not necessarily represent those of their affiliated organizations, or those of the publisher, the editors and the reviewers. Any product that may be evaluated in this article, or claim that may be made by its manufacturer, is not guaranteed or endorsed by the publisher.

References

Aird, J., Alexander, D. M., Ballantyne, D. R., Civano, F., Del-Moro, A., Hickox, R. C., et al. (2015a). The NuSTAR extragalactic survey: first direct measurements of the ≳10 KeV X-ray luminosity function for active galactic nuclei at z>0.1. *ApJ* 815, 66. doi:10.1088/0004-637X/815/1/66

Aird, J., Coil, A. L., Georgakakis, A., Nandra, K., Barro, G., and Pérez-González, P. G. (2015b). The evolution of the X-ray luminosity functions of unabsorbed and absorbed AGNs out to z ~ 5. *MNRAS* 451, 1892–1927. doi:10.1093/mnras/stv1062

Akylas, A., Georgakakis, A., Georgantopoulos, I., Brightman, M., and Nandra, K. (2012). Constraining the fraction of Compton-thick AGN in the Universe by modelling the diffuse X-ray background spectrum. *A&A* 546, A98. doi:10.1051/0004-6361/201219387

Alexander, D. M., Bauer, F. E., Brandt, W. N., Schneider, D. P., Hornschemeier, A. E., Vignali, C., et al. (2003). The Chandra deep field North survey. XIII. 2 Ms point-source catalogs. *AJ* 126, 539–574. doi:10.1086/376473

Alexander, D. M., Stern, D., Del Moro, A., Lansbury, G. B., Assef, R. J., Aird, J., et al. (2013). The NuSTAR extragalactic survey: a first sensitive look at the high-energy cosmic X-ray background population. *ApJ* 773, 125. doi:10.1088/0004-637X/773/2/125

Ananna, T. T., Treister, E., Urry, C. M., Ricci, C., Hickox, R. C., Padmanabhan, N., et al. (2020). Accretion history of AGNs. II. Constraints on AGN spectral parameters using the cosmic X-ray background. *ApJ* 889, 17. doi:10.3847/1538-4357/ab5aef

Ananna, T. T., Treister, E., Urry, C. M., Ricci, C., Kirkpatrick, A., LaMassa, S., et al. (2019). The accretion history of AGNs. I. Supermassive black hole population synthesis model. *ApJ* 871, 240. doi:10.3847/1538-4357/aafb77

Assef, R. J., Eisenhardt, P. R. M., Stern, D., Tsai, C. W., Wu, J., Wylezalek, D., et al. (2015). Half of the most luminous quasars may Be obscured: investigating the nature of WISE-selected hot dust-obscured galaxies. *ApJ* 804, 27. doi:10.1088/0004-637X/804/1/27

Ballantyne, D. R., Everett, J. E., and Murray, N. (2006). Connecting galaxy evolution, star formation, and the cosmic X-ray background. *ApJ* 639, 740–752. doi:10.1086/499558

Bertin, E., and Arnouts, S. (1996). SExtractor: software for source extraction. *A&AS* 117, 393–404. doi:10.1051/aas:1996164

Bogdan, A., Goulding, A., Natarajan, P., Kovacs, O., Tremblay, G., Chadayammuri, U., et al. (2023). Evidence for heavy seed origin of early supermassive black holes from a z¯10 X-ray quasar. arXiv. doi:10.48550/arXiv.2305.15458

Boorman, P. G., Torres-Albà, N., Annuar, A., Marchesi, S., Pfeifle, R., Stern, D., et al. (2023). The high energy X-ray probe (HEX-P): the circum-nuclear environment of growing supermassive black holes. arXiv. doi:10.48550/arXiv.2311.04949

Brandt, W. N., Ni, Q., Yang, G., Anderson, S. F., Assef, R. J., Barth, A. J., et al. (2018). Active galaxy science in the LSST deep-drilling fields: footprints, cadence requirements, and total-depth requirements. arXiv. doi:10.48550/arXiv.1811.06542

Brightman, M., Nandra, K., Salvato, M., Hsu, L.-T., Aird, J., and Rangel, C. (2014). Compton thick active galactic nuclei in Chandra surveys. *MNRAS* 443, 1999–2017. doi:10.1093/mnras/stu1175

Buchner, J. (2016). *BXA: bayesian X-ray analysis*. Astrophysics Source Code Library, record ascl:1610.011. Available at: https://ui.adsabs.harvard.edu/abs/2016ascl.soft10011B

Buchner, J., Brightman, M., Nandra, K., Nikutta, R., and Bauer, F. E. (2019). X-ray spectral and eclipsing model of the clumpy obscurer in active galactic nuclei. *A&A* 629, A16. doi:10.1051/0004-6361/201834771

Buchner, J., Georgakakis, A., Nandra, K., Brightman, M., Menzel, M.-L., Liu, Z., et al. (2015). Obscuration-dependent evolution of active galactic nuclei. *ApJ* 802, 89. doi:10.1088/0004-637X/802/2/89

Buchner, J., Georgakakis, A., Nandra, K., Hsu, L., Rangel, C., Brightman, M., et al. (2014). X-ray spectral modelling of the AGN obscuring region in the CDFS: Bayesian model selection and catalogue. *A&A* 564, A125. doi:10.1051/0004-6361/201322971

Burlon, D., Ajello, M., Greiner, J., Comastri, A., Merloni, A., and Gehrels, N. (2011). Three-year swift-bat survey of active galactic nuclei: reconciling theory and observations? *Astrophysical J.* 728, 58. doi:10.1088/0004-637x/728/1/58

Cappelluti, N., Brusa, M., Hasinger, G., Comastri, A., Zamorani, G., Finoguenov, A., et al. (2009). The XMM-Newton wide-field survey in the COSMOS field. The point-like X-ray source catalogue. *A&A* 497, 635–648. doi:10.1051/0004-6361/200810794

Cappelluti, N., Li, Y., Ricarte, A., Agarwal, B., Allevato, V., Tasnim Ananna, T., et al. (2017). The Chandra COSMOS legacy survey: energy spectrum of the cosmic X-ray background and constraints on undetected populations. *ApJ* 837, 19. doi:10.3847/1538-4357/aa5ea4

Carroll, C. M., Ananna, T. T., Hickox, R. C., Masini, A., Assef, R. J., Stern, D., et al. (2023). A high fraction of heavily X-ray-obscured active galactic nuclei. *ApJ* 950, 127. doi:10.3847/1538-4357/acc402

Carroll, C. M., Hickox, R. C., Masini, A., Lanz, L., Assef, R. J., Stern, D., et al. (2021). A large population of luminous active galactic nuclei lacking X-ray detections: evidence for heavy obscuration? *ApJ* 908, 185. doi:10.3847/1538-4357/abd185

Chen, C. T. J., Brandt, W. N., Luo, B., Ranalli, P., Yang, G., Alexander, D. M., et al. (2018). The XMM-SERVS survey: new XMM-Newton point-source catalogue for the XMM-LSS field. *MNRAS* 478, 2132–2163. doi:10.1093/mnras/sty1036

Civano, F., Hickox, R. C., Puccetti, S., Comastri, A., Mullaney, J. R., Zappacosta, L., et al. (2015). The nustar extragalactic surveys: overview and catalog from the COSMOS field. *ApJ* 808, 185. doi:10.1088/0004-637X/808/2/185

Civano, F., Marchesi, S., Comastri, A., Urry, M. C., Elvis, M., Cappelluti, N., et al. (2016). The Chandra cosmos legacy survey: overview and point source catalog. *ApJ* 819, 62. doi:10.3847/0004-637X/819/1/62

Comastri, A., Gilli, R., Marconi, A., Risaliti, G., and Salvati, M. (2015). Mass without radiation: heavily obscured AGNs, the X-ray background, and the black hole mass density. *A&A* 574, L10. doi:10.1051/0004-6361/201425496

Comastri, A., Setti, G., Zamorani, G., and Hasinger, G. (1995). The contribution of AGNs to the X-ray background. *A&A* 296, 1. doi:10.48550/arXiv.astro-ph/9409067

Dauser, T., Falkner, S., Lorenz, M., Kirsch, C., Peille, P., Cucchetti, E., et al. (2019). SIXTE: a generic X-ray instrument simulation toolkit. *A&A* 630, A66. doi:10.1051/0004-6361/201935978

Della Ceca, R., Castelli, G., Braito, V., Cagnoni, I., and Maccacaro, T. (1999). A medium survey of the hard X-ray sky with ASCA. II. The source's broadband X-ray spectral properties. *ApJ* 524, 674–683. doi:10.1086/307836

Eraerds, T., Antonelli, V., Davis, C., Hall, D., Hetherington, O., Holland, A., et al. (2021). Enhanced simulations on the athena/wide field imager instrumental background. *J. Astronomical Telesc. Instrum. Syst.* 7, 034001. doi:10.1117/1.JATIS.7.3.034001

Euclid Collaboration, Moneti, A., McCracken, H. J., Shuntov, M., Kauffmann, O. B., Capak, P., et al. (2022). Euclid preparation. XVII. Cosmic dawn survey: spitzer space telescope observations of the Euclid deep fields and calibration fields. *A&A* 658, A126. doi:10.1051/0004-6361/202142361

Gandhi, P., and Fabian, A. C. (2003). X-ray background synthesis: the infrared connection. *MNRAS* 339, 1095–1102. doi:10.1046/j.1365-8711.2003.06259.x

Gandhi, P., Fabian, A. C., Suebsuwong, T., Malzac, J., Miniutti, G., and Wilman, R. J. (2007). Constraints on light bending and reflection from the hard X-ray background. *MNRAS* 382, 1005–1018. doi:10.1111/j.1365-2966.2007.12462.x

Gehrels, N. (1986). Confidence limits for small numbers of events in astrophysical data. *ApJ* 303, 336. doi:10.1086/164079

Giacconi, R., Gursky, H., Paolini, F. R., and Rossi, B. B. (1962). Evidence for x rays from sources outside the solar system. *Phys. Rev. Lett.* 9, 439–443. doi:10.1103/PhysRevLett.9.439

Gilli, R., Comastri, A., and Hasinger, G. (2007). The synthesis of the cosmic X-ray background in the Chandra and XMM-Newton era. *A&A* 463, 79–96. doi:10.1051/0004-6361:20066334

Goulding, A. D., Greene, J. E., Setton, D. J., Labbe, I., Bezanson, R., Miller, T. B., et al. (2023). UNCOVER: the growth of the first massive black holes from JWST/NIRSpec-Spectroscopic redshift confirmation of an X-ray luminous AGN at z = 10.1. *ApJL* 955, L24. doi:10.3847/2041-8213/acf7c5

Harikane, Y., Zhang, Y., Nakajima, K., Ouchi, M., Isobe, Y., Ono, Y., et al. (2023). JWST/NIRSpec first census of broad-line AGNs at z=4-7: detection of 10 faint AGNs with M_BH106-107 M_sun and their host galaxy properties. arXiv. doi:10.48550/arXiv.2303.11946

Harrison, C. M. (2017). Impact of supermassive black hole growth on star formation. *Nat. Astron.* 1, 0165. doi:10.1038/s41550-017-0165

Harrison, F. A., Aird, J., Civano, F., Lansbury, G., Mullaney, J. R., Ballantyne, D. R., et al. (2016). The NuSTAR extragalactic surveys: the number counts of active galactic nuclei and the resolved fraction of the cosmic X-ray background. *ApJ* 831, 185. doi:10.3847/0004-637X/831/2/185

Harrison, F. A., Craig, W. W., Christensen, F. E., Hailey, C. J., Zhang, W. W., Boggs, S. E., et al. (2013). The nuclear spectroscopic telescope array (NuSTAR) high-energy X-ray mission. *ApJ* 770, 103. doi:10.1088/0004-637X/770/2/103

Hasinger, G., Miyaji, T., and Schmidt, M. (2005). Luminosity-dependent evolution of soft X-ray selected AGN. New Chandra and XMM-Newton surveys. *A&A* 441, 417–434. doi:10.1051/0004-6361:20042134

Hickox, R. (2024). PEARLS: NuSTAR and XMM-Newton extragalactic survey of the JWST North Ecliptic Pole time-domain field II. arXiv.

Hickox, R. C., and Markevitch, M. (2006). Absolute measurement of the unresolved cosmic X-ray background in the 0.5-8 keV band with Chandra. *ApJ* 645, 95–114. doi:10.1086/504070

Jansen, F., Lumb, D., Altieri, B., Clavel, J., Ehle, M., Erd, C., et al. (2001). XMM-Newton observatory. I. The spacecraft and operations. *A&A* 365, L1–L6. doi:10.1051/0004-6361:20000036

Kammoun, E., Lohfink, A. M., Masterson, M., Wilkins, D. R., Zhao, X., Baloković, M., et al. (2023). The High Energy X-ray Probe (HEX-P): probing the physics of the X-ray corona in active galactic nuclei. arXiv. doi:10.48550/arXiv.2311.04679

Kirkpatrick, A., Yang, G., Le Bail, A., Troiani, G., Bell, E. F., Cleri, N. J., et al. (2023). CEERS key paper VII: JWST/MIRI reveals a faint population of galaxies at cosmic noon unseen by spitzer. arXiv. doi:10.48550/arXiv.2308.09750

Kollmeier, J. A., Zasowski, G., Rix, H.-W., Johns, M., Anderson, S. F., Drory, N., et al. (2017). SDSS-V: pioneering panoptic spectroscopy. arXiv. doi:10.48550/arXiv.1711.03234

Lansbury, G. B., Alexander, D. M., Aird, J., Gandhi, P., Stern, D., Koss, M., et al. (2017a). The NuSTAR serendipitous survey: hunting for the most extreme obscured AGN at >10 keV. *ApJ* 846, 20. doi:10.3847/1538-4357/aa8176

Lansbury, G. B., Stern, D., Aird, J., Alexander, D. M., Fuentes, C., Harrison, F. A., et al. (2017b). TheNuSTARSerendipitous survey: the 40-month catalog and the properties of the distant high-energy x-ray source population. *Astrophysical J.* 836, 99. doi:10.3847/1538-4357/836/1/99

Lanzuisi, G., Civano, F., Marchesi, S., Comastri, A., Brusa, M., Gilli, R., et al. (2018). The Chandra COSMOS legacy survey: Compton thick AGN at high redshift. *MNRAS* 480, 2578–2592. doi:10.1093/mnras/sty2025

Luo, B., Brandt, W. N., Xue, Y. Q., Lehmer, B., Alexander, D. M., Bauer, F. E., et al. (2017). The Chandra deep field-south survey: 7 Ms source catalogs. *ApJS* 228, 2. doi:10.3847/1538-4365/228/1/2

Madsen, K. K., García, J. A., Stern, D., Armini, R., Basso, S., Coutinho, D., et al. (2023). The high energy X-ray probe (HEX-P): instrument and mission profile. arXiv. doi:10.48550/arXiv.2312.04678

Maiolino, R., Scholtz, J., Curtis-Lake, E., Carniani, S., Baker, W., de Graaff, A., et al. (2023a). JADES. The diverse population of infant Black Holes at 4<z<11: merging, tiny, poor, but mighty. arXiv. doi:10.48550/arXiv.2308.01230

Maiolino, R., Scholtz, J., Witstok, J., Carniani, S., D'Eugenio, F., de Graaff, A., et al. (2023b). A small and vigorous black hole in the early Universe. arXiv:2305.12492. doi:10.48550/arXiv.2305.12492

Marchesi, S., Ajello, M., Marcotulli, L., Comastri, A., Lanzuisi, G., and Vignali, C. (2018). Compton-thick AGNs in the NuSTAR era. *ApJ* 854, 49. doi:10.3847/1538-4357/aaa410

Marchesi, S., Ajello, M., Zhao, X., Comastri, A., La Parola, V., and Segreto, A. (2019). Compton-thick AGNs in the NuSTAR era. V. Joint NuSTAR and XMM-Newton spectral analysis of three "soft-gamma" candidate CT-AGNs in the swift/BAT 100-month catalog. *ApJ* 882, 162. doi:10.3847/1538-4357/ab340a

Marchesi, S., Civano, F., Elvis, M., Salvato, M., Brusa, M., Comastri, A., et al. (2016a). The Chandra COSMOS Legacy survey: optical/IR identifications. *ApJ* 817, 34. doi:10.3847/0004-637X/817/1/34

Marchesi, S., Gilli, R., Lanzuisi, G., Dauser, T., Ettori, S., Vito, F., et al. (2020). Mock catalogs for the extragalactic X-ray sky: simulating AGN surveys with ATHENA and with the AXIS probe. *A&A* 642, A184. doi:10.1051/0004-6361/202038622

Marchesi, S., Lanzuisi, G., Civano, F., Iwasawa, K., Suh, H., Comastri, A., et al. (2016b). The Chandra COSMOS-legacy survey: source X-ray spectral properties. *ApJ* 830, 100. doi:10.3847/0004-637X/830/2/100

Marchesi, S., Tremblay, L., Ajello, M., Marcotulli, L., Paggi, A., Cusumano, G., et al. (2017). Chandra and NuSTAR follow-up observations of swift-BAT-selected AGNs. *ApJ* 848, 53. doi:10.3847/1538-4357/aa8ee6

Marcotulli, L., Ajello, M., Böttcher, M., Coppi, P., Costamante, L., Di Gesu, L., et al. (2023). The High Energy X-ray Probe (HEX-P): the most powerful jets through the lens of a superb X-ray eye. arXiv. doi:10.48550/arXiv.2311.04801

Masini, A., Civano, F., Comastri, A., Fornasini, F., Ballantyne, D. R., Lansbury, G. B., et al. (2018a). The NuSTAR extragalactic surveys: source catalog and the compton-thick fraction in the UDS field. *ApJS* 235, 17. doi:10.3847/1538-4365/aaa83d

Masini, A., Comastri, A., Civano, F., Hickox, R. C., Carroll, C. M., Suh, H., et al. (2018b). The NuSTAR extragalactic surveys: unveiling rare, buried AGNs and detecting the contributors to the peak of the cosmic X-ray background. *ApJ* 867, 162. doi:10.3847/1538-4357/aae539

Mateos, S., Alonso-Herrero, A., Carrera, F. J., Blain, A., Severgnini, P., Caccianiga, A., et al. (2013). Uncovering obscured luminous AGN with WISE. *MNRAS* 434, 941–955. doi:10.1093/mnras/stt953

Meidinger, N., Albrecht, S., Beitler, C., Bonholzer, M., Emberger, V., Frank, J., et al. (2020). "Development status of the wide field imager instrument for Athena," in *Space Telescopes and Instrumentation 2020: Ultraviolet to Gamma Ray*. Editors J-W. A. den Herder, S. Nikzad, and K. Nakazawa (Society of Photo-Optical Instrumentation Engineers SPIE 11444), 114440T. Available at: https://ui.adsabs.harvard.edu/abs/2020SPIE11444E.0TM. doi:10.1117/12.2560507

Moretti, A., Campana, S., Lazzati, D., and Tagliaferri, G. (2003). The resolved fraction of the cosmic X-ray background. *ApJ* 588, 696–703. doi:10.1086/374335

Moretti, A., Vattakunnel, S., Tozzi, P., Salvaterra, R., Severgnini, P., Fugazza, D., et al. (2012). Spectrum of the unresolved cosmic X-ray background: what is unresolved 50 years after its discovery. *A&A* 548, A87. doi:10.1051/0004-6361/201219921

Mullaney, J. R., Del-Moro, A., Aird, J., Alexander, D. M., Civano, F. M., Hickox, R. C., et al. (2015). The NuSTAR extragalactic surveys: initial results and catalog from the extended Chandra deep field south. *ApJ* 808, 184. doi:10.1088/0004-637X/808/2/184

Mushotzky, R. F., Cowie, L. L., Barger, A. J., and Arnaud, K. A. (2000). Resolving the extragalactic hard X-ray background. *Nature* 404, 459–464. doi:10.1038/35006564

Nandra, K., Barret, D., Barcons, X., Fabian, A., den Herder, J.-W., Piro, L., et al. (2013). The hot and energetic universe: a white paper presenting the science theme motivating the Athena+ mission. arXiv. doi:10.48550/arXiv.1306.2307

National Academies of Sciences, Engineering, and Medicine (2021). *Pathways to discovery in astronomy and astrophysics for the 2020s*. Washington, DC: The National Academies Press. doi:10.17226/26141

Ni, Y., Di Matteo, T., Bird, S., Croft, R., Feng, Y., Chen, N., et al. (2022). The ASTRID simulation: the evolution of supermassive black holes. *MNRAS* 513, 670–692. doi:10.1093/mnras/stac351

Oh, K., Koss, M., Markwardt, C. B., Schawinski, K., Baumgartner, W. H., Barthelmy, S. D., et al. (2018). The 105-month swift-BAT all-sky hard x-ray survey. *Astrophysical J. Suppl. Ser.* 235, 4. doi:10.3847/1538-4365/aaa7fd

Padmanabhan, H., and Loeb, A. (2023). Constraining the AGN luminosity function from JWST with the X-ray Background. arXiv. doi:10.48550/arXiv.2310.08633

Park, T., Kashyap, V. L., Siemiginowska, A., van Dyk, D. A., Zezas, A., Heinke, C., et al. (2006). Bayesian estimation of hardness ratios: modeling and computations. *ApJ* 652, 610–628. doi:10.1086/507406

Peca, A., Cappelluti, N., Urry, C. M., LaMassa, S., Marchesi, S., Ananna, T. T., et al. (2023). On the cosmic evolution of AGN obscuration and the X-ray luminosity function: XMM-Newton and Chandra spectral analysis of the 31.3 deg^2 stripe 82X. *ApJ* 943, 162. doi:10.3847/1538-4357/acac28

Pfeifle, R. W., Boorman, P. G., Weaver, K. A., Buchner, J., Civano, F., Madsen, K., et al. (2023). The high energy X-ray probe (HEX-P): the future of hard X-ray dual AGN science. arXiv. doi:10.48550/arXiv.2311.05154

Piotrowska, J. M., García, J. A., Walton, D. J., Beckmann, R. S., Stern, D., Ballantyne, D. R., et al. (2023). The high energy X-ray probe (HEX-P): constraining supermassive black hole growth with population spin measurements. arXiv. doi:10.48550/arXiv.2311.04752

Ranalli, P., Comastri, A., and Setti, G. (2005). The X-ray luminosity function and number counts of spiral galaxies. *A&A* 440, 23–37. doi:10.1051/0004-6361:20042598

Ricci, C., Trakhtenbrot, B., Koss, M. J., Ueda, Y., Del Vecchio, I., Treister, E., et al. (2017). BAT AGN spectroscopic survey. V. X-ray properties of the swift/BAT 70-month AGN catalog. *ApJS* 233, 17. doi:10.3847/1538-4365/aa96ad

Ricci, C., Ueda, Y., Koss, M. J., Trakhtenbrot, B., Bauer, F. E., and Gandhi, P. (2015). Compton-thick accretion in the local universe. *ApJL* 815, L13. doi:10.1088/2041-8205/815/1/L13

Rossland, S., Wik, D. R., Grefenstette, B., Cappelluti, N., Civano, F., Gastaldello, F., et al. (2023). Measuring the cosmic X-ray background in 3-20 KeV with stray light from NuSTAR. *AJ* 166, 20. doi:10.3847/1538-3881/acd0ae

Scolnic, D. M., Lochner, M., Gris, P., Regnault, N., Hložek, R., Aldering, G., et al. (2018). Optimizing the LSST observing strategy for dark energy science: DESC recommendations for the deep drilling fields and other special programs. arXiv. doi:10.48550/arXiv.1812.00516

Silver, R., Torres-Albà, N., Zhao, X., Marchesi, S., Pizzetti, A., Cox, I., et al. (2023). A machine learning algorithm for reliably predicting active galactic nucleus absorbing column densities. *A&A* 675, A65. doi:10.1051/0004-6361/202345980

Stern, D., Assef, R. J., Benford, D. J., Blain, A., Cutri, R., Dey, A., et al. (2012). Mid-infrared selection of active galactic nuclei with the wide-field infrared survey explorer. I. Characterizing WISE-selected active galactic nuclei in COSMOS. *ApJ* 753, 30. doi:10.1088/0004-637X/753/1/30

Stern, D., Eisenhardt, P., Gorjian, V., Kochanek, C. S., Caldwell, N., Eisenstein, D., et al. (2005). Mid-infrared selection of active galaxies. *ApJ* 631, 163–168. doi:10.1086/432523

Stern, D., Lansbury, G. B., Assef, R. J., Brandt, W. N., Alexander, D. M., Ballantyne, D. R., et al. (2014). NuSTAR and XMM-Newton observations of luminous, heavily obscured, WISE-selected quasars at z ˜2. *ApJ* 794, 102. doi:10.1088/0004-637X/794/2/102

Torres-Albà, N., Marchesi, S., Zhao, X., Ajello, M., Silver, R., Ananna, T. T., et al. (2021). Compton-thick AGN in the NuSTAR era VI: the observed compton-thick fraction in the local universe. arXiv.

Tozzi, P., Rosati, P., Nonino, M., Bergeron, J., Borgani, S., Gilli, R., et al. (2001). New results from the X-ray and optical survey of the Chandra deep field-south: the 300 kilosecond exposure. II. *ApJ* 562, 42–51. doi:10.1086/322492

Treister, E., Urry, C. M., and Virani, S. (2009). The space density of compton-thick active galactic nucleus and the X-ray background. *ApJ* 696, 110–120. doi:10.1088/0004-637X/696/1/110

Troxel, M. A., Lin, C., Park, A., Hirata, C., Mandelbaum, R., Jarvis, M., et al. (2023). A joint Roman Space Telescope and Rubin Observatory synthetic wide-field imaging survey. *MNRAS* 522, 2801–2820. doi:10.1093/mnras/stad664

Ueda, Y., Akiyama, M., Hasinger, G., Miyaji, T., and Watson, M. G. (2014). Toward the standard population synthesis model of the X-ray background: evolution of X-ray luminosity and absorption functions of active galactic nuclei including compton-thick populations. *ApJ* 786, 104. doi:10.1088/0004-637X/786/2/104

Ueda, Y., Takahashi, T., Inoue, H., Tsuru, T., Sakano, M., Ishisaki, Y., et al. (1999). LOG N-log S relations and spectral properties of sources from the ASCA large sky survey: their implications for the origin of the cosmic X-ray background (CXB). *ApJ* 518, 656–671. doi:10.1086/307291

Vasudevan, R. V., Fabian, A. C., Reynolds, C. S., Aird, J., Dauser, T., and Gallo, L. C. (2016). A selection effect boosting the contribution from rapidly spinning black holes to the cosmic X-ray background. *MNRAS* 458, 2012–2023. doi:10.1093/mnras/stw363

Vito, F., Brandt, W. N., Yang, G., Gilli, R., Luo, B., Vignali, C., et al. (2018). High-redshift AGN in the Chandra Deep Fields: the obscured fraction and space density of the sub-L_* population. *MNRAS* 473, 2378–2406. doi:10.1093/mnras/stx2486

Vito, F., Gilli, R., Vignali, C., Comastri, A., Brusa, M., Cappelluti, N., et al. (2014). The hard X-ray luminosity function of high-redshift ($3 < z \leq 5$) active galactic nuclei. *MNRAS* 445, 3557–3574. doi:10.1093/mnras/stu2004

Worsley, M. A., Fabian, A. C., Bauer, F. E., Alexander, D. M., Hasinger, G., Mateos, S., et al. (2005). The unresolved hard X-ray background: the missing source population implied by the Chandra and XMM-Newton deep fields. *MNRAS* 357, 1281–1287. doi:10.1111/j.1365-2966.2005.08731.x

Xue, Y. Q., Wang, S. X., Brandt, W. N., Luo, B., Alexander, D. M., Bauer, F. E., et al. (2012). Tracking down the source population responsible for the unresolved cosmic 6-8 keV background. *ApJ* 758, 129. doi:10.1088/0004-637X/758/2/129

Yan, W., Brandt, W. N., Zou, F., Zhu, S., Chen, C.-T. J., Hickox, R. C., et al. (2023). The most obscured AGNs in the XMM-SERVS fields. *ApJ* 951, 27. doi:10.3847/1538-4357/accea6

Yan, W., Hickox, R. C., Hainline, K. N., Stern, D., Lansbury, G., Alexander, D. M., et al. (2019). NuSTAR and keck observations of heavily obscured quasars selected by WISE. *ApJ* 870, 33. doi:10.3847/1538-4357/aaeed4

Yung, L. Y. A., Somerville, R. S., Finkelstein, S. L., Behroozi, P., Davé, R., Ferguson, H. C., et al. (2023). Semi-analytic forecasts for Roman - the beginning of a new era of deep-wide galaxy surveys. *MNRAS* 519, 1578–1600. doi:10.1093/mnras/stac3595

Zappacosta, L., Comastri, A., Civano, F., Puccetti, S., Fiore, F., Aird, J., et al. (2018). The NuSTAR extragalactic surveys: X-ray spectroscopic analysis of the bright hard-band selected sample. *ApJ* 854, 33. doi:10.3847/1538-4357/aaa550

Zhao, X., Civano, F., Willmer, C. N. A., Bonoli, S., Chen, C.-T., Creech, S., et al. (2024). PEARLS: nuSTAR and XMM-Newton extragalactic survey of the JWST north ecliptic pole time-domain field II. *arXiv e-prints*, arXiv:2402.13508. doi:10.48550/arXiv.2402.13508

Zhao, X., Civano, F., Fornasini, F. M., Alexander, D. M., Cappelluti, N., Chen, C. T., et al. (2021). The NuSTAR extragalactic survey of the James webb space telescope North Ecliptic Pole time-domain field. *MNRAS* 508, 5176–5195. doi:10.1093/mnras/stab2885

frontiers | Frontiers in Astronomy and Space Sciences

TYPE Original Research
PUBLISHED 28 March 2024
DOI 10.3389/fspas.2024.1324796

Check for updates

OPEN ACCESS

EDITED BY
Renee Ludlam,
Wayne State University, United States

REVIEWED BY
Lijun Gou,
Chinese Academy of Sciences (CAS), China
Eilat Glikman,
Middlebury College, United States

*CORRESPONDENCE
J. M. Piotrowska,
joannapk@caltech.edu

†CITA National Fellow

RECEIVED 20 October 2023
ACCEPTED 16 February 2024
PUBLISHED 28 March 2024

CITATION
Piotrowska JM, García JA, Walton DJ, Beckmann RS, Stern D, Ballantyne DR, Wilkins DR, Bianchi S, Boorman PG, Buchner J, Chen C-T, Coppi P, Dauser T, Fabian AC, Kammoun E, Madsen K, Mallick L, Matt G, Matzeu G, Nardini E, Pizzetti A, Puccetti S, Ricci C, Tombesi F, Torres-Albà N and Wong K-W (2024), The high energy X-ray probe (HEX-P): constraining supermassive black hole growth with population spin measurements.
Front. Astron. Space Sci. 11:1324796.
doi: 10.3389/fspas.2024.1324796

COPYRIGHT
© 2024 Piotrowska, García, Walton, Beckmann, Stern, Ballantyne, Wilkins, Bianchi, Boorman, Buchner, Chen, Coppi, Dauser, Fabian, Kammoun, Madsen, Mallick, Matt, Matzeu, Nardini, Pizzetti, Puccetti, Ricci, Tombesi, Torres-Albà and Wong. This is an open-access article distributed under the terms of the Creative Commons Attribution License (CC BY). The use, distribution or reproduction in other forums is permitted, provided the original author(s) and the copyright owner(s) are credited and that the original publication in this journal is cited, in accordance with accepted academic practice. No use, distribution or reproduction is permitted which does not comply with these terms.

The high energy X-ray probe (HEX-P): constraining supermassive black hole growth with population spin measurements

J. M. Piotrowska[1]*, J. A. García[1,2], D. J. Walton[3], R. S. Beckmann[4], D. Stern[5], D. R. Ballantyne[6], D. R. Wilkins[7], S. Bianchi[8], P. G. Boorman[1], J. Buchner[9], C.-T. Chen[10,11], P. Coppi[12], T. Dauser[13], A. C. Fabian[4], E. Kammoun[8,14,15], K. Madsen[2], L. Mallick[1,16,17†], G. Matt[8], G. Matzeu[18], E. Nardini[15], A. Pizzetti[19], S. Puccetti[20], C. Ricci[21,22], F. Tombesi[2,23,24,25,26], N. Torres-Albà[19] and K.-W. Wong[27], on behalf of the HEX-P Collaboration

[1]Cahill Center for Astronomy and Astrophysics, California Institute of Technology, Pasadena, CA, United States, [2]X-ray Astrophysics Laboratory, NASA Goddard Space Flight Center, Greenbelt, MD, United States, [3]Centre for Astrophysics Research, University of Hertfordshire, Hatfield, United Kingdom, [4]Institute of Astronomy, University of Cambridge, Cambridge, United Kingdom, [5]Jet Propulsion Laboratory, California Institute of Technology, Pasadena, CA, United States, [6]Center for Relativistic Astrophysics, School of Physics, Georgia Institute of Technology, Atlanta, GA, United States, [7]Kavli Institute for Particle Astrophysics and Cosmology, Stanford University, Stanford, CA, United States, [8]Dipartimento di Matematica e Fisica, Università Roma Tre, Rome, Italy, [9]Max-Planck-Institut für Extraterrestrische Physik (MPE), Garching, Germany, [10]Marshall Space Flight Center, Huntsville, AL, United States, [11]Science and Technology Institute, Universities Space Research Association, Huntsville, AL, United States, [12]Department of Astronomy, Yale University, New Haven, CT, United States, [13]Dr Karl Remeis-Observatory and Erlangen Centre for Astroparticle Physics, FAU Erlangen-Nürnberg, Bamberg, Germany, [14]UMR5277 Institut de Recherche en Astrophysique et Planétologie (IRAP), Toulouse, France, [15]INAF–Osservatorio Astrofisico di Arcetri, Firenze, Italy, [16]University of Manitoba, Department of Physics and Astronomy, Winnipeg, MB, Canada, [17]Canadian Institute for Theoretical Astrophysics, University of Toronto, Toronto, ON, Canada, [18]Quasar Science Resources SL for ESA, European Space Astronomy Centre, Science Operations Department, Madrid, Spain, [19]Department of Physics and Astronomy, Clemson University, Kinard Lab of Physics, Clemson, SC, United States, [20]ASI–Agenzia Spaziale Italiana, Rome, Italy, [21]Instituto de Estudios Astrofísicos, Facultad de Ingeniería y Ciencias, Universidad Diego Portales, Santiago, Chile, [22]Kavli Institute for Astronomy and Astrophysics, Peking University, Beijing, China, [23]Physics Department, Tor Vergata University of Rome, Rome, Italy, [24]INAF–Astronomical Observatory of Rome, Rome, Italy, [25]INFN–Rome Tor Vergata, Rome, Italy, [26]Department of Astronomy, University of Maryland, College Park, MD, United States, [27]Department of Physics, SUNY Brockport, Brockport, NY, United States

Constraining the primary growth channel of supermassive black holes (SMBHs) remains one the most actively debated questions in the context of cosmological structure formation. Owing to the expected connection between SMBH spin parameter evolution and the accretion and merger history of individual black holes, population spin measurements offer a rare observational window into the cosmic growth of SMBHs. As of today, the most common method for estimating SMBH spin relies on modeling the relativistically broaden atomic profiles in the reflection spectrum observed in X-rays. In this paper, we study the observational requirements needed to confidently distinguish between the primary SMBH growth channels based on their distinct spin-mass distributions predicted by the

Horizon-AGN cosmological simulation. Indoing so, we characterize outstanding limitations associated with the existing measurements and discuss the landscape of future observational campaigns which could be planned and executed with future X-ray observatories. We focus our attention on the *High-Energy X-ray Probe (HEX-P)*, a proposed probe-class mission designed to serve the high-energy community in the 2030s.

KEYWORDS

supermassive black holes, AGN, black hole growth, black hole spin, future X-ray observatories

1 Introduction

As of today, the existence of supermassive black holes (SMBHs) residing in the nuclei of galaxies is no longer a subject of scientific dispute. With the presence of an SMBH clearly revealed in the orbital motion of stars in our Galactic center (e.g., Ghez et al., 2008; Genzel et al., 2010) and direct imaging of matter just outside the Event Horizon (Event Horizon Telescope Collaboration et al., 2019; Event Horizon Telescope Collaboration et al., 2022), the focus has now shifted towards understanding the origin and growth of these extreme astrophysical objects with masses above $\gtrsim 10^6 M_\odot$. Decades of extragalactic observations have demonstrated a tight connection between the properties of SMBHs and their galactic hosts, now interpreted as black hole-galaxy co-evolution across cosmic time (see Kormendy and Ho, 2013, for a review). More specifically, SMBHs have been established as key players in shaping galaxy formation, structure and, most of all, in suppressing galactic star formation through a range of highly energetic processes collectively referred to as active galactic nucleus (AGN) feedback (e.g., McNamara et al., 2000; Bower et al., 2006; Terrazas et al., 2016; Henriques et al., 2019; Piotrowska et al., 2022).

Regardless of its exact mode of operation, AGN feedback relies on extracting power from the immediate surroundings of supermassive black holes via accretion. The amount of energy released in the process greatly exceeds the threshold required to offset cooling around galaxies or to unbind baryons within them, rendering SMBHs a formidable source of power capable of affecting their galactic hosts (see Fabian, 2012; Werner et al., 2019, for in-depth reviews). At high accretion rates ($\dot{M}_{\rm BH} \gtrsim 0.01 \dot{M}_{\rm Edd}$, the Eddington accretion rate[1]), matter surrounding an SMBH is thought to infall through a geometrically thin, optically thick accretion disk (Novikov and Thorne, 1973; Shakura and Sunyaev, 1973) in which emitted radiation drives high-velocity *quasar* outflows (e.g., Murray et al., 1995; King et al., 2008; Faucher-Giguère and Quataert, 2012) coupling to the interstellar medium (ISM) and further accelerating it at galaxy-wide scales (e.g., Feruglio et al., 2010; Hopkins and Quataert, 2010; Villar-Martín et al., 2011; Maiolino et al., 2012; Cicone et al., 2014; Fiore et al., 2017). At low accretion rates $\lesssim 10^{-6}\ \dot{M}_{\rm Edd}$, the inflow forms a geometrically thick, optically thin accretion disk (e.g., Yuan and Narayan, 2014; Giustini and Proga, 2019) and launches *relativistic jets* which deposit energy within the circumgalactic medium (CGM) at large distances away from the galactic host (e.g., McNamara et al., 2000; Bîrzan et al., 2004; Hlavacek-Larrondo et al., 2012; 2015; Werner et al., 2019). Across all flavors of AGN feedback processes, the efficiency with which power is extracted from the accretion flow depends on the angular momentum of the SMBH and spans over an order of magnitude in range (e.g., Thorne, 1974; Penna et al., 2010; Avara et al., 2016; Liska et al., 2019), further broadening the range of impact AGN can have on their host galaxies.

Although abundant observational evidence exists for the impact of SMBHs on their surrounding galaxies, relatively little is known about their origins and growth across cosmic time. Understanding how these black holes form and reach their impressive masses is particularly important both in the context of galaxy evolution and recent *James Webb Space Telescope* (*JWST*, Gardner et al., 2023; Rigby et al., 2023) observations, which report black holes with masses $M_{\rm BH} > 10^6 M_\odot$ as early as $z = 10.6$ (Harikane et al., 2023; Maiolino et al., 2023a; Maiolino et al., 2023b). Since cosmic growth via accretion of gas and SMBH-SMBH mergers occurs on timescales beyond direct human observation, one would, ideally, like to characterize SMBH growth histories using alternative observables. An example of such a proxy is black hole angular momentum, $\vec{J}$, which changes its orientation and magnitude in response to the different physical processes that increase $M_{\rm BH}$. Hence, by *measuring the magnitude of SMBH angular momentum J*, usually expressed in terms of the dimensionless spin parameter ($a^* \equiv Jc/GM_{\rm BH}^2$, where c is the speed of light and G is the gravitational constant), *one can extract information about the past record of its growth.* In AGN, spin parameter can be estimated by modelling coronal X-ray radiation reprocessed (or "reflected") by the accretion disk (e.g., Fabian et al., 1989; Laor, 1991). Because the reflected signal depends on the position of the innermost edge of the accretion disk, this relationship can be directly applied to determine $a*$ in nearby SMBHs (see Section 3.2 for an overview of this approach).

As the black hole increases its mass via accretion of surrounding material, its spin changes owing to angular momentum transfer from the accretion flow. If the accreting material settles into a prograde[2] disk, inflow of angular momentum aligned with that of the black hole leads to its efficient spin-up (Bardeen, 1970; Moderski and

1 Accretion rate associated with Eddington luminosity, $L_{\rm Edd}$ at which outward radiation pressure balances the gravitational force outside a massive body with mass M, given by $L_{\rm Edd} = 4\pi GMc/\kappa$, where κ is the opacity of the accreting material, G the gravitational constant and c the speed of light.

2 In a prograde disk, the accreting material and the black hole are both rotating in the same direction.

Sikora, 1996; Moderski et al., 1998). In contrast, chaotic accretion of matter with randomly oriented angular momentum decreases the spin magnitude, ultimately driving it towards $a* \sim 0$ over sufficiently long times (e.g., Berti and Volonteri, 2008; King et al., 2008; Dotti et al., 2013). In the presence of magnetic fields, even in the case of ordered inflow through aligned accretion disks, spin can also be reduced by energy extraction via the Blandford-Znajek process (Blandford and Znajek, 1977). This jet launching mechanism has been shown to drain black hole angular momentum in magnetically arrested disks (MADs) in General-Relativistic magneto-hydrodynamical (GRMHD) simulations of SMBH accretion (e.g., Tchekhovskoy et al., 2011; McKinney et al., 2012; Tchekhovskoy et al., 2012; Narayan et al., 2022; Curd and Narayan, 2023; Lowell et al., 2023). Finally, mergers of SMBH binaries leave behind remnants which can be either spun up or down with respect to their progenitors, contingent on individual spin parameters upon coalescence (e.g., Kesden, 2008; Rezzolla et al., 2008; Tichy and Marronetti, 2008; Barausse and Rezzolla, 2009; Healy et al., 2014; Hofmann et al., 2016).

Depending on the relative contribution of these processes across cosmic time, one would expect different growth histories of SMBHs to leave an imprint on the measured spin parameter. In the cosmological context, this expectation was first explored in semi-analytic models (SAMs) - taking advantage of their low computational cost, several studies have now used SAMs to make spin population predictions for different SMBH accretion and coalescence scenarios. Berti and Volonteri (2008) demonstrated that prolonged episodes of coherent accretion produce SMBH populations spinning at near-maximal rates, while chaotic infall of matter and mergers force the dimensionless spin parameter towards $a* \sim 0$. Dotti et al. (2013) generalized the chaotic accretion paradigm and found that SMBHs are not spun down efficiently when the distribution of accreted angular momenta is not isotropic, allowing black holes to maintain stable high spin values for even modest degrees of anisotropy. By linking the orientation of accreted angular momentum with that of the galactic host, Sesana et al. (2014) further showed that the spin parameter critically depends on the dynamics of the host and that SMBHs residing in spiral galaxies tend to spin fast, biasing the observable samples towards high $a*$ values.

Moving beyond the idealized semi-analytic approach, spin parameter modelling in hydrodynamical cosmological simulations only recently became an area of active development (Dubois et al., 2014c; Fiacconi et al., 2018; Bustamante and Springel, 2019; Talbot et al., 2021; Talbot et al., 2022). As of today, there exist three major simulation suites which trace spin parameter in statistical samples of SMBHs: the *NewHorizon cosmological simulation* (Dubois et al., 2021), on-the-fly[3] spin evolution coupled to AGN feedback prescription in a $(16Mpc)^3$ volume, simulated down to $z = 0.25$ at a maximum spatial resolution of 34 pc; the Bustamante and Springel (2019) *simulation suite*, on-the-fly spin evolution implemented in the moving-mesh code AREPO (Springel, 2010), with a cosmological volume of $(\sim 37Mpc)^3$ and a spatial resolution of ~1 kpc, which is evolved to $z = 0$ with the IllustrisTNG AGN feedback model (Weinberger et al., 2017); and the *Horizon-AGN cosmological simulation* (Dubois et al., 2014b), in which spin evolution is computed via post-processing of the completed Horizon-AGN run Dubois et al., 2014a, followed down to $z = 0$ in a $(\sim 147Mpc)^3$ volume at maximum spatial resolution of $\sim 1kpc$. All three suites produce realistic populations of SMBHs and yield $a*$ population statistics compatible with those observed in the local Universe. With limited sample sizes and generous uncertainty on individual measurements, currently available observations are not constraining enough to indicate preference for any particular model. In the future, increased measurement precision and improved statistics in the $M_{\rm BH} - a*$ plane will be of critical importance for new generations of spin evolution models: with improved calibration targets for subgrid prescriptions, different hydrodynamical cosmological models are likely to further converge over time, allowing us to use $a*$ constraints as an interpretative tool, as opposed to a means of discriminating among modelling approaches.

In this study, we show how future observing programs targeting statistical samples of SMBH spins and masses can be designed to best discriminate between different growth histories of SMBHs. We choose to focus on the Horizon-AGN cosmological simulation to take advantage of its SMBH statistics delivered over a large simulation volume. Treating the simulation suite as a case study, we determine sample sizes and measurement precisions required to differentiate between accretion- and merger-dominated SMBH growth. We then discuss these requirements in the context of the *High-Energy X-ray Probe* (*HEX-P*; Madsen et al. 2023)–a probe-class mission concept which offers sensitive broad-band X-ray coverage (0.2–80 keV) with exceptional spectral, timing and angular capabilities, featuring a High Energy Telescope (HET) that focuses hard X-rays, and a low energy telescope (LET) that focuses low-energy X-rays. Taking into account the *HEX-P* instrument design, we demonstrate the potential for this mission to deliver SMBH spin parameter measurements sufficient to constrain SMBH growth scenarios.

In Section 2 we discuss the challenges associated with spin modelling in cosmological hydrodynamical simulations and briefly describe the Horizon-AGN suite. Section 3 provides an overview of reflection spectroscopy as a tool for measuring $a*$, followed by a discussion on current constraints and their comparison with the Horizon-AGN cosmological model in Section 4. Section 5 motivates a systematic study of the $M_{\rm BH} - a*$ plane with future observing programs, and Section 6 describes a sample of AGN selected from the BAT AGN Spectroscopic Survey appropriate for such a study. In Section 7 we determine minimum sample requirements for differentiating between accretion- and merger-dominated SMBH growth, followed by *HEX-P* spin parameter recovery simulations in Section 8. In Section 9 we demonstrate the potential for *HEX-P* to characterize SMBH growth histories through population spin measurements and present our final remarks in Section 10.

2 SMBH spin in cosmological hydrodynamical simulations

Tracing the change in SMBH spin in the context of large-scale evolution of the Universe is a complex problem spanning a broad range of spatial and temporal scales. Transfer of angular momentum via accretion in disks occurs on size scales between ~1 and a

3 The term *on-the-fly* refers to a spin calculation explicitly included at runtime within the simulation, as opposed to in post-processing after the simulation run is completed.

few 10^2 gravitational radii $R_G = GM_{\rm BH}/c^2$ (e.g., Fausnaugh et al., 2016; Jiang et al., 2017; Cackett et al., 2018; Edelson et al., 2019; Guo et al., 2022; Homayouni et al., 2022), which then couples to gas inflows from the host galaxy on scales of several hundred pc (e.g., García-Burillo et al., 2005; Hopkins and Quataert, 2010; Wong et al., 2011; Wong et al., 2014; Alexander and Hickox, 2012; Russell et al., 2015; Russell et al., 2018), ultimately fuelled by gas accretion from within the cosmic web on the intergalactic scales of hundreds of kpc (e.g., Sancisi et al., 2008; Putman et al., 2012; Tumlinson et al., 2017). At the same time, gas flows at all scales are affected by the non-trivial interplay of feedback processes from both stars (e.g., Katz et al., 1996; Cole et al., 2000; Kereš et al., 2005; Hopkins et al., 2014) and AGN (e.g., Bower et al., 2006; Croton et al., 2006; Fabian, 2012; Kormendy and Ho, 2013), disk instabilities (e.g., Schwarz, 1981; Athanassoula et al., 1983; Kuijken and Merrifield, 1995; Debattista et al., 2006) and galaxy-galaxy interactions (e.g., Toomre and Toomre, 1972; Sanders et al., 1988; Barnes and Hernquist, 1992; Di Matteo et al., 2005; Springel et al., 2005; Hopkins et al., 2006) all of which, ideally, need to be taken into account in a comprehensive modelling of SMBH spin evolution. The dynamic range in size scales alone renders it computationally unfeasible to directly follow SMBH evolution, even with current state-of-the-art hardware and numerical methods (see Vogelsberger et al., 2020; Crain and van de Voort, 2023, for reviews of the current state of the field). Hence, to overcome these limitations, cosmological simulations replace missing baryonic physics with *subgrid*[4] prescriptions—semi-analytic models relying on astrophysical scaling relations to predict large scale hydrodynamic effects of unresolved AGN accretion, spin evolution and feedback.

There currently exist three cosmological hydrodynamical simulations which either model spin on-the-fly (Bustamante and Springel, 2019; Dubois et al., 2021) or calculate its evolution in post-processing (Dubois et al., 2014b) (see Section 1). Although these three studies differ significantly in their subgrid prescriptions, in addition to spanning different cosmological volumes and final simulation redshifts, they all deliver SMBH spin distributions broadly consistent with the currently available observational constraints. As spin modelling in a full cosmological context is still in its infancy, the agreement between both models themselves and with the observable Universe is likely to improve once better constraints are available for subgrid parameter tuning. Thus, the study presented here does not focus on differentiating among currently available models, but rather on demonstrating the capability of *HEX-P* to identify different SMBH growth channels within a single realization of a sophisticated full-physics model of the Universe.

2.1 Horizon-AGN cosmological model

In our study we make use of the Horizon-AGN cosmological simulation (Dubois et al., 2014a), post-processed to trace SMBH spin evolution in response to local hydrodynamics of gas, accretion and SMBH mergers (Dubois et al., 2014b). Our choice of the simulation suite is motivated by its large volume of $(\sim 100{\rm cMpc})^3$, generous statistics and great success in reproducing realistic SMBH and galaxy samples across cosmic time (Dubois et al., 2016; Volonteri et al., 2016; Beckmann et al., 2017; Kaviraj et al., 2017). Most importantly, however, accretion-dominated and accretion + merger growth histories of SMBHs in Horizon-AGN have been shown to result in distinct spin parameter distributions (Beckmann et al., 2023), hence the suite offers a promising opportunity for studying the SMBH growth signal with *HEX-P* reflection spectroscopy. The full Horizon-AGN suite, including its spin parameter evolution model, are described in detail in Dubois et al. (2014a) and Dubois et al. (2014b); here we only provide a brief overview of SMBH treatment in the simulation.

Horizon-AGN is a suite of cosmological, hydrodynamical simulations performed with the RAMSES code (Teyssier, 2002) for ΛCDM cosmology with cosmological parameter values based on WMAP-7 observations ($H_0 = 70.4{\rm kms}^{-1}Mpc^{-1}$, $\Omega_m = 0.272$, $\Omega_b = 0.045$, $\Omega_\Lambda = 0.728$ and $\sigma_8 = 0.81$; Komatsu et al., 2011). The hydrodynamics are computed on an adaptively refined Cartesian grid coupled to subgrid prescriptions for baryonic interactions, including gas cooling, star formation, black hole accretion and feedback processes described in detail in Dubois et al. (2014a). The simulation only includes black holes of the supermassive kind, seeding them in $z > 1.5$ gas cells once these exceed a star formation threshold of $n_0 = 0.1{\rm H}cm^{-1}$ in density. Once seeded, the SMBHs then accrete via a boosted Bondi-Hoyle-Lyttleton prescription ($\dot{M}_{\rm BH} = 4\pi\alpha G^2 M_{\rm BH}^2\bar{\rho}/(\bar{c}_s^2 + \bar{u}^2)^{3/2}$, where $\bar{u}$, $\bar{\rho}$ and $\bar{c}_s$ are gas velocity, density and speed of sound averaged in the SMBH vicinity, and G is the gravitational constant; Hoyle and Lyttleton, 1939; Bondi and Hoyle, 1944; Bondi, 1952) capped at the Eddington rate. A fraction $\epsilon_r = 0.1$ of the accreted rest-mass energy is then released as AGN feedback with $\dot{E}_{\rm AGN} = \epsilon_r \dot{M}_{\rm BH} c^2$, and the fraction of power coupled to gas is controlled by the accretion rate-dependent feedback mode. For Eddington ratios $f_{\rm Edd} \equiv \dot{M}_{\rm BH}/\dot{M}_{\rm Edd} > 0.01$, the AGN is in the "quasar" mode and isotropically injects 0.15 $\dot{E}_{\rm BH}$ as thermal energy around the SMBH particle. For $f_{\rm Edd} < 0.01$ the AGN switches to "radio" mode feedback, releasing all $\dot{E}_{\rm BH}$ in biconical outflows. In a post-processing procedure introduced in Dubois et al. (2014b), SMBH are assumed to begin with a spin of $a* = 0$, which subsequently evolves in response to accretion of gas from the hydrodynamical grid and SMBH-SMBH mergers across cosmic time. The spin evolution model combines semi-analytic considerations and calibrations extracted from GRMHD simulations to model the two phenomena, including spin evolution in misaligned disks via the Bardeen-Peterson effect. The prescription, however, does not model SMBH spin-down due to jets via the Blandford-Znajek mechanism.

3 Observations of black holes

Astrophysical black holes are unique objects of great interest as they represent the ultimate test of General Relativity as a theory for gravity. Despite their exotic phenomenology, black holes are also objects of outstanding simplicity; owing to the no-hair theorem (Israel, 1967; Israel, 1968; Carter, 1971), they are fully described by only three physical quantities: mass, angular momentum (or spin),

4 Capturing physics at scales smaller than those allowed by numerical resolution via semi-analytic prescriptions coupled to quantities directly resolved in the simulation. See Vogelsberger et al. (2020) and Crain and van de Voort (2023) for comprehensive reviews of the methodology.

and electric charge. Furthermore, charge is quickly neutralized in any realistic astrophysical environment (Michel, 1972; Wald, 1984; Novikov and Frolov, 1989; Treves and Turolla, 1999; Bambi, 2017), leaving just mass and spin as the fundamental parameters to be constrained by observations.

3.1 Mass

Of the two properties describing a black hole, mass is likely the most straightforward to measure (both for stellar mass black holes and SMBHs). Indeed, a range of techniques has now been developed for SMBH mass estimation, appropriate for both local and distant sources. For a relatively nearby system (such as the SMBH in the center of our Galaxy), it is possible to resolve the motion of individual stars and model the underlying gravitational potential to estimate its associated black hole mass (e.g., Ghez et al., 1998; Ghez et al., 2008; Genzel et al., 2010; Gravity Collaboration et al., 2018). Owing to extremely high resolution requirements, such studies can only be undertaken within the Milky Way, while extragalactic $M_{\rm BH}$ measurements are instead forced to rely on stellar, gas and maser kinematics (e.g., Kormendy et al., 1998; Magorrian et al., 1998; Gebhardt et al., 2000).

One of the most robust methods for measuring $M_{\rm BH}$ for active SMBHs in other galaxies involves reverberation mapping of broad emission lines (Blandford and McKee, 1982; Peterson, 1993). In this approach, the velocity dispersion of gas in the broad line region (BLR) is combined with a measurement of the time delay between variations in the continuum and the line emission to infer the dynamics of the accretion disks (see, e.g., Peterson et al., 2004, for a description of the methodology). The mass estimate relies on the proportionality[5] $M_{\rm BH} \propto R_{\rm BLR}(\Delta V)^2$ between SMBH mass, the line-of-sight velocity of BLR gas (ΔV, encoded in emission line profiles) and the distance between the black hole and the BLR ($R_{\rm BLR}$, inferred from the time lag measurement). Since observations of this kind require monitoring over long times at prime facilities, the current sample of SMBH masses measured via reverberation contains only ~100 objects in total (e.g., Woo et al., 2015).

Because of the limited number of direct SMBH mass measurements, statistical studies commonly rely on empirical calibrations to estimate $M_{\rm BH}$. A common alternative to the expensive reverberation mapping observations combines continuum luminosity measurements and BLR emission line width to estimate $M_{\rm BH}$. Known as the "single-epoch virial BH mass estimator", the method relies on a tight relation between continuum (or line) luminosity and $R_{\rm BLR}$ observed among the reverberation mapping targets, providing a calibrated estimator without the need for a time-lag measurement in each source (see Shen, 2013, for an in-depth review of the method and its limitations). Owing to a broad similarity in continuum and emission line strength among quasars, this method has been successfully applied in estimating $M_{\rm BH}$ in various quasar samples at both low and high redshift, using observations in X-ray, rest-frame UV and optical wavelengths (e.g., Vestergaard, 2002; Greene and Ho, 2005; Wang et al., 2009; Trakhtenbrot and Netzer, 2012).

Absent necessary nuclear emission lines, another common flavor of empirical calibrations makes use of the measured properties of SMBH galactic hosts to estimate their mass. Among these, the relationship between stellar velocity dispersion in the galactic bulge and SMBH mass measured via reverberation mapping, the $M_{\rm BH} - \sigma*$ relation, boasts the least scatter, yielding a systematic uncertainty of $\sim 0.3 - 0.5$ dex in $\log(M_{\rm BH})$ (Ferrarese and Merritt, 2000; Hopkins et al., 2011; McConnell and Ma, 2013; Saglia et al., 2016). Although subject to significant scatter at present, these calibrations will improve with the arrival of future large multi-epoch observation programs like the Black Hole Mapper (Kollmeier et al., 2019). The planned ~1000 optical reverberation mapping $M_{\rm BH}$ estimates will significantly increase the robustness and precision of the $M_{\rm BH} - \sigma*$ estimation. Other techniques have also been recently proposed to measure $M_{\rm BH}$ using X-ray variability, such as X-ray reverberation (Alston et al., 2020) and X-ray spectral-timing (Ponti et al., 2012; Ingram et al., 2022), both of which can be model dependent and carry systematic uncertainties that still need to be understood.

3.2 Spin

The estimation of black hole spin, on the other hand, is a more difficult task as it mainly impacts the environment extremely close to the black hole. For example, the black hole's angular momentum determines the radius of the innermost stable circular orbit, ISCO ($R_{\rm ISCO}$, which varies from 9 $R_{\rm G}$ for a maximal retrograde spin to ~1.2 $R_{\rm G}$ for a maximal prograde spin of $a* = 0.998$, where $R_{\rm G} = GM_{\rm BH}/c^2$ is the gravitational radius; Bardeen et al., 1972; Thorne, 1974). In principle, the spin of a black hole can be constrained through a variety of methods, most of which involve determining $R_{\rm ISCO}$, but for AGN the most reliable method currently available comes via characterization of relativistic reflection from the innermost accretion disk (sometimes referred to as the iron-line method; see Reynolds 2021for a recent review).

For moderately high accretion rates, most of the infalling material is expected to flow through a thin, optically-thick accretion disk (Shakura and Sunyaev, 1973). Some of the thermal emission from the disk, which peaks in the UV for most AGN, is Compton up-scattered into a much higher energy continuum by a "corona" of hot electrons ($kT_{\rm e} \sim 100$ keV; Fabian et al., 2015; Baloković et al., 2020), which is the primary source of X-ray emission in AGN[6]. This X-ray emission re-irradiates the surface of the disk, producing a further "reflected" emission component that contains a diverse range of atomic spectral features both in emission and absorption. Among these, the inner-shell transitions from Fe ions—predominantly the Kα emission line at 6.4–6.97 keV (depending on the ionization state)—together with a strong absorption K-edge around 7–8 keV, are typically the most prominent. Additionally, reflection spectra exhibit a characteristic high-energy continuum, peaking at ~30 keV, often referred to as the "Compton hump" (George and Fabian,

5 The proportionality constant, known as the virial factor, is challenging to determine for individual objects owing to the unknown geometry of the BLR gas (e.g., Brewer et al., 2011; Pancoast et al., 2014).

6 The precise nature of the corona is still poorly understood, but is also an area of AGN physics that *HEX-P* will help uncover (Kammoun et al. 2023).

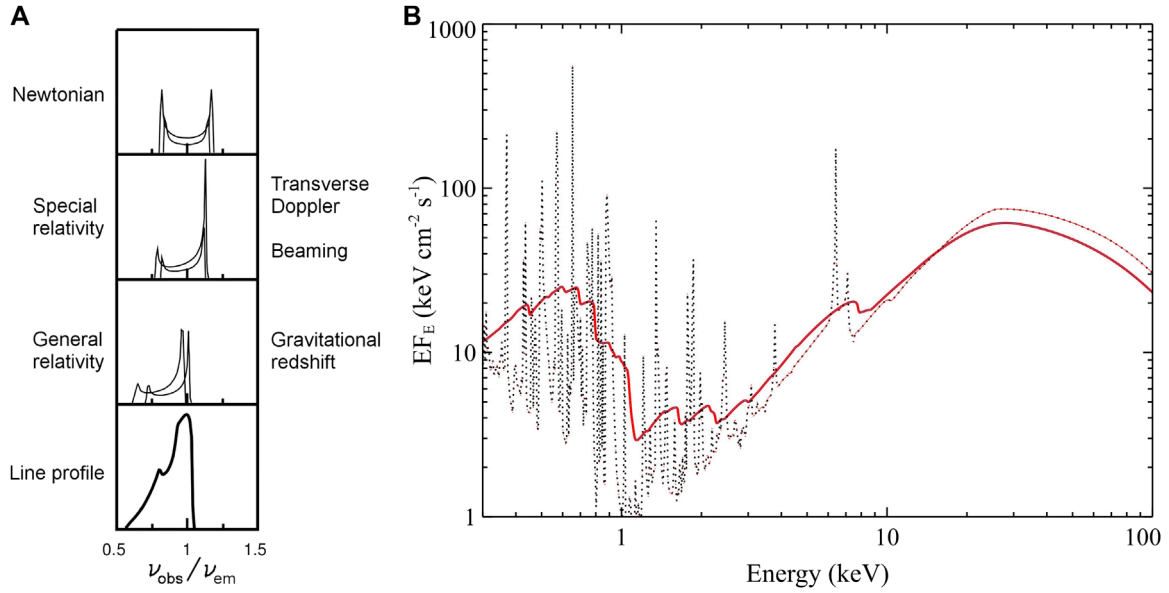

FIGURE 1
(A): The broadening experienced by a narrow emission line from an accretion disk around a black hole (from Fabian et al., 2000). The top three panels show the effects of Newtonian gravity, Special Relativity and General Relativity, respectively, on the line profiles for two example radii within the disk, while the bottom panel shows the broadened and skewed "diskline" profile expected when these combined effects are integrated over the full radial profile of the disk. **(B)**: An example of these relativistic effects applied to a typical reflection spectrum from moderately ionized material (as may be expected for the accretion disk in an AGN). Here we use the XILLVER reflection model for the rest-frame reflection spectrum (dotted line; García and Kallman, 2010) and apply the relativistic blurring with the RELCONV model (solid line; Dauser et al., 2010).

1991; Ross and Fabian, 2005; García and Kallman, 2010). Although the emission lines are narrow in the frame of the disk, by the time the material in the disk approaches the ISCO it is orbiting at relativistic speeds, and the gravitational redshift is also very strong. The combination of these effects serves to broaden and skew the emission lines from our perspective as a distant, external observer, resulting in a characteristic "diskline" emission profile (Fabian et al., 1989; Laor, 1991; Brenneman and Reynolds, 2006; Dauser et al., 2010; see Figure 1). Provided that the disk extends all the way into the ISCO orbit, also expected at moderately high accretion rates, then characterizing the relativistic blurring gives a measurement of $R_{\rm ISCO}$, and thus of $a*$. These distortions are most often discussed in the context of the iron emission line specifically, as it is typically the strongest spectroscopically isolated emission line in the reflection spectrum. While the iron emission provides the cleanest view of the broadened line profile, these relativistic effects impact the whole reflection spectrum (see Figure 1).

This approach to measuring spin is particularly powerful as it can be applied to black holes of all masses, not just the SMBHs powering AGN (e.g., Walton et al., 2012). Indeed, relativistically broadened Fe K lines have been observed in the spectra of a large fraction of AGN with high signal-to-noise (S/N) X-ray spectra (e.g., Tanaka et al., 1995; Miniutti et al., 2007; Fabian et al., 2009; de La Calle Pérez et al., 2010; Brenneman et al., 2011; Gallo et al., 2011; Nardini et al., 2011; Parker et al., 2014; Ricci et al., 2014; Wilkins et al., 2015; Jiang et al., 2018; Walton et al., 2019) as well as most well-studied black hole X-ray binaries (e.g., Miniutti et al., 2004; Miller et al., 2009; Reis et al., 2009; Duro et al., 2011; King et al., 2014; García et al., 2015; Walton et al., 2017; Xu et al., 2018; Kara et al., 2019; Tao et al., 2019; Jiang et al., 2022; Draghis et al., 2023; see also Connors et al. (2023) for additional discussion of black hole X-ray binary studies with *HEX-P*). Broadband X-ray spectroscopy is particularly critical for properly characterizing the reflected emission: its key features span the entire observable X-ray band (a diverse set of emission lines from lighter elements at energies $\lesssim 2keV$, the iron emission line at ~6–7 keV and the Compton hump at ~30 keV) and their proper modelling requires an accurate characterization of the continuum across the entire broadband range. The *NuSTAR* era has therefore marked a period of exciting progress in this field, finally providing high S/N spectroscopy up to ~80 keV for AGN. *NuSTAR* observations have unambiguously revealed the high-energy reflected continuum associated with the broad iron emission, and have been particularly powerful when paired with simultaneous lower-energy coverage from, e.g., *XMM-Newton*, confirming our ability to measure spin via reflection spectroscopy (e.g., Risaliti et al., 2013; Marinucci et al., 2014; Walton et al., 2014; Buisson et al., 2018; García et al., 2019; Chamani et al., 2020; Wilkins et al., 2022). As we further show in Section 4, however, these currently available samples are still insufficient to characterize modelled SMBH growth histories in the observable Universe.

4 Current constraints: The spin–mass plane

The most recent systematic compilations of SMBH spins and masses from the literature are presented in Reynolds (2021) and Bambi et al. (2021). In addition, there have been a few more measurements made since the publication of these reviews

(Walton et al., 2021; Mallick et al., 2022; Sisk-Reynés et al., 2022), resulting in a current sample size of 46 SMBHs with at least initial spin constraints. All but three of these sources are from the local Universe ($z \leq 0.30$, and even then most have $z \leq 0.10$); the two highest redshift constraints to date come from strongly-lensed quasars ($z = 0.66$ and $z = 1.70$; Reis et al., 2014; Reynolds et al., 2014).

Figure 2 shows the current constraints in the spin-mass plane for SMBHs with masses above $10^6 M_\odot$, compared against two distinct SMBH populations in the Horizon-AGN cosmological simulation. Grey filled diamonds indicate measurements with 1σ error bars[7], while open diamonds mark lower limits on $a*$. Many of the measurements show evidence for rapidly rotating black holes, particularly for masses in the range $M_{\rm BH} \sim 10^6$–$10^7 M_\odot$. There are hints in the current data of trends towards lower spins, or at least an increase in the spread of spin measurements, at higher masses, particularly for $M_{\rm BH} > 10^8 M_\odot$.

In order to better capture these trends, we further calculate mean spin parameter values in three bins of SMBH mass between 10^6 and $10^{10} M_\odot$[8], marked with open black squares. In the mean calculation we treat all available constraints as uncensored measurements and hence arrive at lower limit estimates in each bin, which indicate a tentative decrease in $a*$ with increasing $M_{\rm BH}$. We note, however, that there are still only a few measurements in the high-mass regime, and the uncertainties on those are also large. Furthermore, although a few sample-based efforts to constrain SMBH spin via systematic relativistic reflection analyses exist (e.g., Walton et al., 2013; Mallick et al., 2022), the majority of these measurements come from independent analyses of individual sources. As such, they are heterogeneous in regard to the reflection and relativistic blurring models used, the precise assumptions adopted in the use of these models, and the energy range over which the analysis has been performed. Moreover, *NuSTAR* has only contributed to ~half of these measurements, so not all are based on high S/N broadband X-ray spectroscopy.

The blue and orange shaded regions in Figure 2 indicate regions of the spin-mass parameter plane occupied by different SMBH growth histories in the Horizon-AGN cosmological simulation, described further in Section 4.1. To enable a fair comparison with current measurement constraints, both simulated SMBH populations have been corrected to best account for biases present in the observations. Among these, a potential likely bias towards high $a*$ values resulting from the expected spin-dependence of the radiative efficiency ($\eta(a*)$) in a relativistic thin-disk solution (Novikov and Thorne, 1973) is frequently discussed in the literature as at least part of the reason for the observed prevalence of near-maximal spin values (e.g., Brenneman et al., 2011; Reynolds et al., 2012). Under the simplifying assumption of a uniform distribution of AGN in the local Universe, the probability of observing a given spin value $a*$ scales with $\eta(a*)$ to power $\frac{3}{2}$ for sources with equal accretion rates in flux-limited surveys (see Supplementary Appendix S1 for further details). The superlinear scaling combined with the steep increase of $\eta(a*)$ for $a* > 0.8$ can have profound implications for inferred spin population statistics in observations.

Figure 3 shows the change in radiative efficiency with spin in geometrically thin relativistic disks (left panel) together with the potential impact the $\eta - a*$ bias can have on the observed spin parameter distributions (two panels on the right). Using a uniform distribution of $a* \sim U(0, 0.998)$ and a normal distribution $a* \sim N(0.5, 0.15)$ as examples, the two panels on the right demonstrate how a probability density function (PDF) of the expected measurements is distorted towards high spin values, shifting the expected mean observed spin values towards $a* \approx 0.67$ and $a* \approx 0.54$ for the two respective input distributions. As demonstrated in the figure, the impact of the $\eta - a*$ bias is critically dependent on the underlying true spin parameter distribution. Therefore, the strength of this effect will differ from our test cases for realistic samples of AGN observations.

Finally, we also note that radiative efficiency estimation for individual sources is challenging in practice. In the case of SMBH populations, however, one can obtain meaningful constraints on typical $\eta(a*)$ by comparing energy density of AGN radiation with local $M_{\rm BH}$ density (e.g., Soltan, 1982; Fabian and Iwasawa, 1999; Marconi et al., 2004; Raimundo et al., 2012). Most recent studies indicate $\eta(a*) \sim 0.12$–0.20, hence favoring spinning SMBH populations and implying $\boldsymbol{a* \gtrsim 0.5}$ (Shankar et al., 2020).

4.1 Connecting to SMBH growth histories in Horizon-AGN

As discussed in Section 2, different modes of SMBH growth leave distinct imprints on their angular momenta. Hence, once integrated over the lifetime of individual black holes, different SMBH growth histories, e.g., accretion-vs. merger-dominated scenarios, yield distinguishable distributions of their spin parameter $a*$. Beckmann et al. (2023) (hereafter B23) study such signatures in the $z = 0.0556$ snapshot of the Horizon-AGN cosmological simulation, finding that black holes grown exclusively via accretion (nearly merger-free) have a spin distribution that is distinct from the rest of the black hole population at $>5\sigma$ significance. As shown in Figure 3 of B23, SMBHs which acquired <10% of their mass in mergers have a significantly narrower distribution of spin parameter values than the remainder of the black hole population, concentrated at spin values close to $a* = 0.998$. The striking contrast between $a*$ populations presents a promising prospect for extending the study into two dimensions—distinguishing SMBH growth histories with measurements in the $M_{\rm BH} - a*$ plane.

To extract predictions for the observable signatures of different SMBH growth histories in the spin-mass plane from Horizon-AGN, we first identify the loci occupied by each history in the $M_{\rm BH} - a*$ parameter space. From here onwards we focus on the $z = 0.0556$ snapshot of the simulation studied in B23, which is well suited for our intended target sample of local AGN (see Section 6.1). Inspired by B23, we use a threshold on $f_{\rm BH,merge}$, the fraction of mass acquired

7 Measurements reported in the literature commonly quote 90% confidence intervals for spin parameter measurements. In order to translate these values to 1σ estimates, we divide the confidence interval by a factor of 1.64, making the simplifying assumption that the current constrains follow split normal distributions.

8 Our choice of binning scheme is discussed in Section 7.1.

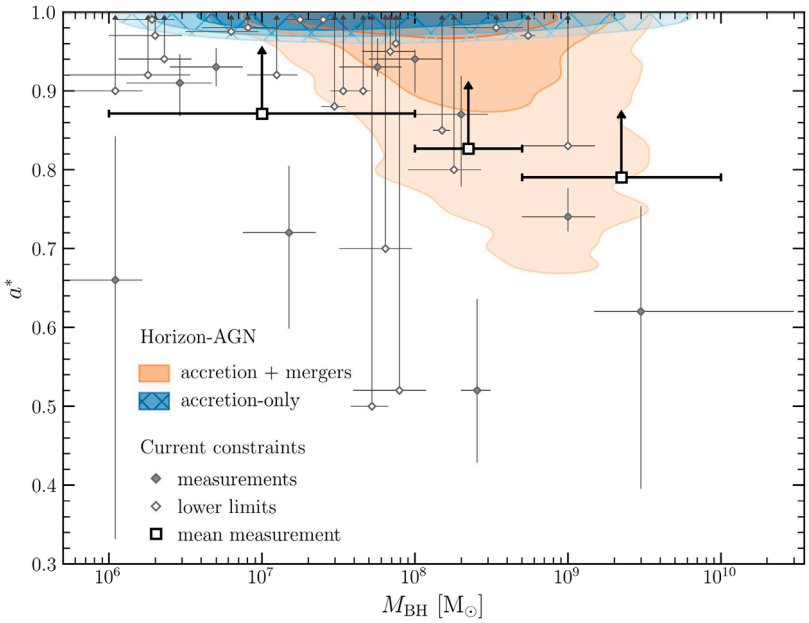

FIGURE 2
Current observational constraints in the $M_{\rm BH} - a*$ plane (open and filled gray diamonds), compared against the locus occupied by the Horizon-AGN cosmological simulation (logarithmically spaced contours) for black holes with $M_{\rm BH} \geq 10^6 M_\odot$ (the range covered by Horizon-AGN). Error bars associated with filled diamonds indicate 1σ uncertainty on $a*$ measurement. Blue, hatched: SMBHs which acquired less than 10% of their mass in mergers (i.e., accretion-only growth), orange: SMBHs with >10% mass grown in mergers (i.e., accretion + mergers growth). Both contours account for the radiative efficiency—spin bias in flux-limited AGN samples. Existing constraints suggest a decreasing trend in $a*$ with $M_{\rm BH}$, as shown by lower limits on mean $a*$ values in $M_{\rm BH}$ bins (black open squares). However, current results are not able to differentiate between SMBH growth scenarios (i.e., orange vs. blue contours).

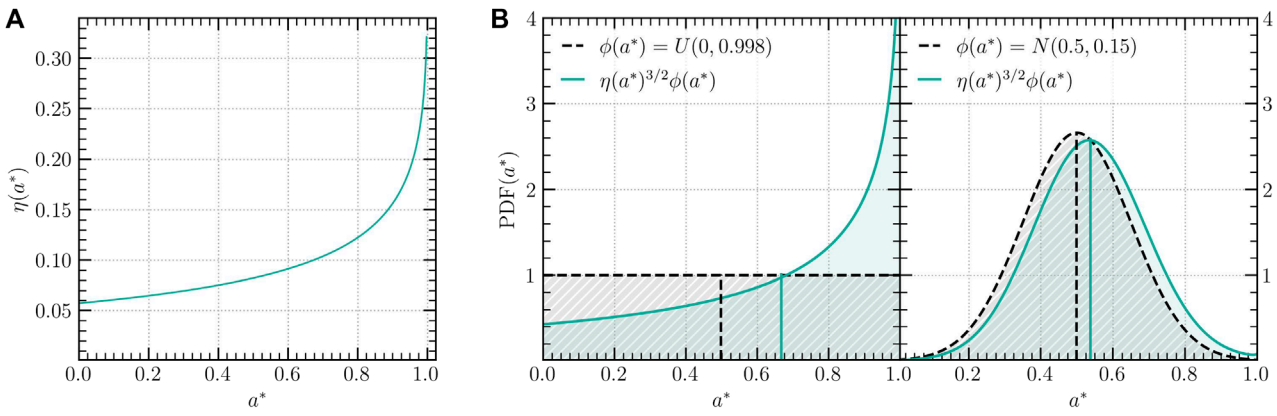

FIGURE 3
(A): Efficiency $\eta(a)$ as a function of spin parameter a for a thin disk solution (Novikov and Thorne, 1973). **(B)**: The effect of spin-dependence of η on the measurement spin population statistics, illustrated with changes to the probability density function (PDF, shaded regions) and its associated mean spin parameter value (vertical lines). Grey hatched regions in the middle and rightmost panels correspond to "raw" PDFs for a uniform distribution $a* \sim U(0, 0.998)$ and a normal distribution centered on $a* = 0.5$ with $\sigma = 0.15$, respectively, while their colored counterparts to PDFs corrected for the $\eta - a*$ bias. The shift between dashed and solid vertical lines indicates the change in associated mean $a*$ value between raw (dashed) and η-bias corrected distributions (solid). The magnitude of bias critically depends on the true underlying spin parameter PDF.

in mergers, to identify the *accretion-only* and *accretion + mergers* growth channels. We adopt $f_{\rm BH,merge} < 0.1$ for accretion-only and $f_{\rm BH,merge} \geq 0.1$ for accretion + mergers, which yield populations of 2,137 and 4,714 black holes respectively. Since the accretion-only population in the simulation is limited to $M_{\rm BH} < 10^{8.5} M_\odot$, to showcase its spin predictions across the entire mass range in Figure 2, we extend the dataset over the missing $M_{\rm BH}$ range with random draws from the accretion-only $a*$ probability density function (PDF). More specifically, we calculate the accretion-only PDF for $M_{\rm BH} > 10^8 M_\odot$ and take random draws from it to generate

$M_{BH} - a*$ value pairs with M_{BH} distribution matching that of the accretion + mergers population above $10^8 M_\odot$. In this way we mimic the effect of switching off spin evolution due to merger events studied for the $z = 0$ snapshot in Dubois et al. (2014b) (see Figure 7 in that publication), arriving at an expected $a*$ measurement across the whole range in M_{BH} for the accretion-only growth channel. We note that although the Eddington-limited subgrid model for SMBH growth in Horizon-AGN does not produce merger-free populations at very high M_{BH}, one could still expect highly spinning black holes at the high-mass end from models which include super-Eddington accretion rates in cosmological hydrodynamical simulations (e.g., Massonneau et al., 2023)[9].

Figure 2 compares loci in the $M_{BH} - a*$ plane occupied by black holes with accretion-only (blue hatched contours) and accretion + mergers (orange filled contours) growth histories in Horizon-AGN. Current observational constraints for $M_{BH} > 10^6 M_\odot$ are shown as individual grey points, with open diamonds corresponding to lower limits and filled diamonds representing measurements and their corresponding 1σ uncertainties. To ensure a meaningful comparison between observations and the cosmological simulation, both of the 2D spin distributions extracted from Horizon-AGN are corrected for the $\eta(a*) - a*$ bias and hence are vertically shifted upwards with respect to the raw output of the simulation. Figure 2 clearly demonstrates that the *two SMBH growth scenarios yield different signatures in the spin–mass parameter space*. At $M_{BH} \gtrsim 10^8 M_\odot$ the two growth histories begin separating, with mergers pushing the expected spin parameter values down towards values as low as $a* \sim 0.6$ with increasing M_{BH}, while the accretion-only scenario remains concentrated at near-maximal spin values. For black hole masses $<10^8$ $M_\odot$ both accretion-only and accretion + mergers populations are concentrated around near-maximal $a*$ values. This degree of overlap is further exacerbated by the spin-dependent radiative efficiency correction, which shifts the orange contours upwards, bringing the two populations towards near-identical loci. Overall, in the context of the Horizon-AGN cosmological simulation, Figure 2 presents a promising opportunity for testing and differentiating between SMBH growth channels in X-ray observations of AGN, even in the presence of the expected $\eta(a*) - a*$ bias.

5 The need for a systematic study of the spin–mass plane

Another critical conclusion drawn from Figure 2 is the necessity of obtaining high-precision spin measurements for large statistical samples of local AGN. Although the current observational constraints are broadly consistent with the accretion + mergers growth channel and show a hint of decrease in $a*$ with M_{BH} above $10^8 M_\odot$, the limited number of measurements at these masses and the relatively poor precision of these measurements mean the current data are not sufficient for a statistical assessment of these trends. More importantly for our discussion, the current sample of 10 measurements and 23 upper limits presented in the figure is not capable of differentiating between the two signatures of SMBH growth histories predicted by Horizon-AGN.

The current state-of-the-art spin measurements also offer a rather limited opportunity for the validation and improvement of the SMBH spin evolution models used in cosmological simulations of SMBH growth. When compared against other hydrodynamical simulations which cover a similar range in M_{BH} (e.g., Bustamante and Springel, 2019), Horizon-AGN produces spin population statistics with only subtle differences in their $M_{BH} - a*$ loci. In general this is encouraging, as it suggests that the qualitative trends implied by these simulations (i.e., Figure 2) are robust. The discrepancies that do exist between them, however, are a combined result of differences in subgrid prescriptions for SMBH seeding, accretion and feedback, and hence carry important information about the validity of a given numerical approach. With the measurement precision and sample size offered by the current constraints, one cannot determine which model implementation (if any) is a closer approximation of the observable Universe. Consequently, the current constraints allow enough room to validate a range of models, while, at the same time, are not strong enough to serve as observational calibrators for future generations of subgrid cosmological SMBH models.

In summary, Figure 2 demonstrates that *a systematic study of the spin-mass plane is necessary for differentiating between different growth histories of SMBHs in the local Universe*. A comprehensive characterisation of M_{BH} and $a*$ properties of local AGN will also play a critical role in calibrating subgrid models of cosmological structure formation by delivering improved constraints on physical properties of SMBH. To establish measurement requirements for these survey observations we take the two SMBH growth histories in Horizon-AGN as a case study, and investigate the precision and sample sizes that would be required to differentiate between these two possibilities in realistic samples of observable sources.

6 The BASS sample

In order to assess the number of known AGN for which spin constraints may be possible, either now or in the moderately near future, we turn to the BAT AGN Spectroscopic Survey (BASS; Koss et al., 2017). This is a major multi-wavelength effort to characterise AGN detected in the very high energy X-ray survey conducted by the Burst Alert Telescope (BAT, 14–195 keV; Barthelmy et al., 2005) onboard the *Neil Gehrels Swift Observatory* (hereafter *Swift*; Gehrels et al., 2004). The latest 105-month release of the BAT source catalogue (Oh et al., 2018) contains 1,632 sources in total, of which 1,105 have been identified as AGN. BASS provides black hole mass estimates (drawn from a variety of methods including Hβ line widths, stellar velocity dispersions and literature searches[10]) and Eddington ratios for the majority of these (e.g., Koss et al., 2022), as well as initial constraints on their broadband spectral properties by combining the BAT data with

9 We also note that efficient SMBH merging is, in part, a consequence of the limitations associated with modelling black hole mergers in cosmological simulations, which do not explicitly follow the SMBH orbital angular momentum loss via dynamical friction.

10 The method used to estimate the mass for each source is also provided in the BASS catalogue.

the best soft X-ray coverage available (e.g., from *XMM-Newton*; Ricci et al., 2017).

6.1 Sources with spin measurement potential

Not all AGN are well suited to making spin measurements. In particular, the very hard X-ray selection of the BAT survey means it is sensitive to even heavily obscured AGN (including "Compton thick" sources with $N_{\rm H} > 1.5 \times 10^{24}$ cm^{-2}; e.g., Arévalo et al., 2014; Annuar et al., 2015), and determining the contribution from relativistic reflection becomes increasingly challenging as the source becomes more obscured. Furthermore, there is a general expectation that at low accretion rates the optically-thick accretion disk becomes truncated at radii larger than the ISCO (Narayan and Yi, 1994; Esin et al., 1997; Tomsick et al., 2009), such that the inner radius of the disk no longer provides direct information about the spin. As such, in order to compile a sample of AGN for which spin measurements should be possible, we apply several selection criteria to the BASS sample. First, we select sources with fairly low levels of obscuration, requiring a neutral column density of $N_{\rm H} \leq 10^{22}$ cm^{-2}. Second, we select sources with Eddington ratios of $\lambda = L_{\rm bol}/L_{\rm Edd} \geq 0.01$, so that we may have confidence that the accretion disk should extend to the ISCO (note also that this selection naturally means a black hole mass estimate is available, otherwise it would not have been possible to estimate λ). We further place an upper limit of $\lambda < 0.7$ to select sources for which thin disk approximation is appropriate (e.g., Steiner et al., 2010). We also require that the sources exhibit sufficiently strong reflection features in order for spin measurements to be feasible. We therefore then select sources for which the initial X-ray spectroscopy conducted by Ricci et al. (2017) indicates a reflection fraction consistent with $R \geq 1$ (note that Ricci et al., 2017 use the definition of the reflection fraction from Magdziarz and Zdziarski, 1995). For the same reason, we also exclude blazars from our sample. Finally, after having made these cuts to the BASS data, we also exclude a small number of remaining sources for which the initial X-ray spectroscopy implies an unreasonably hard photon index ($\Gamma \leq 1.5$), taking this as an indication that either the source is actually obscured but that the absorption is sufficiently complex that it was not well characterized by the simple spectral models used in Ricci et al. (2017) or that the spectrum has a low signal-to-noise ratio.

We do not expect these selections to introduce any significant biases that would cause the observed spin distribution to deviate from the intrinsic one (besides the $\eta - a*$ bias that has already been discussed in Section 4). Selecting based on obscuration properties and the exclusion of blazars are both expected to be related mainly to our viewing angle to these AGN (e.g., Antonucci, 1993), which is not dependent on the spin of their central SMBHs. The Eddington ratio selection relates specifically to the accretion rate onto the AGN "today", while the spin of the SMBH will be mainly determined by its long-term growth history instead. Indeed, the Horizon-AGN simulation shows no connection between SMBH spin and the instantaneous accretion rate in the analysed snapshot. Finally, the reflection fraction selection still permits spins across the full range of possible prograde spin values ($a* = 0$–0.998), as even Schwarzschild black holes ($a* = 0$) should result in reflection from the disc with $R \geq 1$ if the disc reaches the ISCO (e.g., Dauser et al., 2016).

Our various cuts leave a sample of 192 AGN from BASS for which spin measurements should be possible. All of these sources are relatively local, with a median redshift of $z \sim 0.05$ (see "BASS parent" in the right panel of Figure 4), consistent with the $z = 0.0556$ snapshot of the Horizon-AGN simulation we use in this work. Conveniently, these sources all have an estimate of $M_{\rm BH}$, among which ~80% are based on single-epoch virial Hβ and Hα estimators, ~8% on the $\boldsymbol{M_{\rm BH} - \sigma *}$ relation and the remaining ~12% are drawn from reverberation mapping and resolved stellar and gas dynamics published in the literature. Together, the 192 AGN span a broad range of black hole masses, $5.5 \lesssim \log(M_{\rm BH}/{\rm M}_\odot) \lesssim 10.0$ (middle and left panels in Figure 4), which is well suited to placing constraints on different potential black hole growth models. The sample is also particularly appropriate for comparisons against Horizon-AGN specifically, with the $M_{\rm BH}$ distribution in our parent BASS sample showing good qualitative agreement with the black holes extracted from the cosmological simulation (left panel in Figure 4). Finally, we note that while targeting all hard X-ray detected *Swift*-BAT AGN, the BASS survey is not designed to probe a representative sample of mass assembly histories of their galactic hosts. In consequence, our BASS parent sample may not be perfectly representative of all SMBH growth channels present in the observable Universe.

7 Sample size and spin uncertainty requirements

In order to design observational strategies for differentiating between SMBH growth scenarios with spin parameter measurements, we need to establish the sample size and maximum spin measurement uncertainty (σ_{a*}) necessary for such work. Both requirements are imposed by a combination of two independent factors: the difference between the SMBH growth history models as a function of mass in Horizon-AGN, and the SMBH mass distribution of our parent BASS sample (Section 6.1). In order to determine these requirements, below we simulate a set of potential survey programmes covering a range of realistic measurement uncertainties and sample sizes.

7.1 Simulating realistic samples informed by Horizon-AGN

Figure 2 shows that the two SMBH growth scenarios separate in the $M_{\rm BH} - a*$ plane above $10^8 {\rm M}_\odot$, with the strongest difference at the high-$M_{\rm BH}$ end. It is also apparent that at high masses the accretion + mergers distribution (orange) spans a broad range in spin parameter values. Therefore, in order to differentiate between the two growth scenarios with realistic samples, we base our strategy on a simple statistical approach—discretising the spin–mass plane by calculating sample means in bins of $M_{\rm BH}$. This way we can both reduce the impact of the uncertainty on individual $M_{\rm BH} - a*$ measurements and coarsely capture the two-dimensional trends which would otherwise require large sample

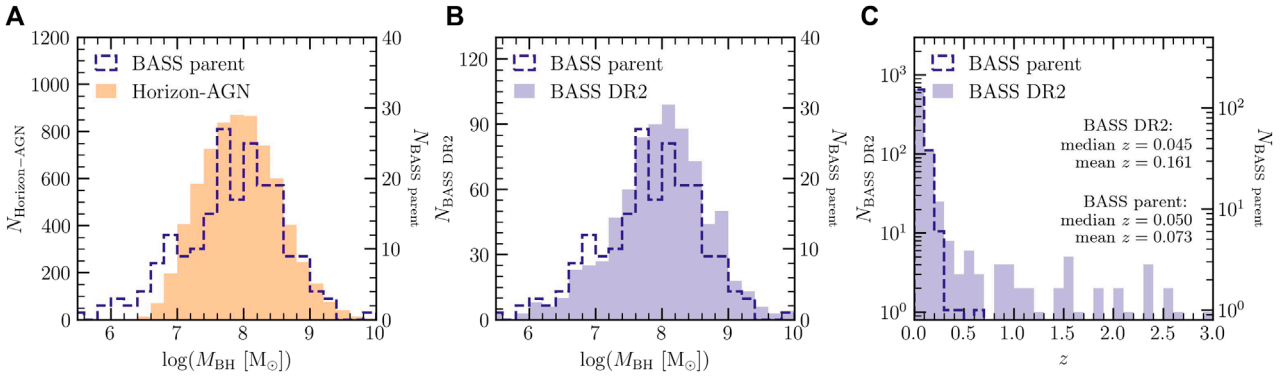

FIGURE 4
(A): comparison of SMBH mass distributions between our parent BASS sample (BASS parent, Section 6.1 and the Horizon-AGN cosmological simulation, demonstrating good agreement between potential AGN targets and the cosmological model. **(B)**: $M_{\rm BH}$ comparison between the whole BASS catalogue (BASS DR2) and out parent BASS sample. The distributions in $M_{\rm BH}$ are comparable, demonstrating that our sample selection criteria do not introduce additional bias with respect to the full BASS DR2 catalogue. **(C)**: comparison of redshift distributions between our parent BASS sample and the full BASS DR2 AGN catalogue sources. As expected, our sample selection removes the highest-redshift sources. However, the median redshift remains comparable at $z = 0.05$.

sizes for a direct comparison between 2D distributions. To best capture the signal we select one bin below $M_{\rm BH} = 10^8 {\rm M}_\odot$ (where both scenarios make consistent predictions) and for higher masses we split the sample into two bins above and below $\log(M_{\rm BH}/{\rm M}_\odot) = 8.7$ ($M_{\rm BH} \approx 5 \times 10^8 {\rm M}_\odot$). This choice is motivated by the SMBH mass distribution shown in the left panel of Figure 4; there are 9 AGN with $\log(M_{\rm BH}/{\rm M}_\odot) > 8.7$ among the brightest 100 X-ray sources in the 2–10 keV band in our parent BASS selection (which we consider as an initial plausible sample size), which yield a Poisson signal-to-noise ratio of 3 for source number count in the highest mass bin. On the low-mass end we restrict the mass bin to $M_{\rm BH} > 10^6 {\rm M}_\odot$ to match the Horizon-AGN $M_{\rm BH}$ distribution. Our final binning scheme results in the following ranges in $\log(M_{\rm BH}/{\rm M}_\odot)$ [6.0, 8.0] [8.0, 8.7] and [8.7, 10.0].

By estimating mean $a*$ values, we take advantage of the $\sqrt{N}$ scaling with sample size N of the standard error on the mean, which allows us to clearly separate the two SMBH growth scenarios in the coarsely binned $M_{\rm BH} - a*$ plane. With $M_{\rm BH}$ ranges in place, we can now determine the minimum sample size and uncertainty required for a series of mean $a*$ measurements to differentiate between the orange and blue SMBH populations in Figure 2. We proceed by selecting the K brightest sources from our parent BASS sample for a set of different values for K, thus imposing a single X-ray flux limit across the whole range in SMBH mass in each case. This way we match the assumptions discussed earlier in Section 4 and hence can implement the radiative efficiency - spin parameter bias expected for flux-limited AGN samples in the local Universe. We then extract $a*$ distributions for both SMBH growth histories in each $M_{\rm BH}$ bin from Horizon-AGN and correct them for the $\eta(a*)$ bias (see Supplementary Appendix S1 for details).

To simulate realistic samples of AGN, we take a total of $K = \Sigma K_i$ random draws from the bias-corrected spin distributions across all $M_{\rm BH}$ bins, with the sample sizes K_i in each individual bin determined by the number of BASS sources which fall within this SMBH mass range[11], among the K brightest AGN from our selection in Section 6.1. We perform the spin draws separately for each SMBH growth model, and hence for each realization of a potential observational sample of a total of K AGN, we have a paired set of predicted spin values for the accretion-only and accretion + mergers growth models. To simulate the effect of measurement uncertainty we then perturb the spin values drawn above by further random draws from a normal distribution $N(0, \sigma_{a*})$, where σ_{a*} is the assumed uncertainty on the spin measurements[12], and where we consider a range of values for σ_{a*}. For each a_i^*, the normal distribution is singly truncated at $\sigma_i = (0.998 - a_i^*)/\sigma_{a*}$ to account for the theoretical upper limit on the spin parameter of $a* = 0.998$. This way, each potential AGN sample from a given SMBH growth history consists of K spin measurements expected from $\eta(a*)$ bias-corrected Horizon-AGN distributions, post-processed to account for measurement uncertainty.

As a final step in each simulated AGN sample, for each mass bin we calculate the mean spin value together with its corresponding standard error on the mean: $\mu_{\rm acc} \pm \delta_{\rm acc}$ for the accretion-only scenario and $\mu_{\rm acc+mer} \pm \delta_{\rm acc+mer}$ for accretion + mergers. To calculate the standard error, we necessarily assume that each paired draw consists of $a*$ measurements without lower limits in both SMBH growth histories. However, we note that some lower limits are likely to be present in real observations. Finally, we check the probability of the two mean measurements in a mass bin Ω being drawn from the same underlying distribution by calculating the right-tail p-value

11 Throughout the study we treat the three sources with $M_{\rm BH} < 10^6 {\rm M}_\odot$ in the parent BASS sample as belonging to the lowest mass bin, given the large uncertainty associated with low $M_{\rm BH}$ estimates.

12 Note that at this point we simply assume all spin measurements to have the same uncertainty; more realistic scenarios that include the expected dependence of measurement uncertainties as a function of spin are investigated in Section 9.

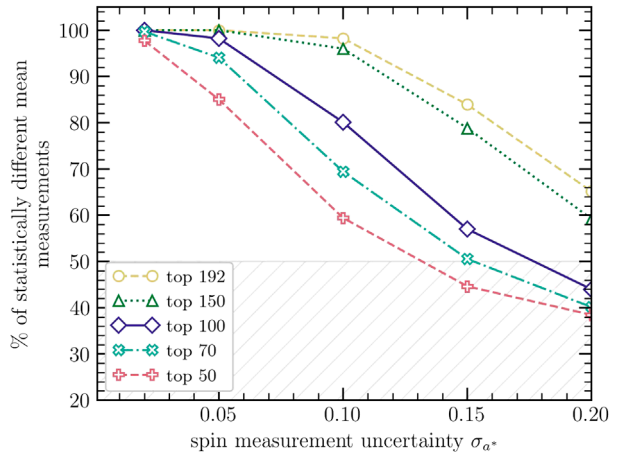

FIGURE 5
Minimum spin measurement uncertainty (σ_{a*}) and sample size required for simulated observations to differentiate between accretion-only and merger and accretion SMBH growth scenarios drawn from the HorizonAGN cosmological simulation. Individual curves show the simulated observations performed for the top 50, 70, 100, 150 and 192 brightest X-ray sources in the 2–10 keV band in our parent BASS sample. In order for a median (50th percentile) simulated measurement to tell SMBH growth histories apart, one requires Gaussian spin measurement uncertainty of $\lesssim 0.15$ across the entire range in $a*$ for a sample of 70 sources.

(p_Ω) of $\mu_{\rm acc} - \mu_{\rm acc+mer}$ belonging to $N(0, \sqrt{\delta^2_{\rm acc} + \delta^2_{\rm acc+mer}})$. In this way, we calculate the probability that a given paired set of predicted spin values in a bin cannot differentiate between the accretion-only and accretion + mergers growth scenarios. For our simulated AGN samples, we consider spin measurement uncertainties in the range $\sigma_{a*} \in [0.02, 0.05, 0.10, 0.15, 0.20]$, and sample sizes of $K \in [50, 70, 100, 150, 192]$. For each combination of these values we repeat the above process 10^4 times, generating a large set of potential AGN samples, together with their corresponding mean spin parameter measurements as a function of mass.

Figure 5 shows the fraction of these simulated AGN samples which result in a statistically different measurement of mean spin parameter value between the accretion-only and accretion + mergers SMBH growth scenarios as a function of $a*$ measurement uncertainty and sample size. In order to take full advantage of the difference between the two predictions at high SMBH masses, in each realization of a potential AGN sample we combine the results for both of the mass bins with $M_{\rm BH} > 10^8 {\rm M}_\odot$. Since these can be treated as independent measurements, the combined probability of the simulated accretion-only and accretion + mergers samples being drawn from the same distribution in the $M_{\rm BH} - a*$ plane for *both* mass bins becomes $p_{\rm total} = p_{[8,8.7]} \times p_{[8.7,10]}$. The vertical axis in Figure 5 shows the fraction of simulated measurements which result in $p_{\rm total} < 0.01$ as a function of σ_{a*} in the x-axis. Different lines and markers correspond to the top 192, 150, 100, 70 and 50 brightest AGN in our parent BASS sample. Whenever the curves enter the gray hatched region, the median measurement expected from the 10^4 realizations of potential AGN samples will not differentiate between the accretion-only and accretion + mergers BH growth scenarios.

As expected, Figure 5 shows that increasing the uncertainty on individual spin measurements at fixed sample size decreases the fraction of simulated samples capable of differentiating between the two SMBH growth histories. Similarly, at fixed uncertainty, a larger sample size results in higher chances for a single realization of such a sample to tell the two growth histories apart. In the context of minimum survey requirements, we find that for a sample size of >70 AGN we would need a maximum of $\sigma_{a*} \lesssim 0.15$ for a median expected measurement to differentiate between the accretion-only and accretion + mergers SMBH populations. In order to be conservative, we therefore suggest that a sample size of $K = 100$ AGN drawn from our BASS selection with spins measured to a precision of $\sigma_{a*} \lesssim 0.15$ would be sufficient to distinguish between these different SMBH growth scenarios.

8 *HEX-P* simulations

Given the importance of simultaneous broadband X-ray spectroscopy for providing observational constraints on SMBH spin, a mission with the profile of *HEX-P* is ideally suited to building the significant samples of SMBH spin measurements required to finally connect these measurements to cosmological BH growth models. We now present a set of simulations that showcase the anticipated capabilities of *HEX-P* in this regard.

8.1 Mission design

The Low Energy Telescope (LET) onboard *HEX-P* consists of a segmented mirror assembly coated with Ir on monocrystalline silicon that achieves a half power diameter of 3.5″, and a low-energy DEPFET detector, of the same type as the Wide Field Imager (WFI; Meidinger et al., 2020) onboard Athena (Nandra et al., 2013). It has 512×512 pixels that cover a field of view of $11.3' \times 11.3'$. It has an effective passband of 0.2–20 keV, and a full frame readout time of 2 ms, which can be operated in a 128 and 64 channel window mode for higher count-rates to mitigate pile-up by allowing a faster readout. Pile-up effects remain below an acceptable limit of ~1% for fluxes up to ~100 mCrab in the smallest window configuration (64w). Excising the core of the PSF, a common practice in X-ray astronomy, allows for observations of brighter sources, with a typical loss of up to ~60% of the total photon counts.

The High Energy Telescope (HET) consists of two co-aligned telescopes and detector modules. The optics are made of Ni-electroformed full shell mirror substrates, leveraging the heritage of *XMM-Newton*, and coated with Pt/C and W/Si multilayers for an effective passband of 2–80 keV. The high-energy detectors are of the same type as flown on *NuSTAR*, and they consist of 16 CZT sensors per focal plane, tiled 4×4, for a total of 128×128 pixel spanning a field of view of $13.4' \times 13.4'$.

8.2 Instrumental responses

All the mission simulations presented here were produced with a set of response files that represent the observatory performance

based on current best estimates as of spring 2023 (see Madsen et al. 2023). The effective area is derived from raytracing calculations for the mirror design including obscuration by all known structures. The detector responses are based on simulations performed by the respective hardware groups, with an optical blocking filter for the LET and a Be window and thermal insulation for the HET. The LET background was derived from a GEANT4 simulation (Eraerds et al., 2021) of the WFI instrument, and the background simulation for the HET was derived from a GEANT4 simulation of the *NuSTAR* instrument. Both simulations adopt the planned L1 orbit of *HEX-P*. The broad X-ray passband and superior sensitivity will provide a unique opportunity to study accretion onto SMBHs across a wide range of energies, luminosities, and dynamical regimes.

8.3 Spectral simulations

To assess the ability of *HEX-P* to constrain black hole growth models via AGN spin measurements, we perform a series of spectral simulations covering a range of spin values relevant to the cosmological simulations discussed above: $a* = 0.5, 0.7, 0.9, 0.95$. We first focus on the lowest spin value among this set, $a* = 0.5$, and perform a set of simulations at different exposures in the range 50–200 ks. For each exposure, we simulate 100 different spectra using the above response files and the XSPEC spectral fitting package (v12.11.1; Arnaud, 1996) in order to determine the minimum exposure that provides the *HEX-P* data quality needed for an average 1σ constraint on the spin of $\sigma_{a*} \leq 0.15$, as required above. We then perform further sets of 100 simulations with this exposure for each of the spin values listed above to map out the expected uncertainty as a function of input spin (as it is well-established that for a given observational setup, tighter constraints are obtained for higher spin values, e.g., Bonson and Gallo, 2016; Choudhury et al., 2017; Kammoun et al., 2018; Barret and Cappi, 2019).

We make use of the RELXILL family of disk reflection models (Dauser et al., 2014; García et al., 2014) for these simulations, and construct a spectral model that draws on the typical properties of the 192 BASS AGN selected above (Section 6.1), general expectations for the unobscured AGN selected based on the unified model for AGN, and typical results seen from AGN for which detailed reflection studies have already been possible in the literature. We specifically make use of the RELXILLLPCP model, which assumes a simple lamppost geometry for the corona, and that the ionizing continuum is a thermal Comptonization model (specifically the NTHCOMP model; Zdziarski et al., 1996; Zycki et al., 1999).

For the key model parameters, we assume the spectrum of the primary continuum has parameters $\Gamma = 2.0$ and $kT_e = 100$ keV for the photon index and electron temperature, respectively, relatively typical parameters for unobscured AGN (Ricci et al., 2017; Baloković et al., 2020). This illuminates a geometrically thin accretion disk which is assumed to extend down to the ISCO. AGN with moderate-to-low levels of obscuration are generally expected to be viewed at moderate-to-low inclinations in the unified model (Antonucci, 1993), so we assume an inclination of 45°. The disk is assumed to be ionized, with an ionization parameter[13] of $\log[\xi/(\text{ergcms})] = 2$ (typical of values reported from relativistic reflection analyses in the literature, e.g., Ballantyne et al., 2011; Walton et al., 2013; Jiang et al., 2019; Mallick et al., 2022), and to have solar iron abundance (i.e., $A_{\rm Fe} = 1$). We assume the corona has a height of $h = 5R_{\rm G}$ for the $a* = 0.5$ simulations, and then that it has constant height in vertical horizon units as we subsequently vary the spin. This is equivalent to assuming the scale of the corona contracts slightly as the inner radius of the disk moves inwards, as might be expected should the corona be related to magnetic reconnection around the inner disk (e.g., Merloni and Fabian, 2001); in gravitational radii, these coronal heights correspond to values in the range ~4–5 $R_{\rm G}$, which are relatively standard values inferred for the sizes of X-ray coronae (e.g., De Marco et al., 2013; Reis and Miller, 2013; Kara et al., 2016; Mallick et al., 2021). The reflection fraction is calculated self-consistently based on the combination of $a*$ and h, both when computing the simulations and also when subsequently fitting the simulated data to explore constraints on $a*$.

As we need a sample of ~100 AGN to distinguish the black hole growth models, we normalize all of our simulations to have a 2–10 keV flux of 6×10^{-12} erg cm^{-2} s^{-1}, corresponding to the flux of the 100th brightest source in the sample of AGN selected above (see Section 6.1). At this flux level, we find that a *HEX-P* exposure of 150 ks is required to provide an average uncertainty of $\sigma_{a*} \leq 0.15$ for an input spin value of $a* = 0.5$. We also find that, as broadly expected, the typical uncertainty on the spin measurements *HEX-P* will decrease for more rapidly rotating black holes (see Figure 6). Although our results do differ quantitatively to the prior efforts that have also come to similar conclusions, the overall quantitative trend we find is consistent with these previous works (e.g., Bonson and Gallo, 2016; Kammoun et al., 2018). These quantitative differences mainly relate to the fact that we are simulating *HEX-P* spectra instead of *XMM-Newton* + *NuSTAR* spectra, with some contribution from the fact that different model versions and slightly different assumptions are used here. An example spectrum from one of our simulations for $a* = 0.9$ is shown in Figure 7, along with the projected constraints on $a*$, h and source inclination i for that simulation.

9 Constraining SMBH growth channels with *HEX-P*

Having established the minimum survey requirements, we now demonstrate *HEX-P*'s ability to differentiate between accretion-only and accretion + mergers SMBH growth scenarios. To this end we repeat the simulations introduced in Section 7.1 for the brightest 100 sources in the parent BASS sample (Section 6.1), this time replacing the constant spin parameter uncertainty σ_{a*} assumed previously with the $a*$-dependent uncertainties $\sigma(a*)$ obtained from spectral simulations in Section 8.3 (see Figure 6), i.e., now specifically simulating observational campaigns with *HEX-P*. Similarly to our initial tests, we simulate 10^4 paired AGN

13 The ionization parameter has its usual definition of $\xi = L/nR^2$, where L is the ionizing luminosity, n is the number density of the plasma, and R is the distance between the plasma and the ionizing source

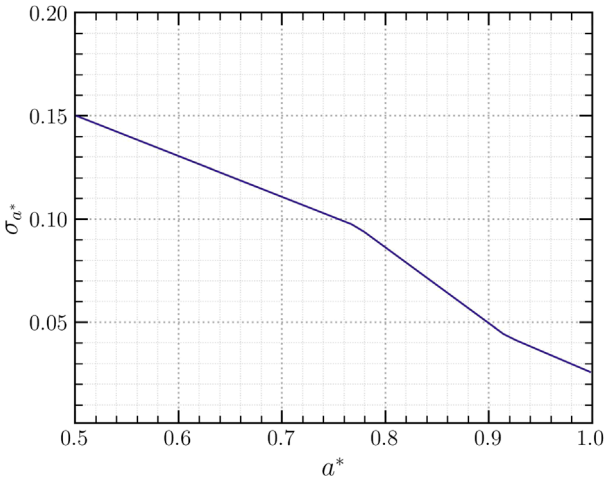

FIGURE 6
Spin parameter measurement uncertainty $\sigma(a*)$ vs. spin parameter $a*$, extracted from the *HEX-P* spectral simulations of relativistic reflection in AGN discussed in Section 8.3 (which assume a 2–10 keV flux of 6×10^{-12} erg cm^{-2} s^{-1} and an exposure time of 150 ks).

samples to assess the probability with which *HEX-P* will confidently discriminate between SMBH growth histories.

Figure 8 illustrates the observational constraints that would be expected for one such paired set of simulated AGN samples, randomly selected from our set of simulations, comparing the accretion-only (blue circles) and accretion + mergers (orange squares) SMBH growth scenarios against the current spin parameter constraints for $M_{\rm BH} > 10^6 M_\odot$ (gray diamonds). In order to account for the existence of lower limits expected in realistic measurements, by analogy with the measurements collected from the literature, we use open symbols to indicate right-censored spin draws, i.e., a_i^* for which $0.998 - a_i^* < \sigma(a_i^*)$. Vertical error bars mark 1σ uncertainties in both simulated and existing $M_{\rm BH} - a*$ constraints, allowing for a direct comparison between the two. All BASS $M_{\rm BH}$ measurements in the figure are assigned a **± 0.5 *dex*** uncertainty expected for their estimate via the single-epoch virial method (Shen, 2013). Figure 8 demonstrates the potential for such a *HEX-P* spin measurement campaign to map the spin-mass plane with unprecedented accuracy. In comparison with currently available constraints, the *simulated observations offer clear improvements in measurement precision, control of sample selection biases, and a greater than twofold increase in sample size*.

Moving on from an individual realization, the top panels in Figure 9 present the distribution of mean $a*$ measurements (μ) for the whole suite of 10^4 simulations for the accretion + mergers (orange) and accretion-only (blue) SMBH growth histories for the three bins of $M_{\rm BH}$. Vertical dashed lines mark μ at which each distribution peaks, indicating the most likely expected mean spin parameter measurement for each growth scenario. Similarly, bottom panels present the corresponding distributions of the standard errors on the mean (δ) together with their peaks marked with vertical dashed lines. The mean spin parameter values from Horizon-AGN together with their most likely measurements expected from *HEX-P* observations are summarized in Table 1.

Together, Figure 9 and Table 1 demonstrate the potential of mean $a*$ measurements in bins of $M_{\rm BH}$ for differentiating between the accretion-only and accretion + mergers SMBH growth scenarios within the Horizon-AGN cosmological model. As expected from Figure 2, the simulated constraints in the lowest mass bin are consistent between the two SMBH populations, but become statistically separable for $M_{\rm BH} > 10^8 M_\odot$. In all three panels in Figure 9, the distributions of mean accretion-only measurements are narrower than the accretion + mergers distributions, with consistently high peak values matching the true $\eta(a*)$ bias-corrected mean $a*$ in Horizon-AGN to within <2%. The orange distributions, on the other hand, peak at progressively lower values with increasing $M_{\rm BH}$, following the trend expected from the cosmological simulation to within <2% as well. We also note that the simulated accretion + mergers mean spin measurements form a visibly left-skewed distribution, primarily owing to the progressive spin parameter uncertainty prescription in our simulations which assumes larger σ_{a^*} for lower spin values based on our *HEX-P* spectral simulations (Section 8.3)[14]. The middle mass bin shows a non-neglible overlap between the accretion-only and accretion + mergers distributions, with their two peaks clearly separated by $\Delta_\mu \simeq 0.03$. For $\log(M_{\rm BH}/M_\odot) > 8.7$ the two SMBH growth scenarios form nearly non-overlapping distributions with peak mean spin parameter values separated by $\Delta_\mu \simeq 0.16$, despite the modest number of only 9 BASS sources available in the mass bin. We note, however, that small sample statistics do lead to a significant spread in the simulated values for accretion + mergers scenario.

In Figure 10 we summarize the prospects for constraining the cosmic growth history of SMBHs via X-ray reflection spectroscopy with a *HEX-P* spin survey similar to the design outlined above. The figure shows the expected mean $a*$ measurements in three bins of $M_{\rm BH}$ for accretion-only (blue circles) and accretion + mergers (orange squares) scenarios, inferred from our suite of simulated observations of the brightest 100 AGN in our parent BASS sample. The y-axis locus of individual points correspond to the vertical dashed lines in the top panels of Figure 9, while the length of the error bars correspond to the vertical dashed lines in the bottom panels. Since it is likely that observations of high-$a*$ SMBHs will result in a significant fraction of constraints that are lower limits, we mark the prediction for the accretion-only growth scenario as a lower limit. We also compare the results of our simulations to the current constraints, showing mean spin parameter values in identical mass bins for $M_{\rm BH} - a*$ measurements calculated earlier in Section 4.1 (and presented earlier in Figure 2).

Figure 10 clearly demonstrates that *future HEX-P spin measurements will allow us to differentiate between the two SMBH growth channels as inferred from the Horizon-AGN cosmological model*. The expected mean measurements in the highest mass bin alone reject the null hypothesis of the accretion-only and accretion + mergers results being drawn from the same distribution at the level of 2.8σ ($p_{[8.7-10.0]} = 2.5\times10^{-3}$). Across the whole suite of our simulations, >82% (>36%) of paired simulated measurements in the highest mass bin reject the null hypothesis at $>2\sigma$ ($>3\sigma$) confidence

14 The skewness is also present in the accretion-only scenario, however, this effect is less visibly apparent due to the narrow width of the distribution.

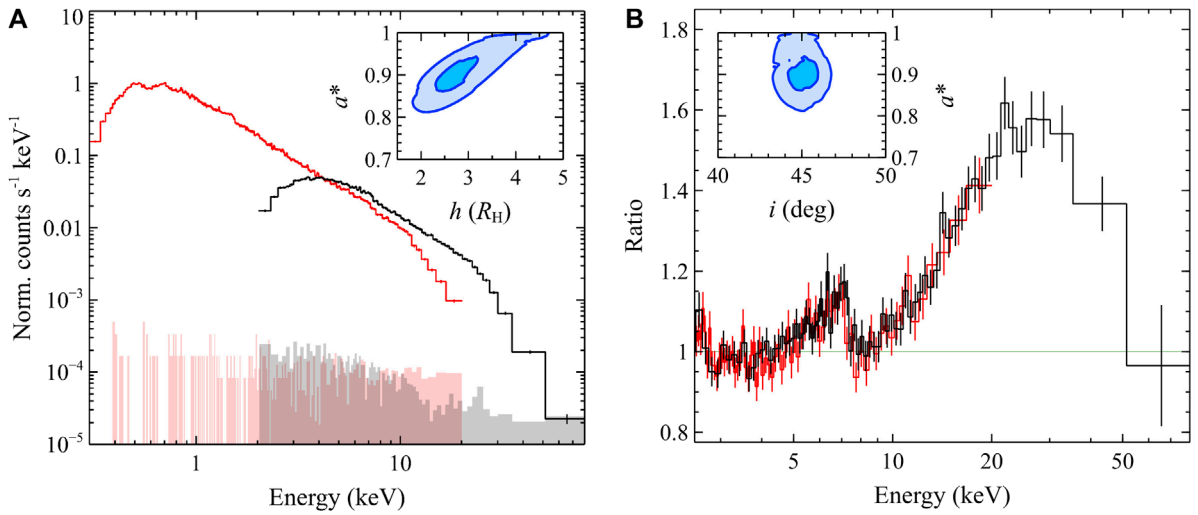

FIGURE 7
(A): Count spectra for the LET (red) and the HET (black) for one of our *HEX-P* spectral simulations with $a*=0.9$, along with their corresponding instrumental backgrounds (shaded regions). **(B)**: The same simulated spectra plotted as a ratio to a simple CUTOFFPL continuum model (a powerlaw with an exponential high-energy cutoff), fit to the 2–4, 8–10 and 50–80 keV bands (where the primary continuum would be expected to dominate). We zoom in on the data above 2 keV to highlight the key reflection features: the relativistically broadened Fe Kα peaking at ~6–7 keV and the Compton hump peaking at ~30 keV. The two insets show the projected constraints on $a*$, h and source inclination i for this simulation (displayed as 2-D confidence contours, with the 1σ and 2σ levels shown).

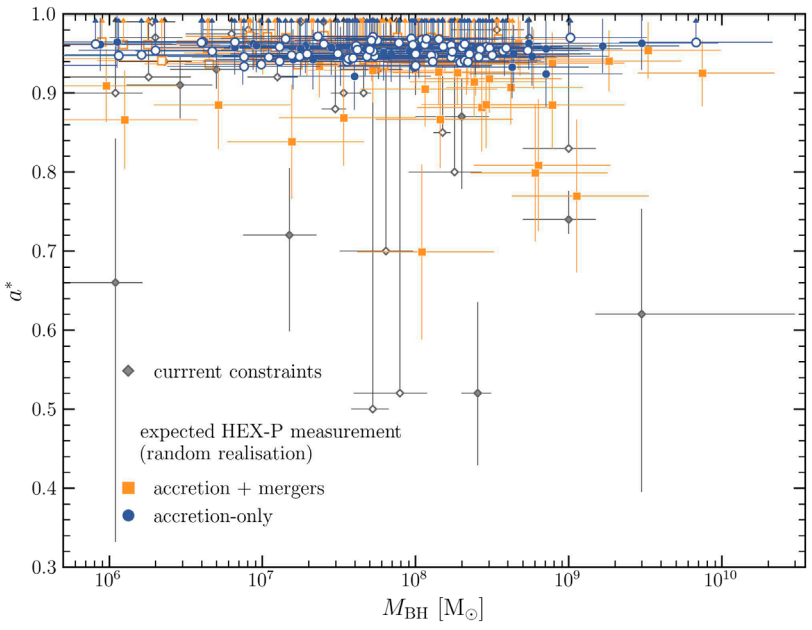

FIGURE 8
Comparison between current published constraints (grey diamonds) and a random realization of simulated *HEX-P* measurements for the accretion-only (blue circles) and accretion + mergers SMBH growth scenarios (orange squares). Empty symbols show lower limits on $a*$, while filled symbols denote measurements with vertical errorbars marking their corresponding 1σ confidence ranges. With its expected spin measurement uncertainty, *HEX-P will provide unprecedented constraints on the* $M_{BH}-a*$ *plane for SMBHs in the local Universe.*

level. When we combine the measurements for both mass bins above $10^8 M_\odot$ in SMBH mass, the expected *HEX-P* measurement can differentiate between the two growth histories at ~4.3σ and across all simulated measurements at >3σ (>4σ) confidence level in >88% (>65%) of all paired draws. Figure 10 also illustrates that the current spin constraints are not yet sufficient to make the distinction between these different growth scenarios; a dedicated SMBH spin survey with improved individual constraints, a larger sample size

TABLE 1 Summary of mean spin parameter values in simulated *HEX-P* observations and Horizon-AGN.

$\log(M_{BH}/M_{\odot})$ bin		[6.0, 8.0]	[8.0, 8.7]	[8.7, 10.0]
Horizon-AGN	accretion-only	0.996	0.993	0.993
	accretion + mergers	0.959	0.905	0.768
Horizon-AGN	accretion-only	0.996	0.995	0.995
with $\eta(a*)$ bias	accretion + mergers	0.981	0.953	0.851
Expected measurement	accretion-only	0.977 ± 0.002	0.975 ± 0.003	0.976 ± 0.005
	accretion + mergers	0.966 ± 0.004	0.945 ± 0.011	0.86 ± 0.04

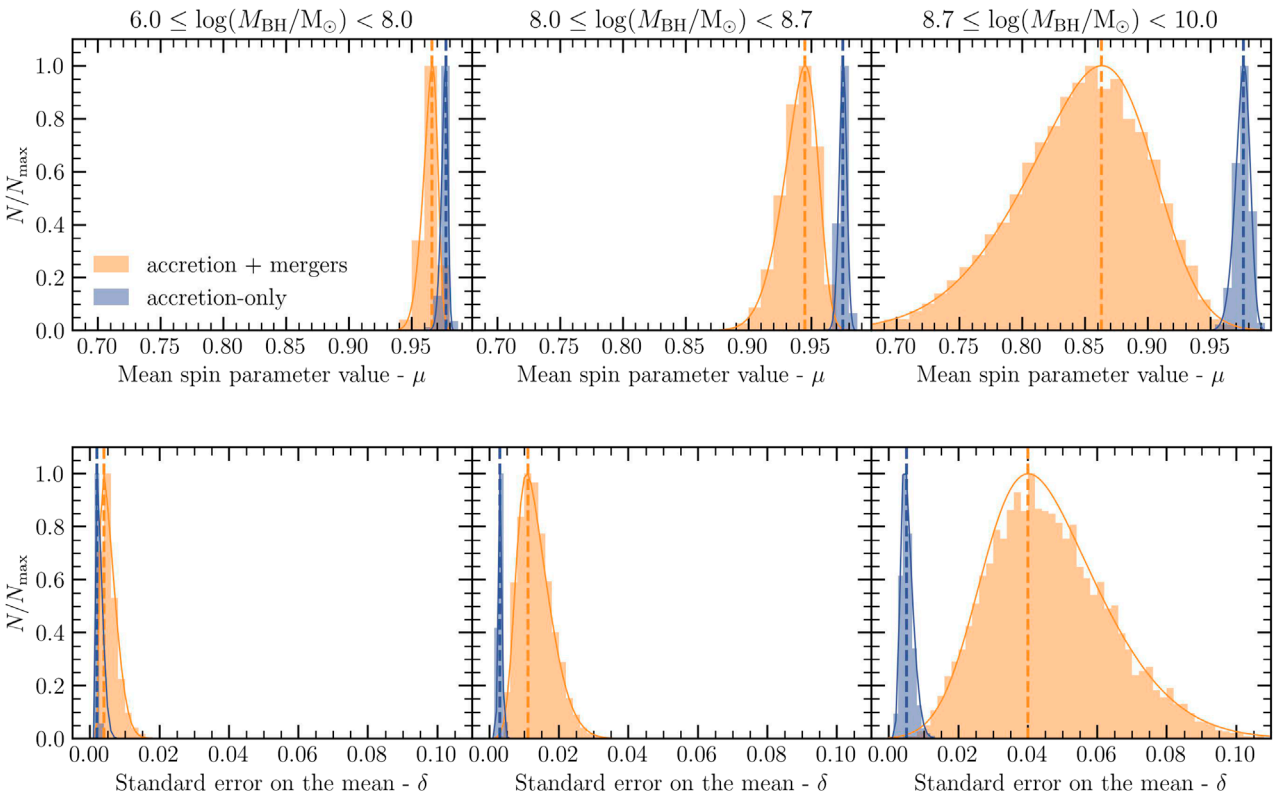

FIGURE 9
Summary of mean spin parameter estimates for 10^4 realisations of simulated *HEX-P* observing campaigns. **(A)**: distribution of expected mean $a*$ estimates (μ) in bins of M_{BH} for accretion-only (blue) and accretion + mergers (orange) SMBH growth scenarios. **(B)**: corresponding distributions of the standard errors on the mean (δ). Peak locations in each distribution are marked with vertical dashed lines. Differences between the mean spin measurements for the two scenarios become apparent for $M_{BH} > 10^8 M_{\odot}$ with the most massive bin showing the strongest signal.

and well-controlled biases—similar to the one envisioned here for *HEX-P*—is required to drive the combined SMBH spin constraints towards distinguishing the models.

10 Final remarks

We have shown that a sample of 100 AGN with the data quality determined in Section 7 and the mass distribution of the 100 brightest sources in our BASS selection (Section 6.1) is sufficient to distinguish between different cosmological SMBH growth scenarios. We now assess the level of observational investment from *HEX-P* that would be required to achieve this result. Given that a 150 ks *HEX-P* exposure provides the necessary data quality for our required spin constraints ($\sigma_{a*} \leq 0.15$ for $a* = 0.5$) for a source with a 2–10 keV flux of 6×10^{-12} erg cm^{-2} s^{-1}, we calculate a rough estimate for how long it would take for *HEX-P* to provide this level of data quality for all 100 sources by scaling this 150 ks

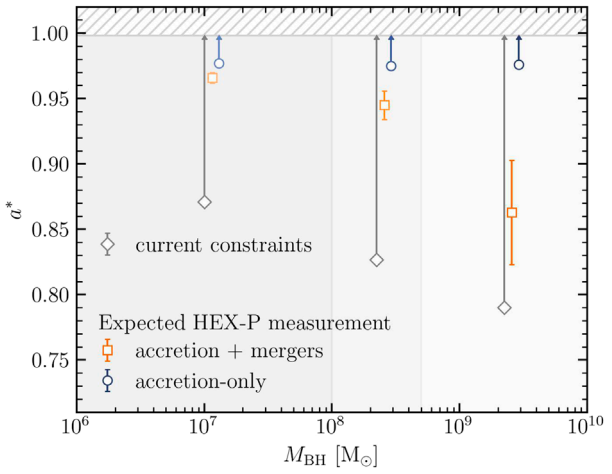

FIGURE 10
Comparison of mean spin parameter measurements in bins of M_{BH} between published constraints (grey diamonds) and expected *HEX-P* measurements for accretion-only (blue circles) and accretion + mergers (orange squares) SMBH growth scenarios. For *HEX-P* measurements we show the most likely result from our simulations, corresponding to the vertical dashed lines in Figure 9. Background shading marks our M_{BH} binning scheme, while the gray hatching at the top indicates the spin parameter range forbidden by the Thorne (1974) limit. The expected *HEX-P spin parameter measurements will allow us to differentiate between SMBH growth histories*, unlike $M_{BH} - a*$ constraints placed until now.

exposure to the actual observed 2–10 keV flux for each source (as reported in the BASS catalogue). Formally, this is a slightly conservative approach, as the instrumental background will make a smaller contribution for higher source fluxes, though even for the faintest sources, the background only impacts the highest energies probed by each detector (see Figure 7), so this simplification will only have a minimal effect across this sample. Summing the exposure required for each of the brightest 100 sources, we find that a total observing investment of ~10 Ms from *HEX-P* is necessary.

While this is a significant investment, it is a program that is achievable when spread over the full 5-year lifetime of *HEX-P*. This unique capability highlights *HEX-P*'s transformative nature as a next-generation X-ray observatory, allowing it to complete large observing programs otherwise unfeasible with coordinated exposures between separate hard and soft X-ray facilities. Collecting a sample of a 100 SMBH spin parameter measurements from *NuSTAR* observations combined with a soft X-ray observatory would require no less than 30 years to complete, given $a*$ publication trends since the mission's launch (see Figure 1 in Madsen et al. 2023). The strictly simultaneous broadband X-ray coverage of *HEX-P*, critical for SMBH spin parameter recovery, would render a large sample size straightforward to achieve, owing to flexible scheduling absent multi-facility coordination restrictions. In particular, a spin survey such as this could serve a similar function to the *HEX-P* mission as the ongoing *Swift*/BAT survey conducted by *NuSTAR* (e.g., Baloković et al., 2020). This program gradually builds up *NuSTAR* observations of hard X-ray sources detected by the *Swift*/BAT detector via regular scheduling of short "filler" observations within the primarily Guest Observer program. Indeed, even the longest exposures required here–150 ks – could be split into 3×50 ks observations for ease of scheduling. The regular inclusion of such observations in the schedule allows for increased flexibility to respond to transient phenomena (i.e., target-of-opportunity observations), as these survey observations can easily be rescheduled since they have no real time constraints and the simultaneity of the coverage across the full 0.2–80 keV bandpass is already guaranteed.

Most importantly, our study demonstrates that in the light of theoretical predictions delivered by state-of-the-art cosmological hydrodynamical simulations tracing SMBH spin evolution, only large statistical samples of consistent measurements are capable of isolating SMBH growth channels. Once radiative efficiency-spin bias is accounted for, the differences in statistical properties of SMBH populations in the $M_{BH} - a*$ plane decrease in magnitude, requiring both high precision on individual measurements and numerous AGN observations at $M_{BH} > 10^8 M_\odot$ to constrain average trends in spin parameter as a function of SMBH mass. Although such measurements are, in principle, possible with currently available instruments, they critically require simultaneous observations with soft and hard X-ray observatories (e.g., *XMM-Newton* and *NuSTAR*). The necessary exposure time comparable to the expected *HEX-P* investment for these observatories renders such a study unfeasible due to the limitations associated with program allocation and scheduling conflicts among individual instruments.

Beyond distinguishing cosmological SMBH growth scenarios via spin measurements, the high-S/N broadband X-ray data generated by such a survey would provide a legacy for the *HEX-P* mission, and broader studies of AGN in general. For example, inner disk inclinations will be well constrained (see Figure 7), providing further tests of the broad applicability of the Unified Model (Antonucci, 1993) as well as allowing for additional sanity checks of the reflection results/searches for disk warps via comparison of these inclinations with constraints from the outer disk from, e.g., VLT/GRAVITY (see the cases of NGC3783 and IRAS 09149–2461, where the inner and outer disk inclinations from reflectionstudies and GRAVITY are in excellent agreement: Brenneman et al., 2011; Walton et al., 2020; GRAVITY Collaboration et al., 2020; GRAVITY Collaboration et al., 2021). These observations would also provide strong constraints on the X-ray corona for a large sample of AGN, both in terms of its location (see Figure 7) and its plasma physics via temperature measurements; all these observations will allow for important constraints on the electron temperature, facilitating further tests of coronal models (e.g., Fabian et al., 2015; see also Kammoun et al. 2023). All-in-all, while a program of this nature would be a major investment, the scientific return provided would be suitably vast.

Data availability statement

The raw data supporting the conclusions of this article will be made available by the authors, without undue reservation.

Author contributions

JP: Conceptualization, Formal Analysis, Investigation, Methodology, Visualization, Writing–original draft, Writing–review and editing. JG: Conceptualization, Funding acquisition, Investigation, Project administration, Resources, Writing–original draft, Writing–review and editing. DW: Conceptualization, Formal Analysis, Investigation, Methodology, Writing–original draft, Writing–review and editing. RB: Conceptualization, Data curation, Writing–review and editing. DS: Writing–review and editing. DB: Writing–review and editing. DW: Writing–review and editing. SB: Writing–review and editing. PB: Writing–review and editing. JB: Writing–review and editing. C-TC: Writing–review and editing. PC: Writing–review and editing. TD: Writing–review and editing. AF: Writing–review and editing. EK: Writing–review and editing. KM: Writing–review and editing. LM: Writing–review and editing. GiM: Writing–review and editing. GaM: Writing–review and editing. EN: Writing–review and editing. AP: Writing–review and editing. SP: Writing–review and editing. CR: Writing–review and editing. FT: Writing–review and editing. NT-A: Writing–review and editing. K-WW: Writing–review and editing.

Funding

The author(s) declare financial support was received for the research, authorship, and/or publication of this article. JP and JG acknowledge support from NASA grants 80NSSC21K1567 and 80NSSC22K1120. The work of DS was carried out at the Jet Propulsion Laboratory, California Institute of Technology, under a contract with NASA. CR acknowledges support from the Fondecyt Regular (grant 1230345) and ANID BASAL (project FB210003). LM acknowledges support from the CITA National Fellowship.

Acknowledgments

We would like to thank the anonymous referees for carefully reading the manuscript and for providing constructive comments which helped improve the quality of the paper. We would also like to acknowledge the journal editor, Renee Ludlam, recognizing her very smooth handling of the peer review process.

Conflict of interest

The authors declare that the research was conducted in the absence of any commercial or financial relationships that could be construed as a potential conflict of interest.

Publisher's note

All claims expressed in this article are solely those of the authors and do not necessarily represent those of their affiliated organizations, or those of the publisher, the editors and the reviewers. Any product that may be evaluated in this article, or claim that may be made by its manufacturer, is not guaranteed or endorsed by the publisher.

Supplementary material

The Supplementary Material for this article can be found online at: https://www.frontiersin.org/articles/10.3389/fspas.2024.1324796/full#supplementary-material

References

Alexander, D. M., and Hickox, R. C. (2012). What drives the growth of black holes? *New Astron. Rev.* 56, 93–121. doi:10.1016/j.newar.2011.11.003

Alston, W. N., Fabian, A. C., Kara, E., Parker, M. L., Dovciak, M., Pinto, C., et al. (2020). A dynamic black hole corona in an active galaxy through X-ray reverberation mapping. *Nat. Astron.* 4, 597–602. doi:10.1038/s41550-019-1002-x

Annuar, A., Gandhi, P., Alexander, D. M., Lansbury, G. B., Arévalo, P., Ballantyne, D. R., et al. (2015). NuSTAR observations of the compton-thick active galactic nucleus and ultraluminous X-ray source candidate in NGC 5643. *Astrophysical J.* 815, 36. doi:10.1088/0004-637X/815/1/36

Antonucci, R. (1993). Unified models for active galactic nuclei and quasars. *ARA&A* 31, 473–521. doi:10.1146/annurev.aa.31.090193.002353

Arévalo, P., Bauer, F. E., Puccetti, S., Walton, D. J., Koss, M., Boggs, S. E., et al. (2014). The 2-79 keV X-ray spectrum of the circinus galaxy with NuSTAR, XMM-Newton, and chandra: a fully compton-thick active galactic nucleus. *Astrophysical J.* 791, 81. doi:10.1088/0004-637X/791/2/81

Arnaud, K. A. (1996). "XSPEC: the first ten years," in *Astronomical data analysis software and systems V*. Editors G. H. Jacoby, and J. Barnes (San Francisco: Astron. Soc. Pac.), 17.

Athanassoula, E., Bienayme, O., Martinet, L., and Pfenniger, D. (1983). Orbits as building blocks of a barred galaxy model. *A&A* 127, 349–360.

Avara, M. J., McKinney, J. C., and Reynolds, C. S. (2016). Efficiency of thin magnetically arrested discs around black holes. *MNRAS* 462, 636–648. doi:10.1093/mnras/stw1643

Ballantyne, D. R., McDuffie, J. R., and Rusin, J. S. (2011). A correlation between the ionization state of the inner accretion disk and the Eddington ratio of active galactic nuclei. *Astrophysical J.* 734, 112. doi:10.1088/0004-637X/734/2/112

Baloković, M., Harrison, F. A., Madejski, G., Comastri, A., Ricci, C., Annuar, A., et al. (2020). NuSTAR survey of obscured swift/BAT-selected active galactic nuclei. II. Median high-energy cutoff in seyfert II hard X-ray spectra. *Astrophysical J.* 905, 41. doi:10.3847/1538-4357/abc342

Bambi, C. (2017). *Black holes: a laboratory for testing strong gravity*. Singapore: Springer Nature. doi:10.1007/978-981-10-4524-0

Bambi, C., Brenneman, L. W., Dauser, T., García, J. A., Grinberg, V., Ingram, A., et al. (2021). Towards precision measurements of accreting black holes using X-ray reflection spectroscopy. *Space Sci. Rev.* 217, 65. doi:10.1007/s11214-021-00841-8

Barausse, E., and Rezzolla, L. (2009). Predicting the direction of the final spin from the coalescence of two black holes. *Astrophysical J.* 704, L40–L44. doi:10.1088/0004-637X/704/1/L40

Bardeen, J. M. (1970). Kerr metric black holes. *Nat* 226, 64–65. doi:10.1038/226064a0

Bardeen, J. M., Press, W. H., and Teukolsky, S. A. (1972). Rotating black holes: locally nonrotating frames, energy extraction, and scalar synchrotron radiation. *Astrophysical J.* 178, 347–370. doi:10.1086/151796

Barnes, J. E., and Hernquist, L. (1992). Dynamics of interacting galaxies. *ARA&A* 30, 705–742. doi:10.1146/annurev.aa.30.090192.003421

Barret, D., and Cappi, M. (2019). Inferring black hole spins and probing accretion/ejection flows in AGNs with the Athena X-ray Integral Field Unit. *A&A* 628, A5. doi:10.1051/0004-6361/201935817

Barthelmy, S. D., Barbier, L. M., Cummings, J. R., Fenimore, E. E., Gehrels, N., Hullinger, D., et al. (2005). The Burst Alert telescope (BAT) on the SWIFT midex mission. *Space Sci. Rev.* 120, 143–164. doi:10.1007/s11214-005-5096-3

Beckmann, R. S., Devriendt, J., Slyz, A., Peirani, S., Richardson, M. L. A., Dubois, Y., et al. (2017). Cosmic evolution of stellar quenching by AGN feedback: clues from the Horizon-AGN simulation. *MNRAS* 472, 949–965. doi:10.1093/mnras/stx1831

Beckmann, R. S., Smethurst, R. J., Simmons, B. D., Coil, A., Dubois, Y., Garland, I. L., et al. (2023). Supermassive black holes in merger-free galaxies have higher spins which are preferentially aligned with their host galaxy. *MNRAS* 527, 10867–10877. doi:10.1093/mnras/stad1795

Berti, E., and Volonteri, M. (2008). Cosmological black hole spin evolution by mergers and accretion. *Astrophysical J.* 684, 822–828. doi:10.1086/590379

Birzan, L., Rafferty, D. A., McNamara, B. R., Wise, M. W., and Nulsen, P. E. J. (2004). A systematic study of radio-induced x-ray cavities in clusters, groups, and galaxies. *Astrophysical J.* 607, 800–809. doi:10.1086/383519

Blandford, R. D., and McKee, C. F. (1982). Reverberation mapping of the emission line regions of Seyfert galaxies and quasars. *Astrophysical J.* 255, 419–439. doi:10.1086/159843

Blandford, R. D., and Znajek, R. L. (1977). Electromagnetic extraction of energy from Kerr black holes. *MNRAS* 179, 433–456. doi:10.1093/mnras/179.3.433

Bondi, H. (1952). On spherically symmetrical accretion. *MNRAS* 112, 195–204. doi:10.1093/mnras/112.2.195

Bondi, H., and Hoyle, F. (1944). On the mechanism of accretion by stars. *MNRAS* 104, 273–282. doi:10.1093/mnras/104.5.273

Bonson, K., and Gallo, L. C. (2016). How well can we measure supermassive black hole spin? *MNRAS* 458, 1927–1938. doi:10.1093/mnras/stw466

Bower, R. G., Benson, A. J., Malbon, R., Helly, J. C., Frenk, C. S., Baugh, C. M., et al. (2006). Breaking the hierarchy of galaxy formation. *MNRAS* 370, 645–655. doi:10.1111/j.1365-2966.2006.10519.x

Brenneman, L. W., and Reynolds, C. S. (2006). Constraining black hole spin via X-ray spectroscopy. *Astrophysical J.* 652, 1028–1043. doi:10.1086/508146

Brenneman, L. W., Reynolds, C. S., Nowak, M. A., Reis, R. C., Trippe, M., Fabian, A. C., et al. (2011). The spin of the supermassive black hole in NGC 3783. *Astrophysical J.* 736, 103. doi:10.1088/0004-637X/736/2/103

Brewer, B. J., Treu, T., Pancoast, A., Barth, A. J., Bennert, V. N., Bentz, M. C., et al. (2011). The mass of the black hole in arp 151 from bayesian modeling of reverberation mapping data. *Astrophysical J.* 733, L33. doi:10.1088/2041-8205/733/2/L33

Buisson, D. J. K., Parker, M. L., Kara, E., Vasudevan, R. V., Lohfink, A. M., Pinto, C., et al. (2018). NuSTAR observations of Mrk 766: distinguishing reflection from absorption. *MNRAS* 480, 3689–3701. doi:10.1093/mnras/sty2081

Bustamante, S., and Springel, V. (2019). Spin evolution and feedback of supermassive black holes in cosmological simulations. *MNRAS* 490, 4133–4153. doi:10.1093/mnras/stz2836

Cackett, E. M., Chiang, C.-Y., McHardy, I., Edelson, R., Goad, M. R., Horne, K., et al. (2018). Accretion disk reverberation with hubble space telescope observations of NGC 4593: evidence for diffuse continuum lags. *Astrophysical J.* 857, 53. doi:10.3847/1538-4357/aab4f7

Carter, B. (1971). Axisymmetric black hole has only two degrees of freedom. *Phys. Rev. Lett.* 26, 331–333. doi:10.1103/PhysRevLett.26.331

Chamani, W., Koljonen, K., and Savolainen, T. (2020). Joint XMM-Newton and NuSTAR observations of the reflection spectrum of III Zw 2. *A&A* 635, A172. doi:10.1051/0004-6361/201936992

Choudhury, K., García, J. A., Steiner, J. F., and Bambi, C. (2017). Testing the performance and accuracy of the RELXILL model for the relativistic X-ray reflection from accretion disks. *Astrophysical J.* 851, 57. doi:10.3847/1538-4357/aa9925

Cicone, C., Maiolino, R., Sturm, E., Graciá-Carpio, J., Feruglio, C., Neri, R., et al. (2014). Massive molecular outflows and evidence for AGN feedback from CO observations. *A&A* 562, A21. doi:10.1051/0004-6361/201322464

Cole, S., Lacey, C. G., Baugh, C. M., and Frenk, C. S. (2000). Hierarchical galaxy formation. *MNRAS* 319, 168–204. doi:10.1046/j.1365-8711.2000.03879.x

Connors, R., Tomsick, J., Draghis, P., Coughenour, B., Shaw, A., Garcia, J., et al. (2023). *The high energy X-ray probe (HEX-P): probing accretion onto stellar mass black holes*. arXiv e-prints , arXiv:2311.04782.

Crain, R. A., and van de Voort, F. (2023). Hydrodynamical simulations of the galaxy population: enduring successes and outstanding challenges. *ARA&A* 61, 473–515. doi:10.1146/annurev-astro-041923-043618

Croton, D. J., Springel, V., White, S. D. M., De Lucia, G., Frenk, C. S., Gao, L., et al. (2006). The many lives of active galactic nuclei: cooling flows, black holes and the luminosities and colours of galaxies. *MNRAS* 365, 11–28. doi:10.1111/j.1365-2966.2005.09675.x

Curd, B., and Narayan, R. (2023). GRRMHD simulations of MAD accretion discs declining from super-Eddington to sub-Eddington accretion rates. *MNRAS* 518, 3441–3461. doi:10.1093/mnras/stac3330

Dauser, T., García, J., Parker, M. L., Fabian, A. C., and Wilms, J. (2014). The role of the reflection fraction in constraining black hole spin. *MNRAS* 444, L100–L104. doi:10.1093/mnrasl/slu125

Dauser, T., García, J., and Wilms, J. (2016). Relativistic reflection: review and recent developments in modeling. *Astron. Nachrichten* 337, 362–367. doi:10.1002/asna.201612314

Dauser, T., Wilms, J., Reynolds, C. S., and Brenneman, L. W. (2010). Broad emission lines for a negatively spinning black hole. *MNRAS* 409, 1534–1540. doi:10.1111/j.1365-2966.2010.17393.x

Debattista, V. P., Mayer, L., Carollo, C. M., Moore, B., Wadsley, J., and Quinn, T. (2006). The secular evolution of disk structural parameters. *Astrophysical J.* 645, 209–227. doi:10.1086/504147

de La Calle Pérez, I., Longinotti, A. L., Guainazzi, M., Bianchi, S., Dovčiak, M., Cappi, M., et al. (2010). FERO: finding extreme relativistic objects. I. Statistics of relativistic Fe K_α lines in radio-quiet Type 1 AGN. *A&A* 524, A50. doi:10.1051/0004-6361/200913798

De Marco, B., Ponti, G., Cappi, M., Dadina, M., Uttley, P., Cackett, E. M., et al. (2013). Discovery of a relation between black hole mass and soft X-ray time lags in active galactic nuclei. *MNRAS* 431, 2441–2452. doi:10.1093/mnras/stt339

Di Matteo, T., Springel, V., and Hernquist, L. (2005). Energy input from quasars regulates the growth and activity of black holes and their host galaxies. *Nat* 433, 604–607. doi:10.1038/nature03335

Dotti, M., Colpi, M., Pallini, S., Perego, A., and Volonteri, M. (2013). On the orientation and magnitude of the black hole spin in galactic nuclei. *Astrophysical J.* 762, 68. doi:10.1088/0004-637X/762/2/68

Draghis, P. A., Miller, J. M., Zoghbi, A., Reynolds, M., Costantini, E., Gallo, L. C., et al. (2023). A systematic view of ten new black hole spins. *Astrophysical J.* 946, 19. doi:10.3847/1538-4357/acafe7

Dubois, Y., Beckmann, R., Bournaud, F., Choi, H., Devriendt, J., Jackson, R., et al. (2021). Introducing the NEWHORIZON simulation: galaxy properties with resolved internal dynamics across cosmic time. *A&A* 651, A109. doi:10.1051/0004-6361/202039429

Dubois, Y., Peirani, S., Pichon, C., Devriendt, J., Gavazzi, R., Welker, C., et al. (2016). The HORIZON-AGN simulation: morphological diversity of galaxies promoted by AGN feedback. *MNRAS* 463, 3948–3964. doi:10.1093/mnras/stw2265

Dubois, Y., Pichon, C., Welker, C., Le Borgne, D., Devriendt, J., Laigle, C., et al. (2014a). Dancing in the dark: galactic properties trace spin swings along the cosmic web. *MNRAS* 444, 1453–1468. doi:10.1093/mnras/stu1227

Dubois, Y., Volonteri, M., and Silk, J. (2014b). Black hole evolution - III. Statistical properties of mass growth and spin evolution using large-scale hydrodynamical cosmological simulations. *MNRAS* 440, 1590–1606. doi:10.1093/mnras/stu373

Dubois, Y., Volonteri, M., Silk, J., Devriendt, J., and Slyz, A. (2014c). Black hole evolution - II. Spinning black holes in a supernova-driven turbulent interstellar medium. *MNRAS* 440, 2333–2346. doi:10.1093/mnras/stu425

Duro, R., Dauser, T., Wilms, J., Pottschmidt, K., Nowak, M. A., Fritz, S., et al. (2011). The broad iron Kα line of Cygnus X-1 as seen by XMM-Newton in the EPIC-pn modified timing mode. *A&A* 533, L3. doi:10.1051/0004-6361/201117446

Edelson, R., Gelbord, J., Cackett, E., Peterson, B. M., Horne, K., Barth, A. J., et al. (2019). The first Swift intensive AGN accretion disk reverberation mapping survey. *Astrophysical J.* 870, 123. doi:10.3847/1538-4357/aaf3b4

Eraerds, T., Antonelli, V., Davis, C., Hall, D., Hetherington, O., Holland, A., et al. (2021). Enhanced simulations on the athena/wide field imager instrumental background. *J. Astronomical Telesc. Instrum. Syst.* 7, 034001. doi:10.1117/1.JATIS.7.3.034001

Esin, A. A., McClintock, J. E., and Narayan, R. (1997). Advection-dominated accretion and the spectral states of black hole X-ray binaries: application to nova muscae 1991. *Astrophysical J.* 489, 865–889. doi:10.1086/304829

Event Horizon Telescope Collaboration, Akiyama, K., Alberdi, A., Alef, W., Asada, K., Azulay, R., et al. (2019). First M87 event horizon telescope results. I. The shadow of the supermassive black hole. *Astrophysical J.* 875, L1. doi:10.3847/2041-8213/ab0ec7

Event Horizon Telescope Collaboration, Akiyama, K., Alberdi, A., Alef, W., Algaba, J. C., Anantua, R., et al. (2022). First Sagittarius A ∗ event horizon telescope results. I. The shadow of the supermassive black hole in the center of the Milky way. *Astrophysical J.* 930, L12. doi:10.3847/2041-8213/ac6674

Fabian, A. C. (2012). Observational evidence of active galactic nuclei feedback. *ARA&A* 50, 455–489. doi:10.1146/annurev-astro-081811-125521

Fabian, A. C., and Iwasawa, K. (1999). The mass density in black holes inferred from the X-ray background. *MNRAS* 303, L34–L36. doi:10.1046/j.1365-8711.1999.02404.x

Fabian, A. C., Iwasawa, K., Reynolds, C. S., and Young, A. J. (2000). Broad iron lines in active galactic nuclei. *PASP* 112, 1145–1161. doi:10.1086/316610

Fabian, A. C., Lohfink, A., Kara, E., Parker, M. L., Vasudevan, R., and Reynolds, C. S. (2015). Properties of AGN coronae in the NuSTAR era. *MNRAS* 451, 4375–4383. doi:10.1093/mnras/stv1218

Fabian, A. C., Rees, M. J., Stella, L., and White, N. E. (1989). X-ray fluorescence from the inner disc in Cygnus X-1. *MNRAS* 238, 729–736. doi:10.1093/mnras/238.3.729

Fabian, A. C., Zoghbi, A., Ross, R. R., Uttley, P., Gallo, L. C., Brandt, W. N., et al. (2009). Broad line emission from iron K- and L-shell transitions in the active galaxy 1H0707-495. *Nat* 459, 540–542. doi:10.1038/nature08007

Faucher-Giguère, C.-A., and Quataert, E. (2012). The physics of galactic winds driven by active galactic nuclei. *MNRAS* 425, 605–622. doi:10.1111/j.1365-2966.2012.21512.x

Fausnaugh, M. M., Denney, K. D., Barth, A. J., Bentz, M. C., Bottorff, M. C., Carini, M. T., et al. (2016). Space telescope and optical reverberation mapping project. III. Optical continuum emission and broadband time delays in NGC 5548. *Astrophysical J.* 821, 56. doi:10.3847/0004-637X/821/1/56

Ferrarese, L., and Merritt, D. (2000). A fundamental relation between supermassive black holes and their host galaxies. *Astrophysical JournalL* 539, L9–L12. doi:10.1086/312838

Feruglio, C., Maiolino, R., Piconcelli, E., Menci, N., Aussel, H., Lamastra, A., et al. (2010). Quasar feedback revealed by giant molecular outflows. *A&A* 518, L155. doi:10.1051/0004-6361/201015164

Fiacconi, D., Sijacki, D., and Pringle, J. E. (2018). Galactic nuclei evolution with spinning black holes: method and implementation. *MNRAS* 477, 3807–3835. doi:10.1093/mnras/sty893

Fiore, F., Feruglio, C., Shankar, F., Bischetti, M., Bongiorno, A., Brusa, M., et al. (2017). AGN wind scaling relations and the co-evolution of black holes and galaxies. *A&A* 601, A143. doi:10.1051/0004-6361/201629478

Gallo, L. C., Miniutti, G., Miller, J. M., Brenneman, L. W., Fabian, A. C., Guainazzi, M., et al. (2011). Multi-epoch X-ray observations of the Seyfert 1.2 galaxy Mrk 79: bulk motion of the illuminating X-ray source. *MNRAS* 411, 607–619. doi:10.1111/j.1365-2966.2010.17705.x

García, J., Dauser, T., Lohfink, A., Kallman, T. R., Steiner, J. F., McClintock, J. E., et al. (2014). Improved reflection models of black hole accretion disks: treating the angular distribution of X-rays. *Astrophysical J.* 782, 76. doi:10.1088/0004-637X/782/2/76

García, J., and Kallman, T. R. (2010). X-Ray reflected spectra from accretion disk models. I. Constant density atmospheres. *Astrophysical J.* 718, 695–706. doi:10.1088/0004-637X/718/2/695

García, J. A., Kara, E., Walton, D., Beuchert, T., Dauser, T., Gatuzz, E., et al. (2019). Implications of the warm corona and relativistic reflection models for the soft excess in mrk 509. *Astrophysical J.* 871, 88. doi:10.3847/1538-4357/aaf739

García, J. A., Steiner, J. F., McClintock, J. E., Remillard, R. A., Grinberg, V., and Dauser, T. (2015). X-ray reflection spectroscopy of the black hole GX 339–4: exploring the hard state with unprecedented sensitivity. *Astrophysical J.* 813, 84. doi:10.1088/0004-637X/813/2/84

García-Burillo, S., Combes, F., Schinnerer, E., Boone, F., and Hunt, L. K. (2005). Molecular gas in NUclei of GAlaxies (NUGA): IV. Gravitational torques and AGN feeding. *A&A* 441, 1011–1030. doi:10.1051/0004-6361:20052900

Gardner, J. P., Mather, J. C., Abbott, R., Abell, J. S., Abernathy, M., Abney, F. E., et al. (2023). The James Webb space telescope mission. *PASP* 135, 068001. doi:10.1088/1538-3873/acd1b5

Gebhardt, K., Richstone, D., Kormendy, J., Lauer, T. R., Ajhar, E. A., Bender, R., et al. (2000). Axisymmetric, three-integral models of galaxies: a massive black hole in NGC 3379. *AJ* 119, 1157–1171. doi:10.1086/301240

Gehrels, N., Chincarini, G., Giommi, P., Mason, K. O., Nousek, J. A., Wells, A. A., et al. (2004). The*Swift*Gamma-ray Burst mission. *Astrophysical J.* 611, 1005–1020. doi:10.1086/422091

Genzel, R., Eisenhauer, F., and Gillessen, S. (2010). The Galactic Center massive black hole and nuclear star cluster. *Rev. Mod. Phys.* 82, 3121–3195. doi:10.1103/RevModPhys.82.3121

George, I. M., and Fabian, A. C. (1991). X-ray reflection from cold matter in active galactic nuclei and X-ray binaries. *MNRAS* 249, 352–367. doi:10.1093/mnras/249.2.352

Ghez, A. M., Klein, B. L., Morris, M., and Becklin, E. E. (1998). High proper-motion stars in the vicinity of Sagittarius A ∗ : evidence for a supermassive black hole at the center of our galaxy. *Astrophysical J.* 509, 678–686. doi:10.1086/306528

Ghez, A. M., Salim, S., Weinberg, N. N., Lu, J. R., Do, T., Dunn, J. K., et al. (2008). Measuring distance and properties of the Milky way's central supermassive black hole with stellar orbits. *Astrophysical J.* 689, 1044–1062. doi:10.1086/592738

Giustini, M., and Proga, D. (2019). A global view of the inner accretion and ejection flow around super massive black holes. Radiation-driven accretion disk winds in a physical context. *A&A* 630, A94. doi:10.1051/0004-6361/201833810

Gravity Collaboration, Abuter, R., Amorim, A., Anugu, N., Bauböck, M., Benisty, M., et al. (2018). Detection of the gravitational redshift in the orbit of the star S2 near the Galactic centre massive black hole. *A&A* 615, L15. doi:10.1051/0004-6361/201833718

GRAVITY Collaboration, Amorim, A., Brandner, W., Clénet, Y., Davies, R., de Zeeuw, P. T., et al. (2020). *The spatially resolved broad line region of IRAS 09149-6206*. arXiv e-prints , arXiv:2009.08463.

GRAVITY Collaboration, Amorim, A., Bauböck, M., Brandner, W., Bolzer, M., Clénet, Y., et al. (2021). The central parsec of NGC 3783: a rotating broad emission line region, asymmetric hot dust structure, and compact coronal line region. *A&A* 648, A117. doi:10.1051/0004-6361/202040061

Greene, J. E., and Ho, L. C. (2005). Estimating black hole masses in active galaxies using the Hα emission line. *Astrophysical J.* 630, 122–129. doi:10.1086/431897

Guo, W.-J., Li, Y.-R., Zhang, Z.-X., Ho, L. C., and Wang, J.-M. (2022). Accretion disk size measurements of active galactic nuclei monitored by the zwicky transient facility. *Astrophysical J.* 929, 19. doi:10.3847/1538-4357/ac4e84

Harikane, Y., Zhang, Y., Nakajima, K., Ouchi, M., Isobe, Y., Ono, Y., et al. (2023). *JWST/NIRSpec first census of broad-line AGNs at z=4-7: detection of 10 faint AGNs with M_BH˜106-107 M_sun and their host galaxy properties*. arXiv e-prints , arXiv:2303.11946.

Healy, J., Lousto, C. O., and Zlochower, Y. (2014). Remnant mass, spin, and recoil from spin aligned black-hole binaries. *Phys. Rev. D.* 90, 104004. doi:10.1103/PhysRevD.90.104004

Henriques, B. M. B., White, S. D. M., Lilly, S. J., Bell, E. F., Bluck, A. F. L., and Terrazas, B. A. (2019). The origin of the mass scales for maximal star formation efficiency and quenching: the critical role of supernovae. *MNRAS* 485, 3446–3456. doi:10.1093/mnras/stz577

Hlavacek-Larrondo, J., Fabian, A. C., Edge, A. C., Ebeling, H., Sanders, J. S., Hogan, M. T., et al. (2012). Extreme AGN feedback in the MAssive Cluster Survey: a detailed study of X-ray cavities at z ∼0.3. *Mon. Notices R. Astronomical Soc.* 421, 1360–1384. doi:10.1111/j.1365-2966.2011.20405.x

Hlavacek-Larrondo, J., McDonald, M., Benson, B. A., Forman, W. R., Allen, S. W., Bleem, L. E., et al. (2015). X-ray cavities in a sample of 83 spt-selected clusters of galaxies: tracing the evolution of agn feedback in clusters of galaxies out to z = 1.2. *Astrophysical J.* 805, 35. doi:10.1088/0004-637X/805/1/35

Hofmann, F., Barausse, E., and Rezzolla, L. (2016). The final spin from binary black holes in quasi-circular orbits. *Astrophysical J.* 825, L19. doi:10.3847/2041-8205/825/2/L19

Homayouni, Y., Sturm, M. R., Trump, J. R., Horne, K., Grier, C. J., Shen, Y., et al. (2022). The sloan digital sky survey reverberation mapping project: UV-optical accretion disk measurements with the hubble space telescope. *Astrophysical J.* 926, 225. doi:10.3847/1538-4357/ac478b

Hopkins, P. F., Hernquist, L., Cox, T. J., Di Matteo, T., Robertson, B., and Springel, V. (2006). A unified, merger-driven model of the origin of starbursts, quasars, the cosmic X-ray background, supermassive black holes, and galaxy spheroids. *Astrophys. J. Suppl. S* 163, 1–49. doi:10.1086/499298

Hopkins, P. F., Kereš, D., Oñorbe, J., Faucher-Giguère, C.-A., Quataert, E., Murray, N., et al. (2014). Galaxies on FIRE (Feedback in Realistic Environments): stellar feedback explains cosmologically inefficient star formation. *MNRAS* 445, 581–603. doi:10.1093/mnras/stu1738

Hopkins, P. F., and Quataert, E. (2010). How do massive black holes get their gas? *MNRAS* 407, 1529–1564. doi:10.1111/j.1365-2966.2010.17064.x

Hopkins, P. F., Quataert, E., and Murray, N. (2011). Self-regulated star formation in galaxies via momentum input from massive stars. *MNRAS* 417, 950–973. doi:10.1111/j.1365-2966.2011.19306.x

Hoyle, F., and Lyttleton, R. A. (1939). The effect of interstellar matter on climatic variation. *Proc. Camb. Philosophical Soc.* 35, 405–415. doi:10.1017/S0305004100021150

Ingram, A., Mastroserio, G., van der Klis, M., Nathan, E., Connors, R., Dauser, T., et al. (2022). On measuring the Hubble constant with X-ray reverberation mapping of active galactic nuclei. *MNRAS* 509, 619–633. doi:10.1093/mnras/stab2950

Israel, W. (1967). Event horizons in static vacuum space-times. *Phys. Rev.* 164, 1776–1779. doi:10.1103/PhysRev.164.1776

Israel, W. (1968). Event horizons in static electrovac space-times. *Commun. Math. Phys.* 8, 245–260. doi:10.1007/BF01645859

Jiang, J., Buisson, D. J. K., Dauser, T., Fabian, A. C., Fürst, F., Gallo, L. C., et al. (2022). A NuSTAR and Swift view of the hard state of MAXI J1813-095. *MNRAS* 514, 1952–1960. doi:10.1093/mnras/stac1401

Jiang, J., Fabian, A. C., Dauser, T., Gallo, L., García, J. A., Kara, E., et al. (2019). High Density Reflection Spectroscopy - II. The density of the inner black hole accretion disc in AGN. *MNRAS* 489, 3436–3455. doi:10.1093/mnras/stz2326

Jiang, J., Parker, M. L., Fabian, A. C., Alston, W. N., Buisson, D. J. K., Cackett, E. M., et al. (2018). The 1.5 Ms observing campaign on IRAS 13224-3809 - I. X-ray spectral analysis. *MNRAS* 477, 3711–3726. doi:10.1093/mnras/sty836

Jiang, Y.-F., Green, P. J., Greene, J. E., Morganson, E., Shen, Y., Pancoast, A., et al. (2017). Detection of time lags between quasar continuum emission bands based on pan-STARRS light curves. *Astrophysical J.* 836, 186. doi:10.3847/1538-4357/aa5b91

Kammoun, E., Lohfink, A. M., Masterson, M., Wilkins, D. R., Zhao, X., Baloković, M., et al. (2023). *The High Energy X-ray Probe (HEX-P): probing the physics of the X-ray corona in active galactic nuclei*. *arXiv e-prints* arXiv:2311.04679. doi:10.3389/fspas.2023.1308056

Kammoun, E. S., Nardini, E., and Risaliti, G. (2018). Testing the accuracy of reflection-based supermassive black hole spin measurements in AGN. *A&A* 614, A44. doi:10.1051/0004-6361/201732377

Kara, E., Alston, W. N., Fabian, A. C., Cackett, E. M., Uttley, P., Reynolds, C. S., et al. (2016). A global look at X-ray time lags in Seyfert galaxies. *MNRAS* 462, 511–531. doi:10.1093/mnras/stw1695

Kara, E., Steiner, J. F., Fabian, A. C., Cackett, E. M., Uttley, P., Remillard, R. A., et al. (2019). The corona contracts in a black-hole transient. *Nat* 565, 198–201. doi:10.1038/s41586-018-0803-x

Katz, N., Weinberg, D. H., and Hernquist, L. (1996). Cosmological simulations with TreeSPH. *Astrophysical JournalS* 105, 19. doi:10.1086/192305

Kaviraj, S., Laigle, C., Kimm, T., Devriendt, J. E. G., Dubois, Y., Pichon, C., et al. (2017). The Horizon-AGN simulation: evolution of galaxy properties over cosmic time. *MNRAS* 467, stx126–4752. doi:10.1093/mnras/stx126

Kereš, D., Katz, N., Weinberg, D. H., and Davé, R. (2005). How do galaxies get their gas? *MNRAS* 363, 2–28. doi:10.1111/j.1365-2966.2005.09451.x

Kesden, M. (2008). Can binary mergers produce maximally spinning black holes? *Phys. Rev. D.* 78, 084030. doi:10.1103/PhysRevD.78.084030

King, A. L., Walton, D. J., Miller, J. M., Barret, D., Boggs, S. E., Christensen, F. E., et al. (2014). The disk wind in the rapidly spinning stellar-mass black hole 4U 1630-472 observed with NuSTAR. *Astrophysical J.* 784, L2. doi:10.1088/2041-8205/784/1/L2

King, A. R., Pringle, J. E., and Hofmann, J. A. (2008). The evolution of black hole mass and spin in active galactic nuclei. *MNRAS* 385, 1621–1627. doi:10.1111/j.1365-2966.2008.12943.x

Kollmeier, J., Anderson, S. F., Blanc, G. A., Blanton, M. R., Covey, K. R., Crane, J., et al. (2019). SDSS-V pioneering panoptic spectroscopy. *Bull. Am. Astronomical Soc.* 51, 274.

Komatsu, E., Smith, K. M., Dunkley, J., Bennett, C. L., Gold, B., Hinshaw, G., et al. (2011). Seven-year wilkinson microwave anisotropy probe (WMAP) observations: cosmological interpretation. *Astrophysical JournalS* 192, 18. doi:10.1088/0067-0049/192/2/18

Kormendy, J., Bender, R., Evans, A. S., and Richstone, D. (1998). The mass distribution in the elliptical galaxy NGC 3377: evidence for a 2 × 10[TSUP]8[/TSUP] [ITAL]M[/ITAL] [TINF] [sun] [/TINF] black hole. *AJ* 115, 1823–1839. doi:10.1086/300313

Kormendy, J., and Ho, L. C. (2013). Coevolution (or not) of supermassive black holes and host galaxies. *ARA&A* 51, 511–653. doi:10.1146/annurev-astro-082708-101811

Koss, M., Trakhtenbrot, B., Ricci, C., Lamperti, I., Oh, K., Berney, S., et al. (2017). BAT AGN spectroscopic survey. I. Spectral measurements, derived quantities, and AGN demographics. *Astrophysical J.* 850, 74. doi:10.3847/1538-4357/aa8ec9

Koss, M. J., Trakhtenbrot, B., Ricci, C., Oh, K., Bauer, F. E., Stern, D., et al. (2022). *VizieR online data catalog: BASS. XXV. DR2 stellar velocity dispersions (Koss+, 2022).* Strasbourg, France: VizieR Online Data Catalog.

Kuijken, K., and Merrifield, M. R. (1995). Establishing the connection between peanut-shaped bulges and galactic bars. *Astrophysical J.* 443, L13. doi:10.1086/187824

Laor, A. (1991). Line profiles from a disk around a rotating black hole. *Astrophysical J.* 376, 90–94. doi:10.1086/170257

Liska, M., Tchekhovskoy, A., Ingram, A., and van der Klis, M. (2019). Bardeen-Petterson alignment, jets, and magnetic truncation in GRMHD simulations of tilted thin accretion discs. *MNRAS* 487, 550–561. doi:10.1093/mnras/stz834

Lowell, B., Jacquemin-Ide, J., Tchekhovskoy, A., and Duncan, A. (2023). *Rapid black hole spin-down by thick magnetically arrested disks. arXiv e-prints* arXiv:2302.01351.

Madsen, K. K., García, J. A., Stern, D., Armini, R., Basso, S., Coutinho, D., et al. (2023). *The high energy X-ray probe (HEX-P): instrument and mission profile. arXiv e-print*s , arXiv:2312.04678.

Magdziarz, P., and Zdziarski, A. A. (1995). Angle-dependent Compton reflection of X-rays and gamma-rays. *MNRAS* 273, 837–848. doi:10.1093/mnras/273.3.837

Magorrian, J., Tremaine, S., Richstone, D., Bender, R., Bower, G., Dressler, A., et al. (1998). The demography of massive dark objects in galaxy centers. *AJ* 115, 2285–2305. doi:10.1086/300353

Maiolino, R., Gallerani, S., Neri, R., Cicone, C., Ferrara, A., Genzel, R., et al. (2012). Evidence of strong quasar feedback in the early Universe. *MNRAS* 425, L66–L70. doi:10.1111/j.1745-3933.2012.01303.x

Maiolino, R., Scholtz, J., Curtis-Lake, E., Carniani, S., Baker, W., de Graaff, A., et al. (2023a). *JADES. The diverse population of infant Black Holes at 4<z<11: merging, tiny, poor, but mighty. arXiv e-print*s , arXiv:2308.01230.

Maiolino, R., Scholtz, J., Witstok, J., Carniani, S., D'Eugenio, F., de Graaff, A., et al. (2023b). *A small and vigorous black hole in the early Universe. arXiv e-*prints , arXiv:2305.12492.

Mallick, L., Fabian, A. C., García, J. A., Tomsick, J. A., Parker, M. L., Dauser, T., et al. (2022). High-density disc reflection spectroscopy of low-mass active galactic nuclei. *MNRAS* 513, 4361–4379. doi:10.1093/mnras/stac990

Mallick, L., Wilkins, D. R., Alston, W. N., Markowitz, A., De Marco, B., Parker, M. L., et al. (2021). Discovery of soft and hard X-ray time lags in low-mass AGNs. *MNRAS* 503, 3775–3783. doi:10.1093/mnras/stab627

Marconi, A., Risaliti, G., Gilli, R., Hunt, L. K., Maiolino, R., and Salvati, M. (2004). Local supermassive black holes, relics of active galactic nuclei and the X-ray background. *MNRAS* 351, 169–185. doi:10.1111/j.1365-2966.2004.07765.x

Marinucci, A., Matt, G., Kara, E., Miniutti, G., Elvis, M., Arevalo, P., et al. (2014). Simultaneous NuSTAR and XMM-Newton 0.5-80 keV spectroscopy of the narrow-line Seyfert 1 galaxy SWIFT J2127.4+5654. *MNRAS* 440, 2347–2356. doi:10.1093/mnras/stu404

Massonneau, W., Volonteri, M., Dubois, Y., and Beckmann, R. S. (2023). How the super-Eddington regime regulates black hole growth in high-redshift galaxies. *A&A* 670, A180. doi:10.1051/0004-6361/202243170

McConnell, N. J., and Ma, C.-P. (2013). Revisiting the scaling relations of black hole masses and host galaxy properties. *Astrophysical J.* 764, 184. doi:10.1088/0004-637X/764/2/184

McKinney, J. C., Tchekhovskoy, A., and Blandford, R. D. (2012). General relativistic magnetohydrodynamic simulations of magnetically choked accretion flows around black holes. *Mon. Notices R. Astronomical Soc.* 423, 3083–3117. doi:10.1111/j.1365-2966.2012.21074.x

McNamara, B. R., Wise, M., Nulsen, P. E. J., David, L. P., Sarazin, C. L., Bautz, M., et al. (2000). [ITAL]Chandra[/ITAL] X-ray observations of the Hydra A cluster: an interaction between the radio source and the X-ray–emitting gas. *Astrophysical J.* 534, L135–L138. doi:10.1086/312662

Meidinger, N., Albrecht, S., Beitler, C., Bonholzer, M., Emberger, V., Frank, J., et al. (2020). "Development status of the wide field imager instrument for Athena," in *Space telescopes and instrumentation 2020: ultraviolet to gamma ray*. Editors J.-W. A. den Herder, S. Nikzad, and K. Nakazawa (Online-Only, California, CA: SPIE), 114440T. doi:10.1117/12.2560507

Merloni, A., and Fabian, A. C. (2001). Accretion disc coronae as magnetic reservoirs. *MNRAS* 321, 549–552. doi:10.1046/j.1365-8711.2001.04060.x

Michel, F. C. (1972). Accretion of matter by condensed objects. *Astrophysics Space Sci.* 15, 153–160. doi:10.1007/BF00649949

Miller, J. M., Reynolds, C. S., Fabian, A. C., Miniutti, G., and Gallo, L. C. (2009). Stellar-mass black hole spin constraints from disk reflection and continuum modeling. *Astrophysical J.* Melville, NY, United States: AIP Publishing 697, 900–912. doi:10.1088/0004-637X/697/1/900

Miniutti, G., Fabian, A. C., and Miller, J. M. (2004). The relativistic Fe emission line in XTE J1650-500 with BeppoSAX: evidence for black hole spin and light-bending effects? *MNRAS* 351, 466–472. doi:10.1111/j.1365-2966.2004.07794.x

Miniutti, G., Ponti, G., Dadina, M., Cappi, M., and Malaguti, G. (2007). IRAS 13197-1627 has them all: Compton-thin absorption, photoionized gas, thermal plasmas and a broad Fe line. *MNRAS* 375, 227–239. doi:10.1111/j.1365-2966.2006.11291.x

Moderski, R., and Sikora, M. (1996). On black hole evolution in active galactic nuclei. *MNRAS* 283, 854–864. doi:10.1093/mnras/283.3.854

Moderski, R., Sikora, M., and Lasota, J. P. (1998). On the spin paradigm and the radio dichotomy of quasars. *MNRAS* 301, 142–148. doi:10.1046/j.1365-8711.1998.02009.x

Murray, N., Chiang, J., Grossman, S. A., and Voit, G. M. (1995). Accretion disk winds from active galactic nuclei. *Astrophysical J.* 451, 498. doi:10.1086/176238

Nandra, K., Barret, D., Barcons, X., Fabian, A., den Herder, J.-W., Piro, L., et al. (2013). *The hot and energetic Universe: a white paper presenting the science theme motivating the Athena+ mission. arXiv e-prints* arXiv:1306.2307.

Narayan, R., Chael, A., Chatterjee, K., Ricarte, A., and Curd, B. (2022). Jets in magnetically arrested hot accretion flows: geometry, power, and black hole spin-down. *Mon. Notices R. Astronomical Soc.* 511, 3795–3813. doi:10.1093/mnras/stac285

Narayan, R., and Yi, I. (1994). Advection-dominated accretion: a self-similar solution. *Astrophysical J.* 428, L13. doi:10.1086/187381

Nardini, E., Fabian, A. C., Reis, R. C., and Walton, D. J. (2011). A reflection origin for the soft and hard X-ray excess of Ark 120. *MNRAS* 410, 1251–1261. doi:10.1111/j.1365-2966.2010.17518.x

Novikov, I. D., and Frolov, V. P. (1989). *Physics of black holes*. Dordrecht, Netherlands: Kluwer Academic.

Novikov, I. D., and Thorne, K. S. (1973). Astrophysics of black holes. *Black Holes Les. Astres Occlus*, 343–450.

Oh, K., Koss, M., Markwardt, C. B., Schawinski, K., Baumgartner, W. H., Barthelmy, S. D., et al. (2018). The 105-month swift-BAT all-sky hard X-ray survey. *Astrophysical JournalS* 235, 4. doi:10.3847/1538-4365/aaa7fd

Pancoast, A., Brewer, B. J., and Treu, T. (2014). Modelling reverberation mapping data - I. Improved geometric and dynamical models and comparison with cross-correlation results. *MNRAS* 445, 3055–3072. doi:10.1093/mnras/stu1809

Parker, M. L., Wilkins, D. R., Fabian, A. C., Grupe, D., Dauser, T., Matt, G., et al. (2014). The NuSTAR spectrum of Mrk 335: extreme relativistic effects within two gravitational radii of the event horizon? *MNRAS* 443, 1723–1732. doi:10.1093/mnras/stu1246

Penna, R. F., McKinney, J. C., Narayan, R., Tchekhovskoy, A., Shafee, R., and McClintock, J. E. (2010). Simulations of magnetized discs around black holes: effects

of black hole spin, disc thickness and magnetic field geometry. *MNRAS* 408, 752–782. doi:10.1111/j.1365-2966.2010.17170.x

Peterson, B. M. (1993). Reverberation mapping of active galactic nuclei. *PASP* 105, 247. doi:10.1086/133140

Peterson, B. M., Ferrarese, L., Gilbert, K. M., Kaspi, S., Malkan, M. A., Maoz, D., et al. (2004). Central masses and broad-line region sizes of active galactic nuclei. II. A homogeneous analysis of a large reverberation-mapping database. *Astrophysical J.* 613, 682–699. doi:10.1086/423269

Piotrowska, J. M., Bluck, A. F. L., Maiolino, R., and Peng, Y. (2022). On the quenching of star formation in observed and simulated central galaxies: evidence for the role of integrated AGN feedback. *MNRAS* 512, 1052–1090. doi:10.1093/mnras/stab3673

Ponti, G., Papadakis, I., Bianchi, S., Guainazzi, M., Matt, G., Uttley, P., et al. (2012). CAIXA: a catalogue of AGN in the*XMM-Newton*archive: III. Excess variance analysis. *A&A* 542, A83. doi:10.1051/0004-6361/201118326

Putman, M. E., Peek, J. E. G., and Joung, M. R. (2012). Gaseous galaxy halos. *ARA&A* 50, 491–529. doi:10.1146/annurev-astro-081811-125612

Raimundo, S. I., Fabian, A. C., Vasudevan, R. V., Gandhi, P., and Wu, J. (2012). Can we measure the accretion efficiency of active galactic nuclei? *MNRAS* 419, 2529–2544. doi:10.1111/j.1365-2966.2011.19904.x

Reis, R. C., Fabian, A. C., Ross, R. R., and Miller, J. M. (2009). Determining the spin of two stellar-mass black holes from disc reflection signatures. *MNRAS* 395, 1257–1264. doi:10.1111/j.1365-2966.2009.14622.x

Reis, R. C., and Miller, J. M. (2013). On the size and location of the X-ray emitting coronae around black holes. *Astrophysical J.* 769, L7. doi:10.1088/2041-8205/769/1/L7

Reis, R. C., Reynolds, M. T., Miller, J. M., and Walton, D. J. (2014). Reflection from the strong gravity regime in a lensed quasar at redshift z = 0.658. *Nat* 507, 207–209. doi:10.1038/nature13031

Reynolds, C. S. (2021). Observational constraints on black hole spin. *ARA&A* 59, 117–154. doi:10.1146/annurev-astro-112420-035022

Reynolds, C. S., Brenneman, L. W., Lohfink, A. M., Trippe, M. L., Miller, J. M., Reis, R. C., et al. (2012). "Probing relativistic astrophysics around SMBHs: the Suzaku AGN spin survey," in *Suzaku 2011: exploring the X-ray Universe: suzaku and beyond*. Editors R. Petre, K. Mitsuda, and L. Angelini doi:10.1063/1.3696170

Reynolds, M. T., Walton, D. J., Miller, J. M., and Reis, R. C. (2014). A rapidly spinning black hole powers the einstein cross. *Astrophysical J.* 792, L19. doi:10.1088/2041-8205/792/1/L19

Rezzolla, L., Diener, P., Dorband, E. N., Pollney, D., Reisswig, C., Schnetter, E., et al. (2008). The final spin from the coalescence of aligned-spin black hole binaries. *Astrophysical J.* 674, L29–L32. doi:10.1086/528935

Ricci, C., Tazaki, F., Ueda, Y., Paltani, S., Boissay, R., and Terashima, Y. (2014). Suzaku observation of IRAS 00521-7054, a peculiar type-II AGN with a very broad feature at 6 keV. *Astrophysical J.* 795, 147. doi:10.1088/0004-637X/795/2/147

Ricci, C., Trakhtenbrot, B., Koss, M. J., Ueda, Y., Del Vecchio, I., Treister, E., et al. (2017). BAT AGN spectroscopic survey. V. X-ray properties of the Swift/BAT 70-month AGN catalog. *Astrophysical JournalS* 233, 17. doi:10.3847/1538-4365/aa96ad

Rigby, J., Perrin, M., McElwain, M., Kimble, R., Friedman, S., Lallo, M., et al. (2023). The science performance of JWST as characterized in commissioning. *PASP* 135, 048001. doi:10.1088/1538-3873/acb293

Risaliti, G., Harrison, F. A., Madsen, K. K., Walton, D. J., Boggs, S. E., Christensen, F. E., et al. (2013). A rapidly spinning supermassive black hole at the centre of NGC1365. *Nat* 494, 449–451. doi:10.1038/nature11938

Ross, R. R., and Fabian, A. C. (2005). A comprehensive range of X-ray ionized-reflection models. *MNRAS* 358, 211–216. doi:10.1111/j.1365-2966.2005.08797.x

Russell, H. R., Fabian, A. C., McNamara, B. R., and Broderick, A. E. (2015). Inside the Bondi radius of M87. *MNRAS* 451, 588–600. doi:10.1093/mnras/stv954

Russell, H. R., Fabian, A. C., McNamara, B. R., Miller, J. M., Nulsen, P. E. J., Piotrowska, J. M., et al. (2018). The imprints of AGN feedback within a supermassive black hole's sphere of influence. *MNRAS* 477, 3583–3599. doi:10.1093/mnras/sty835

Saglia, R. P., Opitsch, M., Erwin, P., Thomas, J., Beifiori, A., Fabricius, M., et al. (2016). The SINFONI black hole survey: the black hole fundamental plane revisited and the paths of (Co)evolution of supermassive black holes and bulges. *Astrophysical J.* 818, 47. doi:10.3847/0004-637X/818/1/47

Sancisi, R., Fraternali, F., Oosterloo, T., and van der Hulst, T. (2008). Cold gas accretion in galaxies. *Astronomy Astrophysics Rev.* 15, 189–223. doi:10.1007/s00159-008-0010-0

Sanders, D. B., Soifer, B. T., Elias, J. H., Madore, B. F., Matthews, K., Neugebauer, G., et al. (1988). Ultraluminous infrared galaxies and the origin of quasars. *Astrophysical J.* 325, 74. doi:10.1086/165983

Schwarz, M. P. (1981). The response of gas in a galactic disk to bar forcing. *Astrophysical J.* 247, 77–88. doi:10.1086/159011

Sesana, A., Barausse, E., Dotti, M., and Rossi, E. M. (2014). Linking the spin evolution of massive black holes to galaxy kinematics. *Astrophysical J.* 794, 104. doi:10.1088/0004-637X/794/2/104

Shakura, N. I., and Sunyaev, R. A. (1973). Black holes in binary systems. Observational appearance. *A&A* 24, 337–355.

Shankar, F., Allevato, V., Bernardi, M., Marsden, C., Lapi, A., Menci, N., et al. (2020). Constraining black hole-galaxy scaling relations and radiative efficiency from galaxy clustering. *Nat. Astron.* 4, 282–291. doi:10.1038/s41550-019-0949-y

Shen, Y. (2013). The mass of quasars. *Bull. Astronomical Soc. India* 41, 61–115. doi:10.48550/arXiv.1302.2643

Sisk-Reynés, J., Reynolds, C. S., Matthews, J. H., and Smith, R. N. (2022). Evidence for a moderate spin from X-ray reflection of the high-mass supermassive black hole in the cluster-hosted quasar H1821+643. *MNRAS* 514, 2568–2580. doi:10.1093/mnras/stac1389

Soltan, A. (1982). Masses of quasars. *MNRAS* 200, 115–122. doi:10.1093/mnras/200.1.115

Springel, V. (2010). E pur si muove: galilean-invariant cosmological hydrodynamical simulations on a moving mesh. *MNRAS* 401, 791–851. doi:10.1111/j.1365-2966.2009.15715.x

Springel, V., Di Matteo, T., and Hernquist, L. (2005). Black holes in galaxy mergers: the formation of red elliptical galaxies. *Astrophysical J.* 620, L79–L82. doi:10.1086/428772

Steiner, J. F., McClintock, J. E., Remillard, R. A., Gou, L., Yamada, S., and Narayan, R. (2010). The constant inner-disk radius of LMC X-3: a basis for measuring black hole spin. *Astrophysical J.* 718, L117–L121. doi:10.1088/2041-8205/718/2/L117

Talbot, R. Y., Bourne, M. A., and Sijacki, D. (2021). Blandford-Znajek jets in galaxy formation simulations: method and implementation. *MNRAS* 504, 3619–3650. doi:10.1093/mnras/stab804

Talbot, R. Y., Sijacki, D., and Bourne, M. A. (2022). Blandford-Znajek jets in galaxy formation simulations: exploring the diversity of outflows produced by spin-driven AGN jets in Seyfert galaxies. *MNRAS* 514, 4535–4559. doi:10.1093/mnras/stac1566

Tanaka, Y., Nandra, K., Fabian, A. C., Inoue, H., Otani, C., Dotani, T., et al. (1995). Gravitationally redshifted emission implying an accretion disk and massive black hole in the active galaxy MCG-6-30-15. *Nat* 375, 659–661. doi:10.1038/375659a0

Tao, L., Tomsick, J. A., Qu, J., Zhang, S., Zhang, S., and Bu, Q. (2019). The spin of the black hole GRS 1716-249 determined from the hard intermediate state. *Astrophysical J.* 887, 184. doi:10.3847/1538-4357/ab5282

Tchekhovskoy, A., McKinney, J. C., and Narayan, R. (2012). General relativistic modeling of magnetized jets from accreting black holes. *J. Phys. Conf. Ser.* 372, 012040. doi:10.1088/1742-6596/372/1/012040

Tchekhovskoy, A., Narayan, R., and McKinney, J. C. (2011). Efficient generation of jets from magnetically arrested accretion on a rapidly spinning black hole. *MNRAS* 418, L79–L83. doi:10.1111/j.1745-3933.2011.01147.x

Terrazas, B. A., Bell, E. F., Henriques, B. M. B., White, S. D. M., Cattaneo, A., and Woo, J. (2016). Quiescence correlates strongly with directly measured black hole mass in central galaxies. *Astrophysical JournalL* 830, L12. doi:10.3847/2041-8205/830/1/L12

Teyssier, R. (2002). Cosmological hydrodynamics with adaptive mesh refinement. A new high resolution code called RAMSES. *A&A* 385, 337–364. doi:10.1051/0004-6361:20011817

Thorne, K. S. (1974). Disk-accretion onto a black hole. II. Evolution of the hole. *Astrophysical J.* 191, 507–520. doi:10.1086/152991

Tichy, W., and Marronetti, P. (2008). Final mass and spin of black-hole mergers. *Phys. Rev. D.* 78, 081501. doi:10.1103/PhysRevD.78.081501

Tomsick, J. A., Yamaoka, K., Corbel, S., Kaaret, P., Kalemci, E., and Migliari, S. (2009). Truncation of the inner accretion disk around a black hole at low luminosity. *Astrophysical J.* 707, L87–L91. doi:10.1088/0004-637X/707/1/L87

Toomre, A., and Toomre, J. (1972). Galactic bridges and tails. *Astrophysical J.* 178, 623–666. doi:10.1086/151823

Trakhtenbrot, B., and Netzer, H. (2012). Black hole growth to z = 2 - I. Improved virial methods for measuring M_{BH} and L/L_{Edd}. *MNRAS* 427, 3081–3102. doi:10.1111/j.1365-2966.2012.22056.x

Treves, A., and Turolla, R. (1999). Vacuum breakdown near a black hole charged by hypercritical accretion. *Astrophysical J.* 517, 396–398. doi:10.1086/307159

Tumlinson, J., Peeples, M. S., and Werk, J. K. (2017). The circumgalactic medium. *ARA&A* 55, 389–432. doi:10.1146/annurev-astro-091916-055240

Vestergaard, M. (2002). Determining central black hole masses in distant active galaxies. *Astrophysical J.* 571, 733–752. doi:10.1086/340045

Villar-Martín, M., Humphrey, A., Delgado, R. G., Colina, L., and Arribas, S. (2011). Ionized outflows in SDSS type 2 quasars at z - 0.3-0.6. *MNRAS* 418, 2032–2042. doi:10.1111/j.1365-2966.2011.19622.x

Vogelsberger, M., Marinacci, F., Torrey, P., and Puchwein, E. (2020). Cosmological simulations of galaxy formation. *Nat. Rev. Phys.* 2, 42–66. doi:10.1038/s42254-019-0127-2

Volonteri, M., Dubois, Y., Pichon, C., and Devriendt, J. (2016). The cosmic evolution of massive black holes in the Horizon-AGN simulation. *MNRAS* 460, 2979–2996. doi:10.1093/mnras/stw1123

Wald, R. M. (1984). *General relativity*. Chicago, IL, United States: the University of Chicago Press.

Walton, D. J., Alston, W. N., Kosec, P., Fabian, A. C., Gallo, L. C., Garcia, J. A., et al. (2020). A full characterization of the supermassive black hole in IRAS 09149-6206. *MNRAS* 499, 1480–1498. doi:10.1093/mnras/staa2961

Walton, D. J., Baloković, M., Fabian, A. C., Gallo, L. C., Koss, M., Nardini, E., et al. (2021). Extreme relativistic reflection in the active galaxy ESO 033-G002. *MNRAS* 506, 1557–1572. doi:10.1093/mnras/stab1290

Walton, D. J., Mooley, K., King, A. L., Tomsick, J. A., Miller, J. M., Dauser, T., et al. (2017). Living on a flare: relativistic reflection in V404 cyg observed by NuSTAR during its summer 2015 outburst. *Astrophysical J.* 839, 110. doi:10.3847/1538-4357/aa67e8

Walton, D. J., Nardini, E., Fabian, A. C., Gallo, L. C., and Reis, R. C. (2013). Suzaku observations of 'bare' active galactic nuclei. *MNRAS* 428, 2901–2920. doi:10.1093/mnras/sts227

Walton, D. J., Nardini, E., Gallo, L. C., Reynolds, M. T., Ricci, C., Dauser, T., et al. (2019). A low-flux state in IRAS 00521-7054 seen with NuSTAR and XMM-Newton: relativistic reflection and an ultrafast outflow. *MNRAS* 484, 2544–2555. doi:10.1093/mnras/stz115

Walton, D. J., Reis, R. C., Cackett, E. M., Fabian, A. C., and Miller, J. M. (2012). The similarity of broad iron lines in X-ray binaries and active galactic nuclei. *MNRAS* 422, 2510–2531. doi:10.1111/j.1365-2966.2012.20809.x

Walton, D. J., Risaliti, G., Harrison, F. A., Fabian, A. C., Miller, J. M., Arevalo, P., et al. (2014). NuSTAR and XMM-Newton observations of NGC 1365: extreme absorption variability and a constant inner accretion disk. *Astrophysical J.* 788, 76. doi:10.1088/0004-637X/788/1/76

Wang, J.-G., Dong, X.-B., Wang, T.-G., Ho, L. C., Yuan, W., Wang, H., et al. (2009). Estimating black hole masses in active galactic nuclei using the Mg II λ2800 emission line. *Astrophysical J.* 707, 1334–1346. doi:10.1088/0004-637X/707/2/1334

Weinberger, R., Springel, V., Hernquist, L., Pillepich, A., Marinacci, F., Pakmor, R., et al. (2017). Simulating galaxy formation with black hole driven thermal and kinetic feedback. *MNRAS* 465, 3291–3308. doi:10.1093/mnras/stw2944

Werner, N., McNamara, B. R., Churazov, E., and Scannapieco, E. (2019). Hot atmospheres, cold gas, AGN feedback and the evolution of early type galaxies: a topical perspective. *Space Sci. Rev.* 215, 5. doi:10.1007/s11214-018-0571-9

Wilkins, D. R., Gallo, L. C., Costantini, E., Brandt, W. N., and Blandford, R. D. (2022). Acceleration and cooling of the corona during X-ray flares from the Seyfert galaxy I Zw 1. *MNRAS* 512, 761–775. doi:10.1093/mnras/stac416

Wilkins, D. R., Gallo, L. C., Grupe, D., Bonson, K., Komossa, S., and Fabian, A. C. (2015). Flaring from the supermassive black hole in Mrk 335 studied with Swift and NuSTAR. *MNRAS* 454, 4440–4451. doi:10.1093/mnras/stv2130

Wong, K.-W., Irwin, J. A., Shcherbakov, R. V., Yukita, M., Million, E. T., and Bregman, J. N. (2014). The megasecond chandra X-ray visionary project observation of NGC 3115: witnessing the flow of hot gas within the Bondi radius. *Astrophysical J.* 780, 9. doi:10.1088/0004-637X/780/1/9

Wong, K.-W., Irwin, J. A., Yukita, M., Million, E. T., Mathews, W. G., and Bregman, J. N. (2011). Resolving the Bondi accretion flow toward the supermassive black hole of NGC 3115 with chandra. *Astrophysical J.* 736, L23. doi:10.1088/2041-8205/736/1/L23

Woo, J.-H., Yoon, Y., Park, S., Park, D., and Kim, S. C. (2015). The black hole mass-stellar velocity dispersion relation of narrow-line seyfert 1 galaxies. *Astrophysical J.* 801, 38. doi:10.1088/0004-637X/801/1/38

Xu, Y., Harrison, F. A., García, J. A., Fabian, A. C., Fürst, F., Gandhi, P., et al. (2018). Reflection spectra of the black hole binary candidate MAXI j1535-571 in the hard state observed by NuSTAR. *Astrophysical J.* 852, L34. doi:10.3847/2041-8213/aaa4b2

Yuan, F., and Narayan, R. (2014). Hot accretion flows around black holes. *ARA&A* 52, 529–588. doi:10.1146/annurev-astro-082812-141003

Zdziarski, A. A., Johnson, W. N., and Magdziarz, P. (1996). Broad-band γ-ray and X-ray spectra of NGC 4151 and their implications for physical processes and geometry. *MNRAS* 283, 193–206. doi:10.1093/mnras/283.1.193

Zycki, P. T., Done, C., and Smith, D. A. (1999). The 1989 May outburst of the soft X-ray transient GS 2023+338 (V404 Cyg). *MNRAS* 309, 561–575. doi:10.1046/j.1365-8711.1999.02885.x

frontiers | Frontiers in Astronomy and Space Sciences

TYPE Original Research
PUBLISHED 14 May 2024
DOI 10.3389/fspas.2024.1335459

Check for updates

OPEN ACCESS

EDITED BY
Esra Bulbul,
Max Planck Institute for Extraterrestrial Physics, Germany

REVIEWED BY
Zhiyuan Ma,
University of Massachusetts Amherst, United States
Swayamtrupta Panda,
Laboratório Nacional de Astrofísica, Brazil

*CORRESPONDENCE
P. G. Boorman,
boorman@caltech.edu

†NASA Postdoctoral Program Fellow

‡NHFP Einstein Fellow

RECEIVED 08 November 2023
ACCEPTED 21 February 2024
PUBLISHED 14 May 2024

CITATION
Boorman PG, Torres-Albà N, Annuar A, Marchesi S, Pfeifle RW, Stern D, Civano F, Baloković M, Buchner J, Ricci C, Alexander DM, Brandt WN, Brightman M, Chen CT, Creech S, Gandhi P, García JA, Harrison F, Hickox R, Kammoun E, LaMassa S, Lanzuisi G, Marcotulli L, Madsen K, Matt G, Matzeu G, Nardini E, Piotrowska JM, Pizzetti A, Puccetti S, Sicilian D, Silver R, Walton DJ, Wilkins DR, Zhao X and The HEX-P Collaboration (2024), The High-Energy X-ray Probe (HEX-P): the circum-nuclear environment of growing supermassive black holes.
Front. Astron. Space Sci. 11:1335459.
doi: 10.3389/fspas.2024.1335459

COPYRIGHT
© 2024 Boorman, Torres-Albà, Annuar, Marchesi, Pfeifle, Stern, Civano, Baloković, Buchner, Ricci, Alexander, Brandt, Brightman, Chen, Creech, Gandhi, García, Harrison, Hickox, Kammoun, LaMassa, Lanzuisi, Marcotulli, Madsen, Matt, Matzeu, Nardini, Piotrowska, Pizzetti, Puccetti, Sicilian, Silver, Walton, Wilkins and Zhao. This is an open-access article distributed under the terms of the Creative Commons Attribution License (CC BY). The use, distribution or reproduction in other forums is permitted, provided the original author(s) and the copyright owner(s) are credited and that the original publication in this journal is cited, in accordance with accepted academic practice. No use, distribution or reproduction is permitted which does not comply with these terms.

The High-Energy X-ray Probe (HEX-P): the circum-nuclear environment of growing supermassive black holes

P. G. Boorman[1]*, N. Torres-Albà[2], A. Annuar[3], S. Marchesi[2,4,5], R. W. Pfeifle[6,7†], D. Stern[8], F. Civano[6], M. Baloković[9,10], J. Buchner[11], C. Ricci[12,13], D. M. Alexander[14], W. N. Brandt[15,16,17], M. Brightman[1], C. T. Chen[18,19], S. Creech[20,21], P. Gandhi[22], J. A. García[1,6], F. Harrison[1], R. Hickox[23], E. Kammoun[24,25], S. LaMassa[26], G. Lanzuisi[5], L. Marcotulli[9,10‡], K. Madsen[6], G. Matt[24], G. Matzeu[27], E. Nardini[25], J. M. Piotrowska[1], A. Pizzetti[2], S. Puccetti[28], D. Sicilian[29], R. Silver[6†], D. J. Walton[30], D. R. Wilkins[31], X. Zhao[32] and The HEX-P Collaboration

[1]Cahill Center for Astrophysics, California Institute of Technology, Pasadena, CA, United States, [2]Department of Physics and Astronomy, Clemson University, Kinard Lab of Physics, Clemson, SC, United States, [3]Department of Applied Physics, Faculty of Science and Technology, Universiti Kebangsaan Malaysia, Bangi, Malaysia, [4]Dipartimento di Fisica e Astronomia (DIFA), Università di Bologna, Bologna, Italy, [5]INAF—Osservatorio di Astrofisica e Scienza dello Spazio di Bologna, Bologna, Italy, [6]X-ray Astrophysics Laboratory, NASA Goddard Space Flight Center, Greenbelt, MD, United States, [7]Oak Ridge Associated Universities, NASA NPP Program, Oak Ridge, TN, United States, [8]Jet Propulsion Laboratory, California Institute of Technology, Pasadena, CA, United States, [9]Yale Center for Astronomy and Astrophysics, New Haven, CT, United States, [10]Department of Physics, Yale University, New Haven, CT, United States, [11]Max-Planck-Institut für extraterrestrische Physik, Garching, Germany, [12]Instituto de Estudios Astrofísicos, Facultad de Ingeniería y Ciencias, Universidad Diego Portales, Santiago, Chile, [13]Kavli Institute for Astronomy and Astrophysics, Peking University, Beijing, China, [14]Centre for Extragalactic Astronomy, Department of Physics, Durham University, Durham, United Kingdom, [15]Department of Astronomy and Astrophysics, The Pennsylvania State University, University Park, PA, United States, [16]Institute for Gravitation and the Cosmos, The Pennsylvania State University, University Park, PA, United States, [17]Department of Physics, The Pennsylvania State University, University Park, PA, United States, [18]Science and Technology Institute, Universities Space Research Association, Huntsville, AL, United States, [19]Astrophysics Office, NASA Marshall Space Flight Center, Huntsville, AL, United States, [20]Department of Physics and Astronomy, University of Utah, Salt Lake City, UT, United States, [21]Astrophysics Science Division, SURA/GSFC/CRESST II, Greenbelt, MD, United States, [22]Department of Physics and Astronomy, Faculty of Physical Sciences and Engineering, University of Southampton, Southampton, United Kingdom, [23]Department of Physics and Astronomy, Dartmouth College, Hanover, NH, United States, [24]Dipartimento di Matematica e Fisica, Universitá degli Studi Roma Tre, Roma, Italy, [25]INAF—Osservatorio Astrofisico di Arcetri, Firenze, Italy, [26]Space Telescope Science Institute, Baltimore, MD, United States, [27]European Space Agency (ESA), European Space Astronomy Centre (ESAC), Madrid, Spain, [28]ASI—Agenzia Spaziale Italiana, Via del Politecnico snc, Roma, Italy, [29]Department of Physics, University of Miami, Coral Gables, FL, United States, [30]Centre for Astrophysics Research, University of Hertfordshire, College Lane, Hatfield, United Kingdom, [31]Kavli Institute for Particle Astrophysics and Cosmology, Stanford University, Stanford, CA, United States, [32]Harvard-Smithsonian Center for Astrophysics, Cambridge, MA, United States

Ever since the discovery of the first active galactic nuclei (AGN), substantial observational and theoretical effort has been invested into understanding how massive black holes have evolved across cosmic time. Circum-nuclear obscuration is now established as a crucial component, with almost every AGN observed known to display signatures of some level of obscuration in their X-ray spectra. However, despite more than six decades of effort, substantial

open questions remain: *how does the accretion power impact the structure of the circum-nuclear obscurer? What are the dynamical properties of the obscurer? Can dense circum-nuclear obscuration exist around intrinsically weak AGN? How many intermediate mass black holes occupy the centers of dwarf galaxies?* In this paper, we showcase a number of next-generation prospects attainable with the *High-Energy X-ray Probe* (*HEX-P*[1]) to contribute toward solving these questions in the 2030s. The uniquely broad (0.2–80 keV) and strictly simultaneous X-ray passband of *HEX-P* makes it ideally suited for studying the temporal co-evolution between the central engine and circum-nuclear obscurer. Improved sensitivities and reduced background will enable the development of spectroscopic models complemented by current and future multi-wavelength observations. We show that the angular resolution of *HEX-P* both below and above 10 keV will enable the discovery and confirmation of accreting massive black holes at both low accretion power and low black hole masses even when concealed by thick obscuration. In combination with other next-generation observations of the dusty hearts of nearby galaxies, *HEX-P* will be pivotal in paving the way toward a complete picture of black hole growth and galaxy co-evolution.

KEYWORDS

X-ray, active galactic nuclei, obscuration, black hole, galaxies, Compton-thick, high energy, spectral modeling

1 Introduction

1.1 The prevalence of obscured accretion onto supermassive black holes

It is now well established that obscuration is an omnipresent ingredient in the growth of supermassive black holes. Prime evidence arises from X-ray surveys and population synthesis studies, which have found heavily obscured AGN to dramatically dominate the AGN population at all but the strongest accretion powers, irrespective of redshift (Comastri et al., 1995; Gandhi and Fabian, 2003; Gilli et al., 2007; Treister et al., 2009; Akylas et al., 2012; Buchner et al., 2014; 2015; Ueda et al., 2014; Aird et al., 2015; Brandt and Alexander, 2015; Lansbury et al., 2017; Ananna et al., 2019; Ananna et al., 2022; Ricci et al., 2022). Though some portion resides on galactic scales (Buchner et al., 2017; Gilli et al., 2022; Andonie et al., 2023), the densest *Compton-thick* obscuration ($N_{\rm H} > 1.5 \times 10^{24}$ cm^{-2})[2] is expected to reside on circum-nuclear parsec scales, similar to the sizes invoked in unified schemes (Antonucci, 1993; Urry and Padovani, 1995; Netzer, 2015; Ramos Almeida and Ricci, 2017).

The Compton-thick fraction is often inferred to be similarly substantial to the obscured (i.e., 10^{22} cm^{-2} < $N_{\rm H}$ < 1.5×10^{24} cm^{-2}) AGN population across cosmic time (see discussion in Comastri et al., 2015; Civano et al., 2023), even after considering the non-trivial dependence with the nature of the intrinsic X-ray-emitting corona and/or accretion flow (Gandhi et al., 2007; Vasudevan et al., 2016; Kammoun et al., 2023; Piotrowska et al., 2023). For example, the latest population synthesis models from Ananna et al. (2019) constrain the abundance of Compton-thick AGN to be 50% ± 9% within z = 0.1 and 56 ± 9% within z = 1 of all AGN.

Theoretical models of supermassive black hole growth additionally suggest that enhanced circum-nuclear obscuration is intricately linked to not only just supermassive black hole accretion (Fabian, 1999) but also galaxy–supermassive black hole co-evolution (Anglés-Alcázar et al., 2021) and galaxy–galaxy interactions as a whole (Springel et al., 2005; Hopkins et al., 2006; Pfeifle et al., 2023). Although it is still uncertain as to the exact role that the dense circum-nuclear obscurer plays, some viable options include a feeding reservoir for the central black hole (Storchi-Bergmann and Schnorr-Müller, 2019) or by-product of the central engine itself (Wada, 2012). Compton-thick AGN are hence pertinent targets to unveil the drivers of galaxy growth and understand the co-evolution between supermassive black holes and galaxies, as highlighted in the Astro2020 Decadal Survey[3].

However, Compton-thick AGN are one of the most difficult classes of AGN to detect and study (Hickox and Alexander, 2018; Asmus et al., 2020; Brandt and Yang, 2022). For energies E < 10 keV, the intrinsic X-ray flux from the corona is mostly extinguished via the photoelectric effect and only a few percent of the intrinsic flux escapes (Gupta et al., 2021). Some fluxes survive in the form of narrow X-ray fluorescent lines at specific energies, with those arising from neutral iron K at 6.4 keV (rest

1 https://hexp.org

2 The Compton-thick threshold is generally adopted to be the inverse of the Thomson-scattering cross section, though the actual threshold will depend on other factors, such as abundances. See Section 2.1 and Equation 2.3 of the `MYtorus` manual (http://mytorus.com/mytorus-instructions.html) for more information.

3 https://www.nationalacademies.org/our-work/decadal-survey-on-astronomy-and-astrophysics-2020-astro2020

frame) typically being the strongest. The remaining AGN fluxes observed are dominated by X-ray photons that have undergone Compton recoil in one or multiple scatterings and escaped the obscurer, giving rise to the underlying Compton-scattered continuum. At ~20–40 keV, the continuum peaks into a broad Compton hump with overall shape determined by the geometry of the obscurer (Matt et al., 2000; Murphy and Yaqoob, 2009; Buchner et al., 2019).

1.2 X-ray spectroscopic modeling of circum-nuclear obscuration

Many X-ray spectroscopic models describing the broadband X-ray emission from obscured AGN are available to date with varying geometric prescriptions for the obscurer. Such variations can be broadly separated into (1) *ad hoc* (i.e., computationally convenient) geometries, such as smooth density obscurers (`etorus`, Ikeda et al., 2009; `MYtorus`, Murphy and Yaqoob, 2009; `BNsphere`, Brightman and Nandra, 2011a; `RXtorus`, Paltani and Ricci, 2017; `borus`, Baloković et al., 2018; 2019; `wedge`, Buchner et al., 2019), clumpy obscurers (`Ctorus`, Liu and Li, 2014; `XCLUMPY`, Tanimoto et al., 2019; `UXCLUMPY`, Buchner et al., 2019), and combinations of different unique geometric components (see the polar gas simulations from Liu et al., 2019; McKaig et al., 2022 or the broadband physical model of the Circinus Galaxy in Andonie et al., 2022) and (2) geometries that emerge from radiative hydrodynamical simulations (`warpeddisk`, `radiativefountain`; Buchner et al., 2021). There has also been a surge in the availability of ray tracing packages designed to enable the production of bespoke user-defined X-ray spectral models in arbitrary geometries and the inclusion of additional physical processes (MONACO: Odaka et al., 2011 and Odaka et al., 2016; RefleX[4]: Paltani and Ricci, 2017 and Ricci and Paltani, 2023; XARS[5]: Buchner et al., 2019; SKIRT[6]: Vander Meulen et al., 2023).

The ability for accurate and precise inference from circum-nuclear obscuration models with ever-increasing numbers of fit parameters is currently met by substantial challenges. The first is exploring the degenerate and multi-modal (i.e., non-identifiable) parameter spaces inherent to the spectral model libraries that result from ray tracing simulations. A typical model to explain the 0.2–80 keV spectra of obscured AGN can consist of $\gtrsim 10$ parameters describing the intrinsic X-ray spectrum, the geometric prescription of the surrounding circum-nuclear obscurer, and other contaminating soft X-ray emissions. The corresponding multi-dimensional parameter spaces are very complex and do not necessarily lead to unique spectral solutions when compared with alternative geometric models of the obscurer (Saha et al., 2022; Kallová et al., 2023). As such, parameter exploration, model verification, and model comparison are all non-trivial and can be exceedingly expensive to compute with increased numbers of fit parameters (van Dyk et al., 2001; Buchner et al., 2014; Buchner and Boorman, 2023). Increased complexity of obscuration models will also require more ray tracing simulations to compute. Due to the corresponding trade-off between exploring fewer geometries *versus* coarser parameter grid resolution, the conventional use of multi-dimensional tables and grid interpolation to fit spectra may become obsolete entirely. A promising alternative is emulation, which has been shown to accelerate the computation time associated with radiative transfer simulations (Kerzendorf et al., 2021; Rino-Silvestre et al., 2022) and avoid the requirement for coarse gridding of parameters into multi-dimensional tables entirely (Matzeu et al., 2022).

The second challenge is the observational requirement for high-quality *broadband* spectroscopy of Compton-thick AGN to test complex physical models. Valuable insights have been attained with focusing X-ray optics < 10 keV, typically capable of isolating the Fe Kα complex and underlying reflection continuum from contaminating non-AGN spectral features (Risaliti et al., 1999; Brightman and Nandra, 2011a; LaMassa et al., 2017). However, without similar sensitivities > 10 keV, strong ambiguity still remains relating to the shape of the Compton hump (see discussion in Brightman et al., 2015; LaMassa et al., 2019; 2023). Hard X-ray sensitivities provided by coded aperture masks have limited previous studies to higher observed X-ray fluxes (Yaqoob, 2012; Gandhi et al., 2013; 2015; Ricci et al., 2017c) and reduced spectral resolution that is insufficient to strongly constrain geometrical properties of the circum-nuclear environment (see discussion in Baloković, 2017; Tanimoto et al., 2022).

NuSTAR (Harrison et al., 2013) provided the first focusing hard X-ray telescope in orbit, opening a new era into the pursuit and understanding of heavily obscured accretion onto supermassive black holes (see Section 2). To date, *NuSTAR* has provided the most sensitive insights into the X-ray obscuration of the brightest Compton-thick AGN known (Arévalo et al., 2014; Puccetti et al., 2014; Bauer et al., 2015; Puccetti et al., 2016), as well as the wider population identified previously with wide-field hard X-ray monitoring surveys (Annuar et al., 2015; Gandhi et al., 2017; Marchesi et al., 2017; 2019b; Torres-Albà et al., 2021; Traina et al., 2021; Zhao et al., 2021; Pizzetti et al., 2022; Silver et al., 2022; Tanimoto et al., 2022). *NuSTAR* has also enabled unambiguous Compton-thick line-of-sight column density classifications for a bulk of the previously published candidate Compton-thick sources that had not been detected > 10 keV before (Baloković et al., 2014; Gandhi et al., 2014; Ptak et al., 2015; Boorman et al., 2016; Masini et al., 2016; Annuar et al., 2017; Ricci et al., 2017; LaMassa et al., 2019; Kammoun et al., 2020). Broadband X-ray spectroscopy has thus proven to be a crucial tool for understanding the obscurer, provided consistent sensitivities are attainable with simultaneous soft X-ray observations across the entire passband (Marchesi et al., 2018; Marchesi et al., 2019a).

Additional complexities arising from the symbiotic relationship between the central engine and the obscurer can introduce systematics, for example, the relationship between the black hole mass-scaled luminosity and covering factor (Fabian et al., 2008; Ricci et al., 2017d).

4 https://www.astro.unige.ch/reflex/

5 https://github.com/JohannesBuchner/xars

6 https://skirt.ugent.be/root/_contributing.html#ContributingRepositories

1.3 Complex structure revealed by variability

There is mounting evidence that the obscurer can be clumpy rather than smooth. This was initially motivated by infrared spectra of AGN, which showed less prominent silicate features than expected from smooth obscuration models (Jaffe et al., 2004; Elitzur, 2006; Hönig and Beckert, 2007; Risaliti et al., 2007; Nenkova et al., 2008). Models such as chaotic cold accretion (Gaspari et al., 2013; Gaspari et al., 2015; Gaspari et al., 2020) suggest clumpy accretion from random angles onto the central 100 pc induced by radiative cooling and turbulence (see Rose et al., 2019; Gaspari et al., 2020; Maccagni et al., 2021; Temi et al., 2022). Obscurer geometries arising from radiation-driven outflows also can produce dynamic, filamentary, and clumpy structures (Vollmer and Duschl, 2002; Wada, 2012; Chan and Krolik, 2016, and references therein). Such clumpy/filamentary models of AGN obscuration predict observed changes in the line-of-sight obscuration.

In X-rays, an inhomogeneity in the circum-nuclear material can vary (i) the accretion luminosity and/or (ii) obscuration level. Such changes can be detected and disambiguated with sufficiently sensitive time-resolved X-ray spectroscopy with a wide-enough passband (Ricci and Trakhtenbrot, 2022). For line-of-sight column density variations $\Delta\ N_{\rm H} \lesssim 10^{23}$ cm^{-2}, the photoelectric turnover is at $\lesssim$ 10 keV and has been used to robustly confirm obscuration variations (Risaliti et al., 2002; 2005; Markowitz et al., 2014). However, for variations $\Delta\ N_{\rm H} \gtrsim 10^{23}$–$10^{24}$ cm^{-2}, sensitive broadband spectroscopy is advantageous to provide constraints on the underlying absorbed spectrum below 10 keV and the reprocessed spectrum above 10 keV to avoid strong degeneracy between the spectral slope, obscuration level, and amount of reprocessing (Walton et al., 2014; Rivers et al., 2015; Lefkir et al., 2023). Decoupling such large changes in obscuration from intrinsic flux variations exclusively in Compton-thick AGN is currently even less represented in the literature, owing in part to the observational demand for observing variations in the Compton hump that are non-trivial to disentangle at $\gtrsim$ 10–20 keV in all but the brightest targets (Puccetti et al., 2014; Marinucci et al., 2016; Nardini, 2017; Zaino et al., 2020; Kayal et al., 2023).

Column density variations are expected to occur over periods of time from ~1 day up to several months, assuming a typical range of obscuring cloud filling factors, velocities, and distances from the accreting black hole (Nenkova et al., 2008). Tentative column density variability timescales on the order of years also exist (Gandhi et al., 2017; Masini et al., 2017; Laha et al., 2020; Torres-Albà et al., 2023), but additional sensitive monitoring is required to quantify its prevalence in the obscured AGN population. Thus, X-ray obscuration variability is a powerful tool for providing reliable constraints on the location of obscuring clouds and their distances from the accreting supermassive black hole (Markowitz et al., 2014; Buchner et al., 2019). By combining numerous epochs of broadband X-ray observations with physical obscuration models, the global properties of the circum-nuclear environment (such as covering factor and average column density) can be decoupled from the epoch-dependent variable components to provide the tightest constraints on obscurer properties in the heavily obscured AGN population currently known (Ricci et al., 2016; Baloković et al., 2018; Marchesi et al., 2022; Pizzetti et al., 2022; Kayal et al., 2023; Torres-Albà et al., 2023). For such observations, simultaneous observations from ~ 0.2–80 keV are essential. These are challenging to achieve, currently requiring the coordination of complementary missions (e.g., *XMM-Newton* and *NuSTAR*), which has limited the sample size for such studies (see Section 4).

1.4 The circum-nuclear environment at low accretion power

Volume-limited multi-wavelength surveys have revealed that the majority of supermassive black holes in the nearby universe are underfed (Ho, 1997, 2008; Baldi et al., 2018, 2021a, 2021b; Williams et al., 2022). This implies that the majority of local galaxies host low-luminosity AGN, often parameterized to have bolometric luminosities $L_{\rm bol} \lesssim 10^{42}$ erg s^{-1}, and/or Eddington-scaled bolometric luminosities (also known as the Eddington ratio) of $\lambda_{\rm Edd} = L_{\rm bol}/L_{\rm Edd} \lesssim 10^{-3}$ (Elitzur, 2006; Hönig and Beckert, 2007; Kawamuro et al., 2016). However, our understanding of the circum-nuclear environment in AGN at low luminosities and accretion powers is currently very incomplete.

Low-luminosity AGN are known to lack an ultraviolet bump in their spectral energy distribution (Ho, 1999; Nemmen et al., 2006; Eracleous et al., 2010) and share similar characteristics to low-luminosity/quiescent accreting stellar mass black holes (Nagar et al., 2005; Körding et al., 2006; Svoboda et al., 2017; Fernández-Ontiveros and Muñoz-Darias, 2021; Moravec et al., 2022), suggesting the absence of a standard optically thick, geometrically thin accretion disc (Shakura and Sunyaev, 1973). At X-ray wavelengths, the absence of Fe Kα emission lines and/or the Compton hump in some low-luminosity AGN also supports this notion, indicating the truncation or absence of a standard accretion disc (Terashima, 2002; González-Martín et al., 2009; Younes et al., 2011; Ursini et al., 2015; Young et al., 2018; Younes et al., 2019; Osorio-Clavijo et al., 2022). Some studies have predicted the collapse and disappearance of the broad-line region and obscuring structure in low-luminosity AGN due to insufficient radiation pressure (Elitzur, 2006; Hönig and Beckert, 2007; Elitzur and Ho, 2009). Although there is some observational evidence supporting these predictions, data are often limited due to the relative difficulty of selecting and studying low-luminosity AGN relative to their more luminous counterparts (Maoz et al., 2005; Ho, 2008; Trump et al., 2011; Hernández-García et al., 2016; Ricci et al., 2017d; González-Martín et al., 2017). Measurements of the obscuring covering factor on a source-by-source basis in large samples via X-ray spectroscopic modeling have provided additional clues supporting this notion, though with considerable uncertainties (Brightman and Nandra, 2011b; Vasudevan et al., 2013; Brightman et al., 2015; Baloković, 2017).

1.5 Accreting intermediate mass black holes

Large numbers of intermediate mass black holes with masses $M_{\rm BH} \sim 10^2$–10^5 M$_\odot$ are required to exist throughout cosmic history to give rise to the $\sim 10^9$ M$_\odot$ supermassive black holes observed within mere hundreds of million years from the Big Bang

(Bañados et al., 2018) up to the present day. A large ongoing challenge, however, is to observationally identify intermediate mass black holes and to understand how they were formed (Greene et al., 2020). Dwarf galaxies are useful to search for intermediate mass black holes. To explain their low masses, dwarf galaxies are expected to have undergone fewer mergers than more massive galaxies that in turn restricts the availability of fuel for the central black holes to grow. Dwarf galaxies in the local universe are hence expected to contain the seeds of the first supermassive black holes, and the dwarf galaxy black hole occupation fraction is a crucial piece of the puzzle (Volonteri et al., 2008; Volonteri, 2010; Greene, 2012; Reines, 2022).

A useful strategy is to search for intermediate mass black hole signatures during episodes of accretion as AGN. The difficulty is that any biases imposed on selecting accreting supermassive black holes in AGN are exacerbated in the case of intermediate mass black holes in low-mass galaxies. Dwarf galaxies often have high levels of star formation that can be significantly stronger than the optical emission associated with the accretion disc surrounding accreting intermediate mass black holes (Moran et al., 2014; Trump et al., 2015). Optical spectroscopy has proven to be a useful tool for identifying unobscured dwarf AGN signatures (Greene and Ho, 2004; 2007; Reines et al., 2013; Baldassare et al., 2018). However, this technique requires that host galaxy dilution be minimal and that the AGN be largely unobscured while accreting at high rates, close to the Eddington limit. X-ray observations are less affected by host galaxy contamination but soft X-rays can be readily absorbed leading to the same biases encountered for more massive black holes in AGN (Brandt and Alexander, 2015; Hickox and Alexander, 2018). Broadband X-ray observations that include hard X-rays are hence crucial to disentangle obscured accreting massive black holes from individual host galaxy X-ray binaries that often have different predicted hard X-ray spectral shapes (see discussion in Lehmer et al., 2023). Detailed broadband X-ray spectroscopic studies of obscured massive black holes in low-mass galaxies are currently rare though due to the requirement for sufficient sensitivities (Ansh et al., 2023; Mohanadas and Annuar, 2023).

1.6 The *HEX-P* perspective

The *High-Energy X-ray Probe* (*HEX-P*; Madsen et al., 2023) is a probe-class mission concept that offers sensitive coverage (0.2–80 keV) of the X-ray spectrum with exceptional spectral, timing, and angular capabilities. It features a high-energy telescope (HET) that focuses hard X-rays, and one low-energy telescope (LET) that focuses soft X-rays in a parallel structure.

The LET (0.2–25 keV) consists of a segmented mirror assembly coated with Iridium on monocrystalline silicon that achieves a half power diameter of 3.5" and a low-energy DEPFET detector of the same type as the Wide Field Imager (WFI; Meidinger et al., 2020) that will be onboard *Athena* (Nandra et al., 2013). It has 512 × 512 pixels that cover a field of view of 11.3' × 11.3'. It has an effective passband of 0.2–25 keV and a full frame readout time of 2 ms, which can be operated in a 128- and 64-channel window mode for higher count-rates to mitigate pile-up and achieve faster readout. Pile-up effects remain below an acceptable limit of ~1% for fluxes up to ~100 mCrab in the smallest window configuration. Excising the core of the PSF, a common practice in X-ray astronomy, will allow for observations of brighter sources, with a typical loss of up to ~ 60% of the total photon counts.

The HET (2–80 keV) consists of two co-aligned telescopes and detector modules. The optics are made of Ni-electroformed full-shell mirror substrates, leveraging the heritage of *XMM-Newton* (Jansen et al., 2001), and coated with Pt/C and W/Si multilayers for an effective passband of 2–80 keV. The high-energy detectors are of the same type as those onboard *NuSTAR* (Harrison et al., 2013), and they consist of 16 CZT sensors per focal plane, tiled 4 × 4, for a total of 128 × 128 pixels spanning a field of view slightly larger than that for the LET, of 13.4' × 13.4'.

The unique improvements yielded by *HEX-P* will provide significant advancements in the study of supermassive black hole growth. Enhanced sensitivity above 10 keV relative to *NuSTAR* will enable detailed modeling constraints of the faintest Compton-thick AGN currently known (see Section 5; Pfeifle et al., 2023) and the completion of the local AGN census that is predominantly restricted by our ability to uncover Compton-thick AGN (Asmus et al., 2020; Civano et al., 2023). The strictly simultaneous broadband coverage will also remove any ambiguity associated with spectral component variability that can significantly affect the inference of key system parameters (see discussion in Baloković et al., 2018; Baloković et al., 2021; Torres-Albà et al., 2023; Section 4). Lastly, the extended passband of the LET up to energies of ~ 25 keV will provide sensitive overlapping X-ray spectroscopy in both *HEX-P* telescopes. The energy range ~ 5–8 keV contains the iron K lines which hold enormous diagnostic value for the structure of the circum-nuclear obscurer when combined with the underlying continuum ≳ 10 keV (Baloković et al., 2018). Having three individual instruments across this wavelength range will also provide independent verification for blue-shifted absorption features arising from outflowing material that have proven difficult to detect in heavily obscured AGN to date (Matzeu et al., 2019). At higher energies, the passband between ~8 and 25 keV encompasses the first inflection point of the Compton hump that holds exciting potential as a fingerprint-like identifier for the circum-nuclear obscurer(s) surrounding the AGN (see Buchner et al., 2019; Buchner et al., 2021).

The paper is organized as follows: Section 2 presents the latest compilation of published Compton-thick AGN within ~ 400 Mpc, confirmed in part by *NuSTAR* observations. To our knowledge, this is the largest compilation of local Compton-thick AGN constructed to date and combines sources selected at a variety of different wavelengths. In Section 3, we present a detailed X-ray spectral analysis of local megamaser AGN, highlighting the prospects for *HEX-P* and next-generation obscuration models to study the effects of radiative feedback from AGN. Section 4 showcases the future possibilities with multi-epoch studies attainable with high sensitivity, strictly simultaneous, broadband X-ray spectroscopy. The current and future prospects behind the behavior of dense AGN obscurers at extremely low luminosities are discussed in Section 5, followed by the prospects for detecting faint obscured AGN in dwarf galaxies in Section 6. We then provide a quantitative estimate of the volume accessible by *HEX-P* for robust characterization of Compton-thick obscuration and compare it to the current state of the art in Section 7. We present our summary in Section 8.

All the *HEX-P* simulations presented in this work were produced with a set of response files that represent the observatory performance based on current best estimates as of Spring 2023

(v07; see Madsen et al., 2023 for corresponding LET and HET sensitivity curves). The effective area is derived from ray tracing of the mirror design that includes obscuration by all known structures. The detector responses are based on simulations performed by the respective hardware groups, with an optical blocking filter for the LET and a Beryllium window and thermal insulation for the HET. The LET background was derived from a Geant4 simulation (Eraerds et al., 2021) of the WFI instrument, and the HET background was derived from a Geant4 simulation of the *NuSTAR* instrument. Both background simulations adopt the planned L1 orbit for *HEX-P*.

2 The Database of Compton-thick AGN

To understand the Compton-thick AGN population uncovered to date and as a natural starting point for our *HEX-P* simulations, we construct a comprehensive list of Compton-thick AGN identified in the literature. To ensure accurate modeling of the underlying Compton scattered continuum in such sources, we limit our search to targets confirmed with spectral modeling that included *NuSTAR* data. Whilst other X-ray instruments such as the *Suzaku*/Hard X-ray Detector, the *Swift*/Burst Alert Telescope, and *INTEGRAL* have provided hard X-ray spectroscopic constraints for some Compton-thick AGN (Yaqoob, 2012; Gandhi et al., 2013; Gandhi et al., 2015; Vasylenko et al., 2013; Ricci et al., 2015), we limit ourselves to the requirement for *NuSTAR* due to its 100-fold increase in sensitivity above 10 keV relative to previous missions (Harrison et al., 2013). The resulting Database of Compton-thick AGN (DoCTA) was created as follows:

1. *Literature search*: We first identified a list of peer-reviewed publications with a NASA ADS[7] search query for any refereed paper containing the phrase 'Compton-thick' and '*NuSTAR*' somewhere in the main body of text. The search returned 690 refereed publications.
2. *Literature refinement*: We manually filtered through the list of publications identified in Step 1, finding ~90 publications that use AGN X-ray spectroscopic modeling with *NuSTAR* (often but not always complemented by soft X-ray spectroscopy from a different instrument) to constrain line-of-sight column density via obscuration models of some form.
3. *Line-of-sight column density*[8]: We sought to extract the line-of-sight column density of each system for every acceptable model fit presented per publication. Our reasoning behind this strategy was to be as complete with the literature as possible, enabling inclusion of sources that are classified as Compton-thick with a specific model setup, but not in others. A number of sources have line-of-sight column density measurement upper bounds *consistent* with the Compton-thick limit, but to be conservative, we only consider sources with at least one line-of-sight column density measurement that is lower 90% confidence bound above a Compton-thick threshold of 1.5×10^{24} cm^{-2}, corresponding to the inverse Thomson cross-section.
4. *Computing unabsorbed luminosities:* To understand the fundamental demographics of the sample, we next estimated intrinsic luminosity. Given the inevitably large number of local AGN selected, a large number of redshift-independent distances are available for the sources. We cross-matched the initial set of objects from Step 3 with the NASA Extragalactic Database[9] using sexagesimal coordinates to remove duplicates arising from different published identifiers. We then downloaded all redshift-independent distances per source and used the median distance for sources where one or more values were available. To overcome possible effects from discrepant distance estimates to a given source, we additionally store the distances used by each work and manually correct intrinsic 2–10 keV luminosities into fluxes when intrinsic fluxes are not provided. We use the median redshift-independent distance listed on NED where available, otherwise the luminosity distance is calculated assuming the cosmological parameters $H_0 = 70.0$ km s^{-1} Mpc^{-1}, $\Omega_\Lambda = 0.7$, and $\Omega_M = 0.3$.

Section 8 presents all published values of line-of-sight column density and intrinsic flux for each of the 66 Compton-thick AGN in DoCTA. A wide range of possible scientific applications are clearly provided with DoCTA. The primary focus for this work is to assess the ability of current circum-nuclear obscuration models paired with modern broadband X-ray spectral sensitivity to provide unique solutions for intrinsic luminosity and line-of-sight column density, in the absence of considerable source variability (see Figure 3 and Section 4 for more information on this assumption).

Figure 1 presents the distance vs. unabsorbed 2–10 keV X-ray luminosity for every intrinsic 2–10 keV luminosity measurement of every source in DoCTA. The *left* panel shows that DoCTA is limited to $\lesssim 100$ Mpc for the conventional Seyfert definition with unabsorbed 2–10 keV luminosity, $L_{2-10\ \mathrm{keV}} > 10^{42}$ erg s^{-1}. Beyond ~ 250 Mpc, only quasars ($L_{2-10\ \mathrm{keV}} > 10^{44}$ erg s^{-1}) have been found as Compton-thick. Overall, there is a significant range of published intrinsic luminosities per source, with some estimates ranging over > 3 orders of magnitude in the most extreme cases. This trend is shown in Figure 1, which marks the range in intrinsic luminosity reported in the spectral fits included in DoCTA. Under the assumption of negligible source variability (see Figure 3), such variations can arise from choosing different circum-nuclear obscuration models. This also leads to a significant systematic uncertainty in parameter inference (i.e., not only unabsorbed luminosity but also line-of-sight column density and covering factors). It is concerning that this occurs even in the local universe where the observing conditions are optimal (e.g., bright fluxes thanks to source proximity and spatial separation of nearby nuclear contaminants). Some sources, particularly at larger distances, appear to show little luminosity variation. However, this may be because

7 https://ui.adsabs.harvard.edu

8 We refer to "line-of-sight" or "angle-averaged" column densities throughout this work to distinguish between the Thomson depth of material along the line-of-sight and the angle-averaged Thomson depth of material out of the line-of-sight, respectively.

9 https://ned.ipac.caltech.edu

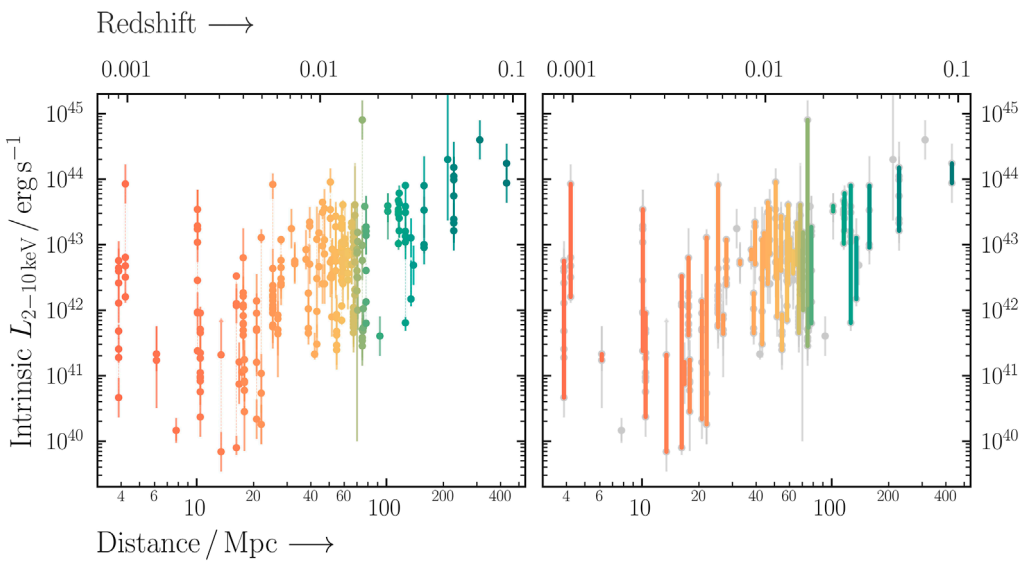

FIGURE 1
(*Left*) Distance vs. intrinsic (i.e., unabsorbed) 2–10 keV luminosity reported in the literature for all local Compton-thick AGN. We have only included Compton-thick classifications that included *NuSTAR* data in the spectral analysis. Multiple reported luminosities for a single source are connected by a vertical dashed line. (*Right*) Same as the *left* panel, with vertical bars indicate the range in best-fit luminosities for each source. For most sources, the reported luminosities vary over one to two orders of magnitude and, in some extreme cases, over three orders of magnitude. The color coding is used to distinguish between different sources and does not correspond to a physical parameter. For analyses lacking an intrinsic flux uncertainty measurement, we conservatively assume a symmetric uncertainty in logarithmic space of 0.3 dex.

those targets have been studied in fewer publications than famous nearby sources (e.g., the Circinus Galaxy and NGC 4945).

Figure 2 presents distance vs. line-of-sight column density from the literature for every available measurement of every source in DoCTA. Similar to Figure 1, we find a significant range of measured line-of-sight column densities. Such a range can arise from subtle differences in the physical properties of the obscurer assumed in different models. For example, line-of-sight column density is inextricably linked to predicted intrinsic luminosity since an increase in line-of-sight column density requires an increase in intrinsic luminosity to explain the additional absorption. Alternatively, parameter differences across obscuration models can arise from how the parameters are represented in the corresponding table models used in the spectral fitting (e.g., the number of parameter grid points). A primary effect of such confusion is that a significant number of sources have published measured line-of-sight column densities both above and below the Compton-thick limit (horizontal dashed line) to 90% confidence. Such uncertainty can clearly have fundamental model-dependent effects on measurements of the Compton-thick AGN abundance for example. A subset of the DoCTA sources are known as changing-obscuration AGN (Ricci and Trakhtenbrot, 2022), in which the line-of-sight column density varies both below and above the Compton-thick threshold (e.g., NGC 1358; Marchesi et al., 2022). However, Compton-thick changing-obscuration events are rarely observed at present, meaning that the wide range in line-of-sight column densities is not expected to be dominated by changing-obscuration AGN.

A large number of different model prescriptions for the obscuration-based reprocessed spectrum in AGN are available in the literature today, as well as different bespoke setups that incorporate those models. A prime example of the latter is the use of decoupled models, in which the global average properties of the reprocessor are decoupled from the reprocessing effects along the line-of-sight (see Yaqoob, 2012 for a detailed review of such techniques). On the practical side, decoupled model fitting often improves the fit due to the larger range of spectral shapes attainable. On the theoretical side, it can be interpreted as flux variability or line-of-sight column density variations arising from a clumpy obscurer. As such, decoupled model setups can often include an overall scaling of the intrinsic continuum relative to the reprocessed one. LaMassa et al. (2019) have shown the effect of manually altering the contribution from reprocessing in the broadband spectral fitting of NGC 4968, finding that an increase in reprocessed flux corresponds to an overall decrease in intrinsic continuum flux, as expected.

Many obscured AGN are variable in hard X-rays (Torres-Albà et al., 2023), such as bright Compton-thick AGN (Puccetti et al., 2014; Marinucci et al., 2016; Marchesi et al., 2022). To understand the high-energy (E > 10 keV) spectral constraints for the DoCTA population and to qualitatively understand the possibility of variability impacting the ranges shown in Figures 1, 2, we extracted all archival *NuSTAR* data available per source with > 10 ks of net exposure time in both focal plane modules (FPMA and FPMB). While intra-observation variability is not unheard of in Compton-thick AGN (Puccetti et al., 2014), it is currently rare in the literature, so we choose to extract epoch-averaged spectra. The *NuSTAR* data for both FPMA and FPMB were processed using the *NuSTAR* Data Analysis Software package within `HEAsoft`. The task `nupipeline` was used to generate cleaned event files. Spectra and corresponding response files were generated using `nuproducts` with circular source regions of 20 pixels (~49") and background regions as large as possible on the same detector as the target. Each

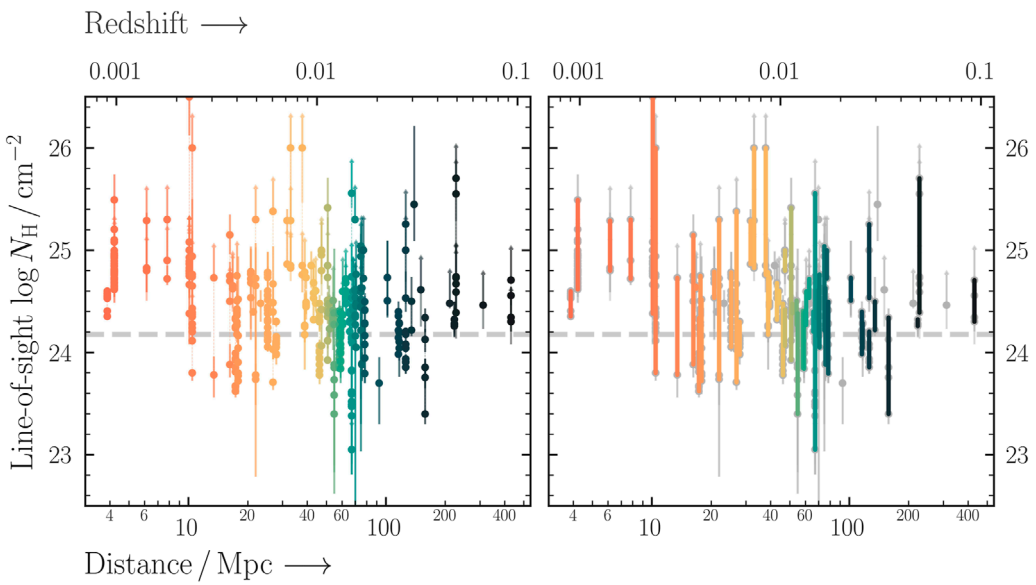

FIGURE 2
Left and *right* panels are the same as in Figure 1, apart from the reported line-of-sight column density that is shown on the vertical axis. The Compton-thick threshold adopted for this work is shown with a horizontal dashed line. The large range between reported line-of-sight log N_H values and the large number of lower limits per source in the Compton-thick regime highlights the challenge with current models to constrain the upper boundary of column density for Compton-thick AGN. We additionally note that the upper bound for each N_H measurement considered during fitting depends on a given specific model setup. The large range itself is fundamentally due to modeling degeneracies remaining in low signal-to-noise ratio of hard X-ray data and variability in time relative to the complementary soft X-ray observations. Both issues will be directly addressed with *HEX-P*.

spectrum was then binned using the optimal binning scheme of Kaastra and Bleeker (2016).

Figure 3 presents residuals in the form of `(data-model)/error` for every extracted *NuSTAR* spectrum after fitting a simple `zcutoffpl` model in PyXspec to the first observed spectrum per source in the 3–78 keV band. We then plot the residuals for every observation per source relative to the fit of the original spectral fit to highlight source variability that has been detected by *NuSTAR*. The figure is organized vertically into bins of *NuSTAR*/FPMA 3–78 keV signal-to-noise ratio, increasing from the bottom to top row. A number of interesting features are visible from Figure 3. First, there is a large diversity in shapes of the Fe K complex (rest frame 6.4 keV is marked with a vertical line in each panel) and Compton hump across the sample. A number of factors can contribute to observed spectral diversity in heavily obscured AGN, whether it be from contamination in the Fe K band and softer energies ($E \lesssim 8$ keV) arising from competing spectral components (Annuar et al., 2015; Reynolds et al., 2015; Farrah et al., 2016; Gandhi et al., 2017) or due to the structure of the obscurer itself at $E \gtrsim 8$ keV (Buchner et al., 2019; 2021). As noted by Bauer et al. (2015), it is physically unlikely for a single-column density obscurer to surround AGN and a plausible alternative could be a continuous distribution of obscurers with varying column densities and other geometric parameters, consistent with galactic molecular cloud studies (Goodman et al., 2009).

Most of the highest signal-to-noise ratio Compton-thick AGN on the top row of Figure 3 display significant spectral variability with *NuSTAR* (Puccetti et al., 2014; Marinucci et al., 2016; Marchesi et al., 2022; Kayal et al., 2023). Only a small number of targets have been selected for *NuSTAR* follow-up because of known variability, and with sufficient sensitivity, repeated observations of others may well show that obscurer-based variability is ubiquitous amongst Compton-thick AGN. For the remainder of the DoCTA population, there are either insufficient *NuSTAR* epochs to search for variability (see panels with $N_{obs} = 1$ in the figure) or the visual difference in the observed reflection spectra is small. Furthermore, the lowest third of DoCTA sources in terms of signal-to-noise ratio have insufficient data quality to reveal any spectral variability in detail (see Section 4 for further discussion).

HEX-P is optimized in many ways to guide the future development of X-ray spectral models. First, the improved broadband sensitivity achieved by reducing the background level will result in a significant improvement in the observed signal-to-noise ratio for the bulk of the Compton-thick AGN population present in DoCTA. Such improvements will fundamentally decrease the number of possibilities for non-unique spectral fits in which parameter posteriors are significantly different. Second, the extended range of the LET to energies > 10 keV means that there will be three instruments in total providing sensitive spectra over the energy range corresponding to the inflection point of the Compton hump. Detailed spectral modeling of Compton hump diversity is currently an under-used resource for constraining the covering factor of material with different column densities surrounding the central engine (Buchner et al., 2019). Lastly, the simultaneous broadband focusing capabilities of *HEX-P* are a novel concept amongst previous, current, and future planned X-ray missions. Broadband coverage removes any possible issues that can arise from variability or significantly mismatched data quality in soft and hard X-ray bands.

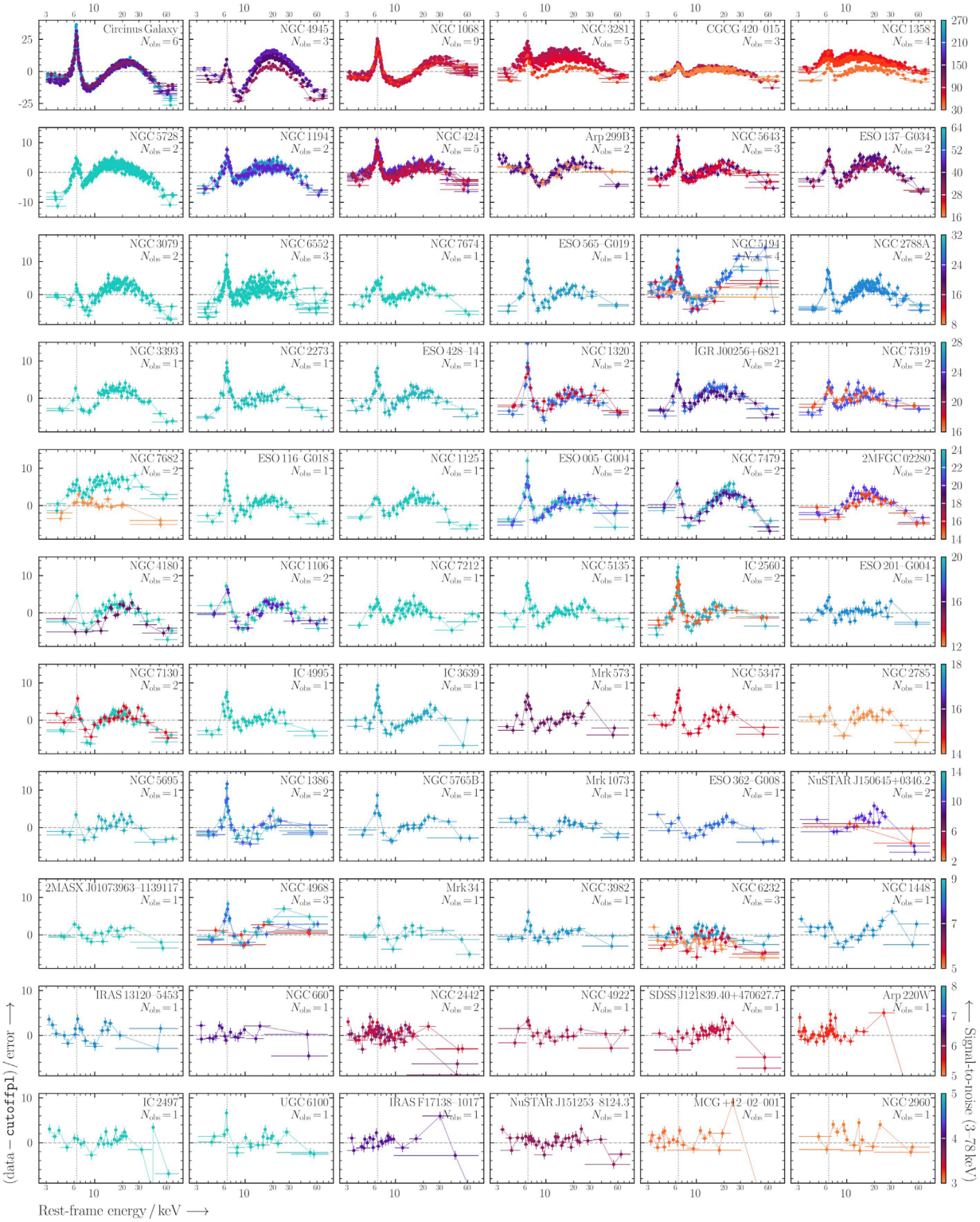

FIGURE 3
Every Compton-thick AGN in DoCTA confirmed by *NuSTAR*: each panel plots the relative residual for a simple `cutoffpl` fit to each *NuSTAR* spectrum with >10 ks of data and is colored by the signal-to-noise ratio in the 3–78 keV band.

3 Developing next-generation models of the circum-nuclear environment

All physical obscurer models feature multiple geometric degrees of freedom that are unique to the geometry assumed (e.g., some combination of line-of-sight column density, global obscurer column density, inclination angle, covering factors, etc.). However, the relative importance for each parameter in a given model fit is often non-trivial with many inter-parameter dependencies and multi-modal solutions to consider. Studies of the obscuration properties of AGN have shown that the covering factor is related to the Eddington-scaled accretion rate (Fabian, 1999; Fabian et al., 2008; Ricci et al., 2017d), meaning that the geometry of the obscurer may be inherently related to the intrinsic properties of the central engine itself. An optimal sample of AGN to observe in X-rays for the development of future obscuration models would hence include 1) Compton-thick obscuration to ensure that the reprocessed emission dominates the observed spectrum, 2) known inclination to remove a geometrical degree of freedom, and 3) precise measurements of black hole mass and multi-wavelength coverage to provide an independent estimate of Eddington-scaled accretion rate.

Disc megamasers satisfy all three criteria. The 22-GHz radio emission line emitted by water vapor is produced by maser amplification[10] and requires highly inclined sight lines to be detected (Zaw et al., 2020). In agreement with the unified model of AGN (Antonucci, 1993; Urry and Padovani, 1995; Netzer, 2015), megamasers are thus often found in Compton-thick AGN in which highly inclined lines-of-sight lead to the highest column densities toward the central engine (Greenhill et al., 2008; Masini et al., 2016; Panessa et al., 2020). Accurate very long baseline interferometry maser mapping additionally provides one of the most precise estimates of the central black hole mass currently known, enabling accurate measurements of Eddington-scaled accretion rate as long as robust bolometric luminosity estimates are available (Brightman et al., 2016). We additionally note that under the unified model, the privileged inclination angles required for 22 GHz water megamaser detection would be purely an orientation effect, with the circum-nuclear obscurer being somewhat similar in all AGN. Thus, future astrophysical surveys of megamasers may be an extremely useful tool not just for studying the circum-nuclear properties of obscured AGN, but the entire AGN population.

In the following sections, we analyze a sample of confirmed Compton-thick AGN with detected water megamaser emission as a basis for developing the next generation of physically motivated obscuration models for *HEX-P*.

3.1 *NuSTAR*-confirmed Compton-thick megamasers

As a basis for our simulations, we selected a sample of 10 Compton-thick AGN in DoCTA with confirmed 22 GHz megamaser in the literature (Masini et al., 2016; Panessa et al., 2020). We additionally included NGC 2960 from Masini et al. (2016) since the target was one of the lowest signal-to-noise ratio sources in their analysis, providing an interesting comparison for *HEX-P*. The sample considered is shown in Table 1. To ensure accurate spectral simulations, we then complemented the longest *NuSTAR* exposure available per source with the *Chandra* observation that was closest in time to the *NuSTAR* observation. Each *Chandra* observation was reprocessed using the `chandra_repro` command in `CIAO` (Fruscione et al., 2006), before creating circular source + background and annular background-only regions centered on the target with each level 2 event file. Owing to the poorer angular resolution of *NuSTAR* compared to *Chandra*, we additionally created circular source + background regions for all clearly visible off-nuclear sources that were within the *NuSTAR* extraction region. Spectra and response files were then produced using the `specextract` command. The breakdown of the sample in terms of source properties and X-ray observations are shown in Table 1. The level of flux contaminating the *NuSTAR* spectra from extracted off-nuclear sources was found to be negligible compared to all AGN apart from NGC 5643. The source has a well-studied ultraluminous X-ray source that has to be accounted for in our spectral analysis (Annuar et al., 2015). We note that at a separation of ~ 50", the AGN and ultraluminous X-ray source would be easily resolved by both the HET and LET onboard *HEX-P* (see Section 5.1).

For X-ray spectral fitting, we use BXA v2.9 that connects the PyMultiNest nested sampling algorithm (Feroz et al., 2009; Buchner et al., 2014) to PyXspec (Gordon and Arnaud, 2021), the Python wrapper for the X-ray spectral fitting environment `Xspec` (Arnaud, 1996). We chose to fit each AGN component with the `UXCLUMPY` model and its associated omnidirectional Thomson scattered emission table. Since we primarily require a good enough description of the observed *Chandra* + *NuSTAR* spectra to perform *HEX-P* simulations, we did not test additional physically motivated models. `UXCLUMPY` does, however, include two unique geometrical parameters that describe the covering factor of material in the obscurer: `TORsigma`, the angular dispersion of the cloud distribution, and `CTKcover`, the covering factor of an additional inner ring of Compton-thick clouds surrounding the AGN. Our spectral model for the AGN in `Xspec` parlance is as follows:

$$\begin{aligned}\text{AGN Model} = {} & \overbrace{\texttt{constant}}^{\text{Cross-calibration}} \times \overbrace{\texttt{TBabs}}^{\text{Galactic absorption}} \\ & \times \left[\overbrace{\texttt{apec}}^{\text{Thermal}} + \overbrace{\texttt{uxclumpy_cutoff_transmit}}^{\text{Transmitted emission}} \right. \\ & \left. + \overbrace{\texttt{uxclumpy_cutoff_reflect}}^{\text{Reprocessed emission}} + \overbrace{\texttt{constant}}^{\text{Scattered fraction}} \right. \\ & \left. \times \underbrace{\texttt{uxclumpy_cutoff_omni}}_{\text{Warm mirror emission}} \right]. \end{aligned} \tag{1}$$

For the ultraluminous X-ray source in NGC 5643, we additionally include the following model:

$$\begin{aligned}\text{ULX Model} = {} & \overbrace{\texttt{constant}}^{\text{Contamination factor}} \times \overbrace{\texttt{TBabs}}^{\text{Galactic absorption}} \\ & \times \left[\overbrace{\texttt{zTBabs}}^{\text{Intrinsic absorption}} \times \overbrace{\texttt{zcutoffpl}}^{\text{Hard X-ray power-law}} + \overbrace{\texttt{diskpbb}}^{\text{Thermal emission}} \right]. \end{aligned} \tag{2}$$

We assumed non-informative priors for line-of-sight column density, intrinsic power-law exponential cutoff, intrinsic power-law normalization, the omnidirectional scattered fraction, Compton-thick inner ring covering factor, cosine of the obscurer dispersion,

10 The name megamaser is assigned to sources with 22 GHz luminosities in excess of 10 $L_{\odot}$.

TABLE 1 Megamaser sample properties and X-ray observations used in this work.

Name (1)	z (2)	D Mpc (3)	Type (4)	M_{BH} 10^6 $M_\odot$ (5)	Ref. (6)	Obs. ID *NuSTAR* (7)	T/ks *NuSTAR* (8)	Obs. ID *Chandra* (9)	T/ks *Chandra* (10)
IC 2560	0.00976	32.9	i	3.5 ± 0.5	1	50001039004	49.6	4908	55.7
NGC 1194	0.01360	61.3	z	65 ± 3	2	60501011002	58.3	22881	21.1
NGC 1386	0.00290	16.2	i	$1.2^{+1.1}_{-0.6}$	3	60201024002	26.4	13257	34.3
NGC 2273	0.00614	30.3	i	7.5 ± 0.4	2	60001064002	23.2	19377	10.1
NGC 2960	0.01650	92.5	i	11.6 ± 0.5	2	60001069002	20.7	22270	10.1
NGC 3079	0.00369	17.6	i	$2.4^{+2.4}_{-1.2}$	3	60662004002	24.6	20947	45.1
NGC 3393	0.01250	56.3	z	31 ± 2	4	60061205002	15.7	13968	28.5
NGC 5643	0.00400	10.5	i	—	—	60061362006	48.1	17664	42.1
NGC 5728	0.00932	27.9	i	—	—	60662002002	24.9	23254	20.1
NGC 7479	0.00792	25.2	i	—	—	60061316002	23.6	10120	10.2

Notes. (1)—Galaxy identifier. (2)—Spectroscopic redshift. (3)—Distance in Mpc. (4)—Distance type: i = redshift-independent, z = redshift dependent. (5)—Black hole mass in 10^6 $M_\odot$ derived exclusively from megamaser emission. (6)—Black hole mass reference: 1: Yamauchi et al. (2012), 2: Kuo et al. (2011), 3: McConnell and Ma (2013), 4: Kondratko et al. (2008). (7)—*NuSTAR*, observation ID. (8)—*NuSTAR*/FPMA, exposure time in ks. (9)—*Chandra* observation ID. (10)—*Chandra* exposure time in ks.

thermal soft–excess temperature, and its associated normalization. For the intrinsic power-law photon index, we assumed a Gaussian prior with mean 1.8 and standard deviation 0.15 in agreement with numerous X-ray surveys (Ricci et al., 2017c). Finally, for cross-calibrations between *Chandra* and FPMB relative to FPMA, we assumed log-Gaussian priors with mean 0 and standard deviation 0.03, consistent with the values of Madsen et al. (2015). In total, there were 11 free parameters in the UXCLUMPY AGN model.

We find all sources to have column densities in excess of 10^{24} cm^{-2} to 90% confidence. Interestingly, this includes NGC 2960 for which we find a line-of-sight column density solution of $N_H > 1.5 \times 10^{24}$ cm^{-2} to 98.2% confidence by fitting the combined *Chandra* and *NuSTAR* data. Previous works that analyzed the *NuSTAR* data alone consistently found $N_H < 10^{24}$ cm^{-2} using the MYTorus obscuration model (Masini et al., 2016). Due to our Compton-thick solution, we include NGC 2960 in DoCTA *ex post facto*. Figure 3 shows that the *NuSTAR* spectra of NGC 2960 are amongst the lowest signal-to-noise in the 3–78 keV band of all other Compton-thick AGN studied with *NuSTAR* to date. Its low signal-to-noise ratio spectrum thus makes NGC 2960 a challenging and very conservative example to showcase the spectral constraints attainable with *HEX-P*.

3.2 Simulating the faint megamaser NGC 2960

We simulate a grid of *NuSTAR* and *HEX-P* spectra to quantify the relative improvement in physical parameter inference attainable with *HEX-P* observations of NGC 2960. Whilst the Compton-thick solution for NGC 2960 that we report here was acquired with the inclusion of *Chandra* data, we restrict our simulations to purely *NuSTAR* due to the relative scarcity of simultaneous observations publicly available (see Figure 6) and as an extrapolation for the discovery space in hard X-rays of new Compton-thick AGN previously missed. In total, we simulate a range of exposures between 10 ks and 100 ks with 10 realizations per exposure. Each simulated spectrum had the same starting spectrum, namely, the maximum *a posteriori* spectral fit acquired with *Chandra* + *NuSTAR*. However, we additionally set the obscurer dispersion to 60° as this parameter was unconstrained and the Compton-thick inner ring covering factor to 30% since it was only constrained to an approximate upper limit of $\lesssim$ 40% with *NuSTAR*.

The results of the NGC 2960 simulation grid are shown in Figure 4 in terms of 90% posterior parameter constraints on the Eddington ratio (*top panel*) and line-of-sight column density (*bottom panel*) as a function of the exposure time. For Eddington ratio error propagation, we sampled from the black hole mass and associated uncertainties in Table 1. However, for the bolometric correction, we use the Compton-thick bolometric correction from Brightman et al. (2016) of 27.5 that focuses on Compton-thick megamasers. To focus on the improvements attainable purely from X-ray spectral fitting as opposed to other systematics, we assume zero uncertainty on bolometric correction. We justify this choice by assuming the plethora of next-generation multi-wavelength observatories that will be available for quasi-simultaneous observations with *HEX-P* that will provide precise photometric data across the electromagnetic spectrum for accurate measurements of bolometric output. Such observatories include the *James Webb Space Telescope* (Rieke et al. 2015), *Euclid* (Laureijs et al., 2011; Racca et al., 2016), the 4-m multi-object spectroscopic telescope (de Jong et al., 2012), the *Nancy Grace Roman Space Telescope* (Spergel et al., 2015; Akeson et al., 2019), and the Vera C. Rubin Observatory (Ivezić et al., 2019).

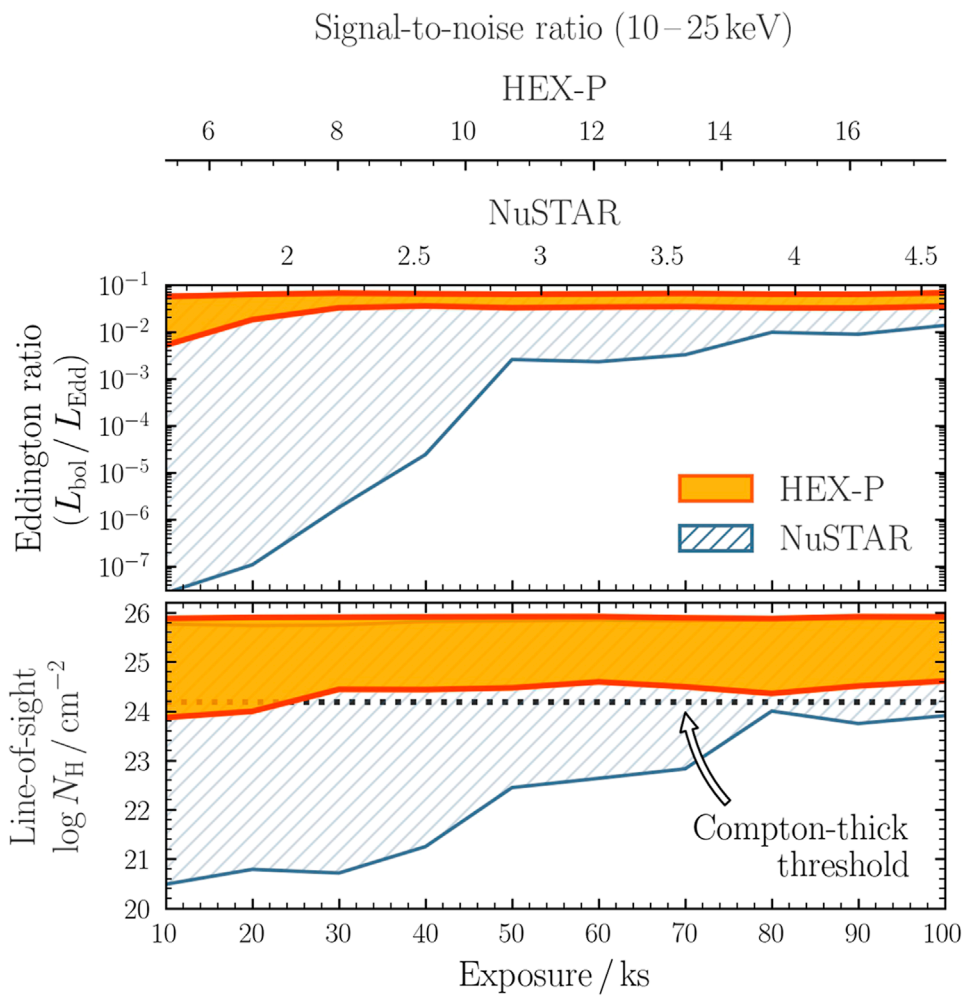

FIGURE 4
Simulated parameter constraints for one of the faintest Compton-thick AGN candidates known: NGC 2960. Bottom panel: Line-of-sight column density posterior 90% quantile range as a function of exposure time for *NuSTAR* (gray hatched region) and *HEX-P* (orange filled region). *HEX-P* could stringently confirm the target as Compton-thick (horizontal dotted line) with a modest ~ 25 ks exposure, which is not possible with *NuSTAR* alone in less than 100 ks Top panel: Same as the bottom one, but for the constrained Eddington ratio. *HEX-P* could constrain the intrinsic luminosity and hence the accretion rate, to comparable precision of the black hole mass for exposures ≳ 30 ks. The top axes show the average measured signal-to-noise ratio in the 10–25 keV band for *NuSTAR* and *HEX-P*, which is found to be ~ 4× higher than that for *NuSTAR* on average.

Even for the low signal-to-noise ratio challenge that NGC 2960 poses, *HEX-P* can achieve Eddington ratio uncertainties comparable to the uncertainties on black hole mass for exposures ≳ 30 ks. By contrast, *NuSTAR* does not reach a similar uncertainty regime for the entire range of exposures considered in the simulations. *HEX-P* can additionally classify the target as Compton-thick to 90% confidence for exposures ≳ 25 ks—a feat that is not possible from purely *NuSTAR* spectroscopy in our simulated range of exposures. We note that the remaining posterior uncertainty above the Compton-thick limit at all exposures with *HEX-P* arises from the stability of the Compton-scattered component in UXCLUMPY. The overall shape of the reprocessed component does not change substantially for line-of-sight column densities $N_H \gtrsim 5 \times 10^{24}$ cm^{-2}, such that constraining line-of-sight column densities to more than a lower limit is currently difficult. The top axis of Figure 4 shows the measured signal-to-noise ratio in the 10–25 keV band for *NuSTAR* and *HEX-P*. The reduced background and simultaneous coverage from three different instruments can boost the signal-to-noise ratio by factors of ~ 4 relative to that of *NuSTAR*. In the case of NGC 2960, the boost in observed signal-to-noise ratio means that a 10-ks exposure with *HEX-P* would require ≫ 100 ks of *NuSTAR* exposure to reach an equivalent 10–25 keV spectral quality. The 10–25 keV energy band holds a plethora of information, not only regarding the line-of-sight column density but also the overall structure of the circum-nuclear obscurer (see Buchner et al., 2019, 2021).

3.3 Prospects for a new era of spectral models

From the signal-to-noise ratio improvements highlighted in Figure 4 and the exceedingly low signal-to-noise ratio of the

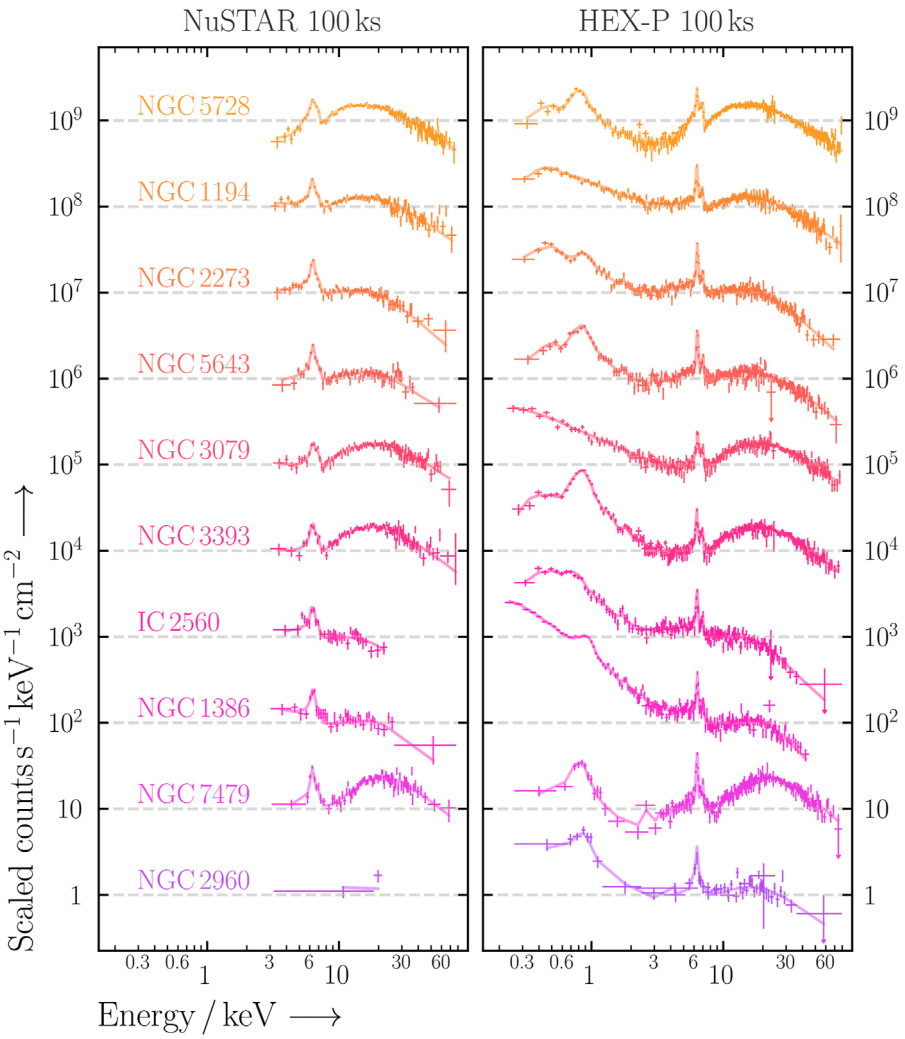

FIGURE 5
Simulating the spectral prospects attainable with *NuSTAR* (*left*) and *HEX-P* (*right*) with 100 ks observations of the Compton-thick megamasers considered in this work. Both panels show the folded simulated spectra from each telescope, normalized by their respective effective areas. *HEX-P* offers a greatly expanded passband, with improved sensitivities up to the highest energies with higher spectral resolution. For each spectrum, any spectral bins with negative lower bounds are shown with The "upper limit arrows" refer to the arrows plotted in the figure that point downwards, and any data that are completely background dominated are omitted for clarity.

NuSTAR data for NGC 2960, it is clear that every known Compton-thick AGN will benefit greatly from modest *HEX-P* observations. Next, we simulate our sample of Compton-thick megamasers for 100 ks with both *NuSTAR* and *HEX-P* to visually showcase the spectral improvements attainable, which will allow the development of next-generation spectral models. In Figure 5, we present a comparison between *NuSTAR* (*left* column) and *HEX-P* (*right* column), ordered from bottom to top by observed 2–10 keV flux. We note that this is already not a like-for-like comparison since *NuSTAR*'s low Earth orbit leads to an ~50% observing efficiency, compared to an ~100% observing efficiency for *HEX-P* observations of $\lesssim$2 weeks in duration. Despite this, a number of crucial improvements are still visible.

Hard X-ray sensitivity: Whether it be due to the overall spectral slope, high-energy cutoff, structural properties of the obscurer or some combination of each, every AGN has a very distinctive spectral shape >10 keV that is clearly detected with *HEX-P*. By contrast, a large number of the simulated *NuSTAR* spectra are not well detected at $\gtrsim$20 keV. These improvements offer a number of useful avenues for model constraints and development. Extending the range of detectable energies to $\gtrsim$50 keV with *HEX-P* will also enable a dramatic reduction in confusion arising from different model components. For example, the high-energy exponential cutoff associated with the intrinsic coronal emission can be extremely difficult to disentangle from the turnover of the Compton hump (Baloković et al., 2019; Kammoun et al., 2023). Furthermore, the covering factor is very dependent on the Compton hump shape, and reducing the measurement uncertainties at $\gtrsim$20 keV will greatly advance our ability to detect it.

Spectral resolution: From Figure 5, it is clear that the spectral resolution arising from the LET is superior to that of *NuSTAR*.

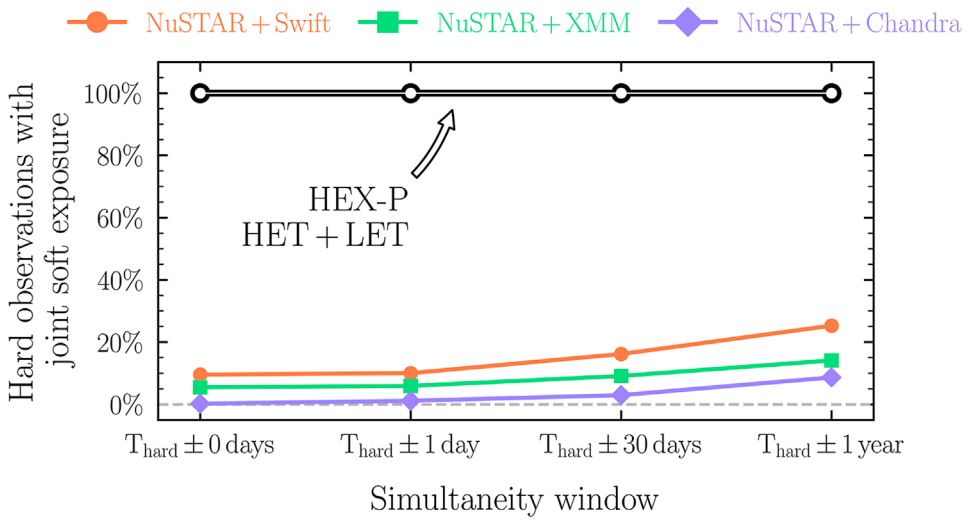

FIGURE 6
Percentage of hard X-ray observations with overlapping soft X-ray exposure available for *NuSTAR* vs. *HEX-P*. To be conservative, in each time window (shown along the horizontal axis), we consider any hard X-ray observation with > 20% of its total exposure overlapping with a soft X-ray observation to be "joint." Archival *NuSTAR* observations were considered for any *Swift*/BAT AGN from the 70-month compilation of Ricci et al. (2017c), obscured with line-of-sight column density $N_H > 10^{22}$ cm^{-2}. Clearly, the complimentary data provided by the LET + HET onboard *HEX-P* will, for the very first time, provide complete simultaneous coverage across the hard and soft X-ray bands.

By combining high spectral resolution measurements of the Fe K region (which includes the Fe Kα and Fe Kβ lines) with sensitive measurements of the underlying reflection continuum up to energies $\gtrsim 20$ keV will enable detailed studies of fluorescence emission in heavily obscured AGN, such as metallicities, dynamics, and emission origins.

Simultaneous soft X-ray coverage: Figure 5 clearly shows the vast range in predicted spectral shapes from our broadband *Chandra* + *NuSTAR* fitting that are not accessible with *NuSTAR*. Whilst quasi-simultaneous soft X-ray coverage is a common strategy for *NuSTAR* observations, exposure times and the corresponding signal-to-noise ratios are often not consistent across instruments (see Figure 6), leading to discrepant measurements of line-of-sight column density (Marchesi et al., 2018). With *HEX-P*, well-matched sensitivities with 100% observing simultaneity will enable broadband X-ray spectral fitting effectively devoid of mismatched signal-to-noise ratio issues.

4 Uncovering the dynamics of the thickest obscurers

Multi-epoch X-ray observations have proven to be a powerful tool for constraining the structure and dynamics of the obscurer. The ability to determine the amount of obscuring material along the line-of-sight as a function of time can be used to place constraints on the sizes of obscuring clumps, as well as their distance from the supermassive black hole (Elvis et al., 2004; Risaliti et al., 2009; Markowitz et al., 2014). Even for sources with sparsely sampled light curves, changes in line-of-sight column densities as a function of time can be used to gain insights into the general scales associated with the obscurer (Laha et al., 2020).

Since the launch of *NuSTAR*, broadband X-ray coverage has allowed the use of complex reflector models, which in turn can constrain global properties of the obscurer such as obscuring covering factor (parameterized as the fraction of sky covered when viewed from the perspective of the corona), inclination angle, and the global obscuring column density out of the line-of-sight (Baloković et al., 2018; Zhao et al., 2019a; Marchesi et al., 2019b; Buchner et al., 2019; Zhao et al., 2019b; Baloković et al., 2021; Zhao et al., 2021). Some works have suggested a correlation between the global properties of the obscurer and the characteristic changes in line-of-sight column densities as a function of the timescale (Pizzetti et al., 2022; Torres-Albà et al., 2023). An advantage of multi-epoch fitting is that parameters unexpected to vary over the relatively short timescales associated with the observations (e.g., the obscurer covering factor or global obscurer column density out of the line-of-sight) can be tied across observing epochs. Such an approach typically leads to more precise constraints on obscurer parameters since there are typically fewer regions of the parameter space compatible with multiple spectra than a single epoch-averaged spectrum (see Baloković et al., 2018; Marchesi et al., 2022; Pizzetti et al., 2022; Torres-Albà et al., 2023).

HEX-P, with its capability to simultaneously observe the soft and hard X-ray bands to greatly improved sensitivity limits, will prove a key instrument for time domain studies (Brightman et al., 2023), such as the time-resolved characterization AGN obscuration in X-rays. Non-simultaneous soft and hard band observations impose significant difficulty in disentangling intrinsic coronal luminosity variability from obscuration-related variability. For example, Torres-Albà et al. (2023) found that for up to 7/12 nearby obscured AGN with confirmed long-term X-ray variability, the two variability

options could not be distinguished due to non-simultaneous soft and hard X-ray observations.

With the results of Torres-Albà et al. (2023) in mind, we sought to assess the current availability of multi-epoch broadband X-ray observations amongst the obscured AGN population. We queried the High-Energy Astrophysics Science Archive Research Center[11] for targeted *NuSTAR* observations of any AGN in the 70-month BAT catalog with line-of-sight column densities $N_{\rm H} > 10^{22}$ cm^{-2}, according to the X-ray spectral fitting catalogs of Ricci et al. (2017c). We then searched for soft X-ray coverage from *XMM-Newton*, *Swift*/XRT, or *Chandra* for each of the 372 obscured AGN with available *NuSTAR* observations (439 *NuSTAR* observations in total). Figure 6 quantifies the frequency of joint soft + *NuSTAR* observations in the obscured AGN sample as a function of ever-increasing hard X-ray observation simultaneity window. To be conservative, we consider any *NuSTAR* observation with > 20% of its total exposure with joint soft exposure within each considered time window to be 'joint'. Even by liberally considering the non-simultaneous scenario of soft observations within 1 year of the *NuSTAR* observations, only ~ 25% have > 20% of their exposure coincident with *NuSTAR* exposure. Even though almost every *NuSTAR* observation considered should have a quasi-simultaneous short (~1–2 ks) *Swift*/XRT coordinated observation, the XRT exposures are typically far shorter than each corresponding *NuSTAR* observation. Having considerably different *NuSTAR* and soft X-ray exposure times can give rise to dramatically different data quality across the spectral passband. Data quality mismatches have been shown to influence measurements of obscuration parameters in heavily obscured AGN considerably (Marchesi et al., 2018; Tanimoto et al., 2022. *HEX-P* will clearly revolutionize the field, providing 100% strictly simultaneous broadband coverage for all observations.

In the sections that follow, we quantify the advances *HEX-P* will make toward multi-epoch observations of obscured AGN with detailed simulations.

4.1 Case study I: non-Compton-thick obscured AGN

First, we consider an obscured but not Compton-thick AGN (line-of-sight $N_{\rm H} \lesssim 10^{24}$ cm^{-2}) that presents both intrinsic luminosity and line-of-sight obscuration variability over three epochs of observation. To make our simulations conservative, we normalize the source flux to NGC 835—the faintest AGN in the sample of Torres-Albà et al. (2023) with confirmed line-of-sight column density variability. We parameterize the obscurer with the `borus02` model (Baloković et al., 2018) in the decoupled mode, in which the obscurer properties were tuned to match the properties derived by Zhao et al. (2021) for a sample of ~ 100 obscured AGN. We simulate and fit with the same model to avoid any systematic uncertainties associated with the *a priori* unknown obscurer that could be more dramatic for the less sensitive *NuSTAR* data than *HEX-P* (i.e., fewer model spectra can accommodate a given *HEX-P* spectrum than *NuSTAR* with reduced sensitivities and passband; see Saha et al., 2022). We consider three different line-of-sight column densities, namely, $N_{\rm H} = 1, 3, 6 \times 10^{23}$ cm^{-2}. To model additional flux variability, we include a cross-normalization constant to the intrinsic AGN emission to simulate 50%, 100%, and 200% flux variability for each of the three observational epochs, respectively. We pair line-of-sight column densities with different flux variability constant values per observational epoch to show increased intrinsic flux with increased line-of-sight column density. We then run spectral simulations of 20 ks exposure times with *NuSTAR* and *HEX-P* before refitting to quantitatively compare each mission's ability to disentangle the two separate forms of variability we consider.

Figure 7 shows the results of our simulations. The *left* panel presents the simulated *HEX-P* spectra, in which the variations in column density from the photoelectric turnover and intrinsic flux from the overall normalizations are clearly visible. The *right* panel shows the resulting constraints in terms of intrinsic flux and line-of-sight column density for both *HEX-P* and the equivalent simulated *NuSTAR* spectra. Overall, we find uncertainties ~ 3–4 times larger with *NuSTAR* than with *HEX-P*. We additionally find the *NuSTAR* constraints on line-of-sight column density to be systematically lower than for *HEX-P*, likely caused by the difficulties associated with constraining the photoelectric turnover purely from a passband above 3 keV. The *NuSTAR* constraints can only place upper limits on the lowest line-of-sight column density scenario that we considered, primarily due to its lack of simultaneous soft band coverage encompassing the photoelectric turnover at soft energies. At higher column densities, the remaining two scenarios are consistent within 99% confidence in terms of both line-of-sight column density constraints and intrinsic flux. By contrast, even for a short 20 ks snapshot, *HEX-P* has no issue in disentangling intrinsic flux variability from line-of-sight column density variability for the full range of column densities considered. The broader passband is crucial, enabling proper characterization of obscuration changes visible through the photoelectric turnover that are degenerate with intrinsic flux changes at harder energies.

4.2 Case study II: Compton-thick AGN

As discussed in Section 1, there have been comparatively few detailed multi-epoch broadband spectroscopic studies of Compton-thick AGN to date, which are dominated by the brightest sources known (Puccetti et al., 2014; Marinucci et al., 2016). An additional limitation with observing variability in Compton-thick AGN is that eclipsing events or intrinsic flux variations are more likely to manifest at ≳10 keV, where the effects of photoelectric absorption are reduced and Compton scattering dominates providing excess detectable flux (Marinucci et al., 2016; Zaino et al., 2020). The improved sensitivity at >10 keV with *HEX-P* will lead to new insights into broadband variability characteristics of Compton-thick AGN that have not been possible to date. To simulate the prospects attainable with *HEX-P*, we use the faintest Compton-thick AGN with a published multi-epoch *NuSTAR*-based campaign to date as the baseline. The nearby Seyfert 2 galaxy NGC 1358 (z = 0.0134) was subjected to a multi-epoch monitoring campaign with *NuSTAR* and *XMM-Newton* between 2017 and 2022 and was found to be highly variable in line-of-sight column density by Marchesi et al. (2022).

11 https://heasarc.gsfc.nasa.gov

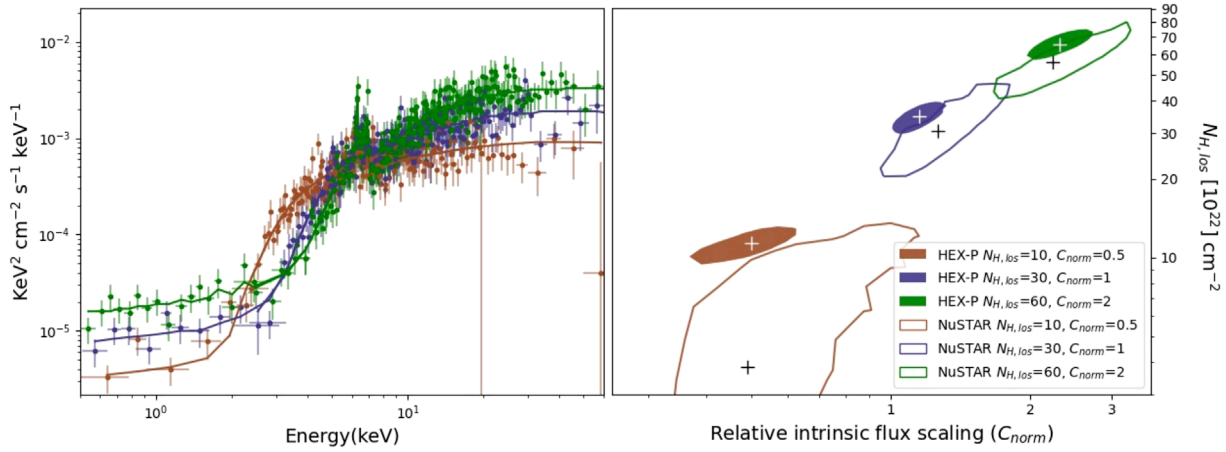

FIGURE 7
Left panel: *HEX-P*/LET + HET spectra simulated with 20 ks exposures from the model described in Section 4.1, based on NGC 835 as a baseline. Colors correspond to the different combinations of line-of-sight column density and intrinsic flux scaling. *Right* panel: Corresponding 99% confidence contours between intrinsic flux scaling vs. line-of-sight column density derived from *HEX-P* (filled) and *NuSTAR* (empty). The crosses represent the best-fit values.

For our *HEX-P* simulations, we use decoupled `borus02` and choose a range of line-of-sight column densities consistent with those measured for NGC 1358 by Marchesi et al. (2022) that varied above and below the Compton-thick limit in a changing-look behavior. The specific line-of-sight column densities that we considered were $N_{\rm H}$ = 0.8, 1.4, 2×10^{24} cm^{-2}. To make our simulations applicable to the wider AGN population, we choose a value of Γ = 1.8, consistent with the broader population of low-redshift Seyfert galaxies (Ricci et al., 2017c). The Thomson-scattered flux fraction is set to 2%, which is again conservative, considering the latest relationships between scattered fraction and line-of-sight column density from Gupta et al. (2021). We additionally include a thermal `apec` component (with temperature kT = 0.3 keV) to model the remaining soft excess flux that the Thomson-scattered power-law does not account for. The global obscuring column density out of the line-of-sight is assumed to be $N_{\rm H} = 3.2\times10^{23}$ cm^{-2} with a covering factor of 15% within the `borus02` model.

The intrinsic 2–10 keV luminosity of NGC 1358 was found by Marchesi et al. (2022) to be $L_{2-10\ \rm keV}$ ~6–9 × 10^{42} erg s^{-1} with a corresponding observed 2–10 keV flux $F_{2-10\ \rm keV}$ = 4–12 × 10^{-13} erg s^{-1} cm^{-2}. To understand the new parameter space that *HEX-P* will probe, we simulate a fiducial source more than an order of magnitude fainter than NGC 1358 with $L_{2-10\ \rm keV}$ = 5 × 10^{41} erg s^{-1}, corresponding to the observed fluxes of $F_{2-10\ \rm keV}$ = 11, 6, 4 × 10^{-14} erg s^{-1} cm^{-2} for each line-of-sight column density considered. We note that equivalent fluxes (and hence spectroscopic constraints) would be constrained for a target at 10 times the distance of NGC 1358 (i.e., D ~500–600 Mpc) with Seyfert-like luminosities of $L_{2-10\ \rm keV}$ ~ 5 × 10^{43} erg s^{-1}. In comparison, it is currently very difficult to perform detailed X-ray spectroscopic modeling of Seyfert-luminosity Compton-thick AGN with *NuSTAR* at comparable distances (Giman et al., 2023).

We simulate one 30-ks *HEX-P* observation for each line-of-sight column density state mentioned above. The line-of-sight column density is recovered to high accuracy with relative uncertainties ≤20%. Owing to the strong advantage of linking parameters that are not expected to vary between epochs, the global column density is precisely recovered with uncertainties < 0.3 dex, and the obscuration covering factor is correctly found to be < 20% to high confidence. Our simulations thus clearly show that a *HEX-P* monitoring campaign would allow us to characterize the properties of the clumpy obscuring medium in heavily obscured AGN with unprecedented quality to far fainter flux levels than are attainable with current X-ray observatories. Such capabilities are critical for constraining the dynamics of the obscurer in the wider Compton-thick AGN population that is currently impossible.

5 The circum-nuclear obscurer of AGN at low accretion power

Our knowledge of the obscurer surrounding low-accretion-power AGN is currently severely incomplete. A root cause is the considerable challenge to select and classify true low-accretion-power AGN, especially at high line-of-sight column densities. *NuSTAR* has provided an unprecedented view into the hard X-ray properties of the circum-nuclear environment of low-luminosity AGN for the first time (Ursini et al., 2015; Annuar et al., 2017; Young et al., 2018; Younes et al., 2019; Annuar et al., 2020; Diaz et al., 2020; Baloković et al., 2021; Diaz et al., 2023). *NuSTAR* has also led to the discovery and classification of a few low-luminosity Compton-thick AGN (Annuar et al., 2017; Brightman et al., 2018; Da Silva et al., 2021), providing exciting evidence that suggests AGN can sustain a significant obscuration structure at low luminosities. However, current observational studies of Compton-thick low-luminosity AGN are often hindered by the requirement for deep integration times to obtain sufficient counts for detailed X-ray spectral modeling (Annuar et al., 2020).

Given the current scarcity of *bona fide* low-luminosity Compton-thick AGN confirmed by broadband X-ray studies that

include hard X-ray observations with *NuSTAR*, we sought to investigate the prospects attainable with *HEX-P* for identifying, classifying, and studying this elusive population in the nearby universe. We tuned our simulations to the properties of four *bona fide* low-luminosity AGN with heavy obscuration in the literature; M51a (Brightman et al., 2018), NGC 660 (Annuar et al., 2020), NGC 1448 (Annuar et al., 2017), and NGC 2442 (Da Silva et al., 2021). We note all sources have column density classifications based in part with *NuSTAR*. In addition, all are confirmed Compton-thick apart from NGC 660 which has both Compton-thick and sub-Compton-thick (but still heavily obscured) solutions in Annuar et al. (2020). With this caveat in mind, for the remainder of this section, we refer to this sample of four sources as the low-luminosity Compton-thick AGN sample.

5.1 Selecting and classifying low-luminosity Compton-thick AGN

A major challenge for studies of low-luminosity AGN is confidently associating detected sources with accretion onto a supermassive black hole, as opposed to off-nuclear accretion onto low-mass compact objects such as ultraluminous X-ray sources, other individual X-ray binaries, or jetted emission (see Bachetti et al., 2023; Lehmer et al., 2023; Connors et al., 2023; Marcotulli et al., 2023 for the *HEX-P* perspective on ultraluminous X-ray sources, other extragalactic accreting compact objects, and resolved AGN jets). A major advantage arises from spectral coverage at $\gtrsim 10$ keV in which the spectral curvature from accreting supermassive black holes can be dramatically different from that of low-mass accreting compact objects. However, an additional difficulty with classification is being able to resolve emission components into individual sources to confidently ascertain the spectral parameters of the central AGN. Given the dramatic improvement in X-ray angular resolution of *HEX-P* compared to both *XMM-Newton* and *NuSTAR*, we sought to test *HEX-P*'s ability to resolve contaminating sources in the host galaxy from low-luminosity AGN.

We base our simulations on the central region of M 51 which is known to host a Compton-thick low-luminosity AGN and a number of bright off-nuclear X-ray sources (Brightman et al., 2018). Our main consideration here was "ULX-3," which is situated ~ 30" from the central AGN and is the closest spatial contamination of all four sources in the Compton-thick low-luminosity AGN sample. Though spatially resolved with *Chandra*, the close separation led to strong contamination with *NuSTAR* that must be accounted for by simultaneously fitting both data sets to infer spectral parameters of the central AGN and ULX-3.

To demonstrate *HEX-P*'s unique capability to spatially resolve closely separated sources in both the soft and hard X-ray energy bands, we compare current constraints from *Chandra* and *NuSTAR* to that of *HEX-P* with simulations. We simulate *HEX-P* soft (<10 keV) and hard (>10 keV) X-ray imaging of M51a and the nearby ultraluminous X-ray source (ULX-3, Brightman et al., 2018) using the Simulated Observations of X-ray Sources (SOXS, ZuHone et al., 2023) and Simulation of X-ray Telescopes (SIXTE, Dauser et al., 2019) software suites. We rely upon SOXS for creating SIMulated inPUT (SIMPUT) files, which incorporates our spectral and spatial models for individual targets. For simplicity, we choose all emission to have energies > 2 keV, in order to exclude any softer extended X-ray emission from the simulation and to enable a more direct study of the resolving power of *HEX-P*.

We use point source models to simulate the spatial morphology of M51a and ULX-3. For spectral modeling, we fit the *Chandra* spectra for M51a and ULX-3 simultaneously with the unresolved *NuSTAR* spectrum of both sources using the same UXCLUMPY-based model described in Section 3 combined with the ultraluminous X-ray source model used to fit NGC 5643. We allow the AGN model to vary for the M51a *Chandra* spectrum and combine the *NuSTAR* spectrum and *vice versa* for ULX-3. The individual AGN and ULX-3 maximum *a posteriori* models found with BXA were then used in conjunction with the spatial model to generate a SIMPUT file. Next, we use SIXTE to produce the telescope event files, energy-filtered imaging, and spectroscopic data products. In order to compare *HEX-P*'s capabilities with current facilities, we also use archival event files for *Chandra*/ACIS-S (0.1–8 keV) and *NuSTAR*/FPMA + FPMB (3–78 keV).

We show the simulated *HEX-P*/LET and HET imaging in Figure 8, juxtaposed with the simulated *Chandra* and *NuSTAR* imaging of the same sources. Despite resolving the AGN and ultraluminous X-ray source well, *Chandra* could only study the targets below 8 keV. As discussed throughout this paper, this limitation considerably restricts the ability for physical inference of the obscurer. It is also clear from the figure that while *NuSTAR* has access to soft (< 10 keV) and hard (> 10 keV) X-ray energies, it cannot spatially resolve the X-ray sources well on these spatial scales. *HEX-P* provides a unique combination of high spatial resolution *broadband* observations, enabling a new era of spatially resolved closely separated nuclear sources. These simulations showcase the power and complementary nature of *HEX-P*/LET and HET imaging to provide enhanced searches of heavily obscured low-luminosity AGN in our nearby galactic neighborhood.

5.2 The nature of the obscurer at low accretion powers

The covering factor of the obscurer at low accretion powers is currently very uncertain, due in part to the difficulty associated with selecting heavily obscured low-luminosity AGN relative to their less obscured counterparts. Here, we investigate the ability of *HEX-P* to study the covering factor of Compton-thick AGN via detailed spectral modeling of individual sources.

To provide a firm basis for our simulations, we begin from all archival *Chandra* and *NuSTAR* data available for NGC 660, NGC 2442, and NGC 1448. For NGC 2442, there were two archival *NuSTAR* and two archival *Chandra* observations. We extracted the spectra following the same criteria as throughout this paper, before manually checking for significant variability between observations. Due to the lack of strong variability, we then co-added all *NuSTAR*/FPMA, *NuSTAR*/FPMB, and *Chandra* spectra individually to provide ~49.5 ks of total *Chandra* exposure and ~ 112 ks of *NuSTAR* exposure. For NGC 1448 and NGC 660, we extracted the *Chandra* and *NuSTAR* data following the methods from Annuar et al. (2017) and Annuar et al. (2020),

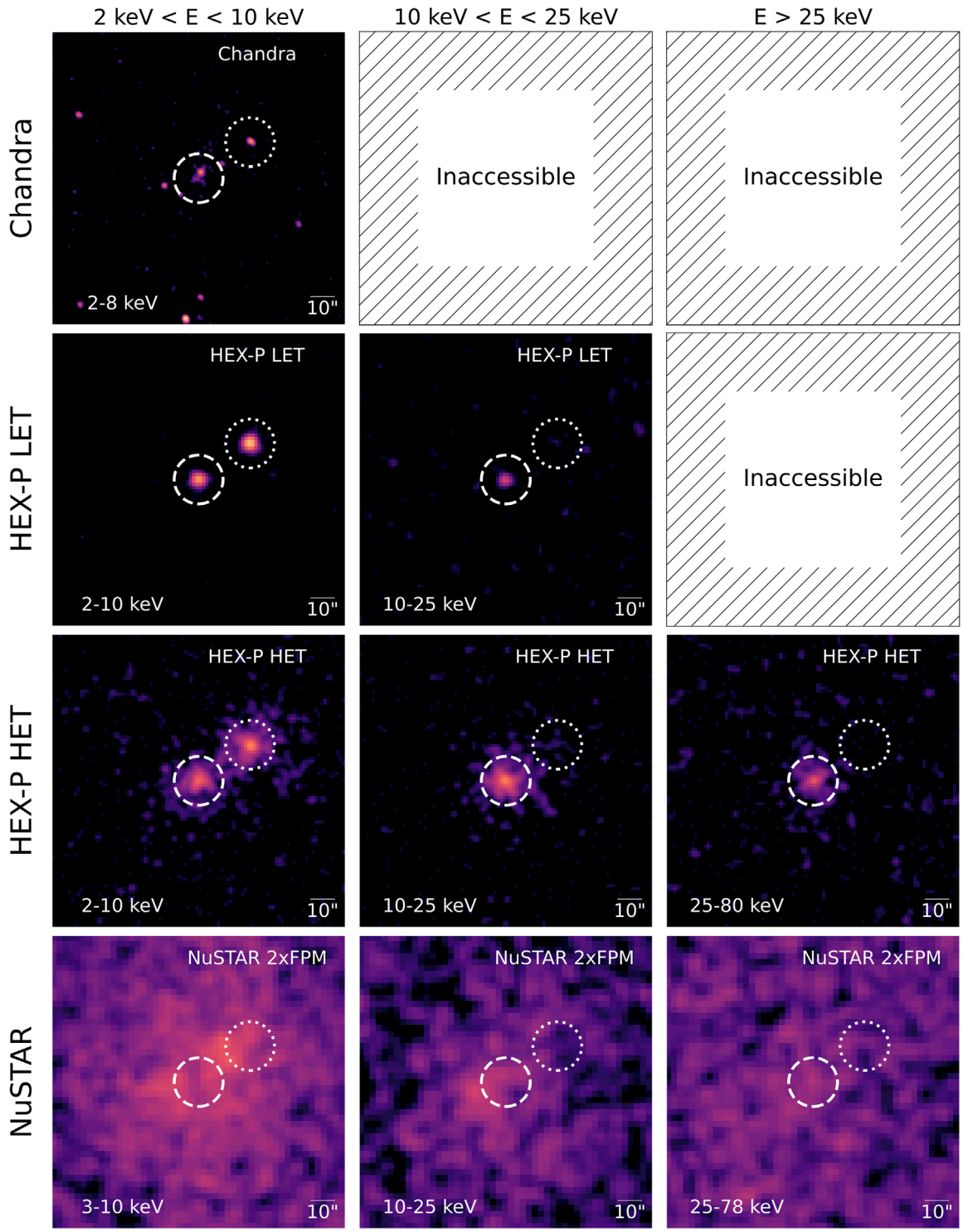

FIGURE 8
Comparing the energy coverage and spatial resolution of *Chandra*, *NuSTAR*, and *HEX-P* for the case of M51a and the nearby ULX-3. The rows represent *Chandra*, *HEX-P*/LET, *HEX-P*/HET, and *NuSTAR*, from top to bottom. The columns represent increasing energy bands, with *left* showing 2 keV < *E* <10 keV; *middle*, 10 keV < *E* < 25 keV; and *right*, *E* >25 keV. For instruments without access to a specific energy passband, the panel is marked as "inaccessible." All tiles are centered on M51a (dashed circle) and the off-center source is ULX-3 (dotted circle). Clearly, *Chandra* can spatially resolve M51a and ULX-3 but does not have access to harder X-ray energies (>10 keV). By contrast, *NuSTAR* has broadband coverage (3 – 78 keV), but lacks the angular resolution to resolve the two sources. *HEX-P* will provide spatially resolved measurements of M51a and ULX-3 in both the 2–25 keV passband with the LET and the 2–80 keV passband with the HET. The half-power diameters are 3.5″ for the LET and 10″, 17″, and 23″ at 10, 30, and 60 keV, respectively, for the HET.

respectively. We additionally included the same absorbed power-law model components from Annuar et al. (2017) for two off-nuclear contaminants inevitably included in the NGC 1448 *NuSTAR* extraction region that were resolved by *Chandra*. The two contaminant model components were kept frozen to their best-fit values from Annuar et al. (2017) for all fitting that involved *NuSTAR*. However, given the results of Section 5.1, *HEX-P* could easily resolve these contaminants from the AGN such that any spectral simulations and corresponding fitting of *HEX-P* spectra only considered the AGN component in NGC 1448.

We then performed spectral modeling using the UXCLUMPY model (Buchner et al., 2019), which included emission from a clumpy obscurer, soft X-ray excess emission from an omnipresent warm mirror, and a thermal component with apec. We experimented with a number of spectral fitting setups, but due to the low signal-to-noise ratio of the observed spectra, a number of unphysical parameter constraints had to be avoided. One example is the tendency for the fit to prefer a low covering-factor obscurer (i.e., the TORsigma parameter in UXCLUMPY tended toward its minimum) in exchange for a hard X-ray photon index and overall unobscured spectrum. Similar degeneracies are well documented in the literature (Brightman et al., 2015), and as such, we opted to freeze TORsigma to a fiducial value of 60° for the spectral fitting of archival data.

Interestingly, the resulting parameter posteriors indicated a diversity in CTKcover between sources, suggesting a diversity in Compton hump shapes across the three sources fit here[12]. From each acquired modal posterior model spectrum, we simulated the corresponding *HEX-P*/LET and *HEX-P*/HET spectra with 100 ks exposures before re-running the same spectral fits with TORsigma additionally left free to vary. Given the distribution of column densities assigned to clouds in the UXCLUMPY model (Buchner et al., 2019), it is difficult to parametrically calculate a covering factor for a particular cloud configuration. We instead used pre-tabulated calculations of covering factor for all material with $N_{\rm H} > 10^{22}$ cm^{-2} and $N_{\rm H} > 10^{24}$ cm^{-2} for a two-dimensional grid of TORsigma and CTKcover values. We used grid interpolation to propagate all posterior uncertainties from TORsigma and CTKcover into posteriors for both of these column density regimes.

To investigate *HEX-P*'s ability to probe the precise relationships between accretion power and covering factor in Compton-thick low-luminosity AGN, we required an estimate of the Eddington ratio for each target. The black hole masses that we used were $\log M_{\rm BH}/M_{\odot} = 7.35 \pm 0.50$ (Annuar et al., 2020)[13], 7.28 ± 0.33 (Davis et al., 2014), and $6.0^{+0.1}_{-0.5}$ (Annuar et al., 2017) for NGC 660, NGC 2442, and NGC 1448, respectively. We then used the bolometric correction relationship shown in Eq. (2) of Nemmen et al. (2014) for low-luminosity AGN to estimate the posterior distribution on the bolometric correction.

The corresponding two-dimensional contours shown in Figure 9 give the posteriors on the Eddington ratio vs. covering factor for material with $N_{\rm H} > 10^{22}$ cm^{-2} and $N_{\rm H} > 10^{24}$ cm^{-2} in the *left* and *right* panels, respectively. Both covering factors are calculated from the Supplementary Appendix Table 2 in Section 8, which lists the spherically averaged angle covering factors above two column densities. *HEX-P* spectroscopy can thus constrain the covering factor to within $\lesssim$20% in the lowest luminosity Compton-thick AGN currently known. Such observations are critical to understand the presence and corresponding importance of circum-nuclear obscuration in the low-luminosity regime.

6 An intermediate mass black hole confirmed with megamaser emission

To explore the parameter space attainable with *HEX-P* in the search for obscured intermediate mass black holes, we start from the work of Chen et al. (2017) who selected a sample of 10 low-mass AGN from the 40-month *NuSTAR* serendipitous survey. Of this sample, IC 750 has a confirmed 22 GHz water megamaser signature (Zaw et al., 2020), placing a tight upper bound on the central black hole mass in the intermediate mass range of $M_{\rm BH} < 1.4 \times 10^5$ M$_{\odot}$. As discussed in Section 3, megamasers are ideal targets for *HEX-P* to aid the development of future circum-nuclear obscuration models, and hence IC 750 provides an extension to the black hole mass range of known megamaser AGN. Furthermore, Chen et al. (2017) performed phenomenological X-ray spectral fitting to an ~30 ks *Chandra* spectrum of IC 750, finding the source to be heavily obscured with line-of-sight $N_{\rm H} \sim 1.2 \times 10^{23}$ cm^{-2}. As discussed by Chen et al. (2017) and throughout this work, X-ray spectral fitting to a predominantly soft band spectrum without sensitive broadband coverage can give rise to wide systematic uncertainties on the properties of the obscurer.

We downloaded and reprocessed all archival *Chandra* data sets of IC 750 using the chandra_repro command available in CIAO (Fruscione et al., 2006). The level 2 event files were then used to create the circular source + background and annular background-only regions centered on the target. We made sure to make the source + background regions small enough to remove as much contamination as possible from the $E < 2$ keV diffuse extended emission reported by Chen et al. (2017). The background regions were created to be as large as possible whilst avoiding off-nuclear sources and chip gaps. Source + background, background, and response spectral files were then produced using the specextract command.

After a variety of different tests of significant spectral variability, we chose to co-add the six individual X-ray spectra using the ftool command addspec. The resulting co-added spectrum contained a net exposure of 177 ks with 441 source counts detected in the 0.5–8 keV band (see the *left* panel of Figure 10). As an initial assessment of the spectrum, we fit a similar model to Chen et al. (2017), namely, an absorbed power-law with an additional thermal component provided by apec and a narrow Gaussian line to represent the Fe K complex. The corresponding folded spectrum with shaded posterior and two-dimensional posterior between observed 0.5–8 keV luminosity and Fe K equivalent width are shown

12 The clouds that form the inner ring described by CTKcover in UXCLUMPY are assigned log $N_{\rm H}$ drawn from a log-normal distribution with $N_{\rm H} = 10^{25.5 \pm 0.5}$ cm^{-2}.

13 We conservatively assumed 0.5 dex uncertainty for NGC 660 when propagating uncertainties on the Eddington ratio posterior.

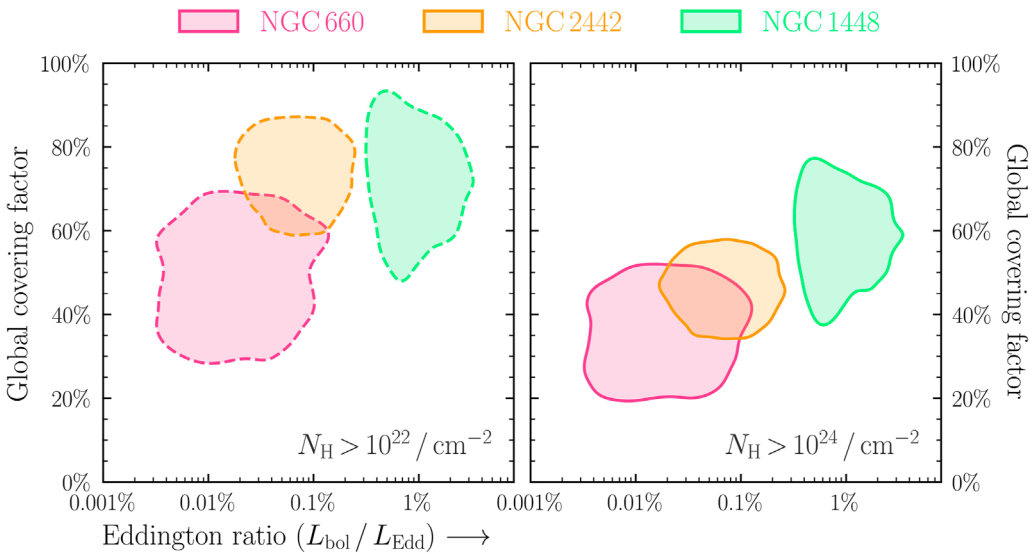

FIGURE 9
HEX-P 100 ks simulation contours for *NuSTAR*-confirmed low-luminosity Compton-thick AGN. The posterior contours show Eddington ratio vs. covering factor for material in the UXCLUMPY geometry with *left:* $N_H > 10^{22}$ cm^{-2} and *right:* $N_H > 10^{24}$ cm^{-2}. Note: due to the overall similar correlations between TORsigma, CTKcover, and the global covering factors of material with $N_H > 10^{22}$ cm^{-2} and $N_H > 10^{24}$ cm^{-2} (see Section 8), the propagated uncertainties in global covering factor have similar shapes. Performing similar spectral fitting to archival *NuSTAR* + *Chandra* data was insufficient to break degeneracies associated with the covering factor, photon index, and line-of-sight column density—see Section 5.2 for details. For both panels, the contours encompass 90% of the probability.

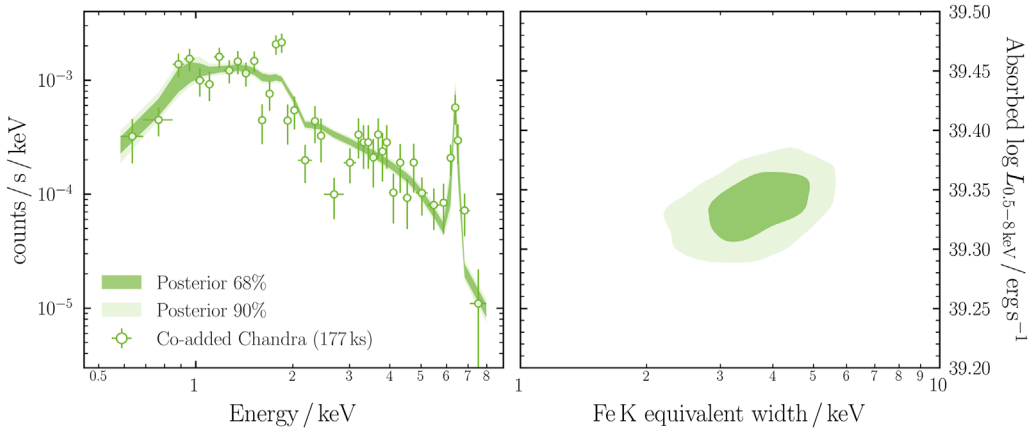

FIGURE 10
(*Left*) Co-added *Chandra* spectrum of IC 750, fit with a phenomenological model. (*Right*) Posterior 2D contour between observed 0.5–8 keV luminosity and Fe K equivalent width derived from the spectral fit shown in the *left* panel.

in the *left* and *right* panels of Figure 10, respectively. Despite the observed (i.e., absorption uncorrected) 0.5–8 keV luminosity being consistent with ultraluminous X-ray sources (Earnshaw et al., 2019), the observed Fe K equivalent width is enormous with a value of > 2 keV at > 99% confidence. The probability of such large equivalent widths to occur in lower obscuration AGN or off-nuclear ultraluminous X-ray sources is virtually impossible. Such high equivalent widths are even rare for Compton-thick AGN, though not unheard of (see Levenson et al., 2002; Boorman et al., 2018), and strongly indicate a deeply buried accreting massive black hole.

6.1 Inferring the obscuration geometry with *HEX-P*

To provide a basis for *HEX-P* simulations, we next turned to physically motivated spectral models of obscuration. To test the distinguishing power of broadband X-ray spectroscopy, we fit the existing co-added *Chandra* spectrum with two distinctive physical X-ray obscuration models: BNsphere (Brightman and Nandra, 2011a), representing a spherical distribution of matter, and UXCLUMPY (Buchner et al., 2019), representing a clumpy distribution of matter. Despite using the BNsphere model, we

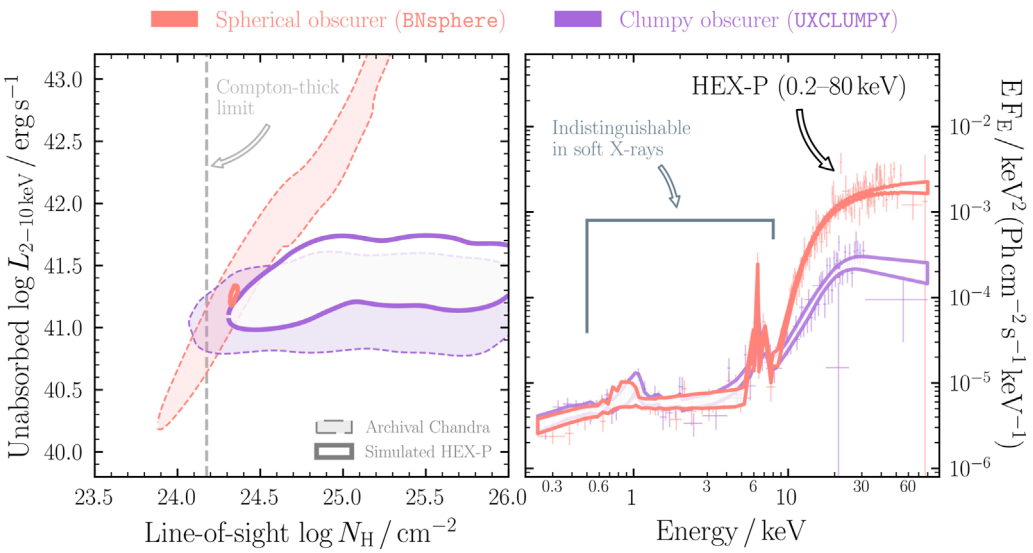

FIGURE 11
(*Left*) Posterior 2D contours between intrinsic 2–10 keV luminosity and line-of-sight column density derived with the BNsphere and UXCLUMPY physically motivated obscuration models. The posterior contours derived from fitting the archival *Chandra* data are shown with light shading bounded by a dashed line. The constraints from fitting simulated *HEX-P* spectra are shown with transparent white contours bounded by thick lines. *HEX-P* can easily constrain the target to be Compton-thick with high confidence and precisely measure the intrinsic luminosity of the buried X-ray corona. (*Right*) Simulated *HEX-P* spectra with posterior range derived from spectral fitting. The soft X-ray band covered by archival *Chandra* spectroscopy is insufficient to distinguish spectral models. By contrast, the broad passband of *HEX-P* encompasses stark spectral differences in the Compton hump, enabling geometrical constraints on the obscurer. Both panels show posterior ranges encompassing 99% probability.

include a soft X-ray excess component in both model fits that is often attributed to a small fraction of intrinsic X-ray fluxes escaping through less-obscured sight-lines. Though unlikely in a spherical model (i.e., there are no less-obscured sight-lines when surrounded by fully covering obscuration), by allowing a small amount of fluxes to escape, we approximately reproduce a leaky-sphere geometry akin to that described in Greenwell et al. (2022). Some contribution to the soft X-ray excess in obscured AGN may still come from larger scales than the circum-nuclear obscurer (see discussion in Gupta et al., 2021), such that our approximation is justified. Both physically motivated obscurer model setups are assumed to be coupled (i.e., the line-of-sight obscuration is assumed to be the same as the global obscuration level out of the line-of-sight).

The line-of-sight column density vs. intrinsic luminosity posterior distributions from the spectral fits to the existing *Chandra* data are shown in the *left* panel of Figure 11 with light shading, encompassed by a dashed line. BNsphere and UXCLUMPY found IC 750 to have line-of-sight column density in excess of the Compton-thick limit to ~85% and ~99% probability[14], making IC 750 a firm Compton-thick accreting intermediate mass black hole candidate.

However, as shown in the *right* panel of Figure 11, the existing soft band *Chandra* spectral coverage is incapable of distinguishing the two obscuration models. This means that the true range of the intrinsic luminosity posterior that we have derived from the spectral fitting spans ~4 dex, and the properties of the obscurer cannot be constrained (see LaMassa et al., 2017, 2019 for more discussion on this). We next simulate *HEX-P*/LET and HET spectra from the modal posterior parameter values derived by fitting the *Chandra* data, using exactly the same exposure as the co-added *Chandra* spectrum for both models and re-fit with BXA. The resulting posterior contours and simulated spectra unfolded with the best-fitting model posteriors are shown with transparent white contours encompassed by thick borders in the *left* and *right* panels of Figure 11, respectively. Clearly the broadband coverage provided by *HEX-P* could dramatically decrease the luminosity degeneracy of the BNsphere model fit, as well as definitively constrain the line-of-sight column density as Compton-thick. The dramatic difference between the two model fits in the *right* panel at energies > 10 keV is crucial since *HEX-P* can not only precisely measure intrinsic luminosities and line-of-sight column densities but also distinguish between obscuration geometries.

HEX-P is hence well poised to find, classify, and study obscured accretion onto intermediate mass black holes. Gaining access to spectroscopic information of sufficient sensitivity at > 10 keV is additionally crucial to decipher genuine intermediate mass black hole accretion from other lower mass compact object accretion in the host galaxy.

7 The discovery space for Compton-thick AGN

The Compton-thick population remains extremely elusive and uncertain, not just in X-ray surveys of the distant universe but even in our nearest cosmic volumes < 100 Mpc (Ricci et al.,

14 We note that the BNsphere posterior gives a >99% probability for a line-of-sight column density in excess of 10^{24} cm^{-2}.

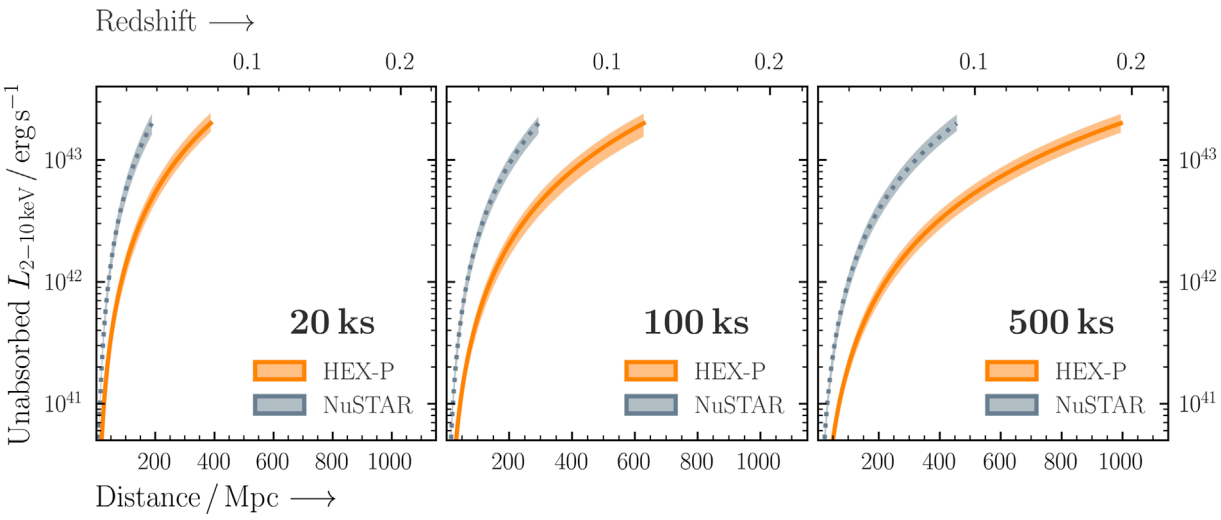

FIGURE 12
Sensitivity curves with 90% probability ranges for the discovery and detailed study of Compton-thick AGN in hard X-rays. *Left*, *center*, and *right* panels correspond to exposure times of 20 ks, 100 ks, and 500 ks, respectively. Across all panels, each curve shows the combination of distance (horizontal axis) and unabsorbed X-ray luminosity in the 2–10 keV band (vertical axis) that gives an observed signal-to-noise ratio of 8 in the hard 10–25 keV band. The simulations detailed in Figure 4 show that this requirement on signal-to-noise is sufficient to correctly classify an AGN as Compton-thick to 90% confidence. By increasing the volume for discovery and detailed study by an order of magnitude relative to *NuSTAR*, *HEX-P* will open up a new era in the pursuit of a complete AGN census.

2015; Asmus et al., 2020; Torres-Albà et al., 2021). A big open question is the volume for which we can reliably classify AGN as Compton-thick and whether the spectral data are sufficient to constrain the morphology of the circum-nuclear obscurer. Here, we demonstrate the much larger search volume accessible with *HEX-P* than *NuSTAR* for the detailed study of Compton-thick AGN.

We build upon the simulations of NGC 2960 detailed in Section 3.2 and shown in Figure 4 and characterize the luminosity and distance space that can be accessed with a given exposure time. We created a large grid of spectral simulations for a Compton-thick AGN UXCLUMPY model with line-of-sight column density $N_{\mathrm{H}} = 1.5 \times 10^{24}$ cm^{-2} and a ∼50% covering factor of material with $N_{\mathrm{H}} > 10^{22}$ cm^{-2}. We simulate spectra with 20 ks, 100 ks, and 500 ks exposures for a grid of distance and unabsorbed 2–10 keV luminosities. For each grid point, we generate 10 realizations to estimate the scatter arising from statistical fluctuations. For each exposure time and each luminosity, we identify the distance out to which line-of-sight column densities $N_{\mathrm{H}} < 1.5 \times 10^{24}$ cm^{-2} can be ruled out to 90% significance based on the 10–25 keV signal-to-noise ratio (as per Figure 4).

HEX-P will double the distance out to which Compton-thick AGN can be securely discovered, over what was possible with *NuSTAR*. This is demonstrated in Figure 12, in three separate panels for the considered exposure times. Each panel plots the unabsorbed 2–10 keV luminosity as a function of distance. We note that for Compton-thick column densities, the corresponding observed 2–10 keV luminosities would be ∼1–2 dex lower, dependent upon the choice of spectral model. We choose a fiducial unabsorbed 2–10 keV luminosity of 2×10^{43} erg s^{-1} to define the limiting distance for Compton-thick AGN classifications in our simulations. Figure 12 shows that irrespective of exposure time, *HEX-P* can provide detailed spectral classifications of Compton-thick AGN to ≳2× the distance of *NuSTAR*, increasing the available volume and number of target sources by ∼8–10×. Even for the shortest exposure considered of 20 ks, *HEX-P* would provide full characterization of the Compton-thick AGN population with unabsorbed 2–10 keV luminosities $L_{2-10\ \mathrm{keV}} > 10^{42}$ erg s^{-1} within 100 Mpc. This encompasses the current volume cut of the highly complete multi-wavelength selected Local AGN Survey that predicts 362^{+145}_{-116} AGN within the volume with 61 AGN previously unidentified (LASr; Asmus et al., 2020).

For very long exposures ≳300 ks, the effective volume for sensitive *HEX-P* spectral modeling of the Compton-thick population extends to ∼1 Gpc for Seyfert-luminosity AGN with unabsorbed 2–10 keV luminosities $L_{2-10\ \mathrm{keV}} \gtrsim 10^{43}$ erg s^{-1}. The corresponding large accessible volume for detailed spectral modeling is testament to the vast jump in sensitivity provided by *HEX-P*. This will be pivotal in probing the dusty hearts of galaxies such as mergers, ultra/luminous infrared galaxies, and compact obscured nuclei that have been suggested to host deeply buried Compton-thick AGN (Iwasawa et al., 2011; Torres-Albà et al., 2018; Aalto et al., 2019; Ricci et al., 2021; Falstad et al., 2021; Pfeifle et al., 2023. Together with the planned *HEX-P* extragalactic surveys (Civano et al., 2023) and a wide array of multi-wavelength facilities, detailed studies of Compton-thick AGN will pave the way toward a complete census of black hole growth across cosmic time.

8 Summary

In this paper, we detail many aspects of heavily obscured AGN studies performed in the literature to date with an extrapolation to the prospects attainable with the next-generation *HEX-P* concept.

We begin by compiling an up-to-date and highly complete catalog of Compton-thick AGN confirmed with spectroscopic fitting that incorporated *NuSTAR* (DoCTA; see Section 2). We show that there is an enormous range of measured line-of-sight column density and intrinsic luminosity for the targets, highlighting the requirement for improved broadband spectroscopy paired with next-generation multi-wavelength models of the circum-nuclear obscurer.

The key findings from our *HEX-P* simulations are as follows:

- *The development of future AGN models with HEX-P:* With the findings of DoCTA in mind, we present an analysis of archival *NuSTAR* + *Chandra* data for 10 Compton-thick megamaser AGN. Megamasers have some of the best constrained black hole masses with known inclinations that would help create physically motivated models of the obscurer that depend on accretion power. We showcase *HEX-P* simulations for the faintest megamaser in our sample, finding that an exposure of 25 ks suffices to classify the target as Compton-thick to better than 90% confidence and to measure the intrinsic accretion rate precisely.
- *Strictly simultaneous broadband X-ray spectroscopy: HEX-P* will provide highly sensitive and strictly simultaneous X-ray spectroscopic observations in the 0.2–80 keV passband for the first time. We show that future *HEX-P* monitoring campaigns of heavily obscured AGN will disentangle obscuration-based variations from intrinsic flux variations to much greater precision than is possible with current instruments.
- *The nature of the circum-nuclear environment at low accretion power:* It is currently extremely difficult to constrain the geometry of circum-nuclear obscuration at low intrinsic AGN power. We show that the enhanced sensitivities and angular resolution of *HEX-P* are essential for 1) disentangling true low-luminosity AGN from off-nuclear compact objects and 2) constraining the covering factor of the obscurer in sources with $L_{\rm bol} \lesssim 10^{42}$ erg s^{-1}.
- *The obscured growth of intermediate mass black holes:* Current estimates of the black hole occupation fraction rely on the detection of dwarf AGN that are biased toward unobscured sources. We show detailed *HEX-P* simulations of one candidate Compton-thick intermediate mass AGN in the literature. We show that sensitive broadband spectroscopy from *HEX-P* is sufficient to not only constrain the line-of-sight column density into the Compton-thick regime but also differentiate between alternative physical prescriptions for the geometry of the obscurer.
- *A new discovery space for Compton-thick AGN:* We determine the accessible volume for accurate characterization of Compton-thick AGN. We find the improved sensitivities provided by *HEX-P* will more than double the distance and increase the accessible volume by up to an order of magnitude relative to *NuSTAR*.

Data availability statement

Publicly available data sets were analyzed in this study. These data can be found at https://heasarc.gsfc.nasa.gov/cgi-bin/W3Browse/w3browse.pl.

Author contributions

PB: conceptualization, data curation, formal analysis, investigation, methodology, project administration, supervision, validation, visualization, writing—original draft, and writing–review and editing. NT-A: conceptualization, formal analysis, validation, visualization, writing—original draft, and writing–review and editing. AA: conceptualization, data curation, formal analysis, investigation, writing–original draft, and writing–review and editing. SM: conceptualization, data curation, formal analysis, investigation, writing–original draft, and writing–review and editing. RP: conceptualization, data curation, formal analysis, investigation, visualization, writing–original draft, and writing–review and editing. DSt: conceptualization and writing–review and editing. FC: conceptualization, and writing–review and editing. MBa: conceptualization, and writing–review and editing. JB: conceptualization, writing–original draft, and writing–review and editing. CR: conceptualization and writing–review and editing. DA: writing–review and editing. WB: conceptualization and writing–review and editing. MBr: writing–review and editing. CC: conceptualization and writing–review and editing. SC: writing–review and editing. PG: conceptualization and writing–review and editing. JG: conceptualization and writing–review and editing. FH: writing–review and editing. RH: conceptualization, writing–review and editing. EK: writing–review and editing. SL: writing–review and editing. GL: writing–review and editing. LM: writing–review and editing. KM: writing–review and editing. G. Matt: writing–review and editing. GM: writing–review and editing. EN: conceptualization and writing–review and editing. JP: writing–review and editing. AP: writing–review and editing. SP: writing–review and editing. DSi: writing–review and editing. RS: writing–review and editing. DJW: writing–review and editing. DRW: writing–review and editing. XZ: conceptualization and writing–review and editing.

Funding

The author(s) declare that financial support was received for the research, authorship, and/or publication of this article. The work of DS was carried out at the Jet Propulsion Laboratory, California Institute of Technology, under a contract with NASA. NT-A acknowledges funding from NASA under contracts 80NSSC19K0531, 80NSSC20K0045, and 80NSSC20K834. RP gratefully acknowledges support through an appointment to the NASA Postdoctoral Program at Goddard Space Flight Center, administered by ORAU through a contract with NASA. JP acknowledges support from NASA grants 80NSSC21K1567 and 80NSSC22K1120. MBa acknowledges support from the YCAA Prize Postdoctoral Fellowship. CR acknowledges support from the Fondecyt Regular grant 1230345 and ANID BASAL project FB210003.

Acknowledgments

The authors thank both referees for their constructive feedback and comments that helped improve the clarity of the paper. PB

would like to additionally thank Abhijeet Borkar for their useful comments and discussions related to the megamaser section of the manuscript. This work made use of data from the NuSTAR mission, a project led by the California Institute of Technology, managed by the Jet Propulsion Laboratory, and funded by the National Aeronautics and Space Administration. We thank the NuSTAR Operations, Software and Calibration teams for support with the execution and analysis of these observations. This research has made use of the NuSTAR Data Analysis Software (NuSTARDAS) jointly developed by the ASI Science Data Center (ASDC, Italy) and the California Institute of Technology (USA). This research has made use of data obtained from the Chandra Data Archive and the Chandra Source Catalog, and software provided by the Chandra X-ray Center (CXC) in the application packages CIAO and Sherpa. This research has made use of the NASA/IPAC Extragalactic Database (NED), which is operated by the Jet Propulsion Laboratory, California Institute of Technology, under contract with the National Aeronautics and Space Administration. This research has made use of NASA's Astrophysics Data System Bibliographic Services. This work made use of Astropy:[15] a community-developed core Python package and an ecosystem of tools and resources for astronomy (Astropy Collaboration et al., 2013; Astropy Collaboration, 2018; Astropy Collaboration, 2022). This paper made extensive use of the matplotlib (Hunter, 2007), Scipy (Virtanen et al., 2020) and Pandas (McKinney, 2010) Python packages.

Conflict of interest

The authors declare that the research was conducted in the absence of any commercial or financial relationships that could be construed as a potential conflict of interest.

The author(s) declared that they were an editorial board member of Frontiers, at the time of submission. This had no impact on the peer review process and the final decision.

Publisher's note

All claims expressed in this article are solely those of the authors and do not necessarily represent those of their affiliated organizations, or those of the publisher, the editors, and the reviewers. Any product that may be evaluated in this article, or claim that may be made by its manufacturer, is not guaranteed or endorsed by the publisher.

Supplementary material

The Supplementary Material for this article can be found online at: https://www.frontiersin.org/articles/10.3389/fspas.2024.1335459/full#supplementary-material

References

Aalto, S., Muller, S., König, S., Falstad, N., Mangum, J., Sakamoto, K., et al. (2019). The hidden heart of the luminous infrared galaxy IC 860. I. A molecular inflow feeding opaque, extreme nuclear activity. *A&A* 627, A147. doi:10.1051/0004-6361/201935480

Aird, J., Coil, A. L., Georgakakis, A., Nandra, K., Barro, G., and Pérez-González, P. G. (2015). The evolution of the X-ray luminosity functions of unabsorbed and absorbed AGNs out to z ~ 5. *MNRAS* 451, 1892–1927. doi:10.1093/mnras/stv1062

Akeson, R., Armus, L., Bachelet, E., Bailey, V., Bartusek, L., Bellini, A., et al. (2019). *The wide field infrared survey telescope: 100 hubbles for the 2020s. arXiv e-prints* , arXiv:1902.05569. doi:10.48550/arXiv.1902.05569

Akylas, A., Georgakakis, A., Georgantopoulos, I., Brightman, M., and Nandra, K. (2012). Constraining the fraction of Compton-thick AGN in the Universe by modelling the diffuse X-ray background spectrum. *A&A* 546, A98. doi:10.1051/0004-6361/201219387

Ananna, T. T., Treister, E., Urry, C. M., Ricci, C., Kirkpatrick, A., LaMassa, S., et al. (2019). The accretion history of AGNs. I. Supermassive black hole population synthesis model. *ApJ* 871, 240. doi:10.3847/1538-4357/aafb77

Ananna, T. T., Urry, C. M., Ricci, C., Natarajan, P., Hickox, R. C., Trakhtenbrot, B., et al. (2022). Probing the structure and evolution of BASS active galactic nuclei through Eddington ratios. *ApJ* 939, L13. doi:10.3847/2041-8213/ac9979

Andonie, C., Alexander, D. M., Greenwell, C., Puglisi, A., Laloux, B., Alonso-Tetilla, A. V., et al. (2023). Obscuration beyond the nucleus: infrared quasars can be buried in extreme compact starbursts. *MNRAS* 527, L144–L150. doi:10.1093/mnrasl/slad144

Andonie, C., Ricci, C., Paltani, S., Arévalo, P., Treister, E., Bauer, F., et al. (2022). A multiwavelength-motivated X-ray model for the Circinus Galaxy. *MNRAS* 511, 5768–5781. doi:10.1093/mnras/stac403

Anglés-Alcázar, D., Quataert, E., Hopkins, P. F., Somerville, R. S., Hayward, C. C., Faucher-Giguère, C.-A., et al. (2021). Cosmological simulations of quasar fueling to subparsec scales using Lagrangian hyper-refinement. *ApJ* 917, 53. doi:10.3847/1538-4357/ac09e8

Annuar, A., Alexander, D. M., Gandhi, P., Lansbury, G. B., Asmus, D., Ballantyne, D. R., et al. (2017). A new compton-thick AGN in our cosmic backyard: unveiling the buried nucleus in NGC 1448 with NuSTAR. *ApJ* 836, 165. doi:10.3847/1538-4357/836/2/165

Annuar, A., Gandhi, P., Alexander, D. M., Anathpindika, S., Asmus, D., Ballantyne, D. R., et al. (2020). A deep x-ray view of the bare agn ark120. v. spin determination from disc-comptonisation efficiency method. *Mon. Notices R. Astronomical Soc.* 492, 5481–5500. doi:10.1093/mnras/staa205

Annuar, A., Gandhi, P., Alexander, D. M., Lansbury, G. B., Arévalo, P., Ballantyne, D. R., et al. (2015). NuSTAR observations of the compton-thick active galactic nucleus and ultraluminous X-ray source candidate in NGC 5643. *ApJ* 815, 36. doi:10.1088/0004-637X/815/1/36

Ansh, S., Chen, C.-T. J., Brandt, W. N., Hood, C. E., Kammoun, E. S., Lansbury, G., et al. (2023). NuSTAR observations of a heavily X-ray-obscured AGN in the dwarf galaxy J144013+024744. *ApJ* 942, 82. doi:10.3847/1538-4357/ac9382

Antonucci, R. (1993). Unified models for active galactic nuclei and quasars. *ARA&A* 31, 473–521. doi:10.1146/annurev.aa.31.090193.002353

Arévalo, P., Bauer, F. E., Puccetti, S., Walton, D. J., Koss, M., Boggs, S. E., et al. (2014). The 2-79 keV X-ray spectrum of the Circinus galaxy with NuSTAR, xmm-Newton, and chandra: a fully compton-thick active galactic nucleus. *ApJ* 791, 81. doi:10.1088/0004-637X/791/2/81

Arnaud, K. A. (1996). "XSPEC: the first ten years," in *Astronomical data analysis software and systems V*. Editors G. H. Jacoby, and J. Barnes (Astronomical Society of the Pacific), 17.

Asmus, D., Greenwell, C. L., Gandhi, P., Boorman, P. G., Aird, J., Alexander, D. M., et al. (2020). Local AGN survey (LASr): I. Galaxy sample, infrared colour selection, and predictions for AGN within 100 Mpc. *MNRAS* 494, 1784–1816. doi:10.1093/mnras/staa766

Astropy Collaboration, Robitaille, T. P., Tollerud, E. J., Greenfield, P., Droettboom, M., Bray, E., et al. (2013). Astropy: a community Python package for astronomy. *A&A* 558, A33. doi:10.1051/0004-6361/201322068

Astropy Collaboration, Price-Whelan, A. M., Sipőcz, B. M., Günther, H. M., Lim, P. L., Crawford, S. M., et al. (2018). The Astropy project: building an open-science project and status of the v2.0 core package. *AJ* 156, 123. doi:10.3847/1538-3881/aabc4f

15 http://www.astropy.org

Astropy Collaboration, Price-Whelan, A. M., Lim, P. L., Earl, N., Starkman, N., Bradley, L., et al. (2022). The Astropy project: sustaining and growing a community-oriented open-source project and the latest major release (v5.0) of the core package. *ApJ* 935, 167. doi:10.3847/1538-4357/ac7c74

Bachetti, M., Middleton, M. J., Pinto, C., Gúrpide, A., Walton, D. J., Brightman, M., et al. (2023). *The high energy X-ray probe (HEX-P): studying extreme accretion with ultraluminous X-ray sources. arXiv e-prints* , arXiv:2311.04733. doi:10.48550/arXiv.2311.04733

Baldassare, V. F., Geha, M., and Greene, J. (2018). Identifying AGNs in low-mass galaxies via long-term optical variability. *ApJ* 868, 152. doi:10.3847/1538-4357/aae6cf

Baldi, R. D., Williams, D. R. A., Beswick, R. J., McHardy, I., Dullo, B. T., Knapen, J. H., et al. (2021a). LeMMINGs III. The e-MERLIN legacy survey of the Palomar sample: exploring the origin of nuclear radio emission in active and inactive galaxies through the [O III] - radio connection. *MNRAS* 508, 2019–2038. doi:10.1093/mnras/stab2613

Baldi, R. D., Williams, D. R. A., McHardy, I. M., Beswick, R. J., Argo, M. K., Dullo, B. T., et al. (2018). LeMMINGs - I. The eMERLIN legacy survey of nearby galaxies. 1.5-GHz parsec-scale radio structures and cores. *MNRAS* 476, 3478–3522. doi:10.1093/mnras/sty342

Baldi, R. D., Williams, D. R. A., McHardy, I. M., Beswick, R. J., Brinks, E., Dullo, B. T., et al. (2021b). LeMMINGs - II. The e-MERLIN legacy survey of nearby galaxies. The deepest radio view of the Palomar sample on parsec scale. *MNRAS* 500, 4749–4767. doi:10.1093/mnras/staa3519

Baloković, M. (2017). "Unveiling the structure of active galactic nuclei with hard X-ray spectroscopy,". Ph.D. thesis (California Institute of Technology).

Baloković, M., Brightman, M., Harrison, F. A., Comastri, A., Ricci, C., Buchner, J., et al. (2018). New spectral model for constraining torus covering factors from broadband X-ray spectra of active galactic nuclei. *ApJ* 854, 42. doi:10.3847/1538-4357/aaa7eb

Baloković, M., Cabral, S. E., Brenneman, L., and Urry, C. M. (2021). Properties of the obscuring torus in NGC 1052 from multiepoch broadband X-ray spectroscopy. *ApJ* 916, 90. doi:10.3847/1538-4357/abff4d

Baloković, M., Comastri, A., Harrison, F. A., Alexander, D. M., Ballantyne, D. R., Bauer, F. E., et al. (2014). The NuSTAR view of nearby compton-thick active galactic nuclei: the cases of NGC 424, NGC 1320, and IC 2560. *ApJ* 794, 111. doi:10.1088/0004-637X/794/2/111

Baloković, M., García, J. A., and Cabral, S. E. (2019). New tools for self-consistent modeling of the AGN torus and corona. *Res. Notes Am. Astronomical Soc.* 3, 173. doi:10.3847/2515-5172/ab578e

Bañados, E., Venemans, B. P., Mazzucchelli, C., Farina, E. P., Walter, F., Wang, F., et al. (2018). An 800-million-solar-mass black hole in a significantly neutral Universe at a redshift of 7.5. *Nature* 553, 473–476. doi:10.1038/nature25180

Bauer, F. E., Arévalo, P., Walton, D. J., Koss, M. J., Puccetti, S., Gandhi, P., et al. (2015). NuSTAR spectroscopy of multi-component X-ray reflection from NGC 1068. *ApJ* 812, 116. doi:10.1088/0004-637X/812/2/116

Boorman, P. G., Gandhi, P., Alexander, D. M., Annuar, A., Ballantyne, D. R., Bauer, F., et al. (2016). IC 3639—a new *bona fide* compton-thick AGN unveiled by NuSTAR. *ApJ* 833, 245. doi:10.3847/1538-4357/833/2/245

Boorman, P. G., Gandhi, P., Baloković, M., Brightman, M., Harrison, F., Ricci, C., et al. (2018). An Iwasawa-Taniguchi effect for Compton-thick active galactic nuclei. *MNRAS* 477, 3775–3790. doi:10.1093/mnras/sty861

Brandt, W. N., and Alexander, D. M. (2015). Cosmic X-ray surveys of distant active galaxies. The demographics, physics, and ecology of growing supermassive black holes. *A&A Rev.* 23, 1. doi:10.1007/s00159-014-0081-z

Brandt, W. N., and Yang, G. (2022). "Surveys of the cosmic X-ray background," in *Handbook of X-ray and gamma-ray Astrophysics*. Editors C. Bambi, and A. Santangelo (Singapore: Springer Nature), 78. doi:10.1007/978-981-16-4544-0_130-1

Brightman, M., Baloković, M., Stern, D., Arévalo, P., Ballantyne, D. R., Bauer, F. E., et al. (2015). Determining the covering factor of compton-thick active galactic nuclei with NuSTAR. *ApJ* 805, 41. doi:10.1088/0004-637X/805/1/41

Brightman, M., Margutti, R., Polzin, A., Jaodand, A., Hotokezaka, K., Alford, J. A. J., et al. (2023). *The High Energy X-ray Probe (HEX-P): sensitive broadband X-ray observations of transient phenomena in the 2030s. arXiv e-prints* , arXiv:2311.04856. doi:10.48550/arXiv.2311.04856

Brightman, M., Masini, A., Ballantyne, D. R., Baloković, M., Brandt, W. N., Chen, C. T., et al. (2016). A growth-rate indicator for compton-thick active galactic nuclei. *ApJ* 826, 93. doi:10.3847/0004-637X/826/1/93

Brightman, M., Masini, A., Ballantyne, D. R., Baloković, M., Brandt, W. N., Chen, C.-T. J., et al. (2018). Bat agn spectroscopic survey. vii. the covering factor of dust and gas in swift/bat active galactic nuclei. *Astrophysical J.* 867, 110. doi:10.3847/1538-4357/aae4da

Brightman, M., and Nandra, K. (2011a). An XMM-Newton spectral survey of 12 μm selected galaxies - I. X-ray data. *MNRAS* 413, 1206–1235. doi:10.1111/j.1365-2966.2011.18207.x

Brightman, M., and Nandra, K. (2011b). An XMM-Newton spectral survey of 12 μm selected galaxies - II. Implications for AGN selection and unification. *MNRAS* 414, 3084–3104. doi:10.1111/j.1365-2966.2011.18612.x

Buchner, J., and Boorman, P. (2023). *Statistical aspects of X-ray spectral analysis. arXiv e-prints* , arXiv:2309.05705. doi:10.48550/arXiv.2309.05705

Buchner, J., Brightman, M., Baloković, M., Wada, K., Bauer, F. E., and Nandra, K. (2021). Physically motivated X-ray obscurer models. *A&A* 651, A58. doi:10.1051/0004-6361/201834963

Buchner, J., Brightman, M., Nandra, K., Nikutta, R., and Bauer, F. E. (2019). X-ray spectral and eclipsing model of the clumpy obscurer in active galactic nuclei. *A&A* 629, A16. doi:10.1051/0004-6361/201834771

Buchner, J., Georgakakis, A., Nandra, K., Brightman, M., Menzel, M.-L., Liu, Z., et al. (2015). Obscuration-dependent evolution of active galactic nuclei. *ApJ* 802, 89. doi:10.1088/0004-637X/802/2/89

Buchner, J., Georgakakis, A., Nandra, K., Hsu, L., Rangel, C., Brightman, M., et al. (2014). X-ray spectral modelling of the AGN obscuring region in the CDFS: bayesian model selection and catalogue. *A&A* 564, A125. doi:10.1051/0004-6361/201322971

Buchner, J., Schulze, S., and Bauer, F. E. (2017). Galaxy gas as obscurer - I. GRBs x-ray galaxies and find an $N_H{}^3\alpha$ M_{star} relation. *MNRAS* 464, 4545–4566. doi:10.1093/mnras/stw2423

Chan, C.-H., and Krolik, J. H. (2016). Radiation-driven outflows from and radiative support in dusty tori of active galactic nuclei. *ApJ* 825, 67. doi:10.3847/0004-637X/825/1/67

Chen, C. T. J., Brandt, W. N., Reines, A. E., Lansbury, G., Stern, D., Alexander, D. M., et al. (2017). Hard X-ray-selected AGNs in low-mass galaxies from the NuSTAR serendipitous survey. *ApJ* 837, 48. doi:10.3847/1538-4357/aa5d5b

Civano, F., Zhao, X., Boorman, P., Marchesi, S., Ananna, T., Creech, S., et al. (2023). *The high energy X-ray probe (HEX-P): bringing the cosmic X-ray background into focus. arXiv e-prints* , arXiv:2311.04832. doi:10.48550/arXiv.2311.04832

Comastri, A., Gilli, R., Marconi, A., Risaliti, G., and Salvati, M. (2015). Mass without radiation: heavily obscured AGNs, the X-ray background, and the black hole mass density. *A&A* 574, L10. doi:10.1051/0004-6361/201425496

Comastri, A., Setti, G., Zamorani, G., and Hasinger, G. (1995). The contribution of AGNs to the X-ray background. *A&A* 296, 1. doi:10.48550/arXiv.astro-ph/9409067

Connors, R., Tomsick, J., Draghis, P., Coughenour, B., Shaw, A., Garcia, J., et al. (2023). *The high energy X-ray probe (HEX-P): probing accretion onto stellar mass black holes. arXiv e-prints* , arXiv:2311.04782. doi:10.48550/arXiv.2311.04782

Da Silva, R. L., Ricci, C., Sani, E., Koss, M. J., Trakhtenbrot, B., Lamperti, I., et al. (2021). A catalog of low-mass black holes in active galactic nuclei. iv. the catalog content and properties, and constraints on the host galaxies. *Astrophysical J.* 911, 150. doi:10.3847/1538-4357/abec74

Dauser, T., Falkner, S., Lorenz, M., Kirsch, C., Peille, P., Cucchetti, E., et al. (2019). SIXTE: a generic X-ray instrument simulation toolkit. *A&A* 630, A66. doi:10.1051/0004-6361/201935978

Davis, B. L., Berrier, J. C., Johns, L., Shields, D. W., Hartley, M. T., Kennefick, D., et al. (2014). The black hole mass function derived from local spiral galaxies. *ApJ* 789, 124. doi:10.1088/0004-637X/789/2/124

de Jong, R. S., Bellido-Tirado, O., Chiappini, C., Depagne, É., Haynes, R., Johl, D., et al. (2012). "4MOST: 4-metre multi-object spectroscopic telescope," in *Ground-based and airborne instrumentation for astronomy IV*. Editors I. S. McLean, S. K. Ramsay, and H. Takami, 84460T. doi:10.1117/12.926239

Diaz, Y., Arévalo, P., Hernández-García, L., Bassani, L., Malizia, A., González-Martín, O., et al. (2020). Constraining X-ray reflection in the low-luminosity AGN NGC 3718 using NuSTAR and XMM-Newton. *MNRAS* 496, 5399–5413. doi:10.1093/mnras/staa1762

Diaz, Y., Hernàndez-García, L., Arévalo, P., López-Navas, E., Ricci, C., Koss, M., et al. (2023). Constraining the X-ray reflection in low accretion-rate active galactic nuclei using XMM-Newton, NuSTAR, and Swift. *A&A* 669, A114. doi:10.1051/0004-6361/202244678

Earnshaw, H. P., Roberts, T. P., Middleton, M. J., Walton, D. J., and Mateos, S. (2019). A new, clean catalogue of extragalactic non-nuclear X-ray sources in nearby galaxies. *MNRAS* 483, 5554–5573. doi:10.1093/mnras/sty3403

Elitzur, M. (2006). The obscuring torus in AGN. *New Astron. Rev.* 50, 728–731. doi:10.1016/j.newar.2006.06.027

Elitzur, M., and Ho, L. C. (2009). The disk-wind connection in agn: us 322, an interesting case. *Astrophysical J.* 701, L91–L94. doi:10.1088/0004-637X/701/2/L91

Elvis, M., Risaliti, G., Nicastro, F., Miller, J. M., Fiore, F., and Puccetti, S. (2004). An unveiling event in the type 2 active galactic nucleus NGC 4388:A challenge for a parsec-scale absorber. *ApJ* 615, L25–L28. doi:10.1086/424380

Eracleous, M., Hwang, J. A., and Flohic, H. M. L. G. (2010). The narrow-line region of narrow-line and broad-line seyfert 1 galaxies. *Astrophysical J.* 711, 796–811. doi:10.1088/0004-637X/711/2/796

Eraerds, T., Antonelli, V., Davis, C., Hall, D., Hetherington, O., Holland, A., et al. (2021). Enhanced simulations on the athena/wide field imager instrumental background. *J. Astronomical Telesc. Instrum. Syst.* 7, 034001. doi:10.1117/1.JATIS.7.3.034001

Fabian, A. C. (1999). The obscured growth of massive black holes. *MNRAS* 308, L39–L43. doi:10.1046/j.1365-8711.1999.03017.x

Fabian, A. C., Vasudevan, R. V., and Gandhi, P. (2008). The effect of radiation pressure on dusty absorbing gas around active galactic nuclei. *MNRAS* 385, L43–L47. doi:10.1111/j.1745-3933.2008.00430.x

Falstad, N., Aalto, S., König, S., Onishi, K., Muller, S., Gorski, M., et al. (2021). CON-quest. Searching for the most obscured galaxy nuclei. *A&A* 649, A105. doi:10.1051/0004-6361/202039291

Farrah, D., Baloković, M., Stern, D., Harris, K., Kunimoto, M., Walton, D. J., et al. (2016). The geometry of the infrared and X-ray obscurer in a dusty hyperluminous quasar. *ApJ* 831, 76. doi:10.3847/0004-637X/831/1/76

Fernández-Ontiveros, J. A., and Muñoz-Darias, T. (2021). X-ray binary accretion states in active galactic nuclei? Sensing the accretion disc of supermassive black holes with mid-infrared nebular lines. *MNRAS* 504, 5726–5740. doi:10.1093/mnras/stab1108

Feroz, F., Hobson, M. P., and Bridges, M. (2009). MULTINEST: an efficient and robust Bayesian inference tool for cosmology and particle physics. *MNRAS* 398, 1601–1614. doi:10.1111/j.1365-2966.2009.14548.x

Fruscione, A., McDowell, J. C., Allen, G. E., Brickhouse, N. S., Burke, D. J., Davis, J. E., et al. (2006). "CIAO: chandra's data analysis system," in *Society of photo-optical instrumentation engineers (SPIE) conference series*. Editors D. R. Silva, and R. E. Doxsey, 62701V. doi:10.1117/12.671760

Gandhi, P., Annuar, A., Lansbury, G. B., Stern, D., Alexander, D. M., Bauer, F. E., et al. (2017). The weak Fe fluorescence line and long-term X-ray evolution of the Compton-thick active galactic nucleus in NGC 7674. *MNRAS* 467, 4606–4621. doi:10.1093/mnras/stx357

Gandhi, P., and Fabian, A. C. (2003). X-ray background synthesis: the infrared connection. *MNRAS* 339, 1095–1102. doi:10.1046/j.1365-8711.2003.06259.x

Gandhi, P., Fabian, A. C., Suebsuwong, T., Malzac, J., Miniutti, G., and Wilman, R. J. (2007). Constraints on light bending and reflection from the hard X-ray background. *MNRAS* 382, 1005–1018. doi:10.1111/j.1365-2966.2007.12462.x

Gandhi, P., Lansbury, G. B., Alexander, D. M., Stern, D., Arévalo, P., Ballantyne, D. R., et al. (2014). NuSTAR unveils a compton-thick type 2 quasar in mrk 34. *ApJ* 792, 117. doi:10.1088/0004-637X/792/2/117

Gandhi, P., Terashima, Y., Yamada, S., Mushotzky, R. F., Ueda, Y., Baumgartner, W. H., et al. (2013). Reflection-dominated nuclear X-ray emission in the early-type galaxy ESO 565-g019. *ApJ* 773, 51. doi:10.1088/0004-637X/773/1/51

Gandhi, P., Yamada, S., Ricci, C., Asmus, D., Mushotzky, R. F., Ueda, Y., et al. (2015). A Compton-thick AGN in the barred spiral galaxy NGC 4785. *MNRAS* 449, 1845–1855. doi:10.1093/mnras/stv344

Gaspari, M., Brighenti, F., and Temi, P. (2015). Chaotic cold accretion on to black holes in rotating atmospheres. *A&A* 579, A62. doi:10.1051/0004-6361/201526151

Gaspari, M., Ruszkowski, M., and Oh, S. P. (2013). Chaotic cold accretion on to black holes. *MNRAS* 432, 3401–3422. doi:10.1093/mnras/stt692

Gaspari, M., Tombesi, F., and Cappi, M. (2020). Linking macro-meso- and microscales in multiphase AGN feeding and feedback. *Nat. Astron.* 4, 10–13. doi:10.1038/s41550-019-0970-1

Georgantopoulos, I., and Akylas, A. (2019). NuSTAR observations of heavily obscured Swift/BAT AGNs: constraints on the Compton-thick AGNs fraction. *A&A* 621, A28. doi:10.1051/0004-6361/201833038

Gilli, R., Comastri, A., and Hasinger, G. (2007). The synthesis of the cosmic X-ray background in the Chandra and XMM-Newton era. *A&A* 463, 79–96. doi:10.1051/0004-6361:20066334

Gilli, R., Norman, C., Calura, F., Vito, F., Decarli, R., Marchesi, S., et al. (2022). Supermassive black holes at high redshift are expected to be obscured by their massive host galaxies' interstellar medium. *A&A* 666, A17. doi:10.1051/0004-6361/202243708

Giman, A., Boorman, P., Harrison, F., Stern, D., and Baloković, M. (2023). *In prep*. ApJ.

González-Martín, O., Hernández-García, L., Masegosa, J., Marquez, I., and Esquej, P. (2017). A universal scaling for the energetics of relativistic jets from black hole systems. *Astrophysical J.* 835, 16. doi:10.3847/1538-4357/835/1/16

González-Martín, O., Masegosa, J., Márquez, I., Guerrero, M. A., and Dultzin-Hacyan, D. (2009). Unification of x-ray winds in seyfert galaxies: from ultra-fast outflows to warm absorbers. *Mon. Notices R. Astronomical Soc.* 397, L79–L83. doi:10.1111/j.1745-3933.2009.00757.x

Goodman, A. A., Pineda, J. E., and Schnee, S. L. (2009). The "true" column density distribution in star-forming molecular clouds. *ApJ* 692, 91–103. doi:10.1088/0004-637X/692/1/91

Gordon, C., and Arnaud, K. (2021). *PyXspec: Python interface to XSPEC spectral-fitting program*. Astrophysics Source Code Library. record ascl:2101.014.

Greene, J. E. (2012). Low-mass black holes as the remnants of primordial black hole formation. *Nat. Commun.* 3, 1304. doi:10.1038/ncomms2314

Greene, J. E., and Ho, L. C. (2004). Active galactic nuclei with candidate intermediate-mass black holes. *ApJ* 610, 722–736. doi:10.1086/421719

Greene, J. E., and Ho, L. C. (2007). A new sample of low-mass black holes in active galaxies. *ApJ* 670, 92–104. doi:10.1086/522082

Greene, J. E., Strader, J., and Ho, L. C. (2020). Intermediate-mass black holes. *ARA&A* 58, 257–312. doi:10.1146/annurev-astro-032620-021835

Greenhill, L. J., Tilak, A., and Madejski, G. (2008). Prevalence of high X-ray obscuring columns among AGNs that host H_2O masers. *ApJ* 686, L13–L16. doi:10.1086/592782

Greenwell, C., Gandhi, P., Lansbury, G., Boorman, P., Mainieri, V., and Stern, D. (2022). XMM and NuSTAR observations of an optically quiescent quasar. *ApJ* 934, L34. doi:10.3847/2041-8213/ac83a0

Gupta, K. K., Ricci, C., Tortosa, A., Ueda, Y., Kawamuro, T., Koss, M., et al. (2021). BAT AGN Spectroscopic Survey XXVII: scattered X-Ray radiation in obscured active galactic nuclei. *MNRAS* 504, 428–443. doi:10.1093/mnras/stab839

Harrison, F. A., Craig, W. W., Christensen, F. E., Hailey, C. J., Zhang, W. W., Boggs, S. E., et al. (2013). The nuclear spectroscopic telescope array (NuSTAR) high-energy X-ray mission. *ApJ* 770, 103. doi:10.1088/0004-637X/770/2/103

Hernández-García, L., Masegosa, J., González-Martín, O., and Márquez, I. (2016). Subarcsecond imaging of the water maser in ngc 1068 with kvn and vera. *Astrophysical J.* 824, L27. doi:10.3847/2041-8205/824/2/L27

Hickox, R. C., and Alexander, D. M. (2018). Obscured active galactic nuclei. *ARA&A* 56, 625–671. doi:10.1146/annurev-astro-081817-051803

Ho, L. C. (1997). Nuclear activity in nearby galaxies. *Rev. Mex. Astron. Astrofísica* 6, 55–63. doi:10.48550/arXiv.astro-ph/9607118

Ho, L. C. (1999). Narrow-line seyfert 1 galaxies and their place in the universe. *Astrophysical J. Suppl. Ser.* 120, 73–112. doi:10.1086/313181

Ho, L. C. (2008). Nuclear activity in nearby galaxies. *Annu. Rev. Astronomy Astrophysics* 46, 475–539. doi:10.1146/annurev.astro.45.051806.110546

Hönig, S. F., and Beckert, T. (2007). The unified model of active galactic nuclei. *Astrophysical J.* 746, 214–234. doi:10.1088/0004-637X/746/2/214

Hopkins, P. F., Hernquist, L., Cox, T. J., Di Matteo, T., Robertson, B., and Springel, V. (2006). A unified, merger-driven model of the origin of starbursts, quasars, the cosmic X-ray background, supermassive black holes, and galaxy spheroids. *ApJS* 163, 1–49. doi:10.1086/499298

Hunter, J. D. (2007). Matplotlib: a 2d graphics environment. *Comput. Sci. Eng.* 9, 90–95. doi:10.1109/MCSE.2007.55

Ikeda, S., Awaki, H., and Terashima, Y. (2009). Study on X-ray spectra of obscured active galactic nuclei based on Monte Carlo simulation—an interpretation of observed wide-band spectra. *ApJ* 692, 608–617. doi:10.1088/0004-637X/692/1/608

Ivezić, Ž., Kahn, S. M., Tyson, J. A., Abel, B., Acosta, E., Allsman, R., et al. (2019). LSST: from science drivers to reference design and anticipated data products. *ApJ* 873, 111. doi:10.3847/1538-4357/ab042c

Iwasawa, K., Sanders, D. B., Teng, S. H., U, V., Armus, L., Evans, A. S., et al. (2011). C-GOALS: chandra observations of a complete sample of luminous infrared galaxies from the IRAS Revised Bright Galaxy Survey. *A&A* 529, A106. doi:10.1051/0004-6361/201015264

Jaffe, W., Meisenheimer, K., Röttgering, H. J. A., Leinert, C., Richichi, A., Chesneau, O., et al. (2004). The central dusty torus in the active nucleus of NGC 1068. *Nature* 429, 47–49. doi:10.1038/nature02531

Jansen, F., Lumb, D., Altieri, B., Clavel, J., Ehle, M., Erd, C., et al. (2001). XMM-Newton observatory. I. The spacecraft and operations. *A&A* 365, L1–L6. doi:10.1051/0004-6361:20000036

Kaastra, J. S., and Bleeker, J. A. M. (2016). Optimal binning of X-ray spectra and response matrix design. *A&A* 587, A151. doi:10.1051/0004-6361/201527395

Kallová, K., Boorman, P., and Ricci, C. (2023). Investigating model dependencies for obscured Active Galactic Nuclei: a case study of NGC 3982. *In prep*. ApJ.

Kammoun, E., Lohfink, A. M., Masterson, M., Wilkins, D. R., Zhao, X., Baloković, M., et al. (2023). *The High Energy X-ray Probe (HEX-P): probing the physics of the X-ray corona in active galactic nuclei. arXiv e-prints* , arXiv:2311.04679. doi:10.48550/arXiv.2311.04679

Kammoun, E. S., Miller, J. M., Koss, M., Oh, K., Zoghbi, A., Mushotzky, R. F., et al. (2020). A hard look at local, optically selected, obscured seyfert galaxies. *ApJ* 901, 161. doi:10.3847/1538-4357/abb29f

Kammoun, E. S., Miller, J. M., Zoghbi, A., Oh, K., Koss, M., Mushotzky, R. F., et al. (2019). A hard look at NGC 5347: revealing a nearby compton-thick AGN. *ApJ* 877, 102. doi:10.3847/1538-4357/ab1c5f

Kawamuro, T., Ueda, Y., Tazaki, F., Terashima, Y., Mushotzky, R., Mori, M., et al. (2016). Low-luminosity active galactic nuclei as observed with suzaku. *Astrophysical J.* 831, 37. doi:10.3847/0004-637X/831/1/37

Kayal, A., Singh, V., Ricci, C., Mithun, N. P. S., Vadawale, S., Dewangan, G., et al. (2023). Multi-epoch hard X-ray view of compton-thick AGN Circinus galaxy. *MNRAS* 522, 4098–4115. doi:10.1093/mnras/stad1216

Kerzendorf, W. E., Vogl, C., Buchner, J., Contardo, G., Williamson, M., and van der Smagt, P. (2021). Dalek: a deep learning emulator for tardis. *ApJ* 910, L23. doi:10.3847/2041-8213/abeb1b

Kondratko, P. T., Greenhill, L. J., and Moran, J. M. (2008). The parsec-scale accretion disk in NGC 3393. *ApJ* 678, 87–95. doi:10.1086/586879

Körding, E. G., Jester, S., and Fender, R. (2006). Accretion states and radio loudness in active galactic nuclei: analogies with X-ray binaries. *MNRAS* 372, 1366–1378. doi:10.1111/j.1365-2966.2006.10954.x

Koss, M. J., Assef, R., Baloković, M., Stern, D., Gandhi, P., Lamperti, I., et al. (2016). A new population of compton-thick AGNs identified using the spectral curvature above 10 keV. *ApJ* 825, 85. doi:10.3847/0004-637X/825/2/85

Koss, M. J., Romero-Cañizales, C., Baronchelli, L., Teng, S. H., Baloković, M., Puccetti, S., et al. (2015). Broadband observations of the compton-thick nucleus of NGC 3393. *ApJ* 807, 149. doi:10.1088/0004-637X/807/2/149

Kuo, C. Y., Braatz, J. A., Condon, J. J., Impellizzeri, C. M. V., Lo, K. Y., Zaw, I., et al. (2011). The megamaser cosmology project. III. Accurate masses of seven supermassive black holes in active galaxies with circumnuclear megamaser disks. *ApJ* 727, 20. doi:10.1088/0004-637X/727/1/20

La Caria, M. M., Vignali, C., Lanzuisi, G., Gruppioni, C., and Pozzi, F. (2019). Broad-band X-ray analysis of local mid-infrared-selected Compton-thick AGN candidates. *MNRAS* 487, 1662–1674. doi:10.1093/mnras/stz1381

Laha, S., Markowitz, A. G., Krumpe, M., Nikutta, R., Rothschild, R., and Saha, T. (2020). The variable and non-variable X-ray absorbers in compton-thin type II active galactic nuclei. *ApJ* 897, 66. doi:10.3847/1538-4357/ab92ab

LaMassa, S. M., Yaqoob, T., Boorman, P. G., Tzanavaris, P., Levenson, N. A., Gandhi, P., et al. (2019). NuSTAR uncovers an extremely local compton-thick AGN in NGC 4968. *ApJ* 887, 173. doi:10.3847/1538-4357/ab552c

LaMassa, S. M., Yaqoob, T., Levenson, N. A., Boorman, P., Heckman, T. M., Gandhi, P., et al. (2017). Chandra reveals heavy obscuration and circumnuclear star formation in seyfert 2 galaxy NGC 4968. *ApJ* 835, 91. doi:10.3847/1538-4357/835/1/91

LaMassa, S. M., Yaqoob, T., Tzanavaris, P., Gandhi, P., Heckman, T., Lansbury, G., et al. (2023). The complex X-ray obscuration environment in the radio-loud type 2 quasar 3C 223. *ApJ* 944, 152. doi:10.3847/1538-4357/acb3bb

Lansbury, G. B., Gandhi, P., Alexander, D. M., Assef, R. J., Aird, J., Annuar, A., et al. (2015). NuSTAR reveals extreme absorption in z < 0.5 type 2 quasars. *ApJ* 809, 115. doi:10.1088/0004-637X/809/2/115

Lansbury, G. B., Stern, D., Aird, J., Alexander, D. M., Fuentes, C., Harrison, F. A., et al. (2017). The NuSTAR serendipitous survey: the 40-month catalog and the properties of the distant high-energy X-ray source population. *ApJ* 836, 99. doi:10.3847/1538-4357/836/1/99

Laureijs, R., Amiaux, J., Arduini, S., Auguères, J. L., Brinchmann, J., Cole, R., et al. (2011). *Euclid definition study report. arXiv e-prints* , arXiv:1110.3193. doi:10.48550/arXiv.1110.3193

Lefkir, M., Kammoun, E., Barret, D., Boorman, P., Matzeu, G., Miller, J. M., et al. (2023). A hard look at the X-ray spectral variability of NGC 7582. *MNRAS* 522, 1169–1182. doi:10.1093/mnras/stad995

Lehmer, B. D., Garofali, K., Binder, B. A., Fornasini, F., Vulic, N., Zezas, A., et al. (2023). *The high energy X-ray probe: resolved X-ray populations in extragalactic environments. arXiv e-prints* , arXiv:2311.04735. doi:10.48550/arXiv.2311.04735

Levenson, N. A., Krolik, J. H., Życki, P. T., Heckman, T. M., Weaver, K. A., Awaki, H., et al. (2002). Extreme X-ray iron lines in active galactic nuclei. *ApJ* 573, L81–L84. doi:10.1086/342092

Liu, J., Hönig, S. F., Ricci, C., and Paltani, S. (2019). X-ray signatures of the polar dusty gas in AGN. *MNRAS* 490, 4344–4352. doi:10.1093/mnras/stz2908

Liu, Y., and Li, X. (2014). An X-ray spectral model for clumpy tori in active galactic nuclei. *ApJ* 787, 52. doi:10.1088/0004-637X/787/1/52

Maccagni, F. M., Serra, P., Gaspari, M., Kleiner, D., Morokuma-Matsui, K., Oosterloo, T. A., et al. (2021). AGN feeding and feedback in Fornax A. Kinematical analysis of the multi-phase ISM. *A&A* 656, A45. doi:10.1051/0004-6361/202141143

Madsen, K., García, J., Grefenstette, B., Stern, D., and The HEX-P Team (2023). *In prep*. Frontiers in Astronomy and Space Sciences.

Madsen, K. K., Harrison, F. A., Markwardt, C. B., An, H., Grefenstette, B. W., Bachetti, M., et al. (2015). Calibration of the NuSTAR high-energy focusing X-ray telescope. *ApJS* 220, 8. doi:10.1088/0067-0049/220/1/8

Maoz, D., Nagar, N. M., Falcke, H., and Wilson, A. S. (2005). The murmur of the sleeping black hole: detection of nuclear ultraviolet variability in LINER galaxies. *Astrophysical J.* 625, 699–715. doi:10.1086/429795

Marchesi, S., Ajello, M., Marcotulli, L., Comastri, A., Lanzuisi, G., and Vignali, C. (2018). Compton-thick AGNs in the NuSTAR era. *ApJ* 854, 49. doi:10.3847/1538-4357/aaa410

Marchesi, S., Ajello, M., Zhao, X., Comastri, A., La Parola, V., and Segreto, A. (2019a). Compton-thick AGNs in the NuSTAR era. V. Joint NuSTAR and XMM-Newton spectral analysis of three "soft-gamma" candidate CT-AGNs in the swift/BAT 100-month catalog. *ApJ* 882, 162. doi:10.3847/1538-4357/ab340a

Marchesi, S., Ajello, M., Zhao, X., Marcotulli, L., Baloković, M., Brightman, M., et al. (2019b). Compton-thick AGNs in the NuSTAR era. III. A systematic study of the torus covering factor. *ApJ* 872, 8. doi:10.3847/1538-4357/aafbeb

Marchesi, S., Tremblay, L., Ajello, M., Marcotulli, L., Paggi, A., Cusumano, G., et al. (2017). Chandra and NuSTAR follow-up observations of swift-BAT-selected AGNs. *ApJ* 848, 53. doi:10.3847/1538-4357/aa8ee6

Marchesi, S., Zhao, X., Torres-Albà, N., Ajello, M., Gaspari, M., Pizzetti, A., et al. (2022). Compton-thick AGN in the NuSTAR era. VIII. A joint NuSTAR-XMM-Newton monitoring of the changing-look compton-thick AGN NGC 1358. *ApJ* 935, 114. doi:10.3847/1538-4357/ac80be

Marcotulli, L., Ajello, M., Böttcher, M., Coppi, P., Costamante, L., Di Gesu, L., et al. (2023). *The High Energy X-ray Probe (HEX-P): the most powerful jets through the lens of a superb X-ray eye. arXiv e-prints* , arXiv:2311.04801. doi:10.48550/arXiv.2311.04801

Marinucci, A., Bianchi, S., Matt, G., Alexander, D. M., Baloković, M., Bauer, F. E., et al. (2016). NuSTAR catches the unveiling nucleus of NGC 1068. *MNRAS* 456, L94–L98. doi:10.1093/mnrasl/slv178

Markowitz, A. G., Krumpe, M., and Nikutta, R. (2014). First X-ray-based statistical tests for clumpy-torus models: eclipse events from 230 years of monitoring of Seyfert AGN. *MNRAS* 439, 1403–1458. doi:10.1093/mnras/stt2492

Masini, A., Comastri, A., Baloković, M., Zaw, I., Puccetti, S., Ballantyne, D. R., et al. (2016). NuSTAR observations of water megamaser AGN. *A&A* 589, A59. doi:10.1051/0004-6361/201527689

Masini, A., Comastri, A., Hickox, R. C., Koss, M., Civano, F., Brigthman, M., et al. (2019). Measuring the obscuring column of a disk megamaser AGN in a nearby merger. *ApJ* 882, 83. doi:10.3847/1538-4357/ab3214

Masini, A., Comastri, A., Puccetti, S., Baloković, M., Gandhi, P., Guainazzi, M., et al. (2017). The Phoenix galaxy as seen by NuSTAR. *A&A* 597, A100. doi:10.1051/0004-6361/201629444

Matt, G., Fabian, A. C., Guainazzi, M., Iwasawa, K., Bassani, L., and Malaguti, G. (2000). The X-ray spectra of Compton-thick Seyfert 2 galaxies as seen by BeppoSAX. *MNRAS* 318, 173–179. doi:10.1046/j.1365-8711.2000.03721.x

Matzeu, G. A., Braito, V., Reeves, J. N., Severgnini, P., Ballo, L., Caccianiga, A., et al. (2019). Evidence for a clumpy disc-wind in the star-forming Seyfert 2 galaxy MCG-03-58-007. *MNRAS* 483, 2836–2850. doi:10.1093/mnras/sty3327

Matzeu, G. A., Lieu, M., Costa, M. T., Reeves, J. N., Braito, V., Dadina, M., et al. (2022). A new emulated Monte Carlo radiative transfer disc-wind model: X-Ray Accretion Disc-wind Emulator - XRADE. *MNRAS* 515, 6172–6190. doi:10.1093/mnras/stac2155

McConnell, N. J., and Ma, C.-P. (2013). Revisiting the scaling relations of black hole masses and host galaxy properties. *ApJ* 764, 184. doi:10.1088/0004-637X/764/2/184

McKaig, J., Ricci, C., Paltani, S., and Satyapal, S. (2022). X-ray simulations of polar gas in accreting supermassive black holes. *MNRAS* 512, 2961–2971. doi:10.1093/mnras/stab3178

McKinney, W. (2010). "Data structures for statistical computing in Python," in *Proceedings of the 9th Python in science conference*. Editors S. van der Walt, and J. Millman, 56–61. doi:10.25080/Majora-92bf1922-00a

Meidinger, N., Albrecht, S., Beitler, C., Bonholzer, M., Emberger, V., Frank, J., et al. (2020). "Development status of the wide field imager instrument for Athena," in Society of Photo-Optical Instrumentation Engineers (SPIE) Conference Series, 114440T. doi:10.1117/12.2560507

Mohanadas, P., and Annuar, A. (2023). NGC 4117: a new compton-thick AGN revealed by broadband X-ray spectral analysis. *Res. Astronomy Astrophysics* 23, 055002. doi:10.1088/1674-4527/acc151

Moran, E. C., Shahinyan, K., Sugarman, H. R., Vélez, D. O., and Eracleous, M. (2014). Black holes at the centers of nearby dwarf galaxies. *AJ* 148, 136. doi:10.1088/0004-6256/148/6/136

Moravec, E., Svoboda, J., Borkar, A., Boorman, P., Kynoch, D., Panessa, F., et al. (2022). Do radio active galactic nuclei reflect X-ray binary spectral states? *A&A* 662, A28. doi:10.1051/0004-6361/202142870

Murphy, K. D., and Yaqoob, T. (2009). An X-ray spectral model for Compton-thick toroidal reprocessors. *MNRAS* 397, 1549–1562. doi:10.1111/j.1365-2966.2009.15025.x

Nagar, N. M., Falcke, H., Wilson, A. S., and Ho, L. C. (2005). Accretion disk model for low-luminosity active galactic nuclei. *Astrophysical J.* 620, 83–89. doi:10.1086/427175

Nandra, K., Barret, D., Barcons, X., Fabian, A., den Herder, J.-W., Piro, L., et al. (2013). *The hot and energetic Universe: a white paper presenting the science theme motivating the Athena+ mission. arXiv e-prints* , arXiv:1306.2307. doi:10.48550/arXiv.1306.2307

Nardini, E. (2017). Nuclear absorption and emission in the AGN merger NGC 6240: the hard X-ray view. *MNRAS* 471, 3483–3493. doi:10.1093/mnras/stx1878

Nemmen, R. S., Storchi-Bergmann, T., and Eracleous, M. (2014). Spectral models for low-luminosity active galactic nuclei in LINERs: the role of advection-dominated accretion and jets. *MNRAS* 438, 2804–2827. doi:10.1093/mnras/stt2388

Nemmen, R. S., Storchi-Bergmann, T., Yuan, F., Eracleous, M., Terashima, Y., and Wilson, A. S. (2006). Radiatively inefficient accretion flow in the nucleus of NGC 1097. *Astrophysical J.* 643, 652–659. doi:10.1086/500571

Nenkova, M., Sirocky, M. M., Ivezić, Ž., and Elitzur, M. (2008). AGN dusty tori. I. Handling of clumpy media. *ApJ* 685, 147–159. doi:10.1086/590482

Netzer, H. (2015). Revisiting the unified model of active galactic nuclei. *ARA&A* 53, 365–408. doi:10.1146/annurev-astro-082214-122302

Odaka, H., Aharonian, F., Watanabe, S., Tanaka, Y., Khangulyan, D., and Takahashi, T. (2011). X-ray diagnostics of giant molecular clouds in the galactic center region and past activity of sgr A. *ApJ* 740, 103. doi:10.1088/0004-637X/740/2/103

Odaka, H., Yoneda, H., Takahashi, T., and Fabian, A. (2016). Sensitivity of the Fe Kα Compton shoulder to the geometry and variability of the X-ray illumination of cosmic objects. *MNRAS* 462, 2366–2381. doi:10.1093/mnras/stw1764

Osorio-Clavijo, N., González-Martín, O., Sánchez, S. F., Esparza-Arredondo, D., Masegosa, J., Victoria-Ceballos, C., et al. (2022). Observational hints on the torus obscuring gas behaviour through X-rays with NuSTAR data. *MNRAS* 510, 5102–5118. doi:10.1093/mnras/stab3752

Paltani, S., and Ricci, C. (2017). RefleX: X-ray absorption and reflection in active galactic nuclei for arbitrary geometries. *A&A* 607, A31. doi:10.1051/0004-6361/201629623

Panessa, F., Castangia, P., Malizia, A., Bassani, L., Tarchi, A., Bazzano, A., et al. (2020). Water megamaser emission in hard X-ray selected AGN. *A&A* 641, A162. doi:10.1051/0004-6361/201937407

Pfeifle, R. W., Boorman, P. G., Weaver, K. A., Buchner, J., Civano, F., Madsen, K., et al. (2023). *The high energy X-ray probe (HEX-P): the future of hard X-ray dual AGN science. arXiv e-prints* , arXiv:2311.05154. doi:10.48550/arXiv.2311.05154

Piotrowska, J. M., García, J. A., Walton, D. J., Beckmann, R. S., Stern, D., Ballantyne, D. R., et al. (2023). *The high energy X-ray probe (HEX-P): constraining supermassive black hole growth with population spin measurements. arXiv e-prints* , arXiv:2311.04752. doi:10.48550/arXiv.2311.04752

Pizzetti, A., Torres-Albà, N., Marchesi, S., Ajello, M., Silver, R., and Zhao, X. (2022). A multiepoch X-ray study of the nearby seyfert 2 galaxy NGC 7479: linking column density variability to the torus geometry. *ApJ* 936, 149. doi:10.3847/1538-4357/ac86c6

Ptak, A., Hornschemeier, A., Zezas, A., Lehmer, B., Yukita, M., Wik, D., et al. (2015). A focused, hard X-ray look at arp 299 with NuSTAR. *ApJ* 800, 104. doi:10.1088/0004-637X/800/2/104

Puccetti, S., Comastri, A., Bauer, F. E., Brandt, W. N., Fiore, F., Harrison, F. A., et al. (2016). Hard X-ray emission of the luminous infrared galaxy NGC 6240 as observed by NuSTAR. *A&A* 585, A157. doi:10.1051/0004-6361/201527189

Puccetti, S., Comastri, A., Fiore, F., Arévalo, P., Risaliti, G., Bauer, F. E., et al. (2014). The variable hard X-ray emission of NGC 4945 as observed by NuSTAR. *ApJ* 793, 26. doi:10.1088/0004-637X/793/1/26

Racca, G. D., Laureijs, R., Stagnaro, L., Salvignol, J.-C., Lorenzo Alvarez, J., Saavedra Criado, G., et al. (2016). "The Euclid mission design," in *Space telescopes and instrumentation 2016: optical, infrared, and millimeter wave*. Editors H. A. MacEwen, G. G. Fazio, M. Lystrup, N. Batalha, N. Siegler, and E. C. Tong, 99040O. doi:10.1117/12.2230762

Ramos Almeida, C., and Ricci, C. (2017). Nuclear obscuration in active galactic nuclei. *Nat. Astron.* 1, 679–689. doi:10.1038/s41550-017-0232-z

Reines, A. E. (2022). Hunting for massive black holes in dwarf galaxies. *Nat. Astron.* 6, 26–34. doi:10.1038/s41550-021-01556-0

Reines, A. E., Greene, J. E., and Geha, M. (2013). Dwarf galaxies with optical signatures of active massive black holes. *ApJ* 775, 116. doi:10.1088/0004-637X/775/2/116

Reynolds, C. S., Lohfink, A. M., Ogle, P. M., Harrison, F. A., Madsen, K. K., Fabian, A. C., et al. (2015). NuSTAR observations of the powerful radio galaxy Cygnus A. *ApJ* 808, 154. doi:10.1088/0004-637X/808/2/154

Ricci, C., Ananna, T. T., Temple, M. J., Urry, C. M., Koss, M. J., Trakhtenbrot, B., et al. (2022). BASS XXXVII: the role of radiative feedback in the growth and obscuration properties of nearby supermassive black holes. *ApJ* 938, 67. doi:10.3847/1538-4357/ac8e67

Ricci, C., Bauer, F. E., Arevalo, P., Boggs, S., Brandt, W. N., Christensen, F. E., et al. (2016). IC 751: a new changing look AGN discovered by NuSTAR. *ApJ* 820, 5. doi:10.3847/0004-637X/820/1/5

Ricci, C., Bauer, F. E., Treister, E., Schawinski, K., Privon, G. C., Blecha, L., et al. (2017). Growing supermassive black holes in the late stages of galaxy mergers are heavily obscured. *MNRAS* 468, stx173–1299. doi:10.1093/mnras/stx173

Ricci, C., and Paltani, S. (2023). Ray-tracing simulations and spectral models of X-ray radiation in dusty media. *ApJ* 945, 55. doi:10.3847/1538-4357/acb5a6

Ricci, C., Privon, G. C., Pfeifle, R. W., Armus, L., Iwasawa, K., Torres-Albà, N., et al. (2021). A hard X-ray view of luminous and ultra-luminous infrared galaxies in GOALS - I. AGN obscuration along the merger sequence. *MNRAS* 506, 5935–5950. doi:10.1093/mnras/stab2052

Ricci, C., and Trakhtenbrot, B. (2022). *Changing-look active galactic nuclei. arXiv e-prints* , arXiv:2211.05132. doi:10.48550/arXiv.2211.05132

Ricci, C., Trakhtenbrot, B., Koss, M. J., Ueda, Y., Del Vecchio, I., Treister, E., et al. (2017c). BAT AGN spectroscopic survey. V. X-ray properties of the swift/BAT 70-month AGN catalog. *ApJS* 233, 17. doi:10.3847/1538-4365/aa96ad

Ricci, C., Trakhtenbrot, B., Koss, M. J., Ueda, Y., Schawinski, K., Oh, K., et al. (2017d). The close environments of accreting massive black holes are shaped by radiative feedback. *Nature* 549, 488–491. doi:10.1038/nature23906

Ricci, C., Ueda, Y., Koss, M. J., Trakhtenbrot, B., Bauer, F. E., and Gandhi, P. (2015). Compton-thick accretion in the local universe. *ApJ* 815, L13. doi:10.1088/2041-8205/815/1/L13

Rieke, G. H., Wright, G. S., Böker, T., Bouwman, J., Colina, L., Glasse, A., et al. (2015). The mid-infrared instrument for the James Webb space telescope, I: introduction. *PASP* 127, 584–594. doi:10.1086/682252

Rino-Silvestre, J., González-Gaitán, S., Stalevski, M., Smole, M., Guilherme-Garcia, P., Carvalho, J. P., et al. (2022). *EmulART: emulating Radiative Transfer – a pilot study on autoencoder based dimensionality reduction for radiative transfer models. arXiv e-prints*, arXiv:2210.15400. doi:10.48550/arXiv.2210.15400

Risaliti, G., Elvis, M., Fabbiano, G., Baldi, A., and Zezas, A. (2005). Rapid compton-thick/compton-thin transitions in the seyfert 2 galaxy NGC 1365. *ApJ* 623, L93–L96. doi:10.1086/430252

Risaliti, G., Elvis, M., Fabbiano, G., Baldi, A., Zezas, A., and Salvati, M. (2007). Occultation measurement of the size of the X-ray-emitting region in the active galactic nucleus of NGC 1365. *ApJ* 659, L111–L114. doi:10.1086/517884

Risaliti, G., Elvis, M., and Nicastro, F. (2002). Ubiquitous variability of X-ray-absorbing column densities in seyfert 2 galaxies. *ApJ* 571, 234–246. doi:10.1086/324146

Risaliti, G., Maiolino, R., and Salvati, M. (1999). The distribution of absorbing column densities among seyfert 2 galaxies. *ApJ* 522, 157–164. doi:10.1086/307623

Risaliti, G., Salvati, M., Elvis, M., Fabbiano, G., Baldi, A., Bianchi, S., et al. (2009). The XMM-Newton long look of NGC 1365: uncovering of the obscured X-ray source. *MNRAS* 393, L1–L5. doi:10.1111/j.1745-3933.2008.00580.x

Rivers, E., Baloković, M., Arévalo, P., Bauer, F. E., Boggs, S. E., Brandt, W. N., et al. (2015). The NuSTAR view of reflection and absorption in NGC 7582. *ApJ* 815, 55. doi:10.1088/0004-637X/815/1/55

Rose, T., Edge, A. C., Combes, F., Gaspari, M., Hamer, S., Nesvadba, N., et al. (2019). Constraining cold accretion on to supermassive black holes: molecular gas in the cores of eight brightest cluster galaxies revealed by joint CO and CN absorption. *MNRAS* 489, 349–365. doi:10.1093/mnras/stz2138

Saade, M. L., Brightman, M., Stern, D., Malkan, M. A., and García, J. A. (2022). NuSTAR observations of AGNs with low observed X-ray to [O III] luminosity ratios: heavily obscured AGNs or turned-off AGNs? *ApJ* 936, 162. doi:10.3847/1538-4357/ac88cf

Saha, T., Markowitz, A. G., and Buchner, J. (2022). Inferring the morphology of AGN torus using X-ray spectra: a reliability study. *MNRAS* 509, 5485–5510. doi:10.1093/mnras/stab3250

Sartori, L. F., Schawinski, K., Koss, M. J., Ricci, C., Treister, E., Stern, D., et al. (2018). Joint NuSTAR and Chandra analysis of the obscured quasar in IC 2497 - hanny's Voorwerp system. *MNRAS* 474, 2444–2451. doi:10.1093/mnras/stx2952

Semena, A. N., Sazonov, S. Y., and Krivonos, R. A. (2019). Spectral properties of heavily obscured seyfert galaxies from the INTEGRAL all-sky survey. *Astron. Lett.* 45, 490–520. doi:10.1134/S1063773719080085

Sengupta, D., Marchesi, S., Vignali, C., Torres-Albà, N., Bertola, E., Pizzetti, A., et al. (2023). Compton-thick AGN in the NuSTAR era X: analysing seven local CT-AGN candidates. *A&A* 676, A103. doi:10.1051/0004-6361/202245646

Shakura, N. I., and Sunyaev, R. A. (1973). Black holes in binary systems. Observational appearance. *A&A* 24, 337–355.

Silver, R., Torres-Albà, N., Zhao, X., Marchesi, S., Pizzetti, A., Cox, I., et al. (2022). Compton-thick AGN in the NuSTAR era. IX. A joint NuSTAR and xmm-Newton analysis of four local AGN. *ApJ* 940, 148. doi:10.3847/1538-4357/ac9bf8

Spergel, D., Gehrels, N., Baltay, C., Bennett, D., Breckinridge, J., Donahue, M., et al. (2015). *Wide-field InfrarRed survey telescope-astrophysics focused telescope assets WFIRST-AFTA 2015 report. arXiv e-prints* , arXiv:1503.03757. doi:10.48550/arXiv.1503.03757

Springel, V., Di Matteo, T., and Hernquist, L. (2005). Modelling feedback from stars and black holes in galaxy mergers. *MNRAS* 361, 776–794. doi:10.1111/j.1365-2966.2005.09238.x

Storchi-Bergmann, T., and Schnorr-Müller, A. (2019). Observational constraints on the feeding of supermassive black holes. *Nat. Astron.* 3, 48–61. doi:10.1038/s41550-018-0611-0

Svoboda, J., Guainazzi, M., and Merloni, A. (2017). AGN spectral states from simultaneous UV and X-ray observations by XMM-Newton. *A&A* 603, A127. doi:10.1051/0004-6361/201630181

Tanimoto, A., Ueda, Y., Odaka, H., Kawaguchi, T., Fukazawa, Y., and Kawamuro, T. (2019). XCLUMPY: X-ray spectral model from clumpy torus and its application to the Circinus galaxy. *ApJ* 877, 95. doi:10.3847/1538-4357/ab1b20

Tanimoto, A., Ueda, Y., Odaka, H., Ogawa, S., Yamada, S., Kawaguchi, T., et al. (2020). Application of an X-ray clumpy torus model (XCLUMPY) to 10 obscured active galactic nuclei observed with suzaku and NuSTAR. *ApJ* 897, 2. doi:10.3847/1538-4357/ab96bc

Tanimoto, A., Ueda, Y., Odaka, H., Yamada, S., and Ricci, C. (2022). NuSTAR observations of 52 compton-thick active galactic nuclei selected by the swift/burst Alert telescope all-sky hard X-ray survey. *ApJS* 260, 30. doi:10.3847/1538-4365/ac5f59

Temi, P., Gaspari, M., Brighenti, F., Werner, N., Grossova, R., Gitti, M., et al. (2022). Probing multiphase gas in local massive elliptical galaxies via multiwavelength observations. *ApJ* 928, 150. doi:10.3847/1538-4357/ac5036

Teng, S. H., Rigby, J. R., Stern, D., Ptak, A., Alexander, D. M., Bauer, F. E., et al. (2015). A NuSTAR survey of nearby ultraluminous infrared galaxies. *ApJ* 814, 56. doi:10.1088/0004-637X/814/1/56

Terashima, Y. (2002). Asca observations of "type 2" liners: evidence for a stellar source of ionization. *Astrophysical J.* 576, 653–666. doi:10.1086/341772

Torres-Albà, N., Iwasawa, K., Díaz-Santos, T., Charmandaris, V., Ricci, C., Chu, J. K., et al. (2018). C-GOALS. II. Chandra observations of the lower luminosity sample of nearby luminous infrared galaxies in GOALS. *A&A* 620, A140. doi:10.1051/0004-6361/201834105

Torres-Albà, N., Marchesi, S., Zhao, X., Ajello, M., Silver, R., Ananna, T. T., et al. (2021). Compton-thick AGN in the NuSTAR era VI: the observed compton-thick fraction in the local universe. *ApJ* 922, 252. doi:10.3847/1538-4357/ac1c73

Torres-Albà, N., Marchesi, S., Zhao, X., Cox, I., Pizzetti, A., Ajello, M., et al. (2023). *Hydrogen column density variability in a sample of local compton-thin AGN*. *arXiv e-prints* , arXiv:2301.07138. doi:10.48550/arXiv.2301.07138

Traina, A., Marchesi, S., Vignali, C., Torres-Albà, N., Ajello, M., Pizzetti, A., et al. (2021). Compton-thick AGN in the NuSTAR era VII. A joint NuSTAR, chandra, and xmm-Newton analysis of two nearby, heavily obscured sources. *ApJ* 922, 159. doi:10.3847/1538-4357/ac1fee

Treister, E., Urry, C. M., and Virani, S. (2009). The space density of compton-thick active galactic nucleus and the X-ray background. *ApJ* 696, 110–120. doi:10.1088/0004-637X/696/1/110

Trump, J. R., Impey, C. D., Kelly, B. C., Civano, F., Gabor, J. M., Diamond-Stanic, A. M., et al. (2011). Mid-infrared selection of active galactic nuclei with the wide-field infrared survey explorer. i. characterizing wise-selected agns in cosmos. *Astrophysical J.* 733, 60. doi:10.1088/0004-637X/733/1/60

Trump, J. R., Sun, M., Zeimann, G. R., Luck, C., Bridge, J. S., Grier, C. J., et al. (2015). The biases of optical line-ratio selection for active galactic nuclei and the intrinsic relationship between black hole accretion and galaxy star formation. *ApJ* 811, 26. doi:10.1088/0004-637X/811/1/26

Turner, T. J., Reeves, J. N., Braito, V., Yaqoob, T., Kraemer, S. B., and Severgnini, P. (2020). Elucidating the global distribution of reprocessing gas in NGC 1194. *MNRAS* 498, 1983–1991. doi:10.1093/mnras/staa2401

Ueda, Y., Akiyama, M., Hasinger, G., Miyaji, T., and Watson, M. G. (2014). Toward the standard population synthesis model of the X-ray background: evolution of X-ray luminosity and absorption functions of active galactic nuclei including compton-thick populations. *ApJ* 786, 104. doi:10.1088/0004-637X/786/2/104

Uematsu, R., Ueda, Y., Tanimoto, A., Kawamuro, T., Setoguchi, K., Ogawa, S., et al. (2021). X-ray constraint on the location of the AGN torus in the Circinus galaxy. *ApJ* 913, 17. doi:10.3847/1538-4357/abf0a2

Urry, C. M., and Padovani, P. (1995). Unified schemes for radio-loud active galactic nuclei. *PASP* 107, 803. doi:10.1086/133630

Ursini, F., Boissay-Malaquin, R., Marinucci, A., Matt, G., Bianchi, S., Capalbi, M., et al. (2015). Simultaneous x-ray/optical/uv snapshots of active galactic nuclei from xmm-Newton: spectral energy distributions for the reverberation mapped sample. *Mon. Notices R. Astronomical Soc.* 452, 3266–3272. doi:10.1093/mnras/stv1527

Vander Meulen, B., Camps, P., Stalevski, M., and Baes, M. (2023). *X-ray radiative transfer in full 3D with SKIRT*. *arXiv e-prints* , arXiv:2304.10563. doi:10.48550/arXiv.2304.10563

van Dyk, D. A., Connors, A., Kashyap, V. L., and Siemiginowska, A. (2001). Analysis of energy spectra with low photon counts via bayesian posterior simulation. *ApJ* 548, 224–243. doi:10.1086/318656

Vasudevan, R. V., Brandt, W. N., Mushotzky, R. F., Winter, L. M., Baumgartner, W. H., Shimizu, T. T., et al. (2013). X-ray properties of the northern galactic cap sources in the 58 Month swift/BAT catalog. *ApJ* 763, 111. doi:10.1088/0004-637X/763/2/111

Vasudevan, R. V., Fabian, A. C., Reynolds, C. S., Aird, J., Dauser, T., and Gallo, L. C. (2016). A selection effect boosting the contribution from rapidly spinning black holes to the cosmic X-ray background. *MNRAS* 458, 2012–2023. doi:10.1093/mnras/stw363

Vasylenko, A. A., Fedorova, E., and Zhdanov, V. I. (2013). Observations of Sy2 galaxy NGC 3281 by XMM-Newton and INTEGRAL satellites. *Adv. Astronomy Space Phys.* 3, 120–125. doi:10.48550/arXiv.1311.1691

Vignali, C., Severgnini, P., Piconcelli, E., Lanzuisi, G., Gilli, R., Mignoli, M., et al. (2018). NuSTAR reveals that the heavily obscured nucleus of NGC 2785 was the contaminant of IRAS 09104+4109 in the BeppoSAX/PDS hard X-rays. *A&A* 619, A16. doi:10.1051/0004-6361/201833805

Virtanen, P., Gommers, R., Oliphant, T. E., Haberland, M., Reddy, T., Cournapeau, D., et al. (2020). SciPy 1.0: fundamental algorithms for scientific computing in Python. *Nat. Methods* 17, 261–272. doi:10.1038/s41592-019-0686-2

Vollmer, B., and Duschl, W. J. (2002). The dynamics of the circumnuclear disk and its environment in the galactic centre. *A&A* 388, 128–148. doi:10.1051/0004-6361:20020422

Volonteri, M. (2010). Formation of supermassive black holes. *A&A Rev.* 18, 279–315. doi:10.1007/s00159-010-0029-x

Volonteri, M., Lodato, G., and Natarajan, P. (2008). The evolution of massive black hole seeds. *MNRAS* 383, 1079–1088. doi:10.1111/j.1365-2966.2007.12589.x

Wada, K. (2012). Radiation-driven fountain and origin of torus around active galactic nuclei. *ApJ* 758, 66. doi:10.1088/0004-637X/758/1/66

Walton, D. J., Risaliti, G., Harrison, F. A., Fabian, A. C., Miller, J. M., Arevalo, P., et al. (2014). NuSTAR and XMM-Newton observations of NGC 1365: extreme absorption variability and a constant inner accretion disk. *ApJ* 788, 76. doi:10.1088/0004-637X/788/1/76

Williams, D. R. A., Pahari, M., Baldi, R. D., McHardy, I. M., Mathur, S., Beswick, R. J., et al. (2022). LeMMINGs - IV. The X-ray properties of a statistically complete sample of the nuclei in active and inactive galaxies from the Palomar sample. *MNRAS* 510, 4909–4928. doi:10.1093/mnras/stab3310

Yamada, S., Ueda, Y., Tanimoto, A., Imanishi, M., Toba, Y., Ricci, C., et al. (2021). Comprehensive broadband X-ray and multiwavelength study of active galactic nuclei in 57 local luminous and ultraluminous infrared galaxies observed with NuSTAR and/or swift/BAT. *ApJS* 257, 61. doi:10.3847/1538-4365/ac17f5

Yamada, S., Ueda, Y., Tanimoto, A., Oda, S., Imanishi, M., Toba, Y., et al. (2020). Nature of compton-thick active galactic nuclei in "nonmerging" luminous infrared galaxies UGC 2608 and NGC 5135 revealed with broadband X-ray spectroscopy. *ApJ* 897, 107. doi:10.3847/1538-4357/ab94b1

Yamauchi, A., Nakai, N., Ishihara, Y., Diamond, P., and Sato, N. (2012). Water-vapor maser disk at the nucleus of the seyfert 2 galaxy IC 2560 and its distance. *PASJ* 64, 103. doi:10.1093/pasj/64.5.103

Yaqoob, T. (2012). The nature of the Compton-thick X-ray reprocessor in NGC 4945. *MNRAS* 423, 3360–3396. doi:10.1111/j.1365-2966.2012.21129.x

Younes, G., Porquet, D., Sabra, B., Reeves, J. N., and Grosso, N. (2011). Discovery of relativistic fe kα emission in the seyfert 1.9 galaxy mcg-05-23-16. *Astronomy Astrophysics* 530, A149. doi:10.1051/0004-6361/201116806

Younes, G., Porquet, D., Sabra, B., Reeves, J. N., and Grosso, N. (2019). A systematic study of the properties of relativistic fe kα lines in agn. *Astronomy Astrophysics* 628, A56. doi:10.1051/0004-6361/201834282

Young, A. J., McHardy, I. M., Emmanoulopoulos, D., and Nandra, K. (2018). Nustar and xmm-Newton observations of the hard state in the seyfert 1.5 galaxy mcg–5-23-16. *Astrophysical J.* 853, 56. doi:10.3847/1538-4357/aaa5aa

Zaino, A., Bianchi, S., Marinucci, A., Matt, G., Bauer, F. E., Brandt, W. N., et al. (2020). Probing the circumnuclear absorbing medium of the buried AGN in NGC 1068 through NuSTAR observations. *MNRAS* 492, 3872–3884. doi:10.1093/mnras/staa107

Zaw, I., Rosenthal, M. J., Katkov, I. Y., Gelfand, J. D., Chen, Y.-P., Greenhill, L. J., et al. (2020). An accreting, anomalously low-mass black hole at the center of low-mass galaxy IC 750. *ApJ* 897, 111. doi:10.3847/1538-4357/ab9944

Zhao, X., Marchesi, S., and Ajello, M. (2019a). Compton-thick AGN in the NuSTAR era. IV. A deep NuSTAR and xmm-Newton view of the candidate compton-thick AGN in eso 116-g018. *ApJ* 871, 182. doi:10.3847/1538-4357/aaf80b

Zhao, X., Marchesi, S., Ajello, M., Baloković, M., and Fischer, T. (2020). A broadband X-ray study of a sample of AGNs with [O III] measured inclinations. *ApJ* 894, 71. doi:10.3847/1538-4357/ab879d

Zhao, X., Marchesi, S., Ajello, M., Cole, D., Hu, Z., Silver, R., et al. (2021). The properties of the AGN torus as revealed from a set of unbiased NuSTAR observations. *A&A* 650, A57. doi:10.1051/0004-6361/202140297

Zhao, X., Marchesi, S., Ajello, M., Marcotulli, L., Cusumano, G., La Parola, V., et al. (2019b). Compton-thick AGNs in the NuSTAR era. II. A deep NuSTAR and xmm-Newton view of the candidate compton-thick AGN in NGC 1358. *ApJ* 870, 60. doi:10.3847/1538-4357/aaf1a0

ZuHone, J. A., Vikhlinin, A., Tremblay, G. R., Randall, S. W., Andrade-Santos, F., and Bourdin, H. (2023). *SOXS: simulated observations of X-ray sources*. Astrophysics Source Code Library. record ascl:2301.024.

frontiers | Frontiers in Astronomy and Space Sciences

TYPE Original Research
PUBLISHED 20 May 2024
DOI 10.3389/fspas.2024.1304652

Check for updates

OPEN ACCESS

EDITED BY
Murray Brightman,
California Institute of Technology,
United States

REVIEWED BY
Roberto Serafinelli,
Astronomical Observatory of Rome (INAF),
Italy
Erika Maria Benitez,
National Autonomous University of Mexico,
Mexico

*CORRESPONDENCE
Ryan W. Pfeifle,
ryan.w.pfeifle@nasa.gov

RECEIVED 29 September 2023
ACCEPTED 02 February 2024
PUBLISHED 20 May 2024

CITATION
Pfeifle RW, Boorman PG, Weaver KA, Buchner J, Civano F, Madsen K, Stern D, Torres-Albà N, Nardini E, Ricci C, Marchesi S, Ballantyne DR, Sicilian D, Chen C-T, Kammoun E, Hickox RC, García JA and Mallick L (2024), The high energy X-ray probe (HEX-P): the future of hard X-ray dual AGN science.
Front. Astron. Space Sci. 11:1304652.
doi: 10.3389/fspas.2024.1304652

COPYRIGHT
© 2024 Pfeifle, Boorman, Weaver, Buchner, Civano, Madsen, Stern, Torres-Albà, Nardini, Ricci, Marchesi, Ballantyne, Sicilian, Chen, Kammoun, Hickox, García and Mallick. This is an open-access article distributed under the terms of the Creative Commons Attribution License (CC BY). The use, distribution or reproduction in other forums is permitted, provided the original author(s) and the copyright owner(s) are credited and that the original publication in this journal is cited, in accordance with accepted academic practice. No use, distribution or reproduction is permitted which does not comply with these terms.

The high energy X-ray probe (HEX-P): the future of hard X-ray dual AGN science

Ryan W. Pfeifle[1,2]*, Peter G. Boorman[3], Kimberly A. Weaver[1], Johannes Buchner[4], Francesca Civano[1], Kristin Madsen[1], Daniel Stern[5], Núria Torres-Albà[6], Emanuele Nardini[7], Claudio Ricci[8,9,10], Stefano Marchesi[6,11,12], D. R. Ballantyne[13], Dominic Sicilian[14], Chien-Ting Chen[15,16], Elias Kammoun[7,17,18], Ryan C. Hickox[19], Javier A. García[1,3] and Labani Mallick[3,20,21]

[1]X-ray Astrophysics Laboratory, NASA Goddard Space Flight Center, Greenbelt, MD, United States, [2]NASA Postdoctoral Program Fellow, Oak Ridge Associated Universities, NASA NPP Program, Oak Ridge, TN, United States, [3]Cahill Center for Astrophysics, California Institute of Technology, Pasadena, CA, United States, [4]Max Planck Institute for Extraterrestrial Physics, Garching, Germany, [5]Jet Propulsion Laboratory, California Institute of Technology, Pasadena, CA, United States, [6]Department of Physics and Astronomy, Clemson University, Clemson, SC, United States, [7]INAF—Osservatorio Astrofisico di Arcetri, Firenze, Italy, [8]Instituto de Estudios Astrofísicos, Facultad de Ingeniería y Ciencias, Universidad Diego Portales, Santiago, Chile, [9]Kavli Institute for Astronomy and Astrophysics, Peking University, Beijing, China, [10]George Mason University, Department of Physics and Astronomy, MS3F3, Fairfax, VA, United States, [11]Dipartimento di Fisica e Astronomia (DIFA) Augusto Righi, Università di Bologna, Firenze, Italy, [12]INAF—Osservatorio di Astrofisico e Scienza dello Spazio (OAS), Bologna, Italy, [13]Center for Relativistic Astrophysics, School of Physics, George Institute of Technology, Atlanta, GA, United States, [14]Department of Physics, University of Miami, Coral Gables, FL, United States, [15]Science and Technology Institute, Universities Space Research Association, Huntsville, AL, United States, [16]Astrophysics Office, NASA Marshall Space Flight Center, Huntsville, AL, United States, [17]UMR5277 Institut de Recherche en Astrophysique et Planétologie (IRAP), CNRS, UPS, CNES, Université de Toulouse, Toulouse, France, [18]Dipartimento di Matematica e Fisica, Università Roma Tre, Rome, Italy, [19]Department of Physics and Astronomy, Dartmouth College, Hanover, NH, United States, [20]CITA National Fellow, University of Manitoba, Winnipeg, MB, Canada, [21]Canadian Institute for Theoretical Astrophysics, University of Toronto, Toronto, ON, Canada

A fundamental goal of modern-day astrophysics is to understand the connection between supermassive black hole (SMBH) growth and galaxy evolution. Merging galaxies offer one of the most dramatic channels for galaxy evolution known, capable of driving inflows of gas into galactic nuclei, potentially fueling both star formation and central SMBH activity. Dual active galactic nuclei (dual AGNs) in late-stage mergers with nuclear pair separations <10 kpc are thus ideal candidates to study SMBH growth along the merger sequence since they coincide with the most transformative period for galaxies. However, dual AGNs can be extremely difficult to confirm and study. Hard X-ray (>10 keV) studies offer a relatively contamination-free tool for probing the dense obscuring environments predicted to surround the majority of dual AGN in late-stage mergers. To date, only a handful of the brightest and closest systems have been studied at these energies due to the demanding instrumental requirements involved. We demonstrate the unique capabilities of *HEX-P* to spatially resolve the soft and - for the first time - hard X-ray counterparts of closely-separated (~2″ – 5″) dual AGNs in the local Universe. By incorporating physically-motivated obscuration models, we reproduce realistic broadband X-ray spectra expected for deeply embedded accreting SMBHs.

Hard X-ray spatially resolved observations of dual AGNs—accessible only to *HEX-P*—will hence transform our understanding of dual AGN in the nearby Universe.

KEYWORDS

dual AGN, galaxy merger, x-ray astronomy, active galactic nucleus, galaxy interaction

1 Introduction

It has long been known that galaxy interactions and mergers give rise to gravitational torques that can transform the structure and composition of the constituent galaxies (e.g., Toomre and Toomre, 1972). These torques can funnel vast quantities of gas into the central nuclei of the galaxies (e.g., Barnes and Hernquist, 1991; Barnes and Hernquist, 1996), creating reservoirs that can then fuel star formation as well as the central supermassive black holes (SMBHs), which ignite as active galactic nuclei (AGNs) (Hopkins et al., 2006; Hopkins et al., 2008). A natural product of galaxy mergers are dual AGNs, that is, synchronized SMBH growth in both galaxies (Van Wassenhove et al., 2012). Simulations of galaxy mergers predict that the growth of the central SMBHs is better synchronized in the latest stages of the merger sequence, when the central nuclei are separated by $\lesssim 10$ kpc (Van Wassenhove et al., 2012; Capelo et al., 2015; Blecha et al., 2018), though dual AGNs can be found across the full merger sequence, from separations below 1 kpc (e.g., Komossa et al., 2003; Koss et al., 2023) and up to ~50 kpc or more (Liu et al., 2011; Koss et al., 2012; De Rosa et al., 2018; De Rosa et al., 2023), and the synchronized activation of a dual AGN is a strong function of progenitor mass ratios, morphological types, gas masses, and radiative feedback (e.g., Callegari et al., 2009; 2011; Van Wassenhove et al., 2012; Capelo et al., 2015; Blecha et al., 2018; Li et al., 2021). Dual AGNs represent a potentially important phase of SMBH growth: they are predicted to be heavily obscured across the merger sequence (Blecha et al., 2018) and in late-stage mergers they are expected to coincide with the most obscured and expeditious growth of the two SMBHs (Capelo et al., 2015; Blecha et al., 2018). These predictions find support in observations showing that, relative to mass- and redshift-matched control galaxies, the AGN fraction in galaxy mergers increases with decreasing nuclear pair separation (Ellison et al., 2011; Satyapal et al., 2014; Weston et al., 2017), where the increase in AGN fraction is most dramatic when selecting AGNs based on mid-IR colors (Satyapal et al., 2014; Weston et al., 2017). A large fraction of known dual AGNs show evidence for heavy obscuration (see Section 5.2 in Pfeifle et al., 2023) which is consistent with theoretical predictions, but such evidence is admittedly still relatively circumstantial and may depend upon selection method; statistically complete studies of dual AGNs are still needed. Nonetheless, with additional evidence of dramatic AGN feedback in known dual AGNs (Müller-Sánchez et al., 2018), dual AGNs in late-stage mergers may represent one of the most transformative phases of the entire merger sequence for both the SMBHs and their hosts. Dual AGNs also represent the observational forerunner to gravitationally-bound binary SMBHs, the inspiral and coalescence of which will emit the most titanic of gravitational wave signals (GW); GWs emitted during the inspiral and coalescence of higher redshift, intermediate-mass SMBH binaries (total binary mass of 10^3–10^7 $M_\odot$) will be accessible to future space-based GW facilities (e.g., LISA, Amaro-Seoane et al., 2023, which will be sensitive these mHz frequencies). These expectations are bolstered by the recent detection of a nHz frequency GW background by Pulsar Timing Arrays (Agazie et al., 2023), the origin of which is most likely attributable to a population of SMBH binaries.

Despite this presumed importance, dual AGNs have remained relatively elusive, and a variety of selection strategies have been pursued to uncover them: optical spectroscopic emission line ratios Liu et al. (2011), double-peaked emission lines (e.g., Zhou et al., 2004; Wang et al., 2009; Liu et al., 2010; Smith et al., 2010; Comerford et al., 2011; Comerford et al., 2012; Ge et al., 2012), infrared colors (Imanishi and Saito, 2014; Satyapal et al., 2017; Ellison et al., 2017; Pfeifle et al., 2019b; Pfeifle et al., 2019a; Imanishi et al., 2020; Barrows et al., 2023), hard X-ray selection (Koss et al., 2012), and most recently varstrometry (Hwang et al., 2020; Shen et al., 2021; Schwartzman et al., 2023) and Gaia multi-source strategies (Shen et al., 2019; Mannucci et al., 2022; Ciurlo et al., 2023). Serendipitous (e.g., Komossa et al., 2003; Guainazzi et al., 2005; Piconcelli et al., 2010) and follow-up X-ray observations (Bianchi et al., 2008; Comerford et al., 2011; Koss et al., 2012; Liu et al., 2013; Comerford et al., 2015; Satyapal et al., 2017; Pfeifle et al., 2019b; Pfeifle et al., 2019a; Hou et al., 2019; Gross et al., 2019; Hou et al., 2020; Hou et al., 2023) are a common method by which dual AGNs are confirmed, particularly in cases where dual AGNs cannot be selected through common optical diagnostics (e.g., NGC 6240, Komossa et al., 2003). These investigations have revealed a prevalence of high column densities in the known population of dual AGNs (e.g., Komossa et al., 2003; Bianchi et al., 2008; Piconcelli et al., 2010; Ptak et al., 2015; Nardini, 2017; De Rosa et al., 2018; Pfeifle et al., 2019b; Pfeifle et al., 2019a; De Rosa et al., 2023); see discussion in Pfeifle et al. (2023). Radio imaging is also an effective method of selecting (Fu et al., 2015a) as well as confirming (e.g., Fu et al., 2011; Frey et al., 2012; Fu et al., 2015b; Müller-Sánchez et al., 2015; Rubinur et al., 2019; Rubinur et al., 2021; Gross et al., 2023) or rejecting dual AGN candidates (e.g., Gabányi et al., 2014; Gabányi et al., 2016; Fu et al., 2015b; Müller-Sánchez et al., 2015; Rubinur et al., 2019). Radio emission is insensitive to the line-of-sight obscuration and therefore radio observations are not biased against the detection of heavily obscured dual AGNs, though confirmation and characterization via radio imaging is not always unambiguous (e.g., Müller-Sánchez et al., 2015; Veres et al., 2021) and does require that one or both AGNs be emitting in the radio, which is not always the case (e.g., Gabányi et al., 2016).

While *Chandra* and *XMM-Newton* have been used effectively in the past to identify, confirm, and/or characterize dual AGN systems, their soft X-ray bandpasses (0.5–10 keV) bias them against detecting and properly characterizing the X-ray spectral properties and the circumnuclear obscurers in heavily obscured

dual AGNs with column densities $N_H > 5 \times 10^{23}$–10^{24} cm^{-2}, as predicted (Hopkins et al., 2008; Capelo et al., 2015; Capelo et al., 2017; Blecha et al., 2018) and observed (e.g., Komossa et al., 2003; Ballo et al., 2004; Bianchi et al., 2008; Mazzarella et al., 2012; Koss et al., 2016; De Rosa et al., 2018; Iwasawa et al., 2018; Pfeifle et al., 2019a; Iwasawa et al., 2020; Guainazzi et al., 2021; De Rosa et al., 2023), particularly in late-stage mergers (e.g., Ricci et al., 2017; Ricci et al., 2021). In fact, this is a particular concern in LIRGs and ULIRGs; though the statistics are small, a higher fraction of dual AGNs were identified among the lower IR luminosity GOALS sample (Torres-Albà et al., 2018) than the brighter IR luminosity sample (Iwasawa et al., 2011), which can possibly be interpreted as the dual AGNs in the high luminosity sample being too obscured for *XMM-Newton* or *Chandra* to detect and too close together to be resolved by *NuSTAR* (Torres-Albà et al., 2018). Hard X-ray bandpasses (>10 keV), on the other hand, provide access to harder X-ray features, such as Compton reflection, that are vital for providing accurate constraints on the X-ray properties of heavily obscured AGNs. *NuSTAR*, with its sensitivity over the 3–78 keV bandpass, has detected and studied the hard X-ray dual AGN counterparts (when present) in Arp 299 (though only one of the dual AGNs was detected, Ptak et al., 2015, but see Section 5 below), ESO 509-IG066 (Kosec et al., 2017), MCG+04-48-002/NGC 6921 (Koss et al., 2016), and NGC 833/NGC 835 Oda et al. (2018), all of which are local, relatively bright, and have separations large enough for *NuSTAR* to spatially resolve (~16″ – 91″, though at 16″ the two sources would appear as a convolved, elongated single source). However, hard X-ray observations of dual AGNs with *NuSTAR* are relatively uncommon (only about 15 *NuSTAR* observations of dual AGNs and candidates have been published previously in the literature; see also Section 5.3 in Pfeifle et al., 2023), and most dual AGN studies performed with *NuSTAR* suffer from non-detections due to *NuSTAR*'s sensitivity limit (e.g., Ptak et al., 2015; Ricci et al., 2017; Inaba et al., 2022; Pfeifle et al., 2023) and/or convolved sources due to *NuSTAR*'s angular resolution (half power diameter ~58″, 18″ FWHM; Nardini, 2017; Yamada et al., 2018; Iwasawa et al., 2018; Pfeifle et al., 2019a; Iwasawa et al., 2020; Pfeifle et al., 2023). This requires a great deal of care and caution when performing the spectroscopic analysis and interpreting the results (e.g., the case of NGC 6240, Nardini, 2017). To usher in revolutionary advances in hard X-ray dual AGN science, new facilities with higher spatial resolution and greater sensitivity at hard X-ray energies (>10 keV) are required.

In this paper, we discuss the feasibility of hard X-ray dual AGN science with the High Energy X-ray Probe (HEX-P) mission concept. The current mission design for *HEX-P* is described in Section 2. In Section 3 we describe our *HEX-P* imaging and spectroscopic simulations, generated using the SOXS (ZuHone et al., 2023) and SIXTE (Dauser et al., 2019) software packages. We outline the potential for resolving hard and soft X-ray signatures from dual AGNs with *HEX-P* using the instrument and facility design described in Section 4.1, the feasibility of using nested sampling and Bayesian statistical source detection techniques to probe closely-separated hard X-ray sources in Section 4.1, and we compare these results to what is currently possible with *NuSTAR* in Section 4.2. In Section 5, we examine simulated hard X-ray imaging and spectra for the dual AGN in Arp 299 as a test case for *HEX-P* dual AGN science, wherein we use physically-motivated obscuration models and Bayesian fitting techniques to constrain the line-of-sight column densities, photon indices, and other spectroscopic parameters of the AGNs. We discuss the issue of spectral contamination for closely separated sources in Section 6. In Section 7 we briefly outline synergies with upcoming ground-based and space-based facilities. We provide concluding remarks in Section 8.

2 Mission design

The *HEX-P* (Madsen et al., 2023) is a probe-class mission concept that offers sensitive broad-band spectral coverage (0.2–80 keV) with exceptional spectral, timing, and angular capabilities (see Madsen et al., 2023, for further details). It features two high-energy telescopes (HETs) that focus hard X-rays, and one low-energy telescope (LET) that focuses lower energy X-rays.

The LET consists of a segmented mirror assembly coated with Ir on monocrystalline silicon that achieves a half power diameter (HPD) of 3.5″, and a low-energy DEPFET detector, of the same type as the Wide Field Imager (WFI; Meidinger et al., 2020) onboard Athena (Nandra et al., 2013). It has 512 × 512 pixels that cover a field of view of 11.3′ x 11.3′. It has an effective passband of 0.2–25 keV, and a full frame readout time of 2 ms, which can be operated in a 128 and 64 channel window mode for higher count-rates to mitigate pile-up and faster readout. Pile-up effects remain below an acceptable limit of ~1% for a flux up to ~100 mCrab (2–10 keV) in the smallest window configuration. Excising the core of the PSF, a common practice in X-ray astronomy, will allow for observations of brighter sources, with a typical loss of up to ~60% of the total photon counts.

The HET consists of two co-aligned telescopes and detector modules. The optics are made of Ni-electroformed full shell mirror substrates, leveraging the heritage of XMM-Newton (Jansen et al., 2001), and coated with Pt/C and W/Si multilayers for an effective passband of 2–80 keV. The high-energy detectors are of the same type as flown on *NuSTAR* (Harrison et al., 2013), and they consist of 16 CZT sensors per focal plane, tiled 4 × 4, for a total of 128 × 128 pixel spanning a field of view slightly larger than for the LET, 13.4′x13.4′.

The broad X-ray passband and superior sensitivity (minimum detectable 10–20 keV flux $F_{10-20\,\mathrm{keV}} = 1.4 \times 10^{-15}$ erg cm^{-2} s^{-1} in 1 Ms; see Table 2 in Madsen et al., 2023) will provide a unique opportunity to study dual AGNs and galaxy mergers across a wide range of energies, luminosity ratios, pair separations, and dynamical regimes.

All the simulations presented here were produced with a set of response files that represent the observatory performance based on current best estimates as of Spring 2023 (see Madsen et al., 2023). The effective area is derived from ray-tracing calculations for the mirror design including obscuration by all known structures. The detector responses are based on simulations performed by the respective hardware groups, with an optical blocking filter for the LET and a Be window and thermal insulation for the HET. The LET background was derived from a GEANT4 simulation (Eraerds et al., 2021) of the WFI instrument, and the HET backgrounds was derived from a GEANT4 simulation of the *NuSTAR* instrument. Both simulations adopt the L1 orbit for HEX-P.

3 Simulating dual AGNs using SOXS and SIXTE

To simulate *HEX-P* observations of dual AGNs, we rely upon two software suites: 1) the Simulated Observations of X-ray Sources (soxs, ZuHone et al., 2023) suite, to create the SIMulated inPUT (SIMPUT) files that store the spatial and spectral models used for the simulations, and 2) the Simulation of X-ray Telescopes (sixte, Dauser et al. (2019)) suite, which was used to generate the actual simulated observations.

Each simulation includes two AGNs represented as point source spatial models (hereafter AGN 1 and AGN 2), and we produced simulations for a variety of separations, ranging from 50″ down to 20″ in increments of 10″ as well as from 20″ down to 0″ in increments of 2″. Here, the 0″ case represents the "null" expectation of what a single source would look like at the combined flux level of the AGNs in our simulations and it is included for visual comparison purposes. For illustrative purposes in this work, we also include simulations of AGNs separated by 15″, 5″, 3″, and 1″. We use the following components to develop the spectral models for the AGNs: 1) an absorbed power law ($\Gamma = 1.8$) that accounts for photoelectric absorption and Compton scattering; 2) reprocessed emission from a torus (borus, Baloković et al. (2018), which self consistently accounts for absorption, fluorescence, and Compton scattering for a toroidal distribution of obscuring gas); 3) two soft X-ray thermal components (apec) to model emission due to star formation, motivated by the common presence of soft thermal components in many dual AGNs and candidate systems (see, e.g., Section 5.4 in Pfeifle et al. (2023)); 4) a power law to model Thomson scattering (0.5%). This AGN spectroscopic model is described in xspec as:

$$tbabs \times (borus + ztbabs \times cabs \times cutoffpl + const \times cutoffpl + apec + apec)$$

Each AGN spectrum is simulated at a redshift of $z = 0.05$ ($D_L = 222.3$ Mpc). We assume an approximately edge-on torus viewing angle of $\theta_{view} = 70°$ and a covering factor of C = 85%; the former assumption was a conservative choice that satisfied our fundamental requirement that the sight line be obscured but not grazing the torus, while the latter assumption is motivated by the expectation that mergers should result in heavily obscured AGNs with high covering factors (Ricci et al., 2017). AGNs 1 and 2 have observed (uncorrected for intrinsic absorption) 2–10 keV fluxes normalized to 1.0×10^{-13} and 5.0×10^{-14} erg cm^{-2} s^{-1}, respectively. For each choice of separation, we run the spectral model of each AGN over a small list of line-of-sight column densities, $\log(N_H/\mathrm{cm}^2) = 22, 23, 24$ (for simplicity we assume the average torus column density and the line-of-sight column density are equal); we therefore end up with nine SIMPUT files for each separation, where each SIMPUT file probes a separate pairing in terms of obscuration; i.e., one Compton-thick pair ($N_{H,1\ and\ 2} = 10^{24}$ cm^{-2}), four Compton-thick and Compton-thin pairs ($N_{H,1\ or\ 2} = 10^{24}$ cm^{-2} and $N_{H,1\ or\ 2} = 10^{23}$ cm^{-2}, $N_{H,1\ or\ 2} = 10^{24}$ cm^{-2} and $N_{H,1\ or\ 2} = 10^{22}$ cm^{-2}), and four Compton-thin-Compton-thin pairs ($N_{H,1\ and\ 2} = 10^{23}$ cm^{-2}, $N_{H,1\ or\ 2} = 10^{22}$ cm^{-2} and $N_{H,1\ or\ 2} = 10^{23}$ cm^{-2}, $N_{H,1\ and\ 2} = 10^{22}$ cm^{-2}). soxs is then used to convolve the spatial and spectral models to produce the SIMPUT files for each AGN pairing.

Each SIMPUT file generated above was fed to sixte in order to generate the *HEX-P* HET and LET event files. For each AGN pairing, we assumed a 50 ks exposure (which could be the typical exposure time in the *HEX-P* wide area survey, and is also similar in length to archival *NuSTAR* observations of dual AGNs, i.e., ~20 – 60 ks) and generated event files for HET 1, HET 2, an effective (co-added) 2-camera HET event file, and a LET event file using the v7 *HEX-P* response files (see Madsen et al., 2023). Science images were generated for all three *HEX-P* cameras using the imgev command and spectra were extracted using the makespec command from 10" apertures (unless stated otherwise in the text) centered on the AGN positions. We performed the same set of commands in sixte for the analogous *NuSTAR* simulated imaging using the *NuSTAR* response files[1] and a background file derived from the COSMOS field (Civano et al., 2015).

4 Hard X-ray imaging results for dual AGNs

4.1 HEX-P HET and LET imaging of dual AGNs

We show a subset of our dual AGN simulation suite in Figure 1 and Figure 2 for the 0.2–25 keV LET and (co-added two-camera) 2–80 keV HET imaging, respectively, with each panel representing a distinct pair separation, ranging from 50″ down to 0″ in 10″ or 5″ intervals. AGN 1 (centered in the field of view) is clearly seen in the center of each panel, while AGN 2 can be seen moving closer in from the left with each successive panel. These images clearly show the two AGNs are distinguishable by eye down to ~5″ in both the HET and LET; we include a finer grid of separations in Figure 9 with separations ranging from 5″ down to 1″ in 1″ intervals, which demonstrates that the AGNs can be distinguished by eye even down to ~4″ in HET imaging and ~3″ in LET imaging.

Probing dual AGNs with *HEX-P* down to separations $\lesssim 5''$ is a particularly important task, as dual AGNs are predicted to experience the peak of their merger-driven luminosities and obscuration in late-stage mergers (Capelo et al., 2015; Blecha et al., 2018) when the nuclei of the galaxies are separated by $\lesssim 10$ kpc ($\lesssim 10.2''$ at $z = 0.05$). *HEX-P*'s access to X-ray energies beyond 10 keV will be vital to constraining the intrinsic luminosities and distinct column densities along the line-of-sight to each AGN in a merging system, an impossibility with *NuSTAR* for all but the nearest and brightest (Nardini, 2017) and/or most widely-separated dual AGNs known (e.g., Ptak et al. (2015); Kosec et al. (2017); Oda et al. (2018)). Furthermore, broadband coverage is fundamental not only to detect obscured AGN, but also to accurately characterize the properties of their obscurers, including line-of-sight column densities, covering factors, and obscurer geometries; broadband hard X-ray coverage with *NuSTAR*, for example, has led to dramatic refinements in AGN column density estimates compared to constraints derived from only soft X-ray or joint soft and ultra-hard X-ray coverage (e.g., Marchesi et al. (2018); Marchesi et al. (2019). Here we discuss the possibility of probing

1 https://www.nustar.caltech.edu/page/response_files

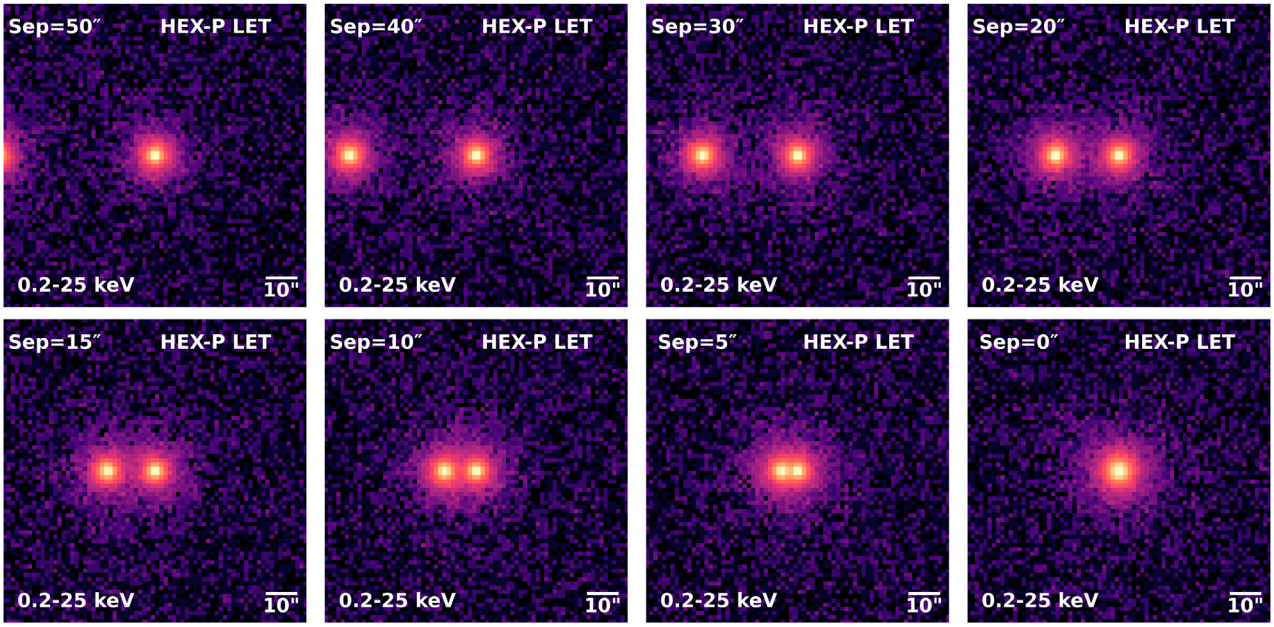

FIGURE 1
This 8-panel figure shows the LET 0.2–25 keV 50 ks images (1-pixel smoothing). Panels represent angular separations ranging from 50″ down to 0″. The two AGNs are distinguishable by eye down to 5″ and can be identified using Bayesian detection methods (see Section 4.1) down to separations of ~2″. The "null" case of 0″ (representing a single AGN at the combined flux level of our sources) is included for visual comparison. The AGNs have observed 2–10 keV fluxes of 1.0×10^{-13} and 5.0×10^{-14} erg cm^{-2} s^{-1}. These panels display the case in which both AGNs are Compton-thick, though the Compton-thick/Compton-thin and Compton-thin/Compton-thin cases show similar X-ray morphologies.

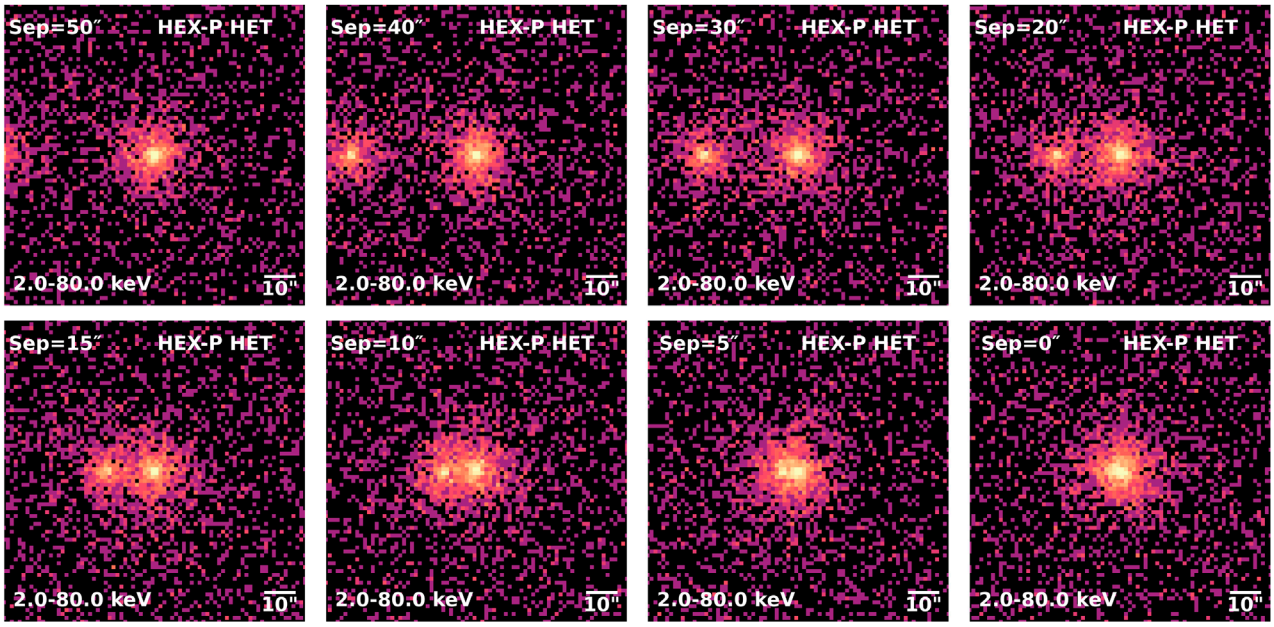

FIGURE 2
This 8-panel figure shows the effective 2-camera HET 2–80 keV, 50 ks images (1-pixel smoothing). As in Figure 1, panels represent angular separations ranging from 50″ down to 0″. The two AGNs are distinguishable by eye down to 5″ and can be identified using Bayesian detection methods (see Section 4.1 down to separations of ~2″. The AGNs have observed 2–10 keV fluxes of 1.0×10^{-13} and 5.0×10^{-14} erg cm^{-2} s^{-1}. These panels display the case in which both AGNs are Compton-thick, though the Compton-thick/Compton-thin and Compton-thin/Compton-thin cases show similar X-ray morphologies.

dual AGNs with separations $1'' < r_p < 5''$ in the hard X-rays with *HEX-P*.

We analyse each simulated event file with a single and double point source model, with wide, uninformative priors on the location and the total counts of each point source, I. The first point source is assumed to be located near the image centre ±10px. Both models also include a background count rate, B, that is constant across the image and left free during the fit. A standard Poisson likelihood is used, with the symmetric PSF model PSF(Δr) extracted from simulations:

$$\mathcal{L} \propto \frac{\prod_{i \in \text{events}} M(x_i, y_i | x_c, y_c, I, B)}{e^{\iint M(x,y|x_c,y_c,I,B)\, \mathrm{d}x\, \mathrm{d}y}}$$

For the single point source model,

$$M(x, y | x_c, y_c, I, B) = I \times \mathrm{PSF}\left(\sqrt{(x_i - x_c)^2 + (y_i - y_c)^2}\right) + B$$

while for the two point source model there are two centres and intensities.

The Akaike Information Criterion (AIC; Akaike, 1974) of the two models is compared to determine whether the single or double source model is preferred. In order for this comparison to take place, we first calibrated our detection algorithm using simulations of convolved X-ray sources, where we simulated two co-spatial X-ray sources with identical fluxes to those in our AGN simulations described in Section 3. We simulated 100 cases of convolved sources for the LET as well as for the HET, ran the detection algorithm on each case, and recorded the resulting AIC values. This calibration set the baseline for an acceptable AIC threshold to differentiate between a single and dual source case. We are able to detect X-ray point sources in both the LET 0.2–25 keV bandpass and the HET 2–80 keV bandpass down to separations of $2''$. This result comes with the caveat that this detection routine is a proof-of-concept and the results are subject to change based on the exposure time and the fluxes of the sources: all else being equal, we cannot necessarily differentiate between multiple sources at $2''$ or $3''$ separations for lower exposure times; alternatively, we can probe down to closer pair separations ($<2''$) for higher flux levels (a more rigorous examination is left to future works). Nonetheless, this is essentially an order-of-magnitude improvement over current capabilities with *NuSTAR*. An additional caveat with this analysis is that these simulations deal strictly with on-axis observations of dual AGNs: at off-axis angles, the minimum separation at which dual AGNs are resolvable by *HEX-P* is expected to increase as the effective area and/or PSF changes across the LET ($11.3'$x$11.3'$) and HET ($13.7'$x$13.7'$) fields of view. Therefore, dual AGNs observed off-axis either in single, pointed observations or as a part of large surveys may be convolved rather than resolved at smaller pair separations.

While dual AGNs are predicted to be heavily obscured in late-stage mergers (Blecha et al., 2018), there are cases of heavily obscured dual AGNs in widely-separated merging pairs of galaxies (Koss et al., 2012; De Rosa et al., 2018; De Rosa et al., 2023). Given that dual AGNs are also predicted to become heavily obscured after only the second pericenter passage (Blecha et al., 2018), and that AGNs are expected to flicker on and off across the merger sequence (e.g., the AGN duty cycle $\ll$ the merger timescale Schawinski et al., 2015; Goulding et al., 2019), *HEX-P* may reveal multi-modal distributions of heavily obscured AGNs across the merger sequence, rather than only during the latest stages of the merger sequence.

4.2 A substantial improvement over *NuSTAR*

In an analogous fashion to the *HEX-P* simulated event files displayed in Figures 1, 2, we have used identical input models, exposure times, and separations to develop *NuSTAR* dual AGN imaging that incorporates the *NuSTAR* background derived from the COSMOS field (Civano et al., 2015). Figure 3 displays these simulated *NuSTAR* images (where the color scale matches that of the HET imaging in Figure 2), in which the positions of the AGNs are denoted with black crosses; AGN 1 can be seen in a few (but not all) of the panels above the background while AGN 2 is virtually imperceptible in almost every panel. This figure clearly illustrates that - at these realistic observed 2–10 keV flux levels of 1×10^{-13} and 5×10^{-14} erg cm^{-2} s^{-1}—*NuSTAR* cannot reliably identify dual AGNs in these pairings; it is important to note that dual AGNs separated by ~$20''$ and $0''$ are essentially indistinguishable, emphasizing that *NuSTAR* cannot be used to reliably resolve $<20''$ dual AGNs. *HEX-P*, on the other hand, can spatially resolve each AGN in both the HET and LET imaging down to separations of ~$5''$ (and ~$2''$ when rigorous detection algorithms are used; see Section 4.1); this is a substantial improvement over *NuSTAR* and emphasizes that the future of hard X-ray dual AGN science relies critically upon access to facilities such as *HEX-P*.

4.3 A substantial improvement over soft X-ray missions

In Figure 4 we display a simulated 50 ks *Chandra* 2–8 keV image alongside the 2–25 keV LET and 2–80 keV HET imaging for the case where the AGNs are separated by $10''$. While *Chandra* can clearly resolve two X-ray cores emitted by the AGNs at >2 keV, the detections are obviously limited to energies <8 keV. To offer a quantitative comparison between *Chandra* and *HEX-P*, we extracted (background subtracted) counts for each AGN in the *Chandra*, LET, and HET imaging. The AGNs are detected with 175 ± 14 counts (AGN 1) and 67 ± 9 counts (AGN 2) in the 2–8 keV *Chandra* band when using $3''$ extraction apertures (~100% EEF); it is important to note that most dual AGNs and candidates are observed for <30 ks, so with a more realistic exposure time these sources would only have been detected with $\lesssim 100$ and $\lesssim 40$ counts. Contrasting this with the detections in LET, we detect 215 ± 16 and 129 ± 13 counts in the LET 2–25 keV band for the two AGNs when using $3.5''$ extraction apertures (~50% EEF). At this separation, the two AGNs begin to severely contaminate one another in the HET imaging when using $8.5''$ (50% EEF) apertures, so we instead excise only the inner $3.5''$ of each hard X-ray source (20%–25% EEF): we find the two AGNs are detected in the HET with 278 ± 17 and 189 ± 14 counts in the 2–80 keV band; these comparisons demonstrate that, given the same exposure time, *HEX-P* offers comparable, if not superior, photometric analyses on top of access to the hard X-rays.

To compare the spectroscopic capabilities of *HEX-P* to *Chandra*, we extracted the spectrum of the weaker of the two AGNs (AGN

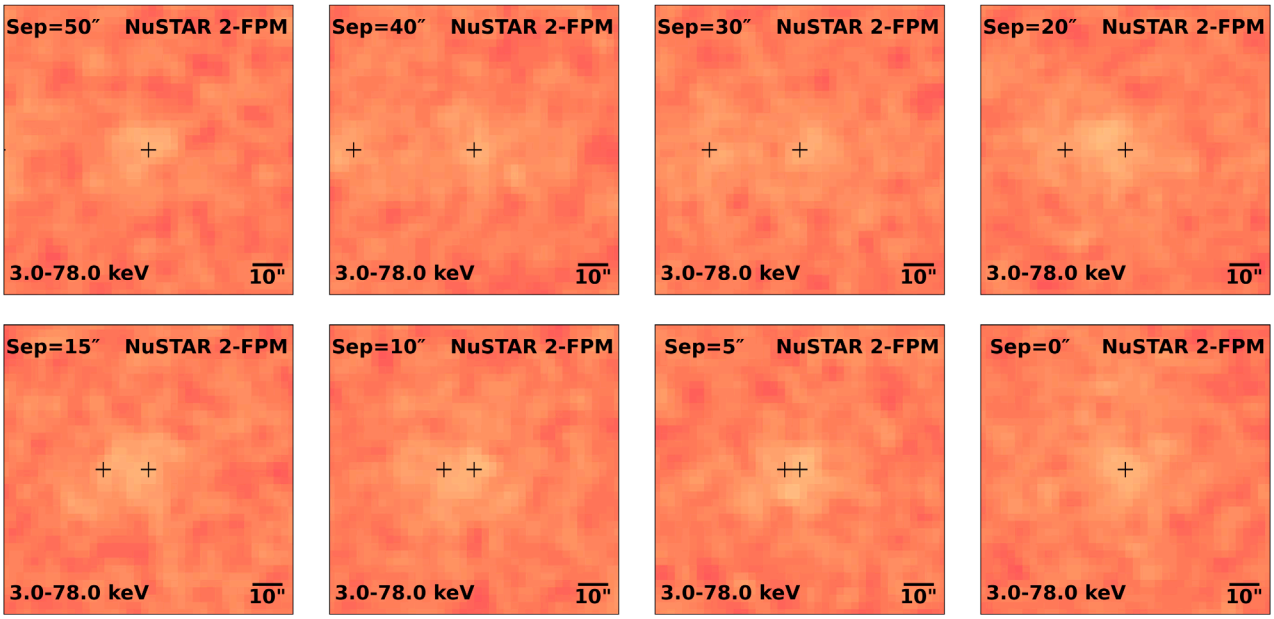

FIGURE 3
This 8-panel figure shows simulated two-camera 3–78 keV FPMA + B 50 ks imaging with *NuSTAR* (smoothed by 1-pixel) for the same suite of dual AGNs described in Section 3. The suite of AGNs range in separation from 50″ down to 0″; the scale bar in the bottom right corner of each panel indicates an angular scale of 10″. These panels use the same scaling as in Figure 1 for the *HEX-P* HET 2–80 keV imaging. The primary AGN can be seen above the background in some panels, but the weaker secondary AGN is essentially imperceptible above the background in all of the panels. Black markers are included to denote the positions of the two AGNs.

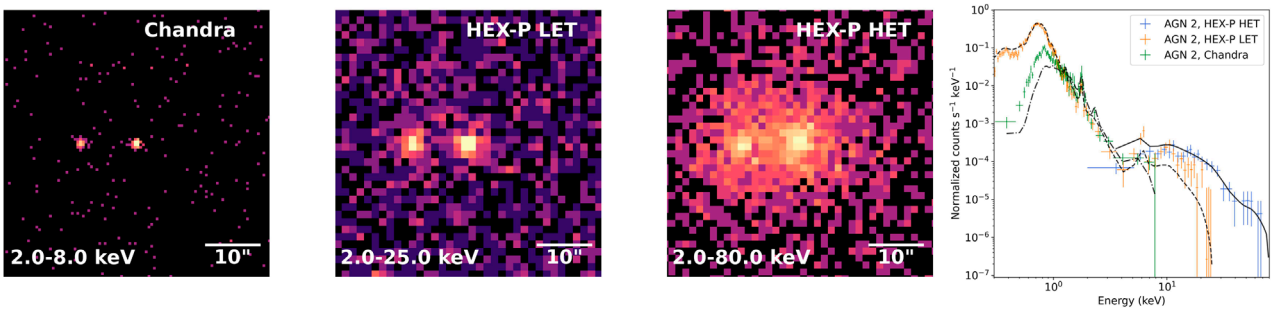

FIGURE 4
This four-panel figure shows a comparison between simulated Chandra, *HEX-P* LET, and *HEX-P* HET imaging and spectroscopy. The three X-ray imaging panels show the *Chandra* 2–8 keV, *HEX-P* LET 2–25 keV, and *HEX-P HET* 2–180 keV energy bands. The fourth panel displays the extracted *Chandra* (green), *HEX-P* LET (orange), and HET (blue) spectra for AGN 2 (the weaker of the two AGNs, see Section 3), binned at 3σ. The black solid, dashed, and dash-dotted lines show the result of fitting a simple phenomenological power law model to the HEX-P HET, LET, and Chandra spectra, respectively.

2) from the *Chandra* and *HEX-P* images using a 3″ aperture for the *Chandra* image, a 3.5″ aperture for LET, and a 3.5″ aperture in HET; these apertures represent the ~100%, ~50%, and 22% EEF for each instrument. This comparison therefore represents the "best-case" scenario for a *Chandra* exposure, a "standard case" for a LET exposure, and a "poor case" scenario for HET. The spectra (Chandra: green points, LET: orange points, HET: blue points) are shown in the fourth panel of Figure 4 and binned at 3σ per bin for visualization purposes. Only LET and HET can access energies beyond 10 keV, where HET can reach out even to 80 keV. The Compton-hump beyond 10 keV is a spectral feature critical for accurate constraints on the line-of-sight absorbing columns (e.g., Boorman et al. (2023)), and it is clearly accessible to the HET. The Fe Kα emission line is another crucial spectral imprint of cold reflection, and a simple fit using a phenomenological power law model reveals that the addition of a Gaussian emission line to account for Fe Kα does not statistically improve the fit to the simulated *Chandra* spectrum, but it *does* statistically improve the fit to the LET spectrum. Thus, this case study illustrates clearly that *HEX-P* can simultaneously access two AGN reflection features important for accurate column density constraints that would, in this case, be inaccessible to soft X-ray missions. It is important to

note, too, that while soft X-ray missions can in principle detect the Fe Kα emission line, intrinsic parameter estimations (including column density determination) can still be degenerate when using the Fe Kα emission line alone (e.g., LaMassa et al. (2017)) without harder X-ray features, whereas constraints that use the Fe Kα line and the Compton-hump in tandem offer clearer and more reliable constraints (e.g., LaMassa et al. (2019)). Without simultaneous access to these X-ray spectral features, soft X-ray missions will continue to be at a disadvantage when it comes to answering open questions related to dual AGN obscuration and fueling in the X-rays.

4.4 Hard X-ray dual AGN science as a function of redshift

Current hard X-ray facilities (e.g., *NuSTAR*) limit the study of distinct AGNs within dual AGN pairings to only the nearest, brightest, and/or more widely-separated systems. Here we illustrate the imaging capabilities of HEX-P as a function of redshift for different pair separations. Figure 5 shows the distribution of angular separations for optical dual AGN candidates from Liu et al. (2011) as a function of redshift out to $z \sim 0.3$. The overlaid black dash-dotted line indicates the angular resolution of *NuSTAR* (18″ FWHM, 58″ HPD, Harrison et al., 2013), while the red dashed, dash-dotted, and dotted curves indicate nuclear pair separations of 30, 20, and 10 kpc. Overlaid on this figure, we have also plotted the corresponding *HEX-P* 2–10 keV luminosity limits (vertical dotted, black lines) as a function of redshift, informed by the limiting flux of 3.8×10^{-14} erg cm^{-2} s^{-1} for a 50 ks exposure; the vast majority of dual AGNs have 2–10 keV luminosities $\lesssim 10^{43}$ erg s^{-1}. Therefore, $z \approx 0.3$ is an approximate redshift limit for dual AGN studies with *HEX-P*. Even late-stage mergers ($\lesssim$ 10 kpc) become virtually inaccessible to *NuSTAR* already by $z \approx 0.025$, and more widely separated pairs (~30 kpc) become inaccessible by only $z \approx 0.09$. *HEX-P*, on the other hand, thanks to resolving separations of ~5″ (possibly even ~2″), can distinguish AGNs in late-stage mergers out to redshifts of $z \sim 0.1$ (or even $z \sim 0.2$ with Bayesian analyses, Section 4.1) and can access distinct AGNs in ~30 kpc-separated duals out to $z \sim 0.3$. Though *distinct* AGNs within late-stage mergers will not be probed beyond $z \sim 0.1$–0.2, *HEX-P* will be able to probe the "gross" X-ray properties of these systems[2]; even when unresolved, *HEX-P* is required to probe the Compton hump and understand the circumstances of the nuclear environment properly, which cannot be done using soft X-ray, optical, near-IR, or radio observations. *HEX-P* will probe distinct AGNs in early-stage mergers well beyond $z \sim 0.1$ and aid in our understanding of dual AGN activation and obscuration across the merger sequence.

2 Selected presumably in the soft X-rays with *Chandra*, via high-resolution radio imaging, space-based high-resolution optical or near-IR spectroscopy (e.g., Hubble Space Telescope or JWST), or via ground-based adaptive-optics-assisted optical or near-IR observations. However, some fraction of dual AGNs will be missed at optical wavelengths (e.g., Koss et al., 2012) and require the detection of distinct X-ray AGNs for unambiguous confirmation.

5 A test case for HEX-P: Arp 299

One illustrative case study for examining the effectiveness of *HEX-P* over *NuSTAR*, in terms of spectroscopic and imaging constraints, is Arp 299, a local (44 Mpc, or $z \sim 0.01$) dual AGN comprising an X-ray bright and heavily obscured AGN in the southwest nucleus (Arp 299-B, detected by *Chandra* and *NuSTAR*, Ballo et al. (2004); Ptak et al. (2015)) and an AGN in the northeast nucleus (Arp 299-A) identified as a flat spectrum radio source (Pérez-Torres et al., 2010), and tentatively identified via mid-IR SEDs (Alonso-Herrero et al., 2013) and ionized Fe Kα emission (Ballo et al., 2004). As reported by Ptak et al. (2015), Arp 299-B is detected by *NuSTAR* with a hard X-ray flux of $F_{10-30keV} = 3.5 \times 10^{-12}$ erg cm^{-2} s^{-1}, while Arp 299-A is dominated by X-ray binaries below 10 keV and contains no hard X-ray emitting AGN above a 10–30 keV limit of $<3.5 \times 10^{-13}$ erg cm^{-2} s^{-1}. Here we demonstrate that *HEX-P* would not only clearly detect both of the reported AGNs in Arp 299 in the 0.2–80 keV band but would spatially resolve the AGNs in both HET and LET imaging.

Our input models are informed by the model choices and spectral fitting results in Ptak et al. (2015). Specifically, we adopt the following model to describe the spectrum of each nucleus:

$$tbabs \times (borus + ztbabs \times cabs \times zcutoffpl + zcutoffpl)$$

where we have used the BORUS02 model (Baloković et al., 2018) rather than MYTorus, which was used by Ptak et al. (2015). This model incorporates host galaxy absorption (TBABS), reflected emission (BORUS02), an absorbed intrinsic power law that accounts for photoelectric absorption and Compton scattering, and a cut-off power law to account for soft X-ray emission from X-ray binaries. For Arp 299-B, we assume $\Gamma = 1.95$, $N_H = 4 \times 10^{24}$ cm^{-2} (for simplicity we assume the average torus column density and the line-of-sight column density are equal), covering factor $\cos(\theta_{open}) = 0.85$, and we normalize the 10–30 keV emission to 3.5×10^{-12} erg cm^{-2} s^{-1}. For Arp 299-A, we assume $\Gamma = 1.8$, $N_H = 5 \times 10^{22}$ cm^{-2} (since it is likely an unobscured, low luminosity AGN, e.g., Ptak et al. (2015)), and covering factor $\cos(\theta_{open}) = 0.5$; while (Ptak et al., 2015) placed an upper limit of $<3.5 \times 10^{-13}$ erg cm^{-2} s^{-1} on the 10–30 keV flux of Arp 299-A (<10% of the observed flux of Arp 299-B), we conservatively assume that Arp 299-A (here, AGN 2) exhibits an observed 10–30 keV flux of 7×10^{-14} erg cm^{-2} s^{-1} (i.e. 2% of the 10–30 keV observed flux of Arp 299-B). For both AGNs 1 and 2, we assume $\Gamma = 1.8$ and a cutoff energy of 7 keV for the power law component driven by X-ray binaries; for simplicity, we assume these components contribute equally to the total 2–10 keV XRB-driven flux (8.1×10^{-13} erg cm^{-2} s^{-1}) found by Ptak et al. (2015), and we therefore normalize both components to 4.05×10^{-13} erg cm^{-2} s^{-1} in the 2–10 keV band. For our spatial models, we adopt the positions given in Table 1 of Ptak et al. (2015). We once again simulated these AGNs using SOXS for SIMPUT file creation and SIXTE for event file and spectroscopic data product creation.

We show the simulated *HEX-P* LET and HET images in Figure 6 juxtaposed with the tricolor optical *ugz* imaging from the Dark Energy Camera Legacy Survey (DeCaLs) Legacy Viewer[3] and

3 https://www.legacysurvey.org/viewer

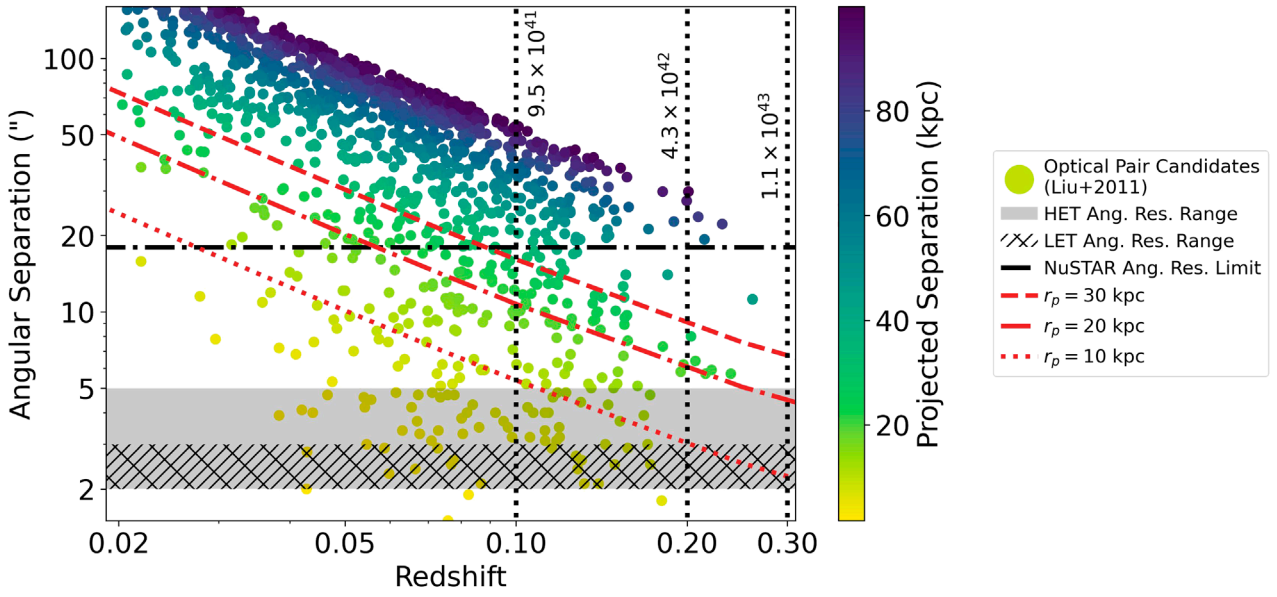

FIGURE 5
Redshift vs. angular separation. We have plotted the sample of optical dual AGN candidates from Liu et al. (2011) at $z < 0.3$. Markers are color coded according to the projected separation of the pair (given on the auxiliary axis). Red dashed, dash dotted, and dotted lines indicate projected separations of 30, 20, and 10 kpc. The grey, shaded region indicates the HET angular resolution limits when examining sources visually by eye (~5″) and when using Bayesian detection algorithms (~2″, see Section 4.1); the hashed and shaded region similarly indicates the LET angular resolution limits (~3″ by eye, ~2″ using Bayesian detection routines). The angular resolution limits derived via the Bayesian detection algorithm in Section 4.1 are subject to change based upon the exposure time and source fluxes; here they refer specifically to the 50 ks exposure time and source fluxes listed in Section 3. *NuSTAR*'s angular resolution limit (18″ PSF, Harrison et al., 2013) is denoted with a dashed-dotted black line. Vertical, dotted lines denote the observed 2–10 keV AGN luminosity that corresponds to the *HEX-P* flux sensitivity limit of 3.8×10^{-14} erg cm^{-2} s^{-1} in a 50 ks exposure (signal-to-noise of 5).

simulated *NuSTAR* FPM imaging. Each row in Figure 6 represents a distinct energy band: 2–10 keV (top row), 10–25 keV (middle row), and 25–80 keV (bottom row; the *NuSTAR* imaging corresponds to 25–78 keV here). At 21″ separation, the soft (<10keV) X-ray components in the *NuSTAR* imaging were spatially blended, and above 10 keV the secondary nucleus is not detected by *NuSTAR* (see Figure 6 in Ptak et al., 2015). However, *HEX-P* clearly resolves the two nuclei in both the LET and HET imaging and detects the simulated low luminosity AGN in Arp 299-A at energies beyond 10 keV. Note, Arp 299-A is not seen in the HET 25–80 keV imaging; this is due to the AGN emitting mostly at softer X-ray energies and is not due to the HET PSF.

To demonstrate *HEX-P*'s spectroscopic capabilities, we fit LET and HET spectra extracted with 8″ and 18″ radius apertures, respectively. These aperture choices represent an enclosed energy fraction (EEF) of ~100% and naturally suffer from cross-contamination; in practice, aperture sizes that represent only 50%–60% EEF are more commonly used when extracting X-ray spectra and would suffer from less cross-contamination, but our aperture choices provide an additional test for *HEX*-P's spectroscopic capabilities in discerning the properties of the distinct AGNs when spectral contamination is present. Arp 299 represents a prime example in which the LET spectra will be uncontaminated while each HET spectrum will contain contributions from both AGNs, which are separated by 21″. Here we show how the LET can be used to improve the reliability of HET spectral fitting.

We perform the fitting of our simulated Arp 299 *HEX-P* spectra using v2.9 of the Bayesian X-ray Analysis (BXA; Buchner et al., 2014a; Buchner, 2021a) software package, which connects PyXspec (Arnaud, 1996) to the nested sampling (Skilling, 2004; Buchner, 2023) algorithm MLFriends (Buchner et al., 2014b; Buchner, 2019) implemented in UltraNest (Buchner, 2021b). Our reasoning for using nested sampling here is two-fold. First, the global parameter exploration enables the traversal of high dimensionality parameter spaces in an efficient manner that is minimally affected by local minima. Second, the pre-defined convergence criteria for nested sampling ensures our fitting process is devoid of biases that can be imposed when fitting of simulated data is not performed in a blind manner (see, e.g., Kammoun et al., 2022).

The resolving ability of the LET ensures negligible cross-contamination in the spectral extraction of both sources. However, despite the angular resolution of the HET being a considerable improvement over *NuSTAR* (see Figure 2), some cross-contamination remains (see also Figure 8). For this reason, we chose to fit the simulated LET and HET spectra for both AGN 1 and AGN 2 simultaneously whilst incorporating nuisance parameters to describe the amount of flux contamination in each source. Our spectral model thus includes the main spectral components used to simulate the AGNs, as well as a multiplicative factor to each AGN component to account for the relative contamination in each AGN HET spectrum. We manually set the cross-contamination to zero for the LET spectra, since any contamination is negligible, and assume that each HET spectrum contains 100% of the AGN emission that the extraction region was centered on and some fraction of the other AGN flux contaminating that extraction region.

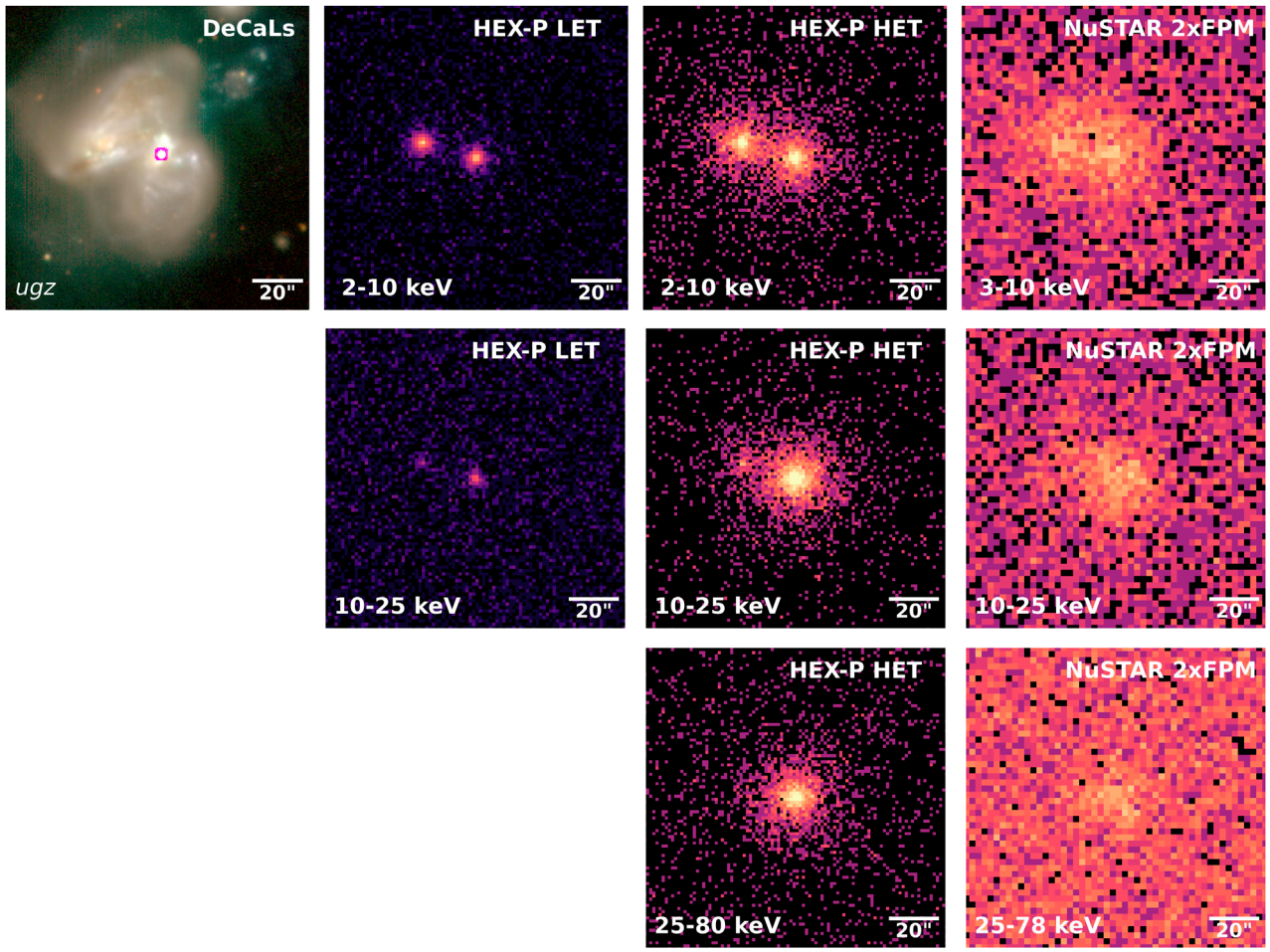

FIGURE 6
The Arp 299 case study: optical *ugz* imaging from DeCaLs (left column), simulated LET and HET (2-camera) *HEX-P* imaging (middle two columns), and simulated 3–78 keV *NuSTAR* imaging (right column) of Arp 299. The energy band or filter is indicated in the bottom left corner of each panel, while the facility or image source resides in the top right corner of each panel. Each row indicates a distinct energy band: the top, middle, and bottom row corresponds to 2–10 keV, 10–25 keV, and 25–80 keV (or 25–78 keV for *NuSTAR*), respectively. Scale bars in the bottom right corners indicate 20″. The LET and HET images were simulated following the procedure in Section 5 and include spectral and spatial models for the X-ray binary populations and the two AGNs in the merger system. For simplicity, we assume the X-ray binary populations are limited to the nuclei and model them as point sources coincident with the nuclei rather than as extended sources. While the two AGNs cannot be clearly detected in the *NuSTAR* imaging (nor was Arp 299-A detected above 10 keV by *NuSTAR*) (Ptak et al., 2015), the two AGNs can be clearly spatially resolved by both the LET and HET in the 2–10 keV and 10–25 keV bands.

We assigned log-uniform priors for all line-of-sight absorption (10^{22}–10^{25} cm^{-2}), cross-contamination factors (range of 0.001 to 1), high-energy cut-offs and normalizations. We additionally created custom cos-uniform priors (priors uniformly sampled over the angle range in cosine units) for all variable obscurer geometric angles (namely, the torus opening angle [0–84.3 degrees] and line-of-sight inclination [60–87.1 degrees] for both AGNs). Finally, the AGN photon indices were assigned Gaussian priors with mean 1.9 and 0.15 standard deviation and the X-ray binary photon index was assigned a uniform prior.

Figure 7 presents the fit acquired with BXA using a total of 18 free parameters. Owing to the combined broadband, sensitive coverage with the LET and HETs, we constrain the overall intrinsic X-ray luminosities and line-of-sight obscuration (log $[N_{\rm H}/{\rm cm}^{-2}]$ = $24.60^{+0.04}_{-0.04}$ for Arp-299B and log $[N_{\rm H}/{\rm cm}^{-2}]$ = $22.43^{+0.64}_{-0.29}$ for Arp-299A) for both AGN well. These column densities also agree within the errors with that found by Ptak et al. (2015) using the real *Chandra* and *NuSTAR* observations, which we would expect given that we used the results from Ptak et al. (2015) as inputs for our simulated spectra. We additionally note that owing to the simultaneous broadband coverage of the LET and HETs, the spectral fit is additionally devoid of any variability concerns across the full ~0.2–80 keV passband. By using BXA, we additionally recover the complex posterior degeneracies intricately associated with various system parameters, e.g., torus covering factors/opening angles (log $[\theta_{\rm open}]$= $0.88^{+0.08}_{-0.13}$ for Arp-299B and log $[\theta_{\rm open}]$= $0.54^{+0.30}_{-0.29}$ for Arp-299A), photon index ($\Gamma = 1.94^{+0.06}_{-0.10}$ for Arp-299B and $\Gamma = 1.89^{+0.14}_{-0.13}$ for Arp-299A), and intrinsic coronal normalisation, the latter two of which are important when propagating uncertainties into intrinsic luminosity estimates or Eddington ratios. These results

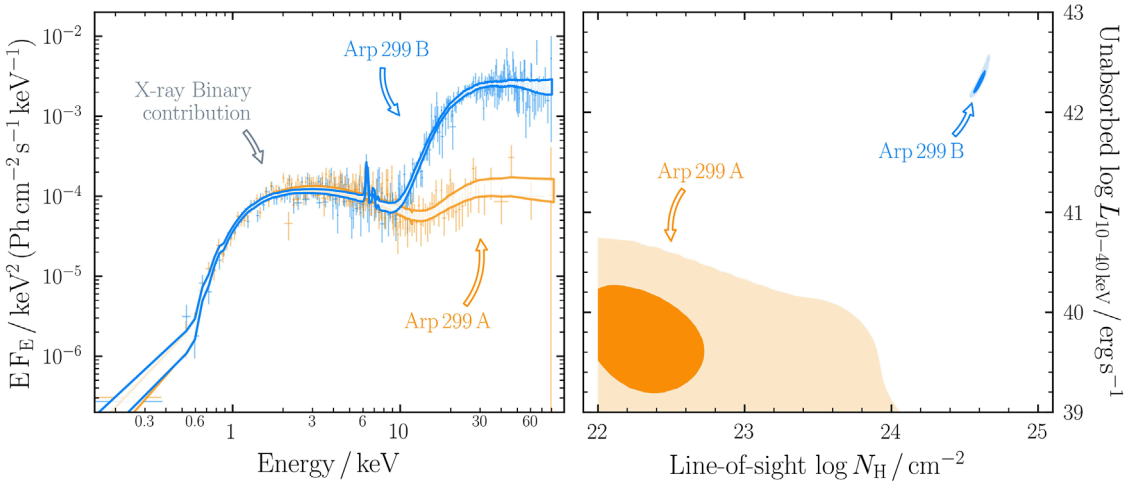

FIGURE 7
Simulated *HEX-P* HET (2-camera, co-added) and LET spectra, and the best-fitting models for the simulated Arp 299-A and Arp 299-B sources. The left panel shows the spectra unfolded with the best-fitting models while the right panel shows the contours for the best-fitting line-of-sight column densities and unabsorbed 10–40 keV luminosity in units of erg s^{-1}. Blue and orange data points and model curves correspond to the Arp 299-B and Arp 299-A, respectively. While we find a slightly harder power law slope for the X-ray binary power law component, we recover very similar values for the AGN power law slopes and column densities to those used in the input models.

clearly demonstrate our ability to reliably recover the intrinsic properties for each AGN despite the cross-contamination in the HET imaging.

6 Spectroscopic fitting of dual AGNs

Simultaneous fitting of soft (*Chandra* and/or *XMM-Newton*) and hard (*NuSTAR*) X-ray spectra has been successfully performed in the past for a few closely separated dual AGN (e.g., NGC 6240, Mrk 273, Mrk 266, Nardini, 2017; Iwasawa et al., 2018; Iwasawa et al., 2020). At these pair separations (~10″ or lower), careful modeling using tools like BXA (Buchner et al., 2014b, see above) should be employed, as the spectra will be convolved at these pair separations and will contain contributions from both AGNs. We illustrate the level of flux contamination in Figure 8, which shows the estimated HET flux for each AGN as a function of pair separation, extracted from the co-added HET images using 18″ radius apertures (~100% EEF; diamonds) and 8.5″ apertures (~50% EEF; squares) for each AGN. As the pair separation decreases, the two AGNs naturally contribute more to each other's observed flux as a result of the ~17.5″ HPD of the HET. The large jump in the observed fluxes at angular separations smaller than ~18″ extracted from the 18″ radius (~100% EEF) apertures, particularly for the weaker AGN, is due to the aperture size rather than the HET PSF. When 8.5″ radius apertures are used (~50% EEF), we find that spectral contamination appears to be modest at separations of >12″ and becomes more significant at separations <12″, despite our ability to visually resolve the two AGNs in the imaging. The LET, on the other hand, will offer relatively contamination-free spectra down to closer pair separations ($\lesssim 6''$). For this reason, it will become increasingly important at smaller pair separations to fit LET and HET AGN spectra simultaneously,

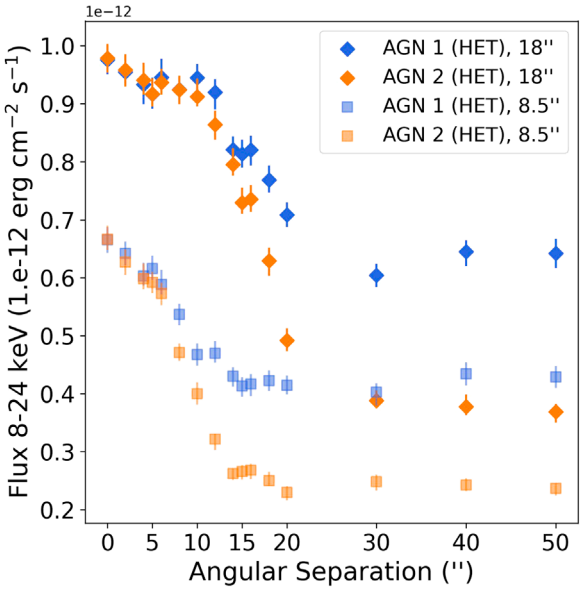

FIGURE 8
8–24 keV observed fluxes from AGN 1 and 2 (from our general suite of simulations described in Section 3 and Section 4.1) as a function of pair separation. Diamonds correspond to spectra extracted from 2-camera HET imaging using 18″ radius apertures (~100% EEF), while squares correspond to spectra extracted from 2-camera HET imaging using 8.5″ radius apertures (~50% EEF); these spectra were fit in XSPEC using the same input spectral model used to simulate the data, where only the normalizations were free to vary in order to recover the observed flux. While the sharp increase in spectral contamination (traced by the increasing flux of each AGN) at ~18″ for the larger apertures is due to our choice of aperture size, the sharp increase in contamination observed at ~10″ for the smaller apertures is more likely due to the size of the HET PSF itself.

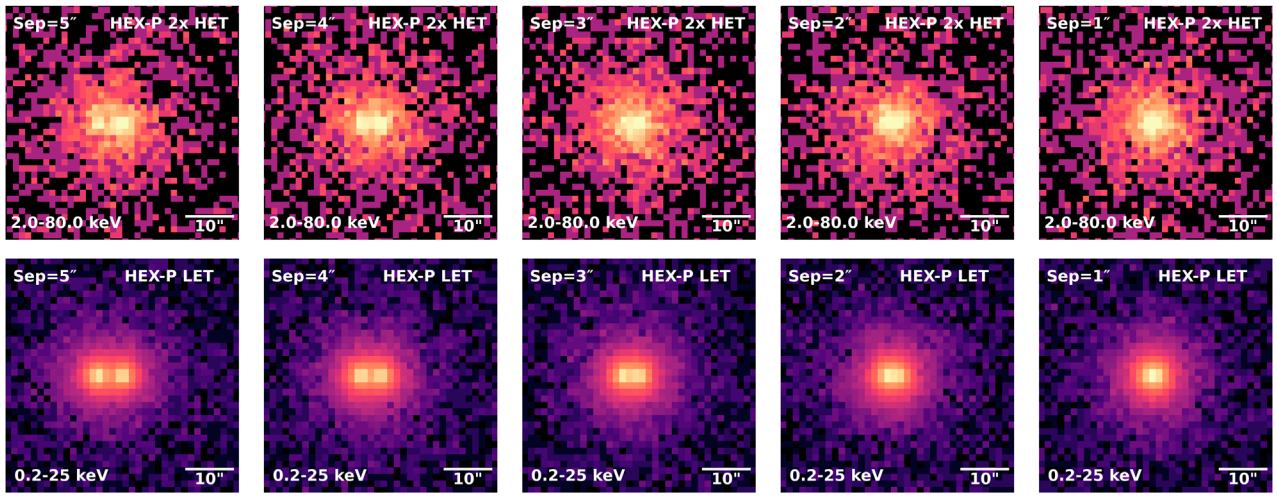

FIGURE 9
This 8-panel figure highlights the *HEX-P* HET and LET imaging for pair separations ranging from 5″ down to 1″. With the exception of the choice of pair separations, these panels are identical in design as Figures 1, 2. Here we can identify pairs of sources down to ~4″ in the HET and ~3″ in the LET by eye. See Section 4.1 on algorithmically detecting even more closely separated sources in *HEX-P* imaging.

because the LET spectra will bolster the accuracy of the X-ray spectral parameters derived from HET spectra.

7 Synergies with upcoming facilities

Given that dual AGNs are predicted to exhibit extremely red infrared colors (Blecha et al., 2018) in concert with high absorbing columns (e.g., Capelo et al. (2015); Blecha et al. (2018)), infrared observations are a natural choice to pair with hard and soft X-ray imaging and spectroscopy from *HEX-P*. *Euclid*, the recently launched ESA near-IR and optical imaging and spectroscopy mission (Laureijs et al., 2011), will provide sub-arcsecond near-IR and optical imaging and near-IR spectroscopy across approximately one third of the sky by the time *HEX-P* launches in the early 2030s. By the very nature of its mission design, *Euclid* will act as a new dual AGN survey facility, forming an enormous archival sample of interacting and merging galaxies from which promising near-IR dual AGNs can be selected and followed-up with *HEX-P*. *JWST* will also offer unprecedented near- and mid-IR imaging and spectroscopic observations of small samples of dual AGNs (and candidates) found both within deep surveys (e.g., Comerford et al. (2009); Civano et al. (2010); Civano et al. (2012)) and through targeted observations, and will provide the opportunity to probe not only heavily obscured AGNs but also heavily obscured star formation in, for example, dual AGNs hosted by LIRGs and ULIRGs (e.g.; Komossa et al. (2003); Iwasawa et al. (2011); Torres-Albà et al. (2018)). On the other hand, Extremely Large Telescopes (ELTs)—expected to come online in the 2030s–will usher in vast improvements in ground-based near-IR and optical spectroscopy and imaging and will experience substantially lower observational overheads and lower subscription rates than *JWST*. ELTs will therefore be paramount for targeting large samples of dual AGNs and may, like *Euclid*, represent the optimal dual AGN survey facilities that can work in tandem with *HEX-P*. In the meantime, high cadence, high resolution ($\lesssim 1''$ angular resolution) optical imaging with the upcoming Vera C. Rubin Observatory (Ivezić et al., 2019)—in concert with presently available optical and near-IR data from *Euclid*–will also aid in the development and preliminary analyses of large samples of dual AGN candidates. The *Nancy Grace Roman Telescope* (NGR), slated for launch in the 2030s, will operate at infrared wavelengths with a FOV 100× larger than *HST* with imaging sensitivity and PSF sizes superior to both *HST* and *Euclid*. *NGR*'s combination of FOV and wavelength coverage will make it an optimal facility for serendipitous dual AGN searches and studies and will complement both *Euclid* and *HEX-P*. Another important upcoming facility will be the 'next-generation VLA' (ngVLA, e.g., Burke-Spolaor et al. (2018)), which will boast 10× the sensitivity of the Jansky VLA and ALMA with 30× longer baselines that will enable 0.01″-0.001″ resolution across the 1.2–116 GHz frequency range. Since radio is also immune to obscuration, the ngVLA will have the sensitivity and resolution to detect dual AGNs to $z \sim 1$, if they are sufficiently luminous in the radio. *HEX-P* and the ngVLA could work as separate follow-up facilities, or *HEX-P* could work in tandem with the ngVLA to confirm dual AGNs and measure the obscuring columns and try to constrain torus parameters (the latter of which the ngVLA would not be able to do). A joint HEX-P/ngVLA coverage strategy may be able to simultaneously circumvent X-ray and radio selection biases. In a similar vein, *HEX-P* observations in combination with ALMA 100–200 GHz continuum observations (Ricci et al., 2023) could offer unprecedented views to the most heavily obscured dual AGNs. Due to the reduced opacities in these ALMA bands, one can probe through very high column densities.

8 Conclusion

The *HEX-P* Probe-class mission concept combines high spatial resolution X-ray imaging (~17.5″ HPD HET, ~3.5″ HPD LET) and broad spectral coverage (0.2–80 keV) with superior sensitivity to faint fluxes than current facilities and will usher in revolutionary new insights into dual AGN growth across the merger sequence.

Hard X-ray imaging and spectroscopy is particularly important to the field of dual AGN science, as these systems are expected to be heavily obscured (e.g., Komossa et al. (2003); Bianchi et al. (2008); Mazzarella et al. (2012); Capelo et al. (2015); Blecha et al. (2018); Pfeifle et al. (2019b)), making optical and soft X-ray missions biased against their detection and accurate analysis; *HEX-P* is the only Probe mission concept that can fulfil this scientific need. In this work, we have used a suite of dual AGN simulations - developed using SOXS (ZuHone et al., 2023) and SIXTE (Dauser et al., 2019) - to demonstrate the following:

- Without the aid of specialized detection algorithms, the spatial resolution of *HEX-P* LET and HET will allow us to resolve dual AGNs down to ~3″ and ~5″, respectively (5″corresponds to ~4.9 kpc at $z = 0.05$). NuSTAR, on the other hand, cannot spatially resolve dual AGNs below ~18″ (~17.9 kpc at $z = 0.05$).
- With the aid of Bayesian detection algorithms like that employed in this work, *HEX-P* will be able to confirm dual AGNs down to separations of ~2" (~2.0 kpc at z = 0.05) in both HET and LET imaging. The exact spatial resolution limit is determined by a combination of source flux levels and observation exposure time.
- Given *HEX-P*'s spatial resolution for both the LET and HET, *HEX-P* will have the capability to probe dual AGNs in late-stage mergers (<10 kpc) out to $z \sim 0.1$, and intermediate-stage mergers (~30 kpc) out to redshifts of $z \sim 0.3$. This is a dramatic improvement over *NuSTAR*, which cannot probe dual AGNs with even 50 kpc separations beyond $z \sim 0.25$.
- *HEX-P* will enable distinct (relatively contamination free) spectral analyses with the LET in the 0.2–25 keV band down to separations of ~6 – 8″, while the HET will offer relatively contamination free spectral analyses down to separations of ~10″ (assuming apertures encompassing ~50% EEF are employed). At small angular separations, this contamination can be mitigated by fitting LET and HET spectra simultaneously, and including model component constants that account for spectral contamination.

HEX-P is poised to transform the landscape of dual AGN science, offering one of the cleanest methods of AGN detection that will be largely obscuration independent given the hard X-ray bandpass and enhanced faint source sensitivity of the HET. *HEX-P* will play a key role in uncovering heretofore unconfirmed dual AGNs in candidate systems, determining the occupation fraction of hard X-ray emitting and obscured dual AGNs in known and currently unknown dual AGN populations, and studying the fueling and obscuration levels of dual AGNs across the merger sequence and as a function of AGN type in the local Universe. Such observations will refine previously proposed correlations between the projected pair separations of the AGNs and their X-ray luminosities (Koss et al., 2012; Hou et al., 2020) and column densities (Guainazzi et al., 2021). Bayesian detection algorithms akin to BAYMAX (Foord et al., 2019; Foord et al., 2020; Foord et al., 2021) will provide statistically powerful improvements to the detectability of closely-separated sources, and such Bayesian methods will provide more accurate constraints on the flux ratios of close angular pairs and thereby improve the statistical priors used during the spectral fitting process. Furthermore, with the high sensitivity and angular resolution of the LET, *HEX-P* will allow the simultaneous examination of the host stellar populations via the detection of hot star formation-driven components in the soft X-rays, often observed in dual AGNs (see Section 5.4 in Pfeifle et al. (2023)). Thus, *HEX-P* will also probe connections between the properties of the host stellar populations and dual AGN activation and obscuration.

Data availability statement

The datasets presented in this study can be found in online repositories[4]. The names of the repository/repositories and accession number(s) can be found below: https://github.com/thatastroguy/HEXP.

Author contributions

RP: Conceptualization, Formal Analysis, Investigation, Methodology, Software, Visualization, Writing–original draft, Writing–review and editing. PB: Conceptualization, Formal Analysis, Software, Visualization, Writing–original draft, Writing–review and editing. KW: Writing–review and editing. JB: Conceptualization, Methodology, Software, Writing–review and editing. FC: Writing–review and editing. KM: Writing–original draft, Writing–review and editing. DS: Conceptualization, Writing–review and editing. NT-A: Writing–review and editing. EN: Writing–review and editing. CR: Writing–review and editing. SM: Writing–review and editing. DB: Writing–review and editing. Dominic Sicilian: Writing–review and editing. C-TC: Software, Writing–review and editing. EK: Writing–review and editing. RH: Conceptualization, Writing–review and editing. JG: Writing–review and editing. LM: Writing–review and editing.

Funding

The author(s) declare that financial support was received for the research, authorship, and/or publication of this article. RP gratefully acknowledges support through an appointment to the NASA Postdoctoral Program at Goddard Space Flight Center, administered by ORAU through a contract with NASA. The work of DS was carried out at the Jet Propulsion Laboratory, California Institute of Technology, under a contract with NASA. CR acknowledges support from Fondecyt Regular grant 1230345 and ANID BASAL project FB210003. EK acknowledges financial support from the Centre National d'Etudes Spatiales (CNES). LM is supported by the CITA National Fellowship.

4 https://github.com/thatastroguy/HEXP

Acknowledgments

We thank both reviewers for their thoughtful reviews that helped to improve our manuscript. We thank the SIXTE support team (with particular thanks to Ole König) for their assistance in generating spectra from simulated event files and for assistance with the documentation.

Conflict of interest

The authors declare that the research was conducted in the absence of any commercial or financial relationships that could be construed as a potential conflict of interest.

The author(s) declared that they were an editorial board member of Frontiers, at the time of submission. This had no impact on the peer review process and the final decision.

Publisher's note

All claims expressed in this article are solely those of the authors and do not necessarily represent those of their affiliated organizations, or those of the publisher, the editors and the reviewers. Any product that may be evaluated in this article, or claim that may be made by its manufacturer, is not guaranteed or endorsed by the publisher.

References

Agazie, G., Anumarlapudi, A., Archibald, A. M., Arzoumanian, Z., Baker, P. T., Bécsy, B., et al. (2023). The NANOGrav 15 yr data set: evidence for a gravitational-wave background. *ApJL* 951, L8. doi:10.3847/2041-8213/acdac6

Akaike, H. (1974). A new look at the statistical model identification. *IEEE Trans. Automatic Control* 19, 716–723. doi:10.1109/tac.1974.1100705

Alonso-Herrero, A., Roche, P. F., Esquej, P., González-Martín, O., Pereira-Santaella, M., Ramos Almeida, C., et al. (2013). Uncovering the deeply embedded active galactic nucleus activity in the nuclear regions of the interacting galaxy Arp 299. *ApJL* 779, L14. doi:10.1088/2041-8205/779/1/L14

Amaro-Seoane, P., Andrews, J., Arca Sedda, M., Askar, A., Baghi, Q., Balasov, R., et al. (2023). Astrophysics with the laser interferometer space antenna. *Living Rev. Relativ.* 26, 2. doi:10.1007/s41114-022-00041-y

Arnaud, K. A. (1996). "XSPEC: the first ten years," in *Astronomical data analysis software and systems V. Of astronomical Society of the pacific conference series*. Editors G. H. Jacoby, and J. Barnes, 101, 17.

Ballo, L., Braito, V., Della Ceca, R., Maraschi, L., Tavecchio, F., and Dadina, M. (2004). Arp 299: a second merging system with two active nuclei? *ApJ* 600, 634–639. doi:10.1086/379887

Baloković, M., Brightman, M., Harrison, F. A., Comastri, A., Ricci, C., Buchner, J., et al. (2018). New spectral model for constraining torus covering factors from broadband X-ray spectra of active galactic nuclei. *ApJ* 854, 42. doi:10.3847/1538-4357/aaa7eb

Barnes, J. E., and Hernquist, L. (1996). Transformations of galaxies. II. Gasdynamics in merging disk galaxies. *ApJ* 471, 115–142. doi:10.1086/177957

Barnes, J. E., and Hernquist, L. E. (1991). Fueling starburst galaxies with gas-rich mergers. *ApJL* 370, L65. doi:10.1086/185978

Barrows, R. S., Comerford, J. M., Stern, D., and Assef, R. J. (2023). A census of WISE-selected dual and offset AGNs across the sky: new constraints on merger-driven triggering of obscured AGNs. *ApJ* 951, 92. doi:10.3847/1538-4357/acd2d3

Bianchi, S., Chiaberge, M., Piconcelli, E., Guainazzi, M., and Matt, G. (2008). Chandra unveils a binary active galactic nucleus in Mrk 463. *MNRAS* 386, 105–110. doi:10.1111/j.1365-2966.2008.13078.x

Blecha, L., Snyder, G. F., Satyapal, S., and Ellison, S. L. (2018). The power of infrared AGN selection in mergers: a theoretical study. *MNRAS* 478, 3056–3071. doi:10.1093/mnras/sty1274

Boorman, P. G., Torres-Albà, N., Annuar, A., Marchesi, S., Pfeifle, R., Stern, D., et al. (2023). *The high energy X-ray probe (HEX-P): the circum-nuclear environment of growing supermassive black holes. arXiv e-prints* , arXiv:2311.04949. doi:10.48550/arXiv.2311.04949

Buchner, J. (2019). Collaborative nested sampling: big data versus complex physical models. *PASP* 131, 108005. doi:10.1088/1538-3873/aae7fc

Buchner, J. (2021a). Bayesian X-ray analysis (BXA) v4.0. *J. Open Source Softw.* 6, 3045. doi:10.21105/joss.03045

Buchner, J. (2021b). UltraNest - a robust, general purpose Bayesian inference engine. *J. Open Source Softw.* 6, 3001. doi:10.21105/joss.03001

Buchner, J. (2023). Nested sampling methods. *Stat. Surv.* 17, 09675. doi:10.1214/23-SS144

Buchner, J., Georgakakis, A., Nandra, K., Hsu, L., Rangel, C., Brightman, M., et al. (2014a). X-ray spectral modelling of the AGN obscuring region in the CDFS: Bayesian model selection and catalogue. *A&A* 564, A125. doi:10.1051/0004-6361/201322971

Buchner, J., Georgakakis, A., Nandra, K., Hsu, L., Rangel, C., Brightman, M., et al. (2014b). X-ray spectral modelling of the AGN obscuring region in the CDFS: Bayesian model selection and catalogue. *A&A* 564, A125. doi:10.1051/0004-6361/201322971

Burke-Spolaor, S., Blecha, L., Bogdanovic, T., Comerford, J. M., Lazio, T. J. W., Liu, X., et al. (2018). *The next-generation very large array: supermassive black hole pairs and binaries. arXiv e-prints* , arXiv:1808.04368. doi:10.48550/arXiv.1808.04368

Callegari, S., Kazantzidis, S., Mayer, L., Colpi, M., Bellovary, J. M., Quinn, T., et al. (2011). Growing massive black hole pairs in minor mergers of disk galaxies. *ApJ* 729, 85. doi:10.1088/0004-637X/729/2/85

Callegari, S., Mayer, L., Kazantzidis, S., Colpi, M., Governato, F., Quinn, T., et al. (2009). Pairing of supermassive black holes in unequal-mass galaxy mergers. *ApJL* 696, L89–L92. doi:10.1088/0004-637X/696/1/L89

Capelo, P. R., Dotti, M., Volonteri, M., Mayer, L., Bellovary, J. M., and Shen, S. (2017). A survey of dual active galactic nuclei in simulations of galaxy mergers: frequency and properties. *MNRAS* 469, 4437–4454. doi:10.1093/mnras/stx1067

Capelo, P. R., Volonteri, M., Dotti, M., Bellovary, J. M., Mayer, L., and Governato, F. (2015). Growth and activity of black holes in galaxy mergers with varying mass ratios. *MNRAS* 447, 2123–2143. doi:10.1093/mnras/stu2500

Ciurlo, A., Mannucci, F., Yeh, S., Amiri, A., Carniani, S., Cicone, C., et al. (2023). New multiple AGN systems with subarcsec separation: confirmation of candidates selected via the novel GMP method. *A&A* 671, L4. doi:10.1051/0004-6361/202345853

Civano, F., Elvis, M., Lanzuisi, G., Aldcroft, T., Trichas, M., Bongiorno, A., et al. (2012). Chandra high-resolution observations of CID-42, a candidate recoiling supermassive black hole. *ApJ* 752, 49. doi:10.1088/0004-637X/752/1/49

Civano, F., Elvis, M., Lanzuisi, G., Jahnke, K., Zamorani, G., Blecha, L., et al. (2010). A runaway black hole in COSMOS: gravitational wave or slingshot recoil? *ApJ* 717, 209–222. doi:10.1088/0004-637X/717/1/209

Civano, F., Hickox, R. C., Puccetti, S., Comastri, A., Mullaney, J. R., Zappacosta, L., et al. (2015). The nustar extragalactic surveys: overview and catalog from the COSMOS field. *ApJ* 808, 185. doi:10.1088/0004-637X/808/2/185

Comerford, J. M., Gerke, B. F., Stern, D., Cooper, M. C., Weiner, B. J., Newman, J. A., et al. (2012). Kiloparsec-scale spatial offsets in double-peaked narrow-line active galactic nuclei. I. Markers for selection of compelling dual active galactic nucleus candidates. *ApJ* 753, 42. doi:10.1088/0004-637X/753/1/42

Comerford, J. M., Griffith, R. L., Gerke, B. F., Cooper, M. C., Newman, J. A., Davis, M., et al. (2009). 1.75 h^{-1} kpc separation dual active galactic nuclei at z = 0.36 in the cosmos field. *ApJL* 702, L82–L86. –L86. doi:10.1088/0004-637X/702/1/L82

Comerford, J. M., Pooley, D., Barrows, R. S., Greene, J. E., Zakamska, N. L., Madejski, G. M., et al. (2015). Merger-driven fueling of active galactic nuclei: six dual and of agns discovered with*chandra*and*hubble space telescope*observations. *ApJ* 806, 219. doi:10.1088/0004-637X/806/2/219

Comerford, J. M., Pooley, D., Gerke, B. F., and Madejski, G. M. (2011). Chandra observations of a 1.9 kpc separation double X-ray source in a candidate dual active galactic nucleus galaxy at z = 0.16. *ApJL* 737, L19. doi:10.1088/2041-8205/737/1/L19

Dauser, T., Falkner, S., Lorenz, M., Kirsch, C., Peille, P., Cucchetti, E., et al. (2019). SIXTE: a generic X-ray instrument simulation toolkit. *A&A* 630, A66. doi:10.1051/0004-6361/201935978

De Rosa, A., Vignali, C., Husemann, B., Bianchi, S., Bogdanović, T., Guainazzi, M., et al. (2018). Disclosing the properties of low-redshift dual AGN through XMM-Newton and SDSS spectroscopy. *MNRAS* 480, 1639–1655. doi:10.1093/mnras/sty1867

De Rosa, A., Vignali, C., Severgnini, P., Bianchi, S., Bogdanović, T., Charisi, M., et al. (2023). The X-ray view of optically selected dual AGN. *MNRAS* 519, 5149–5160. doi:10.1093/mnras/stac3664

Ellison, S. L., Patton, D. R., Mendel, J. T., and Scudder, J. M. (2011). Galaxy pairs in the Sloan Digital Sky Survey - IV. Interactions trigger active galactic nuclei. *MNRAS* 418, 2043–2053. doi:10.1111/j.1365-2966.2011.19624.x

Ellison, S. L., Secrest, N. J., Mendel, J. T., Satyapal, S., and Simard, L. (2017). Discovery of a dual active galactic nucleus with ~8 kpc separation. *MNRAS* 470, L49–L53. doi:10.1093/mnrasl/slx076

Eraerds, T., Antonelli, V., Davis, C., Hall, D., Hetherington, O., Holland, A., et al. (2021). Enhanced simulations on the athena/wide field imager instrumental background. *J. Astronomical Telesc. Instrum. Syst.* 7, 034001. doi:10.1117/1.JATIS.7.3.034001

Foord, A., Gültekin, K., Nevin, R., Comerford, J. M., Hodges-Kluck, E., Barrows, R. S., et al. (2020). A second look at 12 candidate dual AGNs using BAYMAX. *ApJ* 892, 29. doi:10.3847/1538-4357/ab72fa

Foord, A., Gültekin, K., Reynolds, M. T., Hodges-Kluck, E., Cackett, E. M., Comerford, J. M., et al. (2019). A bayesian analysis of SDSS J0914+0853, a low-mass dual AGN candidate. *ApJ* 877, 17. doi:10.3847/1538-4357/ab18a3

Foord, A., Gültekin, K., Runnoe, J. C., and Koss, M. J. (2021). AGN triality of triple mergers: detection of faint X-ray point sources. *ApJ* 907, 71. doi:10.3847/1538-4357/abce5d

Frey, S., Paragi, Z., An, T., and Gabányi, K. É. (2012). Two in one? A possible dual radio-emitting nucleus in the quasar SDSS J1425+3231. *MNRAS* 425, 1185–1191. doi:10.1111/j.1365-2966.2012.21491.x

Fu, H., Myers, A. D., Djorgovski, S. G., Yan, L., Wrobel, J. M., and Stockton, A. (2015a). Radio-selected binary active galactic nuclei from the very large array stripe 82 survey. *ApJ* 799, 72. doi:10.1088/0004-637X/799/1/72

Fu, H., Wrobel, J. M., Myers, A. D., Djorgovski, S. G., and Yan, L. (2015b). Binary active galactic nuclei in stripe 82: constraints on synchronized black hole accretion in major mergers. *ApJL* 815, L6. doi:10.1088/2041-8205/815/1/L6

Fu, H., Zhang, Z.-Y., Assef, R. J., Stockton, A., Myers, A. D., Yan, L., et al. (2011). A kiloparsec-scale binary active galactic nucleus confirmed by the expanded very large array. *ApJL* 740, L44. doi:10.1088/2041-8205/740/2/L44

Gabányi, K. É., An, T., Frey, S., Komossa, S., Paragi, Z., Hong, X. Y., et al. (2016). Four dual AGN candidates observed with the VLBA. *ApJ* 826, 106. doi:10.3847/0004-637X/826/2/106

Gabányi, K. É., Frey, S., Xiao, T., Paragi, Z., An, T., Kun, E., et al. (2014). A single radio-emitting nucleus in the dual AGN candidate NGC 5515. *MNRAS* 443, 1509–1514. doi:10.1093/mnras/stu1234

Ge, J.-Q., Hu, C., Wang, J.-M., Bai, J.-M., and Zhang, S. (2012). Double-peaked narrow emission-line galaxies from the sloan digital sky survey. I. Sample and basic properties. *ApJS* 201, 31. doi:10.1088/0067-0049/201/2/31

Goulding, A. D., Pardo, K., Greene, J. E., Mingarelli, C. M. F., Nyland, K., and Strauss, M. A. (2019). Discovery of a close-separation binary quasar at the heart of a z ~ 0.2 merging galaxy and its implications for low-frequency gravitational waves. *ApJL* 879, L21. doi:10.3847/2041-8213/ab2a14

Gross, A. C., Fu, H., Myers, A. D., Djorgovski, S. G., Steffen, J. L., and Wrobel, J. M. (2023). Testing the radio-selection method of dual active galactic nuclei in the stripe 82 field. *ApJ* 945, 73. doi:10.3847/1538-4357/acb646

Gross, A. C., Fu, H., Myers, A. D., Wrobel, J. M., and Djorgovski, S. G. (2019). X-ray properties of radio-selected dual active galactic nuclei. *ApJ* 883, 50. doi:10.3847/1538-4357/ab3795

Guainazzi, M., De Rosa, A., Bianchi, S., Husemann, B., Bogdanovic, T., Komossa, S., et al. (2021). An XMM-Newton study of active-inactive galaxy pairs. *MNRAS* 504, 393–405. doi:10.1093/mnras/stab808

Guainazzi, M., Piconcelli, E., Jiménez-Bailón, E., and Matt, G. (2005). The early stage of a cosmic collision? XMM-Newton unveils two obscured AGN in the galaxy pair ESO509-IG066. *A&A* 429, L9–L12. doi:10.1051/0004-6361:200400104

Harrison, F. A., Craig, W. W., Christensen, F. E., Hailey, C. J., Zhang, W. W., Boggs, S. E., et al. (2013). The nuclear spectroscopic telescope array (NuSTAR) high-energy X-ray mission. *ApJ* 770, 103. doi:10.1088/0004-637X/770/2/103

Hopkins, P. F., Hernquist, L., Cox, T. J., Di Matteo, T., Robertson, B., and Springel, V. (2006). A unified, merger-driven model of the origin of starbursts, quasars, the cosmic X-ray background, supermassive black holes, and galaxy spheroids. *ApJS* 163, 1–49. doi:10.1086/499298

Hopkins, P. F., Hernquist, L., Cox, T. J., and Kereš, D. (2008). A cosmological framework for the Co-evolution of quasars, supermassive black holes, and elliptical galaxies. I. Galaxy mergers and quasar activity. *ApJS* 175, 356–389. doi:10.1086/524362

Hou, M., Li, Z., and Liu, X. (2020). A Chandra X-ray survey of optically selected AGN pairs. *ApJ* 900, 79. doi:10.3847/1538-4357/aba4a7

Hou, M., Li, Z., Liu, X., Li, Z., Li, R., Wang, R., et al. (2023). NOEMA detection of circumnuclear molecular gas in X-ray weak dual active galactic nuclei: No evidence for heavy obscuration. *ApJ* 943, 50. doi:10.3847/1538-4357/acaaf9

Hou, M., Liu, X., Guo, H., Li, Z., Shen, Y., and Green, P. J. (2019). Active galactic nucleus pairs from the sloan digital sky survey. III. Chandra X-ray observations unveil obscured double nuclei. *ApJ* 882, 41. doi:10.3847/1538-4357/ab3225

Hwang, H.-C., Hamer, J. H., Zakamska, N. L., and Schlaufman, K. C. (2020). Very wide companion fraction from Gaia DR2: a weak or no enhancement for hot Jupiter hosts, and a strong enhancement for contact binaries. *MNRAS* 497, 2250–2259. doi:10.1093/mnras/staa2124

Imanishi, M., Kawamuro, T., Kikuta, S., Nakano, S., and Saito, Y. (2020). Subaru infrared adaptive optics-assisted high-spatial-resolution imaging search for luminous dual active galactic nuclei in nearby ultraluminous infrared galaxies. *ApJ* 891, 140. doi:10.3847/1538-4357/ab733e

Imanishi, M., and Saito, Y. (2014). Subaru adaptive-optics high-spatial-resolution infrared K- and L'-band imaging search for deeply buried dual AGNs in merging galaxies. *ApJ* 780, 106. doi:10.1088/0004-637X/780/1/106

Inaba, K., Ueda, Y., Yamada, S., Ogawa, S., Uematsu, R., Tanimoto, A., et al. (2022). Broadband X-ray spectral analysis of the dual AGN system Mrk 739. *ApJ* 939, 88. doi:10.3847/1538-4357/ac97ec

Ivezić, Ž., Kahn, S. M., Tyson, J. A., Abel, B., Acosta, E., Allsman, R., et al. (2019). LSST: from science drivers to reference design and anticipated data products. *ApJ* 873, 111. doi:10.3847/1538-4357/ab042c

Iwasawa, K., Ricci, C., Privon, G. C., Torres-Albà, N., Inami, H., Charmandaris, V., et al. (2020). A Compton-thick nucleus in the dual active galactic nuclei of Mrk 266. *A&A* 640, A95. doi:10.1051/0004-6361/202038513

Iwasawa, K., Sanders, D. B., Teng, S. H., U, V., Armus, L., Evans, A. S., et al. (2011). C-GOALS: Chandra observations of a complete sample of luminous infrared galaxies from the IRAS Revised Bright Galaxy Survey. *A&A* 529, A106. doi:10.1051/0004-6361/201015264

Iwasawa, K., U, V., Mazzarella, J. M., Medling, A. M., Sanders, D. B., and Evans, A. S. (2018). Testing a double AGN hypothesis for Mrk 273. *A&A* 611, A71. doi:10.1051/0004-6361/201731662

Jansen, F., Lumb, D., Altieri, B., Clavel, J., Ehle, M., Erd, C., et al. (2001). XMM-Newton observatory. I. The spacecraft and operations. *A&A* 365, L1–L6. doi:10.1051/0004-6361:20000036

Kammoun, E. S., Barret, D., Peille, P., Willingale, R., Dauser, T., Wilms, J., et al. (2022). The defocused observations of bright sources with Athena/X-IFU. *A&A* 664, A29. doi:10.1051/0004-6361/202243606

Komossa, S., Burwitz, V., Hasinger, G., Predehl, P., Kaastra, J. S., and Ikebe, Y. (2003). Discovery of a binary active galactic nucleus in the ultraluminous infrared galaxy NGC 6240 using Chandra. *ApJL* 582, L15–L19. doi:10.1086/346145

Kosec, P., Brightman, M., Stern, D., Müller-Sánchez, F., Koss, M., Oh, K., et al. (2017). Investigating the evolution of the dual AGN system ESO 509-ig066. *ApJ* 850, 168. doi:10.3847/1538-4357/aa932e

Koss, M., Mushotzky, R., Treister, E., Veilleux, S., Vasudevan, R., and Trippe, M. (2012). Understanding dual active galactic nucleus activation in the nearby Universe. *ApJL* 746, L22. doi:10.1088/2041-8205/746/2/L22

Koss, M. J., Glidden, A., Baloković, M., Stern, D., Lamperti, I., Assef, R., et al. (2016). NuSTAR resolves the first dual AGN above 10 keV in SWIFT J2028.5+2543. *ApJL* 824, L4. doi:10.3847/2041-8205/824/1/L4

Koss, M. J., Treister, E., Kakkad, D., Casey-Clyde, J. A., Kawamuro, T., Williams, J., et al. (2023). UGC 4211: a confirmed dual active galactic nucleus in the local Universe at 230 pc nuclear separation. *ApJL* 942, L24. doi:10.3847/2041-8213/aca8f0

LaMassa, S. M., Yaqoob, T., Boorman, P. G., Tzanavaris, P., Levenson, N. A., Gandhi, P., et al. (2019). NuSTAR uncovers an extremely local compton-thick AGN in NGC 4968. *ApJ* 887, 173. doi:10.3847/1538-4357/ab552c

LaMassa, S. M., Yaqoob, T., Levenson, N. A., Boorman, P., Heckman, T. M., Gandhi, P., et al. (2017). Chandra reveals heavy obscuration and circumnuclear star formation in seyfert 2 galaxy NGC 4968. *ApJ* 835, 91. doi:10.3847/1538-4357/835/1/91

Laureijs, R., Amiaux, J., Arduini, S., Augueres, J. L., Brinchmann, J., Cole, R., et al. (2011). *Euclid definition study report. arXiv e-prints* , arXiv:1110.3193. doi:10.48550/arXiv.1110.3193

Li, K., Ballantyne, D. R., and Bogdanović, T. (2021). The detectability of kiloparsec-scale dual active galactic nuclei: the impact of galactic structure and black hole orbital properties. *ApJ* 916, 110. doi:10.3847/1538-4357/ac06a0

Liu, X., Civano, F., Shen, Y., Green, P., Greene, J. E., and Strauss, M. A. (2013). Chandra X-ray and Hubble space telescope imaging of optically selected kiloparsec-scale binary active galactic nuclei. I. Nature of the nuclear ionizing sources. *ApJ* 762, 110. doi:10.1088/0004-637X/762/2/110

Liu, X., Shen, Y., Strauss, M. A., and Greene, J. E. (2010). Type 2 active galactic nuclei with double-peaked [O III] lines: narrow-line region kinematics or merging supermassive black hole pairs? *ApJ* 708, 427–434. doi:10.1088/0004-637X/708/1/427

Liu, X., Shen, Y., Strauss, M. A., and Hao, L. (2011). Active galactic nucleus pairs from the sloan digital sky survey. I. The frequency on ˜5-100 kpc scales. *ApJ* 737, 101. doi:10.1088/0004-637X/737/2/101

Madsen, K. K., García, J. A., Stern, D., Armini, R., Basso, S., Coutinho, D., et al. (2023). *The high energy X-ray probe (HEX-P): instrument and mission profile. arXiv e-prints* , arXiv:2312.04678. doi:10.48550/arXiv.2312.04678

Mannucci, F., Pancino, E., Belfiore, F., Cicone, C., Ciurlo, A., Cresci, G., et al. (2022). Unveiling the population of dual and lensed active galactic nuclei at sub-arcsec separations. *Nat. Astron.* 6, 1185–1192. doi:10.1038/s41550-022-01761-5

Marchesi, S., Ajello, M., Marcotulli, L., Comastri, A., Lanzuisi, G., and Vignali, C. (2018). Compton-thick AGNs in the NuSTAR era. *ApJ* 854, 49. doi:10.3847/1538-4357/aaa410

Marchesi, S., Ajello, M., Zhao, X., Comastri, A., La Parola, V., and Segreto, A. (2019). Compton-thick AGNs in the NuSTAR era. V. Joint NuSTAR and XMM-Newton spectral analysis of three "soft-gamma" candidate CT-AGNs in the swift/BAT 100-month catalog. *ApJ* 882, 162. doi:10.3847/1538-4357/ab340a

Mazzarella, J. M., Iwasawa, K., Vavilkin, T., Armus, L., Kim, D. C., Bothun, G., et al. (2012). Investigation of dual active nuclei, outflows, shock-heated gas, and young star clusters in markarian 266. *AJ* 144, 125. doi:10.1088/0004-6256/144/5/125

Meidinger, N., Albrecht, S., Beitler, C., Bonholzer, M., Emberger, V., Frank, J., et al. (2020). "Development status of the wide field imager instrument for Athena," in Society of Photo-Optical Instrumentation Engineers (SPIE) Conference Series, 114440T. doi:10.1117/12.2560507

Müller-Sánchez, F., Comerford, J. M., Nevin, R., Barrows, R. S., Cooper, M. C., and Greene, J. E. (2015). The origin of double-peaked narrow lines in active galactic nuclei. I. Very large array detections of dual AGNs and AGN outflows. *ApJ* 813, 103. doi:10.1088/0004-637X/813/2/103

Müller-Sánchez, F., Nevin, R., Comerford, J. M., Davies, R. I., Privon, G. C., and Treister, E. (2018). Two separate outflows in the dual supermassive black hole system NGC 6240. *Nature* 556, 345–348. doi:10.1038/s41586-018-0033-2

Nandra, K., Barret, D., Barcons, X., Fabian, A., den Herder, J.-W., Piro, L., et al. (2013). *The hot and energetic Universe: a white paper presenting the science theme motivating the Athena+ mission. arXiv e-prints* , arXiv:1306.2307. doi:10.48550/arXiv.1306.2307

Nardini, E. (2017). Nuclear absorption and emission in the AGN merger NGC 6240: the hard X-ray view. *MNRAS* 471, 3483–3493. doi:10.1093/mnras/stx1878

Oda, S., Ueda, Y., Tanimoto, A., and Ricci, C. (2018). Hard X-ray view of HCG 16 (Arp 318). *ApJ* 855, 79. doi:10.3847/1538-4357/aaaccc

Pérez-Torres, M. A., Alberdi, A., Romero-Cañizales, C., and Bondi, M. (2010). Serendipitous discovery of the long-sought active galactic nucleus in Arp 299-A. *A&A* 519, L5. doi:10.1051/0004-6361/201015462

Pfeifle, R. W., Satyapal, S., Manzano-King, C., Cann, J., Sexton, R. O., Rothberg, B., et al. (2019a). A triple AGN in a mid-infrared selected late-stage galaxy merger. *ApJ* 883, 167. doi:10.3847/1538-4357/ab3a9b

Pfeifle, R. W., Satyapal, S., Secrest, N. J., Gliozzi, M., Ricci, C., Ellison, S. L., et al. (2019b). Buried black hole growth in IR-selected mergers: new results from Chandra. *ApJ* 875, 117. doi:10.3847/1538-4357/ab07bc

Pfeifle, R. W., Weaver, K., Satyapal, S., Ricci, C., Secrest, N. J., Gliozzi, M., et al. (2023). *NuSTAR observations of four mid-IR selected dual AGN candidates in galaxy mergers. arXiv e-prints* , arXiv:2306.16437. doi:10.48550/arXiv.2306.16437

Piconcelli, E., Vignali, C., Bianchi, S., Mathur, S., Fiore, F., Guainazzi, M., et al. (2010). Witnessing the key early phase of quasar evolution: an obscured active galactic nucleus pair in the interacting galaxy IRAS 20210+1121. *ApJL* 722, L147–L151. doi:10.1088/2041-8205/722/2/L147

Ptak, A., Hornschemeier, A., Zezas, A., Lehmer, B., Yukita, M., Wik, D., et al. (2015). A focused, hard X-ray look at Arp 299 with NuSTAR. *ApJ* 800, 104. doi:10.1088/0004-637X/800/2/104

Ricci, C., Bauer, F. E., Treister, E., Schawinski, K., Privon, G. C., Blecha, L., et al. (2017). Growing supermassive black holes in the late stages of galaxy mergers are heavily obscured. *MNRAS* 468, stx173–1299. doi:10.1093/mnras/stx173

Ricci, C., Chang, C.-S., Kawamuro, T., Privon, G. C., Mushotzky, R., Trakhtenbrot, B., et al. (2023). A tight correlation between millimeter and X-ray emission in accreting massive black holes from <100 mas resolution ALMA observations. *ApJL* 952, L28. doi:10.3847/2041-8213/acda27

Ricci, C., Privon, G. C., Pfeifle, R. W., Armus, L., Iwasawa, K., Torres-Albà, N., et al. (2021). A hard X-ray view of luminous and ultra-luminous infrared galaxies in GOALS - I. AGN obscuration along the merger sequence. *MNRAS* 506, 5935–5950. doi:10.1093/mnras/stab2052

Rubinur, K., Das, M., and Kharb, P. (2019). Searching for dual AGN in galaxies with double-peaked emission line spectra using radio observations. *MNRAS* 484, 4933–4950. doi:10.1093/mnras/stz334

Rubinur, K., Kharb, P., Das, M., Rahna, P. T., Honey, M., Paswan, A., et al. (2021). A multiwavelength study of the dual nuclei in Mrk 212. *MNRAS* 500, 3908–3919. doi:10.1093/mnras/staa3375

Satyapal, S., Ellison, S. L., McAlpine, W., Hickox, R. C., Patton, D. R., and Mendel, J. T. (2014). Galaxy pairs in the sloan digital sky survey - IX. Merger-Induced AGN activity as traced by the wide-field infrared survey explorer. *MNRAS* 441, 1297–1304. doi:10.1093/mnras/stu650

Satyapal, S., Secrest, N. J., Ricci, C., Ellison, S. L., Rothberg, B., Blecha, L., et al. (2017). Buried AGNs in advanced mergers: mid-infrared color selection as a dual AGN candidate finder. *ApJ* 848, 126. doi:10.3847/1538-4357/aa88ca

Schawinski, K., Koss, M., Berney, S., and Sartori, L. F. (2015). Active galactic nuclei flicker: an observational estimate of the duration of black hole growth phases of ~10^5 yr. *MNRAS* 451, 2517–2523. doi:10.1093/mnras/stv1136

Schwartzman, E., Clarke, T. E., Nyland, K., Secrest, N. J., Pfeifle, R. W., Schmitt, H. R., et al. (2023). *VaDAR: varstrometry for dual AGN using radio interferometry. arXiv e-prints* , arXiv:2306.13219. doi:10.48550/arXiv.2306.13219

Shen, Y., Chen, Y.-C., Hwang, H.-C., Liu, X., Zakamska, N., Oguri, M., et al. (2021). A hidden population of high-redshift double quasars unveiled by astrometry. *Nat. Astron.* 5, 569–574. doi:10.1038/s41550-021-01323-1

Shen, Y., Hwang, H.-C., Zakamska, N., and Liu, X. (2019). Varstrometry for off-nucleus and dual sub-kpc AGN (VODKA): how well centered are low-z AGN? *ApJL* 885, L4. doi:10.3847/2041-8213/ab4b54

Skilling, J. (2004). Nested sampling. *AIP Conf. Proc.* 735, 395. doi:10.1063/1.1835238

Smith, K. L., Shields, G. A., Bonning, E. W., McMullen, C. C., Rosario, D. J., and Salviander, S. (2010). A search for binary active galactic nuclei: double-peaked [O III] AGNs in the sloan digital sky survey. *ApJ* 716, 866–877. doi:10.1088/0004-637X/716/1/866

Toomre, A., and Toomre, J. (1972). Galactic bridges and tails. *ApJ* 178, 623–666. doi:10.1086/151823

Torres-Albà, N., Iwasawa, K., Díaz-Santos, T., Charmandaris, V., Ricci, C., Chu, J. K., et al. (2018). C-GOALS. II. Chandra observations of the lower luminosity sample of nearby luminous infrared galaxies in GOALS. *A&A* 620, A140. doi:10.1051/0004-6361/201834105

Van Wassenhove, S., Volonteri, M., Mayer, L., Dotti, M., Bellovary, J., and Callegari, S. (2012). Observability of dual active galactic nuclei in merging galaxies. *ApJL* 748, L7. doi:10.1088/2041-8205/748/1/L7

Veres, P. M., Gabányi, K. É., Frey, S., Paragi, Z., Kun, E., and An, T. (2021). European vlbi network observations of the proposed dual agn sdss j101022.95+141300.9. *ApJ* 922, 99. doi:10.3847/1538-4357/ac307d

Wang, J.-M., Chen, Y.-M., Hu, C., Mao, W.-M., Zhang, S., and Bian, W.-H. (2009). Active galactic nuclei with double-peaked narrow lines: are they dual active galactic nuclei? *ApJL* 705, L76–L80. doi:10.1088/0004-637X/705/1/L76

Weston, M. E., McIntosh, D. H., Brodwin, M., Mann, J., Cooper, A., McConnell, A., et al. (2017). Incidence of WISE -selected obscured AGNs in major mergers and interactions from the SDSS. *MNRAS* 464, 3882–3906. doi:10.1093/mnras/stw2620

Yamada, S., Ueda, Y., Oda, S., Tanimoto, A., Imanishi, M., Terashima, Y., et al. (2018). Broadband X-ray spectral analysis of the double-nucleus luminous infrared galaxy Mrk 463. *ApJ* 858, 106. doi:10.3847/1538-4357/aabacb

Zhou, H., Wang, T., Zhang, X., Dong, X., and Li, C. (2004). Obscured binary quasar cores in SDSS J104807.74+005543.5? *ApJL* 604, L33–L36. doi:10.1086/383310

ZuHone, J. A., Vikhlinin, A., Tremblay, G. R., Randall, S. W., Andrade-Santos, F., and Bourdin, H. (2023). *SOXS: simulated observations of X-ray sources*. Astrophysics Source Code Library. record ascl:2301.024.

frontiers | Frontiers in Astronomy and Space Sciences

TYPE Original Research
PUBLISHED 19 August 2024
DOI 10.3389/fspas.2024.1290057

Check for updates

OPEN ACCESS

EDITED BY
Aditi Agarwal,
Centre for Cosmology and Science Popularization, India

REVIEWED BY
Reinaldo Roberto Rosa,
National Institute of Space Research (INPE), Brazil
Carlos Frajuca,
Federal University of Rio Grande, Brazil
Fabrizio Tavecchio,
National Institute of Astrophysics (INAF), Italy
Francesco Massaro,
University of Turin, Italy

*CORRESPONDENCE
Lea Marcotulli,
lea.marcotulli@yale.edu

†NHFP Einstein Fellow

RECEIVED 06 September 2023
ACCEPTED 10 July 2024
PUBLISHED 19 August 2024

CITATION
Marcotulli L, Ajello M, Böttcher M, Coppi P, Costamante L, Di Gesu L, Errando M, García JA, Gokus A, Liodakis I, Madejski G, Madsen K, Moretti A, Middei R, McBride F, Petropoulou M, Rani B, Sbarrato T, Stern D, Vasilopoulos G, Zacharias M, Zhang H and the HEX-P Collaboration (2024) The high energy X-ray probe (HEX-P): the most powerful jets through the lens of a superb X-ray eye. *Front. Astron. Space Sci.* 11:1290057. doi: 10.3389/fspas.2024.1290057

COPYRIGHT
© 2024 Marcotulli, Ajello, Boettcher, Coppi, Costamante, Di Gesu, Errando, García, Gokus, Liodakis, Madejski, Madsen, Moretti, Middei, McBride, Petropoulou, Rani, Sbarrato, Stern, Vasilopoulos, Zacharias, Zhang and the HEX-P Collaboration. This is an open-access article distributed under the terms of the Creative Commons Attribution License (CC BY). The use, distribution or reproduction in other forums is permitted, provided the original author(s) and the copyright owner(s) are credited and that the original publication in this journal is cited, in accordance with accepted academic practice. No use, distribution or reproduction is permitted which does not comply with these terms.

The high energy X-ray probe (HEX-P): the most powerful jets through the lens of a superb X-ray eye

Lea Marcotulli[1,2*†], Marco Ajello[3], Markus Böttcher[4], Paolo Coppi[5], Luigi Costamante[6], Laura Di Gesu[6], Manel Errando[7], Javier A. García[8,9], Andrea Gokus[7], Ioannis Liodakis[10,11], Greg Madejski[12], Kristin Madsen[8], Alberto Moretti[13], Riccardo Middei[6,14], Felicia McBride[15], Maria Petropoulou[16], Bindu Rani[17,18], Tullia Sbarrato[19], Daniel Stern[20], Georgios Vasilopoulos[16], Michael Zacharias[21,4], Haocheng Zhang[17,18] and the HEX-P Collaboration

[1]Yale Center for Astronomy and Astrophysics, New Haven, CT, United States, [2]Department of Physics, Yale University, New Haven, CT, United States, [3]Department of Physics and Astronomy, Clemson University, Kinard Lab of Physics, Clemson, SC, United States, [4]Centre for Space Research, North-West University, Potchefstroom, South Africa, [5]Department of Astronomy, Yale University, New Haven, CT, United States, [6]Space Science Data Center, Agenzia Spaziale Italiana, Roma, Italy, [7]Department of Physics & McDonnell Center for the Space Sciences, Washington University in St. Louis, St Louis, MO, United States, [8]X-ray Astrophysics Laboratory, NASA Goddard Space Flight Center, Greenbelt, MD, United States, [9]Cahill Center for Astrophysics, California Institute of Technology, Pasadena, CA, United States, [10]Finnish Centre for Astronomy with ESO, University of Turku, Turku, Finland, [11]NASA Marshall Space Flight Center, Huntsville, AL, United States, [12]SLAC National Accelerator Center and Kavli Institute for Particle Astrophysics and Cosmology, Stanford University, Stanford, CA, United States, [13]INAF - Osservatorio Astronomico di Brera, Milano, Italy, [14]INAF Osservatorio Astronomico di Roma, Frascati, Monte Porzio Catone, Italy, [15]Department of Physics and Astronomy, Bowdoin College, Brunswick, ME, United States, [16]Department of Physics, National and Kapodistrian University of Athens, University Campus Zografos, Athens, Greece, [17]NASA Goddard Space Flight Center, Greenbelt, MD, United States, [18]University of Maryland, Baltimore County, Baltimore, MD, United States, [19]INAF - Osservatorio Astronomico di Brera, Merate, Italy, [20]Jet Propulsion Laboratory, California Institute of Technology, Pasadena, CA, United States, [21]Landessternwarte, Universität Heidelberg, Heidelberg, Germany

A fraction of the active supermassive black holes at the centers of galaxies in our Universe are capable of launching extreme kiloparsec-long relativistic jets. These jets are known multiband (radio to γ-ray) and multimessenger (neutrino) emitters, and some of them have been monitored over decades at all accessible wavelengths. However, several open questions remain unanswered about the processes powering these highly energetic phenomena. These jets intrinsically produce soft-to-hard X-ray emission that extends from $E > 0.1$ keV up to $E > 100$ keV, and simultaneous broadband X-ray coverage, combined with excellent timing and imaging capabilities, is required to uncover the physics of jets. Indeed, truly simultaneous soft-to-hard X-ray coverage, in synergy with current and upcoming high-energy facilities (such as IXPE, COSI, CTAO, etc.) and neutrino detectors (e.g., IceCube), would enable us to disentangle the particle population responsible for the high-energy radiation from these jets. A sensitive hard X-ray survey ($F_{20-80\,\mathrm{keV}} < 10^{-15}$ erg cm^{-2} s^{-1}) could unveil the bulk of their population in the early Universe. Acceleration and radiative processes responsible for the majority of their X-ray emission would be

pinned down by microsecond timing capabilities at both soft and hard X-rays. Furthermore, imaging jet structures for the first time in the hard X-ray regime could unravel the origin of their high-energy emission. The proposed Probe-class mission concept High Energy X-ray Probe (HEX-P) combines all these required capabilities, making it the crucial next-generation X-ray telescope in the multi-messenger, time-domain era. HEX-P will be the ideal mission to unravel the science behind the most powerful accelerators in the Universe.

KEYWORDS

blazar, supermassive black hole, jet, high energy astrophysical phenomena, X-ray mission, time domain astrophysics, multimessenger astronomy

1 Introduction

The high-energy ($E > 1$ keV) extragalactic sky is filled with accreting supermassive black holes (known as active galactic nuclei, AGN, Ajello et al., 2008; Ajello et al., 2009; Gilli, 2013; Ueda et al., 2014; Cappelluti et al., 2017; Ananna et al., 2020). These monstrous objects, reaching masses of billions or more Suns, are feeding from the gas that surrounds them, emitting copious amounts of radiation. A fraction of these black hole systems also powers relativistic jets from their core. When the jet is closely aligned to the Earth's line of sight (viewing angles, $\theta_V < 5° - 10°$), these objects are known as blazars; otherwise they are classified as misaligned AGNs or radio galaxies (e.g., Urry and Padovani, 1995; Hovatta et al., 2009; Pushkarev et al., 2017). Although continuous multi-band monitoring of these sources has been ongoing for more than 2 decades (e.g., Urry et al., 1997; Kataoka et al., 1999; Komossa et al., 2021; Weaver et al., 2022; de Jaeger et al., 2023; Otero-Santos et al., 2023), many open questions remain regarding the nature of these extreme jets.

A unique mission such as the High Energy X-ray Probe (HEX-P; Madsen et al., 2023), with its broadband X-ray coverage ($0.2 - 80$ keV), unprecedented sensitivity ($F_{0.5-2\,\mathrm{keV}} < 10^{-16}$ erg cm^{-2} s^{-1} and $F_{3-24\,\mathrm{keV}} < 10^{-15}$ erg cm^{-2} s^{-1} in a 1 Ms exposure, Civano et al., 2023), good timing resolution ($\Delta t \sim 2\,\mu$s) across a wide range of energies and angular resolution in the hard X-ray band $3 - 4$ times better than NuSTAR, will enable us to answer several open science questions regarding blazars. HEX-P will allow us, for the first time, to: (1) spatially resolve extragalactic nearby jets in hard X-rays; (2) detect spectral signatures (e.g., spectral curvatures, exponential cut-off) that will uniquely point us to the preferred high-energy emission mechanisms in jets, and, by extension, their composition; and (3) in synergy with the current and upcoming landscape of experiments (e.g., COSI, IXPE, CTAO, IceCube Gen 2), reveal the preferred particle acceleration and emission mechanism of the brightest objects in the Universe, fulfilling the promises of multi-wavelength and multi-messenger science. In this paper, we explore some of the open issues in blazar science, and more broadly jetted AGN, and how HEX-P will revolutionize our understanding of these sources.

The peculiar jet orientation in blazars allows for extreme relativistic beaming, opening a window for studies of particle acceleration mechanisms and jet structure (Madau et al., 1987; Dermer, 1995; Dondi and Ghisellini, 1995). These sources are extremely bright multi-wavelength emitters (from radio up to TeV energies; see Massaro et al., 2008; Madejski and Sikora, 2016; Blandford et al., 2019), reaching apparent bolometric luminosities of $> 10^{48}$erg s^{-1} (e.g., Massaro et al., 2015; Ghisellini et al., 2017; Paliya et al., 2019b; Ajello et al., 2020). Blazars are also likely multi-messenger sources, as they are able to accelerate protons and produce both high-energy neutrinos and γ-rays (e.g., IceCube Collaboration et al., 2018). Phenomenologically speaking, blazars have been divided into several subcategories. Objects with broad and strong emission lines (equivalent width, EW > 5Å) in optical spectra are classified as Flat Spectrum Radio Quasars (FSRQs). When these lines are weak or absent, these sources are known as BL Lacertae objects (BL Lacs, e.g., Schmidt, 1968; Stein et al., 1976). Their electromagnetic broadband spectral energy distribution (SED) is characterized by two broad "humps", a low-energy hump peaking in the IR–X-ray range, and a high-energy hump peaking in the MeV–γ-ray range. It is now well understood that most of the radiation from radio to optical/X-ray frequencies of these jets is produced by synchrotron radiation of electrons moving at relativistic speeds in magnetic fields in the jets (e.g., Pian et al., 1998; Padovani et al., 2002). This scenario is further strengthened by the high polarization degree measured in these sources at radio to optical frequencies, and now also in X-rays for the two nearest blazars (e.g., Jorstad et al., 2007; Blinov et al., 2021; Liodakis et al., 2022; Zhang et al., 2023; Zobnina et al., 2023). Based on the location of their synchrotron spectral peak (Abdo et al., 2010a), these sources have later been classified as low- (LSP, $\nu_{\mathrm{synch,peak}} < 10^{14.5}$ Hz), intermediate- (ISP, $10^{14.5}$ Hz $< \nu_{\mathrm{synch,peak}} < 10^{15}$ Hz) and high-synchrotron peaked (HSP, $\nu_{\mathrm{synch,peak}} > 10^{15}$ Hz) sources. FSRQs usually belong to the LSP class, being the most luminous of the class, detected up to the highest redshifts ($z > 4$). BL Lacs instead span the whole range of classifications, are less luminous, and are typically found at $z < 1$ (Shen et al., 2011; Ajello et al., 2014; Massaro et al., 2016; Peña-Herazo et al., 2021; Middei et al., 2022; Rajagopal et al., 2023). However, the physical origin of the high-energy part of the SED is still a matter of debate. In the leptonic scenario (e.g., Ghisellini and Maraschi, 1989; Dermer et al., 1992; Sikora et al., 1994), the X-ray to very high energy (VHE, $E > 100$ GeV) γ-ray emission is explained by inverse Compton scattering by the same population of electrons that produces the synchrotron emission (e.g., Beckmann et al., 2002; Tagliaferri et al., 2002). These electrons scatter the photon fields either within the jet structure (referred to as synchrotron self-Compton; SSC) or those external to

the jet (for example, the accretion disk, the broad-line region, or an infrared-emitting dust torus; this emission is referred to as external Compton; EC). As an alternative to the leptonic inverse-Compton interpretation, the high-energy emission could also be produced by ultra-relativistic protons through proton synchrotron emission and emission from electromagnetic cascades initiated by photo-pion production and Bethe-Heitler pair production processes (e.g., Mannheim, 1993; Mücke et al., 2003).

Clues towards the jets' particle composition lie in the simultaneous characterization of the X-ray spectrum from soft X-rays ($E \sim 1$ keV) to hard ($E \gtrsim 10$ keV) X-rays (e.g., Maraschi, 1999). As pioneered by missions such as BeppoSAX (Boella et al., 1997) and Suzaku (Koyama et al., 2007; Takahashi et al., 2007), and later confirmed by blazar studies using combined observations from soft (e.g., Swift/XRT, XMM-Newtown, Chandra) and hard (Swift/BAT, NuSTAR) X-ray instruments, simultaneous coverage at these energies is crucial for several blazar classes: it allows characterization of the synchrotron peak of the most extreme BL Lac sources (e.g., Costamante et al., 2001; Reimer et al., 2008), pinpointing the high-energy peak of the most luminous MeV-peaked blazars (e.g., Ghisellini et al., 1999; Tagliaferri et al., 2015; Marcotulli et al., 2020), and characterization of the transition between the low- and high-energy humps of the SED (e.g., Abdo et al., 2010b; Böttcher et al., 2013), the shape of which is fundamental to unveil the nature of the particle population in the jet. The superior broadband sensitivity, imaging capabilities, and lower backgrounds, of HEX-P would allow us to study in detail a larger number of blazars of different types, sampling their SED at flux levels order of magnitude lower than previously achievable by past broadband X-ray missions. Due to its coverage of the full X-ray energy range, HEX-P will be complementary for blazar science to many other recent or near-future experiments, such as the recently launched Imaging X-ray Polarimetry Explorer (IXPE; 2 – 8 keV, Weisskopf, 2022), the approved Compton Spectrometer and Imager (COSI; Tomsick et al., 2019), and the order-of-magnitude improvement in sensitivity to high-energy γ-rays above 100 GeV provided by the upcoming Cherenkov Telescope Array Observatory (CTAO; Cherenkov Telescope Array Consortium et al., 2019).

Another observational multi-band characteristic of blazars is their variability, with flaring timescales ranging from months down to minutes, flux enhancements of up to several orders of magnitude, and cross-correlated variability patterns (or lack thereof) observed between different energy bands. To explain this behavior, several particle acceleration mechanisms have been proposed to act in these jets, related to magnetic reconnection occurring inside the jet (e.g., Giannios, 2013; Christie et al., 2019; Zhang H. et al., 2022) for the fastest time scales observed, or mildly relativistic shocks (Rees, 1978; Marscher and Gear, 1985) to describe variability on longer time scales. The most rapid variations, which are shorter than 10 min, have been observed at γ-ray energies for a handful of sources (Albert et al., 2007; Aleksić et al., 2014a; Ackermann et al., 2016a; Aharonian et al., 2017; Meyer et al., 2019). In the X-ray energy range from $\sim$ 0.5–20 keV, variability on similar time scales has also been found for several sources (e.g., Catanese and Sambruna, 2000; Zhu et al., 2018; Zhang Z. et al., 2019; Zhang et al., 2021b; Chatterjee et al., 2021; Mohorian et al., 2022). At optical and near-infrared wavelengths, rapid variability has also been detected within a day or shorter (e.g., Gopal-Krishna et al., 2011; Sandrinelli et al., 2014; Agarwal et al., 2015). Typically, those rapid variations occur when a blazar is in a bright state. Often, spectral changes in the high-energy regime are correlated with an increase in luminosity, where the brighter emission leads to a harder spectrum in the X-ray band for HSP sources (e.g., Bhatta et al., 2018; Wang et al., 2018; Giommi et al., 2021), and in the γ-ray band for LSP sources (e.g., Abdo et al., 2010c; Williamson et al., 2014). Long-term variability is usually also present across all wavelengths (e.g., Mao and Zhang, 2016; Gaur et al., 2019; Rajput et al., 2020; Safna et al., 2020; Mundo and Mushotzky, 2023). However, correlation studies between several energy bands are still inconclusive in diagnosing the production sites of flares (e.g., single zone versus multi-zone scenarios), the mechanisms of particle acceleration, and the particle species responsible for the flares in different wavelengths. Strictly simultaneous multi-wavelength observations and monitoring of flaring blazars must be performed to constrain jet physics. In particular, simultaneously characterizing the transition between the soft and hard X-rays in blazars belonging to different subclasses will provide unprecedented insight into these acceleration processes.

Flaring can lead to a deeper understanding of the physics in AGN jets in terms of particle acceleration mechanisms and dissipative locations in the jet. Additionally, together with neutrino observations, flaring can be pivotal for understanding the particle content responsible for the photon emission. The association of the γ-ray flaring blazar TXS 0506 + 056 with the IceCube neutrino event IceCube-170922A was the first, and so far most convincing, evidence that blazars can accelerate protons to very high energies (IceCube Collaboration et al., 2018). However, the lack of simultaneous broadband coverage from X-ray to MeV γ-rays has prevented us from constraining the relevant models sufficiently well to probe the transition between the synchrotron and high-energy emission part of the spectrum, where signatures of electromagnetic cascades associated with the neutrino-producing photo-hadronic interactions should emerge (Murase et al., 2018). In particular, studies of a previous neutrino flare potentially linked to TXS 0506 + 056 show that the complete lack of sensitive simultaneous broad X-ray spectral and temporal coverage significantly hampered any conclusion on the emission mechanism (e.g., Reimer et al., 2019; Petropoulou et al., 2020; Zhang B. T. et al., 2020). Simultaneous hard X-ray ($E > 10$ keV) observations would be able to probe the transition regime between the low-energy and high-energy peak, and the evolution of the spectral shape at different epochs (pre/post neutrino event), hence removing degeneracies on parameters in the tested models. Moreover, in the context of a one-zone hybrid lepto-hadronic scenario, Petropoulou et al. (2020) found that the maximal neutrino flux is strongly correlated with the X-ray flux in the case of the source, which underscores the importance of X-ray measurements for constraining the blazar neutrino output. Simultaneous broadband coverage of neutrino alerts in the direction of blazar sources could be the tipping point for jet models as well as confirming AGN as one of the sources of high-energy cosmic rays.

In terms of population studies, there appears to exist an anti-correlation between the synchrotron peak position and the intrinsic bolometric luminosity of blazars, the so-called blazar sequence (see Fossati et al., 1998; Ghisellini et al., 1998; Ghisellini et al., 2017). If real, this would imply that more luminous sources (found at the highest redshifts) have higher accretion rates ($L_{\rm disk}/L_{\rm Edd} \gtrsim 10^{-2}$), hence host more radiatively efficient accretion

disks than less luminous (and lower redshift) ones. Opponents of the sequence, however, argue that this is a mere selection effect (e.g., Nieppola et al., 2008; Giommi et al., 2012; Keenan et al., 2021). A mission with high sensitivity in the broad X-ray band such as HEX-P will be key to narrowing down this issue. On the one hand, HEX-P's superior sensitivity will allow us to detect tens to hundreds of sources beyond $z \gtrsim 4$, as predicted by current X-ray blazar evolutionary models (the so-called MeV blazars; see, Marcotulli et al., 2022). Multi-band coverage will enable us to pinpoint the location of the high-energy peak and the intrinsic jet luminosity (probing the low-synchrotron-peak-frequency end of the blazar sequence). On the other hand, HEX-P has the potential to discover a handful of MeV-peaked BL Lac sources in the local Universe. Predicted by the blazar sequence, these jets may have been missed by current surveys due to being too faint or overwhelmed by galaxy emission. If found by HEX-P, they would confirm that the blazar sequence is real and clarify its physical origin.

Finally, jets of active galaxies have been observed to extend up to hundreds of kiloparsecs into the intergalactic medium. They are spatially best resolved in the radio band, using very-long-baseline interferometry (VLBI) observations, where low-energy synchrotron emission can be observed along the entire jet (e.g., Linfield, 1981; Boccardi et al., 2016). Moreover, many jets also show extended components (straight jets or hotspots along the jet flow) in various other energy bands including the X-ray domain (Chartas et al., 2000; Harris and Krawczynski, 2006; Stawarz et al., 2013; Marshall et al., 2018; Meyer et al., 2018), even up to the TeV energy band (e.g., Abramowski et al., 2012; H. E. S. S. Collaboration et al., 2020; Archer et al., 2020). The origin of the X-ray (and high-energy) emission from extended jets is certainly non-thermal (see e.g., Harris and Krawczynski, 2002; Harris and Krawczynski, 2006). However, it is unclear whether synchrotron radiation or inverse-Compton emission dominates. The former process seems to well describe the emission arising from low-power jets while for high-power radio galaxies and QSOs the dominant mechanism could be inverse Compton, in most cases having seed photons provided by the CMB radiation (e.g., Harris and Grindlay, 1979; Stawarz et al., 2003; Atoyan and Dermer, 2004; Zacharias and Wagner, 2016; Meyer et al., 2017; Roychowdhury et al., 2022). Observations with a mission such as HEX-P will be crucial for resolving, for the very first time in the hard X-ray band beyond 10keV, nearby bright jets and disentangling these scenarios.

The paper is organized as follows: Section 2 describes the HEX-P mission design; Section 3 details the setup for the simulations performed throughout the paper; Section 4 addresses the contribution of HEX-P to the multi-messenger and time domain astrophysics of blazars; Section 5 highlights the prospects for different blazar classes; Section 6 showcases the importance of HEX-P in resolving jets in the hard X-ray band; and Section 7 summarizes the main science cases that HEX-P will be able to address with respect to the most powerful jets in the Universe.

2 Mission design

HEX-P (Madsen et al., 2023)is a Probe-class mission concept that offers sensitive broad-band coverage (0.2 – 80 keV) of the X-ray spectrum with exceptional spectral, timing, and angular capabilities. It features two high-energy telescopes (HETs) that focus hard X-rays, and one low-energy telescope (LET) that focuses lower energy X-rays.

The LET consists of a segmented mirror assembly coated with iridium on monocrystalline silicon that achieves a half-power diameter of 3.5″, and a low-energy DEPFET detector, of the same type as the Wide Field Imager (WFI; Meidinger et al., 2020) onboard Athena (Nandra et al., 2013). It has 512×512 pixels that cover a field of view of $11.3' \times 11.3'$. It has an effective passband of 0.2 – 25 keV, and a full frame readout time of 2 ms, which can be operated in a 128 and 64 channel window mode for higher count-rates to mitigate pile-up and faster readout. Pile-up effects remain below an acceptable limit of ~1% for a flux up to ~100 mCrab (2.4×10^{-9} erg cm^{-2} s^{-1}, in the 2 – 10 keV band) in the smallest window configuration. Excising the core of the PSF, a common practice in X-ray astronomy, will allow for observations of brighter sources, with a typical loss of up to ~60% of the total photon counts.

The HET consists of two co-aligned telescopes and detector modules. The optics are made of Ni-electroformed full shell mirror substrates, leveraging the experience of XMM-Newton (Jansen et al., 2001), and coated with Pt/C and W/Si multilayers for an effective passband of 2 – 80 keV, achieving a half-power diameter 3 – 4 times better than that of NuSTAR. The high-energy detectors are of the same type as flown on NuSTAR (Harrison et al., 2013), and they consist of 16 CZT sensors per focal plane, tiled 4×4, for a total of 128×128 pixels spanning a field of view slightly larger than for the LET, of $13.4' \times 13.4'$.

3 Simulations

All the simulations presented here were produced with a set of response files that represent the observatory performance based on current best estimates as of Spring 2023 (see Madsen et al., 2023). The effective area is derived from ray-tracing calculations for the mirror design including obscuration by all known structures. The detector responses are based on simulations performed by the respective hardware groups, with an optical blocking filter for the LET and a Beryllium window and thermal insulation for the HET. The LET background was derived from a GEANT4 simulation (Eraerds et al., 2021) of the WFI instrument, and the HET background was derived from a GEANT4 simulation of the NuSTAR instrument; both backgrounds assume HEX-P's Lagrange point L1 orbit.

The spectral simulations were performed in XSPEC (Arnaud, 1996) via the "fakeit" command with V07[1] response files, selecting an 80% PSF correction. The data are assumed to be extracted from a 10 arcsec region, with the anticipated background for the telescope being positioned at L1. The images and light curves were simulated using the SIXTE toolkit (Dauser et al., 2019), using the same response files as the spectral simulation.

The differential sensitivity curves shown throughout the paper are obtained by calculating for each energy bin (LET: $\Delta E = 0.01$ keV, HET: $\Delta E = 0.04$ keV) the minimum detectable flux for a signal-to-noise ratio (SNR) of 5 in exposures of 100 ks and 1 Ms.

1 https://hexp.org/response-files/

4 Time domain and multi-messenger astrophysics

4.1 Leptonic vs. hadronic populations in blazar jets

4.1.1 Probing the relativistic leptonic population in blazar jets

As discussed in Section 1, the location of the two peaks of the blazar's broadband SED generally depends on its apparent luminosity (e.g., Ghisellini et al., 2017). For HSP sources, the flux in the spectral regime corresponding to the X-ray energy (0.1 – 100 keV) is typically lower than that of the peaks. Thus in an SED plot ($log(E \times F(E))$ vs. $log(E)$, it appears as a "valley" (although note that the peak of the synchrotron component of HSPs and some LSPs and ISPs during flares can extend to the X-ray bands). Figure 1 shows the multi-epoch broadband SED for the HSP blazar PKS 2155–304, highlighting the data taken by Madejski et al. (2016) during a non-flaring period of the object, illustrating this "valley". Recent measurements by the IXPE satellite have revealed that the soft X-ray (0.2 – 8 keV) emission of such sources is also polarized (Liodakis et al., 2022), confirming the synchrotron process as the dominant emission mechanism for the entire low-energy "hump" in blazar SEDs. This suggests that hard X-ray studies probe emission by the most energetic particles in the jet (e.g., Ravasio et al., 2003; Massaro et al., 2004; Massaro et al., 2006), since in the synchrotron process, the radiated photon energy goes as the square of the energy of the radiating particle. As the highest energy particles in the distribution radiate more efficiently, we expect to see a cut-off informing us about the maximum Lorentz factor of the particles in the jet ($\gamma_{\rm max}$) and, in general, constraining the spectral evolution of the electron distribution (e.g., Hota et al., 2021). However, given the weak $E \times F(E)$ flux in the X-ray band and a soft X-ray spectrum ($\Gamma_{\rm X} > 2$, Middei et al., 2022), current instruments cannot accurately measure the spectral cutoff of the synchrotron tail during non-flaring states of ISP/HSP blazars. For example, past 20 keV NuSTAR data are dominated by the instrumental background, and hence cannot inform us about the underlying energy distribution beyond that energy. With broadband coverage in both soft and hard X-ray energies, HEX-P will be able to accurately measure the spectral shape of the synchrotron tail, setting important constraints on the acceleration process of the radiating particles. Moreover, in the leptonic scenario, VHE γ-ray photons are produced by the same electrons that generate the X-ray synchrotron emission. Thus, HEX-P will probe the true electron distribution generating (by the inverse Compton process) the intrinsic VHE spectrum of HSPs, as well as flaring LSPs and ISPs that extend to X-rays. These constraints on the shape of the particle population are crucial as VHE photons from blazars are attenuated by γ-γ interactions with low-energy photons associated with the extragalactic background light (EBL). In synergy with CTAO, this can provide unprecedentedly strong constraints on the EBL (e.g., Desai et al., 2019).

To see the improvement of a mission such as HEX-P for this scenario, we simulated a 100 ks observation of a broken power-law X-ray spectrum of PKS 2155–304 at the same flux level as the observation shown in Madejski et al. (2016), $F_{2-10\,\rm keV} = 1.3 \times 10^{-11}$ erg cm^{-2} s^{-1}. The spectral index is $\Gamma_{0.2-20\,\rm keV} = 2.74$, the break occurs at $E = 20$ keV after which the spectrum steepens to $\Gamma_{20-50\,\rm keV} = 4.0$. The simulated spectrum and model residuals for a power-law (PL) and broken powerlaw model (BPL) are shown in Figure 2. From these plots things to notice are that: (i) the low background of the HET would enable us to reach $E \sim 40$ keV; and (ii) it would ascertain the presence of such break above $E > 20$ keV at a $\sim 5\sigma$ level. The high background of NuSTAR would not enable us to go past $E \sim 20$ keV, even with a 1 Ms exposure. Moreover, we checked that for a 1 Ms HEX-P exposure, we would be able to detect the same break at a 2.5σ confidence level for a source with $F_{2-10\,\rm keV} = 9 \times 10^{-13}$ erg cm^{-2} s^{-1} (~92% of ISP/HSP blazars with $\Gamma_{\rm X} > 2$ in Middei et al., 2022 have $F_{2-10\,\rm keV} > 9 \times 10^{-13}$ erg cm^{-2} s^{-1}).

In the case of LSP sources, the X-ray band already probes the onset of the high-energy SED "hump". In the context of synchro-Compton models for relativistic jets, this part of the spectrum is produced by the lowest-energy part of the distribution of radiating particles. In these sources, therefore, HEX-P will probe the low-energy tail of the particle distribution, possibly revealing the presence of low-energy cutoffs thanks to the long arm provided by broad-band sensitivity out to 80 keV in a single observation (e.g., Fabian et al., 2001; Tavecchio et al., 2007; Sbarrato et al., 2016). The broad-band capability of HEX-P is also important in ISPs sources, where the X-ray band corresponds to the cross-over between the synchrotron and inverse Compton peaks, i.e., the "valley" floor (see e.g., ON 231 and TXS 0506 + 056, Tagliaferri et al., 2000; IceCube Collaboration et al., 2018), and the hard-X-ray range provides constraints on the slope of the low-energy electrons. In both cases, given the observed photon spectrum, it is possible to infer the distribution of energies of radiating particles, and for relativistic jets, the low-energy radiating particles are the most numerous. This, in turn, provides good estimates of the total particle content of the jet, and strong constraints on the total kinetic power of the jet (Madejski et al., 2016), as well as its electron-positron pair content. Thus, for high-luminosity sources, hard X-ray observations by HEX-P will provide estimates of the jet power. We note that, in principle, one could study the low-energy end of particle distributions by examining the lowest energy part of the low-energy "hump". However, the region producing the high-energy (X-to-γ-rays) bump of the SED is assumed compact and close to the central black hole. The synchrotron emission from this region at the lowest radio frequencies is self-absorbed, thus the observed emission is optically thick and the SED at these frequencies is the sum of the compact core plus extended jet (e.g., Ghisellini and Tavecchio, 2009; Massaro et al., 2013; Giroletti et al., 2016; Fan and Wu, 2018; Boula and Mastichiadis, 2022). This hampers robust measurements of the total content of low-energy particles in the jet close to the base of the jet.

4.1.2 Probing the relativistic hadronic population in blazar jets

The high-energy blazar spectral component may consist of one or multiple radiation processes. In the leptonic model, the high-energy component may have contributions from both SSC and EC, while in the hadronic model, the hadronic cascading component can be considerable in the X-ray to MeV γ-ray range. In either case, the hard X-rays often mark the transition from one radiation process to another, which usually manifests itself

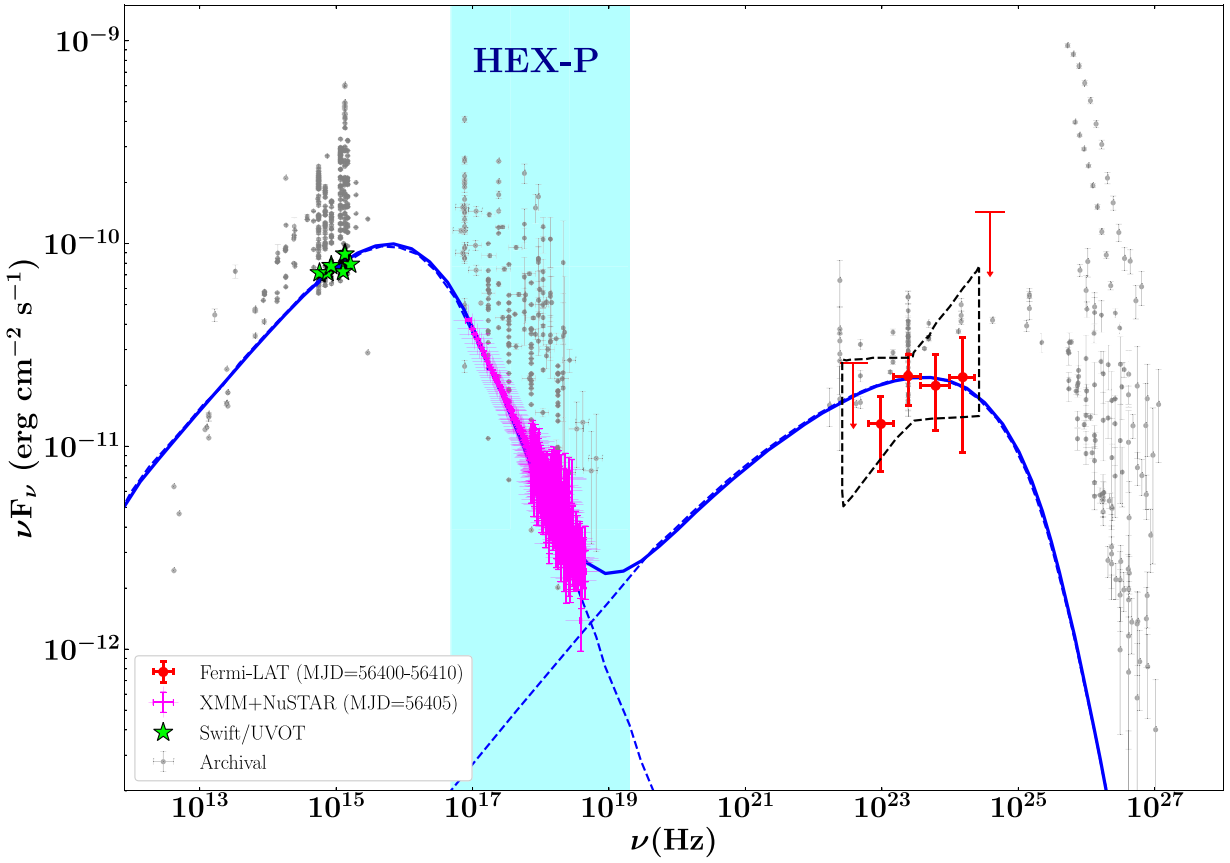

FIGURE 1
Broadband SED of the HSP blazar PKS 2155−304 adapted from Madejski et al. (2016). In gray, we show the multi-epoch multi-band archival data for the source, as an example of the extreme multi-band variability of blazar sources. The low-state was characterized by Madejski et al. (2016), collecting contemporaneous data from: NuSTAR and XMM-Newton-pn (MJD = 56405; magenta points), Swift-UVOT (fluxes corrected for Galactic reddening; green stars), and Fermi-LAT obtained for 10 days centered on the NuSTAR observation (data points in red; broad-band spectral fit "butterfly" in black). Also shown is a basic SED model including synchrotron and SSC components (blue lines). As mentioned in the text, the X-ray data occupy the "valley" in the SED. Highlighted in cyan is the energy band that will be simultaneously covered by HEX-P.

through a change in the spectral shape (e.g., Böttcher et al., 2013; Petropoulou et al., 2015; Gao et al., 2017). But if the high-energy component is dominated by only one radiation mechanism (such as SSC), we expect a smooth, power-law like, hard X-ray spectrum. With its unprecedented spectral resolution and broadband coverage, HEX-P will be able to identify the presence of more than one radiation mechanism at X-ray energies.

To illustrate the capabilities of HEX-P in identifying spectral breaks due to the transition from leptonic to hadronic emission components, we choose Ap Librae, an intriguing LSP at redshift $z \simeq 0.049$ (Disney et al., 1974) that has been detected at VHE (H. E. S. S. Collaboration et al., 2015). It is the only TeV BL Lac object with a detected kpc-scale X-ray jet (Kaufmann et al., 2013). VHE data in combination with the X-ray and high-energy (HE, 0.1 – 300 GeV) γ-ray observations with Fermi-LAT, revealed an unexpected broad high-energy hump, spanning more than nine orders of magnitude in energy (from X-rays to TeV γ-rays). Petropoulou et al. (2017) demonstrated that the superposition of different emission components related to photohadronic interactions in the blazar core can explain the broad high-energy component of Ap Librae without invoking external radiation fields or particle acceleration at kpc scales (for large-scale jet scenarios, see Section 6 and, e.g.,; Zacharias and Wagner, 2016; Roychowdhury et al., 2022).

We adopt Model A from Petropoulou et al. (2017) (see in Figure 3A) to simulate spectra for HEX-P, assuming a 50 ks exposure. The model predicts a broadband X-ray spectrum with leptonic and hadronic contributions in the energy range probed by HEX-P. More specifically, inverse Compton scattered (ICS) emission by accelerated electrons in the jet contributes mostly at hard X-rays (> 10 keV), while synchrotron emission from secondary leptons produced in a hadronic-initiated cascade is dominating in soft X-rays. The simulation results are presented in the Figure 3B. The residuals of a power-law fit to the broadband spectrum have some structure which is improved when the spectrum is modeled with a tabulated leptohadronic model. In the latter case the statistical improvement is of the order of 100 using χ^2 or c-statistics for 5,800 degrees of freedom (unbinned data). Moreover, the residuals at 2 keV, where the spectral break is expected, are reduced in the leptohadronic model. We caution, however, that similar spectral breaks may also occur in a purely leptonic scenario, at the transition from SSC to EC emission, if a sufficiently dense external radiation field exists.

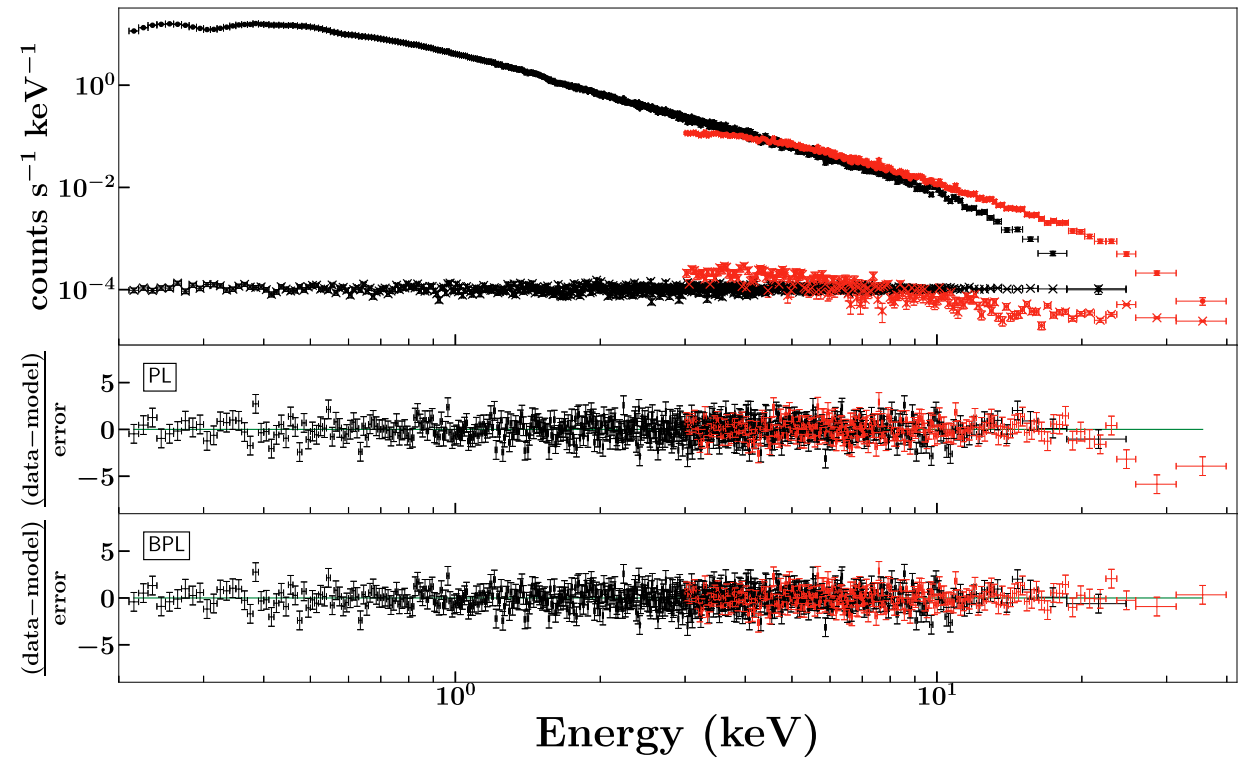

FIGURE 2
Simulated 100 ks observation of PKS 2155−304 with the LET (black data points) and the HET (red data points) assuming a broken power-law energy distribution of the underlying emission, with a break happening at ~20 keV. The top panel also shows the background levels of the LET and the HET. The bottom panels show the residuals for a power-law and a broken power-law model. The low background of the HET would enable us to sample the distribution up to $E \sim 40$ keV, hence disentangling the presence/absence of such a break at a ~5σ level. The higher NuSTAR background would not allow us to detect anything beyond $E \sim 20$ keV for such a soft spectrum, even for a 1 Ms exposure.

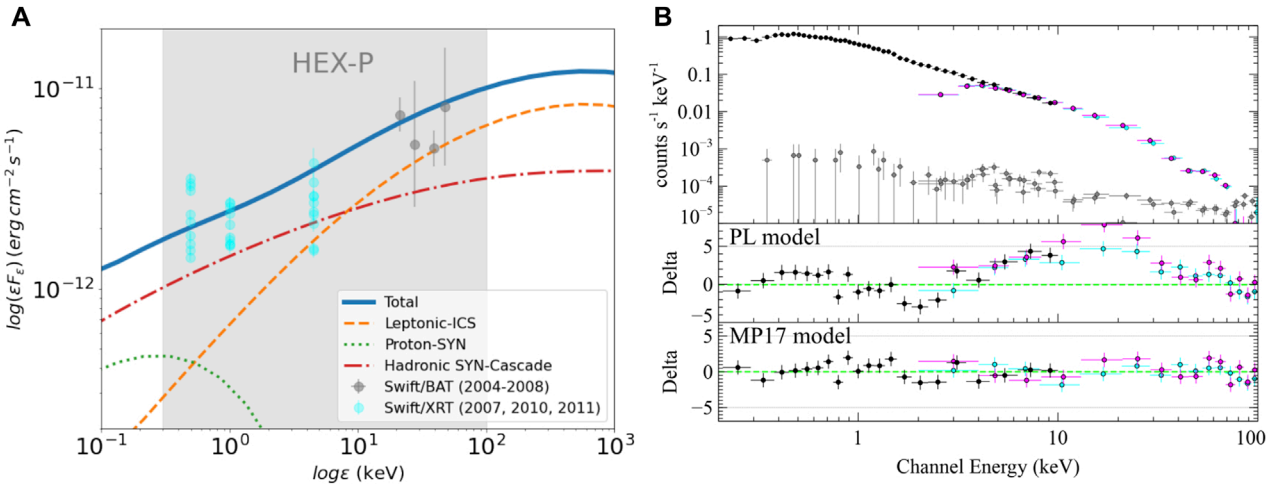

FIGURE 3
(A): Theoretical spectrum for the core emission of Ap Librae from Petropoulou et al. (2017) showing hadronic and leptonic contributions in the 0.2–100 keV range. Colored markers show non-simultaneous observations in soft and hard X-rays obtained with Swift/XRT and Swift/BAT, respectively. A smooth spectral break is evident at ~2 keV due to the onset of leptonic inverse Compton scatter (ICS) over the hadronic synchrotron (SYN) cascade emission. **(B)**: Simulated spectrum of Ap Librae for 50 ks exposure with HEX-P based on the theoretical spectrum shown on the left (top); background contribution is shown with gray shaded points. LET data are shown in black. Magenta and cyan colors correspond to the two high-energy detectors. Residual plots (i.e., (data-model)/error) of a power-law fit (middle) and a fit with a tabulated leptohadronic model (bottom) to the simulated spectrum. The residuals indicate that the power law model is disfavored.

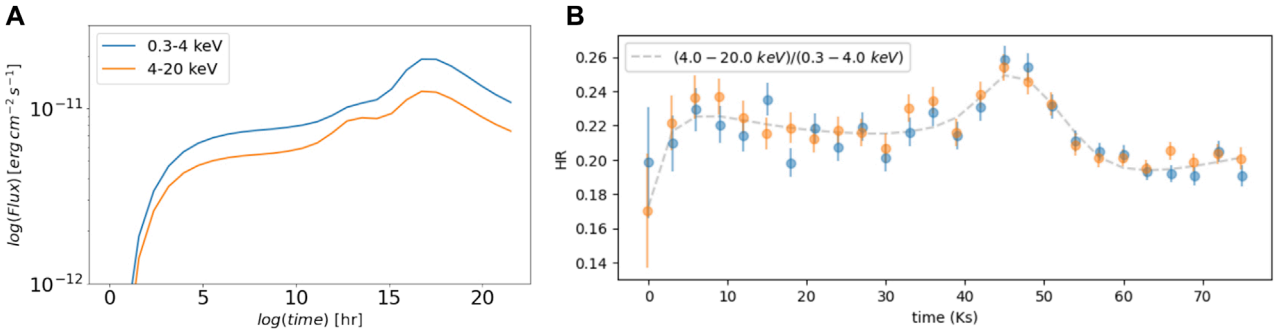

FIGURE 4
(A): Theoretical soft (0.3–4 keV) and hard (4–20 keV) X-ray light curves of a hypothetical flare from Ap Librae with a total duration of 21 h. **(B)**: Evolution of the hardness ratio (HR) during the flare. The HR evolution based on the tabulated model is shown with dashed line, while the results of two simulations are overplotted with colored markers. Each point is obtained assuming a 3 ks observation with HEX-P.

To demonstrate also the capabilities of HEX-P in detecting spectral changes during the course of an X-ray flare, we simulate a ~1-day long flare based on Model A of Petropoulou et al. (2017) by introducing variations in the injection rate of accelerated electrons and protons in the blazar core. The injection rate of both particle species is modeled with a Lorentzian as a function of time. The applied changes in the proton injection rate lag behind the variations in the electron injection rate by ~3 hr. As a result, we expect to see first an increase in the hard X-ray flux, followed by an increase in softer X-rays where the hadronic cascade emission dominates (see left panel in Figure 3). The theoretical light curves of the flare in soft and hard X-rays are presented in the Figure 4A. We simulate 27 HEX-P spectra, 3 ks exposures each, and compute the hardness ratio (HR), defined as the ratio of counts in the 4–20 keV and 0.3–4 keV ranges. In Figure 4 we show the evolution of HR with time for two different simulations (blue and orange markers) that illustrate the statistical variance of the HR. Both simulations recover the expected changes in the HR shown by the dashed line.

4.2 Multimessenger follow-up: cosmics rays and neutrinos

Cosmic rays were first detected at the beginning of the 20th century (Wulf, 1909; Hess, 1912; Pacini, 1912), yet, more than 100 years later, the sources of the high and ultra-high energy cosmic rays remain unclear. Since protons are deflected in magnetic fields, they are not reliable tracers of their origin. Neutrinos that are produced in proton-proton and proton-photon interactions travel in a straight path, but are much harder to detect.

Blazars and AGN have long been suspected to be neutrino emitters. Material in the accretion disk and in the vicinity of the supermassive black hole includes partially or fully ionized gas, which is available for injection into the relativistic outflows. Protons in the jet can interact with photons from a stationary photon field (e.g., thermal UV emission from the disk), and produce neutral and charged pions. Charged pions decay into several products including several neutrinos, while neutral pions produce high-energy photons, detectable by HEX-P. These photo-pion processes are expected to happen in AGN jets (Biermann and Strittmatter, 1987; Mannheim et al., 1992; Mannheim, 1993) and AGN cores (Eichler, 1979; Berezinskii and Ginzburg, 1981; Protheroe and Kazanas, 1983; Begelman et al., 1990; Stecker et al., 1991). The photo-hadronic interactions likely responsible for the neutrino production in blazar jets inevitably lead to the development of electromagnetic cascades. These are initiated by synchrotron or inverse-Compton scattering by secondary electron-positron pairs produced in photo-pion and Bethe-Heitler pair production processes, and the subsequent decay of charged and neutral pions and muons. The radiative output of these cascades is expected to peak in the hard X-ray – soft γ-ray band (e.g., Petropoulou and Mastichiadis, 2015; Keivani et al., 2018; Murase et al., 2018; Gao et al., 2019; Zacharias, 2021).

Follow-up of IceCube neutrino alerts has been promising for identifying the source of astrophysical neutrinos and therefore cosmic rays. The associations of blazars with VHE neutrino events detected by IceCube have attracted much attention in the recent literature, with increasing evidence pointing towards blazars being responsible for at least part of the IceCube VHE neutrino flux (e.g., Krauß et al., 2014; Kadler et al., 2016; Garrappa et al., 2019; Plavin et al., 2020; Buson et al., 2022; Plavin et al., 2022). In 2017, a high-energy IceCube event (IceCube-170922A) was found in positional and temporal coincidence with a blazar flare from TXS 0506 + 056 (IceCube Collaboration et al., 2018), following the previous, lower-confidence coincidence of a PeV neutrino event and a blazar flare (Kadler et al., 2016). Surprisingly, an earlier neutrino flare consistent with the position of TXS 0506 + 056 between September 2014 and March 2015 is not accompanied by a γ-ray flare. In TXS 0506 + 056, X-ray observations in the soft and hard X-ray band were crucial in constraining the hadronic contribution in order to determine that the source is a likely neutrino counterpart. These cascading signatures were studied in detail for TXS 0506 + 056 by Reimer et al. (2019), who used the measured VHE neutrino flux from the neutrino flare coincident with the direction of TXS 0506 + 056 in 2014–2015 (IceCube Collaboration et al., 2018) to constrain the source parameters of the photo-hadronic interactions leading to the neutrino production. A crucial parameter in these calculations is the maximum optical depth to $\gamma\gamma$ absorption within the source (typically peaking at TeV – PeV γ-ray energies), which determines the intensity of the cascades. In this case, the hadronic contributions

to the electromagnetic SED were found to be small, but consistent with the neutrino detection. Such small hadronic contributions are generally expected (Krauß et al., 2018), as electrons and positrons are much lighter, they are easier to accelerate and we therefore expect a high fraction of leptonic emission from AGN jets. The soft X-ray emission in the 2–10 keV band can be associated with either the synchrotron peak or the high-energy peak, depending on the peak frequencies. The purely leptonic synchrotron peak does not provide any information about hadronic fluxes. Only for the most extreme high-peaked blazars does the hard X-ray band not fall on the high-energy peak. In order to reliably constrain the contributions to the high-energy peak from pion cascades, it is necessary to have data in the hard X-ray band, which can only be provided by HEX-P with high angular resolution.

Previous detections of possible blazar counterparts were followed by the detection of possible Seyfert AGN counterparts, that can only be identified in the X-ray band: IceCube-190331A (Krauß et al., 2020) and the recently discovered neutrino source NGC 1068 (IceCube Collaboration et al., 2022). X-ray follow-up of likely-cosmic neutrino alerts has thus proven its utility for identifying possible neutrino counterparts, and most importantly for measuring hadronic contributions to the high-energy emission. HEX-P has a response rate of the order of 1 day (see Madsen et al., 2023). While we may detect neutrino from sources in quiesence, a short flare lasting less than a day or week does not increase the fluence of the source significantly to explain the neutrino event. As only the total flare fluence is relevant, sources in quiescence or long-lasting outbursts are the most promising source of neutrinos from blazars (Kreter et al., 2020b). The response time to triggers from HEX-P is therefore well suited to perform multimessenger follow-up observations.

Blazars have been ruled out as the dominant source of IceCube neutrino events in the TeV energy band through stacking analyses (e.g., Hooper et al., 2019). Blazars, especially BL Lacs are expected to produce neutrinos in the energy range of PeV to EeV (e.g., Murase et al., 2014; Padovani et al., 2015). These are energies that will be covered by the Askaryan Radio Array (ARA; Allison et al., 2016), currently under construction, as well as the IceCube-Gen 2 detector (Grant et al., 2019). IceCube Gen 2 with a 8 cubic kilometer volume is expected to be completed in 2032, which would coincide with the expected start of the HEX-P mission.

HEX-P will identify possible neutrino emitters and constrain the fluxes and emission mechanisms. One of the main challenges of neutrino follow-up is the large uncertainty regions of both cascade and track events. Track events are more promising for a direct identification of a counterpart source due to their smaller angular uncertainties, $\gtrsim 0.5°$. This currently requires Swift-XRT tiling observations with at least 7 pointings to fully cover the uncertainty area. This can often be reduced by using knowledge of previously catalogued X-ray sources. eROSITA will be crucial in providing a pre-identification of potential counterparts. HEX-P has a field of view of $\approx 13' \times 13'$. This will allow follow-up of known brighter X-ray sources in only a few pointings.

In order to test whether HEX-P observations are able to distinguish between a single power-law and the curved up-turns expected from proton-induced cascades, we performed detailed simulations. Three model cascade spectra (synchrotron-supported cascades) from Figure 12 of Reimer et al. (2019) (for $\tau_{\gamma\gamma}^{\max} = 1, 10$, and 100) were used as input to simulate 50 ks observations with HEX-P, which were subsequently fitted with both a single power-law and a broken power-law model. An example for $\tau_{\gamma\gamma}^{\max} = 10$ is shown in Figure 5. In all three cases, a single power-law could clearly be rejected, while a broken power-law was strongly preferred. Although this is not the only possible interpretation for such upturns, HEX-P can reveal and constrain this expected feature of the proton-induced cascades associated with photo-pion neutrino production.

4.3 Variability studies of blazars

Variability is a defining feature of all blazar subclasses, and studies have been conducted across the entire electromagnetic spectrum for many years, both with a focus on long-term (weeks to years) as well as short-term (days to hours) time scales. It is increasingly recognized that simultaneous broadband variability study is crucial to understand blazar physics. But the sample sizes of these studies depend largely on monitoring capabilities in the different energy bands. In the soft X-rays, monitoring campaigns can be performed for certain objects with Swift/XRT (Giommi et al., 2019; 2021), while observations with, e.g., XMM-Newton enable investigation of variability on time scales of hours (e.g., Zhang et al., 2006; Devanand et al., 2022; Noel et al., 2022). Long-term monitoring in the hard X-ray range is possible with Swift/BAT and MAXI (and in the past with RXTE), though, only for the brightest blazars. Variability studies above 10 keV on intraday time scales have been performed with RXTE (Wang et al., 2018) and later NuSTAR (Bhatta et al., 2018). Since no existing X-ray telescopes have sensitive broadband capabilities, simultaneous coverage of soft to hard X-ray variability has to be performed by carefully coordinating multiple X-ray telescopes pointing, which has only been arranged for a small number of observations.

The combination of high sensitivity and time resolution on the order of milliseconds and up to 80 keV will enable HEX-P to probe rapid variability, i.e., fluctuations within several minutes, at hard X-ray energies for a sample of bright blazars, which has not been feasible so far. In particular, we will be able to probe HSPs, for which minute timescale variability has been seen in gamma-rays and which could become evident only in hard-X-rays, since produced by higher-energy electrons, or a hardening at high energies as the result of the harder emission of freshly accelerated electrons on top of a more persistent, softer component.

In the case of FSRQs, HEX-P follow-up observations of flaring blazars will yield an unprecedented view up to 80 keV, i.e., full coverage of the rising half of the high-energy hump, and enable time-resolved spectral studies, which might be able to track changes in the high-energy emission related to, e.g., a change from SSC to EC emission over the course of a flaring event. This part of the spectrum can be a mixture of SSC and EC under the leptonic scenario, while under the hadronic scenario it may consist of SSC, hadronic cascades, EC, or proton synchrotron (Böttcher et al., 2013; Cerruti et al., 2015; Zhang et al., 2016). Theoretical studies have shown that these radiation processes can have different variability patterns, which can lead to distinguishable spectral and temporal signatures in the broadband X-rays. For instance, in the leptonic model EC often peaks at higher energy than SSC, thus the X-ray band can become dominated by a softer SSC spectrum from

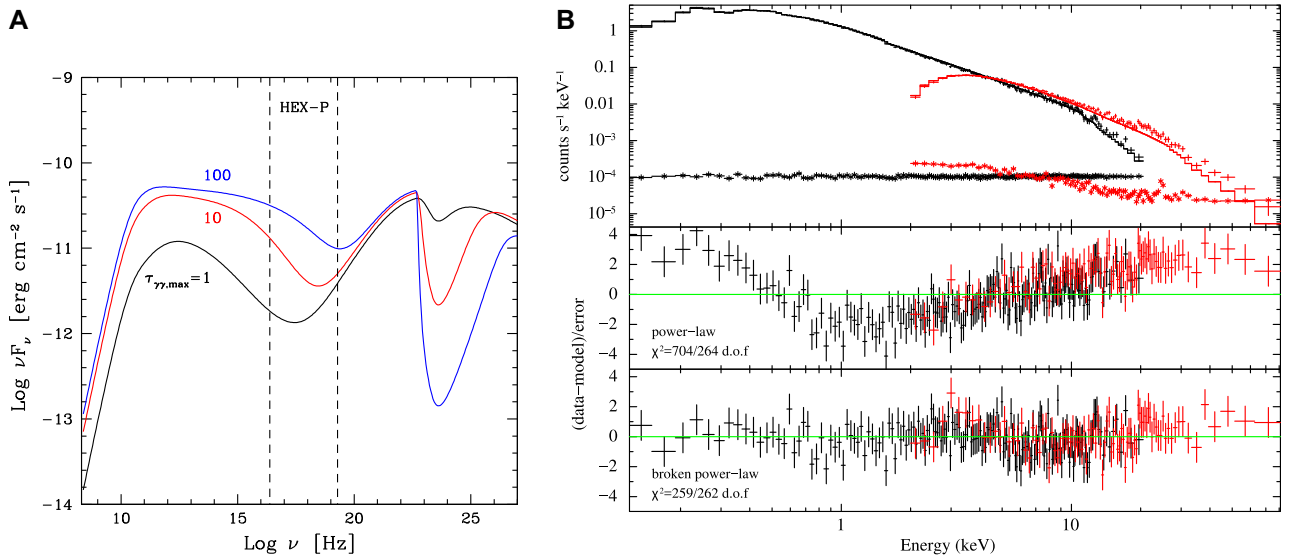

FIGURE 5
(A): Theoretical SEDs of TXS 0506 + 056 (including EBL absorption) calculated from simulations of photo-pion induced synchrotron-supported cascades, for values of $\tau_{\gamma\gamma}^{max}$ = 1,10 and 100; based on Figure 12 of Reimer et al. (2019). Spectral breaks are present in the HEX-P band. **(B)**: Simulated 50-ks observation of TXS 0506 + 056 for the model spectrum with $\tau_{\gamma\gamma}^{max}$ = 10 (red line in left panel). LET data are shown in black, HET in red. The background contribution is also shown in the upper plot. The spectrum is fitted with pure power-law and broken power-law models. The residuals indicate that the broken power-law is clearly preferred.

higher-energy electrons (thus more variable) over a harder EC component by lower-energy electrons, leading to a "softer-when-brighter" behavior (see e.g., Ghisellini et al., 1999; Diltz et al., 2015; Zhang et al., 2015). Simultaneous broadband X-ray variability can therefore track the transition from SSC to EC, as well as unveil possible bulk-compton emission components, which are expected to be transient (Celotti et al., 2007). They can thus probe the underlying particle evolution, and put constraints on the origin of SSC and EC emissions.

Observations have shown that blazars of all types (low, intermediate or high-synchrotron-peaked objects) may experience epochs of extreme particle acceleration, resulting in its synchrotron peak shifting into or across the X-ray band. Most dramatic events have been shown for example, by Mkn 501 in 1997 (Pian et al., 1998; Tavecchio et al., 2001), 1ES 1959 + 650 in 2002 (Krawczynski et al., 2004) and more recently, again by Mkn 501 (Aliu et al., 2016; MAGIC Collaboration et al., 2020), Mkn 421 (Tramacere et al., 2009; MAGIC Collaboration et al., 2020), PKS 2005−489 (Tagliaferri et al., 2001; Chase et al., 2023) and 1ES 1215 + 303 (Valverde et al., 2020). Such phenomena are often referred to as the peak shift. The physical cause is generally understood as the emerging of a new hard emission component from freshly accelerated electrons, injected by a new dissipation event. The mechanism and location of this acceleration are instead still uncertain, being debated among shock acceleration (either in internal shocks or a standing shock), magnetic reconnection and/or hadronic origins (Böttcher et al., 2013; Zhang H. et al., 2022). Due to the significant spectral changes, observing these events needs broadband coverage. Temporal slicing of the SED evolution is therefore important to elucidate the formation of such extreme physical conditions. In Figure 6 we show as an example of a simulated magnetic reconnection event for a high-peaked BL Lac object using the model of Zhang Z. et al. (2021). With very good broadband sensitivity and timing capability, HEX-P can track the peak shifts and spectral variations in greater detail than previously possible, revealing the physical driver of such extreme particle acceleration and probe potential hadronic origins. As such, HEX-P will serve as a space-based time domain astronomy instrument; a field that has been identified as one of the key research topics in the Astro2020 decadal survey[2] (National Academies of Sciences, Engineering, and Medicine, 2021).

For high-peaked BL Lac objects, spectral changes have been observed during flares, during which the spectrum often becomes harder when the source gets brighter. The study of light curves covering different energy ranges can reveal the existence of lags, which are indicators of the efficiency of the underlying acceleration and cooling processes. Interestingly, these lags are not consistent: for example, the well-studied source Mrk 421 has shown both soft and hard lags at different times, without, so far, a consistent pattern (Zhang et al., 2010; Kapanadze et al., 2016; Noel et al., 2022). HEX-P will be an essential instrument for these studies, in particular for flare follow-up observations, as it covers both the soft and hard X-ray range with high sensitivity.

One key discovery in the last decades has been flux variations close to or below the light-crossing time scale of the super-massive black hole (SMBH, Aharonian et al., 2007b; Aleksić et al., 2014b; Ackermann et al., 2016b), which revealed extreme particle acceleration in very localized regions. These rapid flux variations

2 https://cor.gsfc.nasa.gov/Astro2020/26141.pdf

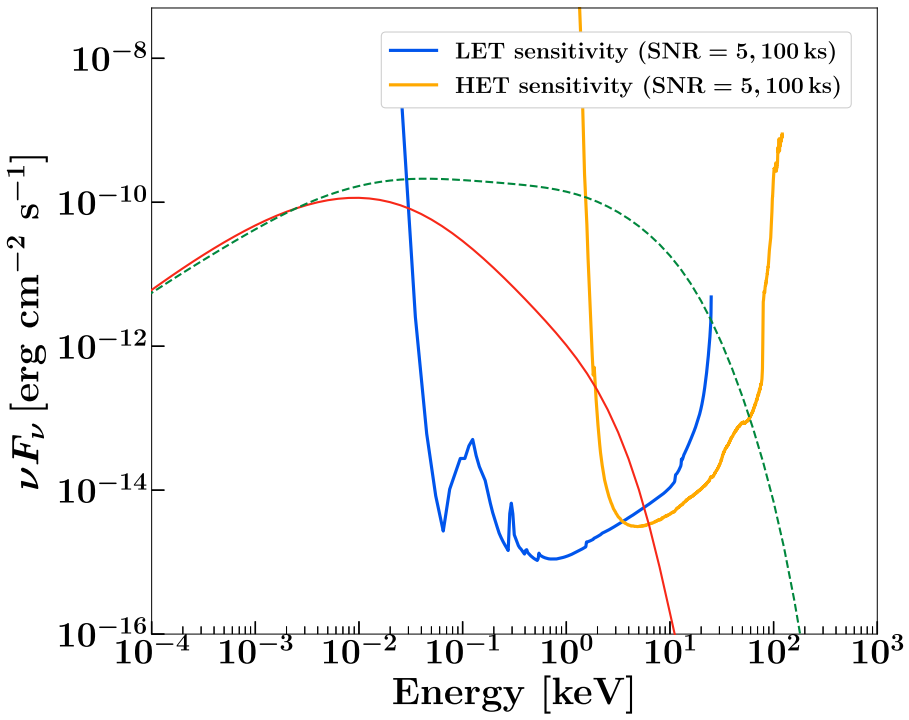

FIGURE 6
Simulated synchrotron peak of a high-peaked BL Lac object in quiet state (red line) versus the shifted synchrotron peak from the same source during flaring activity (dashed green line). Both the quiescent and the flaring state are produced by the magnetic reconnection in the same current sheet using the numerical simulation from Zhang H. et al. (2021). Both the quiescent and flaring state spectra result from plasmoids in the magnetic reconnection region, which has a fixed amount of initial magnetic energy. However, the flare is due to a major plasmoid merger event, which leads to significant dissipation of magnetic energy and efficient acceleration of nonthermal particles. The newly accelerated particles reach a much higher energy and harder spectrum than particles in other plasmoids, producing a peak shift. The sensitivity curves for both the LET and HET of HEX-P illustrate the excellent capability of the X-ray telescope to precisely measure changes in the position and shape of the synchrotron peak of blazars.

provide invaluable information about the particle acceleration mechanisms in jets and are broadly connected to the capability of the jet of accelerating protons and producing neutrinos. Observed, so far, in a few exceptional flares, such rapid gamma-ray variability has shown the limitations of standard emission models (Begelman et al., 2008; Ghisellini and Tavecchio, 2008; H. E. S. S. Collaboration et al., 2019) and prompted more sophisticated scenarios (see, e.g., Aharonian et al., 2017), such as turbulent, multi-zone emission (Marscher, 2014), magnetic reconnection inside the jet or in the jet launching region (see, e.g., Cerutti et al., 2012; Giannios, 2013; Kadowaki et al., 2015; Christie et al., 2019; Zhang H. et al., 2021), jet-star interactions (Barkov et al., 2012), or acceleration in the black-hole magnetosphere (Levinson and Rieger, 2011). These scenarios predict different signatures in both spectral and temporal behaviors, but require broadband time-domain observations to further understand the jet physics. HEX-P would be able to detect a break in the broad band X-ray spectra that is predicted by some models (jet-star interaction) due to the emergence of an additional synchrotron component, which would rise in the hard X-ray band. Alternatively, simulations of processes dominated by magnetic reconnection and turbulence predict distinct temporal patterns in the X-ray band (e.g., Zhang H. et al., 2020; Zhang H. et al., 2023). Those require highly resolved timing data across the full X-ray band in order to be detected, which HEX-P would be able to provide. At VHE, CTAO is expected to probe broadband (sub-TeV to >100 TeV) minute-scale variability in several other sources with less exceptional flares, as well as on sub-minute timescales for events like the one detected from the blazar PKS 2155–304 in 2006 (Aharonian et al., 2007b; Sol et al., 2013).

Current theories suggest that such short timescale variability should also be present in X-ray synchrotron emission, but so far the few simultaneous data show that, even when tightly correlated, the (soft) X-ray variations have typically been of much lower amplitude than at VHE (Aharonian et al., 2009a) and in general on longer timescales (tens of minutes). While X-ray synchrotron emission may suffer from a stronger dilution of variable flux by brighter persistent emission, a key issue in observation is that current X-ray instruments lack the same broadband sensitivity as the VHE telescopes. The synchrotron emission of the rapidly-variable TeV electrons could peak at higher X-ray energies, in a band not yet investigated because of the lack of large collection areas above 5–8 keV. Additionally, several models, such as magnetic reconnection, predict distinct variability patterns in soft and hard X-ray bands (Figure 7), which require broadband coverage with good temporal sensitivity (Zhang H. et al., 2021). HEX-P will be able to probe, for the first time, such short timescales simultaneously at both soft and hard X-ray energies.

Another aspect is the different inter-band variability among X-ray bands. The interplay between acceleration, cooling, and

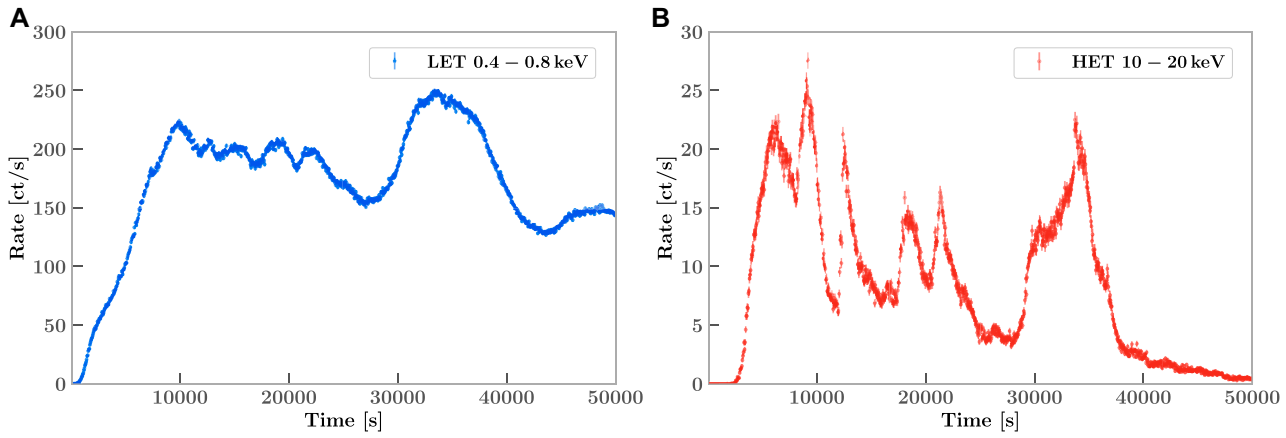

FIGURE 7
Simulated 50 ks light curves as detected by the LET [0.4 – 0.8 keV, **(A)**] and by the HET [10 – 20 keV, **(B)**] of a flaring blazar (such as Mrk 421) based on the magnetic reconnection model of Zhang H. et al. (2021). The soft and hard X-ray bands show distinct flaring patterns, which can be detected by HEX-P to identify reconnection and constrain its physical conditions.

escape timescales of electrons at a shock front or dissipation region can produce different and characteristic patterns in the variation of spectral index vs. flux. For example, such variations can have different "hysteresis loops" (e.g., Kirk et al., 1998; Kirk and Mastichiadis, 1999; Böttcher and Chiang, 2002; Abeysekara et al., 2017; Wang et al., 2018; Böttcher, 2019; Chandra et al., 2021). The timescales of the flux rise and fall provide information on the acceleration mechanisms, if nearly instantaneous or progressive, and these could be different between hard and soft X-rays. So far, such studies have been limited to a few objects observed during large flares over 1 decade in energy. HEX-P will be able to investigate these relations over more than 2 decades in energy, and at lower fluxes and/or shorter timescales (see Madsen et al., 2023, for HEX-P repointing capabilities).

4.4 Synergies with other telescopes

4.4.1 CTAO

In HSP blazars, electrons accelerated to TeV energies emit by synchrotron typically in the X-ray band and by SSC in the VHE band. The possibility to perform extended simultaneous X-ray–VHE observations therefore provides a powerful diagnostic tool to understand particle acceleration and emission, allowing the evolution of a single freshly-accelerated electron population to be sampled by two different emission mechanisms. This is especially important during flares with hour and sub-hour variability. To perform such studies, an X-ray satellite must have a large visibility window at any given epoch for most of the sky and must be able to point in an antisolar direction. A large visibility window increases the chance that a source can be observed when it is found flaring, while the antisolar direction enables simultaneous observations at night with ground-based telescopes when the target culminates at the highest altitudes above the horizon, and thus can be followed by Cherenkov telescopes continuously under the best conditions for at least several hours. Such studies are not possible with XMM-Newton due to its strong solar panel constraints (Costamante, 2004). Chandra showed the potential for such studies with the detection of large flares by PKS 2155–304 in 2006, albeit with a much lower collecting area than XMM-Newon (Aharonian et al., 2009a). At an L1 orbit, HEX-P will fulfill all these operational requirements, allowing us to perform such studies for the first time with a sensitive, flagship-class X-ray telescope.

4.4.2 IXPE & COSI

High-energy polarization, a recently opened new window to the Universe, will play a very important role in future efforts to understand the matter content and high-energy emission processes in jets. In a leptohadronic scenario, emission at the trough can be dominated either by proton synchrotron or synchrotron from secondaries (Zhang H. et al., 2019), and hence it can be highly polarized in the X-ray and MeV bands. Recent IXPE observations have demonstrated that determining the shape of the X-ray spectrum is crucial to correctly recover the polarization parameters, regardless if X-rays are part of the synchrotron or high-energy spectrum (Ehlert et al., 2022; Di Gesu et al., 2022; Liodakis et al., 2022; Middei et al., 2023a; b). This is particularly important for sources like TXS 0506 + 056, i.e., ISP blazars, where the X-rays lie in the trough between the low- and high-energy humps of the SED (Peirson et al., 2022; 2023). Additionally, IceCube observations of TXS 0506 + 056 suggest that the hadronic spectral component, potentially peaking in the MeV band, can be variable (IceCube Collaboration et al., 2018). Therefore, both the spectral shape and variability of the hadronic contribution can have significant effects on the X-ray to MeV polarization degree and angle (Zhang et al., 2016), therefore requiring broadband coverage in X-ray and MeV bands. However, IXPE and future X-ray polarimeters, like the enhanced X-ray Timing and Polarimetry mission (eXTP), have limited energy ranges. For example, IXPE is sensitive in the 2–8 keV band. On the other hand, future MeV missions, such as the Compton Spectrometer and Imager (COSI, Tomsick et al., 2019), observe in the MeV band (0.2 – 5 MeV), which cannot fully capture the rising part of the hadronic component (in the X-ray bands) and its variability. In the X-ray band, the

spectrum of the HSP blazars often shows significant curvature up to tens of keV, often modeled with a log-parabola model (see, Donato et al., 2005; Bhatta et al., 2018; Middei et al., 2022). For some ISP blazars the spectrum is often characterized best with the sum of a soft and a hard powerlaw or a power law with an exponential cut-off and a hard powerlaw. HEX-P's broad energy range can uniquely allow for the accurate modeling of the broadband X-ray spectral shape and transition region in a large number of blazars, paving the way for detecting polarization from the jet's high-energy component. Coordinated observations with missions current or future X-ray polarimeters (e.g., IXPE, eXTP etc.), and future MeV missions (COSI, ASTROGAM, AMEGO-X; De Angelis et al., 2017; Tomsick et al., 2019; Caputo et al., 2022) will enable measurements that can pinpoint or rule out hadronic processes by comparing the predicted and observed polarization degrees.

4.4.3 SPT (CMB)

As discussed in Section 4.3, truly simultaneous, broad-band monitoring is key in unraveling blazar jets structure as well as the emission mechanisms and thus particle acceleration processes operating in blazars. One important spectral band is the millimeter regime, where, for the high-luminosity (FSRQ-type) blazars, the low-energy part of the SED peaks: blazars are generally strong mm sources and their mm emission can even be used to find counterparts of un-identified Fermi-LAT gamma-ray sources (see e.g., Zhang L. et al., 2022). This is the spectral regime where the blazar synchrotron emission is believed to become optically thin, and thus reveals the entire volume of the jet rather than its surface.

Time-resolved blazar studies in the mm band were usually conducted by individual radio/mm telescopes, generally dedicated to a single object at a time, and clearly revealed the large amplitude variability on time scales of days. Such studies also revealed a strong degree of polarization (in some cases, more than 20%), which is key in determining the orientation and uniformity of the magnetic field. Current and planned Cosmic Microwave Background (CMB) facilities will provide such data as a part of the CMB measurements: while the astrophysical sources are "noise" for CMB maps, the data – obtained "for free" – are very valuable for studies of such sources. This holds particularly true for blazars, since the current and planned CMB facilities collect data by continually scanning relatively large regions of the sky, and subsequently combining the data to form sky maps. Such time-resolved data result, generally, in a relatively well-sampled time series for many sources. Importantly, these CMB facilities, in addition to flux, also collect polarization information, thus providing time series in both intensity and polarization. One recent "proof of concept" example is observations of the blazar PKS 2326–502 with the South Pole Telescope (SPT; Hood et al., 2023) which revealed correlated flaring in the mm (at 150 GHz) and GeV-range gamma-ray bands, measured with the Fermi-LAT. For bright blazars in the millimeter band, SPT will provide a time-resolved flux and polarization time series in the SPT bands. Correlating such time series with hard X-ray flux will provide additional constraints on the origin of hard X-ray flux in blazars. Moreover, for HSP objects, the combination of SPT, HEX-P, and other observatories at IR/optical wavelengths would allow us to sample the energy distribution of the accelerated particles from the lowest to the highest energies, simultaneously sampling the SED over 5 orders of magnitude and informing us about the full particle populations in the jet.

The next-generation CMB facility is known as "CMB Stage 4" and is planned for deployment in the early 2030s. This matches well with the proposed timeline for HEX-P. CMB Stage 4, described in Carlstrom et al. (2019) and Abazajian et al. (2022)[3] is significantly more sensitive than the current CMB facilities and, in its full form, will cover well over 50% of the sky. The facility will have detectors sensitive over the range of 30 GHz–280 GHz. While the details of the instrumental sensitivity are still under development, it is expected that in 24 h worth of sky scanning, CMB Stage 4 should be able to measure a source flux of 30 milliJansky (5 σ). This complements the blazar studies undertaken with HEX-P *without altering the strategy of the anticipated CMB studies*, and such synergistic studies (with various classes of astrophysical sources, not just blazars) are already part of the instrument design and the data management plan.

5 Source classes (MeV blazars, extreme BL lacs, and masquerading BL lacs)

5.1 The accretion flow to jet power connection

Flat Spectrum Radio Quasars are defined as blazars with strong broad emission lines. They are generally associated with strong jet emission, peaking at low frequencies both in synchrotron and inverse Compton components. Similar to low-peaked BL Lacs, their high-energy component dominates the X-ray emission, particularly the rising section of the hump. Depending on redshift, different parts of this emission are mapped with specific telescopes: among the most widely used X-ray instruments, Swift/XRT, XMM-Newton and the Chandra X-ray Observatory map the softer X-ray emission (< 10 keV), while Swift/BAT reaches 500 keV, and INTEGRAL reaches 10 MeV (see e.g., Giommi et al., 2019; Marcotulli et al., 2022). NuSTAR provides a sort of "link", by covering the energy range between 3 and 80 keV (Ghisellini et al., 2019). The two instruments onboard HEX-P guarantee an energy range that can overlap with all X-ray telescopes currently available to the astronomical community. With a single observatory, the inverse Compton component of low-frequency peaked blazars, including FSRQs, can be mapped throughout cosmic time, by focusing on their evolution and possible variability, spanning across the whole inverse Compton emission of this AGN class. On the soft X-ray side, LET will be able to shed light on the amount of possible absorption or instrinsic breaks at soft energies. The nature of such a soft break is still under scrutiny, and the recent analysis performed on different samples of FSRQs do not allow us to constrain whether they are due to excess aborption or intrinsic jet features, such as peculiar energy distributions of the electrons involved in jets' high-energy emission (see e.g., Gaur et al., 2021, for a thorough discussion). The significant increase in sensitivity given by the LET and HET combination will likely make a difference in discriminating between the two possibilities. The HET instead will extend spectroscopic studies

3 https://cmb-s4.org/

currently done by Swift/XRT, Chandra and XMM-Newton up to significantly higher energies, getting simultaneously close to the inverse Compton peak. The wide spectral coverage will allow us for the first time to uniformly characterize this section of FSRQ SEDs, crucial for the study and interpretation of jet physics and emission processes.

Even though FSRQs have been known and studied for more than 60 years, many open questions remain about their relativistic jets: how do they relate to the accretion flow, whether their launching system can be associated with it, and how the accretion-jet system evolves accross cosmic time. The better insight on the electron energy distribution, and a better mapping of the spectral evolution of the inverse Compton emission in time will already be a significant advancement in relativistic jet physics. Nonetheless, HEX-P's wide energy coverage and deep sensitivity has the potential to make even bigger improvements on our knowledge.

The connection between accretion flow and the relativistic jet in blazars is in fact a key ingredient to understand the process behind jet launch and acceleration. Relativistic jets are generally associated with geometrically thick accretion flows when their launching mechanism is modelled: an accretion flow funnel close to the central black hole, along with a strong magnetic field, are effective ingredients to accelerate plasma along the polar direction (Tchekhovskoy et al., 2011). In contrast, a geometrically thin accretion disk has not historically been considered a solid basis for an effective jet collimation. FSRQs show that a relativistic jet can coexist with an optically thick, highly UV-luminous accretion flow, since they show a distinct and luminous optical-UV thermal continuum that cannot be justified with jet emission, with strong and broad emission lines, along with powerful relativistic jets. Such optical-UV features are most likely interpreted as coming from a geometrically thin, optically-thick accretion disk ionizing gas clouds in its vicinity (e.g., Padovani et al., 2017). Moreover, the direct correlation between jet and accretion power in blazars suggests a significant role in the jet launching process by the accretion disk, or at least in providing power for the overall process (Jolley and Kuncic, 2008; Ghisellini et al., 2014). The coexistence of these two structures is thus under deep scrutiny: coordinated multiwavelength observations of high-energy jet emission and optical-UV radiation from the disk are crucial to test the actual relation between disk and outflows. In particular, analogous to the cyclic X-ray binaries evolution, FSRQs might show variations in geometry and emission physics of the central part of their accretion flows, corresponding to jet launching or rebrightening. In case of an accretion rate fluctuation, a thin accretion disk might thicken towards its inner radii, providing a temporary funnel, allowing for significant magnetic field advection and ultimately accelerating a new emitting region in the relativistic jet. Coordinated fluctuations would also be expected during flux variations, and they would be easily identified during coordinated optical and X-ray monitoring. On the other hand, no thick component might be necessary: in this case, the launching mechanism might be different from what we currently expect, and this specific multiwavelength simultaneous or correlated variability would not be observed. Coordinated optical-UV and X-ray observations can thus provide unique insights into the most powerful engines in the Universe. HEX-P is crucial in this sense, being able to thoroughly map the jet emission profile and its evolution over a broad energy range. Changes in jet power or acceleration would be easily detectable thanks to changes in the inverse Compton profile, well explored by the combined effort of LET and HET.

A good knowledge of the emission profile of high-energy blazar SEDs is crucial to nail the connection between jet and accretion flow in these sources. A reliable representation of the median blazar SED is necessary to identify variations in the jet emission, possibly linked to accretion fluctuations. The current state-of-the-art is mainly focused at low redshift. Blazars with different jet powers are known to differ in their pre-peak inverse Compton slope and inverse Compton peak frequency. Even though the overall SED blazar shape is always characterized by the two prominent synchrotron and inverse Compton humps, their relative dominance and peak positions vary significantly depending on the jet power. Whether physically motivated or just an observing bias, blazars appear to peak at lower frequencies and have a harder X-ray spectrum when they are intrinsically more powerful. This has been tested among the known γ-ray detected blazars, that are mainly concentrated below $z \sim 3$, but a detailed study of the inverse Compton emission evolution across cosmic time is still incomplete. A significant limit is posed by the narrow X-ray coverage of the currently available sensitive X-ray observing facilities: hard X-rays are needed to explore the inverse Compton peak position, and no current telescope reaches deep enough to detect high redshift sources ($z > 3$). In this sense, HEX-P will be transformative. For the very first time, the astronomical community will have the possibility to explore the evolution of AGN high-energy jet emission. At $z > 3$, blazars appear to host among the most powerful jets known, with very high inverse Compton luminosities ($L_\gamma > 10^{47}$erg s^{-1}) and MeV-peaking inverse Compton humps. This is likely a selection bias: we are currently observing and classifying only the most powerful sources (Marcotulli et al., 2020; Sbarrato, 2021). The possibility to consistently study most of the pre-peak inverse Compton SED over a wide redshift range ($1 < z < 4$), offered by HEX-P, will probe inverse Compton evolution across cosmic time. Limited (in numbers) but self-consistent (in method) results could already be drawn from a 1 Ms wide-field survey (see Section 5.5). Figure 8 shows how the expected HEX-P sensitivity limits and energy ranges will allow a comprehensive study of the most powerful FSRQs over a large redshift range.

5.2 Supermassive black holes at the dawn of time

Due to their high luminosities, we are able to trace blazars, particularly FSRQs, back to the early Universe. The entire broadband spectrum of these objects is shifted towards lower energies, and because of their high-energy hump peaking in the MeV band, they have been coined "MeV blazars" (Bloemen et al., 1995). These sources are more luminous in the hard X-ray band (Sbarrato et al., 2012), and studies made use of the NuSTAR satellite to analyse and characterise the emission processes responsible for the high-energy hump, in combination with Fermi-LAT at gamma-ray energies (Sbarrato et al., 2013; Tagliaferri et al., 2015; Marcotulli et al., 2017; 2020). The most puzzling findings about SMBHs hosted by quasars in the early Universe is that some of them exceed one billion solar masses, detected out to redshift of $z > 7$ (Fan et al., 2001; Mortlock et al., 2011; Wu et al., 2015). Obviously, there is a bias

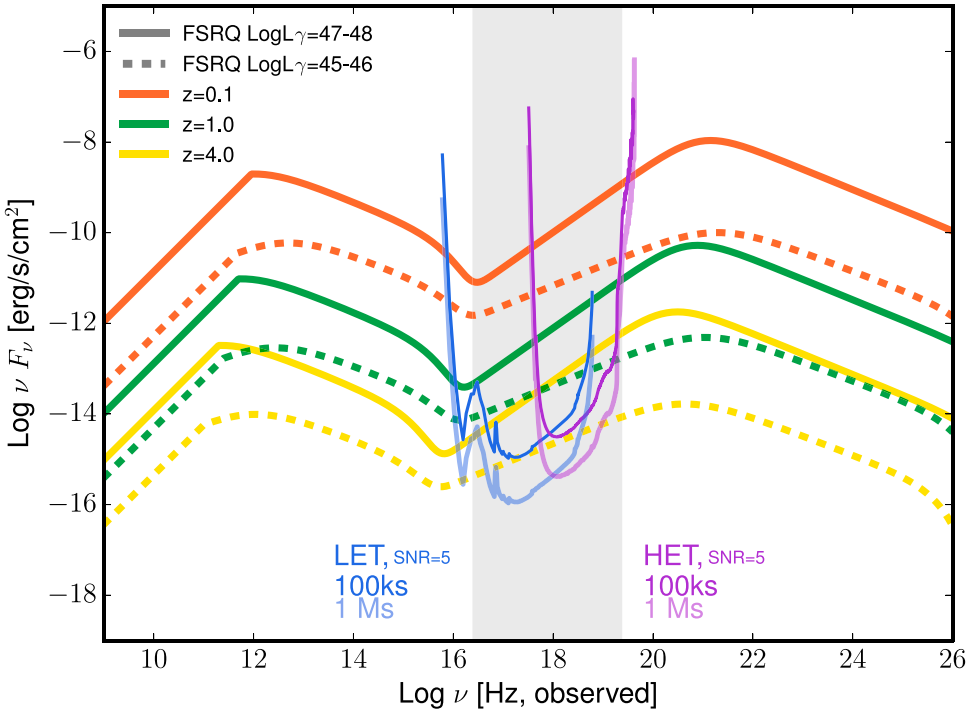

FIGURE 8
FSRQ SEDs with different powers and redshifts, compared with LET (blue) and HET (purple) differential sensitivities, calculated with 100 ks (thin, bright) and 1 Ms (thick, faint) exposures. The SEDs assume the Ghisellini et al. (2017) phenomenological models, corresponding to $L_\gamma = 10^{47} - 10^{48}$ erg s^{-1} (solid lines) and $L_\gamma = 10^{45} - 10^{46}$ erg s^{-1} (dashed lines). Different colours correspond to different redshifts. Note that the most powerful blazars will be easily detectable up to 80 keV and up to $z \sim 4$. HET detections will be more challenging for less powerful FSRQs or sources in a low jet state.

towards the most luminous objects being detected, but the discovery of such massive black holes questions our understanding of how SMBHs form and how fast they can grow. Current theories involve either the creation of ~100 $M_\odot$ BH seeds as remnants of Population III stars (Madau and Rees, 2001; Schneider et al., 2002), which then require sustained super-Eddington accretion growth periods (Begelman and Volonteri, 2017; Yang et al., 2020; Johnson and Upton Sanderbeck, 2022), or the direct collapse of gas into 10^4 – 10^6 $M_\odot$ SMBHs in pre-galactic discs or halos (e.g., Bromm and Loeb, 2003; Begelman et al., 2006; Lodato and Natarajan, 2006). Another hypothesis is the formation of massive BH seeds within star clusters with masses of ~1000 $M_\odot$, which then grow due to the copious supply of matter in the star cluster (Devecchi and Volonteri, 2009; Alexander and Natarajan, 2014).

A fraction of these SMBHs will power jets that, if pointing towards us, should appear as MeV blazars. In particular, the detection of these sources in the gamma-ray band is limited by the sensitivity of current instruments, paired with a very low flux due to the immense distances. Less than 30 high-redshift ($z \geq 2.5$) blazars have been detected at gamma-ray energies with *Fermi*-LAT (Acero et al., 2015; Ackermann et al., 2017; Liao et al., 2018; Abdollahi et al., 2020; Kreter et al., 2020a), with the most distant source having a redshift of $z = 4.72$. In addition, EBL absorption attenuates high-energy gamma-ray emission above ~ 10 GeV (H. E. S. S. Collaboration et al., 2013; Ackermann et al., 2017; Domínguez et al., 2023). The large majority of high-z blazar detections at gamma-ray energies were only possible due to flaring episodes (Paliya et al., 2019a; Kreter et al., 2020a), which biases our studies towards more variable sources. At X-ray energies, instruments like *ROSAT* and *Swift*/BAT have been able to perform unbiased all-sky surveys, but have a limited sensitivity. Pointing observatories like *Chandra*, *XMM-Newton*, and *NuSTAR* have been used to study a selected sample of high-redshift blazars (e.g., Bassett et al., 2004; Young et al., 2009; Ighina et al., 2019). In particular, *NuSTAR*, with its sensitivity reaching up to 80 keV, has significantly contributed to the study of high-z blazars by providing hard X-ray data that is essential to constrain the shape and peak of the high-energy hump of the blazars' SEDs (e.g., Marcotulli et al., 2017; Paliya et al., 2020; Middei et al., 2022). Similarly, HEX-P will enable us to continue studying blazars in the early Universe.

AGN create feedback mechanisms in their host galaxies and can be linked to their evolution (Silk and Rees, 1998). On large scales, jets influence their surroundings by creating shocks in the surrounding gas (Schoenmakers et al., 2000; Rawlings and Jarvis, 2004; Shabala et al., 2011; Raouf et al., 2017), leading to truncation of star formation. Studying AGN-galaxy co-evolution in the early Universe has been difficult and so far has only been done up to redshift $z = 4$ for jetted AGN (Poitevineau et al., 2023). Due to its superior sensitivity compared to current X-ray telescopes, HEX-P will detect sources with fluxes as low as 10^{-16} erg cm^{-2} s^{-1} Civano et al. (2023). With this sensitivity, and the anticipated survey area, we used the prediction on the source count distribution of blazars from Marcotulli et al. (2022) employing a density and a luminosity evolution model to predict how many MeV blazars

could be detected. This number ranges from 50 for the luminosity evolution and 1,000 for the density evolution (see Figure 11). This will include a large number of newly detected extragalactic objects, including high-redshift blazars. The discovery of new sources will be less biased towards the most luminous sources, and enable us to get a better understanding of the cosmic evolution of blazars (see Section 5.5), while hard X-ray data above 20 keV will help distinguish the different high-energy processes in blazar jets, and allow comparisons of local and early Universe objects.

5.3 Extreme BL lacs

Observations in the last 2 decades have shown that BL Lacs can reach much higher SED peak energies than previously thought, surpassing by 1–3 orders of magnitude or more the values of the bulk of the HSP population. They have been thus called *extreme BL Lacs* (Costamante et al., 2001). They come in two flavours: extreme synchrotron and extreme-TeV objects, depending on whether they show extreme peak energies in the synchrotron or gamma-ray emission. By convention, an HSP blazar starts to be called extreme if the ν_{peak} is above 1 keV or 1 TeV, respectively, but these sources have displayed peak energies in excess of 100 keV (both in flaring and quiescent states; Pian et al., 1998; Costamante et al., 2001) and 10 TeV (Aharonian et al., 2007a), respectively.

Conventional one-zone leptonic models (see also Section 4.1.1) struggle to model SEDs peaking at such high-energies, especially in gamma-rays. They generally require extreme conditions with very low magnetic fields, several orders of magnitude below equipartition, unusually hard electron distributions and very low radiative efficiency (Costamante et al., 2018; Biteau et al., 2020; Zech and Lemoine, 2021). The relation between extreme synchrotron and extreme TeV emission is still not well established: they should be correlated in a standard SSC scenario, but there are objects which are extreme in synchrotron but not in gamma-rays, and *vice versa*, although extreme-TeV sources do tend to display also extreme synchrotron peaks more often than the other way round (Biteau et al., 2020). Some objects show large peak variability, both in amplitude as well as in energy, with shifts by more than 3 orders of magnitude during flares (see, e.g., Mkn 501, Ahnen et al., 2018; MAGIC Collaboration et al., 2020). Others instead show rather steady extreme features over several years, a fact that could hint at the contribution of different mechanisms to the gamma-ray emission, in addition to inverse Compton emission by ultrarelativistic electrons (Biteau et al., 2020).

The location of the synchrotron peak in the SED and the slope of the spectrum around it are essential parameters to constrain the emission models and to study the origin of the peak itself (if due to cooling, escape, or the end of the accelerated particles' distribution). So far, this has been possible only for peaks up to 2 – 5 keV with great sensitivity, or up to 30 – 50 keV for only the brightest objects.

Thanks to the unique combination of broad-band coverage, low background, and large collecting area from 0.2 to 80 keV with a single observation, HEX-P is ideally suited to identify and study these objects: it can directly measure or constrain the peak emission at flux levels or timescales one to two orders of magnitude lower than any current instrument (see Figure 9).

In this respect, the synergy with the upcoming CTAO—which will bring a similar improvement of one to two orders of magnitude in sensitivity at multi-TeV energies—cannot be understated. Besides characterizing VHE spectra over a wide energy band, simultaneous observations can test if and when these are indeed the same electrons emitting by two different mechanisms (synchrotron and SSC), as indicated by the tight correlations observed in HSPs down to minute timescales in Mkn 421 (Maraschi et al., 1999; Fossati et al., 2008; Baloković et al., 2016; MAGIC Collaboration et al., 2021) and PKS 2155−304 (Aharonian et al., 2009a). CTAO and HEX-P coordinated observations will also test if the same relations that hold in extreme BL Lacs are observed in normal HSPs.

A crucial advancement enabled by HEX-P is in population studies of extreme blazars. Their overall luminosities tend to be low ($\sim 10^{44-45}$ erg s^{-1}) compared to regular HSPs, more or less in agreement with the blazar-sequence framework (Ghisellini et al., 1998; 2017). So far, they have only been found at low redshift (up to $z \sim 0.3$). However, it is not clear if this is an intrinsic characteristic or simply a bias due to the low fluxes and limited observations.

With 50 ks exposures, HEX-P can discover and characterize such sources down to a 2 – 10 keV flux of $F_{2-10\,\mathrm{keV}} = 10^{-13}$ erg cm^{-2}s^{-1} out to ~30 keV. For example, with a photon index Γ = 1.8, the 1-sigma error on the slope would be ±0.04 full band, and ±0.20 above 3 keV (vs. ±1.0 with NuSTAR, for the same exposure time—and twice the clock time given the inefficiency of NuSTAR's low-Earth orbit compared to HEX-P's L1 orbit). With Γ = 1.6 and $F_{2-10\,\mathrm{keV}} = 5 \times 10^{-14}$ erg cm^{-2}s^{-1}, an extreme BL Lac can still be detected up to ~20 keV with a slope uncertainty of ±0.08 full band and ±0.25 above 3 keV (compared to ±1.2 with NuSTAR). HEX-P can therefore discover and characterize sources similar to 1ES 1426 + 428 (i.e., $L \sim 10^{44}$ erg s^{-1}) down to a luminosity of 1×10^{43} erg/s, or up to z = 0.7.

For objects with peak fluxes around 10^{-12} erg cm^{-2}s^{-1}, HEX-P can also fully characterize the curvature of the synchrotron emission. For example, with a SED peaking at 30 keV and a curvature parameter $\beta = 0.2$ (typical of HSPs), HEX-P can constrain the peak energy to better than 30% and the curvature to within 10% (Figure 9).

CTAO is expected to discover many more TeV-emitting HSPs, as allowed by a 10-fold improvement in sensitivity at 1 TeV with respect to present arrays. Just from the planned CTAO extragalactic survey, which will cover ~25% of the sky, about 110–180 new detections are expected (Cherenkov Telescope Array Consortium et al., 2019), about 1/4 of which could be extreme-TeV according to the present number of extreme vs. standard objects among TeV-detected HSPs with known redshift (see e.g., Biteau et al., 2020; Costamante, 2020). Above a radio flux of 3.5 mJy at 1.4 GHz, the inferred surface density of $\sim 4.5 \times 10^{-3}$ deg^{-2} for extreme-synchrotron objects corresponds to a total number over the sky of ~200 (Biteau et al., 2020). Searches for these extreme blazars will benefit from the eROSITA all-sky survey. This survey is expected to have a point-source sensitivity of 6×10^{-15} erg cm^{-2} s^{-1} in the 0.2 – 2 keV band (Brunner et al., 2022), making it more than ten times deeper than the ROSAT all-sky survey (Boller et al., 2016). Additionally, eROSITA will offer enhanced sensitivity in the 2 – 5 keV band, enabling the identification of further extreme blazar candidates. This will be particularly advantageous for low-luminosity

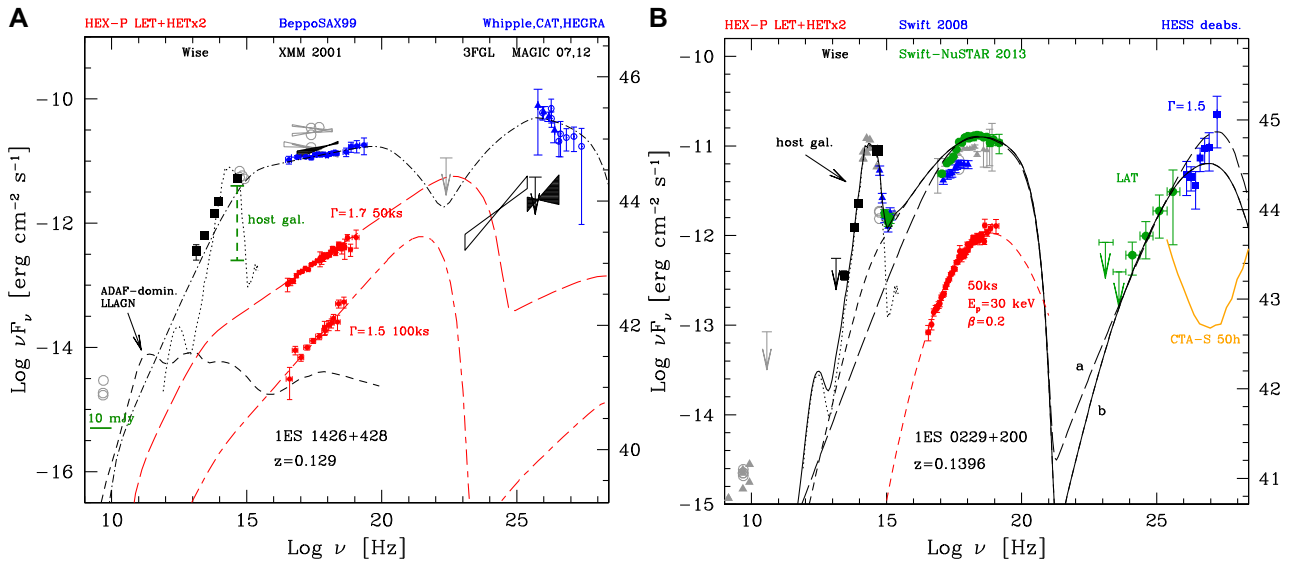

FIGURE 9
HEX-P simulated SEDs of two prototypical extreme BL Lacs, assuming lower flux levels. **(A)**: 50 ks and 100 ks simulations of two extreme sources with hard power-law X-ray spectra, possibly peaking in the MeV range (adapted from Ghisellini, 1999b; Costamante et al., 2007). For reference, the figure shows also the average SED of an advection-dominated accretion flow low luminosity AGN (Nemmen et al., 2014) at 30 × higher luminosity, and in the optical the expected range of luminosities for the host elliptical galaxy (from 1ES1426 + 428 itself to a typical AGN-hosting galaxy). **(B)**: 50 ks observation of a 1ES 0229 + 200-like object, but peaking at 30 keV with curvature β = 0.2 and at a flux level one order of magnitude fainter.

extreme HSP BL Lac objects, which can then be confirmed and characterized by HEX-P.

5.3.1 MeV-synchrotron BL lacs

In principle, blazars could reach even higher energies than shown by extreme BL Lacs. Expressing the acceleration time t_{acc} in terms of the gyroradius r_g, $t_{acc} = \eta(E)\ r_g/c$ (see e.g., Aharonian, 2004), where the factor $\eta(E) \geq 1$ characterizes the energy-dependent rate of acceleration (where unity corresponds to the maximum possible rate in shock acceleration, when a particle gains all its energy in 1 gyroradius). Therefore, even extreme BL Lacs (where $h\nu_{peak}/\delta \sim 1-10$ keV, with δ being the beaming factor) are in fact *not* extreme accelerators ($\eta \gtrsim 10^4 - 10^5$). In the Crab nebula, for example, unbeamed synchrotron emission up to 10 – 20 MeV is observed, meaning electrons are accelerated at ~10% of the maximum rate.

There might be blazars where the acceleration reaches even higher rates than observed so far, yielding a synchrotron peak in the MeV range (Ghisellini, 1999b; a). For example, $h\nu_{peak} \sim 6 - 300$ MeV for $\eta \approx 20 - 1000$ and $\delta = 10 - 40$. The luminosities are expected to be at the low end among blazars, if these objects follow the blazar sequence trend. Such objects could have easily escaped detection so far. At radio wavelengths, the flux is expected to be weak, likely below the typical level of large-area sky surveys or the selection cuts for blazar samples. In the optical band, the non-thermal continuum could be hidden one to two orders of magnitude below the host-galaxy thermal emission. In soft X-rays, the jet emission is expected to be low, thus possibly hidden under (or mixed with) the emission of the corona. In the VHE band, the SSC flux is likely too faint for detection, with the emission severely inhibited by Klein-Nishina effects. In summary, they could be faint at all frequencies except the hard X-ray and MeV bands, where they emit all their power and could reach luminosities ~10^{43-45} erg s^{-1}. As a result, even if already detected in present or future deep X-ray surveys, such sources might not be recognized as blazars, having been more likely classified as radio-quiet AGN.

The brightest among such objects could be detectable by COSI, but only HEX-P can pin-point and reveal the exceptional jet emission and extreme accelerator inside otherwise unremarkable objects. HEX-P can identify such a source with a peak luminosity of 10^{43} erg s^{-1} up to $z = 0.5$, with the observational signature of a hard X-ray spectrum (Γ = 1.5–1.7), connecting by power-law to the possible COSI (or even Fermi-LAT) detections.

5.4 Masquerading BL lacs

Masquerading BL Lacs are objects that are classified as BL Lacs because of the lack of broad emission lines in their optical spectra, but are very likely FSRQs in disguise (Giommi et al., 2013). In these objects the jet is well aligned with our line of sight and its synchrotron emission overwhelms the disk and broad line region (BLR) emission, making the latter undetectable. Several spectroscopic and photometric campaigns have started collecting accurate redshift measurements of BL Lac sources detected in γ-ray catalogs, unveiling a few objects at high redshifts. ($z > 0.8$; Shaw et al., 2013; Massaro et al., 2014; Paggi et al., 2014; Ricci et al., 2015; Álvarez Crespo et al., 2016a; b; Paiano et al., 2017; Marchesi et al., 2018; Desai et al., 2019; Kaur et al., 2019; Rajagopal et al., 2021; Sheng et al., 2022; Rajagopal et al., 2023). The community has shown renewed interest in them after TXS 0506 + 056, a BL Lac associated with the high-energy neutrino

IceCube-170922A, was revealed to be a masquerading BL Lac (Padovani et al., 2019). Indeed, neutrino emission in blazars via photo-hadronic interactions requires external photon fields, something that a masquerading BL Lac can provide. In the last few years, more masqueranding BL Lacs potentially associated with IceCube neutrinos have been discovered (Padovani et al., 2022a; Padovani et al., 2022b). Distinguishing a BL Lac from a masquerading one is often complex and requires SED modeling with high quality data. This becomes somewhat easier when sources are detected at high redshift ($z > 1$). In that case, the large radio power and Compton dominance gives away their true nature (Rau et al., 2012). High-redshift masquerading BL Lacs have also been dubbed 'blue FSRQs' (Ghisellini et al., 2012) because of their blue SED which typically shows synchrotron peak frequencies greater than 10^{15} Hz and very hard γ-ray spectra. This implies that the electrons experience weak radiative cooling, a condition satisfied if the location of the emission region is outside the BLR (Ghisellini et al., 2012). The hard γ-ray spectra and large distances make masquerading BL Lacs powerful probes of the extragalactic background light (Ackermann et al., 2012; Fermi-LAT Collaboration et al., 2018), the integrated emission of all star-forming activity in the Universe.

HEX-P's deep, broadband sensitivity is a unique advantage compared to other instruments for studying masquerading BL Lacs. By measuring the synchrotron component to high energies, HEX-P can put constraints on the maximum Lorentz factor ($\gamma_{\rm max}$) of the electron population, at least up to the energy where the inverse Compton emission starts to dominate. This is something that is generally unconstrained given the limited sensitivity of X-ray instruments above 40 keV. In Figure 10 we show an example of a simulated SED for the high-redshift ($z = 1.34$) BL Lac 4FGL J2146.5–1,344 studied by Rajagopal et al. (2020). In just 40 ks, HEX-P will be able to characterize the X-ray range in the SED of the source from 0.2 keV up to 30 keV, enabling us to accurately determine parameters such as the electrons' $\gamma_{\rm max}$ and to detect a possible break in the high-energy spectrum of the source. We note that to achieve the same quality spectrum > 10 keV, it would require > 100 ks NuSTAR observations (and > 200 ks clock-time, given NuSTAR's low-Earth orbit). Even in sources which are more typically ISP much of the time, like TXS 0506 + 056, HEX-P's broadband sensitivity will be crucial to identify epochs and states when the synchrotron emission enters the X-ray band, which typically yields enhanced gamma-ray activity in the VHE band through SSC emission. Constraining both the spectrum and the lower limit of $\gamma_{\rm max}$, HEX-P will provide fundamental information to elucidate the origin of possible VHE gamma-ray flares to be compared with epochs of higher neutrino fluxes.

5.5 Blazar evolution

As a source class, blazars have been shown to follow different evolutionary paths in the X-ray band. The powerful FSRQs evolve positively (i.e., there is an increasing number of sources at higher redshift, and/or the sources' luminosity increases with redshift) up to redshift $z > 4$ (e.g., Ajello et al., 2009; Marcotulli et al., 2022). BL Lac sources, fainter and for which redshifts are often tenuous, appear not to evolve, or to evolve negatively in the X-ray band (Beckmann et al., 2003; Ajello et al., 2009).

The latest blazar evolutionary model in the hard X-ray band has confirmed that the peak of the evolution of the most luminous FSRQs ($L_X > 10^{47}$ erg s^{-1}) lies beyond redshift 4 (Marcotulli et al., 2022). These sources are powered by the most massive black holes (see Section 5.2), and hence closely trace the evolution of the most massive black holes in the Universe. However, owing to the sensitivity limits of current X-ray surveys (e.g., Oh et al., 2018), we have yet to detect a turnover in the luminosity function at the lowest X-ray luminosities. This break, expected both as a result of beaming (Urry and Shafer, 1984) and due to the preferred evolutionary path, hampers the determination of how these sources evolve through cosmic time, i.e., whether there are more (density evolution) or more luminous (luminosity evolution) sources at earlier times. If we could tell the two evolution scenarios apart, this would have a profound impact on our current understanding of SMBH evolution. Moreover, studies based on radio-selected samples, found that blazar evolution follows the trend observed in the overall AGN population with a density peak at $z \sim 2-3$ (Caccianiga et al., 2019; Ighina et al., 2021; Diana et al., 2022). Only by finding the bulk of the X-ray blazar population at $z > 4$ would enable us to confirm the location of the peak, which in turn will inform us of the SMBH space density at those distances.

Using the latest hard X-ray luminosity function, we calculated the number of blazars detectable at different redshift bins in a 1 deg^2 survey, as planned for the HEX-P mission (Civano et al., 2023) with the predicted source sensitivity in the 8 – 24 keV band for the HET instruments. The right panel of Figure 11 shows these predictions based on the luminosity (pink hatched boxes) and density evolution model (green solid boxes). As can be seen, depending on the chosen evolution model, the number of sources detected at different redshifts is significantly different, with the luminosity evolution prediction extending up to $z > 8$. With its sensitivity, HEX-P would be able to answer these questions: are FSRQs evolving in density or luminosity? Where is the peak of the population? We note that blazars, or possibly nascent jets, have been already detected beyond $z = 6$ (e.g., Zhu et al., 2019; Belladitta et al., 2020). The left panel of Figure 11 shows the predicted source count distribution ($\log N - \log S$; i.e., number of sources as function of energy flux) of X-ray blazars in the 8 – 24 keV band as extrapolated from the X-ray best-fit luminosity evolution function in the same 1 deg^2 survey. With the capabilities of the HET, we will finally be able to detect the break in $\log N - \log S$ and break the degeneracy that would lead us to understand for the very first time the type of evolution taking place in this source class.

Moreover, these sources, though contributing only ~2 – 10% to the cosmic X-ray background above 14 keV, are predicted to be the major contributors to the MeV background. Assuming a luminosity evolution scenario, estimates are of the order of 70%, while for the density evolution, they are up to 100% (Marcotulli et al., 2022). However, such numbers are derived from extrapolations of the best-fit X-ray luminosity function to the MeV band, assuming an average high-energy (X-to-γ-ray) SED of the MeV blazar class derived from time-averaged Swift/BAT and Fermi-LAT data. As shown in (Marcotulli et al. 2020), (Figures 3–5), quasi-simultaneous soft (Swift/XRT) and sensitive hard (NuSTAR) X-ray data, combined with γ-ray ones, are necessary to constrain the location (both

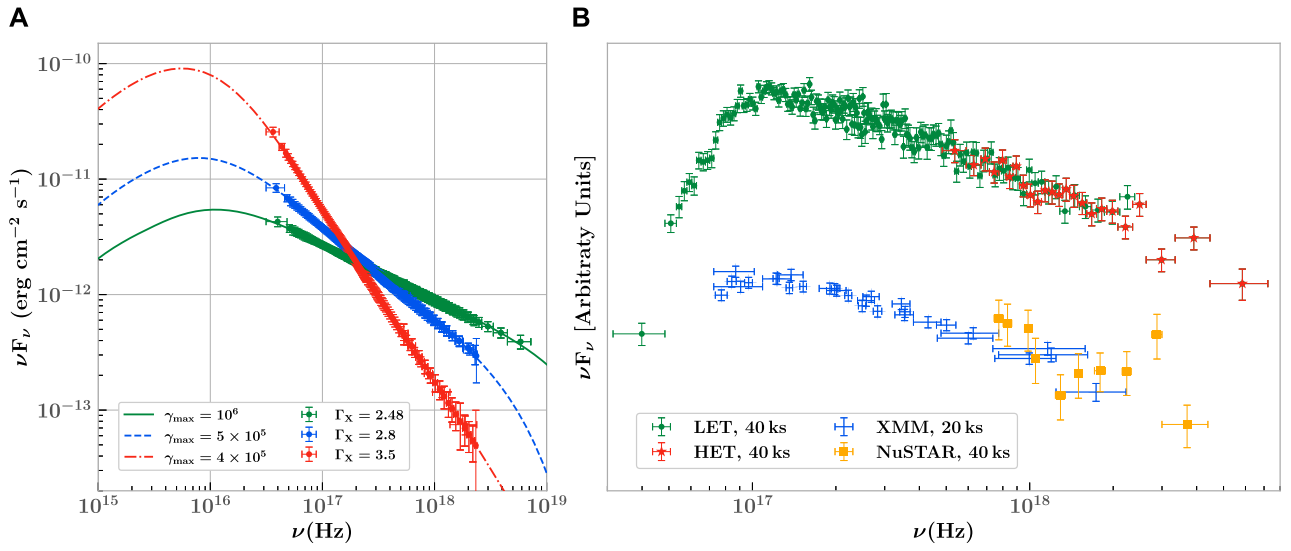

FIGURE 10
(A): Simulated SED of the high-redshift BL Lac 4FGL J2146.5–1,344 ($z = 1.34$; Rajagopal et al., 2020). The left panel shows the simulated HEX-P SED with different spectral indices (Γ_X). In only 40 ks, HEX-P will characterize the source spectrum from 0.2 keV to 30 keV. This will provide crucial constraints on the shape of the high-energy particle population (e.g., the maximum Lorentz factor, γ_{max}), the total jet power, and the true nature of the emitter (whether it is a high-luminosity BL Lac or a masquerading FSRQ). **(B)**: comparison of 40 ks HEX-P simulations to observations carried out by Rajagopal et al. (2020), which entailed simultaneous observations of 4FGL J2146.5–1,344 with XMM-Newton (20 ks) and NuSTAR (40 ks). HEX-P data quality for a similar exposure will highly enhance our S/N and improve determination of important spectral parameters (such as photon index and flux) as well as enable us to detect spectral curvature beyond 10 keV, which would require a > 100 ks NuSTAR exposure (and > 200 ks clock-time, given NuSTAR's low-Earth orbit).

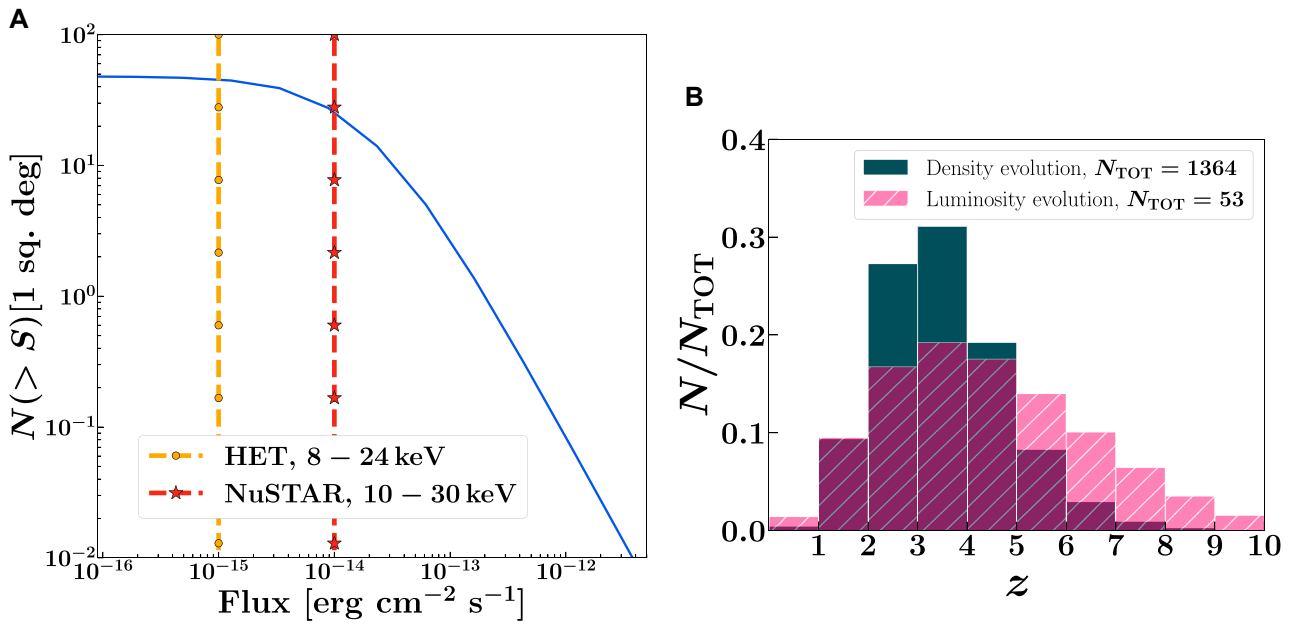

FIGURE 11
(A): Blazar source count distribution, *logN-logS* (blue line), derived from the best-fit luminosity evolution model of Marcotulli et al. (2022) expected for a 1 deg^2 survey. The yellow dash-circle line indicates the HET 8 – 24 keV source sensitivity for the planned 1 deg^2 wide survey (Civano et al., 2023) For comparison, the red dash-star line represents the NuSTAR source sensitivity in the 10 – 30 keV band. HEX-P sensitivity would allow us for the very first time to detect the break of the luminosity function (which is yet to be seen by current facilities). This would lead us to definitely constrain which kind of evolution X-ray detected FSRQs have undergone, as measuring such break would solve the degeneracy between a density versus a luminosity evolution. **(B)**: Predicted relative number of FSRQs (N/N_{TOT}) that would be detected by HEX-P in the planned 1 deg^2 wide survey as a function of redshift. Prediction using the best-fit density evolution model are shown as solid dark green bars, and using the best-fit luminosity evolution model as hatched pink bars (Marcotulli et al., 2022). Depending on the number of sources detected by HEX-P as a function of redshift, we would be able to determine for the very first time the evolution properties of the population.

in flux and energy) of the high-energy SED peak, translating to constraints on the contribution of this class to the background. The average Swift-BAT uncertainty on the spectral index is $\bar{\Gamma}_{\mathrm{BAT,err}} = 0.2$ (Oh et al., 2018). A difference of 0.2 on the hard X-ray spectrum implies a factor of 10 difference in the contribution of blazars to the MeV background. Besides allowing us to detect the bulk of the high-redshift population, HEX-P, with its lower background at hard X-rays, will allow probing the high-energy SED very close to its peak ($E \sim 50-80$ keV at $z = 4$ corresponds to $E_{\mathrm{rest}} \sim 250-400$ keV and at $z = 5$ to $E_{\mathrm{rest}} \sim 300-480$ keV wrt a peak at $E_{\mathrm{rest,peak}} = 3-17$ MeV, Marcotulli et al., 2022) pinpointing its location and the shape of the spectrum with uncertainties of the order of $\Gamma_{0.2-70\ \mathrm{keV,err}} = 0.01$. This, together with the knowledge of the preferred evolution model, will provide tighter constraints on the contribution of MeV blazars to the cosmic MeV background, allowing us to constrain the uncertainties on the level of contribution of blazars to the MeV background from an order of magnitude down to 20%.

Similarly, the prospects to finally disentangle the preferred evolutionary paths for BL Lacs in the X-ray band are bright with HEX-P. Current photometric and spectroscopic follow-up of γ-ray detected BL Lacs are increasing the redshift completeness of this challenging source class. A sensitive X-ray telescope such as HEX-P would enable a complete sample of X-ray selected BL Lacs, even to lower luminosity (see Section 5.3.1), and determine for the first time their evolution in the full 0.2 – 80 keV band.

6 Resolving nearby jets

6.1 Blazars

Jets of active galaxies can be hundreds to thousands of kiloparsecs long (e.g., Oei et al., 2022). The extended structure is most easily observed in the radio band, where the low-energy synchrotron emission can be observed along the entire jet. However, many jets also show extended components (extended jets and/or hotspots along the jet flow) in other energy bands, including the X-ray domain. Observations with Chandra increased the number of resolved X-ray jets considerably and rekindled the debate on the X-ray emission processes in extended jets (see Harris and Krawczynski, 2006, for a review). Especially the explanation of hard X-ray spectra (harder than the radio-through-optical extrapolation) was strongly debated. Two main models emerged: Inverse-Compton scattering of CMB photons by low-energy electrons (which would produce the radio through optical emission through synchrotron emission; Tavecchio et al., 2000) or synchrotron emission of a second, high-energy electron population (e.g., Hardcastle, 2006; Jester et al., 2006). While the IC/CMB model was favored for some time, several studies over recent years have shown that this may not be the correct interpretation for many sources due to a lack of associated γ-rays (e.g., Breiding et al., 2017; Meyer et al., 2017).

For example, an extended X-ray jet has been observed in the flat-spectrum radio quasar 3C 273 (Marshall et al., 2001), revealing a ~10" extended structure with knots. No cut-off is observed in the X-ray spectrum. Multi-wavelength data suggest that the X-ray component is inverse-Compton emission (Uchiyama et al., 2006) or a second synchrotron component.

However, in a notable counterexample, the synchrotron explanation probably does not work for the blazar AP Librae (Zacharias and Wagner, 2016; Roychowdhury et al., 2022), one of the few BL Lac objects with a resolved, 10" long X-ray jet (Kaufmann et al., 2013). The shape of the SED requires at least two emission zones. In fact, the VHE γ-ray emission observed with H.E.S.S. (H. E. S. S. Collaboration et al., 2015). has been interpreted as inverse-Compton scattering of dust emission from the inner 1kpc of the jet (Roychowdhury et al., 2022).

A recent study by Reddy et al. (2023) on jet knots revealed that in most knots the X-ray emission peak is located upstream of the radio emission peak. This might suggest a cooling effect on the particle flow across a shock pointing towards the synchrotron process in both energy bands, as the IC/CMB model requires a one-zone interpretation, where the fluxes should peak at the same location.

Hence, the debate continues. Observations with HEX-P will be crucial for studies of the hard X-ray emission of nearby, resolved blazar jets. The X-ray spectra do not show any spectral feature; they are described well with a power-law (e.g., Haardt et al., 1999; Marshall et al., 2001; Kaufmann et al., 2013). This suggests efficient particle acceleration in large-scale jets potentially up to the synchrotron-burnoff limit (de Jager et al., 1996). Unfortunately, the spectral range of the synchrotron-burnoff limit (50MeV modulo beaming) is currently not well accessible, as the *Fermi*-LAT instrument cannot resolve extended blazar jets (e.g., Breiding et al., 2017) in order to derive the spectrum at these energies. The observation of a break or a cut-off in the hard X-ray domain would provide important information on the acceleration and radiation processes inside the extended jets. This would constrain both synchrotron and inverse-Compton models.

Using the 47 sources labeled as *BL Lac* or *CDQ* in the Atlas-X[4] (Reddy et al., 2023) and the XJET[5] catalogs (most of which are blazars), we determine that HEX-P's angular resolution of ≤5" is sufficient to resolve up to 20 known (blazar) jets at hard X-rays. Six sources have jets longer than 10" including, for example, 3C 273 (cf., Figure 12), 9 sources range between 5" and 10", while 5 jets are about 5" long which might still be detectable. To showcase the excellent imaging capabilities of HEX-P to resolve jets at different separations from the core and with different jet/core flux ratios, we performed several simulations using as a base image the blazar 3C 273 (Chandra obsid:4,876). All the images shown in Figure 12 have been produced using a 100 ks exposure with the LET instrument and they cover the 8 – 25 keV range. From the top panel to the bottom one, we increased the jet separation from the core from 5″ to 20″. From the left panel to the right one, we increase the ratio of fluxes between jet and core ($F_{\mathrm{jet}}/F_{\mathrm{core}}$) from 0.01 to 1. The real 3C 273 system as seen by HEX-P would be the left panel, second row. As can be seen, HEX-P imaging capabilities would be key to resolving blazar jets for the first time at > 10 keV even when the jet is a few times fainter than the core and at very close separation. We would also note that the highest redshift ($z > 5$) resolved X-ray jets are found at a separation of 5″ and

4 https://astro.umbc.edu/Atlas-X/

5 https://hea-www.cfa.harvard.edu/XJET/

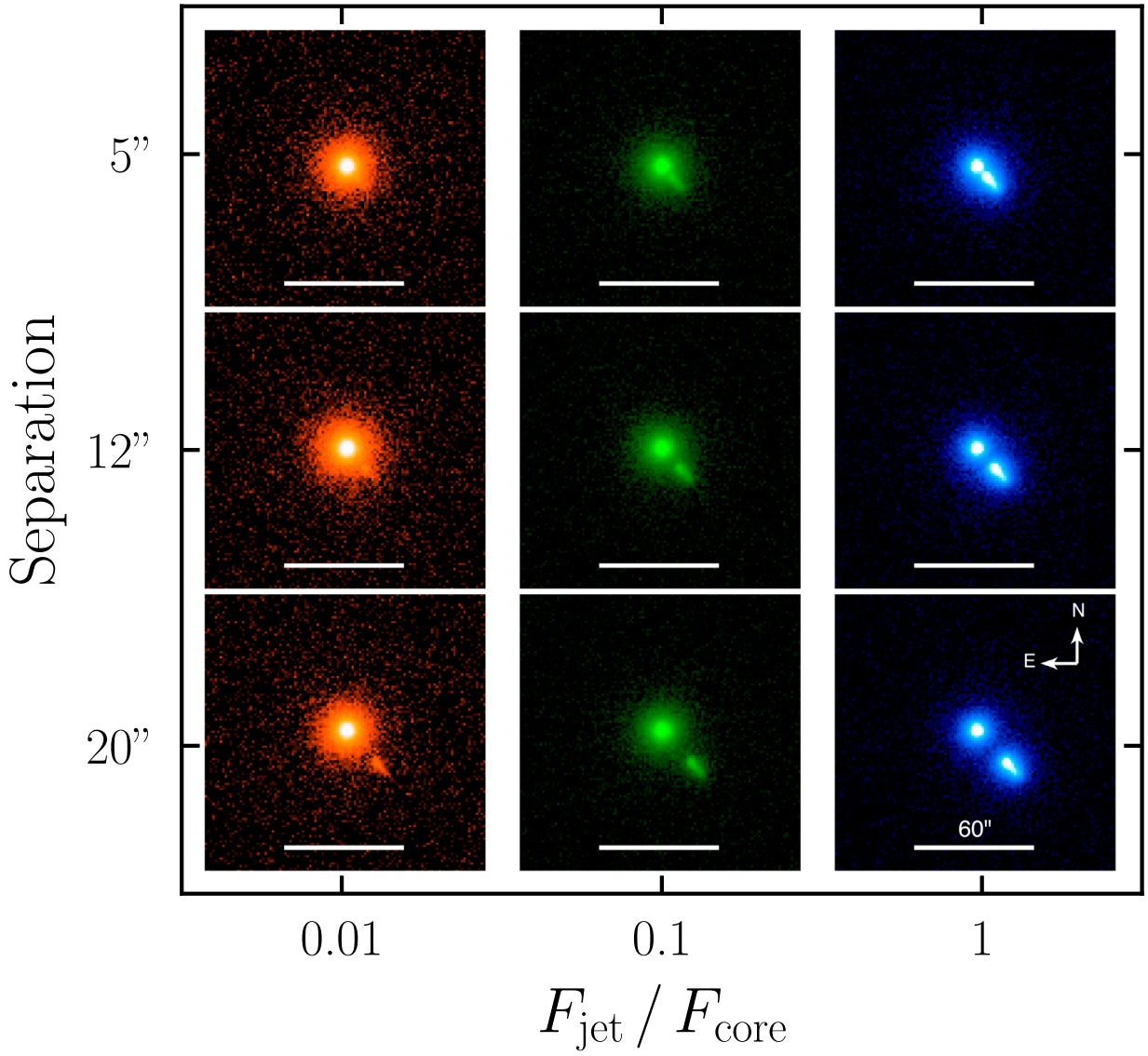

FIGURE 12
SIXTE simulations using as base image the blazar 3C 273 (Chandra obsid:4,876). All the images have been produced using 100 ks exposure with the LET instrument and they cover the 8 – 25 keV range. The field of view in all images is $2' \times 2'$ and we have over-plotted a white line of length 60″ for scale. For reference, 60″ is the NuSTAR PSF. From top to bottom: the jet separation from the core increases from 5″ to 20″. From left to right: the ratio of fluxes between jet and core ($F_{\rm jet}/F_{\rm core}$) increases from 0.01 to 1. The real 3C 273 system as seen by HEX-P would be the left panel, second row. All the other simulations showcase the excellent imaging capabilities of HEX-P to resolve jets at different separation from the core and with different flux ratios. As can been seen, HEX-P imaging capabilities would be key to resolve blazar jets for the first time >10 keV even when the jet is few times fainter than the core and at very close separation.

8″ from the core and a flux ration $F_{\rm jet}/F_{\rm core} \sim 0.06$ (Ighina et al., 2022) and $F_{\rm jet}/F_{\rm core} < 0.1$ (Belladitta et al., 2020; Connor et al., 2021). Therefore, HEX-P would have the capability of resolving those jets.

This implies that HEX-P will help determine the spectral features (e.g., breaks or cut-offs, if present) at X-rays beyond 10keV, which are so far unknown. In turn, the acceleration processes in extended jets will be strongly constrained, which will significantly enhance the modeling of these extended structures (Potter and Cotter, 2015; Lucchini et al., 2019; Zacharias et al., 2022), and which would greatly enhance the theoretical understanding of jets as a whole.

6.2 TeV-detected radio galaxies

Radio galaxies are typically non-aligned AGN with significantly reduced Doppler beaming. Depending on the X-ray production process, their extended X-ray jets may still be observable, as beaming is not as important depending on the particle energies in the jet. Here, we discuss a special class of radio galaxies, namely, those which are detected at VHE γ-ray energies. So far, six bona-fide radio galaxies are listed in the TeVCAT,[6] of which three have extended

6 http://tevcat2.uchicago.edu/

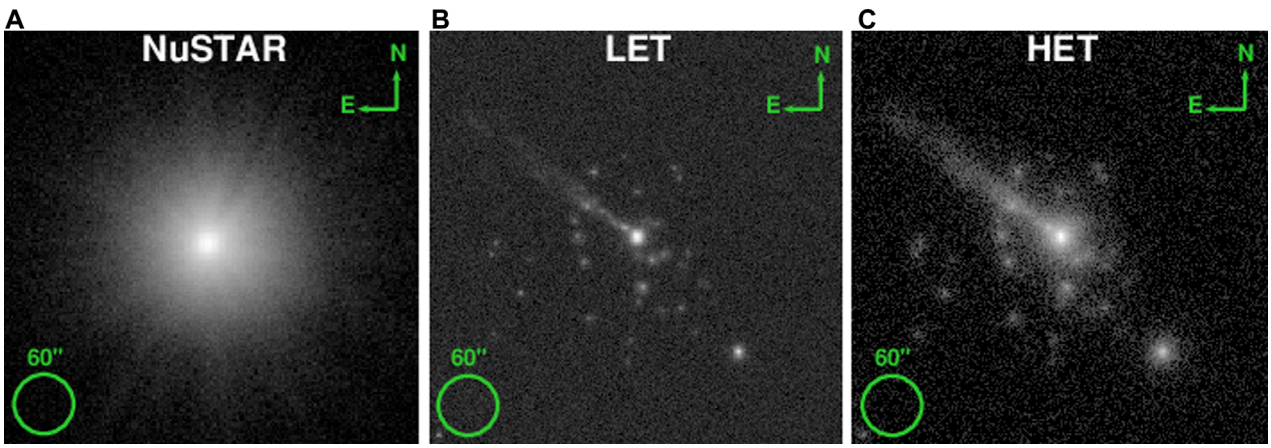

FIGURE 13
(A): NuSTAR FPMA 3 – 80 keV image of the radio galaxy Centaurus A (obsid: 60001081002). **(B, C)**: SIXTE simulations of the same galaxy with HEX-P based on the Chandra image of the source (Middle: 500 ks observation in the 8 – 20 keV range with the LET; Right: 500 ks observation in the 20 – 50 keV range with the HET). HEX-P would enable us, for the first time, to resolve extended jets in the hard X-ray band as well as study point sources visible in the Chandra image at soft X-rays (see Lehmer et al., 2023). The images are all $7' \times 7'$ and we have over-plotted a green circle of diameter $1'$ for scale.

X-ray jets: M 87 (Aharonian et al., 2006; Acciari et al., 2009; Abramowski et al., 2012), Centaurus A (Aharonian et al., 2009b; H. E. S. S. Collaboration et al., 2020), and 3C 264 (Archer et al., 2020, however, the X-ray jet is less than 5" long). Centaurus A is a special case, as it is not only the closest AGN to Earth, but also, so far, the only AGN where the TeV emission is spatially extended along the axis of the X-ray and radio jet (H. E. S. S. Collaboration et al., 2020). This could indicate the presence of high-energy particles on kpc scales that are inverse Compton scattering dust emission or starlight, or it could be associated with synchrotron radiation from ultra-high energy electrons (e.g., Wang et al., 2021).

Observations with HEX-P of these extended jets, coupled with the knowledge that these jets emit TeV γ rays at large distances from the black hole, will be crucial for constraining the location and physics of the γ-ray production. As mentioned above, cut offs or breaks in the X-ray spectra would reveal maximum particle energies (or at least the acceleration efficiency) indicating that such a particle population would probably not produce γ rays. Determining spatially resolved spectra of nearby jets (such as Centaurus A; see Figure 13) would allow us to pinpoint the regions where the extended γ-ray emission is produced.

Along with HEX-P and its broad X-ray coverage, multiwavelength observations with future high-angular-resolution instruments will be crucial to unlock the secrets of these objects. Most notably, collaborative observations by HEX-P with CTAO will be important to constrain the jet morphology and processes.

7 Conclusion

The HEX-P mission offers several key strengths for studying jetted AGN. Its broad-band sensitivity, spanning from 0.2 to 80 keV, provides deep coverage in relatively short exposure times. Additionally, HEX-P exhibits excellent angular resolution at high energies and the unique capability to point in the antisolar direction. These remarkable capabilities set HEX-P apart from both current and currently planned X-ray observatories, making it an unparalleled asset for the study of blazars in the next decade. In particular:

- HEX-P's potential extends to time-domain and multi-messenger studies. HEX-P has the capability to independently discover the expected signatures of hadronic accelerators. In Section 4.1, we illustrated how HEX-P can detect spectral changes during an X-ray flare as expected from the presence of a hadronic component. Moreover, by observing blazars that are detected by IceCube, HEX-P can identify the X-ray signatures expected from hadronic sources. In Section 4.2, we demonstrated that HEX-P can detect the signature of proton-induced cascades associated with neutrino emission. It accomplishes this by distinguishing between power-law emission, typical of a leptonic synchrotron component, from broken power laws, expected in the case of proton-induced cascades. Note, however, that these signatures are not unique to hadronic processes and may also arise in multi-component leptonic emission scenarios.
- The deep broad-band sensitivity of HEX-P will enable the study of rapid variability on minute timescales. As shown in Section 4.3, these investigations provide insight into the connection between the acceleration and cooling of charged particles. Previously, such studies were limited to only a few objects over an energy band spanning less than 1 decade. HEX-P will expand this research to a significantly larger number of objects and offer an energy band spanning more than 2 decades. Furthermore, HEX-P's ability to pinpoint extremely fast variability, comparable to the light-crossing time of the system, will reveal invaluable information about particle acceleration mechanisms. In Section 4.3, we demonstrated how HEX-P can measure the lightcurve of a fast flaring blazar (e.g., Mrk 421) at both low (< 10 keV) and high (> 10 keV)

X-ray energies, thereby identifying the signature of magnetic reconnection.

- Section 5 showed how HEX-P will allow investigation of the accretion-jet connection by measuring the average X-ray SED of selected blazars and constrain variation in the SED linked to possible accretion fluctuations. Moreover, HEX-P will detect and study MeV blazars (the most luminous type of blazars) well above the current $z \approx 3$ limit and possibly all the way to $z = 6$.
- As shown in Section 6, for the first time above 20 keV, HEX-P will be able to resolve jets of blazars and radio galaxies, thus pinpointing the regions where the extended emission is produced. HEX-P will be able to discriminate between the emission of the core and that of the jet allowing to constrain potential spectral cut-offs in the jet. This would yield an important constraints on the maximum energy of the particle population.

Lastly, HEX-P exhibits strong synergies with current and future planned facilities, including CTAO, IceCube, IXPE, COSI, and the current and future CMB facilities (Section 4.4). These collaborations enable the study of extremely fast flaring blazars, the detection and study of multi-messenger sources, and the investigation of hadronic emission components in blazars. An early 2030s launch of HEX-P will significantly enhance the science provided by those facilities and answer many key questions about the most powerful jets in the Universe.

Data availability statement

The original contributions presented in the study are included in the article, further inquiries can be directed to the corresponding author.

Author contributions

LM: Writing–original draft, Writing–review and editing. MA: Writing–original draft, Writing–review and editing. MB: Writing–original draft, Writing–review and editing. PC: Writing–review and editing. LC: Writing–original draft, Writing–review and editing. LG: Writing–review and editing. ME: Writing–original draft, Writing–review and editing. JG: Writing–review and editing. AG: Writing–original draft, Writing–review and editing. IL: Writing–original draft, Writing–review and editing. GM: Writing–original draft, Writing–review and editing. KM: Writing–review and editing. AM: Writing–review and editing. RM: Writing–review and editing. FM: Writing–original draft, Writing–review and editing. MP: Writing–original draft, Writing–review and editing. BR: Writing–review and editing. TS: Writing–original draft, Writing–review and editing. DS: Writing–review and editing. GV: Writing–original draft. MZ: Writing–original draft, Writing–review and editing. HZ: Writing–original draft, Writing–review and editing.

Funding

The author(s) declare that financial support was received for the research, authorship, and/or publication of this article. The work of D.S. was carried out at the Jet Propulsion Laboratory, California Institute of Technology, under a contract with NASA. Support for this work was provided by NASA through the NASA Hubble Fellowship grant #HST-HF2-51486.001-A awarded by the Space Telescope Science Institute, which is operated by the Association of Universities for Research in Astronomy, Inc., for NASA, under contract NAS5-26555. IL was supported by the NASA Postdoctoral Program at the Marshall Space Flight Center, administered by Oak Ridge Associated Universities under contract with NASA. MZ acknowledges funding by the Deutsche Forschungsgemeinschaft (DFG, German Reserach Foundation)–project number 460248186 (PUNCH4NFDI). RM acknowledges financial support from the ASI-INAF agreement n. 2022-14-HH.0. HZ is supported by NASA under award number 80GSFC21M0002. HZ's work is supported by Fermi GI program cycle 16 under the award number 22-FERMI22-0015.

Acknowledgments

We thank both anonymous referees for their meaningful comments that helped us to improve the manuscript.

Conflict of interest

The authors declare that the research was conducted in the absence of any commercial or financial relationships that could be construed as a potential conflict of interest.

The reviewer FT declared a shared affiliation with the author(s) AM, MR and TS to the handling editor at the time of review.

Publisher's note

All claims expressed in this article are solely those of the authors and do not necessarily represent those of their affiliated organizations, or those of the publisher, the editors and the reviewers. Any product that may be evaluated in this article, or claim that may be made by its manufacturer, is not guaranteed or endorsed by the publisher.

References

Abazajian, K., Addison, G. E., Adshead, P., Ahmed, Z., Akerib, D., Ali, A., et al. (2022). CMB-S4: forecasting constraints on primordial gravitational waves. *Astrophys. J.* 926, 54. doi:10.3847/1538-4357/ac1596

Abdo, A. A., Ackermann, M., Agudo, I., Ajello, M., Aller, H. D., Aller, M. F., et al. (2010a). The spectral energy distribution of Fermi bright blazars. *Astrophys. J.* 716, 30–70. doi:10.1088/0004-637X/716/1/30

Abdo, A. A., Ackermann, M., Ajello, M., Antolini, E., Baldini, L., Ballet, J., et al. (2010b). Suzaku observations of luminous quasars: revealing the nature of high-energy blazar emission in low-level activity states. *Astrophys. J.* 716, 835–849. doi:10.1088/0004-637X/716/1/835

Abdo, A. A., Ackermann, M., Ajello, M., Atwood, W. B., Axelsson, M., Baldini, L., et al. (2010c). Spectral properties of bright fermi-detected blazars in the gamma-ray band. *Astrophys. J.* 710, 1271–1285. doi:10.1088/0004-637X/710/2/1271

Abdollahi, S., Acero, F., Ackermann, M., Ajello, M., Atwood, W. B., Axelsson, M., et al. (2020). Fermi large area telescope fourth source catalog. *Astrophys. J. Suppl. Ser.* 247, 33. doi:10.3847/1538-4365/ab6bcb

Abdollahi, S., Ackermann, M., Ajello, M., Atwood, W. B., Baldini, L., Ballet, J., et al. (2018). A gamma-ray determination of the Universe's star formation history. *Science* 362, 1031–1034. doi:10.1126/science.aat8123

Abeysekara, A. U., Archambault, S., Archer, A., Benbow, W., Bird, R., Buchovecky, M., et al. (2017). A search for spectral hysteresis and energy-dependent time lags from X-ray and TeV gamma-ray observations of mrk 421. *Astrophys. J.* 834, 2. doi:10.3847/1538-4357/834/1/2

Abramowski, A., Acero, F., Aharonian, F., Akhperjanian, A. G., Anton, G., Balzer, A., et al. (2012). the 2010 very high energy γ-ray flare and 10 years of multi-wavelength observations of m 87. *Astrophys. J.* 746, 151. doi:10.1088/0004-637X/746/2/151

Acciari, V. A., Aliu, E., Arlen, T., Bautista, M., Beilicke, M., Benbow, W., et al. (2009). Radio imaging of the very-high-energy γ-ray emission region in the central engine of a radio galaxy. *Science* 325, 444–448. doi:10.1126/science.1175406

Acero, F., Ackermann, M., Ajello, M., Albert, A., Atwood, W. B., Axelsson, M., et al. (2015). Fermi large area telescope third source catalog. *Astrophys. J. Suppl. Ser.* 218, 23. doi:10.1088/0067-0049/218/2/23

Ackermann, M., Ajello, M., Allafort, A., Schady, P., Baldini, L., Ballet, J., et al. (2012). The imprint of the extragalactic background light in the gamma-ray spectra of blazars. *Science* 338, 1190–1192. doi:10.1126/science.1227160

Ackermann, M., Ajello, M., Baldini, L., Ballet, J., Barbiellini, G., Bastieri, D., et al. (2017). Gamma-ray blazars within the first 2 billion years. *Astrophys. J. Lett.* 837, L5. doi:10.3847/2041-8213/aa5fff

Ackermann, M., Anantua, R., Asano, K., Baldini, L., Barbiellini, G., Bastieri, D., et al. (2016a). *Minute-timescale >100 MeV γ-Ray variability during the giant outburst of quasar 3C 279 observed by fermi-LAT in 2015 june 824*, L20. doi:10.3847/2041-8205/824/2/L20

Ackermann, M., Anantua, R., Asano, K., Baldini, L., Barbiellini, G., Bastieri, D., et al. (2016b). MINUTE-TIMESCALE >100 MeV γ-RAY VARIABILITY DURING THE GIANT OUTBURST OF QUASAR 3C 279 OBSERVED BY FERMI-LAT IN 2015 JUNE. *Astrophys. J. Lett.* 824, L20. doi:10.3847/2041-8205/824/2/L20

Agarwal, A., Gupta, A. C., Bachev, R., Strigachev, A., Semkov, E., Wiita, P. J., et al. (2015). Multiband optical-NIR variability of blazars on diverse time-scales. *Mon. Not. R. Astron. Soc.* 451, 3882–3897. doi:10.1093/mnras/stv1208

Aharonian, F., Akhperjanian, A. G., Anton, G., Barres de Almeida, U., Bazer-Bachi, A. R., Becherini, Y., et al. (2009a). Simultaneous multiwavelength observations of the second exceptionaly-ray flare of PKS 2155–304 in July 2006. *Astron. Astrophys.* 502, 749–770. doi:10.1051/0004-6361/200912128

Aharonian, F., Akhperjanian, A. G., Anton, G., de Almeida, U. B., Bazer-Bachi, A. R., Becherini, Y., et al. (2009b). discovery of very high energy γ-ray emission from centaurus a with h.e.s.s. *Astrophys. J. Lett.* 695, L40–L44. doi:10.1088/0004-637X/695/1/L40

Aharonian, F., Akhperjanian, A. G., Barres de Almeida, U., Bazer-Bachi, A. R., Behera, B., Beilicke, M., et al. (2007a). New constraints on the mid-IR EBL from the HESS discovery of VHE γ-rays from 1ES 0229+200. *Astron. Astrophys.* 475, L9–L13. doi:10.1051/0004-6361:20078462

Aharonian, F., Akhperjanian, A. G., Bazer-Bachi, A. R., Behera, B., Beilicke, M., Benbow, W., et al. (2007b). An exceptional very high energy gamma-ray flare of PKS 2155-304. *Astrophys. J. Lett.* 664, L71–L74. doi:10.1086/520635

Aharonian, F., Akhperjanian, A. G., Bazer-Bachi, A. R., Beilicke, M., Benbow, W., Berge, D., et al. (2006). Fast variability of Tera–Electron volt γ rays from the radio galaxy M87. *Science* 314, 1424–1427. doi:10.1126/science.1134408

Aharonian, F. A. (2004). *Very high energy cosmic gamma radiation: a crucial window on the extreme Universe*. World Scientific. doi:10.1142/4657

Aharonian, F. A., Barkov, M. V., and Khangulyan, D. (2017). Scenarios for ultrafast gamma-ray variability in AGN. *Astrophys. J.* 841, 61. doi:10.3847/1538-4357/aa7049

Ahnen, M. L., Ansoldi, S., Antonelli, L. A., Arcaro, C., Babić, A., Banerjee, B., et al. (2018). Extreme HBL behavior of markarian 501 during 2012. *Astron. Astrophys.* 620, A181. doi:10.1051/0004-6361/201833704

Ajello, M., Angioni, R., Axelsson, M., Ballet, J., Barbiellini, G., Bastieri, D., et al. (2020). The fourth catalog of active galactic nuclei detected by the Fermi large area telescope. *Astrophys. J.* 892, 105. doi:10.3847/1538-4357/ab791e

Ajello, M., Costamante, L., Sambruna, R. M., Gehrels, N., Chiang, J., Rau, A., et al. (2009). The evolution of Swift/BAT blazars and the origin of the MeV background. *Astrophys. J.* 699, 603–625. doi:10.1088/0004-637X/699/1/603

Ajello, M., Greiner, J., Sato, G., Willis, D. R., Kanbach, G., Strong, A. W., et al. (2008). Cosmic X-ray background and Earth albedo spectra with Swift BAT. *Astrophys. J.* 689, 666–677. doi:10.1086/592595

Ajello, M., Romani, R. W., Gasparrini, D., Shaw, M. S., Bolmer, J., Cotter, G., et al. (2014). The cosmic evolution of Fermi BL Lacertae objects. *Astrophys. J.* 780, 73. doi:10.1088/0004-637X/780/1/73

Albert, J., Aliu, E., Anderhub, H., Antoranz, P., Armada, A., Baixeras, C., et al. (2007). *Variable very high energy γ-Ray emission from markarian 501 669*, 862–883. doi:10.1086/521382

Aleksić, J., Ansoldi, S., Antonelli, L. A., Antoranz, P., Babic, A., Bangale, P., et al. (2014a). Black hole lightning due to particle acceleration at subhorizon scales. *Science* 346, 1080–1084. doi:10.1126/science.1256183

Aleksić, J., Antonelli, L. A., Antoranz, P., Babic, A., Barres de Almeida, U., Barrio, J. A., et al. (2014b). Rapid and multiband variability of the TeV bright active nucleus of the galaxy IC 310. *Astron. Astrophys.* 563, A91. doi:10.1051/0004-6361/201321938

Alexander, T., and Natarajan, P. (2014). Rapid growth of seed black holes in the early universe by supra-exponential accretion. *Science* 345, 1330–1333. doi:10.1126/science.1251053

Aliu, E., Archambault, S., Archer, A., Arlen, T., Aune, T., Barnacka, A., et al. (2016). Very high energy outburst of Markarian 501 in May 2009. *Astron. Astrophys.* 594, A76. doi:10.1051/0004-6361/201628744

Allison, P., Bard, R., Beatty, J. J., Besson, D. Z., Bora, C., Chen, C. C., et al. (2016). Performance of two Askaryan Radio Array stations and first results in the search for ultrahigh energy neutrinos. *Phys. Rev. D.* 93, 082003. doi:10.1103/physrevd.93.082003

Álvarez Crespo, N., Masetti, N., Ricci, F., Landoni, M., Patiño-Álvarez, V., Massaro, F., et al. (2016a). Optical spectroscopic observations of gamma-ray blazar candidates. V. TNG, KPNO, and OAN observations of blazar candidates of uncertain type in the northern hemisphere. *Astron. J.* 151, 32. doi:10.3847/0004-6256/151/2/32

Álvarez Crespo, N., Massaro, F., Milisavljevic, D., Landoni, M., Chavushyan, V., Patiño-Álvarez, V., et al. (2016b). Optical spectroscopic observations of gamma-ray blazar candidates. VI. Further observations from TNG, WHT, OAN, SOAR, and magellan telescopes. *Astron. J.* 151, 95. doi:10.3847/0004-6256/151/4/95

Ananna, T. T., Treister, E., Urry, C. M., Ricci, C., Hickox, R. C., Padmanabhan, N., et al. (2020). Accretion history of AGNs. II. Constraints on AGN spectral parameters using the cosmic X-ray background. *Astrophys. J.* 889, 17. doi:10.3847/1538-4357/ab5aef

Archer, A., Benbow, W., Bird, R., Brill, A., Buchovecky, M., Buckley, J. H., et al. (2020). VERITAS discovery of VHE emission from the radio galaxy 3C 264: a multiwavelength study. *Astrophys. J.* 896, 41. doi:10.3847/1538-4357/ab910e

Arnaud, K. A. (1996). "XSPEC: the first ten years," in *Astronomical data analysis software and systems V*. Editors G. H. Jacoby, and J. Barnes (Astronomical Society of the Pacific Conference Series), 101.

Atoyan, A., and Dermer, C. D. (2004). Synchrotron versus compton interpretations for extended X-ray jets. *Astrophys. J.* 613, 151–158. doi:10.1086/422499

Baloković, M., Paneque, D., Madejski, G., Furniss, A., Chiang, J., Ajello, M., et al. (2016). Multiwavelength study of quiescent states of mrk 421 with unprecedented hard X-ray coverage provided by NuSTAR in 2013. *Astrophys. J.* 819, 156. doi:10.3847/0004-637X/819/2/156

Barkov, M. V., Aharonian, F. A., Bogovalov, S. V., Kelner, S. R., and Khangulyan, D. (2012). Rapid TeV variability in blazars as a result of jet-star interaction. *Astrophys. J.* 749, 119. doi:10.1088/0004-637X/749/2/119

Bassett, L. C., Brandt, W. N., Schneider, D. P., Vignali, C., Chartas, G., and Garmire, G. P. (2004). Chandra observations of radio-loud quasars at z>4: X-rays from the radio beacons of the early universe. *Astron. J.* 128, 523–533. doi:10.1086/422019

Beckmann, V., Engels, D., Bade, N., and Wucknitz, O. (2003). The HRX-BL lac sample - evolution of BL lac objects. *Astron. Astrophys.* 401, 927–938. doi:10.1051/0004-6361:20030184

Beckmann, V., Wolter, A., Celotti, A., Costamante, L., Ghisellini, G., Maccacaro, T., et al. (2002). BeppoSAX spectral survey of BL Lacs - new spectra and results. *Astron. Astrophys.* 383, 410–422. doi:10.1051/0004-6361:20011752

Begelman, M. C., Fabian, A. C., and Rees, M. J. (2008). Implications of very rapid TeV variability in blazars. *Mon. Not. R. Astron. Soc.* 384, L19–L23. doi:10.1111/j.1745-3933.2007.00413.x

Begelman, M. C., Rudak, B., and Sikora, M. (1990). Consequences of relativistic proton injection in active galactic nuclei. *Astrophys. J.* 362, 38. doi:10.1086/169241

Begelman, M. C., and Volonteri, M. (2017). Hyperaccreting black holes in galactic nuclei. *Mon. Not. R. Astron. Soc.* 464, 1102–1107. doi:10.1093/mnras/stw2446

Begelman, M. C., Volonteri, M., and Rees, M. J. (2006). Formation of supermassive black holes by direct collapse in pre-galactic haloes. *Mon. Not. R. Astron. Soc.* 370, 289–298. doi:10.1111/j.1365-2966.2006.10467.x

Belladitta, S., Moretti, A., Caccianiga, A., Spingola, C., Severgnini, P., Della Ceca, R., et al. (2020). The first blazar observed at z > 6. *Astron. Astrophys.* 635, L7. doi:10.1051/0004-6361/201937395

Berezinskii, V. S., and Ginzburg, V. L. (1981). On high-energy neutrino radiation of quasars and active galactic nuclei. *Mon. Not. R. Astron. Soc.* 194, 3–14. doi:10.1093/mnras/194.1.3

Bhatta, G., Mohorian, M., and Bilinsky, I. (2018). Hard X-ray properties of NuSTAR blazars. *Astron. Astrophys.* 619, A93. doi:10.1051/0004-6361/201833628

Biermann, P. L., and Strittmatter, P. A. (1987). Synchrotron emission from shock waves in active galactic nuclei. *Astrophys. J.* 322, 643. doi:10.1086/165759

Biteau, J., Prandini, E., Costamante, L., Lemoine, M., Padovani, P., Pueschel, E., et al. (2020). Progress in unveiling extreme particle acceleration in persistent astrophysical jets. *Nat. Astron.* 4, 124–131. doi:10.1038/s41550-019-0988-4

Blandford, R., Meier, D., and Readhead, A. (2019). Relativistic jets from active galactic nuclei. *ARAA* 57, 467–509. doi:10.1146/annurev-astro-081817-051948

Blinov, D., Kiehlmann, S., Pavlidou, V., Panopoulou, G. V., Skalidis, R., Angelakis, E., et al. (2021). RoboPol: AGN polarimetric monitoring data. *Mon. Not. R. Astron. Soc.* 501, 3715–3726. doi:10.1093/mnras/staa3777

Bloemen, H., Bennett, K., Blom, J. J., Collmar, W., Hermsen, W., Lichti, G. G., et al. (1995). New COMPTEL gamma-ray source (GRO J0516-609) near PKS 0506-612/0522-611: first evidence for "MeV Blazars". *Astron. Astrophys.* 293, L1–L4.

Boccardi, B., Krichbaum, T. P., Bach, U., Bremer, M., and Zensus, J. A. (2016). First 3 mm-VLBI imaging of the two-sided jet in Cygnus A. Zooming into the launching region. *Astron. Astrophys.* 588, L9. doi:10.1051/0004-6361/201628412

Boella, G., Butler, R. C., Perola, G. C., Piro, L., Scarsi, L., and Bleeker, J. A. M. (1997). BeppoSAX, the wide band mission for X-ray astronomy. *Astron. Astrophys. Suppl. Ser.* 122, 299–307. doi:10.1051/aas:1997136

Boller, T., Freyberg, M. J., Trümper, J., Haberl, F., Voges, W., and Nandra, K. (2016). Second ROSAT all-sky survey (2RXS) source catalogue. *Astron. Astrophys.* 588, A103. doi:10.1051/0004-6361/201525648

Böttcher, M. (2019). Progress in multi-wavelength and multi-messenger observations of blazars and theoretical challenges. *Galaxies* 7, 20. doi:10.3390/galaxies7010020

Böttcher, M., and Chiang, J. (2002). X-ray spectral variability signatures of flares in BL Lacertae objects. *Astrophys. J.* 581, 127–142. doi:10.1086/344155

Böttcher, M., Reimer, A., Sweeney, K., and Prakash, A. (2013). Leptonic and hadronic modeling of fermi-detected blazars. *Astrophys. J.* 768, 54. doi:10.1088/0004-637X/768/1/54

Boula, S., and Mastichiadis, A. (2022). Expanding one-zone model for blazar emission. *Astron. Astrophys.* 657, A20. doi:10.1051/0004-6361/202142126

Breiding, P., Meyer, E. T., Georganopoulos, M., Keenan, M. E., DeNigris, N. S., and Hewitt, J. (2017). Fermi non-detections of four X-ray jet sources and implications for the IC/CMB mechanism. *Astrophys. J.* 849, 95. doi:10.3847/1538-4357/aa907a

Bromm, V., and Loeb, A. (2003). Formation of the first supermassive black holes. *Astrophys. J.* 596, 34–46. doi:10.1086/377529

Brunner, H., Liu, T., Lamer, G., Georgakakis, A., Merloni, A., Brusa, M., et al. (2022). The eROSITA final equatorial depth survey (eFEDS). X-Ray catalogue. *Astron. Astrophys.* 661, A1. doi:10.1051/0004-6361/202141266

Buson, S., Tramacere, A., Pfeiffer, L., Oswald, L., de Menezes, R., Azzollini, A., et al. (2022). Beginning a journey across the universe: the discovery of extragalactic neutrino factories. *Astrophys. J. Lett.* 933, L43. doi:10.3847/2041-8213/ac7d5b

Caccianiga, A., Moretti, A., Belladitta, S., Della Ceca, R., Antón, S., Ballo, L., et al. (2019). The space density of z > 4 blazars. *Mon. Not. R. Astron. Soc.* 484, 204–217. doi:10.1093/mnras/sty3526

Cappelluti, N., Li, Y., Ricarte, A., Agarwal, B., Allevato, V., Tasnim Ananna, T., et al. (2017). The Chandra COSMOS legacy survey: energy spectrum of the cosmic X-ray background and constraints on undetected populations. *Astrophys. J.* 837, 19. doi:10.3847/1538-4357/aa5ea4

Caputo, R., Ajello, M., Kierans, C., Perkins, J., Racusin, J., Baldini, L., et al. (2022). *The all-sky medium energy gamma-ray observatory eXplorer (AMEGO-X) mission concept*. arXiv e-prints , arXiv:2208.04990.

Carlstrom, J., Abazajian, K., Addison, G., Adshead, P., Ahmed, Z., Allen, S. W., et al. (2019). CMB-S4. *Bull. Am. Astron. Soc.* 51, 209. doi:10.48550/arXiv.1908.01062

Catanese, M., and Sambruna, R. M. (2000). A rapid X-ray flare from markarian 501. *Astrophys. J. Lett.* 534, L39–L42. doi:10.1086/312637

Celotti, A., Ghisellini, G., and Fabian, A. C. (2007). Bulk Comptonization spectra in blazars. *Mon. Not. R. Astron. Soc.* 375, 417–424. doi:10.1111/j.1365-2966.2006.11289.x

Cerruti, M., Zech, A., Boisson, C., and Inoue, S. (2015). A hadronic origin for ultra-high-frequency-peaked BL Lac objects. *Mon. Not. R. Astron. Soc.* 448, 910–927. doi:10.1093/mnras/stu2691

Cerutti, B., Werner, G. R., Uzdensky, D. A., and Begelman, M. C. (2012). Beaming and rapid variability of high-energy radiation from relativistic pair plasma reconnection. *Astrophys. J. Lett.* 754, L33. doi:10.1088/2041-8205/754/2/L33

Chandra, S., Boettcher, M., Goswami, P., Singh, K. P., Zacharias, M., Kaur, N., et al. (2021). X-ray observations of 1ES 1959+650 in its high-activity state in 2016-2017 with AstroSat and Swift. *Astrophys. J.* 918, 67. doi:10.3847/1538-4357/ac01d1

Chartas, G., Worrall, D. M., Birkinshaw, M., Cresitello-Dittmar, M., Cui, W., Ghosh, K. K., et al. (2000). The Chandra X-ray observatory resolves the X-ray morphology and spectra of a jet in PKS 0637-752. *Astrophys. J.* 542, 655–666. doi:10.1086/317049

Chase, O., McBride, F., Gokus, A., Lucchini, M., Zhang, H., Ojha, R., et al. (2023). The peculiar variable X-ray spectrum of the active galactic nucleus PKS 2005-489. *Astrophys. J.* 948, 2. doi:10.3847/1538-4357/acc575

Chatterjee, R., Das, S., Khasnovis, A., Ghosh, R., Kumari, N., Naik, S., et al. (2021). Short-timescale variability of the blazar Mrk 421 from AstroSat and simultaneous multi-wavelength observations. *J. Astrophys. Astron.* 42, 80. doi:10.1007/s12036-021-09709-3

Cherenkov Telescope Array Consortium, Acharya, B. S., Agudo, I., Al Samarai, I., Alfaro, R., Alfaro, J., et al. (2019). *Science with the Cherenkov telescope Array*. World Scientific. doi:10.1142/10986

Christie, I. M., Petropoulou, M., Sironi, L., and Giannios, D. (2019). Radiative signatures of plasmoid-dominated reconnection in blazar jets. *Mon. Not. R. Astron. Soc.* 482, 65–82. doi:10.1093/mnras/sty2636

Civano, F., Zhao, X., Boorman, P., Marchesi, S., Ananna, T., Creech, S., et al. (2023). The high energy X-ray probe (HEX-P): bringing the cosmic X-ray background into focus. *arXiv e-prints*, 04832doi. arXiv:2311. doi:10.48550/arXiv.2311.04832

Connor, T., Bañados, E., Stern, D., Carilli, C., Fabian, A., Momjian, E., et al. (2021). Enhanced X-ray emission from the most radio-powerful quasar in the universe's first billion years. *Astrophys. J.* 911, 120. doi:10.3847/1538-4357/abe710

Costamante, L. (2004). A brief (blazar oriented) overview on topics for multiwavelength observations with TeV photons. *NAR* 48, 497–503. doi:10.1016/j.newar.2003.12.029

Costamante, L. (2020). TeV-peaked candidate BL Lac objects. *Mon. Not. R. Astron. Soc.* 491, 2771–2778. doi:10.1093/mnras/stz3018

Costamante, L., Aharonian, F., and Khangulyan, D. (2007). "GLAST answers about high-energy peaked BL Lacs: double-humped γ-ray peak and extreme accelerators," in *The first GLAST symposium*. Editors S. Ritz, P. Michelson, and C. A. Meegan (American Institute of Physics Conference Series), 921, 157–159. doi:10.1063/1.2757291

Costamante, L., Bonnoli, G., Tavecchio, F., Ghisellini, G., Tagliaferri, G., and Khangulyan, D. (2018). The nustar view on hard-tev bl lacs. *Mon. Not. R. Astron. Soc.* 477, 4257–4268. doi:10.1093/mnras/sty857

Costamante, L., Ghisellini, G., Giommi, P., Tagliaferri, G., Celotti, A., Chiaberge, M., et al. (2001). Extreme synchrotron BL Lac objects. Stretching the blazar sequence. *Astron. Astrophys.* 371, 512–526. doi:10.1051/0004-6361:20010412

Dauser, T., Falkner, S., Lorenz, M., Kirsch, C., Peille, P., Cucchetti, E., et al. (2019). SIXTE: a generic X-ray instrument simulation toolkit. *Astron. Astrophys.* 630, A66. doi:10.1051/0004-6361/201935978

De Angelis, A., Tatischeff, V., Tavani, M., Oberlack, U., Grenier, I., Hanlon, L., et al. (2017). The e-ASTROGAM mission. Exploring the extreme Universe with gamma rays in the MeV - GeV range. *Exp. Astron.* 44, 25–82. doi:10.1007/s10686-017-9533-6

de Jaeger, T., Shappee, B. J., Kochanek, C. S., Hinkle, J. T., Garrappa, S., Liodakis, I., et al. (2023). Optical/γ-ray blazar flare correlations: understanding the high-energy emission process using ASAS-SN and Fermi light curves. *Mon. Not. R. Astron. Soc.* 519, 6349–6380. doi:10.1093/mnras/stad060

de Jager, O. C., Harding, A. K., Michelson, P. F., Nel, H. I., Nolan, P. L., Sreekumar, P., et al. (1996). Gamma-ray observations of the Crab nebula: a study of the synchro-compton spectrum. *Astrophys. J.* 457, 253. doi:10.1086/176726

Dermer, C. D. (1995). On the beaming statistics of gamma-ray sources. *Astrophys. J. Lett.* 446, L63. doi:10.1086/187931

Dermer, C. D., Schlickeiser, R., and Mastichiadis, A. (1992). High-energy gamma radiation from extragalactic radio sources. *Astron. Astrophys.* 256, L27–L30. doi:10.1086/187931

Desai, A., Helgason, K., Ajello, M., Paliya, V., Domínguez, A., Finke, J., et al. (2019). A GeV-TeV measurement of the extragalactic background light. *Astrophys. J. Lett.* 874, L7. doi:10.3847/2041-8213/ab0c10

Desai, A., Marchesi, S., Rajagopal, M., and Ajello, M. (2019). Identifying the 3fhl catalog. III. results of the CTIO-COSMOS optical spectroscopy campaign. *APSS* 241, 5. doi:10.3847/1538-4365/ab01fc

Devanand, P. U., Gupta, A. C., Jithesh, V., and Wiita, P. J. (2022). Study of X-ray intraday variability of HBL blazars based on observations obtained with XMM-Newton. *Astrophys. J.* 939, 80. doi:10.3847/1538-4357/ac9064

Devecchi, B., and Volonteri, M. (2009). Formation of the first nuclear clusters and massive black holes at high redshift. *Astrophys. J.* 694, 302–313. doi:10.1088/0004-637X/694/1/302

Diana, A., Caccianiga, A., Ighina, L., Belladitta, S., Moretti, A., and Della Ceca, R. (2022). The evolution of the heaviest supermassive black holes in jetted AGNs. *Mon. Not. R. Astron. Soc.* 511, 5436–5447. doi:10.1093/mnras/stac364

Di Gesu, L., Donnarumma, I., Tavecchio, F., Agudo, I., Barnounin, T., Cibrario, N., et al. (2022). The X-ray polarization view of mrk 421 in an average flux state as observed by the imaging X-ray Polarimetry explorer. *Astrophys. J. Lett.* 938, L7. doi:10.3847/2041-8213/ac913a

Diltz, C., Böttcher, M., and Fossati, G. (2015). Time dependent hadronic modeling of flat spectrum radio quasars. *Astrophys. J.* 802, 133. doi:10.1088/0004-637X/802/2/133

Disney, M. J., Peterson, B. A., and Rodgers, A. W. (1974). The redshift and composite nature of AP Librae (pks 1514-24). *Astrophys. J. Lett.* 194, L79. doi:10.1086/181673

Domínguez, A., Láinez, M., Paliya, V. S., Álvarez-Crespo, N., Ajello, M., Finke, J., et al. (2023). *Constraints on redshifts of blazars from extragalactic background light attenuation using Fermi-LAT data*. arXiv e-prints , arXiv:2307.10083doi. doi:10.48550/arXiv.2307.10083

Donato, D., Sambruna, R. M., and Gliozzi, M. (2005). Six years of BeppoSAX observations of blazars: a spectral catalog. *Astron. Astrophys.* 433, 1163–1169. doi:10.1051/0004-6361:20034555

Dondi, L., and Ghisellini, G. (1995). Gamma-ray-loud blazars and beaming. *Mon. Not. R. Astron. Soc.* 273, 583–595. doi:10.1093/mnras/273.3.583

Ehlert, S. R., Ferrazzoli, R., Marinucci, A., Marshall, H. L., Middei, R., Pacciani, L., et al. (2022). Limits on X-ray polarization at the core of Centaurus A as observed with the imaging X-ray Polarimetry explorer. *Astrophys. J.* 935, 116. doi:10.3847/1538-4357/ac8056

Eichler, D. (1979). High-energy neutrino astronomy: a probe of galactic nuclei? *Astrophys. J.* 232, 106–112. doi:10.1086/157269

Eraerds, T., Antonelli, V., Davis, C., Hall, D., Hetherington, O., Holland, A., et al. (2021). Enhanced simulations on the athena/wide field imager instrumental background. *J. Astron. Telesc. Instrum. Syst.* 7, 034001. doi:10.1117/1.JATIS.7.3.034001

Fabian, A. C., Celotti, A., Iwasawa, K., McMahon, R. G., Carilli, C. L., Brandt, W. N., et al. (2001). PMN J0525-3343: soft X-ray spectral flattening in a blazar at z=4.4. *Mon. Not. R. Astron. Soc.* 323, 373–379. doi:10.1046/j.1365-8711.2001.04181.x

Fan, X., Narayanan, V. K., Lupton, R. H., Strauss, M. A., Knapp, G. R., Becker, R. H., et al. (2001). A survey of [CLC] [ITAL]z[/ITAL] [/CLC] > 5.8 quasars in the sloan digital sky survey. I. Discovery of three new quasars and the spatial density of luminous quasars at [CLC] [ITAL]z[/ITAL] [/CLC] ~ 6. *Astron. J.* 122, 2833–2849. doi:10.1086/324111

Fan, X.-L., and Wu, Q. (2018). The radio/gamma connection of blazars from high to low radio frequencies. *Astrophys. J.* 869, 133. doi:10.3847/1538-4357/aaeece

Fermi-LAT Collaboration, Abdollahi, S., Ackermann, M., Ajello, M., Atwood, W.-B., Baldini, L., et al. (2018). A gamma-ray determination of the Universe's star formation history. *Science* 362, 1031–1034. doi:10.1126/science.aat8123

Fossati, G., Buckley, J. H., Bond, I. H., Bradbury, S. M., Carter-Lewis, D. A., Chow, Y. C. K., et al. (2008). Multiwavelength observations of markarian 421 in 2001 March: an unprecedented view on the X-ray/TeV correlated variability. *Astrophys. J.* 677, 906–925. doi:10.1086/527311

Fossati, G., Maraschi, L., Celotti, A., Comastri, A., and Ghisellini, G. (1998). A unifying view of the spectral energy distributions of blazars. *Mon. Not. R. Astron. Soc.* 299, 433–448. doi:10.1046/j.1365-8711.1998.01828.x

Gao, S., Fedynitch, A., Winter, W., and Pohl, M. (2019). Modelling the coincident observation of a high-energy neutrino and a bright blazar flare. *Nat. Astron.* 3, 88–92. doi:10.1038/s41550-018-0610-1

Gao, S., Pohl, M., and Winter, W. (2017). On the direct correlation between gamma-rays and PeV neutrinos from blazars. *Astrophys. J.* 843, 109. doi:10.3847/1538-4357/aa7754

Garrappa, S., Buson, S., Franckowiak, A., Shappee, B. J., Beacom, J. F., Dong, S., et al. (2019). Investigation of two fermi-LAT gamma-ray blazars coincident with high-energy neutrinos detected by IceCube. *Astrophys. J.* 880, 103. doi:10.3847/1538-4357/ab2ada

Gaur, H., Gupta, A. C., Bachev, R., Strigachev, A., Semkov, E., Wiita, P. J., et al. (2019). Optical variability of TeV blazars on long time-scales. *Mon. Not. R. Astron. Soc.* 484, 5633–5644. doi:10.1093/mnras/stz322

Gaur, H., Mohan, P., and Pandey, A. (2021). Breaks in the X-ray spectra of high-redshift blazars and the intervening medium. *Astrophys. J.* 914, 46. doi:10.3847/1538-4357/abfa9d

Ghisellini, G. (1999a). Extreme blazars. *Astropart. Phys.* 11, 11–18. doi:10.1016/S0927-6505(99)00018-3

Ghisellini, G. (1999b). Mev synchrotron BL Lacs. *Astrophys. Lett. Commun.* 39, 17. doi:10.48550/arXiv.astro-ph/9812419

Ghisellini, G., Celotti, A., Fossati, G., Maraschi, L., and Comastri, A. (1998). A theoretical unifying scheme for gamma-ray bright blazars. *Mon. Not. R. Astron. Soc.* 301, 451–468. doi:10.1046/j.1365-8711.1998.02032.x

Ghisellini, G., Costamante, L., Tagliaferri, G., Maraschi, L., Celotti, A., Fossati, G., et al. (1999). The blazar PKS 0528+134: new results from BeppoSAX observations. *Astron. Astrophys.* 348, 63–70. doi:10.48550/arXiv.astro-ph/9906165

Ghisellini, G., and Maraschi, L. (1989). Bulk acceleration in relativistic jets and the spectral properties of blazars. *Astrophys. J.* 340, 181–189. doi:10.1086/167383

Ghisellini, G., Perri, M., Costamante, L., Tagliaferri, G., Sbarrato, T., Campitiello, S., et al. (2019). A *NuSTAR* view of powerful γ-ray loud blazars. *Astron. Astrophys.* 627, A72. doi:10.1051/0004-6361/201935750

Ghisellini, G., Righi, C., Costamante, L., and Tavecchio, F. (2017). The Fermi blazar sequence. *Mon. Not. R. Astron. Soc.* 469, 255–266. doi:10.1093/mnras/stx806

Ghisellini, G., and Tavecchio, F. (2008). Rapid variability in TeV blazars: the case of PKS2155-304. *Mon. Not. R. Astron. Soc.* 386, L28–L32. doi:10.1111/j.1745-3933.2008.00454.x

Ghisellini, G., and Tavecchio, F. (2009). Canonical high-power blazars. *Mon. Not. R. Astron. Soc.* 397, 985–1002. doi:10.1111/j.1365-2966.2009.15007.x

Ghisellini, G., Tavecchio, F., Foschini, L., Sbarrato, T., Ghirlanda, G., and Maraschi, L. (2012). Blue Fermi flat spectrum radio quasars. *Mon. Not. R. Astron. Soc.* 425, 1371–1379. doi:10.1111/j.1365-2966.2012.21554.x

Ghisellini, G., Tavecchio, F., Maraschi, L., Celotti, A., and Sbarrato, T. (2014). The power of relativistic jets is larger than the luminosity of their accretion disks. *Nature* 515, 376–378. doi:10.1038/nature13856

Giannios, D. (2013). Reconnection-driven plasmoids in blazars: fast flares on a slow envelope. *Mon. Not. R. Astron. Soc.* 431, 355–363. doi:10.1093/mnras/stt167

Gilli, R. (2013). The cosmic X-ray background: abundance and evolution of hidden black holes. *MEMSAI* 84, 647. . doi:10.48550/arXiv.1304.3665

Giommi, P., Brandt, C. H., Barres de Almeida, U., Pollock, A. M. T., Arneodo, F., Chang, Y. L., et al. (2019). Open Universe for Blazars: a new generation of astronomical products based on 14 years of Swift-XRT data. *Astron. Astrophys.* 631, A116. doi:10.1051/0004-6361/201935646

Giommi, P., Padovani, P., and Polenta, G. (2013). A simplified view of blazars: the γ-ray case. *Mon. Not. R. Astron. Soc.* 431, 1914–1922. doi:10.1093/mnras/stt305

Giommi, P., Padovani, P., Polenta, G., Turriziani, S., D'Elia, V., and Piranomonte, S. (2012). A simplified view of blazars: clearing the fog around long-standing selection effects. *Mon. Not. R. Astron. Soc.* 420, 2899–2911. doi:10.1111/j.1365-2966.2011.20044.x

Giommi, P., Perri, M., Capalbi, M., D'Elia, V., Barres de Almeida, U., Brandt, C. H., et al. (2021). X-ray spectra, light curves and SEDs of blazars frequently observed by Swift. *Mon. Not. R. Astron. Soc.* 507, 5690–5702. doi:10.1093/mnras/stab2425

Giroletti, M., Massaro, F., D'Abrusco, R., Lico, R., Burlon, D., Hurley-Walker, N., et al. (2016). High-energy sources at low radio frequency: the Murchison Widefield Array view of Fermi blazars. *Astron. Astrophys.* 588, A141. doi:10.1051/0004-6361/201527817

Gopal-Krishna, Goyal, A., Joshi, S., Karthick, C., Sagar, R., Wiita, P. J., et al. (2011). Rapid optical variability of TeV blazars. *Mon. Not. R. Astron. Soc.* 416, 101–117. doi:10.1111/j.1365-2966.2011.19014.x

Grant, D., Ackermann, M., Karle, A., and Kowalski, M. (2019). Neutrino astronomy with the next generation IceCube neutrino observatory. *Bull. Am. Astron. Soc.* 51, 288. doi:10.48550/arXiv.1911.02561

Haardt, F., Grandi, P., Celotti, A., Treves, A., Ghisellini, G., Maraschi, L., et al. (1999). BeppoSAX observations of 3C 273. *Nucl. Phys. B Proc. Suppl.* 69, 449–452. doi:10.1016/S0920-5632(98)00260-6

Hardcastle, M. J. (2006). Testing the beamed inverse-Compton model for jet X-ray emission: velocity structure and deceleration. *Mon. Not. R. Astron. Soc.* 366, 1465–1474. doi:10.1111/j.1365-2966.2005.09923.x

Harris, D. E., and Grindlay, J. E. (1979). The prospects for X-ray detection of inverse-Compton emission from radio source electrons and photons of the microwave background. *Mon. Not. R. Astron. Soc.* 188, 25–37. doi:10.1093/mnras/188.1.25

Harris, D. E., and Krawczynski, H. (2002). X-ray emission processes in radio jets. *Astrophys. J.* 565, 244–255. doi:10.1086/324544

Harris, D. E., and Krawczynski, H. (2006). X-ray emission from extragalactic jets. *ARAA* 44, 463–506. doi:10.1146/annurev.astro.44.051905.092446

Harrison, F. A., Craig, W. W., Christensen, F. E., Hailey, C. J., Zhang, W. W., Boggs, S. E., et al. (2013). The nuclear spectroscopic telescope Array (NuSTAR) high-energy X-ray mission. *Astrophys. J.* 770, 103. doi:10.1088/0004-637X/770/2/103

Hess, V. (1912). *On the observations of the penetrating radiation during seven balloon flights*, 15. arXiv:1808.02927.

H. E. S. S., Collaboration, Abdalla, H., Adam, R., Aharonian, F., Ait Benkhali, F., Angüner, E. O., et al.(2019). Constraints on the emission region of 3C 279 during strong flares in 2014 and 2015 through VHE γ-ray observations with H.E.S.S. *Astron. Astrophys.* 627, A159. doi:10.1051/0004-6361/201935704

H. E. S. S., Collaboration, Abdalla, H., Adam, R., Aharonian, F., Ait Benkhali, F., Angüner, E. O., et al.(2020). Resolving acceleration to very high energies along the jet of Centaurus A. *Nat* 582, 356–359. doi:10.1038/s41586-020-2354-1

H. E. S. S., Collaboration, Abramowski, A., Acero, F., Aharonian, F., Akhperjanian, A. G., Anton, G., et al.(2013). Measurement of the extragalactic background light imprint on the spectra of the brightest blazars observed with H.E.S.S. *Astron. Astrophys.* 550, A4. doi:10.1051/0004-6361/201220355

H. E. S. S., Collaboration, Abramowski, A., Aharonian, F., Ait Benkhali, F., Akhperjanian, A. G., Angüner, E., et al.(2015). The high-energyγ-ray emission of AP Librae. *Astron. Astrophys.* 573, A31. doi:10.1051/0004-6361/201321436

Hood, I. J. C., Simpson, A., McDaniel, A., Foster, A., Ade, P. A. R., Ajello, M., et al. (2023). Simultaneous millimeter-wave, gamma-ray, and optical monitoring of the blazar PKS 2326-502 during a flaring state. *Astrophys. J. Lett.* 945, L23. doi:10.3847/2041-8213/acbf45

Hooper, D., Linden, T., and Vieregg, A. (2019). Active galactic nuclei and the origin of IceCube's diffuse neutrino flux. *J. Cosmol. Astropart. Phys.* 2019, 012. doi:10.1088/1475-7516/2019/02/012

Hota, J., Shah, Z., Khatoon, R., Misra, R., Pradhan, A. C., and Gogoi, R. (2021). Understanding the X-ray spectral curvature of Mkn 421 using broad-band AstroSat observations. *Mon. Not. R. Astron. Soc.* 508, 5921–5934. doi:10.1093/mnras/stab2903

Hovatta, T., Valtaoja, E., Tornikoski, M., and Lähteenmäki, A. (2009). Doppler factors, Lorentz factors and viewing angles for quasars, BL Lacertae objects and radio galaxies. *Astron. Astrophys.* 494, 527–537. doi:10.1051/0004-6361:200811150

IceCube Collaboration, Fermi-LAT Collaboration, INTEGRAL Team, Swift/NuSTAR Team, Ackermann, M., Adams, J., et al. (2018b). Multimessenger observations of a flaring blazar coincident with high-energy neutrino IceCube-170922A. *Science* 361, eaat1378. doi:10.1126/science.aat1378

IceCube Collaboration, Aartsen, M. G., Ackermann, M., Adams, J., Aguilar, J. A., Ahlers, M., et al. (2018a). Neutrino emission from the direction of the blazar TXS 0506+056 prior to the IceCube-170922A alert. *Science* 361, 147–151. doi:10.1126/science.aat2890

IceCube Collaboration, Abbasi, R., Ackermann, M., Adams, J., Aguilar, J. A., Ahlers, M., et al. (2022). Evidence for neutrino emission from the nearby active galaxy NGC 1068. *Science* 378, 538–543. doi:10.1126/science.abg3395

Ighina, L., Caccianiga, A., Moretti, A., Belladitta, S., Della Ceca, R., Ballo, L., et al. (2019). X-ray properties of z > 4 blazars. *Mon. Not. R. Astron. Soc.* 489, 2732–2745. doi:10.1093/mnras/stz2340

Ighina, L., Caccianiga, A., Moretti, A., Belladitta, S., Della Ceca, R., and Diana, A. (2021). The impact of the CMB on the evolution of high-z blazars. *Mon. Not. R. Astron. Soc.* 505, 4120–4128. doi:10.1093/mnras/stab1612

Ighina, L., Moretti, A., Tavecchio, F., Caccianiga, A., Belladitta, S., Dallacasa, D., et al. (2022). Direct observation of an extended X-ray jet at z = 6.1. *Astron. Astrophys.* 659, A93. doi:10.1051/0004-6361/202142676

Jansen, F., Lumb, D., Altieri, B., Clavel, J., Ehle, M., Erd, C., et al. (2001). XMM-Newton observatory. I. The spacecraft and operations. *Astron. Astrophys.* 365, L1–L6. doi:10.1051/0004-6361:20000036

Jester, S., Harris, D. E., Marshall, H. L., and Meisenheimer, K. (2006). New Chandra observations of the jet in 3C 273. I. Softer X-ray than radio spectra and the X-ray emission mechanism. *Astrophys. J.* 648, 900–909. doi:10.1086/505962

Johnson, J. L., and Upton Sanderbeck, P. R. (2022). A simple condition for sustained super-eddington black hole growth. *Astrophys. J.* 934, 58. doi:10.3847/1538-4357/ac7b81

Jolley, E. J. D., and Kuncic, Z. (2008). Jet-enhanced accretion growth of supermassive black holes. *Mon. Not. R. Astron. Soc.* 386, 989–994. doi:10.1111/j.1365-2966.2008.13082.x

Jorstad, S. G., Marscher, A. P., Stevens, J. A., Smith, P. S., Forster, J. R., Gear, W. K., et al. (2007). Multiwaveband polarimetric observations of 15 active galactic nuclei at high frequencies: correlated polarization behavior. *Astron. J.* 134, 799–824. doi:10.1086/519996

Kadler, M., Krauß, F., Mannheim, K., Ojha, R., Müller, C., Schulz, R., et al. (2016). Coincidence of a high-fluence blazar outburst with a PeV-energy neutrino event. *Nat. Phys.* 12, 807–814. doi:10.1038/nphys3715

Kadowaki, L. H. S., de Gouveia Dal Pino, E. M., and Singh, C. B. (2015). The role of fast magnetic reconnection on the radio and gamma-ray emission from the nuclear regions of microquasars and low luminosity AGNs. *Astrophys. J.* 802, 113. doi:10.1088/0004-637X/802/2/113

Kapanadze, B., Dorner, D., Vercellone, S., Romano, P., Aller, H., Aller, M., et al. (2016). X-ray flaring activity of mrk 421 in the first half of 2013. *Astrophys. J.* 831, 102. doi:10.3847/0004-637X/831/1/102

Kataoka, J., Mattox, J. R., Quinn, J., Kubo, H., Makino, F., Takahashi, T., et al. (1999). High-energy emission from the TEV blazar markarian 501 during multiwavelength observations in 1996. *Astrophys. J.* 514, 138–147. doi:10.1086/306918

Kaufmann, S., Wagner, S. J., and Tibolla, O. (2013). Discovery of an extended X-ray jet in AP Librae. *Astrophys. J.* 776, 68. doi:10.1088/0004-637X/776/2/68

Kaur, A., Ajello, M., Marchesi, S., and Omodei, N. (2019). Identifying the 3FHL catalog. I. Archival Swift observations and source classification. *Astrophys. J.* 871, 94. doi:10.3847/1538-4357/aaf649

Keenan, M., Meyer, E. T., Georganopoulos, M., Reddy, K., and French, O. J. (2021). The relativistic jet dichotomy and the end of the blazar sequence. *Mon. Not. R. Astron. Soc.* 505, 4726–4745. doi:10.1093/mnras/stab1182

Keivani, A., Murase, K., Petropoulou, M., Fox, D. B., Cenko, S. B., Chaty, S., et al. (2018). A multimessenger picture of the flaring blazar TXS 0506+056: implications for high-energy neutrino emission and cosmic-ray acceleration. *Astrophys. J.* 864, 84. doi:10.3847/1538-4357/aad59a

Kirk, J. G., and Mastichiadis, A. (1999). Variability patterns of synchrotron and inverse Compton emission in blazars. *Astropart. Phys.* 11, 45–48. doi:10.1016/S0927-6505(99)00023-7

Kirk, J. G., Rieger, F. M., and Mastichiadis, A. (1998). Particle acceleration and synchrotron emission in blazar jets. *Astron. Astrophys.* 333, 452–458. doi:10.48550/arXiv.astro-ph/9801265

Komossa, S., Grupe, D., Gallo, L. C., Gonzalez, A., Yao, S., Hollett, A. R., et al. (2021). MOMO. IV. The complete Swift X-ray and UV/optical light curve and characteristic variability of the blazar OJ 287 during the last two decades. *Astrophys. J.* 923, 51. doi:10.3847/1538-4357/ac1442

Koyama, K., Tsunemi, H., Dotani, T., Bautz, M. W., Hayashida, K., Tsuru, T. G., et al. (2007). X-ray imaging spectrometer (XIS) on board Suzaku. *Publ. Astron. Soc. Jpn. Nihon. Tenmon. Gakkai.* 59, 23–33. doi:10.1093/pasj/59.sp1.S23

Krauß, F., Calamari, E., Keivani, A., Coleiro, A., Evans, P. A., Fox, D. B., et al. (2020). Multimessenger observations of counterparts to IceCube-190331A. *Mon. Not. R. Astron. Soc.* 497, 2553–2561. doi:10.1093/mnras/staa2148

Krauß, F., Deoskar, K., Baxter, C., Kadler, M., Kreter, M., Langejahn, M., et al. (2018). Fermi/LAT counterparts of IceCube neutrinos above 100 TeV. *Astron. Astrophys.* 620, A174. doi:10.1051/0004-6361/201834183

Krauß, F., Kadler, M., Mannheim, K., Schulz, R., Trüstedt, J., Wilms, J., et al. (2014). TANAMI blazars in the IceCube PeV-neutrino fields. *Astron. Astrophys.* 566, L7. doi:10.1051/0004-6361/201424219

Krawczynski, H., Hughes, S. B., Horan, D., Aharonian, F., Aller, M. F., Aller, H., et al. (2004). Multiwavelength observations of strong flares from the TeV blazar 1ES 1959+650. *Astrophys. J.* 601, 151–164. doi:10.1086/380393

Kreter, M., Gokus, A., Krauss, F., Kadler, M., Ojha, R., Buson, S., et al. (2020a). Search for high-redshift blazars with Fermi/LAT. *Astrophys. J.* 903, 128. doi:10.3847/1538-4357/abb8da

Kreter, M., Kadler, M., Krauß, F., Mannheim, K., Buson, S., Ojha, R., et al. (2020b). On the detection potential of blazar flares for current neutrino telescopes. *Astrophys. J.* 902, 133. doi:10.3847/1538-4357/abb5b1

Lehmer, B. D., Garofali, K., Binder, B. A., Fornasini, F., Vulic, N., Zezas, A., et al. (2023). *The high energy X-ray probe: resolved X-ray populations in extragalactic environments*. arXiv e-prints , arXiv:2311.04735. doi:10.48550/arXiv.2311.04735

Levinson, A., and Rieger, F. (2011). Variable TeV emission as a manifestation of jet formation in M87? *Astrophys. J.* 730, 123. doi:10.1088/0004-637X/730/2/123

Liao, N.-H., Li, S., and Fan, Y.-Z. (2018). Fermi-LAT detection of a transient γ-ray source in the direction of a distant blazar B3 1428+422 at z = 4.72. *Astrophys. J. Lett.* 865, L17. doi:10.3847/2041-8213/aae20d

Linfield, R. (1981). VLBI observations of jets in double radio galaxies. *Astrophys. J.* 244, 436–446. doi:10.1086/158720

Liodakis, I., Marscher, A. P., Agudo, I., Berdyugin, A. V., Bernardos, M. I., Bonnoli, G., et al. (2022). Polarized blazar X-rays imply particle acceleration in shocks. *Nature* 611, 677–681. doi:10.1038/s41586-022-05338-0

Lodato, G., and Natarajan, P. (2006). Supermassive black hole formation during the assembly of pre-galactic discs. *Mon. Not. R. Astron. Soc.* 371, 1813–1823. doi:10.1111/j.1365-2966.2006.10801.x

Lucchini, M., Markoff, S., Crumley, P., Krauß, F., and Connors, R. M. T. (2019). Breaking degeneracy in jet dynamics: multi-epoch joint modelling of the BL Lac PKS 2155-304. *Mon. Not. R. Astron. Soc.* 482, 4798–4812. doi:10.1093/mnras/sty2929

Madau, P., Ghisellini, G., and Persic, M. (1987). Beaming in blazars. *Mon. Not. R. Astron. Soc.* 224, 257–264. doi:10.1093/mnras/224.1.257

Madau, P., and Rees, M. J. (2001). Massive black holes as population III remnants. *Astrophys. J. Lett.* 551, L27–L30. doi:10.1086/319848

Madejski, G. G., and Sikora, M. (2016). Gamma-ray observations of active galactic nuclei. *ARAA* 54, 725–760. doi:10.1146/annurev-astro-081913-040044

Madejski, G. M., Nalewajko, K., Madsen, K. K., Chiang, J., Baloković, M., Paneque, D., et al. (2016). First NuSTAR observations of the BL lac-type blazar PKS 2155-304: constraints on the jet content and distribution of radiating particles. *Astrophys. J.* 831, 142. doi:10.3847/0004-637X/831/2/142

Madsen, K. K., García, J. A., Stern, D., Armini, R., Basso, S., Coutinho, D., et al. (2023). *The high energy X-ray probe (HEX-P): instrument and mission profile*. arXiv e-prints , arXiv:2312.04678. doi:10.48550/arXiv.2312.04678

MAGIC Collaboration, Acciari, V. A., Ansoldi, S., Antonelli, L. A., Babić, A., Banerjee, B., et al. (2020). Study of the variable broadband emission of Markarian 501 during the most extreme Swift X-ray activity. *Astron. Astrophys.* 637, A86. doi:10.1051/0004-6361/201834603

MAGIC Collaboration, Acciari, V. A., Ansoldi, S., Antonelli, L. A., Arbet Engels, A., Artero, M., et al. (2021). Investigation of the correlation patterns and the

Compton dominance variability of Mrk 421 in 2017. *Astron. Astrophys.* 655, A89. doi:10.1051/0004-6361/202141004

Mannheim, K. (1993). The proton blazar. *Astron. Astrophys.* 269, 67–76. doi:10.48550/arXiv.astro-ph/9302006

Mannheim, K., Stanev, T., and Biermann, P. L. (1992). Neutrinos from flat-spectrum radio quasars. *Astron. Astrophys.* 260, L1–L3. doi:10.48550/arXiv.astro-ph/9302006

Mao, L., and Zhang, X. (2016). Long-term optical variability properties of blazars in the SDSS Stripe 82. *APSS* 361, 345. doi:10.1007/s10509-016-2934-6

Maraschi, L. (1999). A first look at blazars with BeppoSAX. *Nucl. Phys. B Proc. Suppl.* 69, 389–396. doi:10.1016/S0920-5632(98)00247-3

Maraschi, L., Fossati, G., Tavecchio, F., Chiappetti, L., Celotti, A., Ghisellini, G., et al. (1999). Simultaneous X-Ray and T[CLC]e[/CLC]V Observations of a Rapid Flare from Markarian 421. *Astrophys. J. Lett.* 526, L81–L84. doi:10.1086/312370

Marchesi, S., Kaur, A., and Ajello, M. (2018). Identifying the 3FHL catalog. II. Results of the KOSMOS optical spectroscopy campaign. *Astron. J.* 156, 212. doi:10.3847/1538-3881/aae201

Marcotulli, L., Ajello, M., Urry, C. M., Paliya, V. S., Koss, M., Oh, K., et al. (2022). BASS. XXXIII. Swift-BAT blazars and their jets through cosmic time. *Astrophys. J.* 940, 77. doi:10.3847/1538-4357/ac937f

Marcotulli, L., Paliya, V., Ajello, M., Kaur, A., Marchesi, S., Rajagopal, M., et al. (2020). NuSTAR perspective on high-redshift MeV blazars. *Astrophys. J.* 889, 164. doi:10.3847/1538-4357/ab65f5

Marcotulli, L., Paliya, V. S., Ajello, M., Kaur, A., Hartmann, D. H., Gasparrini, D., et al. (2017). High-redshift blazars through NuSTAR eyes. *Astrophys. J.* 839, 96. doi:10.3847/1538-4357/aa6a17

Marscher, A. P. (2014). Turbulent, extreme multi-zone model for simulating flux and polarization variability in blazars. *Astrophys. J.* 780, 87. doi:10.1088/0004-637X/780/1/87

Marscher, A. P., and Gear, W. K. (1985). Models for high-frequency radio outbursts in extragalactic sources, with application to the early 1983 millimeter-to-infrared flare of 3C 273. *Astrophys. J.* 298, 114–127. doi:10.1086/163592

Marshall, H. L., Gelbord, J. M., Worrall, D. M., Birkinshaw, M., Schwartz, D. A., Jauncey, D. L., et al. (2018). An X-ray imaging survey of quasar jets: the complete survey. *Astrophys. J.* 856, 66. doi:10.3847/1538-4357/aaaf66

Marshall, H. L., Harris, D. E., Grimes, J. P., Drake, J. J., Fruscione, A., Juda, M., et al. (2001). Structure of the X-ray emission from the jet of 3C 273. *Astrophys. J. Lett.* 549, L167–L171. doi:10.1086/319161

Massaro, E., Maselli, A., Leto, C., Marchegiani, P., Perri, M., Giommi, P., et al. (2015). The 5th edition of the Roma-BZCAT. A short presentation. *APSS* 357, 75. doi:10.1007/s10509-015-2254-2

Massaro, E., Perri, M., Giommi, P., and Nesci, R. (2004). Log-parabolic spectra and particle acceleration in the BL Lac object Mkn 421: spectral analysis of the complete BeppoSAX wide band X-ray data set. *Astron. Astrophys.* 413, 489–503. doi:10.1051/0004-6361:20031558

Massaro, E., Tramacere, A., Perri, M., Giommi, P., and Tosti, G. (2006). Log-parabolic spectra and particle acceleration in blazars: III. SSC emission in the TeV band from Mkn 501. *Astron. Astrophys.* 448, 861–871. doi:10.1051/0004-6361:20053644

Massaro, F., Álvarez Crespo, N., D'Abrusco, R., Landoni, M., Masetti, N., Ricci, F., et al. (2016). The gamma-ray blazar quest: new optical spectra, state of art and future perspectives. *APSS* 361, 337. doi:10.1007/s10509-016-2926-6

Massaro, F., Giroletti, M., Paggi, A., D'Abrusco, R., Tosti, G., and Funk, S. (2013). Blazar spectral properties at 74 MHz. *Astrophys. J. Suppl. Ser.* 208, 15. doi:10.1088/0067-0049/208/2/15

Massaro, F., Masetti, N., D'Abrusco, R., Paggi, A., and Funk, S. (2014). Optical spectroscopic observations of blazars and γ-ray blazar candidates in the sloan digital sky survey data release nine. *Astron. J.* 148, 66. doi:10.1088/0004-6256/148/4/66

Massaro, F., Tramacere, A., Cavaliere, A., Perri, M., and Giommi, P. (2008). X-ray spectral evolution of TeV BL Lacertae objects: eleven years of observations with BeppoSAX, XMM-Newton and Swift satellites. *Astron. Astrophys.* 478, 395–401. doi:10.1051/0004-6361:20078639

Meidinger, N., Albrecht, S., Beitler, C., Bonholzer, M., Emberger, V., Frank, J., et al. (2020). "Development status of the wide field imager instrument for Athena," in *Space telescopes and instrumentation 2020: ultraviolet to gamma ray*. Editors J.-W. A. den Herder, S. Nikzad, and K. Nakazawa (Society of Photo-Optical Instrumentation Engineers Conference Series), 11444. doi:10.1117/12.2560507

Meyer, E. T., Breiding, P., Georganopoulos, M., Oteo, I., Zwaan, M. A., Laing, R., et al. (2017). New ALMA and Fermi/LAT observations of the large-scale jet of PKS 0637-752 strengthen the case against the IC/CMB model. *Astrophys. J. Lett.* 835, L35. doi:10.3847/2041-8213/835/2/L35

Meyer, E. T., Petropoulou, M., Georganopoulos, M., Chiaberge, M., Breiding, P., and Sparks, W. B. (2018). Detection of an optical/UV jet/counterjet and multiple spectral components in M84. *Astrophys. J.* 860, 9. doi:10.3847/1538-4357/aabf39

Meyer, M., Scargle, J. D., and Blandford, R. D. (2019). *Characterizing the gamma-ray variability of the brightest flat spectrum radio quasars observed with the Fermi LAT 877*, 39. doi:10.3847/1538-4357/ab1651

Middei, R., Giommi, P., Perri, M., Turriziani, S., Sahakyan, N., Chang, Y. L., et al. (2022). The first hard X-ray spectral catalogue of Blazars observed by NuSTAR. *Mon. Not. R. Astron. Soc.* 514, 3179–3190. doi:10.1093/mnras/stac1185

Middei, R., Liodakis, I., Perri, M., Puccetti, S., Cavazzuti, E., Di Gesu, L., et al. (2023a). X-ray polarization observations of BL Lacertae. *Astrophys. J. Lett.* 942, L10. doi:10.3847/2041-8213/aca281

Middei, R., Perri, M., Puccetti, S., Liodakis, I., Di Gesu, L., Marscher, A. P., et al. (2023b). IXPE and multiwavelength observations of blazar PG 1553+113 reveal an orphan optical polarization swing. *Astrophys. J. Lett.* 953, L28. doi:10.3847/2041-8213/acec3e

Mohorian, M., Bhatta, G., Adhikari, T. P., Dhital, N., Pánis, R., Dinesh, A., et al. (2022). X-ray timing and spectral variability properties of blazars S5 0716 + 714, OJ 287, Mrk 501, and RBS 2070. *Mon. Not. R. Astron. Soc.* 510, 5280–5301. doi:10.1093/mnras/stab3738

Mortlock, D. J., Warren, S. J., Venemans, B. P., Patel, M., Hewett, P. C., McMahon, R. G., et al. (2011). A luminous quasar at a redshift of z = 7.085. *Nature* 474, 616–619. doi:10.1038/nature10159

Mücke, A., Protheroe, R. J., Engel, R., Rachen, J. P., and Stanev, T. (2003). BL Lac objects in the synchrotron proton blazar model. *Astropart. Phys.* 18, 593–613. doi:10.1016/S0927-6505(02)00185-8

Mundo, S. A., and Mushotzky, R. (2023). Long-term hard X-ray variability properties of Swift-BAT blazars. *Mon. Not. R. Astron. Soc.* 526, 4040–4050. doi:10.1093/mnras/stad2991

Murase, K., Inoue, Y., and Dermer, C. D. (2014). Diffuse neutrino intensity from the inner jets of active galactic nuclei: impacts of external photon fields and the blazar sequence. *Phys. Rev. D.* 90, 023007. doi:10.1103/PhysRevD.90.023007

Murase, K., Oikonomou, F., and Petropoulou, M. (2018). Blazar flares as an origin of high-energy cosmic neutrinos? *Astrophys. J.* 865, 124. doi:10.3847/1538-4357/aada00

Nandra, K., Barret, D., Barcons, X., Fabian, A., den Herder, J.-W., Piro, L., et al. (2013). *The hot and energetic universe: a white paper presenting the science theme motivating the Athena+ mission. arXiv e-prints* , arXiv:1306.2307. doi:10.48550/arXiv.1306.2307

National Academies of Sciences, Engineering, and Medicine (2021). *Pathways to discovery in astronomy and astrophysics for the 2020s*. Washington, DC: The National Academies Press. doi:10.17226/26141

Nemmen, R. S., Storchi-Bergmann, T., and Eracleous, M. (2014). Spectral models for low-luminosity active galactic nuclei in LINERs: the role of advection-dominated accretion and jets. *Mon. Not. R. Astron. Soc.* 438, 2804–2827. doi:10.1093/mnras/stt2388

Nieppola, E., Valtaoja, E., Tornikoski, M., Hovatta, T., and Kotiranta, M. (2008). Blazar sequence - an artefact of Doppler boosting. *Astron. Astrophys.* 488, 867–872. doi:10.1051/0004-6361:200809716

Noel, A. P., Gaur, H., Gupta, A. C., Wierzcholska, A., Ostrowski, M., Dhiman, V., et al. (2022). X-ray intraday variability of the TeV blazar markarian 421 with XMM-Newton. *Astrophys. J. Suppl. Ser.* 262, 4. doi:10.3847/1538-4365/ac7799

Oei, M. S. S. L., van Weeren, R. J., Hardcastle, M. J., Botteon, A., Shimwell, T. W., Dabhade, P., et al. (2022). The discovery of a radio galaxy of at least 5 Mpc. *Astron. Astrophys.* 660, A2. doi:10.1051/0004-6361/202142778

Oh, K., Koss, M., Markwardt, C. B., Schawinski, K., Baumgartner, W. H., Barthelmy, S. D., et al. (2018). The 105-month swift-BAT all-sky hard X-ray survey. *Astrophys. J. Suppl. Ser.* 235, 4. doi:10.3847/1538-4365/aaa7fd

Otero-Santos, J., Acosta-Pulido, J. A., Becerra González, J., Raiteri, C. M., Carnerero, M. I., Castro Segura, N., et al. (2023). Variability and evolution of the optical polarization of a sample of gamma-ray blazars. *Mon. Not. R. Astron. Soc.* 523, 4504–4519. doi:10.1093/mnras/stad1722

Pacini, D. (1912). La radiazione penetrante alla superficie ed in seno alle acque. *Il Nuovo Cimento* 3, 93–100. doi:10.1007/bf02957440

Padovani, P., Alexander, D. M., Assef, R. J., De Marco, B., Giommi, P., Hickox, R. C., et al. (2017). Active galactic nuclei: what's in a name? *AAPR* 25, 2. doi:10.1007/s00159-017-0102-9

Padovani, P., Boccardi, B., Falomo, R., and Giommi, P. (2022a). PKS 1424+240: yet another masquerading BL Lac object as a possible IceCube neutrino source. *Mon. Not. R. Astron. Soc.* 511, 4697–4701. doi:10.1093/mnras/stac376

Padovani, P., Costamante, L., Ghisellini, G., Giommi, P., and Perlman, E. (2002). BeppoSAX observations of synchrotron X-ray emission from radio quasars. *Astrophys. J.* 581, 895–911. doi:10.1086/344406

Padovani, P., Giommi, P., Falomo, R., Oikonomou, F., Petropoulou, M., Glauch, T., et al. (2022b). The spectra of IceCube neutrino (SIN) candidate sources - II. Source characterization. *Mon. Not. R. Astron. Soc.* 510, 2671–2688. doi:10.1093/mnras/stab3630

Padovani, P., Oikonomou, F., Petropoulou, M., Giommi, P., and Resconi, E. (2019). TXS 0506+056, the first cosmic neutrino source, is not a BL Lac. *Mon. Not. R. Astron. Soc.* 484, L104–L108. doi:10.1093/mnrasl/slz011

Padovani, P., Petropoulou, M., Giommi, P., and Resconi, E. (2015). A simplified view of blazars: the neutrino background. *Mon. Not. R. Astron. Soc.* 452, 1877–1887. doi:10.1093/mnras/stv1467

Paggi, A., Milisavljevic, D., Masetti, N., Jiménez-Bailón, E., Chavushyan, V., D'Abrusco, R., et al. (2014). Optical spectroscopic observations of γ-ray blazar candidates. i. preliminary results. *Astron. J.* 147, 112. doi:10.1088/0004-6256/147/5/112

Paiano, S., Falomo, R., Franceschini, A., Treves, A., and Scarpa, R. (2017). Optical spectroscopic survey of a sample of unidentified Fermi objects. *Astrophys. J.* 851, 135. doi:10.3847/1538-4357/aa9af4

Paliya, V. S., Ajello, M., Cao, H. M., Giroletti, M., Kaur, A., Madejski, G., et al. (2020). Blazars at the cosmic dawn. *Astrophys. J.* 897, 177. doi:10.3847/1538-4357/ab9c1a

Paliya, V. S., Ajello, M., Ojha, R., Angioni, R., Cheung, C. C., Tanada, K., et al. (2019a). Detection of a gamma-ray flare from the high-redshift blazar DA 193. *Astrophys. J.* 871, 211. doi:10.3847/1538-4357/aafa10

Paliya, V. S., Koss, M., Trakhtenbrot, B., Ricci, C., Oh, K., Ajello, M., et al. (2019b). BAT AGN spectroscopic survey. XVI. General physical characteristics of BAT blazars. *Astrophys. J.* 881, 154. doi:10.3847/1538-4357/ab2f8b

Peirson, A. L., Liodakis, I., and Romani, R. W. (2022). Testing high-energy emission models for blazars with X-ray Polarimetry. *Astrophys. J.* 931, 59. doi:10.3847/1538-4357/ac6a54

Peirson, A. L., Negro, M., Liodakis, I., Middei, R., Kim, D. E., Marscher, A. P., et al. (2023). X-ray polarization of BL Lacertae in outburst. *Astrophys. J. Lett.* 948, L25. doi:10.3847/2041-8213/acd242

Peña-Herazo, H. A., Paggi, A., García-Pérez, A., Amaya-Almazán, R. A., Massaro, F., Ricci, F., et al. (2021). Optical spectroscopic observations of gamma-ray blazar candidates. XI. Optical observations from SOAR, blanco, NTT and OAN-SPM. The story so far. *Astron. J.* 162, 177. doi:10.3847/1538-3881/ac1da7

Petropoulou, M., Dimitrakoudis, S., Padovani, P., Mastichiadis, A., and Resconi, E. (2015). Photohadronic origin of γ-ray BL Lac emission: implications for IceCube neutrinos. *Mon. Not. R. Astron. Soc.* 448, 2412–2429. doi:10.1093/mnras/stv179

Petropoulou, M., and Mastichiadis, A. (2015). Bethe–Heitler emission in BL Lacs: filling the gap between X-rays and γ-rays. *Mon. Not. R. Astron. Soc.* 447, 36–48. doi:10.1093/mnras/stu2364

Petropoulou, M., Murase, K., Santander, M., Buson, S., Tohuvavohu, A., Kawamuro, T., et al. (2020). Multi-epoch modeling of TXS 0506+056 and implications for long-term high-energy neutrino emission. *Astrophys. J.* 891, 115. doi:10.3847/1538-4357/ab76d0

Petropoulou, M., Vasilopoulos, G., and Giannios, D. (2017). The TeV emission of Ap Librae: a hadronic interpretation and prospects for CTA. *Mon. Not. R. Astron. Soc.* 464, 2213–2222. doi:10.1093/mnras/stw2453

Pian, E., Vacanti, G., Tagliaferri, G., Ghisellini, G., Maraschi, L., Treves, A., et al. (1998). [ITAL]BeppoSAX[/ITAL] observations of unprecedented synchrotron activity in the BL Lacertae object markarian 501. *Astrophys. J. Lett.* 492, L17–L20. doi:10.1086/311083

Plavin, A., Kovalev, Y. Y., Kovalev, Y. A., and Troitsky, S. (2020). Observational evidence for the origin of high-energy neutrinos in parsec-scale nuclei of radio-bright active galaxies. *Astrophys. J.* 894, 101. doi:10.3847/1538-4357/ab86bd

Plavin, A. V., Kovalev, Y. Y., Kovalev, Y. A., and Troitsky, S. V. (2022). Growing evidence for high-energy neutrinos originating in radio blazars. *arXiv e-prints*. arXiv:2211.09631doi. doi:10.48550/arXiv.2211.09631

Poitevineau, R., Castignani, G., and Combes, F. (2023). Black hole and galaxy co-evolution in radio-loud active galactic nuclei at $z \sim 0.3$–4. *Astron. Astrophys.* 672, A164. doi:10.1051/0004-6361/202244560

Potter, W. J., and Cotter, G. (2015). New constraints on the structure and dynamics of black hole jets. *Mon. Not. R. Astron. Soc.* 453, 4071–4089. doi:10.1093/mnras/stv1657

Protheroe, R. J., and Kazanas, D. (1983). On the origin of relativistic particles and gamma-rays in quasars. *Astrophys. J.* 265, 620–624. doi:10.1086/160707

Pushkarev, A. B., Kovalev, Y. Y., Lister, M. L., and Savolainen, T. (2017). MOJAVE - XIV. Shapes and opening angles of AGN jets. *Mon. Not. R. Astron. Soc.* 468, 4992–5003. doi:10.1093/mnras/stx854

Rajagopal, M., Marchesi, S., Kaur, A., Domínguez, A., Silver, R., and Ajello, M. (2021). Identifying the 3FHL catalog. V. Results of the CTIO-COSMOS optical spectroscopy campaign 2019. *Astrophys. J. Suppl. Ser.* 254, 26. doi:10.3847/1538-4365/abf656

Rajagopal, M., Marcotulli, L., Ajello, M., Kaur, A., Paliya, V., and Hartmann, D. (2020). NuSTAR observations and multiwavelength modeling of the high-redshift BL Lacertae object 4FGL j2146.5-1344. *Astrophys. J.* 889, 102. doi:10.3847/1538-4357/ab6226

Rajagopal, M., Marcotulli, L., Labrie, K., Marchesi, S., and Ajello, M. (2023). Identifying the 3FHL catalog. VI. Results of the 2019 gemini optical spectroscopy. *Astron. J.* 165, 42. doi:10.3847/1538-3881/aca1be

Rajput, B., Stalin, C. S., and Rakshit, S. (2020). Long term γ-ray variability of blazars. *Astron. Astrophys.* 634, A80. doi:10.1051/0004-6361/201936769

Raouf, M., Shabala, S. S., Croton, D. J., Khosroshahi, H. G., and Bernyk, M. (2017). The many lives of active galactic nuclei-II: the formation and evolution of radio jets and their impact on galaxy evolution. *Mon. Not. R. Astron. Soc.* 471, 658–670. doi:10.1093/mnras/stx1598

Rau, A., Schady, P., Greiner, J., Salvato, M., Ajello, M., Bottacini, E., et al. (2012). BL Lacertae objects beyond redshift 1.3 - UV-to-NIR photometry and photometric redshift for Fermi/LAT blazars. *Astron. Astrophys.* 538, A26. doi:10.1051/0004-6361/201118159

Ravasio, M., Tagliaferri, G., Ghisellini, G., Tavecchio, F., Böttcher, M., and Sikora, M. (2003). <*b*>*Beppo*</*b*>SAX and multiwavelength observations of BL Lacertae in 2000. *Astron. Astrophys.* 408, 479–491. doi:10.1051/0004-6361:20031015

Rawlings, S., and Jarvis, M. J. (2004). Evidence that powerful radio jets have a profound influence on the evolution of galaxies. *Mon. Not. R. Astron. Soc.* 355, L9–L12. doi:10.1111/j.1365-2966.2004.08234.x

Reddy, K., Georganopoulos, M., Meyer, E. T., Keenan, M., and Kollmann, K. E. (2023). Offsets between X-ray and radio components in X-ray jets: the AtlasX. *Astrophys. J. Suppl. Ser.* 265, 8. doi:10.3847/1538-4365/aca321

Rees, M. J. (1978). The M87 jet: internal shocks in a plasma beam? *Mon. Not. R. Astron. Soc.* 184, 61P–65P. doi:10.1093/mnras/184.1.61P

Reimer, A., Böttcher, M., and Buson, S. (2019). Cascading constraints from neutrino-emitting blazars: the case of TXS 0506+056. *Astrophys. J.* 881, 46. doi:10.3847/1538-4357/ab2bff

Reimer, A., Costamante, L., Madejski, G., Reimer, O., and Dorner, D. (2008). A hard X-ray view of two distant VHE blazars: 1ES 1101-232 and 1ES 1553+113. *Astrophys. J.* 682, 775–783. doi:10.1086/589641

Ricci, F., Massaro, F., Landoni, M., D'Abrusco, R., Milisavljevic, D., Stern, D., et al. (2015). Optical spectroscopic observations of gamma-ray blazar candidates. IV. Results of the 2014 follow-up campaign. *Astron. J.* 149, 160. doi:10.1088/0004-6256/149/5/160

Roychowdhury, A., Meyer, E. T., Georganopoulos, M., Breiding, P., and Petropoulou, M. (2022). Circumnuclear dust in AP Librae and the source of its VHE emission. *ApJ* 924, 57. doi:10.3847/1538-4357/ac34f1

Safna, P. Z., Stalin, C. S., Rakshit, S., and Mathew, B. (2020). Long-term optical and infrared variability characteristics of Fermi blazars. *Mon. Not. R. Astron. Soc.* 498, 3578–3591. doi:10.1093/mnras/staa2622

Sandrinelli, A., Covino, S., and Treves, A. (2014). Long and short term variability of seven blazars in six near-infrared/optical bands. *Astron. Astrophys.* 562, A79. doi:10.1051/0004-6361/201321558

Sbarrato, T. (2021). Big and Young supermassive black holes in the early universe. *Galaxies* 9, 23. doi:10.3390/galaxies9020023

Sbarrato, T., Ghisellini, G., Nardini, M., Tagliaferri, G., Foschini, L., Ghirlanda, G., et al. (2012). SDSS J102623.61+254259.5: the second most distant blazar at z = 5.3. *Mon. Not. R. Astron. Soc.* 426, L91–L95. doi:10.1111/j.1745-3933.2012.01332.x

Sbarrato, T., Ghisellini, G., Tagliaferri, G., Perri, M., Madejski, G. M., Stern, D., et al. (2016). Extremes of the jet-accretion power relation of blazars, as explored by NuSTAR. *Mon. Not. R. Astron. Soc.* 462, 1542–1550. doi:10.1093/mnras/stw1730

Sbarrato, T., Tagliaferri, G., Ghisellini, G., Perri, M., Puccetti, S., Baloković, M., et al. (2013). NuSTAR detection of the blazar B2 1023+25 at redshift 5.3. *Astrophys. J.* 777, 147. doi:10.1088/0004-637X/777/2/147

Schmidt, M. (1968). Space distribution and luminosity functions of quasi-stellar radio sources. *Astrophys. J.* 151, 393. doi:10.1086/149446

Schneider, R., Ferrara, A., Natarajan, P., and Omukai, K. (2002). First stars, very massive black holes, and metals. *Astrophys. J.* 571, 30–39. doi:10.1086/339917

Schoenmakers, A. P., de Bruyn, A. G., Röttgering, H. J. A., van der Laan, H., and Kaiser, C. R. (2000). Radio galaxies with a 'double-double morphology' - I. Analysis of the radio properties and evidence for interrupted activity in active galactic nuclei. *Mon. Not. R. Astron. Soc.* 315, 371–380. doi:10.1046/j.1365-8711.2000.03430.x

Shabala, S. S., Kaviraj, S., and Silk, J. (2011). Active galactic nucleus feedback drives the colour evolution of local galaxies. *Mon. Not. R. Astron. Soc.* 413, 2815–2826. doi:10.1111/j.1365-2966.2011.18353.x

Shaw, M. S., Romani, R. W., Cotter, G., Healey, S. E., Michelson, P. F., Readhead, A. C. S., et al. (2013). Spectroscopy of the largest ever γ-ray-selected bl lac sample. *Astrophys. J.* 764, 135. doi:10.1088/0004-637X/764/2/135

Shen, Y., Richards, G. T., Strauss, M. A., Hall, P. B., Schneider, D. P., Snedden, S., et al. (2011). A catalog of quasar properties from sloan digital sky survey data release 7. *Astrophys. J. Suppl. Ser.* 194, 45. doi:10.1088/0067-0049/194/2/45

Sheng, Y., Rajagopal, M., Kaur, A., Ajello, M., Dominguez, A., Rau, A., et al. (2022). *Revealing high-z Fermi-LAT BL Lacs using Swift and SARA data with photometric analysis*. arXiv e-prints , arXiv:2209.09877. doi:10.48550/arXiv.2209.09877

Sikora, M., Begelman, M. C., and Rees, M. J. (1994). Comptonization of diffuse ambient radiation by a relativistic jet: the source of gamma rays from blazars? *Astrophys. J.* 421, 153. doi:10.1086/173633

Silk, J., and Rees, M. J. (1998). Quasars and galaxy formation. *Astron. Astrophys.* 331, L1–L4. doi:10.48550/arXiv.astro-ph/9801013

Sol, H., Zech, A., Boisson, C., Barres de Almeida, U., Biteau, J., Contreras, J. L., et al. (2013). Active galactic nuclei under the scrutiny of CTA. *Astropart. Phys.* 43, 215–240. doi:10.1016/j.astropartphys.2012.12.005

Stawarz, Ł., Sikora, M., and Ostrowski, M. (2003). High-energy gamma rays from FR I jets. *Astrophys. J.* 597, 186–201. doi:10.1086/378290

Stawarz, Ł., Tanaka, Y. T., Madejski, G., O'Sullivan, S. P., Cheung, C. C., Feain, I. J., et al. (2013). Giant lobes of Centaurus A radio galaxy observed with the Suzaku X-ray satellite. *Astrophys. J.* 766, 48. doi:10.1088/0004-637X/766/1/48

Stecker, F. W., Done, C., Salamon, M. H., and Sommers, P. (1991). High-energy neutrinos from active galactic nuclei. *Phys. Rev. Lett.* 66, 2697–2700. doi:10.1103/physrevlett.66.2697

Stein, W. A., Odell, S. L., and Strittmatter, P. A. (1976). The BL Lacertae objects. *ARAA* 14, 173–195. doi:10.1146/annurev.aa.14.090176.001133

Tagliaferri, G., Ghisellini, G., Giommi, P., Celotti, A., Chiaberge, M., Chiappetti, L., et al. (2001). The 0.1-200 keV spectrum of the blazar PKS 2005-489 during an active state. *Astron. Astrophys.* 368, 38–43. doi:10.1051/0004-6361:20010011

Tagliaferri, G., Ghisellini, G., Giommi, P., Chiappetti, L., Maraschi, L., Celotti, A., et al. (2000). The concave X-ray spectrum of the blazar ON 231: the signature of intermediate BL Lacertae objects. *Astron. Astrophys.* 354, 431–438. doi:10.48550/arXiv.astro-ph/9912055

Tagliaferri, G., Ghisellini, G., Perri, M., Hayashida, M., Baloković, M., Covino, S., et al. (2015). NuSTAR and multifrequency study of the two high-redshift blazars S5 0836+710 and PKS 2149-306. *Astrophys. J.* 807, 167. doi:10.1088/0004-637X/807/2/167

Tagliaferri, G., Ghisellini, G., and Ravasio, M. (2002). *BeppoSAX ToO observations on BLAZARS. arXiv e-prints* , astro-ph/0207017 10. 48550/arXiv.astro-ph/0207017.

Takahashi, T., Abe, K., Endo, M., Endo, Y., Ezoe, Y., Fukazawa, Y., et al. (2007). Hard X-ray detector (HXD) on board Suzaku, *Publ. Astron. Soc. Jpn. Nihon. Tenmon. Gakkai.* 59, 35–51. doi:10.1093/pasj/59.sp1.S35

Tavecchio, F., Maraschi, L., Ghisellini, G., Kataoka, J., Foschini, L., Sambruna, R. M., et al. (2007). Low-energy cutoffs and hard X-ray spectra in high-z radio-loud quasars: the Suzaku view of RBS 315. *Astrophys. J.* 665, 980–989. doi:10.1086/519156

Tavecchio, F., Maraschi, L., Pian, E., Chiappetti, L., Celotti, A., Fossati, G., et al. (2001). Theoretical implications from the spectral evolution of markarian 501 observed with BeppoSAX. *Astrophys. J.* 554, 725–733. doi:10.1086/321394

Tavecchio, F., Maraschi, L., Sambruna, R. M., and Urry, C. M. (2000). The X-ray jet of PKS 0637-752: inverse compton radiation from the cosmic microwave background? *Astrophys. J. Lett.* 544, L23–L26. doi:10.1086/317292

Tchekhovskoy, A., Narayan, R., and McKinney, J. C. (2011). Efficient generation of jets from magnetically arrested accretion on a rapidly spinning black hole. *Mon. Not. R. Astron. Soc.* 418, L79–L83. doi:10.1111/j.1745-3933.2011.01147.x

Tomsick, J., Zoglauer, A., Sleator, C., Lazar, H., Beechert, J., Boggs, S., et al. (2019). The compton spectrometer and imager. *Bull. Am. Astron. Soc.* 51, 98. doi:10.48550/arXiv.1908.04334

Tramacere, A., Giommi, P., Perri, M., Verrecchia, F., and Tosti, G. (2009). Swift observations of the very intense flaring activity of Mrk 421 during 2006. I. Phenomenological picture of electron acceleration and predictions for MeV/GeV emission. *Astron. Astrophys.* 501, 879–898. doi:10.1051/0004-6361/200810865

Uchiyama, Y., Urry, C. M., Cheung, C. C., Jester, S., Van Duyne, J., Coppi, P., et al. (2006). Shedding new light on the 3C 273 jet with the spitzer space telescope. *Astrophys. J.* 648, 910–921. doi:10.1086/505964

Ueda, Y., Akiyama, M., Hasinger, G., Miyaji, T., and Watson, M. G. (2014). Toward the standard population synthesis model of the X-ray background: evolution of X-ray luminosity and absorption functions of active galactic nuclei including compton-thick populations. *Astrophys. J.* 786, 104. doi:10.1088/0004-637X/786/2/104

Urry, C. M., and Padovani, P. (1995). Unified schemes for radio-loud active galactic nuclei. *PASP* 107, 803. doi:10.1086/133630

Urry, C. M., and Shafer, R. A. (1984). Luminosity enhancement in relativistic jets and altered luminosity functions for beamed objects. *Astrophys. J.* 280, 569–573. doi:10.1086/162027

Urry, C. M., Treves, A., Maraschi, L., Marshall, H. L., Kii, T., Madejski, G., et al. (1997). Multiwavelength monitoring of the BL Lacertae object PKS 2155-304 in 1994 may. III. Probing the inner jet through multiwavelength correlations. *Astrophys. J.* 486, 799–809. doi:10.1086/304536

Valverde, J., Horan, D., Bernard, D., Fegan, S., Fermi-LAT Collaboration, Abeysekara, A. U., et al. (2020). A decade of multiwavelength observations of the TeV blazar 1ES 1215+303: extreme shift of the synchrotron peak frequency and long-term optical-gamma-ray flux increase. *Astrophys. J.* 891, 170. doi:10.3847/1538-4357/ab765d

Wang, J.-S., Reville, B., Liu, R.-Y., Rieger, F. M., and Aharonian, F. A. (2021). Particle acceleration in shearing flows: the case for large-scale jets. *Mon. Not. R. Astron. Soc.* 505, 1334–1341. doi:10.1093/mnras/stab1458

Wang, Y., Xue, Y., Zhu, S., and Fan, J. (2018). Systematic investigation of X-ray spectral variability of TeV blazars during flares in the RXTE era. *Astrophys. J.* 867, 68. doi:10.3847/1538-4357/aae307

Weaver, Z. R., Jorstad, S. G., Marscher, A. P., Morozova, D. A., Troitsky, I. S., Agudo, I., et al. (2022). Kinematics of parsec-scale jets of gamma-ray blazars at 43 GHz during 10 yr of the VLBA-BU-BLAZAR Program. *Astrophys. J. Suppl. Ser.* 260, 12. doi:10.3847/1538-4365/ac589c

Weisskopf, M. (2022). "The imaging X-ray Polarimetry explorer (IXPE) mission overview," in *AAS/High energy astrophysics division* (AAS/High Energy Astrophysics Division), 54.

Williamson, K. E., Jorstad, S. G., Marscher, A. P., Larionov, V. M., Smith, P. S., Agudo, I., et al. (2014). Comprehensive monitoring of gamma-ray bright blazars. I. Statistical study of optical, X-ray, and gamma-ray spectral slopes. *Astrophys. J.* 789, 135. doi:10.1088/0004-637X/789/2/135

Wu, X.-B., Wang, F., Fan, X., Yi, W., Zuo, W., Bian, F., et al. (2015). An ultraluminous quasar with a twelve-billion-solar-mass black hole at redshift 6.30. *Nature* 518, 512–515. doi:10.1038/nature14241

Wulf, T. (1909). Beobachtungen über die Strahlung hoher Durchdringungsfähigkeit auf dem Eiffelturm. *Phys. Z.* 10, 997.

Yang, X., Yao, S., Yang, J., Ho, L. C., An, T., Wang, R., et al. (2020). Radio activity of supermassive black holes with extremely high accretion rates. *Astrophys. J.* 904, 200. doi:10.3847/1538-4357/abb775

Young, M., Elvis, M., and Risaliti, G. (2009). The fifth data release sloan digital sky survey/XMM-Newton quasar survey. *Astrophys. J. Suppl. Ser.* 183, 17–32. doi:10.1088/0067-0049/183/1/17

Zacharias, M. (2021). Studying the influence of external photon fields on blazar spectra using a one-zone hadro-leptonic time-dependent model. *Physics* 3, 1098–1111. doi:10.3390/physics3040069

Zacharias, M., Reimer, A., Boisson, C., and Zech, A. (2022). EXHALE-JET: an extended hadro-leptonic jet model for blazars - I. Code description and initial results. *Mon. Not. R. Astron. Soc.* 512, 3948–3971. doi:10.1093/mnras/stac754

Zacharias, M., and Wagner, S. J. (2016). The extended jet of AP Librae: origin of the very high-energy γ-ray emission? *A&A* 588, A110. doi:10.1051/0004-6361/201526698

Zech, A., and Lemoine, M. (2021). Electron-proton co-acceleration on relativistic shocks in extreme-TeV blazars. *Astron. Astrophys.* 654, A96. doi:10.1051/0004-6361/202141062

Zhang, B. T., Petropoulou, M., Murase, K., and Oikonomou, F. (2020a). A neutral beam model for high-energy neutrino emission from the blazar TXS 0506+056. *Astrophys. J.* 889, 118. doi:10.3847/1538-4357/ab659a

Zhang, H., Chen, X., Böttcher, M., Guo, F., and Li, H. (2015). Polarization swings reveal magnetic energy dissipation in blazars. *Astrophys. J.* 804, 58. doi:10.1088/0004-637X/804/1/58

Zhang, H., Diltz, C., and Böttcher, M. (2016). Radiation and polarization signatures of the 3D multizone time-dependent hadronic blazar model. *Astrophys. J.* 829, 69. doi:10.3847/0004-637X/829/2/69

Zhang, H., Fang, K., Li, H., Giannios, D., Böttcher, M., and Buson, S. (2019a). Probing the emission mechanism and magnetic field of neutrino blazars with multiwavelength polarization signatures. *Astrophys. J.* 876, 109. doi:10.3847/1538-4357/ab158d

Zhang, H., Li, X., Giannios, D., and Guo, F. (2021a). First-principles prediction of X-ray polarization from magnetic reconnection in high-frequency BL Lacertae objects. *Astrophys. J.* 912, 129. doi:10.3847/1538-4357/abf2be

Zhang, H., Li, X., Giannios, D., Guo, F., Liu, Y.-H., and Dong, L. (2020b). Radiation and polarization signatures from magnetic reconnection in relativistic jets. I. A systematic study. *Astrophys. J.* 901, 149. doi:10.3847/1538-4357/abb1b0

Zhang, H., Li, X., Giannios, D., Guo, F., Thiersen, H., Böttcher, M., et al. (2022a). Radiation and polarization signatures from magnetic reconnection in relativistic jets. II. Connection with γ-rays. *Astrophys. J.* 924, 90. doi:10.3847/1538-4357/ac3669

Zhang, H., Marscher, A. P., Guo, F., Giannios, D., Li, X., and Negro, M. (2023). First-principles-integrated study of blazar synchrotron radiation and polarization signatures from magnetic turbulence. *Astrophys. J.* 949, 71. doi:10.3847/1538-4357/acc657

Zhang, L., Vieira, J. D., Ajello, M., Malkan, M. A., Archipley, M. A., Capota, J., et al. (2022b). New identifications and multiwavelength properties of extragalactic Fermi gamma-ray sources in the SPT-SZ survey field. *Astrophys. J.* 939, 117. doi:10.3847/1538-4357/ac966f

Zhang, Y., Hou, Z., Shao, L., and Zhang, P. (2010). Discovery of a high confidence soft lag from an X-ray flare of Markarian 421. *Sci. China Phys. Mech. Astron.* 53, 224–227. doi:10.1007/s11433-010-0017-1

Zhang, Y. H., Bai, J. M., Zhang, S. N., Treves, A., Maraschi, L., and Celotti, A. (2006). Multiwavelength observations of the BL Lacertae object PKS 2155-304 with XMM-Newton. *Astrophys. J.* 651, 782–790. doi:10.1086/507601

Zhang, Z., Gupta, A. C., Gaur, H., Wiita, P. J., An, T., Gu, M., et al. (2019b). X-ray intraday variability of the TeV blazar mrk 421 with Suzaku. *Astrophys. J.* 884, 125. doi:10.3847/1538-4357/ab3f3a

Zhang, Z., Gupta, A. C., Gaur, H., Wiita, P. J., An, T., Lu, Y., et al. (2021b). X-ray intraday variability of the TeV blazar PKS 2155-304 with Suzaku during 2005-2014. *Astrophys. J.* 909, 103. doi:10.3847/1538-4357/abdd38

Zhu, S. F., Brandt, W. N., Wu, J., Garmire, G. P., and Miller, B. P. (2019). Investigating the X-ray enhancements of highly radio-loud quasars at z > 4. *Mon. Not. R. Astron. Soc.* 482, 2016–2038. doi:10.1093/mnras/sty2832

Zhu, S. F., Xue, Y. Q., Brandt, W. N., Cui, W., and Wang, Y. J. (2018). Extremely rapid X-ray flares of TeV blazars in the RXTE era. *Astrophys. J.* 853, 34. doi:10.3847/1538-4357/aa9f21

Zobnina, D. I., Aller, H. D., Aller, M. F., Homan, D. C., Kovalev, Y. Y., Lister, M. L., et al. (2023). MOJAVE - XXI. Decade-long linear polarization variability in AGN jets at parsec scales. *Mon. Not. R. Astron. Soc.* 523, 3615–3628. doi:10.1093/mnras/stad1481

frontiers | Frontiers in Astronomy and Space Sciences

TYPE Original Research
PUBLISHED 25 November 2024
DOI 10.3389/fspas.2024.1471585

Check for updates

OPEN ACCESS

EDITED BY
Nicolao Fornengo,
University of Turin, Italy

REVIEWED BY
Mattia Di Mauro,
National Institute of Nuclear Physics of Turin, Italy
Antonio Martin-Carrillo,
University College Dublin, Ireland

*CORRESPONDENCE
Javier A. García,
javier.a.garciamartinez@nasa.gov

†NASA Hubble Fellowship Program (NFHP) Einstein Fellow

RECEIVED 27 July 2024
ACCEPTED 07 October 2024
PUBLISHED 25 November 2024

CITATION
García JA, Stern D, Madsen K, Smith M, Grefenstette B, Ajello M, Alford J, Annuar A, Bachetti M, Baloković M, Beckmann RS, Bianchi S, Biccari D, Boorman P, Brightman M, Buchner J, Bulbul E, Chen C-T, Civano F, Coley J, Connors RMT, Del Santo M, Gesu LD, Draghis PA, Fragile PC, Gúrpide A, Gangi M, Gezari S, Harrison F, Kammoun E, Lanzuisi G, Lehmer B, Lohfink A, Ludlam R, Marchesi S, Marcotulli L, Margutti R, Masterson M, Merloni A, Middleton M, Mori K, Moretti A, Nandra K, Perez K, Pfeifle RW, Pinto C, Piotrowska J, Ponti G, Pottschmidt K, Predehl P, Puccetti S, Rau A, Reynolds S, Santangelo A, Spiga D, Tomsick JA, Torres-Albà N, Walton DJ, Wilkins D, Wilms J, Zhang W and Zhao X (2024) The high energy X-ray probe (HEX-P): science overview. *Front. Astron. Space Sci.* 11:1471585. doi: 10.3389/fspas.2024.1471585

The high energy X-ray probe (HEX-P): science overview

Javier A. García[1,2]*, Daniel Stern[3], Kristin Madsen[1], Miles Smith[3], Brian Grefenstette[2], Marco Ajello[4], Jason Alford[5], Adlyka Annuar[6], Matteo Bachetti[7], Mislav Baloković[8,9], Ricarda S. Beckmann[10], Stefano Bianchi[11], Daniela Biccari[3], Peter Boorman[2], Murray Brightman[2], Johannes Buchner[12], Esra Bulbul[12], Chien-Ting Chen[13,14], Francesca Civano[1], Joel Coley[1,15,16], Riley M. T. Connors[17], Melania Del Santo[18], Laura Di Gesu[19], Paul A. Draghis[20,21], P. Chris Fragile[22], Andrés Gúrpide[23], Manuele Gangi[19], Suvi Gezari[24], Fiona Harrison[2], Elias Kammoun[11,25,26], Giorgio Lanzuisi[27], Bret Lehmer[28], Anne Lohfink[29], Renee Ludlam[30], Stefano Marchesi[4,27], Lea Marcotulli[8,9†], Raffaella Margutti[31], Megan Masterson[20], Andrea Merloni[12], Matthew Middleton[23], Kaya Mori[32], Alberto Moretti[33], Kirpal Nandra[12], Kerstin Perez[32], Ryan W. Pfeifle[1,34], Ciro Pinto[18], Joanna Piotrowska[2], Gabriele Ponti[33], Katja Pottschmidt[16,35], Peter Predehl[12], Simonetta Puccetti[19], Arne Rau[12], Stephen Reynolds[36], Andrea Santangelo[37], Daniele Spiga[33], John A. Tomsick[31], Núria Torres-Albà[4], Dominic J. Walton[38], Daniel Wilkins[39], Joern Wilms[40], Will Zhang[1] and Xiurui Zhao[41,42], on behalf of the HEX-P Collaboration

[1]X-Ray Astrophysics Laboratory, National Aeronautics and Space Administration (NASA) Goddard Space Flight Center, Greenbelt, MD, United States, [2]Cahill Center for Astronomy and Astrophysics, California Institute of Technology, Pasadena, CA, United States, [3]Jet Propulsion Laboratory, California Institute of Technology, Pasadena, CA, United States, [4]Department of Physics and Astronomy, Kinard Lab of Physics, Clemson University, Clemson, SC, United States, [5]Department of Physics, New York University, Abu Dhabi, United Arab Emirates, [6]Department of Applied Physics, Faculty of Science and Technology, Universiti Kebangsaan Malaysia, Selangor, Malaysia, [7]Istituto Nazionale di Astrofisica (INAF)-Osservatorio Astronomico di Cagliari, Selargius, Italy, [8]Department of Astronomy, Yale Center for Astronomy and Astrophysics, New Haven, CT, United States, [9]Department of Physics, Yale University, New Haven, CT, United States, [10]Institute of Astronomy and Kavli Institute for Cosmology, University of Cambridge, Cambridge, United Kingdom, [11]Dipartimento di Matematica e Fisica, Università degli Studi Roma Tre, Rome, Italy, [12]Max-Planck-Institute for Extraterrestrial Physics, Garching, Germany, [13]Science and Technology Institute, Universities Space Research Association, Huntsville, AL, United States, [14]Astrophysics Office, National Aeronautics and Space Administration (NASA) Marshall Space Flight Center, Huntsville, AL, United States, [15]Department of Physics and Astronomy, Howard University, Washington, DC, United States, [16]Center for Research and Exploration in Space Science and Technology (CRESST) and Center for Space Sciences and Technology (CSST), University of Maryland, Baltimore County, Baltimore, MD, United States, [17]Department of Physics, Villanova University, Villanova, PA, United States, [18]Istituto Nazionale di Astrofisica (INAF)/Istituto di Astrofisica Spaziale e Fisica (IASF) Palermo, Palermo, Italy, [19]ASI- Agenzia Spaziale Italiana, Rome, Italy, [20]MIT Kavli Institute for Astrophysics and Space Research, Massachusetts Institute of Technology, Cambridge, MA, United States, [21]Department of Astronomy, University of Michigan, Ann Arbor, MI, United States, [22]Department of Physics and Astronomy, College of Charleston, Charleston, SC, United States, [23]School of Physics and Astronomy, University of Southampton, Southampton, United Kingdom, [24]Space Telescope Science Institute, Baltimore, MD, United States, [25]Institut de Recherche en Astrophysique et Planétologie (IRAP), Université de Toulouse, Centre national de la recherche scientifique (CNRS), Université Paul Sabatier (UPS), Centre National d'études Spatiales (CNES), Toulouse, France, [26]Istituto Nazionale di Astrofisica (INAF) – Osservatorio Astrofisico di Arcetri,

Firenze, Italy, [27]Istituto Nazionale di Astrofisica (INAF) – Osservatorio di Astrofisica e Scienza dello Spazio, Bologna, Italy, [28]Department of Physics, University of Arkansas, Fayetteville, AR, United States, [29]Department of Physics, Montana State University, Bozeman, MT, United States, [30]Department of Physics and Astronomy, Wayne State University, Detroit, MI, United States, [31]Space Sciences Laboratory, University of California, Berkeley, Berkeley, CA, United States, [32]Columbia Astrophysics Laboratory, Columbia University, New York, NY, United States, [33]Istituto Nazionale di Astrofisica (INAF)/Osservatorio Astronomico di Brera, Merate, LC, Italy, [34]Oak Ridge Associated Universities, National Aeronautics and Space Administration (NASA) NASA Postdoctoral Program (NPP) Program, Oak Ridge, TN, United States, [35]Astroparticle Physics Laboratory, National Aeronautics and Space Administration (NASA) Goddard Space Flight Center, Greenbelt, MD, United States, [36]Department of Physics, North Carolina State University, Raleigh, NC, United States, [37]Institute of Astronomy and Astrophysics, University of Tübingen, Tübingen, Germany, [38]Centre for Astrophysics Research, University of Hertfordshire, Hatfield, United Kingdom, [39]Kavli Institute for Particle Astrophysics and Cosmology, Stanford University, Stanford, CA, United States, [40]Erlangen Centre for Astroparticle Physics and Remeis-Observatory, Friedrich-Alexander-Universität Erlangen-Nürnberg, Bamberg, Germany, [41]Department of Astronomy, University of Illinois at Urbana-Champaign, Urbana, IL, United States, [42]Center for Astrophysics | Harvard and Smithsonian, Cambridge, MA, United States

To answer NASA's call for a sensitive X-ray observatory in the 2030s, we present the High Energy X-ray Probe (HEX-P) mission concept. HEX-P is designed to provide the required capabilities to explore current scientific questions and make new discoveries with a broadband X-ray observatory that simultaneously measures sources from 0.2 to 80 keV. HEX-P's main scientific goals include: 1) understand the growth of supermassive black holes and how they drive galaxy evolution; 2) explore the lower mass populations of white dwarfs, neutron stars, and stellar-mass black holes in the nearby universe; 3) explain the physics of the mysterious corona, the luminous plasma close to the central engine of accreting compact objects that dominates cosmic X-ray emission; and 4) find the sources of the highest energy particles in the Galaxy. These goals motivate a sensitive, broadband X-ray observatory with imaging, spectroscopic, and timing capabilities, ensuring a versatile platform to serve a broad General Observer (GO) and Guest Investigator (GI) community. In this paper, we present an overview of these mission goals, which have been extensively discussed in a collection of more than a dozen papers that are part of this Research Topic volume. The proposed investigations will address key questions in all three science themes highlighted by Astro2020, including their associated priority areas. HEX-P will extend the capabilities of the most sensitive low- and high-energy X-ray satellites currently in orbit and will complement existing and planned high-energy, time-domain, and multi-messenger facilities in the next decade.

KEYWORDS

x-ray, HEX-P, mission science, NASA, black holes, supernova, AGN, neutron stars - general

1 Introduction

Across the Universe there are mysteries whose secrets are encoded over three orders of magnitude in X-ray energy and more than nine orders in time. As black holes and neutron stars tear apart companions, the accreting matter shines brightly in X-rays from 0.1 to 100 keV. Broad spectral features tell the story of the interacting system and how it formed. Elsewhere in our Universe, extreme events are occurring as stars explode into their recent ejecta, merging neutron stars create ripples in the cosmic fabric, and stars are shredded as they plunge into black holes. And behind it all, billions of active galactic nuclei (AGN) sum together to produce the cosmic X-ray background that peaks at 25 keV. When resolved into individual sources, their spectra tell the story of whether each AGN is enshrouded in dust and gas, how fast its supermassive central black hole is spinning, and whether it is producing feedback from a powerful outflow. These phenomena vary on timescales of milliseconds to millennia, and decoding their secrets requires simultaneous broadband observations.

At the center of all active galaxies exists a supermassive black hole ($10^6 - 10^{10}\,M_\odot$; SMBH), which is believed to play a crucial role in the evolution of its host galaxy. Accretion onto the SMBH is an efficient process to convert matter into energy, producing powerful radiation that outshines all the stars in the galaxy at high energies and drives a strong wind that both induces and inhibits star formation, shaping the very appearance of the galaxy. Light from a surrounding accretion disk is scattered to X-ray energies by a mysterious plasma, and those X-rays are also seen in reflection off the relativistic disk. The surrounding material is mostly opaque to

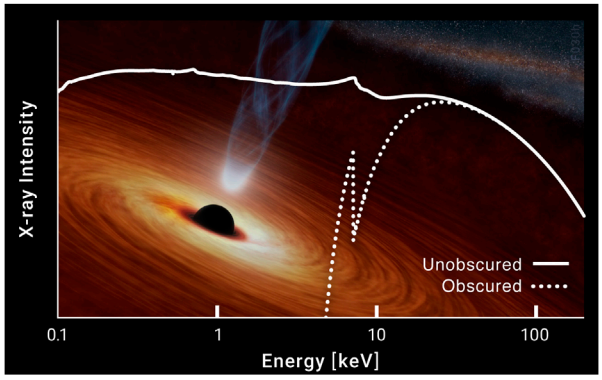

FIGURE 1
The primary emission from accretion is broadband. While accreting sources emit across the full 0.1 – 100 keV X-ray band, gas preferentially absorbs at low energy, making obscured sources best studied above 10 keV.

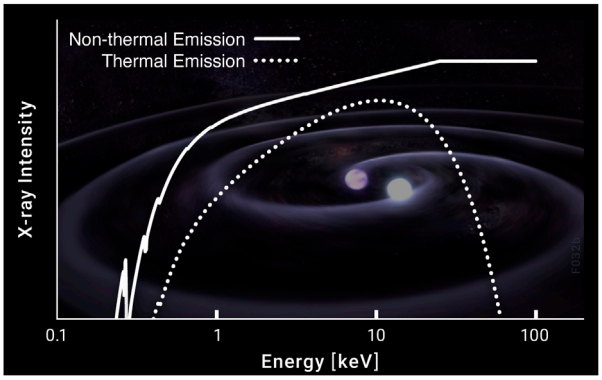

FIGURE 3
The primary emission from accretion is broadband. The X-ray band encodes key spectral features that reveal the physics underlying transient and multi-messenger events, such as sources of gravitational waves.

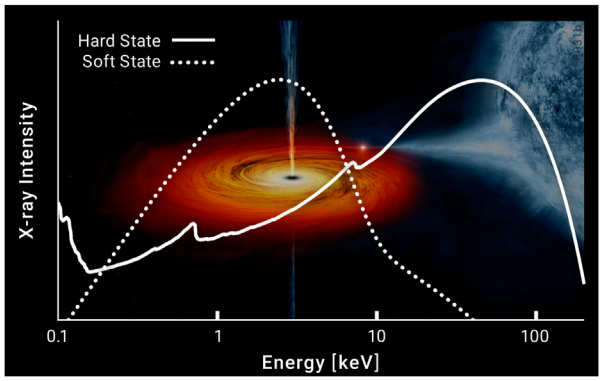

FIGURE 2
The primary emission from accretion is broadband. Accreting binary systems shift between hard and soft states, as emission from the corona (hard) or accretion disk (soft) dominate their energetics.

low-energy radiation, including soft X-rays, but hard X-ray photons ($\gtrsim$ 10 keV) can easily penetrate and escape (Figure 1).

Meanwhile, stellar-mass black holes (~5 – 100 $M_\odot$), which are formed via stellar gravitational collapse, are typically detected in X-rays when in binary systems. Luckily, massive stars are rarely born alone. They form in binaries and multiple systems, exchanging mass as they evolve. The stars' fates become intertwined as their very appearance and lifetimes are influenced by close companions. At late stages, after the more massive star has exploded, close binaries are revealed as the neutron star or black hole remnant violently absorbs matter from its companion. The strong accretion of matter transforms the system into a bright X-ray source, that switches from predominantly soft (< 10 keV) to hard (> 10 keV) states and back again as different physical processes dominate the emission mechanism (Figure 2).

In addition to the extreme environments created by active black holes, our Universe is adorned with a rich tapestry of explosive and energetic events, producing X-rays as jets form, matter collides, and accreting systems are created or destroyed. Our Galaxy contains sites where magnetic fields accelerate ions and electrons to extreme energies, producing high-energy photons as they gyrate in the strong fields and collide with surrounding material. The high-energy spectra of these time-domain and multi-messenger events reveal the nature and physics of the source (Figure 3).

All these exciting astrophysical phenomena require an agile and versatile platform capable of producing simultaneous imaging, spectroscopy, and timing data across the entire X-ray band. The High-Energy X-ray Probe (HEX-P) mission was designed with these requirements in mind. HEX-P is a probe-class mission concept, as directed by the 2020 Decadal Survey on Astronomy and Astrophysics,[1] and was submitted in response to the 2023 NASA Astrophysics Probe Explorer (APEX) call. The observatory combines the power of high angular resolution with broad passband coverage to provide the necessary leap in capabilities to address the important astrophysical questions of the next decade. These were formulated in the Astro2020 Decadal Survey in the Cosmic Ecosystems context as unveiling the "Drivers of Galaxy Growth": *to revolutionize our understanding of the origins and evolution of galaxies, for which new observational capabilities across the electromagnetic spectrum are needed to resolve the rich workings of galaxies on all scales*. HEX-P fills in the important gap between soft X-rays and γ-rays where compact objects, from stellar remnants (neutron stars and black holes) up to supermassive black holes, emit vast amounts of energy through the process of accretion. Powerful ionizing winds from such objects are believed to have a major impact on galaxy evolution, but the growth, numbers, and distribution of these compact objects are poorly understood and only accessible for our closest galactic neighbors.

The current X-ray mission landscape is dominated by oversubscribed observatories far into their extended operation

1 https://www.nationalacademies.org/our-work/decadal-survey-on-astronomy-and-astrophysics-2020-astro2020

phase. The next planned flagship-class X-ray observatory is ESA's NewAthena mission, which is currently scheduled to launch no earlier than 2037. With this current outlook, the science community faces a non-negligible risk of being without a sensitive General Observer (GO) X-ray capability in the 2030s, just at the time that such an observatory is essential to inform the discoveries by the multiple time-domain and multi-messenger facilities coming online in the next decade. HEX-P is designed to bridge this gap with instrumentation that will deliver capabilities to advance our understanding of the X-ray Universe. HEX-P will peer into the hidden regions of the cosmos to reveal the most extreme astrophysical sources and events.

In this paper we present an overview of the core science that drives the HEX-P concept. This is the result of a several-months long study primarily led by members of the high-energy astrophysics community, in a voluntary manner, to determine the most compelling scientific objectives that can be addressed with a mission like HEX-P. A companion paper describing the mission design and implementation is presented by Madsen et al. (2024). More than 200 scientists have produced over a dozen peer-reviewed publications describing a comprehensive yet non-exhaustive list of science uniquely enabled by HEX-P, including topics such as accretion onto supermassive black holes, the cosmic X-ray background, the strong magnetic fields of neutron stars, and resolved studies of X-ray emission in supernova remnants, to name a few. These papers constitute the HEX-P Research Topic published by Frontiers in Astronomy and Space Sciences, which can be accessed freely at their online portal.[2]

2 Observatory and mission overview

The NASA Explorer Nuclear Spectroscopic Telescope Array (NuSTAR) (Harrison et al., 2013) opened the high-energy X-ray band by establishing the power of broad-band X-ray spectroscopy (3 – 80 keV). HEX-P builds on this legacy by expanding the low-energy passband down to 0.2 keV where thermal processes dominate, and by improving the angular resolution with different mirror technologies optimized over the passband. The observatory has a 20-meter focal length and the 0.2 – 80 keV passband is covered by the two instruments, the Low Energy Telescope (LET) and the High Energy Telescope (HET), which are co-aligned and observe the same field. The LET consists of the Low Energy Mirror Assembly (LEMA) and a Low Energy Detector Assembly (LEDA), and the HET of two High Energy Mirror Assemblies (HEMAs) matched to two High Energy Detector Assemblies (HEDAs). HEX-P will be launched into L1, which provides a high observing efficiency (≥90%), which combined with a large field of regard allows for long and uninterrupted exposures. See Madsen et al. (2024) for details on the mission design, instrumentation and implementation. A short summary is provided below.

The LET consists of a segmented mirror assembly coated with Ir on monocrystalline silicon that achieves a half-power diameter (HPD) of 3.5″, and a low-energy DEPFET detector, of the same type as the Wide Field Imager (WFI; Meidinger et al., 2020) onboard NewAthena (Nandra et al., 2013). It has 512 × 512 pixels that cover a field of view of 11.3′ × 11.3′. It has an effective passband of 0.2 – 25 keV, and a full frame readout time of 2 ms, which can be operated in a 128 or 64 channel window mode for higher count-rates to mitigate pile-up and faster readout. Pile-up effects remain below an acceptable limit of ~1% for a flux up to ~100 mCrab (2 – 10 keV) in the smallest window configuration. Excising the core of the PSF, a common practice in X-ray astronomy, will allow for observations of brighter sources, with a typical loss of up to ~60% of the total photon counts.

The HET consists of two co-aligned telescopes and detector modules. The optics are made of Ni-electroformed full shell mirror substrates, leveraging the heritage of XMM-Newton (Jansen et al., 2001), and coated with Pt/C and W/Si multilayers for an effective passband of 2 – 80 keV. The high-energy detectors are of the same type as flown on NuSTAR (Harrison et al., 2013), and they consist of 16 CZT sensors per focal plane, tiled 4 × 4, for a total of 128 × 128 pixels spanning a field of view slightly larger than for the LET, 13.4′ × 13.4′.

All the simulations presented in the collection of HEX-P papers discussed here were produced with a set of response files that represent the observatory performance based on current best estimates as of Spring 2023 (see Madsen et al., 2024). The effective area is derived from ray-tracing calculations for the mirror design including obscuration by all known structures. The detector responses are based on simulations performed by the respective hardware groups, with an optical blocking filter for the LET and a Be window and thermal insulation for the HET. The LET background was derived from a GEANT4 simulation (Eraerds et al., 2021) of the WFI instrument, and the HET backgrounds were derived from a GEANT4 simulation of the NuSTAR instrument. Both simulations adopt the L1 orbit for HEX-P.

The baseline mission is 5 years, with 30% of the observing time dedicated to the Principal Investigator (PI) led program and 70% to a GO program. The GO program will be executed alongside the PI-led, and data will be made available immediately with no proprietary time. With a large propellant capacity and strategic redundancies, HEX-P is designed to operate for more than 20 years.

3 Science enabled by HEX-P

In this Section we summarize the core scientific goals that will be addressed by the HEX-P mission. HEX-P seeks to answer fundamental questions highlighted by the Astro2020 Decadal Survey, delivering transformative science for compact objects and time-domain, multi-messenger astrophysics. The design of HEX-P's capabilities aims to address three main scientific goals to unravel some of the most outstanding questions about the Universe. The mission PI-led program focuses on the massive black holes at the centers of large galaxies (Section 3.1), compact object populations within galaxies (Section 3.2), and the diversity of explosive and multi-messenger phenomena to be uncovered in the coming decades (Section 3.3).

2 https://www.frontiersin.org/research-topics/59532/high-energy-astrophysics-research-enabled-by-the-probe-class-mission-concept-hex-p/overview

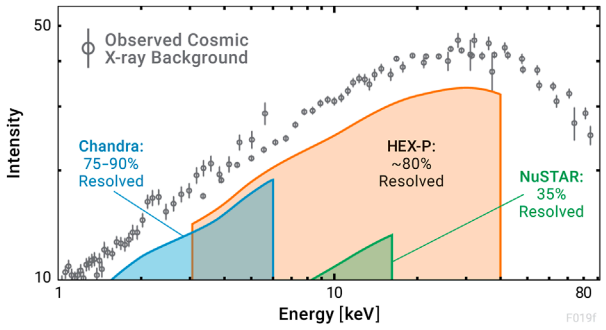

FIGURE 4
The X-ray background, dominated by emission from accreting SMBHs, shows a peak at ~25 keV that the obscured ($N_H > 10^{22}$ cm^{-2}) fraction is higher than the 50% Compton-thick fraction, and missed by low-energy surveys. HEX-P will resolve that population into individual sources and complete our cosmic census of SMBH growth. Adapted from Civano et al. (2024).

3.1 Goal 1: how do supermassive black holes grow and drive galaxy evolution?

Black holes are extremely efficient at converting rest mass energy into radiation, enabling accreting SMBHs at the centers of galaxies to fundamentally affect and regulate the growth of their hosts. However, the extent of this feedback is uncertain, and whether SMBHs play the leading role or a supporting role is a matter of active study and debate. Understanding this process will require improving both our knowledge of black hole growth and constraining the energy they can provide into their host galaxies.

The X-ray background (Figure 4) represents the summed total of all cosmic X-ray emission and provides the most powerful tool for understanding the cosmic history of black hole growth. Leading models imply that at least 90% of the X-ray background is due to accretion onto SMBHs and this has been largely confirmed in ultra-deep surveys by Chandra and XMM-Newton, reaching months-long exposure times (e.g., Luo et al., 2017), that show the low-energy X-ray sky to be dominated by unobscured AGN. However, while lower-energy X-rays are easily absorbed by intervening gas, higher-energy photons are more penetrating (Figure 1). If most AGN were unobscured, the X-ray background would be relatively flat from 1 to 100 keV. Instead, the 20 – 30 keV peak of the X-ray background inform us that there is a significant population of obscured AGN missed by soft X-ray surveys. Without accounting for this hidden population, our knowledge of SMBH growth is highly biased.

HEX-P will transform our understanding of how SMBHs grow and drive galaxy evolution, which is a key question of the Astro2020 Decadal Survey (National Academies of Sciences and Medicine, 2023). This goal motivates three science objectives. Objective 1 addresses this question by completing the cosmic census of AGN, finally revealing the full demographics of SMBH growth. Objective 2 addresses both SMBH and galaxy growth by providing a comprehensive survey of SMBH spin, which is an indicator of the interplay between accretion and mergers in galaxy growth. Spin also constrains the energy budget for AGN-driven feedback. Finally, Objective 3 closes a gap in our understanding of the X-ray background by testing the leading physical model for the X-ray corona to understand the key processes that regulate its temperature and luminosity.

3.1.1 Objective 1: reveal the hidden population of obscured supermassive black holes

Our current understanding of the full census of AGN is highly incomplete. Soft X-ray observatories are strongly biased towards unabsorbed sources (Figure 1), while the shape of the cosmic X-ray background implies approximately half of SMBH growth is obscured. Non-focusing hard X-ray missions resolved just ~2% of the X-ray background at its peak into individual sources (Bottacini et al., 2012), while NuSTAR, the first focusing hard X-ray telescope in orbit, resolved 35% (Harrison et al., 2016). To bring our understanding of the hard X-ray background to the 75 – 90% levels Chandra and XMM-Newton provide below 6 keV and complete the cosmic census of black hole growth requires improvements in both sensitivity and angular resolution in future hard X-ray telescopes.

The deepest NuSTAR survey detects only 4 sources at an 8 – 24 keV depth of 5×10^{-14} erg cm^{-2} s^{-1} (Zhao et al., 2021) (throughout, survey depths are reported at a 99% Poisson reliability threshold at 50% area, i.e., 50% of the total survey area reaches that depth or deeper Zhao et al., 2024). At this depth, NuSTAR is reaching the classical confusion limit in the 3 – 8 keV band, corresponding to 150 sources per deg^2 for the NuSTAR 60″ half-power diameter (HPD). Deeper surveys will require improved angular resolution to detect the hard X-ray sources.

In the study presented by Civano et al. (2024), the authors demonstrate via detailed simulations of extragalactic field observations that HEX-P will detect over 1,000 sources at 10 – 40 keV, compared to the four sources in the deepest NuSTAR survey in the comparable 8 – 24 keV band (Zhao et al., 2024). Their simulations of a deep and a wide area survey include full instrument models and source detection analysis. They show that with HEX-P, the statistical uncertainty in the measured resolved 10 – 40 keV X-ray background fraction is predicted to be ≤6% for a range of population models (Gilli et al., 2007; Ananna et al., 2019), while the resolved fractions from the models themselves differ by more than 20% in the same energy band.

Deep, broadband extragalactic surveys will, for the first time, uncover the full population of accreting SMBHs and constrain their properties. If HEX-P finds that the heavily obscured fraction is constant with luminosity, this would favor radiation-regulated growth in which radiation pressure dictates the geometry of the obscuring structure (Ananna et al., 2022). If HEX-P instead finds fewer obscured AGN, it might favor models where obscuration occurs primarily in the lowest luminosity AGN, below the survey depth (Lawrence, 1991), or that the SMBH spin rather than obscuration is partially responsible for the characteristic ~25 keV peak in the cosmic X-ray background (Vasudevan et al., 2016).

3.1.2 Objective 2: determine the relative importance of accretion versus mergers for SMBH growth

Black holes are the protagonists of one of the most fundamental problems in physics: understanding the complete gravitational collapse of matter to a point that lies within a light-trapping, one-way membrane known as the event horizon. Importantly, only two properties fully define an astrophysical black hole:

its mass M and its angular momentum J, where the latter is commonly reported as the dimensionless spin parameter $a^* = Jc/GM^2$ (where c and G are the speed of light and gravitational constant, respectively); a^* is constrained to values of $-0.998 \leq a^* \leq 0.998$ (Thorne, 1974). Furthermore, mass and spin are fundamentally related. Regardless of its assumed formation channel, a black hole can both increase its mass and change its spin via accretion of matter within its gravitational potential, or via repeated mergers with other black holes. Theoretical models for black hole evolution over cosmic time have specific predictions for how the SMBH mass-spin distribution in the local Universe depends on whether their growth history is dominated by ordered accretion, chaotic accretion or mergers (e.g., Berti and Volonteri, 2008; Dotti et al., 2013; Griffin et al., 2019; Izquierdo-Villalba et al., 2020). Most cosmological simulations predict accretion-dominated growth in lower-mass SMBHs ($< 10^8$ $M_\odot$), leading to near-maximal expected average spins (e.g., Dubois et al., 2014; Dubois et al., 2021). In semi-analytic models where ordered accretion dominates even in the most massive SMBHs ($> 10^9$ $M_\odot$), spin parameter values remain high (Sesana et al., 2014), while other models, which follow the hydrodynamics of gas within galaxies, predict an increasing contribution of chaotic accretion and mergers to SMBH growth, leading to lower spin parameter values (Bustamante and Springel, 2019; Beckmann et al., 2024).

Determining whether mergers play a significant role in the growth of SMBHs observed in the local Universe requires a comprehensive spin survey for a sample of SMBHs across a range in black hole mass. While there exists a selection of well-developed methods for measuring SMBH mass, such as reverberation mapping, single-epoch virial estimation or stellar and gas dynamical modelling (see Peterson, 2014, for an overview of the methods), constraining the spin parameter is significantly more challenging. The most effective method is known as X-ray reflection spectroscopy, and is based on measuring the distortion of atomic spectral features by the strong gravitational potential of the SMBH (see Reynolds, 2021, for a review). The hallmarks of reflection are the inner-shell emission lines of iron (Fe K, ~6.5 keV), the Fe absorption K-edge (~7 keV), and the Compton reflection hump (~30 keV), all observed in the broad HEX-P band (Figure 5A). High spin black holes allow for an inner edge of the accretion disk extended closer to the coordinate system origin than their low spin counterparts, leading to greater relativistic distortion of the spectral features. By measuring the degree of this distortion, one can thus infer the inward radial extent of the accretion disk which serves as a proxy for the innermost stable circular orbit and, by extension, black hole spin. Given the resulting width of these features, high spectral resolution of the instrument is not a priority, especially in the absence of absorption features caused by intervening material in the line of sight.[3] Instead, a broadband coverage is required to robustly constrain the underlying continuum and isolate the spectral reflection signal. This requirement cannot be fulfilled by soft X-ray observatories whose sensitivity drops rapidly above 8 keV.

Piotrowska et al. (2023) present simulated HEX-P spin parameter measurements for a survey of a 100 AGN selected from the Swift-BAT AGN Spectroscopic Survey (Koss et al., 2017). This sample, complete with published SMBH masses (Koss et al., 2022), includes the brightest hard-X-ray-selected unobscured AGN across the sky observed to date. The study makes use of the Horizon-AGN cosmological simulation to determine spin–mass distributions of SMBHs with different growth histories, which occupy distinct loci in the parameter space. In simulating HEX-P observations, the authors account for measurement uncertainty, model limitations and observational biases, including the strong dependence of radiative efficiency on spin which results in a high-spin bias in flux-limited samples (Figure 5A). The suite of simulated measurements demonstrates that HEX-P robustly distinguishes accretion-dominated models from models where mergers play a significant role in SMBH growth in realistic samples of HEX-P X-ray reflection measurements. As shown by the solid white regions in the right panel of Figure 5, current spin constraints are unable to discriminate between these scenarios, as both SMBH growth histories lie well within the currently permitted spin–mass values. Constraints comparable to HEX-P are not feasible with existing facilities as they would require a year of coordinated XMM-Newton and NuSTAR time.

This large survey, besides answering the Astro2020 key question about how SMBHs grow, also addresses the impact of SMBHs on their host galaxies. With inner disk radii closer to the SMBH, higher spin AGN are also more luminous (Novikov and Thorne, 1973) and thus have a greater energy budget to affect their host galaxy's evolution. Blue-shifted absorption due to fierce, outflowing winds is the clearest indicator of feedback on accretion-disk scales and requires continuum measurements at high energies to constrain line properties (e.g., Fe K is shifted to > 8 keV for winds of $> 0.2c$, requiring sensitivity above 10 keV; Tombesi et al., 2010; Tombesi et al., 2011). Parker et al. (2022) highlight the importance of Compton reflection hump measurements to disentangle relativistic reflection from the signal generated by disk winds. Higher spectral resolution at soft energies is less beneficial as the broad features are easily resolved with typical resolution.

3.1.3 Objective 3: test the leading paradigm for the physics of the X-ray corona

Most of the energetic photons in the universe originate from the X-ray corona, a highly luminous plasma of hot electrons close to the central engine of accreting compact objects (Figure 6). Reverberation and microlensing studies indicate that the corona is extremely compact, extending only a few gravitational radii ($R_g = GM/c^2$) from the central accreting object (neutron star or black hole; Pooley et al., 2007; De Marco et al., 2013; Mosquera et al., 2013; Uttley et al., 2014). Incredibly, the coronae of SMBHs in luminous AGN easily outshine all other high-energy emission in the host galaxy. Per volume, AGN coronae are the most luminous, persistent objects in the universe—and reside partnered with the darkest objects in the universe, black holes. However, beyond a few simple characteristics, the origin and physical mechanisms that govern and power the X-ray corona are poorly understood. HEX-P will fundamentally change this, providing key observations and tests of the leading theoretical

3 However, Parker et al. (2022) highlights the importance of Compton reflection hump measurements to disentangle relativistic reflection from disk winds, which imprint absorption features superimposed on the reflection signatures.

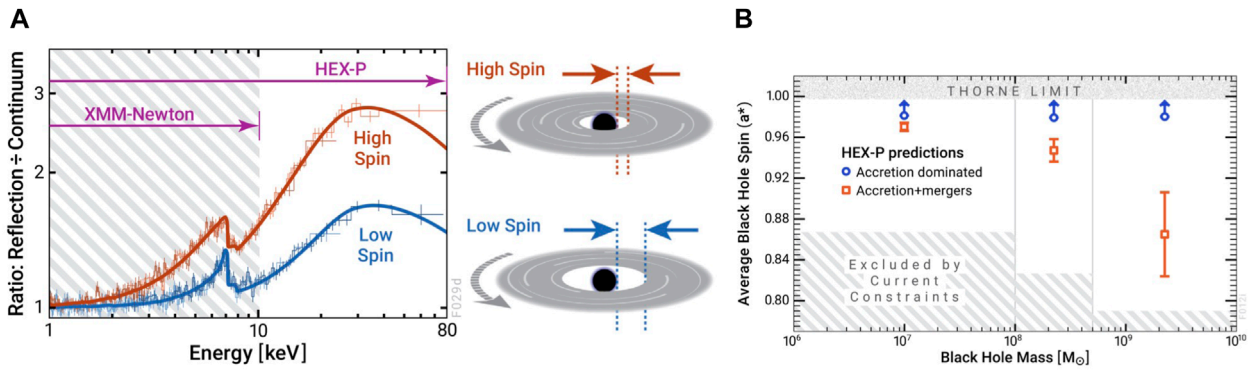

FIGURE 5
(A) Broadband X-ray observations measure SMBH spin from relativistic broadening of the Fe K (~6.5 keV) and Compton hump (~30 keV) features. By virtue of HEX-P's broadband coverage, these simulated spectra have been deconvolved from the continuum, which is poorly constrained by soft X-ray telescopes. **(B)** By measuring average SMBH spins in a range of mass bins, HEX-P will determine whether mergers play a significant role in the growth of the most massive SMBHs. Adapted from Piotrowska et al. (2023).

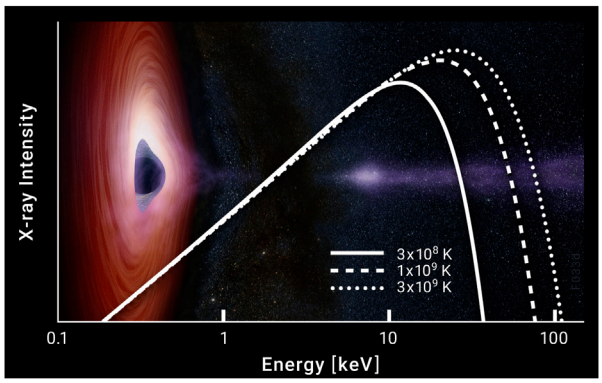

FIGURE 6
Despite its central role powering high-energy emission from compact objects, the nature of the corona is highly uncertain. By directly measuring cut-off energies, related to coronal temperature by $E_{cut} \sim (2-3)kT_e$, HEX-P will test the leading model of coronal physics.

models. Since the corona dominates the intrinsic X-ray emission of accreting objects, understanding it underlies the AGN population studies in Sections 3.1.1, 3.1.2.

The accretion disk, heated by effective viscosity to high temperatures, produces a blackbody spectrum that peaks at ~0.1 – 1 keV for stellar-mass compact objects (Figure 2), and in the UV for SMBHs. Thermal disk photons interact with relativistic electrons in the much hotter corona ($T_e \sim 10^8 - 10^9$ K), increasing the photon energies after repeated inverse Compton scatterings with electrons. The result is a power-law continuum extending up to several hundred keV, and this continuum is more cleanly measured in AGN. For stellar-mass black holes, changes in the X-ray luminosity are also associated with changes in the accretion disk such as the level of the inner-disk truncation, making Galactic binaries poorly suited for this Objective. As coronal photons can only gain so much energy from the relativistic electrons, the power-law-like X-ray spectrum falls off rapidly at a few times the characteristic electron temperature (refereed to as the high-energy cutoff; Titarchuk and Lyubarskij, 1995, and Figure 6). The electron temperature is the result of the corona's heating-to-cooling balance, where heating takes place magnetically and cooling is set by the number of very high-energy X-ray photons produced. Even a small number of such photons in the compact corona produces copious amounts of electron-positron pairs to share the available thermal energy, cooling the electrons rapidly until a balance is reached. The maximum temperature allowed in this pair-production thermostat model is related to the coronal luminosity.

Kammoun et al. (2024) discusses different tests that can be carried out with a mission like HEX-P to validate this paradigm, along with other coronal studies that could be executed as GO programs. One test focuses on a variable AGN (Test 1; Figure 7, left). These sources provide a powerful tool to test the pair-production thermostat model of the X-ray corona since the model predicts specific tracks along the temperature-luminosity plane. As the luminosity increases, the model predicts that more electron-positron pairs are produced, lowering the plasma temperature. Departures from this relation would indicate incomplete physics, invalidating the model.

Another test concerns luminous AGN (Test 2; Figure 7, right). The pair-production model of the corona also predicts that the highest luminosity sources are cooler since more electron-positron pairs are produced, thereby lowering the coronal temperature, and implying a restricted allowed range of temperature. Figure 7 shows simulations of the luminous sources with expected cut-off energies between 50 and 100 keV. Even if the rest-frame cut-offs were ≥200 keV and violating the pair-production model, HEX-P could still constrain the cut-offs to be ≥150 keV (90% confidence), which is still unallowed by the pair-production model. Note that high-luminosity AGN are preferentially at high redshift, thereby shifting cut-offs to lower observed energies where the HEX-P sensitivity is higher.

Tests like these would be prohibitive with current facilities as they would require more than 4 Ms of simultaneous XMM-Newton and NuSTAR observations (clock time) but will take only ~500 ks for HEX-P.

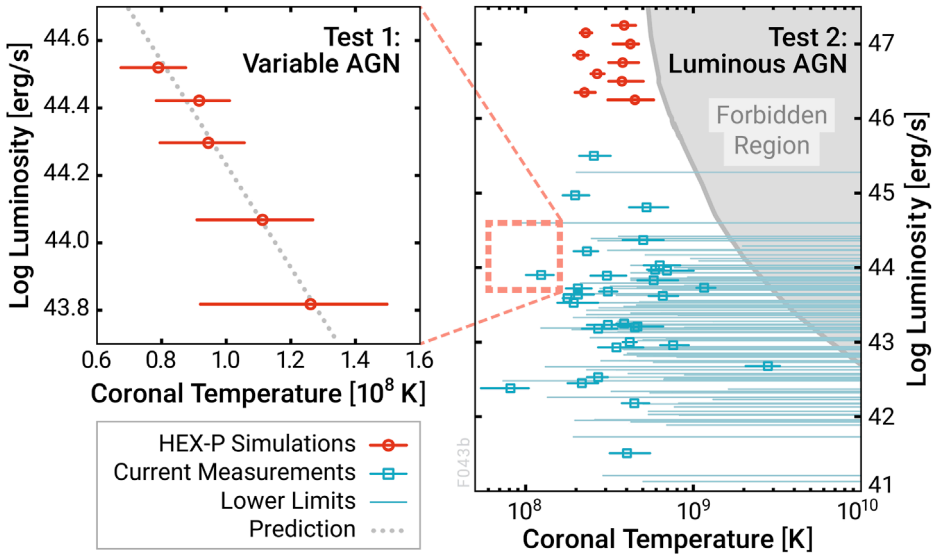

FIGURE 7
HEX-P will validate the pair-production model of the X-ray corona with two tests: measuring how cut-off energy responds to luminosity changes in a variable AGN (Test 1) and observing a sample of luminous AGN (Test 2). Adapted from Kammoun et al. (2024).

3.2 Goal 2: how do binary populations live and die?

Most stars above 8 $M_\odot$ are in binary systems. The fraction of close binaries depends on both mass and metallicity, driven by the opening chapter of star formation as the proto-stellar disk fragments (Moe et al., 2019). The story continues as close binaries exchange mass, potentially share a common envelope, have their outer layers stripped off, or even merge. Stripped envelopes and other mass-loss debris surround a dying star and interact with supernova ejecta, causing a diversity of light-curves. Differences imprinted by instabilities in the proto-stellar disk continue to be seen as stellar remnants accrete from a less massive companion and produce an X-ray signal, and as the closest binaries merge and produce a gravitational wave signal in the final chapter of binary evolution. Understanding the extremes of stellar evolution drives major questions highlighted by Astro2020 with implications ranging from cosmic reionization (e.g., Secunda et al., 2020) to nucleosynthesis (e.g., Drout et al., 2017). These questions require a range of facilities to answer. Sensitive, broadband X-ray observations, both of our Galaxy and of other galaxies (Figure 8) to sample a diversity of environments, play an important role by revealing the late stage where one star has died and is feeding on its companion.

Binaries, consisting of a neutron star or black hole accreting from a stellar companion (i.e., X-ray binaries), and their lower mass cousins with an accreting white dwarf (i.e., cataclysmic variables; CVs), provide unique constraints on how multiplicity affects massive star evolution, as well as on the physics of accretion and its environmental impact. While Chandra and XMM-Newton have surveyed nearby galaxies for more than two decades, such work has been below 10 keV which limits insight into the underlying astrophysics. Advances will require higher energy X-rays to access spectral signatures that distinguish accreting compact object types (e.g., neutron stars versus black holes), measure CV white dwarf mass, and determine accretion state (Remillard and McClintock, 2006). State transitions in X-ray binaries, boundary layer emission from accreting neutron stars, and accretion columns in pulsars all have distinguishable spectral shapes above 10 keV. These questions motivate Objective 4, described next.

3.2.1 Objective 4: determine how different galactic environments build binary systems with compact objects

Mori et al. (2024) presents simulated HEX-P surveys of the central regions of the Milky Way, while Lehmer et al. (2023) presents simulated HEX-P surveys of four nearby galaxies (M31, Maffei 1, NGC 253, and NGC 3310). These studies show how HEX-P observations can be used to investigate how X-ray populations depend on environment and metallicity. Milky Way studies are sensitive to CVs and X-ray binaries, while most detected extragalactic sources will be X-ray binaries. HEX-P's broadband response, high timing resolution, and high angular resolution will enable unprecedented sensitivity for the detection of pulsations from sources in crowded environments where traditional timing-dedicated mission (with high effective areas but little imaging capabilities) would struggle, such as the Galactic Center (Mori et al., 2024) and nearby Galaxies (Bachetti et al., 2023).

3.2.1.1 Milky way

The Galactic Center survey will cover a total area of ≥1 deg^2. The simulations by Mori et al. (2024), based on extrapolating known Chandra sources to higher energy assuming 15 – 30 keV thermal spectra (typical of mCVs), show that HEX-P will detect > 1000 sources within 30′ of Sgr A^* in the 2 – 20 keV band. For comparison, NuSTAR, with its 60″ HPD, provides the current sharpest images of the X-ray sky above 10 keV but is heavily confused and suffers from stray light (both limitations that HEX-P will overcome).

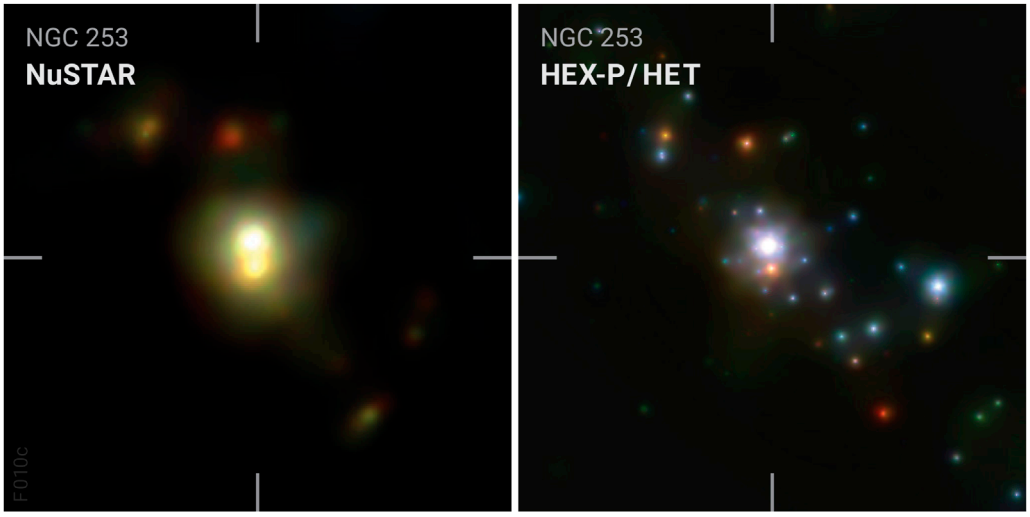

FIGURE 8
HEX-P will provide the first sensitive broadband studies of high-energy populations in the nearby universe. Adapted from Lehmer et al. (2023).

The NuSTAR Galactic Center survey covered a similar area and detected only 66 sources above 10 keV (Hong et al., 2016). HEX-P will be transformative, providing data with sufficient angular resolution, spectral range, and sensitivity to classify the rich binary populations in the center of our Galaxy and study how their properties depend on their environment. The nuclear star cluster in the central 10 pc around Sgr A* is the densest stellar environment in the Galaxy. While NuSTAR discovered diffuse hard X-ray emission from this region (Perez et al., 2015), HEX-P is needed to resolve that emission into individual sources, enabling confirmation of the predicted population of tightly bound black hole binaries in the innermost regions suggested by low energy data (Mori et al., 2021), or finding a central concentration of pulsars, which would have implications for the origin of the Galactic Center GeV excess detected by Fermi (Gautam et al., 2022). Since detecting radio pulsars in this region is challenging due to the large radio dispersion measure, HEX-P is particularly well suited for finding pulsars near Sgr A*.

3.2.1.2 Nearby galaxies

Extragalactic surveys provide additional insight into extreme stars and multiplicity by accessing a wider range of environments. Chandra has been surveying nearby galaxies for over two decades, but its X-ray binary studies are hampered by its limited 0.5 – 8 keV energy range which fails to robustly separate neutron star and black hole X-ray binary populations (Figure 9, left). Rather than observing more galaxies or increasing spectral resolution, the biggest scientific gains will come from broader spectral coverage, which breaks this degeneracy (Figure 9, right; Wik et al., 2014) and identifies accretion states (e.g., soft and hard states; Figure 2). Characteristic pulsations or flaring activity indicative of a neutron star (e.g., Type I and II X-ray bursts) provide additional classification information.

Detailed HEX-P simulations based on Chandra data, including an assumed distribution of neutron star and black hole binaries, realistic spectral models, and confusion from sources below the detection limit, predict over 200 X-ray binaries will be detected in the nearby galaxy survey, including > 130 detected above 12 keV (Lehmer et al., 2023). This is an order of magnitude more than current hard X-ray studies, which suffer from source confusion (Figure 8) and fail to reach typical HMXB depths. Simulations show that HEX-P will robustly characterize compact object types and accretion states in extragalactic environments (Figure 9), enabling the first comprehensive study of binary populations across a wide range of galactic environments, thereby providing key data to constrain high-mass star formation and stellar evolution models.

3.3 Goal 3: what powers the diversity of explosive phenomena across time and multi-messenger domains?

A new generation of time-domain and multi-messenger (TDAMM) facilities will open tremendous discovery space across astrophysics in the coming decade. With deep, multi-color images, Rubin Observatory will profoundly transform our view of the variable sky, while upgraded gamma-ray, neutrino, and gravitational wave facilities transform our view of particle acceleration and compact object mergers. A unifying theme in the diversity of phenomena to be uncovered is their energetic nature, implying they are likely X-ray emitters. However, the prospects for sensitive X-ray follow-up are uncertain. The two flagship-class X-ray missions, Chandra and XMM-Newton, are both in their third decade in orbit, have restricted fields of regard, and lack the agility to regularly and rapidly respond to targets of opportunity (ToOs). To leverage the full potential of TDAMM investments, a sensitive and agile X-ray facility is required. Angular and spectral resolution are less critical than simultaneous broadband sensitivity.

HEX-P is designed to provide the requisite sensitivity and agility, and this priority science area motivates two objectives: understanding the most powerful Galactic accelerators (factories for neutrinos, cosmic rays, and gamma-rays), and providing a community resource for exploring the dynamic universe.

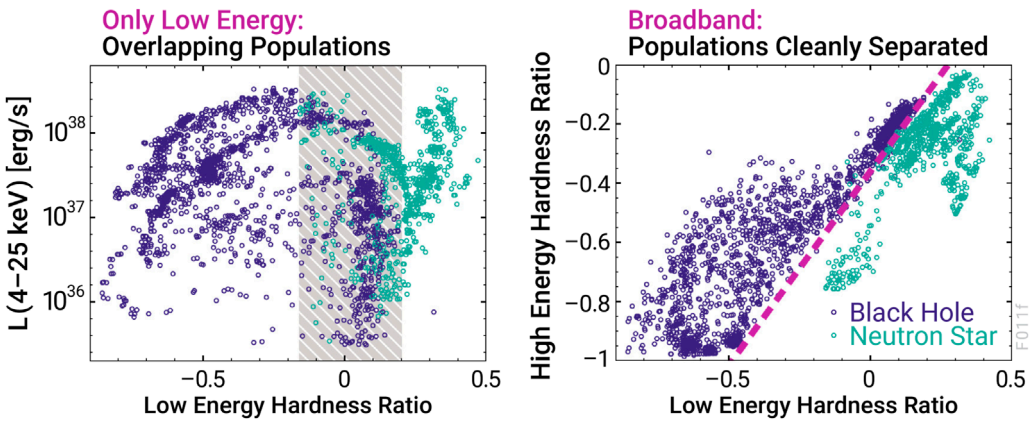

FIGURE 9
Broadband X-ray data cleanly separates black hole and neutron star X-ray binaries. Hardness ratios (HRs) use bands at 4–6 (S), 6–12 (M), and 12–25 (H) keV, and data is from a handful of bright Galactic binaries observed by RXTE. HEX-P will extend these studies into the crowded Milky Way center and to nearby galaxies. Adapted from Lehmer et al. (2023).

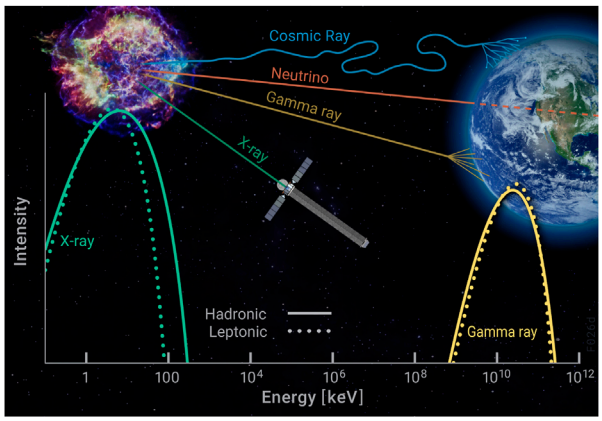

FIGURE 10
HEX-P will study the most energetic particle acceleration sites in the Galaxy, producing PeV cosmic rays, 100 TeV neutrinos, ultra-high energy gamma-rays, and X-rays. Hard X-ray data (> 10 keV) provide unique information to constrain accelerator mechanisms.

3.3.1 Objective 5: find the sources of the most energetic cosmic rays and neutrinos in our galaxy

Cosmic rays, charged extraterrestrial particles that continuously bombard the Earth's atmosphere (Figure 10), exhibit a power-law flux distribution over more than 12 orders of magnitude in energy. Low energy cosmic rays are primarily solar protons, while the most energetic are primarily extragalactic. At the "knee" of the distribution near 10^{15} eV = 1 PeV, the particles are believed to be primarily Galactic from "PeVatron" sources, the most energetic acceleration sites in the Milky Way Galaxy. Understanding these extreme sources requires a multi-messenger approach, addressing the physics of supernova shock waves, pulsar wind nebulae, and other exotic environments, with information from radio, X-rays, gamma-rays, and neutrinos (Figure 10).

Understanding Galactic PeVatron sources requires access to the 40 – 80 keV energy band. Since cosmic rays are charged particles, their trajectories are deflected by interstellar magnetic fields, disguising their origins. Energetic cosmic ray electrons inverse-Compton scatter ambient photons to produce very high-energy emission, up to ~100 TeV (Harding, 1996). However, modeling this emission requires knowledge of the seed photon population (e.g., cosmic microwave background, nearby synchrotron, or nearby thermal sources), and the highest energy emission is affected by quantum electrodynamical effects i.e., Klein-Nishina suppression (Klein and Nishina, 1929). Energetic cosmic-ray electrons also emit synchrotron photons in the X-ray to MeV band. Since this emission reflects the particle spectrum more directly, it provides a key tool for investigating particle acceleration and transport (Reynolds, 2016; Burgess et al., 2022; Mori et al., 2022). A strategic observational campaign, including a list of proposed HEX-P targets, is discussed in detail in Mori et al. (2023).

These targets have significant scientific value beyond the scientific goal of understanding particle acceleration. For example, the morphology and kinematics of the ^{44}Ti emission at 78 keV in supernova remnants is a powerful diagnostic of supernova explosion physics. The capabilities offered by HEX-P in addressing this and other interesting problems on nuclear astrophysics are discussed at length in Reynolds et al. (2023).

3.3.2 Objective 6: provide a community resource to explore the dynamic universe across the X-ray band

HEX-P will be an essential resource in the 2030s, providing sensitive high-energy access to explore explosive events and monitor variable sources with other facilities. HEX-P will devote a fraction of its exposure time to unanticipated transient observations triggered by the community. This time could be considered a form of community GO access, though HEX-P conservatively assesses it as PI-led time since it is allocated by the PI rather than NASA. This will enable HEX-P to provide more flexible and rapid response

to community needs. A few example potential programs are discussed below.

3.3.2.1 Gravitational wave mergers

To date, the binary neutron star merger GW170817 remains the only gravitational wave event with a clear electromagnetic counterpart (Margutti and Chornock, 2021) and this unique event prompted the most intense multiwavelength observational campaign in recent times (Abbott et al., 2017). X-ray observations revealed a slowly rising source appearing 9 days after the merger and peaking at 6 months, indicating that the merger produced a relativistic structured jet whose core was oriented 2° from the line of sight, consistent with an off-axis short gamma-ray burst. The jet structure likely results from the jet interaction with the merger ejecta.

As described in the study by Brightman et al. (2024), HEX-P follow-up of gravitational wave merger counterparts identified by other facilities will provide broadband X-ray light-curves to probe ejecta properties such as energy and angular structure, informing which mergers can launch ultra-relativistic jets (e.g., Sun et al., 2022), and help disambiguate binary neutron star mergers from mergers of neutron stars with black holes. This is a rich, largely unexplored scientific landscape which touches on a wide range of physics from binary star evolution to relativistic jet physics and nucleosynthesis. Determining the merger product constrains the neutron star equation of state, with implications ranging from heavy element abundances to biases in cosmological parameters (Burns, 2020). Theory also predicts that lower mass binary neutron star mergers can form long-lived supermassive neutron star remnants, detectable from the bright hard X-ray emission produced from a resultant magnetar wind nebula (Murase et al., 2018).

3.3.2.2 Fast blue optical transients (FBOTs)

Time-domain surveys are now uncovering new classes of rapidly evolving transients that challenge our notions of energetic events and stellar death. In this rapidly evolving landscape, FBOTs stand out as particularly intriguing. Their short timescales, luminosities that can exceed superluminous supernovae, and lack of UV line blanketing imply a power source other than standard supernova models powered by ^{56}Ni radioactive decay. AT2018cow illustrates the importance of broadband X-ray data for understanding transient phenomena. NuSTAR data taken a week after discovery (Figure 11) revealed excess high-energy emission with properties unprecedented among previous astrophysical transients (Margutti et al., 2019). The high-energy AT2018cow spectrum shows signatures of central engine emission reflecting off spherical optically thick material, potentially a funnel formed by a powerful accretion flow. The high inferred environmental density disfavors an alternative hypothesis that AT2018cow was due to the tidal disruption of a star by an off-center intermediate mass black hole (Perley et al., 2019). This work highlights the importance of access to the hard X-ray range, which HEX-P provides for studying the dynamic universe.

3.3.2.3 Embedded events

Many explosive events are obscured at early times, from circum-burst material, stellar ejecta, or because the event has occurred in a dense environment. Such emission will be highly absorbed, preferentially detected in hard X-rays, and changes in the absorbing column reveal the structure of that material. For example, NuSTAR observations of SN 2023ixf in the Pinwheel Galaxy initially revealed a highly absorbed source just 4 days after the supernova explosion, at a time when Swift only obtained upper limits (Grefenstette et al., 2023). Observations a week later revealed a substantially lower gas column, implying the absorption was due to a thin shell of circumstellar material, likely ejected in the final few to 10 years of the star's life. With more rapid and more sensitive ToO observations, HEX-P's broadband capabilities open a new window into the final stages of stellar evolution, as well as events occurring in dense environments.

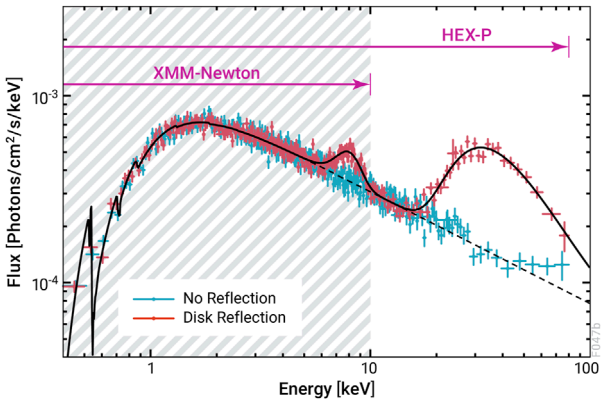

FIGURE 11
Broadband HEX-P data reveals components missed by low-energy observatories. This simulated HEX-P spectrum of AT2018cow, based on NuSTAR observations (Margutti et al., 2019), reveals reflection from a newly formed central engine. Soft X-ray observations only constrain the underlying power-law continuum, with ambiguous hints of Fe K emission.

3.4 Potential for general observer (GO) programs

Examples of potential GO programs that emphasize the range of science enabled by HEX-P are described below. As with the PI-led science described above, each of these programs has been studied in detail and reported in the indicated papers from this Research Topic.

3.4.1 Accretion onto stellar-mass black holes

Accretion of matter onto a black hole is one of the most efficient mechanisms to produce energetic radiation. While SMBHs in centers of galaxies logically provide the most extreme environments, stellar-mass black holes are arguably the best laboratories to understand the physics of accretion and the interaction between radiation and matter in the strong gravity regime. Stellar-mass black holes in binary systems with stellar companions, also known as X-ray binaries, are the primary candidates for such studies. There are close to 30 of these systems confirmed in our Galaxy. They are abundantly bright in X-rays, and relatively nearby (~ few kpc). Their much smaller size compared to SMHBs also means that they regularly display a rich phenomenology on human time scales;

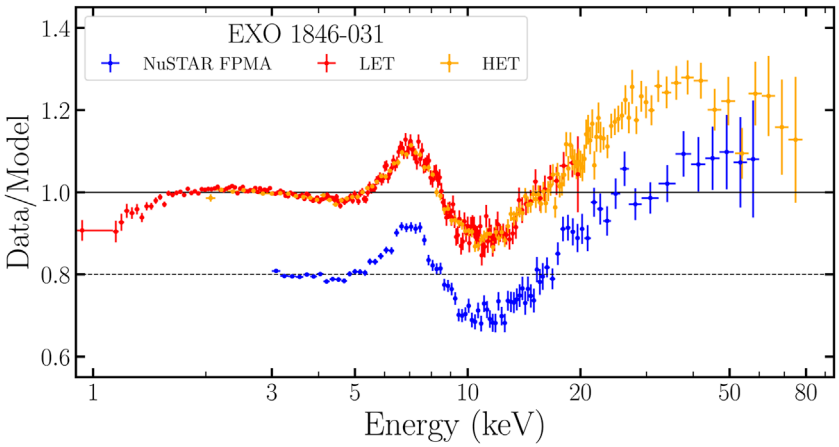

FIGURE 12
X-ray spectra of the black hole binary EXO 1846−031 observed by NuSTAR (blue), and simulated with HEX-P LET (orange) and HET (red). HEX-P's increased sensitivity and broader energy coverage enables better constraints on the physical properties of the system. Adapted from Connors et al. (2024).

i.e., weeks to months, rather than years to megayears (Tanaka and Lewin, 1995; Remillard and McClintock, 2006). Thus, high signal-to-noise data, combined with accelerated evolution, makes black-hole binaries (BHBs) the premier sources to learn about black holes and their effects on space-time, matter and radiation.

Connors et al. (2024) present a study that illustrates the capabilities of HEX-P in measuring the evolving structures of accretion flows in BHBs observed at much lower luminosities than achieved with current facilities. Their simulations demonstrate that HEX-P can accurately measure the inner radius of the accretion disk via reflection spectroscopy at luminosities below 0.1% Eddington (Figure 12). For brighter sources, HEX-P's observations will provide unprecedented data to probe the properties and indirect measurements of the geometry of the X-ray corona.[4] Detailed broadband studies of systems in nearby galaxies could be achieved for black holes accreting above the Eddington limit, which would expand the repertoire of sources available, possibly including those from different populations that have not yet been studied.

3.4.2 Jet physics in blazars

A fraction of accreting SMBHs launch powerful relativistic jets that can reach kpc, even Mpc scales. When the jets align with our line of sight, they appear boosted, producing bright, highly variable multi-band and multi-messenger emission. HEX-P is poised to answer many open questions about what powers these cosmic monsters. HEX-P's ability to pinpoint fast variability (comparable to the system light-crossing time) simultaneously from 0.2 – 80 keV will reveal particle acceleration mechanisms taking place in these jets, such as magnetic reconnection and shocks. The instrument's broadband sensitivity will enable us to disentangle leptonic and hadronic emission mechanisms (Figure 10), potentially detecting proton-induced cascades associated with neutrino emission. Moreover, its sensitivity is paramount to detect a large fraction of the highest redshift ($z > 4$) jets, essential to trace the evolution of jets and SMBHs into the early universe. As described by Marcotulli et al. (2023), HEX-P will also spatially resolve blazar and radio galaxy jets from core emission for the first time above 10 keV (Figure 13), thereby measuring jet spectral cut-offs and constraining the maximum energy of the particle population. Since blazars are strong, multi-messenger and time-variable sources, HEX-P blazar science has strong synergies with many facilities expected to be in operation in the early 2030s, including NASA's IXPE (X-ray; Weisskopf et al., 2022), COSI (γ-ray; Tomsick et al., 2023), and UVEX (ultraviolet; Kulkarni et al., 2021) missions, and the ground-based IceCube (neutrino; IceCube Collaboration, 2005) and CTAO (γ-ray; Hofmann and Zanin, 2023) facilities.

3.4.3 Equation of state (EoS) of ultradense matter

With interior densities several times higher than atomic nuclei and size scales of 10 – 20 km, neutron stars are the densest objects that persist in Nature, and they exist on the verge of imploding into a black hole. Understanding how matter behaves under these extreme conditions is encapsulated in the EoS, relating the mass and radius of the neutron star (Tolman, 1939; Oppenheimer and Volkoff, 1939), and it is best determined through astronomical measurements (Lattimer, 2011).

Each method of determining the EoS of ultradense matter has underlying systematic uncertainties and probes different regions of the mass-radius parameter space (Figure 14). The firmest constraints require multiple approaches. Pulsar timing studies assume simplistic geometrical models (i.e., not physically motivated) of temperature across the neutron star surface (e.g.,; Miller et al., 2019), while gravitational wave studies provide tight radius constraints with

4 While more precise and direct measurements of the geometry of inner accretion flows can be achieved by facilities such as the Event Horizon Telescope (EHT; Doeleman et al., 2009) or Gravity+ (Gravity+ Collaboration et al., 2022), their observations are limited to a few selected of sources.

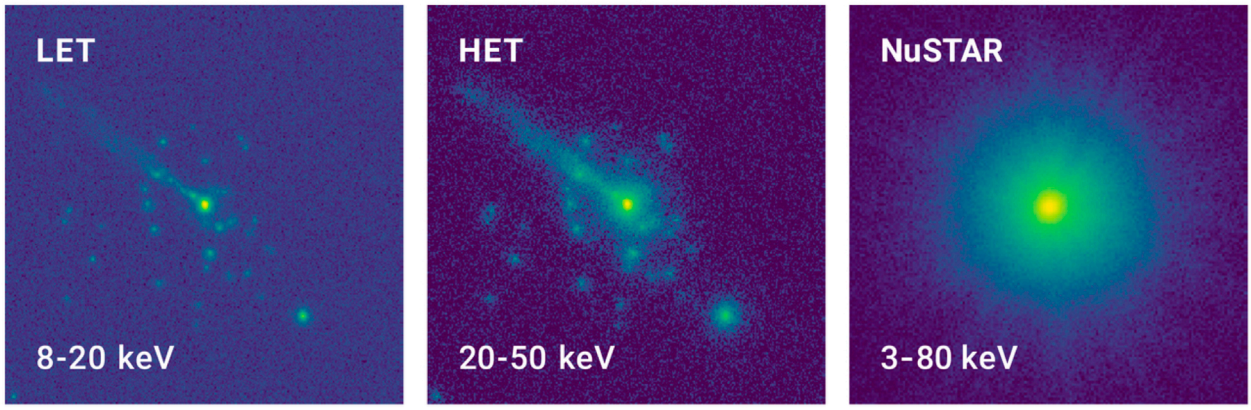

FIGURE 13
HEX-P will resolve the extended jet and point sources above 10 keV, like the one observed in Centaurus A. Adapted from Marcotulli et al. (2023).

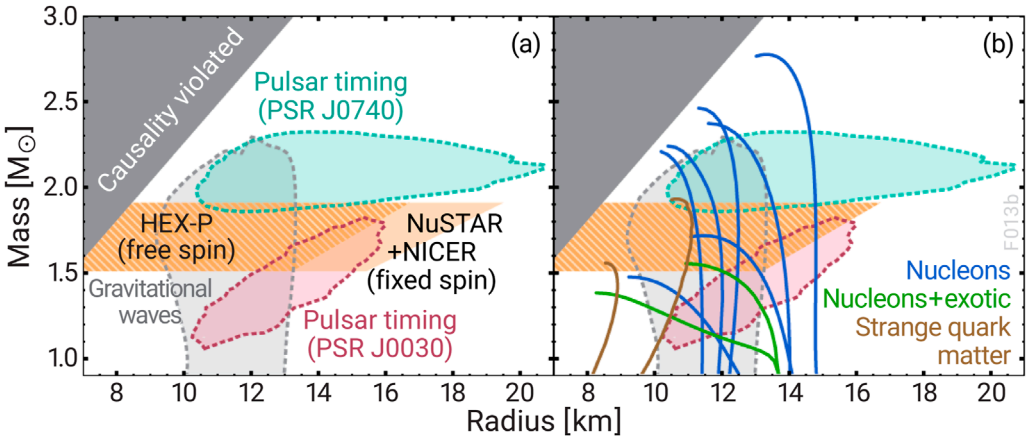

FIGURE 14
(A) Mass and radius constraints from reflection modeling compared to neutron star gravitational wave events and NICER pulsar lightcurve modeling. **(B)** Same as panel **(A)** but including a family of EoS theoretical predictions. Adapted from Ludlam et al. (2023).

poor mass constraints (Raaijmakers et al., 2021). Broadband X-ray studies covering 0.5 – 50 keV robustly measure continuum and reflection features, thereby providing the radius of the inner edge of the accretion disk and placing a strong, physical upper limit on the neutron star size (Ludlam et al., 2022). However, current measurements from coordinated NICER and NuSTAR observations require fixing the neutron star spin (typically assuming no rotation). The study by Ludlam et al. (2023) shows how the improved sensitivity of HEX-P will enable robustly solving for neutron star spin, thereby providing tighter radial constraints with less systematic bias.

3.4.4 Accretion and other physical processes in strong magnetic fields

With magnetic fields reaching typical strengths of $\sim 10^{12}$ G in high-mass X-ray binary systems and $\sim 10^{15}$ G in magnetars, accreting neutron stars provide a unique laboratory to study the extreme physics of accretion in the presence of strong magnetic fields. Neutron star magnetic field strengths are orders of magnitude higher than the strongest magnetic fields achieved in terrestrial laboratories ($\sim 5 \times 10^5$ G). In high-mass binary systems, magnetic field pressure disrupts the inflow of the accreting material, channeling matter onto the magnetic poles. Since the neutron star rotates, radiation is released in a highly anisotropic manner, producing pulsing X-ray emission whose broadband study informs the plasma physics as well as the interaction of radiation with ultra-strong magnetic fields. Magnetars are also useful probes of the physics of the interaction of radiation with ultra-strong magnetic fields, but like some isolated neutron stars, that they are not thought to be accreting. The predictions for HEX-P's unique capabilities in addressing important questions about the physics of magnetars and other isolated neutron stars are extensively discussed in Alford et al. (2024).

Due to the very high magnetic field present in magnetars, electron motion perpendicular to the magnetic field lines becomes quantized, leading to a resonance proportional to the magnetic field strength. This produces absorption-like cyclotron resonant scattering features, or simply cyclotron lines, at 5 – 100 keV. Cyclotron lines represent the most direct way to probe magnetic

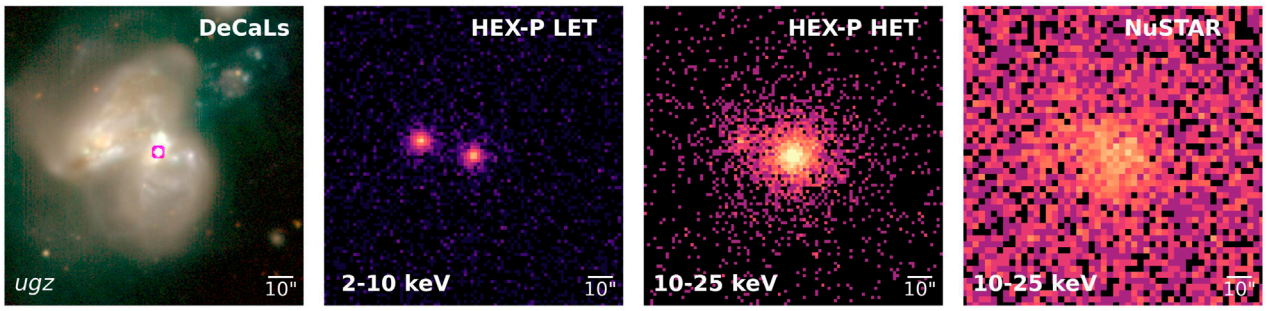

FIGURE 15
HEX-P will resolve obscured AGN in galaxy mergers, such as Arp-299 shown here. Note that the low-energy LET observation finds both components to be comparably bright, while the high-energy HET reveals the western component to be significantly brighter and heavily obscured. Adapted from Pfeifle et al. (2023).

field strengths on or close to the neutron star surface, and they have been detected in about 40 sources (Staubert et al., 2019). Detecting fundamental lines and harmonics, and measuring their dependence on pulsar phase and luminosity, provides crucial insight into the accretion physics, including its geometry, electron bulk motion, turbulence, temperature distribution, and plasma conditions (Kreykenbohm et al., 2002).

Bachetti et al. (2023) presents a comprehensive study of potential HEX-P programs studying ultra-luminous X-ray sources (ULXs), at least some of which are neutron stars accreting at extreme rates, up to ~500 times the Eddington limit (e.g., Bachetti et al., 2014; Fürst et al., 2016; Israel et al., 2017). Cyclotron lines provide the most direct measurement of ULX magnetic field strengths, which may be the key factor enabling their extreme luminosities. HEX-P will also be able to detect and study the radiatively-driven winds discovered in ULXs (Pinto et al., 2016), providing essential information on super-Eddington accretion and unveiling the origin of their surrounding 100-pc interstellar bubbles (Gúrpide et al., 2022).

3.4.5 SMBH activity in merging galaxies

HEX-P is an essential tool for studying SMBH growth. Merging galaxies offer one of the most dramatic channels for galaxy evolution, driving inflows of gas into galactic nuclei and potentially fueling both star formation and central SMBH activity. Dual AGN in late-stage mergers with nuclear pair separations < 10 kpc are ideal candidates to study SMBH growth since they coincide with the most transformative period for galaxies. However, since mergers are also associated with severe gas and dust obscuration (Koss et al., 2018; Blecha et al., 2018; De Rosa et al., 2019), dual AGNs are difficult to confirm and study, particularly with soft X-ray observatories. Hard X-rays offer a powerful tool to penetrate the dense obscuring media predicted to surround dual AGN in late-stage mergers (Figure 15). To date, only a handful of the brightest and closest systems have been studied at these energies due to the demanding instrument requirements involved. HEX-P enables, for the first time, the ability to spatially resolve hard X-ray counterparts of closely separated ($\sim 2-5''$) dual AGN.

The study reported by Pfeifle et al. (2023) shows via simulations that HEX-P will probe dual AGNs in late-stage mergers (< 10 kpc) out to $z \sim 0.1$, and intermediate-stage mergers (~30 kpc) out to $z \sim 0.3$. This is a dramatic improvement over NuSTAR and enables science that cannot be done with a soft X-ray observatory. HEX-P will transform our understanding of the role of AGN triggering and AGN feedback during galactic mergers.

3.4.6 The circum-nuclear environment of growing SMBHs

The vast majority of accretion onto SMBHs takes place within a dense obscuring fortress of gas and dust. This circum-nuclear obscurer connects interstellar space to the accretion disc, and is known to evolve with both the accretion power of the central engine as well as the age of the Universe (e.g., Ueda et al., 2014; Buchner et al., 2014; Ananna et al., 2019). Thus a complete understanding of SMBH growth requires intricate knowledge of the structure and dynamics of the circum-nuclear environment surrounding AGN.

However, our current knowledge of the obscurer is fundamentally incomplete. Estimates of heavily obscured AGN space densities is unconstrained with observations typically suggesting that anywhere between ~ 10%–50% of all SMBH activity takes place within material exceeding the Compton-thick limit (column density $N_{\rm H} > 10^{24}$ cm^{-2}; e.g., Ricci et al., 2015; Kammoun et al., 2020; Torres-Albà et al., 2021). Geometrical parameters describing the obscurer's structure, such as covering factor, impose subtle changes on the observed hard X-ray spectrum of obscured AGN that NuSTAR can only begin to identify in a handful of brightest targets (e.g., Buchner et al., 2021). Furthermore, advances driven by NuSTAR have demonstrated that the obscurer is not static, but predominantly dynamic in nature (e.g., Baloković et al., 2021; Marchesi et al., 2022; Torres-Albà et al., 2023).

Boorman et al. (2023) present a series of simulations to show the exciting ways in which HEX-P will advance our understanding of the circum-nuclear environment surrounding AGN. Dramatic advances in sensitivity driven by reduced backgrounds and enhanced angular resolution will increase the available volume for robustly confirming heavily obscured accretion by more than an order of magnitude. By providing broadband X-ray spectral constraints on select AGN with precise black hole mass estimates, HEX-P will drive the development

of new physically-motivated models that are capable of describing the geometrical structure of the obscurer in relation to the accretion power of the central engine. Also, the strictly simultaneous soft and hard X-ray spectral constraints provided by HEX-P will enable new insights into the dynamical nature of the obscurer via monitoring campaigns. Boorman et al. (2023) show that the passband of HEX-P is sufficient to disentangle intrinsic flux variations from structural changes of the obscurer to high precision, a task virtually impossible with current instrumentation and cadences.

4 Synergies with other facilities

The HEX-P mission will offer powerful synergies with key astronomical facilities expected to be operational in the 2030s, advancing our understanding of the high-energy universe across multiple wavelengths and observational techniques.

HEX-P's high-energy X-ray capabilities will greatly complement JWST's observations in the infrared, allowing for simultaneous studies of the most distant and energetic objects in the universe. While JWST probes the formation of galaxies, stars, and black holes in the early universe through infrared light, HEX-P will trace the high-energy processes occurring within these systems, such as supermassive black hole growth and powerful galactic winds. In obscured AGN, JWST can map the IR emission from the obscuring material, while HEX-P sees the strong X-ray emission from the central engine. Together, they will provide a comprehensive view of the formation and evolution of galaxies and the role of high-energy phenomena in shaping cosmic structure.

In the UV band, the Ultraviolet Explorer (UVEX) and HEX-P will form a powerful combination, covering the ultraviolet and X-ray regimes to study hot, energetic environments like the atmospheres of neutron stars, black hole accretion disks, and supernova remnants. UVEX will capture emissions from ionized gas and hot stars in the ultraviolet, while HEX-P will observe the high-energy processes at play.

In the soft X-rays, HEX-P will complement NewAthena's focus on the soft X-ray band, extending the observational window into the hard X-ray regime. This synergy will allow for simultaneous, multi-band X-ray observations of black holes, galaxy clusters, and neutron stars, revealing more about their energetic environments and evolution. The unrivaled energy resolution of the X-IFU microcalorimeter in NewAthena will reveal the detailed structure of atomic features with unprecedented precision, while HEX-P's broadband coverage will be crucial to uniquely constraint the continuum emission to very high energies.

At very high energies (e.g., gamma rays), HEX-P will synergize with key observatories like COSI, IceCube, and CTAO, creating an observational network to explore the most energetic and extreme phenomena in the universe. This includes detecting processes like gamma-ray bursts (GRBs), supernova explosions, and positron annihilation events with COSI (soft gamma rays); provide X-ray counterparts to IceCube's neutrino detections from the most energetic cosmic accelerators, such as blazars, active galactic nuclei (AGN), and gamma-ray bursts; and complementing CTAO's focus on very-high-energy gamma rays from cosmic sources like AGN, pulsar wind nebulae, and supernova remnants.

As we adventure in the new era of gravitational wave detections, HEX-P will complement Advanced LIGO and LISA's gravitational wave detections by providing rapid follow-up of high-energy X-ray observations of black hole mergers and neutron star collisions. Together, these missions will offer a multi-messenger view of extreme cosmic events, enabling detailed studies of their dynamics and environments.

In the time-domain arena, proposed missions like THESUS (Transient High-Energy Sky and Early Universe Surveyor) and the GAMOW Explorer would deliver new triggers for transient sources. While THESUS will focus on detecting and localizing transient sources like gamma-ray bursts (GRBs) and outbursting X-ray binaries like black holes and neutron stars, HEX-P will provide deeper high-energy follow-up observations, characterizing their X-ray emission. Moreover, by working in tandem with GAMOW's gamma-ray observations, HEX-P will extend the energy range of investigation for phenomena like GRBs and active galactic nuclei (AGN). This collaboration will enable a more comprehensive analysis of the most energetic processes in the universe.

Through all these and many other collaborations, HEX-P will play a pivotal role in multi-messenger and multiwavelength astrophysics, helping to unlock new insights into the fundamental physics of the cosmos.

5 Final remarks

The low-energy capabilities of HEX-P build on the successes of the two current flagship X-ray missions, both soft X-ray observatories that launched in 1999. HEX-P combines greater effective area than Chandra with improved angular resolution over XMM-Newton. HEX-P also has an improved agility to respond to ToO requests, thereby retrieving data prioritized by Astro2020. Broadband X-rays reveal obscured sources, access new spectral features, and improve modeling of soft-band data. Since 2021, $>50\%$ of NuSTAR observations have been coordinated with soft X-ray satellites (i.e., Chandra, XMM-Newton, IXPE, Swift, NICER, XRISM) to provide simultaneous broadband coverage, and a similar reliance on HET is expected for future soft X-ray observatories, such as NewAthena. With sensitivity to 80 keV, HEX-P shrinks the gap between X-ray and gamma-ray facilities, complementing NASA's Compton Spectrometer and Imager (COSI; 0.2–5 MeV; launch in 2027) and the Cherenkov Telescope Array Observatory (CTAO; 0.02–300 TeV; ground-breaking in 2024). Finally, HEX-P provides essential data to probe TDAMM sources to be found in the 2030s by gravitational wave, neutrino, cosmic ray, and photon facilities (e.g., Rubin, Roman, UVEX, and JWST). To leverage the full potential of TDAMM investments, we require a sensitive and agile X-ray facility in the 2030s. Rather than improving angular resolution or spectral resolution, the biggest scientific gains come from simultaneous broad, sensitive spectral coverage.

The work summarized in this paper has been largely led by members of the high-energy astrophysics community, most of whom are not Co-investigators of the HEX-P mission proposal. This exemplifies the strong interests and needs for a facility with capabilities like those in HEX-P. Furthermore, while the science cases discussed in this collection of papers cover the core science of the mission, they do not represent a complete or

comprehensive list of topics that a mission like HEX-P can achieve. The potential for new science reaches far beyond these themes, and perhaps the most promising discoveries are those that will come unexpectedly.

Data availability statement

The raw data supporting the conclusion of this article will be made available by the authors, without undue reservation.

Author contributions

JG: Writing–original draft, Writing–review and editing. DSt: Writing–original draft, Writing–review and editing. KrM: Writing–original draft, Writing–review and editing. MS: Writing–original draft, Writing–review and editing. BG: Writing–original draft, Writing–review and editing. MA: Writing–original draft, Writing–review and editing. JA: Writing–original draft, Writing–review and editing. AA: Writing–original draft, Writing–review and editing. MaB: Writing–original draft, Writing–review and editing. MiB: Writing–original draft, Writing–review and editing. RB: Writing–original draft, Writing–review and editing. SB: Writing–original draft, Writing–review and editing. DB: Writing–original draft, Writing–review and editing. PB: Writing–original draft, Writing–review and editing. MuB: Writing–original draft, Writing–review and editing. JB: Writing–original draft, Writing–review and editing. EB: Writing–original draft, Writing–review and editing. C-TC: Writing–original draft, Writing–review and editing. FC: Writing–original draft, Writing–review and editing. JC: Writing–original draft, Writing–review and editing. RC: Writing–original draft, Writing–review and editing. MD: Writing–original draft, Writing–review and editing. LG: Writing–original draft, Writing–review and editing. PD: Writing–original draft, Writing–review and editing. PF: Writing–original draft, Writing–review and editing. AG: Writing–original draft, Writing–review and editing. MG: Writing–original draft, Writing–review and editing. SG: Writing–original draft, Writing–review and editing. FH: Writing–original draft, Writing–review and editing. EK: Writing–original draft, Writing–review and editing. GL: Writing–original draft, Writing–review and editing. BL: Writing–original draft, Writing–review and editing. AL: Writing–original draft, Writing–review and editing. RL: Writing–original draft, Writing–review and editing. SM: Writing–original draft, Writing–review and editing. LM: Writing–original draft, Writing–review and editing. RM: Writing–original draft, Writing–review and editing. MeM: Writing–original draft, Writing–review and editing. AnM: Writing–original draft, Writing–review and editing. MaM: Writing–original draft, Writing–review and editing. KaM: Writing–original draft, Writing–review and editing. AlM: Writing–original draft, Writing–review and editing. KN: Writing–original draft, Writing–review and editing. KeP: Writing–original draft, Writing–review and editing. RP: Writing–original draft, Writing–review and editing. CP: Writing–original draft, Writing–review and editing. JP: Writing–original draft, Writing–review and editing. GP: Writing–original draft, Writing–review and editing. KaP: Writing–original draft, Writing–review and editing. PP: Writing–original draft, Writing–review and editing. SP: Writing–original draft, Writing–review and editing. AR: Writing–original draft, Writing–review and editing. SR: Writing–original draft, Writing–review and editing. AS: Writing–original draft, Writing–review and editing. DSp: Writing–original draft, Writing–review and editing. JT: Writing–original draft, Writing–review and editing. NT-A: Writing–original draft, Writing–review and editing. DoW: Writing–original draft, Writing–review and editing. DaW: Writing–original draft, Writing–review and editing. JW: Writing–original draft, Writing–review and editing. WZ: Writing–original draft, Writing–review and editing. XZ: Writing–original draft, Writing–review and editing.

Funding

The author(s) declare that financial support was received for the research, authorship, and/or publication of this article. CP acknowledges funds by European Union - Next-Generation EU. JG and JP acknowledge support from NASA grants 80NSSC21K1567 and 80NSSC22K1120.

Acknowledgments

The work of DSt was carried out at the Jet Propulsion Laboratory, California Institute of Technology, under a contract with NASA. We thank the SIXTE support team for their assistance in generating spectra from simulated event files and for assistance with the documentation. We also thank Richard Barkus for his invaluable help with the art work and editing of the figures included in this paper.

Conflict of interest

The authors declare that the research was conducted in the absence of any commercial or financial relationships that could be construed as a potential conflict of interest.

Publisher's note

All claims expressed in this article are solely those of the authors and do not necessarily represent those of their affiliated organizations, or those of the publisher, the editors and the reviewers. Any product that may be evaluated in this article, or claim that may be made by its manufacturer, is not guaranteed or endorsed by the publisher.

References

Abbott, B. P., Abbott, R., Abbott, T. D., Acernese, F., Ackley, K., Adams, C., et al. (2017). Gravitational waves and gamma-rays from a binary neutron star merger: GW170817 and GRB 170817A. *ApJL* 848, L13. doi:10.3847/2041-8213/aa920c

Alford, J. A. J., Younes, G. A., Wadiasingh, Z., Abdelmaguid, M., An, H., Bachetti, M., et al. (2024). The high energy X-ray probe (HEX-P): magnetars and other isolated neutron stars. *Front. Astronomy Space Sci.* 10, 1294449. doi:10.3389/fspas.2023.1294449

Ananna, T. T., Treister, E., Urry, C. M., Ricci, C., Kirkpatrick, A., LaMassa, S., et al. (2019). The accretion history of AGNs. I. Supermassive black hole population synthesis model. *ApJ* 871, 240. doi:10.3847/1538-4357/aafb77

Ananna, T. T., Weigel, A. K., Trakhtenbrot, B., Koss, M. J., Urry, C. M., Ricci, C., et al. (2022). BASS. XXX. Distribution functions of DR2 Eddington ratios, black hole masses, and X-ray luminosities. *ApJS* 261, 9. doi:10.3847/1538-4365/ac5b64

Bachetti, M., Harrison, F. A., Walton, D. J., Grefenstette, B. W., Chakrabarty, D., Fürst, F., et al. (2014). An ultraluminous X-ray source powered by an accreting neutron star. *Nature* 514, 202–204. doi:10.1038/nature13791

Bachetti, M., Middleton, M. J., Pinto, C., Gúrpide, A., Walton, D. J., Brightman, M., et al. (2023). The high energy X-ray probe (HEX-P): studying extreme accretion with ultraluminous X-ray sources. *Front. Astronomy Space Sci.* 10, 1289432. doi:10.3389/fspas.2023.1289432

Baloković, M., Cabral, S. E., Brenneman, L., and Urry, C. M. (2021). Properties of the obscuring torus in NGC 1052 from multiepoch broadband X-ray spectroscopy. *ApJ* 916, 90. doi:10.3847/1538-4357/abff4d

Beckmann, R. S., Smethurst, R. J., Simmons, B. D., Coil, A., Dubois, Y., Garland, I. L., et al. (2024). Supermassive black holes in merger-free galaxies have higher spins which are preferentially aligned with their host galaxy. *MNRAS* 527, 10867–10877. doi:10.1093/mnras/stad1795

Berti, E., and Volonteri, M. (2008). Cosmological black hole spin evolution by mergers and accretion. *ApJ* 684, 822–828. doi:10.1086/590379

Blecha, L., Snyder, G. F., Satyapal, S., and Ellison, S. L. (2018). The power of infrared AGN selection in mergers: a theoretical study. *MNRAS* 478, 3056–3071. doi:10.1093/mnras/sty1274

Boorman, P. G., Torres-Albà, N., Annuar, A., Marchesi, S., Pfeifle, R., Stern, D., et al. (2023). The high energy X-ray probe (HEX-P): the circum-nuclear environment of growing supermassive black holes. doi:10.48550/arXiv.2311.04949

Bottacini, E., Ajello, M., and Greiner, J. (2012). The deep look at the hard X-ray sky: the swift-INTEGRAL X-ray (SIX) survey. *ApJS* 201, 34. doi:10.1088/0067-0049/201/2/34

Brightman, M., Margutti, R., Polzin, A., Jaodand, A., Hotokezaka, K., Alford, J. A. J., et al. (2024). The high energy X-ray probe (HEX-P): sensitive broadband X-ray observations of transient phenomena in the 2030s. *Front. Astronomy Space Sci.* 10, 1292656. doi:10.3389/fspas.2023.1292656

Buchner, J., Brightman, M., Baloković, M., Wada, K., Bauer, F. E., and Nandra, K. (2021). Physically motivated X-ray obscurer models. *Astron. Astrophys.* 651, A58. doi:10.1051/0004-6361/201834963

Buchner, J., Georgakakis, A., Nandra, K., Hsu, L., Rangel, C., Brightman, M., et al. (2014). X-ray spectral modelling of the AGN obscuring region in the CDFS: Bayesian model selection and catalogue. *Astron. Astrophys.* 564, A125. doi:10.1051/0004-6361/201322971

Burgess, D. A., Mori, K., Gelfand, J. D., Hailey, C. J., Tokayer, Y. M., Woo, J., et al. (2022). The eel pulsar wind nebula: a PeVatron-candidate origin for HAWC J1826-128 and HESS J1826-130. *ApJ* 930, 148. doi:10.3847/1538-4357/ac650a

Burns, E. (2020). Neutron star mergers and how to study them. *Living Rev. Relativ.* 23, 4. doi:10.1007/s41114-020-00028-7

Bustamante, S., and Springel, V. (2019). Spin evolution and feedback of supermassive black holes in cosmological simulations. *MNRAS* 490, 4133–4153. doi:10.1093/mnras/stz2836

Civano, F., Zhao, X., Boorman, P. G., Marchesi, S., Ananna, T., Creech, S., et al. (2024). The high energy X-ray probe (HEX-P): bringing the cosmic X-ray background into focus. *Front. Astronomy Space Sci.* 11, 1340719. doi:10.3389/fspas.2024.1340719

Connors, R. M. T., Tomsick, J. A., Draghis, P., Coughenour, B., Shaw, A. W., García, J. A., et al. (2024). The High Energy X-ray Probe (HEX-P): probing accretion onto stellar mass black holes. *Front. Astronomy Space Sci.* 10, 1292682. doi:10.3389/fspas.2023.1292682

De Marco, B., Ponti, G., Cappi, M., Dadina, M., Uttley, P., Cackett, E. M., et al. (2013). Discovery of a relation between black hole mass and soft X-ray time lags in active galactic nuclei. *MNRAS* 431, 2441–2452. doi:10.1093/mnras/stt339

De Rosa, A., Vignali, C., Bogdanović, T., Capelo, P. R., Charisi, M., Dotti, M., et al. (2019). The quest for dual and binary supermassive black holes: a multi-messenger view. *NewAR* 86, 101525. doi:10.1016/j.newar.2020.101525

Doeleman, S., Agol, E., Backer, D., Baganoff, F., Bower, G. C., Broderick, A., et al. (2009). "Imaging an event horizon: submm-VLBI of a super massive black hole," in *astro2010: the astronomy and astrophysics decadal survey*, 2010, 68. doi:10.48550/arXiv.0906.3899

Dotti, M., Colpi, M., Pallini, S., Perego, A., and Volonteri, M. (2013). On the orientation and magnitude of the black hole spin in galactic nuclei. *ApJ* 762, 68. doi:10.1088/0004-637X/762/2/68

Drout, M. R., Piro, A. L., Shappee, B. J., Kilpatrick, C. D., Simon, J. D., Contreras, C., et al. (2017). Light curves of the neutron star merger GW170817/SSS17a: implications for r-process nucleosynthesis. *Science* 358, 1570–1574. doi:10.1126/science.aaq0049

Dubois, Y., Beckmann, R., Bournaud, F., Choi, H., Devriendt, J., Jackson, R., et al. (2021). Introducing the NEWHORIZON simulation: galaxy properties with resolved internal dynamics across cosmic time. *Astron. Astrophys.* 651, A109. doi:10.1051/0004-6361/202039429

Dubois, Y., Pichon, C., Welker, C., Le Borgne, D., Devriendt, J., Laigle, C., et al. (2014). Dancing in the dark: galactic properties trace spin swings along the cosmic web. *MNRAS* 444, 1453–1468. doi:10.1093/mnras/stu1227

Eraerds, T., Antonelli, V., Davis, C., Hall, D. J., Hetherington, O., Holland, A. D., et al. (2021). Enhanced simulations on the athena/wide field imager instrumental background. *J. Astronomical Telesc. Instrum. Syst.* 7, 034001. doi:10.1117/1.JATIS.7.3.034001

Fürst, F., Walton, D. J., Harrison, F. A., Stern, D., Barret, D., Brightman, M., et al. (2016). Discovery of coherent pulsations from the ultraluminous X-ray source NGC 7793 P13. *ApJL* 831, L14. doi:10.3847/2041-8205/831/2/L14

Gautam, A., Crocker, R. M., Ferrario, L., Ruiter, A. J., Ploeg, H., Gordon, C., et al. (2022). Millisecond pulsars from accretion-induced collapse as the origin of the Galactic Centre gamma-ray excess signal. *Nat. Astron.* 6, 703–707. doi:10.1038/s41550-022-01658-3

Gilli, R., Comastri, A., and Hasinger, G. (2007). The synthesis of the cosmic X-ray background in the Chandra and XMM-Newton era. *A&* 463, 79–96. doi:10.1051/0004-6361:20066334

Gravity+ Collaboration, Abuter, R., Alarcon, P., Allouche, F., Amorim, A., Bailet, C., Bedigan, H., et al. (2022). The GRAVITY+ project: towards all-sky, faint-science, high-contrast near-infrared interferometry at the VLTI. *Messenger* 189, 17–22. doi:10.18727/0722-6691/5285

Grefenstette, B. W., Brightman, M., Earnshaw, H. P., Harrison, F. A., and Margutti, R. (2023). Early hard X-rays from the nearby core-collapse supernova SN 2023ixf. *ApJL* 952, L3. doi:10.3847/2041-8213/acdf4e

Griffin, A. J., Lacey, C. G., Gonzalez-Perez, V., Lagos, C. d. P., Baugh, C. M., and Fanidakis, N. (2019). The evolution of SMBH spin and AGN luminosities for $z < 6$ within a semi-analytic model of galaxy formation. *MNRAS* 487, 198–227. doi:10.1093/mnras/stz1216

Gúrpide, A., Parra, M., Godet, O., Contini, T., and Olive, J. F. (2022). MUSE spectroscopy of the ULX NGC 1313 X-1: a shock-ionised bubble, an X-ray photoionised nebula, and two supernova remnants. *A&* 666, A100. doi:10.1051/0004-6361/202142229

Harding, A. K. (1996). Inverse-compton gamma-rays from plerions. *Space Sci. Rev.* 75, 257–268. doi:10.1007/BF00195038

Harrison, F. A., Aird, J., Civano, F., Lansbury, G., Mullaney, J. R., Ballantyne, D. R., et al. (2016). The NuSTAR extragalactic surveys: the number counts of active galactic nuclei and the resolved fraction of the cosmic X-ray background. *ApJ* 831, 185. doi:10.3847/0004-637X/831/2/185

Harrison, F. A., Craig, W. W., Christensen, F. E., Hailey, C. J., Zhang, W. W., Boggs, S. E., et al. (2013). The nuclear spectroscopic telescope Array (NuSTAR) high-energy X-ray mission. *ApJ* 770, 103. doi:10.1088/0004-637X/770/2/103

Hofmann, W., and Zanin, R. (2023). The Cherenkov telescope Array. 1, 47. doi:10.1007/978-981-16-4544-0_70-1

Hong, J., Mori, K., Hailey, C. J., Nynka, M., Zhang, S., Gotthelf, E., et al. (2016). NuSTAR hard X-ray survey of the galactic center region. II. X-ray point sources. *ApJ* 825, 132. doi:10.3847/0004-637X/825/2/132

IceCube Collaboration (2005). The IceCube neutrino telescope. *Nucl. Phys. B Proc. Suppl.* 138, 179–182. doi:10.1016/j.nuclphysbps.2004.11.042

Israel, G. L., Belfiore, A., Stella, L., Esposito, P., Casella, P., De Luca, A., et al. (2017). An accreting pulsar with extreme properties drives an ultraluminous x-ray source in NGC 5907. *Science* 355, 817–819. doi:10.1126/science.aai8635

Izquierdo-Villalba, D., Bonoli, S., Dotti, M., Sesana, A., Rosas-Guevara, Y., and Spinoso, D. (2020). From galactic nuclei to the halo outskirts: tracing supermassive black holes across cosmic history and environments. *MNRAS* 495, 4681–4706. doi:10.1093/mnras/staa1399

Jansen, F., Lumb, D., Altieri, B., Clavel, J., Ehle, M., Erd, C., et al. (2001). XMM-Newton observatory. I. The spacecraft and operations. *A&* 365, L1–L6. doi:10.1051/0004-6361:20000036

Kammoun, E., Lohfink, A. M., Masterson, M., Wilkins, D. R., Zhao, X., Balokovic, M., et al. (2024). The high energy X-ray probe (HEX-P): probing the physics of

the X-ray corona in active galactic nuclei. *Front. Astronomy Space Sci.* 10, 1308056. doi:10.3389/fspas.2023.1308056

Kammoun, E. S., Miller, J. M., Koss, M., Oh, K., Zoghbi, A., Mushotzky, R. F., et al. (2020). A hard look at local, optically selected, obscured seyfert galaxies. *ApJ* 901, 161. doi:10.3847/1538-4357/abb29f

Klein, O., and Nishina, T. (1929). Über die Streuung von Strahlung durch freie Elektronen nach der neuen relativistischen Quantendynamik von Dirac. *Z. fur Phys.* 52, 853–868. doi:10.1007/BF01366453

Koss, M., Trakhtenbrot, B., Ricci, C., Lamperti, I., Oh, K., Berney, S., et al. (2017). BAT AGN spectroscopic survey. I. Spectral measurements, derived quantities, and AGN demographics. *ApJ* 850, 74. doi:10.3847/1538-4357/aa8ec9

Koss, M. J., Blecha, L., Bernhard, P., Hung, C.-L., Lu, J. R., Trakhtenbrot, B., et al. (2018). A population of luminous accreting black holes with hidden mergers. *Nature* 563, 214–216. doi:10.1038/s41586-018-0652-7

Koss, M. J., Trakhtenbrot, B., Ricci, C., Bauer, F. E., Treister, E., Mushotzky, R., et al. (2022). BASS. XXI. The data release 2 overview. *ApJS* 261, 1. doi:10.3847/1538-4365/ac6c8f

Kreykenbohm, I., Coburn, W., Wilms, J., Kretschmar, P., Staubert, R., Heindl, W. A., et al. (2002). Confirmation of two cyclotron lines in Vela X-1. *A&* 395, 129–140. doi:10.1051/0004-6361:20021181

Kulkarni, S. R., Harrison, F. A., Grefenstette, B. W., Earnshaw, H. P., Andreoni, I., Berg, D. A., et al. (2021). Science with the ultraviolet explorer (UVEX). doi:10.48550/arXiv.2111.15608

Lattimer, J. M. (2011). Neutron stars and the dense matter equation of state. *Ap&SS* 336, 67–74. doi:10.1007/s10509-010-0529-1

Lawrence, A. (1991). The relative frequency of broad-lined and narrow-lined active galactic nuclei: implications for unified schemes. *MNRAS* 252, 586–592. doi:10.1093/mnras/252.4.586

Lehmer, B. D., Garofali, K., Binder, B. A., Fornasini, F., Vulic, N., Zezas, A., et al. (2023). The high energy X-ray probe: resolved X-ray populations in extragalactic environments. *Front. Astronomy Space Sci.* 10, 1293918. doi:10.3389/fspas.2023.1293918

Ludlam, R. M., Cackett, E. M., García, J. A., Miller, J. M., Stevens, A. L., Fabian, A. C., et al. (2022). Radius constraints from reflection modeling of Cygnus X-2 with NuSTAR and NICER. *ApJ* 927, 112. doi:10.3847/1538-4357/ac5028

Ludlam, R. M., Malacaria, C., Sokolova-Lapa, E., Fuerst, F., Pradhan, P., Shaw, A. W., et al. (2023). The high energy X-ray probe (HEX-P): a new window into neutron star accretion. *Front. Astronomy Space Sci.* 10, 1292500. doi:10.3389/fspas.2023.1292500

Luo, B., Brandt, W. N., Xue, Y. Q., Lehmer, B., Alexander, D. M., Bauer, F. E., et al. (2017). The Chandra deep field-south survey: 7 Ms source catalogs. *ApJS* 228, 2. doi:10.3847/1538-4365/228/1/2

Madsen, K. K., García, J. A., Stern, D., Amini, R., Basso, S., Coutinho, D., et al. (2024). The high energy X-ray probe (HEX-P): instrument and mission profile. *Front. Astronomy Space Sci.* 11, 1357834. doi:10.3389/fspas.2024.1357834

Marchesi, S., Zhao, X., Torres-Albà, N., Ajello, M., Gaspari, M., Pizzetti, A., et al. (2022). Compton-thick AGN in the NuSTAR era. VIII. A joint NuSTAR-XMM-Newton monitoring of the changing-look compton-thick AGN NGC 1358. *ApJ* 935, 114. doi:10.3847/1538-4357/ac80be

Marcotulli, L., Ajello, M., Böttcher, M., Coppi, P., Costamante, L., Di Gesu, L., et al. (2023). The High Energy X-ray Probe (HEX-P): the most powerful jets through the lens of a superb X-ray eye. doi:10.48550/arXiv.2311.04801

Margutti, R., and Chornock, R. (2021). First multimessenger observations of a neutron star merger. *ARA&* 59, 155–202. doi:10.1146/annurev-astro-112420-030742

Margutti, R., Metzger, B. D., Chornock, R., Vurm, I., Roth, N., Grefenstette, B. W., et al. (2019). An embedded X-ray source shines through the aspherical at 2018cow: revealing the inner workings of the most luminous fast-evolving optical transients. *ApJ* 872, 18. doi:10.3847/1538-4357/aafa01

Meidinger, N., Albrecht, S., Beitler, C., Bonholzer, M., Emberger, V., Frank, J., et al. (2020). "Development status of the wide field imager instrument for Athena," in *Society of photo-optical instrumentation engineers (SPIE) conference series. Vol. 11444*. doi:10.1117/12.2560507114440T

Miller, M. C., Lamb, F. K., Dittmann, A. J., Bogdanov, S., Arzoumanian, Z., Gendreau, K. C., et al. (2019). PSR J0030+0451 mass and radius from NICER data and implications for the properties of neutron star matter. *ApJL* 887, L24. doi:10.3847/2041-8213/ab50c5

Moe, M., Kratter, K. M., and Badenes, C. (2019). The close binary fraction of solar-type stars is strongly anticorrelated with metallicity. *ApJ* 875, 61. doi:10.3847/1538-4357/ab0d88

Mori, K., An, H., Burgess, D., Capasso, M., Dingus, B., Gelfand, J., et al. (2022). "NuSTAR broad-band X-ray observational campaign of energetic pulsar wind nebulae in synergy with VERITAS, HAWC and Fermi gamma-ray telescopes," in 37th International Cosmic Ray Conference, 963. doi:10.22323/1.395.0963963

Mori, K., Hailey, C. J., Schutt, T. Y. E., Mandel, S., Heuer, K., Grindlay, J. E., et al. (2021). The X-ray binary population in the galactic center revealed through multi-decade observations. *ApJ* 921, 148. doi:10.3847/1538-4357/ac1da5

Mori, K., Ponti, G., Bachetti, M., Bodaghee, A., Grindlay, J., Hong, J., et al. (2024). The high energy X-ray probe (HEX-P): resolving the nature of Sgr A* flares, compact object binaries and diffuse X-ray emission in the Galactic center and beyond. *Front. Astronomy Space Sci.* 10, 1292130. doi:10.3389/fspas.2023.1292130

Mori, K., Reynolds, S., An, H., Bamba, A., Krivonos, R., Tsuji, N., et al. (2023). The high energy X-ray probe (HEX-P): galactic PeVatrons, star clusters, superbubbles, microquasar jets, and gamma-ray binaries. *Front. Astronomy Space Sci.* 10, 1303197. doi:10.3389/fspas.2023.1303197

Mosquera, A. M., Kochanek, C. S., Chen, B., Dai, X., Blackburne, J. A., and Chartas, G. (2013). The structure of the X-ray and optical emitting regions of the lensed quasar Q 2237+0305. *ApJ* 769, 53. doi:10.1088/0004-637X/769/1/53

Murase, K., Toomey, M. W., Fang, K., Oikonomou, F., Kimura, S. S., Hotokezaka, K., et al. (2018). Double neutron star mergers and short gamma-ray bursts: long-lasting high-energy signatures and remnant dichotomy. *ApJ* 854, 60. doi:10.3847/1538-4357/aaa48a

Nandra, K., Barret, D., Barcons, X., Fabian, A., den Herder, J.-W., Luigi, P., et al. (2013). The hot and energetic universe: a white paper presenting the science theme motivating the Athena+ mission. doi:10.48550/arXiv.1306.2307

National Academies of Sciences, E. and Medicine (2023). *Pathways to discovery in astronomy and astrophysics for the 2020s*. Washington, DC: The National Academies Press. doi:10.17226/26141

Novikov, I. D., and Thorne, K. S. (1973). "Astrophysics of black holes," in *Black holes (les astres occlus)*, 343–450.

Oppenheimer, J. R., and Volkoff, G. M. (1939). On massive neutron cores. *Phys. Rev.* 55, 374–381. doi:10.1103/PhysRev.55.374

Parker, M. L., Matzeu, G. A., Matthews, J. H., Middleton, M. J., Dauser, T., Jiang, J., et al. (2022). The X-ray disc/wind degeneracy in AGN. *MNRAS* 513, 551–572. doi:10.1093/mnras/stac877

Perez, K., Hailey, C. J., Bauer, F. E., Krivonos, R. A., Mori, K., Baganoff, F. K., et al. (2015). Extended hard-X-ray emission in the inner few parsecs of the Galaxy. *Nature* 520, 646–649. doi:10.1038/nature14353

Perley, D. A., Mazzali, P. A., Yan, L., Cenko, S. B., Gezari, S., Taggart, K., et al. (2019). The fast, luminous ultraviolet transient AT2018cow: extreme supernova, or disruption of a star by an intermediate-mass black hole? *MNRAS* 484, 1031–1049. doi:10.1093/mnras/sty3420

Peterson, B. M. (2014). Measuring the masses of supermassive black holes. *Space Sci. Rev.* 183, 253–275. doi:10.1007/s11214-013-9987-4

Pfeifle, R. W., Boorman, P. G., Weaver, K. A., Buchner, J., Civano, F., Madsen, K., et al. (2023). The high energy X-ray probe (HEX-P): the future of hard X-ray dual AGN science. doi:10.48550/arXiv.2311.05154

Pinto, C., Middleton, M. J., and Fabian, A. C. (2016). Resolved atomic lines reveal outflows in two ultraluminous X-ray sources. *Nature* 533, 64–67. doi:10.1038/nature17417

Piotrowska, J. M., García, J. A., Walton, D. J., Beckmann, R. S., Stern, D., Ballantyne, D. R., et al. (2023). The high energy X-ray probe (HEX-P): constraining supermassive black hole growth with population spin measurements. doi:10.48550/arXiv.2311.04752

Pooley, D., Blackburne, J. A., Rappaport, S., and Schechter, P. L. (2007). X-ray and optical flux ratio anomalies in quadruply lensed quasars. I. Zooming in on quasar emission regions. *ApJ* 661, 19–29. doi:10.1086/512115

Raaijmakers, G., Greif, S. K., Hebeler, K., Hinderer, T., Nissanke, S., Schwenk, A., et al. (2021). Constraints on the dense matter equation of state and neutron star properties from NICER's mass-radius estimate of PSR J0740+6620 and multimessenger observations. *ApJL* 918, L29. doi:10.3847/2041-8213/ac089a

Remillard, R. A., and McClintock, J. E. (2006). X-ray properties of black-hole binaries. *ARA&* 44, 49–92. doi:10.1146/annurev.astro.44.051905.092532

Reynolds, C. (2021). "Observational constraints on black hole spin," in 43rd COSPAR Scientific Assembly, 28 January - 4 February, 1412.43

Reynolds, S., An, H., Abdelmaguid, M., Alford, J., Fryer, C., Mori, K., et al. (2023). The High Energy X-ray Probe (HEX-P): supernova remnants, pulsar wind nebulae, and nuclear astrophysics. *Front. Astronomy Space Sci.* 10, 1321278. doi:10.3389/fspas.2023.1321278

Reynolds, S. P. (2016). Hard X-ray emission from pulsar-wind nebulae. *J. Plasma Phys.* 82, 635820501. doi:10.1017/S0022377816000751

Ricci, C., Ueda, Y., Koss, M. J., Trakhtenbrot, B., Bauer, F. E., and Gandhi, P. (2015). Compton-thick accretion in the local universe. *ApJL* 815, L13. doi:10.1088/2041-8205/815/1/L13

Secunda, A., Cen, R., Kimm, T., Götberg, Y., and de Mink, S. E. (2020). Delayed photons from binary evolution help reionize the universe. *ApJ* 901, 72. doi:10.3847/1538-4357/abaefa

Sesana, A., Barausse, E., Dotti, M., and Rossi, E. M. (2014). Linking the spin evolution of massive black holes to galaxy kinematics. *ApJ* 794, 104. doi:10.1088/0004-637X/794/2/104

Staubert, R., Trümper, J., Kendziorra, E., Klochkov, D., Postnov, K., Kretschmar, P., et al. (2019). Cyclotron lines in highly magnetized neutron stars. *A&* 622, A61. doi:10.1051/0004-6361/201834479

Sun, L., Ruiz, M., Shapiro, S. L., and Tsokaros, A. (2022). Jet launching from binary neutron star mergers: incorporating neutrino transport and magnetic fields. *Phys. Rev. D.* 105, 104028. doi:10.1103/PhysRevD.105.104028

Tanaka, Y., and Lewin, W. H. G. (1995). "Black hole binaries," in *X-Ray binaries*, 126–174.

Thorne, K. S. (1974). Disk-accretion onto a black hole. II. Evolution of the hole. *ApJ* 191, 507–520. doi:10.1086/152991

Titarchuk, L., and Lyubarskij, Y. (1995). Power-law spectra as a result of comptonization of the soft radiation in a plasma cloud. *ApJ* 450, 876. doi:10.1086/176191

Tolman, R. C. (1939). Static solutions of einstein's field equations for spheres of fluid. *Phys. Rev.* 55, 364–373. doi:10.1103/PhysRev.55.364

Tombesi, F., Cappi, M., Reeves, J. N., Palumbo, G. G. C., Braito, V., and Dadina, M. (2011). Evidence for ultra-fast outflows in radio-quiet active galactic nuclei. II. Detailed photoionization modeling of Fe K-shell absorption lines. *ApJ* 742, 44. doi:10.1088/0004-637X/742/1/44

Tombesi, F., Cappi, M., Reeves, J. N., Palumbo, G. G. C., Yaqoob, T., Braito, V., et al. (2010). Evidence for ultra-fast outflows in radio-quiet AGNs: I. Detection and statistical incidence of Fe K-shell absorption lines. *A&* 521, A57. doi:10.1051/0004-6361/200913440

Tomsick, J. A., Boggs, S. E., Zoglauer, A., Hartmann, D., Ajello, M., Burns, E., et al. (2023). The Compton spectrometer and imager. doi:10.48550/arXiv.2308.12362

Torres-Albà, N., Marchesi, S., Zhao, X., Ajello, M., Silver, R., Ananna, T. T., et al. (2021). Compton-thick AGN in the NuSTAR era VI: the observed compton-thick fraction in the local universe. *ApJ* 922, 252. doi:10.3847/1538-4357/ac1c73

Torres-Albà, N., Marchesi, S., Zhao, X., Cox, I., Pizzetti, A., Sengupta, D., et al. (2023). Hydrogen column density variability in a sample of local Compton-thin AGN. *A&* 678, A154. doi:10.1051/0004-6361/202345947

Ueda, Y., Akiyama, M., Hasinger, G., Miyaji, T., and Watson, M. G. (2014). Toward the standard population synthesis model of the X-ray background: evolution of X-ray luminosity and absorption functions of active galactic nuclei including compton-thick populations. *ApJ* 786, 104. doi:10.1088/0004-637X/786/2/104

Uttley, P., Cackett, E. M., Fabian, A. C., Kara, E., and Wilkins, D. R. (2014). X-ray reverberation around accreting black holes. *A& Rev.* 22, 72. doi:10.1007/s00159-014-0072-0

Vasudevan, R. V., Fabian, A. C., Reynolds, C. S., Aird, J., Dauser, T., and Gallo, L. C. (2016). A selection effect boosting the contribution from rapidly spinning black holes to the cosmic X-ray background. *MNRAS* 458, 2012–2023. doi:10.1093/mnras/stw363

Weisskopf, M. C., Soffitta, P., Baldini, L., Ramsey, B. D., O'Dell, S. L., Romani, R. W., et al. (2022). Imaging X-ray polarimetry explorer: prelaunch. *J. Astronomical Telesc. Instrum. Syst.* 8, 026002. doi:10.1117/1.JATIS.8.2.026002

Wik, D. R., Lehmer, B. D., Hornschemeier, A. E., Yukita, M., Ptak, A., Zezas, A., et al. (2014). Spatially resolving a starburst galaxy at hard X-ray energies: NuSTAR, Chandra, and VLBA observations of NGC 253. *ApJ* 797, 79. doi:10.1088/0004-637X/797/2/79

Zhao, X., Civano, F., Fornasini, F. M., Alexander, D. M., Cappelluti, N., Chen, C. T., et al. (2021). The NuSTAR extragalactic survey of the james webb space telescope north ecliptic Pole time-domain field. *MNRAS* 508, 5176–5195. doi:10.1093/mnras/stab2885

Zhao, X., Civano, F., Willmer, C. N. A., Bonoli, S., Chen, C.-T., Creech, S., et al. (2024). PEARLS: NuSTAR and XMM-Newton extragalactic survey of the JWST north ecliptic Pole time-domain field II. *arXiv e-prints* 965, 188. doi:10.3847/1538-4357/ad2b61

Copyright © 2024 García, Stern, Madsen, Smith, Grefenstette, Ajello, Alford, Annuar, Bachetti, Baloković, Beckmann, Bianchi, Biccari, Boorman, Brightman, Buchner, Bulbul, Chen, Civano, Coley, Connors, Del Santo, Gesu, Draghis, Fragile, Gúrpide, Gangi, Gezari, Harrison, Kammoun, Lanzuisi, Lehmer, Lohfink, Ludlam, Marchesi, Marcotulli, Margutti, Masterson, Merloni, Middleton, Mori, Moretti, Nandra, Perez, Pfeifle, Pinto, Piotrowska, Ponti, Pottschmidt, Predehl, Puccetti, Rau, Reynolds, Santangelo, Spiga, Tomsick, Torres-Albà, Walton, Wilkins, Wilms, Zhang and Zhao. This is an open-access article distributed under the terms of the Creative Commons Attribution License (CC BY). The use, distribution or reproduction in other forums is permitted, provided the original author(s) and the copyright owner(s) are credited and that the original publication in this journal is cited, in accordance with accepted academic practice. No use, distribution or reproduction is permitted which does not comply with these terms.

Frontiers in
Astronomy and Space Sciences

Explores planetary science and extragalactic astronomy in all wavelengths

Advances the understanding of our universe - from planetary science to extragalactic astronomy, to high-energy and astroparticle physics.

Discover the latest Research Topics

See more →

Frontiers

Avenue du Tribunal-Fédéral 34
1005 Lausanne, Switzerland
frontiersin.org

Contact us

+41 (0)21 510 17 00
frontiersin.org/about/contact